



T. Pradeep
Publications 2015

Contents

- ❖ **Publications**
- ❖ **Lectures Delivered**
- ❖ **Patents/Technology/New Grants**
- ❖ **Media Reports**

Journal Papers Published in 2015

1. Inter-cluster reactions between Au₂₅(SR)₁₈ and Ag₄₄(SR)₃₀, K. R. Krishnadas, Atanu Ghosh, Ananya Baksi, Indranath Chakraborty, Ganapati Natarajan and T. Pradeep, *J. Am. Chem. Soc.*, (2015) (DOI: 10.1021/jacs.5b09401)
2. Carbon aerogels through organo-inorganic co-assembly and their application in water desalination by capacitive deionization, Rudra Kumar, Soujit Sen Gupta, Shishir Katiyar, V. Kalyan Raman, Siva Kumar Varigala, T. Pradeep and Ashutosh Sharma, *Carbon*, *Carbon*, 99 (2016) 375-383 (DOI: 10.1016/j.carbon.2015.12.004).
3. Metallic nanobrushes made using ambient droplet sprays, Depanjan Sarkar, M. K. Mahitha, Anirban Som, Anyin Li, Michael Wleklinski, R. G. Cooks and T. Pradeep, *Adv. Mater.*, (2015) (DOI: 10.1002/adma.201505127) (In Press).
4. Defining switching efficiency of multi-level resistive memory with PdO as example, K. D. M. Rao, Abhay A. Sagade, Robin John, T. Pradeep and G. U. Kulkarni, *Adv. Electron. Mater.*, (2015) (DOI: 10.1002/aelm.201500286) (In Press).
5. A profile of heavy metals in rice (*Oryza sativa* ssp. *indica*) landraces, Debal Deb, Soujit Sen Gupta and T. Pradeep, *Curr. Sci.*, 109 (2015) 407-409.
6. A low cost approach to synthesize sand like AlOOH nanoarchitecture (SANA) and its application in defluoridation of water, Gaurab Saha, Shihabudheen M. Maliyekkal, P.C. Sabumon and T. Pradeep, *J. Environ. Chem. Eng.* 3 (2015) 1303-1311 (DOI: 10.1016/j.jece.2014.11.030).
7. A unified framework for understanding the structure and modifications of atomically precise monolayer protected gold clusters, Ganapati Natarajan, Ammu Mathew, Yuichi Negishi, Robert L. Whetten and T. Pradeep, *J. Phys. Chem. C*, 119 (2015) 27768–27785 (DOI: 10.1021/acs.jpcc.5b08193).
8. Anisotropic molecular ionization at 1 V from tellurium nanowires (Te NWs), Rahul Narayanan, Depanjan Sarkar, Anirban Som, Michael Wleklinski, R. G. Cooks and T. Pradeep, *Anal. Chem.*, 87 (2015) 10792-10798 (DOI: 10.1021/acs.analchem.5b01596).
9. Cellulose derived graphenic fibers for capacitive desalination of brackish water, Nalenthiran Pugazhenthiran, Soujit Sen Gupta, Anupama Prabhath, Muthu Manikandan, Jakka Ravindran Swathy, V. Kalyan Raman and T. Pradeep, *ACS Appl. Mater. Interfaces*, 7 (2015) 20156-20163 (DOI: 10.1021/acsami.5b05510).
10. Efficient red luminescence from organic-soluble Au₂₅ clusters by ligand structure modification, Ammu Mathew, Elizabeth Varghese, Susobhan Choudhury, Samir Kumar Pal and T. Pradeep, *Nanoscale*, 7 (2015) 14305-14315 (DOI: 10.1039/C5NR03457D).

11. Ambient preparation and reactions of gas phase silver cluster cations and anions, Michael Wleklinski, Depanjan Sarkar, Adam Hollerbach, T. Pradeep, and R. G. Cooks, *Phys. Chem. Chem. Phys.*, 17 (2015) 18364-18373 (DOI: 10.1039/C5CP01538C).
12. Zero volt paper spray ionization and its mechanism, Michael Wleklinski, Yafeng Li, Soumabha Bag, Depanjan Sarkar, Rahul Narayanan, T. Pradeep and R. G. Cooks, *Anal. Chem.*, 87 (2015) 6786-6793 (DOI: 10.1021/acs.analchem.5b01225).
13. Rapid detection of Fusarium wilt in Basil (*Ocimum sp.*) leaves by desorption electrospray ionization mass spectrometry (DESI MS) imaging, R. G. Hemalatha, Hemanta R. Naik, Vasundhara Mariappa and T. Pradeep, *RSC Adv.*, 5 (2015) 50512–50522 (DOI: 10.1039/c4ra16706f).
14. Rapid synthesis of C-TiO₂: Tuning the shape from spherical to rice grain morphology for visible light photocatalytic application, Balaji Sambandam, Anupama Surejan, Ligy Philip and T. Pradeep, *ACS Sustain. Chem. Eng.*, 3 (2015) 1321-1329 (DOI: 10.1021/acssuschemeng.5b00044).
15. Noble metal clusters protected with mixed proteins exhibit intense photoluminescence, Jyoti Sarita Mohanty, Ananya Baksi, Haiwon Lee and T. Pradeep, *RSC Adv.*, 5 (2015) 48039-48045 (DOI:10.1039/c5ra06964e).
16. Simultaneous dehalogenation and removal of persistent halocarbon pesticides from water using graphene nanocomposites: A case study of lindane, Soujit Sen Gupta, Indranath Chakraborty, Shihabudheen M. Maliyekkal, Tuhina A. Maark, Dheeraj K. Pandey, Sarit K. Das and T. Pradeep, *ACS Sustain. Chem. Eng.*, 3 (2015) 1155-1163 (DOI: 10.1021/acssuschemeng.5b00080).
17. Interaction of acetonitrile with water-ice: An infrared spectroscopic study, Radha Gobinda Bhui, Rabin Rajan J. Methikkalam, Bhalamurugan Sivaraman and T. Pradeep, *J. Phys. Chem. C*, 119 (2015) 11524-11532 (DOI: 10.1021/jp512607v).
18. Ambient solid-state mechano-chemical reactions between functionalized carbon nanotubes, Mohamad A. Kabbani, Chandra Sekhar Tiwary, Pedro A. S. Autreto, Gustavo Brunetto, Anirban Som, K. R. Krishnadas, Sehmus Ozden, Ken Hackenberg, Yongji Gong, Douglas S. Galvao, Robert Vajtai, Ahmad T. Kabbani, T. Pradeep and Pulickel M. Ajayan, *Nature Commun.*, 6 (2015) 7291 (DOI: 10.1038/ncomms8231).
19. Initial growth kinetics of luminescent quantum clusters of silver within albumin family protein templates, Kamallesh Chaudhari and T. Pradeep, *J. Phys. Chem. C.*, 119 (2015) 9988-9994 (DOI: 10.1021/acs.jpcc.5b00496).
20. Translocation of uranium from water to foodstuff while cooking, Krishnapriya K. C., Ananya Baksi, Swathi Chaudhari, Soujit Sen Gupta and T. Pradeep, *J. Haz. Mater.*, 297 (2015) 183-190 (DOI: 10.1016/j.jhazmat.2015.04.041).

21. In vitro co-localization of plasmonic nano-bio labels and biomolecules using plasmonic and Raman scattering microspectroscopy, Kamallesh Chaudhari and T. Pradeep, *J. Biomed. Opt.*, 20 (2015) 046011 (DOI: 10.1117/1.JBO.20.4.046011).

22. Ambient ionization mass spectrometry imaging of rohitukine, a chromone anti-cancer alkaloid, during seed development in *Dysoxylum binectariferum* Hook. F (Meliaceae), Mohana Kumara P, Amitava Srimany, Ravikanth G, Uma Shaanker R and T. Pradeep, *Phytochemistry*, 116 (2015) 104-110 (DOI: 10.1016/j.phytochem.2015.02.031).

23. Size evolution of protein protected gold clusters in solution: A combined SAXS-MS investigation, Ananya Baksi, Anuradha Mitra, Jyoti Sarita Mohanty, Haiwon Lee, Goutam De and T. Pradeep, *J. Phys. Chem. C.*, 119 (2015) 2148-2157 (DOI:10.1021/jp509332j).

* Some of these may appear in 2016

** "Papers with T. Pradeep as the/a corresponding author are reproduced in the following pages."

Editorial

1. Advancing the Use of Sustainability Metrics, D. T. Allen, B. J. Hwang, P. Licence, T. Pradeep and B. Subramaniam, *ACS Sustainable Chem. Eng.*, 3 (2015) 2359–2360 (DOI: 10.1021/acssuschemeng.5b01026).

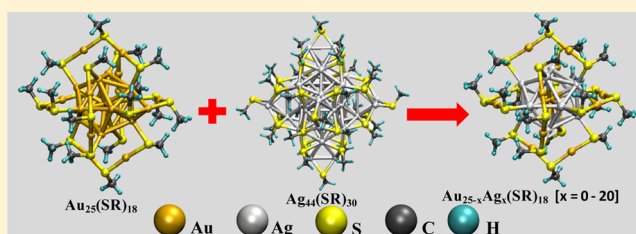
Intercluster Reactions between $\text{Au}_{25}(\text{SR})_{18}$ and $\text{Ag}_{44}(\text{SR})_{30}$

K. R. Krishnadas, Atanu Ghosh, Ananya Baksi, Indranath Chakraborty,[†] Ganapati Natarajan, and Thalappil Pradeep*

DST Unit of Nanoscience (DST UNS) and Thematic Unit of Excellence, Department of Chemistry, Indian Institute of Technology Madras, Chennai, 600 036, India

Supporting Information

ABSTRACT: We present the first example of intercluster reactions between atomically precise, monolayer protected noble metal clusters using $\text{Au}_{25}(\text{SR})_{18}$ and $\text{Ag}_{44}(\text{SR})_{30}$ (RS = alkyl/aryl thiolate) as model compounds. These clusters undergo spontaneous reaction in solution at ambient conditions. Mass spectrometric measurements both by electrospray ionization and matrix assisted laser desorption ionization show that the reaction occurs through the exchange of metal atoms and protecting ligands of the clusters. Intercluster alloying is demonstrated to be a much more facile method for heteroatom doping into $\text{Au}_{25}(\text{SR})_{18}$, as observed by doping up to 20 Ag atoms. We investigated the thermodynamic feasibility of the reaction using DFT calculations and a tentative mechanism has been presented. Metal core-thiolate interfaces in these clusters play a crucial role in inducing these reactions and also affect rates of these reactions. We hope that our work will help accelerate activities in this area to establish chemistry of monolayer protected clusters.



INTRODUCTION

Intercluster reactions between metal clusters are rare, and their chemistry is mostly explored through reactions with small molecules.¹ Monolayer protection² with suitable ligands facilitated the synthesis of highly stable, atomically precise metal clusters in sufficient quantities. This opened up a way to develop an in-depth understanding of their chemistry, conveniently in the solution phase. Reactions of these clusters in solutions are expected to complement the results obtained from gas phase experiments, providing further insights into their properties. Moreover, cluster chemistry in solution has practical applications.^{3,4} Among the ligand-protected metal clusters, thiolate-protected noble metal clusters ($\text{Au}_{25}(\text{SR})_{18}$, for example) have been recognized as a distinct category in view of their unique properties.⁵ The earliest of the chemistry of these clusters has been ligand exchange,⁶ leading to an understanding of the localization of electronic transitions to the Au_nS_m moiety and demonstration of fluorescence resonance energy transfer (FRET).⁶ⁱ Though there have been a few attempts dealing with the reactions of these clusters with halocarbons,⁷ metal ions,^{8,9} metal-thiolates,^{10a} salts^{10b} and one-dimensional nanostructures,¹¹ there has been no example of intercluster chemistry.

EXPERIMENTAL SECTION

Materials. Chloroauric acid trihydrate ($\text{HAuCl}_4 \cdot 3\text{H}_2\text{O}$) was purchased from Sigma-Aldrich. Silver nitrate (AgNO_3) was purchased from RANKEM India. 2-phenylethanethiol (PET), *n*-butanethiol (*n*-BuSH), 4-fluorothiophenol (FTP), 4-mercaptobenzoic acid (MBA), tetraoctylammonium bromide (TOAB), tetraphenylphosphonium bromide (PPh_4Br), sodium borohydride (NaBH_4) were purchased

from Sigma-Aldrich. All the solvents used (tetrahydrofuran (THF), methanol, hexane, dichloromethane (DCM) and dimethylformamide (DMF)) were of analytical grade.

Synthesis of Clusters. $\text{Au}_{25}(\text{PET})_{18}$ and $\text{Au}_{25}(\text{BuS})_{18}$: 2 mL of 50 mM $\text{HAuCl}_4 \cdot 3\text{H}_2\text{O}$ in THF was diluted to 7.5 mL using THF. About 65 mg of TOAB was added to this solution and stirred at 1500 rpm for 30 min at room temperature. The initial yellow color of the solution turned deep red during stirring. About 0.5 mmol of pure thiol was added at a stretch while stirring at the same speed. The deep red color slowly turned to yellow and eventually became colorless after about 45 min. After stirring further for 2 h, 2.5 mL of ice cold aqueous NaBH_4 (0.2 M) was added in one lot. The solution turned black immediately and stirring was continued for 5 h. The solution was rotary evaporated and precipitated with methanol, washed repeatedly with the same and dried.

$\text{Au}_{25}(\text{FTP})_{18}$. Five mg of $\text{Au}_{25}(\text{n-BuS})_{18}$ was dissolved in 0.5 mL of toluene and 150 times (by weight) of pure 4-fluorothiophenol was added to it. The solution was heated at 50 °C in an oil bath while stirring. After about 25 min, clusters were precipitated with hexane and collected by centrifugation. This precipitate was washed with hexane, dissolved in DCM and centrifuged to remove thiolates. This cluster solution was vacuum-dried and stored at 4 °C.

$[\text{PPh}_4]_4[\text{Ag}_{44}(\text{FTP})_{30}]$. The cluster was synthesized following a solid state route.²¹ 20 mg of AgNO_3 and 12 mg of PPh_4Br were ground thoroughly in an agate mortar and pestle for 5 min. About 76 μL of 4-fluorothiophenol was added to it in one shot and the mixture was ground for about 3 more minutes. Dry NaBH_4 (45 mg) was added and the mixture was ground until the pasty mass became brown in color. This was extracted with 7 mL of dichloromethane and kept undisturbed at room temperature until UV/vis spectra showed all the characteristic features of the cluster. The clusters were purified

Received: September 5, 2015

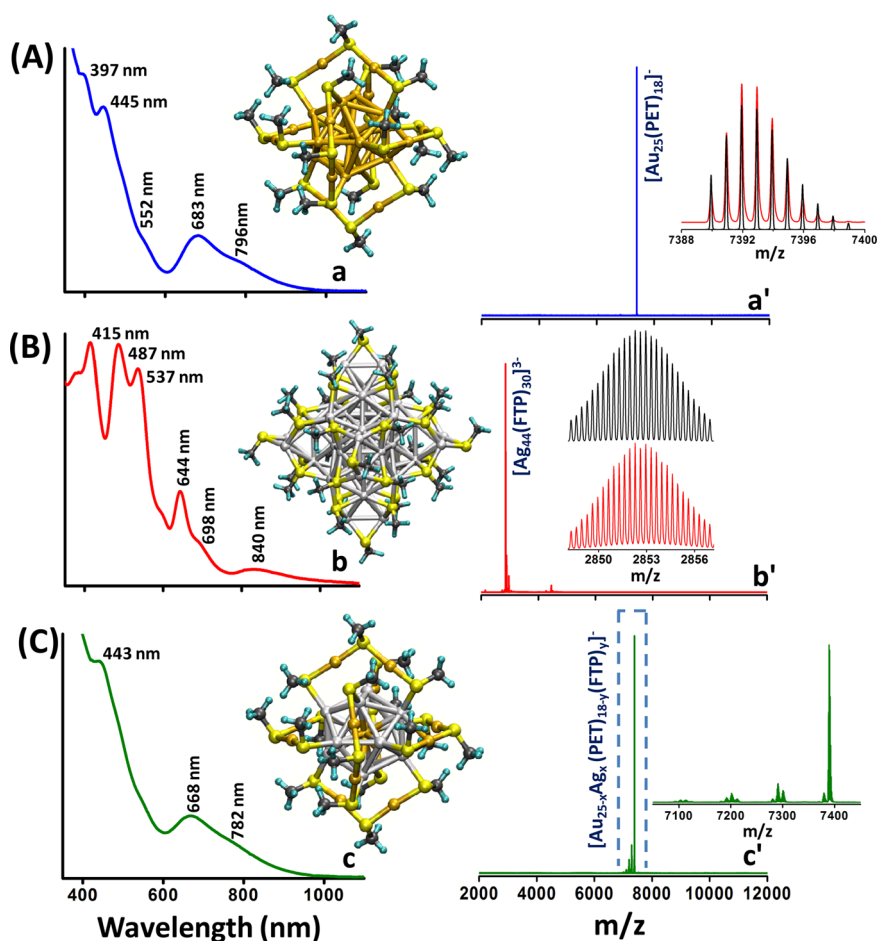


Figure 1. UV/vis absorption and negative ion ESI MS spectra of $\text{Au}_{25}(\text{PET})_{18}$ (A), $\text{Ag}_{44}(\text{FTP})_{30}$ (B) and their 14:1 molar mixture (C) showing changes in the spectral features due to intercluster reaction. In A–C, panels a–c and a'–c' are the UV/vis and ESI MS spectra, respectively. Characteristic peak positions are marked. The corresponding clusters are also shown in between the spectra (modeled assuming the coordinates from the crystal structures). Color codes for the atoms in the inset pictures: Light yellow = sulfur, orange = gold, gray = silver, black = carbon, and cyan = hydrogen. For simplicity, we assumed -SMe ligands, instead of PET and FTP ligands. Inset of a' shows the molecular ion region (m/z 7388–7400) of $\text{Au}_{25}(\text{PET})_{18}$, showing isotope resolution. Inset of b' shows the same for $\text{Ag}_{44}(\text{FTP})_{30}$ in the 3^- charge region (m/z 2848–2857). Theoretical (black) and experimental (red) spectra of ions are compared. The spectra corresponding to the product (marked in open rectangles) is expanded in the inset of c'.

adopting the same protocol used for $\text{Au}_{25}(\text{SR})_{18}$. $\text{Na}_4[\text{Ag}_{44}(\text{MBA})_{30}]$ was synthesized following a reported method^{2e} with slight modifications, as described in [Supporting Information](#).

Intercluster Reactions. Stock solutions of clusters were prepared in dichloromethane, except for $\text{Ag}_{44}(\text{MBA})_{30}$ which was prepared in DMF. Required volumes of each of the stock solutions were added into 1 mL of dichloromethane at room temperature and the mixture was stirred with a pipette. It was not stirred magnetically. The reaction occurred immediately after mixing as observed from the immediate color changes and time-dependent MALDI MS and ESI MS measurements. All reactions were carried out at room temperature ($\sim 30^\circ\text{C}$).

Mass Spectral Measurements. We performed matrix assisted laser desorption ionization (MALDI) and electrospray ionization (ESI) mass spectrometry (MS) measurements. We used Applied Biosystems Voyager DEPro (MALDI) and Waters Synapt G2-Si (ESI and MALDI) mass spectrometers. ESI MS had a maximum resolution of 50 000 in the mass range of interest. More details about the measurements are given in [Supporting Information](#).

Computational Details. We used density functional theory (DFT) as implemented in the real-space grid-based projector augmented wave (GPAW) package.²⁸ Full computational details can be found in the [Supporting Information](#). We calculated the energy difference between the unexchanged cluster and a single Ag atom

exchanged $[\text{Au}_{25}(\text{SR})_{18}]^-$ and a single Au atom exchanged $[\text{Ag}_{44}(\text{SR})_{30}]^{4+}$, for each of the isomers. The three symmetry-unique positions for the Ag atom in $[\text{Au}_{25}(\text{SR})_{18}]^{1-}$ were the central atom (denoted by C), icosahedral vertex atom (I), and the staple gold atom (S). The four symmetry unique positions in $[\text{Ag}_{44}(\text{SR})_{30}]^{4+}$ for the Au atom were the outermost shell in the middle dodecahedron (S), one of the eight cubic vertex positions (D_{cv}) and one of the 12 cube-face capping atoms (D_{cf}), and last, atoms in inner icosahedron (I) (see [Figure S28](#)). We calculated the energy of the overall reaction for the case of a single metal atom exchange in each combination of final substituent positions. We also calculated the energies of the substitution reactions of a single metal atom and single metal–ligand fragment, Ag and Ag-SR into $[\text{Au}_{25}(\text{SR})_{18}]^-$, or, Au and Au-SR into $[\text{Ag}_{44}(\text{SR})_{30}]^{4+}$ for each of the symmetry-unique positions mentioned above. To investigate the feasibility of electron transfer in this system, we compared the relative energies of the HOMO and LUMO states, for both $[\text{Au}_{25}(\text{SR})_{18}]^-$ and $[\text{Ag}_{44}(\text{SR})_{30}]^{4+}$, and their alloys.

RESULTS AND DISCUSSION

(A). Reactions between Clusters Having Different Ligands. Initially we studied the reaction between $\text{Au}_{25}(\text{PET})_{18}$ and $\text{Ag}_{44}(\text{FTP})_{30}$ prepared as described in the [Experimental Section](#). PET and FTP are the ligands protecting

Au_{25} and Ag_{44} clusters, respectively (see the [Experimental Section](#)). Appropriate volumes of their stock solutions were added into a fixed volume of dichloromethane at room temperature ($\sim 30^\circ\text{C}$) (see [Experimental Section](#) for details) to get defined concentrations of the reacting species. UV/visible (UV/vis) absorption features and electrospray ionization mass spectra (ESI MS) of the clusters before and immediately after (within 1 min) mixing are shown in [Figure 1](#). The molecular ion peak of $\text{Au}_{25}(\text{PET})_{18}$ at m/z 7391 is shown in trace a' of [Figure 1A](#) along with the expanded isotopically resolved molecular ion. Typical fragmentation pattern of $\text{Au}_{25}(\text{PET})_{18}$ shown in [Supporting Information](#) ([Figure S1](#)) proves the identity of the cluster. Optical absorption spectrum of $\text{Au}_{25}(\text{PET})_{18}$ shows characteristic peaks^{2c} at 796, 683, 552, 445, and 397 nm (trace a in [Figure 1A](#)). Similarly, $\text{Ag}_{44}(\text{FTP})_{30}$ is characteristic in its optical absorption spectrum^{2e–g} (trace b, [Figure 1B](#)). $[\text{Ag}_{44}(\text{FTP})_{30}]^{3-}$ was the prominent feature in the ESI MS of $\text{Ag}_{44}(\text{SR})_{30}$ (trace b', [Figure 1B](#)). Isotope distributions of the prominent features of these clusters match well with the theoretical patterns as shown in the insets. For example, the spectrum in the m/z 7388–7400 window of $\text{Au}_{25}(\text{PET})_{18}$ (inset of trace a' in [Figure 1A](#)) shows all the isotope features of the molecular ion. Detailed assignment of the spectrum in trace b' of [Figure 1B](#) is given in [Figure S2](#). Absorption features of $\text{Au}_{25}(\text{PET})_{18}$ changed significantly and those due to $\text{Ag}_{44}(\text{FTP})_{30}$ were not observed at all upon mixing the two clusters (trace c in [Figure 1C](#)). Comparing the ESI MS spectra in [Figure 1A–C](#), we notice that a series of peaks at m/z lower than $\text{Au}_{25}(\text{PET})_{18}$ appeared immediately after mixing. (description of these peaks follows later). These changes in the absorption and mass spectral features confirm that the clusters react with each other spontaneously in solution. Time-dependent changes during the reaction at various $\text{Au}_{25}(\text{PET})_{18}:\text{Ag}_{44}(\text{FTP})_{30}$ ratios ([Figures S3–S5](#)) show that a series of peaks at lower m/z than $\text{Au}_{25}(\text{PET})_{18}$ (labeled as group I) and a broad feature at m/z higher than $\text{Ag}_{44}(\text{FTP})_{30}$ (labeled as group II) appeared immediately after mixing the clusters. While a larger distribution of product peaks appeared in group I just after mixing, only 3–4 prominent peaks were observed after 10–15 min. The mass spectra after 1 h were similar to the spectra after 10–15 min, indicating that the reaction got equilibrated/completed in this time scale.

Reaction was studied at various $\text{Au}_{25}(\text{PET})_{18}:\text{Ag}_{44}(\text{FTP})_{30}$ ratios. MALDI MS spectra of these reaction mixtures after 1 h of the reaction are shown in [Figure 2](#). As the concentration of $\text{Ag}_{44}(\text{FTP})_{30}$ was increased, the centroid of group I shifted continually toward lower m/z values. Simultaneously, intensity of group II increased. Peaks in group I of [Figure 2](#) are expanded in the insets. Mass difference between these peaks is either 89 Da or 99 Da. The difference of 89 Da is due to the loss of an Au atom (197 Da) from $\text{Au}_{25}(\text{PET})_{18}$ and a simultaneous inclusion of an Ag (108 Da) atom into it from $\text{Ag}_{44}(\text{FTP})_{30}$. Mass difference of 99 Da is attributed to the loss of an Au-PET moiety (334 Da) and the inclusion of an Ag-FTP moiety (235 Da). Apart from these processes, there is a possibility for the exchange of ligands alone, i.e., FTP-PET exchanges. Because of the broadness of the MALDI MS peaks and small mass difference between FTP and PET ligands (10 Da), unambiguous confirmation of such exchange processes is not possible with MALDI MS measurements alone. Therefore, ESI MS measurements were carried out to reveal the details of the peaks in group I. Group II peaks will be discussed later in the text.

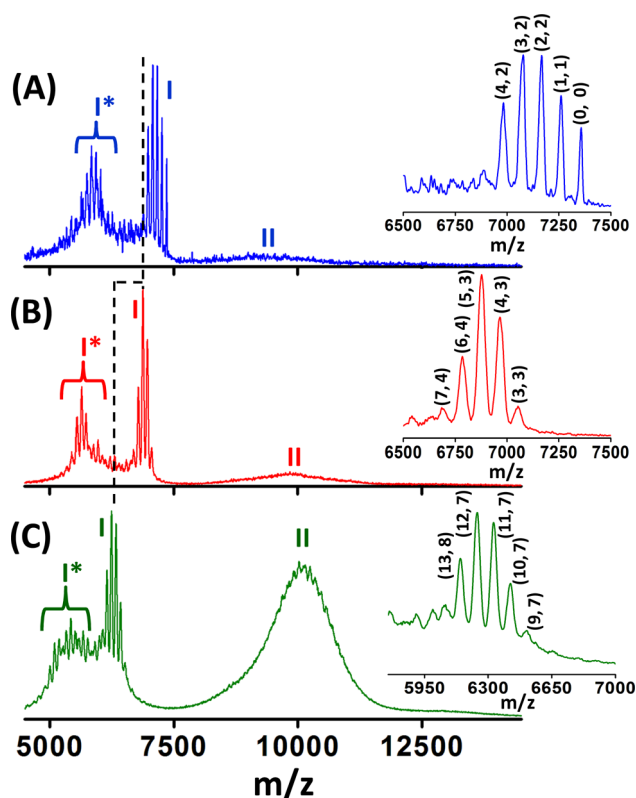


Figure 2. Negative ion mode MALDI MS spectra of the reaction mixtures for the $\text{Au}_{25}(\text{PET})_{18}:\text{Ag}_{44}(\text{FTP})_{30}$ ratio of (A) 14.0:1.0 (B) 7.0:1.0 and (C) 1.7:1.0. Each inset shows the expansion of the collection of peaks labeled I. The numbers (x, y) in parentheses (in the insets), correspond to the general molecular formula, $\text{Au}_{25-x}\text{Ag}_x(\text{PET})_{18-y}(\text{FTP})_y$. Shifts in the centroids of group I with increase in concentration of $\text{Ag}_{44}(\text{FTP})_{30}$ are marked with dotted lines.

ESI MS of the reaction mixtures at various $\text{Au}_{25}(\text{PET})_{18}:\text{Ag}_{44}(\text{FTP})_{30}$ ratios are shown in [Figure 3](#). Reaction products in the $\text{Au}_{25}(\text{PET})_{18}$ region alone are shown here. Two features from each panel (marked in open rectangles) are expanded in the corresponding insets. Expanded features of the panels A–C are given in [Figures S6–S9](#). These data reveal that each feature in these panels is a bunch of peaks separated by m/z 10. For example, the feature (2, 0–4) in [Figure 3A](#) is a collection of (2, 0), (2, 1), (2, 2), (2, 3) and (2, 4) peaks. The first number in parentheses of peak labels gives the number of Ag atoms exchanged. The second number gives the number of FTP ligands exchanged. MALDI MS measurements ([Figure 2](#)) indicated the presence of features separated by either m/z 89 or 99 and ESI MS measurements confirmed these features. For example, the peaks (1, 0), (2, 0), (3, 0), etc. and (1, 2), (2, 2), (3, 2), etc., are separated by m/z 89 Da (see [Figure S10](#)). Peaks such as (1, 1), (2, 2), (3, 3), etc. are separated by m/z 99. Mass difference of 89 Da is due to the Ag–Au exchange and the mass difference of 99 Da is due to the (Au-PET)-(Ag-FTP) exchange, as mentioned earlier. Theoretical and experimental isotope patterns of peaks in the (2, 0–4) feature are shown in [Figure S11](#) which further confirms the inclusion of the FTP ligand into $\text{Au}_{25}(\text{PET})_{18}$. Thus, ESI MS measurements unambiguously confirm that the group I peaks observed in MALDI MS are due to the Ag–Au and (Ag-FTP)-(Au-PET) exchanges between $\text{Au}_{25}(\text{PET})_{18}$ and $\text{Ag}_{44}(\text{FTP})_{30}$. From [Figure 3](#), we see that FTP-PET exchange is also occurring in $\text{Au}_{25}(\text{PET})_{18}$ (see the feature (0, 0–3) in [Figure 3A](#) and

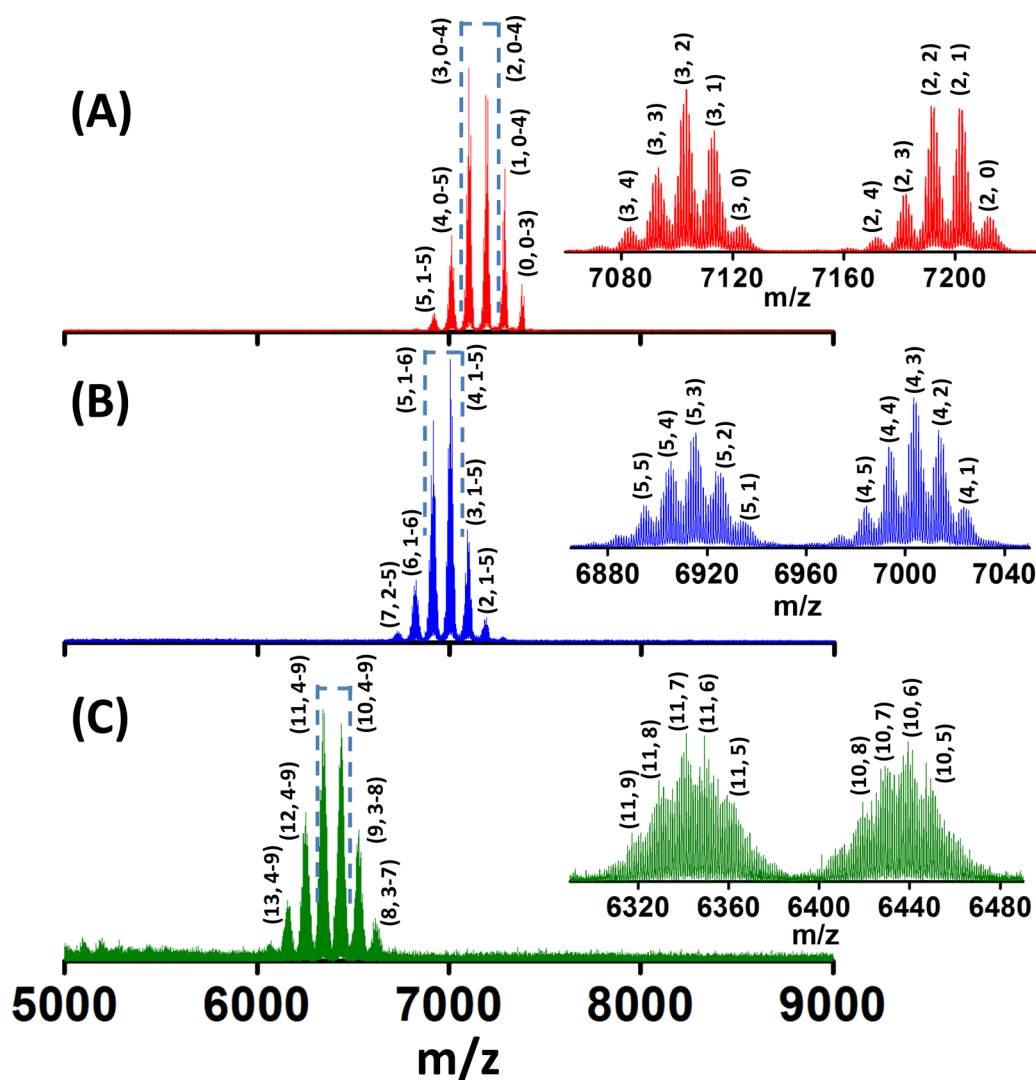


Figure 3. Negative ion mode ESI MS spectra of the reaction mixtures for the $\text{Au}_{25}(\text{PET})_{18}:\text{Ag}_{44}(\text{FTP})_{30}$ ratio of (A) 14.0:1.0 (B) 7.0:1.0 and (C) 1.7:1.0. Each inset shows the expansion of features marked in open rectangles. The numbers (x, y) are according to the general molecular formula, $\text{Au}_{25-x}\text{Ag}_x(\text{PET})_{18-y}(\text{FTP})_y$. Each peak (x, y) has its own isotope pattern and overlap of these features complicate the spectrum.

Figure S10), in addition to Ag–Au and (Ag–FTP)–(Au–PET) exchanges. This aspect will be discussed later. However, the total number of metal atoms and ligands were unchanged in the product clusters in group I. Hence, the series of peaks in group I have been assigned the general formula, $\text{Au}_{25-x}\text{Ag}_x(\text{PET})_{18-y}(\text{FTP})_y$. The larger the concentration of $\text{Ag}_{44}(\text{FTP})_{30}$, the more Ag and FTP ligands are incorporated into $\text{Au}_{25}(\text{PET})_{18}$. Inclusion of up to 1–5, 2–7 and 8–13 Ag atoms were observed for $\text{Au}_{25}(\text{PET})_{18}:\text{Ag}_{44}(\text{FTP})_{30}$ ratios of 14.0:1.0, 7.0:1.0 and 1.7:1.0, respectively. Insets of Figure 3 show that as the number of incorporated Ag atoms increases, peaks within a bunch become less resolved because of the isotope distribution of Ag. While distinct mass separations (of m/z 10) due to pure ligand exchange are seen in the reactions of clusters with differing ligands, these cannot be observed for clusters of the same ligands. We will revisit this aspect later in the text. Temporal changes in the absorption and luminescence spectra during reactions at various $\text{Au}_{25}(\text{PET})_{18}:\text{Ag}_{44}(\text{FTP})_{30}$ ratios are presented in Figures S12–S14. These results confirm the formation of $\text{Au}_{25-x}\text{Ag}_x(\text{PET})_{18-y}(\text{FTP})_y$ bimetallic clusters with mixed ligands.

The maximum numbers of Ag incorporations observed so far in the case of mixed ligand- and all thiolate-protected Au_{25} clusters^{12–14} are 13 and 11, respectively. In contrast to these reports, we observed Ag doping of up to 13–16 and 16–20 atoms into $\text{Au}_{25}(\text{SR})_{18}$ at higher concentrations of $\text{Ag}_{44}(\text{FTP})_{30}$ (see Figures S15 and S16). Absorption spectra of these reaction mixtures are displayed in Figures S17 and S18, respectively. Thus, our experiments demonstrate for the first time that replacement of more than 13 Au atoms with Ag atoms is possible in Au_{25} . It is important to recall that the Au–Ag system is miscible in the entire composition window. This indicates that the intercluster reaction is much more facile in comparison to the coreduction methods used to synthesize $\text{Au}_{25-x}\text{Ag}_x(\text{SR})_{18}$ clusters.

(B). Reaction between Clusters Having Same Ligands.

While the products of intercluster reactions have been assigned in the earlier section, complications arise due to the simultaneous exchange of the metal atoms and the ligands. Definite confirmation of metal atom exchange is possible by using clusters containing the same ligands. For this purpose, we prepared $\text{Au}_{25}(\text{FTP})_{18}$. Reactions of $\text{Au}_{25}(\text{FTP})_{18}$ with $\text{Ag}_{44}(\text{FTP})_{30}$ unambiguously confirm the incorporation of Ag

into $\text{Au}_{25}(\text{FTP})_{18}$. MALDI MS and UV/vis spectra of $\text{Au}_{25}(\text{FTP})_{18}$ shown in Figure S19 confirm the identity of the cluster. Time-dependent changes in the MALDI MS spectra of a mixture of these clusters are given in Figure S20. The mass spectra in the group I region after 1 and 3 h of reaction are shown in Figure 4. The mass difference of 89 Da ($M_{\text{Au}} - M_{\text{Ag}}$)

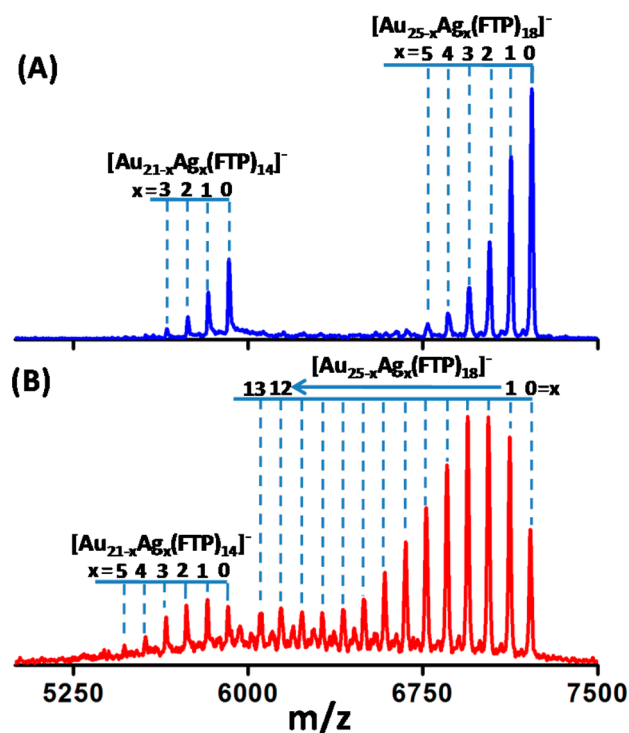


Figure 4. Negative ion mode MALDI MS spectra showing the time-dependent changes in the reaction mixture of $\text{Au}_{25}(\text{FTP})_{18}$ and $\text{Ag}_{44}(\text{FTP})_{30}$ after 1 h (A) and 3 h (B) of the reaction. $[\text{Au}_{21-x}\text{Ag}_x(\text{FTP})_{14}]^-$ are the fragments from the alloy clusters due to the loss of $\text{Au}_4(\text{FTP})_4$ (see Figure S1).

between the peaks in group I clearly confirms the formation of $\text{Au}_{25-x}\text{Ag}_x(\text{FTP})_{18}$ clusters. This shows that Ag inclusion of 1–5 atoms and 1–13 atoms was observed after 1 h and 3 h of the reaction, respectively. After 24 h of reaction, Ag inclusion of up to 17 atoms was observed (see Figure S20 and S21). Analysis of the time-dependent MALDI MS data for clusters with same and different ligands (Figures S3–S5 and S20) show that the ligand shell on the clusters plays an important role in controlling their reactivity (see the text associated with Figure S20).

As we observed both metal and ligand incorporations in $\text{Au}_{25}(\text{PET})_{18}$, we proceeded to develop an understanding of the sequence of events leading to the formation of $\text{Au}_{25-x}\text{Ag}_x(\text{PET})_{18-y}(\text{FTP})_y$ clusters. We wanted to see which of the events, FTP-PET, Ag–Au or (Ag-FTP)-(Au-PET) exchange, is the first step. For this, mass spectra of reaction mixtures were measured immediately after mixing the clusters. These measurements shown in Figure 5 reveal that the Ag–Au, (Ag-FTP)-(Au-PET) and FTP-PET exchanges occur even at the beginning of the reaction. Parent $\text{Au}_{25}(\text{PET})_{18}$ also undergoes FTP-PET exchange (see the peak (0, 1) in Figure 5A and 5B). However, only one FTP-PET exchange was observed for $\text{Au}_{25}(\text{PET})_{18}$ and its relative intensity remained almost the same even at about a 6-fold increase in the concentration of $\text{Ag}_{44}(\text{FTP})_{30}$ (see Figure 5A,B). These

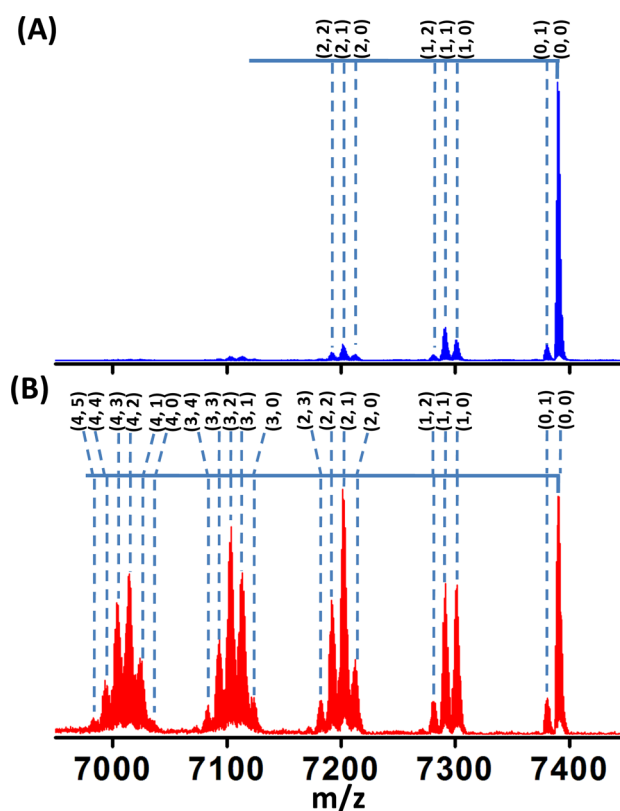


Figure 5. Negative ion mode ESI MS spectra measured immediately after mixing $\text{Au}_{25}(\text{PET})_{18}$ with $\text{Ag}_{44}(\text{FTP})_{30}$ in the $\text{Au}_{25}:\text{Ag}_{44}$ ratio 14:1 (A) and 2.5:1.0 (B). The numbers (x, y) in parentheses are according to the general molecular formula, $\text{Au}_{25-x}\text{Ag}_x(\text{PET})_{18-y}(\text{FTP})_y$.

observations show that Ag–Au and (Ag-FTP)-(Au-PET) exchanges are much faster than pure FTP-PET exchange.

Occurrence of peaks with a separation of m/z 10, in the insets of Figure 3 and Figure S10, may be tempting to conclude that all of these clusters are formed through FTP-PET exchange. For example, the peaks (1, 1) to (1, 4) in Figure S10 may, at first, be considered as the products of sequential FTP-PET exchange of (1, 0) cluster. Mass spectral measurements immediately after mixing (Figure 5 and S22) the clusters reveal that this is not the case. Comparison of Figure 5A and 5B shows that while the relative intensities of the (1, 0) and (1, 1) peaks significantly increases with concentration of $\text{Ag}_{44}(\text{FTP})_{30}$, there is no such notable increase in the intensity of the (0, 1) peak. Also, as mentioned before, only one peak due to FTP-PET exchange of $\text{Au}_{25}(\text{PET})_{18}$ was observed even when the concentration of $\text{Ag}_{44}(\text{FTP})_{30}$ was increased about six times, i.e., no (0, 2) or (0, 3) peaks were observed even at higher concentration of $\text{Ag}_{44}(\text{FTP})_{30}$. These observations suggest that the clusters (1, 0) and (1, 1) are produced from (0, 0), i.e., the parent $\text{Au}_{25}(\text{PET})_{18}$, through Ag–Au and (Ag-FTP)-(Au-PET) exchanges, respectively. For the same reasons, it is unlikely that the (1, 1) clusters are formed by a Ag–Au exchange of (0, 1) because the intensity of the latter is significantly less than that of (0, 0). Even though clusters such as (1, 2) and (2, 3) are observed in the initial stages of reaction (Figure 5A,B), no (0, 2) and (0, 3) clusters were observed. Hence, the (1, 2) and (2, 3) clusters are more likely to be formed by FTP-PET exchange of (1, 1) and (2, 2) clusters and cannot be the result of Ag–Au exchange from (0, 2) and (0, 3) clusters. Thus, it can be concluded that the presence of FTP in the

Table 1. Energies for the Substitution Reaction of (A) Au in $\text{Ag}_{44}(\text{SR})_{30}$, (B) Ag in $\text{Au}_{25}(\text{SR})_{18}$ and (C) the Overall Reaction Energies (in eV) as a Function of Their Positions in the Product Clusters, $\text{Au}_x\text{Ag}_{44-x}(\text{SR})_{30}$ and $\text{Au}_{25-x}\text{Ag}_x(\text{SR})_{18}$ for $x = 1^a$

(A) Location of Au in $\text{Au}_x\text{Ag}_{44-x}(\text{SR})_{30}$		$\Delta E/\text{eV}$	(B) Location of Ag in $\text{Au}_{25-x}\text{Ag}_x(\text{SR})_{18}$		$\Delta E/\text{eV}$
Icosahedron (I)		-0.72	Central atom (C)		+0.71
Dodecahedron: cube vertex (D_{cv})		-0.14			+0.23
Dodecahedron: cube face (D_{cf})		-0.32	Icosahedron (I)		
Staples (S)		-0.48	Staples (S)		+0.44

(C) Location of Ag in $\text{Au}_{25-x}\text{Ag}_x(\text{SR})_{18}$	Locations of Au in $\text{Au}_x\text{Ag}_{44-x}(\text{SR})_{30}$			
	I	D_{cv}	D_{cf}	S
C	-0.015	+0.564	+0.388	+0.226
I	-0.486	+0.093	-0.083	-0.245
S	-0.276	+0.303	+0.127	-0.035

^aLocations of substitution for each cluster are described in the [Computational Details](#).

$\text{Au}_{25-x}\text{Ag}_x(\text{PET})_{18-y}(\text{FTP})_y$ clusters formed is mostly due to (Ag-FTP)-(Au-PET) exchanges rather than due to FTP-PET exchanges.

These observations together suggest that $\text{Au}_{25-x}\text{Ag}_x(\text{PET})_{18-y}(\text{FTP})_y$ clusters were formed principally by two processes: (Ag-FTP)-(Au-PET) and Ag-Au exchanges. For example, the (1, 1) cluster (see [Figure 3](#) for numbering) is formed by the (Ag-FTP)-(Au-PET) exchange from a (0, 0) cluster. The (1, 1) cluster may then undergo Ag-Au or (Ag-FTP)-(Au-PET) exchange, producing (2, 1) or (2, 2) clusters, respectively. These processes continue to give higher Ag- and FTP-incorporated clusters. There may be other complicated events as well.

Transformation of $\text{Au}_{25}(\text{SR})_{18}$ into $\text{Au}_{25-x}\text{Ag}_x(\text{SR})_{18}$ is confirmed from the above measurements. Similarly, our measurements indicate that $\text{Ag}_{44}(\text{SR})_{30}$ has been transformed into $\text{Au}_x\text{Ag}_{44-x}(\text{SR})_{30}$ due to its reaction with $\text{Au}_{25}(\text{SR})_{18}$. As mentioned earlier, the mass spectral features due to $\text{Ag}_{44}(\text{FTP})_{30}$ disappeared immediately after mixing it with $\text{Au}_{25}(\text{PET})_{18}$. MALDI MS measurements show the emergence of a broad peak (group II) at m/z higher than that of $\text{Ag}_{44}(\text{FTP})_{30}$ (see [Figures 2](#) and [S15](#)). Also, the intensity of this peak increased as the concentration of $\text{Ag}_{44}(\text{FTP})_{30}$ increased. The difference between the molecular mass of $\text{Ag}_{44}(\text{FTP})_{30}$ (m/z 8567) and the maxima of group II peaks, at different time intervals (1–24 h) of the reaction between $\text{Ag}_{44}(\text{FTP})_{30}$ and $\text{Au}_{25}(\text{FTP})_{18}$, (see [Figure S23](#)) suggests the formation of $\text{Au}_x\text{Ag}_{44-x}(\text{FTP})_{30}$ with $x = 14$ –16. However, such an analysis may not give accurate compositions of a mixture due to the high energy provided by the MALDI laser. ESI MS measurements (see [Figure S24](#)) clearly indicated the formation of a series of clusters with x varying from 0 to 12. MALDI MS could not resolve the features of these individual clusters due to the broadness of the peaks. Recent reports on the $\text{Au}_x\text{Ag}_{44-x}(\text{SR})_{30}$ clusters¹⁵ (prepared from ionic precursors) indicate that the total number of metal atoms is the same and the structural framework of these clusters is similar to that of $\text{Ag}_{44}(\text{SR})_{30}$. UV/vis spectra of reaction mixtures at higher concentrations of

$\text{Ag}_{44}(\text{FTP})_{30}$ (see [Figure S25B](#)) resemble that of previously reported $\text{Au}_{12}\text{Ag}_{32}(\text{SR})_{30}$ clusters.¹⁵ At lower Ag_{44} concentrations, ([Figure S25A](#)) the absorption spectra resemble $\text{Au}_{25-x}\text{Ag}_x(\text{SR})_{18}$, as seen in previous reports.¹⁶ Hence, our MALDI and ESI MS measurements confirm the formation of $\text{Au}_x\text{Ag}_{44-x}(\text{SR})_{30}$ in the reaction between $\text{Ag}_{44}(\text{FTP})_{30}$ and $\text{Au}_{25}(\text{SR})_{18}$. Reactions were also carried out with Au_{25} and Ag_{44} clusters of different protecting ligands (*n*-butanethiol and 4-mercaptobenzoic acid) (see [Figures S26](#) and [S27](#)). Our experiments show that similar reactions occur between other types of Ag and Au clusters and even with plasmonic nanoparticles. Experiments are in progress in these directions. A discussion of the possible locations of Ag atoms in the alloy clusters, based on the charge states of $\text{Au}_{25}(\text{SR})_{18}$, previous reports of $\text{Au}_{25-x}\text{Ag}_x(\text{SR})_{18}$ clusters and the recent report of $\text{Au}_{25}\text{Ag}_2(\text{SR})_{18}$,¹⁶ is given in the [Supporting Information](#). However, analysis of the structures formed requires more work.

(C). DFT Study of Structural Isomers and Reaction Energetics. To understand the driving force behind the reaction, we used DFT to calculate energies of the reactants [$\text{Au}_{25}(\text{SR})_{18}$ and $\text{Ag}_{44}(\text{SR})_{30}$], the products [$\text{Au}_{25-x}\text{Ag}_x(\text{SR})_{18}$ and $\text{Au}_x\text{Ag}_{44-x}(\text{SR})_{30}$] and the likely species being exchanged in the intermediate steps such as metal atoms (M), and thiolate fragments (M-SR) (see [Tables S1–S7](#), see [Figure S28](#) for a description of the fragments). We calculated the energy of the overall reaction (i.e., $\text{Au}_{25}(\text{SR})_{18} + \text{Ag}_{44}(\text{SR})_{30} \rightarrow \text{Au}_{25-x}\text{Ag}_x(\text{SR})_{18} + \text{Au}_x\text{Ag}_{44-x}(\text{SR})_{30}$) and reaction energies for substitution of metal atom (M = Ag/Au) and metal-thiolate fragments (M-SR) in different combinations of substituent positions in $\text{Au}_{25}(\text{SR})_{18}$ and $\text{Ag}_{44}(\text{SR})_{30}$, respectively (see [Table 1](#) and [Tables S4–S7](#)). The overall reaction, either through M or M-SR substitutions, was found to be exothermic for certain combinations of substituent positions as shown in [Table 1C](#). This can be attributed to the lowering of the total energy by inclusion of (i) Au atoms or Au-SR into $\text{Ag}_{44}(\text{SR})_{30}$ and (ii) Ag-SR into $\text{Au}_{25}(\text{SR})_{18}$, rather than the inclusion of Ag atoms into $\text{Au}_{25}(\text{SR})_{18}$ (see [Tables S4–S7](#)). The more exothermic Au atom or Au-SR substitution into

$\text{Ag}_{44}(\text{SR})_{30}$ and Ag-SR substitution into $\text{Au}_{25}(\text{SR})_{18}$ compensates for the endothermic¹⁷ silver atom inclusion into the $\text{Au}_{25}(\text{SR})_{18}$, in contrast to the exothermic Pd or Pt inclusion.^{18,19} The details are discussed below.

We investigated which substituent atom (M) or M-SR fragment positions in each cluster were most preferred energetically and the dependence of the reaction energy as a function of the final substituent positions. Initially we calculated the energies of different isomers of $\text{Au}_{25-x}\text{Ag}_x(\text{SR})_{18}$ and $\text{Au}_x\text{Ag}_{44-x}(\text{SR})_{30}$ for $x = 1$, relative to the unalloyed clusters. For simplicity, we considered events involving one metal atom substitution into $\text{Au}_{25}(\text{SR})_{18}$ and $\text{Ag}_{44}(\text{SR})_{30}$. There are a large number of symmetry nonequivalent isomers for each substitution; for eg., when $x = 2$ there are 28 isomers for $\text{Au}_{25-x}\text{Ag}_x(\text{SR})_{18}$.²⁰ The preferred locations of substituent metal atoms or fragments in the alloy clusters are indicated by the substitution energy differences between the parent clusters and their alloy isomers, listed in Table 1 A and B.

In case of $\text{Au}_{25-x}\text{Ag}_x(\text{SR})_{18}$, Ag atoms prefer to stay on the icosahedral vertex positions (see Table S2) as in earlier reports.^{14a,c} For $\text{Au}_x\text{Ag}_{44-x}(\text{SR})_{30}$, we found that the order of preference of the position of Au atom is the innermost icosahedron (-0.72 eV), followed by the outermost staple atoms (-0.48 eV), and last, the middle dodecahedral positions D_{cv} and D_{cf} (-0.14 and -0.32 eV) (see Table S1). Reaction energies as a function of substituent positions for $\text{Au}_{25-x}(\text{SR})_{18}$ and $\text{Au}_x\text{Ag}_{44-x}(\text{SR})_{30}$ in the alloy clusters (Table 1C) suggest that at fewer numbers of substituent metal atoms ($x \leq 12$), the most energetically favored final metal atom positions are in the icosahedral sites in both $\text{Au}_{25}(\text{SR})_{18}$ and $\text{Ag}_{44}(\text{SR})_{30}$ (-0.486 eV), and next, in the staples of one cluster and the icosahedral core of the other cluster (-0.245 and -0.276 eV). Two further final metal atom positions in both clusters which are slightly less favorable but still exothermic are the D_{cf} position of $\text{Ag}_{44}(\text{SR})_{30}$ and the icosahedral core of $\text{Au}_{25}(\text{SR})_{18}$ (-0.083 eV) and the staples in both clusters (-0.035 eV), as listed in Table 1C. As mentioned earlier, the similarity of the absorption spectra of the reaction mixture at higher concentrations of $\text{Ag}_{44}(\text{SR})_{30}$ (see Figure S25B) with the previously reported $\text{Au}_{12}\text{Ag}_{32}(\text{SR})_{30}$ also supports this conclusion that Au atoms preferably occupy the icosahedral core of $\text{Au}_x\text{Ag}_{44-x}(\text{SR})_{30}$, and that for $x = 12$, the $\text{Au}_{12}\text{Ag}_{32}(\text{SR})_{30}$ structure would be identical to that of the reported crystal structure of $\text{Au}_{12}\text{Ag}_{32}(\text{SR})_{30}$.^{2e}

We considered the energetics of Au-SH and Ag-SH fragments in the unalloyed clusters, and compared this with the energetics of single metal atom substitution to obtain further clues on the mechanism and its driving force. There are three possible Au-SR fragment positions in $\text{Au}_{25}(\text{SR})_{18}$ and four different Ag-SR fragments in $\text{Ag}_{44}(\text{SR})_{30}$, as shown in Figure S28.

Reaction energies suggest that Ag-SR substitution in $\text{Au}_{25}(\text{SR})_{18}$ is more favorable than the Ag atom exchange in the corresponding position, as seen by comparing the substitution energies in Tables S6 and S7. We also note that the endothermic Ag atom substitution in the icosahedral core of $\text{Au}_{25}(\text{SR})_{18}$ ($+0.22$ eV) becomes slightly exothermic (-0.01 eV) in the case of the Ag-SR fragment (fragment F3 in Figure S28A) involving an icosahedral Ag atom. In contrast, the Au-SR fragment exchanges in $\text{Ag}_{44}(\text{SR})_{30}$ are slightly less favorable than Au atom substitution, but nevertheless still exothermic for the majority of fragment positions (Tables S4 and S5). The substitution energies for the different combinations of final fragment positions in $\text{Ag}_{44}(\text{SR})_{30}$ indicate that the exchange of

fragments involving the terminal ligand and the staple Ag atoms (F1 and F2) are energetically more favored compared to the exchange of fragments involving bridging ligand and Ag atoms in D_{cf} positions (F3). However, in the case of $\text{Au}_{25}(\text{SR})_{18}$, the exchange of fragment F3 involving icosahedral Au atoms is the most favored energetically followed by exchange between the fragments (F1 and F2) containing the staple atoms of both clusters. Overall, the exchange of M-SR fragments between the clusters is an energetically favorable process due to (i) the exothermic Au-SR substitutions in specific positions (F1, F2 and F4) of $\text{Ag}_{44}(\text{SR})_{30}$, (ii) less endothermic (for F1 and F2) and exothermic (for F3) Ag-SR fragment substitutions in $\text{Au}_{25}(\text{SR})_{18}$ (see Tables S5 and S7).

(D). Mechanistic Aspects of the Reaction. We suggest that the metal–thiolate interface plays a significant role in the mechanism of the reaction. In thiolate-protected molecular metal clusters, these interfaces often assume the form of metal–thiolate staple/mount motifs.² Atoms in these motifs are considered to be in M^{I} oxidation state while those in the core are considered to be in M^0 oxidation state. Ag clusters and nanoparticles reduce Au^{I} or $\text{Au}^{\text{I}}\text{-SR}$ thiolates^{8b,c} due to the higher reduction potential of Au^{I} . At the sub-nanometer scale, conversely, gold clusters can also reduce Ag^{I} ions and $\text{Ag}^{\text{I}}\text{-thiolates}$,⁹ even though such reduction is not feasible for the bulk forms of these metals. Therefore, redox processes might also occur between the clusters since they are composed of silver and gold atoms in both the M^0 and M^{I} states. The relative energies of the HOMO (d derived) and LUMO (sp derived) states of the $\text{Au}_{25}(\text{SR})_{18}$ and $\text{Ag}_{44}(\text{SR})_{30}$ and their alloy isomers determine the feasibility of electron transfer from one cluster to another and which would behave like donor or acceptor. The HOMO level of $\text{Ag}_{44}(\text{SR})_{30}$ is about 3.8 eV higher than the LUMO of $\text{Au}_{25}(\text{SR})_{18}$ (see Table S8 and S9). This indicates that an electron transfer into the states above the LUMO of $\text{Au}_{25}(\text{SR})_{18}$ followed by non-radiative relaxation into other levels of the cluster would release enough energy to overcome activation energy barriers and to break bonds, possibly in the staples and the core, leading to partial fragmentation. Although both the clusters are overall negatively charged, locally the electric field in the neighborhood of the ligands is both inhomogeneous²¹ and screened by the solvent molecules. Metallophilic interactions between the Au(I) and Ag(I) centers (closed shell species),^{22,23} could also occur if their relative orientations permit closer approach within less than 3–4 Å. Attractive π – π stacking interactions between these aromatic ligands may also occur. These interactions are expected to bring clusters into proximity and to find their suitable orientation.

The observed intercluster reactions might occur via the following three stages. In the first stage, destabilization of clusters can occur upon their closer approach facilitated by redox processes and/or metallophilic/ π – π interactions. These factors could weaken the M–S bonds in the staples and may result in fragmentation. However, the exact reason behind the destabilization and fragmentation of the clusters cannot be understood from the present studies.

In the next stage, the unstabilized clusters might undergo fragmentation to form small M-SR, $M(\text{SR})_2$, $M_2(\text{SR})_3$, etc. units or clusters with partially opened staples or mounts followed by the nucleophilic attack of these fragments onto the staples of the cluster. Considering the polar nature of the M–S bonds in the staples due to greater electronegativity of the sulfur atom, these fragments become nucleophilic in nature. Anionic fragments such as $M(\text{SR})_2$ and $M_2(\text{SR})_3$ (where M =

Au/Ag), etc., have been observed in mass spectrometry of $\text{Au}_{25}(\text{SR})_{18}$ and $\text{Ag}_{44}(\text{SR})_{30}$.^{24,2e,g} Among these fragments, $\text{Au}(\text{SR})_2$ and the $\text{Ag}(\text{SR})_2$ are the two most abundant species (see Figure S31) and may be the most probable nucleophiles in the reaction. Similar mechanisms have been observed in ligand exchange reactions of monolayer protected clusters^{6k} and metal exchange reactions of small metal–thiolate complexes.²⁵ However, we note that mechanisms of metal exchange in monolayer protected clusters have not yet been investigated thoroughly.

The proposed mechanism for the reaction between $\text{Au}_{25}(\text{SR})_{18}$ and $\text{Ag}(\text{SR})_2$ fragment resulting in the exchange of Au atoms and various Au-SR fragments is depicted in Schemes S1 and S2. However, in the case of $\text{Ag}_{44}(\text{SR})_{30}$ these reactions could consist of several steps of bond-breaking events due to the more complicated bonding network of the $\text{Ag}_2(\text{SR})_5$ mounts. This mechanism shows that even though the M-(SR)₂ unit is involved in the reaction, the net result is the inclusion of either M or M-SR groups depending on the specific reaction pathways. The exchange of the Ag-SR and Au-SR units between the clusters could be facile as they may be considered to be isolobal fragments. Exchange of similar metal–ligand isolobal units are also commonly encountered in coordination complexes.²⁶

In the final stage of the reaction, the open staples or the mounts of the clusters now containing the substituent can rearrange, reconstructing the overall structural framework with substituted metal atoms or ligands resulting in the final products.

An intuitive and alternative way of visualizing the structural changes during the reactions can be inferred from the recent structural model of aspicules²⁰ showing that $\text{Au}_{25}(\text{SR})_{18}$ can be viewed as three interlocked (Borromean) $\text{Au}_8(\text{SR})_6$ rings around the central gold atom (see Figure S29). These rings in the destabilized clusters may undergo opening, and once the staple chains or mounts are opened, they become more flexible and assume elongated conformations which gives the atoms of their free ends greater reach with which to interact with the corresponding open chains or mounts on the other cluster. A similar reorganization of the staples has been proposed (theoretically) earlier.²⁷ The ends of the open chains or mounts can interact more easily exchanging the M and the M-SR units between them. The ring model of $\text{Au}_{25}(\text{SR})_{18}$ also suggests that inclusion of Ag into the Au_{13} core is not as significantly hindered from the steric factors as might be expected when $\text{Au}_{25}(\text{SR})_{18}$ is viewed as separate core covered by $\text{Au}_2(\text{SR})_3$ staples. The opening and reorganization of the chains or mounts away from the core would make the core atoms more exposed, and facile for reaction. This may also be facilitated by structural rearrangements in the core and staples, or $\text{Au}_8(\text{SR})_6$ rings as a whole due to rearrangements in the positions of the individual $\text{Au}_8(\text{SR})_6$ -rings. Similarly, the icosahedral Ag atoms in $\text{Ag}_{44}(\text{SR})_{30}$ become more accessible when certain Ag–S bonds are broken (see Figure S30). Thus, our mechanistic model implies that M and M-SR substitutions in the staples can originate from the reactions and rearrangements involving the metal–thiolate fragments and the open chains and mounts, while substitutions of the core atoms could involve the exposed core of one of the clusters and the fragments or open chains or mounts of the other cluster.

The initially formed alloy clusters with fewer numbers of substituents could also undergo similar reactions producing clusters with higher number of substituents until the

thermodynamic equilibrium for the particular reactant concentration is reached (see Figure S4–S5). Final positions of the substituent metal atoms in the alloy clusters are dictated by their relative energies which depend on the number and positions of substituents, as mentioned earlier.

CONCLUSIONS

In conclusion, we report the first example of intercluster reactions of monolayer protected noble metal clusters. Metal core-thiolate interfaces of these clusters play an important role in these reactions. The reaction results in exchange of the metal atoms as well as the metal–thiolate fragments. The intercluster reaction route seems to be a more facile way than the coreduction route and thiolate reaction route^{10a} for bimetallic clusters. DFT calculations show that in case of $\text{Au}_x\text{Ag}_{44-x}(\text{SR})_{30}$, Au atoms prefer to occupy the icosahedral core followed by the outer staples and last the inner dodecahedron. Calculations also revealed that the overall reaction is energetically favorable due to the lowering of the energy of Au or Au-SR substitution into $\text{Ag}_{44}(\text{SR})_{30}$ rather than the Ag or Ag-SR substitution into $\text{Au}_{25}(\text{SR})_{18}$. A discussion of some of the essential aspects of the reaction mechanism is presented. Further experimental and theoretical efforts are needed to understand the phenomena behind these reactions in detail. We hope that our work will draw greater attention to the role of the monolayers in determining the chemistry of these clusters and the role of metallic core and the surrounding monolayers in determining the chemistry of these clusters.

ASSOCIATED CONTENT

Supporting Information

The Supporting Information is available free of charge on the ACS Publications website at DOI: 10.1021/jacs.5b09401.

Instrumentation, general methods of ESI MS and MALDI MS measurements, computational details, temporal changes in absorption and emission spectra during intercluster reactions, additional ESI MS and MALDI MS spectra, discussion on the charge state of the alloy clusters formed and the position of the Ag atoms in them. (PDF)

AUTHOR INFORMATION

Corresponding Author

*pradeep@iit.ac.in

Present Address

†Currently a postdoctoral fellow at Dept. of Chemistry, University of Illinois at Urbana Champaign.

Notes

The authors declare no competing financial interest.

ACKNOWLEDGMENTS

K. R. K. and A. G. thank U. G. C. for their senior research fellowships. A. B. and I. C. thank IIT Madras for an Institute Post Doctoral Fellowship. We thank Department of Science and Technology for consistently supporting our research program.

REFERENCES

- (1) (a) Kappes, M. M. *Chem. Rev.* **1988**, *88*, 369. (b) Schmid, G. *Chem. Rev.* **1992**, *92*, 1709. (c) Moskovits, M. *Annu. Rev. Phys. Chem.* **1991**, *42*, 465. (d) Luo, Z.; Smith, J. C.; Woodward, W. H.; Castleman, A. W., Jr. *J. Phys. Chem. Lett.* **2012**, *3*, 3818. (e) Luo, Z.; Gamboa, G.

- U.; Smith, J. C.; Reber, A. C.; Reveles, J. U.; Khanna, S. N.; Castleman, A. W., Jr. *J. Am. Chem. Soc.* **2012**, *134*, 18973.
- (2) (a) Heaven, M. W.; Dass, A.; White, P. S.; Holt, K. M.; Murray, R. W. *J. Am. Chem. Soc.* **2008**, *130*, 3754. (b) Akola, J.; Walter, M.; Whetten, R. L.; Häkkinen, H.; Grönbeck, H. *J. Am. Chem. Soc.* **2008**, *130*, 3756. (c) Zhu, M.; Aikens, C. M.; Hollander, F. J.; Schatz, G. C.; Jin, R. *J. Am. Chem. Soc.* **2008**, *130*, 5883. (d) Jadzinsky, P. D.; Calero, G.; Ackerson, C. J.; Bushnell, D. A.; Kornberg, R. D. *Science* **2007**, *318*, 430. (e) Desireddy, A.; Conn, B. E.; Guo, J.; Yoon, B.; Barnett, R. N.; Monahan, B. M.; Kirschbaum, K.; Griffith, W. P.; Whetten, R. L.; Landman, U.; Bigioni, T. P. *Nature* **2013**, *501*, 399. (f) Bakr, O. M.; Amendola, V.; Aikens, C. M.; Wenseleers, W.; Li, R.; Negro, L. D.; Schatz, G. C.; Stellacci, F. *Angew. Chem.* **2009**, *121*, 6035. (g) Harkness, K. M.; Tang, Y.; Dass, A.; Pan, J.; Kothalawala, N.; Reddy, V. J.; Cliffel, D. E.; Demeler, B.; Stellacci, F.; Bakr, O. M.; McLean, J. A. *Nanoscale* **2012**, *4*, 4269. (h) Abdulhalim, L. G.; Ashraf, S.; Katsiev, K.; Kirmani, A. R.; Kothalawala, N.; Anjum, D. H.; Abbas, S.; Amassian, A.; Stellacci, F.; Dass, A.; Hussain, I.; Bakr, O. M. *J. Mater. Chem. A* **2013**, *1*, 10148. (i) Schnöckel, H.; Schnepf, A.; Whetten, R. L.; Schenk, C.; Henke, P. Z. *Anorg. Allg. Chem.* **2011**, *637*, 15. (j) Schnöckel, H. *Chem. Int. Rev.* **2010**, *110*, 4125. (k) Schnepf, A.; Schnöckel, H. *Angew. Chem., Int. Ed.* **2014**, *53*, 3064. (l) Rao, T. U. B.; Nataraju, B.; Pradeep, T. *J. Am. Chem. Soc.* **2010**, *132*, 16304. (m) Hassinen, J.; Pulkkinen, P.; Kalenius, E.; Pradeep, T.; Tenhu, H.; Häkkinen, H.; Ras, R. H. A. *J. Phys. Chem. Lett.* **2014**, *5*, 585. (n) Azubel, M.; Koivisto, J.; Malola, S.; Bushnell, D.; Hura, G. L.; Koh, A. L.; Tsunoyama, H.; Tsukuda, T.; Pettersson, M.; Häkkinen, H.; Kornberg, R. D. *Science* **2014**, *345*, 909. (o) Xu, W. W.; Gao, Y. *J. Phys. Chem. C* **2015**, *119*, 14224. (p) Gao, Y. *J. Phys. Chem. C* **2013**, *117*, 8983. (q) Joshi, C. P.; Bootharaju, M. S.; Alhilaly, M. J.; Bakr, O. M. *J. Am. Chem. Soc.* **2015**, *137*, 11578. (r) Yan, J.; Su, H.; Yang, H.; Malola, S.; Lin, S.; Häkkinen, H.; Zheng, N. *J. Am. Chem. Soc.* **2015**, *137*, 11880.
- (3) (a) Li, G.; Liu, C.; Lei, Y.; Jin, R. *Chem. Commun.* **2012**, *48*, 12005. (b) Yu, C.; Li, G.; Kumar, S.; Kawasaki, H.; Jin, R. *J. Phys. Chem. Lett.* **2013**, *4*, 2847. (c) Oliver-Meseguer, J.; Cabrero-Antonino, J. R.; Domínguez, I.; Leyva-Pérez, A.; Corma, A. *Science* **2012**, *338*, 1452. (d) Yamazoe, S.; Koyasu, K.; Tsukuda, T. *Acc. Chem. Res.* **2014**, *47*, 816. (e) Maity, P.; Xie, S.; Yamauchi, M.; Tsukuda, T. *Nanoscale* **2012**, *4*, 4027.
- (4) (a) Kwak, K.; Kumar, S. S.; Pyo, K.; Lee, D. *ACS Nano* **2014**, *8*, 671. (b) Kumar, S. S.; Kwak, K.; Lee, D. *Anal. Chem.* **2011**, *83*, 3244. (c) Kwak, K.; Kumar, S. S.; Lee, D. *Nanoscale* **2012**, *4*, 4240. (d) Yuan, X.; Luo, Z.; Yu, Y.; Yao, Q.; Xie, J. *Chem. - Asian J.* **2013**, *8*, 858. (e) Xie, J.; Zheng, Y.; Ying, J. Y. *Chem. Commun.* **2010**, *46*, 961. (f) Zheng, K.; Yuan, X.; Goswami, N.; Zhang, Q.; Xie, J. *RSC Adv.* **2014**, *4*, 60581.
- (5) (a) Jin, R. *Nanoscale* **2010**, *2*, 343. (b) Udayabhaskararao, T.; Pradeep, T. *J. Phys. Chem. Lett.* **2013**, *4*, 1553. (c) Mathew, A.; Pradeep, T. *Part. Part. Syst. Character.* **2014**, *31*, 1017.
- (6) (a) Song, Y.; Murray, R. W. *J. Am. Chem. Soc.* **2002**, *124*, 7096. (b) Guo, R.; Song, Y.; Wang, G.; Murray, R. W. *J. Am. Chem. Soc.* **2005**, *127*, 2752. (c) Parker, J. F.; Kacprzak, K. A.; Lopez-Acevedo, O.; Häkkinen, H.; Murray, R. W. *J. Phys. Chem. C* **2010**, *114*, 8276. (d) Dass, A.; Holt, K.; Parker, J. F.; Feldberg, S. W.; Murray, R. W. *J. Phys. Chem. C* **2008**, *112*, 20276. (e) Heinecke, C. L.; Ni, T. W.; Malola, S.; Mäkinen, V.; Wong, O. A.; Häkkinen, H.; Ackerson, C. J. *J. Am. Chem. Soc.* **2012**, *134*, 13316. (f) Ni, T. W.; Tofanelli, M. A.; Phillips, B. D.; Ackerson, C. J. *Inorg. Chem.* **2014**, *53*, 6500. (g) Shichibu, Y.; Negishi, Y.; Tsukuda, T.; Teranishi, T. *J. Am. Chem. Soc.* **2005**, *127*, 13464. (h) Shibu, E. S.; Muhammed, M. A. H.; Tsukuda, T.; Pradeep, T. *J. Phys. Chem. C* **2008**, *112*, 12168–12176. (i) Muhammed, M. A. H.; Shaw, A. K.; Pal, S. K.; Pradeep, T. *J. Phys. Chem. C* **2008**, *112*, 14324. (j) AbdulHalim, L. G.; Kothalawala, N.; Sinatra, L.; Dass, A.; Bakr, O. M. *J. Am. Chem. Soc.* **2014**, *136*, 15865. (k) Fernando, A.; Aikens, C. M. *J. Phys. Chem. C* **2015**, *119*, 20179. (l) Pengo, P.; Bazzo, C.; Boccalon, M.; Pasquato, L. *Chem. Commun.* **2015**, *51*, 3204.
- (7) Bootharaju, M. S.; Deepesh, G. K.; Udayabhaskararao, T.; Pradeep, T. *J. Mater. Chem. A* **2013**, *1*, 611.
- (8) (a) Bootharaju, M. S.; Pradeep, T. *Langmuir* **2011**, *27*, 8134. (b) Krishnadas, K. R.; Udayabhaskararao, T.; Choudhury, S.; Goswami, N.; Pal, S. K.; Pradeep, T. *Eur. J. Inorg. Chem.* **2014**, *5*, 908–916. (c) Udayabhaskararao, T.; Sun, Y.; Goswami, N.; Pal, S. K.; Balasubramanian, K.; Pradeep, T. *Angew. Chem., Int. Ed.* **2012**, *51*, 2155. (d) Chakraborty, L.; Rao, T. U. B.; Pradeep, T. *J. Hazard. Mater.* **2012**, *211–212*, 396.
- (9) (a) Choi, J.-P.; Fields-Zinna, C. A.; Stiles, R. L.; Balasubramanian, R.; Douglas, A. D.; Crowe, M. C.; Murray, R. W. *J. Phys. Chem. C* **2010**, *114*, 15890. (b) Wu, Z. *Angew. Chem., Int. Ed.* **2012**, *51*, 2934–2938. (c) Wang, M.; Wu, Z.; Chu, Z.; Yang, J.; Yao, C. *Chem. - Asian J.* **2014**, *9*, 1006.
- (10) (a) Wang, S.; Song, Y.; Jin, S.; Liu, X.; Zhang, J.; Pei, Y.; Meng, X.; Chen, M.; Li, P.; Zhu, M. *J. Am. Chem. Soc.* **2015**, *137*, 4018. (b) Zhu, M.; Chan, G.; Qian, H.; Jin, R. *Nanoscale* **2011**, *3*, 1703.
- (11) Som, A.; Samal, A. K.; Udayabhaskararao, T.; Bootharaju, M. S.; Pradeep, T. *Chem. Mater.* **2014**, *26*, 3049.
- (12) (a) Shichibu, Y.; Negishi, Y.; Watanabe, T.; Chaki, N. K.; Kawaguchi, H.; Tsukuda, T. *J. Phys. Chem. C* **2007**, *111*, 7845. (b) Wang, S.; Meng, X.; Das, A.; Li, T.; Song, Y.; Cao, T.; Zhu, X.; Zhu, M.; Jin, R. *Angew. Chem., Int. Ed.* **2014**, *53*, 2376–2380.
- (13) Negishi, Y.; Iwai, T.; Ide, M. *Chem. Commun.* **2010**, *46*, 4713.
- (14) (a) Kumara, C.; Aikens, C. M.; Dass, A. *J. Phys. Chem. Lett.* **2014**, *5*, 461. (b) Yamazoe, S.; Kurashige, W.; Nobusada, K.; Negishi, Y.; Tsukuda, T. *J. Phys. Chem. C* **2014**, *118*, 25284. (c) Guidez, E. B.; Mäkinen, V.; Häkkinen, H.; Aikens, C. M. *J. Phys. Chem. C* **2012**, *116*, 20617.
- (15) Yang, H.; Wang, Y.; Huang, H.; Gell, L.; Lehtovaara, L.; Malola, S.; Häkkinen, H.; Zheng, N. *Nat. Commun.* **2013**, *4*, 2422.
- (16) Yao, C.; Chen, J.; Li, M.-B.; Liu, L.; Yang, J.; Wu, Z. *Nano Lett.* **2015**, *15*, 1281.
- (17) Walter, M.; Moseler, M. *J. Phys. Chem. C* **2009**, *113*, 15834.
- (18) Negishi, Y.; Kurashige, W.; Niihori, Y.; Iwasab, T.; Nobusada, K. *Phys. Chem. Chem. Phys.* **2010**, *12*, 6219.
- (19) Guidez, E. B.; Mäkinen, V.; Häkkinen, H.; Aikens, C. M. *J. Phys. Chem. C* **2012**, *116*, 20617.
- (20) Natarajan, G.; Mathew, A.; Negishi, Y.; Whetten, R. L.; Pradeep, T. *J. Phys. Chem. C* **2015**, *119*, 27768.
- (21) Chen, X.; Moore, J. E.; Zekarias, M.; Jensen, L. *Nat. Commun.* **2015**, *6*, 8921.
- (22) Ni, W.-X.; Qiu, Y.-M.; Li, M.; Zheng, J.; Sun, R. W.-Y.; Zhan, S.-Z.; Ng, S. W.; Li, D. *J. Am. Chem. Soc.* **2014**, *136*, 9532.
- (23) Nardi, M. D.; Antonello, S.; Jiang, D.; Pan, F.; Rissanen, K.; Ruzzi, M.; Venzo, A.; Zoleo, A.; Maran, F. *ACS Nano* **2014**, *8*, 8505.
- (24) Angel, L. A.; Majors, L. T.; Dharmaratne, A. C.; Dass, A. *ACS Nano* **2010**, *4*, 4691.
- (25) (a) Autissier, V.; Henderson, R. A. *Inorg. Chem.* **2008**, *47*, 6393. (b) Hagen, K. S.; Stephan, D. W.; Holm, R. H. *Inorg. Chem.* **1982**, *21*, 3928.
- (26) (a) Goldman, A. S.; Tyler, D. R. *J. Am. Chem. Soc.* **1986**, *108*, 89. (b) Hor, T. S. A.; Tan, A. L. C. *J. Coord. Chem.* **1989**, *20*, 311.
- (27) Liu, C.; Lin, S.; Pei, Y.; Zeng, X. C. *J. Am. Chem. Soc.* **2013**, *135*, 18067.
- (28) Enkovaara, J.; et al. *J. Phys.: Condens. Matter* **2010**, *22*, 253202.

Supporting Information for the paper:

Intercluster reactions between $\text{Au}_{25}(\text{SR})_{18}$ and $\text{Ag}_{44}(\text{SR})_{30}$

K. R. Krishnadas, Atanu Ghosh, Ananya Baksi, Indranath Chakraborty[†], Ganapati Natarajan and Thalappil Pradeep*

DST Unit of Nanoscience (DST UNS) and Thematic Unit of Excellence, Department of Chemistry, Indian Institute of Technology Madras, Chennai 600 036, India

[†]Currently a postdoctoral fellow at Dept. of Chemistry, University of Illinois at Urbana Champaign

*Email: pradeep@iitm.ac.in

Table of Contents

Name	Description	Page No.
Figure S1	Collision energy-dependent ESI MS spectra of $\text{Au}_{25}(\text{PET})_{18}$	S7
Figure S2	Detailed ESI MS spectrum of $\text{Ag}_{44}(\text{FTP})_{30}$	S8
Figure S3	MALDI MS spectra showing the temporal evolution of the products formed after mixing of $\text{Au}_{25}(\text{PET})_{18}$ and $\text{Ag}_{44}(\text{FTP})_{30}$ clusters at $\text{Au}_{25}:\text{Ag}_{44}$ ratio of 14:1	S9
Figure S4	MALDI MS spectra showing the temporal evolution of the products formed after mixing of $\text{Au}_{25}(\text{PET})_{18}$ and $\text{Ag}_{44}(\text{FTP})_{30}$ clusters at $\text{Au}_{25}:\text{Ag}_{44}$ ratio of 1.7:1.	S10
Figure S5	MALDI MS spectra showing the temporal evolution of the products formed after mixing of $\text{Au}_{25}(\text{PET})_{18}$ and $\text{Ag}_{44}(\text{FTP})_{30}$ clusters at $\text{Au}_{25}:\text{Ag}_{44}$ ratio of 1.0:1.0.	S11
Figure S6	Expansion of ESI MS features (0, 0-3), (1, 0-4), (2, 0-4) and (3, 0-4), (shown in Figure 3 in main paper)	S12
Figure S7	Expansion of features (4, 1-5), (5, 1-5), (6, 3-8) and (7, 3-8), (shown in Figure 3 in main	S13

	paper)	
Figure S8	Expansion of features (8, 3-9), (9, 3-9), (10, 4-9) and (11, 4-9), (shown in Figure 3 in main paper)	S14
Figure S9	Expansion of features (12, 4-9) and (13, 4-9), (shown in Figure 3 in main paper)	S15
Figure S10	Expansion of the mass spectra in panel A of Figure 3 in main manuscript	S15
Figure S11	Experimental and theoretical isotope distributions of $\text{Au}_{23}\text{Ag}_2(\text{PET})_{18}$, $\text{Au}_{23}\text{Ag}_2(\text{PET})_{17}(\text{FTP})_1$, $\text{Au}_{23}\text{Ag}_2(\text{PET})_{16}(\text{FTP})_2$ and $\text{Au}_{23}\text{Ag}_2(\text{PET})_{15}(\text{FTP})_3$	S16
Figure S12	Time-dependent changes in the UV/Vis and emission spectra during the reaction between $\text{Au}_{25}(\text{PET})_{18}$ and $\text{Ag}_{44}(\text{FTP})_{30}$ clusters taken in the ratio ($\text{Au}_{25}:\text{Ag}_{44}$) of 14:1	S17
Figure S13	Time-dependent UV/Vis spectra and emission spectra during the reaction between $\text{Au}_{25}(\text{PET})_{18}$ and $\text{Ag}_{44}(\text{FTP})_{30}$ clusters taken in the ratio ($\text{Au}_{25}:\text{Ag}_{44}$) of 7:1	S18
Figure S14	Time-dependent UV/Vis spectra and emission spectra during the reaction between $\text{Au}_{25}(\text{PET})_{18}$ and $\text{Ag}_{44}(\text{FTP})_{30}$ clusters taken in the ratio ($\text{Au}_{25}:\text{Ag}_{44}$) of 1.7:1.0.	S18
Figure S15	Negative ion mode MALDI MS spectra of the $\text{Au}_{25-x}\text{Ag}_x(\text{PET})_{18-y}(\text{FTP})_y$ ($x=0,1-13$; $y=0,1-8$) product clusters formed at $\text{Au}_{25}(\text{PET})_{18}:\text{Ag}_{44}(\text{FTP})_{30}$ ratio of 0.7:1 and 1:1	S19
Figure S16	ESI MS spectrum of the mixture of $\text{Au}_{25}(\text{PET})_{18}$ and $\text{Ag}_{44}(\text{FTP})_{30}$ (in $\text{Au}_{25}:\text{Ag}_{44}$ ratio 1:1) measured 1h after mixing	S20
Figure S17	Time-dependent UV/Vis spectra during the reaction between $\text{Au}_{25}(\text{PET})_{18}$ and $\text{Ag}_{44}(\text{FTP})_{30}$ clusters taken in the ratio ($\text{Au}_{25}:\text{Ag}_{44}$) of 1.0:1.0.	S21
Figure S18	Time-dependent UV/Vis spectra during the reaction between $\text{Au}_{25}(\text{PET})_{18}$ and $\text{Ag}_{44}(\text{FTP})_{30}$ clusters taken in the ratio ($\text{Au}_{25}:\text{Ag}_{44}$) of 0.7:1.0.	S21
Figure S19	MALDI MS of the $\text{Au}_{25}(\text{FTP})_{18}$ clusters synthesized through ligand exchange of $\text{Au}_{25}(\text{n-BuS})_{18}$ with 4-fluorothiophenol.	S22

Figure S20	Time-dependent changes in the MALDI MS spectra of the products formed during the reaction between $\text{Au}_{25}(\text{FTP})_{18}$ and $\text{Ag}_{44}(\text{FTP})_{30}$.	S23
Figure S21	MALDI MS spectra of the clusters formed after 24 h in the reaction between $\text{Au}_{25}(\text{FTP})_{18}$ and $\text{Ag}_{44}(\text{FTP})_{30}$.	S24
Figure S22	ESI MS spectra measured immediately after mixing $\text{Au}_{25}(\text{PET})_{18}$ and $\text{Ag}_{44}(\text{FTP})_{30}$ at a $\text{Au}_{25}:\text{Ag}_{44}$ ratio of 1.7:1	S25
Figure S23	Time-dependent changes of group II features appeared in the MALDI MS spectra during the reaction of $\text{Ag}_{44}(\text{FTP})_{30}$ and $\text{Au}_{25}(\text{PET})_{18}$	S26
Figure S24	ESI MS spectra showing the formation of $\text{Au}_x\text{Ag}_{44-x}(\text{FTP})_{30}$ during the reaction between $\text{Au}_{25}(\text{FTP})_{18}$ and $\text{Ag}_{44}(\text{FTP})_{30}$	S27
Figure S25	UV/Vis spectra of the reaction mixtures (after 1h of the reaction) at $\text{Au}_{25}:\text{Ag}_{44}$ ratios of 14:1, 7:1, 1.7:1 (A) and 1:1 and 0.7:1 (B).	S28
Figure S26	Negative ion mode MALDI MS spectra of the products formed immediately and after 1h of mixing $\text{Au}_{25}(\text{n-BuS})_{18}$ and $\text{Ag}_{44}(\text{FTP})_{30}$	S29
Figure S27	MALDI MS spectra of the products formed immediately after mixing $\text{Au}_{25}(\text{PET})_{18}$ and $\text{Ag}_{44}(\text{MBA})_{30}$ clusters.	S30
Figure S28	Structures of $\text{Au}_{25}(\text{SR})_{18}$ and $\text{Ag}_{44}(\text{SR})_{30}$ showing different types of Ag/Au atoms and Ag-S/Au-S bonds	S30
Table S1	Isomers of $\text{Ag}_{43}\text{Au}(\text{SH})_{30}$ and their energies	S31
Table S2	Isomers of $\text{Au}_{24}\text{Ag}(\text{SH})_{18}$ and their energies	S31
Table S3	Energies of undoped clusters, metal atoms, and metal-ligand fragments	S31
Table S4	Energies of the reaction, $\text{Au} + \text{Ag}_{44}(\text{SR})_{30} \rightarrow \text{AuAg}_{43}(\text{SR})_{30} + \text{Ag}$	S32
Table S5	Energies of the reaction, $\text{Au-SR} + \text{Ag}_{44}(\text{SR})_{30} \rightarrow \text{AuAg}_{43}(\text{SR})_{30} + \text{Ag-SR}$	S32

Table S6	Energies of the reaction, $\text{Ag} + \text{Au}_{25}(\text{SR})_{18} \rightarrow \text{Au}_{24}\text{Ag}(\text{SR})_{18} + \text{Au}$	S32
Table S7	Energies of reaction, $\text{Ag-SR} + \text{Au}_{25}(\text{SR})_{18} \rightarrow \text{Au}_{24}\text{Ag}(\text{SR})_{18} + \text{Au-SR}$	S32
Table S8	HOMO-LUMO energy difference of un-exchanged and alloy clusters	S33
Table S9	Energy difference (in eV) between the HOMO of $\text{AuAg}_{43}(\text{SR})_{30}$ and LUMO of $\text{Au}_{24}\text{Ag}(\text{SR})_{18}$ as a function of the substituent positions	S33
Figure S29	Borromean-Rings diagram of $\text{Au}_{25}(\text{SMe})_{18}$	S34
Figure S30	Structure of $\text{Ag}_{44}(\text{SR})_{30}$ showing the accessibility of the icosahedral core Ag atoms	S35
Figure S31	Mass spectra showing the thiolate fragments of $\text{Ag}_{44}(\text{FTP})_{30}$ and $\text{Au}_{25}(\text{PET})_{18}$	S35
Scheme S1	Schematic of the reaction between $\text{Au}_{25}(\text{SR}_1)_2$ with $\text{Ag}(\text{SR}_2)_2$ showing M-SR exchange	S36
Scheme S2	Schematic of the reaction between $\text{Au}_{25}(\text{SR}_1)_2$ with $\text{Ag}(\text{SR}_2)_2$ showing Ag/Au exchange	S37
	Discussion on the charge states of $\text{Au}_{25}(\text{SR})_{18}$ and the position of Ag in the $\text{Au}_{25-x}\text{Ag}_x(\text{PET})_{18-y}(\text{FTP})_y$	S38

Instrumentation

Matrix assisted laser desorption ionization mass spectrometric (MALDI MS) studies were conducted using a Voyager DE PRO Biospectrometry Workstation (Applied Biosystems) matrix assisted laser desorption ionization time-of-flight mass spectrometer (MALDI TOF MS). Spectrometer was operated in the linear mode. The UV/Vis spectra were recorded using a Perkin Elmer Lambda 25 UV/Vis spectrometer. Absorption spectra were typically measured in the range of 200-1100 nm. Luminescence measurements were carried out on a JobinYvonNanoLog instrument.

ESI MS measurements

Waters Synapt G2-Si High Definition Mass Spectrometer equipped with Electrospray ionization, matrix assisted laser desorption ionization and ion mobility separation was used. All the samples were analyzed in negative mode electrospray ionization. The instrumental parameters were first

optimized for $\text{Au}_{25}(\text{PET})_{18}$ and other samples were analyzed using the similar setting with slight modification depending on the sample. About 0.1 mg of as prepared samples were diluted dichloromethane (DCM) and directly infused to the system without any further purification. The instrument was calibrated using NaI as calibrant. The optimized conditions were as follows:

Sample concentration: 0.1 mg/mL
Diluents: DCM
Sample flow rate: 10-20 $\mu\text{L}/\text{min}$
Source Voltage: 2.5-3 kV
Cone Voltage: 120-140 V
Source Offset: 80-120 V
Trap Collision Energy: 0-20 V (For higher $\text{Ag}_{44}(\text{FTP})_{30}$ concentration)
Transfer Collision Energy: 0-2 V
Source Temperature: 80-100°C
Desolvation Temperature: 150-200°C
Desolvation Gas Flow: 400 L/h

For fragmentation of $\text{Au}_{25}(\text{PET})_{18}$, the molecular ion peak was first mass selected in the quadrupole which is situated before T-wave region. Collision induced dissociation was performed in the first T-wave region (trap) and analyzed in the TOF region. A nominal collision energy of 80-120 V was used for the CID experiments. Below 50 V, $\text{Au}_{25}(\text{PET})_{18}$ did not show any considerable fragmentation. Similar fragmentation was observed when the same sample was fragmented in-source without any mass selection.

$\text{Ag}_{44}(\text{FTP})_{30}$ clusters were analyzed in DCM medium as the reaction was carried out in pure DCM. The experimental parameters optimized for $\text{Ag}_{44}(\text{FTP})_{30}$ are as follows:

Sample concentration: 0.05 mg/mL
Diluents: DCM
Sample flow rate: 10 $\mu\text{L}/\text{min}$
Source Voltage: 0.3-1.5 kV
Cone Voltage: 20-60 V
Source Offset: 30-40 V
Trap Collision Energy: 0-4 V
Transfer Collision Energy: 0-2 V
Source Temperature: 80°C
Desolvation Temperature: 150°C
Desolvation Gas Flow: 400 L/h

MALDI MS measurements: The matrix used was trans-2-[3-(4-tertbutylphenyl)-2-methyl-2-propenylidene]malononitrile (DCTB, > 98%). A solution of 6.2 mg of DCTB in 0.5 mL of dichloromethane was used for the measurements. Appropriate volumes of the sample solutions and DCTB solutions in DCM were mixed thoroughly and spotted on the sample plate and allowed to dry at ambient conditions. All the MALDI MS measurements were carried out at the threshold laser fluence in order to minimize fragmentation. All the spectra reported are of negative ions. An average of 100 shots were taken for each mass spectrum.

Synthesis of $\text{Na}_4[\text{Ag}_{44}(\text{MBA})_{30}]$: Initially 128 mg of AgNO_3 was added to a mixture of DMSO and water (4:7 volume ratio) in a beaker under constant stirring. About 173 mg of MBA was then added to the mixture while stirring. This results in the formation of thiolates which gives a cloudy appearance to the solution. About 50% CsOH was then added drop wise till the solution was clear and a greenish yellow color appeared. After this, NaBH_4 solution (283 mg in 9 mL water) was added dropwise. Slowly the color changes to deep brown and after 1 h the color becomes deep red indicating the formation of clusters. This crude cluster solution was purified by precipitating it by the addition of DMF. The precipitate was collected by centrifugation. The centrifugate was then removed and the cluster was extracted in citric acid containing DMF. Role of citric acid is to acidify all the protons of carboxylic acid groups of MBA ligand which will make the cluster soluble in DMF. The resultant cluster solution was then again precipitated using toluene and centrifuged. The acidification step was repeated one more time. After this, the precipitate was redissolved in DMF to get the purified cluster.

Computational Details: The $\text{Ag}(4d^{10}5s^1)$, $\text{Au}(5d^{10}6s^1)$, and $\text{S}(3s^23p^4)$ electrons were treated as valence and the inner electrons were included in a frozen core. The GPAW setups¹ for gold and silver included scalar-relativistic corrections. The exchange-correlation functional employed was the generalized gradient approximation of Perdew, Burke and Ernzerhof (GGA-PBE).² We used a 0.2\AA grid spacing for electron density in all calculations and a convergence criterion of 0.05 eV/\AA for the residual forces on atoms was used in all structure optimizations, without any symmetry constraints. For computational efficiency during the structural optimizations, rather than employing the finite-difference real-space grid method for the expansion of the pseudowavefunctions, we used instead the LCAO method³ as implemented in GPAW by employing a double zeta plus polarization (DZP) basis set. For greater precision in our reaction energy calculations, we then recalculated the total energies at this geometry minimum using the finite-difference method in GPAW. The crystal structures of $\text{Au}_{25}(\text{SR})_{18}$ ⁴ and $\text{Ag}_{44}(\text{SR})_{30}$ ⁵ were used for the initial structures of the calculations. For efficient computations, we terminated each sulfur atom with a hydrogen atom in all the clusters.

The initial structures of $[\text{Au}_{25}(\text{SR})_{18}]^-$ and $[\text{Ag}_{44}(\text{SR})_{30}]^{4+}$ were first geometry optimized, and then a single metal (Ag or Au) atom was replaced in a symmetry non-equivalent position and the geometries of the resulting $[\text{Au}_{24}\text{Ag}(\text{SR})_{18}]^-$ and $[\text{Au}_{43}\text{Au}(\text{SR})_{30}]^{4+}$ configurations were then optimized. The value of the total energy of each isomer was taken at the geometry-optimized configuration using the LCAO method but then recalculated using the more accurate finite-difference method in GPAW. We also computed the total energies of Au and Ag atoms using spin-polarization applying Hund's rule to the ground-state electronic configuration (of the isolated atoms) and the energies in the geometry-optimized configurations of AuSH and AgSH clusters in charge neutral states. The exchange reaction energies of Au(Ag) and Au(Ag)-SH into different positions in both of the clusters were calculated as $E(\text{Reaction}) = E(\text{Products}) - E(\text{Reactants})$

The structures of $\text{Au}_{25}[\text{PET}]_{18}$ and $\text{Ag}_{44}[\text{FTP}]_{30}$ were built up with the help of Avogadro software package⁶ and visualizations were created with Visual Molecular Dynamics (VMD)

software.⁷ The structures have been modeled assuming coordinates from the crystal structures of $\text{Au}_{25}(\text{SR})_{18}$ ⁴ and $\text{Ag}_{44}(\text{SR})_{30}$.⁵

Supporting Information 1

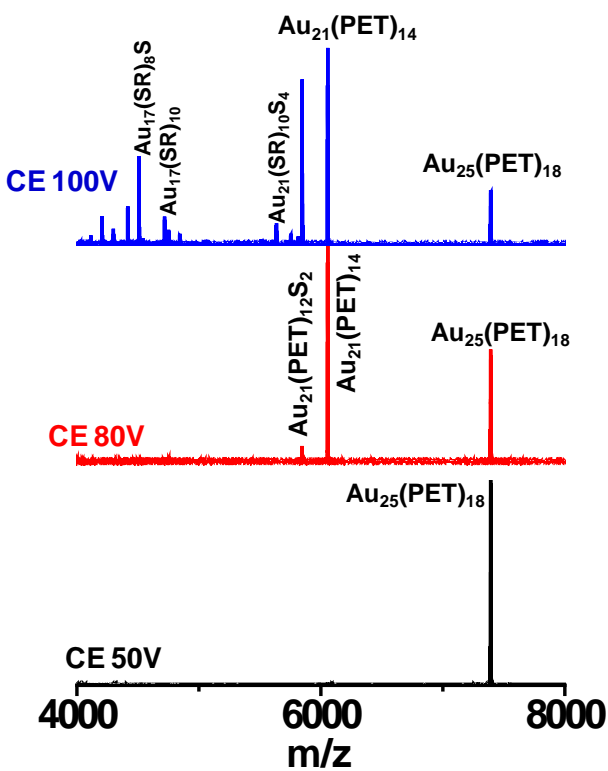


Figure S1. Collision energy-dependent ESI MS spectra of $\text{Au}_{25}(\text{PET})_{18}$. Loss of $\text{Au}_4(\text{SR})_4$ unit resulting in $\text{Au}_{21}(\text{SR})_{14}$ is the typical fragmentation mode of $\text{Au}_{25}(\text{SR})_{18}$.⁸

Supporting Information 2

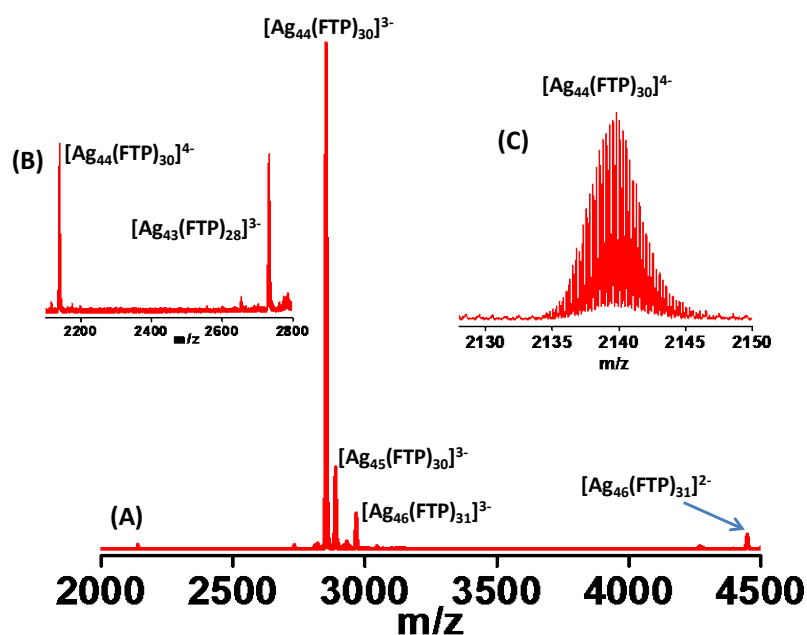


Figure S2. ESI MS spectrum of $\text{Ag}_{44}(\text{FTP})_{30}$ shown in trace b' of Figure 1B. Lower m/z region in A is expanded in B to show the fragmentation of $[\text{Ag}_{44}(\text{FTP})_{30}]^{4-}$ to give $[\text{Ag}_{43}(\text{FTP})_{28}]^{3-}$. Such a fragmentation pattern is in accordance with previous reports (see Ref. 2e and 2g in main manuscript). Isotope distribution of $[\text{Ag}_{44}(\text{FTP})_{30}]^{4-}$ is shown in C. Species such as $[\text{Ag}_{45}(\text{FTP})_{30}]^{3-}$ and $[\text{Ag}_{46}(\text{FTP})_{31}]^{3-}$ were also detected which could be due to minor byproducts.

Supporting Information 3

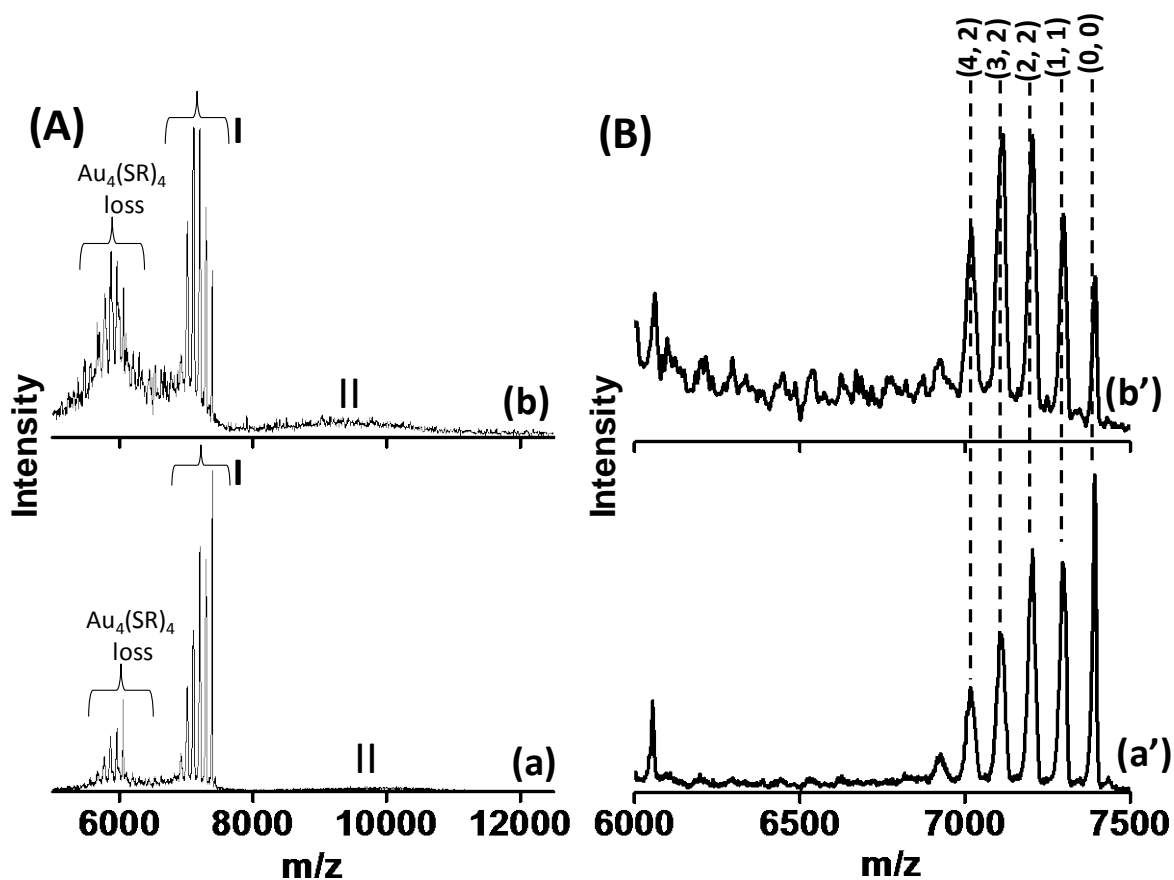


Figure S3. MALDI MS spectra showing the temporal evolution of the products formed after mixing of Au₂₅(PET)₁₈ and Ag₄₄(FTP)₃₀ clusters at Au₂₅:Ag₄₄ ratio of 14:1. Traces a and b in (A) are the mass spectra of the reaction mixture immediately after mixing and after 1h of mixing, respectively. The group I in a and b are expanded in a' and b', respectively. The numbers in parentheses, (x, y), are according to the general molecular formula, Au_{25-x}Ag_x(PET)_{18-y}(FTP)_y. Au₄(SR)₄ loss is a standard fragmentation pattern of Au₂₅(SR)₁₈ clusters (see Figure S1).

Supporting Information 4

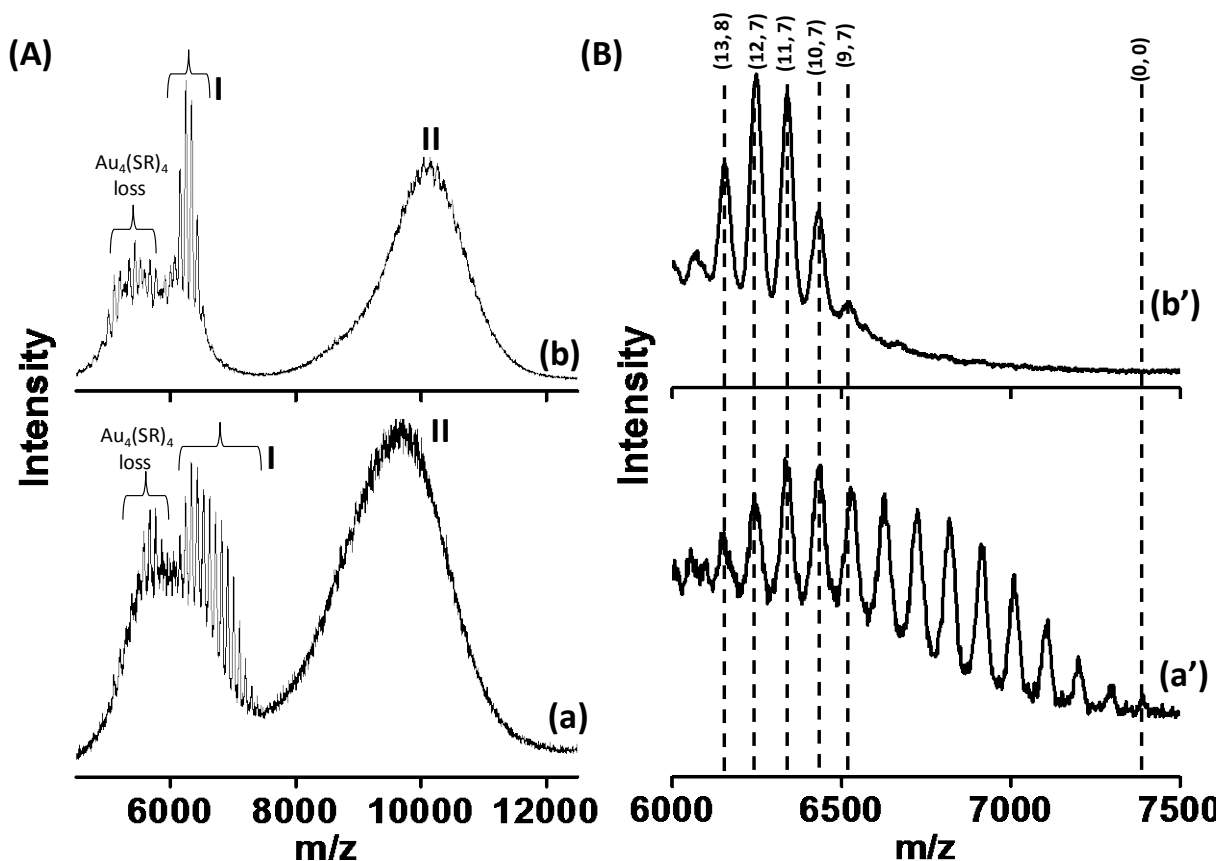


Figure S4. MALDI MS spectra showing the temporal evolution of the products formed after mixing of $\text{Au}_{25}(\text{PET})_{18}$ and $\text{Ag}_{44}(\text{FTP})_{30}$ clusters at $\text{Au}_{25}:\text{Ag}_{44}$ ratio of 1.7:1. Traces a and b in (A) are the mass spectra of the reaction mixture immediately after mixing and after 1h of mixing, respectively. The group I in a and b are expanded in a' and b', respectively. The numbers in parentheses, (x, y), are according to the general molecular formula, $\text{Au}_{25-x}\text{Ag}_x(\text{PET})_{18-y}(\text{FTP})_y$. Au_4SR_4 loss is a standard fragmentation pattern of $\text{Au}_{25}(\text{SR})_{18}$ clusters (see Figure S1).

Supporting Information 5

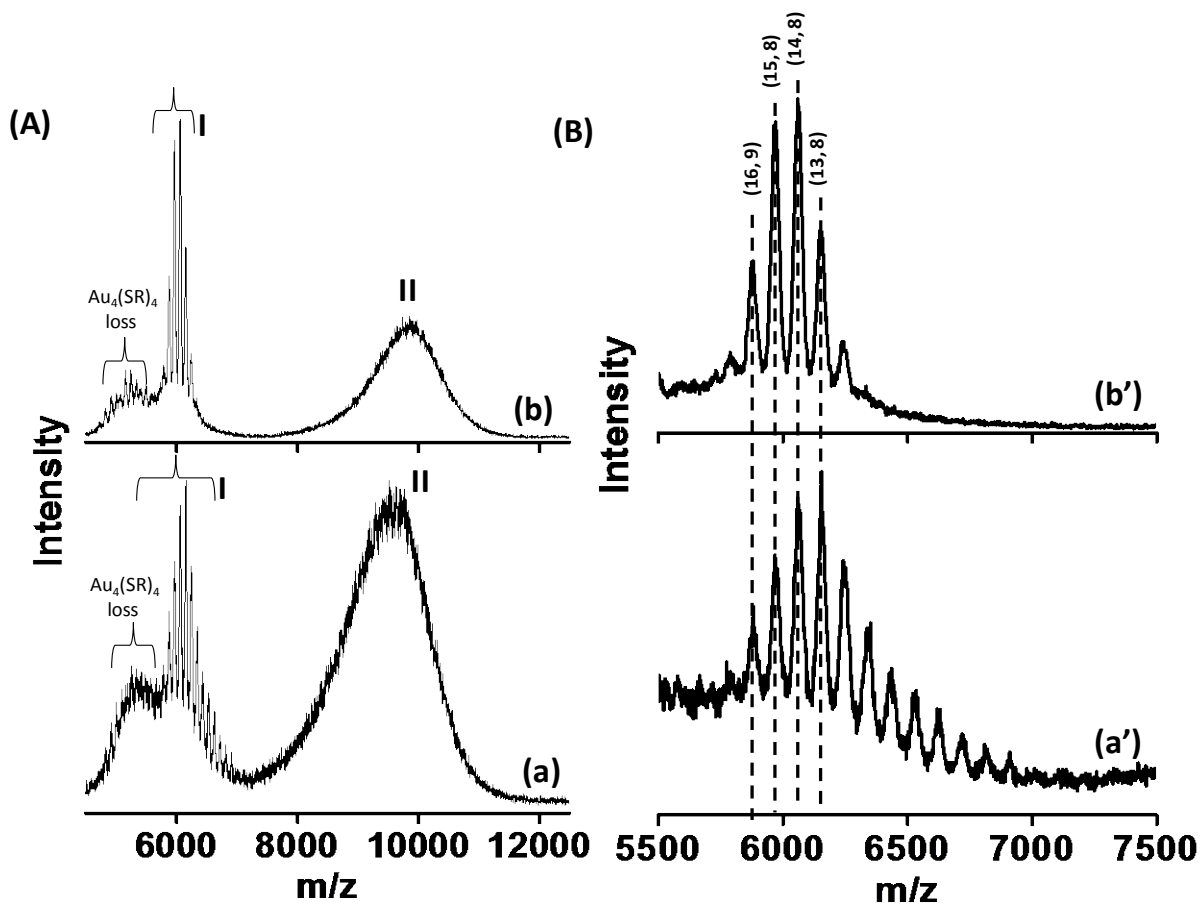


Figure S5. MALDI MS spectra showing the temporal evolution of the products formed after mixing of $\text{Au}_{25}(\text{PET})_{18}$ and $\text{Ag}_{44}(\text{FTP})_{30}$ clusters at $\text{Au}_{25}:\text{Ag}_{44}$ ratio of 1.0:1.0. Traces a and b in (A) are the mass spectra of the reaction mixture immediately after mixing and after 1h of mixing, respectively. The group I in a and b are expanded in a' and b', respectively. The numbers in parenthesis, (x, y), are according to the general molecular formula, $\text{Au}_{25-x}\text{Ag}_x(\text{PET})_{18-y}(\text{FTP})_y$.

Note: In Figures S3, S4 and S14, peaks labels are assigned considering the peak maxima alone. However, ESI MS data (see Figure 3 insets, Figures S5-S9), shows that there are additional peaks in each of these features which is not resolved in MALDI MS due to the broadness of peaks.

Supporting Information 6

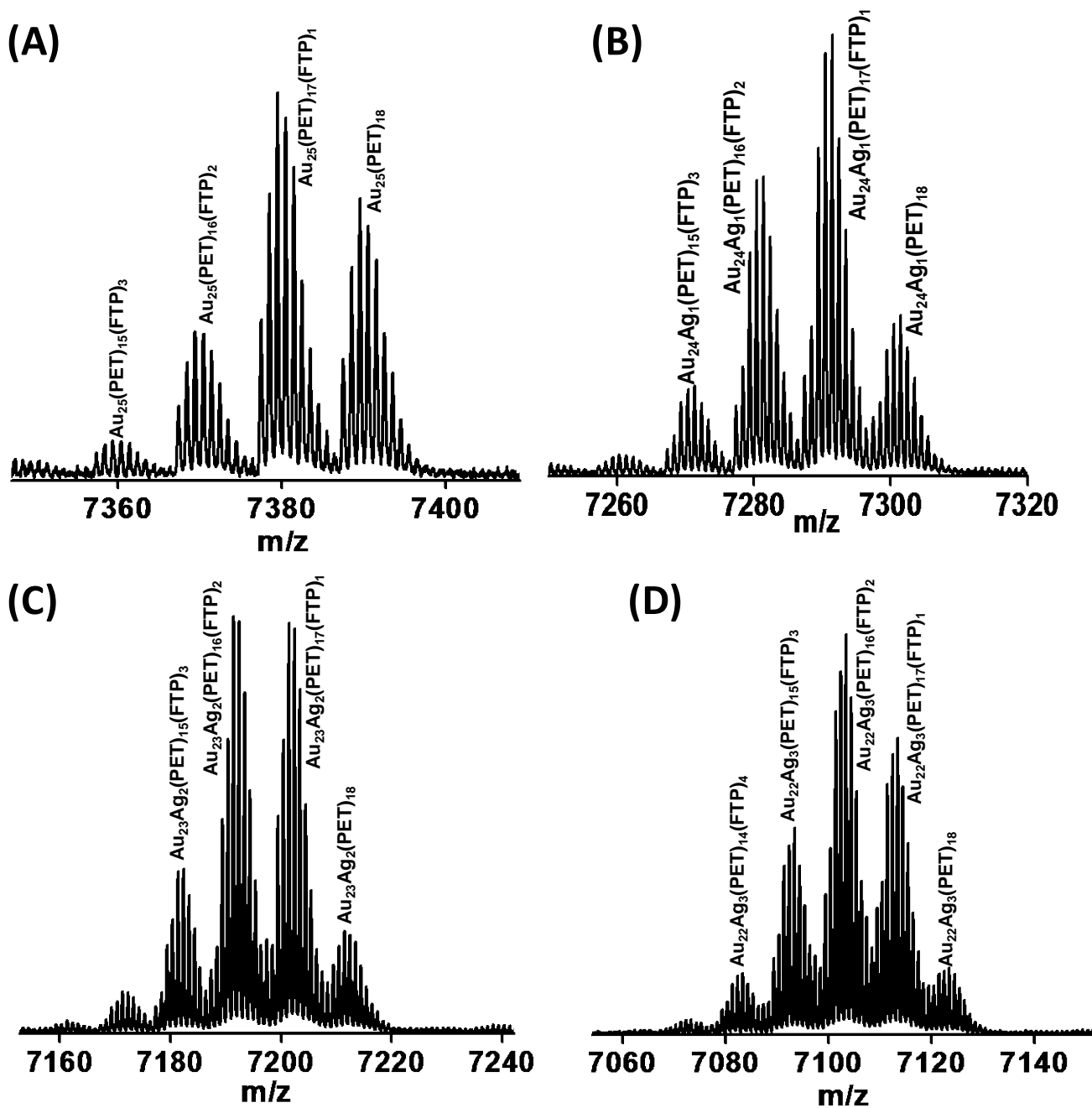


Figure S6. Panels A-D shows the expansion of features (0, 0-3), (1, 0-4), (2, 0-4) and (3, 0-4), (shown in Figure 3), respectively. The numbers, for example, (0, 0-3) is according to the general formula, Au_{25-x}Ag_x(PET)_{18-y}(FTP)_y.

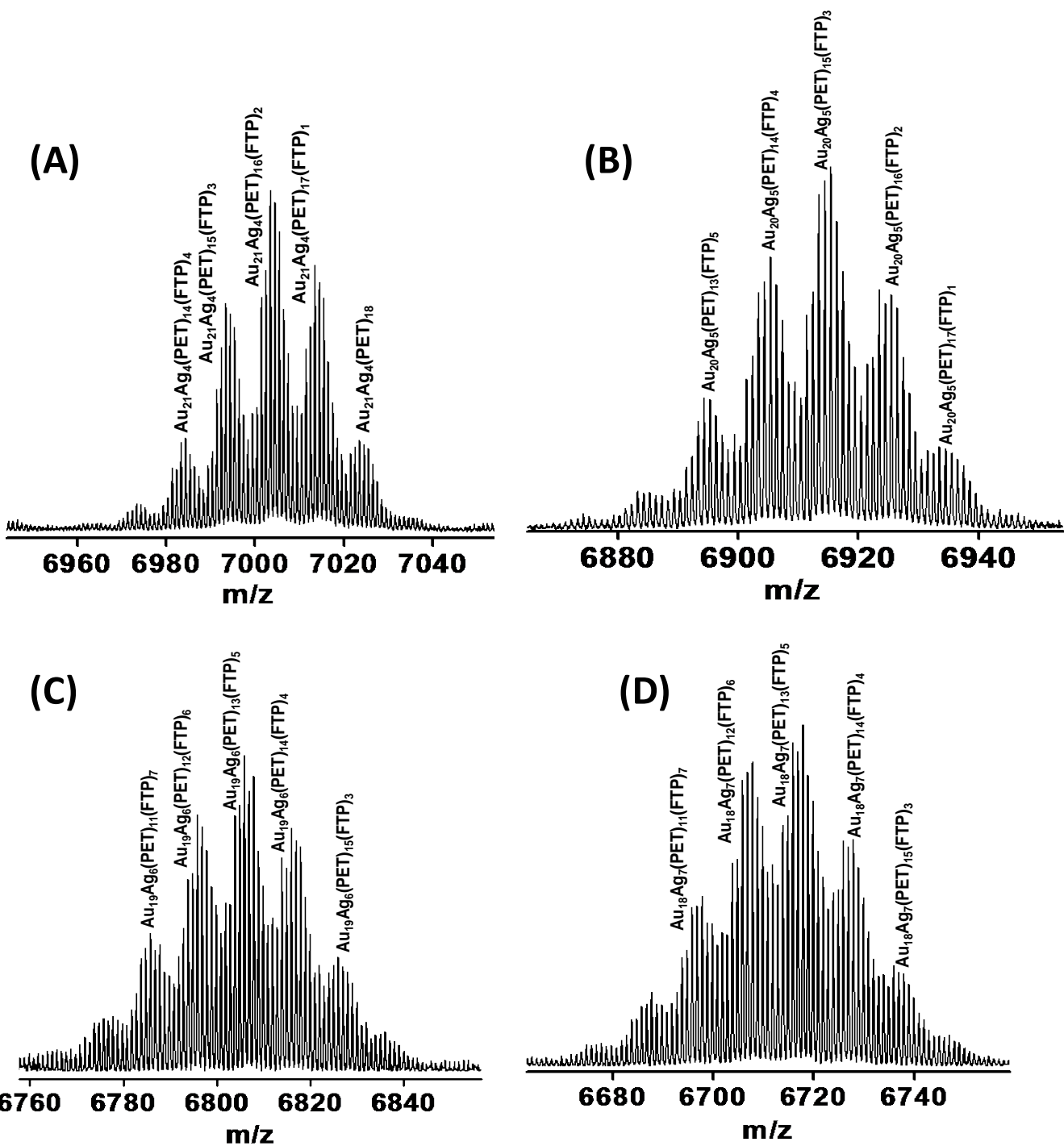


Figure S7. Panels A-D shows the expansion of features (4, 1-5), (5, 1-5), (6, 3-8) and (7, 3-8), (shown in Figure 3) respectively. The numbers, for example, (4, 1-5) is according to the general formula, $Au_{25-x}Ag_x(PET)_{18-y}(FTP)_y$.

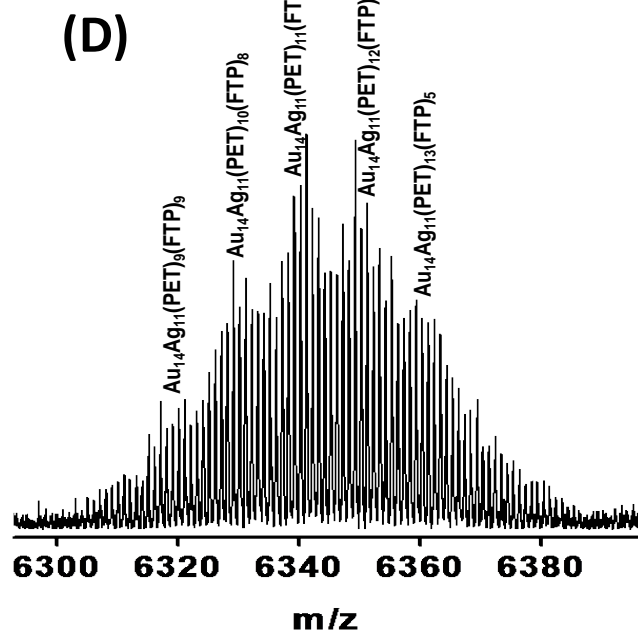
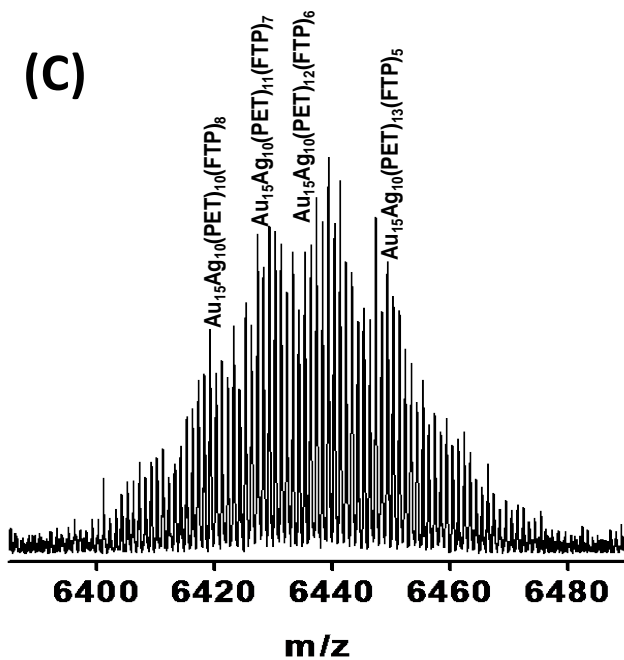
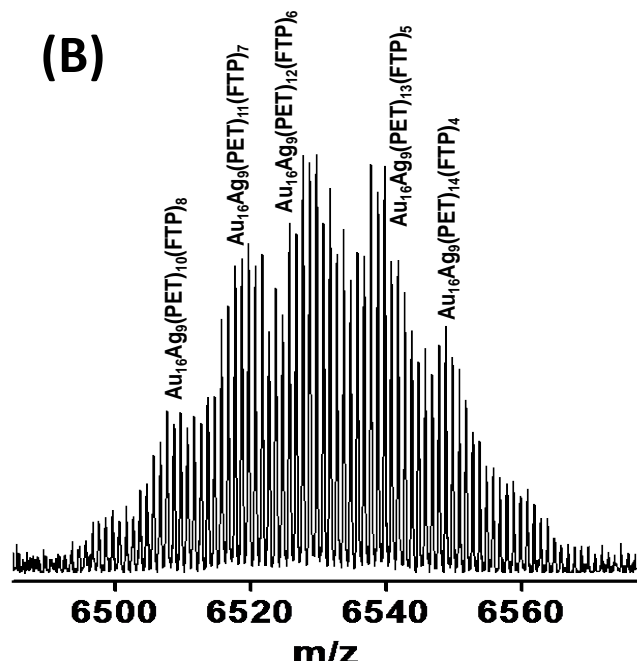
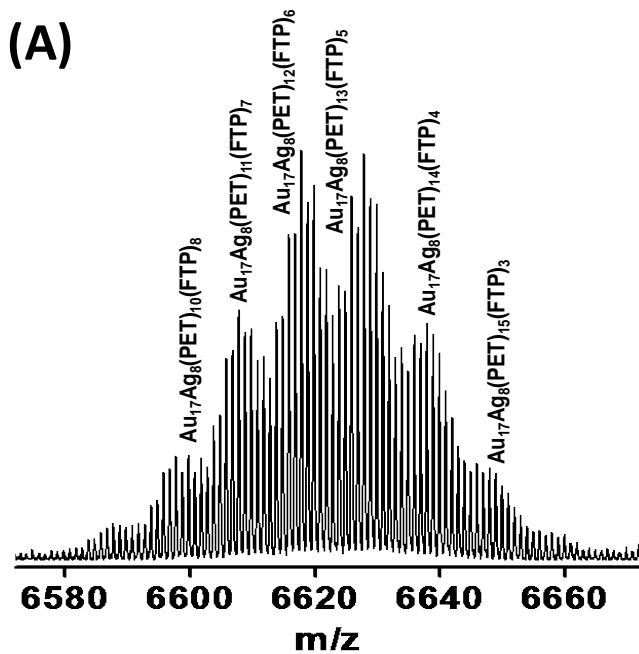


Figure S8. Panels A-D shows the expansion of features (8, 3-9), (9, 3-9), (10, 4-9) and (11, 4-9), (shown in Figure 3) respectively. The numbers, for example, (8, 3-9) is according to the general formula, $\text{Au}_{25-x}\text{Ag}_x(\text{PET})_{18-y}(\text{FTP})_y$.

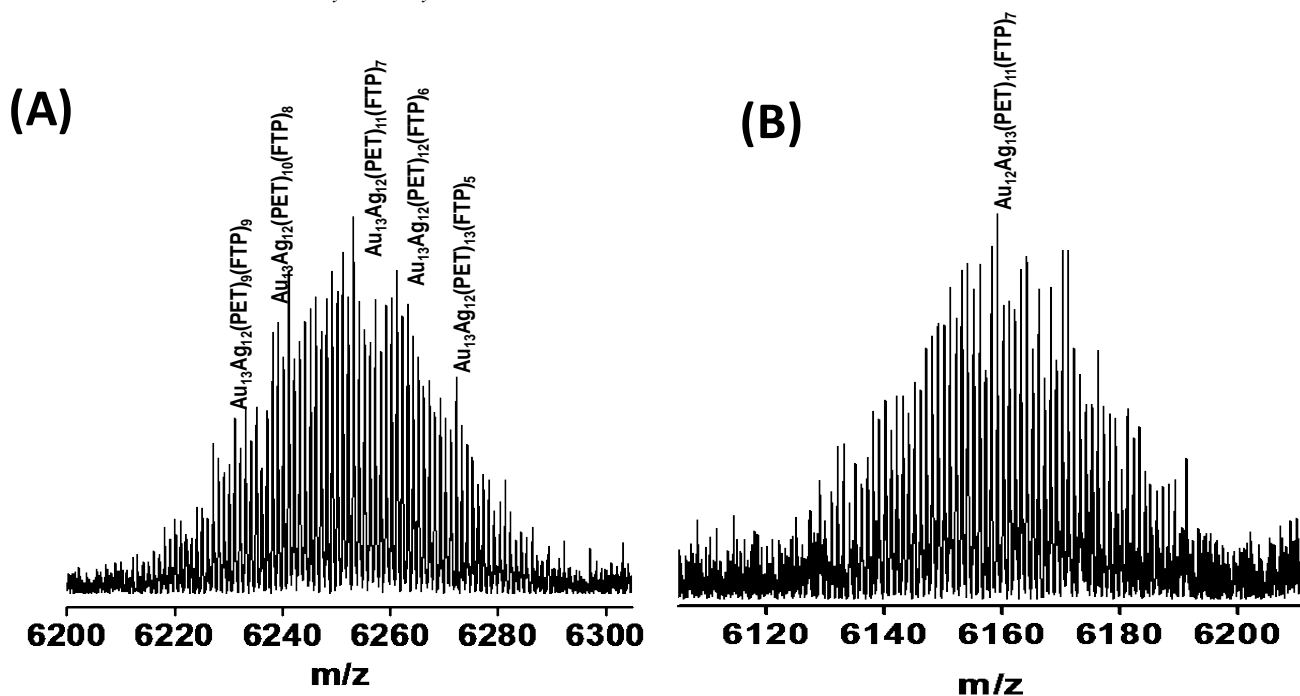


Figure S9. Panels A and B shows the expansion of features (12, 4-9) and (13, 4-9), (shown in Figure 3) respectively. The numbers, for example, (12, 4-9) is according to the general formula, $\text{Au}_{25-x}\text{Ag}_x(\text{PET})_{18-y}(\text{FTP})_y$.

Supporting Information 7

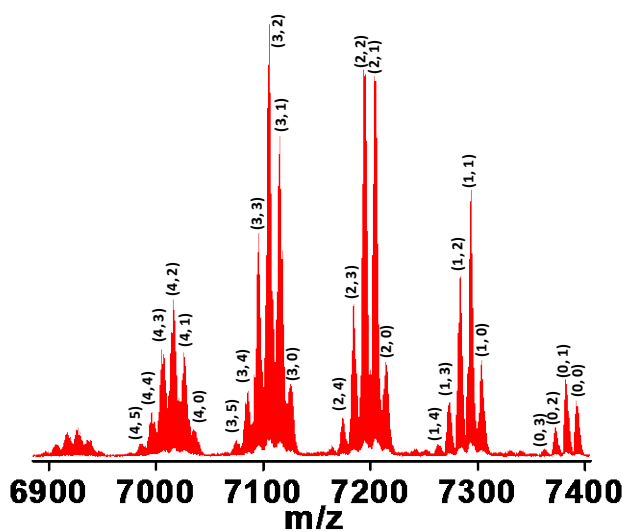


Figure S10. Expansion of the mass spectra in panel A of Figure 3 in the Article.

Supporting Information 8

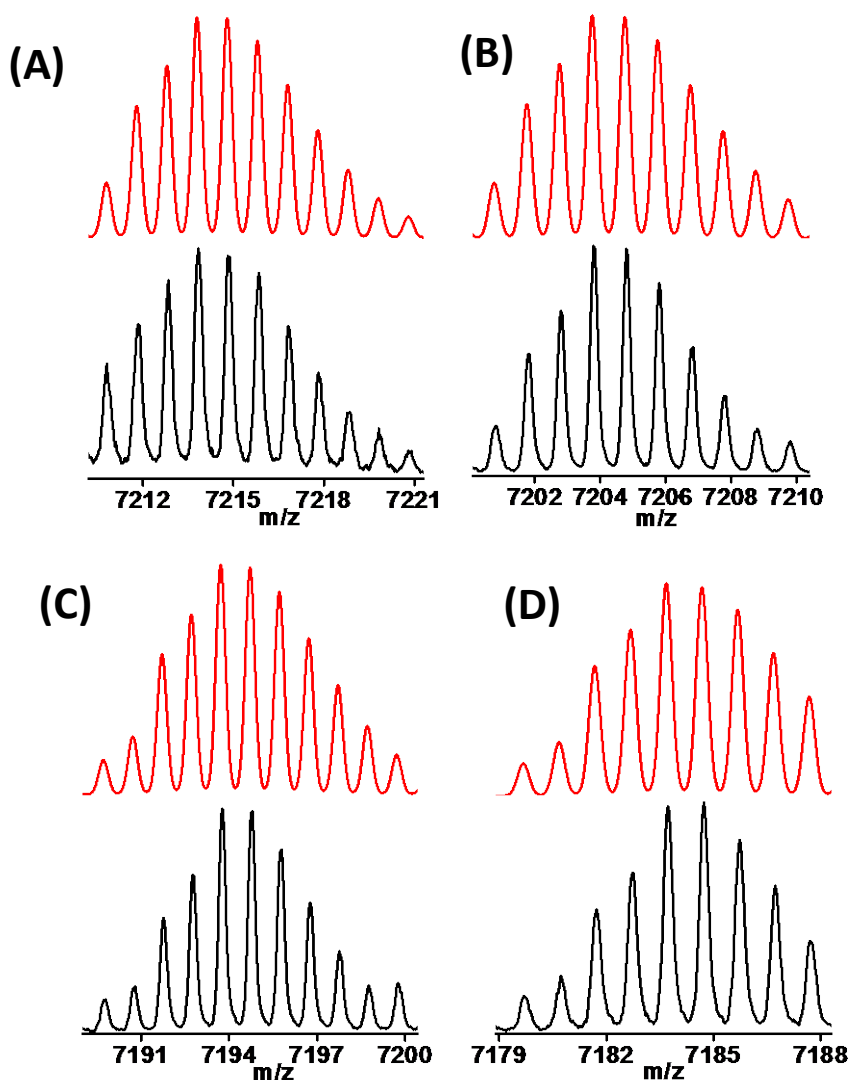


Figure S11. Experimental (black trace) and theoretical (red trace) isotope distributions of (A) $\text{Au}_{23}\text{Ag}_2(\text{PET})_{18}$, (B) $\text{Au}_{23}\text{Ag}_2(\text{PET})_{17}(\text{FTP})_1$, (C) $\text{Au}_{23}\text{Ag}_2(\text{PET})_{16}(\text{FTP})_2$ and (D) $\text{Au}_{23}\text{Ag}_2(\text{PET})_{15}(\text{FTP})_3$. These species corresponds to those labeled as (2, 0), (2, 1), (2, 2) and (2, 3), respectively in Figure 3A inset.

Supporting Information 9

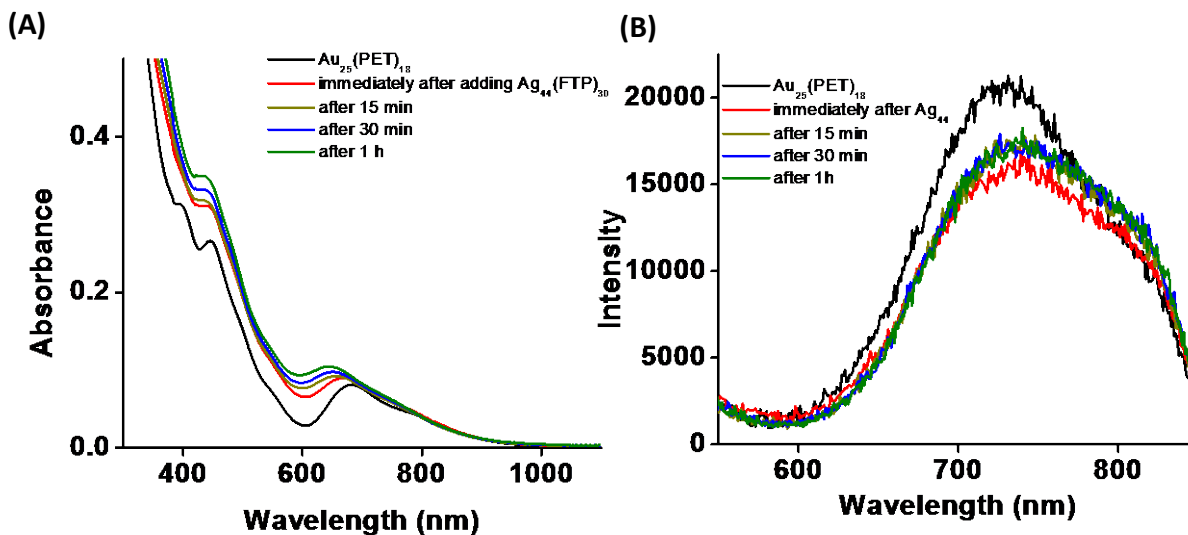


Figure S12. Time-dependent changes in the UV/Vis (A) and emission (B) spectra during the reaction between Au₂₅(PET)₁₈ and Ag₄₄(FTP)₃₀ clusters taken in the ratio (Au₂₅:Ag₄₄) of 14:1. Solvent used was dichloromethane.

Note: Emission spectrum of Au₂₅(PET)₁₈⁻ shows a peak at 720 nm and a hump at 800 nm as reported previously by Jin et al.⁹ When Ag₄₄(FTP)₃₀ was added to Au₂₅(PET)₁₈, in all the cases (Figures S12-S14), there was an immediate decrease in intensity of these features. But, as time goes on, intensity increased with a slight redshift of about 10 nm (for both features).

Supporting Information 10

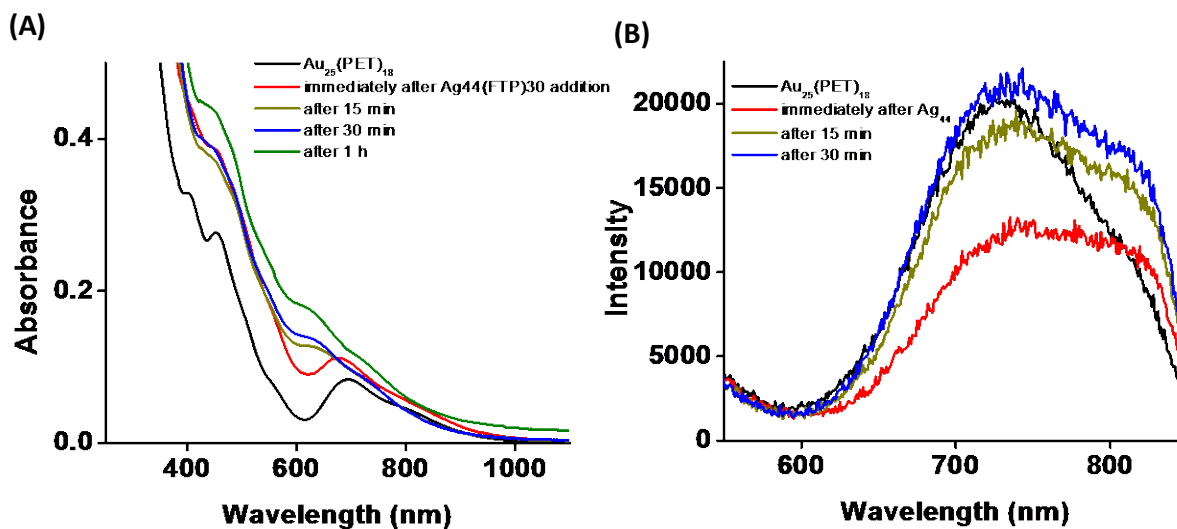


Figure S13. Time-dependent UV/Vis spectra (A) and emission (B) spectra during the reaction between $Au_{25}(PET)_{18}$ and $Ag_{44}(FTP)_{30}$ clusters taken in the ratio ($Au_{25}:Ag_{44}$) of 7:1.

Supporting Information 11

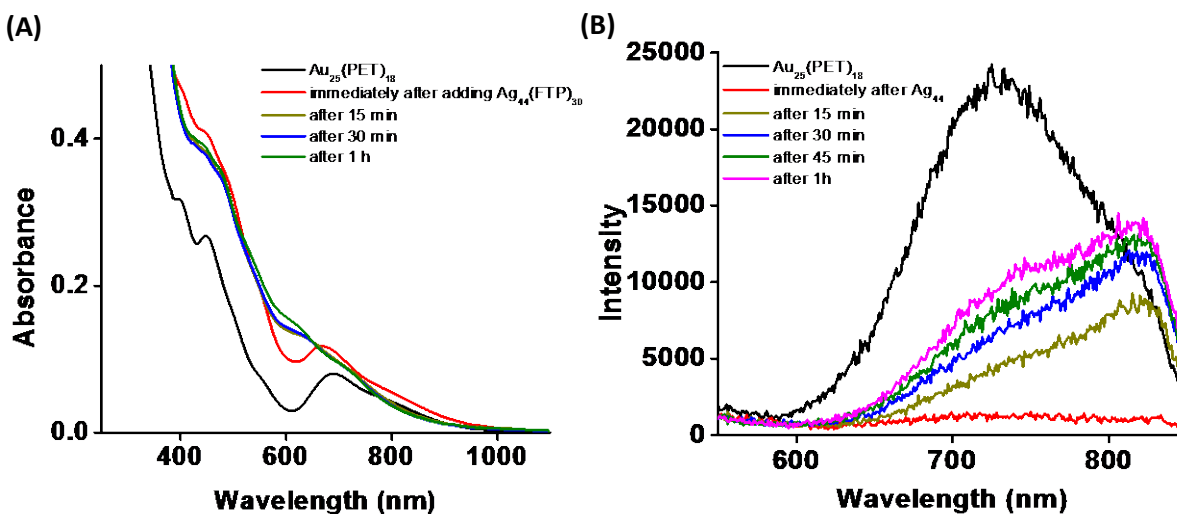


Figure S14. Time-dependent UV/Vis spectra (A) and emission (B) spectra during the reaction between $Au_{25}(PET)_{18}$ and $Ag_{44}(FTP)_{30}$ clusters taken in the ratio ($Au_{25}:Ag_{44}$) of 1.7:1.0.

Supporting Information 12

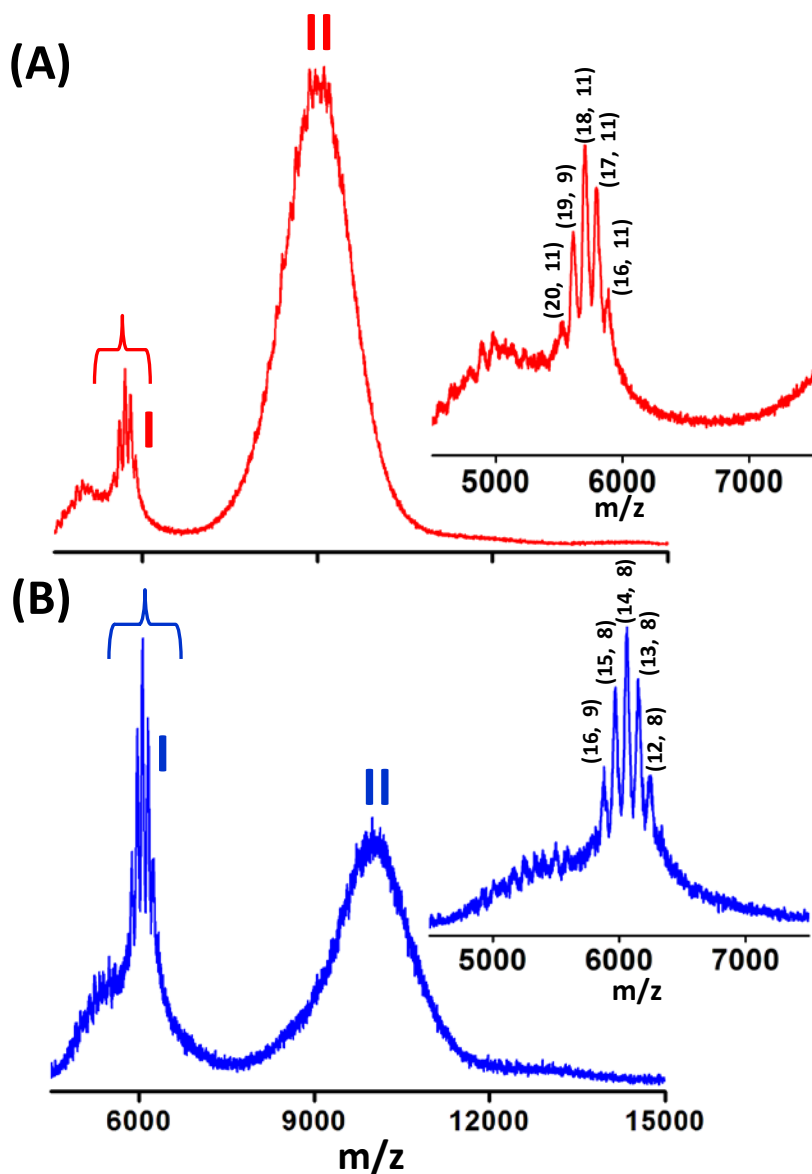


Figure S15. Negative ion mode MALDI MS spectra of the $Au_{25-x}Ag_x(PET)_{18-y}(FTP)_y$ ($x=0,1-13$; $y=0,1-8$) product clusters formed at $Au_{25}(PET)_{18}:Ag_{44}(FTP)_{30}$ ratio of (A) 0.7:1 and (B) 1:1. Group I is expanded in the inset. The numbers (x, y) in parenthesis (in the insets), are according to the general molecular formula, $Au_{25-x}Ag_x(PET)_{18-y}(FTP)_y$.

Supporting Information 13

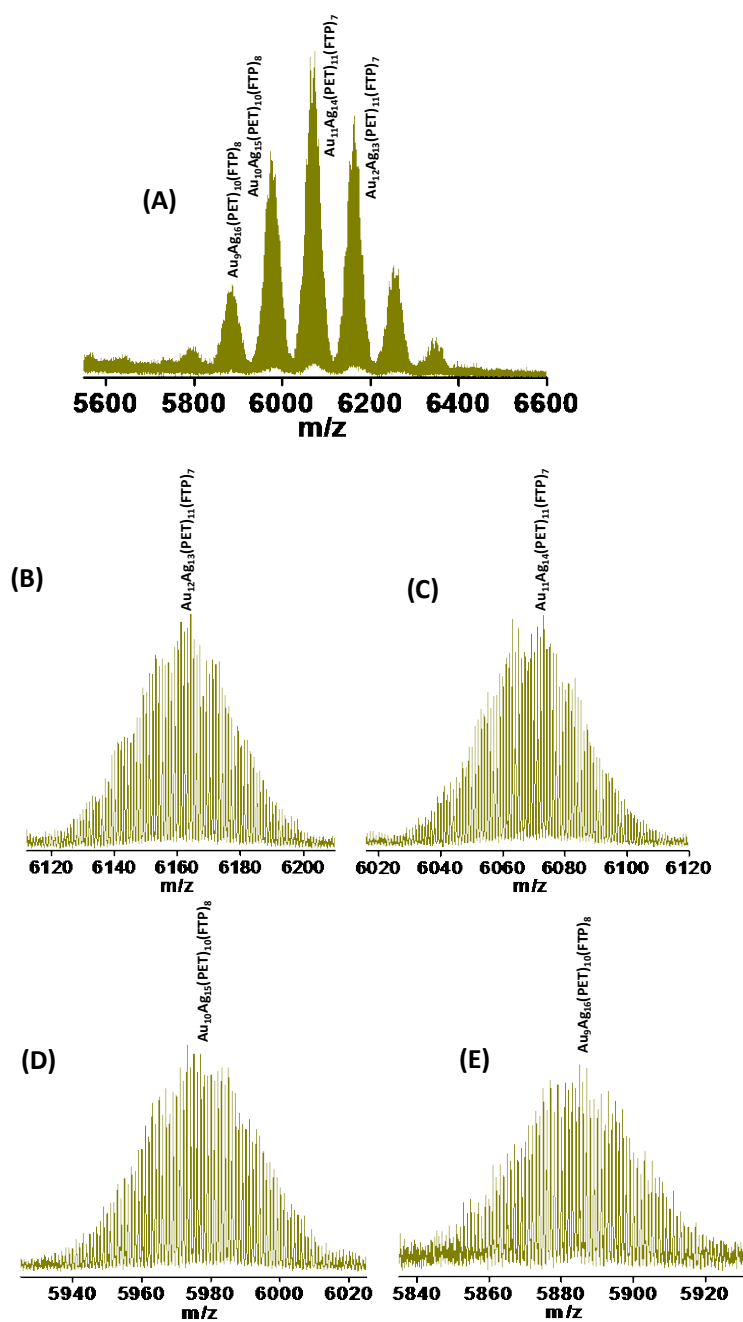


Figure S16. ESI MS spectrum of the mixture of $\text{Au}_{25}(\text{PET})_{18}$ and $\text{Ag}_{44}(\text{FTP})_{30}$ (in $\text{Au}_{25}:\text{Ag}_{44}$ ratio 1:1) measured 1h after mixing. Features labelled in panel A are expanded in panels B-E. The peak labels in B-E are given according to the peak maxima in each bunch. However, due to large number of Ag atoms and resulting isotopic width, features within these bunches are not resolved fully (unlike in the Figure S6 and S7).

Supporting Information 14

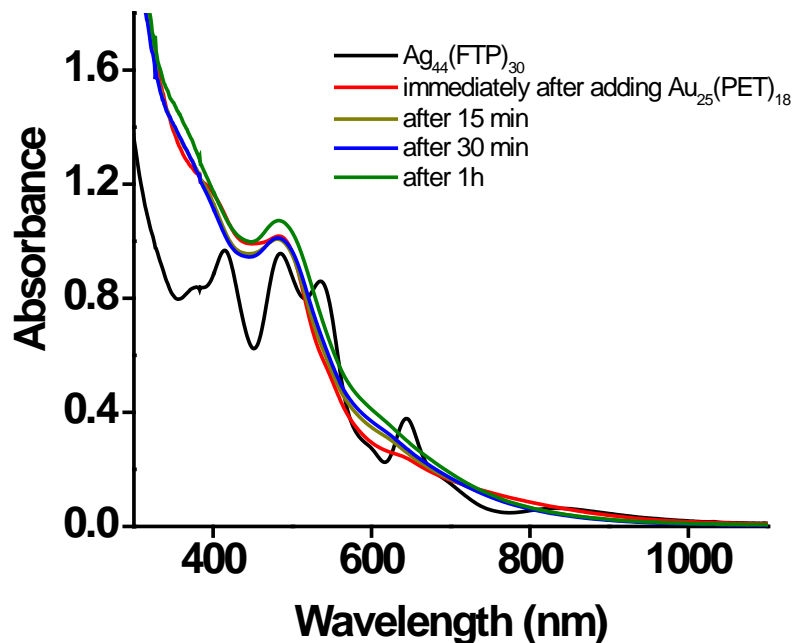


Figure S17. Time-dependent UV/Vis spectra during the reaction between $\text{Au}_{25}(\text{PET})_{18}$ and $\text{Ag}_{44}(\text{FTP})_{30}$ clusters taken in the ratio ($\text{Au}_{25}:\text{Ag}_{44}$) of 1.0:1.0.

Supporting Information 15

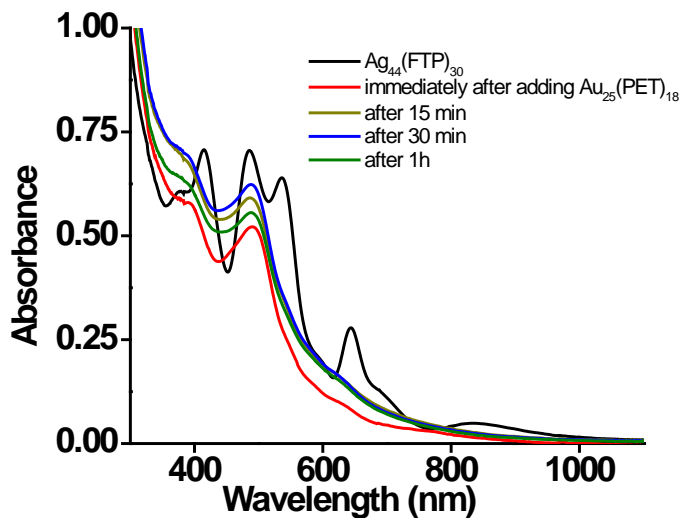


Figure S18. Time-dependent UV/Vis spectra during the reaction between $\text{Au}_{25}(\text{PET})_{18}$ and $\text{Ag}_{44}(\text{FTP})_{30}$ clusters taken in the ratio ($\text{Au}_{25}:\text{Ag}_{44}$) of 0.7:1.0.

Supporting Information 16

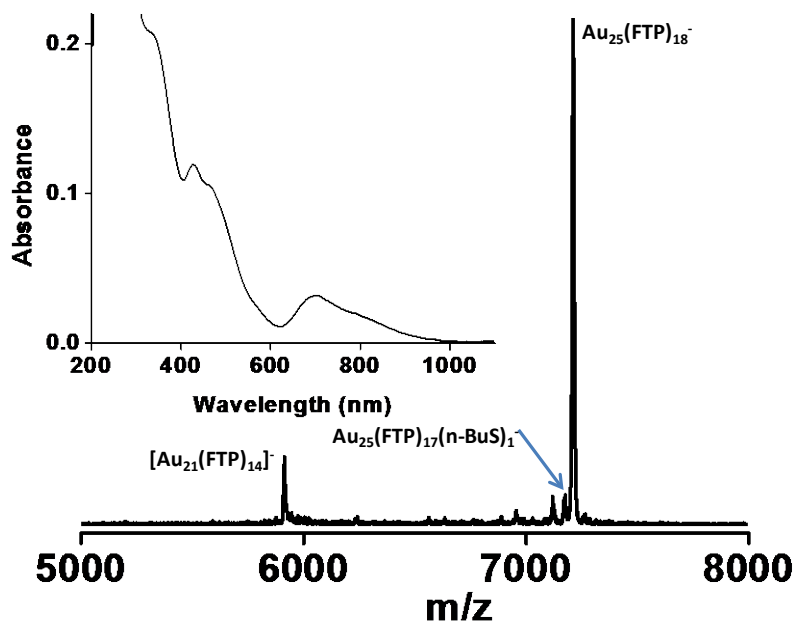


Figure S19. MALDI MS of the Au₂₅(FTP)₁₈ clusters synthesized through ligand exchange of Au₂₅(n-BuS)₁₈ with 4-fluorothiophenol. Inset shows the UV/Vis spectrum of Au₂₅(FTP)₁₈.

Supporting Information 17

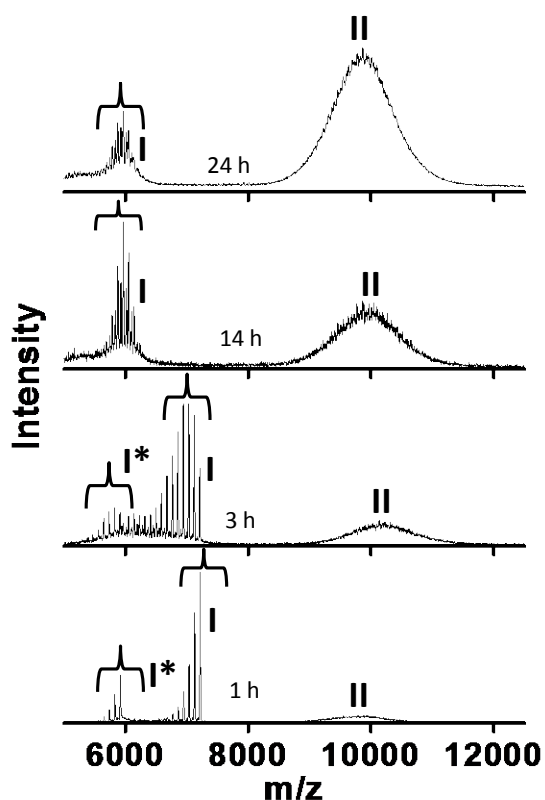


Figure S20. Time-dependent changes in the MALDI MS spectra of the products formed during the reaction between $\text{Au}_{25}(\text{FTP})_{18}$ and $\text{Ag}_{44}(\text{FTP})_{30}$. The spectra for 1 h and 3 h are shown in the main manuscript (Figure 4). The spectrum for 24 h is shown in the Figure S21.

Note: Comparison of group I in Figures S3-S5 and S20 reveal that there is a drastic difference in rates of reactions between Au and Ag clusters depending on whether the same or different ligand is used to protect them. Time-dependent MALDI MS measurements show that irrespective of the concentrations of the reactant clusters, the reaction between $\text{Au}_{25}(\text{PET})_{18}$ and $\text{Ag}_{44}(\text{FTP})_{30}$ got completed/equilibrated within 10-15 min. In contrast, the reaction between $\text{Au}_{25}(\text{FTP})_{18}$ and $\text{Ag}_{44}(\text{FTP})_{30}$ continued for several hours (Figure S20). During the reaction between clusters with different ligands, the mass spectra show peaks arising from the inclusion of one to several Ag atoms, which in turn transform to only 3-4 prominent peaks after about ten minutes. But in the case of clusters having the same ligands, only 1-6 Ag inclusions are observed in group I even after 1 h of the reaction. When the ligands are different, the inter-cluster reaction may be initiated by a fast $(\text{Au-SR})-(\text{Ag-SR}')$ exchange step, starting the disruption of the thiolate staples. This in turn can make the clusters unstable leading to the incorporation of Ag and ligands. Thus, we believe that the nature of the ligand shell on the reactant clusters play an important role in controlling the reactivity of the clusters.

Supporting Information 18

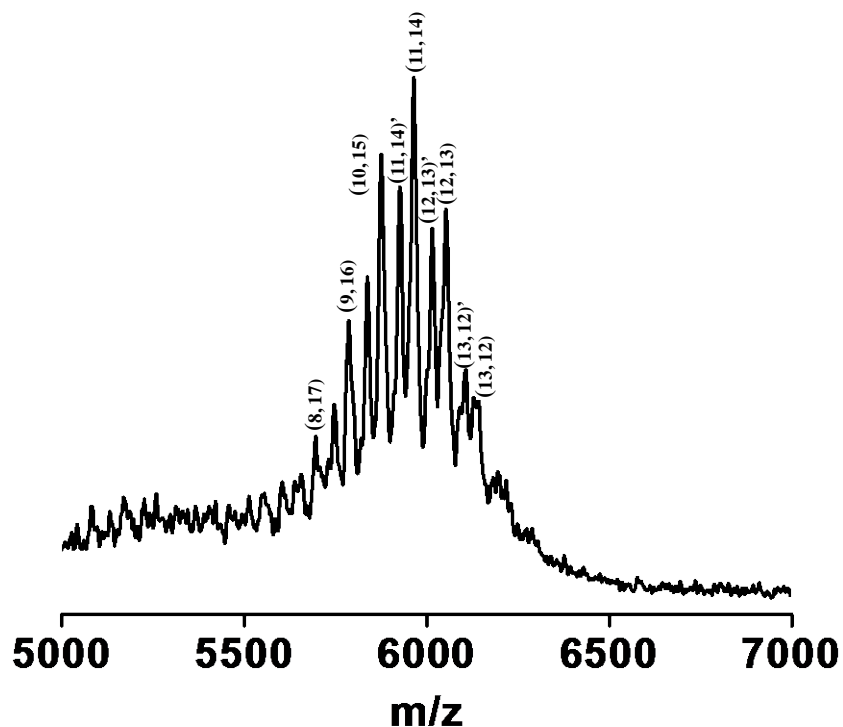


Figure S21. MALDI MS spectra of the clusters formed after 24 h (expansion of the group I in the uppermost panel, i.e., spectrum for 24 h, Figure S20) the reaction between $\text{Au}_{25}(\text{FTP})_{18}$ and $\text{Ag}_{44}(\text{FTP})_{30}$. The peaks labeled as (13, 12)', (12, 13)', etc., are due to the exchange of a single FTP ligand in (13, 12) and (12, 13) clusters with a single n-BuS ligand (mass difference between these peaks are 38 Da, $M_{\text{FTP}} - M_{\text{n-BuS}}$). The numbers in parenthesis, (m, n), are according to the general molecular formula, $\text{Au}_m\text{Ag}_n(\text{FTP})_{18}$.

Supporting Information 19

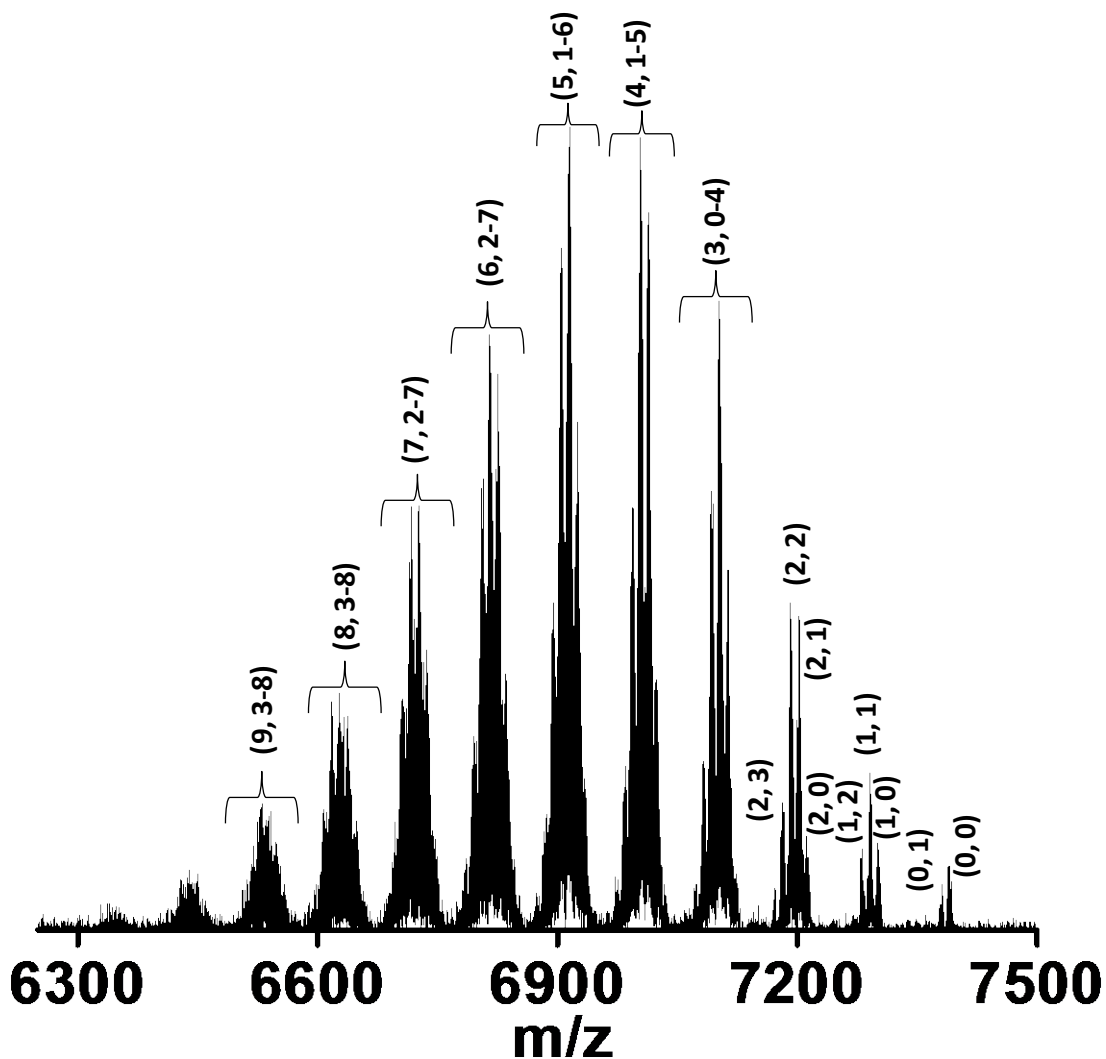


Figure S22: ESI MS spectra measured immediately after mixing $\text{Au}_{25}(\text{PET})_{18}$ and $\text{Ag}_{44}(\text{FTP})_{30}$ at a $\text{Au}_{25}:\text{Ag}_{44}$ ratio of 1.7:1. The numbers (x, y) in parenthesis are according to the general molecular formula, $\text{Au}_{25-x}\text{Ag}_x(\text{PET})_{18-y}(\text{FTP})_y$.

Supporting Information 20

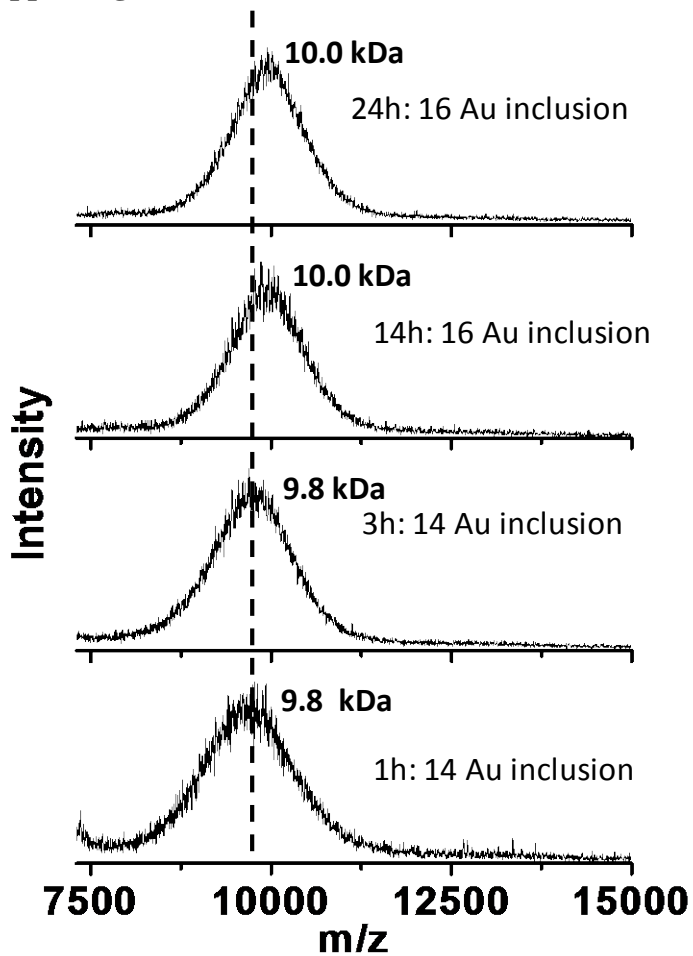


Figure S23. Time-dependent changes of group II features appeared in the MALDI MS spectra during the reaction of $\text{Ag}_{44}(\text{FTP})_{30}$ and $\text{Au}_{25}(\text{PET})_{18}$. Groups II in Figure S20 are expanded here. A gradual shift of the peak maxima to higher m/z is seen.

Supporting Information 21

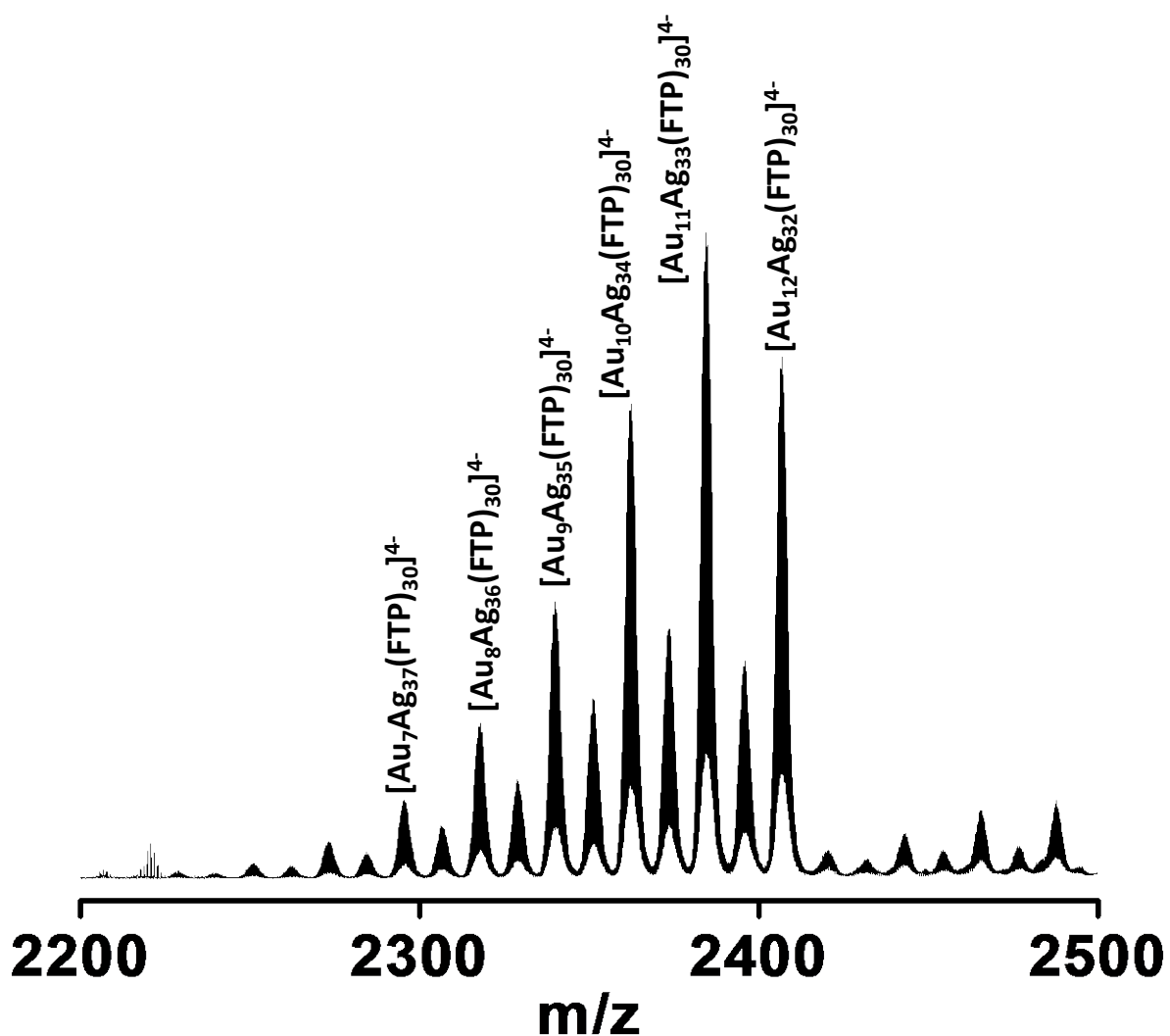


Figure S24. ESI MS spectra showing the formation of $\text{Au}_x\text{Ag}_{44-x}(\text{FTP})_{30}$ during the reaction between $\text{Au}_{25}(\text{FTP})_{18}$ and $\text{Ag}_{44}(\text{FTP})_{30}$ at a $\text{Au}_{25}:\text{Ag}_{44}$ ratio of 0.7:1.0. The peaks in between are due to the n-butanethiol-containing $\text{Au}_x\text{Ag}_{44-x}$ species as the latter could not be completely removed from $\text{Au}_{25}(\text{FTP})_{18}$ (see Figure S21).

Supporting Information 22

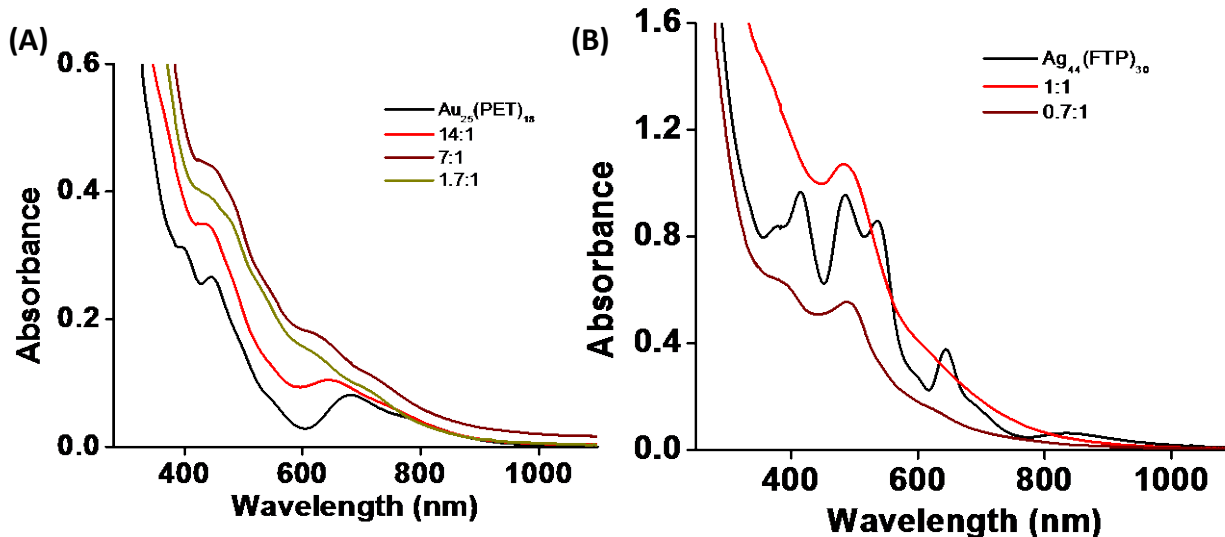


Figure S25. UV/Vis spectra of the reaction mixtures (after 1h of the reaction) at Au₂₅:Ag₄₄ ratios of 14:1, 7:1, 1.7:1 (A) and 1:1 and 0.7:1 (B). At lower Ag₄₄ concentrations (in A) the spectra resembles more with the previously reported spectra of Au_{25-x}Ag_x(SR)₁₈ (see Ref. 16 in main manuscript). At higher concentrations of Ag₄₄ (in B), the spectra resembles more with the previously reported spectra of Au_xAg_{44-x}(SR)₃₀ (see Ref. 15 in the Article).

Supporting Information 23

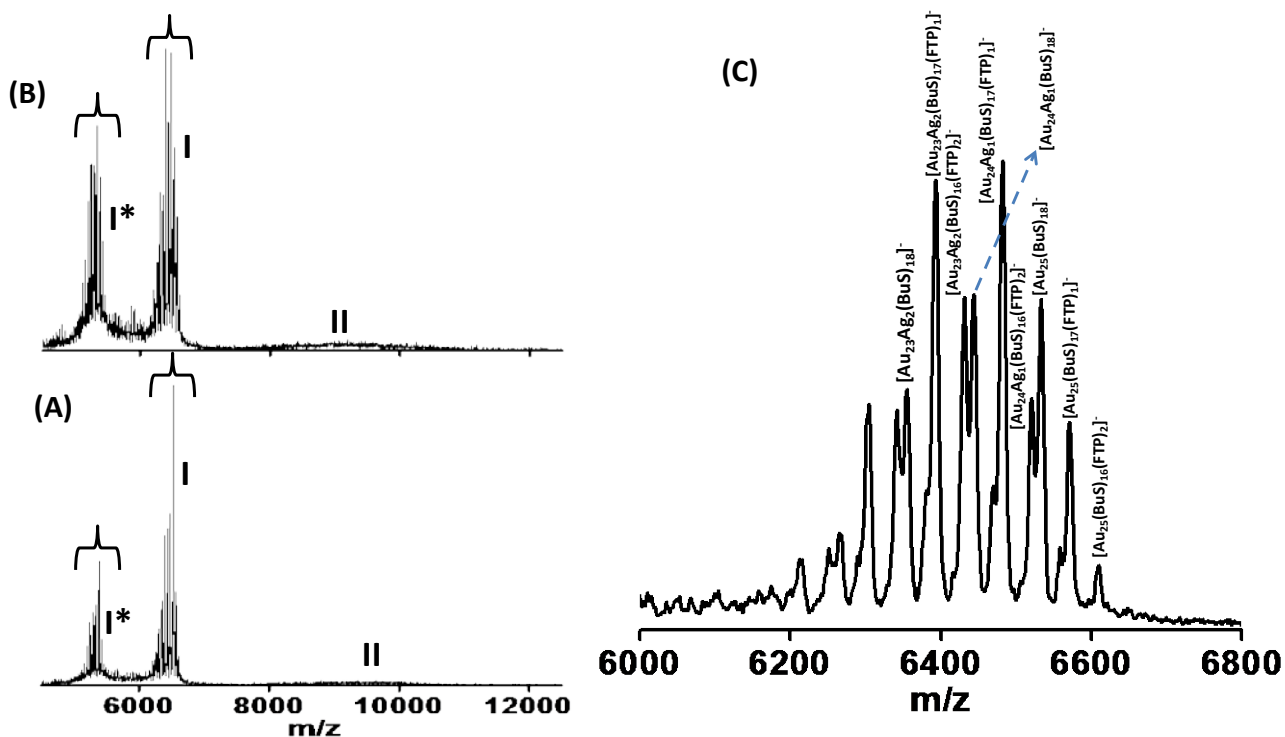


Figure S26. Negative ion mode MALDI MS spectra of the products formed immediately (A) and after 1h (B) of mixing $\text{Au}_{25}(\text{n-BuS})_{18}$ and $\text{Ag}_{44}(\text{FTP})_{30}$ clusters in dichloromethane. Group I in B is expanded in C. Group I are the molecular ion peak of the alloy clusters with mixed ligands formed during the reaction and the group I* are due to their fragments (due to $\text{Au}_4(\text{SR})_4$ loss). Peaks due to BuS-FTP, Ag-Au and (Ag-FTP)-(Au-BuS) exchanges are labeled in C.

Supporting Information 24

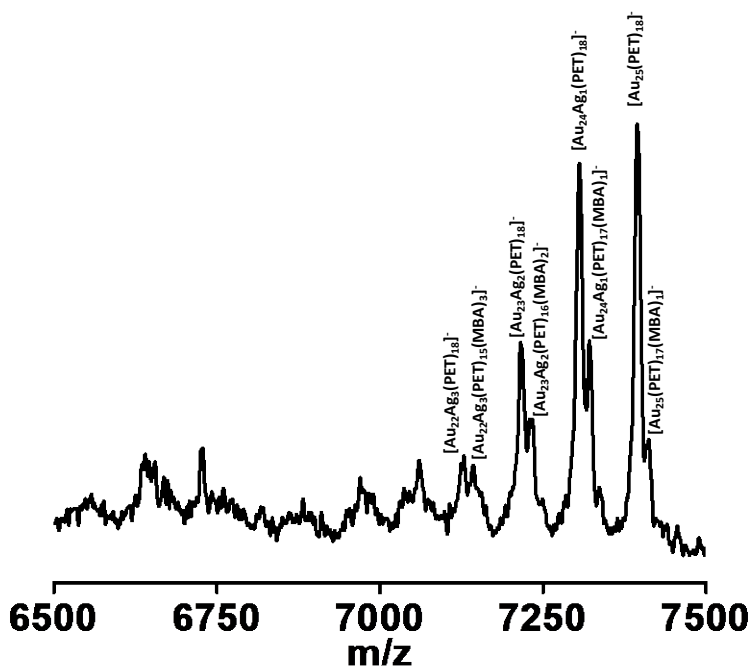


Figure S27. MALDI MS spectra of the products formed immediately after mixing $Au_{25}(PET)_{18}$ and $Ag_{44}(MBA)_{30}$ clusters. Peaks due to MBA-PET, Ag-Au and (Ag-MBA)-(Au-PET) exchanges are marked.

Supporting Information 25

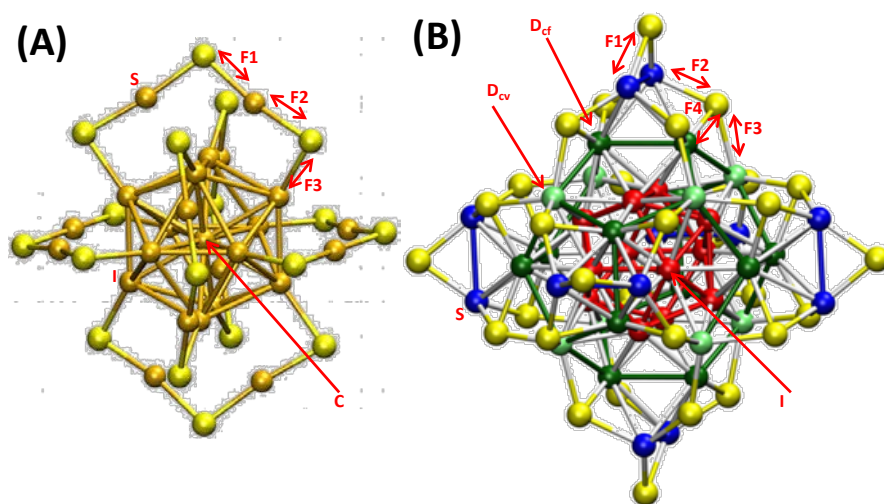


Figure S28. Structures of (A) $Au_{25}(SR)_{18}$ and (B) $Ag_{44}(SR)_{30}$ showing different types of Ag/Au atoms and Ag-S/Au-S bonds. Color codes of Ag atoms: staple (blue), dodecahedron (light and dark green), icosahedron (red). Au atoms are in orange and S atoms are in light yellow. Light green Ag atoms form the vertices of the cube of the Au_{20} dodecahedron and the darker green

Ag atoms are at the faces of this cube. The labels F1-F4 correspond to different types of Ag-S/Au-S bonds. In $\text{Ag}_{44}(\text{SR})_{30}$, F1 involves the terminal ligand while the others involve the bridging ligand. In F3 the bridging ligand binds to the Ag atoms in the cube vertices of the dodecahedron (D_{cv}). In F4 the bridging ligand binds to the cube faces of dodecahedron (D_{cf}).

Supporting Information 26: Results of theoretical calculations

Table S1: Isomers of $\text{Ag}_{43}\text{Au}(\text{SH})_{30}$ and their energies

Isomer	Au location	Energy E/eV	E-E ₀ /eV
I	Central icosahedron	-349.995	-0.72
D_{cv}	Dodecahedron (cube vertex)	-349.416	-0.14
D_{cf}	Dodecahedron(cube face)	-349.592	-0.32
S	Staple	-349.754	-0.48

Table S2: Isomers of $\text{Au}_{24}\text{Ag}(\text{SH})_{18}$ and their energies

Isomer	Ag location	Energy E/eV	E-E ₀ /eV
C	Centre of icosahedron	-219.576	+0.71
I	Icosahedron	-220.047	+0.23
S	Staple	-219.837	+0.44

Table S3: Energies of undoped clusters, metal atoms, and metal-ligand fragments

Structure	E ₀ /eV
$\text{Ag}_{44}(\text{SH})_{30}$	-349.275
$\text{Au}_{25}(\text{SH})_{18}$	-220.281
Ag	-0.1862
Au	-0.2035
AgSH	-8.658
AuSH	-8.902

Table S4. Energies of the reaction, $\text{Au} + \text{Ag}_{44}(\text{SR})_{30} \rightarrow \text{AuAg}_{43}(\text{SR})_{30} + \text{Ag}$

Isomer	Position of Au in $\text{AuAg}_{43}(\text{SR})_{30}$	Energy E/eV
I	Inner icosahedron	-0.70
D _{cv}	Dodecahedron Cube vertex	-0.12
D _{cf}	Dodecahedron Cube face	-0.30
S	Staples	-0.46

Table S5. Energies of the reaction, $\text{Au-SR} + \text{Ag}_{44}(\text{SR})_{30} \rightarrow \text{AuAg}_{43}(\text{SR})_{30} + \text{Ag-SR}$

Position of Au-SR in $\text{AuAg}_{43}(\text{SR})_{30}$	Energy E/eV
Dodecahedron Cube vertex (F3)	+0.10
Dodecahedron Cube face (F4)	-0.07
Staples (F1 and F2)	-0.24

Table S6. Energies of the reaction, $\text{Ag} + \text{Au}_{25}(\text{SR})_{18} \rightarrow \text{Au}_{24}\text{Ag}(\text{SR})_{18} + \text{Au}$

Isomer	Position of Ag in $\text{Au}_{24}\text{Ag}(\text{SR})_{18}$	Energy E/eV
C	Centre of icosahedron	+0.69
I	Icosahedron	+0.22
S	Staples	+0.43

Table S7. Energies of reaction, $\text{Ag-SR} + \text{Au}_{25}(\text{SR})_{18} \rightarrow \text{Au}_{24}\text{Ag}(\text{SR})_{18} + \text{Au-SR}$

Position of Ag-SR in $\text{Au}_{24}\text{Ag}(\text{SR})_{18}$	Energy E/eV
Icosahedron (F3)	-0.01
Staples (F1 and F2)	+0.2

Table S8. HOMO-LUMO energy difference of un-exchanged and alloy clusters

Cluster	Metal substituent position	HOMO/eV	LUMO/eV	HOMO-LUMO Gap/eV	Fermi Energy/eV
Ag₄₄(SH)₃₀	none	2.59	3.45	0.86	3.01
Ag₄₃Au(SH)₃₀	I	2.57	3.44	0.87	3.01
Ag₄₃Au(SH)₃₀	D _{cv}	2.61	3.43	0.82	3.02
Ag₄₃Au(SH)₃₀	D _{cf}	2.63	3.44	0.81	3.04
Ag₄₃Au(SH)₃₀	S	2.63	3.44	0.81	3.04
Au₂₅(SH)₁₈	none	-2.53	-1.24	1.29	-1.88
Au₂₄Ag(SH)₁₈	C	-2.49	-1.35	1.14	-1.92
Au₂₄Ag(SH)₁₈	I	-2.51	-1.22	1.28	-1.86
Au₂₄Ag(SH)₁₈	S	-2.56	-1.30	1.26	-1.93

Table S9. Energy difference (in eV) between the HOMO of AuAg₄₃(SR)₃₀ and LUMO of Au₂₄Ag (SR)₁₈ as a function of the substituent positions. The values showed in bold are those for the most favorable combinations of substituent positions.

Au Position in Ag ₄₄ \ Ag Position in Au ₂₅	I	D _{cv}	D _{cf}	S
C	3.92	3.96	3.98	3.98
I	3.79	3.83	3.86	3.85
S	3.87	3.91	3.93	3.93

Supporting Information 27

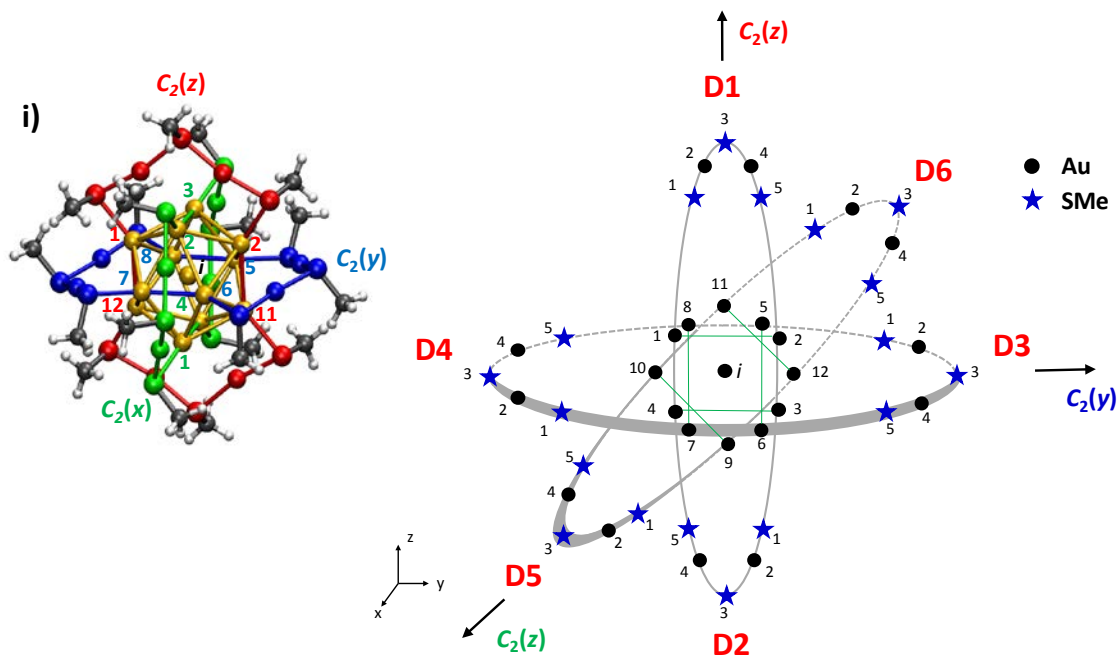


Figure S29. Borromean-Rings diagram of $\text{Au}_{25}(\text{SMe})_{18}$. The rings formed by pairs of coplanar staples are shown as ellipses. Gold atoms are shown by black dots and dark blue stars represent the SMe ligands whose positions are taken to be identical with their sulfur atom. The core Au atoms are numbered from 1 to 12 and the staple atoms are numbered clockwise from end of the staple, from 1 to 5. The lines that join core Au atoms on opposite ends of the same staple are shown by the green lines. The three perpendicular C_2 axes are marked with the associated Cartesian axis direction in brackets. The staple directions are labeled by the six staple locants D1 to D6, marked in red. Inset (i) shows a 3D visualization of the ring structure of the core and staples of $\text{Au}_{25}(\text{SR})_{18}$ aspicule, with each (Au_8S_6) -ring consisting of two coplanar staples and the core atoms that are bonded to these staples. The three rings are colored red, blue and green, and the numbers of the core atoms are marked. This figure and caption are adapted from Ref. 20 of the main manuscript.

Supporting Information 28

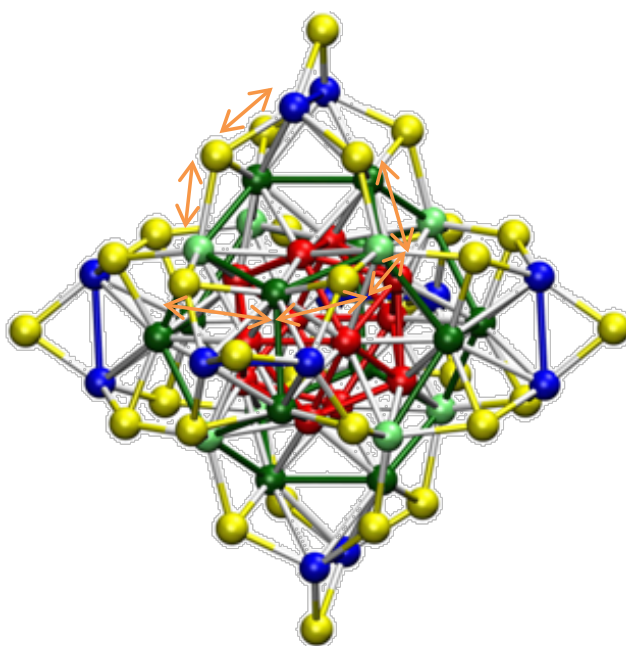


Figure S30. Structure of $\text{Ag}_{44}(\text{SR})_{30}$ showing the accessibility of the icosahedral core Ag atoms. The bonds marked with orange arrows when broken make the core atoms more exposed.

Supporting Information 29

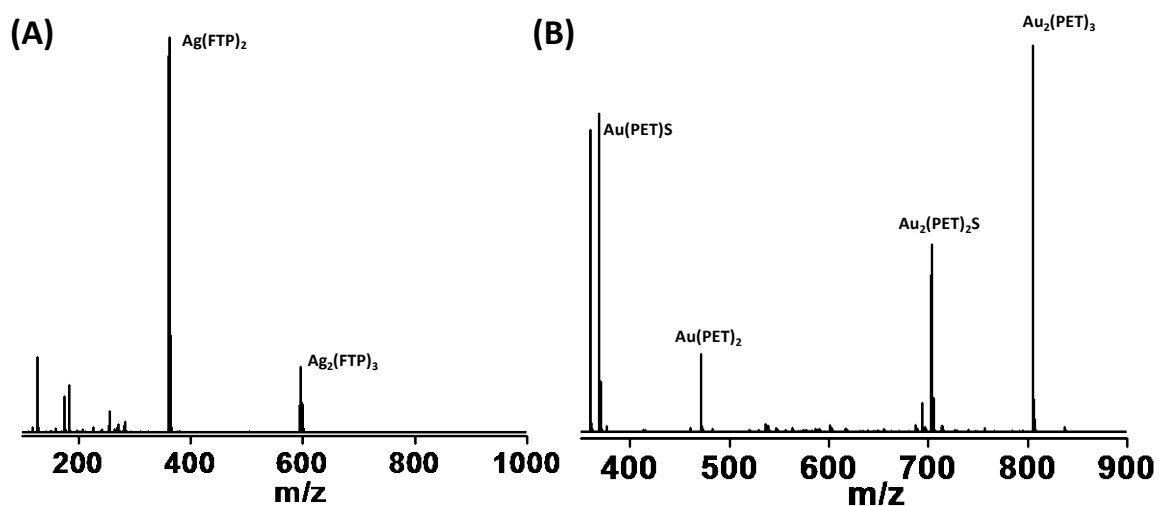
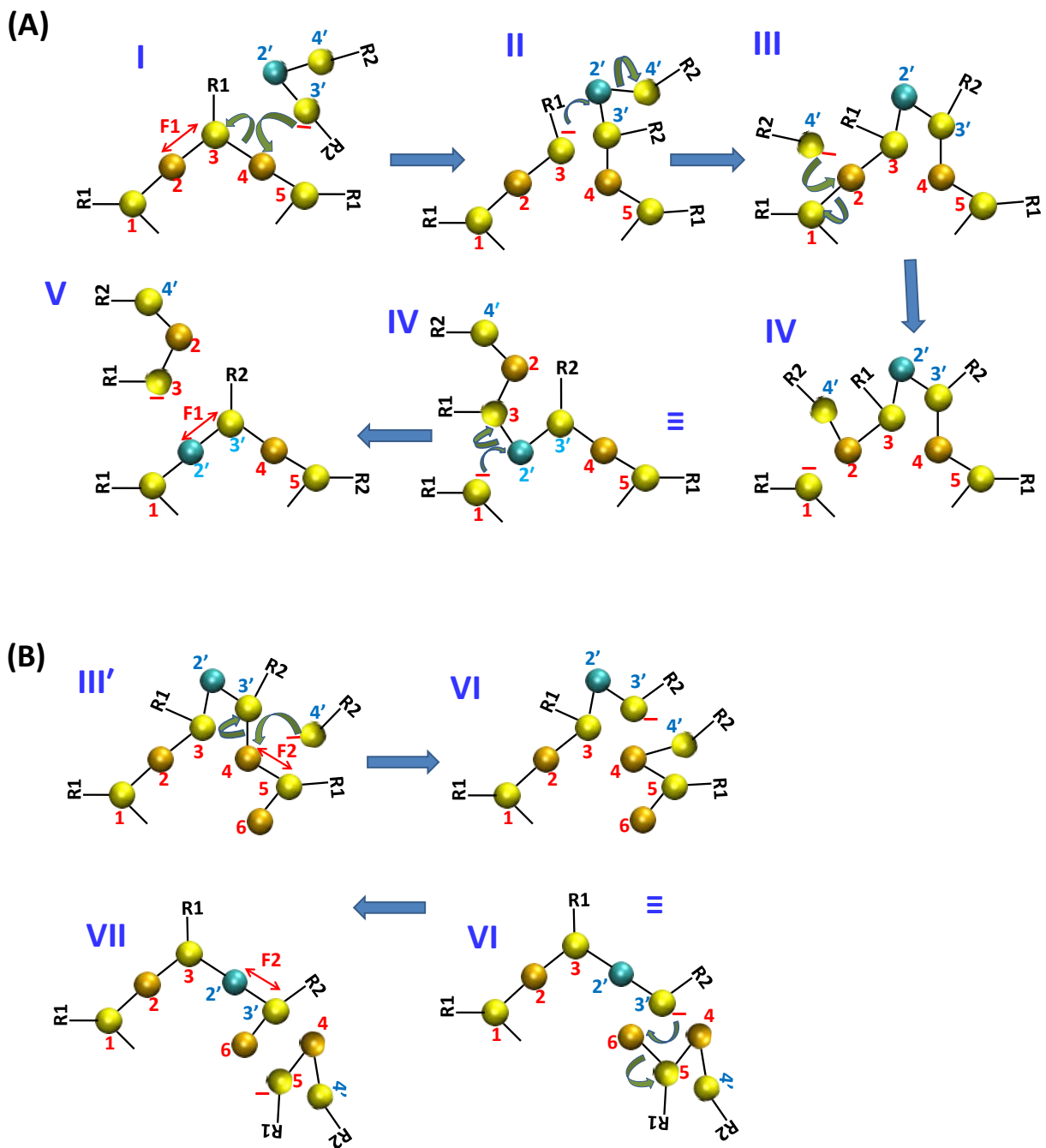


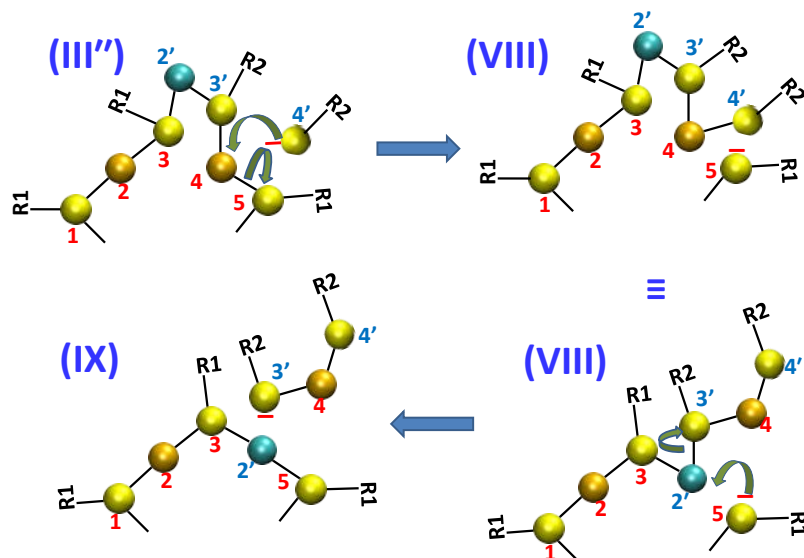
Figure S31. Mass spectra showing the thiolate fragments of (A) $\text{Ag}_{44}(\text{FTP})_{30}$ and (B) $\text{Au}_{25}(\text{PET})_{18}$.

Supporting Information 30: Schematic of the reaction between $\text{Au}_{25}(\text{SR}_1)_2$ with $\text{Ag}(\text{SR}_2)_2$



Scheme S1. Schematic of the reaction between $\text{Ag}(\text{SR}_2)_2$ anion and the staples of $\text{Au}_{25}(\text{SR}_1)_{18}$ resulting in exchange of (A) fragment F1 (B) fragment F2. Color codes of the atoms: dark yellow (Au), light yellow (S), blue (Ag). Au and sulfur atoms in the staple are numbered from 1 to 5 (red). Gold atom labeled as 6 is part of the icosahedral core. Atoms in the $\text{Ag}(\text{SR}_2)_2$ are labeled as 2', 3' and 4' (blue). Structures in the intermediate steps are labeled I to VII. Comparison of structures I and V in (A) shows that the fragment F1 was exchanged between the staples and

fragment. Comparison of structures III' and VII shows that the fragment F2 was exchanged between the staple and fragment.



Scheme S2. Schematic of the reaction between $\text{Ag}(\text{SR}_2)_2$ anion and the staples of $\text{Au}_{25}(\text{SR}_1)_{18}$ resulting in Ag/Au exchange. Color codes of the atoms: dark yellow (Au), light yellow (S), blue (Ag). Au and sulfur atoms in the staple are numbered from 1 to 5 (red). Atoms in the $\text{Ag}(\text{SR}_2)_2$ are labeled as 2', 3' and 4' (blue). Comparison of the structures III'' and IX show that Au atom (4) is exchanged with Ag atom (2').

Note: Structures III, III' and III'' differ only in the position of attack of the R_2S^- and the subsequent bond breaking steps. Also note that structures having the same labels (IV, VIII) are identical and differ only in their orientation. Similar to the schemes S1 and S2, it is possible to draw mechanistic pathways showing the replacement of Au atoms in the icosahedral core (atoms labeled 6, for example) also. But there will be significant steric effects in the various steps.

Discussion on the charge states of $\text{Au}_{25}(\text{SR})_{18}$ and the position of Ag in the $\text{Au}_{25-x}\text{Ag}_x(\text{PET})_{18-y}(\text{FTP})_y$:

$\text{Au}_{25}(\text{SR})_{18}$ exists in two most stable charge states: neutral and anionic.¹⁰ Crystal structures of both the anionic and neutral $\text{Au}_{25}(\text{SR})_{18}$ have been solved.^{4,10a} In the anion, 12 of the 25 Au atoms are part of six $\text{Au}_2(\text{SR})_3$ staples and they are in +1 oxidation state. The 12 terminal sulfurs of the six $\text{Au}_2(\text{SR})_3$ staples bind to the 12 icosahedral core Au (Au_{core}) atoms. Among these twelve $\text{S}_{\text{staple}}\text{-Au}_{\text{core}}$ bonds, six of them localize the valence electrons of those six Au_{core} atoms. The remaining six valence electrons of the Au_{13} core, in addition to that of the central Au and the negative charge, provide eight free electrons fulfilling the magic number criterion for electronic stability. Thus, only seven of the icosahedral Au atoms contribute to the free electron count of the anionic Au_{25} . This implies that any substitution of the $\text{Au}_{\text{staple}}$ with another metal like Ag (having a similar electronic configuration) will not reduce the free electron count and the overall charge of the bimetallic cluster because Ag is likely to exist as Ag(I) in the staples rather than as Ag(0), similar to the Au(I) in $\text{Au}_2(\text{SR})_3$ staples. Substitution of Au_{core} with Ag can alter the free electron count depending upon the nature of Au (i.e., whether the Au is strongly or weakly bound to S_{staple}) that is being replaced and the oxidation state of the incoming Ag (whether Ag(I) or neutral Ag). $\text{Ag}_x\text{Au}_{25-x}(\text{SR})_{18}$ ($x < 6$) clusters synthesized by co-reduction of HAuCl_4 and AgNO_3 by sodium borohydride are also anionic with eight free electrons as in case of undoped anionic $\text{Au}_{25}(\text{SR})_{18}$. Experimental observations and theoretical calculations¹¹ on these clusters show that the incoming Ag atoms are preferably located at the icosahedral positions, replacing the Au_{core} atoms. These observations show that the incoming Ag (upto 6) atoms are present in the icosahedral positions of $\text{Ag}_x\text{Au}_{25-x}(\text{SR})_{18}$ as Ag(0), not as Ag(I). This reduction of the Ag(I) to Ag(0) could be due to the external reducing agent used.

As opposed to the above case, reaction of anionic $\text{Au}_{25}(\text{PET})_{18}$ with Ag(I) salts in acetonitrile results in the formation of neutral $\text{Au}_{25}\text{Ag}_2(\text{PET})_{18}$ and its structure has been predicted through DFT calculations.¹² These calculations show that one of the two incoming Ag(I) is incorporated into the thiolate shell of the clusters as Ag(I)-SR which does not alter the free electron count. The second Ag(I) is situated outside the Au_{13} core and it is bonded to one of the Au_{core} atoms. The bonding of this Ag(I) to icosahedral Au_{core} decreases the free electron count by one. Hence, anionic $\text{Au}_{25}(\text{PET})_{18}$ produces neutral $\text{Au}_{25}\text{Ag}_2(\text{PET})_{18}$ clusters due to its reaction with Ag(I). Thus, it is obvious that incorporation of metals, with similar electronic configuration as Au, into $\text{Au}_{25}(\text{SR})_{18}$ using their cationic precursors in the absence of an external reducing agent will reduce the free electron count if the dopant metal makes any electron localizing bonds to Au_{core} . Further, the report of $\text{Au}_{25}\text{Ag}_2(\text{SR})_{18}$ suggests that the positions of the dopant atoms/ions in the bimetallic clusters vary depending on the nature of the precursors and reaction conditions (whether any external reducing agent is used or not).

In this regard, it is worthwhile to understand the nature of the incoming Ag in the inter-cluster reaction. MALDI and ESI MS features of $\text{Au}_{25-x}\text{Ag}_x(\text{SR})_{18}$ ($x=1-20$) (formed through the inter-cluster reaction route where $\text{Ag}_{44}(\text{SR})_{30}$ was the Ag source and not Ag(I) salts; no external reducing agents were used) in positive ion mode were of very low intensity and low signal to noise ratio compared to those observed in the negative ion mode. This indicates that these clusters are also anionic. This also indicates that Ag inclusion through this reaction has not changed the free electron count and the charge state of the resultant bimetallic cluster, as in the case of the clusters obtained through co-reduction methods. Based on the above discussion, it can

thereby be concluded that both the inter-cluster reaction and co-reduction routes incorporate Ag into Au₂₅(SR)₁₈ as Ag(0). According to the suggested mechanism depicted in the Schemes 1 and 2, replacement of the Au-SR with Ag-SR would not change the overall charge state and the free electron count in the alloy clusters as there are only rearrangement of bonds involved after the nucleophilic attack and no reduction of Ag⁺ or Ag-SR is required. Thus it is likely that in the initial stages of doping, Ag and Ag-SR substituents are more likely to be present on the staples than in the core. Once the staples are opened, substitution of core atoms would become more facile. However, crystal structure data are needed to unambiguously confirm this.

References:

- (1) Enkovaara, J.; et al. *J. Phys.: Condens. Matter* **2010**, *22*, 253202.
- (2) Perdew, J. P.; Burke, K. *Phys. Rev. Lett.* **1996**, *77*, 3865.
- (3) Larsen, A. H.; Vanin, M.; Mortensen, J. J.; Thygesen, K. S.; Jacobsen, K. W. *Phys. Rev. B* **2009**, *80*, 195112.
- (4) (a) Heaven, M. W.; Dass, A.; White, P. S.; Holt, K. M.; Murray, R. W. *J. Am. Chem. Soc.* **2008**, *130*, 3754. (b) Akola, J.; Walter, M.; Whetten, R. L.; Häkkinen, H.; Grönbeck, H. *J. Am. Chem. Soc.* **2008**, *130*, 3756. (c) Zhu, M.; Aikens, C. M.; Hollander, F. J.; Schatz, G. C.; Jin, R. *J. Am. Chem. Soc.* **2008**, *130*, 5883.
- (5) Desireddy, A.; Conn, B. E.; Guo, J.; Yoon, B.; Barnett, R. N.; Monahan, B. M.; Kirschbaum, K.; Griffith, W. P.; Whetten, R. L.; Landman, U.; Bigioni, T. P. *Nature* **2013**, *501*, 399.
- (6) Hanwell, M.; Curtis, D.; Lonie, D.; Vandermeersch, T.; Zurek, E.; Hutchison, G. *J. Cheminf.* **2012**, *4*, 1.
- (7) Humphrey, W.; Dalke, A.; Schulten, K. *J. Mol. Graphics* **1996**, *14*, 33.
- (8) (a) Parker, J. F.; Fields-Zinna, C. A.; Murray, R. W. *Acc. Chem. Res.* **2010**, *43*, 1289. (b) Angel, L. A.; Majors, L. T.; Dharmaratne, A. C.; Dass, A. *ACS Nano* **2010**, *4*, 4691.
- (9) Wu, Z.; Jin, R. *Nano Lett.* **2010**, *10*, 2568–2573.
- (10) (a) Zhu, M.; Eckenhoff, W. T.; Pintauer, T.; Jin, R. *J. Phys. Chem. C* **2008**, *112*, 14221. (b) Antonello, S.; Perera, N. V.; Ruzzi, M.; Gascón, J. A.; Maran, F. *J. Am. Chem. Soc.* **2013**, *135*, 15585. (c) Zhu, M.; Aikens, C. M.; Henrich, M. P.; Gupta, R.; Qian, H.; Schatz, G. C.; Jin, R. *J. Am. Chem. Soc.* **2009**, *131*, 2490–2492. (d) Negishi, Y.; Chaki, N. K.; Shichibu, Y.; Whetten, R. L.; Tsukuda, T. *J. Am. Chem. Soc.* **2007**, *129*, 11322. (e) Ghosh, A.; Hassinen, J.; Pulkkinen, P.; Tenhu, H.; Ras, R. H. A.; Pradeep T. *Anal. Chem.* **2014**, *86*, 12185.
- (11) (a) Kumara, C.; Aikens, C. M.; Dass, A. *J. Phys. Chem. Lett.* **2014**, *5*, 461. (b) Yamazoe, S.; Kurashige, W.; Nobusada, K.; Negishi, Y.; Tsukuda, T. *J. Phys. Chem. C* **2014**, *118*, 25284. (c) Guidez, E. B.; Mäkinen, V.; Häkkinen, H.; Aikens, C. M. *J. Phys. Chem. C* **2012**, *116*, 20617.
- (12) Yao, C.; Chen, J.; Li, M.-B.; Liu, L.; Yang, J.; Wu, Z. *Nano Lett.* **2015**, *15*, 1281.



Carbon aerogels through organo-inorganic co-assembly and their application in water desalination by capacitive deionization



Rudra Kumar ^{a,1}, Soujit Sen Gupta ^{b,1}, Shishir Katiyar ^a, V. Kalyan Raman ^c,
Siva Kumar Varigala ^c, T. Pradeep ^{b,*}, Ashutosh Sharma ^{a,**}

^a DST Unit on Nanoscience, Department of Chemical Engineering, Indian Institute of Technology Kanpur, 208016, India

^b DST Unit on Nanoscience and Thematic Unit of Excellence (TUE), Department of Chemistry, Indian Institute of Technology Madras, Chennai 600036, India

^c Centre of Excellence (Biotechnology) & Water and Wastewater Technology, Thermax Limited, Pune 411019, India

ARTICLE INFO

Article history:

Received 29 June 2015

Received in revised form

26 November 2015

Accepted 2 December 2015

Available online 10 December 2015

ABSTRACT

We report the preparation of a carbon aerogel (CA) material utilizing the simultaneous co-assembly of organic and inorganic precursors, having a high Brunauer–Emmet–Teller surface area of 2600 m²/g, through a one-step sol–gel process. This CA was characterized using different spectroscopic and microscopic techniques. The as-synthesized CA with its tunable porosity, high mechanical strength, transport property and electrical conductivity was found to be a suitable candidate for water desalination via capacitive deionization (CDI). The optimum working potential for CDI was in the range of 1.2–1.4 V. The material was tested for the removal of different ions of varying charges and the experiment was performed for multiple cycles. The result showed high adsorption capacity of 10.54 mg/g for Cl[−] in laboratory batch experiments compared to 3–4 mg/g reported for most of the CDI materials. The materials were also characterized after adsorption/desorption cycles. Adsorption was physical in nature and the ions desorbed completely after reversing the polarity. The result showed that the material can be used for multiple cycles without any change in its spectroscopic and adsorption properties.

© 2015 Elsevier Ltd. All rights reserved.

1. Introduction

Shortage of clean drinking water globally, due to rapid increase in population and industrialization; probably the most important problem of the planet, has to be addressed from multiple directions. Environmental contamination and pollution has led to the deterioration of water quality, even in water rich regions [1]. In order to solve the water crisis, we require clean and cost effective methods [2] for decontaminating polluted waters. Desalinating fresh water from rivers or groundwater can generate water suitable for human consumption [3,4]. Reverse osmosis [5], ultra-filtration [6] and electro-dialysis [7] have been traditionally used to generate drinking water from brackish water. However, all these techniques require heavy equipment and more power and therefore, involve high installation and operational costs.

Among all the water desalination processes, capacitive deionization (CDI) is cost effective and easy to operate. CDI removes primarily ions from water by using two oppositely charged carbon electrodes of high porosity, electrical conductivity and a large surface area. The electrodes are separated by a spacer and connected to a direct current (DC) source by a current collector (typically graphite or titanium sheet). On applying a voltage, the surface of the electrodes gets charged and an electrical double layer is formed between the electrode and the solution. These charged electrodes adsorb the counter ions present in the feed water and thereby, desalinate it. The electrodes are regenerated by reversing the polarity discarding the heavily saline stream generated during this step. No additional efforts are required for this process. Capacitive desalination is attractive because it is a non-membrane based approach which requires low voltage (an applied potential between 0.8 and 2.0 V that is below the hydrolysis potential of water at the electrode surface) and requires only low pressure for operation.

The electrode materials that have been used for wastewater treatment using CDI include porous activated carbons [8], carbon cloth [9,10], activated carbon fiber [11], carbide derived carbon (CDC) [12], carbon nanotubes [13], graphene [14], graphene aerogel

* Corresponding author.

** Corresponding author.

E-mail addresses: pradeep@iitm.ac.in (T. Pradeep), ashutos@iitm.ac.in (A. Sharma).

¹ Both the authors contributed equally.

[15,16], carbon–carbon composite [17], conducting polymer carbon composite [18], and carbon metal oxide composites [19]. Among these materials, carbon aerogels (CA) have high surface area (400–1100 m²/g), low resistivity (~400 Ωm/cm), high electrical conductivity and excellent electrochemical stability in aqueous solutions. The main advantage of carbon aerogel is that its micro and meso-porosity can be tuned by using an easy to implement sol–gel technique [20]. The ion adsorption capacity is dependent on tailoring its microstructure [21] either by using an inorganic precursor (like silica) or metal oxides [22,23]. Yang et al. [24] prepared a carbon aerogel on a silica gel template for CDI of NaCl solution. In another study, manganese and iron oxide-doped carbon aerogel electrodes were tested for CDI of saline water [22]. Both the materials showed enhanced capacity than CA alone.

A unique property of a CA is the presence of inter-connected particles, which along with a simple synthesis procedure, is advantageous when used as an electrode in capacitors, fuel cells and Li ion batteries and catalytically active substrates [25]. Previously, resorcinol–formaldehyde (RF) gels have been used to make CAs by combining the two precursors in suitable molar ratios and employing different processing conditions, such as, reactant concentrations, catalyst concentrations, pH, activation temperature and pyrolysis temperature [26,27]. Recently, Wu et al. [21] have synthesized an ordered mesoporous carbon aerogel by incorporating a carbon precursor in a calcium carbonate based hard template network that was subsequently removed selectively to generate mesopores. Surfactant-assisted soft template has also been reported to create a porous carbon structure [25]. However, such techniques are limited by the template size and the pore structure and are therefore, unable to control the pore size distribution and achieve porosity beyond a narrow range.

It is a standard practice to generate carbon aerogels by supercritical drying of wet RF gels and this method requires high pressures (up to 1000 psi) that raises safety issues [28,29], and makes it expensive and difficult to scale-up for industrial use. To reduce the cost, new techniques are needed which will eliminate the supercritical drying step and substitute it with ambient pressure drying at feasible temperatures, while preserving the mechanical strength and maintaining the porosity of the material. Jung et al. [30] have reported RF derived carbon aerogel electrodes for capacitive deionization, prepared by ambient pressure drying.

In this work, we have used a simple and cost effective sol–gel technique to fabricate a resorcinol–silica composite aerogel monolith with a highly porous structure and high surface area. The interpenetrating network of organic and inorganic phases was self-assembled during the gelation process. After removing the solvent phase present in the monolith, the ambient drying helped to maintain the micro and meso porosity and mechanical integrity of the monolith structure. After carbonization of the prepared monolith, some shrinkage occurred due to the removal of volatile substances generated due to the decomposition of carbonaceous precursors. In further steps, silica was etched from the carbon–silica aerogel to form a carbon aerogel with increased surface area and electrical conductivity. This material was used for water desalination using the CDI technique.

2. Material and methods

2.1. Materials

Resorcinol (R), formaldehyde solution (F), tetraethyl orthosilicate (TEOS), and 3-aminopropyl tri-ethoxysilane (APTES) were purchased from Sigma–Aldrich. Acetone, sodium hydroxide (NaOH), sodium chloride (NaCl), magnesium chloride (MgCl₂), and ferric chloride (FeCl₃) were purchased from LobaChemie. All

reagents were used as-received, without further treatment.

2.2. Synthesis of carbon–silica composite aerogel

Carbon–silica aerogel was prepared by the sol–gel condensation method of resorcinol, formaldehyde and TEOS. Briefly, 0.732 g of resorcinol was mixed in 4.20 mL of acetone, 2.73 mL of TEOS, and 320 μL of APTES, and 240 μL of APTMS was added into the reaction mixture. Finally 1.5 mL of formaldehyde was added and the mixed solution was kept in a polypropylene container. The container was tightly packed to avoid solvent loss. The mixed solution was kept undisturbed at room temperature for 5–6 h for gelation. After gelation was complete, the gel was washed three times with fresh acetone and kept at 60 °C for 10 h in a hot air oven to slowly evaporate the solvents. At this stage, color of the dried gel was reddish brown. Finally, the formed gel was carbonized in a tubular furnace at 900 °C for 1 h in an inert atmosphere using nitrogen gas. The heating rate was maintained at 5 °C/min. The as-synthesized aerogel was the carbon–silica composite aerogel (CSA).

2.3. CDI experimental scheme

CA electrodes of dimension 3 × 3 × 0.5 (l × b × h) cm³ were taken and were separated by a 0.4 mm nylon spacer. Two graphite rods were used as current collectors and were connected to a DC source. This single electrode set-up was immersed in a 100 mL beaker containing 80 mL of NaCl solution of 500 mg/L concentration. Magnetic stirrer was used with a stirring speed of 200 rpm. The electrodes (CA) are connected to the DC source (applied a potential of 1.2 V) such that one of the electrodes becomes positive and the other is negative. When the feed water (NaCl/salt solution) is passed through the electrodes, the cations (Na⁺) and anions (Cl⁻) get adsorbed on the cathode and anode, respectively. This process continues for a certain period of time until the electrodes become saturated enough that it cannot adsorb more ions. At this point, the maximum adsorption capacity of the material is calculated. As the terminals of the DC source are changed, the electrodes also reverse their potential and thereby, desorbing all the adsorbed ions on its surface due to electrostatic repulsion. In this process, the reject comes out as brine and the porous CA material is regenerated to be further used in another adsorption cycle. These steps should continue for multiple times without loss of capacity for ideal CDI electrodes.

2.4. Etching of silica from carbon–silica composite aerogel

Silica was etched from CSA by dipping it in a 2 M NaOH solution at 70–80 °C for 12 h. This step was performed three times for complete removal of silica. After this, the aerogel was washed with water several times to ensure complete removal of NaOH and then dried overnight at 80 °C to remove water. This material was termed as carbon aerogel (CA). The density of the material was found to be 0.13 g/cm³. The ultra low density for this material proves it to be aerogel rather than xerogel as reported elsewhere [31] and was further confirmed by porosity measurements. The total pore volume of the CA was found to be 2.12 cc/g with average pore size of 3.26 nm (data in supporting information (SI), Fig. S1) A schematic of the preparation of CSA and CA by using sol–gel technique is depicted in Fig. 1.

2.5. General characterization

The surface morphology of the prepared samples was characterized by using field emission scanning electron microscopy (FESEM, ZEISS Supra 40VP, Germany). Energy dispersive X-ray

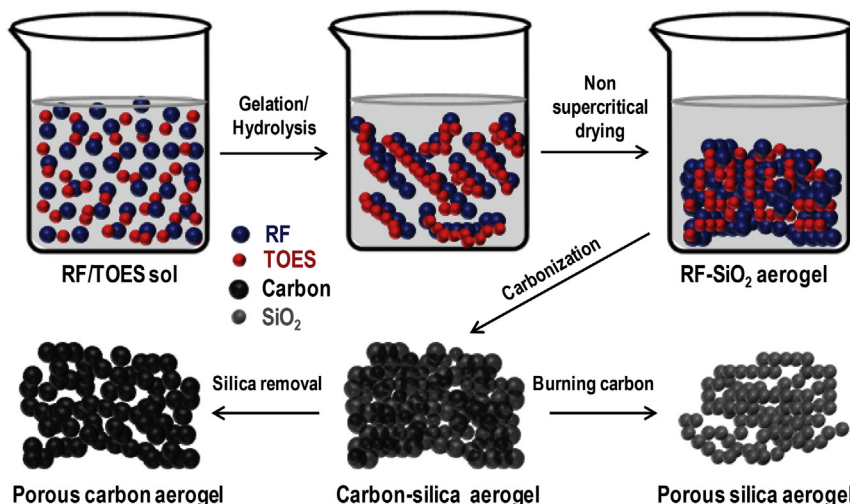


Fig. 1. Schematic of the preparation of carbon aerogel by the sol–gel technique. (A color version of this figure can be viewed online).

spectroscopy (EDS) with elemental mapping (Oxford instruments) was combined with FESEM. The crystal structure of carbon aerogel, before and after desalination, was analyzed by X-ray diffraction (XRD) (PAN Analytic Germany), using a Cu $K\alpha$ radiation ($\lambda = 1.5406 \text{ \AA}$) from 5 to 80° at a scanning speed of 2° per min. Raman spectra (Model: Alpha, Make: Witec, Germany) of the CAs were measured in the frequency range of 400–3000 cm^{-1} with a 514 nm laser source. X-ray photoelectron spectroscopy (XPS) was performed with an Omicron ESCA Probe spectrometer employing a polychromatic Mg $K\alpha$ X-ray source ($h\nu = 1253.6 \text{ eV}$). Majority of the spectra were deconvoluted to their component peaks using the software, CasaXPS. The energy resolution of the XPS spectrometer was set at 0.1 eV at a pass energy of 20.0 eV. The binding energy was corrected with respect to C 1s at 284.5 eV.

The surface area and pore volume of CA was measured by the Brunauer–Emmet–Teller (BET) BET-surface area analyzer (Quantachrome) Autosorb iQ. The pore size distribution (PSD) was obtained from the Barrett–Joyner–Halenda (BJH) method. The mechanical strength of the material was measured by Instron 1195 (in compression mode). The electrical conductivity was measured by a four probe point conductivity equipment (SES Instruments, Roorkee). A Keithley current source-voltmeter was attached to the four probe setup for the collection of data. The electrochemical capacitive behavior of CA was determined by cyclic voltammetry (CV). All electrochemical experiments were carried out at room temperature in a three-electrode cell with 1 M NaCl electrolyte solution. CV was performed at various scan rates using a potentiostat/galvanostat (AUTOLAB 302N) in a potential range of -0.8 V to 0.2 V versus Ag/AgCl (3 M KCl). The specific capacitance was calculated from the CV curve based on the following equation:

$$C_m = \left\{ \frac{1}{mR\Delta V} \right\} \int I(V)dV \quad (1)$$

Where, C_m is the specific capacitance, m is the mass of the active material, R is the scan rate, ΔV is the potential window of scanning, which is the integral area under the CV curve.

3. Results and discussion

The carbon aerogel (CA) prepared by our sol–gel method was characterized using different spectroscopic and microscopic techniques. Fig. 2A shows the photograph of the synthesized CA block of 7 cm (length) \times 3 cm (width) \times 1 cm (thick). The material exhibited

high mechanical strength having Young's modulus of 1.12 MPa which was calculated from compressive stress–strain curve (data are shown in supporting information (SI), Fig. S2) and was found to possess high monolithic integrity, such that it can be used as an electrode, without the need of a binder. This would prove to be an advantage as a binder generally decreases the conductivity of an electrode material, and thereby reduces the adsorption capacity. The electrical conductivity of CA was determined to be between 1 and 80 S/m, and its surface area was found to be $\sim 2600 \text{ m}^2/\text{g}$.

The SEM image of carbon silica aerogel (CSA) presented in Fig. 2B clearly illustrates the spherical nature of the carbon nanosphere. The high resolution SEM image (inset in Fig. 2B) of CSA further reveals that the carbon nanosphere has a uniform size of around 200 nm. Fig. 2B also shows the presence of voids in CSA at the nanoscale, which leads to excellent porosity (mesoporosity of 12.5%). The porosity of the material was tuned by using different concentrations of the silica precursor (TEOS). The porosity was very low in the absence of TEOS, but substantially increased upon addition of the SiO_2 precursor. However, at an optimum amount of TEOS (2%) the porosity reached a maximum and then decreased with further increase in SiO_2 concentration (see Fig. S3) along with a reduction in mechanical strength of CA.

Etching the silica precursor from CSA using 1 M NaOH led to the formation of CA with a increased porosity that enhanced the performance of CDI by 80%. The SEM image of CA is shown in Fig. 2C. Interestingly, while the porosity increased (mesoporosity increased by 15%), the mechanical strength was not adversely affected. XPS was performed to understand the chemical composition of CA. The spectrum displayed in Fig. 2D show that carbon and oxygen are the only two components present in the system. The deconvoluted C 1s spectrum (inset of Fig. 2D) consists of two peaks at 284.5 and 286.7 eV, whose relative intensities suggest that carbon in CA occurs mainly as C=C and partially as C–O. The presence of Si in the parent material (CSA) was confirmed by its XPS spectrum as shown in SI, Fig. S4. The absence of the corresponding peak in Fig. 2D affirms that SiO_2 was completely removed by etching.

The SEM–EDS of CA illustrated in Fig. 3 shows the presence of carbon and oxygen alone, similar to XPS data in Fig. 2D. The elemental mapping performed on the SEM image in Fig. 3(i) depicted the uniform distribution of carbon (see Fig. 3(ii)) and negligible amount of oxygen (see Fig. 3(iii)) in CA. Fig. 3b shows that the elemental ratio of carbon and oxygen in CA is almost around 19:1, which is in good agreement with the deconvoluted XPS spectrum of C 1s in the inset of Fig. 2D. The SEM–EDS and

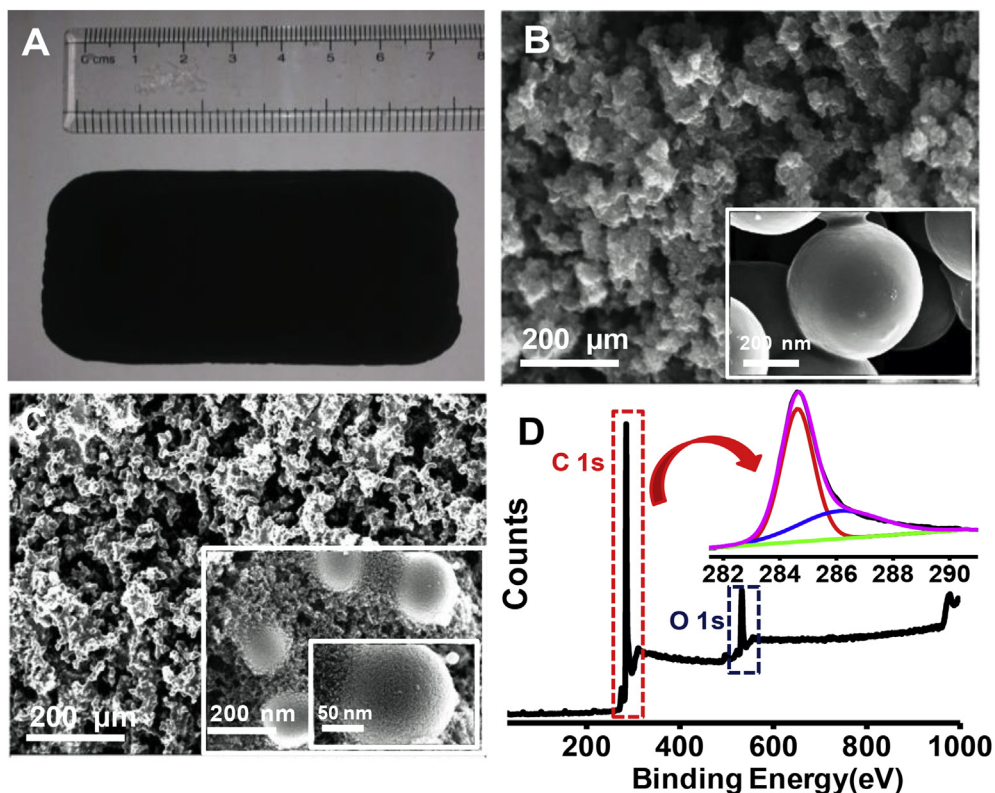


Fig. 2. A) Photograph of carbon aerogel. B & C) FESEM image of Si and Si etched carbon aerogel, the inset in both the figures show higher magnification image and D) XPS spectrum of carbon aerogel, the inset shows the C 1s spectrum. C and O were the only elements noticed. (A color version of this figure can be viewed online).

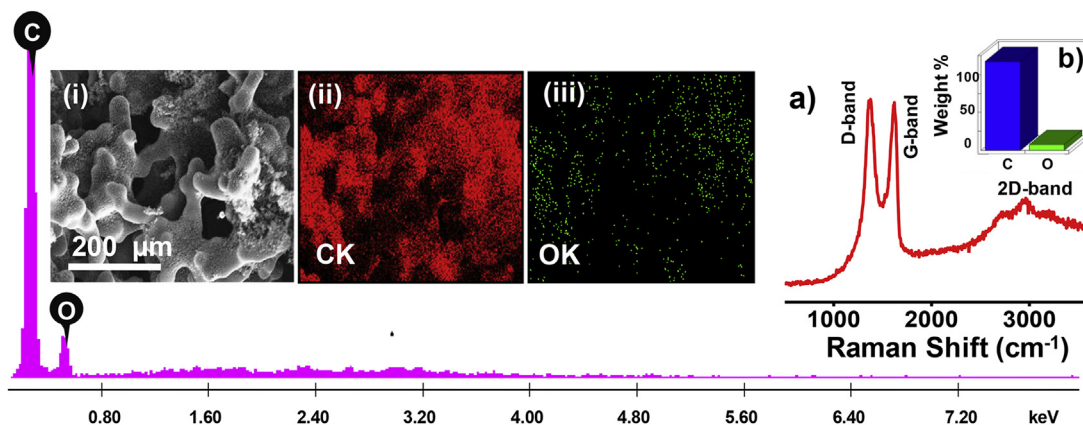


Fig. 3. SEM–EDS of CA showing the presence of carbon and oxygen. The inset displays its i) SEM image and EDS mapping of ii) carbon and iii) oxygen, a) shows the Raman spectrum of CA and b) depicts the elemental ratio of carbon:oxygen in ratio 19:1 (SEM–EDS). (A color version of this figure can be viewed online).

elemental mapping results for CSA are provided in SI Fig. S5. The Raman spectrum of CA is shown in Fig. 3a which shows the presence of D, G and 2D bands at 1383, 1601 and 2769 cm^{-1} , respectively. The presence of these bands suggested that the material is graphenic in nature, as expected after a high temperature treatment.

Electrical conductivity determines the charge transfer and internal resistance of a material and its value at room temperature was evaluated for both CSA and CA using the four probe method. It can be seen from Fig. 4A that for achieving the same current, CA requires a much lower potential than CSA. The electrical conductivities of CSA and CA electrodes were calculated to be 2.3 and 71.0 S/m, respectively. The lower conductivity of CSA is due to the

non-conducting nature of silica that is impregnated in the CSA. This interpenetrating network of silica formed between the carbon matrixes reduces electrically conducting pathways.

CV was performed in 1 M NaCl electrolyte solution in a potential window of -0.2 – 0.8 V to determine the potential of CA as a CDI electrode with high electro-sorptive salt adsorption and specific capacitance. Fig. 4B shows the CV curves of CA obtained at a range of scan rates between 2 and 200 mV/s. It is noticeable that at low scan rates, the CV curve has a rectangular shape, which becomes distorted at high scan rates due to large current and increase resistance. This confirms the picture that at low scan rates, the electrolyte is able to penetrate into the pores of the CA electrode with an unrestricted motion, which does not occur at a high scan

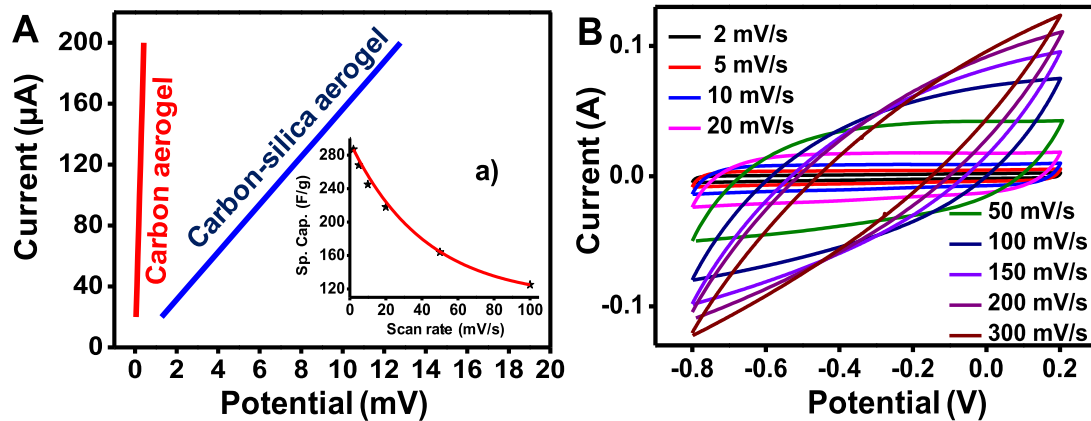


Fig. 4. A) Electrical conductivity of CSA and CA. The inset in the figure shows the variation of specific capacitance with respect to scan rate. B) Cyclic voltammetry of CA using 1 M NaCl as electrolyte. (A color version of this figure can be viewed online).

rate when the ohmic resistance affects the formation of the electrical double layer [32]. The effect of scan rate is also reflected by the specific capacitance which is calculated to be 262 and 86 F/g for CA (inset in Fig. 4A) and 170 and 55 F/g for CSA (from CV curves in SI, Fig. S6) at 2 mV/s and 100 mV/s, respectively calculated from equation (1).

Next, we developed a laboratory batch CDI set-up to examine the desalination performance of CA. The set-up consisted of two CA electrodes (one acting as a positive and the other as a negative electrode) separated by a porous nylon membrane (spacer), and a graphite rod as a current collector. Salt water of known concentration was taken in a glass beaker to function as the electrolyte. The electrodes were dipped into the salt solution along with a conductometer to monitor any change in the conductivity of the solution. Finally, a DC source, which can supply a voltage from 0.0 to 5.0 V, was connected to the graphite rod. The above set-up is illustrated in SI, Fig. S7.

Electrochemical capacity is a measure of the electro-sorptive behavior of an electrode material. The electrical double layer formed onto the pores of the electrode material and the electrolyte leads to the adsorption of charged species over the electrode. The thickness of electrical double layer and the size of the charged species, therefore, govern the adsorption capacity. The former parameter in turn depends on the concentration of electrolyte solution and size of the electrolyte ions. Thus, to understand the effect of these key factors on the electrochemical properties of CA, we chose a set of three different salt solutions, namely, NaCl, MgCl₂ and FeCl₃ as electrolytes.

The voltage required for CDI was first optimized by measuring the adsorption capacity as a function of the applied voltage (between 0.4 and 2.0 V) using the DC source. It can be seen from Fig. 5A that, when using NaCl as the electrolyte, as the applied voltage was increased the removal capacity of the electrodes also increased. The optimum voltage was found to be 1.2 V, as further increase in voltage over 1.8 V led to electrolysis of water in the presence of NaCl, which was evidenced by the decrease in the volume of water upon prolonged operation. In Fig. 5B the desalination capacity of CA at 1.2 V using different salt solutions (200 ppm) is showcased. It can be seen that higher the valence of the metal ion, higher is the efficiency of salt removal, all other parameters being the same. The maximum adsorption capacity of the material was found to be 7.68 and 10.45 mg/g for CSA and CA, respectively. These values are higher than most of the previously reported adsorption capacities for carbon based CDI electrodes in batch mode [33]. Table 1 shows the comparison of efficiency of different electrode materials

reported in the recent past. The rate of adsorption of the material was evaluated and it was noted that a three step event occurred: a) an initial kinetics where the electro-adsorption was 0.280 mg/min for 12 min (fast kinetics as all the vacant sites are available for adsorption), b) 0.098 mg/min from 12 to 80 min (slow kinetics) and c) 0.002 mg/min from 80 to 120 min (very slow kinetics, where equilibrium is reached and no more adsorption occurred); data are shown in SI Fig. S8a. It was observed that the material reached saturation at 80 min from the initiation of the electro-adsorption process. Lagergren pseudo-first-order [34] and Ho's pseudo-second-order [35] mathematical models were used for describing the kinetic data. Details are given in supporting information Fig. S8. The fitting shows that Lagergren pseudo-first-order matches more with the experimental data as shown in SI Fig. S8b.

To test the potential of CA in real time CDI applications for water treatment, we examined desorption from the electrode material, following an adsorption step, by changing the terminal of the DC source. Multiple such adsorption–desorption cycles were carried out to evaluate the efficiency of the electrodes using 200 ppm of NaCl solution. Fig. 5C and D shows that even after five cycles, there was no loss in the adsorption capacity of both CSA and CA. It can also be deduced that the adsorption efficiency of CA is higher than that of CSA. At the end of each adsorption step, ~60 and 100 ppm of metal ions are adsorbed by CSA and CA, respectively. The effect of varying concentration of the electrolyte was analyzed by performing CDI for CA using NaCl solution at three different concentrations (200, 400 and 800 ppm) (SI, Fig. S9). We found that the adsorption capacity of CA did not change as NaCl concentration was increased and for each case it was ~10 mg/g, this indicates that the material has reached saturation limit at 200 ppm itself. These experiments prove that CA is suitable for CDI applications.

The electrode material (CA) was characterized after one adsorption cycle. For this the adsorption process was continued until the electrodes got saturated using NaCl as the electrolyte. It is seen that the cathode contains only positive ions and the anode contains only negatively charged ions. The SEM-EDS of the cathode and anode in Fig. 6A and B confirm the presence of sodium in the former and chloride in the latter. The elemental mapping shows that these ions are uniformly distributed on the surface of the electrodes. The XRD spectrum of CA before and after a single adsorption step is shown in SI Fig. S10. The XPS spectra of the electrodes after the adsorption step in Fig. 6C and D reaffirm the presence of sodium and chloride ions in the anode and cathode, respectively based on the peaks for sodium and chlorine at 1072.1 eV and 198.5 eV, respectively.

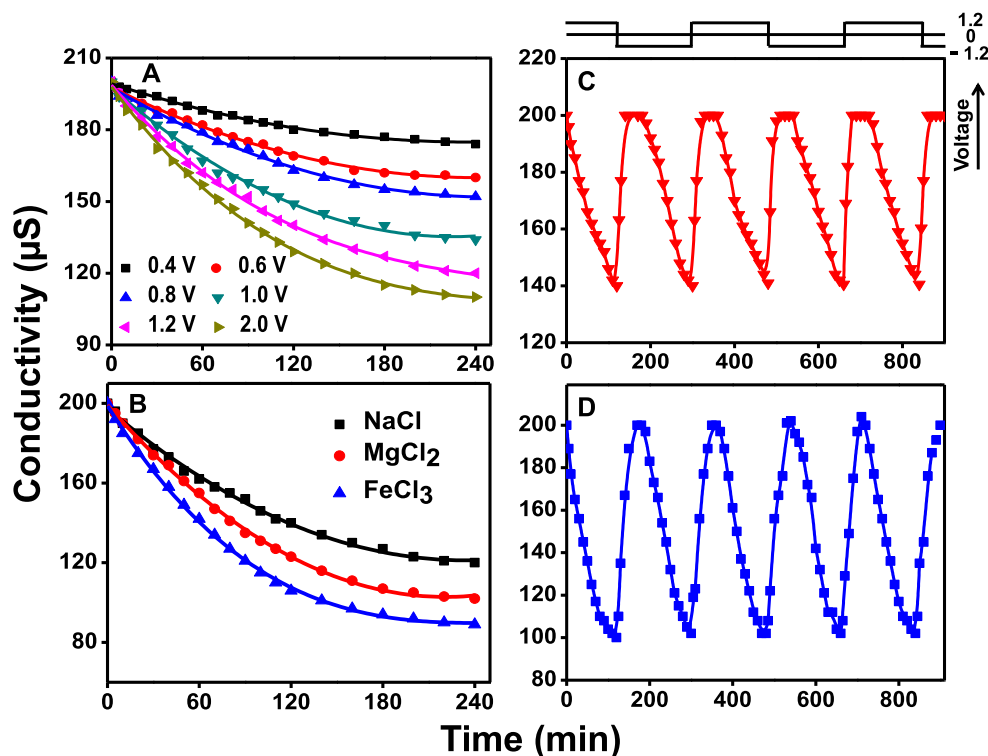


Fig. 5. A) Adsorption capacity of CA (with 1 M NaCl as the electrolyte) as a function of the applied voltage in the range of 0.4–2.0 V and B) CDI performance of CA using different electrolytes at 1.2 V. CDI efficiency of C) CSA and D) CA over five adsorption–desorption cycles. The fit over figure C represents the variation of voltage with respect to time from 1.2 to –1.2 V. (A color version of this figure can be viewed online).

Table 1

Comparison of electrode material efficiency in term of salt adsorption capacity in mg/g reported in the recent past.

First author/journal [ref]	Year of publication	Material	Initial salt concentration (mg/L)	Salt adsorption (mg/g)
Joseph C. Farmer/J. Electrochem. Soc. [36]	1996	CA	50	1.40
		CA	500	2.90
Kai Dai/Mater. Lett. [37]	2005	MWCNT's	3000	1.70
Linda Zou/Water Res. [38]	2008	Mesoporous carbon	25	0.68
Lixia Li/Carbon [39]	2009	Mesoporous carbon	50	0.93
Zheng Peng/J. Mater. Chem. [40]	2012	Mesoporous carbon–CNTs	46	0.63
Min-Woong Ryoo/Water Res. [41]	2003	TiO AC cloth	5844	4.30
Juan Yang/Desalination [42]	2011	MnO ₂ –AC	25	1.00
Yu-Jin Kim/Sep. Purif. Technol. [43]	2010	AC	200	3.70
X.Z. Wang/Electrochem. Solid-State Lett. [44]	2006	CNT-nanofibers	110	3.30
Gang Wang/Electrochim. Acta. [11]	2012	Carbon nanofiber webs	95	4.60
Haibo Li/J. Electroanal. Chem. [42]	2011	SWCNT's	23	0.75
Haibo Li/J. Mater. Chem. [45]	2009	Graphene	25	1.80
Zhuo Wang/Desalination [46]	2012	Functional RGO	65	3.20
Haibo Li/Environ. Sci. Technol. [47]	2010	Graphene-like nanoflakes	25	1.30
Dengsong Zhang/J. Mater. Chem. [48]	2012	Graphene–CNT	29	1.40
Haibo Li/J. Mater. Chem. [49]	2012	Reduced graphene oxide–AC	50	2.90
Yue Wang/Desalination [50]	2014	CNT–CNT	1000	11.00
		Polypyrrole/CNT	1000	43.99
Lumeng Chao/J. Mater. Chem. A [51]	2015	Porous carbon materials	40	34.27
Nalenthiran Pugazhenthiran/ACS Appl. Mater. Interfaces. [52]	2015	Cellulose derived graphenic fibers	500	13.10
Xiaoyu Gu/Electrochem. Acta [53]	2015	Graphene–Fe ₃ O ₄	300	10.30
Xiaoyu Gu/ACS Sustain. Chem. Eng. [54]	2015	Graphene–chitosan–Mn ₃ O ₄	300	12.70
Changming Wang/Desalination [55]	2015	AC	100	14.32

The XPS survey spectrum in Fig. 7A represents CA after adsorption–desorption cycles. Fig. 7a represents the XPS spectrum of CA before adsorption (also shown in Fig. 2D). After the first adsorption cycle, the material was characterized (cathode) and it showed sodium at 1072.1 eV along with carbon and oxygen

(Fig. 7b). The same material after desorption (Fig. 7c) shows a similar survey spectrum as that of the initial material (Fig. 7a). Similarly, the same material was characterized by XPS after tenth adsorption–desorption cycle (Fig. 7d and e). Sodium was getting adsorbed on to the electrodes and was desorbed completely after

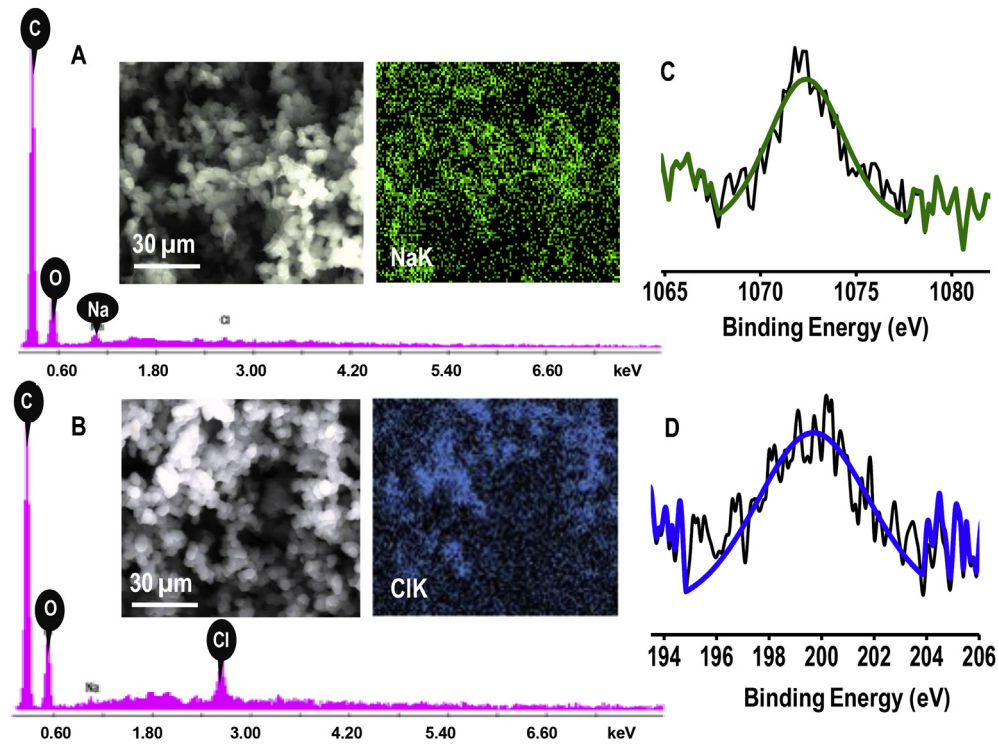


Fig. 6. SEM–EDAX of A) cathode and B) anode and the deconvoluted XPS spectrum of C) sodium in cathode and D) chloride in anode after a single adsorption cycle. (A color version of this figure can be viewed online).

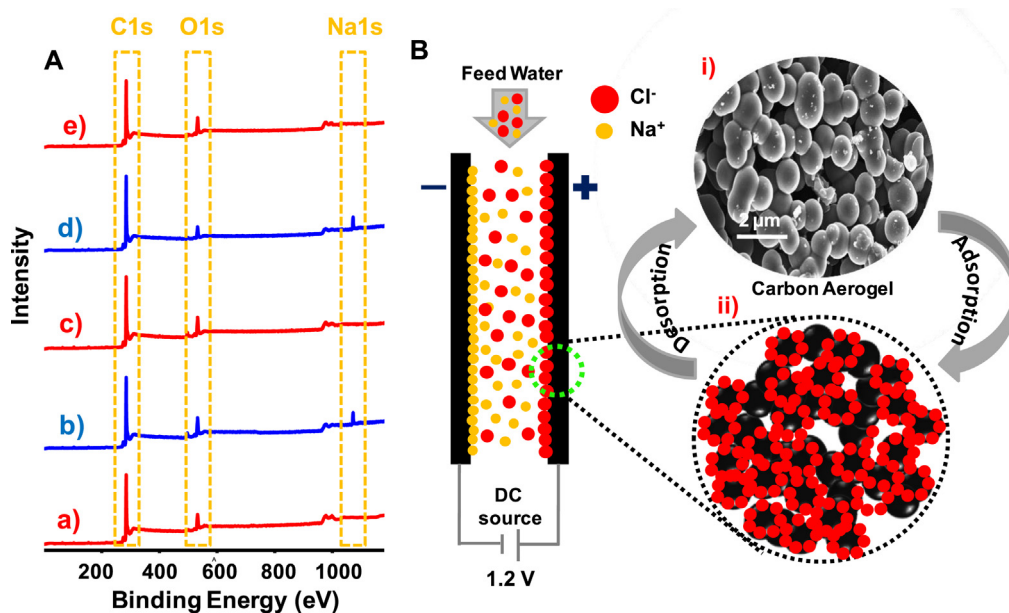


Fig. 7. A) XPS spectrum of carbon aerogel a) before adsorption (pristine CA), b) after adsorption (first cycle), c) after desorption (first cycle), d) after adsorption (tenth cycle) and e) after desorption (tenth cycle). Areas of importance are marked. B) Schematic showing the adsorption–desorption process used in multiple cycles. i) FESEM image of carbon aerogel and ii) the schematic of the anode surface showing the presence of anion on its surface after adsorption. (A color version of this figure can be viewed online).

the desorption cycle. The intensity ratio of carbon:oxygen remains the same even after the tenth cycle which confirms that no oxidation is occurring on the electrode surface during the process. The deconvoluted carbon and oxygen spectra of the material (survey spectra are in traces a, d and e of Fig. 7A) show that there is no change in the oxidation state. The data are shown in SI Fig. S11. The data further confirm that the material can be used for multiple

cycles. The schematic in Fig. 7B shows the adsorption–desorption process used in multiple cycles.

4. Conclusion

In this paper we have synthesized a porous carbon aerogel with tunable porosity, high surface area of 2600 m²/g and good

mechanical strength. We employed a simple and cost effective one step sol–gel process, which avoided supercritical and freeze drying processes and did not require any hard or soft template for fabrication. This process to build a carbon inorganic framework can be easily scaled up for industrial applications such as water desalination. The as-synthesized CA was used as a CDI electrode for water desalination to remove salts such as NaCl, MgCl₂ and FeCl₃. The NaCl removal capacity of CA with and without silica etching was determined to be 10.54 and 7.64 mg/g, respectively at 1.2 V. Multiple adsorption–desorption cycles were performed to test the efficiency of the electrodes and it was illustrated that CA can be scaled up and used in a real time water desalination unit.

Acknowledgment

This work was supported by the DST Unit of Excellence on Soft Nanofabrication at the Indian Institute of Technology Kanpur and the Indian Institute of Technology Madras established by the Department of Science and Technology, New Delhi, India. SSG thanks SERB, CII and Thermax India Pvt. Ltd. for a research fellowship.

Appendix A. Supporting information

Supporting information related to this article can be found at <http://dx.doi.org/10.1016/j.carbon.2015.12.004>.

References

- [1] T.P. Barnett, J.C. Adam, D.P. Lettenmaier, Potential impacts of a warming climate on water availability in snow-dominated regions, *Nature* 438 (7066) (2005) 303–309.
- [2] M.A. Shannon, P.W. Bohn, M. Elimelech, J.G. Georgiadis, B.J. Marinas, A.M. Mayes, Science and technology for water purification in the coming decades, *Nature* 452 (7185) (2008) 301–310.
- [3] M. Elimelech, W.A. Phillip, The future of seawater desalination: energy, technology, and the environment, *Science* 333 (6043) (2011) 712–717.
- [4] R.F. Service, Desalination freshens up, *Science* 313 (5790) (2006) 1088–1090.
- [5] R.J. Petersen, Composite reverse osmosis and nanofiltration membranes, *J. Membr. Sci.* 83 (1) (1993) 81–150.
- [6] R. Gopal, S. Kaur, Z. Ma, C. Chan, S. Ramakrishna, T. Matsuura, Electrospun nanofibrous filtration membrane, *J. Membr. Sci.* 281 (1–2) (2006) 581–586.
- [7] E.G. Akgemci, M. Ersoz, T. Atalay, Transport of formic acid through anion exchange membranes by diffusion dialysis and electro-electro dialysis, *Sep. Sci. Technol.* 39 (1) (2004) 165–184.
- [8] L. Zou, G. Morris, D. Qi, Using activated carbon electrode in electrosorptive deionization of brackish water, *Desalination* 225 (1–3) (2008) 329–340.
- [9] H.-J. Oh, J.-H. Lee, H.-J. Ahn, Y. Jeong, Y.-J. Kim, C.-S. Chi, Nanoporous activated carbon cloth for capacitive deionization of aqueous solution, *Thin Solid Films* 515 (1) (2006) 220–225.
- [10] M.W. Ryoo, G. Seo, Improvement in capacitive deionization function of activated carbon cloth by titania modification, *Water Res.* 37 (7) (2003) 1527–1534.
- [11] G. Wang, C. Pan, L. Wang, Q. Dong, C. Yu, Z. Zhao, et al., Activated carbon nanofiber webs made by electrospinning for capacitive deionization, *Electrochim. Acta* 69 (0) (2012) 65–70.
- [12] S. Porada, L. Weinstein, R. Dash, A. van der Wal, M. Bryjak, Y. Gogotsi, et al., Water desalination using capacitive deionization with microporous carbon electrodes, *ACS Appl. Mater. Interfaces* 4 (3) (2012) 1194–1199.
- [13] L. Tang, Y. Wang, Y. Li, H. Feng, J. Lu, J. Li, Preparation, structure, and electrochemical properties of reduced graphene sheet films, *Adv. Funct. Mater.* 19 (17) (2009) 2782–2789.
- [14] D. Zhang, X. Wen, L. Shi, T. Yan, J. Zhang, Enhanced capacitive deionization of graphene/mesoporous carbon composites, *Nanoscale* 4 (17) (2012) 5440–5446.
- [15] Z. Sui, Q. Meng, X. Zhang, R. Ma, B. Cao, Green synthesis of carbon nanotube-graphene hybrid aerogels and their use as versatile agents for water purification, *J. Mater. Chem.* 22 (18) (2012) 8767–8771.
- [16] H. Yin, S. Zhao, J. Wan, H. Tang, L. Chang, L. He, et al., Three-dimensional graphene/metal oxide nanoparticle hybrids for high-performance capacitive deionization of saline water, *Adv. Mater.* 25 (43) (2013) 6270–6276.
- [17] Z. Peng, D.S. Zhang, L.Y. Shi, T.T. Yan, High performance ordered mesoporous carbon/carbon nanotube composite electrodes for capacitive deionization, *J. Mater. Chem.* 22 (14) (2012) 6603–6612.
- [18] C. Yan, Y.W. Kanaththage, R. Short, C.T. Gibson, L.D. Zou, Graphene/polyaniline nanocomposite as electrode material for membrane capacitive deionization, *Desalination* 344 (2014) 274–279.
- [19] A.G. El-Deen, N.A.M. Barakat, H.Y. Kim, Graphene wrapped MnO₂-nanostructures as effective and stable electrode materials for capacitive deionization desalination technology, *Desalination* 344 (2014) 289–298.
- [20] M. Haro, G. Rasines, C. Macias, C.O. Ania, Stability of a carbon gel electrode when used for the electro-assisted removal of ions from brackish water, *Carbon* 49 (12) (2011) 3723–3730.
- [21] G.-P. Wu, J. Yang, D. Wang, R. Xu, K. Amine, C.-X. Lu, A novel route for preparing mesoporous carbon aerogels using inorganic templates under ambient drying, *Mater. Lett.* 115 (0) (2014) 1–4.
- [22] M.C. Zafra, P. Lavela, G. Rasines, C. MacAs, J.L. Tirado, C.O. Ania, A novel method for metal oxide deposition on carbon aerogels with potential application in capacitive deionization of saline water, *Electrochim. Acta* 135 (0) (2014) 208–216.
- [23] J.Y. Liu, S.P. Wang, J.M. Yang, J.J. Liao, M. Lu, H.J. Pan, et al., ZnCl₂ activated electrospun carbon nanofiber for capacitive desalination, *Desalination* 344 (2014) 446–453.
- [24] C.M. Yang, W.H. Choi, B.K. Na, B.W. Cho, W.I. Cho, Capacitive deionization of NaCl solution with carbon aerogel-silica gel composite electrodes, *Desalination* 174 (2) (2005) 125–133.
- [25] L. Xia, M. Zhang, M. Rong, K. Guo, Y. Hu, Y. Wu, et al., An easy soft-template route to synthesis of wormhole-like mesoporous tungsten carbide/carbon composites, *Compos. Sci. Technol.* 72 (14) (2012) 1651–1655.
- [26] S.A. Al-Muhtaseb, J.A. Ritter, Preparation and properties of resorcinol–formaldehyde organic and carbon gels, *Adv. Mater.* 15 (2) (2003) 101–114.
- [27] G. Rasines, P. Lavela, C. MacAs, M. Haro, C.O. Ania, J.L. Tirado, Electrochemical response of carbon aerogel electrodes in saline water, *J. Electroanal. Chem.* 671 (0) (2012) 92–98.
- [28] S.J. Kim, S.W. Hwang, S.H. Hyun, Preparation of carbon aerogel electrodes for supercapacitor and their electrochemical characteristics, *J. Mater. Sci.* 40 (3) (2005) 725–731.
- [29] S.W. Hwang, S.H. Hyun, Capacitance control of carbon aerogel electrodes, *J. Non-Cryst. Solids* 347 (1–3) (2004) 238–245.
- [30] H.H. Jung, S.W. Hwang, S.H. Hyun, L. Kang-Ho, G.T. Kim, Capacitive deionization characteristics of nanostructured carbon aerogel electrodes synthesized via ambient drying, *Desalination* 216 (1–3) (2007) 377–385.
- [31] H. Sun, Z. Xu, C. Gao, Multifunctional, ultra-flyweight, synergistically assembled carbon aerogels, *Adv. Mater.* 25 (18) (2013) 2554–2560.
- [32] L.G. Austin, E.G. Gagnon, The triangular voltage sweep method for determining double-layer capacity of porous electrodes: part I, Theory, *J. Electrochem. Soc.* 120 (2) (1973) 251–254.
- [33] S. Porada, R. Zhao, A. van der Wal, V. Presser, P.M. Biesheuvel, Review on the science and technology of water desalination by capacitive deionization, *Prog. Mater. Sci.* 58 (8) (2013) 1388–1442.
- [34] S. Lagergren, Zur Theorie der sogenannten Absorption gelöster Stoffe, *PA Norstedt & söner*, 1898.
- [35] Y.S. Ho, Review of second-order models for adsorption systems, *J. Hazard. Mater.* 136 (3) (2006) 681–689.
- [36] J.C. Farmer, D.V. Fix, G.V. Mack, R.W. Pekala, J.F. Poco, Capacitive deionization of NaCl and NaNO₃ solutions with carbon aerogel electrodes, *J. Electrochem. Soc.* 143 (1) (1996) 159–169.
- [37] K. Dai, L. Shi, J. Fang, D. Zhang, B. Yu, NaCl adsorption in multi-walled carbon nanotubes, *Mater. Lett.* 59 (16) (2005) 1989–1992.
- [38] L. Zou, L. Li, H. Song, G. Morris, Using mesoporous carbon electrodes for brackish water desalination, *Water Res.* 42 (8–9) (2008) 2340–2348.
- [39] L. Li, L. Zou, H. Song, G. Morris, Ordered mesoporous carbons synthesized by a modified sol–gel process for electrosorptive removal of sodium chloride, *Carbon* 47 (3) (2009) 775–781.
- [40] Z. Peng, D. Zhang, L. Shi, T. Yan, High performance ordered mesoporous carbon/carbon nanotube composite electrodes for capacitive deionization, *J. Mater. Chem.* 22 (14) (2012) 6603–6612.
- [41] M.-W. Ryoo, G. Seo, Improvement in capacitive deionization function of activated carbon cloth by titania modification, *Water Res.* 37 (7) (2003) 1527–1534.
- [42] H. Li, L. Pan, T. Lu, Y. Zhan, C. Nie, Z. Sun, A comparative study on electro-sorptive behavior of carbon nanotubes and graphene for capacitive deionization, *J. Electroanal. Chem.* 653 (1–2) (2011) 40–44.
- [43] Y.-J. Kim, J.-H. Choi, Enhanced desalination efficiency in capacitive deionization with an ion-selective membrane, *Sep. Purif. Technol.* 71 (1) (2010) 70–75.
- [44] X.Z. Wang, M.G. Li, Y.W. Chen, R.M. Cheng, S.M. Huang, L.K. Pan, et al., Electro-sorption of NaCl solutions with carbon nanotubes and nanofibers composite film electrodes, *Electrochem. Solid-State Lett.* 9 (9) (2006) E23–E26.
- [45] H. Li, T. Lu, L. Pan, Y. Zhang, Z. Sun, Electro-sorption behavior of graphene in NaCl solutions, *J. Mater. Chem.* 19 (37) (2009) 6773–6779.
- [46] Z. Wang, B. Dou, L. Zheng, G. Zhang, Z. Liu, Z. Hao, Effective desalination by capacitive deionization with functional graphene nanocomposite as novel electrode material, *Desalination* 299 (0) (2012) 96–102.
- [47] H. Li, L. Zou, L. Pan, Z. Sun, Novel graphene-like electrodes for capacitive deionization, *Environ. Sci. Technol.* 44 (22) (2010) 8692–8697.
- [48] D. Zhang, T. Yan, L. Shi, Z. Peng, X. Wen, J. Zhang, Enhanced capacitive deionization performance of graphene/carbon nanotube composites, *J. Mater. Chem.* 22 (29) (2012) 14696–14704.
- [49] H. Li, L. Pan, C. Nie, Y. Liu, Z. Sun, Reduced graphene oxide and activated

- carbon composites for capacitive deionization, *J. Mater. Chem.* 22 (31) (2012) 15556–15561.
- [50] Y. Wang, L. Zhang, Y. Wu, S. Xu, J. Wang, Polypyrrole/carbon nanotube composites as cathode material for performance enhancing of capacitive deionization technology, *Desalination* 354 (2014) 62–67.
- [51] L. Chao, Z. Liu, G. Zhang, X. Song, X. Lei, M. Noyong, et al., Enhancement of capacitive deionization capacity of hierarchical porous carbon, *J. Mater. Chem. A* 3 (24) (2015) 12730–12737.
- [52] N. Pugazhenthiran, S. Sen Gupta, A. Prabhath, M. Manikandan, J.R. Swathy, V.K. Raman, et al., Cellulose derived graphenic fibers for capacitive desalination of brackish water, *ACS Appl. Mater. Interfaces* 7 (36) (2015) 20156–20163.
- [53] X. Gu, M. Hu, Z. Du, J. Huang, C. Wang, Fabrication of mesoporous graphene electrodes with enhanced capacitive deionization, *Electrochim. Acta* 182 (2015) 183–191.
- [54] X. Gu, Y. Yang, Y. Hu, M. Hu, C. Wang, Fabrication of graphene-based xerogels for removal of heavy metal ions and capacitive deionization, *ACS Sustain. Chem. Eng.* 3 (6) (2015) 1056–1065.
- [55] C. Wang, H. Song, Q. Zhang, B. Wang, A. Li, Parameter optimization based on capacitive deionization for highly efficient desalination of domestic wastewater biotreated effluent and the fouled electrode regeneration, *Desalination* 365 (2015) 407–415.

Carbon aerogels through organo-inorganic co-assembly and their application in water desalination by capacitive deionization

Rudra Kumar^{1#}, Soujit Sen Gupta^{2#}, Shishir Katiyar¹, V. Kalyan Raman³, Siva Kumar Varigala³, T. Pradeep^{2*} and Ashutosh Sharma^{1*}

¹*DST Unit on Nanoscience, Department of Chemical Engineering, Indian Institute of Technology Kanpur 208016, India*

²*DST Unit on Nanoscience and Thematic Unit of Excellence (TUE), Department of Chemistry, Indian Institute of Technology Madras, Chennai 600036, India*

³*Centre of Excellence (Biotechnology) & Water and wastewater Technology, Thermax Limited, Pune 411019, India*

[#]*Both the authors contributed equally*

^{*}*Email: ashutos@iitk.ac.in; pradeep@iitm.ac.in*

Contents

N ₂ adsorption–desorption isotherm for pore size distribution of CA	Page 2
Compressive stress-strain curve for carbon aerogel	Page 3
Change in porosity with the change in concentration of the SiO ₂ precursor	Page 4
XPS survey spectrum of CSA	Page 5
SEM image and EDS of CSA	Page 6
CV curves of the carbon-silica aerogel	Page 7
Photograph of the CDI laboratory batch experimental set-up	Page 8
Rate of adsorption and kinetics for the CA material	Page 9
CDI performance of CA with different initial concentrations of NaCl	Page 10
XRD of CA before and after single adsorption cycle	Page 11
Decovoluted XPS spectrum of C1s and O1s after different cycles	Page 12

Supporting Information S1

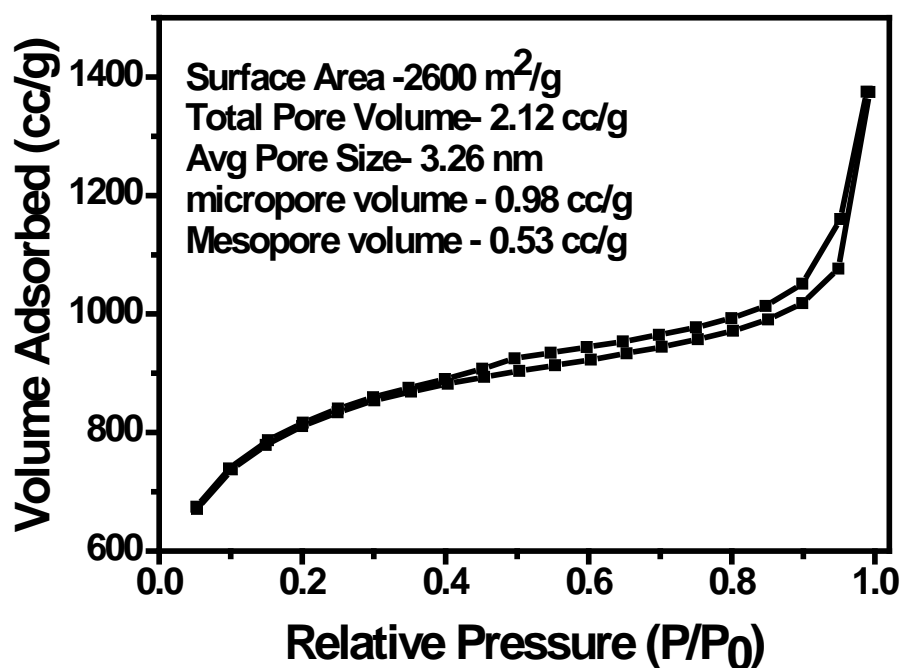


Fig. S1: N₂ adsorption–desorption isotherm and data of pore size distribution of CA.

Porosity measurement of CA sample shows that the total pore volume was 2.12 cc/g and average pore size was 3.26 nm. The pore size distribution (PSD) was obtained from the Barret-Joyner-Halenda (BJH) method.

The hysteresis in the curve at higher P/P₀ value shows the presence of large mesopores which arises due to the cross linking of smaller particles.

Supporting Information S2

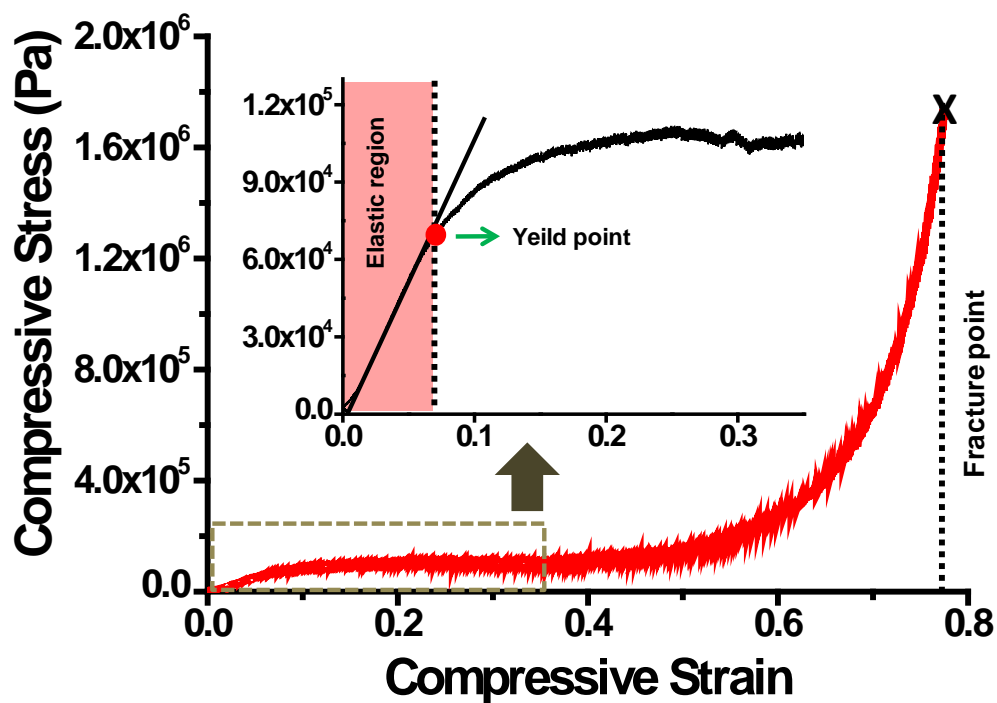


Fig. S2: Compressive stress-strain curve for carbon aerogel. The expanded region shows the elastic region and the yield point (marked). Fracture point is marked in the figure. The Young's modulus was calculated to be 1.12 MPa from the straight line (tangent) drawn in the elastic region.

Supporting Information S3

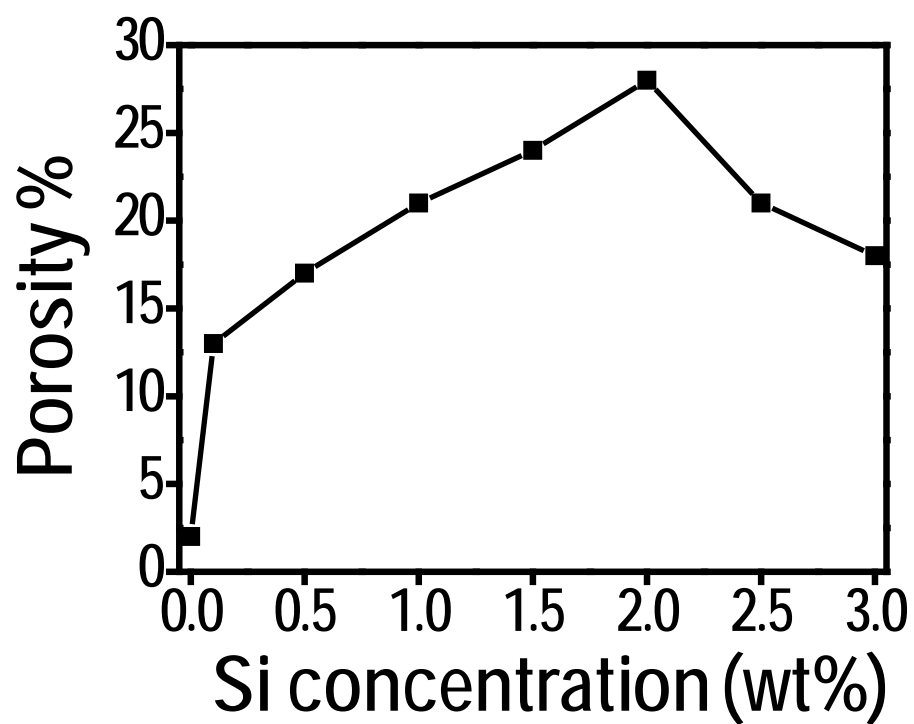


Fig. S3: Variation of porosity of CSA with the change in concentration of the SiO₂ precursor.

Supporting Information S4

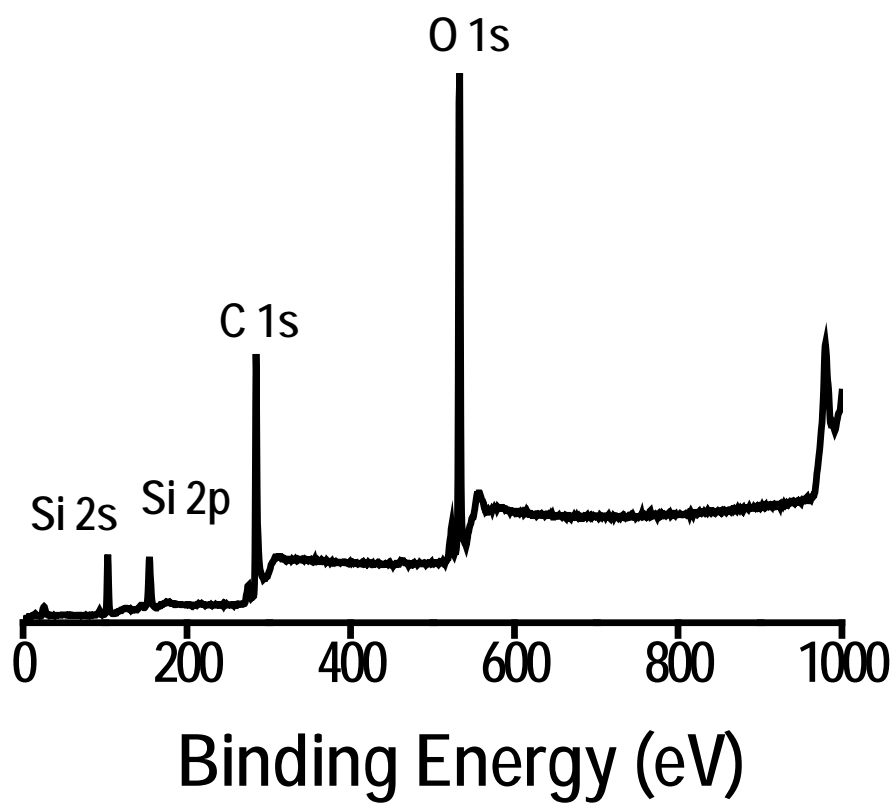


Fig. S4: XPS survey spectrum of CSA.

Supporting Information S5

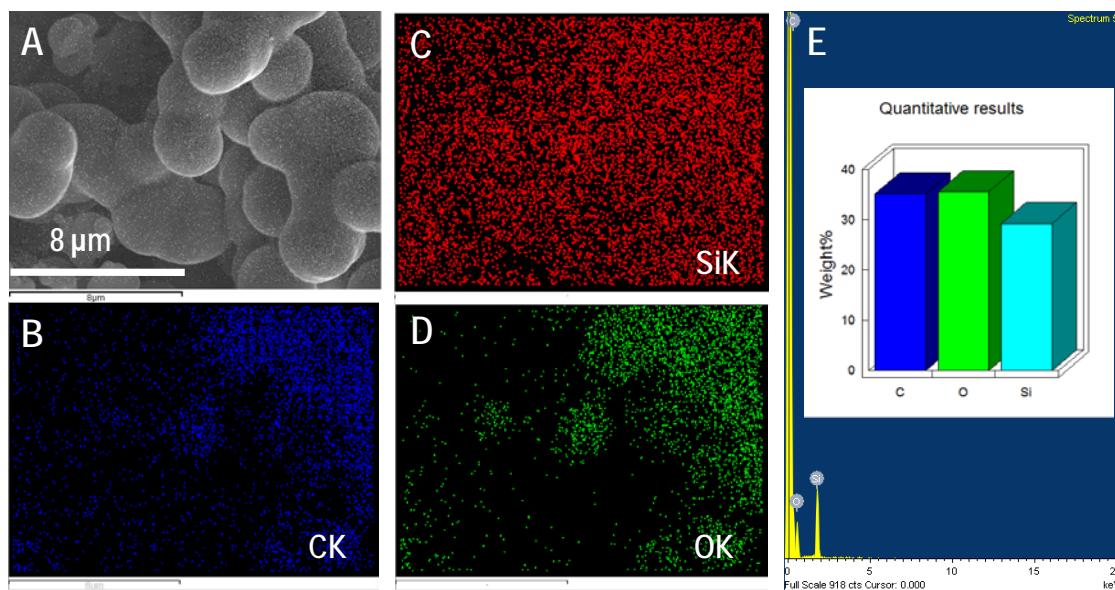


Fig. S5: A) SEM image of CSA B, C,D) EDS mapping of carbon, silica and oxygen and E)SEM-EDS with weight ratio of SiO₂ carbon aerogel.

Supporting Information S6

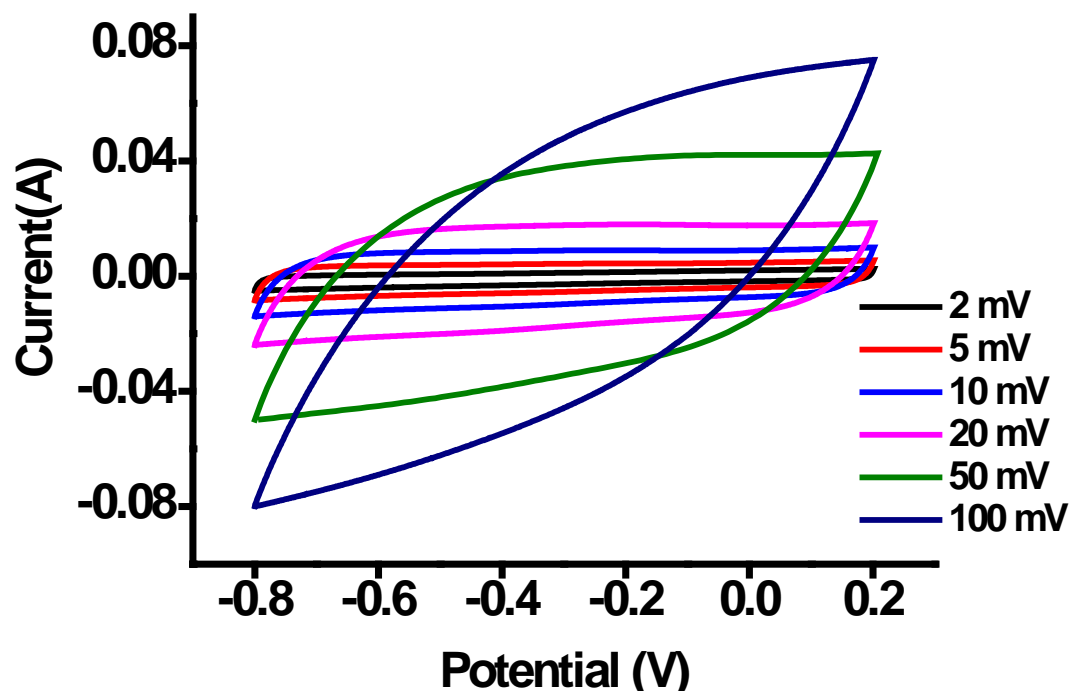


Fig. S6: CV curves of the carbon-silica aerogel at scan rates between 2 to 100 mV/s.

Supporting Information S7



Fig. S7: Photograph of the CDI laboratory batch experimental set-up.

Supporting Information S8

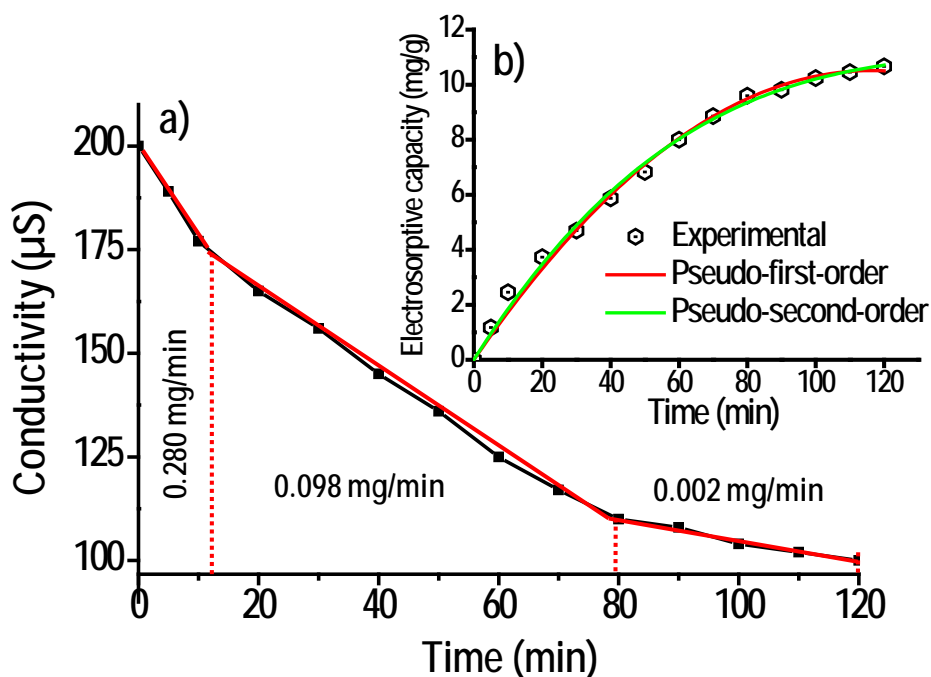


Fig. S8: a) Rate of adsorption for the CA material, having 200 ppm of NaCl solution. The kinetics shows a three step adsorption and b) represents the electrosorption kinetics for the CA electrodes and comparison with existing mathematical models.

The mathematical representations of the models are given below:

Pseudo-first-order equation:
$$q_t = q_e \left(1 - e^{-k_1 t}\right) \quad (1)$$

Pseudo- second-order equation:
$$q_t = \frac{q_e^2 k_2 t}{1 + q_e k_2 t} \quad (2)$$

Here, q_e and q_t (mg/g) denotes the amount of salt ion adsorbed at equilibrium and at time t (h), respectively. k_1 (1/h) and k_2 (g/mg h) are the first-order and second-order rate constants, respectively.

Supporting Information S9

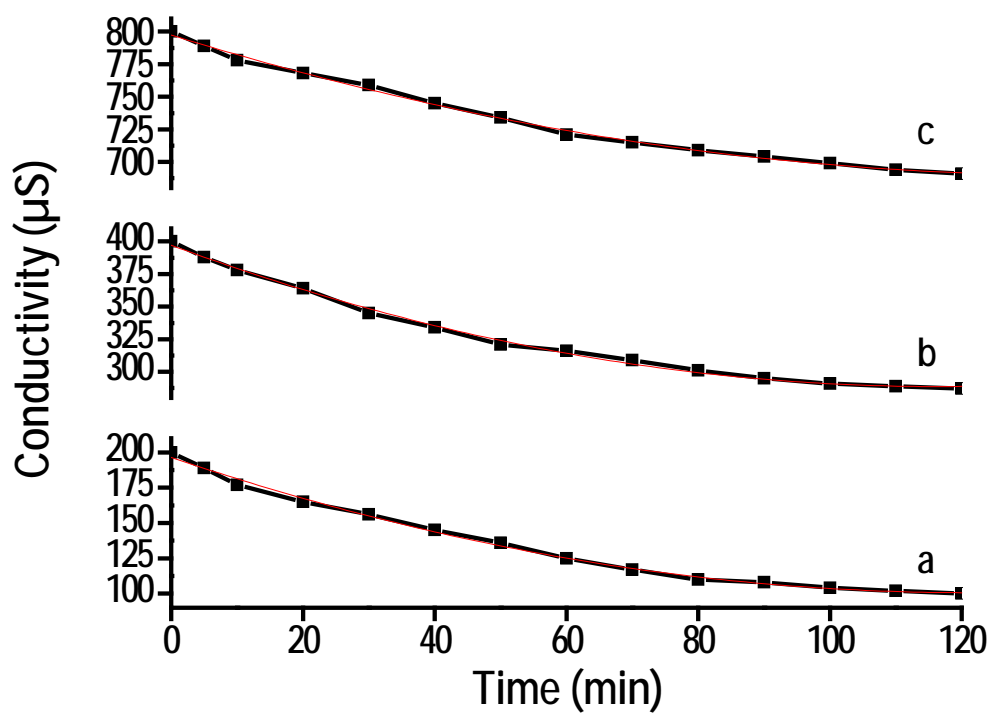


Fig. S9: CDI performance of CA with different initial concentrations of NaCl solution as electrolyte a) 200 ppm, b) 400 ppm and c) 800 ppm.

Supporting Information S10

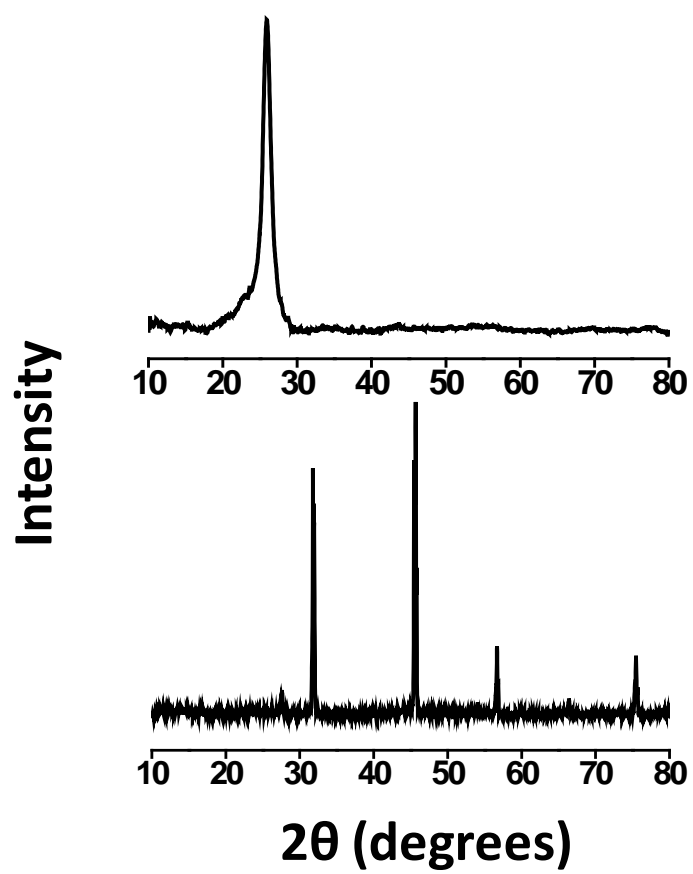


Fig. S10: XRD of CA A) before and B) after a single adsorption cycle.

Supporting Information S11

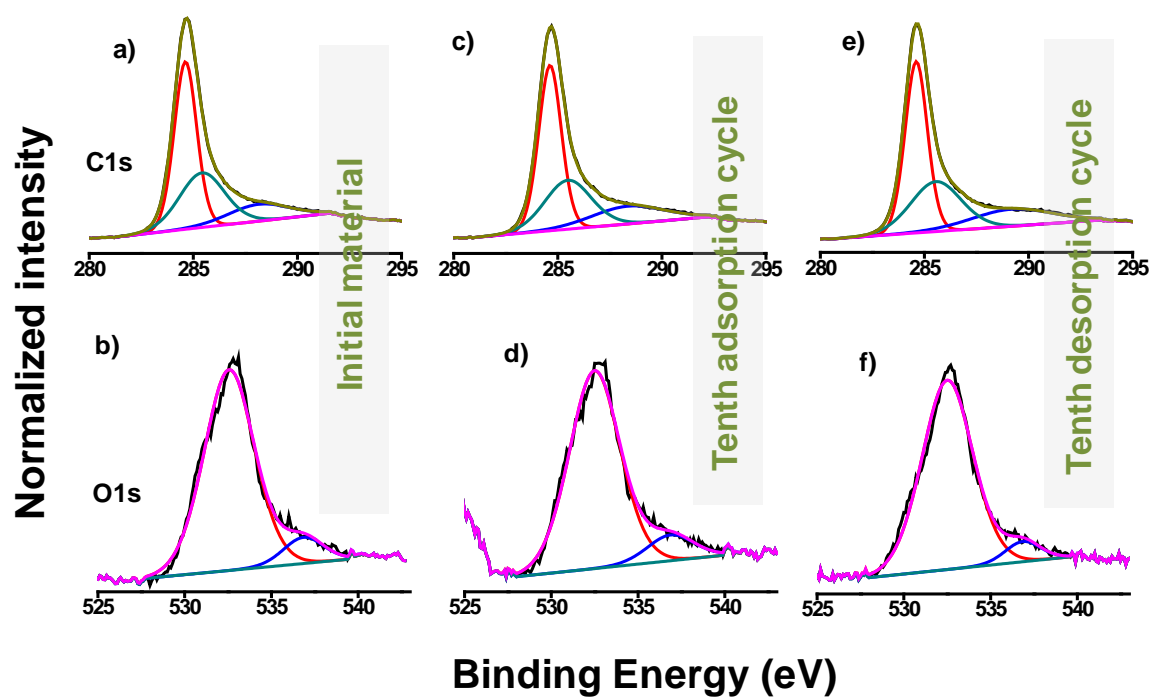


Fig. S11: Decoupled XPS spectrum of C1s and O1s, a & b) of pristine CA, c & d) after tenth adsorption cycle and e & f) after tenth desorption cycle. The corresponding XPS survey spectrum is shown in Figure 6A in the manuscript.

Metallic Nanobrushes Made using Ambient Droplet Sprays

By Depanjan Sarkar, Maheswari Kavirajan Mahitha, Anirban Som, Anyin Li, Michael Wleklinski, Robert Graham Cooks,* and Thalappil Pradeep*

Keywords: 1D nanostructures, droplet spray, mass spectrometry, nanomaterials, nanowires, Raman spectroscopy

There are important implications for science and technology in the ability to create structures composed of tens of micrometer long, uniformly aligned, nanowires. They include improvements in understanding electronic structures of materials, creation of photonic devices, band gap engineering, and surface-derivatized nanostructures for use as sensors and for fundamental studies of catalysis.^[1] While advances in materials science have contributed various methods for the synthesis of aligned nanostructures on surfaces, often such methods involve processing in vacuum and/or the use of special features like magnetic fields,^[2] dipole–dipole attraction,^[3] directional freezing,^[4] and template mediation.^[5] Here, we introduce an ambient solution-state procedure for making oriented 1D nanostructures which can cover and pattern large areas.

Spray pyrolysis is an established method of making materials,^[6] especially thin films. Several variations of this method exist which result in nanoscale oxides^[7] and related materials. However, these methods do not produce metal nanoparticles. Anisotropic growth of nanostructures has not been observed in such cases. Here we report spontaneous electric field induced assembly of charged microdroplets in air, producing nanowires (NWs) by the 1D assembly of nanoparticles (NPs). The possibility of extending this over cm² areas and control of individual wires so prepared are presented here. The possibility to control compositions and novel properties of the structures derived are demonstrated.

In the present experiment, a home-built nanoelectrospray source was directed to deliver charged droplets of silver acetate (AgOAc) in water onto a conductive mesh (usually a transmission electron microscopy (TEM) grid), placed on top of an indium tin oxide (ITO) coated glass collector. The TEM grid was used as a static mask to intercept a portion of the spray plume. The collector was grounded through a picoammeter to monitor the deposition current and a potential in the range of 1–1.5 kV was applied to the solution through a platinum

D. Sarkar, M. K. Mahitha, A. Som, Prof. R. G. Cooks, Prof. T. Pradeep, DST Unit of Nanoscience (DST UNS) and Thematic Unit of Excellence (TUE), Department of Chemistry, Indian Institute of Technology Madras, Chennai, 60036, India
A. Li, M. Wleklinski, Prof. R. G. Cooks, Prof. T. Pradeep, Department of Chemistry, Purdue University, West Lafayette, IN, 47907, USA

Correspondence to: Prof. R. G. Cooks (Email: cooks@purdue.edu), Prof. T. Pradeep (Email: pradeep@iitm.ac.in)
10.1002/adma.201505127

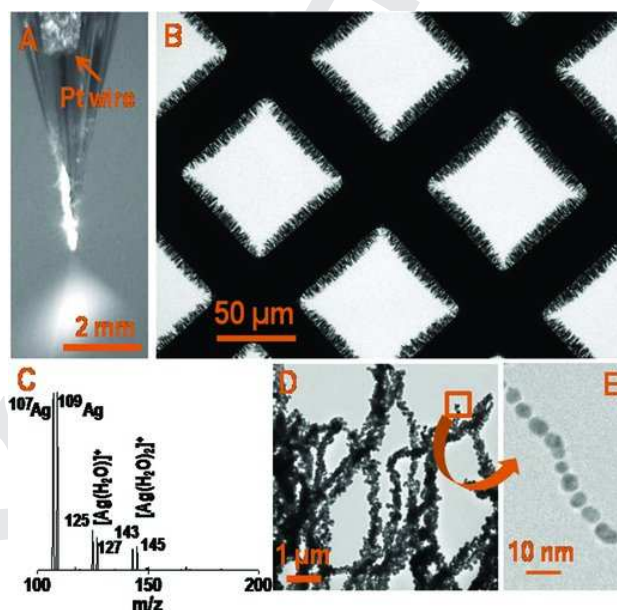


Figure 1. A) Optical image of an electro-spray experiment using AgOAc solution, showing the spray plume, B) large area TEM image of an empty TEM grid (used as mask during deposition) showing uniform NWs all over it, C) mass spectrum collected from the spray showing the presence of Ag and solvated Ag ions, D) TEM image of the nanobrush formed on the mask (an empty TEM grid in this case), showing 1D structure of the NWs, and E) Higher magnification TEM image of single building block (NW) with its pearl necklace morphology.

(Pt) wire electrode. A plume of solvated silver ions (notably, Ag(H₂O)⁺ and Ag(H₂O)₂⁺) was ejected from the nanospray tip, as confirmed by mass spectrometry. Figure 1A,C shows an optical image of the sprayer, the spray plume, and the mass spectrum collected from the plume, respectively.

In the course of silver deposition, a black circular spot (typical diameter 2 mm) due to the impinging plume appeared on the mask itself. Microscopy of this revealed an unprecedented brush-like growth of nanowires, with a linear arrangement of NPs comprising each nanowire. Figure 1B,D shows TEM images of such nanowires at different magnifications. A higher magnification image of the same sample (Figure 1D) clearly shows a structure having linear morphology, some of

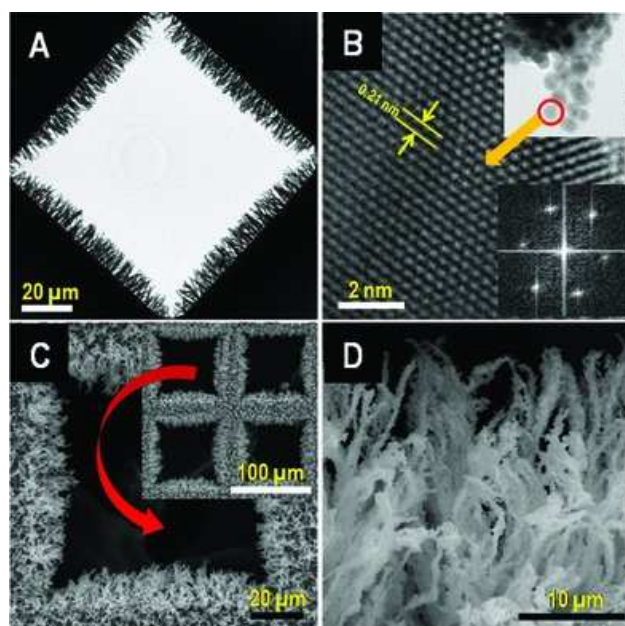


Figure 2. A,B) TEM images and C,D) FESEM images. A) TEM image of a grid after electrolytic spray deposition of Ag, B) HRTEM shows Ag lattice plane in one NP constituting the brush, inset is a high magnification TEM image showing a "pearl necklace" collection of NPs, C) FESEM of the same grid showing Ag growth all over the grid (inset shows large area image), and D) high magnification SEM image of the same grid showing rough edges of the NWs.

them somewhat bent. The growth in each NW is clearly 1D and not dendritic; although the imaging electron beam can cause the wires to adhere (Figures 1C, 2A); they are clearly not branched. This 1D wire-like growth occurred only on the mask: the same ion plume generated a collection of NPs when it fell directly onto the collector (Figure S1, Supporting Information). Close examination showed that the NWs are typically assembled in small groups (nanobristles) and these in turn are arrayed on the surface to create a nanobrush. Each nanobristle is braided. Figure 1D shows a TEM image from the tip of a brush, where it is clearly visible that nanobristles are protruding from the brush. So, this image proves that each brush is a braid of a member of nanowires of 5–7 nm diameter. If we look closely at the nanobristles, they are composed of NPs of similar shape and size, oriented linearly (Figure 1E), reminiscent of the conidial growth of fungi. In short, deposition of the solvated metal ion plume results in neutralization, aggregation, and orientation to form nanostructures.

Detailed examination of the TEM data reveals further interesting features. A TEM image of a single square of the mesh (Figure 2A) shows uniform arrays of bristles of NW structures protruding from the vertical edges of the grid. The apparently continuous nanowires and nanobristles in low magnification (Figures 1B and 2A) images prove, upon closer inspection, to have a "pearl necklace" morphology, derived from individual nanoparticles (Figures 1E and 2B inset). The TEM image in Fig-

ure 2B inset shows the assembly of NPs leading to elongated NW growth and their assembly into bristles. In this experiment, the wire length was kept deliberately small by controlling the deposition time, to reduce electron beam induced distortions of the individual structures. Figure S2 in the Supporting Information shows TEM images of such an aggregated structure where individual NPs of similar sizes are clearly visible. Figure 2B shows a high resolution transmission electron microscopy (HRTEM) image of one of the NPs in a nanowire. The measured Ag (111) lattice spacing (Figure 2B) and scanning electron microscopic–energy dispersive spectroscopy (SEM–EDS) spectrum (Figure S3, Supporting Information), confirm the presence of crystalline AgNPs.

TEM images are 2D projections of 3D objects; hence they may be misinterpreted to imply that the NW structures are formed only at the edges of the square apertures of the mesh. For better understanding of their growth, field emission scanning electron microscopic (FESEM) analysis was performed on the circular plume spot (≈ 1.5 – 2.5 mm in diameter, depending upon the distance of the collector surface from the spray emitter) on the mask. An FESEM image (Figure 2C) of the grid surface shows uniform growth of nanostructures all over the exposed surface of the grid, not only at its edges. A magnified image (Figure 2D) shows that the growth of the metallic brush appears as an extended grassland-like morphology.

The images just discussed were typically of those collected from a sample that had undergone electro spray (1 mM AgOAc solution) for 1 h. Typical deposition currents during electro spray were 40 nA corresponding to an arrival rate of 2×10^{12} ions s^{-1} . On a 2 mm diameter spot, this converts to ≈ 213 monolayers (ML) in 1 h. Using the Ag lattice constant of 0.408 nm, the thickness of 213 contiguous silver layers (of (110) stacking) is about 86.5 nm. The actual measured length of the NWs in a typical experiment is 20 micrometer, ≈ 231 times greater. The major source of this difference is the sparse spacing of the NWs making up the nanobrush surface. Figure 2A shows that in a linear distance of 100 micrometer, only about 50 nanobristles (≈ 60 nm each, composed of ≈ 75 NWs) exist. This $\approx 0.3\%$ occupancy of the available space gives rise to the ≈ 3 orders of magnitude increase in the number of layers of Ag found in the NW forming regions. The NW growth occurs only when the droplets were neutralized on the conducting grid. Powerful organizing forces must be involved in such dramatic structuring of a surface to create these brush structures. Obviously NPs formed by the deposition are arranged by this organization force, as evident from the 1D assembly shown in Figure 1E.

Coulombic assembly and basic mechanism: Aspects of the mechanism of NW growth are the following. First, as just noted, powerful electrostatic forces are involved. Second, the crystalline nature of the NWs suggests that microdroplets or solvated metal ions are deposited on the surfaces and spatial reorganization occurs while solvent is evaporating leaving behind a neutralized silver deposit. Third, small NP "pearls" attach to each other to form the growing nanowire. The edges of these structures are rough, which is ascribed to head-on accumulation of NPs as well as their orthogonal association to form nanobristles. Finally, the NPs constituting the NWs are remarkably uniform in size, especially considering that

www.advmate.de

Author Pr **ADVANCED MATERIALS**

no capping agent is used. These facts are all consistent with a Coulombic control mechanism. The electric field strength near the wires which form on the grounded metal grid is strongly enhanced with field lines radiating out from these structures. The Coulombic force due to the potential difference (≈ 1200 V, and the field strength calculated at this potential difference was 2×10^5 V m⁻¹) between the grid and the emitter harpoons metal ion microdroplets into the high field region and deposits and neutralizes them on the metal grid surface. At high fields, especially after some NW growth, field emission may be important in determining droplet neutralization. The material so formed represents a point of even higher electric field and this leads to the growth of elongated NWs. The fact that lengths of the NWs are attenuated (clearly visible in Figure 2A) in the corners of the grid also supports the role of electric fields in the growth of NWs because of the lower electric fields there. We do not understand why the NPs which make up the NWs have well-defined (5–7 nm) sizes. It could be because each microdroplet contains approximately the same number of Ag ions as there are in a 5–7 nm particle. A deposition current of 40 nA and solvent flow rate of 20 nL min⁻¹ would contain enough silver ions to produce 5–7 nm NPs if the droplets were 260–370 nm in size. Droplets smaller than 500 nm cannot be visualized but have been estimated^[8] as a plausible size in nanoelectrospray ionization. In this mechanism, the next incoming droplet would drop its cargo of Ag making a new NP instead of aggregating with the previous NP. The growth of 1D NWs would be due to preferred deposition at a NW tip (or nascent NW tip), as a result of the enhanced high electric field that exists at the tips of the NWs.^[9] A difficulty with this mechanism is the lack of experimental evidence that the NW geometry depends on spray distance and hence droplet size and the fact that a relatively tight range of droplets sizes must be invoked. Note that the process could continue to extend NWs until very long structures have been grown as shown in Figure 2D and in Figure S4 in the Supporting Information, where an aperture in the grid is almost closed by the inwardly growing NWs. A control experiment demonstrated the role of the electric field in the formation of both the NPs collected on the ITO substrate and the NWs collected on the mask. In this experiment, one TEM grid was laid on top of another with in-plane rotation to avoid complete superimposition so that a portion of the bottom grid is exposed to the impinging ion beam. Deposition of silver ions now gives SEM images (Figure S5, Supporting Information) which demonstrate that the bottom grid did not grow brushes, it only accumulated AgNPs, just as the ITO slide did; on the other hand, brushes formed on the top grid. This experiment was repeated with different concentration of solution. The result obtained in all the cases were same as discussed above. We interpret this result as suggesting that the cavity formed by the grid above the open spots on the bottom surface acts to weaken the electric field at this surface and that a strong electric field is responsible for creating the strong Coulombic force which causes charged microdroplets to be deposited as NWs.

Rapid deposition, use of other substrates and applications: The low dose of silver in these deposition experiment means that it takes a long time to make long wires or large area structures, so higher flux experiments were performed using higher

concentrations of silver salts. Interestingly the structures were unaffected by the increasing concentrations. The TEM images (Figure S6, Supporting Information) show that longer structures were produced using higher concentration in much less time. Figure S6 in the Supporting Information shows TEM images of this growth using electrospray deposition of 10 mM solution. Figure S6 A,B in the Supporting Information shows the growth after 3 and 5 h spray time, respectively. In all the above experiments, copper grids were used as masks for NW deposition, but other mask materials like stainless steel (SS) wire mesh were also used. Figure S7 in the Supporting Information shows similar growth of silver on the SS wire mesh. Metallic or in general, conducting mesh surfaces, appear to be necessary for the growth of nanobrushes. Insulating surfaces do not grow brushes. Figure S7C,D shows SEM images of Ag deposition on cotton cloth. In this case no 1D NWs were seen. Hence we propose that a conducting metallic mesh is required for making these brushes. On the other hand, different underlying substrates gave the same result. Experiments were done with ITO-coated glass slide, copper plate, SS plate, etc., all of them accumulated AgNPs whereas the mesh on top formed NWs. Rapid deposition with morphology control may be important in applications.

Plasmonic nanostructures find use as sensors^[10] being surface enhanced Raman active substrates.^[11] Figure 3A shows a hyperspectral image of the AgNPs in the prepared nanobrush. The scattering spectra collected from these particles show sharp peaks, indicating that they are plasmonic, and have a small range of sizes. The inset a in Figure 3A shows a dark field optical image of Ag brushes protruding from the edge of a TEM grid. Continuous structures are not seen as they would have been broken by the coverslip which presses against them during imaging. Inset b in Figure 3A shows scattering spectrum collected from the AgNPs. The sharpness of the spectra proves that they are plasmonic in nature. X-ray photoelectron spectroscopic (XPS) analysis (Figure S8, Supporting Information) shows that the 3d_{5/2} peak of the brushes occur at 367.9 eV supporting the existence of Ag(0) state in the sample. Figure 3B shows a Raman image of a TEM grid, using 1×10^{-8} M crystal violet (CV) as the analyte. The copper edges of the grid are visible in the Raman image as they contain silver brushes which are SERS active. The inset shows the Raman spectrum of CV; an enhancement factor of 2.4×10^6 was measured.

The surface enhancement exhibited by these structures could be useful in sensing trace amounts of materials from air, automobile emissions or water as many of them have Raman spectral features. The advantages of these substrates in SERS are that the structures are readily made in air and can act like nanoscale brushes to capture particles or bacteria present in the air due to their mechanical porosity.

To demonstrate the capture of micron-sized particles, a mist of bacteria (from a suspension of *Escherichia coli*) was sprayed onto a NW structure, but the structures were easily destroyed by mechanical strain of the spray. To stabilize the structures, a molecular bond between the NPs was first established using 1,8-octanedithiol. After treatment with 1,8-octanedithiol, the brushes were strong enough to withstand a mechanical strain like an incoming spray plume from a commercial water spray

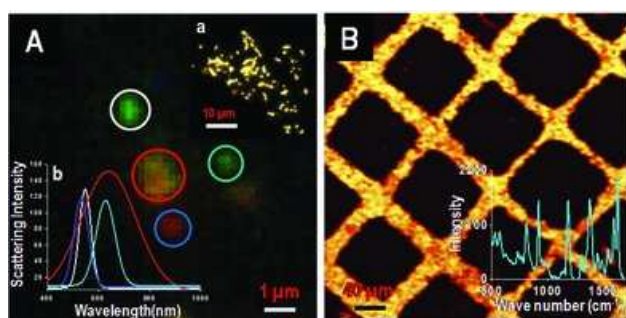


Figure 3. Spectroscopic images of the AgNPs. A) Inset a) shows a large area image, b) scattering spectra collected from AgNPs in a single NW, sharpness of the scattering spectrum taken from the particles shows that they are plasmonic in nature, each scattering spectrum is from an isolated particle or an aggregate (color variation is due to their size differences). Colors of the scattering spectra correspond to particles from which they were collected (with circles of the same color). B) Raman image of the Ag brush containing grid using 1×10^{-8} M crystal violet as analyte. Inset shows the corresponding Raman spectrum.

bottle. A pretreatment of the TEM grid was also performed with the same reagent to ensure strong bonding between the brush and the grid. The procedure of NP stabilization is elaborated in the methods section. This made the structures strong enough to be used as traps for particles in air flows. **Figure 4A,B** shows SEM images of *E. coli* captured by the brushes from a mist of bacterial suspension passing over it. As Ag is known to be antibacterial,^[12] the NWs are expected to kill captured bacteria. In the SEM image in Figure 4B one bacterial cell is visible, trapped in between the Ag brushes. Exploring additional applications, the brushes were shown to capture particulate matter (PM_{2.5}),^[13] when exposed to smoke created by burning incense which produced particles below 2.5 micron size. The SEM images (Figure 4C,D) show the brushes, before and after 60 s exposure to smoke. It is clear that they become thicker after capture. The SEM image shown in Figure 4E was taken after 300 s of exposure to smoke. The image clearly shows the presence of particulate matter in between the brushes also. Raman spectrum shown in the inset also supports the presence of carbonaceous material. SEM images in Figure S9 in the Supporting Information shows changes of Ag brushes with respect to time of smoke exposure. These brushes are not reusable; but can capture much more mass than their own body mass. This is possible due to the fact that they have substantial void space in between. The silver present in the material can be reused, however.

Composition control: Bimetallic brushes can be made by this methodology by changing the precursor composition. In an experiment, a 1:1 mixture of palladium acetate in acetonitrile (1 mM) and silver acetate in water (1 mM) was electro sprayed and collected in the same way as described earlier (same as electro spray deposition of silver acetate). In this case also an empty TEM grid was used as a mask in between the spray tip and the collector surface. After deposition for 2 h at a deposition

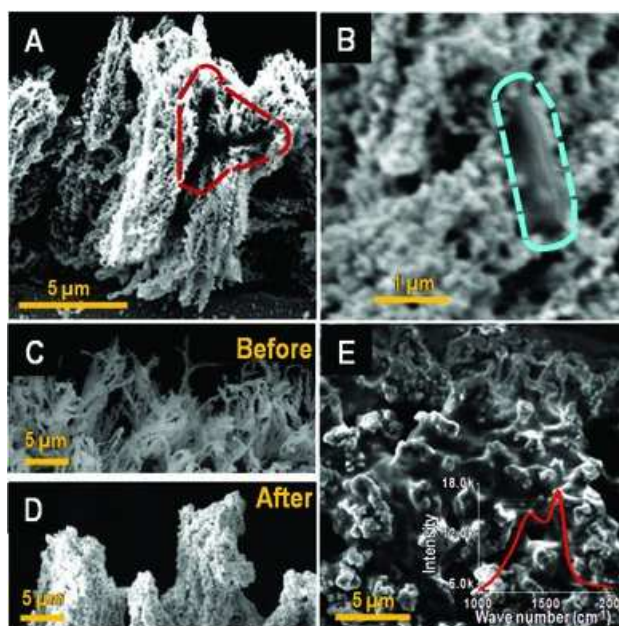


Figure 4. A, B) SEM images of the Ag brush on grid after capturing *E. coli* from corresponding suspensions. The dashed line, in (A) shows an area where *E. coli* is trapped among the brushes, and in (B) it shows the perimeter of a captured bacterium (without sputter coating of a metal film, the nonconductive bacteria show a vague image under SEM), C, D) SEM images of the brushes before and after 60 s exposure of PM_{2.5}, and E) SEM image of the brushes after 60 s exposure of PM_{2.5}, which was generated by burning incense sticks. Inset shows the Raman spectrum taken after PM_{2.5} exposure; clear peak identifies black carbon present in this PM_{2.5}.

current of 45 nA, the mask was examined under an electron microscope. **Figure 5A–C** show SEM images, at different magnifications, of the grid showing the formation of thicker NWs than the earlier case (only Ag deposition). Figure 5D shows a SEM image of a single square of the TEM grid containing Ag brushes on it. Differences in morphology are clearly visible if we compare the images in Figures 5B,D. In the case of AgPd bimetallic structures, the NWs are not 1D in nature. TEM images (Figures 5E,F) taken from the same sample show the presence of crystalline AgPd NPs in each bristle. These brushes are made up of bimetallic NP assembly. Composition variation of Ag and Pd precursors has a significant role on the formation of bimetallic brushes. Control experiments show that when the content of Pd was high in the precursor solution (1:3 Ag/Pd), bimetallic brushes did not form.

Catalysis: These bimetallic structures can be used as catalytic platforms for different chemical reactions. **Figure 6** shows the mass spectrum of diphenylamine (DPA), polymerized using AgPd bimetallic brushes as a catalytic platform. In this experiment, first AgPd bimetallic structures were made on a stainless steel wire mesh and a 100 ppm methanolic solution of DPA was electro sprayed at a deposition current of 40 nA for 10 min. After deposition of DPA, the brushes were washed gently with

www.advmat.de

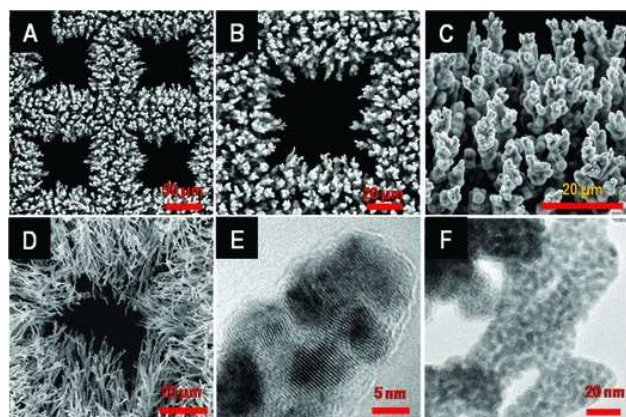
Author Pr **ADVANCED MATERIALS**

Figure 5. A–C) SEM images of AgPd bimetallic nanobrushes at different magnifications, D) SEM image of Ag brush showing different morphology in the case of bimetallic brushes, and E, F) TEM images of bimetallic structures showing the presence of AgPd NPs in each bristle.

methanol and ESI mass spectrum of the solution was taken. It showed that DPA polymerizes on the AgPd bimetallic brushes. Conversion efficiency was calculated as 81% in the case of bimetallic brushes. To prove that these bimetallic brushes are playing a catalytic role in the polymerization reaction, control experiments were done. In one experiment the same solution of DPA was sprayed on an ITO-coated glass slide using the same deposition current (40 nA) as in the earlier case. After deposition was complete, the ITO-coated slide was washed with methanol and mass spectrum was taken. In this case polymerization was not seen, whereas a clear intense peak of DPA was visible in the spectrum at m/z 170 (Figure 6, inset). In another control experiment AgPd particles were deposited on a copper plate. We know that electro spray deposition of metal on copper does not produce any particular morphology: in this process NPs of the metal are deposited on the plate. In the control experiment, a 1:1 mixture of palladium acetate (1mM) in acetonitrile and silver acetate (1mM) in water was electro sprayed on the copper plate at the same deposition current (40 nA). The experiment was repeated with DPA on this bimetallic surface. The mass spectrum (Figure S10, Supporting Information) showed polymerization of DPA with a conversion efficiency of 58%. Although the amount of NPs deposited was more in this case because the whole spray plume was collected (there was no mask in this case), lower conversion efficiency was seen. This supports the fact that brush-like morphology is more efficient in conversion than NPs. This enhanced efficiency may extend to other chemical reactions.

An ambient solution-state method for growing metallic brushes of micrometer length spread over cm^2 areas is presented. The brushes are composed of 1D assemblies of uniform nanoparticles, grown by the Coulombic forces present in the electrolytic spray system. Various control experiments prove that the electric field is the key to the oriented growth. The solvent droplets are shown to deposit the metallic nanoparticle cargo one after the other, upon droplet collision at metallic

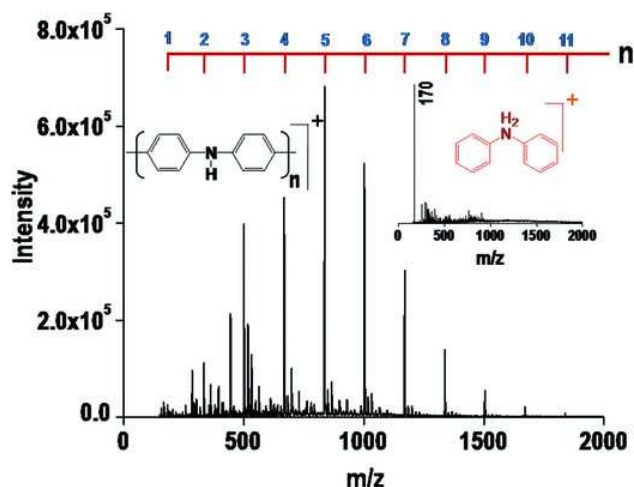


Figure 6. Mass spectrum taken after electro spray deposition of DPA on AgPd nanobrushes, showing polymerization of DPA. Inset shows the mass spectrum taken from electro spray deposited DPA on an ITO-coated glass slide.

surfaces. The growing brushes act as nanoscale antennae. The resulting structures are shown to act as molecular sensors due to their large surface enhanced Raman activity. Their porosity allows them to act as collector surfaces for particulate matter. Composition of such structures can be varied easily. Bimetallic Ag:Pd nanostructures act as catalysts for polymerization reactions. The ease of fabricating such structures directly from solutions and the efficient control of size and composition are expected to generate interest in this method for creating metallic grasslands.

Experimental Section

For all experiments, nanospray emitters were made using a micropipette puller (P-97) purchased from Sutter instrument, USA. MilliQ water was used for the electro spray experiments. A homemade nanospray source was made by pulling a borosilicate glass capillary (1.5 mm outer diameter and 0.86 mm inner diameter) using a micropipette puller and cutting into two pieces. The internal diameter of the spray tip was estimated to be 8–12 μm and electrode used was 0.5 mm diameter platinum wire (Sigma Aldrich, India). The capillary was filled with 1 mM aqueous solution of AgOAc using a micro-injector pipette tip. Experiments with different solvents mixtures (different composition of water/MeOH, water/acetonitrile, etc.) were also done. Water gave the best result among all the solvents, hence for all other experiments water was used as the solvent. The platinum wire was connected to a high voltage power supply through a copper clip, and a potential in the range 1–1.5 kV was applied.

The collector surface, an ITO-coated glass slide in this case, was firmly mounted on a stable platform and a copper TEM grid was placed over it. The collector surface and the grid were grounded through a picoammeter. The spray emitter was manually positioned above the grid center at a distance of 5–

10 mm and deposition was done. Parameters like distance of the spray emitter tip to the substrate and the deposition current, optimized by trial and error, were 5–10 mm and 20–40 nA, respectively. In the case of longer wires, we used 10 mM concentrations of aqueous silver salt (AgOAc). Electro spray of higher concentrations Ag gave similar structures in shorter time. From these images, it is clearly visible that the structures are not dendritic, they are 1D.

To confirm the presence of solvated Ag⁺ ions, mass spectra were collected using an ion trap LTQ XL (Thermo Scientific, San Jose, California) mass spectrometer. Indium tin oxide-coated glass slides (Toshniwal brothers (SR) Pvt. Ltd., India) was the usual deposition substrate. Copper TEM grids with 100 × 100 micron apertures (Tedpella Inc. USA) were used as masks and served as substrates for NW growth. Locally available stainless steel wire mesh was used as substrate when indicated. All TEM measurements were made using a JEOL 3010 (JEOL Japan) transmission electron microscope. A field emission scanning electron microscope (FEI Quanta FEG 200, USA) was used to image these structures. EDS analyses were done with an attachment on the SEM instrument. Some images were collected with a FEI Quanta 100 instrument with tungsten filament source. Raman measurements were made using a Confocal Raman micro spectrometer (Witec GmbH, Germany) with 532 nm and 633 nm laser excitation. Silver acetate and palladium acetate (Sigma Aldrich, India) were used for electro spray. Hyperspectral images were collected with a Cyto viva instrument working in the spectral range of 400–1000 nm. XPS measurements were conducted using an Omicron ESCA probe spectrometer with polychromatic MgK α Xrays ($h\nu = 1253.6$ eV). Microparticles (PM_{2.5}) were generated by burning locally available incense sticks. *E. coli* were purchased commercially from MTCC (identification number MTCC 739).

Mechanical Stabilization of Ag Brushes: The brushes made of bare NPs have weak van der Waals interactions between the constituent NPs. Hence, they are not stable to mechanical strain. To increase stability to forces like the passage of air or immersion in water, postdeposition electro spray of 1,8-octanedithiol was done. It is expected that the terminal SH-groups will bind with two adjacent NPs and strengthen their bonding. Figure S11 in the Supporting Information shows SEM images of a dithiol-stabilized nanobrush on a TEM grid, before and after holding it under water. The image in Figure S11 B in the Supporting Information shows that brushes are lost from the grid due to the strain. Therefore, to bind the brushes to the substrate (TEM grid in this case), the 1,8-octanedithiol was electro sprayed on the substrate prior of creating the brushes. SEM images in Figure S11 C,D in the Supporting Information shows that nanostructures are now stable after water exposure.

Supporting Information

Supporting Information is available from the Wiley Online Library or from the author.

Acknowledgements

D.S., M.K.M. contributed equally to this work. The authors thank the Nano Mission, Department of Science and Technology, Govt. of India for continued support of our research program. D.S. thanks the University Grants Commission and A.S. thanks Council of Scientific and Industrial Research for research fellowships. Financial support from the Separations and Analysis Program, Office of Basic Energy Sciences, US Department of Energy, DE-FG02-06ER15807 is also acknowledged.

Received: October 17, 2015

Revised: November 23, 2015

Published Online: MM DD, YYYY

- [1] P. Christopher, S. Linic, *ChemCatChem* **2010**, *2*, 78.
- [2] a) M. A. Correa-Duarte, M. Grzelczak, V. Salgueirino-Maceira, M. Giersig, L. M. Liz-Marzan, M. Farle, K. Sieradzki, R. Diaz, *J. Phys. Chem. C* **2005**, *109*, 19060; b) S. Kralj, D. Makovec, *ACS Nano* **2015**.
- [3] Z. Tang, N. A. Kotov, M. Giersig, *Science* **2002**, *297*, 237.
- [4] a) X. Shen, L. Chen, D. Li, L. Zhu, H. Wang, C. Liu, Y. Wang, Q. Xiong, H. Chen, *ACS Nano* **2011**, *5*, 8426; b) H. Zhang, I. Hussain, M. Brust, M. F. Butler, S. P. Rannard, A. I. Cooper, *Nat. Mater.* **2005**, *4*, 787.
- [5] a) B. Freund, S. Suresh, *Thin Film Materials Stress, Deformation and Surface Evolution*, Cambridge University Press, **2003**; b) K. Wasa, a. et, *Thin Film Materials Technology: Synthesis of Compound Materials*, William Andrew Publishing, **2004**; c) V. Barth, G. Costantini, K. Kern, *Nature* **2005**, *437*, 671; d) S. I. Stupp, V. LeBonheur, K. Walker, L. S. Li, K. E. Huggins, M. Keser, A. Amstutz, *Science* **1997**, *276*, 384; e) Y. Zhang, L. Zhang, C. Zhou, *Acc. Chem. Res.* **2013**, *46*, 2329; f) Y. Xia, P. Yang, Y. Sun, Y. Wu, B. Mayers, B. Gates, Y. Yin, F. Kim, H. Yan, *Adv. Mater.* **2003**, *15*, 353; g) G. Mondragon-Galicia, C. Gutierrez-Wing, M. Eufemia Fernandez-Garcia, D. Mendoza-Anaya, R. Perez-Hernandez, *RSC Adv.* **2015**, *5*, 42568; h) C. Chuang, S. Cheng, *Nano Res.* **2014**, *7*, 1592; i) S. H. Chung, S. Ramadurgam, C. Yang, *Nanomater. Nanotechnol.* **2014**, *4*, 58317/1; j) H.-W. Liang, J.-W. Liu, H.-S. Qian, S.-H. Yu, *Acc. Chem. Res.* **2013**, *46*, 1450; k) H.-W. Liang, S. Liu, J.-Y. Gong, S.-B. Wang, L. Wang, S.-H. Yu, *Adv. Mater.* **2009**, *21*, 1850; l) P. S. Chinthamanipeta, Q. Lou, D. A. Shipp, *ACS Nano* **2011**, *5*, 450.
- [6] a) G. L. Messing, S. C. Zhang, G. V. Jayanthi, *J. Am. Ceram. Soc.* **1993**, *76*, 2707; b) P. S. Patil, *Mater. Chem. Phys.* **1999**, *59*, 185.
- [7] a) N. Nasiri, R. Bo, F. Wang, L. Fu, A. Tricoli, *Adv. Mater.* **2015**, *27*, 4336; b) K. Okuyama, I. W. Lenggoro, *Chem. Eng. Sci.* **2003**, *58*, 537; c) J. H. Bang, K. S. Suslick, *Adv. Mater.* **2010**, *22*, 1039.
- [8] R. Juraschek, T. Dulcks, M. Karas, *J. Am. Soc. Mass Spectrom.* **1999**, *10*, 300.
- [9] S. Parviainen, F. Djurabekova, A. Pohjonen, K. Nordlund, *Nucl. Instrum. Methods Phys. Res. Sect. B* **2011**, *269*, 1748.
- [10] E. T. Castellana, R. C. Gamez, M. E. Gomez, D. H. Russell, *Langmuir* **2010**, *26*, 6066.
- [11] a) S. Nie, S. R. Emory, *Science* **1997**, *275*, 1102; b) W. Deng, E. M. Goldys, *Analyst* **2014**, *139*, 5321; c) W. Xie, S. Schlucker, *Rep. Prog. Phys.* **2014**, *77*, 116502; d) P. El Khoury, G. E. Johnson, I. V. Novikova, Y. Gong, A. Joly, J. Evans, M. Zamkov, J. Laskin, W. Hess, *Faraday Discuss.* **2014**, *197*, 1; e) W. Hoffmann, G. Verbeck, *Appl. Spectrosc.* **2013**, *67*, 656.

www.advmat.de

Author Pr **ADVANCED
MATERIALS**

- [12] C. Baker, A. Pradhan, L. Pakstis, D. J. Pochan, S. I. Shah, *J. Nanosci. Nanotechnol.* **2005**, *5*, 244.
- [13] C. Liu, P.-C. Hsu, H.-W. Lee, W. Li, M. Ye, G. Zheng, N. Liu, Y. Cui, *Nat. Commun.* **2015**, *6*, 6205.

WILEY-VCH

- Q1 APT to AU: Please provide the highest academic title (either Dr. or Prof.) for all authors, where applicable.
- Q2 APT to AU: If you have not returned the color cost confirmation form already, please email the completed form to the editorial office when you submit your proof corrections. This will confirm that you are willing to support the cost for color publication of the figures. Details about our color policies and a link to the form were included with your acceptance email. If you wish for your figures to be presented in greyscale, please email the editorial office to confirm this.
- Q3 APT to AU: Please update ref. (2b,11d).
- Q4 APT to AU: Please add publisher location to ref. (5a,b).

Supporting Information

Metallic nanobrushes made using ambient droplet sprays

Debanjan Sarkar,^{[a]†} Maheswari Kavirajan Mahitha,^{[a]†} Anirban Som,^[a] Anyin Li,^[b] Michael Wleklinski,^[b] Robert Graham Cooks^{[a,b]} and Thalappil Pradeep^{[a,b]*}*

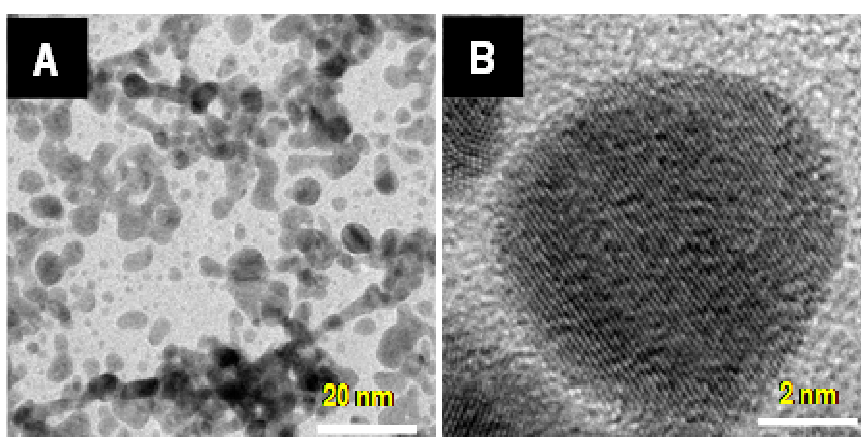


Figure S1. A) TEM image of AgNPs formed on a carbon coated TEM grid, B) HRTEM shows the Ag (111) lattice plane in a single NP.

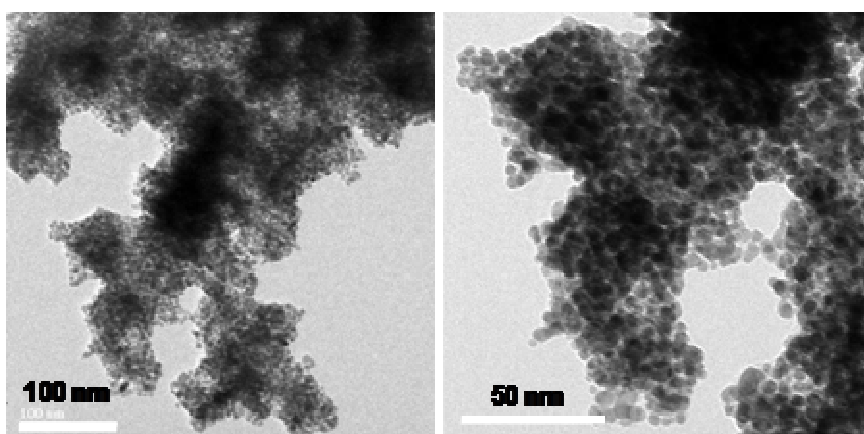


Figure S2. TEM image of Ag brush, formed by accumulation of uniform AgNPs. Images A and B are at different magnifications. In some instances, single NP strings (comprised of 6 nm NPs) have been observed to coalesce to create these nanobristles (as shown in Figure 1).

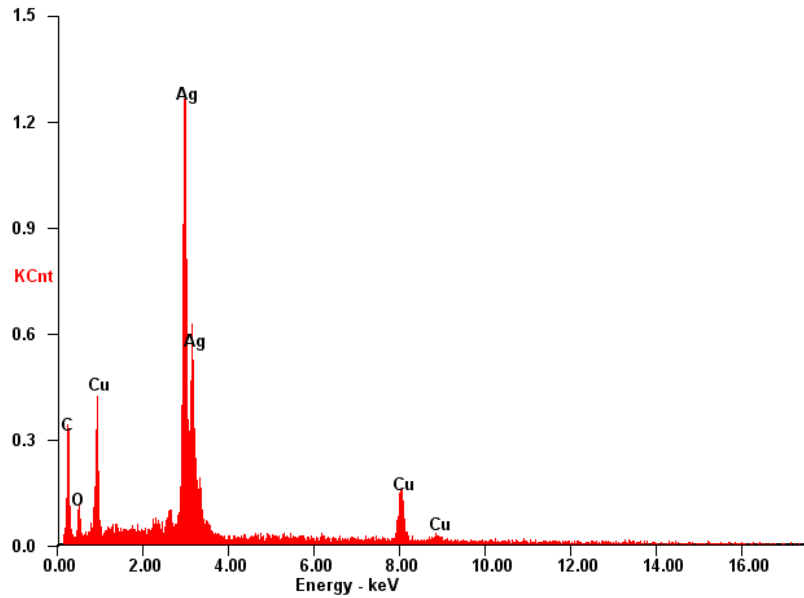


Figure S3. SEM EDS spectrum showing the presence of silver. Cu is from the grid.

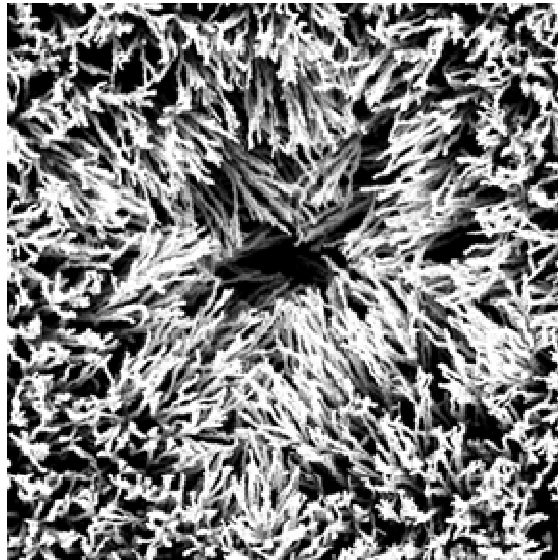


Figure S4. Deposition of 10mM silver acetate at a constant current of 100nA for 7 h, forming 70-80 micron long nanowires which almost completely block a 100 micron square grid element.

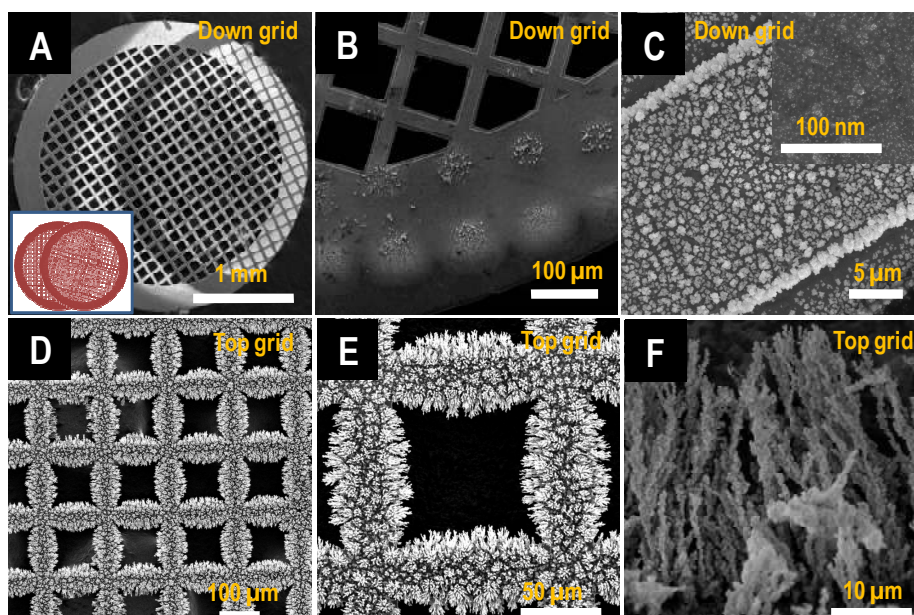


Figure S5. Experiment done using two grids. SEM images at successive magnifications A), B), and C) show formation of NPs on the bottom rim whilst NWs which assemble into nanobrushes form on the top grid as seen in SEM images D), E), and F). Inset in A shows the schematic of the grid position in the experiment.

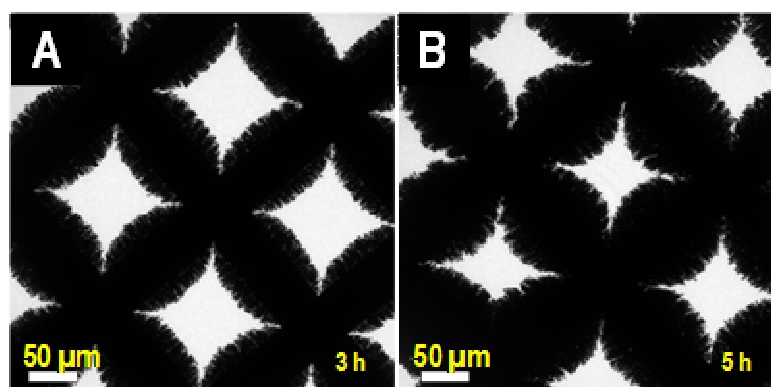


Figure S6. TEM images of Ag brushes formed by electrospray deposition of 10 mM aqueous AgOAc solution, at different times.

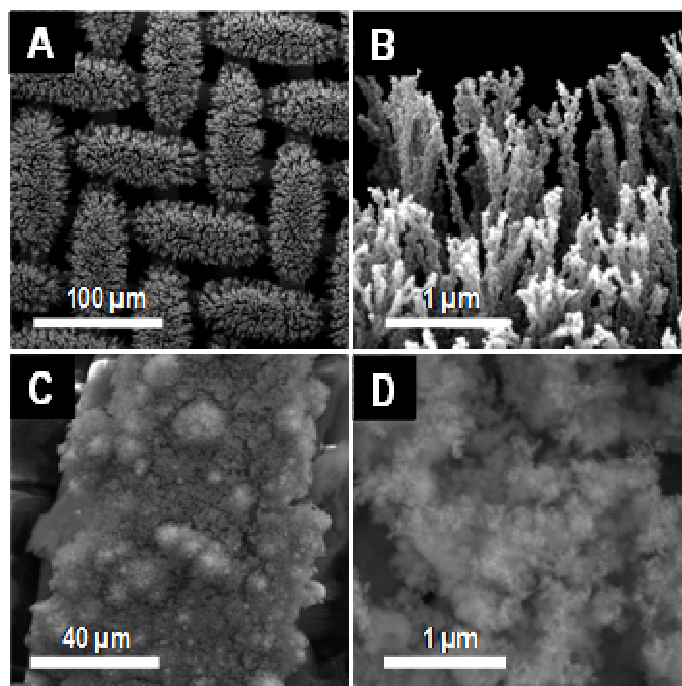


Figure S7. A), B) SEM images of Ag brushes on stainless steel wire mesh and C), D) SEM image of Ag deposition on cotton cloth. No brush-like growth is seen in C and D.

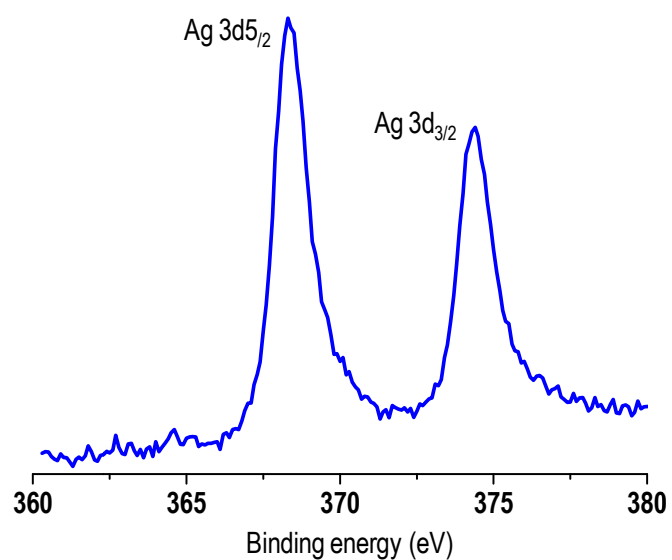


Figure S8. X-ray photoelectron spectrum of Ag brush in the Ag 3d region.

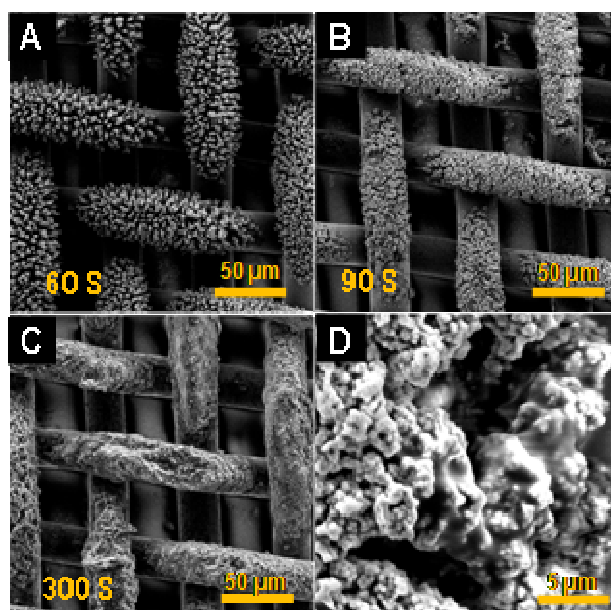


Figure S9. A), B) and C) SEM image of Ag brushes after particulate matter (PM_{2.5}) collection, with increasing time of collection, and D) higher magnification SEM image of the sample shown in C.

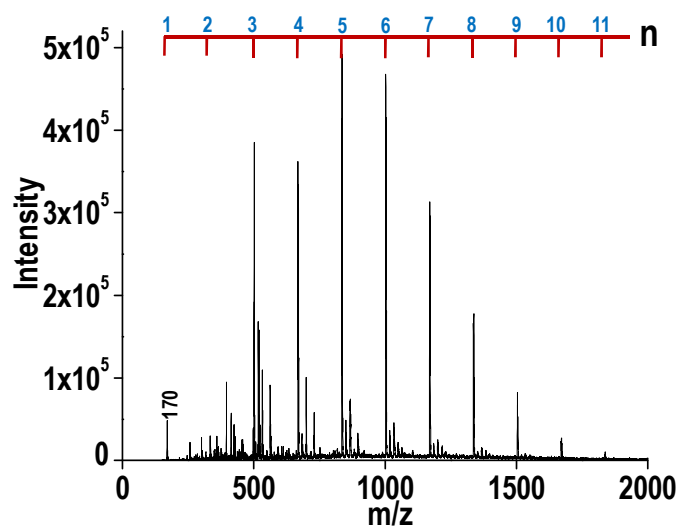


Figure S10: Polymerization of DPA on AgPd NPs. It shows a relatively low conversion efficiency compared to NWs.

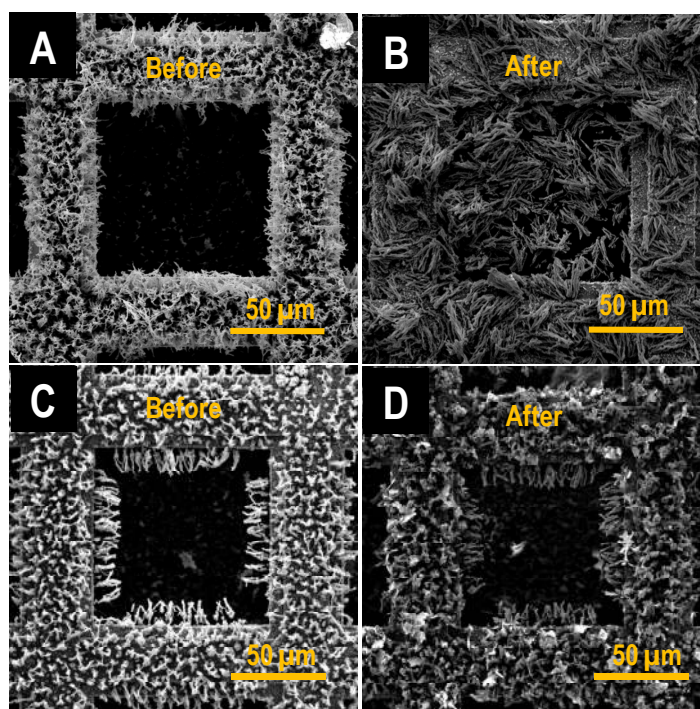


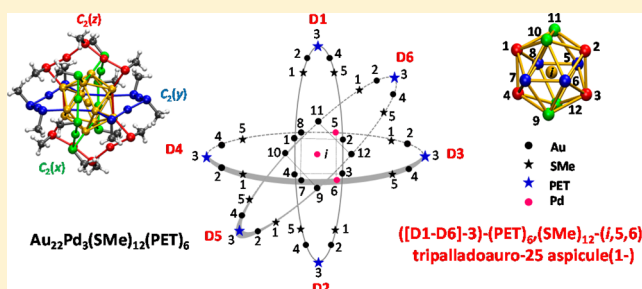
Figure S11. A) and B) SEM image of a Ag nanobrush on a TEM grid stabilized with 1,8-octanedithiol before and after washing in water; C) and D) SEM images of the same, but in this case the grid was pre-treated with 1,8-octanedithiol before building the nanobrush.

A Unified Framework for Understanding the Structure and Modifications of Atomically Precise Monolayer Protected Gold Clusters

Ganapati Natarajan,[†] Ammu Mathew,[†] Yuichi Negishi,[‡] Robert L. Whetten,[§] and Thalappil Pradeep^{*,†}[†]DST Unit of Nanoscience (DST UNS), Department of Chemistry, Indian Institute of Technology Madras, Chennai 600036, India[‡]Department of Applied Chemistry, Tokyo University of Science, 1-3 Kagurazaka, Shinjuku, Tokyo 162-8601, Japan[§]Department of Physics and Astronomy, University of Texas at San Antonio, San Antonio, Texas 78249, United States

Supporting Information

ABSTRACT: Atomically precise monolayer protected clusters are molecules comprising a few-atom cluster core of a noble metal, typically Au or Ag, surrounded by a protective layer of ligands, exhibiting many special optical, electrical, catalytic, and magnetic properties, and are emerging as important materials in biology, medicine, catalysis, energy conversion and storage, and sensing. The structural diversity of these clusters or aspicules, as we definitively term them, meaning shielded molecules, combining the Greek word *aspis* (shield) with molecule, is rapidly increasing due to new compositions and modification routes such as ligand-exchange, alloying, or supramolecular functionalization. We present a structural analysis of the most stable cluster of this kind, $\text{Au}_{25}(\text{SR})_{18}$, and propose a Borromean rings diagram for the cluster, showing its topological configuration of three interlocked (Au_8S_6) -rings. This simplified two-dimensional diagram is used to represent its structure and modifications via ligand or metal atom substitution uniquely. We enumerate and name its isomers with two-ligand or metal atom substituents. Among the several structural insights obtained, the identification of the Borromean rings-interlocked configuration in $\text{Au}_{25}(\text{SR})_{18}$ may explain its high geometric stability and indicate a possible general unified structural viewpoint for these clusters without the division between core and staple motifs. On the basis of our structural analysis, we developed a structure-based nomenclature system that can be applied to both describe and understand the structure and modifications of gold thiolate clusters, $\text{Au}_M(\text{SR})_N$, and is adaptable to the general case of $\text{M}_M(\text{X})_N$ (M, metal and X, ligand). The application of structural analysis and diagrams to $\text{Au}_{38}(\text{SR})_{24}$ and $\text{Au}_{102}(\text{SR})_{44}$, revealing the possible formation of the cluster core by stacking or growth of rings of metal atoms, is also presented.



1. INTRODUCTION

Over the past two decades, since the pioneering work of Brust and Shiffrin on the synthesis of small alkanethiolate monolayer protected clusters of gold,¹ noble metal clusters of ultrasmall size consisting of a few (~ 10 to ~ 1000) atoms surrounded by a monolayer of organic ligands have evolved into an area of intense research.^{2–11} A significant advancement in this area came in late 1998 after the isolation of the very first molecularly precise clusters of this kind, $\text{Au}_{28}\text{SG}_{16}$, by Whetten and co-workers¹² (where SG is glutathione, later reassigned as $\text{Au}_{25}\text{SG}_{18}$ by Tsukuda and co-workers¹³), composed of an Au(0) core and protected with ligands; the cluster itself was synthesized from Au(I)SG polymers. In the subsequent years, research on this class of materials gained momentum.^{6,11,14–18} Properties such as unique absorption,^{6,12,19,20} luminescence,^{10,21–25} unusually strong chiroptical activity,^{26–29} electrical^{30–32} and catalytic properties,^{33–35} magnetic properties,^{36–39} etc., proved these clusters to be unprecedented and useful for a host of potential applications.^{5,7,9–11,40} In that perspective, various synthetic approaches have been developed

to make clusters with different core sizes, surface functionalities, and chemical compositions.^{5,41–47} The molecular science of these materials became even more important as their structures became known from single crystal studies, for example, through the efforts of Kornberg,⁴⁸ Murray,⁴⁹ Jin,^{50–54} Dass,^{55–60} Tsukuda,⁶¹ Bigioni,⁶² Zheng,^{63–66} Ackerson,^{67,68} Zhu,^{69–71} Wang,^{72,73} Maran,⁷¹ Simon,⁷⁴ Wang,⁷⁵ Bakr,⁷⁶ Liu,⁷⁷ and co-workers. Because each composition has a unique structure that depends on the number of metal atoms and ligands, a large variety of fascinating structures exist, but understanding their origin and predicting them remain important challenges that are still not resolved completely.

Modifications may involve changes in the metal core as in the case of $\text{Au}_{25-x}\text{M}_x(\text{SR})_{18}$,^{57,78,79} where M is a metal atom, or in the ligand as in the case of $\text{Au}_{25}(\text{SR}_1)_{18-x}(\text{SR}_2)_x$,^{80,81} where SR_1 and SR_2 are two different thiols. Mixed ligand-exchanged

Received: August 22, 2015

Revised: November 6, 2015

Published: November 6, 2015

clusters containing a distribution of chemical compositions of $\text{Au}_{24}\text{Pd}(\text{SR}_1)_{18-x}(\text{SR}_2)_x$ have been separated and isolated using high-performance liquid chromatography (HPLC), and evidence of isomers in ligand-exchanged clusters was acquired.⁸⁰ Different regioisomers of $\text{Au}_{38}(\text{SR}_1)_{23}(\text{SR}_2)_1$ have also been identified and isolated using HPLC.⁸² Similarly, a small number of experimental studies have determined the precise positions of the substituted ligands or metal atoms by X-ray diffraction or other techniques,^{55,57,67,68} and structural studies by Ackerson and co-workers have found the precise position of ligands exchanged for $\text{Au}_{25}(\text{SR}_1)_{16}(\text{SR}_2)_2$ and also for $\text{Au}_{102}(\text{SR}_1)_{40}(\text{SR}_2)_4$.⁶⁸ A combined experimental and theoretical approach to gain more information on the exact substituent locations may also be fruitful, for example, in the cases of R-1,1'-binaphthyl-2,2'-dithiol (BINAS) ligand-exchanged $\text{Au}_{38}(\text{SR})_{24}$ ⁸³ and copper doping of $\text{Au}_{25}(\text{SR})_{18}$.^{79,84} With the growth of this new family of molecules with associated chemistry, one requires a system to describe the structure and composition, and also to precisely describe the positions of atoms and their connectivity both in the core as well as in the outer shells of these clusters.

Being distinct from both small gas-phase atomic clusters and their monolayer protected nanoparticle counterparts,^{85,86} these clusters may be rightly regarded as molecules because they consist of a finite aggregate of atoms which are chemically bonded to each other, have well-defined and measurable physical and chemical properties, and also form the building blocks of molecular crystals. Hence, the term nanomolecule is frequently used for them. A variety of other names have been used to describe this class of molecules as a whole such as monolayer protected clusters, ligand-stabilized clusters, clusters, nanoclusters, quantum clusters, superatoms, faradaurates, fluorescent nanoparticles, molecular clusters, atomic clusters, etc., to list a few. However, no consensus has been reached on what to call these molecules, and new names are constantly being generated. Many of the names have deficiencies mostly due to either being nonspecific to this class of molecule, and thus are nonunique; for example, the term monolayer protected clusters (MPCs) is also used to describe larger nanoparticles. The ubiquitous term "cluster" has its principal application to atomic/molecular assemblies, typically in the gas phase, and considering the molecular nature of these systems we find that this name is unsuitable for them. The addition of prefixes to yield names such as metallic clusters, molecular clusters, etc., also fails to remedy the situation. IUPAC nomenclature names often include a compact single-word name for the category of molecules such as in fullerene nomenclature.⁸⁷ A unique and specific name is therefore desirable to describe this class of materials that captures their two defining characteristics, first that they are molecules, and second that they have a protecting layer of ligand groups peripheral to an inorganic core. The ligand layer is crucial to the stability of the entire molecule, as it prevents the metal cores from etching or aggregating to form small metal complexes and larger metal nanoparticles, respectively, during synthesis in solution (generally) as well as in the solid phase, and protects the core from reactive molecules and ions. Furthermore, electron transfer from the core to the ligands and reverse is crucial to both the electronic and the geometric stability of the monolayer protected clusters, which leads to the appearance of "magic numbers" of core atoms. Electronic interaction of the core and the ligand layer is thus essential for the stability of the system as a whole. All of these reasons lead us to propose a name capturing the

molecular character of an entity, which itself is protected with molecules. We propose the compound term "aspicule" for this class of molecules; the name is derived by combining the Greek root word *aspis* meaning shield and the word molecule, to denote a shielded molecule. The name aspicule may be extended to other protected metal clusters, composed primarily of other metals rather than gold and silver, and for which the shielding effect of the ligands is crucial to their stability, for example, those containing Pd,⁸⁸ Al, and Ga.^{88,89} We note that the term metal aspicule may be a yet more precise description, and its derivatives such as gold, silver, and palladium aspicules, and so on. We appreciate that several other names already in use such as (nano)clusters, quantum clusters, nanomolecules, faradaurates, etc., may continue to be used. Hereafter, we refer to monolayer protected clusters as aspicules in this Article. We may define the term aspicule precisely to mean those entities that have a molecular formula and consist of a closed cage metal cluster of more than a few atoms in their central region bonded to a surface arrangement of ligands or atoms or ions, which shield the inner metallic core structure from destructive chemical interactions in the solution and solid states. This definition distinguishes aspicules from their larger monolayer protected nanoparticles and nanocrystal counterparts composed of thousands of atoms, which do not have precise molecular formulas (at the current experimental capability, especially using mass spectrometry), but have an overall morphology and lattice arrangement with associated dimensions, and it also distinguishes them from smaller noble metal complexes.

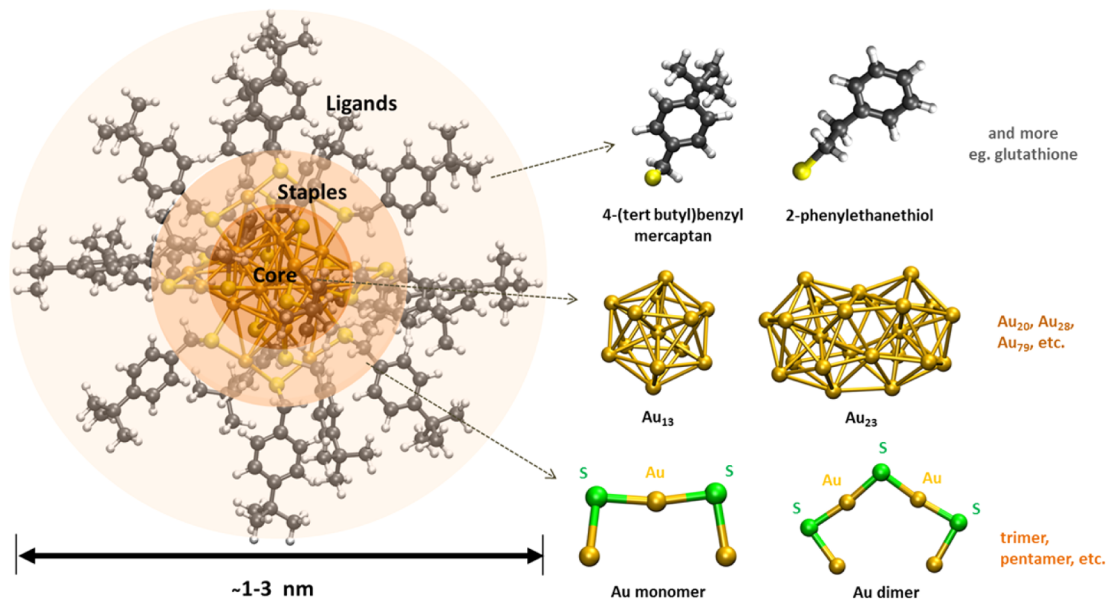
We investigated the structure, symmetry, and network topology of the three aspicules, $\text{Au}_{25}(\text{SR})_{18}$, $\text{Au}_{38}(\text{SR})_{24}$, and $\text{Au}_{102}(\text{SR})_{44}$. We found simplified structural representations, derived structural insights from them, and produced labeled diagrams of these molecules to represent their modifications. As a secondary aspect, we also created an overall framework in the form of a structure-based nomenclature, which integrates our structural analysis and provides names for the structures and their modifications in the general case of $\text{Au}_M(\text{SR})_N$ or $\text{Au}_M(\text{X})_N$. We emphasize that the structural analysis and its insights are the central aspect of this Article, and the nomenclature is only a byproduct.

We begin with a description of the general structure of gold thiolate aspicules, and develop simplified representations of the structure of $\text{Au}_{25}(\text{SR})_{18}$ in section 2.1. This is followed by a systematic presentation of the nomenclature and precise terminologies in sections 2.2–2.5, which can be applied to describe the structure of any gold thiolate aspicule or its chemical modifications at different levels of structural detail. Modifications of $\text{Au}_{25}(\text{SR})_{18}$ are represented using locants and structural diagrams for cases of ligand and metal atom exchange, their two-substituent isomers, and specific supramolecular/conjugated interactions (section 2.6–2.8). Sections 2.9 and 2.10 show how we applied this structural analysis to $\text{Au}_{38}(\text{SR})_{24}$ and $\text{Au}_{102}(\text{SR})_{44}$. Last, in section 2.11, we review some of the main structural insights gained and their implications to the general structure of aspicules.

2. METHODOLOGY, RESULTS, AND DISCUSSION

2.1. Aspicule Structure and Simplified Structural Representation of $\text{Au}_{25}(\text{SR})_{18}$.

The structure of an aspicule may be represented as three concentric shells of atoms: the protective shell of ligand R-groups, an intermediate mantle, and the inner metal core (Scheme 1).

Scheme 1. Generic Structure of Gold Thiolate Aspicules^a

^aSchematic of the shell structure of an aspicule (left), with the size of a typical $\text{Au}_{25}(\text{SR})_{18}$ aspicule (1–3 nm) marked. Examples of the constituent structures of the core, staple, and ligand R-group regions with their terminating sulfur atoms are shown (right).

For example, in $\text{Au}_{25}(\text{SR})_{18}$, the core consists of an Au_{12} icosahedron, plus a single gold atom at the center, while for Au_{38} it is a face-sharing bi-icosahedron with two gold atoms at the center of each icosahedron. The second shell or mantle is the structure that is found between the core and the ligands, which follows the “divide and protect” scheme,⁹⁰ in which the staple-like structures containing both metal and chalcogen (usually sulfur) atoms project out from core atoms and then bond back to a different core atom. This coordinating atom forms bonds linking the core atoms and staple metal atoms, which is sulfur in the case of thiolate ligands. Different sizes of staples (oligomeric forms), which have the general formula $-(\text{S}-\text{Au})_n-\text{S}-$ consisting of repetitive units of the monomer $(\text{S}-\text{Au})$ and a single terminating sulfur atom at one end, are named according to the number of repeating $-(\text{S}-\text{Au})-$ units contained in the staple: monomer $-\text{S}-\text{Au}-\text{S}-$,^{48,51} dimer $-(\text{S}-\text{Au})_2-\text{S}-$,^{49,50} trimer $-(\text{S}-\text{Au})_3-\text{S}-$,⁹¹ tetramer $-(\text{S}-\text{Au})_4-\text{S}-$,⁹² pentamer $-(\text{S}-\text{Au})_5-\text{S}-$,⁹¹ and heptamer $-(\text{S}-\text{Au})_7-\text{S}-$,⁹¹ with smaller staple sizes being found typically in the larger core sizes of aspicules. There are also instances of single sulfur atoms $(-\text{S}-)$ bridging two core atoms.^{59,93,94} The third and outermost layer is the ligand shell where the R-groups of organic thiolates (RS-) of phenylethanethiol (PET), glutathione (SG), 4-*tert*-butylbenzyl mercaptan (BBSH), etc., are bonded to the sulfur atoms in the staples or directly to sulfur atoms that bridge the core atoms. At the outset, we make some general simplifications about the structure. First, we need only consider (in most cases) the structures of the core and mantle shells omitting the ligand R-groups because chalcogen (S, Se, Te) atoms represent the termini of the ligands.

This reduces the total number of atoms to 43 and 62 for $\text{Au}_{25}(\text{SR})_{18}$ and $\text{Au}_{38}(\text{SR})_{24}$, respectively, for example. Second, aspicule structures from experiments are not perfectly symmetric; they exhibit variations in bond length, angles, and also a dihedral distortion in the staples, for example, in $\text{Au}_{25}(\text{SR})_{18}$.⁵⁰ Here, we ignore these minor distortions in the geometry and assume symmetric core and staple structures.

Third, we neglect orientation of the ligand with respect to the staples (*cis-trans*), and also its internal conformation. The directions of the S–C bonds, relative to the staples, may be included at a later stage to give a description of their *cis-trans* isomerism and the inversion symmetry of the coordinating atom–carbon atom (S–C for thiolates) bond directions on opposite sides of a pair of coplanar staples, as found for example in $\text{Au}_{25}(\text{SR})_{18}$. Similarly, the torsional angles of the first ligand C–C bond with respect to the staple Au–S bonds and its own internal torsional angles may be specified using terms such as *trans* and *gauche*(\pm). We consider only gold thiolate (Au–S) aspicules in our examples, but our methods could be applied with some additional modifications to take account of different types of staple motifs for the case of other metals such as silver and different coordinating atoms by substitution of S for Se, P, or Cl, where in the latter two cases there are no staple motifs, for example, in the name.

For concreteness, we will write as though the ligand is methylthiol(ato) (SMe) and the substituted ligands are always PET (2-phenylethanethiol(ato)), and similarly we designate the metal substituent by Pd (palladium) in our examples. Although multiple Pd substituents are a rarer case than Ag substituents, for example, we have used Pd to avoid confusion between majority silver and gold aspicules, which generally have marked structural differences. We assume for simplicity that the charge of the modified aspicules that we present as examples is the same as that of the parent aspicule.

The first objective of our structural analysis is to find a simplified representation of the structure in the form of a diagram, with unique positional labels (locants) for (a) the core atoms, (b) the staples, (c) the ligands, and (d) the staple metal atoms. For this purpose, we made extensive use of the molecular building and visualization software Avogadro⁹⁵ and VMD⁹⁶ for structural manipulation and visualization. The core and staple structure is obtained from the crystal structure/DFT-optimized crystal structure by extracting the entire molecule from the crystalline unit cell, and subsequently

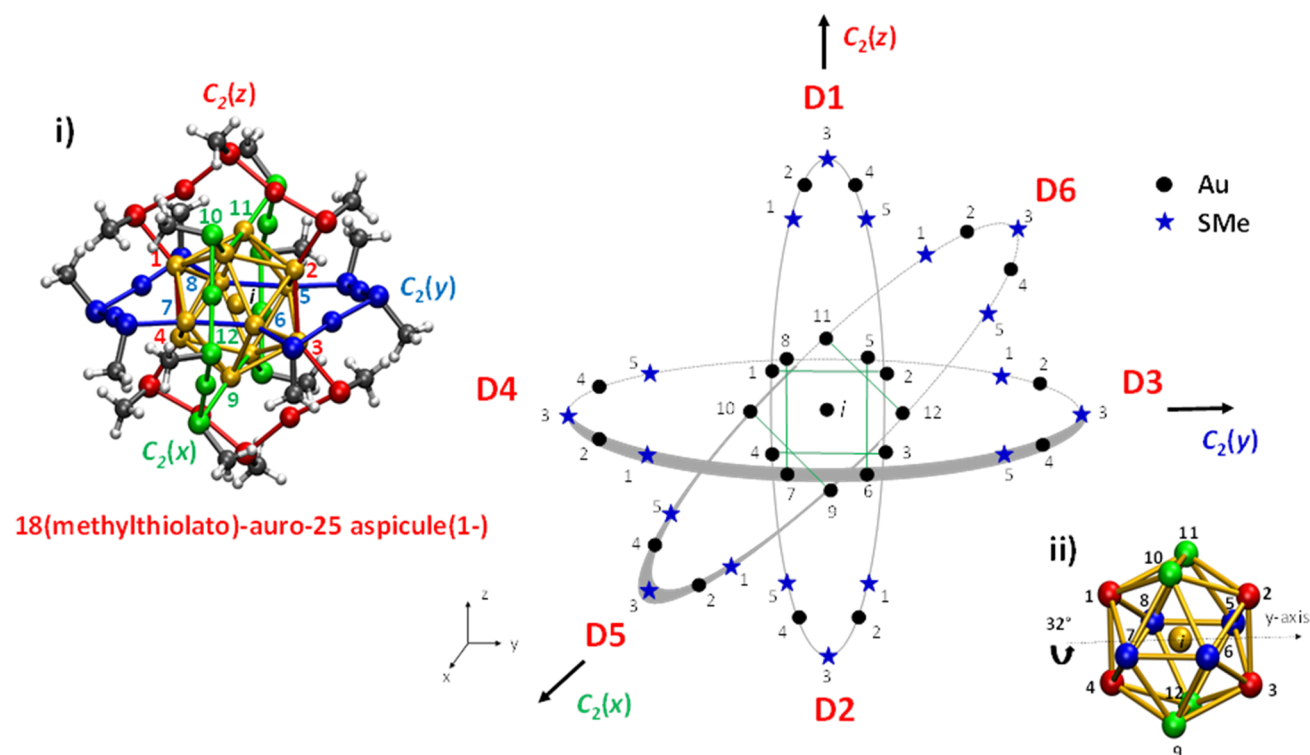


Figure 1. Borromean-rings diagram of $\text{Au}_{25}(\text{SMe})_{18}$. The rings formed by pairs of coplanar staples are shown as ellipses. Gold atoms are shown by black dots, and dark blue stars represent the SMe ligands whose positions are taken to be identical with their sulfur atom. The core Au atoms are numbered from 1 to 12, and the staple atoms are numbered clockwise from the end of the staple, from 1 to 5. The lines that join core Au atoms on opposite ends of the same staple are shown by the green lines. The three perpendicular C_2 axes are marked with the associated Cartesian axis direction in parentheses. The staple directions are labeled by the six staple locants D1 to D6, marked in red. Inset (i) shows a 3D visualization of the ring structure of the core and staples of $\text{Au}_{25}(\text{SR})_{18}$ aspicule, with each (Au_8S_6) -ring consisting of two coplanar staples and the core atoms that are bonded to these staples. The three rings are colored red, blue, and green, and the numbers of the core atoms are marked; the aspicule name for $\text{Au}_{25}(\text{SR})_{18}$ is shown in red below it. The core Au atoms and also Au–Au bonds that are not part of the rings are shown in gold, while the other atoms are colored according to which ring they are part of. Inset (ii) shows a close-up of the numbering scheme of the core atoms marked on the edge-projection of the core icosahedron. The arrow indicates the angle of the anticlockwise rotation about the y -axis, needed to bring the icosahedron into a face-projected view of the face defined by the atoms 6, 7, and 9.

isolating the gold and sulfur atoms from the model by replacing the R-group in the crystal structure by Me or removing it completely, and we refer to the latter as the core and mantle (staple) structure. Initially, a detailed consideration of symmetries and the orientation of $\text{Au}_{25}(\text{SR})_{18}$ was carried out, which is shown in [Supporting Information \(SI 1\)](#).

The general approach we follow is to first simplify the structure and bonding network by focusing on different groups of atoms and bonds, and also selecting representations that capture the entire structure as simply as possible. We considered various possible structural representations and labeling schemes for Au_{25} , such as polyhedral shells ([Figure S2 in SI 2](#)), core and staple motif $\text{Au}_{25}(\text{SR})_{18}$ with Cartesian locant labels for atoms ([Figure S3 in SI 2](#)), and the molecular graph ([Figure S4 in SI 2](#)). The simplest representation we found was based on a simplification of the core and staple structure, which, apart from the central gold atom, shows the staples and only the core Au–Au bonds that lie on three (Au_8S_6) -rings, leading to the diagram shown in [Figure 1](#), and this figure is the central idea of this Article. This simple topological representation is based on a projection of the three-ring structure of $\text{Au}_{25}(\text{SR})_{18}$, and shows all of the essential atoms and the octahedral symmetry; [Figure 1](#) represents the central result of this Article. [Figure 1](#), inset i, shows a 3D visualization of the core and staple structure of $\text{Au}_{25}(\text{SR})_{18}$,

where there are three perpendicular (Au_8S_6) -rings, colored red, blue, and green, with each ring consisting of two coplanar staples and the four core atoms to which their ends are bonded. The presence of these (Au_8S_6) -rings has been noted earlier from the crystal structure;⁴⁹ however, we examined their relative arrangement more closely. We found that the arrangement of these rings is identical to the configuration of interlocked rings known as the Borromean rings. The Borromean rings satisfy the condition that the removal of one ring causes the other two to fall apart, and no two rings are linked together and are therefore the smallest possible “Brunnian link” having only three components (rings). The rings can be viewed as a cover over the central gold atom. The physical significance of these rings is discussed in detail in [section 2.11](#). This ring representation is obtained by omitting the core Au–Au bonds that are not part of the red, blue, and green rings as shown in inset (i). The Borromean-rings condition can be verified by direct observation of inset i of [Figure 1](#). If we imagine the core Au–Au bonds that are not part of the rings (shown in gold) and the central gold atom are not present, then the removal of the green ring allows us to lift the red ring upward and outside of the plane of the blue ring, thus freeing these two rings, which would otherwise be impossible. Structural manifestation of additional stability due to ring

structure is discussed in section 2.11, which renders additional proof to its existence and significance.

Projecting the three-dimensional ring structure onto the plane and representing each ring as an ellipse, and adding symbols for atoms in the appropriate places results in the Borromean-rings diagram at the center of Figure 1. We label each ring of the structure by the symbol of the symmetry axis passing through the bridging sulfurs that lie on the ring, that is, $C_2(y)$ for the blue ring, $C_2(z)$ for the red ring, and $C_2(x)$ for the green ring. The central parts of the ellipses represent the core, and the ends of the ellipses represent the staples. The gold and sulfur atoms are represented by “●” and “★”, respectively, placed according to their connectivity, and we note that the bond distances are not to scale in this schematic representation.

The three-dimensional effect in Figure 1 is brought out by using thicker lines for those ellipse-edges that are projecting out of the plane of the paper, while those that are going into the plane of the paper are shown by thin dashed lines, in the same way as in stereochemical diagrams of molecules. A close-up view of the icosahedral core in its edge projection with core atoms numbered is shown in inset (ii) of Figure 1. We found that this Borromean-rings diagram has the advantage that it allows one to easily visualize ligand-exchanged and alloyed $\text{Au}_{25}(\text{SR})_{18}$ aspicules. Step-by-step instructions for drawing the diagram by hand are provided in Scheme S1 in SI 4. It is possible for a Borromean-rings type of diagram to be extended to $\text{Au}_{144}(\text{SR})_{60}$, because the core and staple structure would most likely be identical to that of the experimentally determined, $\text{Au}_{144}\text{Cl}_{60}$ structure, which contains six ($\text{Au}_{20}\text{Cl}_{10}$)-rings surrounding a central 24-gold-atom vertex-capped icosahedron.⁹⁷

For the purpose of describing modifications precisely, we must assign to each metal atom or ligand of Figure 1 (or, equivalently, a sulfur atom) a unique label, and this assignment is described below. The term substituents is used to denote modifications of the ligands, metal atoms on a staple, or metal atoms in the core, and their positions are all specified using the positional labels of substituents, or locants. The parent structure of $\text{Au}_{25}(\text{SR})_{18}$ has locants as follows: The locants for each of the staples consist of the letter D for dimer, indicating the number of gold atoms in the staple, followed by the staple number that uniquely identifies it. The three C_2 axes have been rotated to coincide with the Cartesian axes as shown in Figure 1. For $\text{Au}_{25}(\text{SR})_{18}$ shown in Figure 1, the staples are labeled as D1 and D2 for the staples pointing in the z - and z' -directions (where the prime denotes the negative Cartesian direction), D3 and D4 for the staples pointing in the y - and y' -directions, and D5 and D6 for the staples in the x - and x' -directions. The core atoms are labeled according to which staple they are bonded to, so that core atoms 1, 2 are associated with staple D1, atoms 2 and 3 with staple D2, atoms 4 and 5 with staple D3, and D4, etc. Each atom on a staple is given a positional number (“staple atom number”), in sequence (as in the IUPAC nomenclature of inorganic chains), beginning with 1 for the sulfur atom at the end of the staple bonded to the core atom that has lowest locant, and counting clockwise the atoms in sequence around the dimer staple. The locants of the ligands are formed by the staple locant followed by a hyphen and the staple atom number of the sulfur atoms (1, 3, or 5). Hence, the sulfur atoms on the D1 staple, for example, are referred to as D1-1, D1-3, and D1-5, while the staple metal atoms are referred to as D1-2 and D1-4.

We used the Borromean-rings diagram to represent the ligand-exchange and alloy modifications, and their respective isomers, of $\text{Au}_{25}(\text{SR})_{18}$ (see sections 2.6 and 2.7). On the basis of this labeled diagram, we created a structure-based nomenclature as a tool for understanding the structure, to refer to the positions of the substituent atoms, and also to name the structure and their modifications precisely in the general cases of $\text{Au}_M(\text{SR})_N$ and $\text{Au}_M(\text{X})_N$.

2.2. Development of a Structure-Based Nomenclature. Precise and systematic structure-based names for these molecules would also enable the structure and details of ligand-exchanged and alloyed molecules to be conveyed accurately and efficiently in a standardized format. There is also a need to depict them on paper, retaining the essential structural details. These requirements are fulfilled by a structural nomenclature, which provides a framework within which it is possible to associate with a molecule a unique name containing essential structural aspects such as the bonding topology and geometry, and compositional information.

Structure-based nomenclatures also serve as a framework and a tool for understanding the molecule itself and its modifications, because the structural representations shown in the diagrams also carry physical significance. By means of the unique labels (locants) for the atoms, we may specify the positions of modifications in the name, even in cases where modifications break the symmetry. The lack of structural nomenclature is not exclusive to monolayer protected clusters but applies to nanomaterials as a whole, and some effort has been initiated to create a unified framework and classification of nanomaterials.⁹⁸ IUPAC (International Union of Pure and Applied Chemistry) nomenclature exists for certain nanomaterials such as fullerenes⁸⁷ and boranes,⁹⁹ and we therefore anticipate that nomenclature would be useful in the case of this category of materials as well.

The following criteria were forefront while developing this nomenclature: It should (i) be symmetry based, (ii) be universal and be able to describe the structure and/or modifications of any aspicule, (iii) have resemblance to IUPAC nomenclature, and (iv) be simple enough to use and remember, so that it would be useful to workers in the field. The latter condition also entails that the resulting names of aspicules should be as succinct as possible, and that diagrams of their structure should be drawable by hand, if possible, after some training. Throughout, we follow the general IUPAC convention of placing the substituent locants as a prefix to the name of the substituent with a hyphen between the prefix and the substituent name. Three stages are involved in the development and application of a structure-based nomenclature.

(1) Structural and symmetry analysis: Finding a suitable structural representation for the aspicule so that a diagram of the structure can be drawn. Selecting a standard symmetry-based orientation. This is an important aspect as a unique representation is needed to locate atoms.

(2) Locant assignment: Assigning unique labels to the relevant parts of the structural diagram in a systematic way so that modifications can be named.

(3) Naming: Assigning names that contain information (descriptors) about different structural, compositional, and molecular properties, for both the parent structure and its modifications. Creation of syntax for linking these descriptors to form the names.

On the basis of the three-shell description, a name that completely describes the parent structure of an aspicule would contain the following information.

(1) Core: The geometric shape of the core and its composition.

(2) Staples: The number and size of each type of staple and the connectivity of the atoms of the staple to the core atoms at their ends.

(3) Ligands: The number and type of each ligand R-group and their positions of attachment on the staples. Stereo-descriptor prefixes may be used for *cis-trans* isomerism of the ligands with respect to the staple, and their internal conformation.

(4) Other details: The total number of metal atoms, the name of this class of molecules (aspicule), and the electrical charge; the latter two may be appended to the name as part of a final suffix. The geometric shape of the core and the principal symmetry axis, and the formula name of the crystal counterion, may also be added in parentheses as an additional suffix.

Stereodescriptor prefixes for the intrinsic chirality of the core and staple structure may be added to the front of the name, describing the type of isomerism, which may be configurational, the latter being defined by the relative position of the substituents on the staples.

We have developed a complete structural nomenclature, which we call “aspicule structural nomenclature”. It incorporates all of the above aspects of the structure, and is presented in SI 5. Describing the connectivity of the staples to the core atoms increases the lengths of the structural names, and detailed names with this information intact may be found in SI 5 and Tables S7 and S10 in SI 9. For this reason, we have chosen in this Article to describe the modifications of parent aspicules, and we have condensed the names by omitting the unnecessary details of the structure. We term this reduced version “aspicule nomenclature”, and the resulting names are “aspicule names”. In aspicule nomenclature, a parent aspicule name has three parts: the first part describes the ligands consisting of their type and number, while the second part describes the names of the metal present, both in the core and in the staples, and includes the total number of metal atoms. The third part of the name specifies the name of the family of molecules (aspicule) and the electrical charge. Structural details such as geometric isomerism and chirality can be included as prefixes to the front of the whole name.

The nomenclature has been developed to be valid for any gold thiolate aspicule and utilizes the core and staple motif picture of the structure. Before describing the nomenclature in detail, we present as an introduction the name for $\text{Au}_{25}(\text{SMe})_{18}$ according to our nomenclature, which is 18(methylthiolato)-auro-25 aspicule(1-) or $(\text{SMe})_{18}$ -auro-25 aspicule(1-), in its condensed form. The name for $\text{Au}_{25}(\text{SMe})_{16}(\text{PET})_2$, based on the locants of Figure 1, which has two PET ligands exchanged at the bridging positions on the D1 and D2 staples, is (D1-3,D2-3)-di(2-phenylethanethiolato),16(methylthiolato)-auro-25 aspicule(1-) or, in its condensed form, (D1-3,D2-3)-(PET)₂, $(\text{SMe})_{16}$ -auro-25 aspicule(1-). In this name, the locant prefix (D2-3,D2-3) denotes that the ligand exchange occurs at the two bridging sulfur atoms on opposite dimer staples in the *z*- and *z'*-directions, D1 and D2. We now systematically present the aspicule nomenclature in sections 2.3–2.5, apply it to modifications and isomers of $\text{Au}_{25}(\text{SR})_{18}$ in sections 2.6–2.8, and finally in sections 2.9 and 2.10 we show how it can be applied to $\text{Au}_{38}(\text{SR})_{24}$ and $\text{Au}_{102}(\text{SR})_{44}$ and their modifications.

2.3. Symmetry Axes, Orientation, and Diagrams.

Locants are generally assigned with respect to a single symmetry axis by counting atoms lying in the parallel planes lying perpendicular to the symmetry axis.

2.3.1. Principal Symmetry Axis. Before locant assignment can be carried out, the aspicule symmetry axes, around which the numbering of staples and core atoms will take place, must be identified and must be oriented in a standard way. Usually, the highest axis of rotational symmetry may be chosen as the principal axis about which numbering of the staples and core atoms is carried out. The chosen axis of rotational symmetry should, if possible, apply to both the core and the staples of the aspicule, because these two parts of the structure may not share all of the axes of rotational symmetry present. If any of staples do not share the core symmetry axis, but are nevertheless spatially distributed around this axis, we may choose the highest rotational symmetry axis of the core as the principal one. The principal symmetry axis is oriented to coincide with the *z*-axis, with its top end being associated with the *z*-direction.

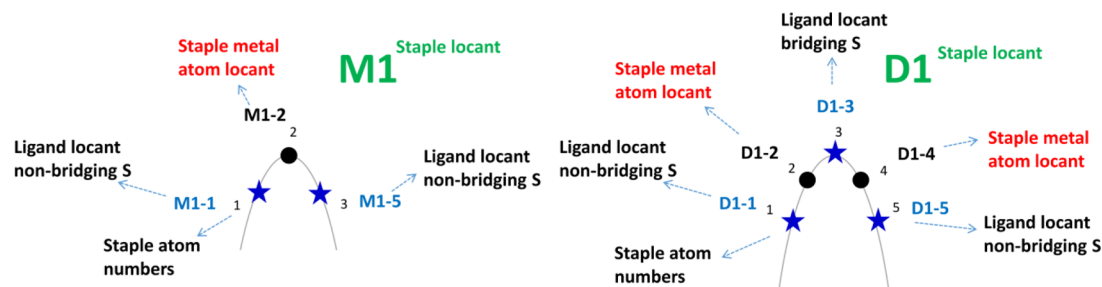
2.3.2. Orientation and Diagram. The aspicule should then be rotated into a unique standard orientation, which is as unique as its symmetry permits. This could be achieved by bringing other symmetry axes or some other distinctive structural feature, such as a particular staple, into a fixed orientation with respect to the Cartesian axes.

Visualization of the 3D structure of a molecule may serve as a diagram, after reduction of the structure to simpler elements such as rings as we demonstrated for $\text{Au}_{25}(\text{SR})_{18}$ so that a two-dimensional diagram can be drawn by hand. In the special case where there are three perpendicular C_2 axes as in $\text{Au}_{25}(\text{SR})_{18}$, it is preferable to align these with respect to standard Cartesian axes, to show the octahedral staple symmetry clearly, and this view may sometimes be preferred over the tomographic representation about a single principal C_3 axis (Figures S5 and S6 in SI 3). For the C_2 axes scheme, we identify three perpendicular planes, which contain the $C_2(x)$, $C_2(y)$, and $C_2(z)$ rings of atoms, and the numbering of staples and core atoms can proceed around the rings that lie perpendicular to each of these three axes.

2.4. Aspicule Locants and Their Assignment. The locants for the staples, ligands and staple metal atoms, and core atoms and their assignment schemes are described in sections 2.4.1–2.4.3.

2.4.1. Staple Locants. The locants of the staples have two parts, first, one or two letters that correspond to the type of staple determined by the number of gold atoms it contains, and this is followed by the identification number of the particular staple. The following upper case letters are used: M for a monomer staple, D for a dimer staple, and TR for a trimer staple. Others are TE (tetramer), P (pentamer), HX (hexamer), HP (heptamer), O (octamer), N (nonamer), D (decamer), U (unadecamer), DO (dodecamer), etc.; the two-letter symbolism is used in some cases to avoid confusion. A slightly more precise way of notating the staple types would be MS, DS, TrS, etc., where S stands for terminating sulfur; however, for simplicity we prefer to omit the S.

Two further cases arise when the ligands are bonded to the core rather than the staples; first, when the ligand (SR) bridges two core atoms, we use the Greek letter μ , as it is conventionally used to denote bridging atoms in IUPAC inorganic nomenclature, in the same manner as the staple type letter, so a set of three bridging ligands would be labeled μ_1, μ_2, μ_3 , etc. Second, if the ligand is only bonded to a single core

Scheme 2. Assignments of Ligand and Staple Metal Atom Locants in Monomer and Dimer Staples^a

^aTaken to be staples M1 and D1 in this example.

atom, we use the letter C, which stands for core, instead. The assignment of the identification numbers of these ligands follows the same procedure as that for the staples. Staples of the same type are numbered in separate sequences, for example, D1–D6 for the six dimer staples of $\text{Au}_{25}(\text{SR})_{18}$ and $\text{Au}_{38}(\text{SR})_{24}$, and M1–M3 for the three monomer staples of $\text{Au}_{38}(\text{SR})_{24}$. Depending on the types of symmetries present, scheme 2.4.1.1 or 2.4.1.2 can be adopted to assign the staple locants.

2.4.1.1. Single Principal Symmetry Axis. **2.4.1.1.1. Staple Groups.** We may consider staples as being grouped, first, by the fact that their bridging sulfur atoms are located on the same planes perpendicular to the principal axis or, second, by the different rings of core atoms to which their ends are bonded.

2.4.1.1.2. Sense of Staple “Rotation”. The direction of “rotation” of a staple can be defined from the projection of the aspicule structure onto a plane perpendicular to the symmetry axis as to whether a clockwise or anticlockwise rotation is needed to bring the core atom bonded to the sulfur atom of the staple with the lowest staple atom number into coincidence with the core atom bonded to the sulfur atom with higher staple atom number on that staple.

2.4.1.1.3. Assignment of Staple Locants. The direction of assigning of the staples in a group is carried out according to the direction of rotation of the staples, being either clockwise (C) or anticlockwise (A). Numbering of staples in each group is carried out starting from the staple group at the top, and if the staples are rotating in clockwise fashion just to the right of the 12 o’ clock position (in the x' -direction), counting clockwise around the principal symmetry axis. While for staples that rotate anticlockwise, these are numbered in an anticlockwise direction from the same 12 o’ clock position. For example, in a case where there are six dimer staples located at the top and bottom regions of the C_3 axis, as in $C\text{-Au}_{38}(\text{SR})_{24}$, the staples would be numbered D1, D2, and D3 in the upper bridging sulfur plane and D4, D5, and D6 in the lower bridging sulfur plane. Hence, in special cases like this where all of the staples “rotate” in the same direction, this scheme is equivalent to numbering the staples winding both around and moving downward with respect to the principal symmetry axis.

2.4.1.2. Special Scheme: Three Perpendicular C_2 Axes for $\text{Au}_{25}(\text{SR})_{18}$. In $\text{Au}_{25}(\text{SR})_{18}$ due to the octahedral arrangement of staples, it is convenient to make further use of symmetry by using the three perpendicular C_2 axes, which, when this aspicule is rotated appropriately, correspond to the x , y , and z Cartesian axes that are oriented as in Figure 1. The staples that lie at either end of each Cartesian (C_2) axis are numbered in sequence according to the reverse order of the six Cartesian directions (so that the z -direction takes priority): z , z' , y , y' , x ,

x' . For $\text{Au}_{25}(\text{SR})_{18}$, the staples directions, respectively, staples D1, D2 are assigned to the z and z' ends of the $C_2(z)$ axis, D3 and D4 are assigned to the y and y' ends of the $C_2(y)$ axis, and staples D5 and D6 to the x and x' ends of the $C_2(x)$ axis.

2.4.2. Ligand Locants and Staple Metal Atom Locants. The ligand and staple metal atom locants are described in sections 2.4.2.2 and 2.4.2.3, and are formed by combining the staple locant with the appropriate staple atom number, described in section 2.4.2.1.

2.4.2.1. Staple Atom Number. Atoms on a staple are assigned a staple atom number, which counts the position of the atoms clockwise from the end of the staple that is bonded to the core atom with the lowest locant. The staple atom numbers for a monomer staple are 1(S_c), 2(Au), 3(S_c) (a total of three atoms), and for a dimer staple they are 1(S_c), 2(Au), 3(S_μ), 4(Au), 5(S_c) (a total of five atoms), where we have indicated the type of atom in brackets and use the subscripts “ μ ” and “ c ” to indicate bridging and nonbridging sulfur positions.

2.4.2.2. Ligand Locants. The position of a ligand on a particular staple is specified by appending to the staple label (D1, M1, etc.) a hyphen and the staple atom number of the sulfur atom, which is bonded to the ligand R-group. In the case where we have no staples, where the ligand or a terminating atom is directly attached to a core atom, we use the core locant as the ligand locant.

2.4.2.3. Staple Metal Atom Locants. The position of a staple metal atom is specified by appending to the staple locant a hyphen followed by the staple atom number of the metal atom substituent.

Scheme 2 illustrates the assignment of ligand and staple metal atom locants of the M1 and D1 staples, for example. The ligand locant D1-3 indicates the third atom counting clockwise around the staple, which is a sulfur atom in the bridging position on dimer staple 1, while D1-1 corresponds to the first nonbridging sulfur atom counting clockwise from the left end of the staple and D1-5 to the fifth atom counting clockwise from the left of the staple, which is the second nonbridging sulfur. Similarly, D1-2 and D1-4 indicate the positions of the two metal atoms on a dimer staple. Examples of monomer ligand and staple metal atom locants are M1-1, M1-2, and M1-3, which correspond to the ligand R-group bonded to the first nonbridging sulfur atom, the central metal atom, and the ligand R-group bonded to the second nonbridging sulfur on the staple.

2.4.3. Core Atom Locants. If the core of an aspicule consists of at least two concentric polyhedra, we term the innermost of these the central polyhedron, which we label separately. The locants of core atoms in the first noncentral polyhedron are

numbers, and if there is more than one such polyhedron comprising the core, we number the inner polyhedron first, and then for the next surrounding polyhedron, we begin the numbering again from one, and so on for each successive outer polyhedron. Furthermore, the locants of the atoms of the outer polyhedra are distinguished from each other by prefixing the number by a letter, which indicates the type of polyhedron or polyhedral fragments.

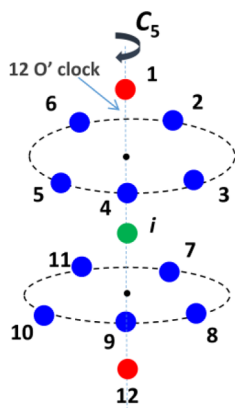
There are two possible schemes described in sections 2.4.3.1 and 2.4.3.2 of assigning core locants. The first is based on numbering around the principal symmetry axis, and is generally applicable, while the second is more convenient for small to medium sized aspicules with, for example, less than 44 metal atoms.

2.4.3.1. Core Ring Locants (Tomographic Representation).

In this section, we describe a general procedure to carry out a tomographic sectioning of the structure around the principal symmetry axis and assign locants to the core atoms.

The numbering of the core ring locant procedure is illustrated in Scheme 3. We assume the core region has been

Scheme 3. Assignment of Core Locants According to the Core Ring Scheme^a



^aThe core icosahedron of $\text{Au}_{25}(\text{SR})_{18}$ with principal C_5 axis is used as an example.

separated into different polyhedrons of atoms, the innermost polyhedron or atom is taken to be the central one, and we then carry out the following five steps:

(1) The core atoms in each polyhedron are sectioned into a set of parallel atomic planes that are perpendicular to the principal symmetry axis.

(2) Core atoms are then identified in each plane, and if there are more than three they are grouped into rings, by joining these coplanar core atoms to their nearest in-plane neighbors by bonds. In the case that there are only two atoms lying in a plane, then the same clockwise numbering scheme is used to number the atom on the right first and then the left.

(3) If there are central atoms or a central polyhedron, these are numbered separately and their locants are written as i , for a single central atom, and i_1, i_2, i_3 , etc., for the atoms of the central polyhedron. If the shape of the central polyhedron is not known a priori, once the core structure has been sectioned into rings, the central atoms may be identified with those that lie on inner concentric rings or isolated atoms at the center of a larger ring. Central atoms may also be identified in rings, or in isolated atoms, which lie on a plane that is sandwiched between neighboring planes above and below it that contain larger rings

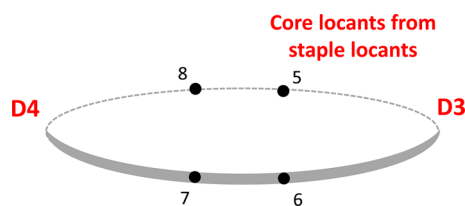
of core atoms, where the size of the ring is defined by its radial dimension.

(4) Numbering of the atoms of a polyhedral cluster in each plane is carried out in a circular manner, counting clockwise around the symmetry axis, and continuing through each of the parallel planes in sequence, from the first plane, which is at the top (or right), to the last plane, which is at the bottom (or left).

(5) In each plane, we give the lowest number to the atom in a ring that is on or just on the right of the 12 o'clock position (which is in the x' direction), viewing the ring from the direction down the symmetry axis from the top to the bottom.

2.4.3.2. Special Assignment Scheme: Core Locants from Staple Locants (for $\text{Au}_{25}(\text{SR})_{18}$). The core atoms are numbered in pairs according to the number of the staple to which they are bonded (see Scheme 4). Core atoms 1 and 2 are bonded to

Scheme 4. Core Locants Associated with the D3 and D4 Staples of the $C_2(y)$ Ring of $\text{Au}_{25}(\text{SR})_{18}$ ^a



^aThe staple atoms are not shown.

staple D1, core atoms 3 and 4 are bonded to staple D2, and in general staple D_n is bonded to core atoms $2n-1$ and $2n$. Core atoms that do not bond to the staples may be numbered in a sequence beginning after the last core atom that is associated with a staple. This scheme is suitable for the smaller aspicules, such as $\text{Au}_{25}(\text{SR})_{18}$, where staples bond to nearly all of the core atoms with the exception of the central one. In the case of aspicules with large cores, where there are many interior core atoms that do not bond to staples, it is best to apply the core ring locant scheme as we will demonstrate for $\text{Au}_{38}(\text{SR})_{24}$ and $\text{Au}_{102}(\text{SR})_{44}$.

2.5. Aspicule Name Syntax. The third part of our nomenclature is naming, and we assemble a three-part name of the form below:

(Ligand Name)-Metal Name aspicule(charge)

The word "aspicule" indicates the family of molecules in an analogous way to the suffix fullerene in IUPAC fullerene nomenclature. The word aspicule is followed without a space by the electrical charge, which is written in parentheses as a final suffix to the name in accord with IUPAC nomenclature, for example, (1-), (1+), or (0), etc. Optionally, the compositional formula name of the counterion of the crystal structure may be specified in parentheses leaving a space after the charge. A further optional structural descriptor, in parentheses, may be specified after the charge or counterion formula, preceded by a space.

In aspicule names, we treat core and staple metal atoms equally and describe them using the single metal name. A hyphen is placed between the last ligand name and the metal name, and the only space in the name is left between the metal name and the suffix. If the ligand name is abbreviated using the $(\text{SR})_n$ notation, then a hyphen is placed between the last ligand name, or $(\text{SR})_n$, and the metal name:

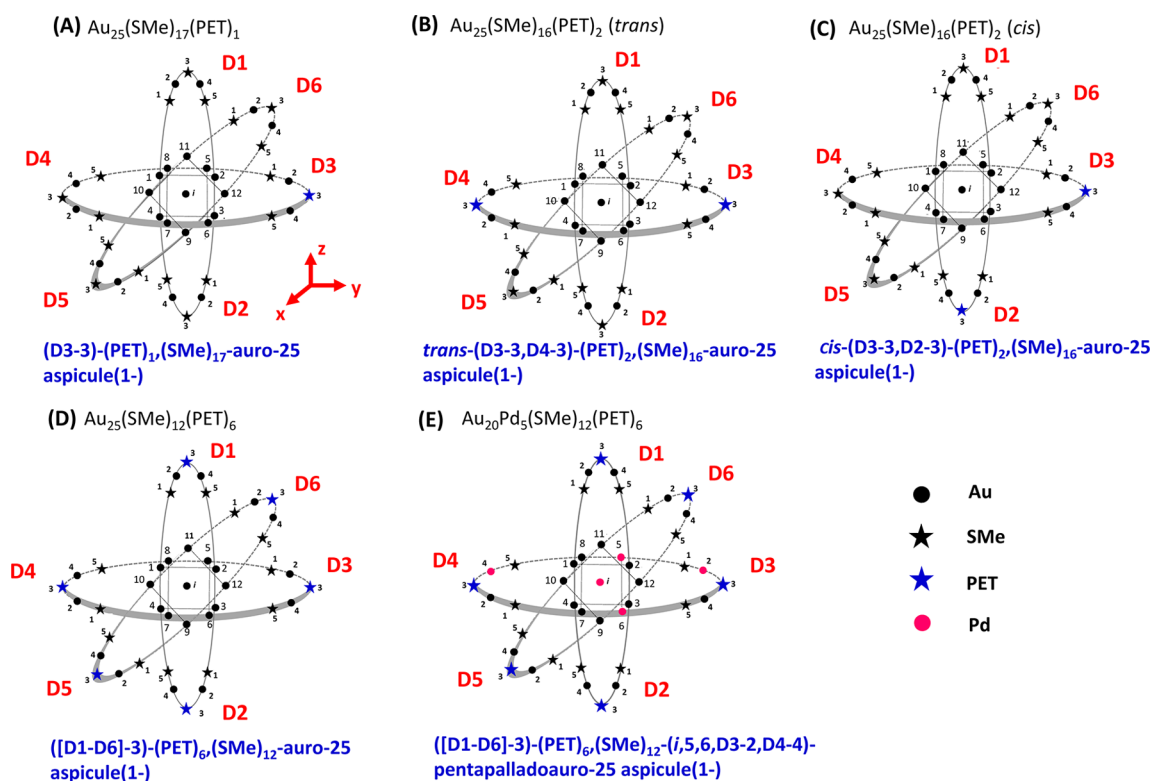


Figure 2. Modifications of $\text{Au}_{25}(\text{SMe})_{18}$ with ligand and metal atom substituents for the following cases: (A) a single bridging ligand (PET) exchange, (B) two bridging ligands exchanged in a *trans* configuration, (C) two bridging ligands exchanged in a *cis* configuration, (D) six bridging ligands exchanged, and (E) six bridging ligands and five metal (Pd) atoms exchanged (which is at present a hypothetical structure). For each example, the current formula name is shown above the diagram and its aspicule name is shown below. The atoms are colored and represented according to the legend, and the ligand (Me and PET) and metal atom type (Pd) are to be taken in a representative sense.

(SR)_n-Metal Name aspicule(charge)

For concreteness, we present as an example the name for $\text{Au}_{25}(\text{SMe})_{18}$ according to our nomenclature, which is 18-(methylthiolato)-auro-25 aspicule(1-) or (SMe)₁₈-auro-25 aspicule(1-), in its condensed form. The name for $\text{Au}_{25}(\text{SMe})_{16}(\text{PET})_2$, based on the locants of Figure 1, which has two PET ligands exchanged at the bridging positions on the D1 and D2 staples, is (D1-3,D2-3)-di(2-phenylethanethiolato),16(methylthiolato)-auro-25 aspicule(1-) or, in its condensed form, (D3-3,D4-3)-(PET)₂(SMe)₁₆-auro-25 aspicule(1-). In this name, the locant prefix (D3-3,D4-3) denotes that the ligand exchange occurs at the two bridging sulfur atoms on opposite dimer staples in the *y*- and *y'*-directions, D3 and D4.

The rules of forming the ligand name and the metal name are formally described in sections 2.5.1 and 2.5.2. In section 2.5.5, we outline the stereodescriptor prefixes to the names.

2.5.1. Ligand Name. The following rules are observed in forming the ligand name of an aspicule:

2.5.1.1. Ligand Name and Number of Ligands. Ligand names may be specified, first, using the IUPAC nomenclature name of the ligand including its thiol group name, all enclosed in brackets. The number of ligands is specified using Greek multiplicative prefixes such as mono-, di-, tri-, etc., as in IUPAC nomenclature, or, as we introduce for brevity, a numerical multiplicative prefix. Thus, (PET)₂ could be written as di(2-phenylethanethiolato), or as 2(2-phenylethanethiolato), where there is no space or hyphen between the prefix and the brackets around the ligand name.

2.5.1.2. Shorter Ligand Names. The second and more compact way of describing the ligands is using the (SR)_n terminology with an acronym for the R-group formed from its systematic name that is prefixed by the element symbol of the chalcogen atom, e.g. SG, or just the acronym of the R-group if it already includes an explicit reference to the thiol group, for example, (PET). In this terminology, the number of each type of ligand is written as a subscript outside the brackets. For brevity, we have chosen in certain places to present ligand names compactly by employing the (SR)_n terminology. If any of the ligands are chiral, the handedness is specified by prefixing a stereodescriptor from IUPAC organic nomenclature to the ligand name in its IUPAC form or before the S in the (SR)_n terminology name.

2.5.1.3. Order and Spacing of Ligand Names. The ordering of the ligand names and their prefixes is in the order of increasing number of the ligand, and a comma separates these different ligand names. A hyphen is used after the ligand names to separate them from the metal name following them.

2.5.1.4. Positions of Ligand Substituents. Each substituent ligand name is prefixed by its comma-separated locants in parentheses, followed by a hyphen to separate it from the ligand name, as in (D1-3,D1-5)-(PET)₂. The ordering of the ligand locants is, first, in the order of the staple number; for example, D1 always precedes D5, and then, second, in order of the positional number on the staple, for example, (D3-3,D3-5). No spaces are left after the commas separating the locants.

2.5.1.5. Example of a Name for $\text{Au}_{25}(\text{SR})_{18}$ with Ligand Substituents. An example of a name for $\text{Au}_{25}(\text{SMe})_{16}(\text{PET})_2$, depicted in Figure 2B, which has two PET ligands substituted is

(D3-3,D4-3)-di(2-phenylethanethiolato),16(methylthiolato)-auro-25 aspicule(1-), or in its compact form (D3-3,D4-3)-(PET)₂(SMe)₁₆-auro-25 aspicule(1-). The first part of this name (D3-3,D4-3)-(PET)₂(SMe)₁₆ indicates that two Me ligand R-groups are substituted by PET ligand R-groups at precisely the D3-3 and D4-3 positions, which are bridging ligand positions on opposite staples. If there are substituents located at the same position on a series of staples, a contraction of the locants of a contiguous sequence of staple numbers is possible. We may condense this by specifying the first and last staples separated by a hyphen, all enclosed in square brackets, followed by the common position on each of the staples; for example, [D1–D6]-3 stands for (D1-3,D2-3,D3-3,D4-3,D5-3,D6-3).

2.5.2. Metal Name. The metal name contains the description of the metal atoms that are present in the core and the staples, and if there is more than one type of metal element, then the positions of the substituents are described using locant prefixes, in a way similar to ligand substituent prefixes.

The following rules are observed in forming the metal name of an aspicule:

2.5.2.1. Metal Element Names. Metal element names are of the form auro, pallado, and so on. These names are formed from the root word of the IUPAC Latin element names and adding an ending “o” to this root, for example, aur-o. We note that these names are also used elsewhere in IUPAC nomenclature for the “metallo” part of the names for metallocenes⁴⁷ (e.g., ferrocene) and metalboranes (e.g., cobaltoborane). In the case that there is more than one type of metal element present, the metal name consists of minority metal element names being prepended to the majority metal element name, giving rise to compound names such as palladoauro, argentoauro, etc. It should be noted that these names have advantages of being unique and forming euphonic combinations, and hence are easy to remember.

2.5.2.2. Number of Metal Substituents. The number of metal atom substituents of a particular element is indicated by prepending the Greek multiplicative prefixes mono-, di-, tri-, tetra-, penta-, hexa-, hepta-, octa-, nona-, deca-, etc., to the substituent metal element name. Optionally, if there are a larger number of metal atom substituents, as might possibly be found in a larger aspicule such as Au₁₀₂(SR)₄₄, the number of substituents can be prefixed in Arabic numerals.

2.5.2.3. Positions of Metal Atom Substituents. The positions of metal atom substituents are described by prefixing their locants to the name of the respective substituent (minority) metal name within the compound metal name; for example, (i,2)-dipalladoauro represents substitution of the central atom and core atom 2. In the case of two minority metals, the locant prefix is inserted before the relevant name with a hyphen before it; for example, with Pd in positions 1 and 2 and Ag in positions 3 and 4, the compound metal name would be (1,2)-dipallado-(3,4)-diargentoauro-25. The ordering of the metal atom locants is to put the core locants first in numerical order, and then the staple metal atom locants.

2.5.2.4. Total Number of Metal Atoms. The total number of metal atoms that is characteristic of the structure is appended to the metal name as a final suffix, with a hyphen separating it from the metal name, for example, auro-25.

2.5.3. Example of a Name with Both Metal and Ligand Substituents. An example of a name for the six-ligand- and five-metal-atom-exchanged Au₂₀Pd₅(SMe)₁₂(PET)₆, shown in

Figure 2E, is ([D1–D6]-3)-hexa(2-phenylethanethiolato)-dodeca(methylthiolato)-(i,5,6,D3-2,D4-4)-pentapalladoauro-25 aspicule(1-), or, in its shorter form, ([D1–D6]-3)-(PET)₆(SMe)₁₂-(i,5,6,D3-2,D4-4)-pentapalladoauro-25 aspicule(1-). The six ligands are exchanged at the bridging sulfur positions, and of the five Pd substitutions, three are in the core and two are in the staples.

2.5.4. Examples of Multimetallic Substituents. A five Pd atom-exchanged structure is certainly hypothetical at present, but we provide this example to show the potential scope of the nomenclature. Recently, trimetallic Au₂₅(SR)₁₈ aspicules have been synthesized.⁸⁴ Examples of hypothetical multimetallic Au₂₅(SR)₁₈ aspicules are the trimetallic Au₂₁Ag₂Pd₂(SMe)₁₈, which has two Pd atoms and two Ag atoms in the core, and could, for example, be named (SMe)₁₈-(i,1)-dipallado-(2,3)-diargentoauro-25 aspicule(1-), and the tetrametallic Au₁₈Ag₃Pd₂Pt₂(SMe)₁₈, one isomer of which might be named (SMe)₁₈-(i,2)-dipallado-(3,4)-diplatio-(5,6,7)-triargentoauro-25 aspicule(1-).

2.5.5. Stereodescriptors and Structure Descriptors.

2.5.5.1. Chirality Intrinsic to the Core and Staple Structure.

The prefixes C and A used for intrinsic chirality are described in sections 2.9 and 2.10 on Au₃₈(SR)₂₄ and Au₁₀₂(SR)₄₄, which are aspicules that have chiral isomers. The chirality of organic ligand can be specified as a prefix to the ligand name following IUPAC organic nomenclature.

2.5.5.2. Geometric Isomerism of Ligands Bonded to the Same Staple. One descriptor of ligand configuration is the direction of the sulfur–carbon (S–C) bonds, which are described by additional prefixes (SI 7), and S–C bond directions are represented diagrammatically for Au₂₅(SR)₁₈ in Figure S7, which is based on the diagram of Figure 1. Because of the presence of a sulfur stereogenic center, the CIP priority and R/S system have been used for this purpose,²⁸ but we present an intuitive scheme based on the direction of the S–C bond with respect to the right-hand screw direction associated with a rotation following the sense of moving around the staple in order of increasing staple atom numbers. We note that for small high symmetry aspicules, each staple may be associated with the Cartesian axis that passes through the center of the core and the central atom of that staple. This provides a spatially intuitive alternative to using the staple locants (D1, D2, etc.), and this hybrid-directional locant scheme (SI 8) has been applied to Figure 1 (Figure S8).

2.5.5.3. Geometric Isomerism of Ligand and Metal Substituents on Different Staples. We observe in Figure 2B and C that concepts from stereochemistry and coordination chemistry such as *cis* and *trans* isomerism are applicable to ligand-exchanged isomers, because if we have substituted ligands at D3-3 and D4-3, it will be *trans*, while if the substitution occurs at D1-3 and D4-3, it would be *cis*. The *cis* and *trans* isomerism also applies to metal atom substituents. The prefixes *cis* and *trans* may be added to the beginning of an aspicule name or terminology to indicate the type of isomer followed by a hyphen between the aspicule name, or the terminology, for example, *cis*-Au₂₅(PET)₂(SMe)₁₆. A more accurate name involving ligand locants would be, for example, *cis*-(D2-3,D3-3)-(PET)₂(SMe)₁₆-auro-25 aspicule(1-).

2.5.5.4. Internal Ligand Conformation and Ligand Chirality. Isomerism arising from changes in the ligand conformation of organic ligands (e.g., rotations about internal bonds) and the chirality of the ligand itself may be included as a

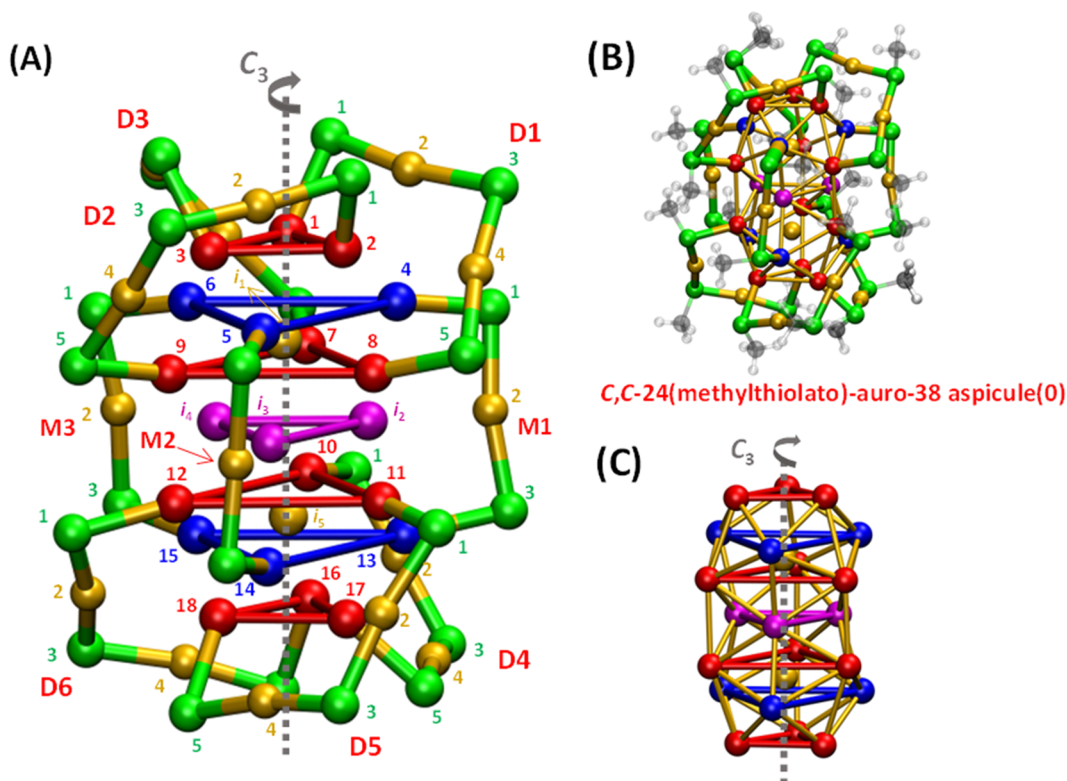


Figure 3. (A) The core and staple structure of $C\text{-Au}_{38}(\text{SMe})_{24}$ with the triangular rings of atoms lying in atomic planes perpendicular to the vertical C_3 axis (marked by the arrow at the top of the figure). The Au–Au bonds of the core have been omitted for clarity. The core atoms and the triangles are colored according to the type of staple they are located in (red for dimer staples and blue for monomer staples and magenta for the face sharing atoms of the bi-icosahedron). The staple and gold atoms at the center of the icosahedra are colored gold, while the sulfur atoms are colored green. Part (B) shows the complete structure of $\text{Au}_{38}(\text{SR})_{24}$ aspicule with Me ligand R-groups, and part (C) shows the bi-icosahedral core with the triangles of atoms in addition to Au–Au bonds. Triangles and the core atoms shown in (B) and (C) follow the same coloring scheme as in (A).

prefix and included as part of the ligand name, and described using terms such as *trans* and *gauche*(\pm).

2.5.5.5. Core Structure Descriptor and Staple Connectivity.

If there is another structural isomer with the same number of metal atoms but with a different core structure and symmetry, the distinction between the two aspicules can first be seen in the ligand name and number of ligands. We may also optionally add a descriptor describing the core polyhedral structure, after the charge, leaving a space. Structural descriptors for different core geometries may be found in SI 5. The main difference between the structural nomenclature and condensed nomenclature is that the staple connectivity to the core information must be included. The names are prefixed by the staple–core locant, which are of the form, for example, D1(1,2), which means that the staple D1 is bonded to core atoms 1 and 2. For $\text{Au}_{25}(\text{SR})_{18}$ in the topological representation with staple locants from the core locants, this connectivity information is actually contained in the staple locants, and the following locant sequence D1(1,2):D2(3,4):D3(5,6):D4(7,8):D5(9,10):D6(11,12) is prefixed to the front of the name to describe the staple–core connectivity of the parent aspicule. In the longer version of the names, the structure descriptor and the principal symmetry axis or axes must also be included. More precise syntax details on the structural nomenclature may be found in SI 5.

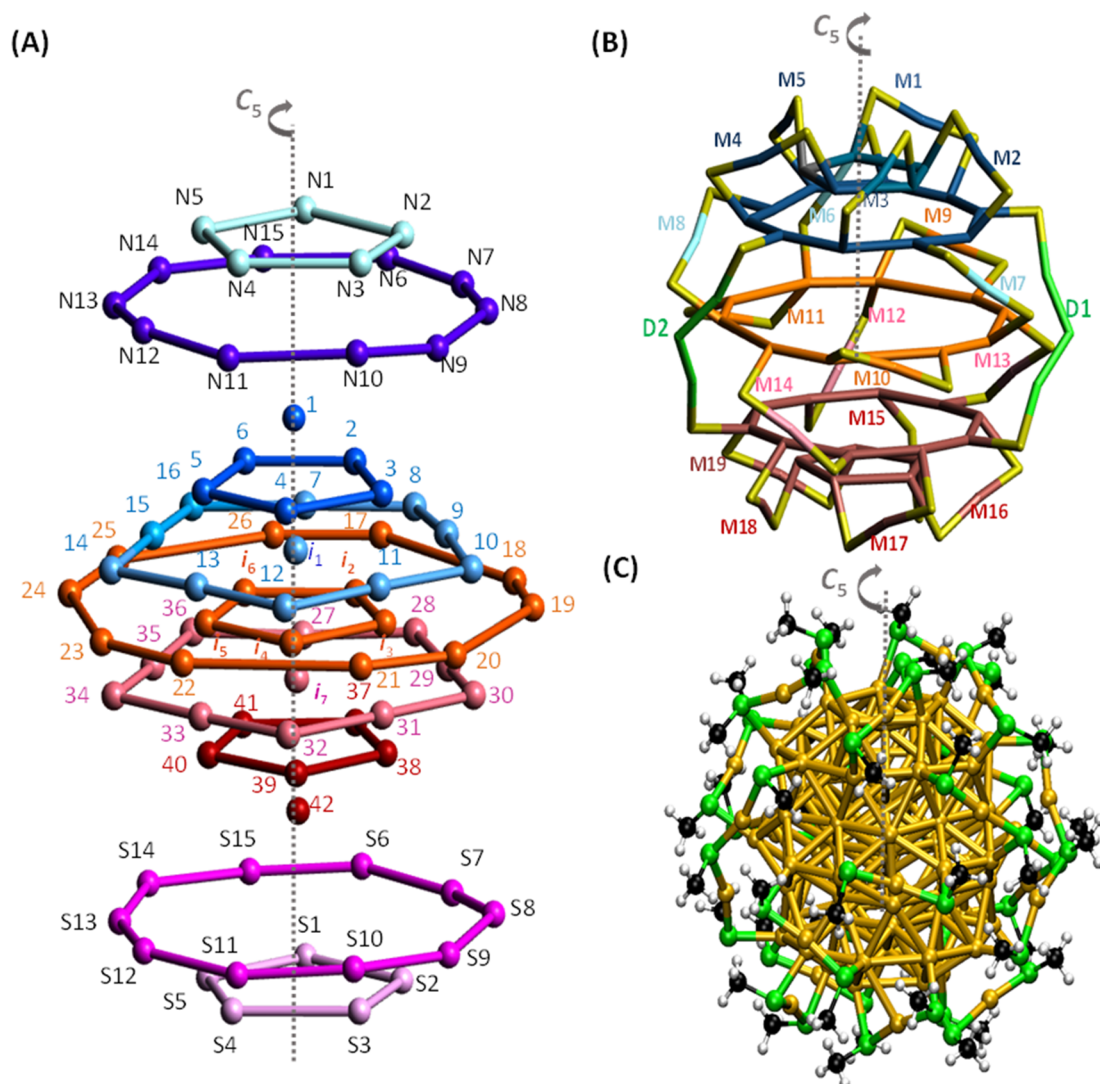
We can improve upon existing terminologies, such the formula name, $\text{Au}_{25}(\text{PET})_2(\text{SMe})_{16}$, by adding a prefix containing the locants of substituents to the relevant part of the formula name. For example, a two PET ligand substitution

of $\text{Au}_{25}(\text{SR})_{18}$ at the bridging positions of D1 and D2 staples would be $\text{Au}_{25}(\text{D1-3,D2-3-PET})_2(\text{SMe})_{16}$, where we have left out the second bracket around the locant prefix and also the first bracket around the ligand name. Several examples of terminologies for ligand and metal-atom-exchanged $\text{Au}_{25}(\text{SR})_{18}$ are shown in Tables S1 and S2 in SI 6.

We stress here that the nomenclature and terminologies described should only be applied to structures that have been determined through either X-ray diffraction or single-particle electron microscopy. A list of many of the known parent structures of $\text{Au}_M(\text{SR})_N$ and closely related structures containing silver, selenium, and chlorine, with their corresponding aspicule names, are given in Table S11 in SI 10.

2.6. Ligand and Metal-Atom Substituents in $\text{Au}_{25}(\text{SR})_{18}$. We considered various examples of ligand-exchanged and alloy modifications of $\text{Au}_{25}(\text{SR})_{18}$ and visualized the modifications using the diagram of Figure 1. Figure 2 shows several examples, including those mentioned earlier, for exchange of Me with a PET R-group for (A) a single bridging ligand, (B) two bridging ligands in a *trans* configuration, (C) two bridging ligands in a *cis* configuration, (D) six bridging ligands, and finally for (E) six bridging ligands and five Pd substituents.

Further examples of aspicule names with substituent positions for modified $\text{Au}_{25}(\text{SR})_{18}$ aspicules may be found in Tables S3 and S4 for different cases such as $\text{Au}_{25}(\text{SR})_{18}$ with six bridging ligand substitutions and one nonbridging ligand substitution, and two cases of metal-atom exchange with Pd



C-44(methylthiolato)-auro-102 aspicule(0)

Figure 4. (A) Core atoms of $C\text{-Au}_{102}(\text{SMe})_{44}$. The 49-atom Marks decahedron is shown at the center, and the two Au_{15} “polar caps” are shown displaced slightly above and below the Marks decahedral core for clarity. The Au_{79} gold core atoms have been divided into rings of atoms lying in planes perpendicular to the C_5 axis. The atoms and the edges of the rings that are shown by connecting “bonds” have both been colored uniquely according to the latitudinal position of the ring in which they lie with blues being used for rings in the Northern “hemisphere” and reds in the Southern “hemisphere”, while the equatorial ring is shown in orange. (B) Staple structure of $C\text{-Au}_{102}(\text{SMe})_{44}$. The staples and those rings of core atoms that bond to the staples have been shown using the stick-bond representation, with their staple locants alongside. The staples are color coded in groups according to their position and size (as described in SI 12). Sulfur atoms on the monomer staples are shown in yellow and on dimer staples in green, while the color scheme for the gold atoms is described in the text. The staple-atom numbers on each of the staples have not been shown, but may be generated from this diagram and the core locants. (C) The complete structure of $C\text{-Au}_{102}(\text{SMe})_{44}$ with representative Me ligand R-groups is shown with its aspicule name in red below it. The gold, sulfur, carbon, and hydrogen atoms are colored gold, green, black, and white, respectively. Because of inherent structural irregularities in the mantle shell, the C_5 axis does not apply to the entire structure, including all of the staples, but only to the Au_{15} polar caps, the M1–M5 and M15–M19 staples bonded to these polar caps, and the Marks decahedral core.

are also presented. Many of these cases have isomers (see below).

2.7. Isomers of Ligand and Metal-Atom-Exchanged $\text{Au}_{25}(\text{SR})_{18}$. We now consider examples of the structures and resulting names of geometric isomers of ligand and metal-atom-exchanged $\text{Au}_{25}(\text{SR})_{18}$. For the simplest case of a single ligand substitution, there are two symmetry-unique isomers, corresponding to exchange at either a bridging sulfur atom or a nonbridging sulfur atom, replacement of the central atom, a core surface metal atom, or an exterior (staple) metal atom. We now consider the case of substitutions of either two ligands or

two metal atoms: how many symmetry-unique isomers are there of each type, and what would be their structures and aspicule names? We used a method which takes into account the C_2 , C_3 , and chiral symmetry operations utilizing the diagram of Figure 1 to enumerate the number of symmetry-unique isomers, and this is described in SI 11. For two-ligand-exchanged $\text{Au}_{25}(\text{SMe})_{16}(\text{PET})_2$, we counted 15 symmetry-unique isomers, and these are shown in Figure S9 in SI 11. In the case of alloying, we counted 28 symmetry-unique isomers for $\text{Au}_{23}\text{Pd}_2(\text{SMe})_{18}$, and we have depicted 18 of these in Figure S10 in SI 11 and provide a complete list of locants for all 28

isomers in Table S12 in SI 11. Examples of possible two metal-atom alloy isomers which involve only the core atoms are shown by visualization of their core icosahedron in Figure S11 in SI 12. The choice of Pd as the substituent is purely representative because it is known that Pd prefers to occupy the central site, while other metals such as silver do not.

2.8. Au₂₅(SR)₁₈ Supramolecular and Conjugated Functionalization. Aspicules whose ligands have either been functionalized or interact supramolecularly can be described by modifying the ligand name appropriately so that the ligand name where the interaction occurs and the type of interaction may be specified. Supramolecular interaction of Au₂₅ with differing numbers of β -cyclodextrin molecules gives rise to Au₂₅(BBSH)_{18-n}(BBSH \cap CD)_n adducts, and these aspicules can be named as shown in Table S5. For the four β -cyclodextrin (CD)-attached Au₂₅(BBSH)₁₄(BBSH \cap CD)₄ supramolecular adduct, we have used the positions of Mathew et al.¹⁰⁰

Fluorescein isothiocyanate (FITC) molecules interact with the amine group of the dansyl glutathione (SDG) ligands of Au₂₅(SDG)₁₈¹⁰¹ to form Au₂₅(SDG)_{18-n}(SDG-FITC)_n adducts, and names for adducts with between one and four FITC molecules are given Table S6. We remark that the above systems are given as examples because their precise structures have not yet been determined experimentally.

2.9. Au₃₈(SR)₂₄. In this section and the next, we describe how we obtained tomographic ring representations of the core and staples of two highly stable aspicules with crystal structures, Au₃₈(SR)₂₄ and Au₁₀₂(SR)₄₄. The tomographic sectioning is more straightforward to carry out than finding the rings containing both the core and the staple atoms as we did for Au₂₅(SR)₁₈; hence, we opted for this kind of representation. The structural insights derived from these representations are outlined in section 2.11, and we also label our diagrams with locants so that modifications can be identified. The core structure of Au₃₈(SR)₂₄ consists of a face-fused bi-icosahedron with two central atoms and six dimer staples, which are arranged in two groups of three staples twisting around the C₃ axis at either end of the bi-icosahedron, and the point group is pseudo D_{3h}.^{51,102} We have used the structure of Qian et al.⁴⁰ for visualization and analysis, and Figure 3B shows this structure with Me ligand R-groups, and also with the core atoms colored according to which plane perpendicular to the C₃ axis they lie in and their bonding environment.

The bi-icosahedral core is sectioned into seven triangles (three-membered rings) located in parallel planes lying perpendicular to the C₃ axis, as shown in Figure 3C. Each triangle of core atoms is colored blue or red according to whether the atoms are bonded to monomer or dimer staple atoms, respectively. The central triangle, shown in magenta of face-sharing atoms, may be grouped with the two central gold atoms to constitute a central trigonal bipyramid whose atoms may be labeled *i*₁–*i*₅. The numbering of the remaining core atoms proceeds from the top red triangle to the bottom red triangle according to the core ring locant scheme.

Figure 3A shows the core and staple structure of Au₃₈(SR)₂₄ with locants. The dimer staples, D1, D2, and D3, are counted in a clockwise manner (D1 → D2 → D3) around the C₃ axis. We count the staple closest and to the right of the *x'* direction going into the paper, because it coincides with the direction of the 12 o'clock position looking down the C₃ axis from the top. This procedure is repeated for the other three dimer staples at the bottom end, D4, D5, and D6, and finally the three centrally located monomer staples are numbered as M1, M2, and M3.

We note that there is already a terminology for chiral and achiral isomers of Au₃₈(SR)₂₄ introduced by Knoppe et al.,¹⁰³ based on IUPAC stereochemical nomenclature of coordination compounds: *A,A*-Au₃₈(SR)₂₄, *C,C*-Au₃₈(SR)₂₄, and the achiral *A,C*-Au₃₈(SR)₂₄ isomer, where *A* and *C* stand for anticlockwise and clockwise. A single prefix, *A* or *C*, may be used if all of the staples “rotate” in the same direction, as appropriate.

In Figure 3A, if we look down the C₃ axis from above, we see that core atom 4 bonded to the lower end of the D1 staple, located in the third triangle from the top, is found in a clockwise direction around the symmetry axis with respect to core atom 1 bonded to the upper end of the staple. This direction of rotation is also the case for the other two staples D2 and D3.^{28,104} A similar scenario is found for D4, D5, and D6, if we now look upward from the bottom of the C₃ axis. Thus, the staples in this enantiomer are considered to be rotating clockwise and have *C* or right-handed chirality. The structure shown in Figure 3 is the chiral *C,C*-Au₃₈(SR)₂₄ or *C*-Au₃₈(SR)₂₄ isomer in this notation.

An example of a name for the parent structure of Au₃₈(SR)₂₄ is *C,C*-24(methylthiolato)-auro-38 aspicule(0), and this would shorten to *C*-(SMe)₂₄-auro-38 aspicule(0). One example with four ligand substitutions in the bridging positions of two dimer and two monomer staples, and with two central Pd atoms, is *C*-(D1-3,D2-3,M1-1,M2-3)-(PET)₄(SMe)₂₀-(*i*₁,*i*₅)-dipalladoauro-38 aspicule(0), or *C*-(D1-3,D2-3,M1-1,M2-3)-tetra(2-phenylethanethiolato),20(methylthiolato)-(*i*₁,*i*₅)-dipalladoauro-38 aspicule(0).

2.10. Au₁₀₂(SR)₄₄. We apply our structural analysis to Au₁₀₂(*p*-MBA)₄₄ or equivalently Au₁₀₂(SMe)₄₄, which was the first aspicule to have its crystal structure determined, and a visualization of the right-handed enantiomer *C*-Au₁₀₂(SMe)₄₄ can be seen in Figure 4C. Au₁₀₂(SR)₄₄ has 89 gold atoms that have pseudo D_{5h} symmetry, apart from the 13 irregularly located ones in the staples around the equatorial region.^{48,105} We used the structure of *C*-Au₁₀₂(SR)₄₄ from Jung et al.¹⁰⁶ for visualization. We select as the principal symmetry axis the C₅ axis passing through the center of the 49-atom Marks decahedron (MD₄₉) located in the inner-core region, and rotate the structure into a standard orientation, as described in SI 13 and shown in Figure 4C. The 10 monomer staples bonded to the “polar caps” also exhibit C₅ symmetry, but the two dimer staples and the remaining nine monomer staples do not; however, this does not affect the choice of the C₅ principal axis.

The three regions of N and S Au₁₅ polar caps, where N (north) and S (south) distinguish the upper and lower fragments, and the outer shell of the Marks decahedron and its central pentagonal bipyramid are numbered in separate groups following the core ring locant procedure, and the result is shown in Figure 4A. Because of the equatorial C₂ symmetry plane, we numbered the south polar Au₁₅ fragment starting from the southernmost ring, rather than the one above it.

The staple locant assignment, shown in Figure 4B, is carried out in six groups, with each group consisting of a set of staples of similar size and latitudinal position. The staples in each group are counted clockwise around the C₅ axis, beginning from the northernmost monomer staple group, proceeding downward through each group in turn until the southernmost monomer staple group and then counting the two dimer staples in the final group. Further details of the standard orientation, locant assignment, the staple groups, and color scheme of Figure 4B are given in SI 13. The staple–core connectivity is

shown in Figure S12 in SI 13, which is similar to Figure 4B, but with the locants for core atoms in the outer shell being shown.

We have not shown the locants for the ligands and the staple metal atoms in Figure 4B, but these may be ascertained by assigning the staple atom numbers to each staple following the schemes in section 2.4.2.1. The parent structure of $\text{Au}_{102}(\text{SMe})_{44}$ can be named immediately as 44-(methylthiolato)-auro-102 aspicule(0) or auro-102 aspicule(0), the latter being the mirror image of the structure of Figure 4C. An example of a modification is the name of one isomer of $\text{C-Au}_{102}(\text{SMe})_{40}(\text{PET})_4$, which has four PET ligands substituted on four monomer staples. The substituent locations are on two different staples bonded to the north polar cap, and on two other staples: one in the northern hemisphere and one in the equatorial staple group. This would be named as C-(M1-1,M2-3,M7-1,M10-3)-tetra(2-phenylethanthiolato),40-(methylthiolato)-auro-102 aspicule(0), or, more compactly, C-(M1-1,M2-3,M7-1,M10-3)-(PET)₄(SMe)₄₀-auro-102 aspicule(0). A comparison of aspicule names for $\text{Au}_{25}(\text{SR})_{18}$, $\text{Au}_{38}(\text{SR})_{24}$, and $\text{Au}_{102}(\text{SR})_{44}$ with a single modification is given in Table S8, while names for these aspicules, which include more structural information, are shown in Tables S9 and S10, and the latter table presents names that include complete staple connectivity to the core. An extension to other multishell core clusters of other metals, such as $(\mu_{12}\text{-Pt})\text{Pd}_{164-x}\text{Pt}_x(\text{CO})_{72}(\text{PPh}_3)_{20}$ ($x \sim 7$) of ref 88, which has both terminal ligands on the surface of the core and intershell bridging ligands inside the core, is possible by assigning its locants following a procedure similar to $\text{Au}_{102}(\text{SR})_{44}$. Because there are no staples, we use ligand locants beginning with the letters μ and C, to denote bridging or terminal sulfur atoms. A basic example of a name with locants for the Pt positions would be $(\text{CO})_{72}(\text{PPh}_3)_{20}$ -(i,1,2,3,4,5,6,7)-octaplatinopallado-165 aspicule(0). The specific locants for the eight Pt atoms are given as an example and are not based upon the structure, apart from the central one. Further prefixes may be inserted specifying ligand positions for modifications or structural descriptors if greater structural detail is required.

2.11. Structural Insights. First and foremost, the identification of a topologically interesting configuration such as the Borromean rings is a very significant but hitherto unrecognized finding in the context of understanding the structure of $\text{Au}_{25}(\text{SR})_{18}$ but also, perhaps, that of the structures of gold thiolate aspicules in general. This is the most important example of an interlocked ring configuration found for an aspicule, which has a known crystal structure, the others being $\text{Au}_{10}(\text{SR})_{10}$ ¹⁰⁷ which is a catenane, and $\text{Au}_{20}(\text{SR})_{16}$ ¹⁰⁸

These two examples suggest that rings and topological linking or interlocking of rings may be a more general feature of part of the inner bonding network of aspicules, and represent a unified view of this part of the structure involving both core and staple atoms, rather than the division between the core and the staples.

A physical distinction of these rings may be seen in the differences found in the lengths of the Au–Au core bonds (colored red, blue, and green in inset (i) of Figure 1), which lie in the (Au_8S_6) -rings, being all of same length (~ 2.79 Å) and slightly shorter⁷¹ than the other Au–Au bonds in the icosahedron (~ 2.99 Å) (colored gold in Figure 1, inset (i)), apart from the bonds to the central atom, which are also of length similar to those in the rings.⁷¹ The geometric stability arising from the greater depth of the energy minimum at the ground-state geometry of $\text{Au}_{25}(\text{SR})_{18}$ may be in part related to

the shorter⁷¹ and therefore stronger bonds in the rings and to the triple-interlocking of the rings around the central atom, which provides a strong framework for the whole molecule.

The second structural viewpoint was the tomographic one, where parallel rings of core atoms and staples winding around a common symmetry axis are found, which might also be generally applicable to many more aspicules. The bonds between core atoms lying on adjacent rings have been left out, which clearly shows the parallel sets of atomic rings, or planes containing single atoms, in the core region and with different groups of staples joining different rings together. We use the term ring in the sense of the connectivity, because the atoms in these rings actually lie in triangles or other polygons (e.g., as shown in Figures 3A and 4A). We may distinguish three types of rings depending on whether all of the atoms in the ring are bonded to each other (e.g., the triangle with atoms 1, 2, and 3 of Figure 3A), some are bonded to each other and some not (e.g., the atoms in the orange equatorial ring in Figure 4A), and last, none of the atoms in the ring are bonded. The latter case occurs if all of the atoms are separated by at least next nearest-neighbor bond distances (e.g., the triangle with atoms 4, 5, 6 in Figure 3A). The core atom ring configurations shown in Figures 3A and 4A suggest a mechanism by which the core forms by stacking (or growth) of ring configurations (with or without intraring bonds) of gold atoms, above and below a central polyhedron or central atom in $\text{Au}_{38}(\text{SR})_{24}$ and $\text{Au}_{102}(\text{SR})_{44}$. From this representation, we cannot, however, conclusively identify the precise structural units that lead to this formation. One further significance of these core rings is that the preferential sites of Ag alloy substituents in $\text{Au}_{38}(\text{SR})_{24}$, for example, lie in these rings.⁵⁵ The smaller triangles at the top, center, and bottom of $\text{Au}_{38}(\text{SR})_{24}$ in Figure 3A are precisely those that are preferred for Ag atom alloying. A slight preference for opposite triangles of Ag atoms lying perpendicular to the C_3 axis in Ag doping of $\text{Au}_{25}(\text{SR})_{18}$ has also been observed.⁵⁷

Third, a detailed understanding of the structure of isomers was obtained through the enumeration and naming of the cases of two ligand or two-metal atom substituents for $\text{Au}_{25}(\text{SR})_{18}$. Here, we took into account symmetry equivalence and chirality, and diagrammatically represented the structures of chiral isomers and *cis*–*trans* analogue isomers.

Finally, we note that a set of symmetry-equivalent sites would only be equivalent with respect to the metal or sulfur atom site positions, but not with respect to the metal or ligand atoms associated with those sites once a modification has broken the symmetry. Hence, the locant system we have presented provides a unique label for each metal atom or ligand and is a more general and precise system for specifying substituent positions.

3. SUMMARY

We carried out a structural simplification of the highly stable $\text{Au}_{25}(\text{SR})_{18}$ and identified within the bonding network the topological configuration consisting of interlocked Au_8S_6 (Borromean) rings, which provides a unified structural viewpoint including both core and staple atoms, and which forms a strongly bonded framework that is possibly responsible for the high geometric stability of this molecule. The Borromean rings diagram of $\text{Au}_{25}(\text{SR})_{18}$ was also used to represent its various modifications, such as ligand-exchange, alloying, and functionalization (supramolecular/conjugated interaction). We also incorporated our methods of structural

analysis into a structure-based nomenclature, including positionally precise terminologies, for gold thiolate aspicules that is symmetry-based, provides a complete framework to describe and understand the structural diversity of $\text{Au}_M(\text{SR})_N$ and $\text{Au}_M(\text{X})_N$ and is adaptable to the general case of $\text{M}_M(\text{X})_N$ with additional modifications to account for any atypical structural features that may be encountered.

Developing simplified structural representations of gold thiolate aspicules of different sizes, both smaller than $\text{Au}_{25}(\text{SR})_{18}$ (e.g., $\text{Au}_{15}(\text{SR})_{13}$ ⁹¹ and $\text{Au}_{18}(\text{SR})_{14}$ ¹⁰⁹) and also larger (e.g., $\text{Au}_{133}(\text{SR})_{52}$ ^{54,60} and $\text{Au}_{144}(\text{SR})_{60}$ ^{111,112}) with coordinating atoms other than sulfur, and also of aspicules with different predominant metals such as silver, for example, $\text{Ag}_{44}(\text{SR})_{30}$ ^{62,63} is the subject of ongoing and further work. Because chirality is found in nearly all aspicules, it is necessary to produce simplified diagrams for each of the enantiomers. Finding symmetry-equivalent isomer structures for the general cases of isomers with n substituent ligands/metal atoms is another possible direction. Finally, we wish to emphasize that this Article is not about the name aspicule for this class of molecules, which may be decided by a consensus of workers in the field, but is focused on understanding the structure and modifications within a unified framework.

■ ASSOCIATED CONTENT

Supporting Information

The Supporting Information is available free of charge on the ACS Publications website at DOI: 10.1021/acs.jpcc.5b08193.

Additional data and systematic instructions for drawing the Borromean rings diagram of $\text{Au}_{25}(\text{SR})_{18}$ (PDF)

■ AUTHOR INFORMATION

Corresponding Author

*E-mail: pradeep@iitm.ac.in.

Author Contributions

G.N. and T.P. carried out structural analysis and developed the nomenclature. G.N., A.M., and T.P. wrote this Article. A.M. also contributed to the production of the figures. Y.N. and R.L. reviewed and commented on the manuscript.

Notes

The authors declare no competing financial interest.

■ ACKNOWLEDGMENTS

G.N. and T.P. thank the DST (India) for funding. A.M. thanks CSIR for her fellowship. G.N. gratefully acknowledges a helpful discussion on the nomenclature of boranes with Sundargopal Ghosh.

■ REFERENCES

- (1) Brust, M.; Walker, M.; Bethell, D.; Schiffrin, D. J.; Whyman, R. Synthesis of Thiol-Derivatized Gold Nanoparticles in a Two-Phase Liquid-Liquid System. *J. Chem. Soc., Chem. Commun.* **1994**, 7, 801–802.
- (2) Jin, R. Quantum Sized, Thiolate-Protected Gold Nanoclusters. *Nanoscale* **2010**, 2, 343–362.
- (3) Häkkinen, H. The Gold-Sulfur Interface at the Nanoscale. *Nat. Chem.* **2012**, 4, 443–455.
- (4) Maity, P.; Xie, S.; Yamanuchi, M.; Tsukuda, T. Recent Progress in the Functionalization Methods of Thiolate Protected Gold Clusters. *Nanoscale* **2012**, 4, 4027–4037.
- (5) Kurashige, W.; Niihori, Y.; Sharma, S.; Negishi, Y. Recent Progress in the Functionalization Methods of Thiolate-Protected Gold Clusters. *J. Phys. Chem. Lett.* **2014**, 5, 4134–4142.

(6) Jin, R. Atomically Precise Metal Nanoclusters: Stable Sizes and Optical Properties. *Nanoscale* **2015**, 7, 1549–1565.

(7) Mathew, A.; Pradeep, T. Noble Metal Clusters: Applications in Energy, Environment, and Biology. *Part. Part. Syst. Char.* **2014**, 31, 1017–1053.

(8) Parker, J. F.; Fields-Zinna, C. A.; Murray, R. W. The Story of a Monodisperse Gold Nanoparticle: $\text{Au}_{25}\text{L}_{18}$. *Acc. Chem. Res.* **2010**, 43, 1289–1296.

(9) Lourdu Xavier, P.; Chaudhari, K.; Baksi, A.; Pradeep, T. Protein-Protected Luminescent Noble Metal Quantum Clusters: An Emerging Trend in Atomic Cluster Nanoscience. *Nano Rev.* **2012**, 3, 14767–14782.

(10) Yuan, X.; Luo, Z.; Yu, Y.; Yao, Q.; Xie, J. Luminescent Noble Metal Nanoclusters as an Emerging Optical Probe for Sensor Development. *Chem. - Asian J.* **2013**, 8, 858–871.

(11) Li, J.; Zhao, T.; Chen, T.; Liu, Y.; Ong, C. N.; Xie, J. Engineering Noble Metal Nanomaterials for Environmental Applications. *Nanoscale* **2015**, 7, 7502–7519.

(12) Schaaff, T. G.; Whetten, R. L. Giant Gold–Glutathione Cluster Compounds: Intense Optical Activity in Metal-Based Transitions. *J. Phys. Chem. B* **2000**, 104, 2630–2641.

(13) Negishi, Y.; Nobusada, K.; Tsukuda, T. Glutathione-Protected Gold Clusters Revisited: Bridging the Gap between Gold(I) Thiolate Complexes and Thiolate-Protected Gold Nanocrystals. *J. Am. Chem. Soc.* **2005**, 127, 5261–5270.

(14) Templeton, A. C.; Wuelfing, W. P.; Murray, R. W. Monolayer-Protected Cluster Molecules. *Acc. Chem. Res.* **2000**, 33, 27–36.

(15) Schaaff, T. G.; Whetten, R. L. Controlled Etching of Au:SR Cluster Compounds. *J. Phys. Chem. B* **1999**, 103, 9394–9396.

(16) Chen, L.-Y.; Wang, C.-W.; Yuan, Z.; Chang, H.-T. Fluorescent Gold Nanoclusters: Recent Advances in Sensing and Imaging. *Anal. Chem.* **2015**, 87, 216–229.

(17) Kumara, C.; Zuo, X.; Cullen, D. A.; Dass, A. Faradaurate-940: Synthesis, Mass Spectrometry, Electron Microscopy, High-Energy X-ray Diffraction, and X-ray Scattering Study of $\text{Au}_{940\pm 20}(\text{SR})_{160\pm 4}$ Nanocrystals. *ACS Nano* **2014**, 8, 6431–6439.

(18) Azubel, M.; Koivisto, J.; Malola, S.; Bushnell, D.; Hura, G. L.; Koh, A. L.; Tsunoyama, H.; Tsukuda, T.; Pettersson, M.; Häkkinen, H.; et al. Electron Microscopy of Gold Nanoparticles at Atomic Resolution. *Science* **2014**, 345, 909–912.

(19) Hostetler, M. J.; Wingate, J. E.; Zhong, C.-J.; Harris, J. E.; Vachet, R. W.; Clark, M. R.; Londono, J. D.; Green, S. J.; Stokes, J. J.; Wignall, G. D.; et al. Alkanethiolate Gold Cluster Molecules with Core Diameters from 1.5 to 5.2 nm: Core and Monolayer Properties as a Function of Core Size. *Langmuir* **1998**, 14, 17–30.

(20) Aikens, C. M. Electronic Structure of Ligand-Passivated Gold and Silver Nanoclusters. *J. Phys. Chem. Lett.* **2011**, 2, 99–104.

(21) Bigioni, T. P.; Whetten, R. L.; Dag, O. Near-Infrared Luminescence from Small Gold Nanocrystals. *J. Phys. Chem. B* **2000**, 104, 6983–6986.

(22) Wu, Z.; Jin, R. On the Ligand's Role in the Fluorescence of Gold Nanoclusters. *Nano Lett.* **2010**, 10, 2568–2573.

(23) Pyo, K.; Thanthirige, V. D.; Kwak, K.; Pandurangan, P.; Ramakrishna, G.; Lee, D. Ultrabright Luminescence from Gold Nanoclusters: Rigidifying the Au(I)-Thiolate Shell. *J. Am. Chem. Soc.* **2015**, 137, 8244–8255.

(24) Diez, I.; Ras, R. H. A. Fluorescent Silver Nanoclusters. *Nanoscale* **2011**, 3, 1963–1970.

(25) Diez, I.; Kanyuk, M. I.; Demchenko, A. P.; Walther, A.; Jiang, H.; Ikkala, O.; Ras, R. H. A. Blue, Green and Red Emissive Silver Nanoclusters Formed in Organic Solvents. *Nanoscale* **2012**, 4, 4434–4437.

(26) Barrabés, N.; Zhang, B.; Bürgi, T. Racemization of Chiral $\text{Pd}_2\text{Au}_{36}(\text{SC}_2\text{H}_4\text{Ph})_{24}$: Doping Increases the Flexibility of the Cluster Surface. *J. Am. Chem. Soc.* **2014**, 136, 14361–14364.

(27) Dolamic, I.; Varnholt, B.; Bürgi, T. Chirality Transfer from Gold Nanocluster to Adsorbate Evidenced by Vibrational Circular Dichroism. *Nat. Commun.* **2015**, 6, 7117.

- (28) Knoppe, S.; Bürgi, T. Chirality in Thiolate-Protected Gold Clusters. *Acc. Chem. Res.* **2014**, *47*, 1318–1326.
- (29) Knoppe, S.; Wong, O. A.; Malola, S.; Häkkinen, H.; Bürgi, T.; Verbiest, T.; Ackerson, C. J. Chiral Phase Transfer and Enantioenrichment of Thiolate-Protected Au₁₀₂ Clusters. *J. Am. Chem. Soc.* **2014**, *136*, 4129–4132.
- (30) Díez, I.; Pusa, M.; Kulmala, S.; Jiang, H.; Walther, A.; Goldmann, A. S.; Mueller, A. H. E.; Ikkala, O.; Ras, R. H. A. Color Tunability and Electrochemiluminescence of Silver Nanoclusters. *Angew. Chem., Int. Ed.* **2009**, *48*, 2122–2125.
- (31) Lee, D.; Donkers, R. L.; Wang, G.; Harper, A. S.; Murray, R. W. Electrochemistry and Optical Absorbance and Luminescence of Molecule-Like Au₃₈ Nanoparticles. *J. Am. Chem. Soc.* **2004**, *126*, 6193–6199.
- (32) Antonello, S.; Holm, A. H.; Instuli, E.; Maran, F. Molecular Electron-Transfer Properties of Au₃₈ Clusters. *J. Am. Chem. Soc.* **2007**, *129*, 9836–9837.
- (33) Turner, M.; Golovko, V. B.; Vaughan, O. P. H.; Abdulkin, P.; Berenguer-Murcia, A.; Tikhov, M. S.; Johnson, B. F. G.; Lambert, R. M. Selective Oxidation with Dioxide by Gold Nanoparticle Catalysts Derived from 55-Atom Clusters. *Nature* **2008**, *454*, 981–983.
- (34) Yamazoe, S.; Koyasu, K.; Tsukuda, T. Nonscalable Oxidation Catalysis of Gold Clusters. *Acc. Chem. Res.* **2014**, *47*, 816–824.
- (35) Li, G.; Jin, R. Atomically Precise Gold Nanoclusters as New Model Catalysts. *Acc. Chem. Res.* **2013**, *46*, 1749–1758.
- (36) McCoy, R. S.; Choi, S.; Collins, G.; Ackerson, B. J.; Ackerson, C. J. Superatom Paramagnetism Enables Gold Nanocluster Heating in Applied Radiofrequency Fields. *ACS Nano* **2013**, *7*, 2610–2616.
- (37) Zhu, M.; Aikens, C. M.; Hendrich, M. P.; Gupta, R.; Qian, H.; Schatz, G. C.; Jin, R. Reversible Switching of Magnetism in Thiolate-Protected Au₂₅ Superatoms. *J. Am. Chem. Soc.* **2009**, *131*, 2490–2492.
- (38) Krishna, K. S.; Tarakeswar, P.; Mujica, V.; Kumar, C. S. Chemically Induced Magnetism in Atomically Precise Gold Clusters. *Small* **2014**, *10*, 907–911.
- (39) Chen, X.; Strange, M.; Häkkinen, H. Nonmagnetic and Magnetic Thiolate-Protected Au₂₅ Superatoms on Cu(111), Ag(111), and Au(111) Surfaces. *Phys. Rev. B: Condens. Matter Mater. Phys.* **2012**, *85*, 085422.
- (40) Choi, S.; Dickson, R. M.; Yu, J. Developing Luminescent Silver Nanodots for Biological Applications. *Chem. Soc. Rev.* **2012**, *41*, 1867–1891.
- (41) Jin, R.; Nobusada, K. Doping and Alloying in Atomically Precise Gold Nanoparticles. *Nano Res.* **2014**, *7*, 285–300.
- (42) Udayabhaskararao, T.; Pradeep, T. New Protocols for the Synthesis of Stable Ag and Au Nanocluster Molecules. *J. Phys. Chem. Lett.* **2013**, *4*, 1553–1564.
- (43) Wilcoxon, J. P.; Abrams, B. L. Synthesis, Structure and Properties of Metal Nanoclusters. *Chem. Soc. Rev.* **2006**, *35*, 1162–1194.
- (44) Takano, S.; Yamazoe, S.; Koyasu, K.; Tsukuda, T. Slow-Reduction Synthesis of a Thiolate-Protected One-Dimensional Gold Cluster Showing an Intense Near-Infrared Absorption. *J. Am. Chem. Soc.* **2015**, *137*, 7027–7030.
- (45) De Nardi, M.; Antonello, S.; Jiang, D.-E.; Pan, F.; Rissanen, K.; Ruzzi, M.; Venzo, A.; Zoleo, A.; Maran, F. Gold Nanowired: A Linear (Au₂₅)_n Polymer from Au₂₅ Molecular Clusters. *ACS Nano* **2014**, *8*, 8505–8512.
- (46) Díez, I.; Pusa, M.; Kulmala, S.; Jiang, H.; Walther, A.; Goldmann, A. S.; Müller, A. H. E.; Ikkala, O.; Ras, R. H. A. Color Tunability and Electrochemiluminescence of Silver Nanoclusters. *Angew. Chem., Int. Ed.* **2009**, *48*, 2122–2125.
- (47) Nishigaki, J.-i.; Koyasu, K.; Tsukuda, T. Chemically Modified Gold Superatoms and Superatomic Molecules. *Chem. Rec.* **2014**, *14*, 897–909.
- (48) Jadzinsky, P. D.; Calero, G.; Ackerson, C. J.; Bushnell, D. A.; Kornberg, R. D. Structure of a Thiol Monolayer-Protected Gold Nanoparticle at 1.1 Å Resolution. *Science* **2007**, *318*, 430–433.
- (49) Heaven, M. W.; Dass, A.; White, P. S.; Holt, K. M.; Murray, R. W. Crystal Structure of the Gold Nanoparticle [N(C₈H₁₇)₄]-[Au₂₅(SCH₂CH₂Ph)₁₈]. *J. Am. Chem. Soc.* **2008**, *130*, 3754–3755.
- (50) Zhu, M.; Aikens, C. M.; Hollander, F. J.; Schatz, G. C.; Jin, R. Correlating the Crystal Structure of a Thiol-Protected Au₂₅ Cluster and Optical Properties. *J. Am. Chem. Soc.* **2008**, *130*, 5883–5885.
- (51) Qian, H.; Eckenhoff, W. T.; Zhu, Y.; Pintauer, T.; Jin, R. Total Structure Determination of Thiolate-Protected Au₃₈ Nanoparticles. *J. Am. Chem. Soc.* **2010**, *132*, 8280–8281.
- (52) Zeng, C.; Qian, H.; Li, T.; Li, G.; Rosi, N. L.; Yoon, B.; Barnett, R. N.; Whetten, R. L.; Landman, U.; Jin, R. Total Structure and Electronic Properties of the Gold Nanocrystal Au₃₆(SR)₂₄. *Angew. Chem., Int. Ed.* **2012**, *51*, 13114–13118.
- (53) Das, A.; Li, T.; Nobusada, K.; Zeng, Q.; Rosi, N. L.; Jin, R. Total Structure and Optical Properties of a Phosphine/Thiolate-Protected Au₂₄ Nanocluster. *J. Am. Chem. Soc.* **2012**, *134*, 20286.
- (54) Zeng, C.; Chen, Y.; Kirschbaum, K.; Appavoo, K.; Sfeir, M. Y.; Jin, R. Structural Patterns at All Scales in a Nonmetallic Chiral Au₁₃₃(SR)₅₂ Nanoparticle. *Sci. Adv.* **2015**, *1*, e1500045.
- (55) Kumara, C.; Gagnon, K. J.; Dass, A. X-ray Crystal Structure of Au_{38-x}Ag_x(SCH₂CH₂Ph)₂₄ Alloy Nanomolecules. *J. Phys. Chem. Lett.* **2015**, *6*, 1223–1228.
- (56) Nimmala, P. R.; Knoppe, S.; Jupally, V. R.; Delcamp, J. H.; Aikens, C. M.; Dass, A. Au₃₆(SPh)₂₄ Nanomolecules: X-ray Crystal Structure, Optical Spectroscopy, Electrochemistry, and Theoretical Analysis. *J. Phys. Chem. B* **2014**, *118*, 14157–14167.
- (57) Kumara, C.; Aikens, C. M.; Dass, A. X-ray Crystal Structure and Theoretical Analysis of Au_{25-x}Ag_x(SCH₂CH₂Ph)₁₈ Alloy. *J. Phys. Chem. Lett.* **2014**, *5*, 461–466.
- (58) Crasto, D.; Barcaro, G.; Stener, M.; Sementa, L.; Fortunelli, A.; Dass, A. Au₂₄(SAdm)₁₆ Nanomolecules: X-ray Crystal Structure, Theoretical Analysis, Adaptability of Adamantane Ligands to Form Au₂₃(SAdm)₁₆ and Au₂₅(SAdm)₁₆, and Its Relation to Au₂₅(SR)₁₈. *J. Am. Chem. Soc.* **2014**, *136*, 14933–14940.
- (59) Crasto, D.; Malola, S.; Brosofsky, G.; Dass, A.; Häkkinen, H. Single Crystal XRD Structure and Theoretical Analysis of the Chiral Au₃₀S(S-t-Bu)₁₈ Cluster. *J. Am. Chem. Soc.* **2014**, *136*, 5000–5005.
- (60) Dass, A.; Theivendran, S.; Nimmala, P. R.; Kumara, C.; Jupally, V. R.; Fortunelli, A.; Sementa, L.; Barcaro, G.; Zuo, X.; Noll, B. C. Au₁₃₃(SPh-tBu)₅₂ Nanomolecules: X-ray Crystallography, Optical, Electrochemical, and Theoretical Analysis. *J. Am. Chem. Soc.* **2015**, *137*, 4610–4613.
- (61) Shichibu, Y.; Negishi, Y.; Watanabe, T.; Chaki, N. K.; Kawaguchi, H.; Tsukuda, T. Biicosahedral Gold Clusters [Au₂₅(PPh₃)₁₀(SC_nH_{2n+1})₅Cl₂]²⁺ (n = 2–18): A Stepping Stone to Cluster-Assembled Materials. *J. Phys. Chem. C* **2007**, *111*, 7845–7847.
- (62) Desiredy, A.; Conn, B. E.; Guo, J.; Yoon, B.; Barnett, R. N.; Monahan, B. M.; Kirschbaum, K.; Griffith, W. P.; Whetten, R. L.; Landman, U.; et al. Ultrastable Silver Nanoparticles. *Nature* **2013**, *501*, 399–402.
- (63) Yang, H.; Wang, Y.; Huang, H.; Gell, L.; Lehtovaara, L.; Malola, S.; Häkkinen, H.; Zheng, N. All-Thiol-Stabilized Ag₄₄ and Au₁₂Ag₃₂ Nanoparticles with Single-Crystal Structures. *Nat. Commun.* **2013**, *4*, 2422.
- (64) Yang, H.; Lei, J.; Wu, B.; Wang, Y.; Zhou, M.; Xia, A.; Zheng, L.; Zheng, N. Crystal Structure of a Luminescent Thiolated Ag Nanocluster with an Octahedral Ag₆⁴⁺ Core. *Chem. Commun.* **2013**, *49*, 300–302.
- (65) Yang, H.; Wang, Y.; Edwards, A. J.; Yan, J.; Zheng, N. High-Yield Synthesis and Crystal Structure of a Green Au₃₀ Cluster Capped by Thiolate and Sulfide. *Chem. Commun.* **2014**, *50*, 14325–14327.
- (66) Wang, Y.; Su, H.; Xu, C.; Li, G.; Gell, L.; Lin, S.; Tang, Z.; Häkkinen, H.; Zheng, N. An Intermetallic Au₂₄Ag₂₀ Superatom Nanocluster Stabilized by Labile Ligands. *J. Am. Chem. Soc.* **2015**, *137*, 4324–4327.
- (67) Ni, T. W.; Tofanelli, M. A.; Phillips, B. D.; Ackerson, C. J. Structural Basis for Ligand Exchange on Au₂₅(SR)₁₈. *Inorg. Chem.* **2014**, *53*, 6500–6502.

- (68) Heinecke, C. L.; Ni, T. W.; Malola, S.; Mäkinen, V.; Wong, O. A.; Häkkinen, H.; Ackerson, C. J. Structural and Theoretical Basis for Ligand Exchange on Thiolate Monolayer Protected Gold Nanoclusters. *J. Am. Chem. Soc.* **2012**, *134*, 13316–13322.
- (69) Jin, S.; Wang, S.; Song, Y.; Zhou, M.; Zhong, J.; Zhang, J.; Xia, A.; Pei, Y.; Chen, M.; Li, P.; et al. Crystal Structure and Optical Properties of the $[\text{Ag}_{62}\text{S}_{12}(\text{SBut})_{32}]^{2+}$ Nanocluster with a Complete Face-Centered Cubic Kernel. *J. Am. Chem. Soc.* **2014**, *136*, 15559–15565.
- (70) Song, Y.; Wang, S.; Zhang, J.; Kang, X.; Chen, S.; Li, P.; Sheng, H.; Zhu, M. Crystal Structure of Selenolate-Protected $\text{Au}_{24}(\text{SeR})_{20}$ Nanocluster. *J. Am. Chem. Soc.* **2014**, *136*, 2963–2965.
- (71) Dainese, T.; Antonello, S.; Gascón, J. A.; Pan, F.; Perera, N. V.; Ruzzi, M.; Venzo, A.; Zoleo, A.; Rissanen, K.; Maran, F. $\text{Au}_{25}(\text{SEt})_{18}$, a Nearly Naked Thiolate-Protected Au_{25} Cluster: Structural Analysis by Single Crystal X-ray Crystallography and Electron Nuclear Double Resonance. *ACS Nano* **2014**, *8*, 3904–3912.
- (72) Wan, X.-K.; Yuan, S.-F.; Lin, Z.-W.; Wang, Q.-M. A Chiral Gold Nanocluster Au_{20} Protected by Tetradentate Phosphine Ligands. *Angew. Chem., Int. Ed.* **2014**, *53*, 2923–2926.
- (73) Wan, X.-K.; Tang, Q.; Yuan, S.-F.; Jiang, D.-E.; Wang, Q.-M. Au_{19} Nanocluster Featuring a V-Shaped Alkynyl-Gold Motif. *J. Am. Chem. Soc.* **2015**, *137*, 652–655.
- (74) Guttrath, B. S.; Oppel, I. M.; Presly, O.; Beljakov, I.; Meded, V.; Wenzel, W.; Simon, U. $[\text{Au}_{14}(\text{PPh}_3)_8(\text{NO}_3)_4]$: An Example of a New Class of $\text{Au}(\text{NO}_3)$ -Ligated Superatom Complexes. *Angew. Chem., Int. Ed.* **2013**, *52*, 3529–3532.
- (75) Chen, J.; Zhang, Q.-F.; Bonaccorso, T. A.; Williard, P. G.; Wang, L.-S. Controlling Gold Nanoclusters by Diphosphine Ligands. *J. Am. Chem. Soc.* **2014**, *136*, 92–95.
- (76) AbdulHalim, L. G.; Bootharaju, M. S.; Tang, Q.; Del Gobbo, S.; AbdulHalim, R. G.; Eddaoudi, M.; Jiang, D.-E.; Bakr, O. M. $\text{Ag}_{29}(\text{BDT})_{12}(\text{TPP})_4$: A Tetravalent Nanocluster. *J. Am. Chem. Soc.* **2015**, *137*, 11970–11975.
- (77) Dhayal, R. S.; Liao, J.-H.; Liu, Y.-C.; Chiang, M.-H.; Kahlal, S.; Saillard, J.-Y.; Liu, C. W. $[\text{Ag}_{21}\{\text{S}_2\text{P}(\text{OiPr})_2\}_{12}]^+$: An Eight-Electron Superatom. *Angew. Chem., Int. Ed.* **2015**, *54*, 3702–3706.
- (78) Kauffman, D. R.; Alfonso, D.; Matranga, C.; Qian, H.; Jin, R. A Quantum Alloy: The Ligand-Protected $\text{Au}_{25-x}\text{Ag}_x(\text{SR})_{18}$. *J. Phys. Chem. C* **2013**, *117*, 7914–7923.
- (79) Yamazoe, S.; Kurashige, W.; Nobusada, K.; Negishi, Y.; Tsukuda, T. Preferential Location of Coinage Metal Dopants (M = Ag or Cu) in $[\text{Au}_{25-x}\text{M}_x(\text{SC}_2\text{H}_4\text{Ph})_{18}]^-$ ($x \sim 1$) As Determined by Extended X-ray Absorption Fine Structure and Density Functional Theory Calculations. *J. Phys. Chem. C* **2014**, *118*, 25284–25290.
- (80) Niihori, Y.; Matsuzaki, M.; Pradeep, T.; Negishi, Y. Separation of Precise Compositions of Noble Metal Clusters Protected with Mixed Ligands. *J. Am. Chem. Soc.* **2013**, *135*, 4946–4949.
- (81) Shibu, E. S.; Muhammed, M. A. H.; Tsukuda, T.; Pradeep, T. Ligand Exchange of $\text{Au}_{25}\text{SG}_{18}$ Leading to Functionalized Gold Clusters: Spectroscopy, Kinetics, and Luminescence. *J. Phys. Chem. C* **2008**, *112*, 12168–12176.
- (82) Beqa, L.; Deschamps, D.; Perrio, S. P.; Gaumont, A.-C.; Knoppe, S.; Bürgi, T. Ligand Exchange Reaction on $\text{Au}_{38}(\text{SR})_{24}$ Separation of $\text{Au}_{38}(\text{SR})_{23}(\text{SR}')_1$ Regioisomers, and Migration of Thiolates. *J. Phys. Chem. C* **2013**, *117*, 21619–21625.
- (83) Molina, B.; Sanchez-Castillo, A.; Knoppe, S.; Garzon, I. L.; Bürgi, T.; Tlahuice-Flores, A. Structures and Chiroptical Properties Of the BINAS-Mono Substituted $\text{Au}_{38}(\text{SCH}_3)_{24}$ Cluster. *Nanoscale* **2013**, *5*, 10956–10962.
- (84) Sharma, S.; Kurashige, W.; Nobusada, K.; Negishi, Y. Effect of Trimetalization in Thiolate-Protected $\text{Au}_{24-n}\text{Cu}_n\text{Pd}$ clusters. *Nanoscale* **2015**, *7*, 10606–10612.
- (85) Sardar, R.; Funston, A. M.; Mulvaney, P.; Murray, R. W. Gold Nanoparticles: Past, Present, and Future. *Langmuir* **2009**, *25*, 13840–13851.
- (86) Eustis, S.; El-Sayed, M. A. Why Gold Nanoparticles Are More Precious Than Pretty Gold: Noble Metal Surface Plasmon Resonance and Its Enhancement of the Radiative and Nonradiative Properties of Nanocrystals of Different Shapes. *Chem. Soc. Rev.* **2006**, *35*, 209–217.
- (87) Godly, E. W.; Taylor, R. Nomenclature and Terminology of Fullerenes: A Preliminary Survey. *Pure Appl. Chem.* **1997**, *69*, 1411–1434.
- (88) Mednikov, E. G.; Jewell, M. C.; Dahl, L. F. Nanosized (μ_{12} -Pt) $\text{Pd}_{164-x}\text{Pt}_x(\text{CO})_{72}(\text{PPh}_3)_{20}$ ($x \approx 7$) Containing Pt-Centered Four-Shell 165-Atom Pd–Pt Core with Unprecedented Intershell Bridging Carbonyl Ligands: Comparative Analysis of Icosahedral Shell-Growth Patterns with Geometrically Related $\text{Pd}_{145}(\text{CO})_x(\text{PEt}_3)_{30}$ ($x \approx 60$) Containing Capped Three-Shell Pd_{145} Core. *J. Am. Chem. Soc.* **2007**, *129*, 11619–11630.
- (89) Schnöckel, H. Structures and Properties of Metalloid Al and Ga Clusters Open Our Eyes to the Diversity and Complexity of Fundamental Chemical and Physical Processes during Formation and Dissolution of Metals. *Chem. Rev.* **2010**, *110*, 4125–4163.
- (90) Häkkinen, H.; Walter, M.; Grönbeck, H. Divide and Protect: Capping Gold Nanoclusters with Molecular Gold-Thiolate Rings. *J. Phys. Chem. B* **2006**, *110*, 9927–9931.
- (91) Tlahuice-Flores, A.; Jose-Yacamán, M.; Whetten, R. L. On the Structure of the Thiolated Au_{15} Cluster. *Phys. Chem. Chem. Phys.* **2013**, *15*, 19557–19560.
- (92) Jiang, D.-E.; Whetten, R. L.; Luo, W.; Dai, S. The Smallest Thiolated Gold Superatom Complexes. *J. Phys. Chem. C* **2009**, *113*, 17291–17295.
- (93) Zeng, C.; Li, T.; Das, A.; Rosi, N. L.; Jin, R. Chiral Structure of Thiolate-Protected 28-Gold Atom Nanocluster Predicted by X-Ray Crystallography. *J. Am. Chem. Soc.* **2013**, *135*, 10011–10013.
- (94) Das, A.; Li, T.; Nobusada, K.; Zeng, C.; Rosi, N. L.; Jin, R. Nonsuperatomic $[\text{Au}_{23}(\text{SC}_6\text{H}_{11})_{16}]^-$ Nanocluster Featuring Bipyramidal Au_{15} Kernel and Trimeric $\text{Au}_3(\text{SR})_4$ Motif. *J. Am. Chem. Soc.* **2013**, *135*, 18264–18267.
- (95) Hanwell, M. D.; Curtis, D. E.; Lonie, D. C.; Vandermeersch, T.; Zurek, E.; Hutchison, G. R. Avogadro: An Advanced Semantic Chemical Editor, Visualization, and Analysis Platform. *J. Cheminf.* **2012**, *4*, 17.
- (96) Humphrey, W.; Dalke, A.; Schulten, K. J. VMD: Visual Molecular Dynamics. *J. Mol. Graphics* **1996**, *14*, 33–38.
- (97) Tlahuice-Flores, A.; Black, D. M.; Bach, S. B. H.; Jose-Yacamán, M.; Whetten, R. L. Structure & Bonding of the Gold-Subhalide Cluster $\text{I-Au}_{144}\text{Cl}_{60}[\text{Z}]$. *Phys. Chem. Chem. Phys.* **2013**, *15*, 19191–19195.
- (98) Tomalia, D. A. In Quest of a Systematic Framework for Unifying and Defining Nanoscience. *J. Nanopart. Res.* **2009**, *11*, 1251–1310.
- (99) Connelly, N. G.; Damhus, T.; Hartshorn, R. M.; Hutton, A. T. *Nomenclature of Inorganic Chemistry: IUPAC Recommendations*; RSC Publishing: Cambridge, 2005.
- (100) Mathew, A.; Natarajan, G.; Lehtovaara, L.; Häkkinen, H.; Kumar, R. M.; Subramanian, V.; Jaleel, A.; Pradeep, T. Supramolecular Functionalization and Concomitant Enhancement in Properties of Au_{25} Clusters. *ACS Nano* **2014**, *8*, 139–152.
- (101) Muhammed, M. A. H.; Shaw, A. K.; Pal, S. K.; Pradeep, T. Quantum Clusters of Gold Exhibiting FRET. *J. Phys. Chem. C* **2008**, *112*, 14324–14330.
- (102) Zeng, C.; Liu, C.; Pei, Y.; Jin, R. Thiol Ligand-Induced Transformation of $\text{Au}_{38}(\text{SC}_2\text{H}_4\text{Ph})_{24}$ to $\text{Au}_{36}(\text{SPh-t-Bu})_{24}$. *ACS Nano* **2013**, *7*, 6138–6145.
- (103) Knoppe, S. On the Stereochemistry of Atomically Defined Gold Clusters: Synthesis, Size-Selection and Stereochemical Characterization of Thiolate-Protected Gold Clusters. Ph.D. Thesis, Université de Genève, 2012.
- (104) Knoppe, S.; Boudon, J.; Dolamic, I.; Dass, A.; Bürgi, T. Size Exclusion Chromatography for Semipreparative Scale Separation of $\text{Au}_{38}(\text{SR})_{24}$ and $\text{Au}_{40}(\text{SR})_{24}$ and Larger Clusters. *Anal. Chem.* **2011**, *83*, 5056–5061.
- (105) Mednikov, E. G.; Dahl, L. F. Crystallographically Proven Nanometer-Sized Gold Thiolate Cluster $\text{Au}_{102}(\text{SR})_{44}$: Its Unexpected Molecular Anatomy and Resulting Stereochemical and Bonding Consequences. *Small* **2008**, *4*, 534–537.

(106) Jung, J.; Kang, S.; Han, Y.-K. Ligand Effects on the Stability of Thiol-Stabilized Gold Nanoclusters: $\text{Au}_{25}(\text{SR})_{18}^-$, $\text{Au}_{38}(\text{SR})_{24}$, and $\text{Au}_{102}(\text{SR})_{44}$. *Nanoscale* **2012**, *4*, 4206–4210.

(107) Wiseman, M. R.; Marsh, P. A.; Bishop, P. T.; Brisdon, B. J.; Mahon, M. F. Homoleptic Gold Thiolate Catenanes. *J. Am. Chem. Soc.* **2000**, *122*, 12598–12599.

(108) Zeng, C.; Liu, C.; Chen, Y.; Rosi, N. L.; Jin, R. Gold-Thiolate Ring as a Protecting Motif in the $\text{Au}_{20}(\text{SR})_{16}$ Nanocluster and Implications. *J. Am. Chem. Soc.* **2014**, *136*, 11922–11925.

(109) Das, A.; Liu, C.; Byun, H. Y.; Nobusada, K.; Zhao, S.; Rosi, N.; Jin, R. Structure Determination of $[\text{Au}_{18}(\text{SR})_{14}]$. *Angew. Chem., Int. Ed.* **2015**, *54*, 3140–3144.

(110) Zeng, C.; Chen, Y.; Li, G.; Jin, R. Synthesis of a $\text{Au}_{44}(\text{SR})_{28}$ Nanocluster: Structure Prediction and Evolution from $\text{Au}_{28}(\text{SR})_{20}$, $\text{Au}_{36}(\text{SR})_{24}$ to $\text{Au}_{44}(\text{SR})_{28}$. *Chem. Commun.* **2014**, *50*, 55–57.

(111) Lopez-Acevedo, O.; Akola, J.; Whetten, R. L.; Grönbeck, H.; Häkkinen, H. Structure and Bonding in the Ubiquitous Icosahedral Metallic Gold Cluster $\text{Au}_{144}(\text{SR})_{60}$. *J. Phys. Chem. C* **2009**, *113*, 5035–5038.

(112) Bahena, D.; Bhattarai, N.; Santiago, U.; Tlahuice, A.; Ponce, A.; Bach, S. B. H.; Yoon, B.; Whetten, R. L.; Landman, U.; Jose-Yacamán, M. STEM Electron Diffraction and High-Resolution Images Used in the Determination of the Crystal Structure of the $\text{Au}_{144}(\text{SR})_{60}$ Cluster. *J. Phys. Chem. Lett.* **2013**, *4*, 975–981.

Supporting Information (SI) for the Paper:

A Unified Framework for Understanding the Structure and Modifications of Atomically Precise Monolayer Protected Gold Clusters

Ganapati Natarajan[†], Ammu Mathew[†], Yuichi Negishi[‡], Robert L. Whetten[§], and Thalappil Pradeep^{*,†}

[†]DST Unit of Nanoscience (DST UNS), Department of Chemistry, Indian Institute of Technology Madras, Chennai, 600036, India.

[‡]Department of Applied Chemistry, Tokyo University of Science, 1-3 Kagurazaka, Shinjuku, Tokyo 162-8601, Japan.

[§]Department of Physics and Astronomy, University of Texas at San Antonio, San Antonio, Texas 78249, United States.

*E-mail: pradeep@iitm.ac.in

Table of Contents

Number	Description	Page no.
1	Symmetries and standard orientation of Au ₂₅ (SR) ₁₈	2
2	Structural representations of Au ₂₅ (SR) ₁₈	4
3	Tomographic diagram with a C ₃ principal axis for Au ₂₅ (SR) ₁₈	8
4	Drawing the Borromean Rings diagram of Au ₂₅ (SR) ₁₈	10
5	Structural nomenclature of aspicles	15
6	Terminologies for Au ₂₅ (SR) ₁₈ with substituent positions	19
7	Borromean-Rings diagram for Au ₂₅ (SR) ₁₈ with S-C bond directions	21
8	Borromean-Rings diagram for Au ₂₅ (SR) ₁₈ with hybrid directional locants	23
9	Tables of names for modifications and structural names for Au ₂₅ (SR) ₁₈ , Au ₃₈ (SR) ₂₄ and Au ₁₀₂ (SR) ₄₄	25
10	Table of crystal structures of Au _M (X) _N and their corresponding nomenclature names	32
11	Isomers of two-substituent isomers of ligand and metal-atom exchanged Au ₂₅ (SR) ₁₈	34
12	Isomers of two metal atom substituents in the icosahedral core of Au ₂₅ (SR) ₁₈	39
13	Staple to core-connectivity diagram, standard orientation and locant assignment for Au ₁₀₂ (SR) ₄₄	40

Supporting Information 1

Symmetries and Standard Orientation of $\text{Au}_{25}(\text{SR})_{18}$

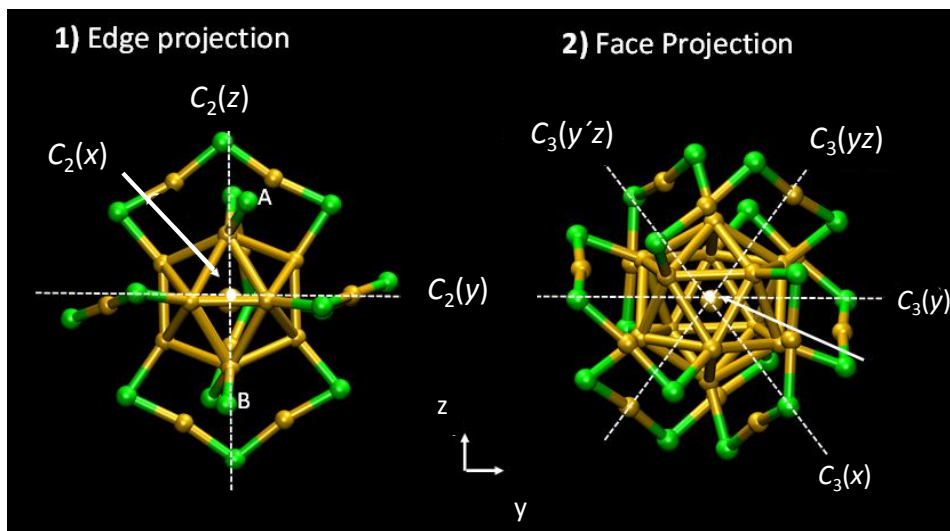


Figure S1: Views of $\text{Au}_{25}(\text{SR})_{18}$ aspicule along different axes of rotational symmetry: 1) C_2 and 2) C_3 axes. In 1) the edge projection of the Au_{12} core is shown with the portion of the front outward pointing staple between sulfur atoms marked A and B deliberately removed to expose the core structure. In 2) the Au_{12} core is seen in the face projection with a C_3 axis pointing outward in the z -direction from the front central triangular face, and the projection of the three other C_3 axes onto the x - y plane are shown and the direction of each of these projected lines of symmetry is indicated in brackets. Gold atoms are shown in gold and the sulfur atoms in green, and the size of the central gold atom has been increased slightly for clarity.

It is appropriate to begin with a review of the molecular symmetry of $\text{Au}_{25}(\text{SR})_{18}$ aspicule which is shown viewed along two different symmetry axes in **Figure S1**.¹ The core icosahedron has 12 vertices (atoms), 20 triangular faces and 30 edges (bonds) and it belongs to the I_h point group. The six dimer staples are arranged in an octahedral manner around the core, so that the central sulfur atom of the staple lies along the directions of the C_2 axes. $\text{Au}_{25}(\text{SR})_{18}$ being a composite entity, consisting of an icosahedral core and an octahedral arrangement of surrounding staples, will have a total symmetry that is reduced from I_h to the octahedral point subgroup of distorted O_h (dO_h).² The dO_h point group lacks C_4 elements, due to the positions of exterior Au atoms in the staples breaking the full octahedral symmetry. There are two types of rotational symmetry axes in $\text{Au}_{25}(\text{SR})_{18}$. Firstly, the four C_3 axes passing through the centre of the icosahedron and through four pairs of opposite triangular faces, one view of which is shown in **Figure S1(2)**. Secondly, the three perpendicular C_2 axes (marked on Figure S1(1) using white dotted lines) which intersect the midpoint of bonds of the icosahedron which lie in the three perpendicular planes that pass through the six pairs of bridging sulfurs which belong to coplanar staples. The

C_2 axes naturally permit a Cartesian axis system to be superimposed on them. Our first objective was to create a labeled diagram of $\text{Au}_{25}(\text{SR})_{18}$ in a standard orientation, as there are visualizations from many different angles in the literature and with the individual Cartesian axes assigned differently with respect to the C_2 axes.

In Figure S1, two views of $\text{Au}_{25}(\text{SR})_{18}$ are shown depending on whether it is viewed along a C_2 or a C_3 axis. We therefore made two conventions: one for the orientation of Cartesian axis and, secondly, for the direction of each of the Cartesian axes with respect to the C_2 axes of $\text{Au}_{25}(\text{SR})_{18}$. We setup Cartesian axes to be fixed in the plane of the paper, as shown in Figure S1, with the y -axis towards the right, the z -axis upwards, and the x -axis coming out of the paper. Secondly, the left hand view, which we term the edge projection, is taken by us to be the standard view used for nomenclature diagrams, unless stated otherwise. The reason for this is that the octahedral arrangement of staples is seen most clearly, while in the face projected view, the staples twist around the core structure.

We defined the standard view of $\text{Au}_{25}(\text{SR})_{18}$ as seen towards the negative z -direction with the rings in each Cartesian plane appearing exactly as shown in Figure S1(1). Viewing the structure along the different Cartesian axes directions will result in a different view of these rings (staples), even though the core always appears in the edge projection.

Supporting Information 2

Structural Representations of Au₂₅(SR)₁₈

A. Polyhedral Shells

The first approach we tried was based on what we term the polyhedral representation of aspicules. The core and mantle regions of several aspicules such as Au₂₅(SR)₁₈ and Au₁₀₂(p-MBA)₄₄³ have been found to consist of a set of polyhedra, one inside the other, and so this appears to be a generic structural characteristic. The polyhedra may be viewed as a generalization of polyhedra for coordination compounds as their sides do not always represent bonds between the atoms, except in the case of the Au₁₂ core, but rather indicate their relative positions in space and symmetries. Polyhedral shells may be defined either by analysis of the bonding network or by classifying atoms according to their element and positional type as shown in the inset of Figure S2(a). The four types of atoms in Au₂₅(SR)₁₈ are: core Au atoms (Au_c), exterior metal atoms in the staples (Au_e), bridging sulfurs (S_μ) which bridge exterior metal atoms and are located at the central position of the staple and lastly the non-bridging sulfur (S_c) atoms which join gold atoms in the core to the exterior gold atoms.

The crystal structure available in the literature for Au₂₅(SR)₁₈ was used.¹ We made extensive use of the molecular building and visualization software Avogadro³ and VMD⁴ for structural manipulation and visualization. We analysed the structure of Au₂₅(PET)₁₈ obtained from its crystal structure by extracting the molecules from the crystalline unit cell, and isolating the gold and sulfur atoms from the model by removing the atoms of the PET ligands, which we refer to as the core and mantle structure. The Au₂₅(SR)₁₈ aspicule is oriented in the edge-projected, octahedral staple configuration shown in Figure S1(1).

For the visualization as concentric shells of polyhedra, the bond radii were chosen such that only the nearest neighbours in each category of atoms would be joined together by a bond. The bond radii between each type of atom in VMD were chosen as 3.2 Å for Au-Au core bonds, 5.5 Å for exterior Au atoms and 5.5 Å for the non-bridging sulfurs and 8.8 Å for the bridging sulfurs. Bonds between the atoms in each category are drawn when the distance between them is less than the bond radii mentioned above. The four polyhedra are shown superimposed on each other in Figure S2(a). Figure S2(a) shows the inner Au icosahedron in gold, the bridging sulfur octahedron in yellow, and the exterior gold icosahedron in blue which protrude out from the green cuboctahedron of non-bridging sulfurs. Figure S2(b) shows only the sulfur polyhedra with the inner sulfur octahedron capping the six square faces of the cuboctahedron. We note that this arrangement of sulfur atoms has already been visualized in the context of ligand exchange.² Thus, by labeling each of the sulfur atoms of the octahedron and the cuboctahedron, we would have a notation for ligand positions.

Generally the positional labels of atoms in a molecule, known as locants, are denoted by numbers or letters in IUPAC nomenclature. Here, we use the Cartesian axis directions, which may also be regarded as Cartesian quadrant bounding directions, to uniquely describe the positions of the atoms in the core and mantle regions⁶. The bridging sulfurs are located at vertices of the yellow octahedron and are labeled by one of the six perpendicular Cartesian

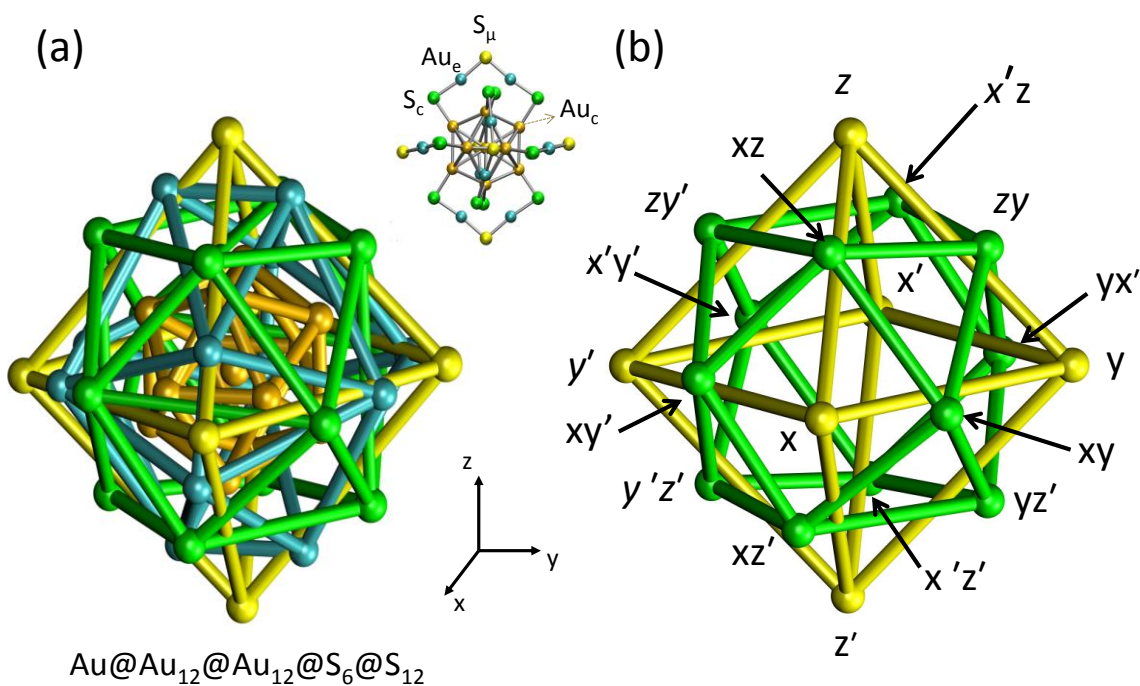


Figure S2. Concentric polyhedral representation of the core and staple atoms of $\text{Au}_{25}(\text{SR})_{18}$ aspicule. Polyhedra formed by connecting atoms of the same category to their nearest neighbors of the same category for (a) both gold and sulfur atoms, and (b) sulfur atoms only with Cartesian atom labels, according to the Cartesian axes shown. The atoms and the lines joining them are colored according to their category as shown in the inset to (a) gold and cyan for the core and exterior gold atoms, while yellow and green represent bridging and non-bridging sulfurs. A shell structure terminology for $\text{Au}_{25}(\text{SR})_{18}$ is given below (a).

directions. Shell directions x, y, z, x', y', z' where the primes indicate the negative direction. The primes on the Cartesian axis directions, eg. x' , represents the negative direction of the x -axis. The non-bridging sulfur atoms are associated with the vertices of the cuboctahedron, or equivalently, a pair of the vertices of the octahedron at either end of the edge. Hence they may be labeled by the associated pairs of Cartesian axes. Figure S3, shows the ball and stick visualization of $\text{Au}_{25}(\text{SR})_{18}$ with Cartesian locant labels. Using the ordering of these twelve Cartesian pairs for the non-bridging sulfurs allows us to preserve this information, by placing the direction for the staple on which the core-bonded sulfur resides first. A simple rule is shown at the top left of Figure S3, which is that the pairs are taken anticlockwise when $x, y,$ and z are arranged in a circle. For example, the nonbridging sulfur at the xz position cannot be referred to as zx because the staple this sulfur is located points in the x direction and not in the z direction. The twelve unique ordered pairs specifying the Cartesian quadrants are $xz, xz', x'z, x'z', yx, yx', y'x, y'x'$ and $zy, zy', z'y$ and $z'y'$. It should be noted that the ordering of these pairs are specific to our conventions and about the relative orientation of the Cartesian axes and the $\text{Au}_{25}(\text{SR})_{18}$ aspicule as described in SI 2.

We can also uniquely identify the core gold and exterior gold atoms using the same twelve Cartesian quadrant specifiers as the non-bridging sulfurs since each pair of these gold atoms are the nearest neighbors of the non-bridging sulfurs. Hence, by adding a ‘*c*’ or an ‘*e*’ to before the direction pair we can indicate the directions of the gold atoms too eg. *c-xy* or *e-xy* indicate the core and exterior gold atoms which are bonded to the non-bridging sulfur located in the *xy*-direction. The interstitial gold atom is identified by the italicized ‘*i*’. Some terminologies for ligand and alloy exchanged $\text{Au}_{25}(\text{SR})_{18}$ are given in Table S2.

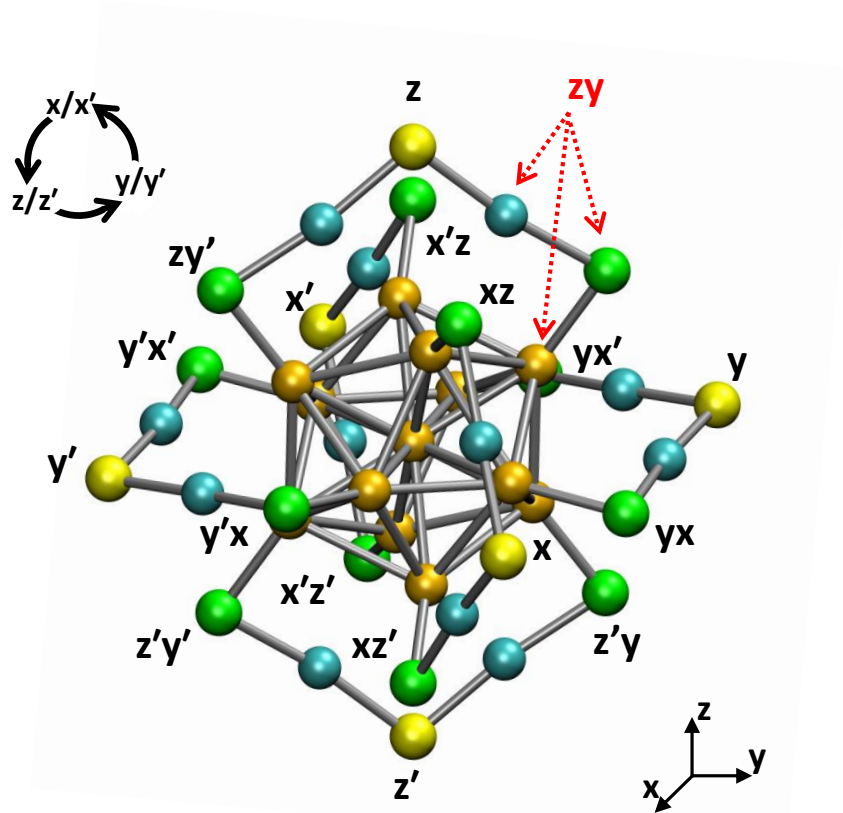


Figure S3. $\text{Au}_{25}(\text{SR})_{18}$ aspicule with Cartesian locant labels for atoms. The core and staple atoms are colored as shown in the inset of Figure S2(a). The same locants are used for core atoms, non-bridging sulfur atoms, and exterior gold atoms which lie in the same Cartesian octant. The red arrows indicate the use of the same *zy* locant for the green non-bridging sulfur atom which applies to it and its two nearest neighbor atoms consisting of a gold core atom and a light blue exterior gold atom.

B. Molecular graph of $\text{Au}_{25}(\text{SR})_{18}$ aspicule

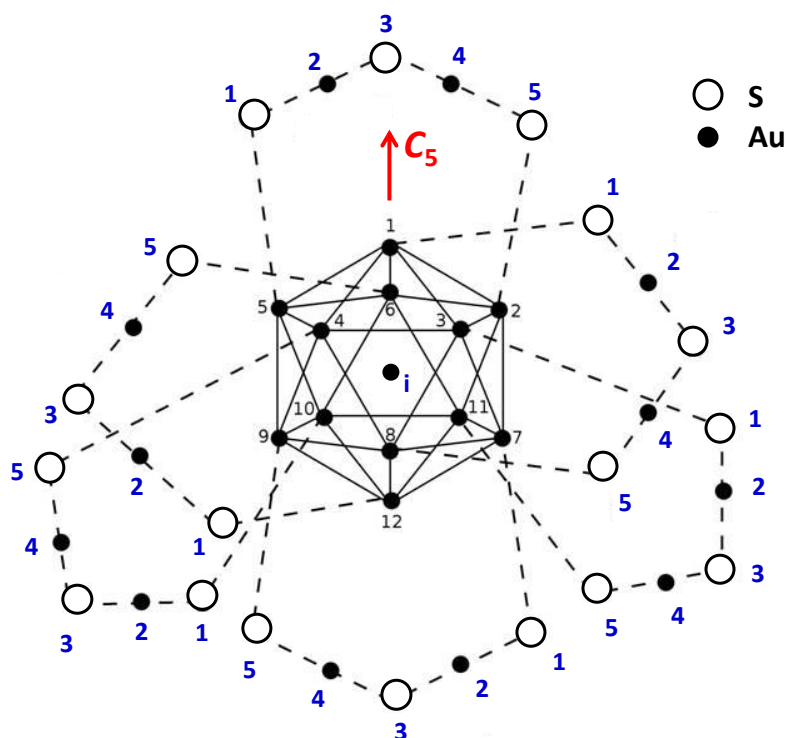


Figure S4. The molecular graph of $\text{Au}_{25}(\text{SR})_{18}$ aspicule. Small black circles show sulfur atoms while large open circles represent sulfur atoms. Au-S bonds are shown by the dashed lines, while Au-Au bonds are shown by the solid lines. The locants of each atom are shown alongside in blue.

The visualizations of $\text{Au}_{25}(\text{SR})_{18}$ in Figures S1, S2 and S3 being in three dimensions are less convenient for developing nomenclature which is generally based on diagrams involving lines and element symbols to represent the bonds and the atoms of the 3D structure on the 2D plane. The molecular graph of $\text{Au}_{25}(\text{SR})_{18}$, shown in Figure S4, is just such a 2D representation showing all Au/S atoms as dots/circles and the bonds as lines joining them. The icosahedron is shown in face projection and the bonds from the aurophilic interactions between the core and exterior Au atoms and those between the interstitial Au atom and the other core atoms have been omitted. The highest symmetry C_5 axis of the icosahedral core is oriented vertically the atoms are numbered on planes perpendicular to this axis, as shown in Figure S4. Numbering of the atoms within a plane is done in a clockwise fashion with the lowest number being to the far right of the C_5 axis. The staple atoms are numbered from 1 to 5, starting at the leftmost atom of the staple and counting clockwise around it. Each staple may be identified by the start and end atoms of the core atoms to which it is bonded. Nevertheless, this diagram is quite difficult to remember and draw by hand due to the use of the face projection so we searched for a simpler representation based on the edge-projected structure of $\text{Au}_{25}(\text{SR})_{18}$ based on its three ring structure.

Supporting Information 3

$\text{Au}_{25}(\text{SR})_{18}$ Tomographic Diagram with a C_3 Principal Axis

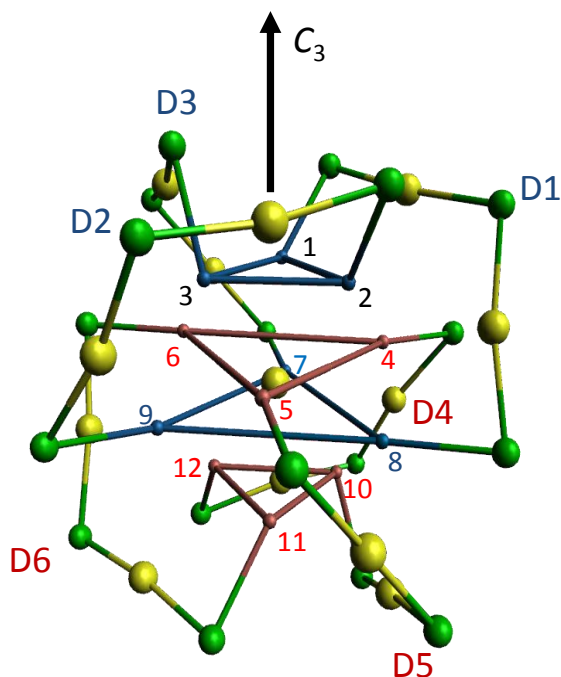


Figure S5. $\text{Au}_{25}(\text{SR})_{18}$ aspicle with locants with the C_3 axis as the principal axis. Only the core and staple structure is shown with the ligands. The connectivity of core atoms in the same plane are indicated by bonds, Both the bonds and core atoms which are shown as small spheres, are colored blue in the case that the core atoms are bonded to the upper group of three dimers staples (D1-D3) and red in the case that they are bonded to the lower group of three dimer staples (D4-D6). The interstitial Au atom as larger yellow sphere, staple Au atoms are shown in yellow and the sulfur atoms in green. The locants of the core atoms are colored by the same scheme as the triangle they lie on. The six dimer staples, D1 to D6, are labeled in red. Staple atom numbers are not shown, but may added according to the rules given in the Manuscript.

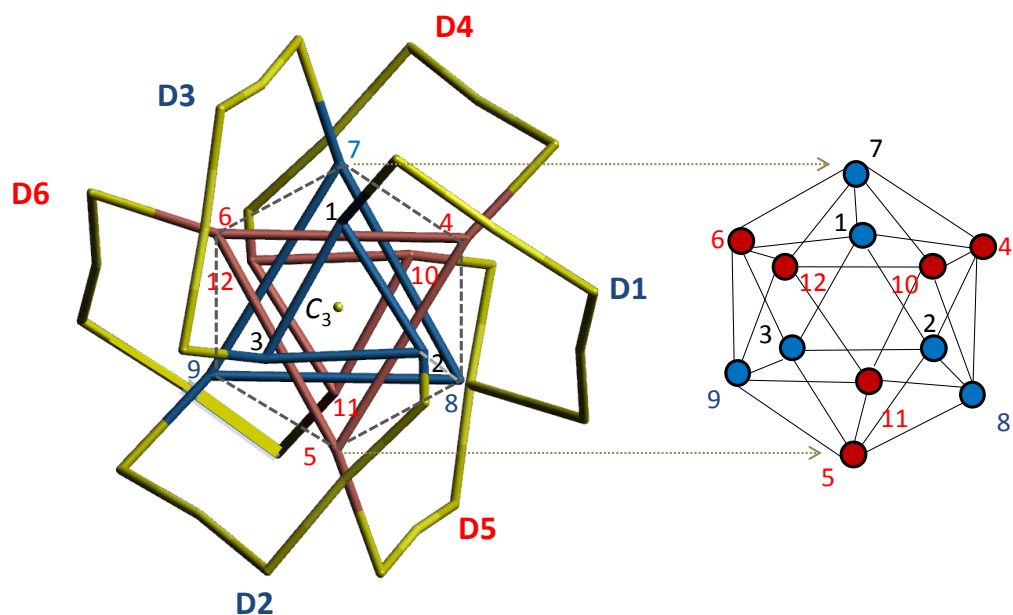


Figure S6. A “Star of David” projection of $\text{Au}_{25}(\text{SR})_{18}$ aspicule in planes perpendicular to the C_3 axis coming out of the plane of the paper with the twelve core atoms of the icosahedron sectioned into four parallel triangles each containing three atoms. The triangles are colored alternately blue and red, with the smaller blue and red triangles being at the front and back, respectively and the larger triangles in the middle. The stick bond representation has been used and the staples are shown in yellow and gold for the sulfur and gold stick bonds respectively. Right: A schematic of the core icosahedron in face-projection with the Au-Au bonds shown as lines and atoms represented by filled circles colored according to the color of the triangle they lie in.

Supporting Information 4

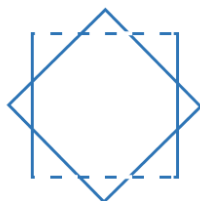
Drawing the Borromean-Rings Diagram of $\text{Au}_{25}(\text{SR})_{18}$

Scheme S1: Visual instructions are shown below for drawing the Borromean-Rings diagram of $\text{Au}_{25}(\text{SR})_{18}$ in nine steps.

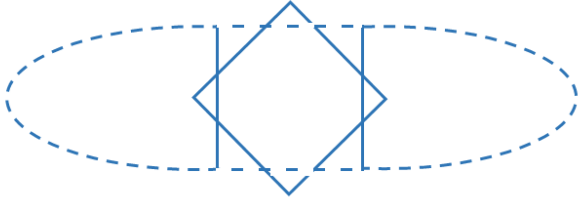
- 1. Draw a square with its horizontal edges as dashed lines and its vertical edges as solid lines**



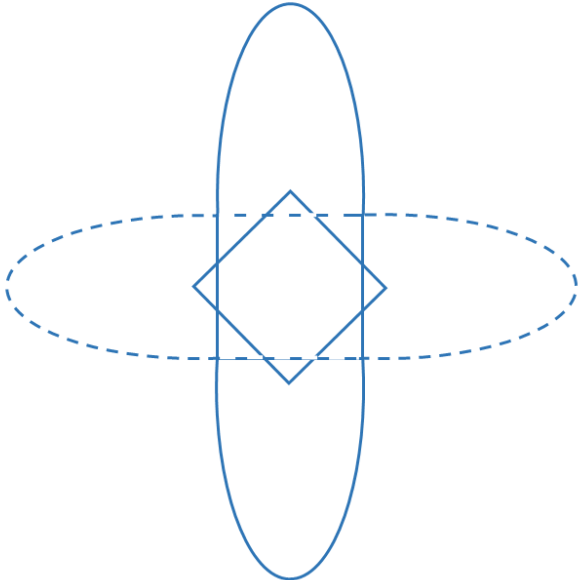
- 2. Draw a second square over the first rotated by 45 degrees**



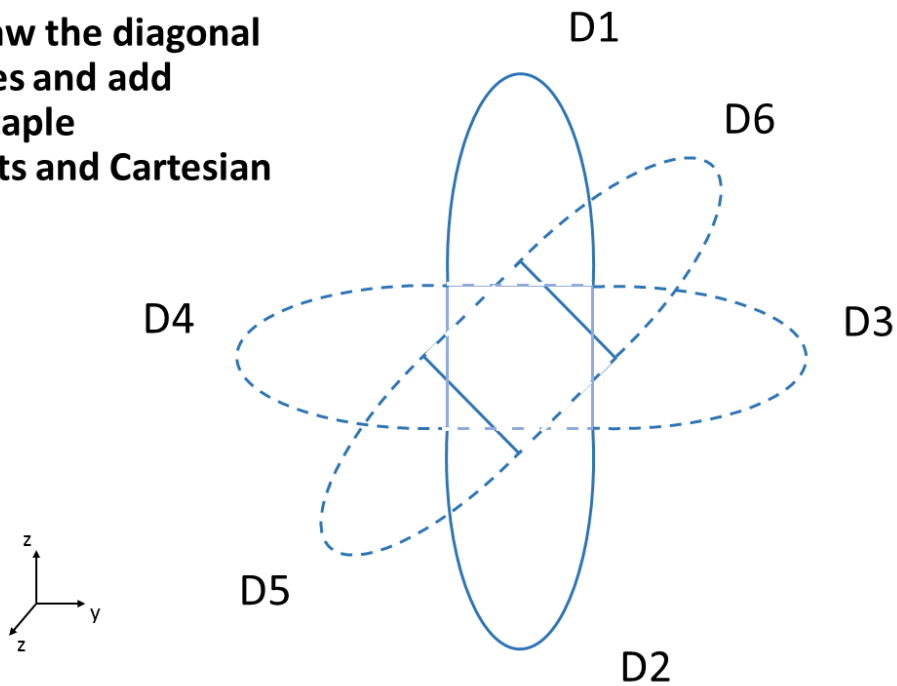
3. Draw the horizontal staples using dashed lines



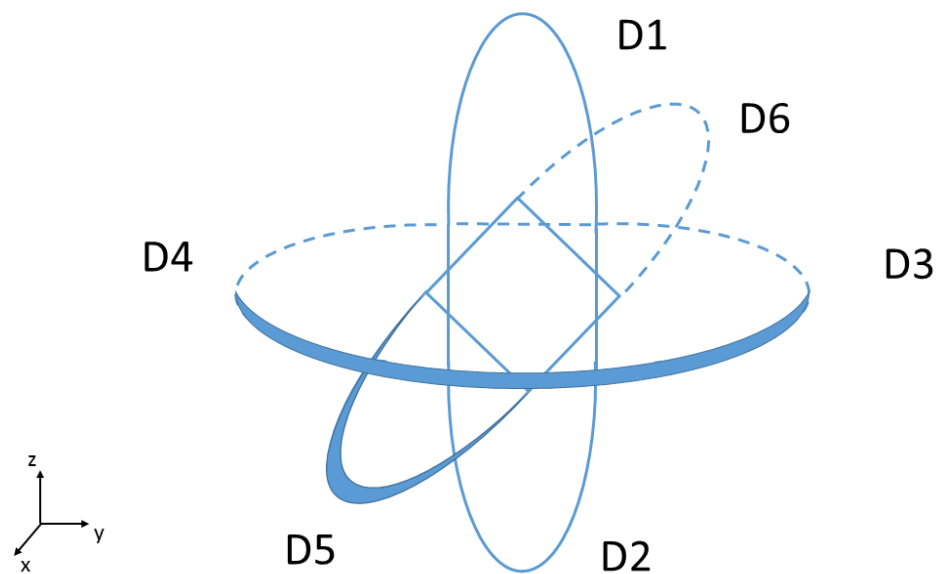
4. Draw the vertical staples using solid lines



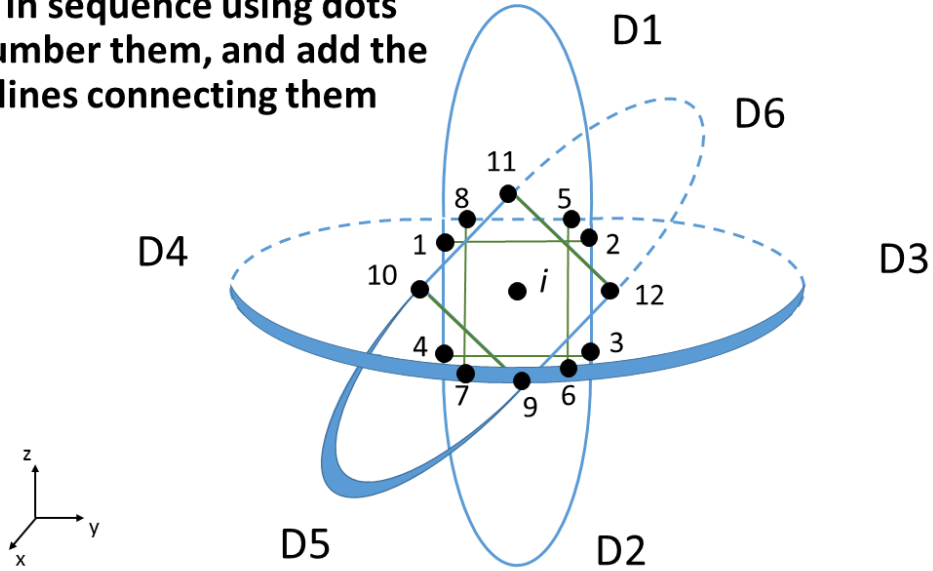
5. Draw the diagonal staples and add the staple locants and Cartesian axes



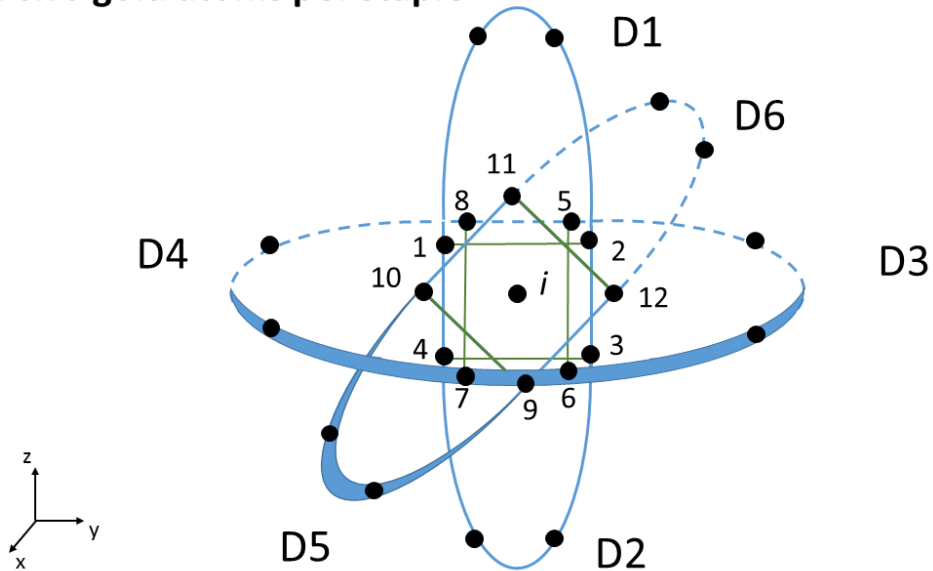
6. Add thick tapering lines as shown to get the 3D-effect



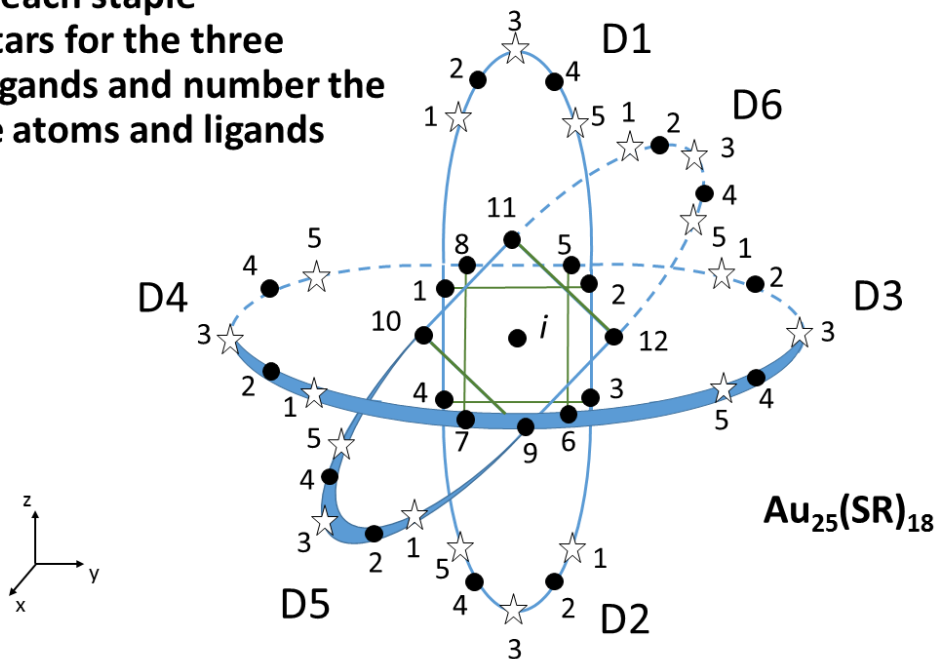
7. Mark the central core gold atoms in sequence using dots and number them, and add the green lines connecting them



8. Add two gold atoms per staple



9. On each staple
add stars for the three
(SR) ligands and number the
staple atoms and ligands



Supporting Information 5

Structural Nomenclature of Aspicules

This section can be appreciated better after going through Figure 1 of the Manuscript. In this section we present names, which can describe the structure of the parent aspicule in detail and also the type and nature of substituents, either metal atoms or ligands. We assume the locant assignment scheme for $\text{Au}_{25}(\text{SR})_{18}$ aspicule shown in Figure 1 in the Manuscript and provide examples for modifications in this structural nomenclature in Table S7.

The general structure of the name would be:

Staple-core locants-(Ligand-Staple name)-(Core name) (Suffix)

where the brackets have been used for clarity but are not included in the actual name.

A name which describes the full structure of $\text{Au}_{25}(\text{SMe})_{18}$, would then be:

D1(1,2):D2(3,4):D3(5,6):D4(7,8):D5(9,10):D6(11,12)-hexa(1,3,5-methylthiolato-2,4-Au)-auro-25 aspicule(1-) (*i@I,3C₂*)

A slightly shorter name using the (SR) terminology for the ligand, as described in the Manuscript) would be:

D1(1,2):D2(3,4):D3(5,6):D4(7,8):D5(9,10):D6(11,12)-(1,3,5-SMe-2,4-Au)₆-auro-25 aspicule(1-) (*i@I,3C₂*)

The above structural name is interpreted as follows: This is an aspicule which has six dimer staples, with locants D1 to D6, and these six staples are attached to the core atoms with numbers 1 and 2, 3 and 4, 5 and 6 and so on. It has SMe ligands at the 1, 3 and 5 positions along each of the staples, counting from the left hand end of the staple. The whole structure has a total of 25 gold atoms and there is a single negative charge on the molecule. Lastly, the core polyhedron is an icosahedron with an additional central atom and the principal symmetry axes used for locant assignment are the three perpendicular C_2 axes (denoted by $3C_2$ which coincide with the Cartesian x, y, z axes oriented in the standard way).

A. Ligand and Staple name

The various parts of the structural name are now described in detail. We regard the staple and its ligands as a branched chain molecule, with the staple being the chain and the ligands the branches. The ligand and staple name is a combined name of the form (in its shorter version): (1,3,5-SMe-2,4-Au).

The name of the ligand (SMe) is prefixed by 1,3,5 followed by a hyphen which are the sulfur positions on the dimer staple, and this is followed by a hyphen and the positions of the Au atoms on the chain. We use square brackets to enclose the ligand name and staple name, and we place

the number of staple/ligand combinations of that kind in the subscript outside the brackets. Hence, when presented with the structure of a modified $\text{Au}_{25}(\text{SR})_{18}$ aspicule, we first identify the different combinations of staple metal atoms and their attached ligands eg. (3-PET,1,5-SMe-2-Pd,4-Au), and we use as many ligand and staple names as are needed to name each of the distinct combinations present. In the case of unmodified $\text{Au}_{25}(\text{SR})_{18}$, we have the same ligand and staple configuration repeated, and so we put its multiplicity in the subscript eg. (1,3,5-SMe-2,4-Au)₆.

Whenever there is more than one ligand-staple name they are separated by a comma. The ligand-staples name and their prefixed staple locants are placed in increasing order of prevalence. Each ligand-staple name is prefixed by the locants of all the staples that are described by it. The description of the staples consists of a staple locant and the staple-core locant described below.

B. Staple locants

1. The locants of the staples have two parts, a letter which corresponds to the type of staple and the number of the staple. The following letters are used: M for a monomer staple, D for a dimer staple and Tr for trimer, etc. Further details on the method of assignment of the staple locants are given in the Manuscript. Examples of staple locants are M1, D1, etc.

2. A consecutive sequence of staples the first and last staple separated by a hyphen, also all enclosed in square brackets eg. [D1-D6].

3. A staple-core locant consist of the pair of comma-separated numbers of the core atoms on which the staples begin and end (eg. 1,2) with each pair being enclosed in brackets and prefixed by the staple locant eg. D1(1,2) is an example of a staple-core locant which signifies that the dimer staple one is bonded to core atoms 1 and 2. Staple-core locants are separated by a colon with spaces either side of it, and there are no spaces after the commas. In $\text{Au}_{25}(\text{SR})_{18}$, from the locants of Manuscript Figure 1, we obtain the six staple-core locants as D1(1,2):D2(3,4):D3(5,6):D4(7,8):D5(9,10):D6(11,12).

We note that if the locants of the molecular graph of Figure S4 are used, a more difficult to remember sequence of staple-core locants results which is D1(1,8):D2(6,12):D3(7,9):D4(3,11):D5(4,10), hence we will employ those of Manuscript Figure 1 for reasons of simplicity.

5. We may also use a contracted staple locant sequence, if all the the locant numbers are in consecutive order by placing an ellipsis between the colons to indicate the missing locants in the sequence: D1(1,2); ... ;D6(11,12)-(1,3,5-SMe-2,4-Au)₆.

There are spaces after the commas when they surround an ellipsis.

C. Core Metal Name

(i) The core metal name contains the description of the metal atoms of the core and staples and their substituents. Metal names of the form auro, pallado and argento, which correspond to the elements Au, Pd and Ag, are assigned using IUPAC inorganic nomenclature. The presence of more than one type of metal element present is indicated by forming compound names, and the

additional metal element is treated as a substituent and hence carries a prefix to indicate the positions of substitution. The following rules are applied:

(i) The minority (substituent) metal element names being placed in front of the majority metal element names such as palladauro and argentoauro.

(ii) The number of metal atom substituents of a particular element is indicated by adding the Latin prefixes mono, di, tri, tetra, penta, hexa, hepta, octa, nona, deca, etc., to the substituent metal element name. Optionally, and if there are larger number of metal atom substituents, the number of them can be prefixed to the substituent name eg. (23)-palladauro-25.

(iii) The sets of locants for the positions of the minority metal atoms, separated by commas and in parentheses, are prefixed to their respective minority metal names. Eg. (1,2)-dipalladauro. For example, a case where there are two types of minority metal element, with Pd in positions 1 and 2 and Ag in positions 3 and 4, might be called (1,2)-dipallado-(3,4)-diargentoauro-25 aspicule(1-). A hyphen is used after the first metal minority atom name to separate it from the locant prefix of second (more numerous) metal element name.

(iv) The number of metal atoms which is characteristic of the structure; eg. auro-25, where a hyphen separates it from the metal name.

D. Suffix of the name

Following the core name we attach a suffix of the form: **aspicule(charge) (structural descriptor)**.

The word aspicule indicates the family of molecules in an analogous way to the suffix fullerene in fullerene nomenclature. The charge is written in brackets as the final suffix eg. (1-), (1+), or (0).

After the charge a space is left and a final suffix consisting of a structural descriptor of the form: **(core polyhedral descriptor, principal symmetry axis)**. The rules below govern the formation of the structural descriptor.

(i) The geometrical shape of each polyhedral cluster comprising the core is designated by a core polyhedral descriptor which is its first letter which is italicized and in capitals, eg. tetrahedro (*T*), octahedro (*O*), dodecahedro (*D*), icosahedro (*I*), or, by forming an acronym out of several of its letters by splitting the name into its distinctive parts eg. rhomboicosidodecahedron (*R-ID*) to form *RID*. If the polyhedron name consists of more than one word for example a Marks decahedron, we use the first letter of each word (*MD*).

(ii) If there is a core atom polyhedron inside the other, we may use, for example, the notation *I@D* for a central icosahedral (*I*) cage within a dodecahedral (*D*) cage.

(iii) If there is a single central atom within the polyhedral core it is designated by adding the symbol '*i*', which stands for interstitial, and if there is more than one central atom each of their

locants may be designated as i_1, i_2, i_3, i_4 , etc., and if these central atoms form a polyhedron we place this polyhedron's acronym first in the core polyhedral descriptor. For example, $\text{Au}_{38}(\text{SR})_{24}$ consists of an interstitial trigonal-bipyramidal (*TBP*) structure capped on its top and bottom by nine-atom caps designated as BIC_{18} , an 18-atom fragment of the bi-icosahedron (*BIC*) and the complete core structure of $\text{Au}_{38}(\text{SR})_{24}$ aspicule would be described as $\text{TBP}@\text{(BIC}_{18})$ which is an alternative way of viewing the structure to a bi-icosahedral core consisting of a face-fused pair of icosahedra. For $\text{Au}_{102}(\text{SR})_{44}$ we find a central pentagonal bipyramid (*PBP*) within a 42-atom Marks decahedral shell (MD_{42}) which may be written as $\text{PBP}@\text{MD}_{42}$, and this comprises the 49-atom Marks decahedron.

E. Stereodescriptor prefixes

A prefix to the front of the name indicating chiral and geometric isomerism may be added as described in the Manuscript, and S-C bond directions may also be included. (See SI 6).

F. Compact structural name

A more compact structural name can be obtained by omitting the connectivity information of the staples to the core atoms and substituting these by the labels of the staples and placing these as a prefix to the ligand-staple name they apply to.

Staple locants-(Ligand-Staple name)-(Core name) (Suffix)

A compact structural name for $\text{Au}_{25}(\text{SR})_{18}$ would be [D1-D6]-(1,3,5-SMe-2,4-Au)₆-auro-25 aspicule(1-) ($i@I,3C_2$).

Examples of aspicule structural names are given in Table S8 for modifications of $\text{Au}_{25}(\text{SR})_{18}$, $\text{Au}_{38}(\text{SR})_{24}$ and $\text{Au}_{102}(\text{SR})_{44}$ and modifications in both compact and standard aspicule structural nomenclature are given in Tables S9 and S10.

Supporting Information 6

Terminologies of Au₂₅(SR)₁₈ with Substituent Positions for Modifications

Table S1: Aspicule terminologies for ligand-exchanged and alloy modifications of Au₂₅(SR)₁₈ aspicules. Only one of the names of the isomers of a given formula name of a modification is presented.

Formula name	Aspicule Formula name
Au ₂₅ (SMe) ₁₈	Au ₂₅ (SMe) ₁₈
Au ₂₅ (SMe) ₁₇ (PET) ₁	Au ₂₅ (SMe) ₁₇ ((D1-3)-PET) ₁
Au ₂₅ (SMe) ₁₆ (PET) ₂	Au ₂₅ (SMe) ₁₆ ((D1-3,D2-3)-PET) ₂
Au ₂₅ (SMe) ₁₂ (PET) ₆	Au ₂₅ (SMe) ₁₂ (([D1-D6]-3)-PET) ₆
Au ₂₅ (SMe) ₁₁ (PET) ₇	Au ₂₅ (SMe) ₁₁ (([D1-D6]-3,D3-5)-PET) ₇
Au ₂₄ Pd(SMe) ₁₈	Au ₂₄ ((i)-Pd)(SMe) ₁₈
Au ₂₂ Pd ₃ (SMe) ₁₈	Au ₂₂ ((i,D1-2,D1-4)-Pd) ₃ (SMe) ₁₈
Au ₂₁ Pd ₄ (SMe) ₁₈	Au ₂₁ ((i,2,D1-2,D1-4)-Pd) ₄ (SMe) ₁₈

Table S2: Precise terminologies for ligand-exchanged and alloy modifications of $\text{Au}_{25}(\text{SR})_{18}$ using formula names and polyhedral shell names. Only one of the names of the isomers of a given formula name of a modification is presented.

Formula name	Aspicule Formula Name	Shell Name
$\text{Au}_{25}(\text{SMe})_{18}$	$\text{Au}_{25}(\text{SMe})_{18}$	$\text{Au}@ \text{Au}_{12}@ \text{Au}_{12}@ \text{S}_6@ \text{S}_{12}@ \text{Me}_{18}$
$\text{Au}_{25}(\text{SMe})_{17}(\text{PET})_1$	$\text{Au}_{25}(\text{SMe})_{17}(\text{D1-3-PET})$	$\text{Au}@ \text{Au}_{12}@ \text{Au}_{12}@ \text{S}_6@ \text{S}_{12}@ (\text{Me}_{17})((\text{D1-3})\text{-PET})$
$\text{Au}_{25}(\text{SMe})_{16}(\text{PET})_2$	$\text{Au}_{25}(\text{SMe})_{16}(\text{D1-3,D2-3-PET})_2$	$\text{Au}@ \text{Au}_{12}@ \text{Au}_{12}@ \text{S}_6@ \text{S}_{12}@ (\text{Me}_{16})((\text{D1-3,D2-3})\text{-PET})_2$
$\text{Au}_{25}(\text{SMe})_{12}(\text{PET})_6$	$\text{Au}_{25}(\text{SMe})_{12}([\text{D1-D6}]\text{-3-PET})_6$	$\text{Au}@ \text{Au}_{12}@ \text{Au}_{12}@ \text{S}_6@ \text{S}_{12}@ (\text{Me}_{12})([\text{D1-D6}]\text{-3-PET})_6$
$\text{Au}_{25}(\text{SMe})_{11}(\text{PET})_7$	$\text{Au}_{25}(\text{SMe})_{11}([\text{D1-D6}]\text{-3,D1-5-PET})_7$	$\text{Au}@ \text{Au}_{12}@ \text{Au}_{12}@ \text{S}_6@ \text{S}_{12}@ (\text{Me}_{11})([\text{D1-D6}]\text{-3,D1-5-PET})_7$
$\text{Au}_{24}\text{Pd}(\text{SMe})_{18}$	$\text{Au}_{24}(i\text{-Pd})(\text{SMe})_{18}$	$\text{Pd}@ \text{Au}_{12}@ \text{Au}_{12}@ \text{S}_6@ \text{S}_{12}@ \text{Me}_{18}$
$\text{Au}_{22}\text{Pd}_3(\text{SMe})_{18}$	$\text{Au}_{22}(i, \text{D1-2,D1-4-Pd})_3(\text{SMe})_{18}$	$\text{Pd}@ \text{Au}_{12}@ ((\text{D1-2,D1-4})\text{-Pd})_2 \text{Au}_{10}@ \text{S}_6@ \text{S}_{12}@ \text{Me}_{18}$
$\text{Au}_{21}\text{Pd}_4(\text{SMe})_{18}$	$\text{Au}_{21}(i, 2, \text{D1-2,D1-4-Pd})_4(\text{SMe})_{18}$	$\text{Pd}@ ((2)\text{-Pd}) \text{Au}_{11}@ ((\text{D1-2,D1-4})\text{-Pd})_2 \text{Au}_{10}@ \text{S}_6@ \text{S}_{12}@ \text{Me}_{18}$

Supporting Information 7

Borromean-Rings Diagram with S-C Bond Directions for $\text{Au}_{25}(\text{SR})_{18}$

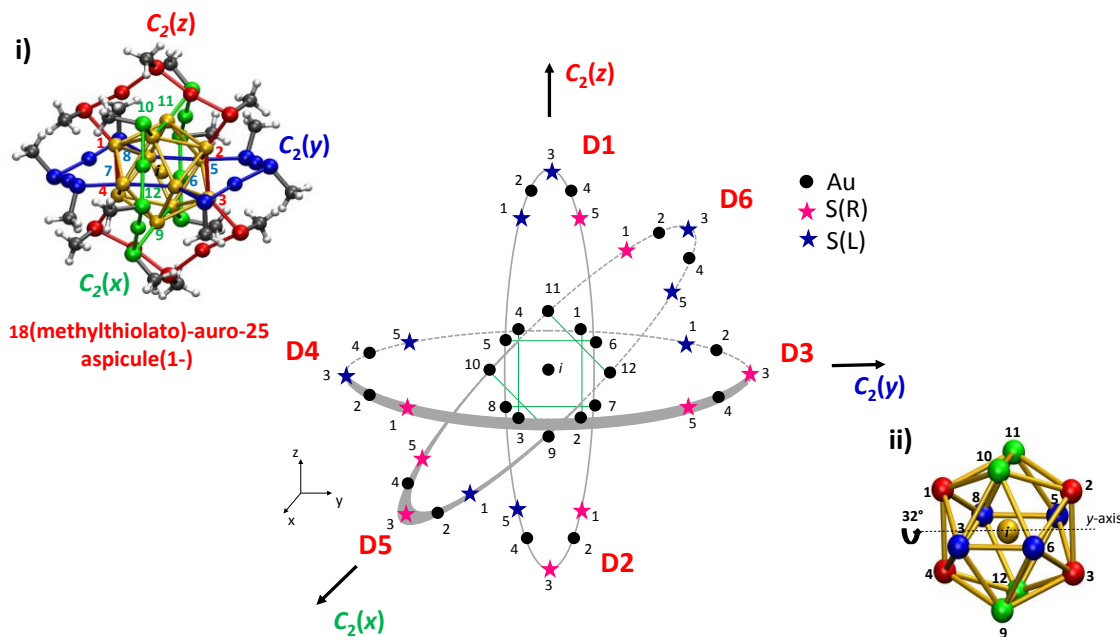


Figure S7. Borromean ring diagram for $\text{Au}_{25}(\text{SR})_{18}$ aspicule including S-C bond directions. Gold atoms are shown by black dots and sulfur atoms (ligands) by magenta and blue stars, respectively. The clockwise direction for each staple is defined by the path around the staple beginning at 1 and ending 5. The magenta stars correspond to an S-C bond direction which is parallel to the direction of a right-handed screw rotating in *clockwise* direction on that staple. The S(R) bond directions are in the z' direction on the $C_2(y)$ ring, the x' -direction on the $C_2(z)$ ring, and the y' -direction for the $C_2(x)$ ring. S(L) sulfur atoms are shown by blue stars are those for which the S-C bond direction is parallel to a right-handed screw rotating *anticlockwise*, and is opposite to the S(R) bond direction on each ring. We have assumed that C-S-Au bond angles are right angles for simplicity.

We may include S-C bond direction information for $\text{Au}_{25}(\text{SR})_{18}$ on a diagram similar to Manuscript Figure 1, and the result can be seen in Figure S7 above. We assumed that C-S-Au bond angles are right angles for simplicity. We indicate the direction of an S-C bond at a particular sulfur atom by the color of the star symbol used to represent it. Hence, blue and magenta stars indicate the direction of the sulfur-carbon (S-C) bond pointing in a clockwise screw and anticlockwise screw direction, respectively, with respect to the clockwise and anticlockwise directions around the staple. We specify the S-C bond directions by R (clockwise), and L (anticlockwise). We may form a prefix by concatenating the S-C bond directions for each ligand counting clockwise around a staple, eg. LRR indicates the S-C bond directions in positions 1(L), 3(R) and 5(R) on the staple. The staple locants of the staples which have a

specific S-C bond direction may be placed as a prefix to that S-C bond-direction-prefix *eg.* (D2,D3,D5)-LRR. We consider the name of $\text{Au}_{25}(\text{SMe})_{12}(\text{PET})_6$ with six substituents at the bridging ligand sites and include the S-C bond directions.

In the aspicule nomenclature, a name for $([\text{D1-D6}]-3)(\text{PET})_6, (\text{SMe})_{12}$ auro-25 aspicule(1-) including the S-C bond direction sequence together with the staple locants could be prefixed to the name to give $((\text{D2,D3,D5})\text{-LRR}, (\text{D1,D4,D6})\text{-RLL})\text{-}([\text{D1-D6}]-3)\text{-}(\text{PET})_6, (\text{SMe})_{12}$ -*i*-auro-25 aspicule(1-).

Supporting Information 8

Borromean-Rings Diagram of $\text{Au}_{25}(\text{SR})_{18}$ with Hybrid Directional Locants

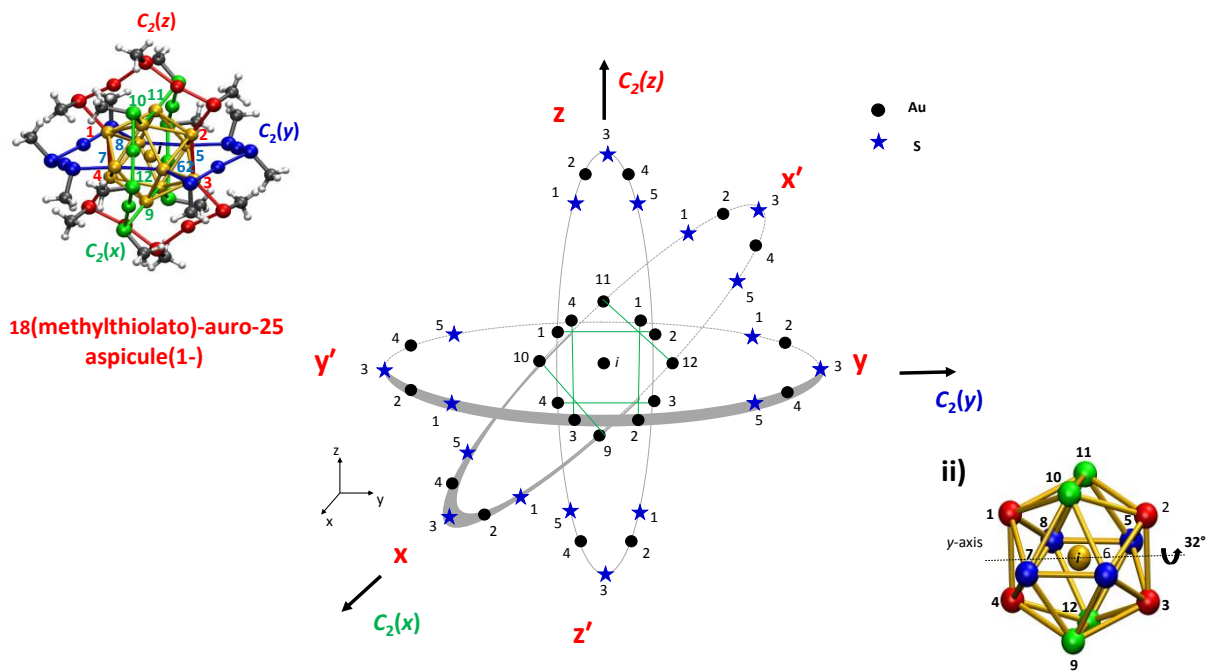


Figure S8. Borromean-Rings diagram of $\text{Au}_{25}(\text{SMe})_{18}$ with *hybrid-directional locants* for the staples. Gold atoms are shown by black dots and SMe ligands by the blue stars. The Cartesian direction associated with each of the staples is marked alongside the relevant staple. Insets (i) shows the 3D ring structure within $\text{Au}_{25}(\text{SMe})_{18}$ and inset (ii) the core icosahedron, respectively.

We introduce just such a hybrid-directional locant scheme for $\text{Au}_{25}(\text{SR})_{18}$. Instead of using the staple type and number (eg. D1, D2, etc.) to specify staple locants we use the direction the central sulfur that the staple points in, according to a Cartesian axis system superimposed on at least one symmetry axis of the aspicule. In the case of $\text{Au}_{25}(\text{SR})_{18}$ we may associate the three C_2 axes of symmetry with a set of Cartesian axis as oriented in supporting information 1. This locant scheme is suitable for smaller aspicules with upto approximately 44 metal atoms and is convenient as it allows the structure to be visualized with or without the aid of a diagram. We note that labeling atoms using directions for $\text{Au}_{102}(\text{SR})_{44}$ and $\text{Au}_{144}(\text{SR})_{60}$ is impractical as the number of staples is large and they are spread out over a wide range of directions.

Figure S8 shows Figure 1 from the manuscript with the positions labelled using Cartesian directions. In this locant scheme, the locants for the core atoms are simply the number which labels them; however, the locants of the staple atoms are formed by combining the direction of the staple with the number of the staple atom counting clockwise from the first sulfur atom on its left side. For example, x3 indicates the bridging sulfur on the x -direction staple, and x1 and x5 indicate the non-bridging sulfurs on that staple. We do not insist on italics to specify the

Cartesian directions in the locants. The name hybrid directional locant stems from this combination of the use of both numerals and Cartesian axis directions such as x , y and z . An example of a name for a ligand substitution on the bridging ligands in the x and x' direction would be (x3,x'3)-(PET)₂,(SMe)₁₆-auro-25 aspicule(1-). We remark that this method of providing locants has the advantage that the position of the substituent is very easy to identify compared to existing locant systems and could be applied to other classes of molecules.

Supporting Information 9

Tables of Names for Au₂₅(SR)₁₈, Au₃₈(SR)₂₄ and Au₁₀₂(SR)₄₄

Table S3: Table of aspicule names for Au₂₅(SMe)₁₈ and some examples of names for ligand-exchange and alloy modifications. The (SR) terminology for the ligands has been used here. Only one of the names of the isomers of a given formula name of a modification is presented.

Formula Name	Aspicule Name
Au ₂₅ (SMe) ₁₈	(SMe) ₁₈ -auro-25 aspicule(1-)
Au ₂₅ (SMe) ₁₇ (PET) ₁ 1 bridging PET ligand	(D1-3)-(PET) ₁ (SMe) ₁₇ -auro-25 aspicule(1-)
Au ₂₅ (SMe) ₁₆ (PET) ₂ Two bridging PET ligands (<i>trans</i>)	(D1-3,D2-3)-(PET) ₂ (SMe) ₁₆ -auro-25 aspicule(1-)
Au ₂₅ (SMe) ₁₆ (PET) ₂ Two bridging PET ligands (<i>cis</i>)	(D1-3,D3-3)-(PET) ₂ (SMe) ₁₆ -auro-25 aspicule(1-)
Au ₂₅ (SMe) ₁₂ (PET) ₆ Six bridging PET ligands	([D1-D6]-3)-(PET) ₆ (SMe) ₁₂ -auro-25 aspicule(1-)
Au ₂₅ (SMe) ₁₁ (PET) ₇ Six bridging ligands and one non-	([D1-D6]-3,D1-5)-(PET) ₇ (SMe) ₁₁ -auro-25 aspicule(1-)
Au ₂₄ Pd(SMe) ₁₈ One central Pd atom	(SMe) ₁₈ - <i>i</i> -monopalladoauro-25 aspicule(1-)
Au ₂₂ Pd ₃ (SMe) ₁₂ (PET) ₆ Three Pd atoms: one central, two in core. Six bridging ligands	([D1-D6]-3)-(PET) ₆ (SMe) ₁₂ -(<i>i</i> ,1,2)-tripalladoauro-25 aspicule(1-)
Au ₂₁ Pd ₄ (SMe) ₁₂ (PET) ₆ Four Pd atoms: one interstitial, two in the core and one on a staple. Six PET bridging ligands	([D1-D6]-3)-(PET) ₆ (SMe) ₁₂ -(<i>i</i> ,1,2,D1-2)-tetrapalladoauro-25 aspicule(1-)

Table S4: Table of aspicule names for $\text{Au}_{25}(\text{SMe})_{18}$ and some examples of names for ligand-exchange and alloy modifications. The IUPAC terminology names for the ligands has been used here. Only one of the names of the isomers of a given formula name of a modification is presented.

Formula Name/Substituent details	Aspicule Name
$\text{Au}_{25}(\text{SMe})_{18}$	18(methylthiolato)-auro-25 aspicule(1-)
$\text{Au}_{25}(\text{SMe})_{17}(\text{PET})_1$ One bridging PET ligand	(D1-3)-mono(2-phenylethanethiolato),17(methylthiolato)-auro-25 aspicule(1-)
$\text{Au}_{25}(\text{SMe})_{16}(\text{PET})_2$ Two bridging PET ligands (<i>trans</i>)	(D1-3,D2-3)-di(2-phenylethanethiolato),16(methylthiolato)-auro-25 aspicule(1-)
$\text{Au}_{25}(\text{SMe})_{16}(\text{PET})_2$ Two bridging PET ligands (<i>cis</i>)	(D1-3,D3-3)-di(2-phenylethanethiolato),16(methylthiolato)-auro-25 aspicule(1-)
$\text{Au}_{25}(\text{SMe})_{12}(\text{PET})_6$ Six bridging PET ligands	([D1-D6]-3)-hexa(2-phenylethanethiolato),dodeca(methylthiolato)-auro-25 aspicule(1-)
$\text{Au}_{25}(\text{SMe})_{11}(\text{PET})_7$ Six bridging and one non-bridging PET ligand	([D1-D6]-3,D1-5)-hepta(2-phenylethanethiolato),unadeca(methylthiolato)-auro-25 aspicule(1-)
$\text{Au}_{24}\text{Pd}(\text{SMe})_{18}$ One central Pd atom	18(methylthiolato)-(i)-monopalladoauro-25 aspicule(1-)
$\text{Au}_{22}\text{Pd}_3(\text{SMe})_{12}(\text{PET})_6$ Three Pd atoms: one central, two in core. Six PET bridging ligands	([D1-D6]-3)-hexa(2-phenylethanethiolato),dodeca(methylthiolato)-(i,1,2)-tripalladoauro-25 aspicule(1-)
$\text{Au}_{21}\text{Pd}_4(\text{SMe})_{12}(\text{PET})_6$ Four Pd atoms: one central, two in the core and one on a staple. Six PET bridging ligands	([D1-D6]-3)-hexa(2-phenylethanethiolato),dodeca(methylthiolato)-(i,1,2,D1-2)-tetrapalladoauro-25 aspicule(1-)

Table S5: Table of names for supramolecular adducts formed between β -CD and $\text{Au}_{25}(\text{BBSH})_{18}$. We provide example names for one possible isomer for each number of attached β -CDs (from 1 to 4). The positions for the four β -CD attached structure are taken from Mathew et al⁵. Only one of the names of the isomers of a given formula name of a modification is presented. The (SR) terminology for the ligands has been used here.

Formula Name	Aspicule name
$\text{Au}_{25}(\text{BBSH})_{17}$ ($\text{BBSH} \cap \text{CD}$) ₁	(D1-3)-(BBSH \cap CD) ₁ ,(BBSH) ₁₇ -auro-25 aspicule(1-)
$\text{Au}_{25}(\text{BBSH})_{16}$ ($\text{BBSH} \cap \text{CD}$) ₂	(D1-3,D2-3)-(BBSH \cap CD) ₂ ,(BBSH) ₁₆ -auro-25 aspicule(1-)
$\text{Au}_{25}(\text{BBSH})_{15}$ ($\text{BBSH} \cap \text{CD}$) ₃	(D3-3,D4-1,D4-5)-(BBSH \cap CD) ₃ ,(BBSH) ₁₅ -auro-25 aspicule(1-)
$\text{Au}_{25}(\text{BBSH})_{14}$ ($\text{BBSH} \cap \text{CD}$) ₄	(D6-1,D2-5,D2-1,D3-5)-(BBSH \cap CD) ₄ ,(BBSH) ₁₄ -auro-25 aspicule(1-)

Table S6: Table of names for some possible conjugated FITC complexes with $\text{Au}_{25}(\text{SR})_{18}$ with dansyl glutathione (SDG) ligands. We provide example names for one possible structural isomer for several numbers of conjugated FITCs. In the ligand name, SDG-FITC, the dash indicates the SDG ligand is conjugated with FITC. Only one of the names of the isomers of a given formula name of a modification is presented.

Formula Name	Aspicule name
$\text{Au}_{25}(\text{SDG})_{18}(\text{FITC})_1$	(D1-3)-(SDG-FITC) ₁ ,(SDG) ₁₇ -auro-25 aspicule(1-)
$\text{Au}_{25}(\text{SDG})_{18}(\text{FITC})_2$	(D1-3,D2-3)-(SDG-FITC) ₂ ,(SDG) ₁₆ -auro-25 aspicule(1-)
$\text{Au}_{25}(\text{SDG})_{18}(\text{FITC})_3$	(D1-3,D3-3,D5-3)-(SDG-FITC) ₃ ,(SDG) ₁₅ -auro-25 aspicule(1-)
$\text{Au}_{25}(\text{SDG})_{18}(\text{FITC})_6$	([D1-D6]-3)-(SDG-FITC) ₆ ,(SDG) ₁₂ -auro-25 aspicule(1-)

Table S7: Aspicule structural names with staple-core locants for ligand-exchanged and alloy-modifications of Au₂₅(SR)₁₈. Only one of the names of the isomers of a given formula name of a modification is presented.

Formula Name/Substituent positions	Structural Aspicule Name
Au ₂₅ (SMe) ₁₈	D1(1,2):D2(3,4):D3(5,6):D4(7,8):D5(9,10):D6(11,12)-(1,3,5-SMe-2,4-Au) ₆ -auro-25 aspicule(1-) (<i>i@I,3C₂</i>)
Au ₂₅ (SMe) ₁₇ (PET) ₁ One bridging PET ligand	D1(1,2)-(3-PET,1,5-SMe-2,4-Au) ₂ ,D2(3,4):D3(5,6):D4(7,8):D5(9,10):D6(11,12)-(1,3,5-SMe-2,4-Au)-auro-25 aspicule(1-) (<i>i@I,3C₂</i>)
Au ₂₅ (SMe) ₁₆ (PET) ₂ Two bridging PET ligands (<i>trans</i>)	D1(1,2):D2(3,4)-(3-PET,1,5-SMe-2,4-Au) ₂ , D3(5,6):D4(7,8):D5(9,10):D6(11,12)-(1,3,5-SMe-2,4-Au) ₄ -auro-25 aspicule(1-) (<i>i@I,3C₂</i>)
Au ₂₅ (SMe) ₁₆ (PET) ₂ Two bridging PET ligands	D1(1,2):D4(7,8)-(3-PET,1,5-SMe-2,4-Au) ₂ ,D2(3,4):D3(5,6):D5(9,10),D6(11,12)-(1,5-SMe,3-PET-2,4-Au) ₄ -auro-25 aspicule(1-) (<i>i@I,3C₂</i>)
Au ₂₅ (SMe) ₁₂ (PET) ₆ Six bridging PET ligands	D1(1,2); ... ;D6(11,12)-(3-PET,1,5-SMe-2,4-Au) ₆ -auro-25 aspicule(1-) (<i>i@I,3C₂</i>)
Au ₂₅ (SMe) ₁₁ (PET) ₇ Six PET bridging ligands and one PET non-bridging ligand	D1(1,2)-(1-SMe,3,5-PET-2,4-Au),D1(1,2); ... ;D6(11,12)-(3-PET,1,5-SMe-2,4-Au) ₅ -auro-25 aspicule(1-) (<i>i@I,3C₂</i>)
Au ₂₄ Pd(SMe) ₁₈ One interstitial Pd atom	D1(1,2):D2(3,4):D3(5,6):D4(7,8):D5(9,10):D6(11,12)-(1,3,5-SMe-2,4-Au) ₆ -monopalladoauro-25 aspicule(1-) (<i>i@I,3C₂</i>)
Au ₂₂ Pd ₃ (SMe) ₁₂ (PET) ₆ Three Pd atoms, one central, and two in the core	D1(1,2); ... ;D6(11,12)-(3-PET,1,5-SMe-2,4-Au) ₆ -(<i>i,1,2</i>)-tripalladoauro-25 aspicule(1-) (<i>i@I,3C₂</i>)
Au ₂₁ Pd ₄ (SMe) ₁₂ (PET) ₆ Four Pd atoms, one central, two in the core and one on a staple. Six PET bridging ligands.	D1(1,2)-(3-PET,1,5-SMe-2-Pd,4-Au) ₁ ,D2(3,4):D3(5,6):D4(7,8):D5(9,10):D6(11,12)-(1,5-SMe,3-PET-2,4-Au) ₅ -(<i>i,1,2,D1-2</i>)-tetrapalladoauro-25 aspicule(1-) (<i>i@I,3C₂</i>)

Table S8: Aspicule names for $\text{Au}_{25}(\text{SR})_{18}$, $\text{Au}_{38}(\text{SR})_{24}$ and $\text{Au}_{102}(\text{SR})_{44}$ and one modification of each. Only one of the names of the isomers of a given formula name of a modification is presented.

Formula Name	Aspicule name
$\text{Au}_{25}(\text{SMe})_{18}$	$(\text{SMe})_{18}\text{-auro-25 aspicule(1-)}$
$\text{Au}_{23}\text{Pd}_2(\text{SMe})_{16}(\text{PET})_2$ Two PET on the bridging ligands opposite each other, and 2 Pd in the core.	$(\text{D1-3,D2-3})\text{-(PET)}_2,(\text{SMe})_{16}\text{-(}i,2\text{)-dipalladoauro-25 aspicule(1-)}$
$\text{Au}_{38}(\text{SMe})_{24}$	$(\text{SMe})_{24}\text{-(}i, i_5\text{)-auro-38 aspicule(0)}$
$\text{Au}_{36}\text{Pd}_2(\text{SMe})_{20}(\text{PET})_4$ Two Pd in interstitials. Two PET ligands in bridging positions on dimer staples and two on monomer staples	$(\text{D1-3,D2-3,M1-1,M2-3})\text{-(PET)}_4,(\text{SMe})_{20}\text{-(}i, i_5\text{)-dipalladoauro-38 aspicule(0)}$
$\text{Au}_{102}(\text{SMe})_{44}$	$(\text{SMe})_{44}\text{-auro-102 aspicule(0)}$
$\text{Au}_{100}\text{Pd}_2(\text{SMe})_{40}(\text{PET})_4$ Two Pd in MD core. Two PET ligands at bridging positions of the dimer staples and two on monomer ligands of the N Au_{15} cap.	$(\text{D1-3,D2-3,M1-1,M2-3})\text{-(PET)}_4,(\text{SMe})_{40}\text{-(1,42)-dipalladoauro-102 aspicule(0)}$

Table S9: Compact aspicule structural names for Au₂₅(SR)₁₈, Au₃₈(SR)₂₄ and Au₁₀₂(SR)₄₄ and one modification of each. Only one of the names of the isomers of a given formula name of a modification is presented.

Formula Name/substituent positions	Compact Aspicule Structural Name	Aspicule name
Au ₂₅ (SMe) ₁₈	[D1-D6]-(1,3,5-SMe-2,4-Au) ₆ -auro-25 aspicule(1-) (<i>i@I,C₂</i>)	(SMe) ₁₈ -auro-25 aspicule(1-)
Au ₂₃ Pd ₂ (SMe) ₁₆ (PET) ₂ Two Pd in the core. Two PET at the bridging ligands	D1,D2-(3-PET,1,5-SMe-2,4-Au) ₂ ,[D3-D6]-(1,3,5-SMe-2,4-Au) ₄ -(<i>i,2</i>)-dipalladoauro-25 aspicule(1-) (<i>i@I,C₂</i>)	(D1-3,D2-3)-(PET) ₂ , (SMe) ₁₆ -(<i>i,2</i>)-dipalladoauro-25 aspicule(1-)
Au ₃₈ (SMe) ₂₄	[D1-D6]-(1,3,5-SMe-2,4-Au) ₆ ,[M1-M3]-(1,3-SMe-2-Au) ₂ -auro-38 aspicule(0) (<i>TBP@BIC₁₈,C₃</i>)	(SMe) ₂₄ -auro-38 aspicule(0)
Au ₃₆ Pd ₂ (SMe) ₂₂ (PET) ₂ Two Pd atoms in the icosahedra centres. Two PET ligands in bridging positions of two dimer staples	D1,D2-(3-PET,1,5-SMe-2,4-Au) ₂ ,[D3-D6]-(1,3,5-SMe-2,4-Au) ₄ ,[M1-M3]-(1,3-SMe-2-Au) ₃ -(<i>i₁,i₅</i>)-dipalladoauro-38 aspicule(0) (<i>TBP@BIC₁₈,C₃</i>)	(D1-3,D2-3)-(PET) ₂ , (SMe) ₂₂ -(<i>i₁,i₅</i>)-dipalladoauro-38 aspicule(0)
Au ₁₀₂ (SMe) ₄₄	[M1-M19]-(1,3-SMe-2,4-Au) ₁₉ ,D1,D2-(1,3-SMe-2,4-Au) ₂ -auro-102 aspicule(0) (<i>PBP@MD₄₂@(N-RID₁₅,S-RID₁₅),C₅</i>)	(SMe) ₄₄ -auro-102 aspicule(0)
Au ₁₀₀ Pd ₂ (SMe) ₄₀ (PET) ₄ Two Pd atoms in the MD core. Two PET ligands at bridging ligands of the dimer staples and two on different monomer staples in different positions.	M1-(1-PET,3-SMe-2-Au),M2-(3-PET,1-SMe-2-Au),[M3-M19]-(1,3-SMe-2-Au) ₁₇ ,D1,D2-(3-PET,1,5-SMe-2,4-Au) ₂ -(1,42)-dipalladoauro-102 aspicule(0) (<i>PBP@MD₄₂@(N-RID₁₅,S-RID₁₅),C₅</i>)	(D1-3,D2-3,M1-1,M2-3)-(PET) ₄ , (SMe) ₄₀ -(1,42)-dipalladoauro-102 aspicule(0)

Table S10: Aspicule structural names and aspicule names for Au₂₅(SR)₁₈, Au₃₈(SR)₂₄ and Au₁₀₂(SR)₄₄ and one modification of each. The ligand-staple names have been shown in bold for clarity. Only one of the names of the isomers of a given formula name of a modification is presented.

Formula Name	Aspicule Structural Name	Aspicule Name
Au ₂₅ (SMe) ₁₈	D1(1,2):D2(3,4):D3(5,6):D4(7,8):D5(9,10)- (1,3,5-SMe-2,4-Au) ₆ -auro-25 aspicule(1-) (<i>i@I,3C₂</i>)	(SMe) ₁₈ -auro-25 aspicule(1-)
Au ₂₃ Pd ₂ (SMe) ₁₆ (PET) ₂ Two PET ligands on the bridging positions, and two Pd atoms in the core	D1(1,2):D2(3,4)- (1,3,5-SMe-2-Au,4-Pd) ₂ , D3(5,6):D4(7,8):D5(9,10):D6(11,12)- (1,3,5-SMe-2,4-Au) ₄ -(<i>i,2</i>)-dipalladoauro-25 aspicule(1-) (<i>i@I,3C₂</i>)	(D1-3,D2-3)-(PET) ₂ , (SMe) ₁₆ -(<i>i,2</i>)-dipalladoauro-25 aspicule(1-)
Au ₃₈ (SMe) ₂₄	D1(1,9):D2(2,10):D3(3,8):D4(14,22):D5(15,23)- (1,3,5-SMe-2,4-Au) ₆ , M1(4,18):M2(5,19):M3(6,20)- (1,3-SMe-2-Au) ₃ -auro-38 aspicule(0) (<i>TBP@BIC₁₈,C₃</i>)	(SMe) ₂₄ -auro-38 aspicule(0)
Au ₃₆ Pd ₂ (SMe) ₂₂ (PET) ₂ Two Pd atoms in central positions, Two PET in dimer staples	D1(1,9):D2(2,10)- (3-PET,1,5-SMe-2,4-Au) ₂ , D3(3,8):D4(14,22):D5(15,23)- (1,3,5-SMe-2,4-Au) ₄ , M1(4,18):M2(5,19):M3(6,20)- (1,3-SMe-2-Au) ₃ -(<i>i₁,i₅</i>)-dipalladoauro-38 aspicule(0) (<i>TBP@BIC₁₈,C₃</i>)	(D1-3,D2-3,M1-1,M2-3)-(PET) ₂ , (SMe) ₂₂ -(<i>i₁,i₅</i>)-dipalladoauro-38 aspicule(0)
Au ₁₀₂ (SMe) ₄₄	M1(N1,N7):M2(N2,N9):M3(N3,N11):M4(N4,N13):M5(N5,N15):M6(N6,31):M7(N10,26):M8(N14,30):M6(17,18):M2(1,22):M8(25,26)M12(17,S15):M13(19,S7):M14(23,S11):M15(S6,S2):M16(S8,S3):M17(S10,S4):M18(S12,S5):M19(S14,S1)- (1,3-SMe-2-Au) ₁₉ , D1(N8,S9):D2(N14,S13)- (1,3,5-SMe-2,4-Au) ₂ -auro-102 aspicule(0) (<i>PBP@MDS₄₂@(N-RID₁₅,S-RID₁₅,C₅)</i>)	(SMe) ₄₄ -auro-102 aspicule(0)
Au ₁₀₀ Pd ₂ (SMe) ₄₀ (PET) ₄ Two Pd in the MD core. Two PET ligands on bridging ligands of the dimer staples and two PET ligands on different positions of monomer staples.	M1(N1,N7):M2(N2,N9)- (1-PET,3-SMe-2-Au) ₂ , D1(N8,S9):D2(N14,S13)- (3-PET,1,5-SMe-2,4-Au) ₂ , M3(N3,N11):M4(N4,N13):M5(N5,N15):M6(N6,31):M7(N10,26):M8(N14,30):M9(17,S15):M10(19,S7):M11(23,S11):M12(17,S15):M13(19,S7):M14(23,S11):M15(S6,S2):M16(S8,S3):M17(S10,S4):M18(S12,S5):M19(S14,S1)- (1,3-SMe-2-Au) ₁₇ -(1,42)-dipalladoauro-102 aspicule(0) (<i>PBP@MD₄₉@(N-RID₁₅,S-RID₁₅,C₅)</i>)	(D1-3,D2-3,M1-1,M2-1)-(PET) ₄ , (SMe) ₄₀ -(1,42)-dipalladoauro-102 aspicule(0)

Supporting Information 10

Table of Crystal Structures and their Corresponding Nomenclature Names

Table S11: A list of crystal structures together with their aspicule names for $Au_M(SR)_N$ is shown below. Both aspicule names with (SR) notation for the ligands and with their IUPAC name are given. A few structurally related compositions containing silver, selenium and chlorine, have also been included in this table. In the case of charged species, the counterion is shown in brackets after the aspicule name. Modifications of these structures may be specified using the locant prefixes as shown in Tables S3-S8. Aspicule structural names with information on the staple type and arrangement and the core shape may be formed from these names in a similar way to those shown in Tables S7, S9, and S10. This table has been based on inputs from the literature³.

No	Crystal structure	Aspicule Name	Ref.
1	$Au_{10}(TBBT)_{10}$	(TBBT) ₁₀ -auro-10 aspicule(0)	6
		10(4-tert-butylbenzenethiolato)-auro-10 aspicule(0)	
2	$Au_{18}(CHT)_{14}$	(CHT) ₁₄ -auro-18 aspicule(0)	7
		14(1-cyclohexanethiolato)-auro-18 aspicule(0)	
3	$Au_{20}(TBBT)_{16}$	(TBBT) ₁₆ -auro-20 aspicule(0)	8
		16(4-tert-butylbenzenethiolato)-auro-20 aspicule(0)	
4	$[Au_{23}(CHT)_{16}]^{1-}$	(CHT) ₁₆ -auro-23 aspicule(1-) (TOAA)	9
		16(1-cyclohexanethiolato)-auro-23 aspicule(1-)	
5	$Au_{24}(ADT)_{16}$	(ADT) ₁₆ -auro-24 aspicule(0)	10
		16(1-adamantanethiolato)-auro-24 aspicule(0)	
6	$Au_{24}(SePh)_{20}$	20(SePh)-auro-24 aspicule(0)	11
		20(phenylselenolato) auro-24 aspicule(0)	
7	$[Au_{25}(PET)_{18}]^{1-}$	(PET) ₁₈ -auro-25 aspicule(1-) (TOAA)	12,1
		18(2-phenylethanethiolato)-auro-25 aspicule(1-) (TOAA)	
8	$[Ag_{25}(PET)_{18}]^{1-}$	(PET) ₁₈ -argento-25 aspicule(1-) (TOAA)	13
		18(2-phenylethanethiolato)-argento-25 aspicule(1-) (TOAA)	
9	$[Au_{25}(SePh)_{18}]^{1-}$	(SePh) ₁₈ -auro-25 aspicule(1-)	14
		18(phenylselenolato)-auro-25 aspicule(1-) (TOAA)	
10	$Au_{28}(TBBT)_{20}$	(TBBT) ₂₀ -auro-28 aspicule(0)	15
		20(4-tert-butylbenzenethiolato)- auro-28 aspicule(0)	
11	$Au_{30}(TBT)_{18}$	(TBT) ₁₈ -auro-30 aspicule(0)	16
		18 (2-methylpropane-2-thiolato)-auro-30 aspicule(0)	
12	$Au_{36}(TBBT)_8Cl_{20}$	(Cl) ₂₀ , (TBBT) ₈ -auro-36 aspicule(0)	17
		20(chlorido), 8(4-tert-butyl-benzenethiolato)-auro-36 aspicule(0)	
13	$Au_{36}(TBT)_{24}$	(TBT) ₂₄ -auro-36 aspicule(0)	18
		24(2-methylpropane-2-thiolato)-auro-36 aspicule(0)	
14	$Au_{38}(PET)_{24}$	(PET) ₂₄ -auro-38 aspicule(0)	19
		24(2-phenylethanethiolato)-auro-38 aspicule(0)	

15	Au ₃₈ S ₂ (PET) ₂₀	(PET) ₂₀ ,S ₂ -auro-38 aspicule(0)	20
		20(2-phenylethanethiolato),di(sulfido)-auro-38 aspicule(0)	
16	Au ₄₀ (<i>o</i> -MBT) ₂₈	(<i>o</i> -MBT) ₂₈ -auro-40 aspicule(0)	21
		28(2-sulfanylbenzenethiolato)-auro-40 aspicule(0)	
17	Au ₅₂ (TBBT) ₃₂	(TBBT) ₃₂ -auro-52 aspicule(0)	22
		32(4-tert-butylbenzenethiolato)-auro-52 aspicule(0)	
18	Au ₆₈ (3-MBA) ₃₄	(3-MBA) ₃₄ -auro-68 aspicule(0)	23
		34(3-mercaptopbenzoic acid)-auro-68 aspicule(0)	
19	Au ₁₀₂ (<i>p</i> -MBA) ₄₄	(<i>p</i> -MBA) ₄₄ -auro-102 aspicule(0)	24
		44(<i>p</i> -mercaptopbenzoic acid)-auro-102 aspicule(0)	
20	Au ₁₃₀ (TBT) ₅₀	(TBT) ₅₀ -auro-130 aspicule(0)	25
		50(2-methylpropane-2-thiolato)-auro-130 aspicule(0)	
21	Au ₁₃₃ (TBT) ₅₂	(TBT) ₅₂ -auro-133 aspicule(0)	26, 27
		52(2-methylpropane-2-thiolato)-auro-133 aspicule(0)	
22	Au ₁₄₄ (PET) ₆₀	(PET) ₆₀ -auro-144 aspicule(0)	28
		60(2-phenylethanethiolato)-auro-144 aspicule(0)	

Supporting Information 11

Isomers with Two-Substituents of Ligand-Exchanged and Alloyed $\text{Au}_{25}(\text{SR})_{18}$

For two ligand exchanges of $\text{Au}_{25}(\text{SMe})_{16}(\text{PET})_2$, we counted 15 symmetry-unique isomers and these are shown in **Figure S9**. In the case of alloying, we found that $\text{Au}_{23}\text{Pd}_2(\text{SMe})_{18}$ has 28 symmetry-unique alloy isomers, and we have shown a selection of eighteen these in Figure S10 and provided locants for the substituent atoms for all the isomers in Table S12. The three-ring diagram of $\text{Au}_{25}(\text{SR})_{18}$ is a useful device for both representing and finding the possible isomers taking into account the $d\text{O}_h$ symmetry elements. Using the Borromean-rings diagram of $\text{Au}_{25}(\text{SR})_{18}$ we can easily identify structures that are equivalent under the C_2 and C_3 rotation operations in the reduced point group of the modified configuration. We checked for chiral isomers of the modified aspicule (which are symmetry-non-equivalent) by testing whether the mirror image was superimposable on the modified aspicule, where this image was obtained by reflection in a plane parallel to the mirror plane of the symmetry element which is broken by the modification. For clarity, when considering ligand exchanges one need not show the Au atoms on the diagram, and when considering alloy exchanges one can dispense with showing the S atoms.

The procedure used to the numbers and structures of the isomers was as follows: First we replaced two ligands (marked by an X) and then identified all the symmetry equivalent isomers to that configuration. The second step was to replace a different pair of ligands from all the previous symmetry equivalent isomers found in the previous steps, and then we repeated this step until there were no more possible symmetry-unique placements.

The whole procedure was repeated for the different classes of ligand placements, which consist of choosing the two ligands to be on the same staple, secondly, to both on a single ring which includes the staple and its coplanar pair, and then thirdly, on two perpendicular rings. The number of ligand isomers can be counted in the following way: there are six isomers on the same ring and nine isomers on perpendicular rings making a total of fifteen. The same procedure was used to enumerate the alloy isomers. The number of alloy isomers can be counted as follows: two involving the central atom, ten on the same ring, and sixteen on perpendicular rings making a total of 28. We neglected the S-C bond directions in this analysis, if they are included then there would be a greater number of different isomers. For six of the alloy isomers (Nos: 2, 10, 11, 12, 17 and 18 in Figure S10) which involve only substitution of two core atoms, the configuration of substituent atoms in the core icosahedron is visualized in Figure S11. These core alloy isomers may be distinguished as to whether the two substituent atoms are nearest neighbors, next-nearest neighbors, and third neighbors on opposite ends of a C_5 axis. It can be seen that although S11(b) and S11(c) appear to be equivalent in that the substituted atoms are nearest neighbors, they are in fact separate isomers since in (c) both substituent atoms are bonded to staples on different rings rather than the same ring, which makes their local bonding geometry slightly different. A similar case as S11(b) and S11(c) also occurs for the next-nearest neighbors S11(e) and S11(f).

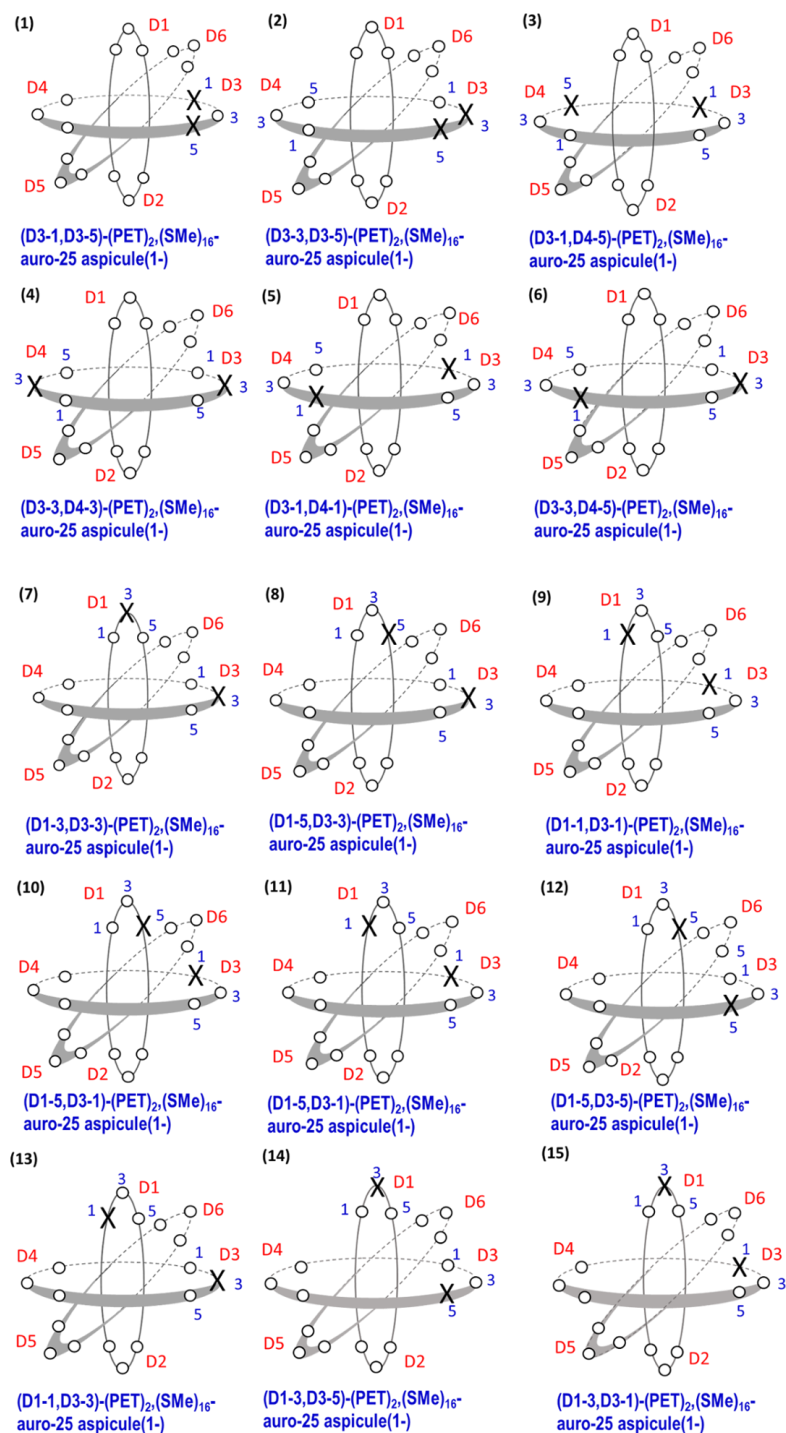
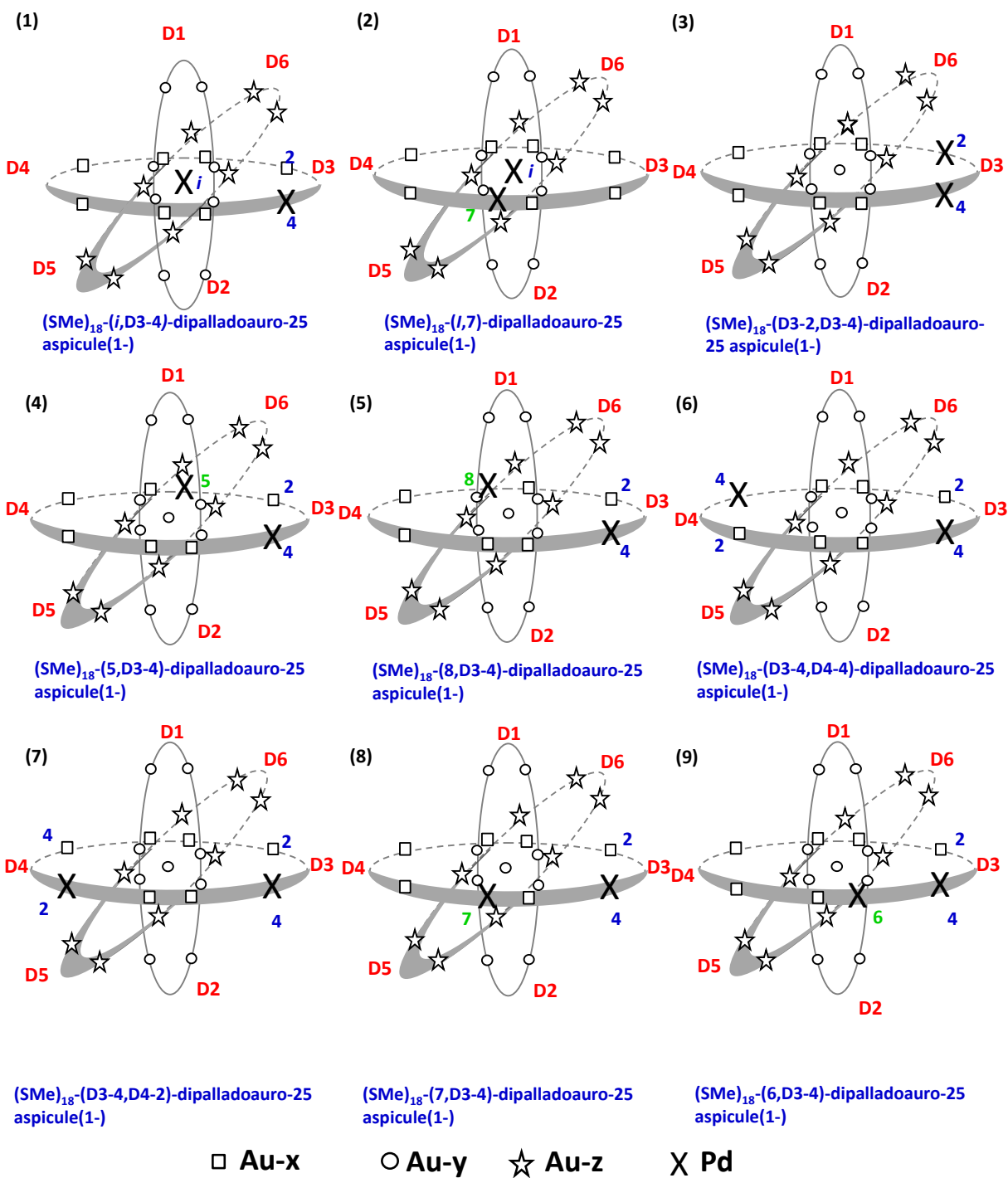


Figure S9. Ligand-exchanged isomers of $Au_{25}(SMe)_{16}(PET)_2$. The fifteen symmetry unique isomers are depicted in the following order: Isomers 1 and 2 have two PET ligands substituted on a D1 staple. Isomers 3, 4, 5, and 6 have PET ligands substituted on the $C_2(x)$ ring. Isomers 7 to 15, have PET ligands substituted on perpendicular $C_2(x)$ and $C_2(y)$ rings. An open circle indicates the sulfur bonded to methyl ligand R-groups, while a cross is used to denote a sulfur atom bonded to a PET ligand. The aspicule names for each isomer are shown underneath their respective diagrams.



Please see the caption on the next page.

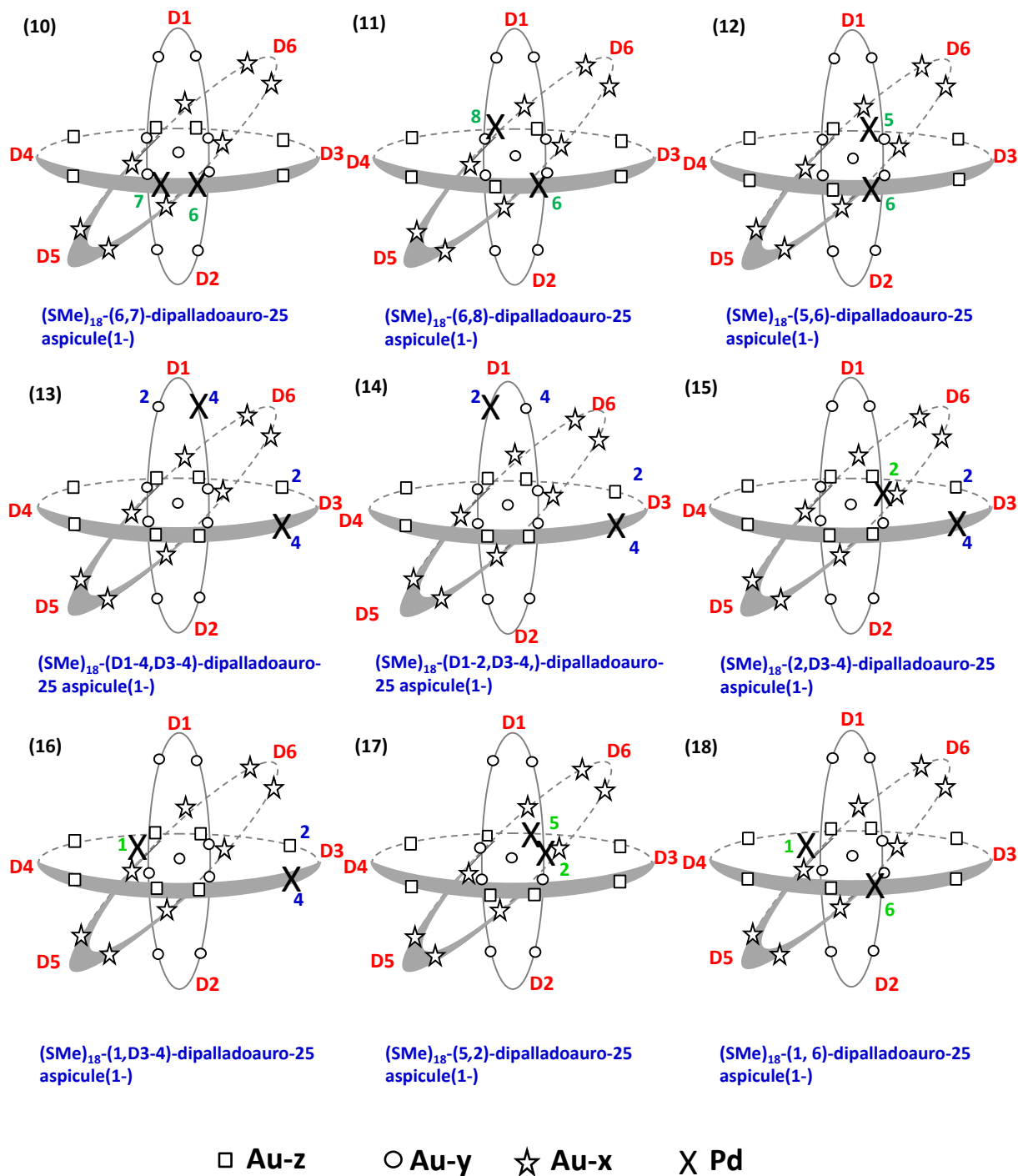


Figure S10. Alloy-exchanged isomers of $\text{Au}_{23}\text{Pd}_2(\text{SMe})_{18}$. A selection of 18 out of the 28 symmetry-unique isomers are depicted in the following order: (1) and (2) substitution of the two Pd atoms with one at the central position (*i*), (3)-(12) on the same $C_2(y)$ -ring, and (13)-(18) on perpendicular $C_2(y)$ and $C_2(z)$ rings. For clarity only the Au atoms have been shown and not the SMe ligands).

Table S12: Examples of locants of Pd atoms for the complete set of 28 symmetry-unique isomers of Au₂₃Pd₂(SMe)₁₈. Isomers involving the central atom are Nos: 1 and 2, those involving the atoms on a single ring are Nos: 3-11 and No: 28. Isomers involving Pd atoms on perpendicular rings are Nos: 12-27.

Isomer number	Aspicule locants	Isomer number	Aspicule Locants	Isomer number	Aspicule Locants
1	(i,D3-4)	14	(D1-2,D3-4)	27	6,D1-2
2	(i,7)	15	(2,D3-4)	28	5,7
3	(D3-2,D3-4)	16	(D1-1,D3-4)		
4	(5,D3-4)	17	(5,2)		
5	(8,D3-4)	18	(1,6)		
6	(D3-4,D4-4)	19	(2,6)		
7	(D3-4,D4-2)	20	(D1-2,D3-2)		
8	(7,D3-4)	21	(D1-4,D3-2)		
9	(6,D3-4)	22	(1,D3-2)		
10	(6,7)	23	(2,D3-2)		
11	(6,8)	24	(6,D1-2)		
12	(5,6)	25	(5,D1-4)		
13	(D1-4,D3-4)	26	(6,D1-4)		

Supporting Information 12

Isomer Diagrams for Two Metal Atom Substituents in the Icosahedral Core of $\text{Au}_{25}(\text{SR})_{18}$

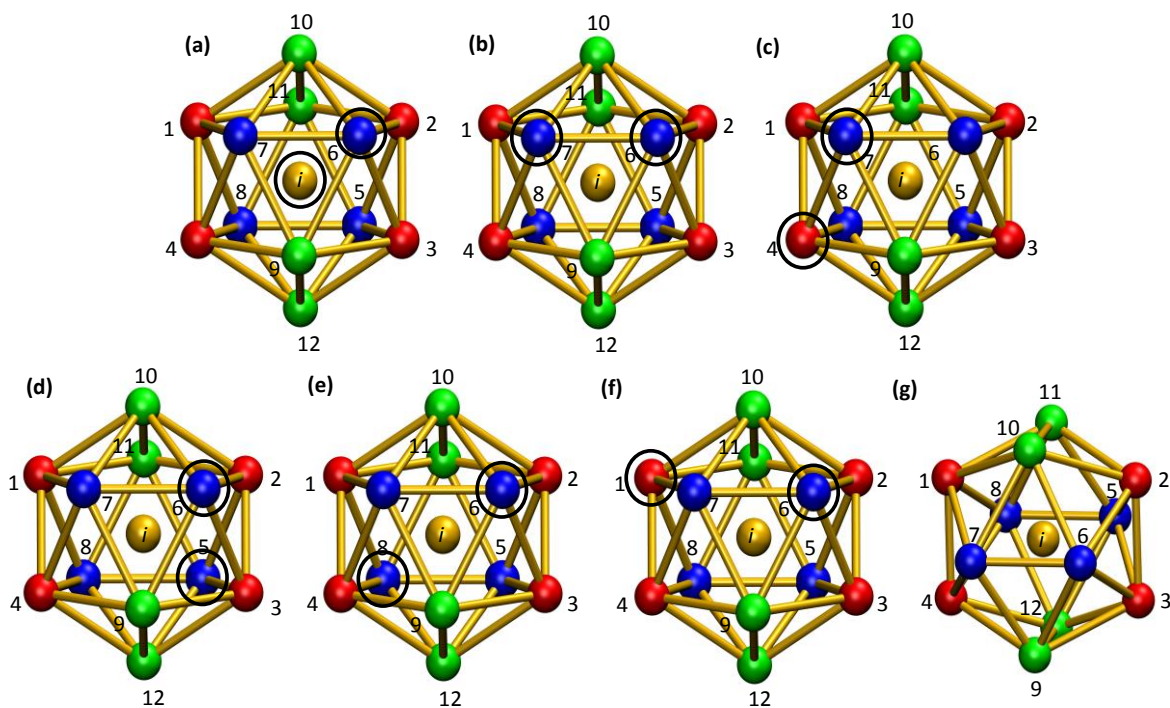


Figure S11. (a)-(f) Alloy isomers of $\text{Au}_{25}(\text{SR})_{18}$ aspicle with two metal (Pd) substituents in the core with nos. 2, 10, 11, 12, 17, 18, respectively in Figure S10. These six symmetry-unique isomers are shown by marking the positions of the substituent atoms using a thick black circle around the respective atom. The core atoms are colored red, green and blue according to inset of Figure 1 in the Manuscript, and the icosahedron is shown in its face projection. (g) The edge projection of an unmodified core icosahedron is shown for reference so that the positions may be understood as they appear on the diagrams of Figures S10.

Supporting Information 13

Staple to Core Connectivity Diagram of $\text{Au}_{102}(\text{SR})_{44}$ and its Standard Orientation and Locant Assignment

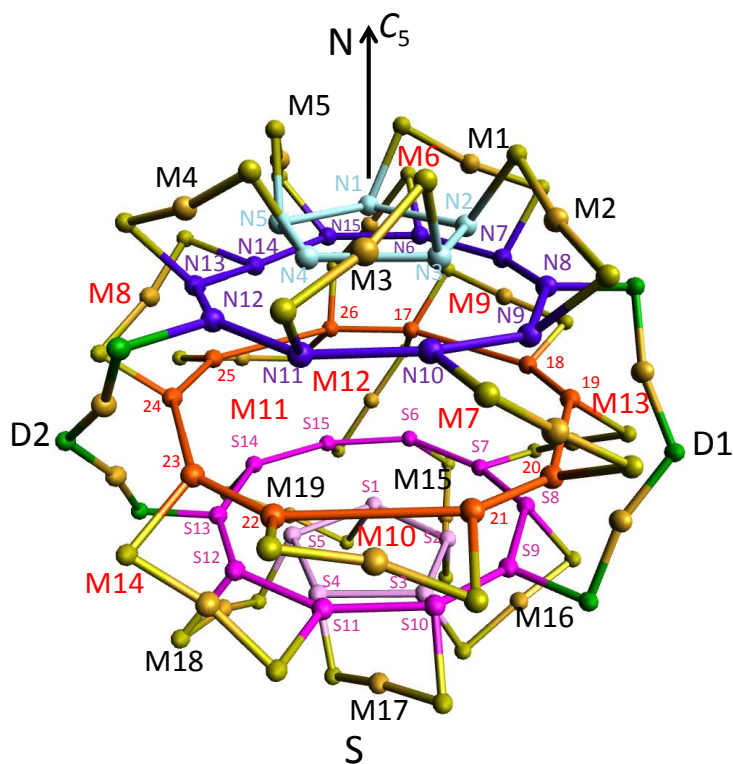


Figure S12. $\text{Au}_{102}(\text{SR})_{44}$ staples and their connectivity to the surface core atoms. The core atoms are shown as rings lying in planes perpendicular to the C_5 symmetry axis marked at the top of the figure. The core atom rings and their colors are the same as in Figure 4 in the Manuscript. Staple gold atoms are colored gold, monomer staple sulfur atoms yellow, while dimer staple sulfur atoms are colored green. The “North” and “South” hemispheres are labeled N and S respectively, and the prefixes N and S are also used in the locants of atoms of the respective Au_{15} polar caps. The arrow at the top indicates the principal C_5 symmetry axis.

The following two sections contain more details about the standard orientation and locant assignment of $\text{Au}_{102}(\text{SR})_{44}$ aspicle²⁹ which is described only briefly in the Manuscript.

(i) Standard orientation of Au₁₀₂(SR)₄₄

We select a standard orientation by placing the C_5 axis along the z -axis (vertical) as shown in **Figure S12** and secondly by using the asymmetry of the dimer and equatorial staple arrangement. Observing that the dimer staples slant at a fairly small angle from the vertical and are located on opposite sides and within one half of the Au₁₀₂(SR)₄₄ "globe", this asymmetry can be used to define the front and reverse of Au₁₀₂(SR)₄₄. The hemisphere with the dimer staples in it is taken to be the front half of Au₁₀₂(SR)₄₄.

(ii) Locant assignment of Au₁₀₂(SR)₄₄

The core atoms of the 49-atom Marks decahedron are numbered as in **Figure 4(A)**, following the core-ring locant scheme. The two Au₁₅ polar caps are labelled as N(North) and S(South), and each polar cap consists of two rings of atoms. The N Au₁₅ polar cap upper ring is shown in light blue and the lower ring in dark blue. The Au₁₅ South polar cap upper ring is shown in purple and lilac for the lower ring. The numbering of the Au₁₅ South (S) polar cap begins from the lower ring rather than the upper ring as an exception to the general rule due to the C_2 symmetry with the Au₁₅ North (N) polar cap. The 49-atom Marks decahedron is divided into six planes of atoms, in which each ring (plane) of atoms in the Marks decahedron is colored differently to indicate its position, blues being used for the Northern hemisphere and reds being used in the Southern hemisphere, while orange represents the equatorial ring of atoms. This 49-atom structure may be further broken down into an outer 42-atom Marks decahedral shell and a central pentagonal bipyramid of atoms, whose atoms are numbered from i_1 to i_7 , once again following the core ring locant scheme.

For the purpose of assigning staple locants and staple core locants we may view the structure of the staples and the outer shell of core atoms in isolation. This structure includes the two Au₁₅ polar caps and an equatorial ring of atoms of the Marks decahedron, to which the staples are connected to, as shown in Figure 4(B). Figure S9 above shows this structure and also the locants of the core atoms to which the staples bond to.

The color scheme below is used for the gold atoms present in the 19 monomer staples of Figure 4(B) which are divided into five groups of (1)-(5) below, with each group being distinguished by its different connectivity to the rings of core atoms:

(1) M1-M5 in dark blue bonded to N Au₁₅ polar cap, (2) M6-M8 in cyan are three staples bonded from N Au₁₅ polar cap to the orange equatorial ring of the Marks decahedron, (3) M9-M11 in orange for staples bonded solely to the equatorial ring of the Marks decahedron, (4) M12-M14, for staples bonded from the equatorial ring to the S polar Au₁₅ cap structure, and finally (5) M15-M19 for those bonded solely to the S Au₁₅ polar cap. The gold atoms in the sixth group comprising the two dimer staples are shown in gold, while dimer-staple sulfur atoms are shown in green and monomer-staple sulfur atoms are shown in yellow.

References

- (1) Zhu, M.; Aikens, C. M.; Hollander, F. J.; Schatz, G. C.; Jin, R. Correlating the Crystal Structure of a Thiol-Protected Au₂₅ Cluster and Optical Properties. *J. Am. Chem. Soc.* **2008**, *130*, 5883-5885.
- (2) Heinecke, C. L.; Ni, T. W.; Malola, S.; Mäkinen, V.; Wong, O. A.; Häkkinen, H.; Ackerson, C. J. Structural and Theoretical Basis for Ligand Exchange on Thiolate Monolayer Protected Gold Nanoclusters. *J. Am. Chem. Soc.* **2012**, *134*, 13316-13322.
- (3) Hanwell, M. D.; Curtis, D. E.; Lonie, D. C.; Vandermeersch, T.; Zurek, E.; Hutchison, G. R. Avogadro: An Advanced Semantic Chemical Editor, Visualization, and Analysis Platform. *J. Cheminform.* **2012**, *4*, 17.
- (4) Humphrey, W.; Dalke, A.; Schulten, K. VMD: Visual Molecular Dynamics. *J. Mol. Graph.* **1996**, *14*, 33-38.
- (5) Mathew, A.; Natarajan, G.; Lehtovaara, L.; Häkkinen, H.; Kumar, R. M.; Subramanian, V.; Jaleel, A.; Pradeep, T. Supramolecular Functionalization and Concomitant Enhancement in Properties of Au₂₅ Clusters. *ACS Nano* **2014**, *8*, 139-152.
- (6) Takano, S.; Tsukuda, T. In Protected Metal Clusters: From Fundamentals to Applications; Tsukuda, T.; Häkkinen, H., Eds.; Elsevier: Amsterdam, **2015**, p20-21.
- (7) Wiseman, M. R.; Marsh, P. A.; Bishop, P. T.; Brisdon, B. J.; Mahon, M. F. Homoleptic Gold Thiolate Catenanes. *J. Am. Chem. Soc.* **2000**, *122*, 12598-12599
- (8) Chen, S.; Wang, S.; Zhong, J.; Song, Y.; Zhang, J.; Sheng, H.; Pei, Y.; Zhu, M. The Structure and Optical Properties of the [Au₁₈(SR)₁₄]. *Angew. Chem. Int. Ed.* **2015**, *54*, 3145-3149.
- (9) Zeng, C.; Liu, C.; Chen, Y.; Rosi, N. L.; Jin, R. Gold-Thiolate Ring as a Protecting Motif in the Au₂₀(SR)₁₆ Nanocluster and Implications. *J. Am. Chem. Soc.* **2014**, *136*, 11922-11925.
- (10) Das, A.; Li, T.; Nobusada, K.; Zeng, C.; Rosi, N. L.; Jin, R. Nonsuperatomic [Au₂₃(SC₆H₁₁)₁₆]⁻ Nanocluster Featuring Bipyramidal Au₁₅ Kernel and Trimeric Au₃(SR)₄ Motif. *J. Am. Chem. Soc.* **2013**, *135*, 18264-18267.
- (11) Crasto, D.; Barcaro, G.; Stener, M.; Sementa, L.; Fortunelli, A.; Dass, A. Au₂₄(SAdm)₁₆ Nanomolecules: X-ray Crystal Structure, Theoretical Analysis, Adaptability of Adamantane Ligands to Form Au₂₃(SAdm)₁₆ and Au₂₅(SAdm)₁₆, and Its Relation to Au₂₅(SR)₁₈. *J. Am. Chem. Soc.* **2014**, *136*, 14933-14940.
- (12) Song, Y.; Wang, S.; Zhang, J.; Kang, X.; Chen, S.; Li, P.; Sheng, H.; Zhu, M. Crystal Structure of Selenolate-Protected Au₂₄(SeR)₂₀ Nanocluster. *J. Am. Chem. Soc.* **2014**, *136*, 2963-2965.
- (13) Heaven, M. W.; Dass, A.; White, P. S.; Holt, K. M.; Murray, R. W. Crystal Structure of the Gold Nanoparticle [N(C₈H₁₇)₄][Au₂₅(SCH₂CH₂Ph)₁₈]. *J. Am. Chem. Soc.* **2008**, *130*, 3754-3755.
- (14) Joshi, C. P.; Bootharaju, M. S.; Alhilaly, M. J.; Bakr, O. M. [Ag₂₅(SR)₁₈]⁻: The "Golden" Silver Nanoparticle. *J. Am. Chem. Soc.* **2015**, *137*, 11578-11581.
- (15) Song, Y.; Zhong, J.; Yang, S.; Wang, S.; Cao, T.; Zhang, J.; Li, P.; Hu, D.; Pei, Y.; Zhu, M. Crystal Structure of Au₂₅(SePh)₁₈ Nanoclusters and Insights into their Electronic, Optical and Catalytic Properties. *Nanoscale* **2014**, *6*, 13977-13986.
- (16) Zeng, C.; Li, T.; Das, A.; Rosi, N. L.; Jin, R. Chiral Structure of Thiolate-Protected 28-Gold Atom Nanocluster Protected by X-Ray Crystallography. *J. Am. Chem. Soc.* **2013**, *135*, 10011-10013.
- (17) Crasto, D.; Malola, S.; Brosofsky, G.; Dass, A.; Häkkinen, H. Single Crystal XRD Structure and Theoretical Analysis of the Chiral Au₃₀S(S-t-Bu)₁₈ Cluster. *J. Am. Chem. Soc.* **2014**, *136*, 5000-5005.
- (18) Yang, S.; Chai, J.; Song, Y.; Kang, X.; Sheng, H.; Chong, H.; Zhu, M. A New Crystal Structure of Au₃₆ with a Au₁₄ Kernel Cocapped by Thiolate and Chloride. *J. Am. Chem. Soc.* **2015**, *137*, 10033-10035.
- (19) Zeng, C.; Qian, H.; Li, T.; Li, G.; Rosi, N. L.; Yoon, B.; Barnett, R. N.; Whetten, R. L.; Landman, U.; Jin, R. Total Structure and Electronic Properties of the Gold Nanocrystal Au₃₆(SR)₂₄. *Angew. Chem. Int. Ed.* **2012**, *124*, 13114-13118.
- (20) Qian, H.; Eckenhoff, W. T.; Zhu, Y.; Pintauer, T.; Jin, R. Total Structure Determination of Thiolate-Protected Au₃₈ Nanoparticles. *J. Am. Chem. Soc.* **2010**, *132*, 8280-8281.
- (21) Liu, C.; Li, T.; Li, G.; Nobusada, K.; Zeng, C.; Pang, G.; Rosi, N. L.; Jin, R. Observation of Body-Centred Cubic Gold Nanocluster. *Angew. Chem. Int. Ed.* **2015**, *54*, 9826-9829.
- (22) Zeng, C.; Chen, Y.; Liu, C.; Nobusada, K.; Rosi, N. L.; Jin, R. Gold tetrahedra coil up: Kekulé-Like and Double Helical Superstructures. *Sci. Adv.* **2015**, *1*, e1500425.
- (23) Azubel, M.; Koivisto, J.; Malola, S.; Bushnell, D.; Hura, G. L.; Koh, A. L.; Tsunoyama, H.; Tsukuda, T.; Pettersson, M.; Häkkinen, H.; Kornberg, R. D. Nanoparticle Imaging Electron Microscopy of Gold Nanoparticles at Atomic Resolution. *Science*, **2014**, *345*, 909-912.

- (24) Jadzinsky, P. D.; Calero, G.; Ackerson, C. J.; Bushnell, D. A.; Kornberg, R. D. Structure of a Thiol Monolayer-Protected Gold Nanoparticle at 1.1 Å Resolution. *Science*, **2007**, *318*, 430-433.
- (25) Chen, Y.; Zeng, C.; Liu, C.; Kirschbaum, K.; Gayathri, C.; Gil, R. R.; Rosi, N. L.; Jin, R. Crystal Structure of the Barrel-Shaped Chiral Au₁₃₀(*p*-MBT)₅₀ Nanocluster. *J. Am. Chem. Soc.* **2015**, *137*, 10076-10079.
- (26) Zeng, C.; Chen, Y.; Kirschbaum, K.; Appavoo, K.; Sfeir, M. Y.; Jin, R. Structural Patterns at All Scales in a Nonmetallic Chiral Au₁₃₃(SR)₅₂ Nanoparticle. *Sci. Adv.* **2015**, *1*, e1500045.
- (27) Dass, A.; Theivendran, S.; Nimmala, P. R.; Kumara, C.; Jupally, V. R.; Fortunelli, A.; Sementa, L.; Barcaro, G.; Zuo, X.; Noll, B. C. Au₁₃₃(SPh-tBu)₅₂ Nanomolecules: X-ray Crystallography, Optical, Electrochemical, and Theoretical Analysis. *J. Am. Chem. Soc.* **2015**, *137*, 4610-4613.
- (28) Bahena, D.; Bhattarai, N.; Santiago, U.; Tlahuice, A.; Ponce, A.; Bach, S. B. H.; Yoon, B.; Whetten, R. L.; Landman, U.; Jose-Yacaman, M. STEM Electron Diffraction and High-Resolution Images Used in the Determination of the Crystal Structure of the Au₁₄₄(SR)₆₀ Cluster. *J. Phys. Chem. Lett.* **2013**, *4*, 975-981.
- (29) Mednikov, E. G.; Dahl, L. F. Crystallographically Proven Nanometer-Sized Gold Thiolate Cluster Au₁₀₂(SR)₄₄: Its Unexpected Molecular Anatomy and Resulting Stereochemical and Bonding Consequences. *Small* **2008**, *4*, 534-537.

Anisotropic Molecular Ionization at 1 V from Tellurium Nanowires (Te NWs)

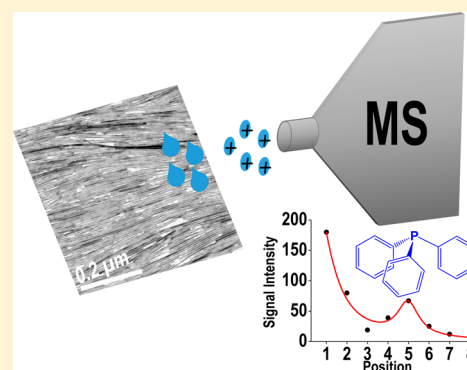
Rahul Narayanan,[†] Depanjan Sarkar,[†] Anirban Som,[†] Michael Wlekinski,[‡] R. Graham Cooks,^{*,†,‡} and Thalappil Pradeep^{*,†}

[†]DST Unit of Nanoscience (DST UNS) and Thematic Unit of Excellence (TUE), Department of Chemistry, Indian Institute of Technology Madras, Chennai 600036, India

[‡]Department of Chemistry, Purdue University, West Lafayette, Indiana 47907, United States

S Supporting Information

ABSTRACT: Ionization of molecular species from one-dimensional (1D) tellurium nanowires (Te NWs) has been achieved at 1 V. Molecules with a range of chemical functional groups gave quality mass spectra with high signal/noise ratios and no fragment ions. Experiments suggest the possibility of emission of microdroplets of solution due to the intense fields at the ends or interfaces of nanostructures. It appears that electrolytic conduction of the solution wetting of the nanostructures and not the electronic conduction of the nanostructures themselves is involved in the ionization event. Anisotropy was seen when two-dimensionally aligned Te NWs were used for ionization. The orientation effect of aligned Te NWs on molecular ion intensity is demonstrated for many analytes including organic molecules and amino acids with experiments done using a silicon substrate having aligned Te NWs. These measurements suggest the possibility of creating a MS source that extends the applicability of mass spectrometry. Analysis of a variety of analytes, including amino acids, pesticides, and drugs, in pure form and in complex mixtures, is reported. These experiments suggest that 1D nanostructures in general could be excellent ionization sources.



Creation of molecular ions using the high electric fields associated with the application of electrical potentials to small objects is embodied in the methods of field ionization (FI) and field desorption (FD) mass spectrometry.^{1,2} These ionization methods, although still in use,³ inconveniently involve unit operations in a vacuum. The development of ambient ionization methods which employ unmodified samples in the open air^{4–13} has led to ionization from solutions on paper substrates^{14–18} by application of voltages in the low kV range. Addition of carbon nanotubes to the paper substrate¹⁹ yields mass spectra with the application of just 3 V. Recently these MS techniques have found a significant role in the study of various biologically important systems also.^{20,21}

We now show that (i) one-dimensional (1D) aligned tellurium nanowires (Te NWs) supported on a suitable substrate give mass spectra with high signal/noise ratios upon application of just 1 V and that (ii) ion emission is strongly anisotropic, the orientation of the support relative to the inlet of the mass spectrometer exerting a strong effect on ion intensity as a result of preferential orientation of the Te NWs. The data suggest that solution-phase emission of charged microdroplets occurs and that electrolytic conduction over the nanostructures is responsible for this effect.

Tellurium is a semiconducting material which has high inherent tendency for anisotropic growth.²² One-dimensional (1D) nanowires of Te can be prepared with ease, in solution.²³

These nanowires can be aligned over a substrate, and this property is utilized for the measurements outlined here. In particular, the high electric fields associated with the nanowires even at low applied voltages facilitate ionization.

EXPERIMENTAL SECTION

Materials. The chemicals used for the synthesis of aligned Te NWs (TeO₂, NaOH, PVP, ammonia solution, N₂H₄·H₂O, and butanol) were purchased from Sigma-Aldrich, India. The medicinal tablets used in these experiments were purchased from a local pharmacy. All the amino acids were bought from Sisco Research Laboratories Pvt. Ltd., Mumbai, India. The pesticides were purchased from Sigma-Aldrich, India. Triphenylphosphine and tributylphosphine were bought from Spectrochem Pvt. Ltd., Mumbai, India and Wako Pure Chemical Industries Ltd., respectively. Diphenylamine (DPA) and triethylamine were from Merck Ltd., Mumbai, India. The salts for the preformed ion study were purchased from Sigma-Aldrich, India.

Synthesis of Te NWs. A well-known synthetic strategy was modified for the preparation of Te NWs.²² For this, a TeO₂ solution was prepared by dissolving 66.3 mg of TeO₂ in a basic

Received: April 28, 2015

Accepted: October 11, 2015

Published: October 11, 2015

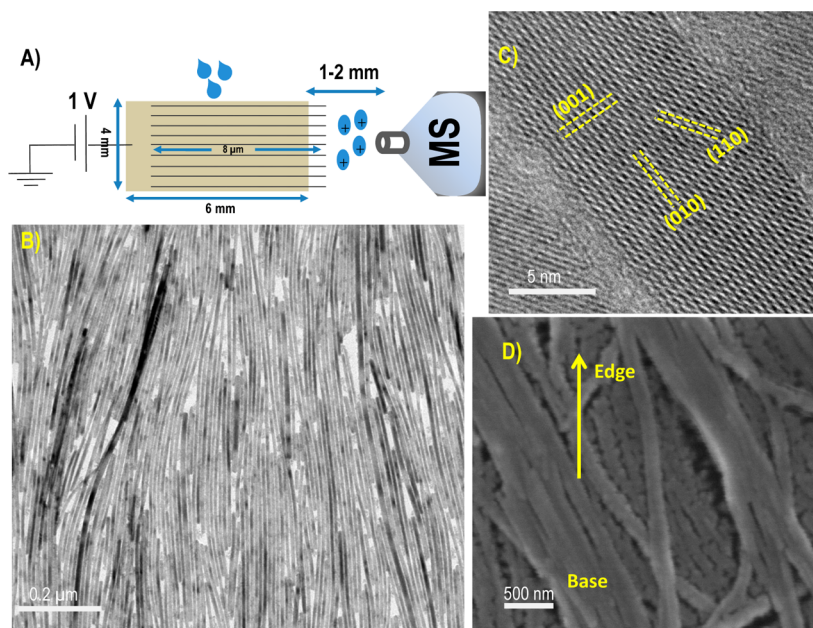


Figure 1. (A) Schematic of the ionization process (include appropriate scale bars), (B) low magnification TEM image of aligned Te NWs, (C) high magnification HRTEM image of TE NWs, and (D) FE SEM image of aligned Te NWs-coated paper clamped onto carbon tape. Various lattice planes observed are marked in C. The edge of the paper substrate is marked in D. The NWs coat the surface uniformly and a thin coating visibly changes the color of the paper. In panels B and C, copper grids were used as substrates.

medium containing 0.3 g of NaOH in 2 mL of distilled water. This solution was mixed with a polyvinylpyrrolidone (PVP) solution containing 500 mg of PVP (30 kDa) in 30 mL of distilled water in a Teflon-lined stainless steel autoclave. To this, 2.5 mL of ammonia and 500 μ L of 99% $\text{N}_2\text{H}_4 \cdot \text{H}_2\text{O}$ were added and stirred for 15 min. The reaction was kept at 180 $^\circ\text{C}$ for 3 h. A dark blue colored Te NWs suspension was obtained from which the Te NWs were precipitated by centrifugation. The NWs were characterized by transmission electron microscopy (10 μ m long wires of \sim 10–12 nm diameter) and by optical absorption spectroscopy.

Freestanding Aligned Layers of Te NWs. The freshly synthesized ultrathin Te NWs were washed thoroughly by centrifuging at 20 000 rpm, and the pellet was dispersed in 1 mL of n-butanol. The resulting suspension was carefully added dropwise to water in a Petri dish to form a thin bluish layer of NWs (8 μ m length and 10 nm diameter) between the water–butanol interface due to their buoyancy and capillary forces.²³ A schematic illustration of NWs alignment is shown in Figure S1. A TEM grid was placed upside down over the surface to capture the NW layer, which was dried and characterized under TEM. The aligned nanostructures can be transferred to other substrates such as a silicon (001) single crystal surface, which were used for the ionization anisotropy experiments discussed later in the paper.

For most experiments, the so-prepared aligned tellurium nanowire suspension in butanol was transferred directly onto a piece of Whatman 42 filter paper. For this, the filter paper was held parallel over the surface of the NW suspension in the Petri dish and the suspension was transferred carefully to the paper (by moving the substrate along the water–butanol interface). The paper was dried under laboratory conditions at room temperature and cut using a pair of scissors in a rectangular shape in dimensions of 4 \times 6 mm (base \times height). In the case of Si, a precut substrate (by using a diamond knife) was used to deposit the Te NWs. It was mounted on a copper clip and held

in front of the mass spectrometer (MS) inlet at a distance of \sim 1–2 mm. This distance was set manually and was not precisely controlled. The copper clip was connected to an external voltage supply, and a voltage of 1 V was applied for all the measurements except when indicated otherwise. The paper was not cut in the triangular shape typically used in paper spray ionization to ensure that the enhanced fields at the (macroscopic) corners of the triangular paper tip did not cause an artifact in the measurement of effects associated with the microscopic NW features. Many samples were analyzed including amino acids, pesticides, and commercial medical tablets. All samples (2 μ L) were used at a concentration of 50 ppm. For all the experiments, HPLC grade methanol (Sigma-Aldrich) and methanol/water (1:1 by volume) were used as solvents. All the mass spectra were recorded at 1 V in positive ion mode with negative ion mode data also being acquired when analyzing preformed ions. The following experimental conditions were maintained for all the measurements: source voltage: \pm 1 V; capillary temperature: 150 $^\circ\text{C}$; capillary voltage: 0 V; and tube lens voltage: 0 V.

Techniques. All the measurements were made using an ion trap LTQ XL (Thermo Scientific, San Jose, California). Collision-induced dissociation was used for MS² analysis. A field emission scanning electron microscope (FE SEM) was used for imaging of the paper. Raman measurements were made using a Witec GmbH Confocal Raman Microspectrometer, Germany with 532 and 633 nm laser excitation sources.

RESULTS AND DISCUSSION

Suitably cut Te NWs-coated paper was supplied with the desired potential, delivered from a power supply, and the modified paper was mounted in front of the MS inlet for the current experiments. A schematic of the process is shown in Figure 1A. Here a rectangular piece of paper was held in front of the MS inlet at a distance of \sim 1–2 mm. The shape of the paper is unimportant in the measurements. Normal paper

(without NWs) does not give detectable ion signals below 500 V (Figure S2B). Various analytes in methanol/water (1:1) at a concentration of 50 ppm were added onto the paper with a micropipette. About 2 μL of sample (i.e., 10^{-7} g, absolute) was used for a single measurement. Under these conditions, the aligned Te NW paper gave ions which were analyzed using an ion trap LTQ XL mass spectrometer. The rectangularly cut paper was examined with a field emission scanning electron microscope (FE SEM). The image, shown in Figure 1D, revealed the presence of aligned Te NWs on the paper. The corresponding low magnification TEM and HRTEM images of Te NWs on a standard copper grid display the same features, as shown in Figure 1B and 1C.

A fascinating feature of ionization at low voltage is the presence of $[\text{M} + \text{H}]^+$ (M = molecule) without any fragment ions. These low voltage mass spectra are characterized by their high signal/noise ratios. Such a low voltage (1 V) mass spectrum of DPA is shown in Figure 2A. The figure represents

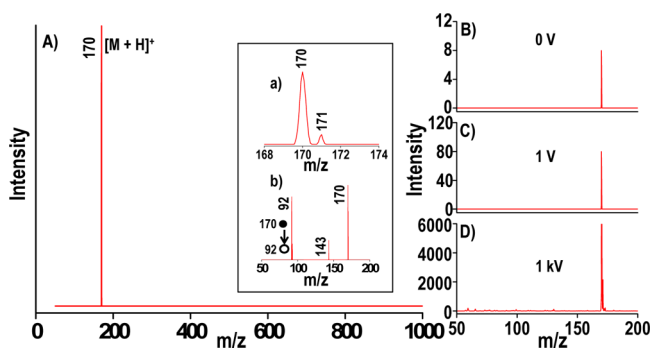


Figure 2. (A) Full scan mass spectrum of 100 ng DPA with inset showing isotopic distribution of the molecular ion peak (a) and MS^2 of molecular ion peak (b). (B), (C), and (D) show mass spectra of DPA at 0 V, 1 V and 1 kV, respectively. There are processes which give minor signals even at 0 V.

a full range mass spectrum which was collected at 1 V by applying 50 ppm of DPA in methanol/water to the substrate. The volume of the sample solution used for a single experiment was 2 μL (corresponding to 100 ng, absolute). Typically, 50 scans were recorded and averaged from this quantity of analyte. The spectrum is characterized by the presence of the protonated molecule at m/z 170 with a well-defined isotopic distribution (shown in the inset). The identity of the protonated molecule was confirmed by MS^2 analysis, which is also shown as an inset. The expected benzene loss product was seen at m/z 92. The results are shown in Figure 2B and Figure 2C, which represent the mass spectrum of diphenylamine at 0 and 1 V, respectively. (There are processes which can give minor signal even at 0 V, but these depend on the experimental and atmospheric conditions.) For comparison, the mass spectrum of diphenylamine at 1 kV (using the same Te NWs-coated paper) is shown in Figure 2D. This has a more noisy background and lower signal/noise ratio than the mass spectrum at 1 V. The variation of S/N ratio as a function of voltage is depicted in Figure S2C. It is important to note that the signal at 1 V is 10^2 times smaller than that at 1 kV. This is an approximation made, as signal intensity is a function of many factors (substrate to MS inlet distance, capillary voltage, capillary temperature, etc.). Integration time for 1 V and 1 kV spectra are 0.4 and 1.5 min, respectively.

The role of aligned nanostructures (Te NWs) in ejecting ions at 1 V has been verified by conducting the same experiment with similarly cut Whatman 42 filter paper (without Te NWs on it). This paper did not give any ions at low voltage demonstrating that 1D nanostructures can act as electrodes that eject ions even at 1 V. The threshold voltage for ion ejection from Whatman 42 filter paper of the same shape and placement without NWs was tested with various analytes and a minimum of 400–500 V was found to be necessary for ejecting ions. The results are shown in Figure S2A and Figure S2B, which represent the mass spectra of DPA from normal Whatman 42 filter paper at 500 V and below 500 V, respectively. The dependence of signal intensity on voltage was tested with nanowire-coated paper and normal Whatman 42 filter paper. The results are shown in Figure S2D and Figure S2E, respectively. Here DPA at 50 ppm was analyzed at various voltages starting from 1 V to 5 kV (for nanowire-coated paper). The data showed an enhancement in signal intensity with increasing voltage, plateauing at 3 kV. Similar results were obtained for normal Whatman filter paper also.

Ionization at 3 V from protruding carbon nanotubes has been suggested to follow a “field ionization of microdroplet” mechanism.^{24,25} The main feature of this mechanism is that ionization occurs in the solution phase. This was supported by various experimental data. The present data also support solution-phase ionization and emission of charged microdroplets. The key role of solvent in the ionization at 1 V was tested with various amines and phosphines by varying the pH. Two amines (diphenylamine and triethylamine) and two phosphines (triphenylphosphine and tributylphosphine) were selected, and mass spectra of these analytes were recorded before and after the addition of dilute acid (HCl). The results are shown in Figure 3. The results show an enhancement in

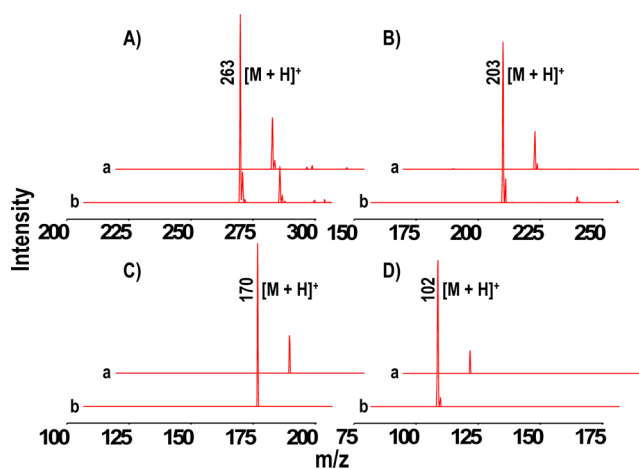


Figure 3. Signal intensity enhancement for various analytes (a, before adding HCl, and b, after adding HCl). (A) Triphenylphosphine, (B) tributylphosphine, (C) diphenylamine, and (D) triethylamine.

intensity of the protonated molecule after the addition of dilute acid (HCl). This reveals the role of solution-phase acid/base equilibria in the ionization process and supports the proposed solution-phase ionization mechanism. This was also supported by another experiment of introducing vapors of a highly volatile analyte species (triethylamine dissolved in acetone) between the tip of the paper and the MS inlet. The absence of a molecular ion peak in this case supports the solution-phase

ionization mechanism and is not consistent with ionization in the gas phase.

Solution-phase ionization at 1 V was further supported by results obtained for salts from which preformed ions of both the polarities are observed in low-voltage mass spectra. Solutions of preformed ions were made in methanol/water (1:1) at a concentration of 50 ppm, and they were introduced onto a rectangularly cut Te NWs-coated paper in volumes of 2 μL at a time (i.e., again in 100 ng amounts). Figure 4 represent

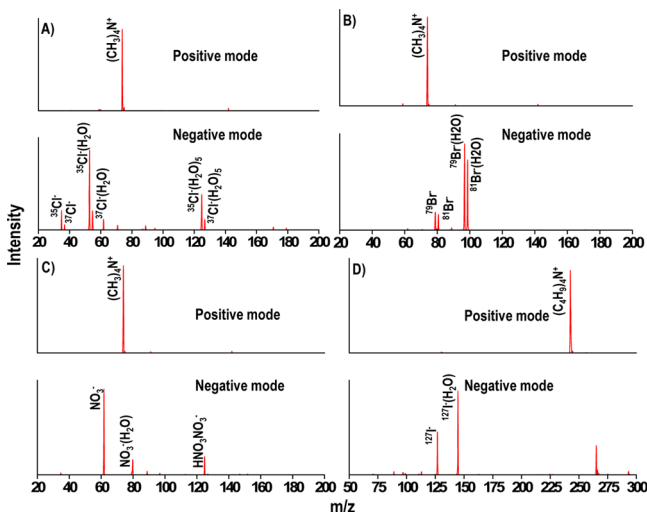


Figure 4. Analysis of preformed ions. (A) Tetramethylammonium chloride, (B) tetramethylammonium bromide, (C) tetramethylammonium nitrate, and (D) tetrabutylammonium iodide.

the results obtained. The mass spectra were collected both in positive and negative modes for the positive and negative counterions, respectively. These experiments also substantiate solution-phase ionization via microdroplet emission.

To evaluate the structural and chemical changes that might have occurred to the Te NWs on the paper due to the applied voltage, Raman spectra of the nanowire-coated paper were recorded before and after the experiment. Three kinds of samples (neutral species, positively charged species, and negatively charged species) were analyzed continuously for 25 min, and Raman spectra of the paper were recorded before and after analysis. These spectra (Figure 5) showed a prominent peak due to the Raman active A_1 singlet mode of the t-Te lattice vibration.²⁶ The other peaks at 267 and 375 cm^{-1} are due to various vibrational modes of Te–O bond.²⁷ These were collected at various points on the paper to ascertain reproducibility. For a better presentation of the Raman spectra before and after experiments, a vertical shift of spectra has been done. There may be a small intensity variation in the spectrum before and after the experiment. That variation in the intensity is due to the changes in the experimental parameters, like the focus spot for Raman measurement, the amount of NWs present at that point (can be seen from the FE SEM images that the NWs concentration is not same at all the points), and so forth. There is no physical degradation seen for the NWs. The data suggest that the Te NWs are unchanged in the course of the experiment.

The experiments presented suggest that ionization does not lead to changes in the electrodes. Tellurium being a semiconductor, application of a potential at the electrode surface should result in a potential drop. We measured a

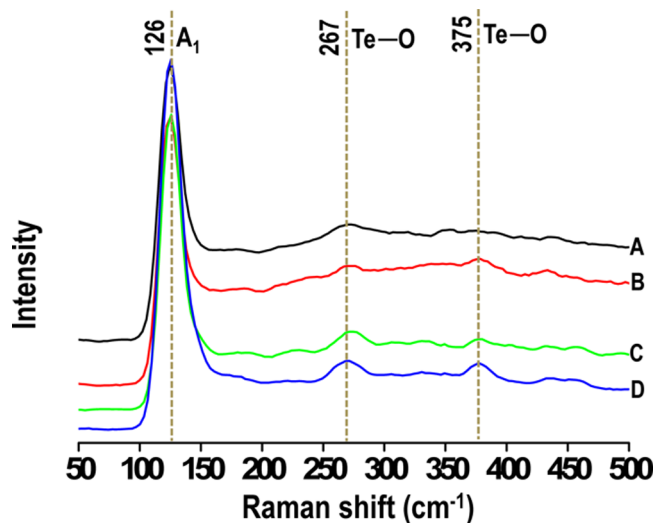


Figure 5. Raman spectra of tellurium-coated paper. (A) Before the experiment, after the experiment for (B) neutral molecules, (C) positive counterpart of a preformed ion, and (D) negative counterpart of a preformed ion. The spectra have been shifted vertically for clarity.

potential drop of 0.40 V upon the application of 1 V on the NWs-coated paper (Supporting Information, SI-3). The existence of ions even under these conditions implies that ion formation is unlikely to be occurring at this reduced potential at the end of the NWs (opposite to the point of electrical contact). Similar to our previous report,¹⁹ experiments with vapors introduced between the electrodes and the mass spectrometer inlet did not produce ions. Creation of ions from solutions and their detection as preformed ions imply ionization in solution, and emission presumably as microdroplets. Conduction seems to involve ions in the solution covering the NWs and droplet emission occurs from the end of the wet electrode where the field is highest. This is supported by the enhancement of ion signals in acidic pH for a range of analytes.

In order to verify the mechanism of ionization, solutions of the same analyte (DPA) were prepared in a homologous series of alcohols with decreasing dielectric constant. Although ions were detected in methanol and ethanol, they were not detectable in butanol and only with substantial reduction in intensity in propanol (see Table S1). These findings highlight the key role of solvents in the ionization mechanism. The mechanism of ionization was tested with another experiment for which solutions of DPA (50 ppm) in butanol with varying conductivity were prepared. This was done by adding an external ionic species, at different concentrations, to the analyte system. Butanol solution of sodium acetate was prepared and was added to the analyte solutions so that the final salt concentrations were 1, 10, 50, 100, and 500 ppm. Mass spectra were collected, and the signal intensity is listed in Table S2. Ions were not detectable up to 50 ppm concentration of sodium acetate (in the analyte system), but ionization started occurring at 100 ppm of sodium acetate. This is ascribed to the enhancement of electrolytic conductivity of the analyte system. This confirms the role of electrolytic conductivity of the solution in ejecting ions from NWs. Electronic conductivity of the nanostructure does not seem to be important. This is supported by the fact that the nature of carbon nanotubes, whether single-walled or multiwalled, did not make a difference in ionization.¹⁹

The dependence of alignment of these nanostructures on molecular ion intensity has been tested with various analytes. To do this, the aligned tellurium nanowire suspension was transferred on to a square cut silicon (001) single crystal substrate and analysis of various molecules was done with the silicon substrate in different positions (from position 1 to 8 as shown in Figure 6A). Alignment of NWs was checked with

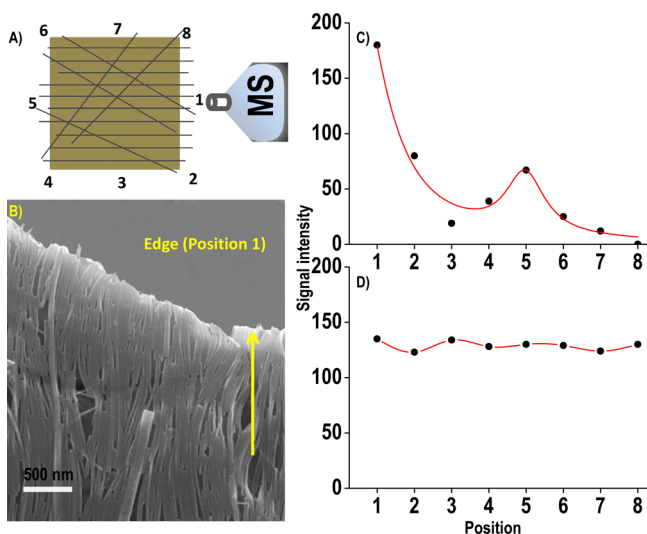


Figure 6. Analysis of TPP at different positions of a silicon (001) single crystal substrate coated with Te NWs. (A) Schematic of the silicon substrate showing different positions (from 1 to 8) which are analyzed consecutively, (B) microscopic image of the silicon substrate coated with aligned Te NWs. At the edge of the Si substrate, the Te NWs would bend downward. Variation in ion intensity of triphenylphosphine collected from (C) aligned Te NWs, and (D) nonaligned Te NWs, both deposited on silicon substrates. Some disorder in the alignment of NWs is shown.

SEM imaging. The substrate with aligned Te NWs was held in front of the MS inlet at an approximate distance of 1 mm, and it was rotated repeatedly in steps of approximately 45° anticlockwise with respect to the MS inlet. The rotation caused different regions of the substrate to face the MS inlet in turn. Measurements were done with various analytes. Results for a set of experiments using TPP are shown in Figure 6C, and others are given in Figure 7. There is a large variation in molecular ion intensity at different positions of the silicon

substrate. In particular, we note that positions 1 and 5 have much larger intensities than others. Analysis of these particular regions under a microscope revealed the difference in alignment of nanostructures in these positions with respect to the MS inlet. The microscopic image is shown in Figure 6B.

The edge of the silicon substrate is marked in the image, and the alignment of nanostructures is shown by an arrow. The positions where ion intensity got enhanced are those at which nanowire alignment is along the axis of the MS inlet. Other regions where intensity is less are those where NWs lie at an angle with respect to the mass spectrometer inlet. At certain positions, most of the NWs are orthogonal to the mass spectrometer inlet. However, even in these positions, certain NWs will be protruding from the substrate oriented toward the inlet as would be expected from Figures 1B and 1D. This makes a gradual variation in ion intensity with positions with maxima at 0 and 180° with respect to the MS inlet.

Positions 1 and 5 are edges of the substrate cut that the tips of NWs facing the MS inlet. The Te NWs at these positions are 8 μm in length and 10 nm in diameter. These are distributed over a 4 mm long edge (the substrate dimension is 4×4 mm). So there can be 4×10^5 wires over the entire edge (assuming monolayer coating). The distribution of NWs is unlikely to be the same at positions 1 and 5, because they are nanoscale materials and the monolayer is made by solution casting. There is difference in morphology as well as number density between these positions (Figure S4A). These contribute to variations in the ion intensity at apparently equivalent positions such as 1 and 5 as well as 7 and 3. To confirm the existence of anisotropy in such ionization events we performed measurements with a variety of analytes as well as varying substrates. The results show the reproducibility of the main finding of anisotropy in the experiment. These data are shown in Figure S5 and S6. The difference in arrangement of NWs can be understood from microscopy, in general as seen in Figure 1B. Nearly similar intensities are observed upon reversal of electrode positions. Because precise position control was not possible in these experiments (note that the control possible in electrode alignment is much smaller than the dimensions of NWs), the observed alignment-dependent intensity variation was confirmed by performing similar measurements with a silicon substrate deposited with nonaligned Te NWs (Figure S4B). In this case, all positions have almost equal intensity. Data using TPP are shown in Figure 6D, and similar results for other analytes are presented in Figure 7. Signal intensity data of DPA

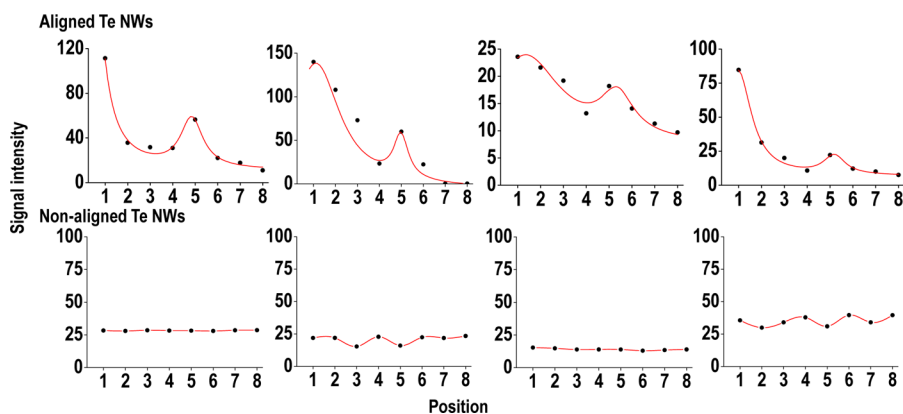


Figure 7. Variation of signal intensity with different orientations of the TeNWs: aligned (top) and nonaligned (bottom) for (A) diphenylamine, (B) isoleucine, (C) threonine, and (D) phenyl alanine. Positions are as in Figure 6.

as a function of position for both types of Te NWs are shown in Table S3.

Because it was difficult to accurately reproduce the position of the substrate containing Te NWs with respect to the entrance to the mass spectrometer, the effects of applied potential were explored by switching from 1 to 0 V keeping other conditions the same. Similarly, orientation was studied under two extreme conditions of parallel and orthogonal. These experiments were done at various pH values for DPA, thymine, adenine, and guanine, and the results are summarized in the Supporting Information, Table S4. These data confirm that (i) there is a significant orientation effect (an order of magnitude or more), (ii) there is an increase in ion signal of about a factor of 2 on going from 0 to 1 V, and (iii) there is a significant pH effect with acidic solutions strongly favoring observation of $[M + H]^+$.

The applicability of this low-voltage ionization has been tested with various analytes. These include amino acids, pesticides, and drugs. The zwitterionic nature of amino acids allows them to exist in solution as charged species. Ionization of these species was achieved at 1 V from Te NWs-coated paper, and the result of an experiment using phenylalanine is shown in Figure 8A. The spectrum is dominated by the protonated

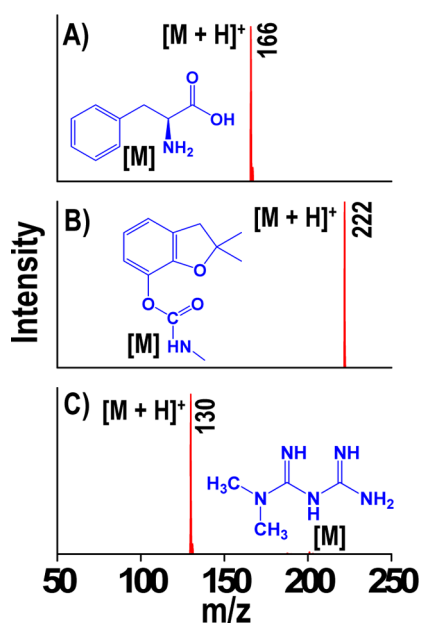


Figure 8. Detection of (A) amino acid (phenyl alanine), (B) carbofuran (from the surface of an orange), and (C) content of a medicinal tablet (metformin) at 1 V.

molecule peak at m/z 166. This study was extended to various amino acids ranging from alanine (m/z 90) to methionine (m/z 150) as shown in Figure S7. Similarly, various pesticides were studied. Pesticides at 50 ppm concentration were applied on the surface of an orange. The rectangle of nanowire-coated paper was rubbed on the orange surface and solvent (methanol/water) added, and mass spectra were collected at 1 V. The spectrum of carbofuran recorded in this way is shown in Figure 8B. The result suggests the possibility of detecting 250 ng of pesticides from fruit surfaces. Results for various pesticides are shown in Figure S8. The figure shows mass spectrum of chlorpyrifos, parathion, and methyl parathion with their MS^2 data, confirming their identity. The ultralow

voltage ionization method has been extended to identify the contents of various medicinal tablets also. A number of tablets were purchased from a local pharmacy, and the tablet surface was rubbed with the Te NWs-coated paper and analyzed using methanol/water at 1 V. Figure 8C presents the mass spectrum of metformin which was analyzed from a metformin tablet. Various other tablets were analyzed and the signal intensity data are given in Table S5.

CONCLUSIONS

In conclusion, we present a widely applicable low voltage ionization process involving one-dimensional nanostructures. Ionized molecular species are detected without accompanying fragment ions. It is shown that ionization is independent of the substrate used for the nanostructures. Ion formation occurs as a result of the enhanced electric fields at the tips of the nanostructures causing charged droplet emission. Electrolytic conduction in solution over the nanostructures is found to be the basis for conductivity. Alignment of nanostructures with respect to the mass spectrometer inlet has a significant effect on ion intensity. The observed anisotropy is ascribed to the effects of NW alignment on the electric field direction, but it might also contain contributions from physical flow profiles across the oriented NWs. High sensitivity and selectivity to the molecular species expressed on surfaces offer certain analytical advantages to this methodology. Simplification of mass spectrometry ionization is possible using easily prepared nanostructures. The data also indicate that there are processes that produce ions at zero applied potential; these processes are studied in a separate publication.²⁸

ASSOCIATED CONTENT

Supporting Information

The Supporting Information is available free of charge on the ACS Publications website at DOI: 10.1021/acs.analchem.5b01596.

Additional information as noted in text (PDF)

AUTHOR INFORMATION

Corresponding Authors

*E-mail: pradeep@iitm.ac.in. Fax: (+) 91-44-22570545.

*E-mail: cooks@purdue.edu.

Notes

The authors declare no competing financial interest.

ACKNOWLEDGMENTS

T.P. acknowledges financial support from the Department of Science and Technology, Government of India, for his research programme on nanomaterials. R.N. and D.S. thank the University Grants Commission for research fellowships. A.S. thanks CSIR for a research fellowship. R.G.C. acknowledges funding from the Separations and Analysis Program, Office of Basic Energy Sciences, U.S. Department of Energy, DE-FG02-06ER15807.

REFERENCES

- (1) Beckey, H. D. *Int. J. Mass Spectrom. Ion Phys.* **1969**, *2*, 500–503.
- (2) Robertson, A. J. B. *J. Phys. E: Sci. Instrum.* **1974**, *7*, 321.
- (3) Hsu, C. S. *Prepr. Symp. Am. Chem. Soc., Div. Fuel Chem.* **2011**, *56*, 421.
- (4) Takats, Z.; Wiseman, J. M.; Gologan, B.; Cooks, R. G. *Science* **2004**, *306*, 471–473.

- (5) Zhang, J.; Huo, F.; Zhou, Z.; Bai, Y.; Liu, H. *Huaxue Jinzhan* **2012**, *24*, 101–109.
- (6) Takats, Z.; Cotte-Rodriguez, I.; Talaty, N.; Chen, H.; Cooks, R. G. *Chem. Commun.* **2005**, 1950–1952.
- (7) Zhang, X.; Wang, N.; Zhou, Y.; Liu, Y.; Zhang, J.; Chen, H. *Anal. Methods* **2013**, *5*, 311–315.
- (8) Monge, M. E.; Harris, G. A.; Dwivedi, P.; Fernandez, F. M. *Chem. Rev.* **2013**, *113*, 2269–2308.
- (9) Ifá, D. R.; Wu, C.; Ouyang, Z.; Cooks, R. G. *Analyst* **2010**, *135*, 669–681.
- (10) Huang, M.-Z.; Cheng, S.-C.; Cho, Y.-T.; Shiea, J. *Anal. Chim. Acta* **2011**, *702*, 1–15.
- (11) Harris, G. A.; Galhena, A. S.; Fernandez, F. M. *Anal. Chem.* **2011**, *83*, 4508–4538.
- (12) Watrous, J. D.; Alexandrov, T.; Dorrestein, P. C. *J. Mass Spectrom.* **2011**, *46*, 209–222.
- (13) *Ambient Ionization Mass Spectrometry*; Domin, M.; Cody, R., Eds.; Royal Society of Chemistry: London, U.K., 2015; Vol. 2.
- (14) Liu, J.; Wang, H.; Manicke, N. E.; Lin, J.-M.; Cooks, R. G.; Ouyang, Z. *Anal. Chem.* **2010**, *82*, 2463–2471.
- (15) Cody, R. B.; Dane, A. J. *Rapid Commun. Mass Spectrom.* **2014**, *28*, 893–898.
- (16) Yang, Q.; Wang, H.; Maas, J. D.; Chappell, W. J.; Manicke, N. E.; Cooks, R. G.; Ouyang, Z. *Int. J. Mass Spectrom.* **2012**, *312*, 201–207.
- (17) Sarkar, D.; Sen Gupta, S.; Narayanan, R.; Pradeep, T. *J. Am. Soc. Mass Spectrom.* **2014**, *25*, 380–387.
- (18) Liu, J.; Manicke, N. E.; Zhou, X.; Cooks, R. G.; Ouyang, Z. *New Dev. Mass Spectrom.* **2015**, *2*, 389–422.
- (19) Narayanan, R.; Sarkar, D.; Cooks, R. G.; Pradeep, T. *Angew. Chem., Int. Ed.* **2014**, *53*, 5936–5940.
- (20) Porcari, A. M.; Fernandes, G. D.; Belaz, K. R. A.; Schwab, N. V.; Santos, V. G.; Alberici, R. M.; Gromova, V. A.; Eberlin, M. N.; Lebedev, A. T.; Tata, A. *Anal. Methods* **2014**, *6*, 2436–2443.
- (21) Douglass, K. A.; Venter, A. R. *J. Mass Spectrom.* **2013**, *48*, 553–560.
- (22) Qian, H. S.; Yu, S. H.; Gong, J. Y.; Luo, L. B.; Fei, L. F. *Langmuir* **2006**, *22*, 3830–3835.
- (23) Moon, G. D.; Lee, T. I.; Kim, B.; Chae, G. S.; Kim, J.; Kim, S. H.; Myoung, J.-M.; Jeong, U. *ACS Nano* **2011**, *5*, 8600–8612.
- (24) Xu, X.; Lu, W.; Cole, R. B. *Anal. Chem.* **1996**, *68*, 4244–4253.
- (25) Wang, G.; Cole, R. B. *Anal. Chim. Acta* **2000**, *406*, 53–65.
- (26) Pine, A. S.; Dresselhaus, G. *Phys. Rev. B* **1971**, *4*, 356–371.
- (27) Samal, A. K.; Pradeep, T. *J. Phys. Chem. C* **2009**, *113*, 13539–13544.
- (28) Wleklinski, M.; Li, Y.; Bag, S.; Narayanan, R.; Sarkar, D.; Pradeep, T.; Cooks, R. G. *Anal. Chem.* **2015**, *87*, 6786.

Supporting information

Anisotropic Molecular Ionization at 1 V from Tellurium Nanowires (Te NWs)

R. Narayanan¹, D. Sarkar¹, A. Som¹, M. Wleklinski², R. G. Cooks^{1,2*} and T. Pradeep^{1*}

Number	Description	Page no.
SI-1	Schematic illustration of NWs alignment	3
SI-2	Low voltage mass spectra using different surfaces	4
SI-3	Calculation of potential drop	4-5
SI-4	FE SEM images	5
SI-5	Anisotropic measurements.	6

SI-6	Anisotropic measurements.	6
SI-7	Analysis of amino acids	7
SI-8	Detection of various pesticides from the surface of an orange	8
Table S1	Signal intensity of diphenylamine in different solvents.	9
Table S2	Signal intensity of diphenylamine in butanol solutions of different conductivity	9
Table S3	Signal intensity of DPA collected from positions 1 to 8 on a silicon substrate coated with aligned and non-aligned Te NWs.	10

Table S4	Variation of protonated molecule signal intensity	11-12
Table S5	Signal intensity of various tablets	13

Supporting information 1:

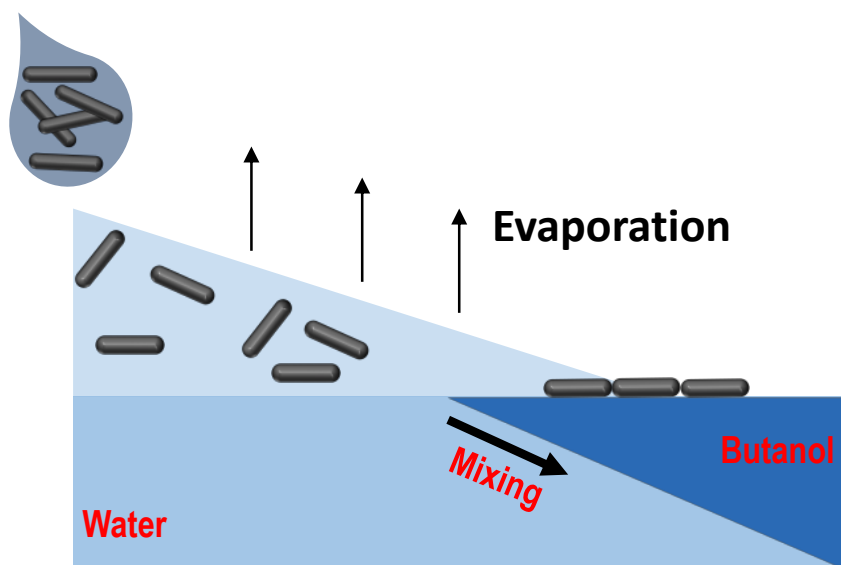


Figure S1. Schematic illustration of Te NWs alignment along water-butanol interface. Here Te NWs suspension was introduced to a petridish containing water with a micropipette. The capillary and buoyancy forces help the NWs to align along the interface. This can be easily transferred to a substrate under study. **Note that the alignment is side by side along the interface.**

Supporting information 2

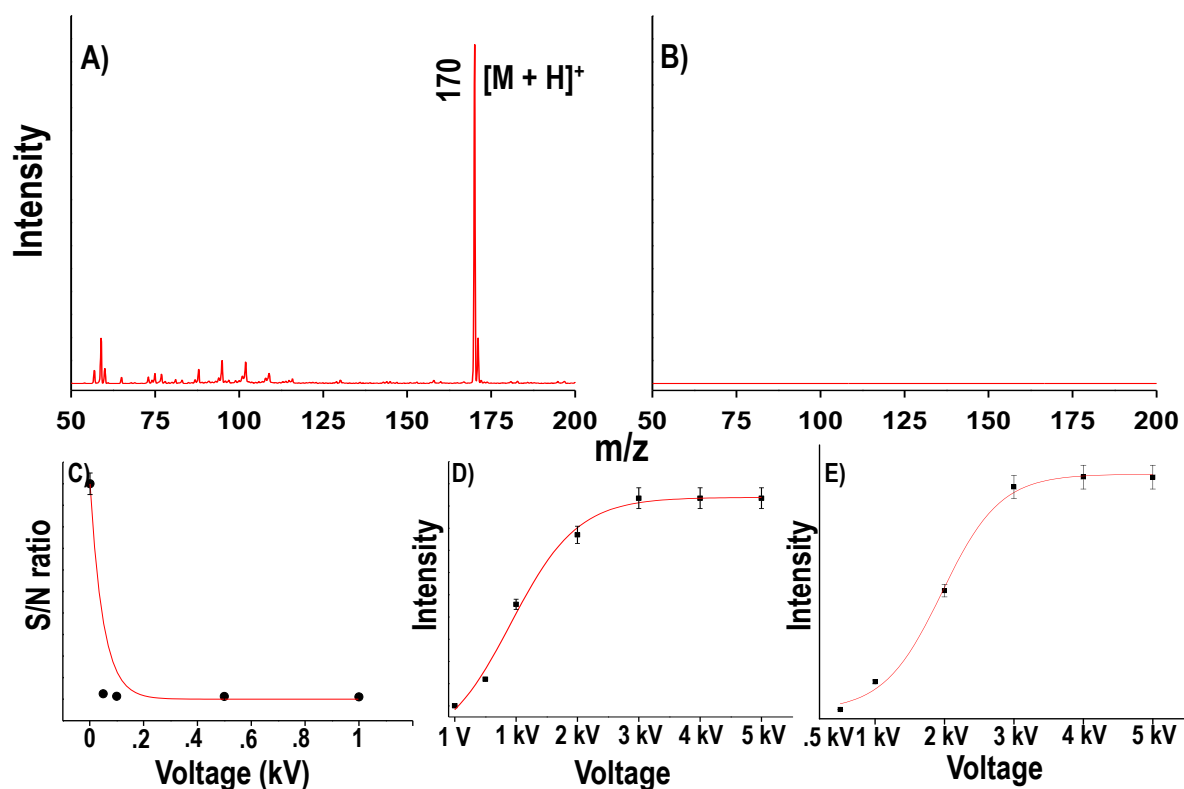


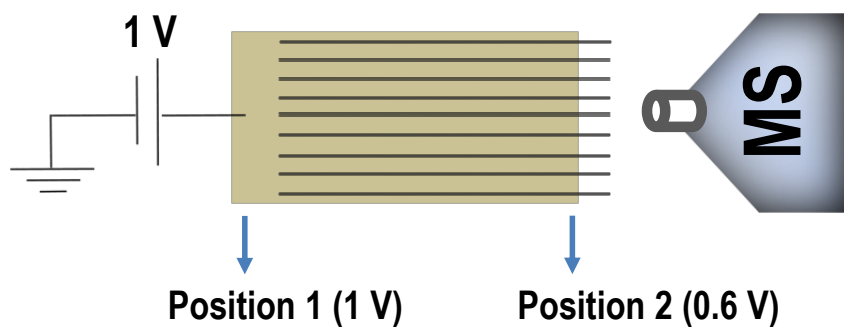
Figure S2. A) Mass spectrum of DPA from normal paper at 500 V, B) spectrum below an applied potential of 500 V, C) variation of S/N ratio with voltage for DPA, D) variation of signal intensity with voltage from a Te NW-coated paper, and E) variation of signal intensity with voltage from an ordinary Whatman filter paper. Parts D) and E) are separately normalized but the maximum ion currents are similar.

Supporting information 3:

Calculation of potential drop

Potential drop was determined manually by measuring the voltage at two positions using a multimeter. Potential at position 1 = 1 V, potential at position 2 = 0.6 V (with respect to the copper clip). So there is a decrease in potential of 0.4 V (1 - 0.6) across the paper due to paper and Te NWs resistances.

Here position 1 refers to paper edge which is near to copper clip and position 2 refers to edge near to MS inlet. This is shown in the schematic below.



Supporting information 4:

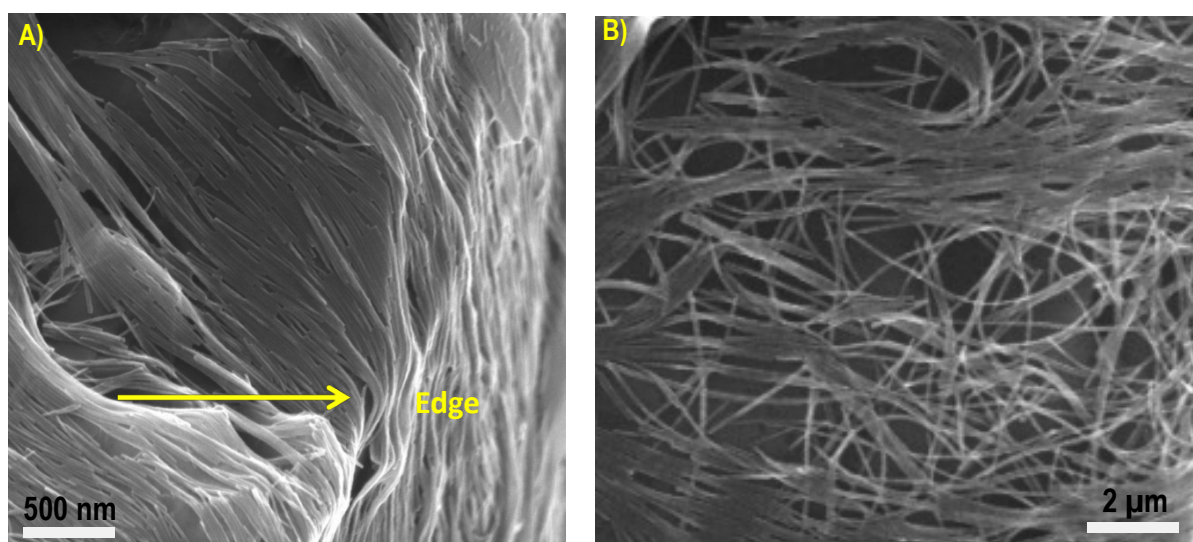


Figure S4. FE SEM image of A) position 5 and B) non-aligned NWs deposited on Si substrate.

Note: The deformation and discontinuity of NWs at position 5 edge is clearly visible in the image. Also there is bending of long NWs at the edge.

Supporting information 5:

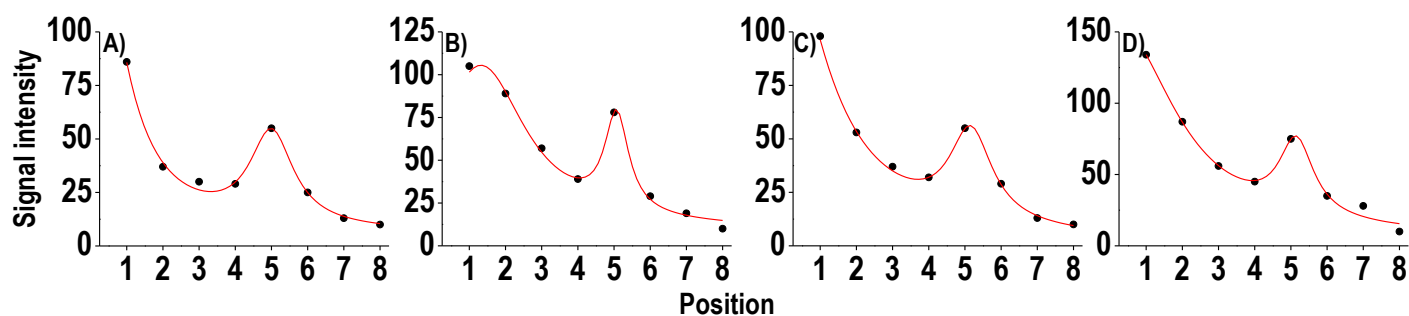


Figure S5. Anisotropic measurements done on multiple analytes with aligned Te NWs on silicon substrate, A) tributylphosphine, B) glutamine, C) alanine, and D) thymine.

Supporting information 6:

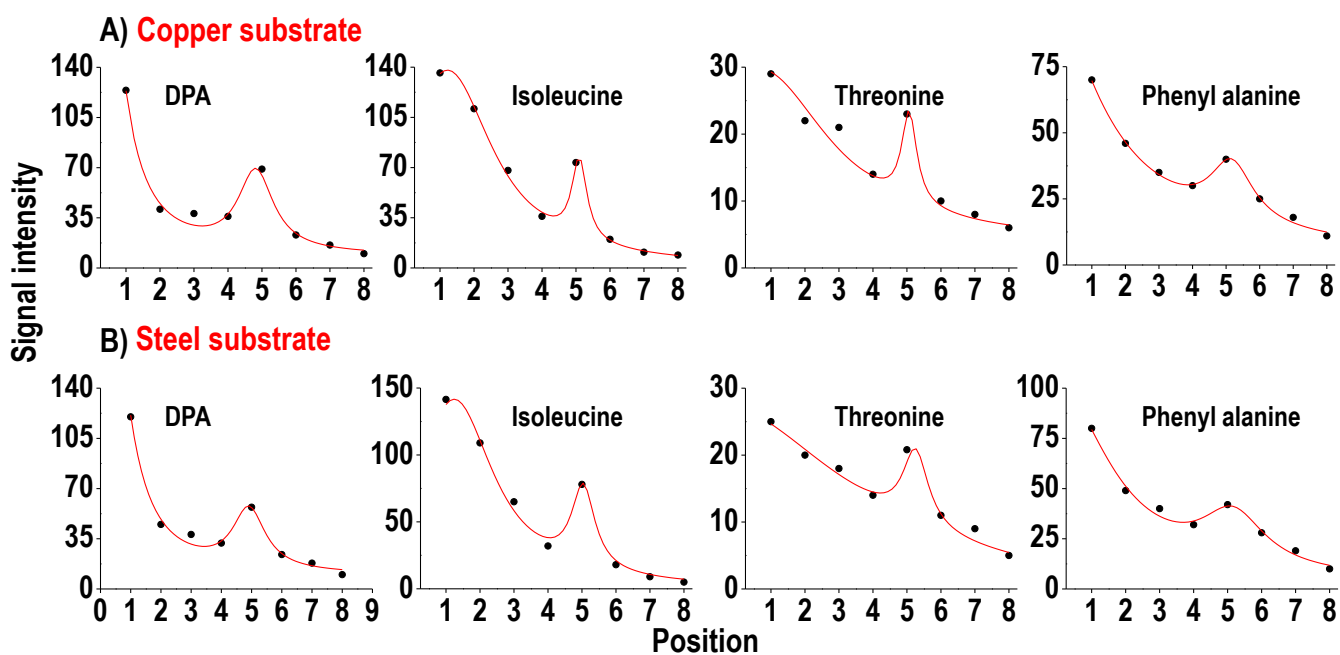


Figure S6. Anisotropic measurements done with aligned Te NWs on A) copper and B) steel substrates. Data with various analytes are shown.

Supporting information 7:

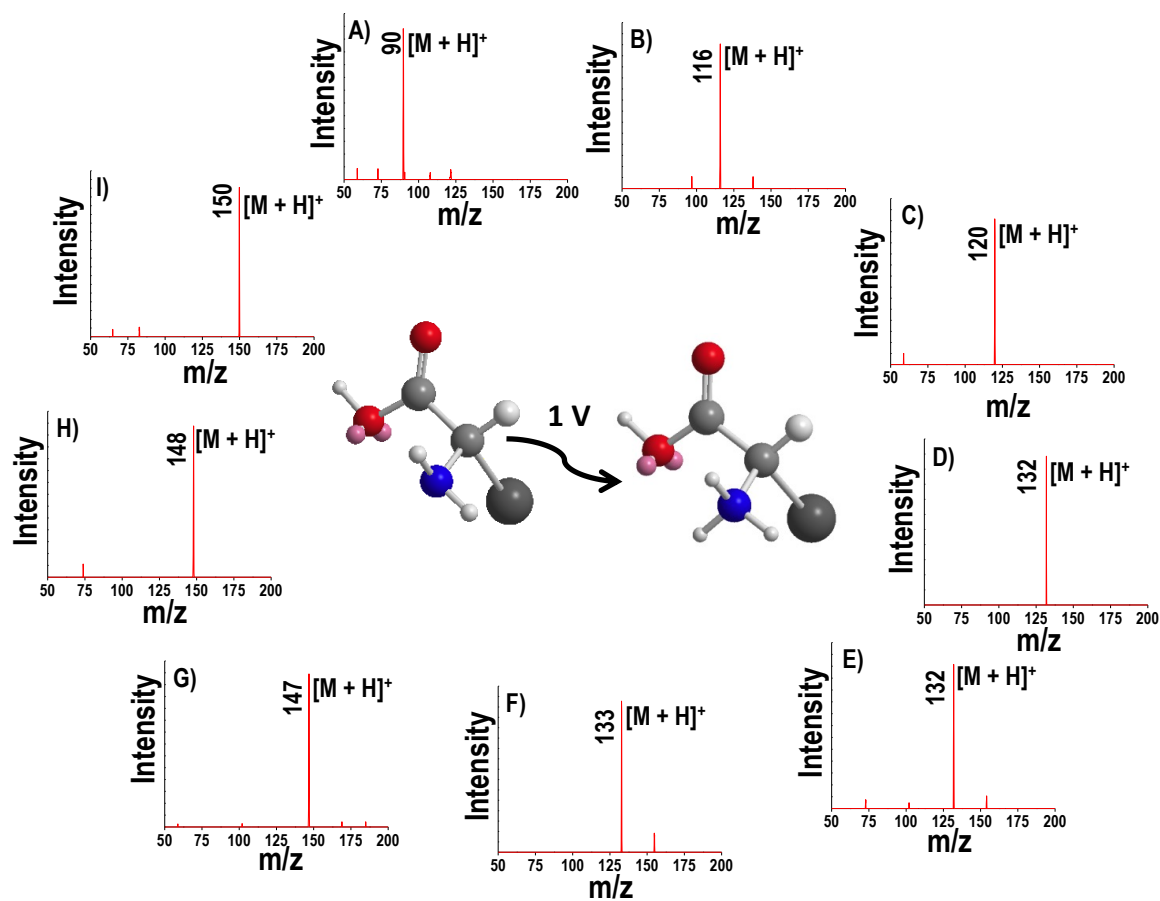


Figure S7. Mass spectra of various amino acids at 1 V using Tellurium nanowire-coated paper. A) Alanine, B) proline, C) threonine, D) isoleucine, E) leucine, F) asparagine, G) glutamine, H) glutamic acid and I) methionine.

Supporting information 8:

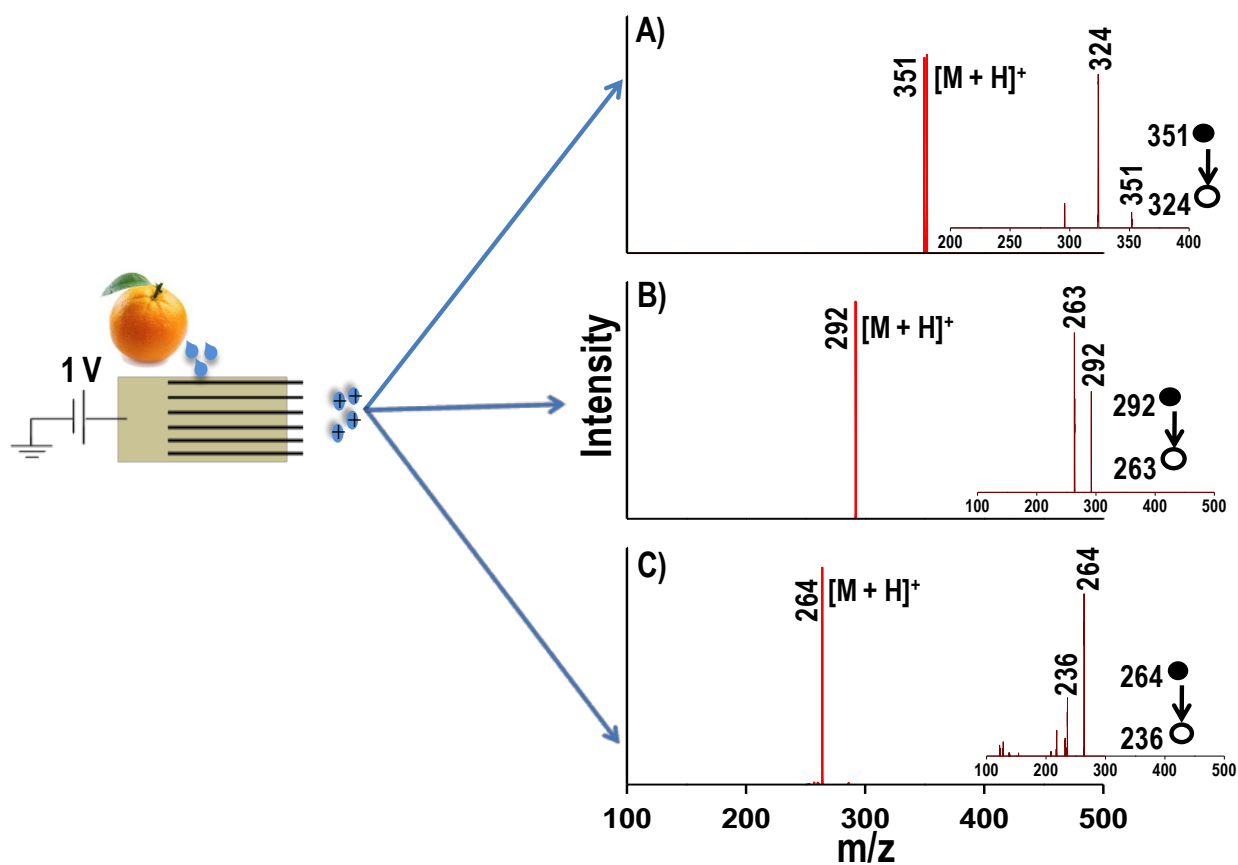


Figure S8. Detection of various pesticides from the surface of an orange at 1 V using tellurium nanowire-coated paper. A) Chloropyrifos, B) parathion and C) methylparathion. MS² data are given along with the mass spectra.

Table S1. Signal intensity of diphenylamine in different solvents at 1 V

No	Analyte system studied	m/z	Signal intensity
1	DPA in methanol	170	4.0×10^{-1}
2	DPA in ethanol	170	3.2×10^{-1}
3	DPA in propanol	170	2.5×10^{-2}
4	DPA in butanol	170	0

Table S2. Signal intensity of diphenylamine in butanol solutions of different conductivity recorded at 1 V.

No	Analyte system studied	m/z	Signal intensity
1	DPA (in butanol without sodium acetate)	170	0
2	DPA (Butanol with 1ppm sodium acetate)	170	0
3	DPA (Butanol with 10 ppm sodium acetate)	170	0
4	DPA (Butanol with 50 ppm sodium acetate)	170	0
5	DPA (Butanol with 100 ppm sodium acetate)	170	3.3×10^1
6	DPA (Butanol with 500 ppm sodium acetate)	170	1.70×10^2

Table S3. Signal intensity of DPA collected from positions 1 to 8 on a silicon substrate coated with aligned and non-aligned Te NWs. Positions are as in Figure 6.

Aligned Te NWs			
No	Position	m/z	Signal intensity
A	1	170	1.12×10^2
B	2	170	3.58×10^1
C	3	170	3.57×10^1
D	4	170	3.13×10^1
E	5	170	5.69×10^1
F	6	170	2.19×10^1
G	7	170	1.77×10^1
h	8	170	1.11×10^1

Non-aligned Te NWs			
No	Position	m/z	Signal intensity
A	1	170	2.84×10^1
B	2	170	2.83×10^1
C	3	170	2.86×10^1
D	4	170	2.82×10^1
E	5	170	2.82×10^1
F	6	170	2.81×10^1
G	7	170	2.87×10^1
h	8	170	2.87×10^1

Table S4. Effects of orientation, voltage and pH on protonated molecule signal intensity.

Compound	Directi on	Voltag e	pH	Sign al	Directio n	Voltag e	pH	Signal
DPA, m/z 170	Parallel	1 V	neutr al	53	Orthogo nal	1 V	Neutra l	0.7
“	“	0 V	neutr al	6	“	0 V	Neutra l	0.4
DPA, m/z 170	Parallel	1 V	14	0	Orthogo nal	1 V	14	0
“	“	1 V	9	0	“	1 V	9	0
“	“	1 V	7	9	“	1 V	7	0
“	“	1 V	2	10	“	1 V	2	2
“	“	0 V	14	0	“	0 V	14	0
“	“	0 V	9	0	“	0 V	9	0
“	“	0 V	7	2	“	0 V	7	0
“	“	0 V	2	6	“	0 V	2	0.5
Compound	Directi on	Voltag e	pH	Sign al	Directio n	Voltag e	pH	Signal
Thymine, m/z 126	Parallel	1 V	7	0	Orthogo nal	1 V	7	0
“	“	1 V	2	1	“	1 V	2	3

“	“	0 V	7	0	“	0 V	7	0
“	“	0 V	2	2	“	0 V	2	0
Adenine, m/z 136	“	1 V	7	8	“	1 V	7	0.6
“	“	1 V	2	2	“	1 V	2	1
“	“	0 V	7	5	“	0 V	7	2
“	“	0 V	2	1	“	0 V	2	0.7
Guanine, m/z 152	“	1 V	7	0	“	1 V	7	0
“	“	1 V	2	2	“	1 V	2	0
“	“	0 V	7	0	“	0 V	7	0
“	“	0 V	2	0	“	0 V	2	0

Note: The data show that signals are detected at 0 V as well in cases where ions exist in solution.

Table S5. Signal intensity of various tablets at 1 V.

NO	Tablet studied	m/z	Signal intensity
2	Diethylcarbamazine (DIET pills)	200	1.37×10^2
3	Trimetazidine (flavdon tablets)	267	1.80×10^2
4	Clopidogrel (from clopidogrel tablets)	322	2.90×10^2
5	Gliclazide (gliclazide tablets)	324	2.85×10^2
6	Levocetirizine (xysal tablets)	389	3.25×10^2

Cellulose Derived Graphenic Fibers for Capacitive Desalination of Brackish Water

Nalenthiran Pugazhenthiran,[†] Soujit Sen Gupta,[†] Anupama Prabath,[†] Muthu Manikandan,[†] Jakka Ravindran Swathy,[†] V. Kalyan Raman,[‡] and Thalappil Pradeep^{*,†}

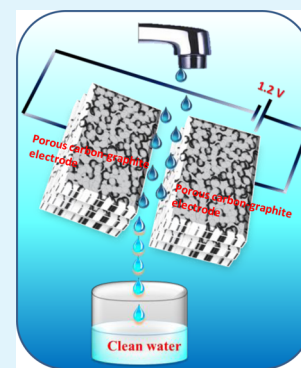
[†]DST Unit of Nanoscience (DST UNS) and Thematic Unit of Excellence (TUE), Department of Chemistry, Indian Institute of Technology Madras, Chennai 600 036, India

[‡]Centre of Excellence (Biotechnology) & Water and Wastewater Technology, Thermax Limited, Pune 411019, India

S Supporting Information

ABSTRACT: We describe a simple and inexpensive cellulose-derived and layer-by-layer stacked carbon fiber network electrode for capacitive deionization (CDI) of brackish water. The microstructure and chemical composition were characterized using spectroscopic and microscopic techniques; electrochemical/electrical performance was evaluated by cyclic voltammetry and 4-probe electrical conductivity and surface area by Brunauer–Emmett–Teller analysis, respectively. The desalination performance was investigated using a laboratory batch model CDI unit, under fixed applied voltage and varying salt concentrations. Electro-adsorption of NaCl on the graphite reinforced-cellulose (GrC) electrode reached equilibrium quickly (within 90 min) and the adsorbed salts were released swiftly (in 40 min) back into the solution, during reversal of applied potential. X-ray photoelectron spectroscopic studies clearly illustrate that sodium and chloride ions were physisorbed on the negative and positive electrodes, respectively during electro-adsorption. This GrC electrode showed an electro-adsorption capacity of 13.1 mg/g of the electrode at a cell potential of 1.2 V, with excellent recyclability and complete regeneration. The electrode has a high tendency for removal of specific anions, such as fluoride, nitrate, chloride, and sulfate from water in the following order: $\text{Cl}^- > \text{NO}_3^- > \text{F}^- > \text{SO}_4^{2-}$. GrC electrodes also showed resistance to biofouling with negligible biofilm formation even after 5 days of incubation in *Pseudomonas putida* bacterial culture. Our unique cost-effective methodology of layer-by-layer stacking of carbon nanofibers and concurrent reinforcement using graphite provides uniform conductivity throughout the electrode with fast electro-adsorption, rapid desorption, and extended reuse, making the electrode affordable for capacitive desalination of brackish water.

KEYWORDS: capacitive deionization, graphene, nanofiber, adsorption, water purification



■ INTRODUCTION

Shortage of clean water is the most exigent problem faced by several communities in the developing world. Access to safe and potable water is threatened by population growth, climate change, and contamination of existing fresh water sources.^{1–3} The need for clean water for domestic, agricultural, and industrial processes has resulted in intense search for alternate sources of water supply, such as brackish groundwater and seawater.^{1,3} Reverse osmosis (RO), ultrafiltration (UF), and distillation processes are the most widely used treatment technologies for water today.⁴ However, excessive energy requirements and the need for skilled personnel to maintain such facilities are limiting their large scale deployment in resource-limited settings.⁵

Capacitive deionization (CDI) is increasingly being considered as a viable solution for water desalination that is more energy efficient than the above-mentioned processes. This technology fundamentally involves adsorption of oppositely charged ions from the electrical double layer region over an electrode upon application of a potential leading to desalination. Subsequent desorption of the adsorbed ions

when the potential is reversed leads to regeneration of the electrodes.^{5–9} Although CDI is associated with high theoretical efficiency, cost effectiveness, and point-of-use (POU) utility, its practical applications for desalination are yet to be realized fully.^{6–10} The existing mainstream CDI materials with their inherent limitations in stability and resistance to biofouling confine such electrodes for larger scale operations. Various methods are used to solve these issues and commercial products are available; although capital costs are higher than RO. An ideal CDI material should exhibit the following characteristics: high specific surface area, high conductivity, fast adsorption/desorption rates, electrochemical stability, resistance to biofilm formation, and easy processability.^{6,11,12}

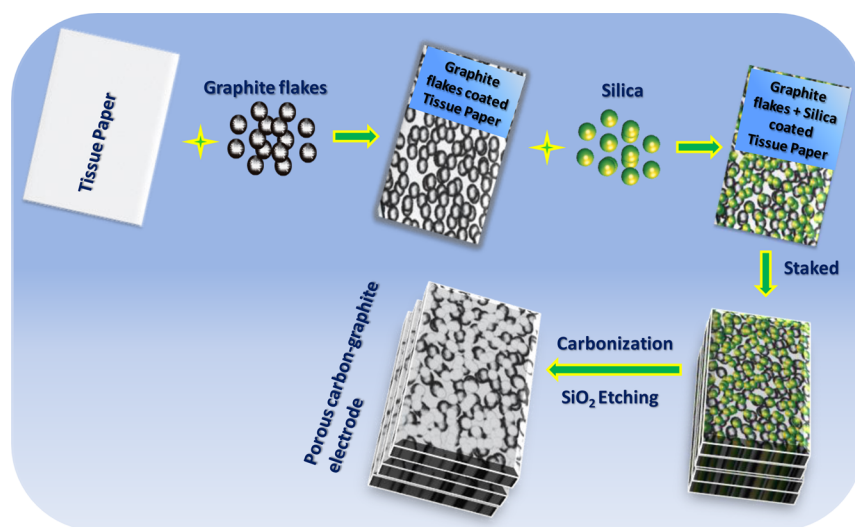
The salt removal efficiency of various forms of carbon used as an electrode for CDI is generally reported in terms of salt (NaCl) adsorbed per gram of carbon. Li et al. and Kim et al. reported the capacity to be 0.275 and 3.7 mg/g, respectively for

Received: June 21, 2015

Accepted: August 25, 2015

Published: August 25, 2015

Scheme 1. Schematic Representation of the Procedure for the Preparation of Layer-by-Layer Stacked Graphite-Reinforced-Carbon (GrC) Fiber Electrodes



activated carbon.^{13,14} In addition, multiwalled carbon nanotubes,¹⁵ single-walled carbon nanotubes,¹⁶ graphene-like nanoflakes,¹⁷ graphene,¹⁸ graphene-carbon nanotubes,¹⁹ carbon nanofiber webs,²⁰ reduced graphene oxide-activated carbon,²¹ Ti–O activated carbon cloth,²² and MnO₂ activated carbon²³ have shown adsorption capacities of 1.7, 0.75, 1.3, 1.8, 1.4, 4.6, 2.9, 4.3, and 1.0 mg/g, respectively. These systems are excellent in terms of electrical conductivity and pore-distribution, but are found lacking in their symmetric adsorption and desorption of counterions, electrochemical stability, and resistance to biofouling. Additionally, they suffer from relatively complicated manufacturing processes and high production cost.⁶ In comparison, mesoporous carbon is an inexpensive and highly porous material with varying pore sizes. This property can help overcome the limited ion accessibility and slow diffusion associated with activated carbon.^{9,24–27} However, the obtained adsorption efficiency is less due to the high inner electrode resistance of reported mesoporous carbon materials.^{24,26,28} Incorporation of conducting polymers, metal oxides, graphene and carbon nanotubes into mesoporous carbon is an effective approach for solving this issue.^{25,29–34} Though these agents locally impart a pseudocapacitance on the surface, they do not contribute much to the adsorption efficiency. Recently, incorporating graphene into a mesoporous carbon increased its conductivity, as a result, it leads to higher adsorption of salt from brackish water compared to a carbon electrode alone.^{13,21,35,36}

With an objective to develop a cost-effective and superior CDI electrode material with high surface area, low electrical resistance, and electrochemical durability, in this work we have synthesized a layer-by-layer stacked graphite reinforced-cellulose (GrC) derived 3D mesoporous fibrous carbon electrode. The material exhibits the above-mentioned characteristics along with superior adsorption capability and resistance to bacterial biofilm formation, while being cost-effective. The CDI performance of this hybrid electrode was evaluated and the effect of biofouling was examined via a temporal study employing a biofilm-forming organism, *Pseudomonas putida*. These characteristics make our graphite reinforced-cellulose derived carbon fiber material a promising candidate for POU water treatment, especially in resource-limited settings.

■ MATERIALS AND METHODS

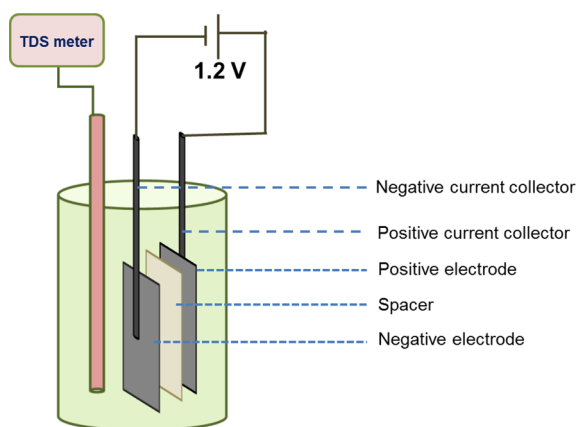
Chemicals. Graphite flakes were a gift sample from Tamil Nadu Minerals Limited (TAMIN) and tissue papers were purchased from a local market in Chennai. Tetraethyl orthosilicate (TEOS) and 3-aminopropyltriethoxysilane (APTES) were purchased from Sigma-Aldrich and used as such. Unless otherwise specified, all the reagents used were of analytical grade and the solutions were prepared using deionized water.

Preparation of Layer-by-Layer Assembly of Graphite Reinforced-Carbon Electrode. The typical procedure for the preparation of a layer-by-layer assembly of a graphite reinforced-carbon (GrC) electrode was as follows (see Scheme 1). First, 5 mg of graphite (TAMIN) powder was coated on a single piece of tissue paper (size 5 × 5 cm and thickness of 0.2 mm) and then 300 μL of a TEOS:APTES mixture (ratio 1:0.5) was sprayed on it. This process was repeated for each layer (total 50 layers were prepared). Next, the entire set of graphite coated tissue paper layers were stacked on one above another and was pressed for 5 min (at 5 ton load) by a press. It was further dried at 60 °C for 3 h, which was followed by carbonization under nitrogen atmosphere at 700 °C for 3 h. After carbonization, silica was etched out from the stacked GrC electrode by aqueous NaOH (1 mM) for 3 h to generate pores. Finally, the electrode was washed with water several times until the pH of the mother liquor reached 7 and then dried overnight at 60 °C to remove water.

Capacitive Deionization Setup. The laboratory-scale CDI batch reactor consisted of a single pair of GrC electrodes and a pair of current collectors, as shown in Scheme 2. The current collectors were made of graphite rods and the electrodes were held at a spacing of ~0.2 mm by a piece of nylon membrane. Power was supplied to the cell by connecting the current collectors to a direct-current (DC) Testronic 30B DC power supply with a voltage range of 0–5 V and a current range of 0–1 A. The conductivity was measured at the cell exit stream by using a conductivity meter (cyberscan PCD 650 Eutech instrument). The approximate volume of the solution in the cell was 80 mL, which was maintained in the system. The temperature of the solution was kept at ~25 °C. Regeneration of the electrodes was carried out by reversing the terminal of the electrodes.

Biofilm Formation. Monoculture biofilms of *Pseudomonas putida* were grown on the surface of the electrodes (a commercial electrode used for capacitive deionization and GrC). The protocol for the biofilm is reported elsewhere.³⁷ A few selected electrodes were immersed in 20 mL of a synthetic medium, inoculated with 10⁸ colony forming units (CFU) of *Pseudomonas putida*. The biofilm was allowed to grow for 5 days while replenishment of the medium was done at an

Scheme 2. Schematic Representation of the Capacitive Deionization Setup



interval of 48 h. Electrodes after biofilm growth were rinsed in distilled water and air-dried for 24 h. The surfaces were sputtered with gold to increase their electrical conductivity before imaging. Scanning electron microscopy (SEM) studies were performed using a FEI QUANTA-200 operated at 12.5 kV.

Characterization Studies. Morphological studies of the electrode surface, elemental analysis, and elemental mapping were carried out using a scanning electron microscope equipped with energy dispersive analysis of X-rays (EDAX or energy dispersive spectroscopy, EDS) (FEI Quanta 200). The high resolution transmission electron microscopy (HRTEM) images of the electrodes were obtained with an instrument, JEM 3010 (JEOL, Japan) which was operated at 200 keV (to reduce beam induced damage) and the samples were drop-cast on carbon-coated copper grids and allowed to dry under ambient conditions. X-ray photoelectron spectroscopy (XPS) measurements were performed using ESCA Probe TPD of Omicron Nanotechnology with polychromatic Mg K α as the X-ray source ($h\nu = 1253.6$ eV) and the binding energy was calibrated with respect to C 1s at 284.5 eV. A Flowsorb II 2300 Micrometrics surface area analyzer was employed for measuring the surface area, pore volume, and pore diameter of the samples. Total sodium and chloride concentrations in the water were estimated using inductively coupled plasma spectroscopy (ICP-MS) (PerkinElmer NexION 300 ICP-MS) and ion chromatography (Metrohm 883 Basic IC plus), respectively. Raman spectra were obtained with a WITec GmbH, Alpha-SNOM alpha 300 S confocal Raman microscope having a 532 nm laser as the excitation source. The electrical conductivity was measured at room temperature by a four probe conductivity instrument (SES Instruments, Roorkee). A Keithley current source-voltmeter was attached to the four probe setup for the collection of data. The electrochemical capacitive behavior of CA was determined by cyclic voltammetry (CV). All electrochemical experiments were carried out at room temperature in a three-electrode cell with 1 M NaCl electrolyte solution.

RESULTS AND DISCUSSION

Characterization of Layer-by-Layer Stacked Assembly of Graphite Reinforced-Carbon (GrC) Electrode. To investigate the morphology of the GrC electrode, FESEM and HRTEM images were analyzed. Figure 1A,B,C shows that the prepared GrC electrodes are collectively intertwined in a unique fiber-like morphology with a thickness of 4–5 μm and a length of ten to several hundred micrometers. The graphite reinforcement into the consecutively stacked layer-by-layer assembly of carbon fiber is also evident from Figure 1A,B, marked in white arrows. This arrangement established an effective way for improving conductivity as well as mechanical strength. The material proved to be superior to similar carbon-carbon composites.^{38–41} The elemental mapping confirmed the

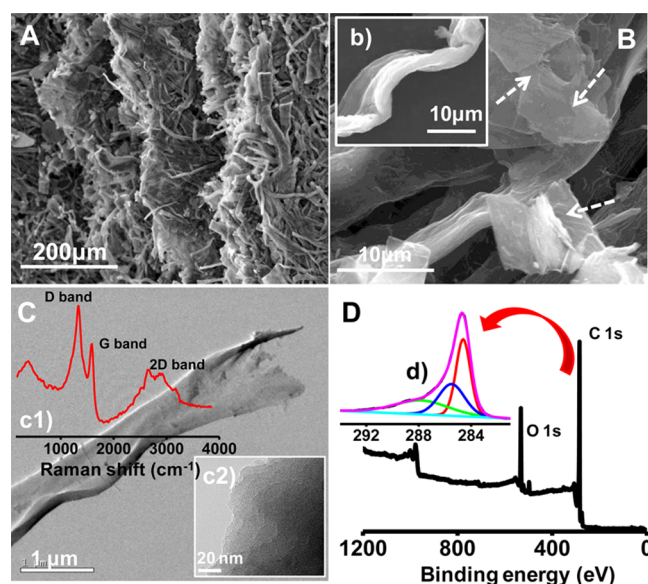


Figure 1. (A and B) FESEM images of layer-by-layer stacked graphite reinforced carbon fiber. The white arrow in panel B shows the presence of graphite flakes. The inset in panel B represents the single layer graphenic carbon (b), (C) TEM image, the inset c1 represents the Raman spectrum of the material and c2 represents the HRTEM image of graphenic carbon, (D) XPS survey spectrum of the material and the inset shows the deconvoluted C 1s spectrum (d).

presence of silica in the initial material (Supporting Information, Figure S1). Figure S2 in the Supporting Information shows the complete etching of silica from the parent material, which led to the characteristic porosity of the GrC electrode. Furthermore, the Raman spectrum of the assembly in inset c1 in Figure 1C clearly shows that the material is graphenic in nature. The spectrum is composed of a primary in-plane vibrational mode at 1580 cm^{-1} (G band) and a second order overtone of a different in-plane vibration at 2690 cm^{-1} (2D band) and a defect band at 1350 cm^{-1} (D band).^{42–44} This graphenic nature of the single carbon fiber represents multilayer graphene as shown in the HRTEM image in the inset of Figure 1C (c2). The X-ray photoelectron survey spectrum of GrC electrode (Figure 1D) shows the presence of carbon and oxygen as the only elements. The deconvoluted C 1s XPS (inset in Figure 1D) spectrum shows the presence of C=C at 284.6 eV and two “oxide” peaks that are shifted to higher binding energy by 1.0 and 1.5 eV, respectively. The first oxide peak is assigned to a carbon atom in alcohol (C—OH) or ether (C—O—C) groups. The second type of oxide corresponds to a C atom in carbonyl (C=O) type groups.

Structural properties (surface area and pore characteristic) and electrical conductivity have a major effect on the CDI performance of carbon materials. Therefore, the specific surface areas and the pore size distributions of the GrC electrode were measured using the BET and BJH methods. The nitrogen adsorption–desorption isotherms observed for the GrC electrode are shown in the Supporting Information, Figure S3. The calculated BET surface area and pore volume of the prepared samples are 598 $\text{m}^2 \text{g}^{-1}$ and 0.358 $\text{cm}^3 \text{g}^{-1}$, respectively. The N_2 adsorption increased for $P/P_0 > 0.1$ owing to capillary condensation and multilayer adsorption of N_2 and the typical type-IV isotherm with H4 hysteresis loops indicate that the layer-by-layer assembly of carbon electrode is mesoporous in nature.^{27,32,44} The BET isotherm results suggest

that the GrC electrode is expected to be a potential candidate for salt adsorption from water in CDI.

Electrical conductivity of the material was around 128 S/m. It is postulated to be due to the layered structure of the electrode. The I - V graph is shown in the Supporting Information, Figure S4A. Cyclic voltammetry was performed with GrC electrodes in a potential window of -0.8 to $+0.2$ V in 1 M NaCl solution as shown in the Supporting Information, Figure S4B. It is noted that at lower scan rates the curves are symmetrical, but at higher scan rates the curves distort. This can be attributed to the enhanced mass-transfer of the ions onto the GrC electrodes at lower scan rate but as the scan rate increases, the ohmic resistance also increases, which leads to the formation electrical double layer and thereby restricts the movement of the ions into the pores. The specific capacitances calculated using the CV curves were 323 and 83 F/g at 2 and 100 mV/s. The superior electrochemical property of the material enhances the electro-adsorption capacity of the GrC electrodes.

CDI Performance of the GrC Electrode. The CDI efficiency of the graphite reinforced-carbon electrode was evaluated using NaCl solution at room temperature with a single CDI cell (as depicted in Scheme 2) at an applied voltage of 1.2 V. Generally, water with total dissolved solids (TDS) higher than 500 mg/L is not considered suitable for consumption.⁴⁵ Bearing this in mind, we chose NaCl concentrations of 500 mg/L to test the CDI performance of these electrode materials. In Figure 2A, the NaCl electro-

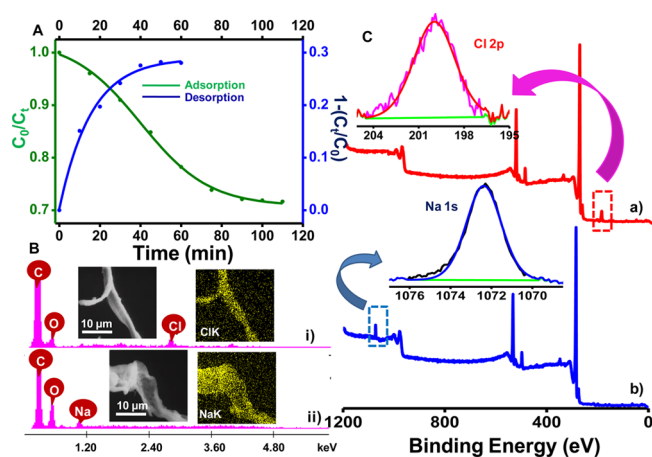


Figure 2. (A) Electro-adsorption/desorption curve of the graphite reinforced-carbon fiber electrode for a single cycle. The electrolyte present is NaCl measured at room temperature. (B) EDS spectra of (i) positive and (ii) negative terminals after single adsorption cycle. The corresponding SEM images along with the elemental maps are shown in the inset. (C) XPS survey spectrum of the material after single adsorption cycle, (a) positive and (b) negative terminals. The inset shows the deconvoluted XPS spectrum of Cl 2p and Na 1s.

adsorption and electro-desorption profiles of the electrode are plotted as a function of time. It is noticeable from the figure that the concentration of NaCl (500 mg/L) in the solution decreases gradually with time and reaches equilibrium. In comparison, when the potential was reversed, a rapid increase in NaCl concentration in solution occurs, which later stabilizes. One can further deduce from the electro-adsorption and electro-desorption profiles that $\sim 30\%$ of NaCl is adsorbed in the first step, which is completely desorbed from the electrode

on reversing the potential.^{26,30,32,44} This implies that our porous carbon-graphite hybrid electrode can be regenerated efficiently.

The NaCl electro-adsorption capacity (q_e) of the electrodes is calculated from the following equation:

$$q_e = \frac{(C_0 - C_f)V}{W} \quad (1)$$

where C_0 and C_f are the initial and final NaCl concentrations (in mg/L) in solution, respectively, V is the volume (in mL) of the NaCl solution used, and W is the mass (in g) of the active material in the working electrode. The q_e of the graphite reinforced-carbon electrode was evaluated as 13.1 mg/g. Notably, the NaCl electro-adsorption capacity of the carbon-graphite hybrid electrode in this work is much higher than that of other recently reported CDI electrode materials, e.g., 0.731 mg/g for graphene incorporated-mesoporous carbon sheet.^{7,34,46–50}

A fast electro-adsorption rate is also an important criterion responsible for allowing practical applications of CDI electrode materials. Various carbon based materials require several hours to reach their electro-adsorption equilibrium.^{47,49} From the time dependent desalination behavior of the GrC electrode in Figure 2A, it is evident that the electro-adsorption of 500 mg/L NaCl reaches equilibrium quickly within 90 min, and the adsorbed salts are swiftly released back into the solution in 40 min during discharge compared to Li et al., which reported around 120 min for electro-adsorption.¹³

Elemental mapping and EDS analysis of the positive and negative electrodes are shown in Figure 2B and the Supporting Information, Figures S5 and S6. It clearly shows that the graphite reinforced-carbon electrodes have the capacity to remove salts from brackish water and get regenerated quickly. The XPS spectra of the positive and negative electrodes after application of potential are presented in Figure 2C. In comparison with Figure 1D, new peaks due to sodium and chloride ions adsorbed on the negative and positive electrode, respectively can be seen in the spectra. Interestingly, adsorption of these ions did not alter the binding energies of the carbon and oxygen peaks. This demonstrates that electro-adsorption of Na^+ and Cl^- ions on the electrodes is via physisorption alone.^{42,51}

Studies were performed to investigate the reversibility of the GrC electrode during adsorption and regeneration. Figure 3A shows the ratio of initial concentration (C_0) to concentration at a time t (C_t) over several consecutive cycles. The symmetrical nature of the electro-adsorption (deionization) and desorption (regeneration) curves is characteristic of first-order kinetics associated with ion uptake and removal by the hybrid electrode.^{52,53} The surface of the electrodes was characterized using XPS as shown in Figure 3B. Interestingly, there was no feature in the XPS spectrum corresponding to the negative and positive ions, and no shift in the binding energy of carbon and oxygen was observed. The EDS elemental mapping of the anode and cathode after the tenth adsorption cycle is shown in Figure 3C,D, and the corresponding EDS maps of the regenerated electrodes are shown in the Supporting Information, Figures S7 and S8. This study confirms that the GrC electrode maintains its adsorption and desorption capacity even after ten consecutive cycles. These results exhibit the high electro-adsorption capacity and a fast and reversible electro-adsorption/desorption.

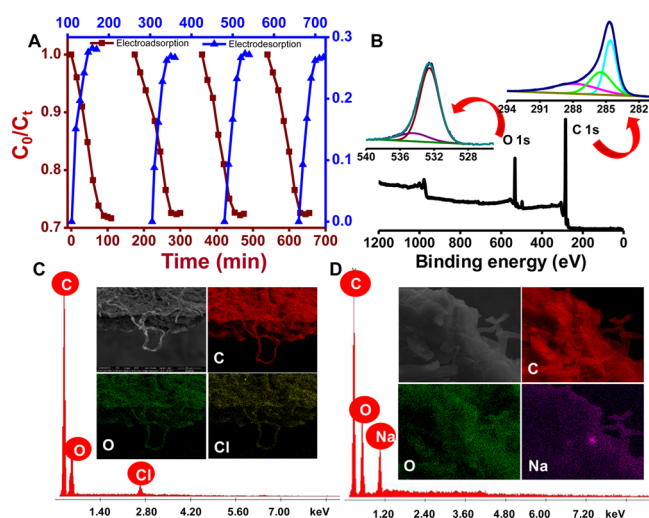


Figure 3. (A) Electro-adsorption/desorption cycles of the material (up to four cycles). (B) XPS spectrum of regenerated positive terminal after the tenth cycle showing the presence of carbon and oxygen only. The inset shows the deconvoluted C 1s and O 1s spectrum. (C and D) EDS spectra at the inset shows the SEM image and the corresponding elemental mapping for carbon, oxygen, and respective adsorbed ions. The electrolyte used in all cases was NaCl.

The electro-adsorption capacity is known to depend strongly on the surface properties, such as surface area, pore microstructure, and pore size distribution as well as solution state properties of the electrode material.^{26,30,32,44,53} The layer-by-layer assembly of our GrC electrodes increases the mass-transfer of ions into the pores, ion electro-adsorption, and energy storage in the electrical double layer of the electrode. This consequently reduces the mass transport resistance of salt ions inside the electrode as well as between the electrode and saline water. This structural feature gives rise to a high electro-adsorption rate of the GrC electrodes and therefore, leads to excellent CDI performance.

The electro-adsorption capacity of the GrC electrodes was further investigated with respect to the effect of cation charge and size. For these solutions of NaCl, MgCl₂, and FeCl₃, each at an initial concentration of 500 ppm, were selected. The electro-adsorption and electro-desorption profiles of the GrC electrode for these solutions are compared with those of NaCl (500 ppm) in the Supporting Information, Figure S9. The concentrations of Mⁿ⁺ in solutions decrease with time and varies in the order Fe³⁺ > Mg²⁺ > Na⁺ during the CDI experiment. The adsorption capacity was found to be 16.9, 14.5, and 13.1 mg/g for FeCl₃, MgCl₂, and NaCl, respectively. It is understandable that the ionic charge, ionic radii, and hydrated radii of different cations may play a major role in governing the electro-adsorption process. The hydrated radius of Fe³⁺ is the largest whereas that of Na⁺ is the smallest in these cations, based on which the electro-adsorption preference should exhibit an opposite trend. The above order can instead be explained in terms of charge of the cations; as cations with higher charge will be more easily adsorbed on the electrode surface on application of a potential at the electrodes. Thus, the trivalent Fe³⁺ ion is most effectively removed, followed by the bivalent Mg²⁺ ion, and then the univalent Na⁺ ion.^{25,53} The GrC electrodes used in this study have a layer-by-layer assembly which allows the cations to move easily over the carbon-graphite electrode through the pores. This is confirmed from

EDS coupled with elemental mapping analysis (Supporting Information, Figures S10–S13).

Anion contamination of both surface water and groundwater is well documented.^{2,3,45} To test the effectiveness of our electrode for electro-adsorption of anions, several experiments were carried out using a solution containing different anions (such as SO₄²⁻, Cl⁻, NO₃⁻, and F⁻). The initial concentration of each of the selected anions was fixed at 50 ppm. About 2 mL aliquots of the analyte were withdrawn at regular intervals, and an analysis via ion chromatography was performed. Figure 4A

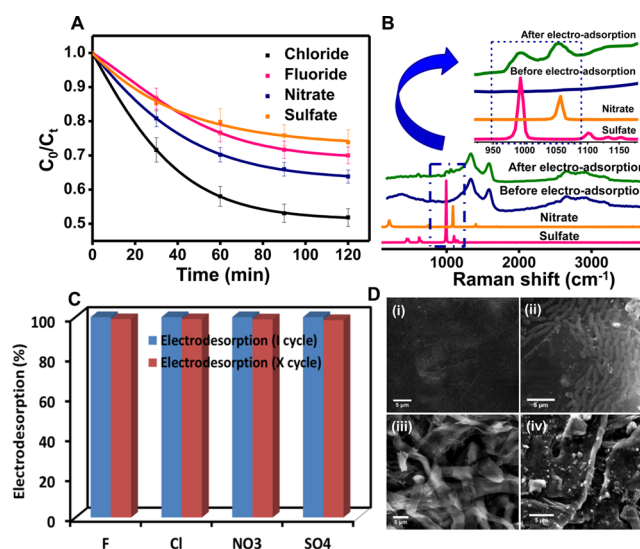


Figure 4. Plot of CDI performance of graphite reinforced carbon fiber electrode in the mixed negative ions (Cl⁻, F⁻, NO₃⁻, SO₄²⁻) system (A). Raman spectra of graphite reinforced carbon fiber electrode before and after electro-adsorption of positive electrode (B), inset shows enlarged Raman spectra of a narrower region. Plot of desorption capability of electrode in 1st and 10th cycle (C). SEM images of desorption before and after 5 days growth of biofilms of *Pseudomonas putida* on commercial electrode (D(i,ii)) and graphite reinforced-carbon fiber electrode (D(iii,iv)).

shows that for each anion the concentration decreases with increase in time, indicating that they are adsorbed on the GrC electrode. These results were further confirmed through Raman spectroscopy (Figure 4B) and elemental mapping (Supporting Information, Figures S14 and S15). Raman spectra evidently indicate the presence of symmetric N–O and S–O stretching vibrations at 1056 and 990 cm⁻¹ for nitrate and sulfate, respectively.⁵⁴ These features appeared clearly in the positive carbon-graphite electrode after electro-adsorption. Elemental mapping of positive and negative electrodes provide further evidence confirming electro-adsorption.

It can also be noticed from the adsorption profiles in Figure 4A that at a given time *t*, the measured anion concentration variation in solution follows the order: Cl⁻ > NO₃⁻ > F⁻ > SO₄²⁻. The size of the hydrated radii of these anions decreases as SO₄²⁻ > F⁻ > Cl⁻, NO₃⁻. Anions with smaller hydrated radii can pass through the pores and arrive at the electrode surface more easily.^{53,55,56} As a result, higher fractions of Cl⁻ and NO₃⁻ are removed than the other two anions. Finally, the recyclability of the GrC electrodes when treating water containing a mixture of anions was tested. We found negligible difference between the first and tenth cycles (Figure 4C), which indicated that the electrodes were completely regenerated even after ten cycles.

Further experiments were performed to test the efficiency of the GrC electrodes at different concentrations of NaCl solution (1000, 500, and 250 mg/L). In each case, we have found that the adsorption capacity of the electrodes is around 13.0 mg/g of material (keeping all other parameters constant). The graph is shown in the [Supporting Information](#), Figure S16.

Biofouling of electrodes is a major issue impeding their utilization in the CDI process and is detrimental to their practical applications.⁶ Though employing conventional biofouling control methods during capacitive desalination process can reduce biofouling of the electrodes, they also generate harmful byproducts requiring additional treatment.⁵⁷ In this context, we tested the effect of biofouling with *Pseudomonas putida* on the graphite reinforced-carbon fiber electrode. The SEM results ([Figure 4D](#)) showed that in comparison with a commercially available electrode, our graphite reinforced-carbon fiber electrode has an enhanced resistance to biofouling. This could be due to the graphenic nature of carbon fibers,⁵⁸ which have been individually proven to be effective antibacterial agents. The fiber-like surface morphology of the electrode could also provide it resistance against bacterial adhesion and proliferation. This is understandable because the surface charge of the carbon fiber-like structure may effectively repel bacteria from initial attachment on the GrC fiber electrode, thereby making it an effective material for long-term use.^{57–59}

CONCLUSIONS

We have synthesized a graphite reinforced-cellulose derived carbon fiber electrode via a simple layer-by-layer stacking method. The reinforced graphite structure increases the conductivity of the electrode and results in excellent electro-adsorption of NaCl (13.1 mg/g). The high electro-adsorption performance is attributed to the layer-by-layer assembly of the hybrid electrode that allows ions to move easily on the carbon-graphite electrode. The graphenic carbon fiber-like surface morphology of the electrode could also provide it resistance against bacterial adhesion and proliferation. The preparation methodology of the carbon fiber electrode opens up a new avenue for the development of high-performance and cost-effective CDI electrodes from renewable sources.

ASSOCIATED CONTENT

Supporting Information

The Supporting Information is available free of charge on the [ACS Publications website](#) at DOI: [10.1021/acsami.5b05510](#).

BET surface area measurement of electrode and EDS coupled with elemental mapping analysis of electrode surface before and after electro-adsorption/desorption, I–V curve and CV curves of the GrC electrode at varying scan rates, CDI results of electro-adsorption and desorption performance of the GrC fiber electrode in different charged species ie., Na⁺, Mg²⁺ and Fe³⁺ and CDI performance of the GrC electrode at different NaCl concentration ([PDF](#)).

AUTHOR INFORMATION

Corresponding Author

*T. Pradeep. E-mail: pradeep@iitm.ac.in. Fax: +91-44-2257-0545.

Notes

The authors declare no competing financial interest.

ACKNOWLEDGMENTS

We thank the Department of Science and Technology and Nano Mission of Government of India for constantly supporting our research program on nanomaterials. S.S.G. thanks the SERB, CII, and Thermax India Pvt. Ltd. for a research fellowship.

REFERENCES

- (1) Hoekstra, A. Y. Water Scarcity Challenges to Business. *Nat. Clim. Change* **2014**, *4*, 318–320.
- (2) Schewe, J.; Heinke, J.; Gerten, D.; Haddeland, I.; Arnell, N. W.; Clark, D. B.; Dankers, R.; Eisner, S.; Fekete, B. M.; Colón-González, F. J.; Gosling, S. N.; Kim, H.; Liu, X.; Masaki, Y.; Portmann, F. T.; Satoh, Y.; Stacke, T.; Tang, Q.; Wada, Y.; Wisser, D.; Albrecht, T.; Frieler, K.; Piontek, F.; Warszawski, L.; Kabat, P. Multimodel Assessment of Water Scarcity under Climate Change. *Proc. Natl. Acad. Sci. U. S. A.* **2014**, *111*, 3245–3250.
- (3) Shannon, M. A.; Bohn, P. W.; Elimelech, M.; Georgiadis, J. G.; Marinas, B. J.; Mayes, A. M. Science and Technology for Water Purification in the Coming Decades. *Nature* **2008**, *452*, 301–310.
- (4) Elimelech, M.; Phillip, W. A. The Future of Seawater Desalination: Energy, Technology, and the Environment. *Science* **2011**, *333*, 712–717.
- (5) Porada, S.; Weinstein, L.; Dash, R.; van der Wal, A.; Bryjak, M.; Gogotsi, Y.; Biesheuvel, P. M. Water Desalination Using Capacitive Deionization with Microporous Carbon Electrodes. *ACS Appl. Mater. Interfaces* **2012**, *4*, 1194–1199.
- (6) Porada, S.; Zhao, R.; van der Wal, A.; Presser, V.; Biesheuvel, P. M. Review on the Science and Technology of Water Desalination by Capacitive Deionization. *Prog. Mater. Sci.* **2013**, *58*, 1388–1442.
- (7) Suss, M. E.; Baumann, T. F.; Bourcier, W. L.; Spadaccini, C. M.; Rose, K. A.; Santiago, J. G.; Stadermann, M. Capacitive Desalination with Flow-Through Electrodes. *Energy Environ. Sci.* **2012**, *5* (11), 9511–9519.
- (8) Suss, M. E.; Biesheuvel, P. M.; Baumann, T. F.; Stadermann, M.; Santiago, J. G. In Situ Spatially and Temporally Resolved Measurements of Salt Concentration between Charging Porous Electrodes for Desalination by Capacitive Deionization. *Environ. Sci. Technol.* **2014**, *48*, 2008–2015.
- (9) Tsouris, C.; Mayes, R.; Kiggans, J.; Sharma, K.; Yiaccoumi, S.; DePaoli, D.; Dai, S. Mesoporous Carbon for Capacitive Deionization of Saline Water. *Environ. Sci. Technol.* **2011**, *45*, 10243–10249.
- (10) Długołęcki, P.; van der Wal, A. Energy Recovery in Membrane Capacitive Deionization. *Environ. Sci. Technol.* **2013**, *47*, 4904–4910.
- (11) Oren, Y. Capacitive Deionization (CDI) for Desalination and Water Treatment — Past, Present and Future (a review). *Desalination* **2008**, *228*, 10–29.
- (12) Zhao, R.; Biesheuvel, P. M.; Miedema, H.; Bruning, H.; van der Wal, A. Charge Efficiency: A Functional Tool to Probe the Double-Layer Structure Inside of Porous Electrodes and Application in the Modeling of Capacitive Deionization. *J. Phys. Chem. Lett.* **2010**, *1*, 205–210.
- (13) Li, L.; Zou, L.; Song, H.; Morris, G. Ordered Mesoporous Carbons Synthesized by a Modified Sol–Gel process for Electro-sorptive Removal of Sodium Chloride. *Carbon* **2009**, *47*, 775–781.
- (14) Kim, Y.-J.; Choi, J.-H. Enhanced Desalination Efficiency in Capacitive Deionization with an Ion-Selective Membrane. *Sep. Purif. Technol.* **2010**, *71*, 70–75.
- (15) Dai, K.; Shi, L.; Fang, J.; Zhang, D.; Yu, B. NaCl Adsorption in Multi-Walled Carbon Nanotubes. *Mater. Lett.* **2005**, *59*, 1989–1992.
- (16) Li, H.; Pan, L.; Lu, T.; Zhan, Y.; Nie, C.; Sun, Z. A Comparative Study on Electro-sorptive Behavior of Carbon Nanotubes and Graphene for Capacitive Deionization. *J. Electroanal. Chem.* **2011**, *653*, 40–44.
- (17) Li, H.; Zou, L.; Pan, L.; Sun, Z. Novel Graphene-Like Electrodes for Capacitive Deionization. *Environ. Sci. Technol.* **2010**, *44*, 8692–8697.

- (18) Li, H.; Lu, T.; Pan, L.; Zhang, Y.; Sun, Z. Electrosorption Behavior of Graphene in NaCl Solutions. *J. Mater. Chem.* **2009**, *19*, 6773–6779.
- (19) Zhang, D.; Yan, T.; Shi, L.; Peng, Z.; Wen, X.; Zhang, J. Enhanced Capacitive Deionization Performance of Graphene/Carbon Nanotube Composites. *J. Mater. Chem.* **2012**, *22*, 14696–14704.
- (20) Wang, G.; Pan, C.; Wang, L.; Dong, Q.; Yu, C.; Zhao, Z.; Qiu, J. Activated Carbon Nanofiber Webs Made by Electrospinning for Capacitive Deionization. *Electrochim. Acta* **2012**, *69*, 65–70.
- (21) Li, H.; Pan, L.; Nie, C.; Liu, Y.; Sun, Z. Reduced Graphene Oxide and Activated Carbon Composites for Capacitive Deionization. *J. Mater. Chem.* **2012**, *22*, 15556–15561.
- (22) Ryou, M.-W.; Seo, G. Improvement in Capacitive Deionization Function of Activated Carbon Cloth by Titania Modification. *Water Res.* **2003**, *37*, 1527–1534.
- (23) Yang, J.; Zou, L.; Song, H.; Hao, Z. Development of Novel MnO₂/Nanoporous Carbon Composite Electrodes in Capacitive Deionization Technology. *Desalination* **2011**, *276*, 199–206.
- (24) Wang, X.; Lee, J. S.; Tsouris, C.; DePaoli, D. W.; Dai, S. Preparation of Activated Mesoporous Carbons for Electrosorption of Ions from Aqueous Solutions. *J. Mater. Chem.* **2010**, *20*, 4602–4608.
- (25) Peng, Z.; Zhang, D.; Shi, L.; Yan, T. High Performance Ordered Mesoporous Carbon/Carbon Nanotube Composite Electrodes For Capacitive Deionization. *J. Mater. Chem.* **2012**, *22*, 6603–6612.
- (26) Porada, S.; Borchardt, L.; Oschatz, M.; Bryjak, M.; Atchison, J. S.; Keesman, K. J.; Kaskel, S.; Biesheuvel, P. M.; Presser, V. Direct Prediction of the Desalination Performance of Porous Carbon Electrodes for Capacitive Deionization. *Energy Environ. Sci.* **2013**, *6*, 3700–3712.
- (27) Peng, Z.; Zhang, D.; Shi, L.; Yan, T.; Yuan, S.; Li, H.; Gao, R.; Fang, J. Comparative Electrodesorption Study of Mesoporous Carbon Electrodes with Various Pore Structures. *J. Phys. Chem. C* **2011**, *115*, 17068–17076.
- (28) Wang, G.; Qian, B.; Dong, Q.; Yang, J.; Zhao, Z.; Qiu, J. Highly Mesoporous Activated Carbon Electrode for Capacitive Deionization. *Sep. Purif. Technol.* **2013**, *103*, 216–221.
- (29) Kim, Y.-J.; Choi, J.-H. Improvement of Desalination Efficiency in Capacitive Deionization using a Carbon Electrode Coated with an Ion-Exchange Polymer. *Water Res.* **2010**, *44*, 990–996.
- (30) El-Deen, A. G.; Choi, J.-H.; Khalil, K. A.; Almajid, A. A.; Barakat, N. A. M. A TiO₂ Nanofiber/Activated Carbon Composite as a Novel Effective Electrode Material for Capacitive Deionization of Brackish Water. *RSC Adv.* **2014**, *4*, 64634–64642.
- (31) Kim, C.; Lee, J.; Kim, S.; Yoon, J. TiO₂ Sol–Gel Spray Method for Carbon Electrode Fabrication to Enhance Desalination Efficiency of Capacitive Deionization. *Desalination* **2014**, *342*, 70–74.
- (32) Wang, H.; Zhang, D.; Yan, T.; Wen, X.; Zhang, J.; Shi, L.; Zhong, Q. Three-Dimensional Macroporous Graphene Architectures as High Performance Electrodes for Capacitive Deionization. *J. Mater. Chem. A* **2013**, *1*, 11778–11789.
- (33) Wang, H.; Shi, L.; Yan, T.; Zhang, J.; Zhong, Q.; Zhang, D. Design of Graphene-Coated Hollow Mesoporous Carbon Spheres as High Performance Electrodes for Capacitive Deionization. *J. Mater. Chem. A* **2014**, *2*, 4739–4750.
- (34) Li, H.; Liang, S.; Li, J.; He, L. The Capacitive Deionization Behaviour of a Carbon Nanotube and Reduced Graphene Oxide Composite. *J. Mater. Chem. A* **2013**, *1*, 6335–6341.
- (35) Bai, Y.; Huang, Z.-H.; Yu, X.-L.; Kang, F. Graphene Oxide-Embedded Porous Carbon Nanofiber Webs by Electrospinning for Capacitive Deionization. *Colloids Surf., A* **2014**, *444*, 153–158.
- (36) Liu, Y.; Xu, X.; Lu, T.; Sun, Z.; Chua, D. H. C.; Pan, L. Nitrogen-Doped Electrospun Reduced Graphene Oxide-Carbon Nanofiber Composite for Capacitive Deionization. *RSC Adv.* **2015**, *5*, 34117–34124.
- (37) Sutherland, I. W. The Biofilm Matrix – An Immobilized but Dynamic Microbial Environment. *Trends Microbiol.* **2001**, *9* (5), 222–227.
- (38) Fitzer, E.; Terwiesch, B. Carbon–Carbon Composites Unidirectionally Reinforced with Carbon and Graphite Fibers. *Carbon* **1972**, *10*, 383–390.
- (39) Fitzer, E. The Future of Carbon-Carbon Composites. *Carbon* **1987**, *25*, 163–190.
- (40) Windhorst, T.; Blount, G. Carbon-Carbon Composites: A Summary of Recent Developments and Applications. *Mater. Eng.* **1997**, *18*, 11–15.
- (41) Manocha, L. M.; Yasuda, E.; Tanabe, Y.; Kimura, S. Effect of Carbon Fiber Surface-Treatment on Mechanical Properties of C/C Composites. *Carbon* **1988**, *26*, 333–337.
- (42) Sreepasad, T. S.; Gupta, S. S.; Maliyekkal, S. M.; Pradeep, T. Immobilized Graphene-Based Composite from Asphalt: Facile Synthesis and Application in Water Purification. *J. Hazard. Mater.* **2013**, *246–247*, 213–220.
- (43) John, R.; Shinde, D. B.; Liu, L.; Ding, F.; Xu, Z.; Vijayan, C.; Pillai, V. K.; Pradeep, T. Sequential Electrochemical Unzipping of Single-Walled Carbon Nanotubes to Graphene Ribbons Revealed by in Situ Raman Spectroscopy and Imaging. *ACS Nano* **2014**, *8*, 234–242.
- (44) Wen, X.; Zhang, D.; Yan, T.; Zhang, J.; Shi, L. Three-Dimensional Graphene-Based Hierarchically Porous Carbon Composites Prepared by a Dual-Template Strategy for Capacitive Deionization. *J. Mater. Chem. A* **2013**, *1*, 12334–12344.
- (45) Sankar, M. U.; Aigal, S.; Maliyekkal, S. M.; Chaudhary, A.; Anshup; Kumar, A. A.; Chaudhari, K.; Pradeep, T. Biopolymer-Reinforced Synthetic Granular Nanocomposites for Affordable Point-of-Use Water Purification. *Proc. Natl. Acad. Sci. U. S. A.* **2013**, *110*, 8459–8464.
- (46) Li, H.; Zaviska, F.; Liang, S.; Li, J.; He, L.; Yang, H. Y. A High Charge Efficiency Electrode by Self-Assembling Sulphonated Reduced Graphene Oxide onto Carbon Fibre: Towards Enhanced Capacitive Deionization. *J. Mater. Chem. A* **2014**, *2*, 3484–3491.
- (47) El-Deen, A. G.; Barakat, N. A. M.; Khalil, K. A.; Kim, H. Y. Development of Multi-Channel Carbon Nanofibers as Effective Electrodes for a Capacitive Deionization Process. *J. Mater. Chem. A* **2013**, *1*, 11001–11010.
- (48) Zhang, D.; Wen, X.; Shi, L.; Yan, T.; Zhang, J. Enhanced Capacitive Deionization of Graphene/Mesoporous Carbon Composites. *Nanoscale* **2012**, *4*, 5440–5446.
- (49) Wen, X.; Zhang, D.; Shi, L.; Yan, T.; Wang, H.; Zhang, J. Three-Dimensional Hierarchical Porous Carbon with a Bimodal Pore Arrangement for Capacitive Deionization. *J. Mater. Chem.* **2012**, *22*, 23835–23844.
- (50) Pasta, M.; Wessells, C. D.; Cui, Y.; La Mantia, F. A Desalination Battery. *Nano Lett.* **2012**, *12*, 839–843.
- (51) Maliyekkal, S. M.; Sreepasad, T. S.; Krishnan, D.; Kouser, S.; Mishra, A. K.; Waghmare, U. V.; Pradeep, T. Graphene: A Reusable Substrate for Unprecedented Adsorption of Pesticides. *Small* **2013**, *9*, 273–283.
- (52) Mossad, M.; Zou, L. Evaluation of the Salt Removal Efficiency of Capacitive Deionisation: Kinetics, Isotherms and Thermodynamics. *Chem. Eng. J.* **2013**, *223* (0), 704–713.
- (53) Mossad, M.; Zou, L. A Study of the Capacitive Deionisation Performance under Various Operational Conditions. *J. Hazard. Mater.* **2012**, *213–214*, 491–497.
- (54) Dudik, J. M.; Johnson, C. R.; Asher, S. A. Wavelength Dependence of the Preresonance Raman Cross Sections of CH₃CN, SO₄²⁻, ClO₄⁻, and NO₃⁻. *J. Chem. Phys.* **1985**, *82*, 1732–1740.
- (55) Pan, L.; Li, H.; Zhan, Y.; Zhang, Y.; Sun, Z. Electrosorption Behavior of Carbon Nanotube and Carbon Nanofiber Film Electrodes. *Curr. Phys. Chem.* **2011**, *1*, 16–26.
- (56) Pan, L.; Wang, X.; Gao, Y.; Zhang, Y.; Chen, Y.; Sun, Z. Electrosorption of Anions with Carbon Nanotube and Nanofiber Composite Film Electrodes. *Desalination* **2009**, *244*, 139–143.
- (57) Nguyen, T.; Roddick, F.; Fan, L. Biofouling of Water Treatment Membranes: A Review of the Underlying Causes, Monitoring Techniques and Control Measures. *Membranes* **2012**, *2*, 804–840.

(58) Chen, J.; Peng, H.; Wang, X.; Shao, F.; Yuan, Z.; Han, H. Graphene Oxide exhibits Broad-Spectrum Antimicrobial Activity against Bacterial Phytopathogens and Fungal Conidia by Intertwining and Membrane Perturbation. *Nanoscale* **2014**, *6*, 1879–1889.

(59) Mansouri, J.; Harrison, S.; Chen, V. Strategies for Controlling Biofouling in Membrane Filtration Systems: Challenges and Opportunities. *J. Mater. Chem.* **2010**, *20*, 4567–4586.

Supporting Information

Cellulose Derived Graphenic Fibers for Capacitive Desalination of Brackish Water

Nalenthiran Pugazhenthiran,¹ Soujit Sen Gupta,¹ Anupama Prabhath,¹ Muthu Manikandan,¹
Jakka Ravindran Swathy,¹ V. Kalyan Raman² and Thalappil Pradeep^{1,*}

¹DST Unit of Nanoscience (DST UNS) and Thematic Unit of Excellence (TUE). Department
of Chemistry, Indian Institute of Technology Madras, Chennai 600 036, India.

²Centre of Excellence (Biotechnology) & Water and wastewater Technology, Thermax
Limited, Pune 411019, India

E-mail: pradeep@iitm.ac.in; Fax: +91-44-2257-0545.

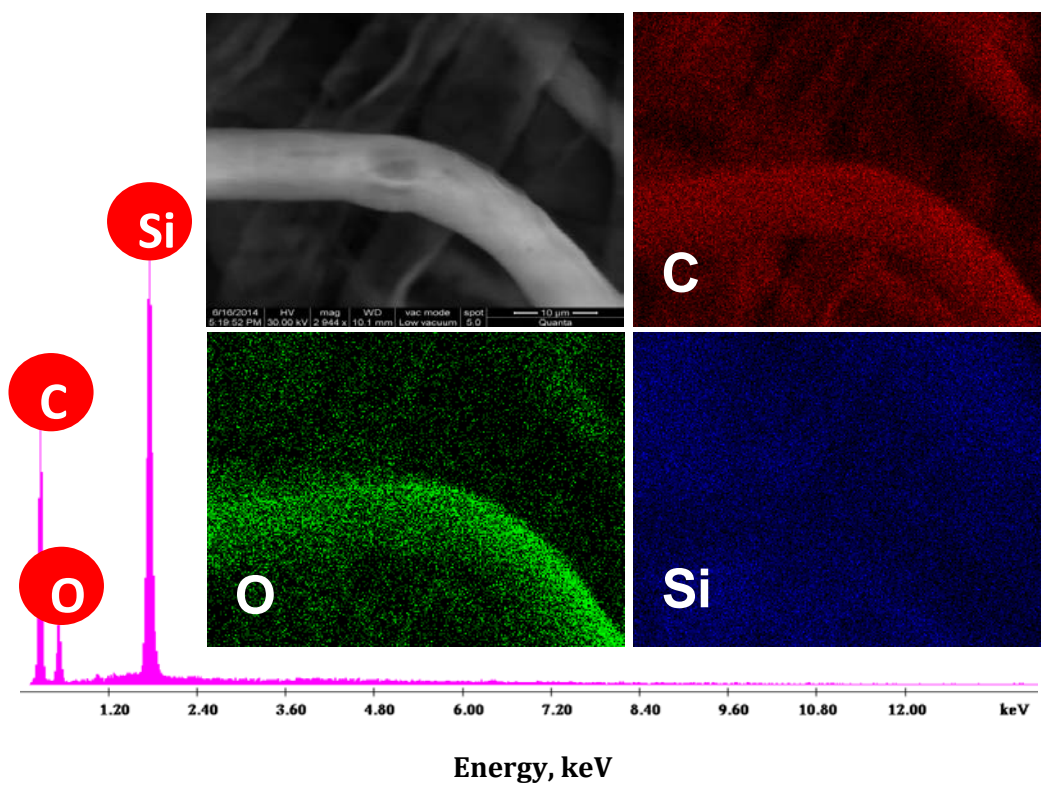


Figure S1. EDS spectrum of the layer-by-layer stacked carbon-graphite electrode before SiO_2 etching. Inset: Its corresponding SEM image and elemental mapping images.

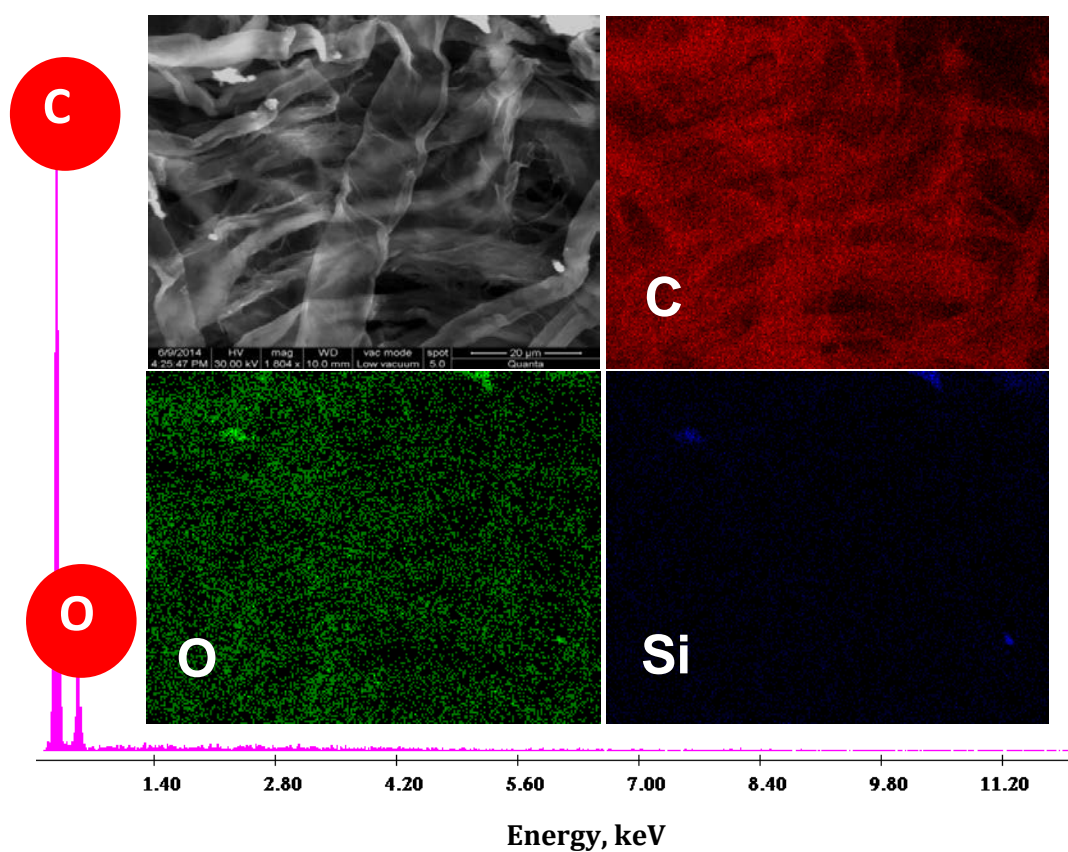


Figure S2. EDS spectrum of the layer-by-layer stacked carbon-graphite electrode after etching SiO₂. Inset: SEM and Elemental mapping images.

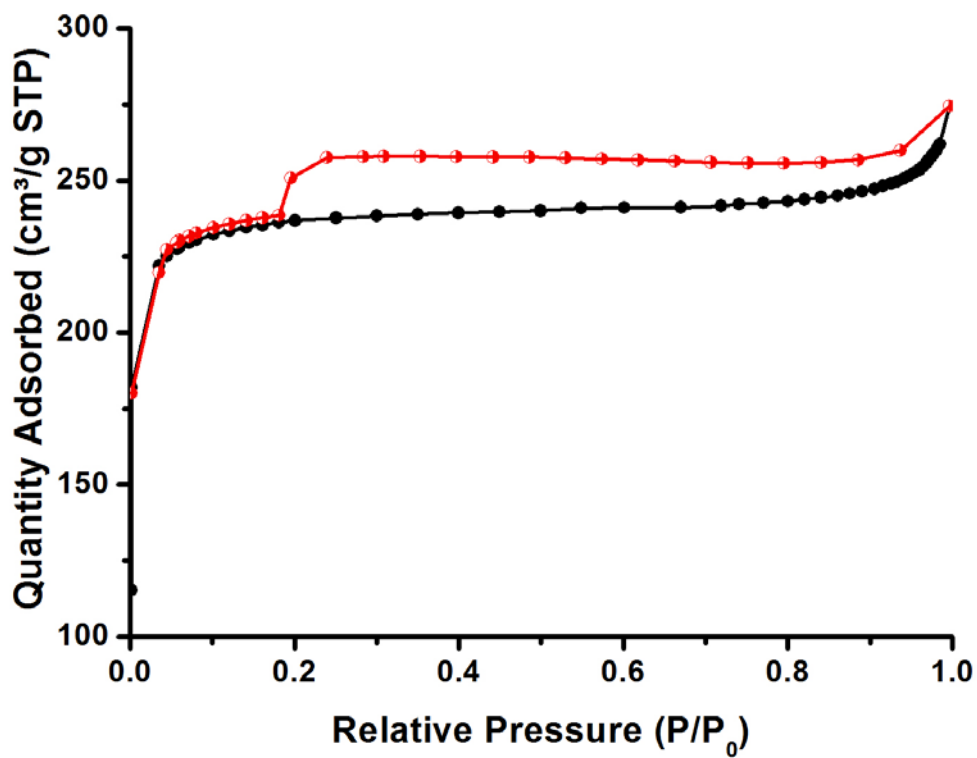


Figure S3. N₂ adsorption–desorption isotherms of graphite-reinforced carbon fiber electrode.

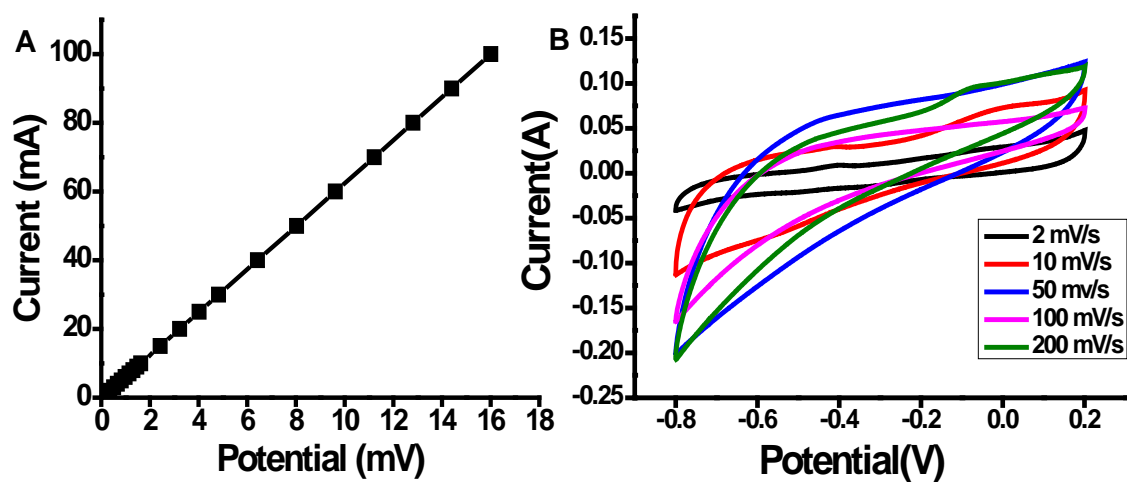


Figure S4:A) I-V curve and B) CV curves of the GrC electrode at varying scan rates

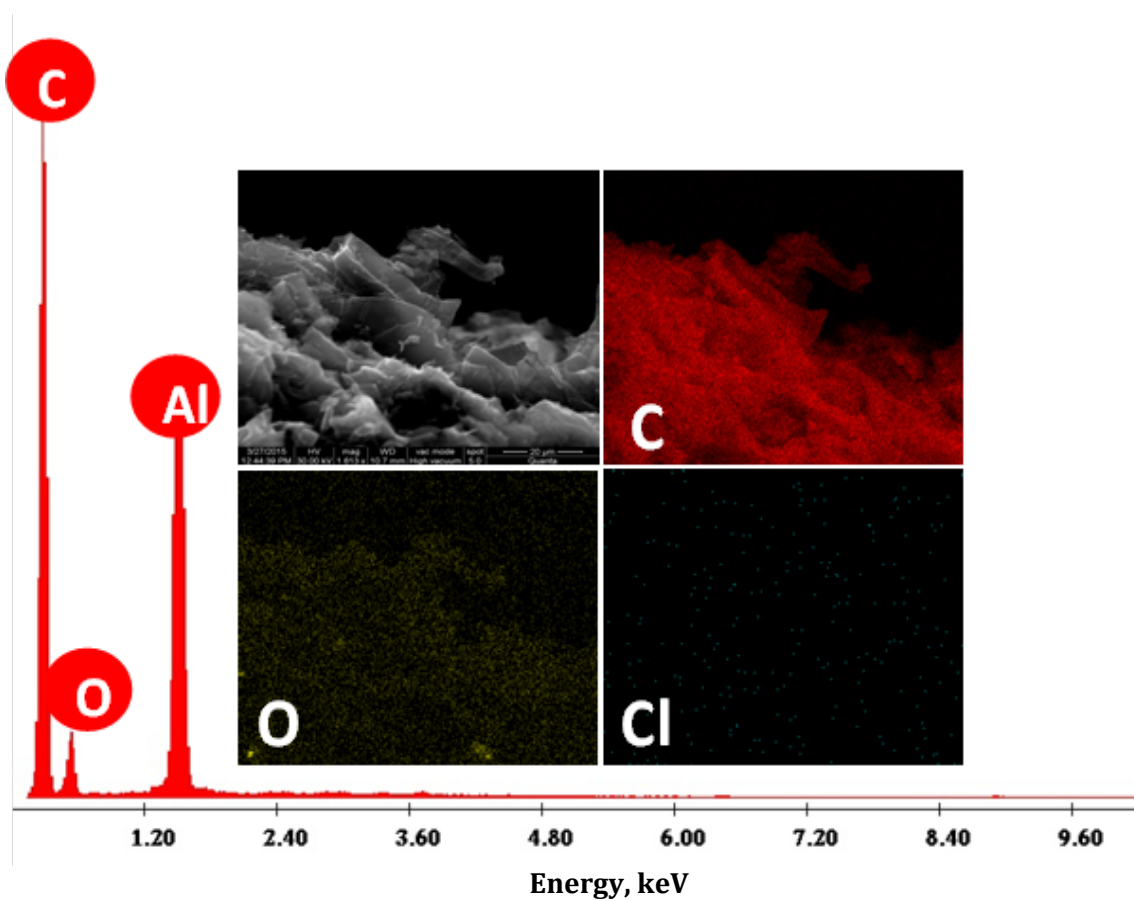


Figure S5. Electro-adsorption and desorption performance of the graphite-reinforced carbon fiber electrode in NaCl solution. EDS spectrum and their elemental mapping images of the regenerated positive terminal carbon-graphite electrode (after first cycle). *Note: Aluminum comes from the SEM sample stubs.*

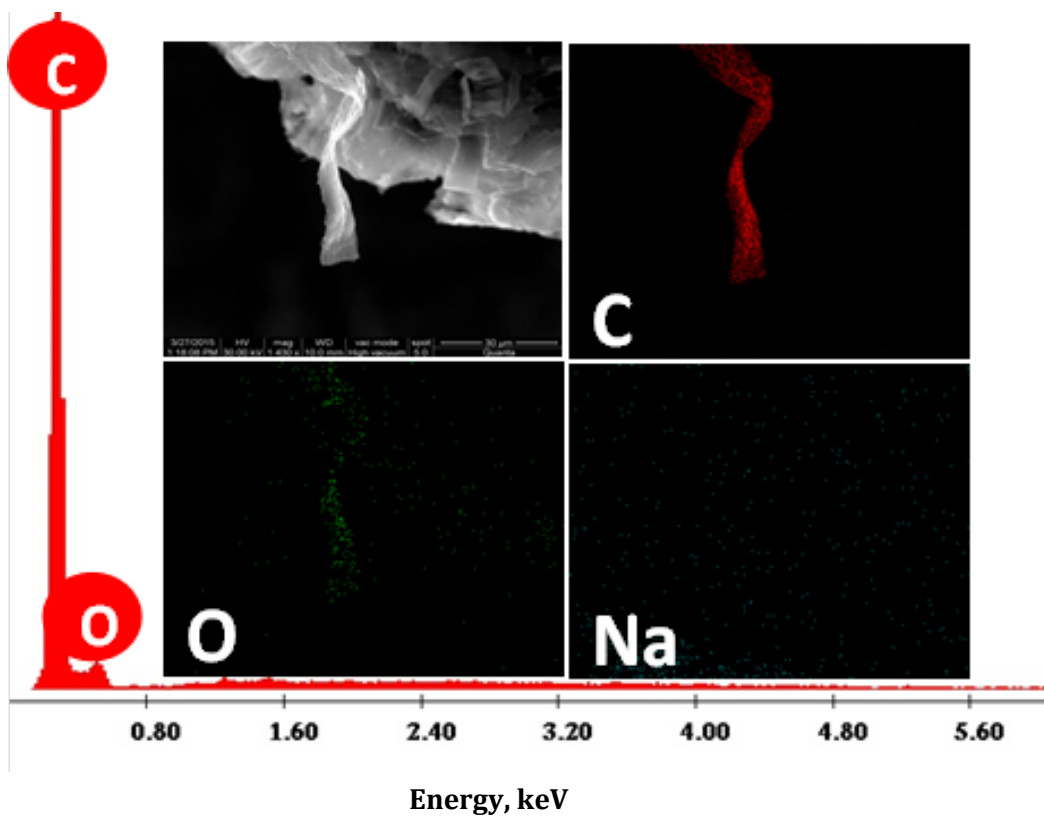


Figure S6. Electro-adsorption and desorption performance of the graphite-reinforced carbon fiber electrode in NaCl solution. EDS spectrum and their elemental mapping images of the regenerated negative terminal carbon-graphite electrode (after first cycle).

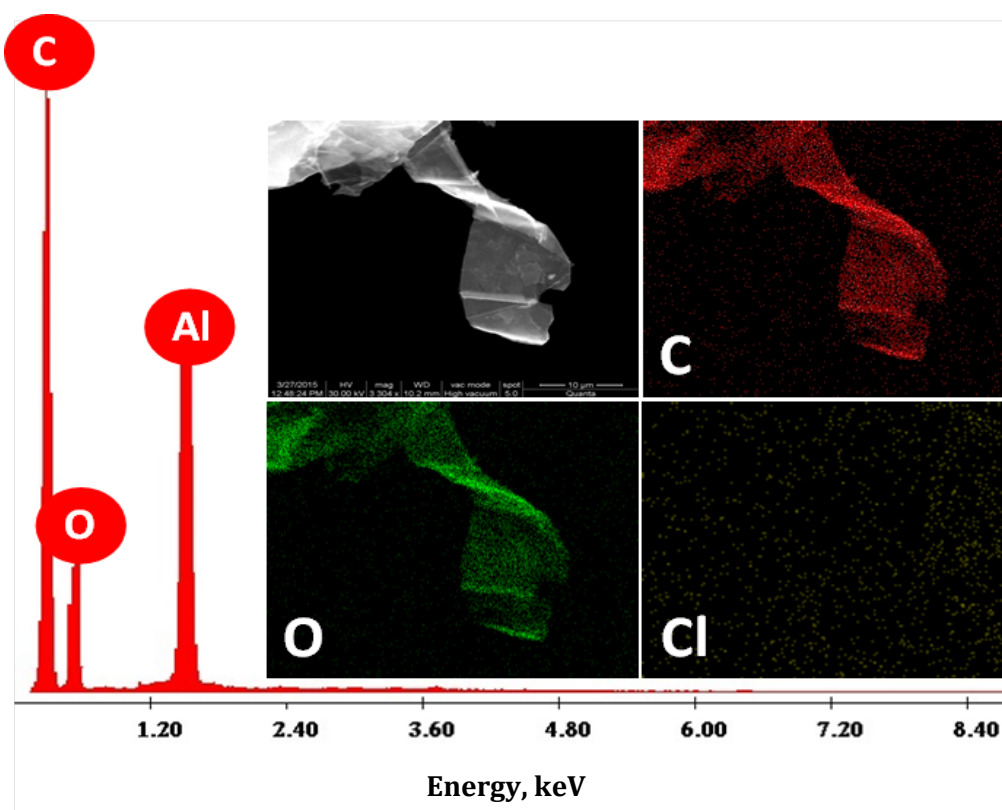


Figure S7. Electro-adsorption and desorption performance of the graphite-reinforced carbon fiber electrode in NaCl solution. EDS spectrum and their elemental mapping images of the regenerated positive terminal carbon-graphite electrode (after ten consecutive cycle). *Note: Aluminum comes from the SEM sample stubs.*

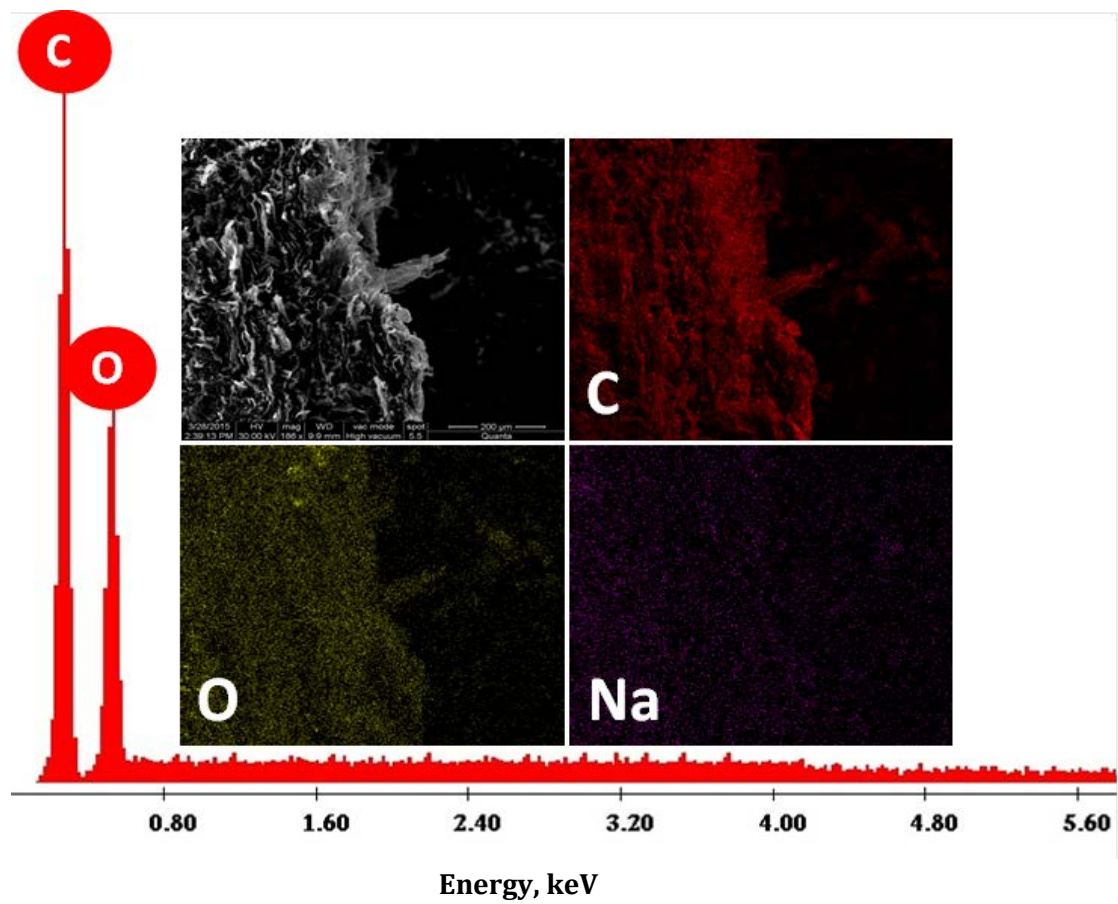


Figure S8. Electro-adsorption and desorption performance of the graphite-reinforced carbon fiber electrode in NaCl solution. EDS spectrum and their elemental mapping images of the regenerated negative terminal carbon-graphite electrode (after ten consecutive cycle).

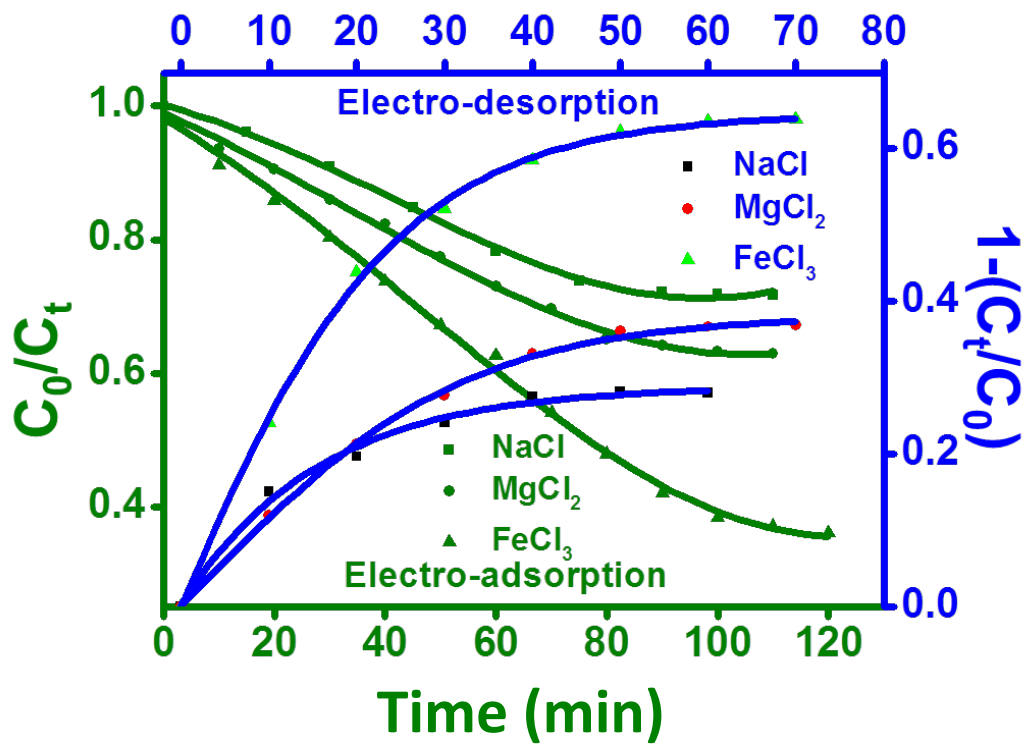


Figure S9. Plot of CDI results of electro-adsorption and desorption performance of the graphite-reinforced carbon fiber electrode in different charged species i.e., Na⁺, Mg²⁺ and Fe³⁺.

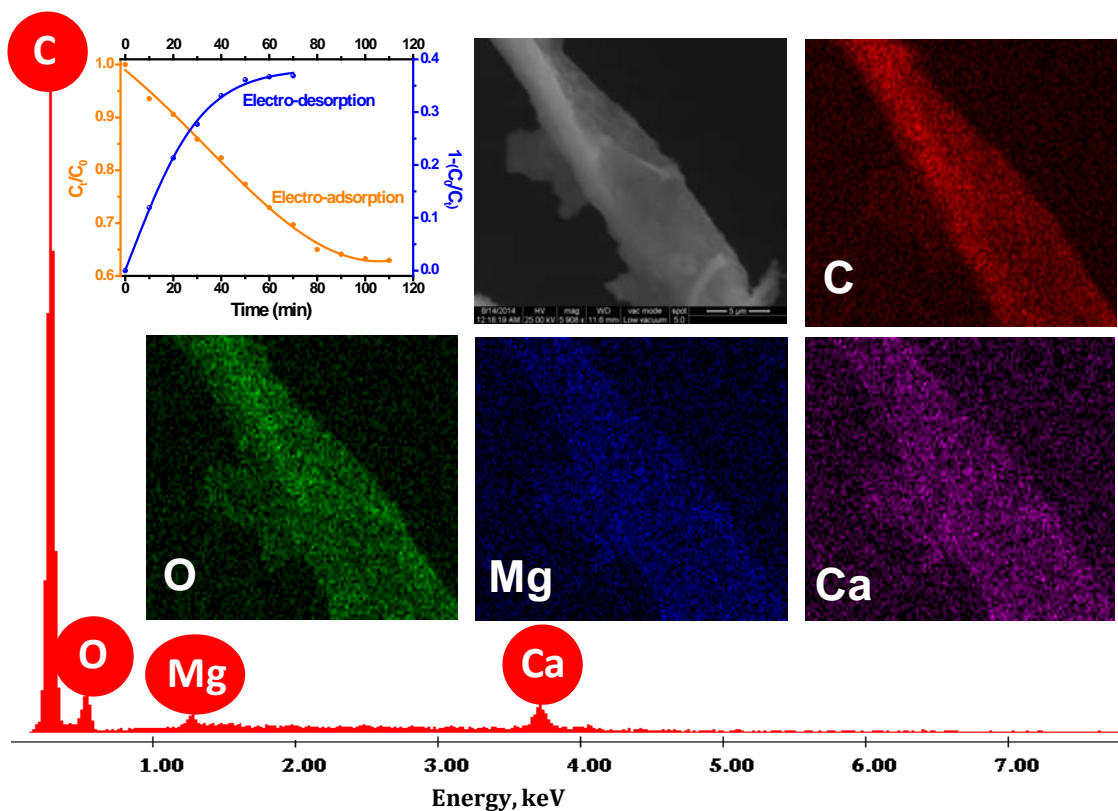


Figure S10. Electro-adsorption and electro-desorption performance of the graphite-reinforced carbon fiber electrode in MgCl_2 solution. EDS spectrum and their elemental mapping images of the negative terminal after electro-adsorption of the carbon-graphite electrode. *Note: Calcium is from the water used.*

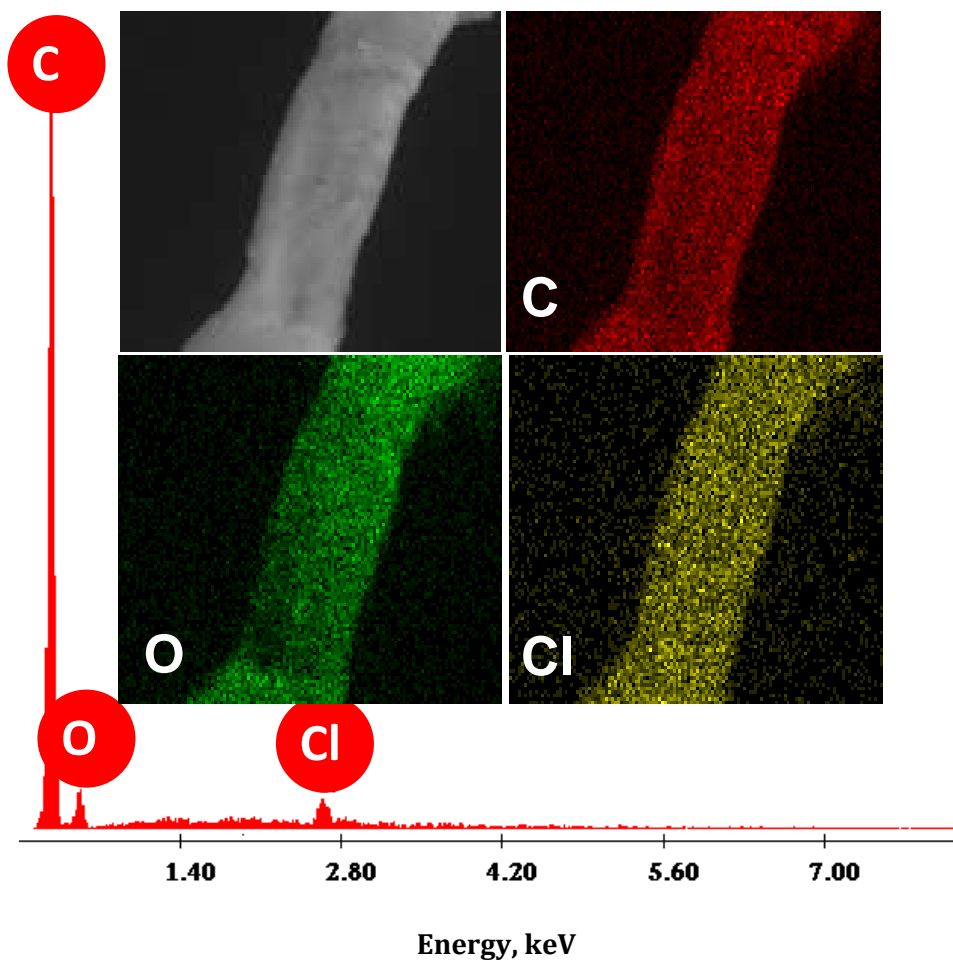


Figure S11. Electro-adsorption and desorption performance of the graphite-reinforced carbon fiber electrode in MgCl_2 solution. EDS spectrum and their elemental mapping images of the positive terminal after electro-adsorption of the carbon-graphite electrode.

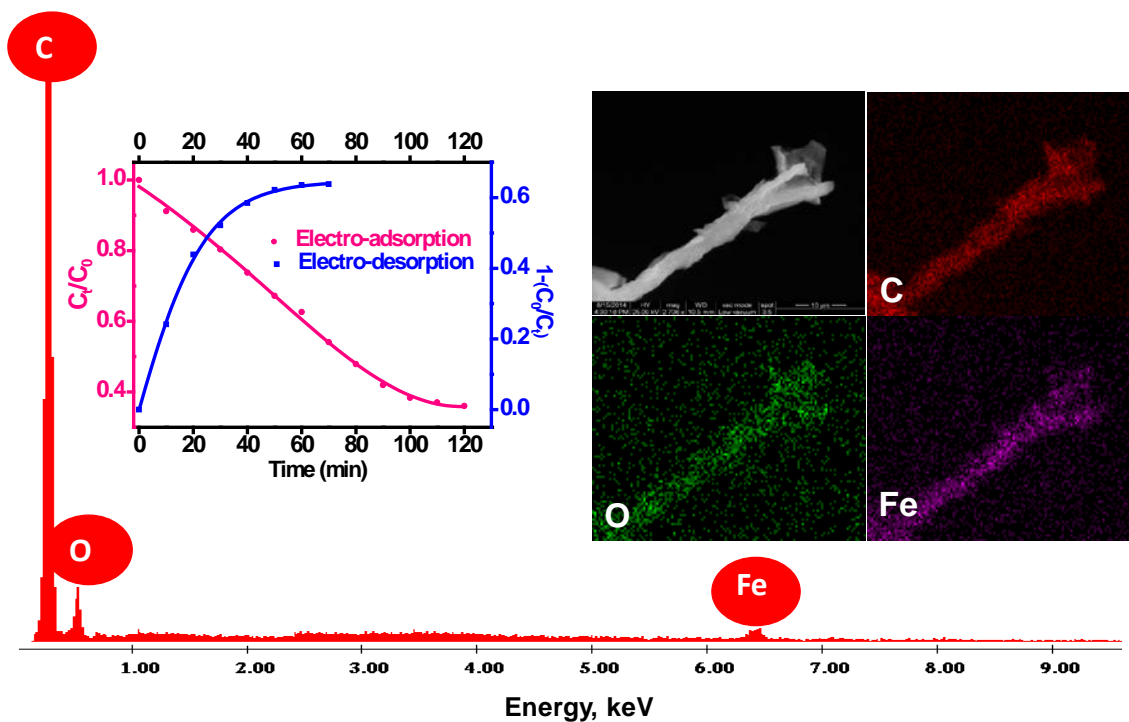


Figure S12. Electro-adsorption and desorption performance of the graphite-reinforced carbon fiber electrode in FeCl_3 solution. EDS spectrum and their elemental mapping images of the negative terminal after electro-adsorption on the carbon-graphite electrode.

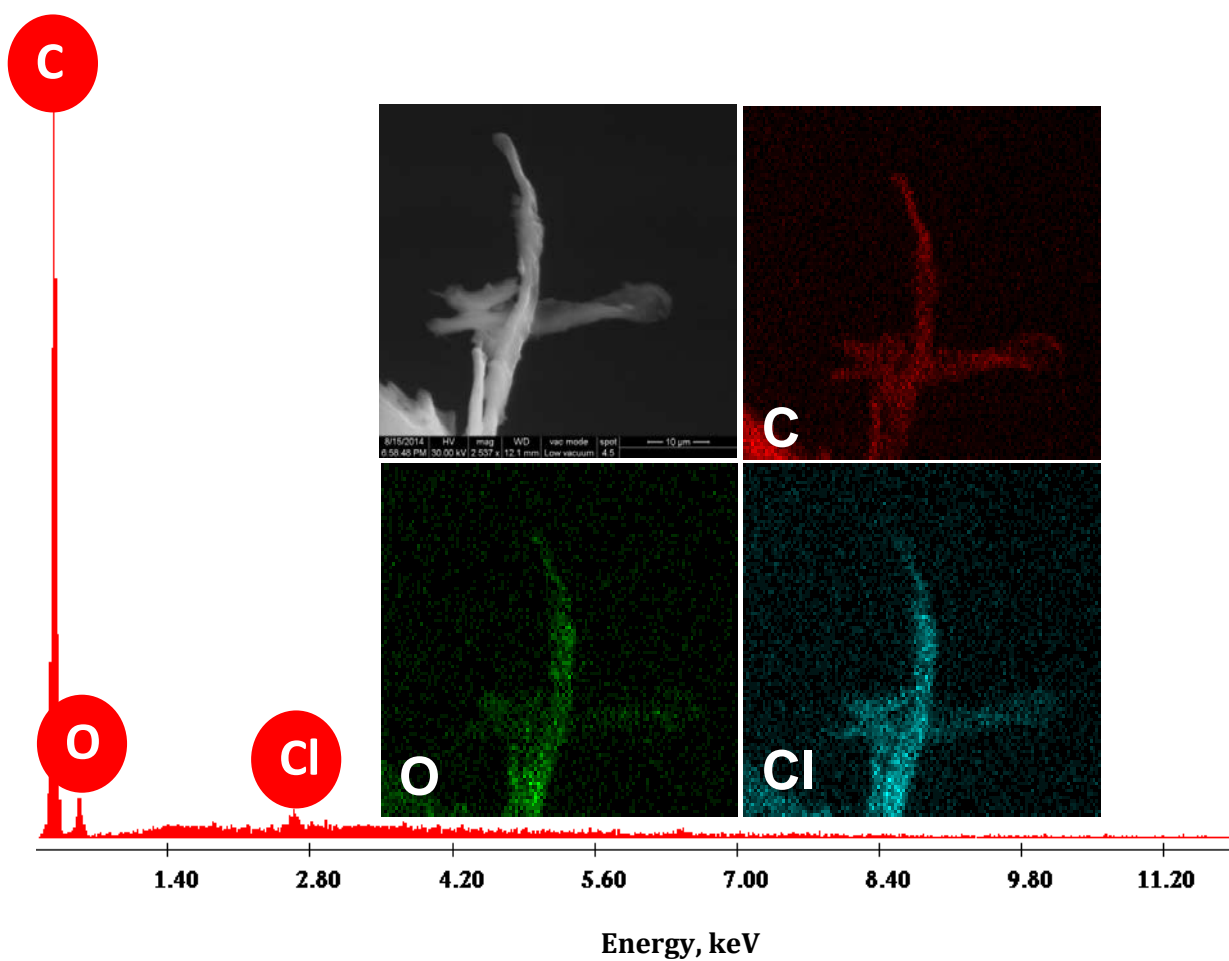


Figure S13. Electro-adsorption and desorption performance of graphite reinforced carbon fiber electrode in FeCl_3 solution. EDS spectrum and their elemental mapping images of the positive terminal after electro-adsorption on the carbon-graphite electrode.

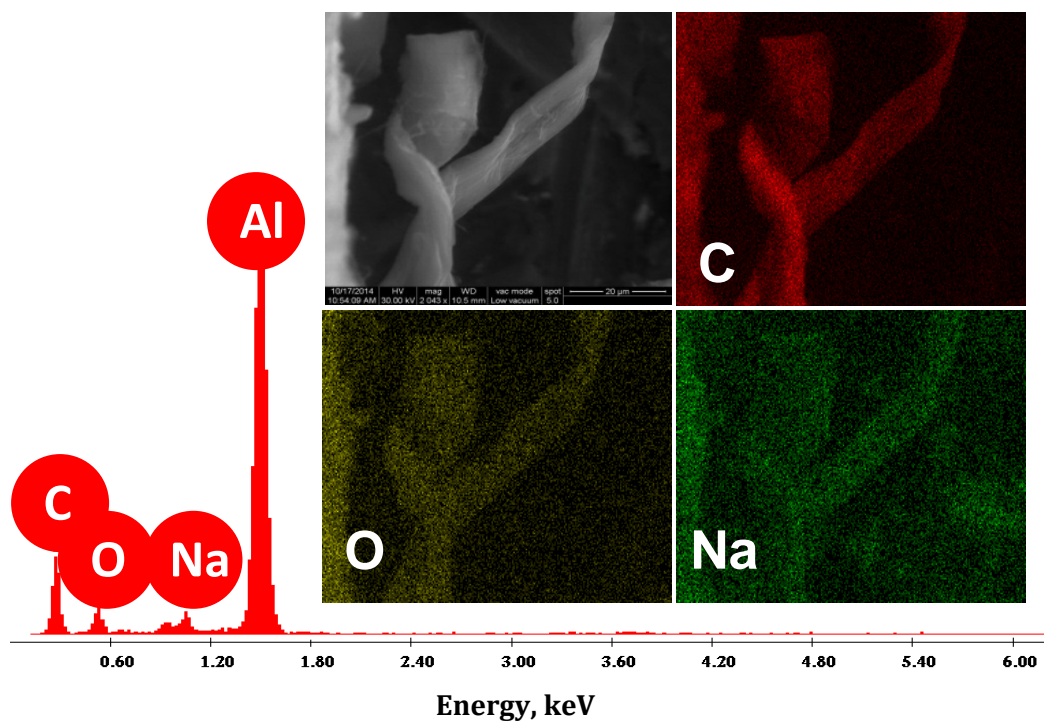


Figure S14. CDI performance of graphite reinforced carbon fiber electrode in the mixed negative ions (Cl^- , F^- , NO_3^- , SO_4^{2-}) system. EDS spectrum and their elemental mapping images of the negative terminal after electro-adsorption on the porous carbon-graphite electrode. *Note: Aluminum comes from the SEM sample stubs.*

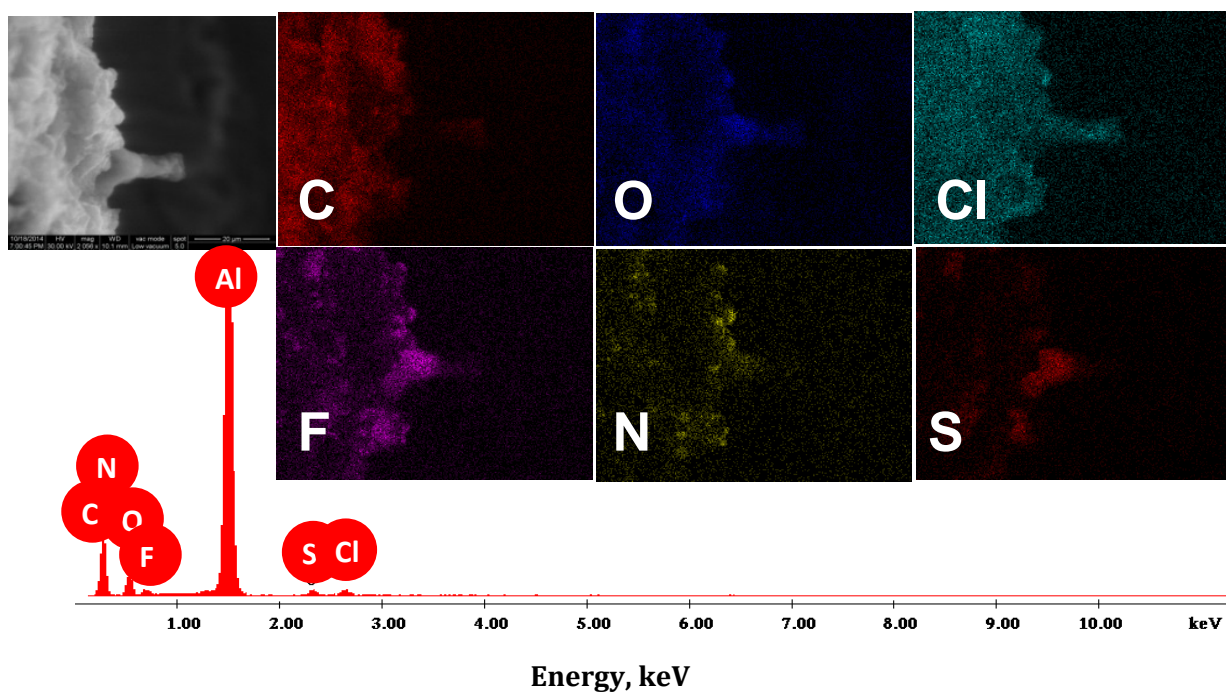


Figure S15. CDI performance of graphite reinforced carbon fiber electrode in the mixed negative ions (Cl^- , F^- , NO_3^- , SO_4^{2-}) system. EDS spectrum and their elemental mapping images of the positive terminal after electro-adsorption on the porous carbon-graphite electrode which shows the presence of O, Cl, F, N and S. *Note: Aluminum comes from the SEM sample stubs.*

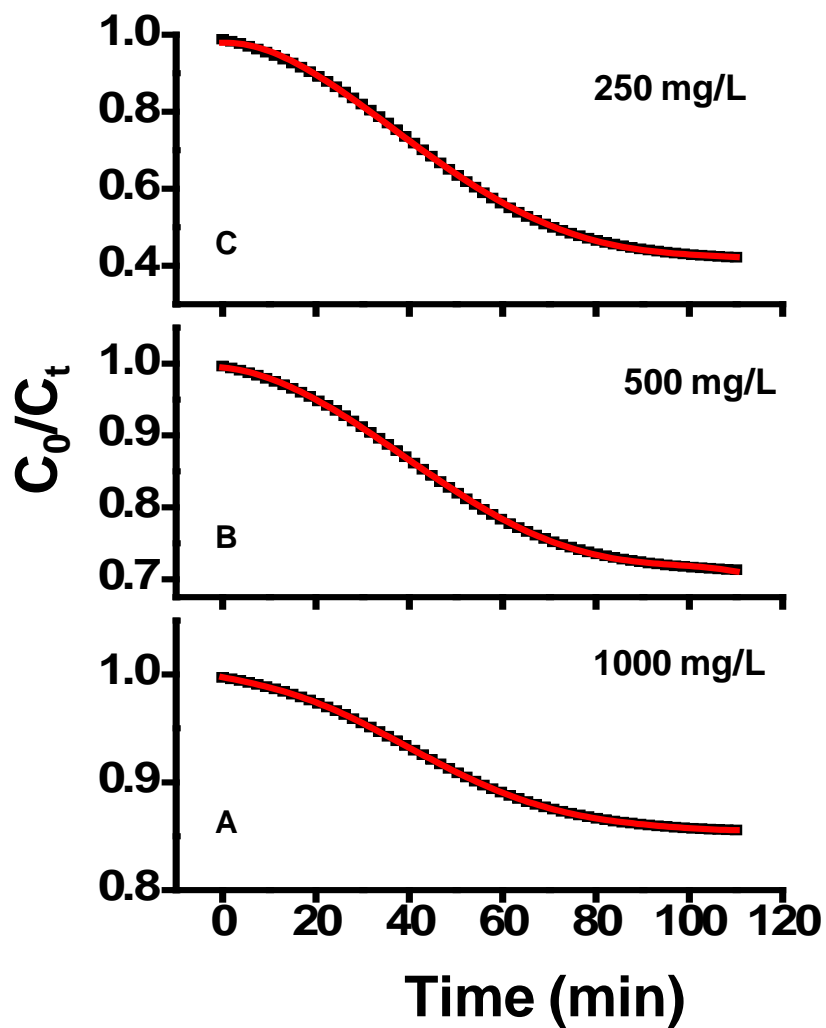


Figure S16. CDI performance of the GrC electrode at different NaCl concentration A) 1000, B) 500 and C) 250 mg/L. All other parameters are kept constant. This measurement was performed as it is known that the salt concentrations used to measure the electrosorption performance influence the observed capacities.



Cite this: *Nanoscale*, 2015, 7, 14305

Efficient red luminescence from organic-soluble Au₂₅ clusters by ligand structure modification†

Ammu Mathew,^a Elizabeth Varghese,^a Susobhan Choudhury,^b Samir Kumar Pal^b and T. Pradeep*^a

An efficient method to enhance visible luminescence in a visibly non-luminescent organic-soluble 4-(*tert* butyl)benzyl mercaptan (SBB)-stabilized Au₂₅ cluster has been developed. This method relies mainly on enhancing the surface charge density on the cluster by creating an additional shell of thiolate on the cluster surface, which enhances visible luminescence. The viability of this method has been demonstrated by imparting red luminescence to various ligand-protected quantum clusters (QCs), observable to the naked eye. The bright red luminescent material derived from Au₂₅SBB₁₈ clusters was characterized using UV-vis and luminescence spectroscopy, TEM, SEM/EDS, XPS, TG, ESI and MALDI mass spectrometry, which collectively proposed an uncommon molecular formula of Au₂₉SBB₂₄S, suggested to be due to different staple motifs protecting the Au₂₅ core. The critical role of temperature on the emergence of luminescence in QCs has been studied. The restoration of the surface ligand shell on the Au₂₅ cluster and subsequent physicochemical modification to the cluster were probed by various mass spectral and spectroscopic techniques. Our results provide fundamental insights into the ligand characteristics determining luminescence in QCs.

Received 26th May 2015,

Accepted 21st July 2015

DOI: 10.1039/c5nr03457d

www.rsc.org/nanoscale

Introduction

Luminescent noble metal quantum clusters (QCs) with intriguing physicochemical properties such as near infrared (NIR) emission, low toxicity, good biocompatibility, *etc.* have shown significant promise in biolabeling, imaging and sensing.^{1–4} Consequently, various attempts have been made to synthesize QCs with visible luminescence. The photophysical properties of QCs largely depend on their structure and chemical environments such as the cluster core size, protecting ligands, solvents, surface charge, *etc.*⁵ A better understanding of the origin of luminescence in such clusters (whether from core or staple atoms) can lead to new approaches for the design and synthesis of clusters with strong luminescence and improved quantum yields (QY). Though size-dependent emission, ranging from UV to IR, is a commonly observed phenomenon in such clusters;⁶ a change in visible emission might not always be a direct indication of change in cluster core size.⁷ A recent study

suggests that nonluminescent oligomeric Au(I)-glutathione complexes can generate very strong luminescence upon aggregation. An aggregation-induced emission (AIE) mechanism was proposed for the synthesis of a highly luminescent Au cluster.⁸ Also similar-sized clusters protected by different ligands often lead to clusters with varying QYs suggesting the strong ligand effects on luminescence.^{9–11} Therefore, appropriate ligands are chosen for specific applications.^{2,3,12} Recently thermal treatment of mercaptosuccinic acid and tiopronin protected Au clusters was found to enhance the quantum efficiency of NIR emission significantly.¹³ However, the vast majority of QCs showing visible luminescence are water-soluble and are prepared in polar solvents with hydrophilic ligands.^{5,7,14–17} Visible luminescence in hydrophobic ligand-stabilized QCs, in nonpolar organic media, is rare.¹⁸ For organic-soluble clusters, emission is typically in the NIR region with weak QYs ($\sim 10^{-4}$ and 10^{-5}).^{9,19–21} Such materials capable of dissolving in non-polar and moderately polar solvents could be of great interest for their applications in biomedicine and imaging.^{22–25} Among the various nonpolar organic ligand-modified QCs known in the literature, Au₂₅SR₁₈ (SR denotes the thiolate ligand) with a known crystal structure,^{26–28} is well-studied. Though various aspects of Au₂₅ such as catalytic,^{29–32} electrochemical,³³ magnetic,^{28,34,35} chiral,³⁶ alloying,^{37–41} ligand exchange,^{42–44} supramolecular functionalization,⁴⁵ *etc.*,^{2,20,46} have been explored, the absence of strong visible luminescence in the organic

^aDST Unit of Nanoscience (DST UNS) and Thematic Unit of Excellence, Department of Chemistry, Indian Institute of Technology Madras, Chennai 600036, India. E-mail: pradeep@iitm.ac.in; Fax: +91-44 2257-0545

^bDepartment of Chemical Biological & Macromolecular Sciences, S. N. Bose National Centre for Basic Sciences, Block JD, Sector III, Salt Lake, Kolkata 700098, India

†Electronic supplementary information (ESI) available: Additional data on characterization of red luminescent Au₂₉ QC and comparison with parent Au₂₅SBB₁₈ are given. See DOI: 10.1039/c5nr03457d

phase hinders their applications in areas such as sensing and imaging. Even though fine-tuning of surface characteristics has been exploited for modifying the physicochemical properties of QCs,^{9,13,16,45} new approaches to make significant modifications in the physical and chemical properties of QCs without disrupting the cluster core are highly desirable. Herein, we describe an efficient strategy to increase the visible luminescence of a visibly non-luminescent and organic thiol-stabilized QC by increasing its surface charge density while preserving its stability. This was achieved by making an additional shell of Au(I)SR thiolate on a visibly non-luminescent Au₂₅ precursor *via* mild thermal annealing.

Results and discussion

For this study, we chose Au₂₅ QCs protected by a 4-(*tert*-butyl)-benzyl mercaptan (SBB) ligand, synthesized and characterized in our previous work,⁴⁵ as they exhibited well-defined optical and mass spectral features. The optical absorption spectrum of Au₂₅SBB₁₈ solution (black trace in Fig. 1A) revealed discrete molecule-like features, characteristic of the cluster. The stability of the cluster was confirmed using optical absorption measurements. Fig. S1A in the ESI† shows the comparison of the UV-vis absorption spectra of as-prepared Au₂₅ (black trace) and the same after 2 months (red trace) of synthesis. Moreover, the Au₂₅SBB₁₈ QCs were stable against thiol-induced etching of the core even in the presence of ten-fold excess BBSH present in solution at room temperature (Fig. S1B†).

Au₂₅ clusters stabilized by hydrophobic ligands such as phenylethanethiol (PET), dodecanethiol (DDT), BBSH, *etc.*, have a weak emission (10^{-5} – 10^{-7} QY) in the visible region and a relatively stronger emission in the NIR region (10^{-3} QY). The fluorescence is influenced by various factors such as the nature of the protecting ligands^{9,10} as well as their charge states.^{9,47,48} Au₂₅SBB₁₈ QCs also showed a strong luminescence in the NIR region in comparison with the visible region (blue and green traces in Fig. S1C†), an expanded version (125 000 times) of the original spectrum is also shown for comparison) and no luminescence was observable to the naked eye (see photographs shown in the inset of Fig. S1C†). Interestingly, heating of purified Au₂₅SBB₁₈ clusters with Au(I)SBB thiolate (1:1 Au³⁺ and BBSH thiol) for 2 h enhanced the visible luminescence significantly (Fig. S2A†), along with increasing amount of thiolate in the solution. This could possibly be due to the surface charge modification of the QCs.^{8,9,49,50} The intensity of luminescence reached a maximum after the addition of 0.05 mL of thiolate to Au₂₅ (1 mL, 0.1 mM) (Fig. S2B†). No further enhancement in the intensity was observed, suggesting the saturation of the cluster surface by the thiolate shell that can directly interact with the cluster core. Moreover, heating the purified cluster solution at 55 °C for a period of 24 h with additionally added Au(I)SBB thiolate was identified to yield a maximum emission intensity (Fig. S2C†). These experiments are described in more detail in the ESI.† The samples were cooled for 3 h before the PL measurement. A bar diagram shown in Fig. S2D† illustrates the improved luminescence obtained by the addition of thio-

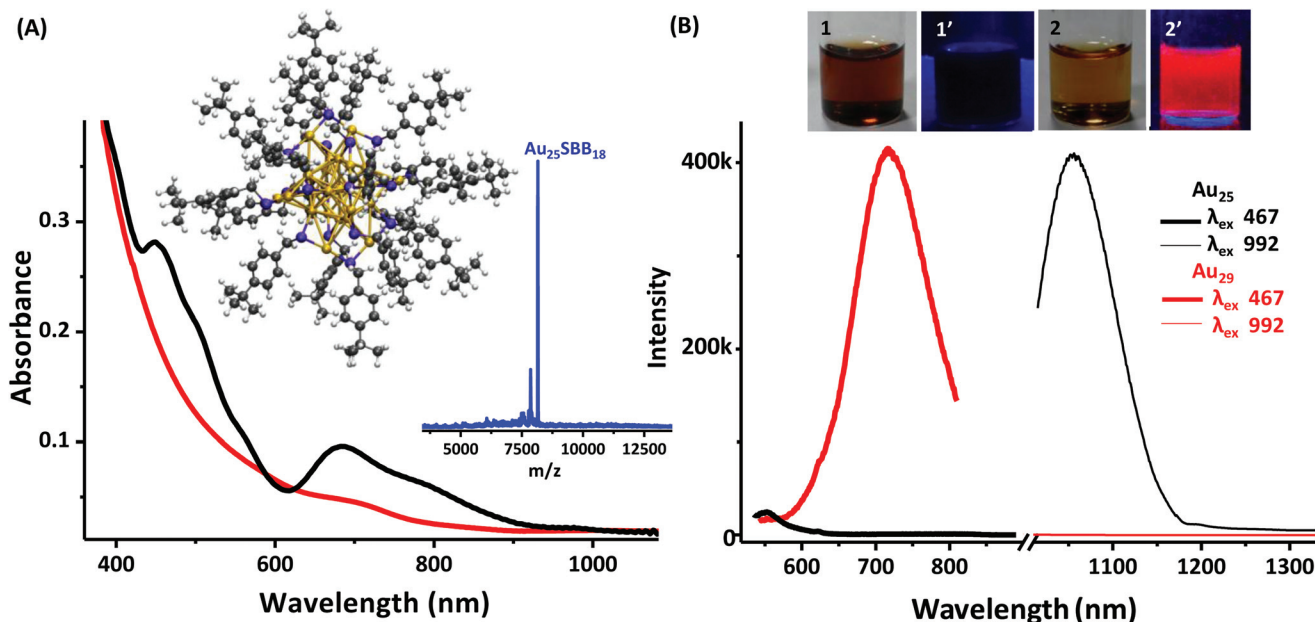


Fig. 1 Comparison of the UV-vis absorption spectrum (A) and emission spectra (B) of Au₂₅SBB₁₈ (black trace) and the resultant red luminescent cluster (red trace) in the visible (thick lines) and NIR range (thin lines), at excitation wavelengths of 467 and 992 nm, respectively. The inset of (A) shows a visualization of the DFT-optimized structure of Au₂₅SBB₁₈. Gold, sulfur, carbon and hydrogen atoms are shown in gold, blue, dark grey, and light grey, respectively. The MALDI mass spectrum of parent Au₂₅SBB₁₈ clusters showing a peak at m/z 8152 Da is also shown in the inset. Photographs of the Au₂₅ (1, 1') and red luminescent (2, 2') clusters in visible light (1, 2) and UV light (1', 2'), respectively are shown in the inset of (B).

late to pure Au₂₅ QCs with heating for 24 h (green bars), in comparison with that without heating for 24 h (red bars). Such a thiolate addition to previously prepared red luminescent clusters resulted only in the quenching of cluster emission due to dilution of the solution (blue bars). Based on the above observation, we optimized the conditions to obtain red luminescent clusters in high yield, which involved the following steps: (i) synthesis of the precursor Au₂₅SBB₁₈ QCs, (ii) thermal treatment of Au₂₅ QCs for 24 h and addition of definite amounts of Au(I)SBB thiolate to the reaction medium at definite intervals and (iii) rapid cooling.

Optical properties of the parent Au₂₅ QCs were modified upon forming the red-emitting cluster (labelled as Au₂₉ in the figure; nuclearity explained later), as depicted in Fig. 1. Though a dampening of the characteristic absorption features of Au₂₅ clusters (black trace in Fig. 1A) was observed for the red-luminescent clusters (red trace), a distinct shoulder at 707 nm was observed in the case of the latter (see Fig. S3†). The dampening could be due to the increased charges on the cluster surface due to thiolate attachment.⁹ Photographs taken under UV light (inset of Fig. 1B) clearly show the drastic change in the visible luminescence of parent Au₂₅SBB₁₈ and red-luminescent clusters. Photoluminescence spectra for both the clusters at excitation wavelengths, 467 (thick line) and 992 nm (thin line), respectively are shown in Fig. 1B. Parent Au₂₅SBB₁₈ emits primarily in the NIR region (see Fig. S1C†) with a peak maximum at 1030 nm (black thin line in Fig. 1B) while the red-emitting cluster showed an emission maximum at 737 nm (red thick line) with a concomitant loss of NIR emission. The fluorescence QY of the resultant red luminescent cluster was calculated to be 1.8% in THF medium at room temperature. This was much higher than that of parent Au₂₅SBB₁₈ clusters (0.04%) and that reported for other organic thiolate ligand protected Au₂₅ clusters.^{9,19–21} Fig. S4† compares the NIR emission (excited at 992 nm) from the parent Au₂₅SBB₁₈ QCs (green trace) and the resultant red luminescent clusters (blue trace). NIR emission from the red luminescent clusters is expanded (140 times, blue dotted line in Fig. S4†) for clarity. The absence of the prominent emission feature at 1030 nm (seen in parent Au₂₅) in the red luminescent cluster indicates the modification of the cluster. Identical concentrations of both the clusters are compared in the spectra, under similar instrumental conditions.

It is likely that the emergence of luminescence could be due to the core etching of the cluster by unreacted ligands as reported in earlier studies.^{51–56} Core etching of nanoparticles/clusters in aqueous medium to form smaller clusters with luminescence is well known in the literature. However, this scenario can be ruled out in our case as the parent Au₂₅SBB₁₈ QCs exhibited high stability against core etching upon heating in the presence of excess BBSH. Intact optical absorption features of Au₂₅SBB₁₈ even in the presence of high thiol concentrations are observed in Fig. S1B.† Fig. S5A† shows the luminescence spectra of the solutions before and after addition of similar amounts of BBSH thiol (instead of Au(I)SBB thiolate) to the Au₂₅ cluster, under identical reaction con-

ditions. Though reports exist on the observation of luminescence from various Au(I) complexes in solution under different conditions,^{8,57} this was ruled out in our case as heating the Au(I)SBB thiolate for 24 h under similar conditions also did not result in luminescent species (Fig. S5B†), validating that the observed luminescence was not from a Au(I)SBB thiolate. Moreover, comparison of the photoluminescence profile of the red luminescent cluster with identical concentrations (with respect to BBSH thiol) of precursor species validates its formation (Fig. S6†).

The red-emitting cluster could be successfully separated by preparative thin layer chromatography (TLC) with dichloromethane in hexane as the eluent (inset of Fig. 2A). TLC as a methodology for separating clusters has been reported earlier.⁵⁸ It is important to have pure QCs in order to determine their molecularity using mass spectrometric techniques. Both the clusters contain a certain amount of free BBSH which is observed as a blue band on the TLC plate, under UV light. Fig. S7† shows the SEM and EDAX images of a TLC plate with the separated red luminescent fraction. Photographs of the plate under UV and visible light (a and a' in Fig. S7†) show the distinct luminescence.

Electrospray ionization mass spectrometry (ESI MS) has been considered as a reliable spectroscopic technique for the precise characterization of the cluster in the absence of crystal structures. Fig. S8A† compares the ESI mass spectra, in the negative ion mode, collected from the parent Au₂₅SBB₁₈ QCs (black trace) and the red luminescent cluster (red trace). In the case of the red luminescent cluster (Fig. 2A), apart from a peak at *m/z* 8152 (marked with a *) corresponding to the parent Au₂₅SBB₁₈ species, three intense peaks at *m/z* 4467, 4656 and 4844 were observed (region marked with a # in Fig. 2A). Fig. S8B† shows an expanded view of the region marked with the symbol, # in Fig. 2A. A difference of *m/z* 188 between the peaks, corresponding to (Au + SBB)/2, was observed between the three peaks marked with i, ii and iii in Fig. 2A. The isotope separation seen in each of the peaks is *m/z* 0.5, suggesting a dianion. From a theoretical prediction and isotope distribution, the peaks were assigned to [Au₂₇(SBB)₂₀S]²⁻, [Au₂₈(SBB)₂₁S]²⁻ and [Au₂₉(SBB)₂₂S]²⁻ corresponding to [Au_{*n*}(SBB)_{*n*}S]²⁻ (*n* = 2–4) in addition to Au₂₅SBB₁₈. The almost equal intensity of the three species indicates that they are formed as a result of fragmentation of a single species, due to asymmetric cleavage of similar bonds, rather than the formation of individual species in solution.

Evidence of the thiolate shell was obtained from matrix-assisted laser desorption ionization (MALDI) mass spectrometry as well (green trace in Fig. 2B). Though weak features were observed after 12 h, distinct peaks corresponding to the addition of the [S(AuSBB)_{*n*}] unit to Au₂₅SBB₁₈ QC emerged after 24 h of the reaction (black to green trace in Fig. 2B). The peaks were separated by a mass difference of *m/z* 376 corresponding to a unit of (Au + SBB) and the highest peak was Au₂₉SBB₂₂S. This is in agreement with ESI MS data shown in Fig. 2A. Time dependent MALDI measurements confirmed that the red luminescent cluster, henceforth termed as Au₂₉,

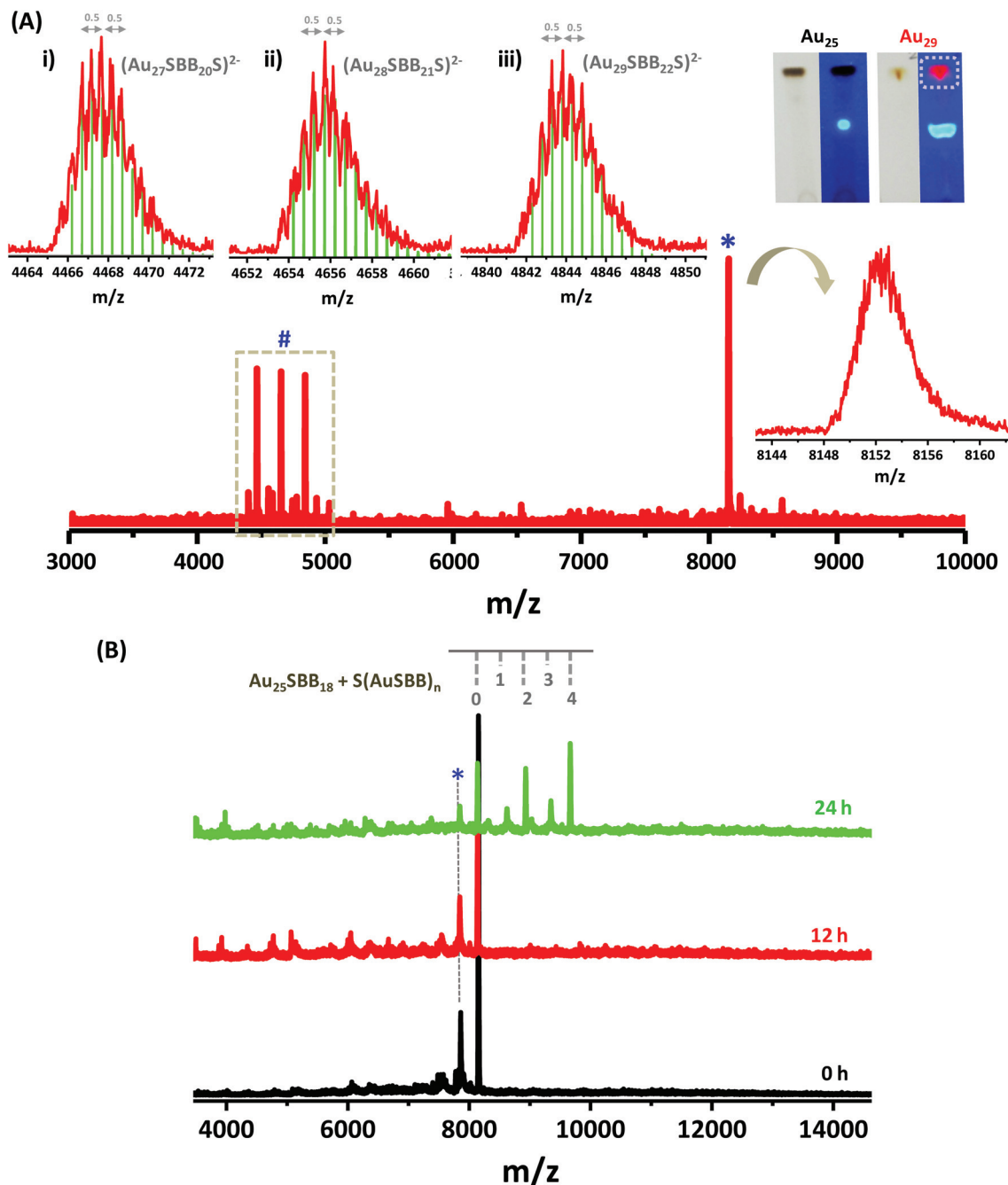


Fig. 2 ESI MS (A) and time dependent evolution of MALDI mass spectra (B) in negative ion mode of the red luminescent Au_{29} cluster. The three prominent peaks (marked with a #) apart from parent $Au_{25}SBB_{18}$ (marked with a * and expanded to depict the isotopic distribution corresponding to -1 charge) are expanded in insets (i–iii). The green lines in (i–iii) are the simulated isotope patterns for (i) $[Au_{27}(SBB)_{20}S]^{2-}$, (ii) $[Au_{28}(SBB)_{21}S]^{2-}$, and (iii) $[Au_{29}(SBB)_{22}S]^{2-}$. Peak separation of m/z 0.5 is marked in the experimental spectra. The inset of (A) also shows the TLC separation of parent Au_{25} and the red luminescent Au_{29} cluster (marked with a dotted circle) eluted with a DCM/hexane mixture (80 : 20) as the eluent. Fragmentation due to the C–S cleavage of the SBB ligand from Au_{25} (marked with an asterisk in B) is also observed.

was formed in solution only after prolonged heating. DCTB was used as the matrix for all measurements. Careful control over the laser power was crucial to observe the peaks without further fragmentation. The additional sulphur present in the cluster is suggestive of an unusual ligand structure. However, the cleavage of the R–S bond is observed in clusters^{45,59} and

crystal structures with additional sulphur atoms.⁶⁰ Moreover, Ag_2S clusters have been formed from $Ag_{25}SR_{18}$ clusters⁶¹ in solution which occurs especially at temperatures used here. Thus, we believe that such clusters of the kind suggested are possible. Recently, an AIE mechanism has been proposed for water soluble glutathione protected Au ^{8,49} and bimetallic

Au/Ag clusters⁵⁰ wherein luminescence properties of the clusters are thought to involve the long Au(I)–thiolate motifs on the cluster surface. While ESI MS shows the formation of clusters larger than Au₂₅ in solution, photoluminescence data from the cluster solutions showed a blue shift in the peak maximum for Au₂₉ QCs compared to parent Au₂₅SBB₁₈. As the charge density has a critical role in the enhancement of luminescence in the QCs,^{9,10} we proceeded to identify the role of the charge state of Au₂₅ QCs in organic media. Unlike Ag clusters, surface oxidation is difficult in Au₂₅ QCs. But, it is likely that partial oxidation of the thiolate staples (Au₂L₃) on the Au₁₃ core can modify their overall charge.

In view of the critical role of surface charge density on the emergence of fluorescence in Au₂₉, X-ray photoelectron spectra (XPS) of parent Au₂₅ and red-emitting Au₂₉ clusters were recorded. The presence of surface thiolates in Au₂₉ was also

evident from the XPS spectra of the two clusters (Fig. 3). Though Au appears to exist in the near metallic (Au⁰) state in both QCs as shown by the binding energy values of 4f_{7/2}, a slight shift (0.4 eV) towards a higher binding energy value is noted for the Au₂₉ species (84.7 eV) relative to the parent Au₂₅ QC (84.3 eV). Note that binding energy values for Au 4f_{7/2} peaks are at 85.4 eV and 84.0 eV for Au⁺ and Au⁰, respectively.⁶² Though small amounts of Au(I) are found on thiolate protected QCs,^{63,64} the observed shift indicates the higher percentage of Au(I) in the Au₂₉ cluster compared to parent Au₂₅. This clearly suggests the existence of oxidized thiolate staples on the cluster surface. The S 2p_{3/2} peak, seen at 163.1 eV (Au₂₅) and 162.8 eV (red luminescent species), for both clusters supports the Au–S thiolate binding to the core⁶⁵ and confirms the existence of only one type of S. On the basis of the above results, the enhanced luminescence in Au₂₅SBB₁₈ upon heating could be attributed

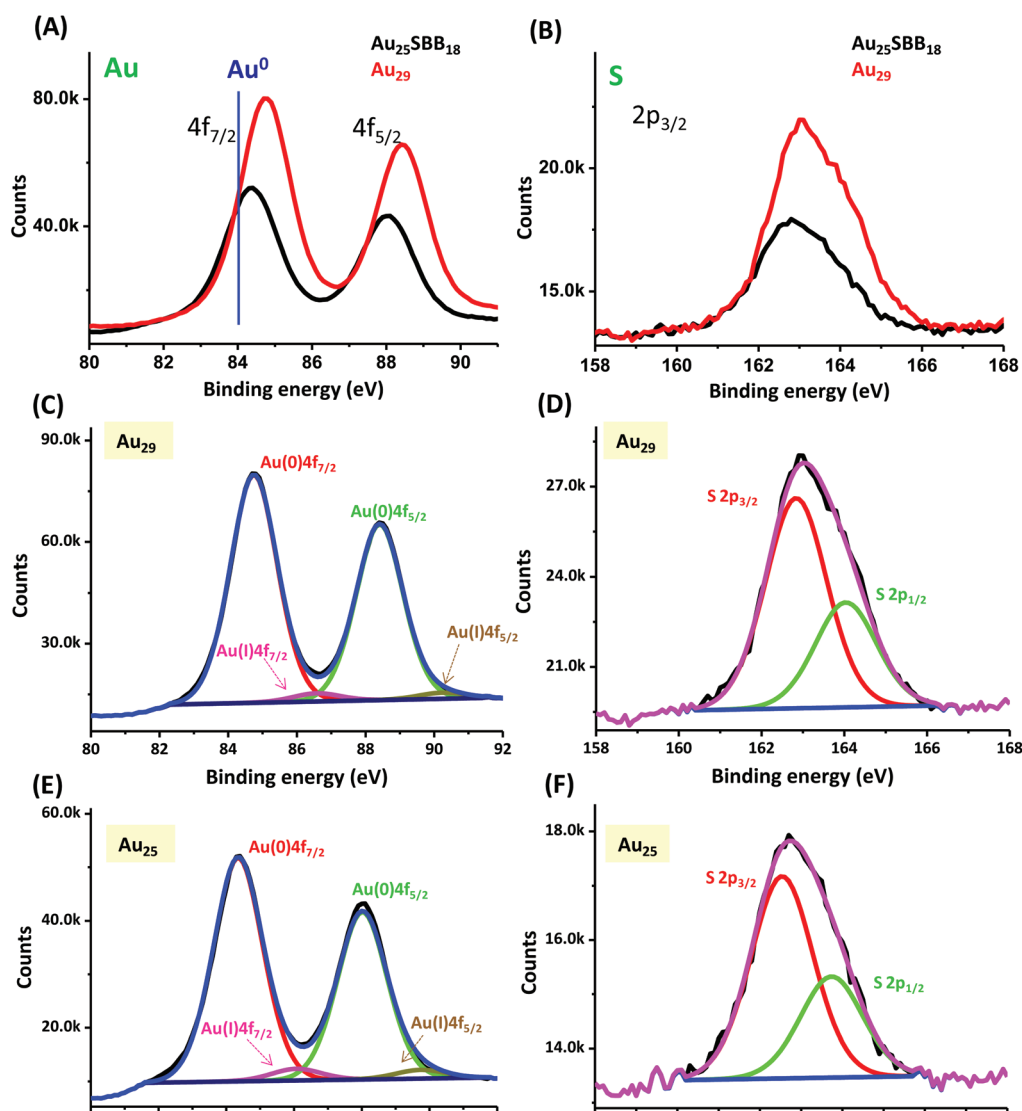


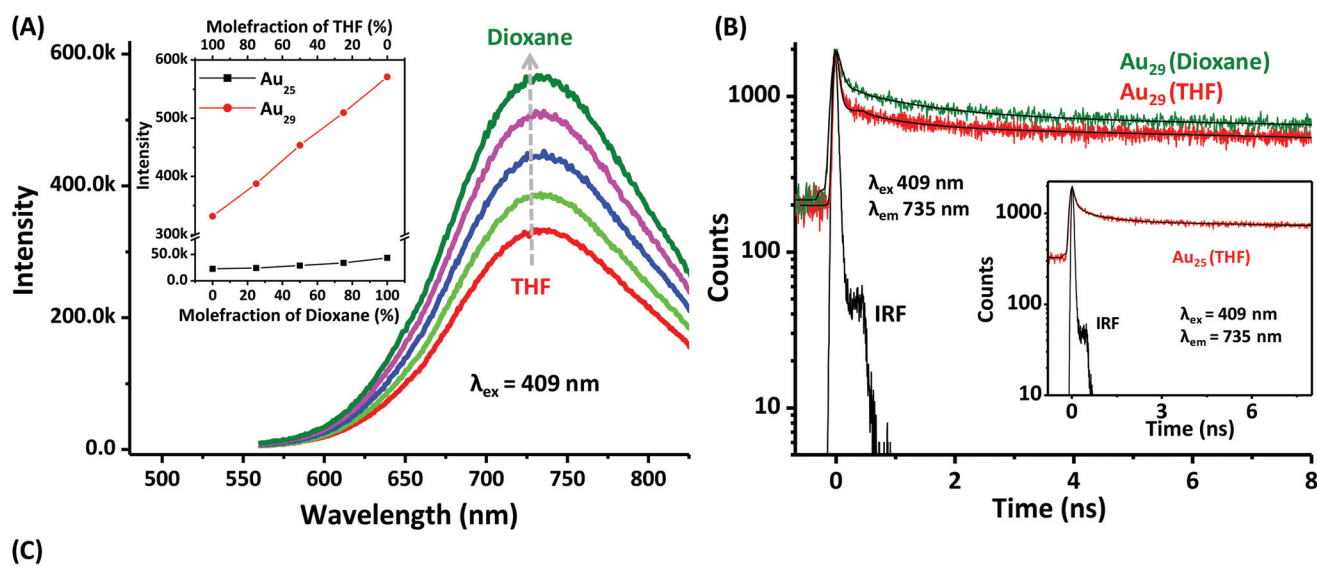
Fig. 3 XPS spectra of Au 4f (A) and S 2p (B) regions in parent Au₂₅SBB₁₈ (black trace) and luminescent Au₂₉ (red trace) clusters. The blue line in (A) indicates the position of Au(0) at 84.0 eV. Deconvoluted XPS spectra of Au 4f (C, E) and S 2p (D, F) regions of the red luminescent Au₂₉ clusters (C, D) and parent Au₂₅SBB₁₈ clusters (E, F) are also shown.

to the charge transfer from the oxidized surface thiolate ligands to the core of QC through the Au-S bonds and direct donation of delocalized electrons from electron-rich ligands to the metal core, as described by Jin *et al.*⁹

The presence of the thiolate shell around the cluster surface was further verified by thermogravimetric analysis (TGA). The red-emitting Au₂₉ QCs showed higher organic content (observed metal to the organic content ratio (57.9% : 42.0%)), than the parent Au₂₅ (60.2% : 39.7%) (Fig. S9†). The observed value was in accordance with the theoretical prediction, confirming the existence of the Au₂₉SBB₂₂S cluster. Additional data were collected which further supported the proposed composition. A slight increase in the average size of the cluster was observed in the transmission electron microscopy (TEM) images of the red luminescent Au₂₉ QCs compared to parent Au₂₅ QCs (Fig. S10†). Au₂₉ QCs also showed a tendency to aggregate. Compared to Au₂₅ QCs (Fig. S10A†) which were well separated on the TEM grid, Au₂₉ QCs (Fig. S10B†) showed a tendency to aggregate and exist as islands throughout the TEM grid. Note that this cannot be an effect of electron beam-induced aggregation, a common phenomenon observed in other Ag and Au clusters, as we observed no such effect on Au₂₅ QCs. Scanning electron

microscopic (SEM) images of the clusters at various stages of the reaction (Fig. S11A and B†) also show distinct changes in morphology. While a powdery texture is usually observed in the case of parent Au₂₅ clusters (marked with a green circle in Fig. S11A†), an amorphous nature was observed for the purified red luminescent Au₂₉ cluster (Fig. S11B†). Energy-dispersive analyses of X-ray (EDAX) mapping and spectra confirmed the presence of the constituent elements in the cluster (Fig. S11C†) and an Au/S ratio of 1 : 0.79 was seen in agreement with Au₂₉SBB₂₂S.

The presence of surface thiolates in red luminescent Au₂₉ QCs was further confirmed by the addition of dilute sodium borohydride to the QCs (Fig. S12†). A drastic quenching of its visible luminescence accompanied by a significant red shift was observed upon addition of increasing amounts of sodium borohydride to the red luminescent Au₂₉ QCs (black to tan trace in Fig. S12A†). The plot shown in Fig. S12B† compares the effect of similar amounts of NaBH₄ on parent Au₂₅ QCs under identical conditions. Though a reduction in the luminescence intensity is noted in the case of parent Au₂₅ QCs as well (red trace in Fig. S12B†), quenching is greater in the case of the Au₂₉ species (black trace). This could be attributed to the reduction of the thiolate shell by sodium borohydride and consequent reduction in the overall surface charge of the cluster.



System	τ_1 (%) ns	τ_2 (%) ns	τ_3 (%) ns	τ_{avg} (ns)
Au ₂₉ (THF)	0.05(84)	0.79(8.5)	35(7.5)	2.77
Au ₂₉ (1, 4-dioxane)	0.05(78)	1.08(10.5)	35(11.5)	4.20
Au ₂₅ (THF)	0.05(77)	0.91(11.5)	35(11.5)	4.15
Au ₂₅ (1, 4-dioxane)	0.06(77)	0.95(10)	34(13)	4.42

Fig. 4 (A) Emission spectra of Au₂₉ QC in THF–1,4 dioxane mixture with different mole fractions of THF. The inset compares the corresponding emission spectra of Au₂₅ QC in THF–1,4 dioxane solvent mixtures (see the text). (B) Picosecond-resolved decay transients of Au₂₉ at 735 nm (ex 409 nm) in both THF and 1,4-dioxane solvents. The corresponding transients for Au₂₅ in THF are shown as an inset. (C) Data corresponding to the picosecond time-resolved luminescence transients of Au₂₉ and Au₂₅ in pure THF and 1,4-dioxane.

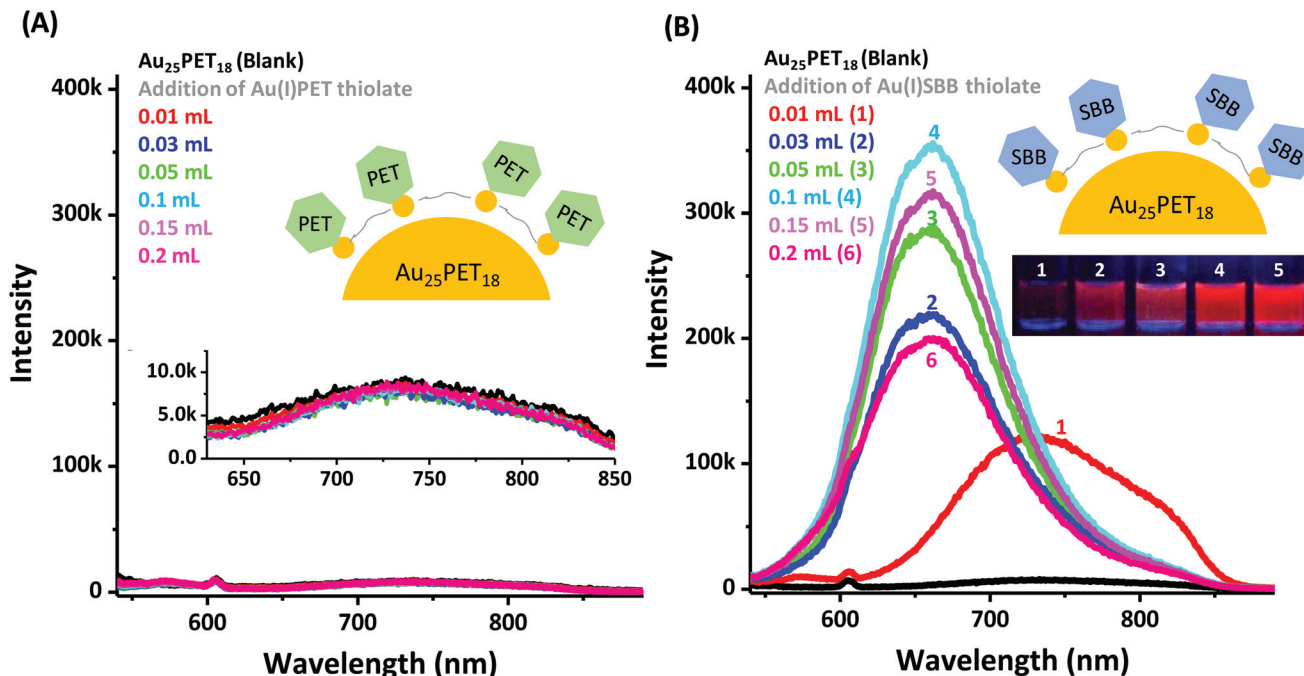


Fig. 5 Changes in emission spectra (λ_{ex} 514 nm) of Au₂₅PET₁₈ QCs upon reaction with various amounts of Au(I)PET thiolate (A) and Au(I)SBB thiolate (B). The inset of (B) shows the photographs of the cluster solution under conditions indicated in the figure. The inset also shows a cartoonic representation of the thiolate shell above Au₂₅PET₁₈ QCs.

The zeta potential of the parent Au₂₅SBB₁₈ QCs and the red luminescent Au₂₉ QCs was determined to be -70.1 mV and $+0.04$ mV at room temperature, respectively. This enhanced charge is in accordance with the thiolate shell over the surface of Au₂₅SBB₁₈.

We conjectured that enhanced charge transfer in Au₂₉ due to the thiolate shell, compared to that in Au₂₅ could be responsible for the enhancement. To confirm this, we have performed solvent dependent luminescence studies on both the QCs. As shown in Fig. 4A, the luminescence from the Au₂₉ cluster in 1,4-dioxane is significantly enhanced compared to that in THF. The enhancement is found to be linear upon increasing the concentration of 1,4-dioxane in THF–dioxane binary mixture. It has to be noted that the dielectric constant of the system can be varied from 7.58 (THF) to 2.25 (1,4-dioxane). The inset of Fig. 4A illustrates the relatively less sensitivity of Au₂₅ QCS towards the polarity of the binary mixture of the host solvent. The observations suggest the higher extent of charge transfer in the case of Au₂₉ QCs in comparison with Au₂₅.

In order to investigate non-radiative processes associated with the increased polarity of the host solvent of the QC, we performed picosecond resolved fluorescence studies (Fig. 4B) and the corresponding time scales are tabulated in the table (Fig. 4C). Au₂₉ QCs show tri-exponential fluorescence relaxation with time constants of 50 ps (84%), 790 ps (8.5%), and 35 ns (7.5%) in THF. Faster and slower time constants are found to be similar in pure 1,4-dioxane. Interestingly, the second time constant of 790 ps in THF is slowed down to

1.08 ns in 1,4-dioxane, revealing that the key time scale accounts for the charge transfer dynamics, which is the consequence of change in polarity.⁶⁶ While the slowest component (35 ns) accounts for the radiative life time of the QC HOMO–LUMO transition,^{67,68} the fastest component of 50 ps can be rationalised to thermalization dynamics in the QC⁶⁹ which depends upon the energy of excitation. We have performed excitation dependent picosecond resolved studies using various excitation lasers (409 nm, 510 nm and 635 nm) and found that the fastest component is gradually decreased with the increase in excitation wavelengths, revealing the vanishing of small contribution of thermalization dynamics at 635 nm excitation (Fig. S14†). We have calculated the non-radiative rate in the case of THF with reference to 1,4-dioxane following the equation,⁷⁰

$$k_{\text{nr}} = \frac{1}{\langle \tau \rangle} - \frac{1}{\langle \tau_0 \rangle}$$

and found it to be $1.2 \times 10^8 \text{ s}^{-1}$. As shown in Fig. 4B, inset, the temporal characteristic of the Au₂₅ cluster shows insignificant dependency on the polarity of the host solvent. Thus the contribution of the charge transfer effect in Au₂₉ QCs in comparison with parent Au₂₅ QCs is confirmed.

The mechanism of increased surface charge responsible for visible luminescence enhancement was verified with the help of other experiments illustrated below. These experiments were intended to prove the possibility of ligand structure-induced changes in luminescence and not to establish the

nature of the metal core or composition of the resulting clusters. Heating Au₂₅SBB₁₈ cluster loaded silica gel at 55 °C (brown colored solid, see photographs shown in Fig. S14†) showed luminescence (for 24 h). Photographs of the Au₂₅SBB₁₈-loaded silica gel before and after heat treatment are shown in the figure. Though no red luminescence was observed from the material before heat treatment, a bright red emission was observed from the silica gel after 24 h of heating in a sand bath (set-up is shown in Fig. S14†). This confirms that the observed luminescence was not a result of solution state dynamics involving other species in solution as solid cluster samples were heated in this case. Here, instead of Au(I) thiolate, silica having hydroxyl groups on its surface may be acting as an electron donor leading to charge transfer and thus causing luminescence enhancement of the adsorbed Au₂₅ QCs.

Further, this strategy is also illustrated for yet another hydrophobic Au₂₅ QC with phenylethanethiol as the protecting ligand. The Au₂₅PET₁₈ cluster was chosen as it is a well-studied and characterized system with known crystal structure.^{26,27} Advantages of a solved X-ray crystal structure in the case of Au₂₅PET₁₈ has triggered a lot of studies in catalysis, chirality, magnetism, *etc.*, involving these clusters which make use of the structure–property correlations to understand their unique properties. Imparting visible luminescence on such materials can add another dimension to these studies. Fig. 5 shows variation in the emission spectra of Au₂₅PET₁₈ QCs upon heating with two different thioliates namely, Au(I)PET (Fig. 5A) and Au(I)SBB (Fig. 5B). Interestingly, a 35 times enhancement in luminescence was observed in the case of the cluster treated with Au(I)SBB thiolate compared to PET thiolate. While addition of Au(I)PET thiolate showed little or no change in the emission intensities of the parent clusters at an excitation of 514 nm, similar amounts of SBB thiolate resulted in drastic enhancement in emission (black to cyan trace in Fig. 5B). The stronger electron donating capability of the BBSH ligand (Ph(*tert*-butyl)CH₂- group) compared to PET (PhC₂H₄- group) might be the reason for this enhancement. Emergence of bright red luminescence in solution is evident from the photographs of the cluster (inset of Fig. 5B). Images 1–5 show increasing amounts of Au(I)SBB thiolate in solution.

Experimental

Materials and methods

Tetrachloroauric(III) acid (HAuCl₄·3H₂O) and methanol were purchased from SRL Chemical Co. Ltd, India. 4-(*t*-Butyl)benzyl mercaptan (CH₃)₃C–C₆H₄–CH₂SH (BBSH), 2-phenylethanethiol C₆H₅–CH₂–CH₂SH (PET) and sodium borohydride (NaBH₄) were purchased from Sigma Aldrich. Silica gel (60–120 mesh) was obtained from Merck, India. Tetrahydrofuran was purchased from Rankem, India. All chemicals were analytical grade and were used without further purification. Glassware was cleaned thoroughly with aqua regia (HCl/HNO₃, 3 : 1 vol%),

rinsed with distilled water, and dried in an oven prior to use. Triply distilled water was used throughout the experiments.

Synthesis of Au₂₅SBB₁₈ and the red luminescent Au₂₉ cluster

Au₂₅SBB₁₈ was synthesized as per our earlier report.⁶ Briefly, 10 mL HAuCl₄·3H₂O (14.5 mM in THF) was added to 15 mL BBSH thiol (89.2 mM in THF) while stirring at 400 rpm at room temperature (29 °C) in a round bottom flask. The solution becomes colorless after 15 min, indicating the formation of the Au(I)SBB thioliates. An aqueous solution of 2.5 mL NaBH₄ (0.4 M) was added rapidly to the reaction mixture under vigorous stirring (1100 rpm) and the solution turned from colorless to black, indicating the formation of clusters. The reaction was allowed to proceed with constant stirring for 3 h under ambient conditions and then for 3 h at 45 °C. The solution was left overnight to yield monodisperse species. The THF solvent was removed under vacuum and the residue was washed repeatedly with a 1 : 1 water : methanol mixture to remove excess BBSH thiol and other side products. The Au₂₅ cluster thus precipitated was dried and used for further experiments. The red luminescent Au₂₉ clusters were synthesized *via* thermal treatment of Au₂₅ clusters followed by rapid cooling. Approximately 10 mg of purified, solid Au₂₅SBB₁₈ (used as the precursor) was dissolved in 3 mL THF and 3 mL water. The cluster phase is separated from the organic layer and the aqueous layer remains colorless. The solution was heated at 55 °C for 24 h with stirring in a sealed container. After 12 h, 0.6 mL of Au(I)SBB thiolate was added to the reaction mixture and the reaction was allowed to proceed for another 12 h. Afterwards, the dark reddish brown upper (organic) layer was collected and cooled to 4 °C for 4 h. Visible bright red luminescence was observed from the cluster after this cooling step. Later the solvent was removed under vacuum and the residue was washed repeatedly with 1 : 1 water/methanol mixture and dried. To synthesize the thiolate, 8 mL HAuCl₄·3H₂O (13 mM in THF) was dissolved in 5 mL THF and to this solution 20 μL BBSH thiol (1 : 1 ratio of Au³⁺ and BBSH thiol) was added while stirring at 300 rpm at room temperature (29 °C). The solution was allowed to equilibrate for 12 h before use.

TLC separation

The cluster samples (both Au₂₅ and Au₂₉) in THF medium (2 mg in 0.3 mL) were pipetted (1 μL each) to the TLC plates and dried in air. After drying, the plate was eluted with a DCM/hexane mixture (the optimal solvent ratio varies with the cluster system⁵⁸). In our case an 80 : 20 mixture of DCM : hexane was used as the eluent. After the separation, the bands were cut from the TLC plate, and the clusters from each band were extracted separately and analyzed. The solid pieces of the TLC plate were removed from these extracts *via* centrifugation.

Instrumentation

Mass spectral studies were carried out using a Voyager DE PRO biospectrometry workstation (Applied Biosystems) matrix-assisted laser desorption ionization (MALDI) time-of-flight (TOF) mass spectrometer in the linear mode as well as using a

MALDI TOF/TOF (UltrafleXtreme, Bruker Daltonics) mass spectrometer. In the case of MALDI TOF MS, a pulsed nitrogen laser of 337 nm was used (a maximum firing rate, 20 Hz; a maximum pulse energy, 300 μJ) for the measurements. The MALDI TOF/TOF mass spectrometer utilizes a 1 kHz smart-beam-II laser, FlashDetector system, and a minimum 4 GHz digitizer. Mass spectra were recorded in positive and negative ion modes and were averaged for 500–700 shots. DCTB (*trans*-2-[3-(4-*t*-butylphenyl)-2-methyl-2-propenylidene]malononitrile) was used as the matrix for all MALDI MS measurements. All spectra were recorded at a threshold laser intensity to keep fragmentation to a minimum. The concentration of the analyte and the mass spectral conditions (laser intensity and spectrometer tune files) were optimized to obtain good quality spectra. UV-vis absorption spectra were recorded using a Perkin-Elmer Lambda 25 spectrophotometer. The experiments were carried out at room temperature, and the absorption spectra were recorded from 200 to 1100 nm. Luminescence measurements were carried out on a Jobin Yvon NanoLog instrument. The band pass for excitation and emission was set at 3 nm. QYs were measured using cluster solutions of appropriate dilutions (~ 0.04 OD absorption at 467 nm) using $[\text{Au}_{25}\text{PET}_{18}]^-$ as a reference (QY 0.01% as reported previously⁹). All picosecond-resolved fluorescence decay transients were measured by using a commercially available spectrophotometer (Life Spec-ps, Edinburgh Instruments, UK) with 90 ps instrument response function (IRF). The excitations at 409 nm, 510 nm and 635 nm were obtained using a pulse laser diode from PicoQuant, Germany. The observed fluorescence transients were fitted by using a nonlinear least squares fitting procedure to a function $\left(X(t) = \int_0^t E(t')R(t-t')dt'\right)$ comprising of convolution of the IRF $(E(t))$ with a sum of exponential $\left(R(t) = A + \sum_{i=1}^N B_i e^{-t/\tau_i}\right)$ with pre-exponential factors (B_i), characteristic lifetimes (τ_i) and a background (A). The relative concentration in a multi exponential decay was finally expressed as:

$$c_n = \frac{B_n}{\sum_{i=1}^N B_i} \times 100$$

The quality of the curve fitting was evaluated by reduced chi-square and residual data. It has to be noted that with our time-resolved instrument, we can resolve at least one fourth of the instrument response time constants after the de-convolution of the IRF. The average lifetime (amplitude-weighted) of a multi-exponential decay is expressed as:

$$\tau_{\text{av}} = \sum_{i=1}^N c_i \tau_i$$

ESI mass spectrometric measurements were done in the negative mode using a Synapt G2 HDMS, quadrupole time-of-flight (Q TOF), ion mobility, orthogonal acceleration mass spectrometer with electrospray ionization having a mass

range of up to 32 kDa. The Synapt instrument used for ESI measurements combined an exact-mass quadrupole and a high resolution time-of-flight mass spectrometer with Triwave technology, enabling measurements in the TOF mode. The purified samples were dispersed in THF and used for both mass spectrometric measurements. The samples were electro-sprayed at a flow rate of $5 \mu\text{L min}^{-1}$ and at a capillary temperature of 150 °C. The spectra were averaged for 80–100 scans. SEM and EDAX images were obtained using a FEI QUANTA-200 SEM. For the SEM and EDAX measurements, samples were either spotted or stuck (in the case of the TLC plate) on a carbon substrate and dried at ambient temperature. TEM was conducted using a JEOL 3011, using a 300 kV instrument with an ultra-high-resolution (UHR) polepiece. The samples were prepared by dropping the dispersion on amorphous carbon films supported on a copper grid and dried under laboratory conditions. The zeta potential measurements were carried out using a Malvern Zetasizer nz (M3-PALS) instrument.

Conclusions

In summary, an efficient method to enhance the visible luminescence in visibly non-luminescent organic-soluble Au_{25} QCs is developed. Our study demonstrates that making an additional shell of thiolate on the cluster surface can increase the surface charge density resulting in enhancement of the visible luminescence. The critical role of temperature in the emergence of luminescence in QCs has been studied in detail. The restoration of the surface ligand shell on the Au_{25} cluster and subsequent physicochemical modification to the cluster was probed by various mass spectral and spectroscopic techniques. This method has been successfully illustrated by imparting visible red luminescence in PET protected Au_{25} QCs. Our results provide fundamental insights into the ligand characteristics on the origin of luminescence in QCs.

Acknowledgements

We thank the Department of Science and Technology, Government of India (DST), for constantly supporting our research program on nanomaterials. A. M. thanks CSIR for a research fellowship. Dr Abdul Jaleel, Mr Arun Surendran and Mr M. Saravanakumar at Rajiv Gandhi Centre for Biotechnology (RGCBC) are thanked for help in mass spectral measurements.

References

- 1 S. Choi, R. M. Dickson and J. Yu, *Chem. Soc. Rev.*, 2012, **41**, 1867–1891.
- 2 A. Mathew and T. Pradeep, *Part. Part. Syst. Charact.*, 2014, **31**, 1017–1053.
- 3 X. Yuan, Z. Luo, Y. Yu, Q. Yao and J. Xie, *Chem. – Asian J.*, 2013, **8**, 858–871.

- 4 A. Mathew, P. R. Sajanlal and T. Pradeep, *Angew. Chem., Int. Ed.*, 2012, **51**, 9596–9600.
- 5 J. Zheng, C. Zhou, M. Yu and J. Liu, *Nanoscale*, 2012, **4**, 4073–4083.
- 6 J. Zheng, C. Zhang and R. M. Dickson, *Phys. Rev. Lett.*, 2004, **93**, 077402.
- 7 A. Mathew, P. R. Sajanlal and T. Pradeep, *J. Mater. Chem.*, 2011, **21**, 11205–11212.
- 8 Z. Luo, X. Yuan, Y. Yu, Q. Zhang, D. T. Leong, J. Y. Lee and J. Xie, *J. Am. Chem. Soc.*, 2012, **134**, 16662–16670.
- 9 Z. Wu and R. Jin, *Nano Lett.*, 2010, **10**, 2568–2573.
- 10 G. Wang, R. Guo, G. Kalyuzhny, J.-P. Choi and R. W. Murray, *J. Phys. Chem. B*, 2006, **110**, 20282–20289.
- 11 G. Wang, T. Huang, R. W. Murray, L. Menard and R. G. Nuzzo, *J. Am. Chem. Soc.*, 2005, **127**, 812–813.
- 12 X. Tan and R. Jin, *Wiley Interdiscip. Rev.: Nanomed. Nanobiotechnol.*, 2013, **5**, 569–581.
- 13 C. V. Conroy, J. Jiang, C. Zhang, T. Ahuja, Z. Tang, C. A. Prickett, J. J. Yang and G. Wang, *Nanoscale*, 2014, **6**, 7416–7423.
- 14 T. Vosch, Y. Antoku, J.-C. Hsiang, C. I. Richards, J. I. Gonzalez and R. M. Dickson, *Proc. Natl. Acad. Sci. U. S. A.*, 2007, **104**, 12616–12621.
- 15 J. Xie, Y. Zheng and J. Y. Ying, *J. Am. Chem. Soc.*, 2009, **131**, 888–889.
- 16 X. Yuan, Z. Luo, Q. Zhang, X. Zhang, Y. Zheng, J. Y. Lee and J. Xie, *ACS Nano*, 2011, **5**, 8800–8808.
- 17 S.-I. Tanaka, J. Miyazaki, D. K. Tiwari, T. Jin and Y. Inouye, *Angew. Chem., Int. Ed.*, 2011, **50**, 431–435.
- 18 A. Das, T. Li, G. Li, K. Nobusada, C. Zeng, N. L. Rosi and R. Jin, *Nanoscale*, 2014, **6**, 6458–6462.
- 19 R. Jin, *Nanoscale*, 2010, **2**, 343–362.
- 20 J. F. Parker, C. A. Fields-Zinna and R. W. Murray, *Acc. Chem. Res.*, 2010, **43**, 1289–1296.
- 21 G. Wang, T. Huang, R. W. Murray, L. Menard and R. G. Nuzzo, *J. Am. Chem. Soc.*, 2004, **127**, 812–813.
- 22 A. Verma, O. Uzun, Y. Hu, Y. Hu, H.-S. Han, N. Watson, S. Chen, D. J. Irvine and F. Stellacci, *Nat. Mater.*, 2008, **7**, 588–595.
- 23 C. M. Jewell, J.-M. Jung, P. U. Atukorale, R. P. Carney, F. Stellacci and D. J. Irvine, *Angew. Chem., Int. Ed.*, 2011, **50**, 12312–12315.
- 24 H.-Y. Lee, S. H. R. Shin, L. L. Abezgaus, S. A. Lewis, A. M. Chirsan, D. D. Danino and K. J. M. Bishop, *J. Am. Chem. Soc.*, 2013, **135**, 5950–5953.
- 25 E. A. Appel, M. W. Tibbitt, M. J. Webber, B. A. Mattix, O. Veisoh and R. Langer, *Nat. Commun.*, 2014, **6**, 6295, DOI: 10.1038/ncomms7295.
- 26 M. W. Heaven, A. Dass, P. S. White, K. M. Holt and R. W. Murray, *J. Am. Chem. Soc.*, 2008, **130**, 3754–3755.
- 27 M. Zhu, C. M. Aikens, F. J. Hollander, G. C. Schatz and R. Jin, *J. Am. Chem. Soc.*, 2008, **130**, 5883–5885.
- 28 T. Dainese, S. Antonello, J. A. Gascon, F. Pan, N. V. Perera, M. Ruzzi, A. Venzo, A. Zoleo, K. Rissanen and F. Maran, *ACS Nano*, 2014, **8**, 3904–3912.
- 29 Y. Zhu, H. Qian, B. A. Drake and R. Jin, *Angew. Chem., Int. Ed.*, 2010, **49**, 1295–1298.
- 30 D. R. Kauffman, D. Alfonso, C. Matranga, H. Qian and R. Jin, *J. Am. Chem. Soc.*, 2012, **134**, 10237–10243.
- 31 X. Nie, H. Qian, Q. Ge, H. Xu and R. Jin, *ACS Nano*, 2012, **6**, 6014–6022.
- 32 S. Yamazoe, K. Koyasu and T. Tsukuda, *Acc. Chem. Res.*, 2014, **47**, 816–824.
- 33 K. Kwak and D. Lee, *J. Phys. Chem. Lett.*, 2012, **3**, 2476–2481.
- 34 M. Zhu, C. M. Aikens, M. P. Hendrich, R. Gupta, H. Qian, G. C. Schatz and R. Jin, *J. Am. Chem. Soc.*, 2009, **131**, 2490–2492.
- 35 S. Antonello, N. V. Perera, M. Ruzzi, J. A. Gascón and F. Maran, *J. Am. Chem. Soc.*, 2013, **135**, 15585–15594.
- 36 M. Zhu, H. Qian, X. Meng, S. Jin, Z. Wu and R. Jin, *Nano Lett.*, 2011, **11**, 3963–3969.
- 37 Y. Negishi, K. Munakata, W. Ohgake and K. Nobusada, *J. Phys. Chem. Lett.*, 2012, **3**, 2209–2214.
- 38 W. Kurashige, K. Munakata, K. Nobusada and Y. Negishi, *Chem. Commun.*, 2013, **49**, 5447–5449.
- 39 D. R. Kauffman, D. Alfonso, C. Matranga, H. Qian and R. Jin, *J. Phys. Chem. C*, 2013, **117**, 7914–7923.
- 40 C. Kumara, C. M. Aikens and A. Dass, *J. Phys. Chem. Lett.*, 2014, **5**, 461–466.
- 41 Y. Negishi, W. Kurashige, Y. Niihori, T. Iwasa and K. Nobusada, *Phys. Chem. Chem. Phys.*, 2010, **12**, 6219–6225.
- 42 A. Tlahuice-Flores, R. L. Whetten and M. Jose-Yacamán, *J. Phys. Chem. C*, 2013, **117**, 20867–20875.
- 43 Y. Niihori, M. Matsuzaki, T. Pradeep and Y. Negishi, *J. Am. Chem. Soc.*, 2013, **135**, 4946–4949.
- 44 E. S. Shibu, M. A. H. Muhammed, T. Tsukuda and T. Pradeep, *J. Phys. Chem. C*, 2008, **112**, 12168–12176.
- 45 A. Mathew, G. Natarajan, L. Lehtovaara, H. Häkkinen, R. M. Kumar, V. Subramanian, A. Jaleel and T. Pradeep, *ACS Nano*, 2014, **8**, 139–152.
- 46 J. Akola, M. Walter, R. L. Whetten, H. Häkkinen and H. Grönbeck, *J. Am. Chem. Soc.*, 2008, **130**, 3756–3757.
- 47 S. H. Yau, O. Varnavski and T. Goodson, *Acc. Chem. Res.*, 2013, **46**, 1506–1516.
- 48 M. S. Devadas, J. Kim, E. Sinn, D. Lee, T. Goodson and G. Ramakrishna, *J. Phys. Chem. C*, 2010, **114**, 22417–22423.
- 49 Y. Yu, Z. Luo, D. M. Chevrier, D. T. Leong, P. Zhang, D.-e. Jiang and J. Xie, *J. Am. Chem. Soc.*, 2014, **136**, 1246–1249.
- 50 X. Dou, X. Yuan, Y. Yu, Z. Luo, Q. Yao, D. T. Leong and J. Xie, *Nanoscale*, 2014, **6**, 157–161.
- 51 M. A. Habeeb Muhammed, P. K. Verma, S. K. Pal, A. Retnakumari, M. Koyakutty, S. Nair and T. Pradeep, *Chem. – Eur. J.*, 2010, **16**, 10103–10112.
- 52 L. Dhanalakshmi, T. Udayabhaskararao and T. Pradeep, *Chem. Commun.*, 2011, **48**, 859–861.
- 53 I. Díez, M. Pusa, S. Kulmala, H. Jiang, A. Walther, A. S. Goldmann, A. H. E. Müller, O. Ikkala and R. H. A. Ras, *Angew. Chem., Int. Ed.*, 2009, **48**, 2122–2125.

- 54 C.-Y. Ke, T.-H. Chen, L.-C. Lu and W.-L. Tseng, *RSC Adv.*, 2014, **4**, 26050–26056.
- 55 X. Le Guével, V. Trouillet, C. Spies, G. Jung and M. Schneider, *J. Phys. Chem. C*, 2012, **116**, 6047–6051.
- 56 M. A. H. Muhammed, F. Aldeek, G. Palui, L. Trapiella-Alfonso and H. Mattoussi, *ACS Nano*, 2012, **6**, 8950–8961.
- 57 D. V. Krupenya, P. A. Snegurov, E. V. Grachova, V. V. Gurzhiy, S. P. Tunik, A. S. Melnikov, P. Y. Serdobintsev, E. G. Vlakh, E. S. Sinitsyna and T. B. Tennikova, *Inorg. Chem.*, 2013, **52**, 12521–12528.
- 58 A. Ghosh, J. Hassinen, P. Pulkkinen, H. Tenhu, R. Ras and T. Pradeep, *Anal. Chem.*, 2014, **86**, 12185–12190.
- 59 I. Chakraborty, A. Govindarajan, J. Erusappan, A. Ghosh, T. Pradeep, B. Yoon, R. L. Whetten and U. Landman, *Nano Lett.*, 2012, **12**, 5861–5866.
- 60 H. Yang, Y. Wang, A. J. Edwards, J. Yan and N. Zheng, *Chem. Commun.*, 2014, **50**, 14325–14327.
- 61 K. P. Remya, T. Udayabhaskararao and T. Pradeep, *J. Phys. Chem. C*, 2012, **116**, 26019–26026.
- 62 K. Chaudhari, P. L. Xavier and T. Pradeep, *ACS Nano*, 2011, **5**, 8816–8827.
- 63 P. D. Jadzinsky, G. Calero, C. J. Ackerson, D. A. Bushnell and R. D. Kornberg, *Science*, 2007, **318**, 430–433.
- 64 R. L. Whetten and R. C. Price, *Science*, 2007, **318**, 407–408.
- 65 G. J. Ashwell, B. Urasinska-Wojcik and L. J. Phillips, *Angew. Chem., Int. Ed.*, 2010, **49**, 3508–3512.
- 66 M. Zhou, S. Long, X. Wan, Y. Li, Y. Niu, Q. Guo, Q.-M. Wang and A. Xia, *Phys. Chem. Chem. Phys.*, 2014, **16**, 18288–18293.
- 67 X. Wen, P. Yu, Y.-R. Toh, A.-C. Hsu, Y.-C. Lee and J. Tang, *J. Phys. Chem. C*, 2012, **116**, 19032–19038.
- 68 E. S. Shibu and T. Pradeep, *Chem. Mater.*, 2011, **23**, 989–999.
- 69 P. F. Barbara, G. C. Walker and T. P. Smith, *Science*, 1992, **256**, 975–981.
- 70 S. Choudhury, S. Batabyal, T. Mondol, D. Sao, P. Lemmens and S. K. Pal, *Chem. – Asian J.*, 2014, **9**, 1395–1402.

Electronic supplementary information (ESI) for the paper:

Efficient red luminescence from organic-soluble Au₂₅ clusters by ligand structure modification

Ammu Mathew,^[a] Elizabeth Varghese,^[a] Susobhan Choudhury,^[b] Samir Kumar Pal,^[b] and T. Pradeep^{[a]*}

[a] DST Unit of Nanoscience (DST UNS) and Thematic Unit of Excellence (TUE), Department of Chemistry, Indian Institute of Technology Madras, Chennai 600036, India.

[b] Department of Chemical Biological & Macromolecular Sciences, S. N. Bose National Centre for Basic Sciences, Block JD, Sector III, Salt Lake, Kolkata 700098, India

*E-mail: pradeep@iitm.ac.in

Table of contents

No.	Description	Pg no.
S1	Stability of UV-vis absorption spectral features of Au ₂₅ SBB ₁₈ clusters	2
S2	Comparison of fluorescence spectral changes of cluster under various experimental conditions	3
S3	UV-vis absorption spectra of parent Au ₂₅ QCs and resultant red luminescent cluster	4
S4	NIR emission from parent Au ₂₅ SBB ₁₈ QCs and red luminescent cluster	5
S5	Control experiments showing effect of BBSH thiol and Au(I)SBB thiolate with heating	6
S6	PL profile showing evolution of red luminescent cluster with time	7
S7	SEM and EDAX data from TLC plate of the red luminescent clusters	8
S8	ESI MS of Au ₂₅ SBB ₁₈ and red luminescent cluster	9
S9	Comparison of TGA data from the QCs	10
S10	TEM images of Au ₂₅ SBB ₁₈ and red luminescent Au ₂₉ clusters	11
S11	SEM and EDAX characterization of red luminescent Au ₂₉ cluster.	12
S12	Effect of addition of sodium borohydride to red luminescent Au ₂₉ cluster	13
S13	Picosecond life time decay of Au ₂₉ QCs upon excitation at different wavelengths.	14
S14	Au ₂₅ SBB ₁₈ -loaded silica gel experiment	15

Supporting information 1

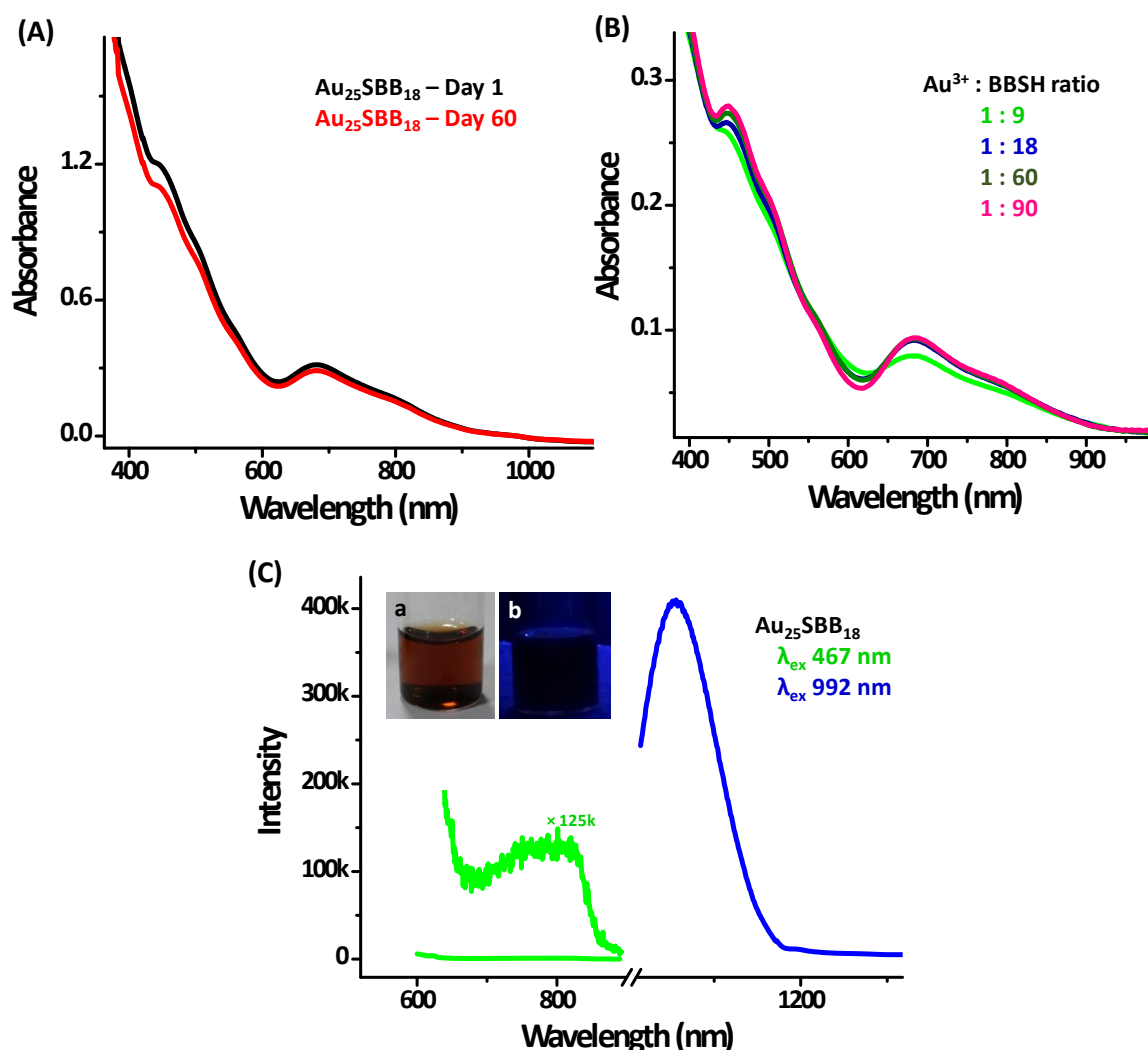


Figure S1. Stability of UV-vis absorption spectral features of $\text{Au}_{25}\text{SBB}_{18}$ clusters (A) with time and (B) against etching using excess BBSH thiol. Various $\text{Au}:\text{BBSH}$ ratios used for etching are indicated. (C) Emission spectra of parent $\text{Au}_{25}\text{SBB}_{18}$ in the visible (λ_{ex} 467 nm, green trace) and NIR (λ_{ex} 992 nm, blue trace) regimes. An expanded version (125k times) of the original spectra is also shown for visualization. Inset shows photographs of the $\text{Au}_{25}\text{SBB}_{18}$ cluster under visible light (a) and UV light (b). Note that no observable visible luminescence is present from the solution.

Supporting information 2

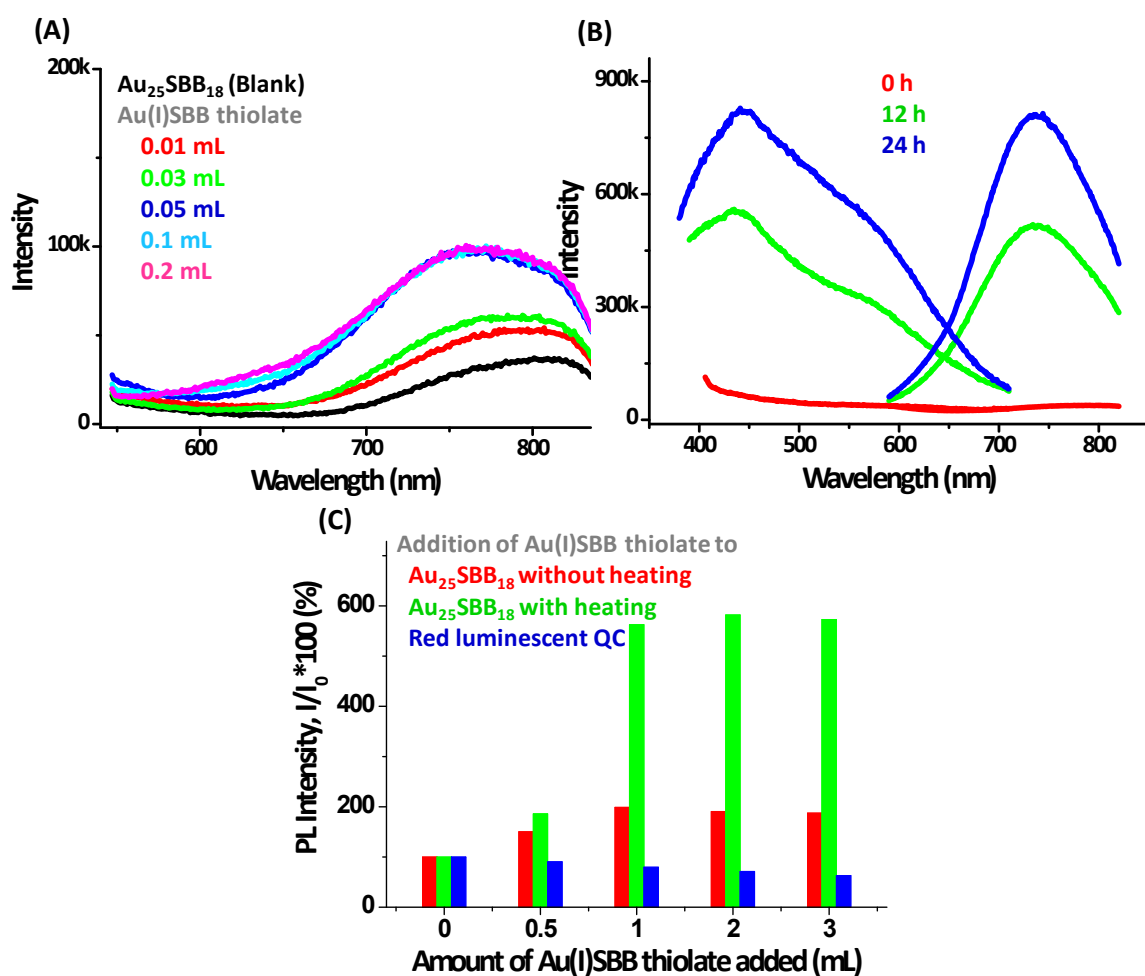


Figure S2. (A) Changes in the emission spectra (λ_{ex} 467 nm) of Au₂₅SBB₁₈ in the visible region upon addition of Au(I)SBB thiolate and heating for 2 h. (B) Evolution of excitation and emission spectra of the red luminescent cluster with increasing reaction time; 0 h (red trace), 12 h (green trace) and 24 h (blue trace). The time shown indicates the time for which sample was heated at 55 °C with stirring. The samples were cooled for 3 h before PL measurement. A 24 h thermal etching treatment was thus identified to obtain clusters with highest luminescence intensity. (C) Bar diagram comparing the changes in relative fluorescence intensity at 737 nm (ex 467 nm) upon addition of Au(I)SBB thiolate to pure Au₂₅ followed by incubation for 24 h (red bars), pure Au₂₅ with heating for 24 h (green bars) and to previously synthesized red luminescent clusters (blue bars).

Supporting information 3

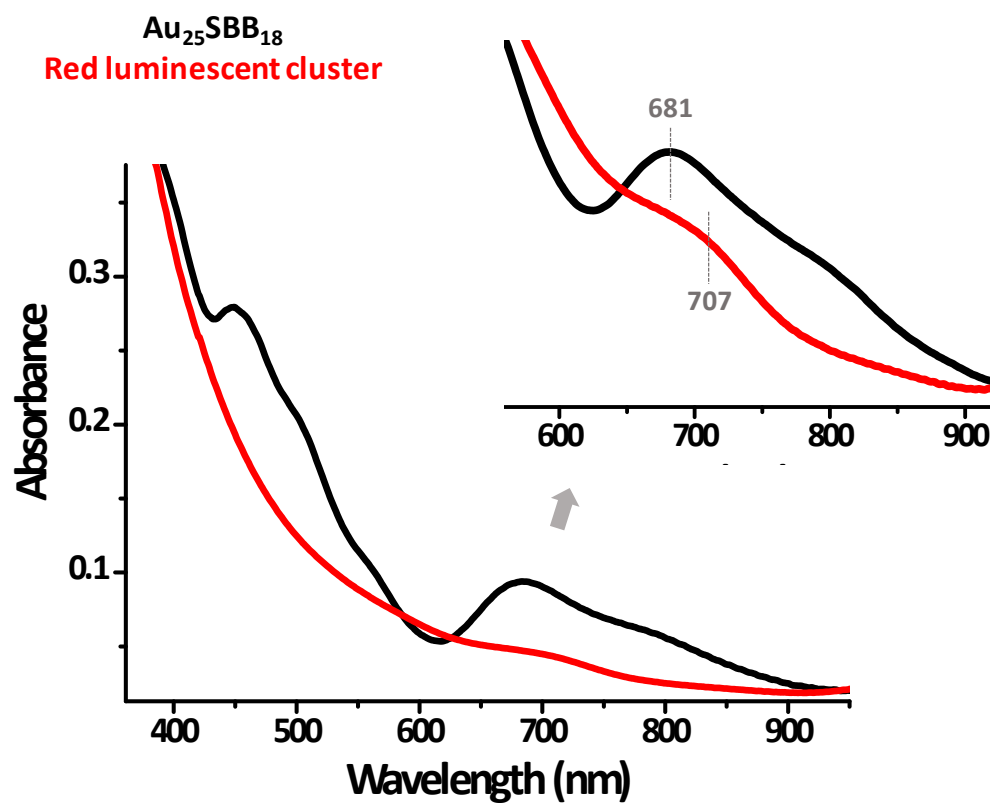


Figure S3. Comparison of UV-vis absorption spectra of parent $\text{Au}_{25}\text{SBB}_{18}$ (black trace) and resultant red luminescent cluster (red trace). Inset shows an expanded view of the spectra.

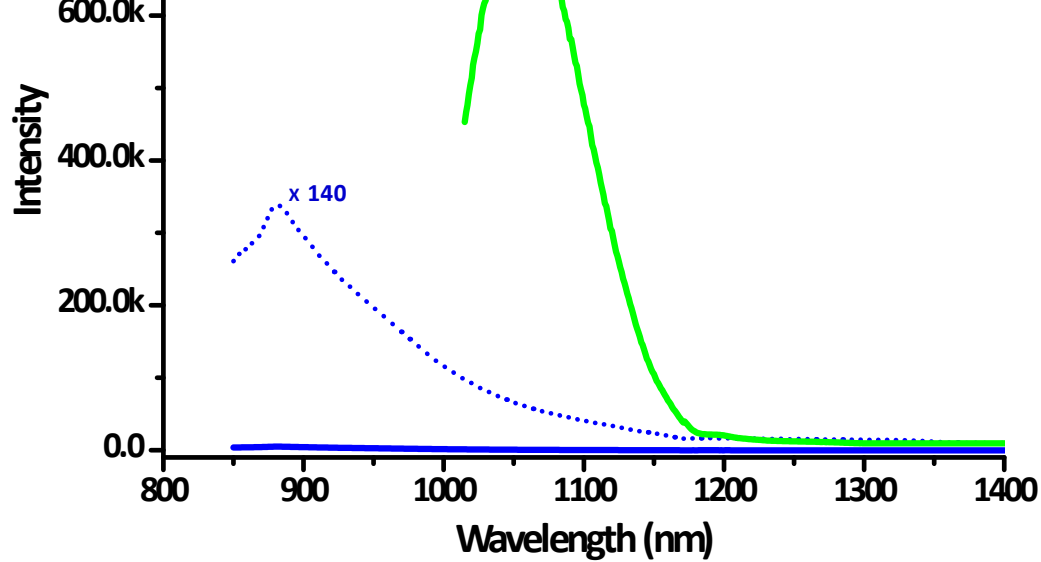


Figure S4. Comparison of emission in the NIR regime (excited at 992 nm) for parent $\text{Au}_{25}\text{SBB}_{18}$ QCs (green trace) and red luminescent Au_{29} (nucularity explained later) clusters (blue trace). An expanded spectra (140 times) showing the NIR features of the red luminescent clusters (blue dotted line) clearly indicates the absence of the prominent emission feature at 1030 nm (seen in parent Au_{25}) in the red luminescent cluster. Spectral features shows a blue shift accompanied by a drastic quenching after the reaction. Identical concentrations of both clusters are compared in the spectra under similar instrumental conditions.

Supporting information 5

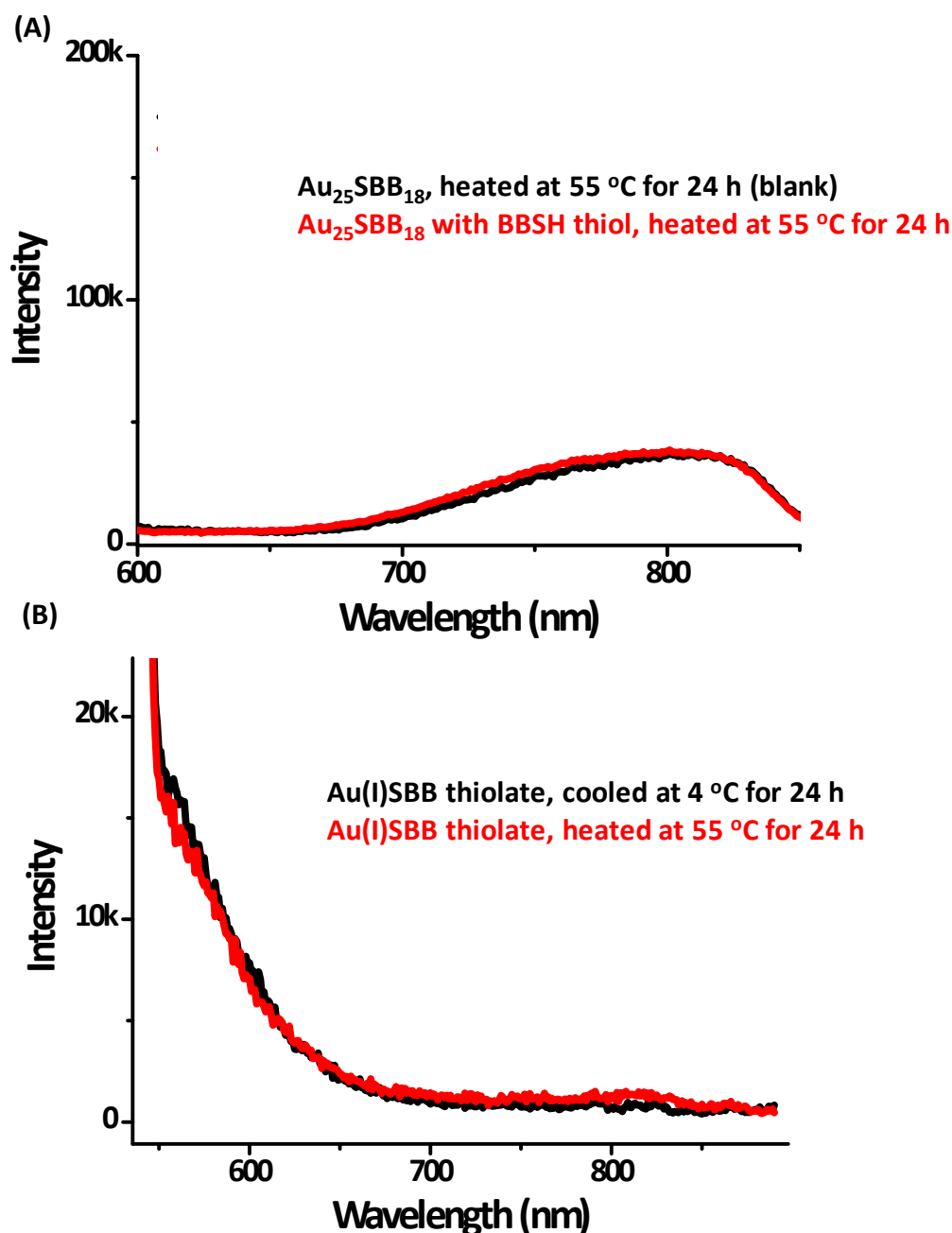


Figure S5. Control experiments showing the effect of emission spectra (ex 467 nm) of $\text{Au}_{25}\text{SBB}_{18}$ upon heating at 55 °C for 24 h in presence of similar concentrations of BBSH thiol (instead of Au(I)SBB thiolate used to synthesize red luminescent clusters) in comparison with parent clusters under identical conditions (A). (B) Effect of emission spectra of Au(I)SBB thiolate upon heating for 24 h at 55 °C. This validates that the visual luminescence enhancement observed upon heating Au_{25} QCs in presence of Au(I)SBB thiolate is neither a consequence of heating Au_{25} in presence of BBSH thiol nor an effect of heating Au(I)SBB thiolate for 24 h.

Supporting information 6

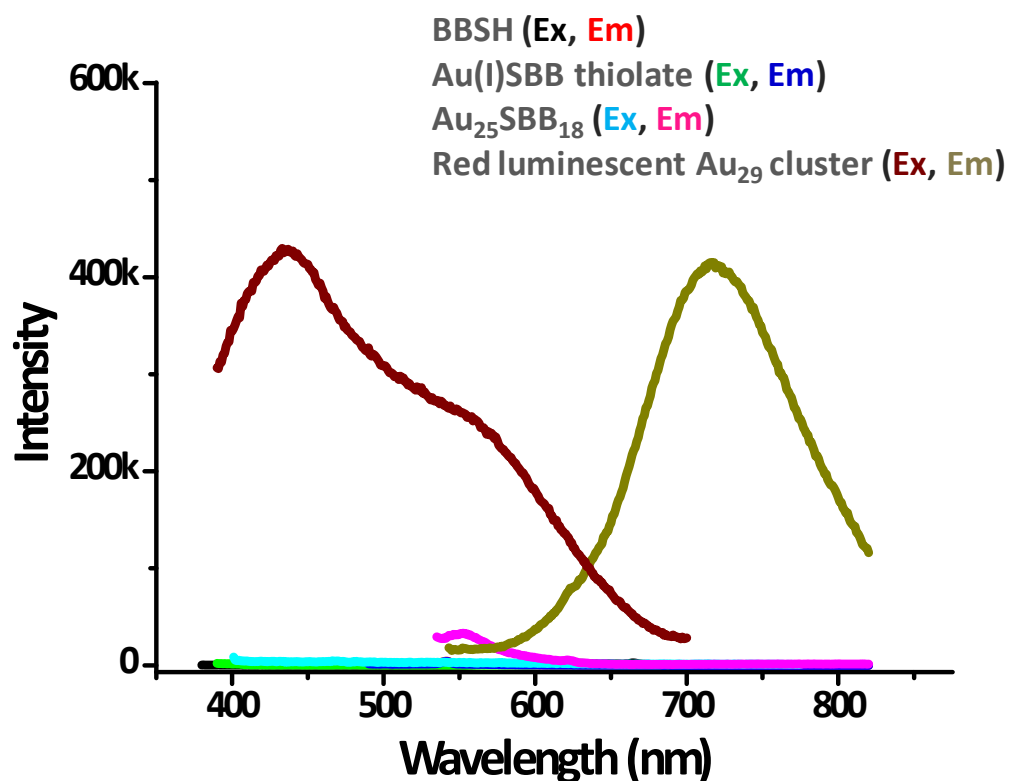


Figure S6. Comparison of excitation and emission spectra of the various reaction intermediates such as BBSH thiol (black and red trace), Au(I)SBB thiolate (green and blue trace), Au₂₅SBB₁₈ (cyan and pink trace) and red luminescent cluster (dark brown and tan trace) respectively. Solutions were diluted in THF so as to maintain identical concentrations (with respect to BBSH thiol). All solutions were measured at λ_{ex} 467 nm and λ_{em} of 737 nm. Slit width was kept at 3 nm for all measurements.

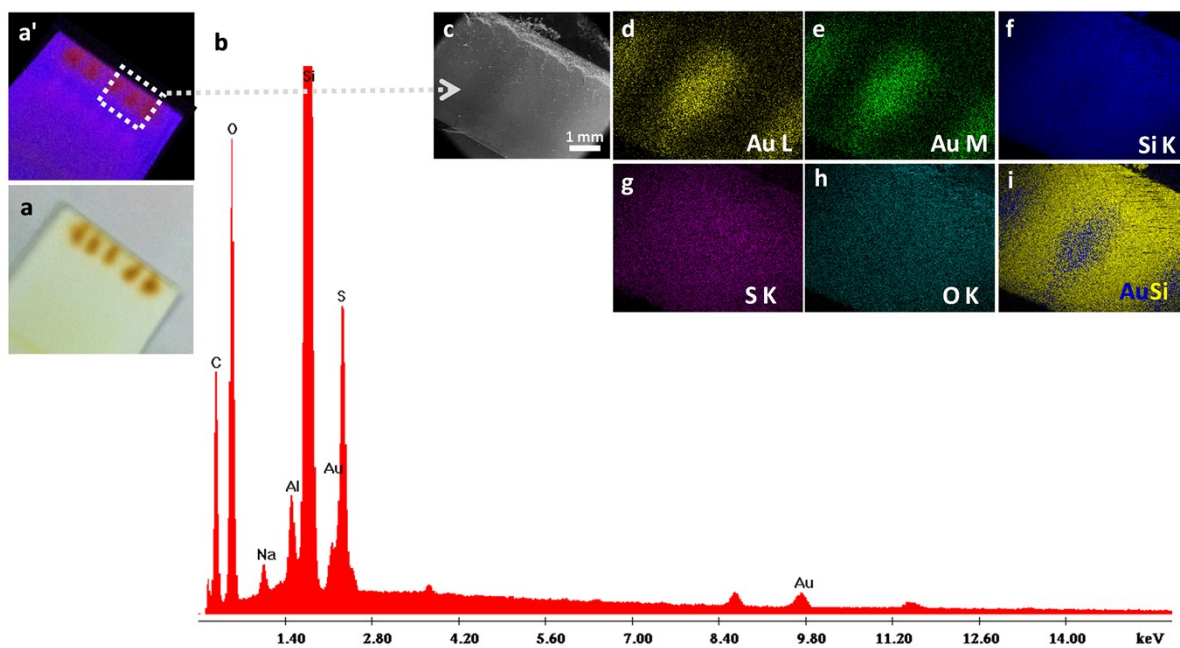


Figure S7. SEM (c), EDAX images (d-i) and EDAX spectrum (b) from the TLC plate with the separated red luminescent fraction (photograph shown as inset) under UV light (a') and visible light (a).

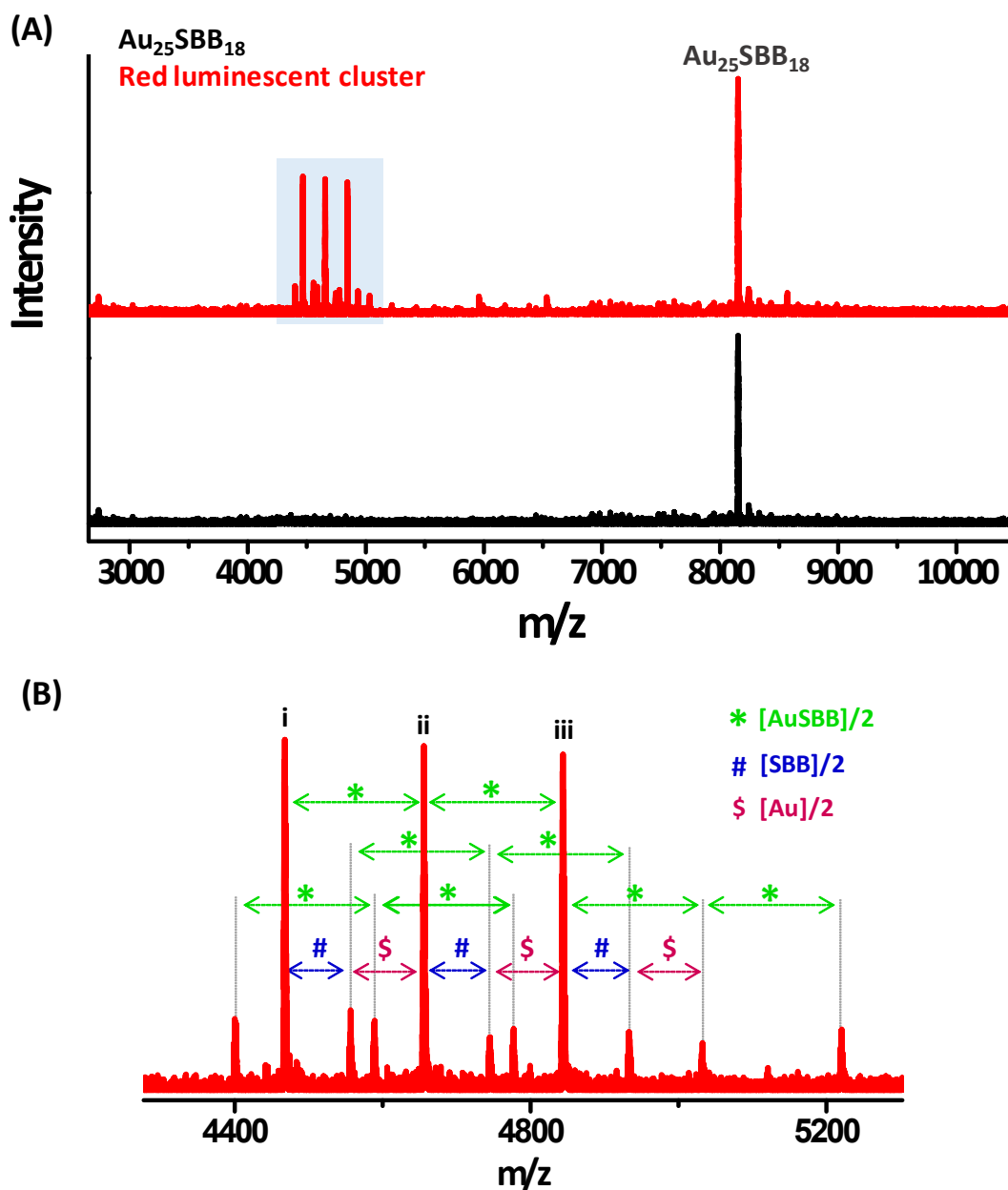


Figure S8. ESI MS of $Au_{25}SBB_{18}$ (black trace) and red luminescent cluster (red trace) in negative ion mode (A). Peak corresponding to Au_{25} is marked in the figure. (B) shows an expanded view of the area marked in (A). A difference of m/z 188, corresponding to $(Au+SBB)/2$, was observed between the three peaks marked i, ii and iii in the figure. Similar intensities of the peaks indicate fragmentation.

Supporting information 9

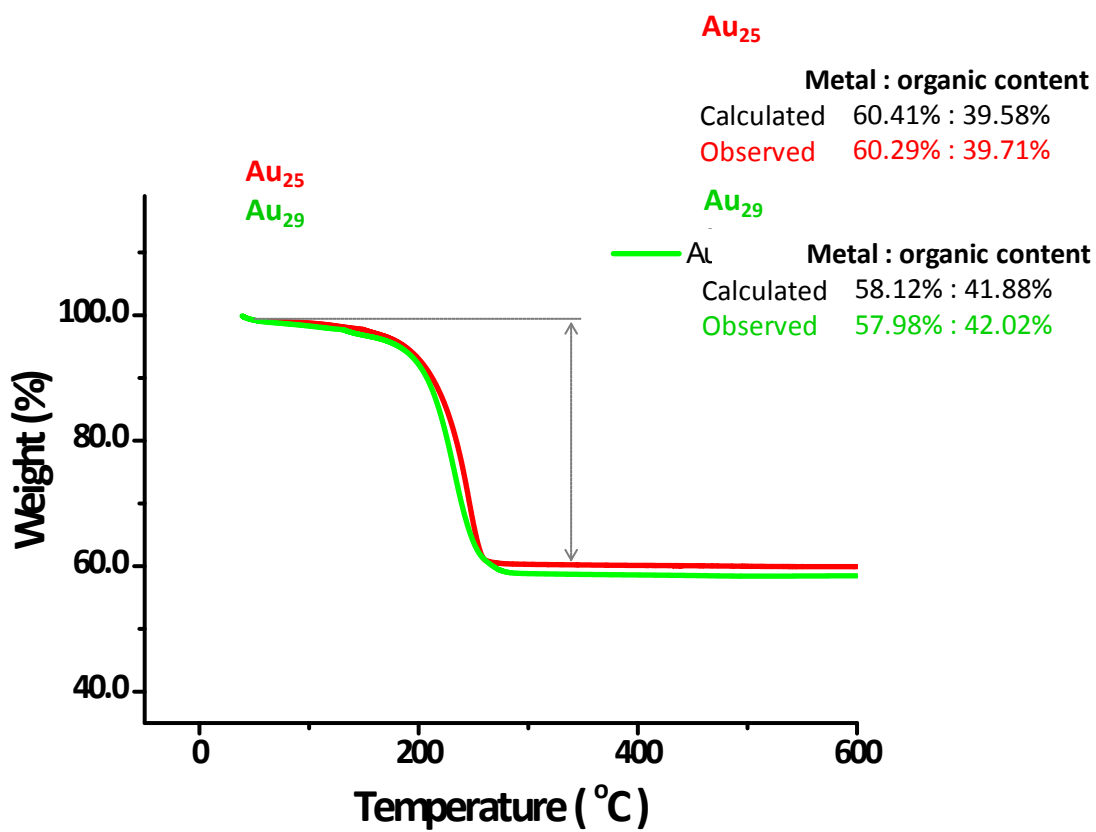


Figure S9. Comparison of TGA data from parent Au₂₅SBB₁₈ (red trace) and red luminescent Au₂₉ QCs (green trace). Though both clusters show similar trend in thiolate desorption the organic content is more in the luminescent Au₂₉ QC as shown. 2.51 mg of Au₂₅SBB₁₈ and 3.32 mg of Au₂₉ was used for analysis under a N₂ atmosphere. Both experimental and calculated values (shown in the inset) are matching confirming the assignment.

Supporting information 10

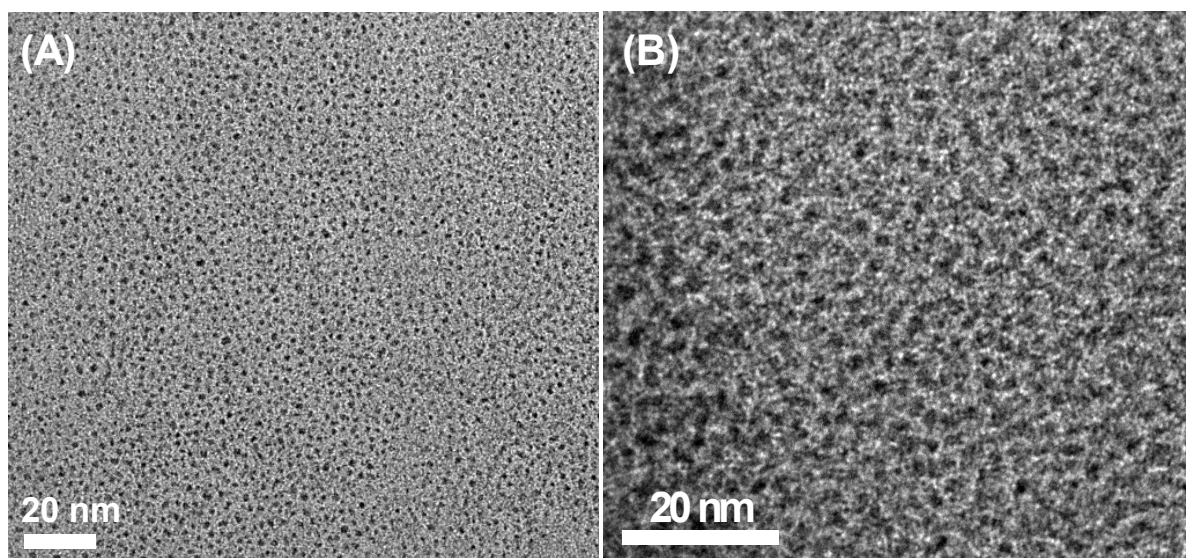


Figure S10. TEM images of (A) $\text{Au}_{25}\text{SBB}_{18}$ and (B) red luminescent Au_{29} clusters.

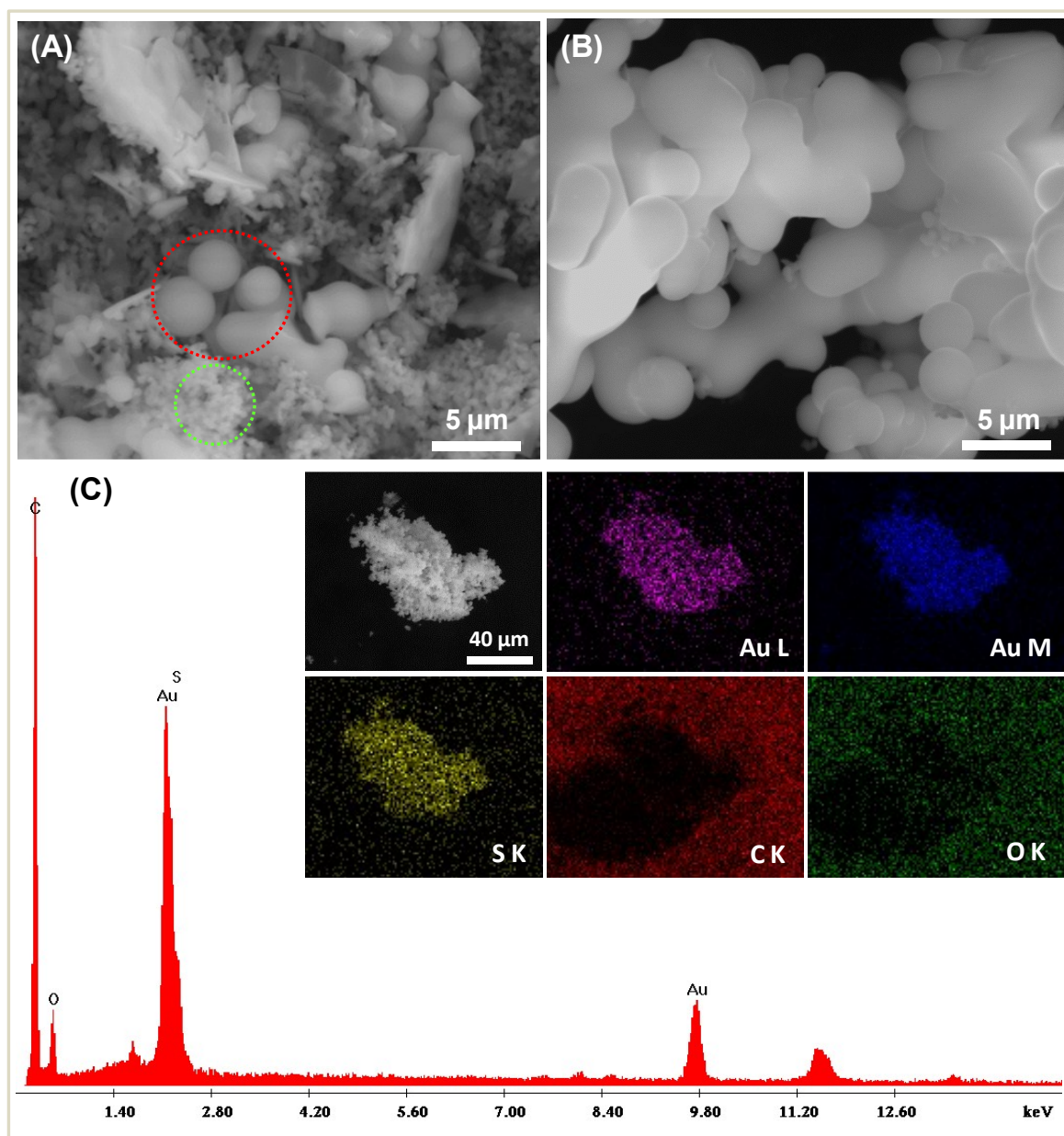


Figure S11. SEM (A, B) and EDAX (C) characterization of red luminescent Au@SBB cluster. SEM images at 6 h (A) and 24 h (B) of reaction are shown. A shows the crude cluster containing mixture of Au₂₅SBB₁₈ (indicated by green circle) and red luminescent Au₂₉ cluster (red circle) obtained after 6 h of heating. Pure red luminescent Au₂₉SBB₂₃ cluster obtained after 24 h heating is shown in B. EDAX mapping and spectra are shown in (C). Carbon and aluminium are from the substrate used for the measurement. Contrast of carbon is low due to the use of carbon tape as the substrate. The scale is same for all images.

Supporting information 12

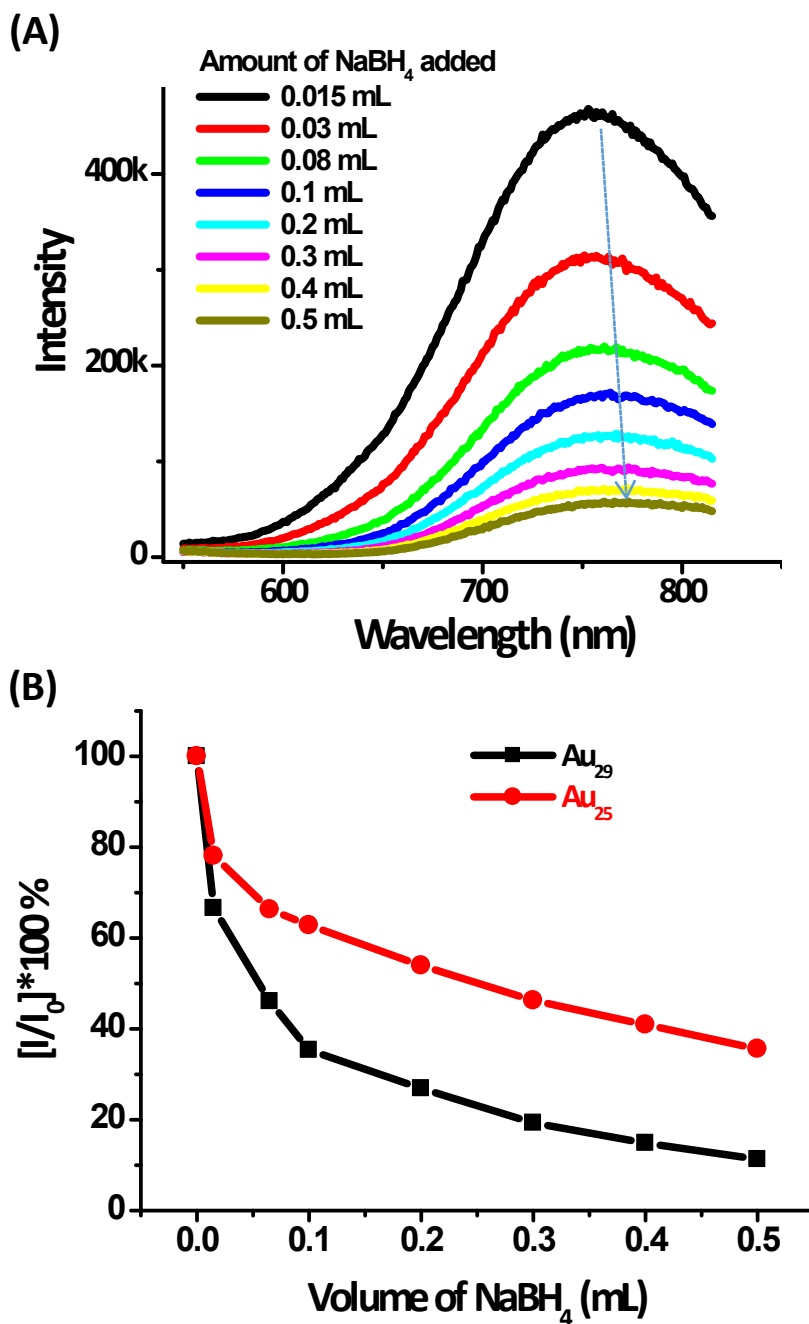


Figure S12. (A) Effect of addition of sodium borohydride to red luminescent Au₂₉ cluster. With increasing amounts of NaBH₄ a emission intensities underwent a drastic quenching along with red shift possibly due to reduction of the surface thiolate shell on the cluster and thus shifting the luminescence to NIR regime. (B) Comparison of change in relative emission intensities of luminescent Au₂₉ and parent Au₂₅SBB₁₈ cluster to equal amounts of NaBH₄.

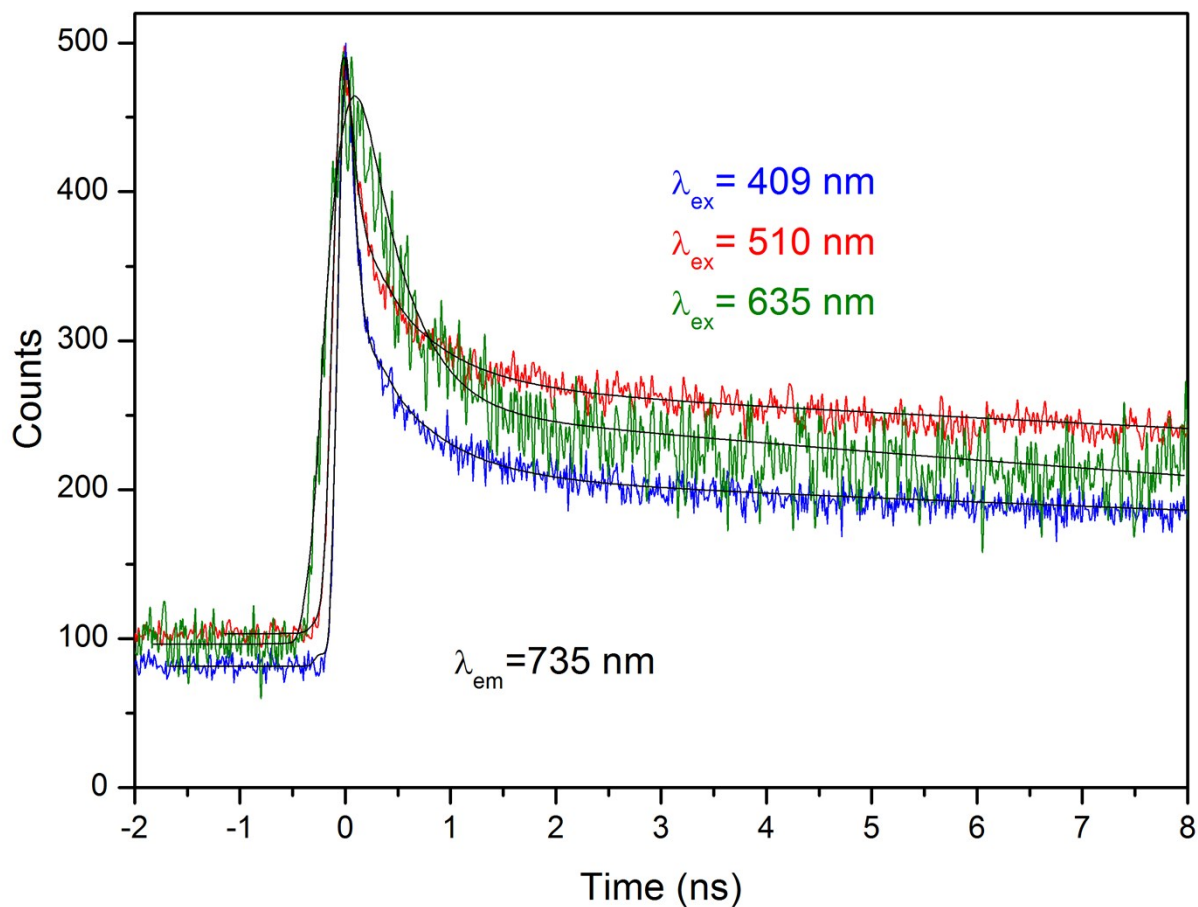


Figure S13. Life time decay of Au₂₉ QCs (emission wavelength of 735 nm) upon excitation at different wavelengths.

Table S1. Picosecond time-resolved fluorescence transients of Au₂₉ clusters in THF upon excitation in three different (409, 510 and 635 nm)

System in THF	τ_1 (%) ns	τ_2 (%) ns	τ_3 (%) ns	τ_{avg} (ns)
Au ₂₉ (Ex 409 nm)	0.05(84)	0.79(8.5)	35(7.5)	2.77
Au ₂₉ (Ex 510 nm)	0.08(70)	0.814(18)	32(12)	4.02
Au ₂₉ (Ex 635 nm)	0.19(60)	1.09(26)	32(14)	4.87

Supporting information 14

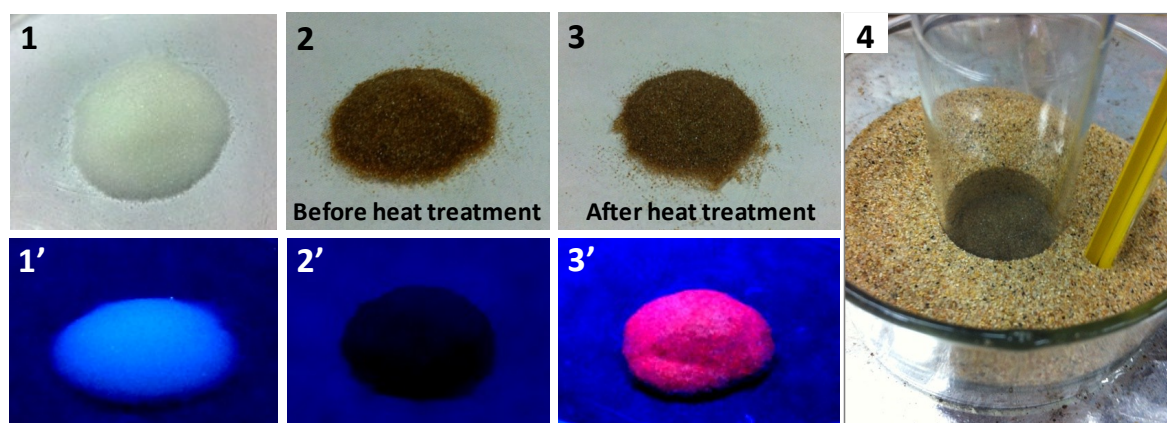


Figure S14. Photographs of silica gel (1, 1'), Au₂₅SBB₁₈-loaded silica gel (2, 2') and Au₂₅SBB₁₈-loaded silica gel after 24 h heat treatment (3, 3') under visible light (1, 2 and 3) and under UV light (1', 2' and 3'). Experimental set-up is shown in (4). Though the Au₂₅SBB₁₈-loaded silica gel powder was initially non-luminescent (see 2, 2'), upon heating it became bright red luminescent (see 3 and 3') with little or no change in the visible color.



Cite this: *Phys. Chem. Chem. Phys.*,
2015, 17, 18364

Ambient preparation and reactions of gas phase silver cluster cations and anions†

Michael Wleklinski,^a Depanjan Sarkar,^b Adam Hollerbach,^a Thalappil Pradeep^b and R. Graham Cooks*^a

Electrospray ionization of metal salt solutions followed by ambient heating transforms the resulting salt clusters into new species, primarily naked ionic metal clusters. The experiment is done by passing the clusters through a heated coiled loop outside the mass spectrometer which releases the counter-anion while generating the anionic or cationic naked metal cluster. The nature of the anion in the starting salt determines the type of metal cluster observed. For example, silver acetate upon heating generates only positive silver clusters, Ag_n^+ , but silver fluoride generates both positive and negative silver clusters, $\text{Ag}_n^{+/-}$ ($3 < n < 20$). Both unheated and heated metal salt sprays yield ions with characteristic geometric and electronic magic numbers. There is also a strong odd/even effect in the cationic and anionic silver clusters. Thermochemical control is suggested as the basis for favored formation of the observed clusters, with anhydride elimination occurring from the acetates and fluorine elimination from the fluorides to give cationic and anionic clusters, respectively. Data on the intermediates observed as the temperature is ramped support this. The naked metal clusters react with gaseous reagents in the open air, including methyl substituted pyridines, hydrocarbons, common organic solvents, ozone, ethylene, and propylene. Argentation of hydrocarbons, including saturated hydrocarbons, is shown to occur and serves as a useful analytical ionization method. The new cluster formation methodology allows investigation of ligand–metal binding including in reactions of industrial importance, such as olefin epoxidation. These reactions provide insight into the physicochemical properties of silver cluster anions and cations. The potential use of the ion source in ion soft landing is demonstrated by reproducing the mass spectra of salts heated in air using a custom surface science instrument.

Received 16th March 2015,
Accepted 11th June 2015

DOI: 10.1039/c5cp01538c

www.rsc.org/pccp

1. Introduction

Transition metals exhibit unique physical, optical, and chemical properties both as bulk materials and in the nanoscale. Silver nanomaterials have applications in water purification,¹ catalysis,² and surface enhanced Raman spectroscopy,^{3,4} among many others. The properties of atomically precise metal clusters are even more fascinating as the addition or removal of a single atom affects the electronic⁵ and chemical⁶ properties of the cluster. Atomically precise metal clusters can be generated both in solution and in the gas phase. Mass spectrometry (MS)

is a critical tool for preparing and understanding the unique properties of metal clusters both in the gas phase^{7,8} and when deposited onto surfaces.^{2,9,10}

The production of gas-phase metal clusters has been demonstrated using a variety of ionization sources, including magnetron sputtering,¹¹ laser ablation,^{12–15} gas aggregation,^{16,17} cold reflux discharge,¹⁸ pulsed arc cluster ion sources,^{19,20} and electrospray ionization (ESI).^{21–26} These sources produce positive, negative, and neutral clusters over a wide size range with a seemingly unlimited choice of elemental compositions.²⁷ Flow tube reactors^{11,28,29} and ion traps^{30,31} are common ways of studying metal clusters in the gas phase. Small silver clusters ($\text{Ag}_n^{+/-}$, $n < 20$), the topic of interest in this paper, have been studied extensively in the gas phase due to their value in partial oxidation and catalytic reactions.^{6,23,24,28,32–38}

The silver cluster, Ag_4H^+ has been used to mediate the carbon–carbon coupling of allyl bromide.²³ In the overall reaction, three molecules of allyl bromide are needed to generate $[\text{Ag}(\text{C}_3\text{H}_5)_2]^+$, $[\text{Ag}_3\text{Br}_3]$, and $\text{CH}_2=\text{CHCH}_3$. The product, $[\text{Ag}(\text{C}_3\text{H}_5)_2]^+$ loses C_6H_{10} , most likely 1,5-hexadiene, upon collisional activation, which represents an example of gas phase carbon–carbon bond coupling.^{39,40}

^a Department of Chemistry and Center for Analytical Instrumentation Development, Purdue University, West Lafayette, Indiana 47907, USA.
E-mail: cooks@purdue.edu

^b DST Unit of Nanoscience (DST UNS) and Thematic Unit of Excellence (TUE), Department of Chemistry, Indian Institute of Technology Madras, Chennai 600 036, India

† Electronic supplementary information (ESI) available: Additional experimental setups, mass spectra of unheated and heated silver salts, tandem MS of silver cluster cations and anions, mass spectra of silver cluster cation/anion reactivity, and tabular results of silver cluster reactivity. See DOI: 10.1039/c5cp01538c

Silver has long served as a catalyst for the partial oxidation of ethylene to ethylene oxide and Ag_2O^+ has been investigated as a model for silver-mediated olefin epoxidation.³⁷ Roithová and Schröder note clean O-atom transfer reactions with ethylene. Propylene undergoes allylic H-atom abstraction and other oxidation pathways but C-H abstraction from propylene leads to the formation of unwanted byproducts, preventing high selectivity in the formation of propylene oxide.⁴¹

The physical and chemical properties of anionic silver clusters in the gas phase have also garnered attention. Measurements on the binding energies of O_2 and observation of cooperative binding of O_2 to silver cluster anions have been reported.^{32,33} Recently, Luo *et al.* noted the enhanced stability of Ag_{13}^- towards etching with O_2 due to a large spin excitation energy.²⁸ The reaction of O_2 with CO in the presence of anionic silver clusters was found to be strongly cluster-size dependent with only Ag_7^- , Ag_9^- , and Ag_{11}^- serving as potential catalytic centers.⁶ Luo *et al.* found that Ag_8^- reacts with chlorine through a harpoon mechanism³⁵ and reported that silver cluster anions activate C-S bonds in ethanethiol to produce such products as Ag_nSH^- and Ag_nSH_2^- .³⁶

While extensive literature exists on the chemistry of gaseous silver clusters in vacuum, there is also a growing community interested in studying their properties on surfaces. For example, size-selected silver cluster cations with different energies were deposited onto Pt(111) and the surface topography was measured with scanning tunneling microscopy. When the energy was less than 1 eV per atom, it was possible to non-destructively deposit the clusters.⁴² Palmer *et al.* deposited size-selected silver clusters on graphite as a method for preparing nanostructured surfaces.⁴³ Recently, Ag_3^+ deposited on alumina was found to be a highly selective catalyst for the epoxidation of propylene by O_2 .² Size selected-silver clusters were deposited on passivated carbon in order to understand the discharge process in lithium-oxygen cells. The size of the deposited silver clusters greatly affected the morphology of lithium peroxide, indicating that precise control of sub-nanometer features on a surface might improve battery technology.⁴⁴

In this study, we describe a novel and facile method for the production of naked metal cluster ions by electrospray

ionization (ESI) and cluster heating in air. When the appropriate silver salt is subjected to these conditions, it is possible to generate silver cluster cations and anions without the use of lasers or collision-induced dissociation (CID). Physicochemical properties are elucidated by subjecting the clusters in the open air to ion/molecule reactions; for example, they can be oxidized in the presence of ozone. The silver clusters can also be used for the analysis of hydrocarbons or to study ligand exchange processes. Finally, it is demonstrated that this ionization source can be coupled to an ion soft landing instrument to perform catalytic studies.

2. Experimental

2.1 Chemicals and materials

Silver fluoride, silver acetate, silver benzoate, 2-ethylpyridine, 3-ethylpyridine, 4-ethylpyridine, 3,4-lutidine, 2,6-lutidine, 2,5-lutidine, 3,5-lutidine, hexadecane, isocetane, squalane, and ethanol were purchased from Sigma Aldrich, USA. HPLC grade methanol was purchased from Mallinckrodt Baker Inc., Phillipsburg, NJ. Deionized water was provided by a Milli-Q Integral water purification system (Barnstead Easy Pure II). Deuterated solvents, such as D_2O and CD_3OD were purchased from Cambridge Isotope Laboratories (Tewksbury, MA). *tert*-Butyl alcohol, 1-propanol, ammonium hydroxide, and pyridine were purchased from Mallinckrodt Chemicals (St. Louis, MI). Isopropyl alcohol, acetic anhydride, and acetone were purchased from Macron (Center Valley, PA). 2,4,6-Trimethylpyridine was purchased from Eastman chemical company (Kingsport, TN). All chemicals were used as received without further purification.

2.2 Experimental methods

A home-built electrosonic spray ionization (ESSI) source was coupled to a heated drying tube as shown in Fig. 1.^{45,46} The heated drying tube is made from 316L stainless steel (AmazonSupply.com, part # S0125028T316SAL 6', O.D. 1/8", I.D. 0.069") and coiled twice to a diameter of 5.5 cm and to a total length of 43 cm. The stainless steel loop was wrapped with heating tape (Omega, part # FGR-030). The ESSI source was typically positioned between 3 mm outside

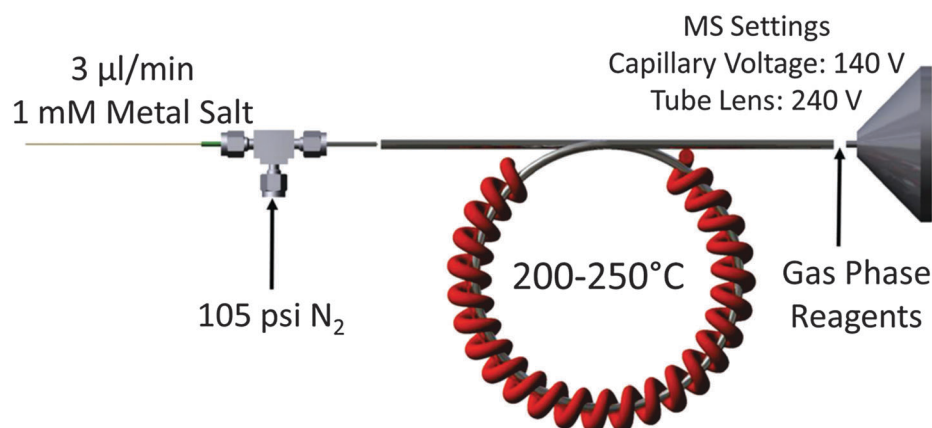


Fig. 1 Apparatus for the production of silver cluster cations and anions.

to 3 mm inside the heating loop, the position being chosen such that the maximum ion signal was obtained. Independent positioning of the ESSI sprayer and heating loop was achieved by using two xyz micrometer moving stages (Parker Automation, Rohnert Park, CA). The distance between the heating loop and linear ion trap mass spectrometer (LTQ, Thermo Scientific, San Jose, CA) inlet was typically between 1 to 10 mm. At shorter distances, the ion signal was higher as more of the electrospray plume entered the MS inlet.

In a typical experiment, a metal salt was dissolved in 1:1 methanol:water at a concentration of 1 mM. Spray was initiated using a voltage of ± 5 kV and N_2 nebulizing gas (105 psi pressure). The electrospray plume entered the heating loop, which was set to 250 °C. The temperature was controlled by the voltage supplied using an autotransformer and monitored by a thermocouple. The ions exiting the loop were analyzed by a LTQ mass spectrometer using the following parameters: capillary temperature 200 °C, capillary voltage ± 140 V, tube lens voltage ± 240 V, maximum injection time 100 ms, and an average of 3 microscans. Automatic instrument tuning was used to optimize the potential applied to all other lenses. For collision-induced dissociation (CID), normalized collision energies of 25–35% (manufacturer's unit), Mathieu parameter q_z values of 0.25–0.35, and isolation windows were typically 2 m/z units larger than the isotopic distribution (e.g. for Ag_6^+ an isolation window of 14 mass units was used). In certain experiments, high mass accuracy (< 5 ppm) was achieved using a hybrid LTQ-Orbitrap mass spectrometer (LTQ-Orbi, Thermo Scientific, San Jose, CA). The mass resolution was set to 30 000 with a typical injection time between 250 ms and 5 s depending on the initial ion intensity. Tandem MS Orbitrap experiments utilized the same conditions as the LTQ.

To perform ion/molecule reactions, the distance between the heating loop and inlet was typically set at 1 cm. Vapors of interest were introduced *via* a cotton swab held between the heating loop and MS inlet (Fig. S1, ESI†). In order to perform sequential ion/molecule reactions, a short piece of metal tubing (2.5 cm) was placed between the inlet and heating loop (Fig. S2, ESI†). One neutral reagent was introduced into the first gap (between the heating loop and the additional metal tubing) and the second reagent was introduced into the second gap (between the added metal tube and the inlet). In addition, some experiments were performed using ozone which was generated by low temperature plasma (LTP) (Fig. S3, ESI†). The low temperature plasma source used has been described previously.^{47,48} Gases were introduced using Swagelok couplings at a flow rate between 0.5–1 L min^{-1} .

3. Results/discussion

3.1 Unheated silver salts

The electrospray of solutions of metal salts has long been known to produce species of the type $[C_nA_{n-1}]^+$ and $[C_nA_{n+1}]^-$ where C is the cation and A is the anion of the salt.⁴⁹ Consistent with this, the mass spectrum of silver acetate recorded with the heating loop turned off shows the formation of simple salt clusters (Fig. 2A).

This spectrum is characterized by a weak geometric magic number for $[Ag_5(CH_3COO)_4]^+$ and $[Ag_8(CH_3COO)_7]^+$, the enhanced stability likely being associated with 3×3 and 3×5 units. For smaller clusters (Ag_3 and smaller), some hydration is present. For larger clusters ($[Ag_4(CH_3COO)_3]^+$ and larger), dissociation (by CID) of the mass-selected ion is dominated by the loss of $Ag_2(CH_3COO)_2$ units, which likely occurs in two separate steps.²⁴ Smaller hydrated clusters undergo water loss followed by ejection of $AgCH_3COO$ while the cluster $[Ag_2(CH_3COO)]^+$ undergoes decarboxylation in agreement with observations by O'Hair *et al.*⁵⁰ Negative ion mode electrospray produces a series of ions $[Ag_n(CH_3COO)_{n+1}]^-$, which do not exhibit any geometric magic numbers (Fig. S4A, ESI†). Dissociation of silver acetate cluster anions is by loss of $Ag(CH_3COO)$. Silver benzoate exhibits similar clustering to that of silver acetate except that the geometric magic numbers are replaced by an abundant ion $[Ag_7(C_7H_6O_2)_6]^+$ (Fig. S4C and E, ESI†). Silver fluoride exhibits a unique unheated mass spectrum. In the positive ion mode, naked silver cluster cations (e.g. Ag_3^+ , Ag_5^+ , Ag_7^+ , Ag_9^+) along with various oxidized and hydrated cations are observed (Fig. S4G, ESI†). In the negative ion mode, extensive clustering of silver with multiple counter anions is observed (Fig. 2C).

3.2 Heated silver salts

The mass spectra of the various silver salts changed significantly when the heating loop was set to 250 °C. Regardless of the silver salt chosen, the positive ion mode mass spectra were all essentially identical (Fig. 2B, Fig. S4D and H, ESI†). These spectra are dominated by the naked metal clusters Ag_n^+ and Ag_n^{2+} . All species undergo expected fragmentations (Fig. S5, ESI†), including the loss of Ag_2 from odd-numbered clusters, coulombic explosion for Ag_{16}^{2+} , and monomer loss from other Ag_n^{2+} ions.^{51–54} The expected odd/even alternation and magic numbers at Ag_3^+ and Ag_9^+ was also observed.⁵⁵ Thus, the fragmentation behavior of the Ag_n^+ and Ag_n^{2+} ions is the same, regardless of the starting material, *viz.* silver benzoate or silver acetate. Moreover, during heating there is no evidence for the formation of silver hydride clusters. Interestingly, only silver fluoride has the ability to generate negatively charged clusters, Ag_n^- (Fig. 2D). Silver acetate and benzoate do not produce silver cluster anions, but instead produce mainly organic fragments, presumably because of the stability of the organic counter anion (Fig. S4B and F, ESI†). The fragmentation of small silver cluster anions ($n < 12$) matches that reported in the literature (Fig. S6, ESI†).⁵⁶ Larger silver cluster anions typically lose neutral Ag upon collisional activation, which has not been reported in literature. For the silver cluster anions, the expected odd/even alternation and magic number at Ag_7^- is observed.²⁸

3.3 Mechanism

The above experiments used heat as well as in-source collisions to transform silver acetate and other silver salts into silver cluster cations and anions. Ready access to these clusters ions facilitated the study of their formation and dissociation as a source of information on their structure and reactivity. Possible intermediates responsible for the formation of silver cluster cations from silver acetate were investigated by monitoring the

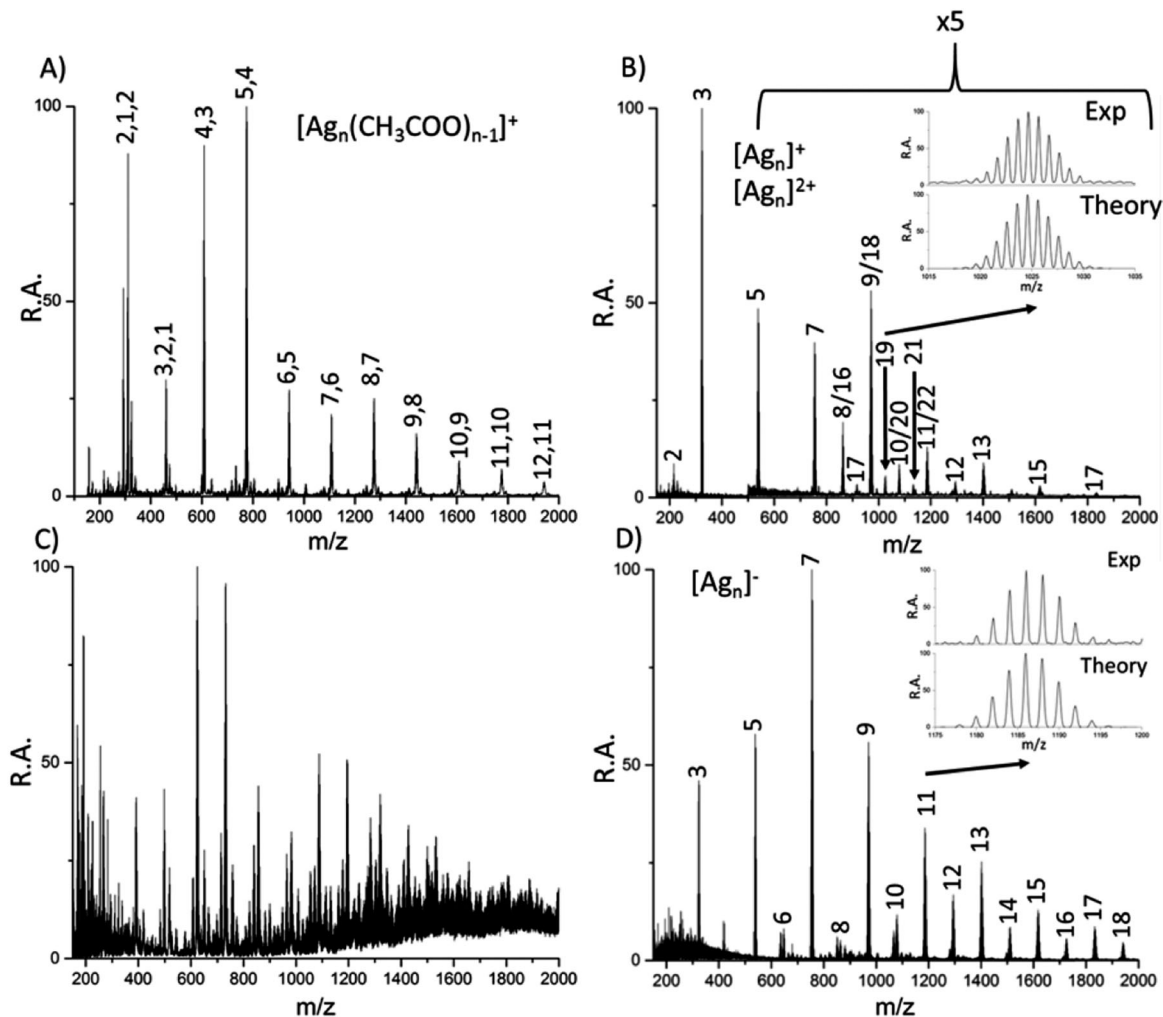
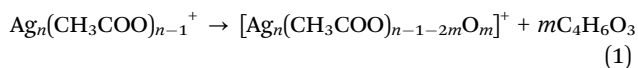


Fig. 2 Positive ion mode mass spectra of (A) unheated and (B) heated electro sprayed silver acetate. Negative ion mode for (C) unheated and (D) heated electro sprayed silver fluoride solution. The numbers above each peak in (A) indicate the number of silver atoms, ligands, and water molecules present. The numbers above each peak in (B) and (D) indicate the number of silver atoms.

total ion chromatogram while the temperature of the loop was ramped from room temperature to 250 °C over the course of a few minutes (Fig. S7, ESI†). At low temperatures, the salt clusters $[\text{Ag}_n(\text{CH}_3\text{COO})_{n-1}]^+$ were observed. At intermediate temperatures (100–150 °C), new species were observed in the MS, including $[\text{Ag}_9(\text{CH}_3\text{COO})_6\text{O}]^+$, $[\text{Ag}_8(\text{CH}_3\text{COO})_5\text{O}]^+$, and $[\text{Ag}_7(\text{CH}_3\text{COO})_4\text{O}]^+$, indicating losses of acetic anhydride ($\text{C}_4\text{H}_6\text{O}_3$), eqn (1). For smaller clusters, an additional water molecule was present on the cluster, as in $[\text{Ag}_6(\text{CH}_3\text{COO})_3\text{OH}_2\text{O}]^+$ and $[\text{Ag}_5(\text{CH}_3\text{COO})_2\text{OH}_2\text{O}]^+$. This may simply be the result of addition of residual water to coordinatively unsaturated metal complexes by ion/molecule reactions in the ion trap, a known process. An alternative to this pathway, the loss of ethenone ($\text{C}_2\text{H}_2\text{O}$) followed by water, is considered less likely as discussed in the ESI.†



Thermochemical considerations are useful in deciding on likely decomposition pathways. For example if $n = 3$, then the

process shown in eqn (1) forms one molecule acetic anhydride and Ag_3O^+ .⁵⁷ The formation of acetic anhydride is exothermic by $-572.5 \text{ kJ mol}^{-1}$, which almost 250 kJ mol^{-1} more exothermic than the alternative pathway (ESI†), suggesting that acetic anhydride formation is the favored pathway leading to oxidized silver cluster cations.

Fig. S8 (ESI†) provides a chart of all ions observed in the full scan mass spectra along with their relationships as established by CID experiments for the decomposition of the silver acetate ions in the positive ion mode. All ions observed in the mass spectra can be explained as possible products of eqn (1) when water and oxygen are allowed to arrive or leave from the cluster. When the heating experiment is performed at the highest temperatures, the formation of simple silver cluster cations and oxidized silver cluster cations was observed. Once the final temperature was reached and some time had passed, the formation of primarily naked metal clusters was observed.

The thermochemical mechanism for cationic cluster formation extends to other silver salts such as the benzoate, which is

assumed to undergo thermal dissociation by similar routes to give silver cation clusters. A method for the production of Ag_n^+ and $\text{Ag}_{n-1}\text{H}^+$ from cluster ions generated from precursor solutions containing silver nitrate and either glycine or *N,N*-dimethyl glycine has been reported by O'Hair, using ion trap CID.²⁴ The choice of precursor compounds is important in these experiments as it can allow the production of $[\text{C}_n\text{A}_{n-1}]^+$ and $[\text{C}_n\text{A}_{n-1}]^-$ where A is an anion with favorable redox properties. For example, glycine contains both an amine and deprotonated carboxylic group, which appear to meet these redox criteria.²⁴ It should be noted that under the conditions of the O'Hair study, silver acetate did not produce silver cluster cations upon CID.²⁴ The heating loop utilized in our work dissociates clusters to this extent at atmospheric pressure, but the similarities and differences between the ion trap CID and ambient heating experiments are not well understood.⁵⁸

Anionic cluster formation can be considered in a similar vein. The loss of fluorine could be by hydrolysis to give the enthalpically favored HF or in a redox process to give the less favored F_2 . The favored formation of the odd-numbered silver anion clusters (Fig. 2D) is simply due to their greater stability than their even-numbered counterparts.²⁸

3.4 Reactivity of silver cluster cations

3.4.1 Alcohol reactivity. Atmospheric pressure ion/molecule reactions were carried out between organic solvents (ethanol, 1-propanol, isopropyl alcohol, *tert*-butyl alcohol, acetone, and acetonitrile) and silver cluster cations generated from silver acetate. Typically, an organic solvent of interest was added to a cotton swab and introduced into the region after the heating tube and before the MS inlet (Fig. S1, ESI†). A summary of the reactions can be found in Tables S1, S2 and Fig. S9 (ESI†). Monomeric Ag^+ reacts to form mainly $[\text{AgL}]^+$ and $[\text{AgL}_2]^+$, except in the case of acetonitrile where the only product is $[\text{AgL}_2]^+$. The cluster Ag_3^+ reacts to form $[\text{Ag}_3\text{L}]^+$ and $[\text{Ag}_3\text{L}_2]^+$, except that acetonitrile behaves differently in forming $[\text{Ag}_3\text{L}_2]^+$ and $[\text{Ag}_3\text{L}_3]^+$. This reactivity differs from reported gas phase reactions, where $[\text{AgL}_2]^+$ and $[\text{Ag}_3\text{L}_3]^+$ are the terminal products for all reagents studied except ethanol, which was reported to be unreactive.⁵⁹ The differences in reactivity are not unexpected given that our experiments were performed in air, and the literature data refers to vacuum, and there are also differences in reaction time. The maximum interaction time in our experiments was on the order of a single scan, *ca.* 0.2–0.5 s, compared to possibly 60 s reported in the literature. The ion/molecule reactions under vacuum do not provide efficient third body stabilization for smaller ions, explaining the difference in reactivity with ethanol.⁵⁹ Tandem mass spectrometry data on the reaction products (*e.g.* $[\text{Ag}_3\text{L}_2]^+$, Fig. S9A, C, E and F, ESI†) indicate that the reagents serve as simple ligands. The reaction product, for example $[\text{Ag}_3\text{L}_2]^+$, loses one ligand for each stage of tandem MS to form bare Ag_3^+ . Simple ligation is the main result observed in these reactions. There appears to be relatively good agreement between silver clusters with alcohols obtained under vacuum and in the open air. Due to the inability to mass select the clusters before reaction, it is possible that some of the reaction products form

from the larger clusters which react with accompanying losses of Ag_n moieties. The loss of Ag upon ligand addition for even-numbered silver cluster cations is an example of such a reaction that has been previously reported.^{59,60}

3.4.2 Methyl substituted pyridine reactivity. Atmospheric pressure ion/molecule reactions were carried out between methyl-substituted pyridines and silver cluster cations generated from silver benzoate (Fig. S10, Tables S3 and S4, ESI†). Ligation of the neutral reagents to the silver cluster was observed with the dominant products being $[\text{AgL}_2]^+$ and $[\text{Ag}_3\text{L}_3]^+$ except in the case of pyridine itself and 2,4,6-trimethylpyridine which also produced species with a smaller number of ligands. The nature of the interaction between Ag_3^+ and the neutral reagent was confirmed by CID (Fig. S11, ESI†) which showed the sequential loss of ligands from the species $[\text{Ag}_3(\text{C}_8\text{H}_{11}\text{N})_3]^+$ and $[\text{Ag}_3(\text{C}_7\text{H}_9\text{N})_3]^+$ generated from 2,4,6-trimethylpyridine and 3,5-lutidine. This confirms that the neutrals are acting as simple ligands on Ag_3^+ .

3.4.3 Ligand exchange. It is obvious from the previous examples that ligation of Ag_3^+ is easily achieved. A further test was made to determine if the generation of mixed-ligand Ag_3^+ species was possible. A slightly modified version of the apparatus of Fig. S1 (ESI†) was used so that multiple neutral reagents could be introduced separately (Fig. S2, ESI†). The system was tested with three mixtures of ligands: ammonia (from ammonium hydroxide) and acetonitrile, 2,6-lutidine and acetonitrile, and acetone and acetonitrile. For the first set of reagents, ammonia and acetonitrile, a variety of mixed ligand species was observed, including $[\text{Ag}_3 + \text{C}_2\text{H}_3\text{N} + \text{NH}_3]^+$, $[\text{Ag}_3 + (\text{C}_2\text{H}_3\text{N})_2 + \text{NH}_3]^+$, and $[\text{Ag}_3 + \text{C}_2\text{H}_3\text{N} + (\text{NH}_3)_2]^+$ as confirmed by MS/MS (Fig. S12, ESI†). 2,6-Lutidine and acetonitrile also generated a mixed ligand species (Fig. S13, ESI†), $[\text{Ag}_3 + \text{C}_7\text{H}_9\text{N} + \text{C}_2\text{H}_3\text{N}]^+$; however, this was the only mixed ligand species observed in this case. In addition, $[\text{Ag}_3 + (\text{C}_7\text{H}_9\text{N})_2]^+$ and $[\text{Ag}_3 + (\text{C}_7\text{H}_9\text{N})_3]^+$ were formed in higher intensity than $[\text{Ag}_3 + \text{C}_7\text{H}_9\text{N} + \text{C}_2\text{H}_3\text{N}]^+$, indicating a preference towards binding 2,6-lutidine. To qualitatively test the effect of the sequence used to introduce neutral reagents, acetone and acetonitrile were used. Acetone was allowed to interact first with the cluster spray followed by the acetonitrile and *vice versa* (Table S5 and Fig. S14, ESI†). When acetone was allowed to react first, it was possible to generate a mixed species as well as species containing either acetone or acetonitrile. This was in stark contrast to the case where acetonitrile was the first reagent as it produced only species with acetonitrile ligands; *i.e.* ligand displacement did not occur due to stronger binding to this ligand.

3.4.4 Hydrocarbon reactivity. Silver cationization is known to selectively ionize unsaturated compounds, including polycyclic aromatic hydrocarbons and alkenes.^{61–64} A series of hydrocarbons was analyzed using ambient ion/molecule reactions in the same manner as other neutral reagents (Fig. S15, ESI†). Both cationization by Ag^+ and Ag_3^+ occurred for hexadecane, isocetance, and squalane. Cationization of a pump oil (Ultragrade 19) sample was also demonstrated, but the identity of the silver adducts is unknown. The fact that heat was required to generate the silver cluster spray is advantageous for the analysis of heavy hydrocarbons, which are difficult to vaporize and often have low

vapor pressures. The convenient ionization of saturated hydrocarbons in the ambient environment is a potential analytical application of this methodology.

3.4.5 Oxidation. Oxidized silver clusters can serve as model catalysts for partial oxidation reactions, including epoxidation.³⁷ Roithová and Schröder produced Ag_2O^+ in vacuum from the dissociation of Ag_2NO_3^+ into NO_2 and Ag_2O^+ . Another possible approach to simple oxides is the direct oxidation of Ag_n^+ clusters, a possibility indicated by the reaction between *neutral* silver clusters and ozone.⁶⁵ Ionic metal cluster oxidation was achieved by utilizing a low power plasma (LTP) source (Fig. 3), which under appropriate conditions serves as a source of ozone.^{47,66} Silver cluster cations were generated from silver fluoride and allowed to interact with the generated ozone (Fig. 3B). A series of oxidized metal clusters was observed which contained multiple oxygen atoms as well as water molecules. The simplest and most notable reaction was the transformation of Ag_3^+ into Ag_3O^+ . It is observed that silver clusters containing at least one oxygen atom can react with water too. It seems that water is only reactive towards already oxidized clusters, since naked silver cluster cations have been reported to be unreactive towards water.⁵⁹ (The water is likely adventitious water in the ambient environment or in the ion trap used for mass analysis.)

3.4.6 Reactions of Ag_n^+ and oxidized Ag_n^+ with ethylene and propylene. Supported silver trimers have been demonstrated to

be catalysts for the direct epoxidation of propylene using gaseous oxygen.² In our study, odd-numbered silver cluster cations interacted with ethylene to produce mono-, bi-, and tri-ligated species (Fig. S16A, ESI[†]). No ligation was observed for even-numbered clusters, either due to their inertness or to the loss of Ag upon reaction to produce the favored odd-numbered cluster. A small amount of $[\text{Ag}_3(\text{C}_2\text{H}_4)_3\text{O}]^+$ was observed, which presumably arises from reaction with the small amount of Ag_3O^+ present within the spray. With the addition of ozone from the LTP source, the mass spectra change significantly. The intensity of $[\text{Ag}_3(\text{C}_2\text{H}_4)_3\text{O}]^+$ increases dramatically and a species $[\text{Ag}_5(\text{C}_2\text{H}_4)_4\text{O}_2]^+$ is observed (Fig. S16B, ESI[†]). It is interesting to note that there appears to be a cooperative effect in the binding of ethylene to oxidized clusters as Ag_3^+ binds one or two ethylenes, but it appears that Ag_3O^+ binds only three ethylenes. The same phenomenon occurs for the binding of one, two, or three ethylenes to Ag_5^+ but Ag_5O^+ only binds four ethylenes. Cooperative binding has been reported for O_2 and CO with anionic silver clusters, but no such reports exist for cationic silver clusters.^{6,32} $[\text{Ag}_3(\text{C}_2\text{H}_4)_3\text{O}]^+$ and $[\text{Ag}_5(\text{C}_2\text{H}_4)_4\text{O}_2]^+$ were subjected to CID to identify any potential epoxide products; however, only the products of ligation were observed. The tandem MS of $[\text{Ag}_5(\text{C}_2\text{H}_4)_4\text{O}_2]^+$ (Fig. S17, ESI[†]) is interesting as the loss of two ethylene molecules is accompanied by the addition of a single water molecule, and the loss of three ethylenes is accompanied by the addition of two water molecules.

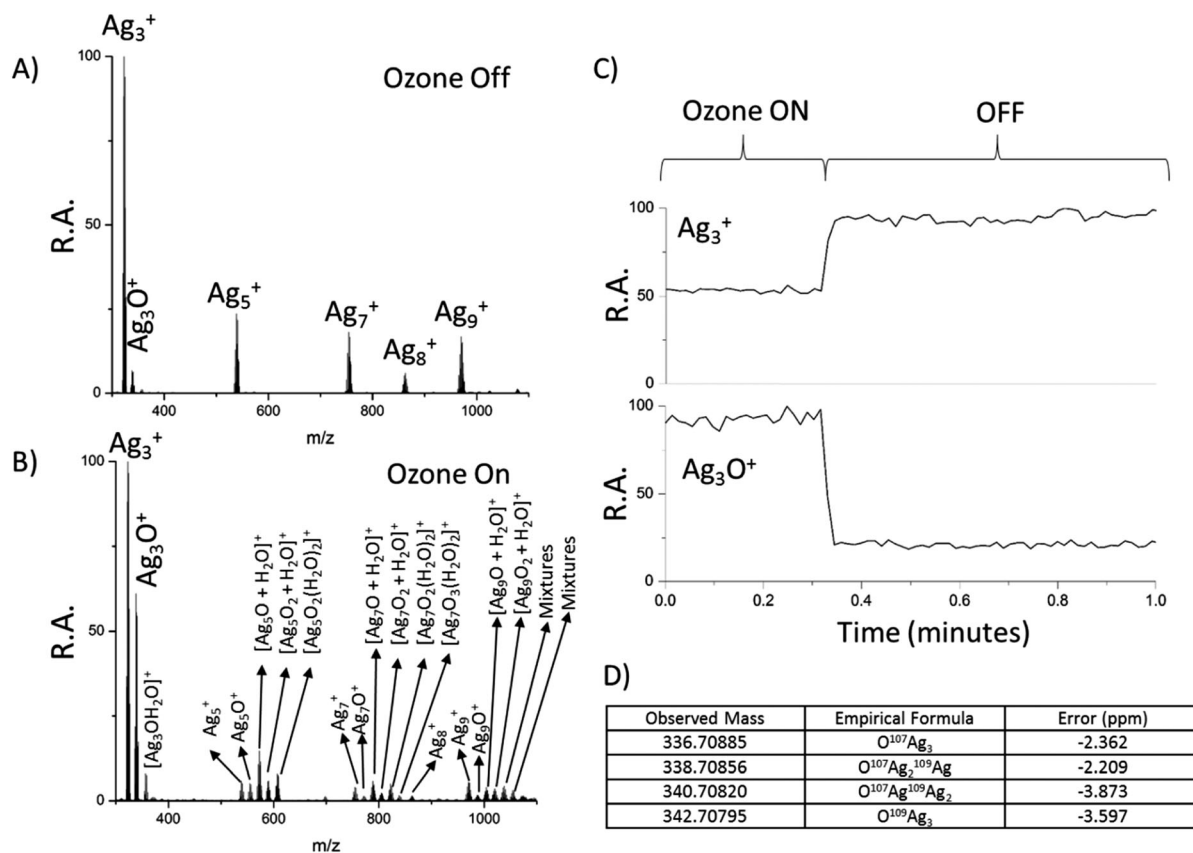


Fig. 3 Mass spectra of silver cluster cations generated from silver fluoride (A) without ozone and (B) with ozone. (C) Shows the selected ion chromatogram of Ag_3^+ (top) and Ag_3O^+ (bottom) in the presence and absence of ozone. (D) High mass accuracy measurements confirm the formation of Ag_3O^+ .

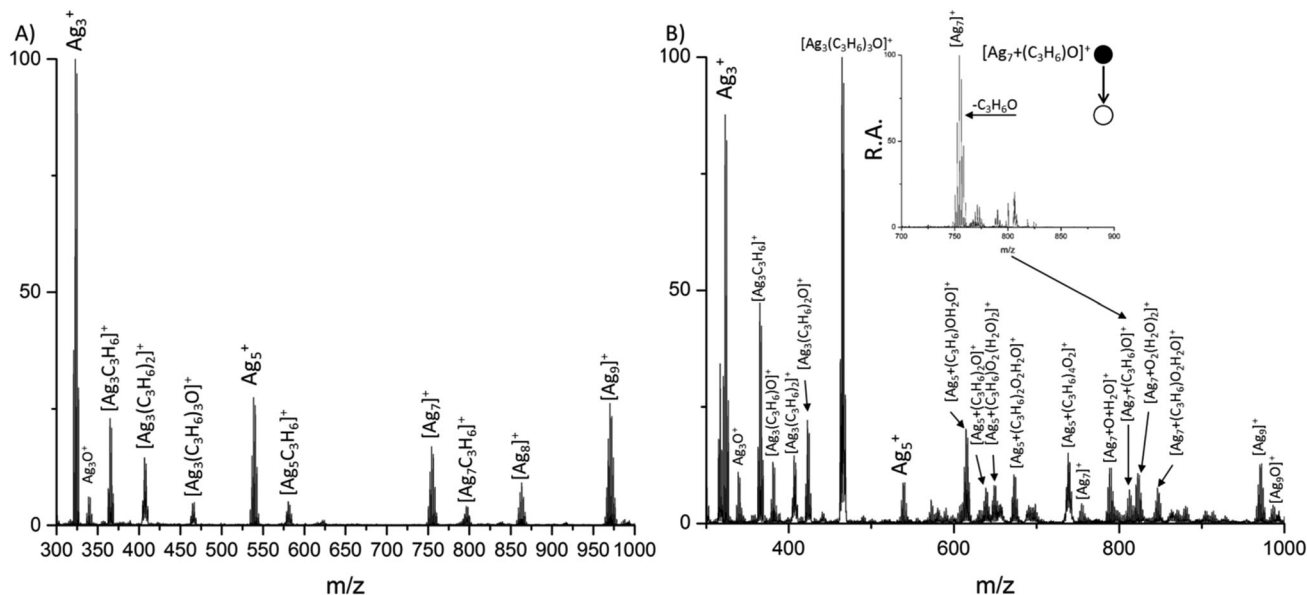


Fig. 4 Reaction of silver cluster cations with (A) propylene and (B) propylene and ozone.

Similar experiments were performed with propylene as the reagent gas. In the absence of ozone, propylene exhibits nearly identical reactivity to ethylene (Fig. 4). The reactivity of ozone and propylene is similar to ozone and ethylene for the Ag_3^+ cluster but differs for the larger clusters (Fig. 4B). A variety of species containing propylene, oxygen, and water are observed for both Ag_5^+ and Ag_7^+ . $[\text{Ag}_7(\text{C}_3\text{H}_6)\text{O}]^+$ is particularly interesting because it fragments to lose neutral $\text{C}_3\text{H}_6\text{O}$, propylene oxide or a structural isomer.

3.5 Reactivity of silver cluster anions

3.5.1 Formation of $[\text{Ag}_n(\text{OH})]^-$. The reactivity of silver cluster anions generated from silver fluoride was examined. The position of the ESI source relative to the heating tube was altered to form an ambient discharge. Without the discharge, naked metal silver clusters are observed (Fig. 5). With the discharge, the even-numbered clusters (especially $n = 6, 8$, and 10) gained an OH group to form $[\text{Ag}_n\text{OH}]^-$, possibly due to reaction with hydroxyl radicals created by the discharge.⁶⁷ The amount of

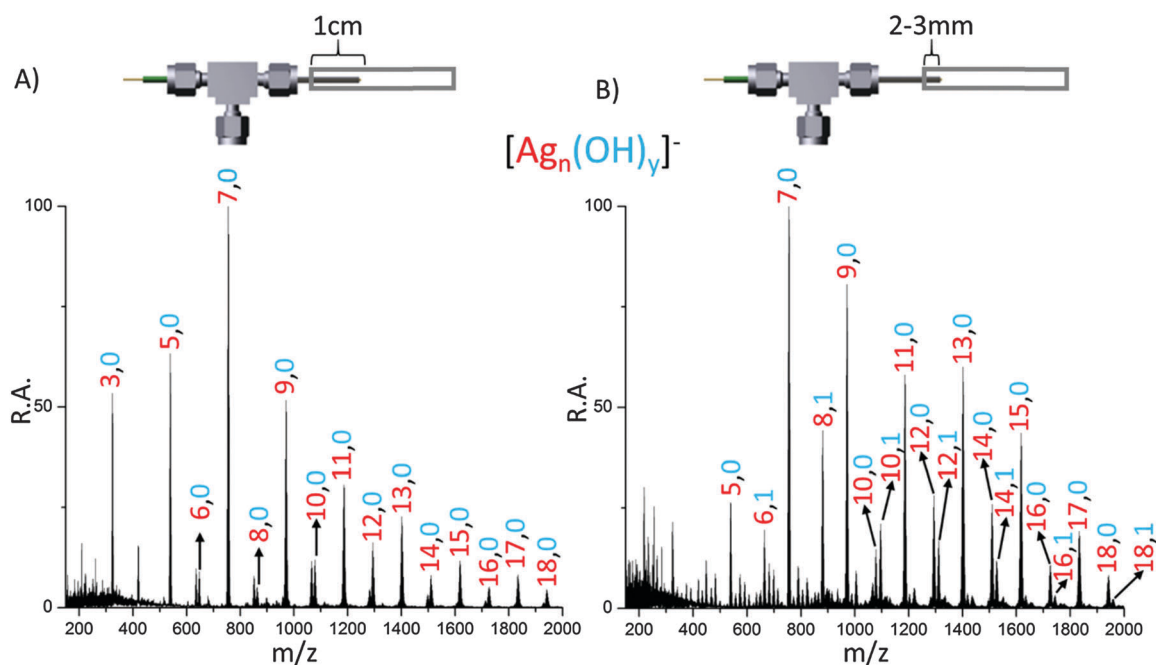


Fig. 5 Mass spectra of silver cluster anions with the ESSI sprayer inserted (A) 1 cm and (B) 2–3 mm inside the heating tube. Red and blue numbers respectively indicate silver atoms and OH molecules.

$[\text{Ag}_n\text{OH}]^-$ varies with cluster size but generally decreases as n increases. Deuterated 1:1 methanol:water was used as the spray solution in an attempt to identify the source of the OH. The intensity of $[\text{Ag}_n\text{OD}]^+$ was at most 30% of the $[\text{Ag}_n\text{OH}]^-$ intensity, indicating that the source of OH must be from elsewhere, such as atmospheric water.

3.6 Ion soft landing

As a proof of principle, the metal cluster ion source was coupled to a homebuilt ion soft landing instrument.^{4,68} Each of the three silver salts was electrosprayed and similar mass spectra were obtained as previously described (Fig. S18, ESI†). For unheated silver acetate and silver benzoate, the same type of salt clustering was observed as previously seen (Fig. 2A). A similar effect was observed for silver fluoride, but the exact number of silver and amount of oxygen or water bound could not be determined with the given instrument resolution. Upon heating, all three salts produced a range of clusters from Ag_3^+ to Ag_{15}^+ without any even-numbered clusters. This set of ions was deposited onto a gold surface and a current of 10 pA could be achieved. Efforts are underway to improve the current of the source so it will be possible to study mass-selected ions on surfaces.

4. Conclusions

The major significance of this study lies in the development of a simple methodology to produce anionic and cationic metal clusters in the ambient environment. In addition (1) insights into the mechanisms of formation of the cluster ions was obtained by studying effects of ambient heating and from thermochemical considerations. The formation of a series of odd-numbered silver anions is most remarkable. (2) Ion/molecule reactions at atmospheric pressure revealed a rich chemistry of the silver cluster cations and anions. Examples of this include, ligation, ligand exchange, cationization of alkanes and olefins, and oxidation reactions. Ligand exchange chemistry shows the relative strength of different ligands towards silver cluster cations, which may be of use in choosing ligands for capping atomically precise clusters. (3) The potential analytical utility of the cluster ions was demonstrated by silver cationization of saturated alkanes. (4) The use of ozone to produce oxidized clusters especially Ag_3O^+ was demonstrated; these silver clusters are especially important as partial oxidation catalysts.

In future work, attempts will be made to operate these ambient sources so as to produce a narrower range of cluster ions, to select clusters of a particular size by ion mobility and to explore further the chemistry of such anionic species Ag_n^- and Ag_nOH^- . Extensions of this approach to the generation of cluster ions from other metals will also be attempted. For example, it is already known that Pd_n^+ , Pd_nO_y^+ , and Pd_nO_y^- (where $3 < n < 13$, and $3 < y < 8$) are formed from palladium acetate. The formation of alloy clusters from a mixture of metal salts is also expected to be straightforward. Given the existence of a rationale for the loss of the counterion as a small stable molecule (acetic anhydride in the case of acetates), other

counterions will be selected to optimize cluster ion formation. The most interesting aspect of the new capabilities provided will be the investigation of processes of industrial significance using metal clusters and metal oxide clusters, which have some of the structural features believed to be important in full scale heterogeneous catalysis (certain metal cluster sizes and compositions).^{8,69,70} The fact that these species can be generated in air compensates to a degree for the fact that they are not atomically precise.

Acknowledgements

Financial support from the Separations and Analysis Program, Office of Basic Energy Sciences, US Department of Energy, DE-FG02-06ER15807 is acknowledged. TP acknowledges DST for funding. DS acknowledges UGC for their research fellowship. Zane Baird is thanked for technical assistance.

References

- 1 M. U. Sankar, S. Aigal, S. M. Maliyekkal, A. Chaudhary, Anshup, A. A. Kumar, K. Chaudhari and T. Pradeep, *Proc. Natl. Acad. Sci. U. S. A.*, 2013, **110**, 8459–8464.
- 2 Y. Lei, F. Mehmood, S. Lee, J. Greeley, B. Lee, S. Seifert, R. E. Winans, J. W. Elam, R. J. Meyer, P. C. Redfern, D. Teschner, R. Schlögl, M. J. Pellin, L. A. Curtiss and S. Vajda, *Science*, 2010, **328**, 224–228.
- 3 A. Li, Z. Baird, S. Bag, D. Sarkar, A. Prabhath, T. Pradeep and R. G. Cooks, *Angew. Chem., Int. Ed.*, 2014, **53**, 12528–12531.
- 4 J. Cyriac, M. Wlekinski, G. Li, L. Gao and R. G. Cooks, *Analyst*, 2012, **137**, 1363–1369.
- 5 D. M. Cox, W. Eberhardt, P. Fayet, Z. Fu, B. Kessler, R. D. Sherwood, D. Sondericker and A. Kaldor, *Z. Phys. D: At., Mol. Clusters*, 1991, **20**, 385–386.
- 6 L. D. Socaciu, J. Hagen, J. Le Roux, D. Popolan, T. M. Bernhardt, L. Wöste and Š. Vajda, *J. Chem. Phys.*, 2004, **120**, 2078–2081.
- 7 P. Jena and A. W. Castleman Jr, *Int. J. Mass Spectrom.*, 2015, **377**, 235–247.
- 8 S. M. Lang and T. M. Bernhardt, *Phys. Chem. Chem. Phys.*, 2012, **14**, 9255–9269.
- 9 S. K. Buratto, M. T. Bowers, H. Metiu, M. Manard, X. Tong, L. Benz, P. Kemper and S. Chrétien, in *The Chemical Physics of Solid Surfaces*, ed. D. P. Woodruff, Elsevier, 2007, vol. 12, pp. 151–199.
- 10 G. E. Johnson, T. Priest and J. Laskin, *J. Phys. Chem. C*, 2012, **116**, 24977–24986.
- 11 Z. Luo, W. H. Woodward, J. C. Smith and A. W. Castleman Jr, *Int. J. Mass Spectrom.*, 2012, **309**, 176–181.
- 12 P. Milani and W. A. deHeer, *Rev. Sci. Instrum.*, 1990, **61**, 1835–1838.
- 13 R. L. Wagner, W. D. Vann and A. W. Castleman, *Rev. Sci. Instrum.*, 1997, **68**, 3010–3013.

- 14 W. Bouwen, P. Thoen, F. Vanhoutte, S. Bouckaert, F. Despa, H. Weidele, R. E. Silverans and P. Lievens, *Rev. Sci. Instrum.*, 2000, **71**, 54–58.
- 15 S. Kéki, L. S. Szilágyi, J. Török, G. Deák and M. Zsuga, *J. Phys. Chem. B*, 2003, **107**, 4818–4825.
- 16 S. H. Baker, S. C. Thornton, A. M. Keen, T. I. Preston, C. Norris, K. W. Edmonds and C. Binns, *Rev. Sci. Instrum.*, 1997, **68**, 1853–1857.
- 17 W. A. de Heer, *Rev. Mod. Phys.*, 1993, **65**, 611–676.
- 18 R. Keller, F. Nöhmayer, P. Spädtke and M. H. Schönenberg, *Vacuum*, 1984, **34**, 31–35.
- 19 H. R. Siekmann, C. Lüder, J. Faehrmann, H. O. Lutz and K. H. Meiwes-Broer, *Z. Phys. D: At., Mol. Clusters*, 1991, **20**, 417–420.
- 20 B. Klipp, M. Grass, J. Müller, D. Stolcic, U. Lutz, G. Ganteför, T. Schlenker, J. Boneberg and P. Leiderer, *Appl. Phys. A: Mater. Sci. Process.*, 2001, **73**, 547–554.
- 21 D. Schröder, J. Roithová and H. Schwarz, *Int. J. Mass Spectrom.*, 2006, **254**, 197–201.
- 22 R. A. J. O'Hair, *Reactive Intermediates*, Wiley-VCH Verlag GmbH & Co. KGaA, 2010, ch. 6, pp. 199–227, DOI: 10.1002/9783527628728.
- 23 G. N. Khairallah and R. A. J. O'Hair, *Angew. Chem., Int. Ed.*, 2005, **44**, 728–731.
- 24 G. N. Khairallah and R. A. J. O'Hair, *Dalton Trans.*, 2005, 2702–2712, DOI: 10.1039/b505645b.
- 25 C. P. G. Butcher, A. Dinca, P. J. Dyson, B. F. G. Johnson, P. R. R. Langridge-Smith and J. S. McIndoe, *Angew. Chem., Int. Ed.*, 2003, **42**, 5752–5755.
- 26 T. Tabarin, R. Antoine, M. Broyer and P. Dugourd, *Eur. Phys. J. D*, 2006, **37**, 237–239.
- 27 G. E. Johnson, E. C. Tyo and A. W. Castleman, *Proc. Natl. Acad. Sci. U. S. A.*, 2008, **105**, 18108–18113.
- 28 Z. Luo, G. U. Gamboa, J. C. Smith, A. C. Reber, J. U. Reveles, S. N. Khanna and A. W. Castleman, *J. Am. Chem. Soc.*, 2012, **134**, 18973–18978.
- 29 R. E. Leuchtner, A. C. Harms and A. W. Castleman, *J. Chem. Phys.*, 1989, **91**, 2753–2754.
- 30 T. M. Bernhardt, *Int. J. Mass Spectrom.*, 2005, **243**, 1–29.
- 31 T. Waters, R. A. J. O'Hair and A. G. Wedd, *J. Am. Chem. Soc.*, 2003, **125**, 3384–3396.
- 32 J. Hagen, L. D. Socaci, J. Le Roux, D. Popolan, T. M. Bernhardt, L. Wöste, R. Mitrić, H. Noack and V. Bonačić-Koutecký, *J. Am. Chem. Soc.*, 2004, **126**, 3442–3443.
- 33 T. M. Bernhardt, J. Hagen, S. M. Lang, D. M. Popolan, L. D. Socaci-Siebert and L. Wöste, *J. Phys. Chem. A*, 2009, **113**, 2724–2733.
- 34 G. N. Khairallah, T. Waters and R. A. J. O'Hair, *Dalton Trans.*, 2009, 2832–2836, DOI: 10.1039/b822371h.
- 35 Z. Luo, C. Berkdemir, J. C. Smith and A. W. Castleman Jr, *Chem. Phys. Lett.*, 2013, **582**, 24–30.
- 36 Z. Luo, G. U. Gamboa, M. Jia, A. C. Reber, S. N. Khanna and A. W. Castleman, *J. Phys. Chem. A*, 2014, **118**, 8345–8350.
- 37 J. Roithová and D. Schröder, *J. Am. Chem. Soc.*, 2007, **129**, 15311–15318.
- 38 R. A. J. O'Hair and N. J. Rijs, *Acc. Chem. Res.*, 2015, **48**, 329–340.
- 39 T. Müller, A. Badu-Tawiah and R. G. Cooks, *Angew. Chem., Int. Ed.*, 2012, **51**, 11832–11835.
- 40 R. M. Bain, C. J. Pulliam and R. G. Cooks, *Chem. Sci.*, 2015, **6**, 397–401.
- 41 T. A. Nijhuis, M. Makkee, J. A. Moulijn and B. M. Weckhuysen, *Ind. Eng. Chem. Res.*, 2006, **45**, 3447–3459.
- 42 K. Bromann, C. Félix, H. Brune, W. Harbich, R. Monot, J. Buttet and K. Kern, *Science*, 1996, **274**, 956–958.
- 43 R. E. Palmer, S. Pratontep and H. G. Boyen, *Nat. Mater.*, 2003, **2**, 443–448.
- 44 J. Lu, L. Cheng, K. C. Lau, E. Tyo, X. Luo, J. Wen, D. Miller, R. S. Assary, H.-H. Wang, P. Redfern, H. Wu, J.-B. Park, Y.-K. Sun, S. Vajda, K. Amine and L. A. Curtiss, *Nat. Commun.*, 2014, **5**, 4895.
- 45 H. Chen, L. S. Eberlin and R. G. Cooks, *J. Am. Chem. Soc.*, 2007, **129**, 5880–5886.
- 46 H. Chen, L. S. Eberlin, M. Neffliu, R. Augusti and R. G. Cooks, *Angew. Chem., Int. Ed.*, 2008, **47**, 3422–3425.
- 47 J. I. Zhang, W. A. Tao and R. G. Cooks, *Anal. Chem.*, 2011, **83**, 4738–4744.
- 48 J. S. Wiley, J. T. Shelley and R. G. Cooks, *Anal. Chem.*, 2013, **85**, 6545–6552.
- 49 C. Hao, R. E. March, T. R. Croley, J. C. Smith and S. P. Rafferty, *J. Mass Spectrom.*, 2001, **36**, 79–96.
- 50 H. Al Sharif, K. L. Vikse, G. N. Khairallah and R. A. J. O'Hair, *Organometallics*, 2013, **32**, 5416–5427.
- 51 S. Krückeberg, G. Dietrich, K. Lützenkirchen, L. Schweikhard, C. Walther and J. Ziegler, *Int. J. Mass Spectrom. Ion Processes*, 1996, **155**, 141–148.
- 52 S. Krückeberg, G. Dietrich, K. Lützenkirchen, L. Schweikhard, C. Walther and J. Ziegler, *Z. Phys. D: At., Mol. Clusters*, 1997, **40**, 341–344.
- 53 S. Krückeberg, G. Dietrich, K. Lützenkirchen, L. Schweikhard, C. Walther and J. Ziegler, *J. Chem. Phys.*, 1999, **110**, 7216–7227.
- 54 S. Krückeberg, G. Dietrich, K. Lützenkirchen, L. Schweikhard, C. Walther and J. Ziegler, *Eur. Phys. J. D*, 1999, **9**, 145–148.
- 55 M. K. Harbola, *Proc. Natl. Acad. Sci. U. S. A.*, 1992, **89**, 1036–1039.
- 56 V. A. Spasov, T. H. Lee, J. P. Maberry and K. M. Ervin, *J. Chem. Phys.*, 1999, **110**, 5208–5217.
- 57 W. M. Haynes and D. R. Lide, *CRC handbook of chemistry and physics: a ready-reference book of chemical and physical data*, CRC Press, Boca Raton, Fla., 2011.
- 58 A. K. Badu-Tawiah, C. Wu and R. G. Cooks, *Anal. Chem.*, 2011, **83**, 2648–2654.
- 59 P. Sharpe and C. J. Cassady, *Chem. Phys. Lett.*, 1992, **191**, 111–116.
- 60 P. Sharpe, J. M. Campbell and C. J. Cassady, *Organometallics*, 1994, **13**, 3077–3084.
- 61 A. Jackson, T. Shum, E. Sokol, A. Dill and R. G. Cooks, *Anal. Bioanal. Chem.*, 2011, **399**, 367–376.
- 62 L. I. Grace, A. Abo-Riziq and M. S. deVries, *J. Am. Soc. Mass Spectrom.*, 2005, **16**, 437–440.
- 63 T. K. Dutta and S. Harayama, *Anal. Chem.*, 2001, **73**, 864–869.
- 64 M. Eftekhari, A. I. Ismail and R. N. Zare, *Rapid Commun. Mass Spectrom.*, 2012, **26**, 1985–1992.

- 65 J. L. Gole, R. Woodward, J. S. Hayden and D. A. Dixon, *J. Phys. Chem.*, 1985, **89**, 4905–4908.
- 66 S. A. Oradu and R. G. Cooks, *Anal. Chem.*, 2012, **84**, 10576–10585.
- 67 F. J. Andrade, J. T. Shelley, W. C. Wetzel, M. R. Webb, G. Gamez, S. J. Ray and G. M. Hieftje, *Anal. Chem.*, 2008, **80**, 2646–2653.
- 68 W.-P. Peng, M. P. Goodwin, Z. Nie, M. Volný, Z. Ouyang and R. G. Cooks, *Anal. Chem.*, 2008, **80**, 6640–6649.
- 69 B. Yoon, H. Häkkinen, U. Landman, A. S. Wörz, J.-M. Antonietti, S. Abbet, K. Judai and U. Heiz, *Science*, 2005, **307**, 403–407.
- 70 N. Nilius, T. Risse, S. Schaueremann, S. Shaikhutdinov, M. Sterrer and H. J. Freund, *Top. Catal.*, 2011, **54**, 4–12.

Supporting Information for
Ambient Preparation and Reactions of Gas Phase Silver Cluster Cations and Anions

Michael Wleklinski¹, Depanjan Sarkar², Adam Hollerbach¹, T. Pradeep², and R. Graham Cooks¹

¹ Department of Chemistry and Center for Analytical Instrumentation Development, Purdue University, West Lafayette, Indiana 47907

² DST Unit of Nanoscience (DST UNS) and Thematic Unit of Excellence (TUE), Department of Chemistry, Indian Institute of Technology Madras, Chennai 600 036, India

* Author for correspondence cooks@purdue.edu

Table of Contents

Mechanism of Formation of Oxo-cations

Supplementary Tables

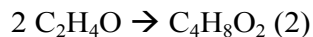
- Table S1: Reaction products of Ag^+ with various reagents (pg. 4)
Table S2: Figure S2: Reaction products of Ag_3^+ with various reagents (pg. 4)
Table S3: Reaction products of Ag^+ with various methyl-substituted pyridines (pg. 5)
Table S4: Reaction products of Ag_3^+ with various methyl-substituted pyridines (pg. 5)
Table S5: Reaction products of Ag_3^+ with acetone, acetonitrile, acetone followed by acetonitrile, and acetonitrile followed by acetone (pg. 6)

Supplementary Figures

- Figure S1: Apparatus for studying atmospheric pressure ion/molecule reactions of silver clusters (cation/anions) with various reagents. (pg. 7)
Figure S2: Apparatus for performing atmospheric pressure ion/molecule ligand exchange reactions of silver clusters cations with various reagents. (pg. 7)
Figure S3: Apparatus for performing ion/molecule reactions using either a gas, low temperature plasma, or both. (pg. 8)
Figure S4: Mass spectra of heated and unheated silver salts. (pg. 9)
Figure S5: Tandem MS of Ag_n^+ and Ag_n^{2+} (pg. 10)
Figure S6: Tandem MS of Ag_n^- (pg. 11)
Figure S7: Selected ion chronograms for ions of interest in the formation of silver cluster cations from a silver acetate precursor (pg. 12)
Figure S8: Tandem MS tree for ions observed when silver acetate is subjected to 100-150 Celsius and harsh in source conditions (pg. 13)
Figure S9: Reaction of silver cluster cations with various reactants. (pg. 14)
Figure S10: Reaction of silver cluster cations with methyl-substituted pyridines. (pg. 15)
Figure S11: Tandem MS data for reaction of silver cluster cations with methyl-substituted pyridine. (pg.16)
Figure S12: Tandem MS data for ligand exchange of ammonia and acetonitrile (pg. 17)
Figure S13: MS data for ligand exchange of 2,6-Lutidine and acetonitrile (pg. 18)
Figure S14: MS data for ligand exchange of acetone and acetonitrile (pg. 19)
Figure S15: Silver cluster cation analysis of hydrocarbons (pg. 20)
Figure S16: Reaction of silver cluster cations with ethylene and ethylene and ozone. (pg. 21)
Figure S17: MS fragmentation tree for $[\text{Ag}_5(\text{C}_2\text{H}_4)\text{O}_2]^+$ (pg. 22)
Figure S18: Mass spectra of heated and unheated silver salts taken on a custom surface science instrument. (pg. 23)

Mechanism of Formation of Oxo-cations

The loss of ethenone from $[\text{Ag}_n(\text{CH}_3\text{COO})_{n-1}]^+$ is possible as evidenced by the observation of $[\text{Ag}_6(\text{CH}_3\text{COO})_3\text{OH}_2\text{O}]^+$ and $[\text{Ag}_5(\text{CH}_3\text{COO})_2\text{OH}_2\text{O}]^+$ (1). The ethenone product can go on to dimerize (2). The heat of formation of ethenone is -47.5 kJ/mol with its dimer having a heat of formation of -190.3 kJ/mol.¹ The hydration energy of Ag_3O^+ is assumed to be close to that of Ag^+ , which is -139 kJ/mol.^{2,3} The observation that multiple ions, including $\text{Ag}_5(\text{CH}_3\text{COO})_2^+$, bind water upon isolation in the ion trap suggests this interaction is quite weak. The formation of 2 ethenone and monohydrated Ag_3O^+ is predicted to be exothermic by -234 kJ/mol, as calculated from the heat of formation and hydration energy. If the ethenone dimerizes, the reaction is even more exothermic at -329.3 kJ/mol. This is still much less favorable than the formation of acetic anhydride, and thus it is assumed to be a minor pathway.



References

1. W. M. Haynes and D. R. Lide, *CRC handbook of chemistry and physics : a ready-reference book of chemical and physical data*, CRC Press, Boca Raton, Fla., 2011.
2. D. Feller, E. D. Glendening and W. A. de Jong, *The Journal of Chemical Physics*, 1999, 110, 1475-1491.
3. B. S. Fox, M. K. Beyer and V. E. Bondybey, *Journal of the American Chemical Society*, 2002, 124, 13613-13623.

Supplementary Tables

Table S1: Reaction products of Ag^+ with various reagents^a

Reactant	Ag^+	$[\text{AgL}]^+$	$[\text{AgL}_2]^+$
Ethanol	9.7%	14%	100%
1-propanol	4.4%	6.7%	100%
Isopropyl Alcohol	24.5%	13.2%	100%
Tert-Butyl Alcohol	18.2%	3.6%	100%
Acetone	24.8%	28.5%	100%
Acetonitrile	9.4%	N.R.	100%

^a L refers to the respective reagent

Table S2: Reaction products of Ag_3^+ with various reactants^a

Reactant	Ag_3^+	$[\text{Ag}_3\text{L}]^+$	$[\text{Ag}_3\text{L}_2]^+$	$[\text{Ag}_3\text{L}_3]^+$
Ethanol	100%	75.4%	57.3%	N.R.
1-propanol	33.0%	48.4%	100%	N.R.
Isopropyl Alcohol	100%	44.2%	73.%	N.R.
Tert-Butyl Alcohol	38.6%	11.0%	100%	N.R.
Acetone	100%	48.5%	51.8%	N.R.
Acetonitrile	44.8%	N.R.	57.5%	100%

^a L refers to the respective reagent

Table S3: Reaction products of Ag⁺ with various methyl-substituted pyridines^a

Reactant	Ag ⁺	[AgL] ⁺	[AgL ₂] ⁺
Pyridine	1.0%	6.3%	100%
2-ethylpyridine	0.1%	1.4%	100%
3-ethylpyridine	0.9%	1.8%	100%
4-ethylpyridine	0.09%	0.9%	100%
3,4-Lutidine	1.8%	2.5%	100%
2,6-Lutidine	3.6%	1.2%	100%
2,5-Lutidine	2.2%	2.0%	100%
3,5-Lutidine	3.1%	1.4%	100%
2,4,6-trimethylpyridine	1.2%	10.6%	100%

^a L refers to the respective reagent

Table S4: Reaction products of Ag₃⁺ with various methyl-substituted pyridines^a

Reactant	Ag ₃ ⁺	[Ag ₃ L] ⁺	[Ag ₃ L ₂] ⁺	[Ag ₃ L ₃] ⁺
Pyridine	28.8%	44.1%	73.8%	100%
2-ethylpyridine	N.R.	N.R.	N.R.	100%
3-ethylpyridine	N.R.	N.R.	N.R.	100%
4-ethylpyridine	N.R.	N.R.	N.R.	100%
3,4-Lutidine	N.R.	N.R.	N.R.	100%
2,6-Lutidine	N.R.	N.R.	N.R.	100%
2,5-Lutidine	N.R.	N.R.	N.R.	100%
3,5-Lutidine	N.R.	N.R.	N.R.	100%
2,4,6-trimethylpyridine	23.2%	52.5%	51.0%	100%

^a L refers to the respective reagent

Table S5: Reaction products of Ag_3^+ with acetone, acetonitrile, acetone followed by acetonitrile, and acetonitrile followed by acetone^a

Compound $[\text{Ag}_3 + (\text{C}_3\text{H}_6\text{O})_x + (\text{C}_2\text{H}_3\text{N})_y]^+$	Acetone Only	Acetonitrile Only	Acetone, then Acetonitrile	Acetonitrile, then Acetone
[1,0]	✓		✓	N.R.
[2,0]	✓		✓	N.R.
[3,0]			N.R.	N.R.
[0,1]		✓	✓	✓
[0,2]		✓	✓	✓
[0,3]		✓	✓	✓
[1,1]			✓	N.R.
[2,1]			N.R.	N.R.
[1,2]			N.R.	N.R.

^a Checkmarks indicate the presence of a species as determined by the appropriate MS/MS experiment.

Supplementary Figures

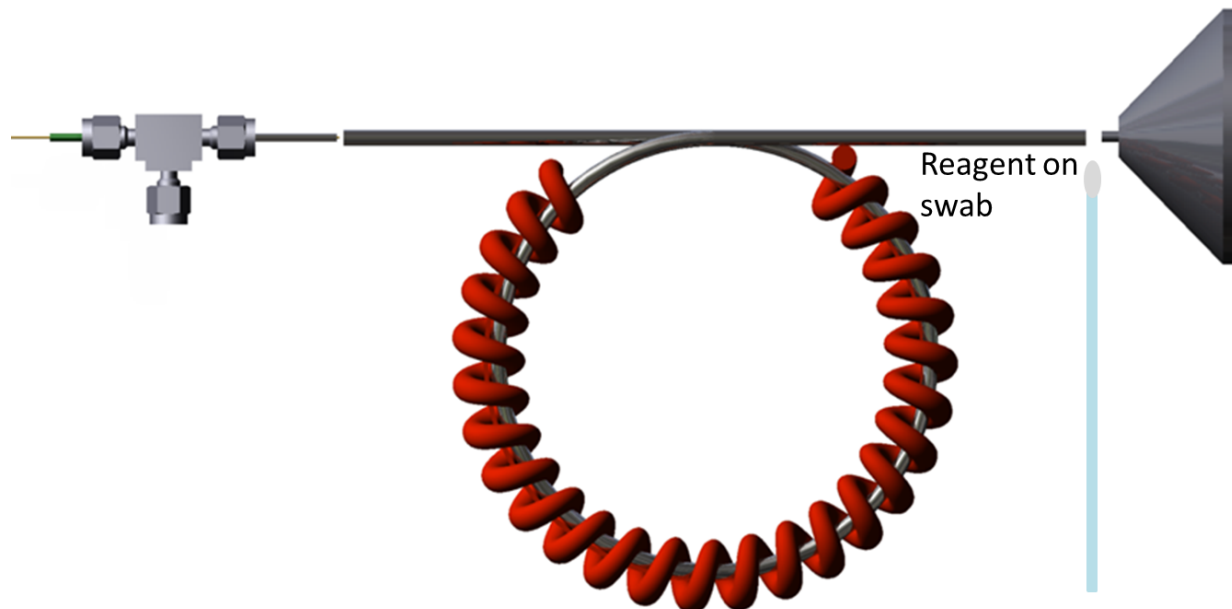


Figure S1: Apparatus for studying atmospheric pressure ion/molecule reactions of silver clusters (cations/anions) with various reagents

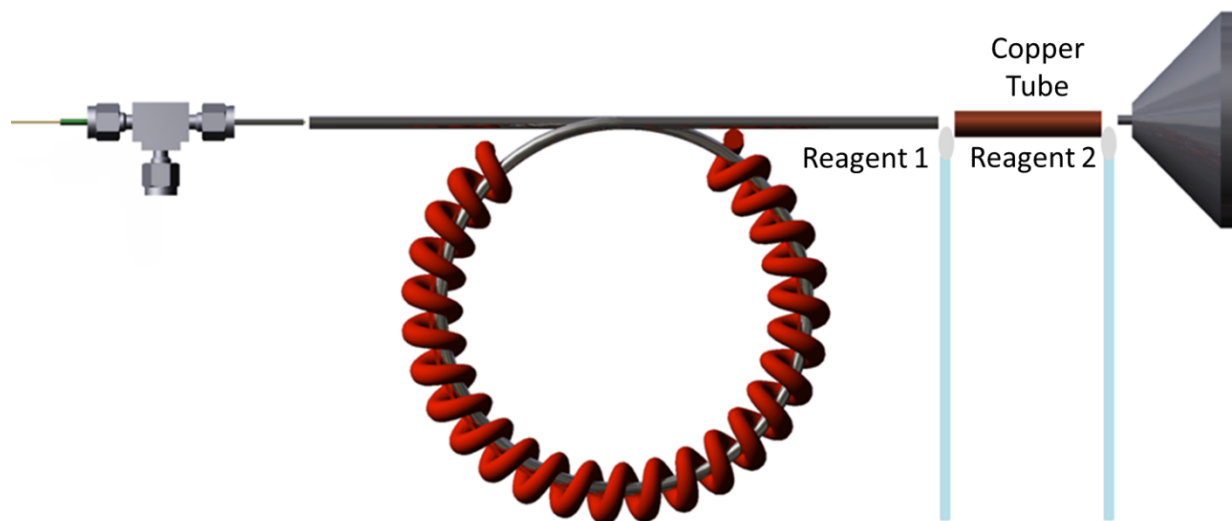


Figure S2: Apparatus for performing atmospheric pressure ion/molecule ligand exchange reactions of silver clusters with various reagents

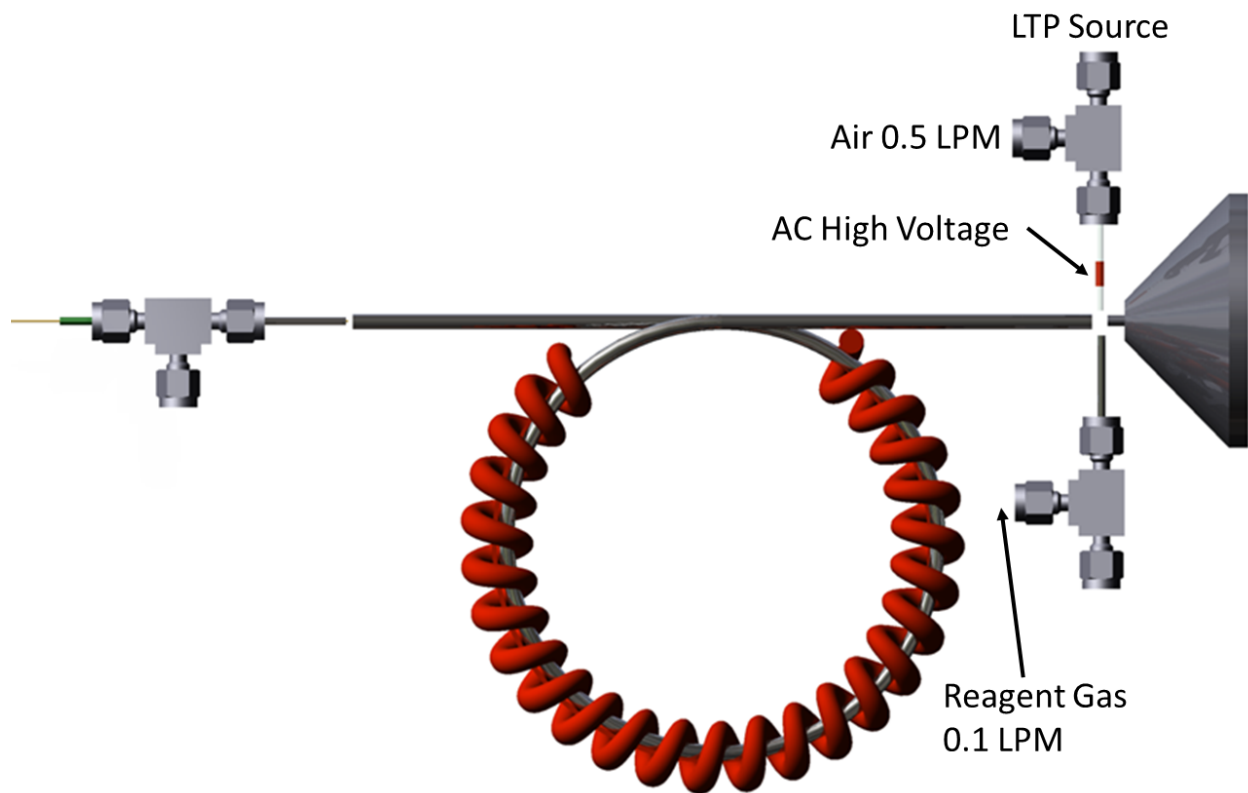


Figure S3: Apparatus for performing ion/molecule reactions using either a gas, low temperature plasma, or both. The low temperature plasma is used to generate reactive species to oxidize silver cluster cations

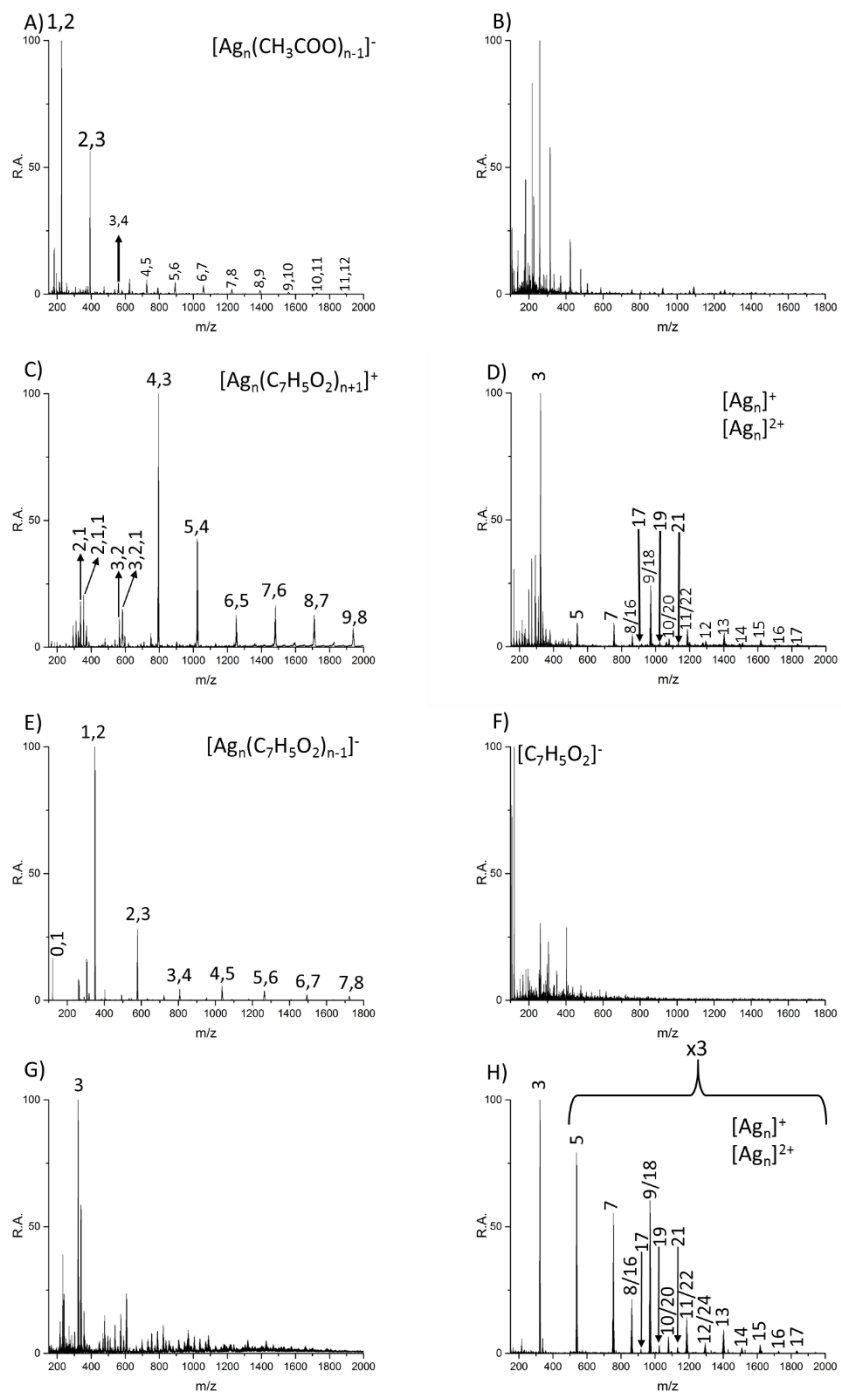


Figure S4: Negative ion mode mass spectra of A) unheated and B) heated silver acetate. Positive ion mode of C) unheated and D) heated silver benzoate. Negative ion mode mass spectra of E) unheated and F) heated silver benzoate. Positive ion mode mass spectra of G) unheated and H) heated silver fluoride. The numbers above each peak indicate the number of silver atoms, ligands, and water present, and the absence of the final number indicates zero water molecules are present

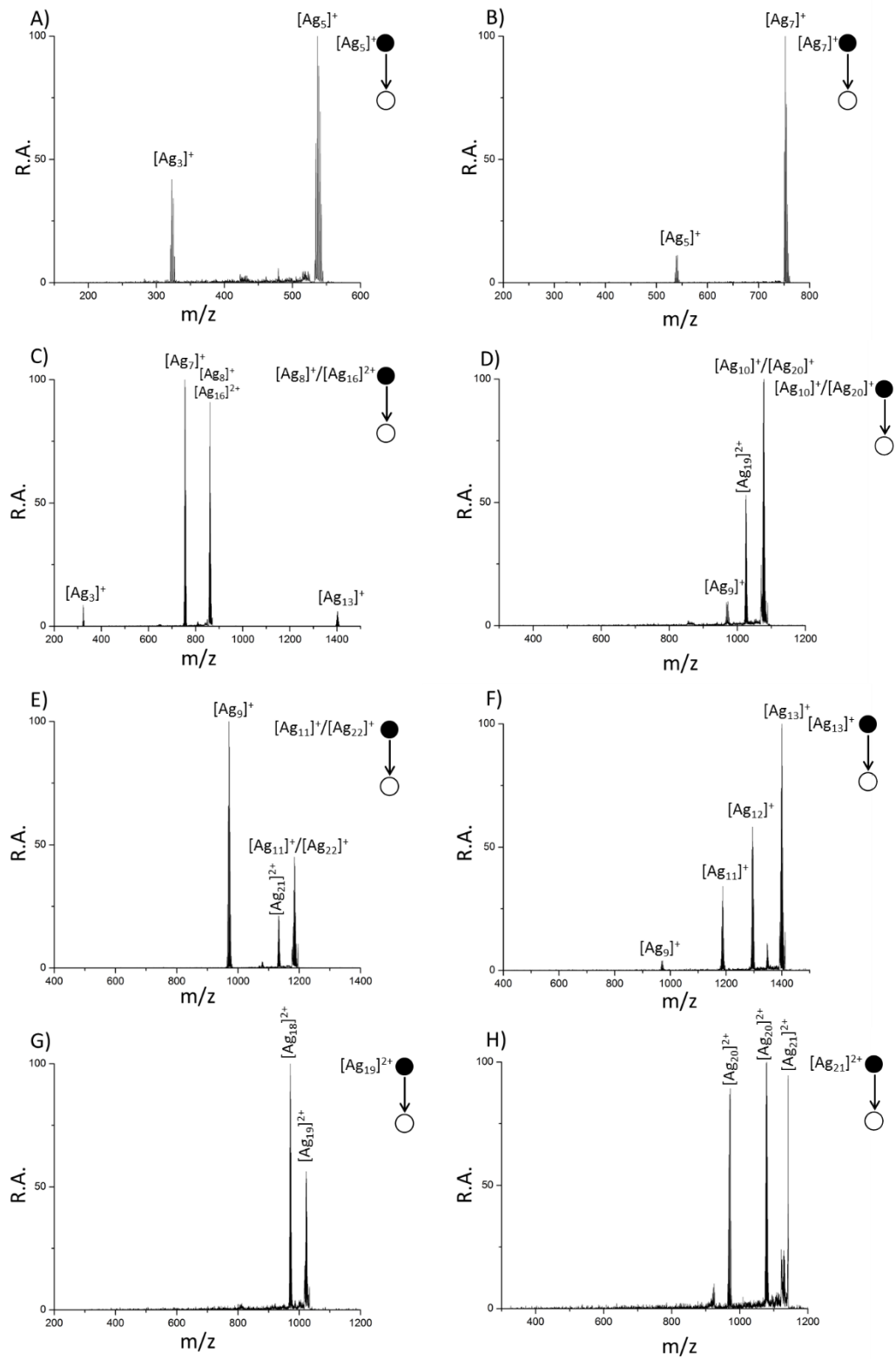


Figure S5: Tandem MS of A) Ag_5^+ , B) Ag_7^+ , C) Ag_8^+/Ag_{16}^{2+} , D) Ag_{10}^+/Ag_{20}^{2+} , E) Ag_{11}^+/Ag_{22}^{2+} , F) Ag_{13}^+ , G) Ag_{19}^{2+} , and H) Ag_{21}^{2+}

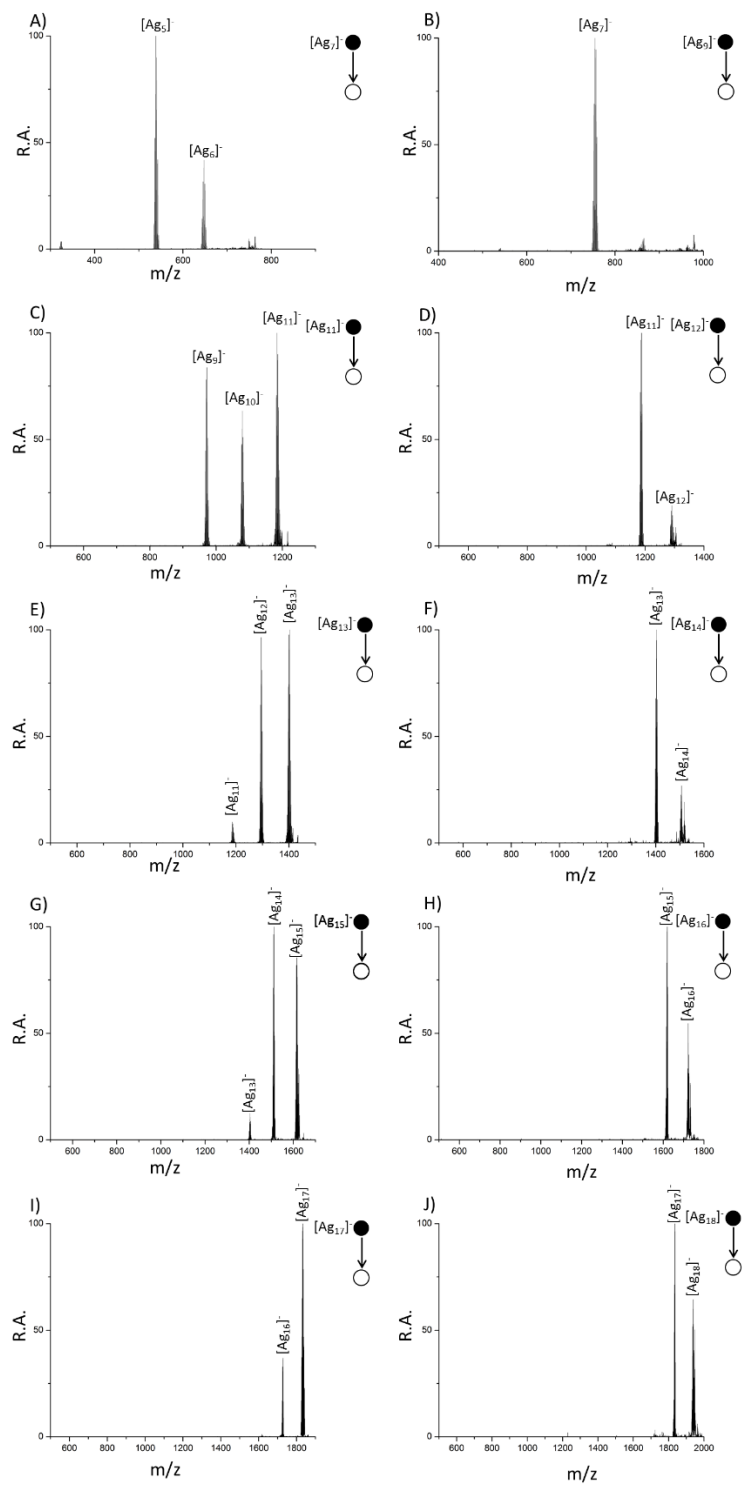


Figure S6: Tandem MS of A) Ag_7^- , B) Ag_9^- , C) Ag_{11}^- , D) Ag_{12}^- , E) Ag_{13}^- , F) Ag_{14}^- , G) Ag_{15}^- , H) Ag_{16}^- , I) Ag_{17}^- , and J) Ag_{18}^-

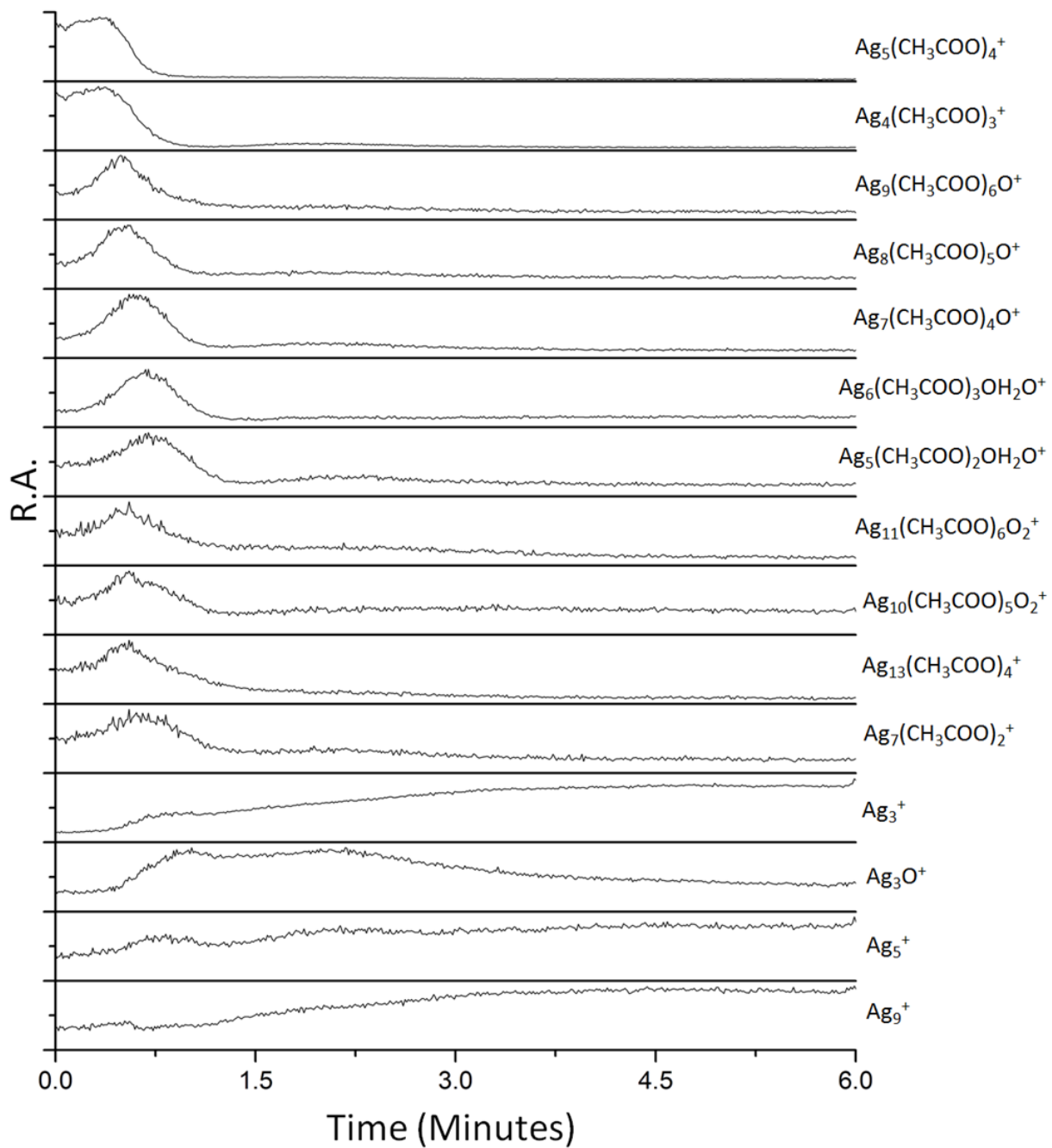


Figure S7: Selected ion chromatograms for ions of interest in the formation of silver cluster cations from a silver acetate precursor. At time zero the heating is turned on and temperature slowly rises to 250 Celsius over the course of a few minutes

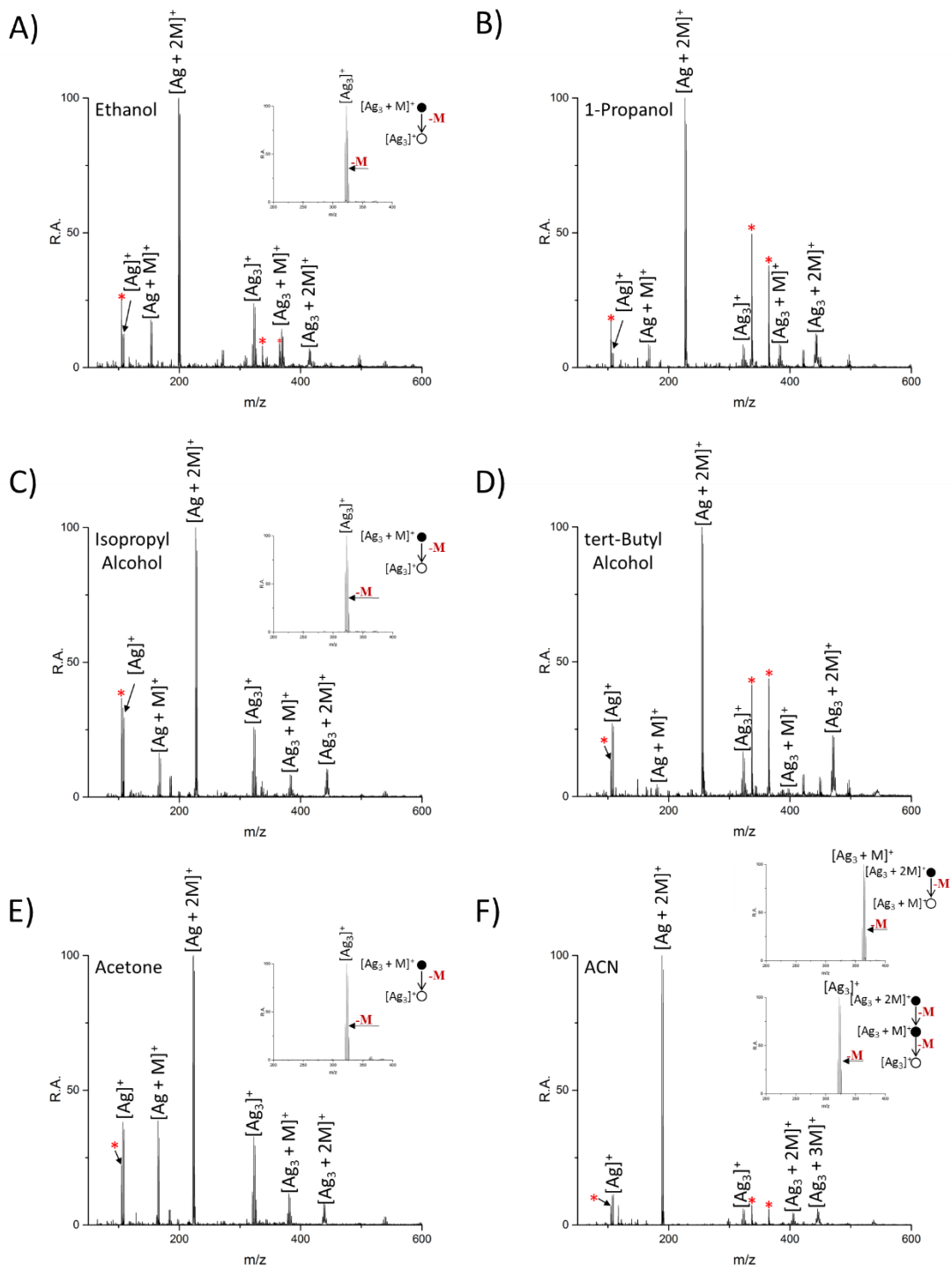


Figure S9: Reaction of silver cluster cations with A) ethanol, B) 1-propanol, C) isopropyl alcohol, D) tert-butyl alcohol, E) acetone, and F) acetonitrile. Tandem MS for selected ions are shown as insets. M stands for the reactant of interest. Peaks at m/z 105, 337, and 365 are common background ions with the first originating from the spray and the latter arising from the cotton swab

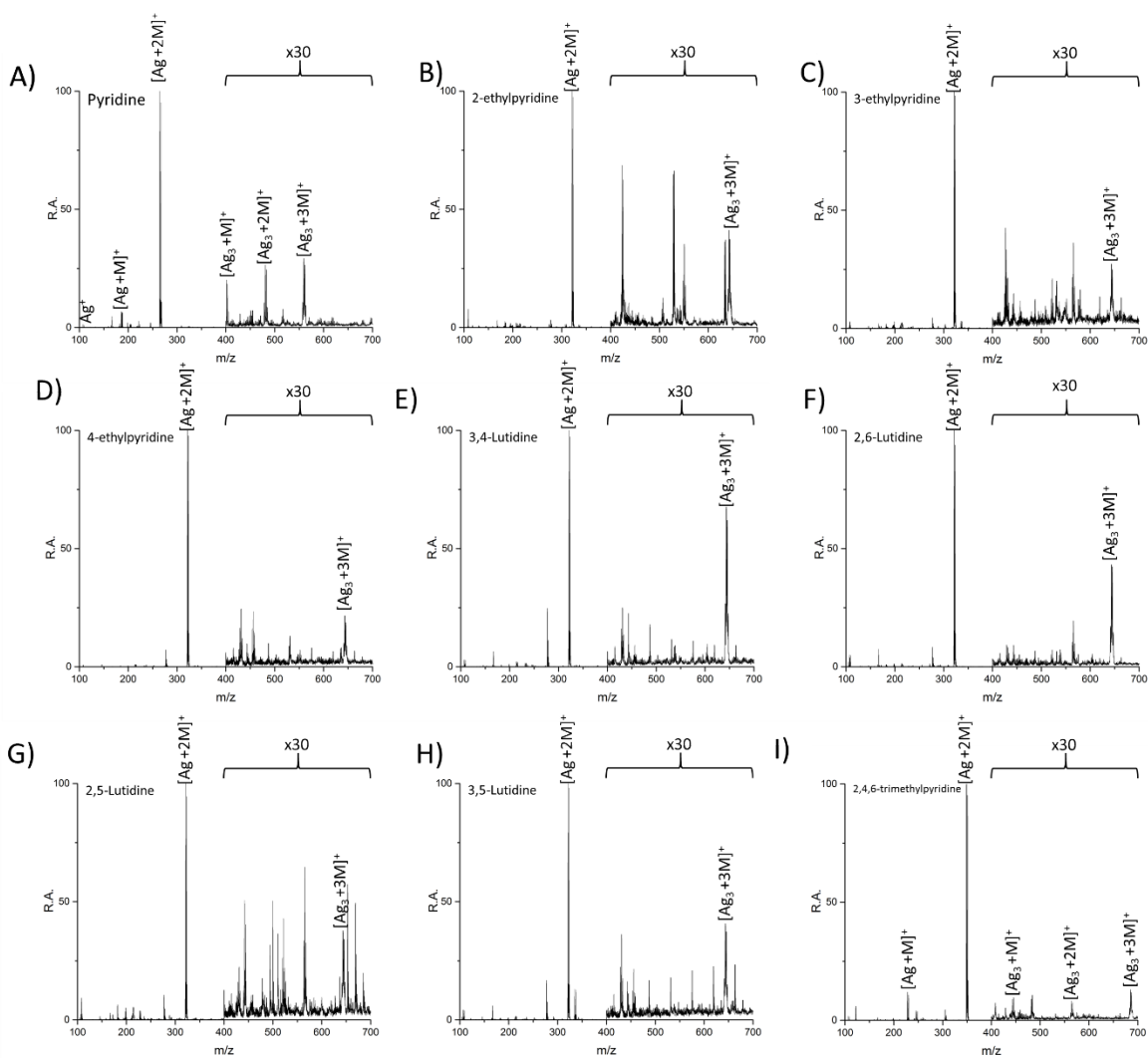


Figure S10: Reaction of silver cluster cations with A) pyridine, B) 2-ethylpyridine, C) 3-ethylpyridine, D) 4-ethylpyridine, E) 3,4-lutidine, F) 2,6-lutidine, G) 2,5-lutidine, H) 3,5-lutidine, and I) 2,4,6-trimethylpyridine. M stands for the reactant of interest

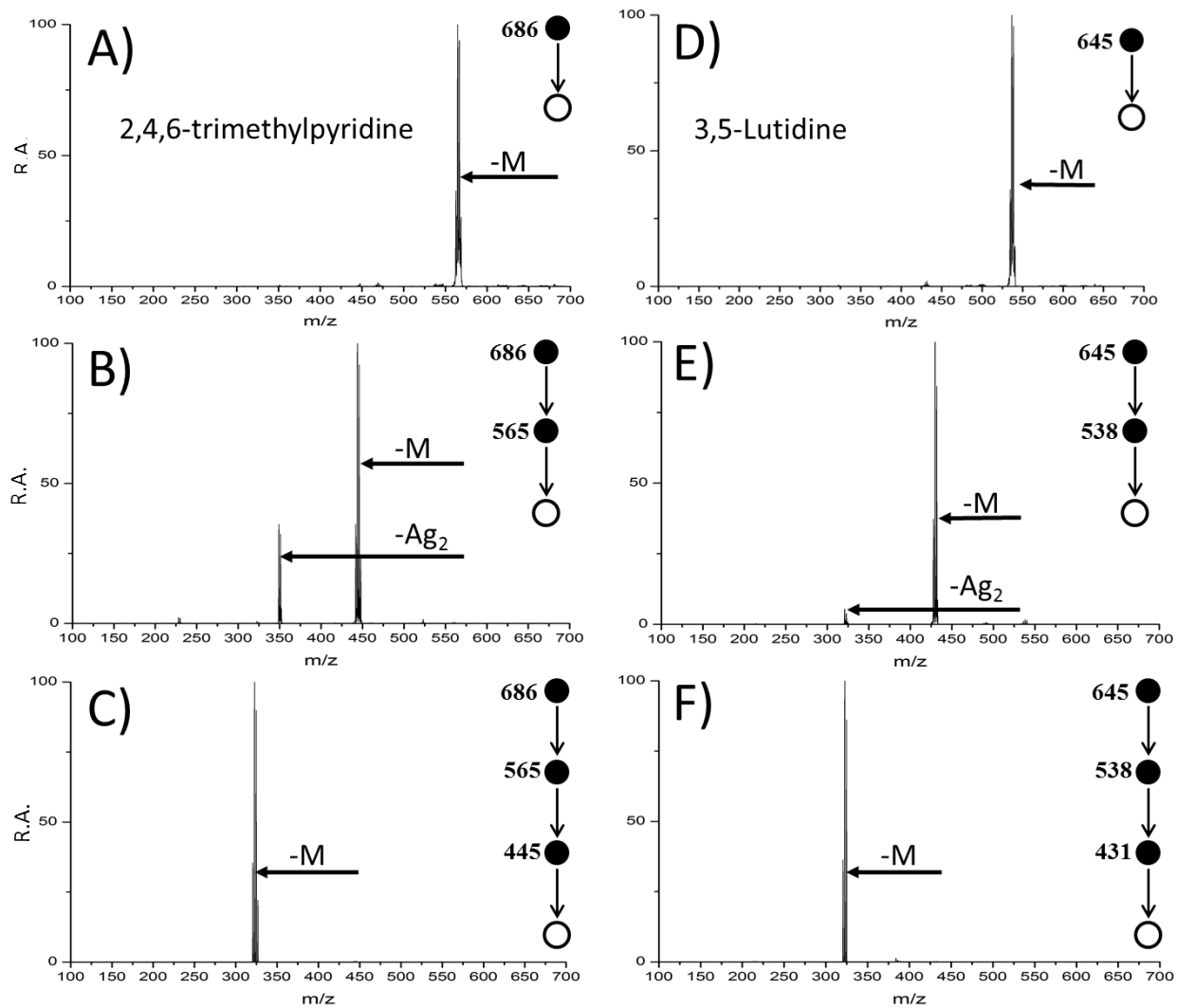


Figure S11: Tandem mass spectrometry data for $[\text{Ag}_3(\text{C}_8\text{H}_{11}\text{N})_3]^+$ (left) and $[\text{Ag}_3(\text{C}_7\text{H}_9\text{N})_3]^+$ (right) where 2,4,6-trimethylpyridine and 3,5-lutidine are the respective neutral reactants. A) MS², B) MS³, C) MS⁴ of $[\text{Ag}_3+(2,4,6\text{-trimethylpyridine})_3]^+$. D) MS², E) MS³, F) MS⁴ of $[\text{Ag}_3+(3,5\text{-lutidine})_3]^+$. M stands for the reactant of interest

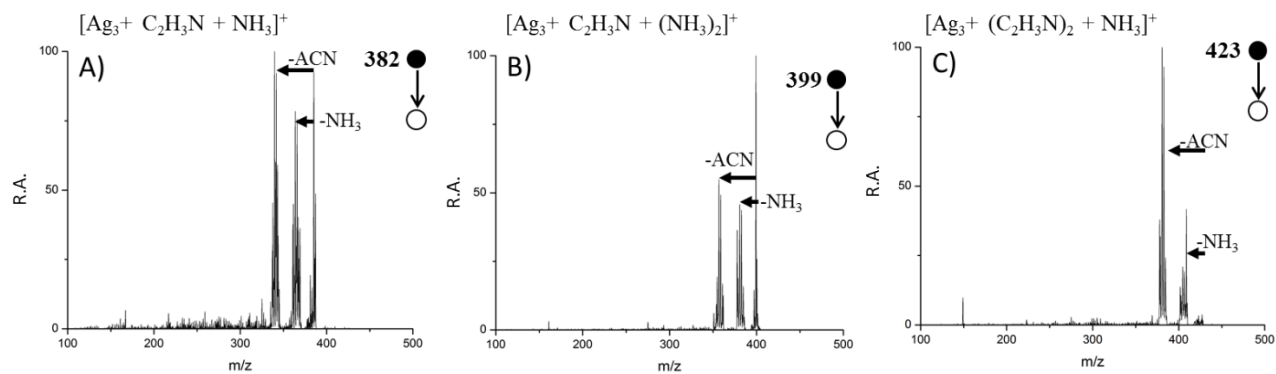


Figure S12: A) MS² of $[\text{Ag}_3 + \text{C}_2\text{H}_3\text{N} + \text{NH}_3]^+$, B) MS² of $[\text{Ag}_3 + \text{C}_2\text{H}_3\text{N} + (\text{NH}_3)_2]^+$, and C) MS² of $[\text{Ag}_3 + (\text{C}_2\text{H}_3\text{N})_2 + \text{NH}_3]^+$ for the reaction of silver clusters with first ammonia (from ammonium hydroxide) then acetonitrile

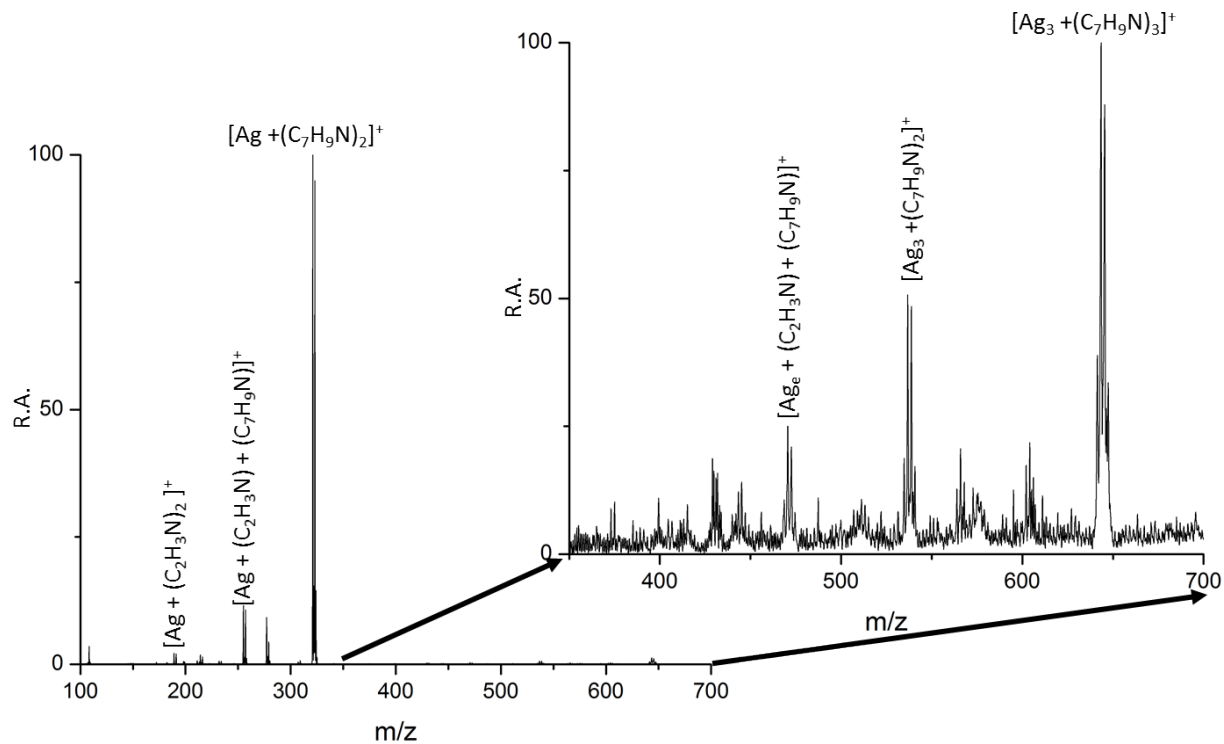


Figure S13: Full MS for the reaction of silver clusters with first 2,6-lutidine then acetonitrile. Inset: Blowup of m/z 350-700

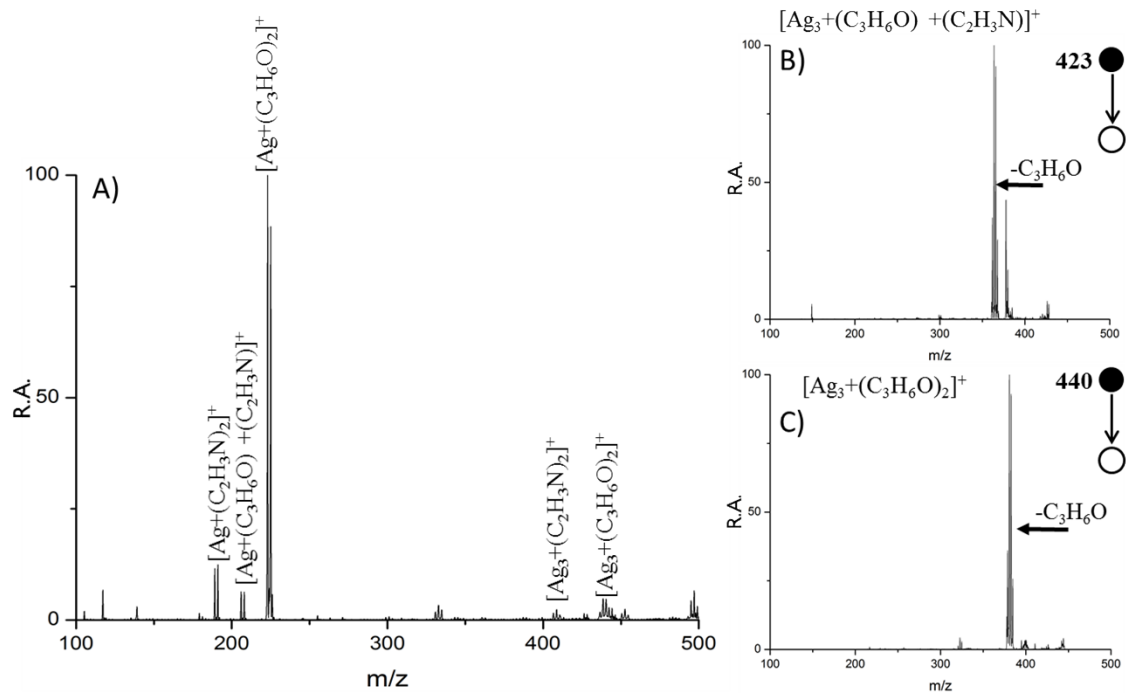


Figure S14: A) Full MS, B) MS^2 of $[\text{Ag}_3+(\text{C}_3\text{H}_6\text{O})+(\text{C}_2\text{H}_3\text{N})]^+$, and C) MS^2 of $[\text{Ag}_3+(\text{C}_3\text{H}_6\text{O})_2]^+$ for the reaction of silver clusters with Ag_3^+ with first acetone, then acetonitrile

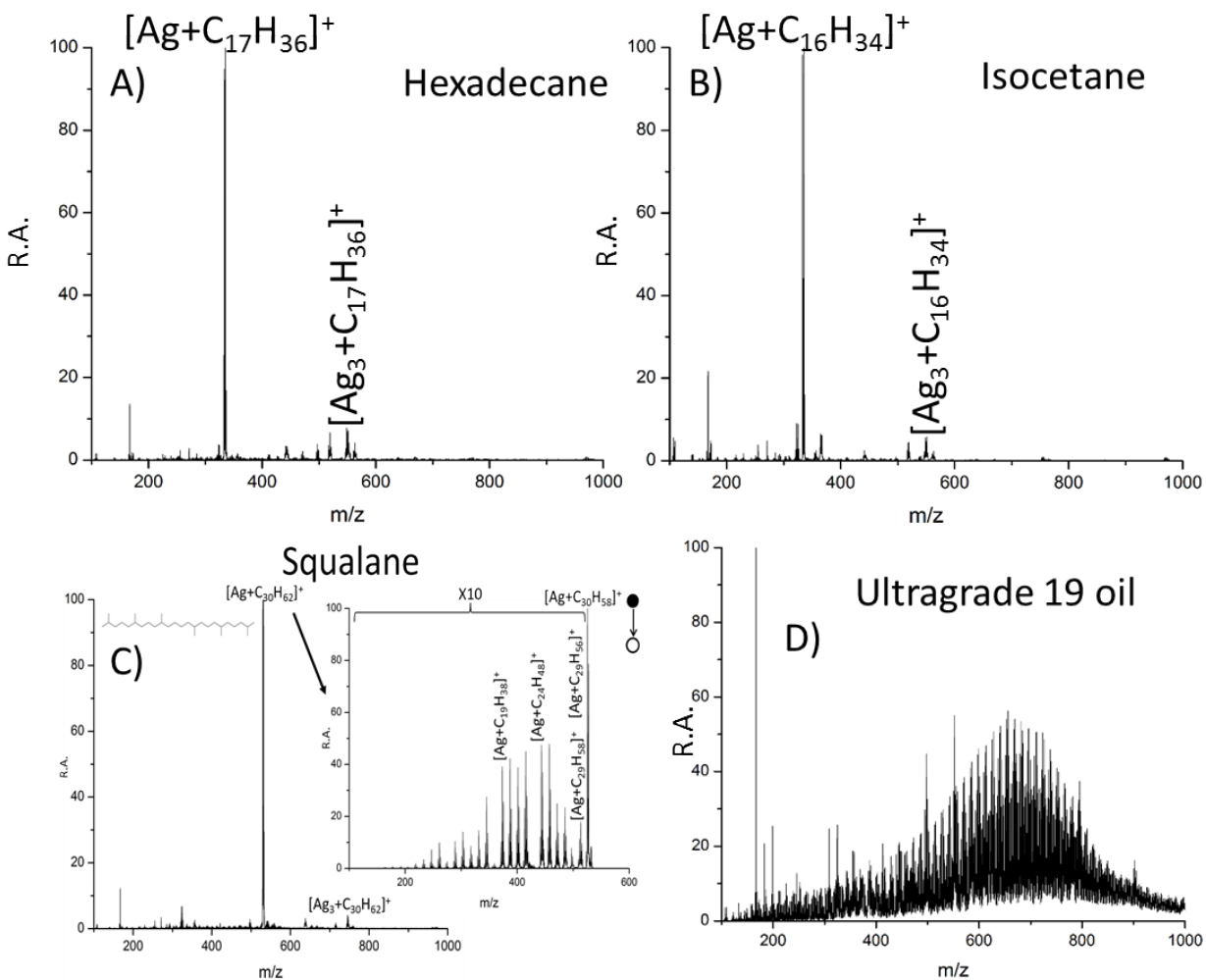


Figure S15: Analysis of A) Hexadecane, B) Isocetane, C) Squalane, and D) Ultragrade 19 oil using silver cluster spray. The inset of C) is the MS^2 of $[Ag+Squalane]^+$

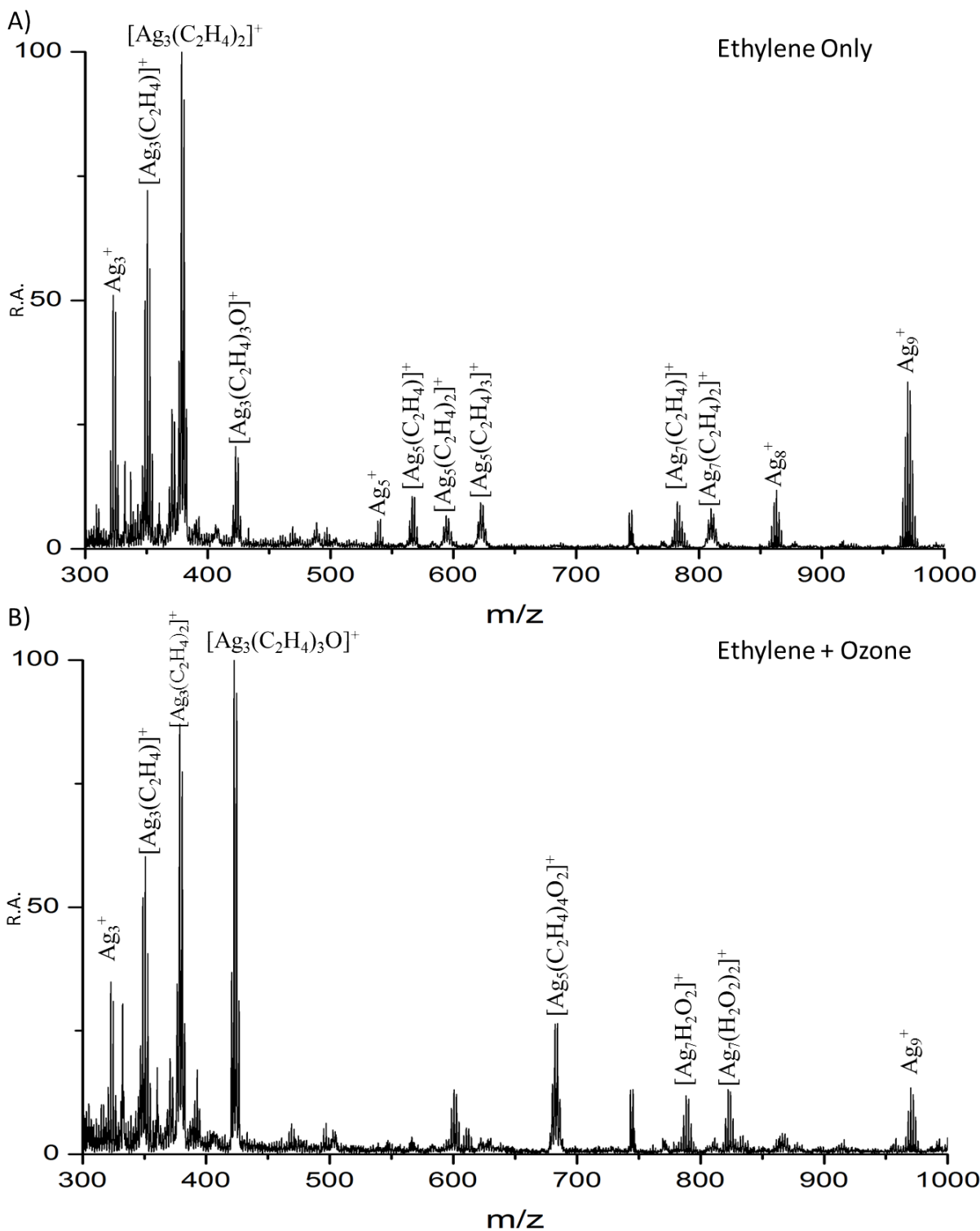


Figure S16: Reaction of silver cluster cations with A) ethylene and B) ethylene and ozone

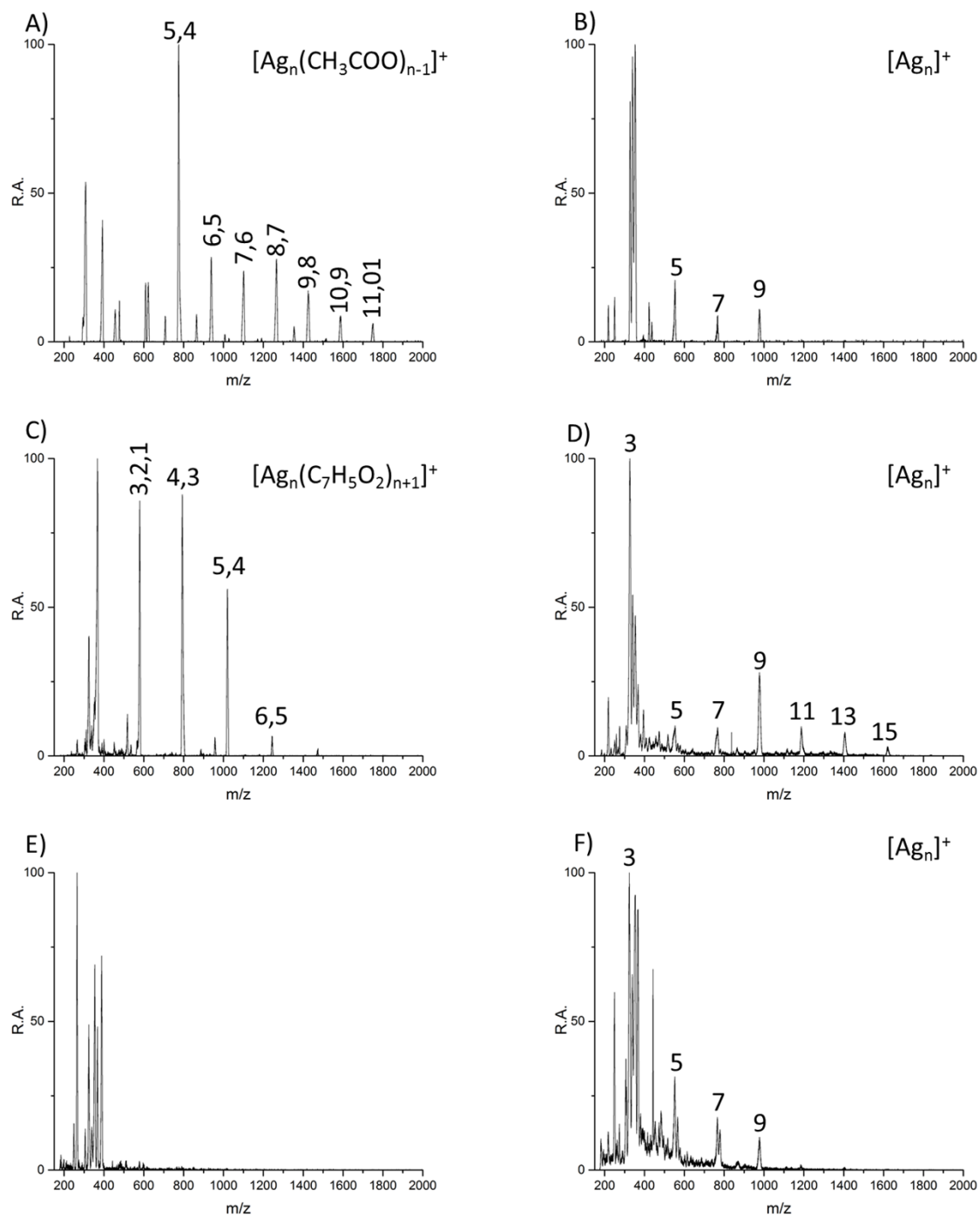


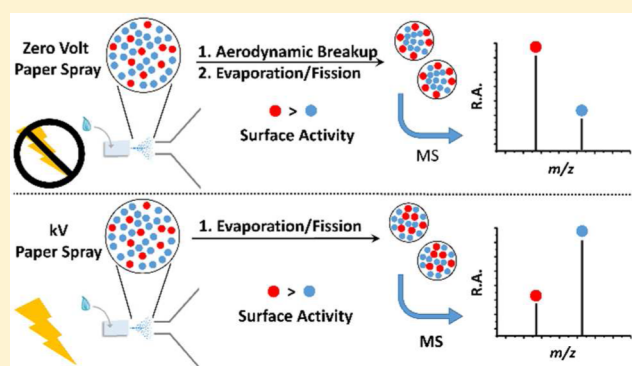
Figure S18: Positive ion mode mass spectra of A) unheated and B) heated silver acetate. Positive ion mode of C) unheated and D) heated silver benzoate. Positive ion mode mass spectra of E) unheated and F) heated silver fluoride. All these mass spectra were collected on a custom surface science instrument. The numbers above each peak indicate the number of silver atoms and ligands present

Zero Volt Paper Spray Ionization and Its Mechanism

Michael Wleklinski,^{†,‡} Yafeng Li,^{†,‡} Soumabha Bag,[†] Depanjan Sarkar,[‡] Rahul Narayanan,[‡] T. Pradeep,[‡] and R. Graham Cooks^{*,†}[†]Department of Chemistry and Center for Analytical Instrumentation Development, Purdue University, West Lafayette, Indiana 47907, United States[‡]DST Unit of Nanoscience (DST UNS) and Thematic Unit of Excellence (TUE), Department of Chemistry, Indian Institute of Technology Madras, Chennai, Tamil Nadu 600 036, India

S Supporting Information

ABSTRACT: The analytical performance and a suggested mechanism for zero volt paper spray using chromatography paper are presented. A spray is generated by the action of the pneumatic force of the mass spectrometer (MS) vacuum at the inlet. Positive and negative ion signals are observed, and comparisons are made with standard kV paper spray (PS) ionization and nanoelectrospray ionization (nESI). While the range of analytes to which zero volt PS is applicable is very similar to kV PS and nESI, differences in the mass spectra of mixtures are interpreted in terms of the more significant effects of analyte surface activity in the gentler zero volt experiment than in the other methods due to the significantly lower charge. The signal intensity of zero volt PS is also lower than in the other methods. A Monte Carlo simulation based on statistical fluctuation of positive and negative ions in solution has been implemented to explain the production of ions from initially uncharged droplets. Uncharged droplets first break up due to aerodynamic forces until they are in the 2–4 μm size range and then undergo Coulombic fission. A model involving statistical charge fluctuations in both phases predicts detection limits similar to those observed experimentally and explains the effects of binary mixture components on relative ionization efficiencies. The proposed mechanism may also play a role in ionization by other voltage-free methods.



Mass spectrometry (MS) is a powerful analytical technique because of its high sensitivity, selectivity, and speed. Ionization, the first step in MS analysis, plays a pivotal role in the experiment. The applicability of MS to complex samples examined without sample pretreatment is the key feature of desorption electrospray ionization (DESI)¹ and other ambient ionization methods.^{2,3} These ionization methods have been used in various fields including drug discovery, metabolomics, forensic science, and biofluid analysis. Ambient ionization methods which avoid the use of a high voltage have obvious advantages, especially for in vivo analysis.⁴

The first voltage-free spray ionization method, thermospray, was developed by Vestal et al. in the 1980s as an interface for LC/MS.^{5,6} In this experiment thermal energy was used to help release solvent and create ionized analytes. A few years later, another important voltage-free spray ionization method (SSI) was introduced by Hirabayashi.^{7,8} In this experiment a high speed gas flow is used to break up the bulk solution into droplets, which go on to evaporate and generate gaseous ions. A variety of compounds^{9–11} can be ionized by SSI, and it has been used for in vivo analysis when combined with ultrasonic aerosolization.⁴ Desorption sonic spray ionization¹² (DeSSI, also referred to as easy ambient sonic-spray ionization, EASI^{13,14}) is another example of a zero voltage spray ionization

method. It represents a particular mode of operation of DESI which removes the high voltage. In SSI and EASI ionization, pneumatic forces play an important role. Another voltage-free ionization method, solvent assisted inlet ionization (SAII) is applicable in LC/MS.^{15–17} Here, as in thermospray, both thermal energy and pneumatic forces appear to contribute to ionization. In addition to these voltage-free spray ionization methods, ultrasound produced by piezoelectric devices has also been used for spray ionization.^{18,19} A low frequency ultrasonicator has been used to analyze biomolecules and monitor organic reactions, reducing background noise by decreasing interference from background electrochemical reactions.^{20,21} In 2013, Chung-Hsuan Chen et al. reported yet another new spray ionization method, Kelvin spray ionization,²² which required no external electric energy, the system itself producing a voltage.

Paper spray (PS), first reported in 2009,²³ has proven practically useful for qualitative and quantitative analysis. The use of paper as the substrate in PS allows ionization of compounds of interest while leaving some of the other

Received: March 11, 2015

Accepted: May 29, 2015

Published: May 29, 2015

components of complex matrices adsorbed to the paper; this feature makes it suitable for the quantification of therapeutic drugs in blood.^{24,25} Paper cut to a sharp point ensures that a kilovolt applied potential will generate an electric field high enough to cause emission of charged analyte-containing solvent droplets; these droplets evaporate and undergo Coulomb explosion and perhaps solvated ion emission to give ESI-like mass spectra.²⁶ A recent variant on the PS method uses paper impregnated with carbon nanotubes as a way to achieve the necessary field strengths while applying only a low voltage.²⁷

We show in this study that by removing the applied voltage entirely, a zero volt form of PS can be performed. This experiment, which is phenomenologically similar to the SAI method, retains the advantages of the paper substrate by allowing complex mixtures to be examined directly without chromatography while removing the electric field and dispensing with the strong pneumatic forces needed in the pneumatically assisted ionization methods of SSI and EASI. In zero volt PS, as in SAI, the vacuum provides a sufficient pneumatic force. Our results demonstrate that zero volt PS gives both positive and negative ions just as does conventional kV PS and nESI, albeit with much lower signal intensities. The reduction in signal intensities roughly parallels that between EASI and DESI. Qualitative mechanisms, which are not fully understood, have been proposed for other zero volt methods, but this paper seeks to develop a quantitative model for zero volt paper spray. Simulations, based on the theory of Dodd,²⁸ have been performed to gain insights into the ionization mechanism. The proposed mechanism includes charge separation during droplet formation due to statistical fluctuations in positive and negative ion distributions¹¹ after aerodynamic droplet breakup as described by Jarrold and co-workers.²⁹ Subsequent solvent evaporation and Coulombic fission processes follow the accepted ESI mechanisms.

EXPERIMENTAL DETAILS

Chemicals and Materials. Deionized water was provided by a Milli-Q Integral water purification system (Barnstead Easy Pure II). Morphine and cocaine were purchased from Cerilliant (Round Rock, Texas). Methanol was from Mallinckrodt Baker Inc. (Phillipsburg, NJ). Deuterated methanol and water were provided by Cambridge Isotope Laboratories (Tewksbury, MA). The paper used as the spray substrate was Whatman 1 chromatography paper (Whatman International Ltd., Maidstone, England). All samples were examined in methanol solution except where noted.

Zero Volt Paper Spray. As is shown in Figure 1, the experimental details of zero volt PS were a little different from those previously reported for kV PS.²³ The choice of paper shape for kV PS is important to generate the required electric fields for ionization; however, the choice of paper shape for zero volt PS is less important than the orientation of the paper relative to the MS inlet. Therefore, a rectangular piece of paper cut to 8 mm × 4 mm and held in place by a toothless alligator clip (McMaster-Carr, USA Part 7236K51) was used, with the center of a straight edge being placed closest to the inlet and on the ion optical axis. This arrangement made it easier to control the distance between the paper and the inlet than in the case of a paper triangle (Figure 1a), increasing the reproducibility of the experiment. A xyz-micrometer moving stage (Parker Automation, USA) was used to set the distance between the front edge of the paper and the MS inlet in the range 0.3 mm to 0.5 mm. A camera (Watec Wat-704R) was used to help in

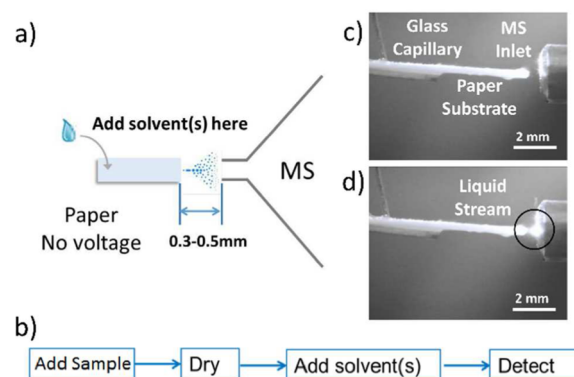


Figure 1. a) Overview of the zero volt paper spray process. The distance between the front edge of the paper and the MS inlet is 0.3–0.5 mm. No voltage is applied to either the paper or the MS inlet capillary. The suction force of the MS inlet causes the release of analyte-containing droplets, which are sampled by the mass spectrometer. b) Sampling and detections procedures. Photographs of the inlet region c) without and d) with solvent. A solvent spray or stream is generated when solvent is applied to the paper, as shown in detail in a video in the Supporting Information.

positioning the paper and to observe the spray which was illuminated by a red laser pointer. No voltage was applied to the paper or the capillary of the MS, instead the spray was generated by the pneumatic forces at play near the MS inlet.

Figure 1b depicts the typical workflow. Typically, 5 μL of sample dissolved in methanol was loaded onto the paper and allowed to dry. During drying, the paper was positioned appropriately with respect to the MS. A methanol and water solvent (1:1 v/v, applied to the paper in three 7 μL aliquots) was used to generate the spray and detect signal. For each 7 μL aliquot of solvent, the signal lasted for about 10 s. Micropipette tips were used to load solvent onto the paper. Sample solutions could also be directly applied to the paper to generate spray. Figures 1c and 1d are photographs taken without and with solvent on the paper, respectively. Clearly, droplets are observed only in the presence of solvent. The spray process was monitored using a 30 Hz camera and details are shown in Figure S1 and the Supporting Information videos. Note that there are similarities to the experiments described by Pagnotti and co-workers.^{15,16}

Computational Resources. All programs used in the simulation of zero volt PS were coded in Python 3.4.2 and computed using computational resources provided by Information Technology at Purdue Research Computing (RCAC) on the Carter supercomputer. Smaller codes were tested on a small desktop computer (core i3).

Instrumentation. Mass spectra were acquired using a Thermo Fisher LTQ mass spectrometer (Thermo Scientific Inc., San Jose, CA). The MS inlet capillary temperature was kept between 150 and 200 $^{\circ}\text{C}$ except where noted, and the tube lens voltage and the capillary voltage were held at zero volt for both positive and negative ion detection. Collision-induced dissociation (CID) was used to carry out tandem mass spectrometry analysis on precursor ions mass-selected using windows of 1.5 mass units. To record the corresponding kV PS spectra, 3.5 kV and 2.0 kV were used in the positive and negative ion modes, respectively, while for nESI 1.5 kV was used in both polarities. The same CID conditions were used for the analysis of the same sample regardless of the ionization method.

RESULTS AND DISCUSSION

Characteristics of Zero Volt PS Mass Spectra. A variety of samples was used to test the ionization capabilities of zero volt PS. As shown in Figure 2, both positive and negative

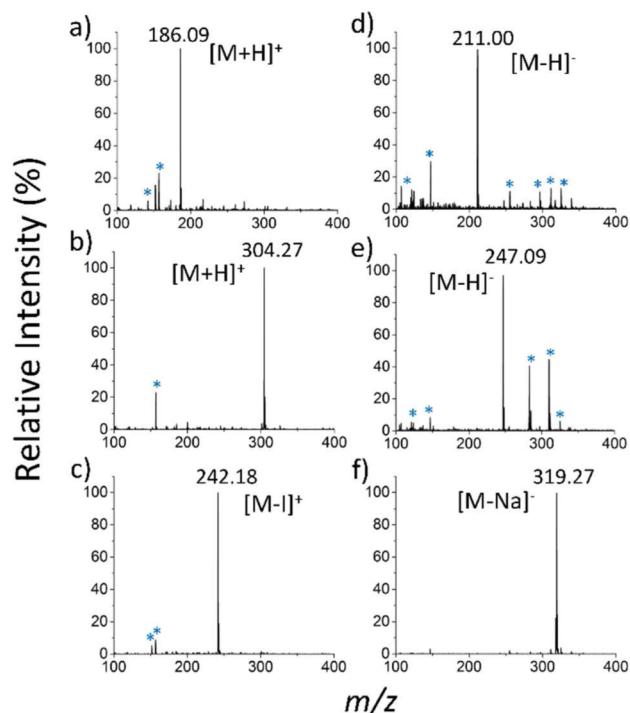


Figure 2. Mass spectra recorded using zero volt PS of three samples examined in the positive ion mode: a) 1 ppm tributylamine; b) 8 ppm cocaine, and c) 1 ppm tetrabutylammonium iodide and three samples examined in the negative ion mode: d) 10 ppm 3,5-dinitrobenzoic acid, e) 10 ppm fludiononil, and f) 10 ppm sodium tetraphenylborate. Methanol and water (v/v 1:1) were used as spray solvent for all samples. Both positive and negative signals were recorded with much lower intensities compared with kV PS and nESI. * Indicates the presence of background species.

spectra were obtained, although the signal intensities were about 2 orders of magnitude lower than those of nESI and kV PS spectra. The MS/MS results for zero volt PS were almost identical to those for the same ions generated by nESI and kV PS (Figures S2 and S3). These results show that the range of analytes to which zero volt PS is applicable is very similar to kV PS and nESI, but the ionization efficiency is much lower.

As noted at the beginning of the paper, ionization without application of a voltage has been observed using several methods. This makes it important to seek to understand the fundamental processes that lead to the formation of ions at zero volts. It is expected that such an enquiry for zero volt PS might be of some later use in guiding mechanistic studies of the other methods. A simple experiment was performed to determine the maximum distance between the paper and MS inlet that still allows observation of signal. It was found that without external forces and with the instrument and paper used, the paper must be within 1 mm of the inlet for the observation of a spray and the corresponding ion signal. At larger distances, an external force such as an applied voltage or additional pneumatic force is needed. A distance of 0.3–0.5 mm was chosen for subsequent experiments to optimize signal intensity and lower its fluctuations. The spray process was monitored using a 30 Hz

camera in an experiment that used 50 ppm of tributylamine fed continuously onto the paper at a flow rate of 15 $\mu\text{L}/\text{min}$. The emission of individual droplets occurs rapidly enough that the chronogram appears to be continuous when observed using an ion injection time of 100 ms (Figure S1f). By illuminating the spray with a hand-held red laser pointer the spray process could be videographed. Figure S1 a-d shows the suction of one droplet over the course of 4 consecutive images. This indicates that a single suction event occurs in a time on the order of ~ 100 ms. This experiment was repeated using manual additions of solvent (7 μL), and similar droplet events are observed. Movies of the continuous and discrete methods of analysis are included in the Supporting Information. The important finding is that signal is observed only when a droplet event is recorded by the camera, indicating that droplets are necessary to produce gas phase ions.

Source of Protons, pH Effect, and Low Voltage Effect. Figure 3 shows the zero volt PS spectrum of 1 ppm

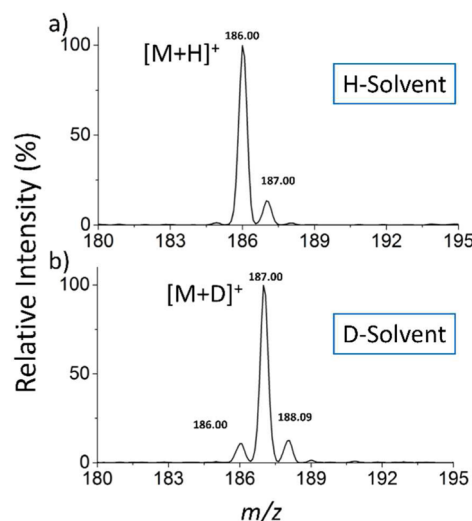


Figure 3. Zero volt PS mass spectra of 1 ppm tributylamine using a) methanol/water (v/v 1:1) and b) deuterated methanol/water (v/v 1:1) as solvent. When deuterated solvent is used, $[\text{M} + \text{D}]^+$ becomes the major peak.

tributylamine using methanol:water 1:1 and deuterated methanol:water 1:1 as solvents, respectively (Figure 3a and 3b). When methanol/water was used, m/z 186 ($[\text{M} + \text{H}]^+$) was the dominant peak, accompanied by an isotopic signal at m/z 187. However, when deuterated methanol/water was used, m/z 187, $[\text{M} + \text{D}]^+$, was dominant, and m/z 188 is its isotopic peak. These results indicate that the protons mainly come from the solvent and that the normal acid/base equilibria occurring in bulk solution are ultimately responsible for the ions seen in the mass spectra. In Figure 3b, there is still a small peak of m/z 186, while in Figure 3a ions of m/z 185 are virtually absent, indicating that a small proportion of tributylamine is still ionized as $[\text{M} + \text{H}]^+$ when deuterated solvents are used. Possible sources of the proton include autoionization ($2 \text{M} \rightleftharpoons [\text{M} + \text{H}]^+ + [\text{M} - \text{H}]^-$), gas phase water molecules, and residual protic compounds in the instrument.

The effects of solvent pH on the spectra have been tested using a representative compound, tributylamine. The intensity of the signal for the protonated molecule is high at pH 7, but when the pH is raised to 10, the intensity drops to zero. Further tests were done by using a series of aromatic heterocyclic

compounds (pyridine, guanine, thymine, and adenine) at neutral and acidic pH (Figure S4). The results show that all four compounds ionize well from acidic solution; pyridine and adenine also ionize at neutral pH, while guanine and thymine do not. These observations are consistent with expectations based on acid/base solution equilibria. The pK_a values of the conjugate acids of thymine and guanine are 0 and 3.2, respectively, while the pyridine and adenine values are significantly higher, 5.25 and 4.1, respectively.³⁰ A series of basic amines including tetramethyl-1,4-butanediamine, diisopropylamine, and methyl amine was also analyzed to investigate the effect of proton affinity (Figure S5). Tetramethyl-1,4-butanediamine has the highest proton affinity (1046.3 kJ/mol) among these analytes and also the highest absolute MS signal intensity. Diisopropyl amine (971.9 kJ/mol) is second in PA, and methyl amine (899 kJ/mol) has the lowest PA and MS signal. Basicity in the gas phase and in solution appear to play important roles in determining the types of ions and conditions (pH) under which they will be observed, similar to the effects observed in electrospray.³¹

To investigate the role low - as opposed to zero - voltages can have on ionization, paper spray experiments were performed using diphenylamine and low and zero volts. The results demonstrate that the small signal at zero volts rises measurably (by a factor of 1.5) upon providing 1 V on the paper (Figure S6) and increases by a factor of 2.5 on raising the potential to 10 V (data not shown). The addition of even a low voltage supplies additional charges, which increases ionization efficiency.

Analyzing Organic Salt/Organic Analyte Mixtures by Zero Volt PS, kV PS, and nESI. A mixture containing 9 ppm cocaine and 0.1 ppm tetrabutylammonium iodide was examined by nESI, kV PS, and zero volt PS. The results are shown in Figure 4a-c. For nESI and kV PS, cocaine (protonated molecule, m/z 304) is the dominant peak, while the signal intensity of tetrabutylammonium (m/z 242) is only about 2% of that of cocaine. For zero volt PS, m/z 304 is still dominant, but the relative intensity of tetrabutylammonium (m/z 242) is much higher than in nESI and kV PS (about 50% relative abundance). The trend is even more obvious in the results of 9 ppm morphine/0.1 ppm tetrabutylammonium iodide (Figure S7a,b,c). The data for nESI (Figure S7a) and kV PS (Figure S7b) show the signal for morphine (m/z 286) to be the base peak, while the relative abundance of tetrabutylammonium (m/z 242) is only about 2% in both cases. By contrast, in the zero volt PS result, it is the ion m/z 242 that constitutes the base peak, while the relative abundance of the protonated morphine ion is only about 10% (Figure S7c). An analogous effect was observed in the negative ion mode, by analyzing a mixture of 36 ppm sodium tetraphenylborate and 3,5-dinitrobenzoic acid (Figure S7 d,e,f).

To account for these results we note the well-known fact both in nESI and in conventional kV PS that the signal intensity is closely related to the concentration of the analyte, at least in the lower concentration range where the available number of charges is sufficient to convert all analyte into the ionic form. The observation that zero volt PS is ca. 2 orders of magnitude less efficient than kV PS and nESI is interpreted simply as the result of the limited number of charges provided by the statistical droplet breakup process versus direct solvent charging. However, this does not explain the large differences between the cocaine/tetrabutylammonium and morphine/tetrabutylammonium ion signals in zero volt PS vs the

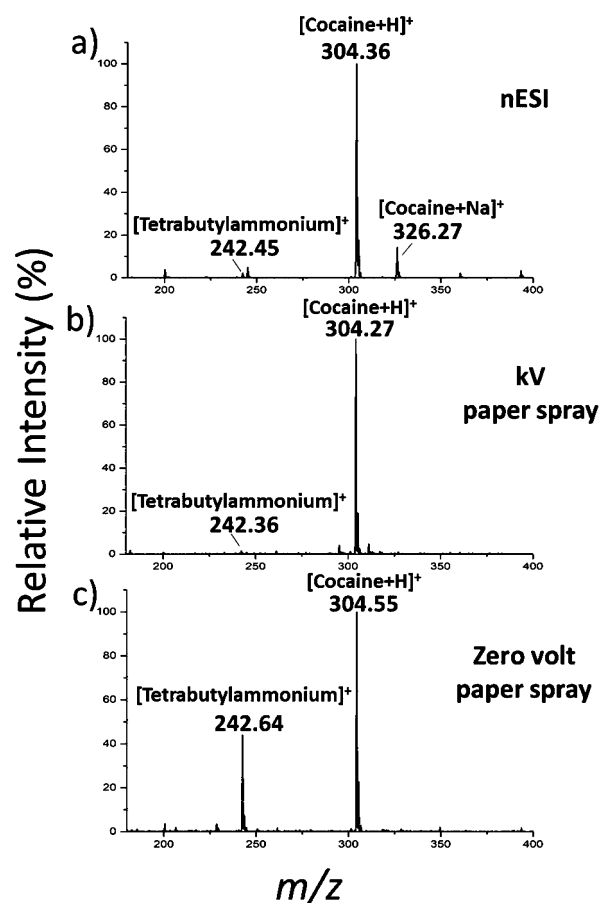
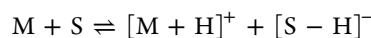


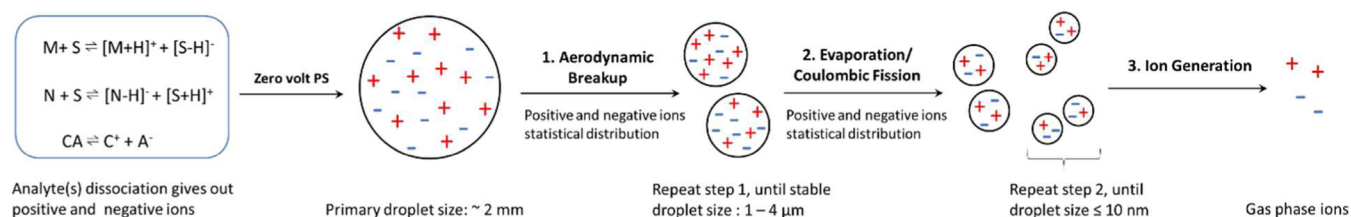
Figure 4. Mass spectra of a mixture of 9 ppm cocaine and 0.1 ppm tetrabutylammonium iodide using a) nESI, b) kV PS, and c) zero volt PS.

conventional PS and nESI methods. The aqueous pK_b of cocaine is 5.39 (15 °C), and morphine is slightly higher, 5.79 (25 °C). This means that morphine should produce somewhat fewer ions than cocaine even when their absolute concentrations are the same. However, the main reason for the low relative intensity of morphine in zero volt PS is likely the lower surface activity of morphine compared to cocaine.³² Evidence for this comes from the fact that when mixed with the very surface active compound tetrabutylammonium iodide, suppression of ionization is much more obvious for morphine than for cocaine in zero volt PS. In kV PS and nESI, the influence of surface activity is not as severe as in zero volt PS since their ionization efficiencies are so high that most of the analytes in the droplets can be ionized and pushed to the droplet surface. A parallel result is observed in negative ion mode where the surface active tetraphenylborate signal is relatively enhanced in zero volt PS as compared to the kV PS and nESI experiments. Given these qualitative explanations we can now test them using a quantitative model of the ionization mechanism.

Overview of Ionization Mechanism for Zero Volt PS. It is well-known that most analytes that can be ionized by ESI (or nESI) or by PS are Bronsted acids or bases. For a basic compound M dissolved in a solvent (S), a certain amount of M exists in the ion pair form (normally as solvent-separated ion pairs) because of the equilibrium:

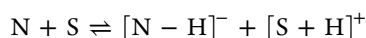


Scheme 1. Overview of the Ionization Mechanism of Zero Volt PS Ionization Including Representations of the Aerodynamic Breakup Process and the Droplet Evaporation/Coulombic Fission^a



^aIn both steps statistical distribution of charge to the fragments is assumed.

For negative ion generation from of an acidic compound N, the equilibrium is



For an ionic compound, say CA, there exists a dissociation equilibrium:



It is these solution-phase ion pairs which can go on to be evaporated and detected in zero volt PS as positively or negatively charged ions.

In zero volt PS, a droplet experiences aerodynamic forces as it is pulled into the mass spectrometer by the suction of the vacuum system. These aerodynamic forces break apart droplets until they reach a size on the order of 1 to 4 μm where the aerodynamic forces are no longer strong enough to cause further droplet breakup.^{29,33} Aerodynamics forces are described by the Weber number, which is defined as

$$We = \frac{\rho_g (V_g - V_d)^2 D_d}{\sigma} \quad (1)$$

where ρ_g is the gas density, V_g is the gas velocity, V_d is the droplet velocity, D_d is the diameter of the droplet, and σ is the surface tension of the solvent.³⁴ The droplet will continue to break up while its Weber number is larger than 10 (Figure S8).^{34,35} During the aerodynamic breakup process, there is a very large chance that the positive charges and negative charges will be unevenly separated, that is to say, many of these progeny droplets will be (slightly) charged. The extent of charging is unknown. However, because the initial Weber number in zero volt paper spray is larger than 1000 a catastrophic breakup of the initial droplet occurs to produce progeny droplets (Figure S8).^{34,36} After aerodynamic breakup it is assumed that droplets will undergo multiple rounds of evaporation and Coulombic fission until they are ionized by either of the main ESI models, the charge residue model or the ion evaporation model^{37,38} or its close analog, solvated ion emission.²⁶ A schematic of the overall mechanism is shown in Scheme 1. The model used here to describe evaporation and fission is similar to other approaches used to model nESI based on Monte Carlo methods,³⁹ except that droplet charging is determined by nonsymmetrical fragmentation as described by Dodd.²⁸ While the charging calculated by Dodd is small,^{28,40} there is enough charge to allow for the Coulombic fission of most 1 to 4 μm droplets to occur after an appropriate evaporation time. Note, too, that we assume statistical breakup and resulting charge distributions in the fragments during the early aerodynamic phase of bulk breakup but are aware of the fact that this is simply a first approximation. Simulations have been done based on the above postulated mechanism. The initial concentration

and diameter for each droplet were specified, but the charge of each droplet was randomly assigned based on a theory described by Dodd.²⁸ To determine the initial charge, the number of ions an analyte forms in solution was calculated based on the initial concentration and dissociation constant of the analyte. Statistical fluctuations in the number of positive and negative ions in each droplet were modeled by a binomial distribution

$$f(z; n, p) = \binom{n}{z} p^z (1 - p)^{n-z} \quad (2)$$

where p is the probability of an ion being charged (either positive or negative), n is the number of ions, and z is number of positive charges. The difference in ion polarity count determines the initial charge. It should be noted that charge is assumed to be carried only by analytes added to the solution. The droplet then evaporates until its diameter reaches the Rayleigh limit (3).^{38,41}

$$D_R = \left(\frac{D_q^2 * e^2}{(\pi^2 * 8 * \epsilon_0 * \sigma)} \right)^{1/3} \quad (3)$$

Here D_R is the diameter of the droplet at the Rayleigh limit, D_q is the charge on the droplet, e is elementary charge, ϵ_0 is the permittivity of a vacuum, and σ is the solvent surface tension.

At the Rayleigh limit a droplet undergoes fission and produces progeny droplets. Accordingly the size of precursor and progeny droplets was calculated according to these equations

$$D_d = (1 - \Delta m)^{1/3} * D_R \quad (4)$$

$$D_{pD} = \left(\frac{\Delta m}{N_{pd}} \right)^{1/3} D_R \quad (5)$$

where N_{pd} is the number of progeny droplets taken to be 10, D_{pd} is the diameter of the progeny droplets, and $\Delta m = 0.02$. The number of analytes in each progeny droplet was determined from two Poisson distributions: the concentration of ions, $N_{anal-IP}$ (both positive and negative), and the concentration of free ions in the outer region of the droplet, N_{anal-q} . The position of a solvated ion within the droplet is determined by its surface activity, S . Surface activity is a number between 0 and 1 describing the probability of a molecule being at the surface or the interior of the droplet. Larger values of surface activity means the analyte competes more strongly for surface sites. Surface activity is modeled by a binomial distribution, similar to eq 2, except that $p = S$, n is the number of ions, and z is the number of ions found in the outer region of

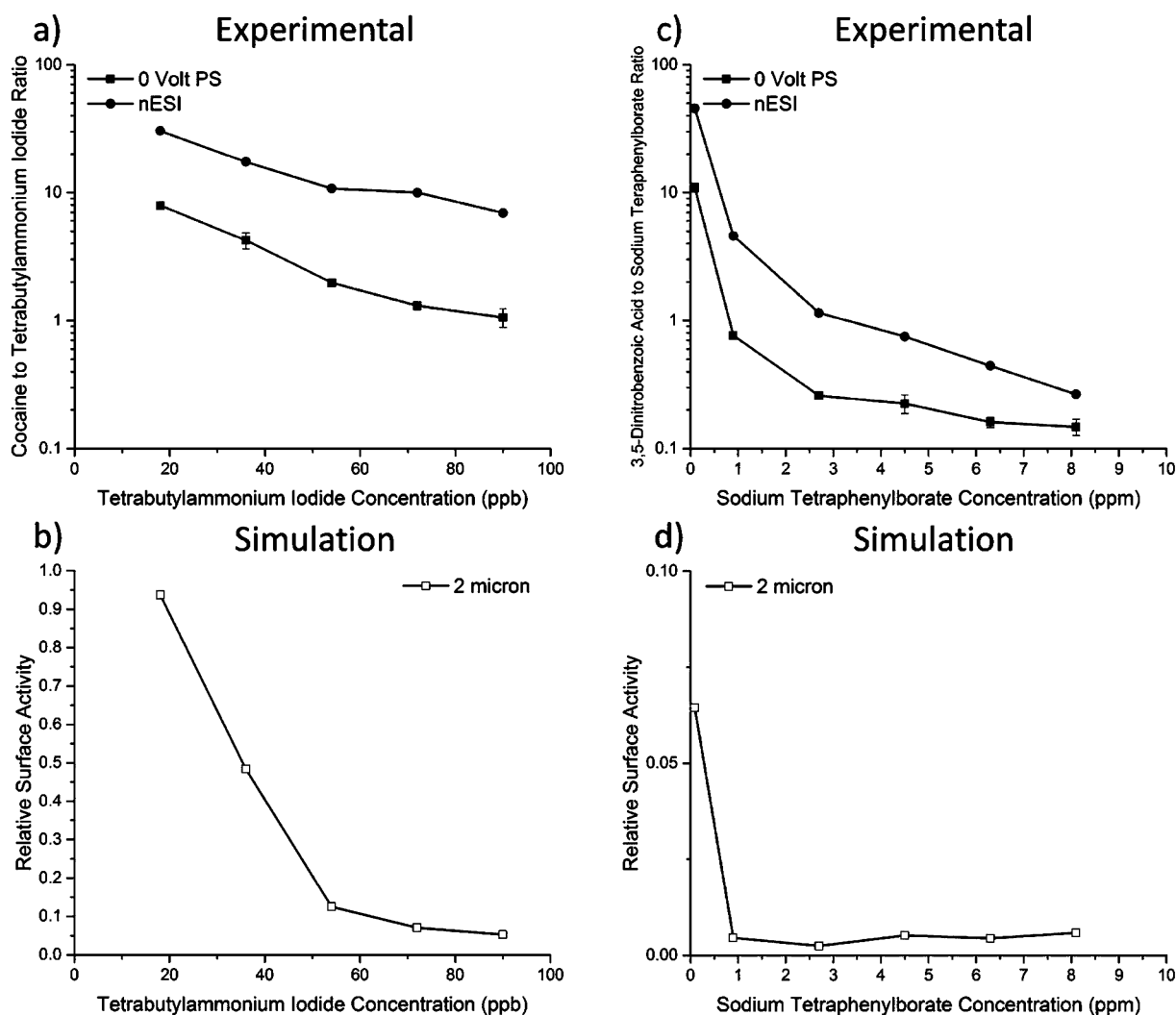


Figure 5. a) Cocaine to tetrabutylammonium cation ratio dependence in positive ion mode for zero volt PS and nESI. Cocaine concentration is held constant at 1 ppm, while tetrabutylammonium iodide concentration changes. b) The relative surface activity of cocaine calculated according to the experimental data in a). c) Ratio dependence of 3,5-dinitrobenzoate to tetraphenylborate in negative ion mode for zero volt PS and nESI. 3,5-Dinitrobenzoic acid concentration is held constant at 20 ppm, while the sodium tetraphenylborate concentration changes. d) Relative surface activity of 3,5-dinitrobenzoic acid calculated according to the experimental data in c). Surface activity of the salt is assumed to be 1 for all simulations.

the droplet.³⁹ The number of ions, $N_{\text{anal-IP}}$, and charges, $N_{\text{anal-q}}$, is chosen randomly from a Poisson distribution.

$$f(N_{\text{anal-IP}}; N_{\text{IP}}) = \frac{e^{-N_{\text{IP}}} N_{\text{IP}}^{N_{\text{anal-IP}}}}{N_{\text{anal-IP}}!} \quad (6)$$

Here N_{IP} is the average number of ions close to the surface. The same equation is used for $N_{\text{anal-q}}$ with the appropriate substitutions. For the progeny droplets, additional charging can arise from the statistical fluctuations in the number of positive and negative ions, and this is modeled in the same manner as above (2). The evaporation/Coulombic fission process continues until all droplets reach a size of 10 nm. At 10 nm, ions free of their counter charge are considered ionized (i.e., considered to undergo subsequent rapid desolvation), which is a simplification of the actual processes that leads to ion formation. Ions are produced from droplet smaller than 10 nm by the ion emission mechanism or by the charge residue model.²⁶ The formation of gas-phase ions from 10 nm droplets is not explicitly modeled here. A more detailed explanation is provided in the Supporting Information.

There are differences, but there are also strong similarities in the ionization mechanism of zero volt PS and conventional kV PS. Both processes involve the key steps of (i) droplet formation and (ii) droplet breakup. Droplet formation is mostly due to pneumatic forces in zero volt paper spray, whereas it is mostly due to electrical forces at kV paper spray. There exists a continuum in behavior between zero volt PS and kV PS as evidenced by the low voltage PS data cited above. Droplet breakup starts with a mechanical breakup process which may or may not occur in kV PS and is then followed by processes analogous to those of kV PS.

Single Analyte Simulation. Simulations were run with 2 μm droplets to investigate the possible limits of detection of zero volt PS. Both sizes lead to indicated limits of detection between 10^{-7} and 10^{-8} M (Figure S8), based on the assumption of being able to detect a single ion. The detection limit determined from simulation is calculated from the ionization efficiency, which is defined as the ratio of the number of ions generated vs the total number of molecules used.⁴² Qualitatively, 18 ppb (4.87×10^{-8} M) of tetrabutylammonium iodide could be detected experimentally,

which is in good agreement with the estimate of detectability by simulation. The simulation was also repeated at three different surface activities, and it was found that the number of ionized molecules decreases as the surface activity decreases (Figure S10). Surface activity has been reported to have a similar effect on the ionization efficiency.^{43,44}

Experimental and Simulated Results and Mechanistic Considerations for Multianalyte Mixtures. A series of mixtures of cocaine and tetrabutylammonium iodide were analyzed with zero volt PS. In Figure 5a the amount of tetrabutylammonium iodide was varied, while the amount of cocaine was held constant at 1 ppm. A similar experiment was performed using 3,5-dinitrobenzoic acid and sodium tetraphenylborate but analyzed in negative ion mode. In Figure 5c the amount of sodium tetraphenylborate was changed, while the concentration of 3,5-dinitrobenzoic acid was held constant at 20 ppm. At each point, the ratio of (de)protonated molecular ion to salt was calculated. Simulations were run in which the more surface active compound (salts in this case) was assumed to have a surface activity of 1 and surface activity of (de)protonated molecular ion relative to the salt was varied until the simulated ratio matched within 1% error of the experimental ratio.

In Figure 5a, as the amount of tetrabutylammonium iodide decreases the ratio of cocaine to tetrabutylammonium iodide increases for both zero volt PS and nESI. Note that nESI has larger ratios than zero volt PS. This is because the kV applied voltage provides protons^{38,45} which can serve to ionize the cocaine but will not cause additional ionization of the tetrabutylammonium iodide salt. Thus, the measured ratio becomes closer to the concentration ratio, with differences being due to intrinsic ionization and detection efficiency. We applied the experimental intensity ratios of zero volt PS to our simulation and calculated the relative surface activity trend. The results are shown in Figure 5b. As the amount of tetrabutylammonium iodide decreases the relative surface activity of cocaine is calculated to increase. This makes sense since as the amount of tetrabutylammonium iodide decreases more cocaine will move toward the droplet surface and can compete against the tetrabutylammonium cation for surface sites.⁴⁶ Tang et al. developed a model, which suggests that at low concentrations, 10^{-8} to 5×10^{-6} M, the ratio of analyte ion signals is dependent upon the relative surface activities of the two analytes.³² This agrees with our simulation results very well. Figure 5c,d display the same general trend observed in Figure 5a,b. As the concentration of sodium tetraphenylborate decreases the ratio of 3,5-dinitrobenzoic acid to sodium tetraphenylborate decreases (Figure 5c), while the relative surface activity of 3,5-dinitrobenzoic acid increases (Figure 5d). A similar set of experiments was performed except that the concentration of the analyte was varied, and the salt concentration was held constant (Figure S11). This produced similar conclusions, and a detailed explanation is provided in the Supporting Information.

CONCLUSION

Chemical analysis at zero volts from paper substrates has been demonstrated. Zero volt PS gives both positive and negative ion signals and allows detection of similar compounds to those seen by kV PS and nESI but with lower ionization efficiency. In spite of the low efficiency, the process is intrinsically very gentle and is more sensitive to surface active compounds. A mechanism for zero volt PS has been proposed based on the statistical

fluctuation of positive and negative ions in droplet solutions during the course of droplet breakup. This model (developed in detail in the Supporting Information) has been used to predict a detection limit similar to that observed experimentally. In the case of multiple analytes, the simulation is also able to calculate the relative surface activity of both positive and negative ions, such as cocaine and 3,5-dinitrobenzoic acid. The relationship of this model to other zero volt spray ionization mechanisms is not known but is of great future interest, especially for the inlet ionization experiments^{15,16} and the nanowire spray⁴⁷ methods. Besides the understanding of its mechanism, zero volt PS also has potential application advantages: it could be used to study systems where there is a need to avoid the influence of external electric fields and at the same time to use paper to eliminate the complex matrix, such as in living organisms analysis. In the course of this work we have learned of related unpublished paper spray ionization experiments done by Dr. Akira Motoyama of Shiseido Company.

ASSOCIATED CONTENT

Supporting Information

Additional information as noted in text. The Supporting Information is available free of charge on the ACS Publications website at DOI: 10.1021/acs.analchem.5b01225.

AUTHOR INFORMATION

Corresponding Author

*E-mail: cooks@purdue.edu.

Author Contributions

#These authors contributed equally.

Notes

The authors declare no competing financial interest.

ACKNOWLEDGMENTS

The support of the National Science Foundation CHE 1307264 is acknowledged. T.P. acknowledges DST for funding. D.S. and R.N. acknowledge UGC for their research fellowship. Yafeng Li is a visiting student from the Institute of Chemistry, Chinese Academy of Sciences, and she acknowledges the Chinese Scholarship Council for financial support.

REFERENCES

- (1) Takáts, Z.; Wiseman, J. M.; Gologan, B.; Cooks, R. G. *Science* **2004**, *306*, 471–473.
- (2) Monge, M. E.; Harris, G. A.; Dwivedi, P.; Fernández, F. M. *Chem. Rev.* **2013**, *113*, 2269–2308.
- (3) *Ambient Ionization Mass Spectrometry*; The Royal Society of Chemistry; 2015; pp P001–508.
- (4) Schäfer, K.-C.; Balog, J.; Szaniszló, T.; Szalay, D.; Mezey, G.; Dénes, J.; Bognár, L.; Oertel, M.; Takáts, Z. *Anal. Chem.* **2011**, *83*, 7729–7735.
- (5) Blakley, C. R.; Carmody, J. J.; Vestal, M. L. *Anal. Chem.* **1980**, *52*, 1636–1641.
- (6) Blakley, C. R.; Vestal, M. L. *Anal. Chem.* **1983**, *55*, 750–754.
- (7) Hirabayashi, A.; Sakairi, M.; Koizumi, H. *Anal. Chem.* **1994**, *66*, 4557–4559.
- (8) Hirabayashi, A.; Sakairi, M.; Koizumi, H. *Anal. Chem.* **1995**, *67*, 2878–2882.
- (9) Hirabayashi, A.; Hirabayashi, Y.; Sakairi, M.; Koizumi, H. *Rapid Commun. Mass Spectrom.* **1996**, *10*, 1703–1705.
- (10) Hirabayashi, Y.; Hirabayashi, A.; Takada, Y.; Sakairi, M.; Koizumi, H. *Anal. Chem.* **1998**, *70*, 1882–1884.
- (11) Ozdemir, A.; Lin, J.-L.; Wang, Y. S.; Chen, C.-H. *RSC Adv.* **2014**, *4*, 61290–61297.

- (12) Haddad, R.; Sparrapan, R.; Eberlin, M. N. *Rapid Commun. Mass Spectrom.* **2006**, *20*, 2901–2905.
- (13) Haddad, R.; Sparrapan, R.; Kotiaho, T.; Eberlin, M. N. *Anal. Chem.* **2008**, *80*, 898–903.
- (14) Haddad, R.; Milagre, H. M. S.; Catharino, R. R.; Eberlin, M. N. *Anal. Chem.* **2008**, *80*, 2744–2750.
- (15) Pagnotti, V. S.; Inutan, E. D.; Marshall, D. D.; McEwen, C. N.; Trimpin, S. *Anal. Chem.* **2011**, *83*, 7591–7594.
- (16) Pagnotti, V. S.; Chubatyi, N. D.; McEwen, C. N. *Anal. Chem.* **2011**, *83*, 3981–3985.
- (17) Wang, B.; Trimpin, S. *Anal. Chem.* **2014**, *86*, 1000–1006.
- (18) Wu, C.-I.; Wang, Y.-S.; Chen, N. G.; Wu, C.-Y.; Chen, C.-H. *Rapid Commun. Mass Spectrom.* **2010**, *24*, 2569–2574.
- (19) Zhu, H.; Li, G.; Huang, G. J. *Am. Soc. Mass Spectrom.* **2014**, *25*, 935–942.
- (20) Chen, T.-Y.; Chao, C.-S.; Mong, K.-K. T.; Chen, Y.-C. *Chem. Commun.* **2010**, *46*, 8347–8349.
- (21) Chen, T.-Y.; Lin, J.-Y.; Chen, J.-Y.; Chen, Y.-C. *J. Am. Soc. Mass Spectrom.* **2010**, *21*, 1547–1553.
- (22) Ozdemir, A.; Lin, J.-L.; Gillig, K. J.; Chen, C.-H. *Analyst* **2013**, *138*, 6913–6923.
- (23) Wang, H.; Liu, J.; Cooks, R. G.; Ouyang, Z. *Angew. Chem., Int. Ed.* **2010**, *49*, 877–880.
- (24) Manicke, N. E.; Yang, Q.; Wang, H.; Oradu, S.; Ouyang, Z.; Cooks, R. G. *Int. J. Mass Spectrom.* **2011**, *300*, 123–129.
- (25) Espy, R. D.; Teunissen, S. F.; Manicke, N. E.; Ren, Y.; Ouyang, Z.; van Asten, A.; Cooks, R. G. *Anal. Chem.* **2014**, *86*, 7712–7718.
- (26) Konermann, L.; Ahadi, E.; Rodriguez, A. D.; Vahidi, S. *Anal. Chem.* **2013**, *85*, 2–9.
- (27) Narayanan, R.; Sarkar, D.; Cooks, R. G.; Pradeep, T. *Angew. Chem., Int. Ed.* **2014**, *53*, 5936–5940.
- (28) Dodd, E. E. *J. Appl. Phys.* **1953**, *24*, 73–80.
- (29) Zilch, L. W.; Maze, J. T.; Smith, J. W.; Ewing, G. E.; Jarrold, M. F. *J. Phys. Chem. A* **2008**, *112*, 13352–13363.
- (30) Yen, T.-Y.; Judith Charles, M.; Voyksner, R. D. *J. Am. Soc. Mass Spectrom.* **1996**, *7*, 1106–1108.
- (31) Ehrmann, B. M.; Henriksen, T.; Cech, N. B. *J. Am. Soc. Mass Spectrom.* **2008**, *19*, 719–728.
- (32) Tang, L.; Kebarle, P. *Anal. Chem.* **1993**, *65*, 3654–3668.
- (33) Wang, R.; Allmendinger, P.; Zhu, L.; Gröhn, A.; Wegner, K.; Frankevich, V.; Zenobi, R. *J. Am. Soc. Mass Spectrom.* **2011**, *22*, 1234–1241.
- (34) Krzeczkowski, S. A. *Int. J. Multiphase Flow* **1980**, *6*, 227–239.
- (35) Wierzbna, A. *Exp. Fluids* **1990**, *9*, 59–64.
- (36) Pilch, M.; Erdman, C. A. *Int. J. Multiphase Flow* **1987**, *13*, 741–757.
- (37) Iribarne, J. V.; Thomson, B. A. *J. Chem. Phys.* **1976**, *64*, 2287–2294.
- (38) Kebarle, P.; Verkerk, U. H. *Mass Spectrom. Rev.* **2009**, *28*, 898–917.
- (39) Hogan, C. J., Jr.; Biswas, P. *J. Am. Soc. Mass Spectrom.* **2008**, *19*, 1098–1107.
- (40) Knochenmuss, R. *Mass Spectrometry* **2013**, *2*, S0006–S0006.
- (41) Rayleigh, L. *Philos. Mag. Ser. 5* **1882**, *14*, 184–186.
- (42) Murray, K. K.; Boyd, R. K.; Eberlin, M. N.; Langley, G. J.; Li, L.; Naito, Y. *Pure Appl. Chem.* **2013**, *85*, 1515–1609.
- (43) Cech, N. B.; Enke, C. G. *Anal. Chem.* **2000**, *72*, 2717–2723.
- (44) Cech, N. B.; Enke, C. G. *Mass Spectrom. Rev.* **2001**, *20*, 362–387.
- (45) Kertesz, V.; Van Berkel, G. J. *Anal. Chem.* **2007**, *79*, 5510–5520.
- (46) Enke, C. G. *Anal. Chem.* **1997**, *69*, 4885–4893.
- (47) Narayanan, R.; Sarkar, D.; Som, A.; Cooks, R. G.; Pradeep, T. **2015**, Unpublished.

Supporting Information for:

Zero Volt Paper Spray Ionization and its Mechanism

Michael Wleklinski,^{1#} Yafeng Li,^{1#} Soumabha Bag,¹ Depanjan Sarkar,² Rahul Narayanan,² T. Pradeep² and R. Graham Cooks^{1*}

¹Department of Chemistry and Center for Analytical Instrumentation Development, Purdue University, West Lafayette, Indiana 47907

²DST Unit of Nanoscience (DST UNS) and Thematic Unit of Excellence (TUE), Department of Chemistry, Indian Institute of Technology Madras, Chennai 600 036, India

* Corresponding Author: cooks@purdue.edu

These authors contributed equally

Keywords: Ambient Ionization; Charged Droplets; Inlet Ionization; Nanoelectrospray; Charge Residue Model; Electrospray Mechanism; Acid/Base Equilibria; Surface Activity; Coulombic Repulsion; Aerodynamic Breakup; Asymmetric Charge Distribution

Abstract: The supporting information includes 11 figures, 4 movies, and further simulation details. Figure S1 shows the process of one droplet being sucked into the mass spectrometer. Figures S2 and S3 display MS/MS data for selected analytes examined in the positive and negative ion modes ionized by paper spray (PS), nano-electrospray ionization (nESI), and zero volt PS. Figures S8 – S10 are supporting information for the simulations developed in this paper. A in depth discussion of the postulated ionization mechanism for zero volt paper spray is provided. A brief discussion of figure S11 is also provided.

Supplementary Figures:

Figure S1: Consecutive camera images of 0V paper spray process.

Figure S2: MS/MS of selected positive mode analytes using PS, nESI, and zero volt PS

Figure S3: MS/MS of selected negative ion mode analytes using PS, nESI, and zero volt PS

Figure S4: 0V paper spray of aromatic heterocycles in neutral and acidic pH

Figure S5: 0V paper spray of amines with different basicities

Figure S6: Comparison of 0 V and 1 V paper spray

Figure S7: Analysis of mixtures selected compounds using nESI, PS, and zero volt PS.

Figure S8: Weber number for methanol droplets under different gas flows

Figure S9: Simulated number of molecules ionized vs analyte concentration at various surface activities

Figure S10: Simulated ionization efficiency vs analyte concentration at various surface activities

Figure S11: Experimental results of binary mixtures and calculated relative surface activity results.

Supplementary Movies:

Movie S1: Video image of the analysis of 50 ppm tributylamine in methanol feed continuously onto the paper at 15 $\mu\text{L}/\text{min}$.

Movie S2: Video image of the analysis of 50 ppm tributylamine in methanol feed continuously onto the paper at 15 $\mu\text{L}/\text{min}$ at $\frac{1}{4}$ speed.

Movie S3: Video image of the analysis of 50 ppm tributylamine in methanol added in 5-7 μL aliquots.

Movie S4: Video image of the analysis of 50 ppm tributylamine in methanol added in 5-7 μL aliquots at $\frac{1}{4}$ speed.

Additional Experimental Details

Chemicals and Materials

Diphenylamine and adenine were purchased from Merck Ltd., Mumbai, India. Guanine was purchased from Spectrochem Pvt. Ltd., Mumbai, India. Diisopropylamine and methylamine were purchased from SD Fine Chem. Ltd, Mumbai, India. Thymine was purchased from Titan Biotech LTD., New Delhi, India. Pyridine was purchased from Qualigens Fine Chemicals, India. Tetramethyl-1,4-butanediamine was purchased from Sigma Aldrich, India. All compounds purchased in India were dissolved in HPLC grade methanol (Sigma Aldrich, India). All other samples were purchased from Sigma (St. Louis, MO, USA).

Additional Simulation Details

Aerodynamic Breakup

When sufficient solvent is applied, droplets are pulled from the filter paper by the suction of the instrument. Typically a few μL of sample is added before each suction event suggesting that the initial droplets will be at least of similar volume. The droplets, initially at zero velocity enter a high speed gas flow (170 m/s) due to the suction of the inlet and experience an aerodynamic force.³ This force causes the droplet to simultaneously accelerate and breakup. The droplet will continue to breakup while its Weber number is larger than 10.^{4,5} The weber number is defined by

$$We = \frac{\rho_g (V_g - V_d)^2 D_d}{\sigma} \quad (1)$$

where ρ_g is the gas density, V_g is the gas velocity, V_d is the droplet velocity, D_d is the diameter of the droplet, and σ is the surface tension of the solvent.⁴ This suggests that droplets will primarily breakup due to aerodynamic forces until they either accelerate to the velocity of the surrounding gas or reach a certain size. There is evidence from charge detection mass spectrometry that water droplets produced by either sonic spray ionization or vibrating orifice aerosol generator reach a common size of about 2.5 μm after traveling through the inlet.⁵ This is also approximately the average size measured for kV PS mass spectrometry.⁶ This suggests that methanol droplets should undergo a similar phenomenon, but in fact could be smaller due to the reduced surface tension of methanol as compared to water. Using this information, it is assumed that droplets may have diameters between 1-4 μm after aerodynamic breakup (Figure S8).

Initial Droplet Conditions for Evaporation and Columbic Fission Cycles

Aerodynamic breakup determines that droplets will have diameters between 1 and 4 μm and this serves as the initial diameter of droplets modeled in this section. The number of analytes in a droplet was calculated based on initial analyte concentration and its dissociation constant to determine the number of ions it will produce. Only ions can be separated into detectable quantities by mass spectrometry, thus solution phase neutrals are ignored in this model. The initial droplet charge was

modeled by the statistical fluctuations of positive and negative ions present in the total population of ions. For a droplet containing n ions, of which the ions are either positively or negatively charged, the overall charge is modeled by a binomial distribution (2).

$$f(z; n, p) = \binom{n}{z} p^z (1 - p)^{n-z} \quad (2)$$

For this distribution, p is the probability of an ion being charged (either positive or negative), n is the number of ions, and z is number of positive charges. The initial number of positive and negative ions is on average, equal; however, statistical fluctuations in the positive and negative ions will produce some net charge. This is simulated by using a binomial random number generator with parameter $p = 0.5$ and n is the previously calculated number of ions. The initial charge is found by subtracting the number of negative ions from the positive ions.

Droplet Evaporation to Rayleigh Limit

With the droplet's initial parameter set (size, charge, number of analytes), evaporation is allowed to occur. The temperature of the droplet was kept constant at 298 K to ease the computation time required. This is justified by the fact that droplets will cool evaporatively,⁷ but will also be warmed by collisional activation, so the temperature will drop initially but may rise later on, thus an accurate model for temperature will be difficult to obtain over the droplet size range of the simulation (4 μm – 10 nm).⁸⁻¹⁰ The droplet is allowed to evaporate until it reaches the Rayleigh limit diameter.^{11,12}

$$D_R = \left(\frac{D_q^2 * e^2}{(\pi^2 * 8 * \epsilon_0 * \gamma)} \right)^{\frac{1}{3}} \quad (3)$$

Here D_q is the charge on the droplet, e is elementary charge, ϵ_0 is the permittivity of a vacuum, and γ is the solvent surface tension. Surface tension was estimated using a regression method developed by Jasper et al.^{13,14}

Droplet Fission and Progeny Droplets

Upon reaching the Rayleigh limit, droplets undergo fission and lose mass and charge in the form of progeny droplets. At this point columbic fission occurs with most reports indicating a small mass loss, Δm , (2%) from the precursor droplet and large charge loss, Δq , (15%).¹⁵⁻¹⁷ From this the diameter of the precursor and progeny droplets can be calculated, assuming that on average 10 progeny droplets are generated in a fission event. The exact number of progeny droplets generated is unknown, but 10 is within the range of typical values reported.¹⁸⁻²⁰ Accordingly the size of precursor and progeny droplets was calculated according to these equations:

$$D_d = (1 - \Delta m)^{\frac{1}{3}} * D_R \quad (4)$$

$$D_{pD} = \left(\frac{\Delta m}{N_{pd}} \right)^{\frac{1}{3}} D_R \quad (5)$$

where N_{pd} is the number of progeny droplets taken to be 10, D_{pd} is the diameter of the progeny droplets, and $\Delta m = 0.02$. At the time of fission only ions that are close to the surface are allowed the possibility of being transferred to a progeny droplet. A volume fraction, V_f , is specified as the volume which can be considered for transfer to progeny droplets. In this simulation it is taken to be 15% of the total volume, but the exact value is unknown. The position of a solvated ion within a droplet is determined by its surface activity, S . Surface activity is a number between 0 and 1 describing the probability of a molecule being at the surface or the interior of the droplet. This is modeled by a binomial distribution, similar to equation (2), except that $p = S$, n is the number of ions, and z is the number of ions found in the outer region of the droplet. Thus when $S = 1$ all ions are located in the outer region, and when $S = 0$, none are located in the outer region. Any ions free of their respective counter charge are assumed to be in the outer region of the droplet. The average number of ions, N_{IP} , and charges, N_q , per progeny droplet are calculated from (6) and (7)

$$N_{IP} = \left(\frac{D_d}{D_{pd}} \right)^3 * V_f * C_{IP} \quad (6)$$

$$N_q = \frac{C_q * \Delta q}{N_{pd}} \quad (7)$$

where C_{IP} and C_q are the number concentration of ions and charges in the outer region of the droplet. The number of ions transferred to progeny droplets can be modeled by a Poisson distribution.²¹ The number of ions, $N_{anal-IP}$, and charges, N_{anal-q} is chosen randomly from a Poisson distribution.

$$f(N_{anal-IP}, N_{IP}) = \frac{e^{-N_{IP}} * N_{IP}^{N_{anal-IP}}}{N_{anal-IP}!} \quad (8)$$

The same equation is used for N_{anal-q} with the appropriate substitutions. At this point, more random charging can occur due to the statistical fluctuations of positive and negative ions present in the total population of positive and negative ions. This is modeled in the same manner as described in the initial droplet conditions section (equation 2). With this information, the charge of the progeny droplet is calculated by subtracting the total population of positive ions from negative ions. This same methodology is completed for all the other progeny droplets, and then the conditions of the precursor droplet are updated based on the total number of ions consumed by the progeny droplets. All droplets (precursor and progeny) larger than 10 nm then undergo more evaporation/fission cycles until all droplets reach 10 nm in size.

Analyte Ion Formation

Once all droplets have reached 10 nm in size the simulation ends. At this time each droplet is analyzed for charge to determine the number of ionized analytes. For example, a droplet containing a +2 charge is assumed to have two ionized molecules. Note that in the simulation the actual ionization event is not modeled explicitly. Gas phase ions could be produced by either the charge residue model or the ion evaporation model. This counting process is repeated for all the droplets of size <10 nm and then ionization efficiency can be calculated. Typically 5,000 – 50,000 precursor droplets are modeled to obtain an estimate of ionization efficiency and total number of ionized molecules. Alternatively this model can be applied to droplets containing multiple analytes, in which case multiple analyte ratios can be calculated. Note that multiple charges on the small analytes of interest are very unlikely and this possibility is ignored.

Experimental and Simulated Results and Mechanistic Considerations for Multi-Analyte Mixtures

In Figure S11a, the amount of tetrabutylammonium iodide was held constant at 0.1 ppm, while that of cocaine was changed. In Figure S11a the ratio of cocaine to tetrabutylammonium iodide increases as the concentration of cocaine increases. Figure S11b shows a similar trend to Figure 5b, but since the amount of cocaine is increased the calculated relative surface activity of cocaine increases. Again this is because as the cocaine concentration increases, more cocaine can occupy the surface increasing its relative surface activity. In Figure S11c, sodium tetraphenylborate was held constant at 5 ppm and 3,5-dinitrobenzoic acid was varied. The data in Figure S11c are consistent with those of Figure S11a in that as the concentration of the analyte increases the ratio of analyte to salt signal increases. Additionally the relative surface activity of 3,5-dinitrobenzoic acid increases (Figure S11d) as the analyte concentration increases. The only noticeable difference is in the nESI results of Figure S11c, which show a drop in the ratio of 3,5-dinitrobenzoic acid to sodium tetraphenylborate in spite of its higher surface activity.

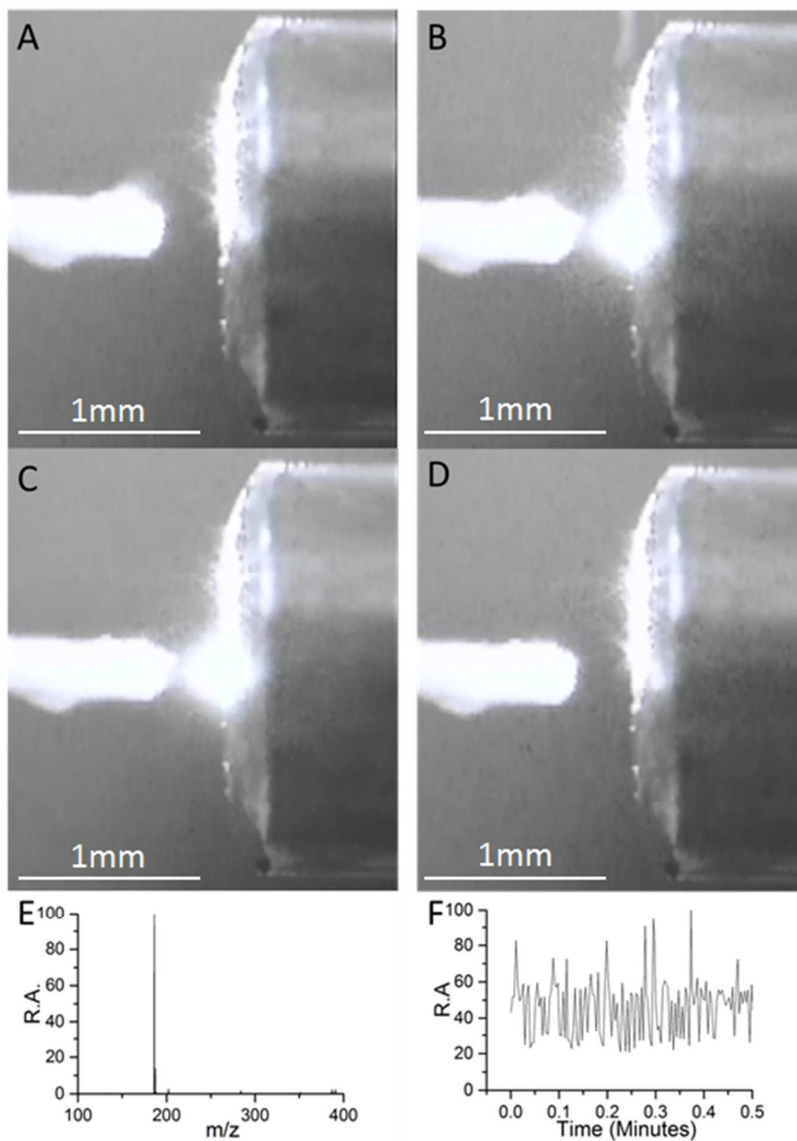


Figure S1. Panels A-D are consecutive images of the spray process occurring at 0 volts. The spray is illuminated with a red laser pointer and captured on a Watec Wat-704R camera. Panels A-D show a droplet event over the course of 4 consecutive scans. The time elapsed is around 100 milliseconds. Panels E and F are the mass spectrum of 50 ppm tributylamine and its corresponding ion chromatogram. Tributylamine was added in a continuous manner at 15 $\mu\text{L}/\text{min}$ through a fused silica capillary.

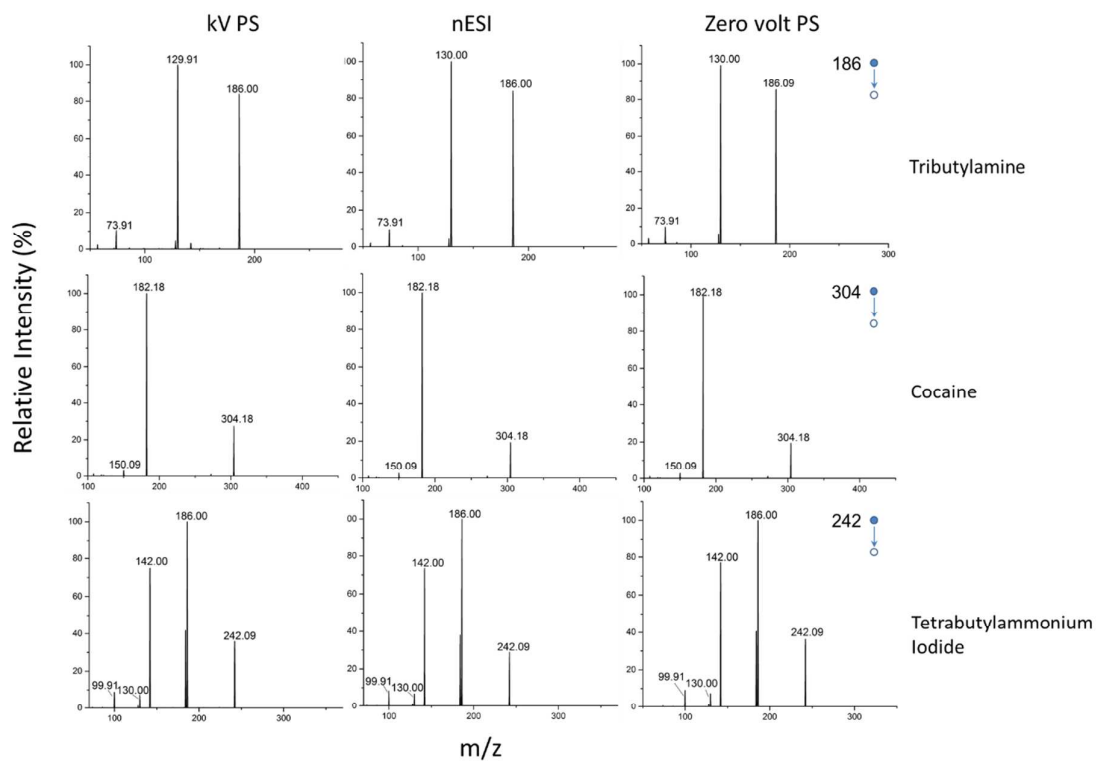


Figure S2. Positive ion mode MS/MS data for tributylamine, cocaine, and tetrabutylammonium iodide taken by kV paper spray, nano-electrospray ionization, and zero volt paper spray.

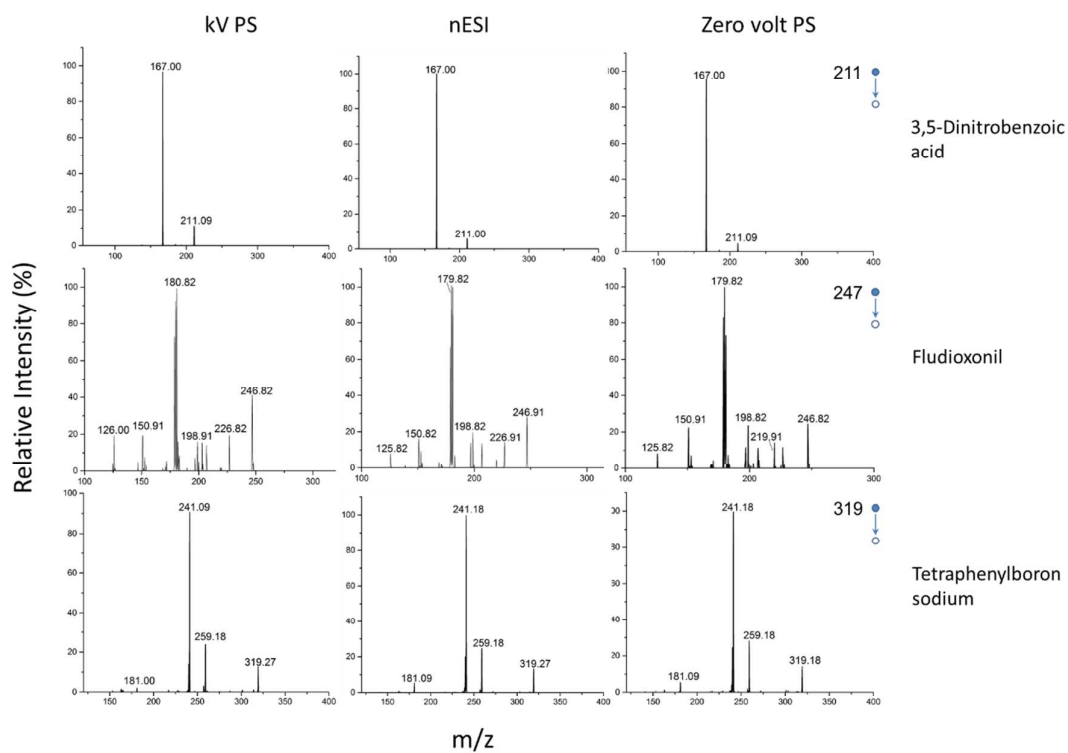


Figure S3: Negative ion mode MS/MS data for 3,5-dinitrobenzoic acid, fludioxonil, and sodium tetraphenylborate taken by kV paper spray, nano-electrospray ionization, and zero volt paper spray.

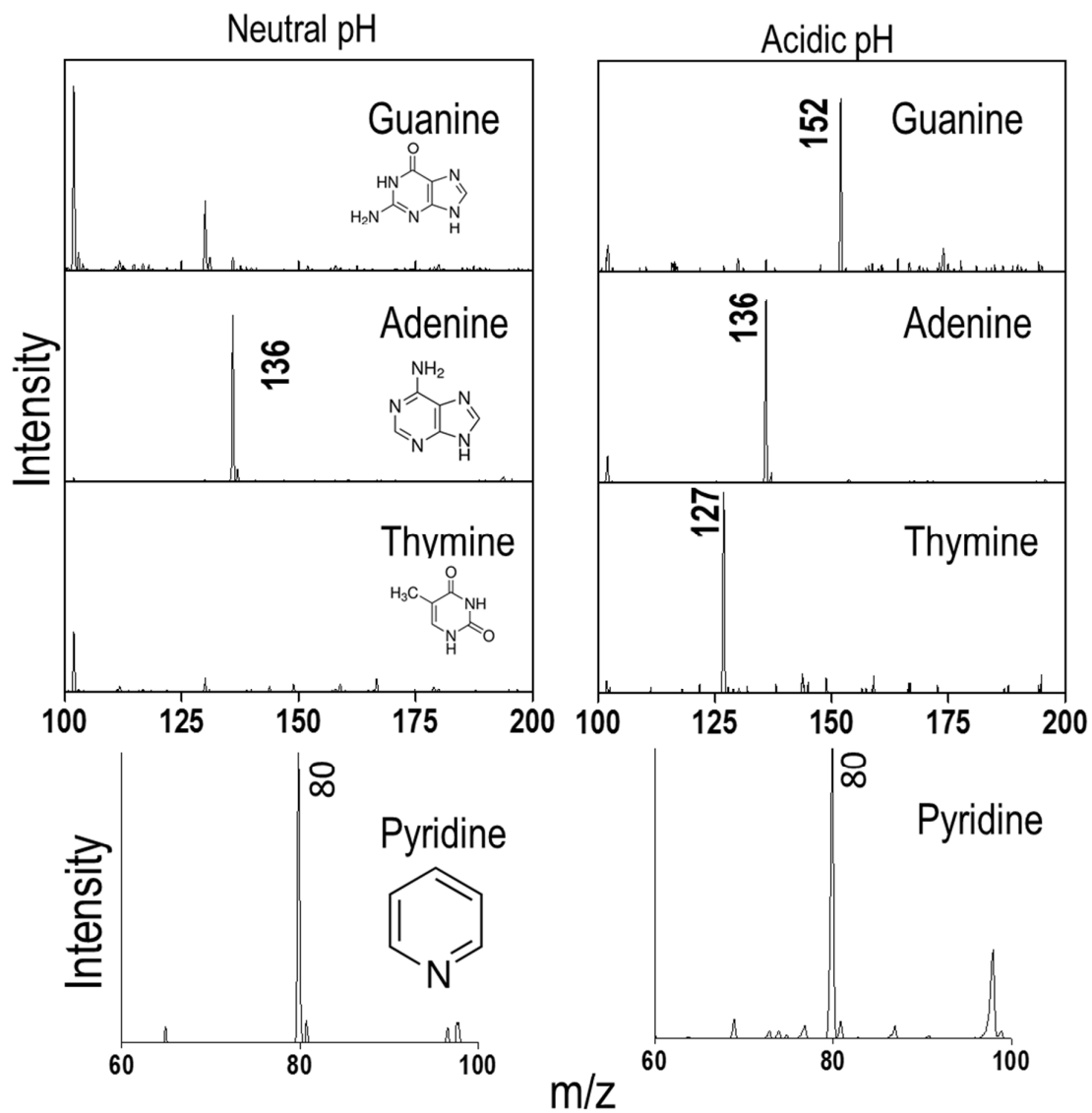


Figure S4: Analysis of aromatic heterocycles, guanine (top, m/z 152), adenine (middle, m/z 136), thymine (middle, m/z 127), and Pyridine (bottom, m/z 80) with 0 V paper spray under both neutral (left) and acidic conditions (right).

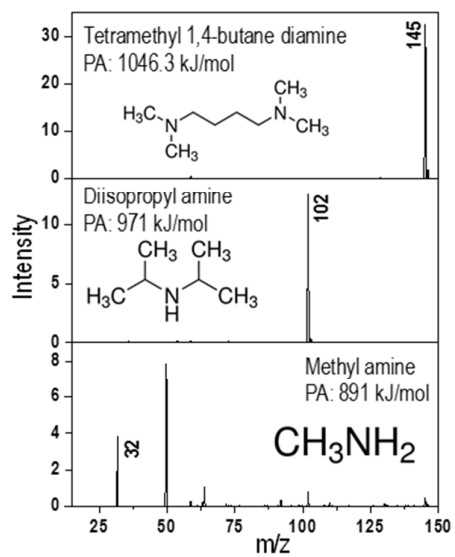


Figure S5: Analysis of three different amines. Tetramethyl-1,4-butanediamine (top, m/z 145), diisopropylamine (middle, m/z 102), and methyl amine (bottom, m/z 32). All samples are dissolved in methanol at neutral with pH 7. Proton affinities are obtained from NIST Webbook.

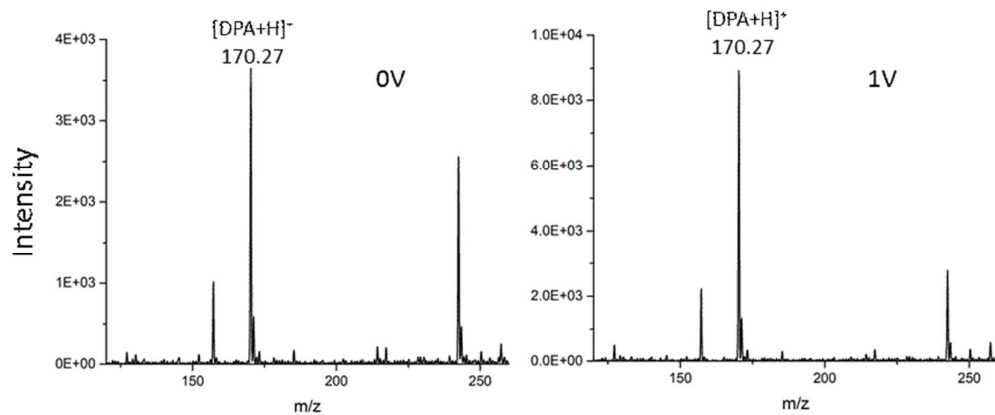


Figure S6: Mass spectra of 50 ppm diphenylamine (DPA) on a paper substrate at 0 V and 1 V, respectively. Note the difference in scales and the fact that the m/z 170 signal intensity is about 1.5 times higher than that at 0 V.

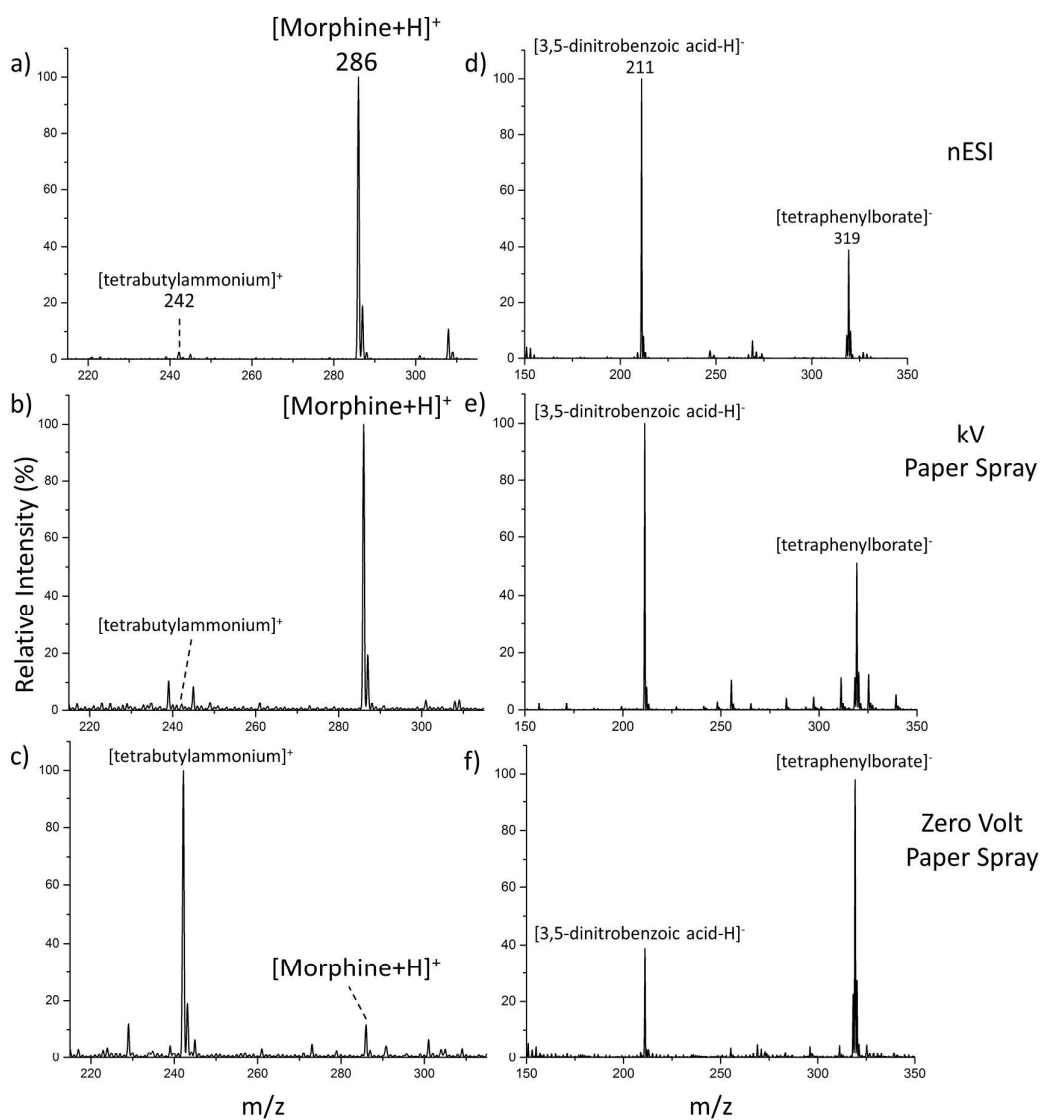


Figure S7: Mass spectra of 5 μ L of a mixture of 9 ppm morphine and 0.1 ppm tetrabutylammoniumiodide using a) nESI, b) kV PS, and c) zero volt PS. Mass spectra of 5 μ L of a mixture of 36 ppm 3,5-dinitrobenzoic acid and 5 ppm sodium tetraphenylborate using d) nESI, e) kV PS, and f) zero volt PS. The relative intensity of tetrabutylammonium signal to morphine in zero volt PS is much higher than in nESI and kV PS in both cases. The same is true of the ratio of tetraphenylborate to 3,5-dinitrobenzoic acid for zero volt PS as compared to nESI and kV PS.

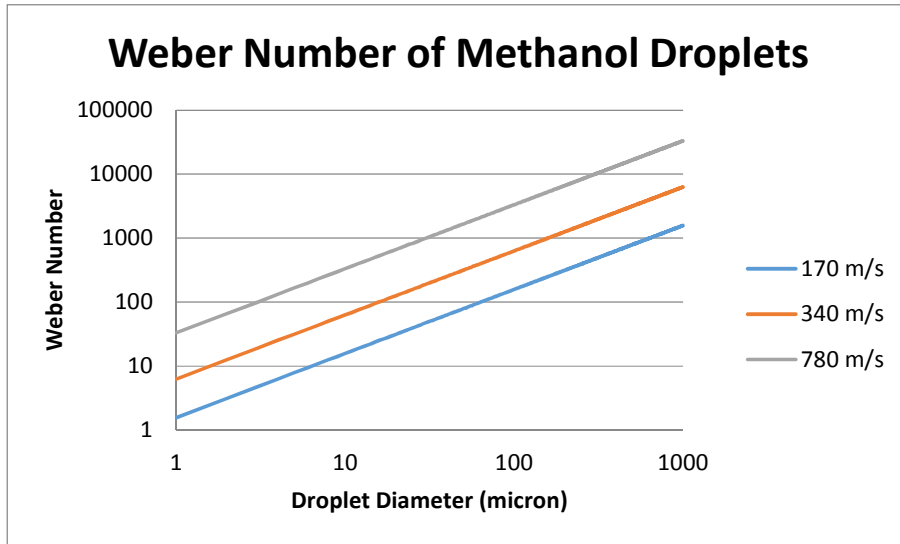


Figure S8. Simulation results of Weber number of methanol droplets. Using this information, it is assumed that droplets may have diameters between 1-4 μm after aerodynamic breakup.

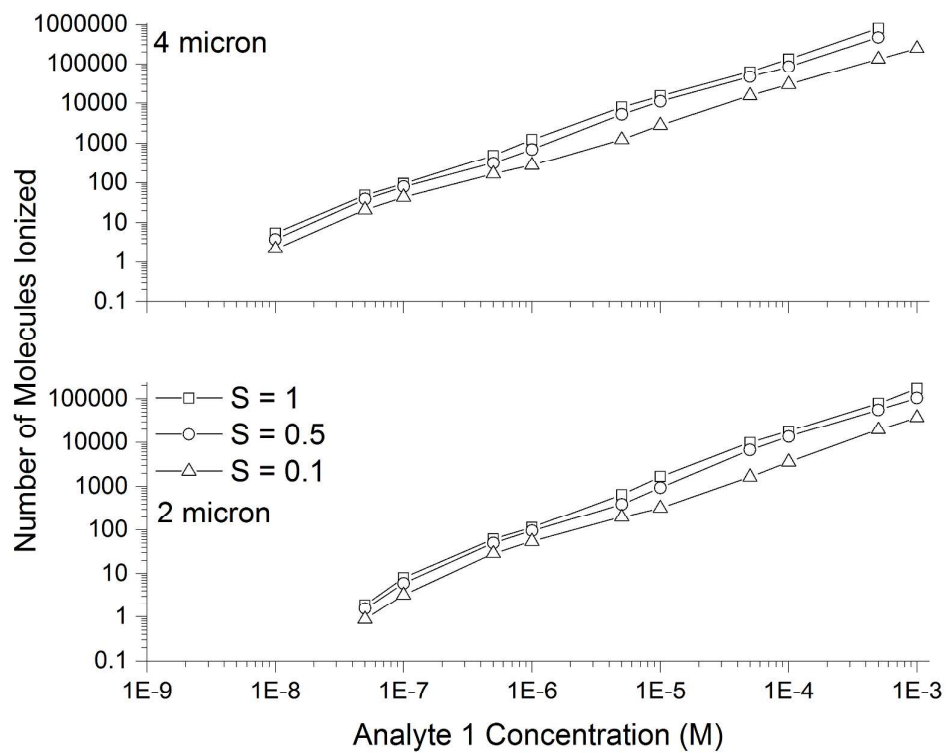


Figure S9. The number of ionized molecules vs. concentration for 2 micron (bottom) and 4 micron (top) droplets. The simulation was run at three different surface activities.

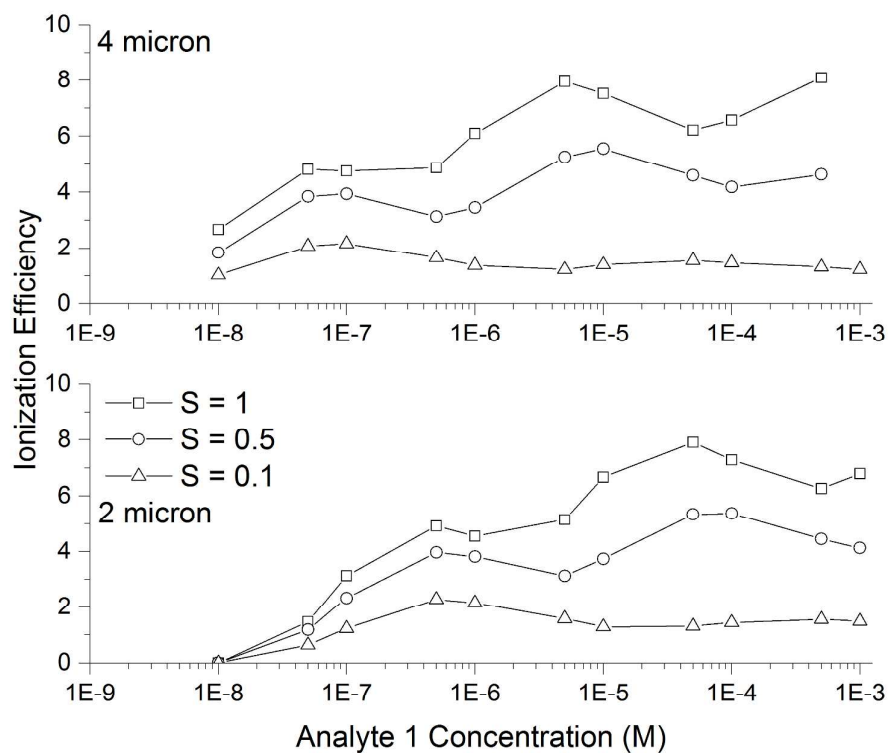


Figure S10. Ionization efficiency vs. concentration of 2 micron (bottom) and 4 micron (top) droplets. The simulation was run at three different surface activities.

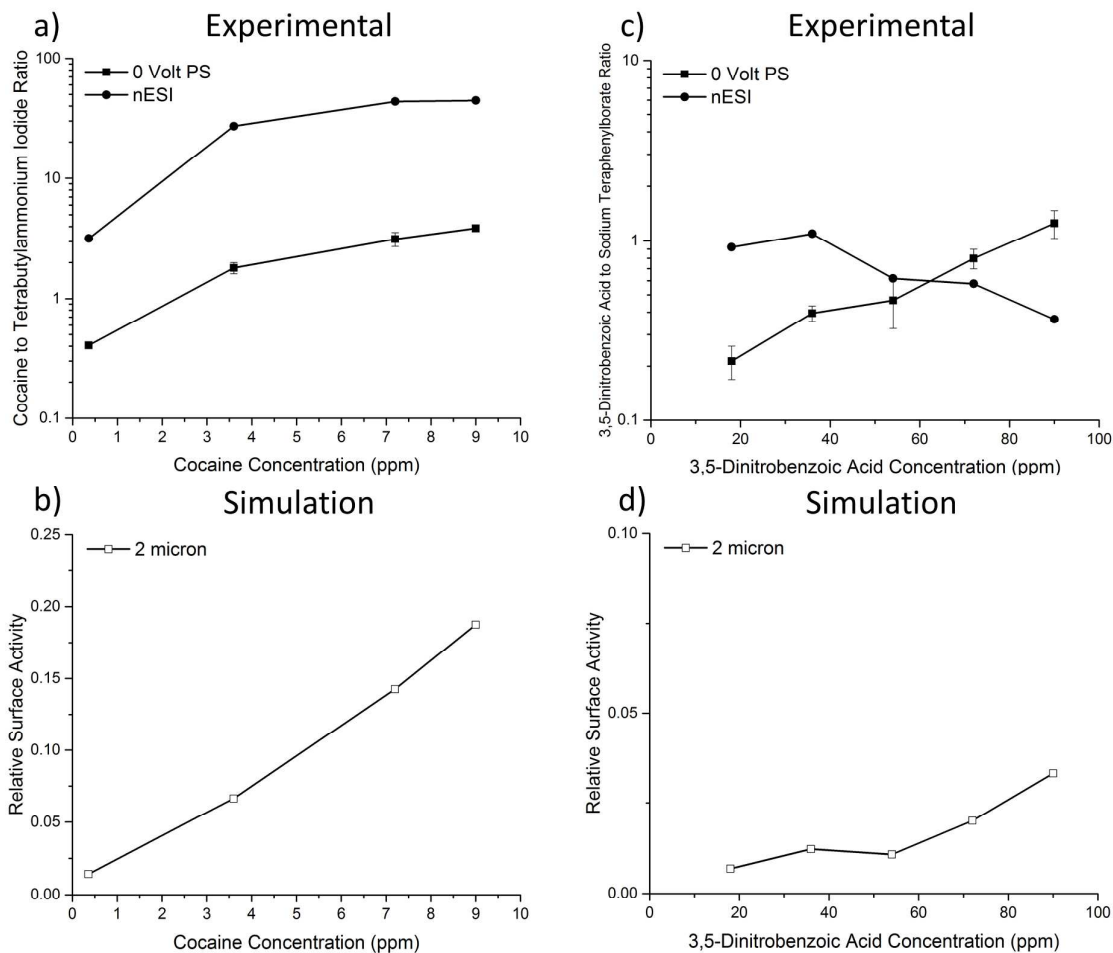


Figure S11. Cocaine to tetrabutylammonium iodide ratio dependence in positive ion mode for zero volt PS and nESI. a) Tetrabutylammonium iodide concentration is held constant at 0.1 ppm, while cocaine concentration changes. b) Relative surface activity of cocaine calculated to match the experimental ratio in part a). c) Sodium tetrphenylborate is held constant at 5 ppm, while 3,5-dinitrobenzoic acid concentration changes. d) Relative surface activity of 3,5-dinitrobenzoic acid calculated to fit experimental data in part c). Surface activity of the salt is assumed to be 1 for simulations.

Supplementary Movies:**Movie Captions:**

Supplementary Movie 1: This movie shows the analysis of 50 ppm tributylamine with zero volt paper spray. Continuous feeding at 15 $\mu\text{L}/\text{min}$ is used to feed the paper. With continuous feeding, a near continuous stream of droplets is observed entering the mass spectrometer inlet.

Supplementary Movie 2: Same as supplementary movie 1 but at $\frac{1}{4}$ speed.

Supplementary Movie 3: This movie shows the analysis of 50 ppm tributylamine with zero volt paper spray. Seven μL aliquot additions are added to the paper to cause generation of droplets. When solvent is added a group of droplet can be seen entering the mass spectrometer inlet.

Supplementary Movie 4: Same as supplementary movie 3 but at $\frac{1}{4}$ speed.

References:

- (1) Qian, H.-S.; Yu, S.-H.; Gong, J.-Y.; Luo, L.-B.; Fei, L.-f. *Langmuir* 2006, 22, 3830-3835.
- (2) Moon, G. D.; Lee, T. I.; Kim, B.; Chae, G.; Kim, J.; Kim, S.; Myoung, J.-M.; Jeong, U. *ACS Nano* 2011, 5, 8600-8612.
- (3) Zilch, L. W.; Maze, J. T.; Smith, J. W.; Ewing, G. E.; Jarrold, M. F. *The Journal of Physical Chemistry A* 2008, 112, 13352-13363.
- (4) Krzeczowski, S. A. *International Journal of Multiphase Flow* 1980, 6, 227-239.
- (5) Wierzba, A. *Experiments in Fluids* 1990, 9, 59-64.
- (6) Espy, R. D.; Muliadi, A. R.; Ouyang, Z.; Cooks, R. G. *International Journal of Mass Spectrometry* 2012, 325-327, 167-171.
- (7) Gibson, S. C.; Feigerle, C. S.; Cook, K. D. *Analytical Chemistry* 2013, 86, 464-472.
- (8) Merenbloom, S.; Flick, T.; Williams, E. J. *Am. Soc. Mass Spectrom.* 2012, 23, 553-562.
- (9) Konermann, L.; McAllister, R. G.; Metwally, H. *The Journal of Physical Chemistry B* 2014, 118, 12025-12033.
- (10) Gabelica, V.; Pauw, E. D. *Mass Spectrometry Reviews* 2005, 24, 566-587.
- (11) Rayleigh, L. *Philosophical Magazine Series 5* 1882, 14, 184-186.
- (12) Kebarle, P.; Verkerk, U. H. *Mass Spectrometry Reviews* 2009, 28, 898-917.
- (13) Lange, N. A.; Speight, J. G. *Lange's handbook of chemistry*, 16th ed.; McGraw-Hill: New York, 2005.
- (14) Jasper, J. J. *Journal of Physical and Chemical Reference Data* 1972, 1, 841-1010.
- (15) Fernández de la Mora, J. *Journal of Colloid and Interface Science* 1996, 178, 209-218.
- (16) Tang, K.; Smith, R. D. *International Journal of Mass Spectrometry* 1999, 185-187, 97-105.
- (17) Cech, N. B.; Enke, C. G. *Analytical Chemistry* 2001, 73, 4632-4639.
- (18) Chen, D.-R.; Pui, D. Y. H.; Kaufman, S. L. *Journal of Aerosol Science* 1995, 26, 963-977.
- (19) Konermann, L. *J. Am. Soc. Mass Spectrom.* 2009, 20, 496-506.
- (20) Kebarle, P.; Tang, L. *Analytical Chemistry* 1993, 65, 972A-986A.
- (21) Hogan Jr, C. J.; Biswas, P. *J. Am. Soc. Mass Spectrom.* 2008, 19, 1098-1107.

PAPER

CrossMark
click for updatesCite this: *RSC Adv.*, 2015, 5, 50512

Rapid detection of *Fusarium* wilt in basil (*Ocimum* sp.) leaves by desorption electrospray ionization mass spectrometry (DESI MS) imaging†

R. G. Hemalatha,^a Hemanta R. Naik,^a Vasundhara Mariappa^b and T. Pradeep^{*a}

Basil (*Ocimum* sp.), a medicinal herb is used fresh and/or dry in various (culinary, cosmetic and pharmaceutical) preparations. *Fusarium* wilt caused by the fungus *Fusarium oxysporum* f. sp. *basilici* is limiting basil cultivation in many countries. Since the leaf is the edible part in basil, new approaches are required to identify, and to prevent the spread of *Fusarium* pathogens. Desorption electrospray ionization mass spectrometry (DESI MS) was used for imaging thin layer chromatography (TLC) – imprints of leaves of three different species of basil (*Ocimum basilicum* L., *O. tenuiflorum* L., and *O. gratissimum* L.), and the molecular manifestations during *Fusarium* contamination are recorded. DESI MS images showed the chemotaxonomic differences of basil species and the changes in metabolite ion peaks during pathogen infection. Besides easy detection of reported toxic metabolite(s) of the pathogen(s), the results include molecular images showing spatial distribution of all coexisting surface-bound metabolites in plant leaves, their fragment ions, and the transient changes in their spatial distribution during *Fusarium* attack under natural conditions. Demonstration of the same protocol to image seedling, young/mature leaves, basil/other related plant (Patchouli – *Pogostemon cablin* (Blanco) Benth.), wilt/other disease symptoms shows that prior knowledge of the metabolite profile of the plant/pathogen is not required. This rapid detection method can be tailored to large scale screening programs for plant diseases suggesting potential implications in agriculture and quarantine requirements.

Received 19th December 2014
Accepted 20th May 2015

DOI: 10.1039/c4ra16706f

www.rsc.org/advances

Introduction

Mass spectrometry in natural product research is unraveling several unprecedented possibilities. From the traditional chemical ionization to the recent ambient ionization, various methods are available to analyze diverse classes of natural compounds.¹ With the advent of desorption electrospray ionization mass spectrometry, the capability of doing ionization outside the mass spectrometer under ambient/native conditions is largely exploited for developing various ambient ionization techniques.² While direct ambient ionization of intact plant material is demonstrated, certain ambient ionization methods like imprint imaging gives the spatial distribution of compounds in two or three dimensional space.³ Imaging mass spectrometry including desorption electrospray mass spectrometry (DESI MS) has been used to study microbes in cultures,^{4,5} but it is necessary to identify disease causing

pathogens in intact plant tissues to isolate contaminated planting materials, especially, in emergencies of disease epidemics like *Fusarium* wilt. The genus *Fusarium* includes several pathogenic fungal species,⁶ whose outbreak has caused huge economic loss in many crops. In this study, we demonstrate the rapid detection of *Fusarium* wilt contamination in leaves of different basil species by DESI MS imaging.

Basil (*Ocimum* sp.) is a traditional, revered home-grown plant with long history of use and cultivation in India. The commercial success of sweet basil (*Ocimum basilicum* L.) as a culinary herb is evident from its widespread use in various popular cuisines. Its quick growing habit and suitability for different climatic conditions has promoted its large scale cultivation, worldwide.⁷ A number of domestic cultivars, breeding lines and hybrids are available with variety of unique aromas/tastes (like clove, citrus, camphor, cinnamon, licorice, etc.) giving them special market price and export quality.⁸ Essential oils, polyphenols, flavonoids and other bioactive molecules in them are commercially exploited as flavoring agents and in perfumes, cosmetics and pharmaceutical preparations.

Fusarium wilt is a production constraint in basil and its occurrence is reported from different parts of the world.⁹ The disease is caused by *Fusarium oxysporum* f. sp. *basilica* (Fob). It is one among the 120 host-specific, individual strains (formae species) of the wilt pathogen, *Fusarium oxysporum* (Fox).¹⁰ The

^aDST Unit on Nanoscience and Thematic Unit of Excellence, Department of Chemistry, Indian Institute of Technology Madras, Chennai, India. E-mail: pradeep@iitm.ac.in; Fax: +91-44-2257-0509; +91-44-2257-0545; Tel: +91-44-22574208

^bMedicinal and Aromatic Section, Department of Horticulture, University of Agricultural Sciences, Bangalore, India

† Electronic supplementary information (ESI) available. See DOI: 10.1039/c4ra16706f

presence of *Fusarium* pathogenic fungal species complex in the common environment causes diseases (like keratitis, fusariosis etc.), in human and animals.^{11,12} The pathogenic species is identified by polymerase chain reaction (PCR) and other molecular methods.¹³ *Fusarium* remains dormant in soil for decades and comes to life on finding a suitable host. The symptomless infection present in plant parts spread through planting materials, irrigation water, farm tools, drainages, etc. The control measures taken up with chemical pesticides and sterilization of soil are inefficient. Resistance to *Fusarium* wilt is searched in accessions of *Ocimum* species and resistant basil varieties have been developed.^{14,15} Planting resistant varieties have also been challenged by new pathogenic races of *Fusarium*, which has resulted in recurrence of *Fusarium* epidemics in several crops including banana and cereals.¹⁶ Besides, aerial dissemination of the pathogens through the infected basil foliage is a major concern.¹⁷ Exceptionally low level of inoculum found in healthy leaves and seeds would introduce the pathogen into a new host or new geographical area. The major concern is that market demand for fresh, green basil leaves remains high; every day tons of basil leaves are transported and used fresh or dry, or extracted/macerated to enhance the flavor of herbal teas, food ingredients and oil.¹⁸ The changes reflected in the preparations, made from infected basil leaves remain elusive. Also, the effect of Fob on human health is not known. Hence, in this study, mass spectrometry based imaging method is demonstrated for rapid detection of *Fusarium* contamination in basil leaves under ambient conditions. Here three different aspects were addressed: the chemotaxonomic differences among three different basil species (*Ocimum basilicum* L., *O. tenuiflorum* L. and *O. gratissimum* L.) grown in natural conditions were unraveled, by imaging the TLC-imprints of their leaves using DESI MS. Likewise, *Fusarium* contaminated leaves were imaged under ambient conditions to delineate them from the healthy ones in all selected basil species. The suitability of the method in screening other related plant/disease is illustrated with Patchouli (*Pogostemon cablin*).

Experimental

Plant material

Two basil species, namely, *O. basilicum* L. and *O. tenuiflorum* L. (syn. *O. sanctum* L.) growing under natural conditions in the Indian Institute of Technology Madras (IITM) campus were used for the study. Young seedlings of Clove basil (*O. gratissimum* L.) and Patchouli (*Pogostemon cablin* (Blanco) Benth.) collected from University of Agricultural Sciences (UAS) campus, Bangalore were grown in a nursery at IITM campus. The study period was from March 2012 to October 2014.

Scanning electron microscopy

The morphology of the lower side of the healthy and *Fusarium* wilt infected leaf of basil and patchouli were observed by scanning electron microscopy (SEM) (FEI QUANTA-200). A small portion of the leaf with and without wilt symptom was fixed on the top of aluminium stub using double sided carbon tape. In

order to minimize the charging effect, SEM measurements were done using the environmental mode with a large field detector.

DESI MS imaging

A Thermo-Fisher Scientific LTQ ion trap mass spectrometer equipped with a DESI ion source was used for the study. Two TLC plates were cut in proportion to the size of the selected, detached leaf; with the leaf placed in between and sandwiched with tissue papers, TLC-imprints were made by applying a pressure of 1–4 tons for 5–10 s. Further details on the method of TLC-imprinting and the chemicals required for imaging are explained in our previous report.¹⁹ DESI MS images were acquired by continuously moving the surface beneath the spray at a constant speed, over the whole TLC-imprinted surface on a row-by-row basis (as shown in TOC graphic). The pixel size (250 × 250 μm) was determined by the total scan time of the mass spectra and the x–y scanner speed. Two operation modes (both negative and positive) and a mass range of *m/z* 50–2000 was used for imaging. Three different solvents (methanol, acetonitrile and chloroform) were used for optimization of the protocol. Elaborate details on processing and interpretation of acquired data with spectrum search tool of online databases were given in our previous report.¹⁹ For this study, the acquired data was also processed using MZmine, open-source software.²⁰

Results and discussion

The antibacterial and antifungal activities of *Ocimum* sp. are well known,²¹ but its susceptibility to *Fusarium* wilt has to be understood in detail to prevent outbreak of the disease. To check the reactions of resistance/susceptibility, in this study, three species of basil and patchouli were grown outdoors at IIT campus, in the same soil next to each other. No known chemical control was applied for *Fusarium* wilt, and resistant varieties were not planted. The selected plant species were grown under natural conditions, with no external application of manures, chemical fungicides or bio-control agents. Though commercial kits are developed for molecular identification of types of *Fusarium* pathogen present in the soil, they require technical knowledge.²² Therefore, customized methods suitable for rapid detection of contaminated leaves within hours is focused for this study. Here, the predominant metabolite ion peaks present on the leaves of healthy *versus* infected ones were compared and the contaminated ones were rapidly identified. To understand the metabolic state of the plant at any given time of pathogen infection, the spatial distribution of untargeted metabolite profile in a healthy leaf for a select mass range was used as base information to identify the infected/contaminated leaves.

The predominant metabolite profile of the selected basil species and patchouli were recorded using TLC-imprints of fresh leaves, as explained in our previous report,¹⁹ Both positive and negative ionization mode data were collected for each species. As the data acquired are voluminous, the peaks that eluted using methanol as spray solvent in the mass range of *m/z* 50–1000 from positive ionization mode alone are given in this manuscript. Fig. 1A and B and 2A–E show the DESI MS spectra

and images for spatial distribution of predominant metabolites of healthy leaf in control plants of all selected species. Illustrations given here show the similarities and variations in metabolite profile within a single leaf (*O. basilicum*-Fig. 1A and B), between young and mature leaf of same species-*O. gratissimum* (Fig. 2C and D), variations within *Ocimum* genus (Fig. 1A, B and 2A–D) and between genus (*Ocimum* and *Pogostemon*-Fig. 1A, 2A–C and E).

It is possible to identify the similarities and differences of the upper and lower leaf surfaces of a single leaf by imaging their TLC-imprints separately. Insets in Fig. 1A(a and b) show the TLC-imprints of upper and lower surfaces, respectively of a single leaf of *O. basilicum*. The corresponding DESI MS images in insets (c and d) of Fig. 1A show the faithful reproduction of TLC-imprints of the upper and lower surfaces as molecular images. As shown in Fig. 1B, the TLC-imprint of the upper leaf surface does not contain any venation pattern; but, on imaging that imprint, vein like spatial distribution was observed in DESI MS images for the metabolite ions m/z 201 and m/z 365 whereas for the ion m/z 797 (Fig. 1B) was exactly similar to the imprint as shown in Fig. 1B; this is an illustration to show that these molecular images are not artifacts. Moreover, it is possible to identify some new information by DESI MS which are not detected by conventional measurements using extracts. An example is the finer molecular detail present on the leaf margin as shown in DESI MS images for m/z 405, m/z 489 in Fig. 1B. Leaf margin (Fig. S1A†) is one of the diagnostic leaf characteristics to categorize some plant species including basil by the morphological features;^{23a} so far molecular methods are used to distinguish physical similarities.^{23b}

The leaves of *O. tenuiflorum* and *O. basilicum* look similar and have to be differentiated based on the colors of their inflorescences (Fig. S1B†). The advantage of DESI MS imaging is that the molecular differences can be identified at any stage of plant growth, without waiting for the flowering stage; here the molecular similarities and differences were understood by comparing the predominant peaks of both species of *O. tenuiflorum* and *O. basilicum* (Fig. 1A and 2A). There were overlaps found in metabolite ions for several major (m/z 201 and m/z 378) and minor peaks (m/z 104, 197, 365, 797, etc.). *De novo* sequencing and transcriptomics information available for *O. basilicum* and *O. tenuiflorum* confirms the presence of transcripts responsible for such similarities and differences in the metabolite profiles.²⁴ In this study, the characteristic predominant peaks for each species of basil are unique (for example m/z 349 for *O. gratissimum*, m/z 378 for *O. tenuiflorum* and m/z 201 for *O. basilicum*), which were used as markers to identify each basil species in further experiments. The reproducibility of these results was confirmed using samples collected from other growing areas for all selected species. It is interesting to note that samples picked from a local market also showed a similar spatial distribution of metabolites; an example is shown in Fig. S2,† wherein the spatial distribution of m/z 104, m/z 197, m/z 797 are similar to those given in Fig. 1A and B. Hence, besides identifying similarities, the predominant peak(s) may be used as unique molecular signatures/metabolite markers in plant species identification.

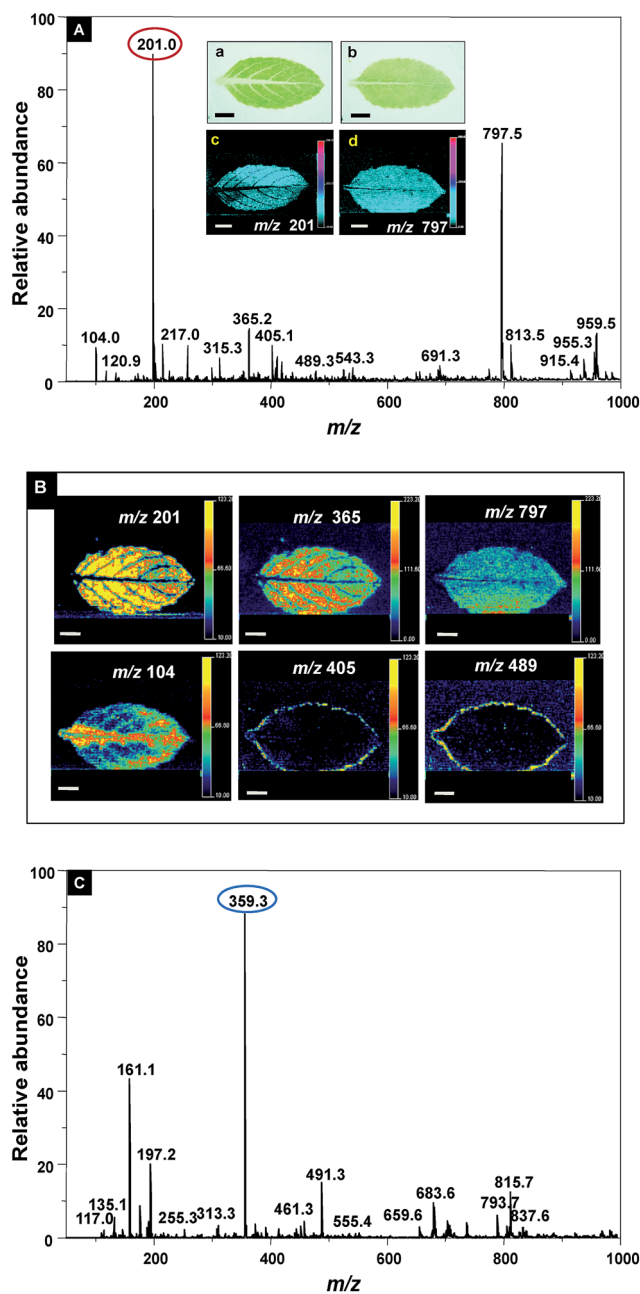


Fig. 1 DESI MS spectrum (A) and images (B) showing the predominant metabolites on the leaf of *O. basilicum*. Spectra shows the predominant metabolite peaks in positive (A) and negative (C) ionization mode, eluted in the mass range of m/z 50–1000 using methanol as spray solvent. Peak(s) which can be used for basil species identification is encircled. Insets in A shows the photographs of TLC-imprints of lower (a) and upper (b) surface of the basil leaf, and the corresponding DESI MS images for the ion m/z 201 and 797 of lower (c) and upper (d) surface are shown below. (B). Images corresponding to various ions from the upper surface of the leaf. The scale is uniform in all the images (5 mm). The major peaks where differences are seen are highlighted as DESI MS images.

Solvent plays a major role in the elution of each category of the compound.²⁵ When different solvents (methanol, acetonitrile, chloroform) were used, there were differences in metabolite profile recorded, as shown in Fig. 3A for *O. gratissimum*.

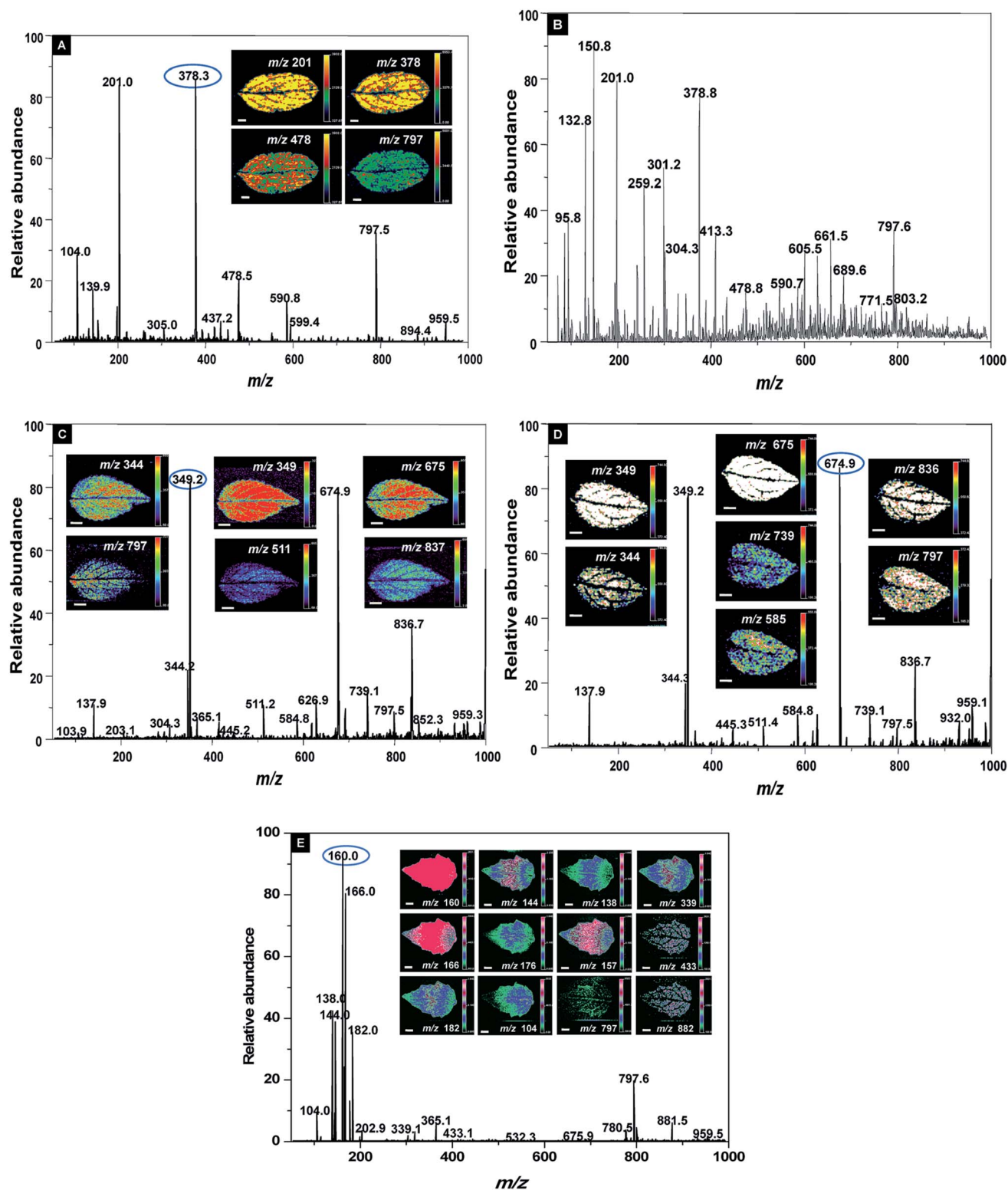


Fig. 2 DESI MS spectra and images showing the variations in predominant metabolites using (A) TLC-imprint, (B) direct detection from detached leaf of *O. tenuiflorum*. Other illustrations are showing variations between (C) mature leaf versus (D) young leaf of *O. gratissimum* and (E) *P. cablin*. The scale is uniform in all the images (5 mm). Predominant peak representing species identity is encircled. The major peaks where differences in spatial distribution are seen are highlighted as DESI MS images.

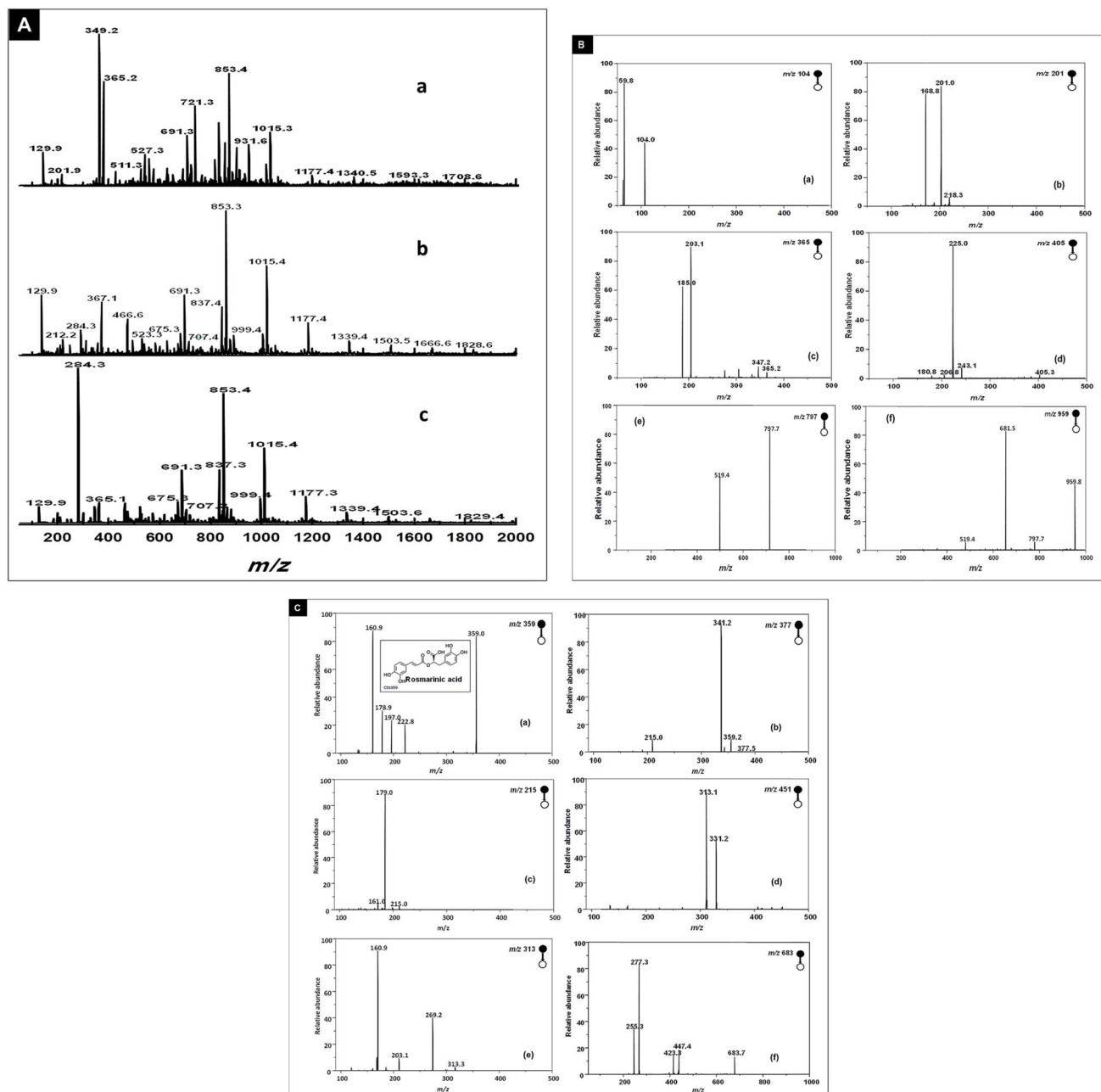


Fig. 3 ESI MS mass spectra (A) showing differences in metabolite profile of the leaf of *O. gratissimum* due to solvents (a-methanol, b-acetonitrile and c-chloroform). ESI MS-tandem mass spectra for selected metabolite ion peaks of leaf of *O. basilicum* in positive (B) and negative (C) ionization mode.

Illustrations with *O. gratissimum* show the differences in the metabolite profiles between DESI MS of leaf imprint (Fig. 2C) and ESI MS from leaf extract (Fig. 3A(a-c)). Besides, there were differences between the metabolite profile of TLC-imprint (Fig. 2A) and that of a direct leaf tissue (Fig. 2B). As reported with barley leaf,^{3b} the detached leaves of basil became dry and deformed quickly; hence, imprint imaging was followed for the study.

The metabolite distribution can be acquired in positive and negative ionization modes, as illustrated with *O. basilicum* (Fig. 1A and C). Tandem mass spectral imaging was done on respective ionization modes to get the fragmentation pattern for

identification of the predominant metabolite ion peaks. Few examples are shown in Fig. 3B and C. Elaborate details for finding metabolite adducts and matching tandem mass spectral data using database search is given in our previous report.¹⁹ For this study, the data acquired were also analyzed using MZmine software,²⁰ which has various processing algorithms for peak picking, base line correction *etc.* Peak lists were created and searched against the online databases. Different biomolecules tentatively identified by MZmine in this study include several terpene alcohols, fatty acids, phenolic and flavonoid glycosides *etc.* Literature abounds with gas or liquid chromatography based

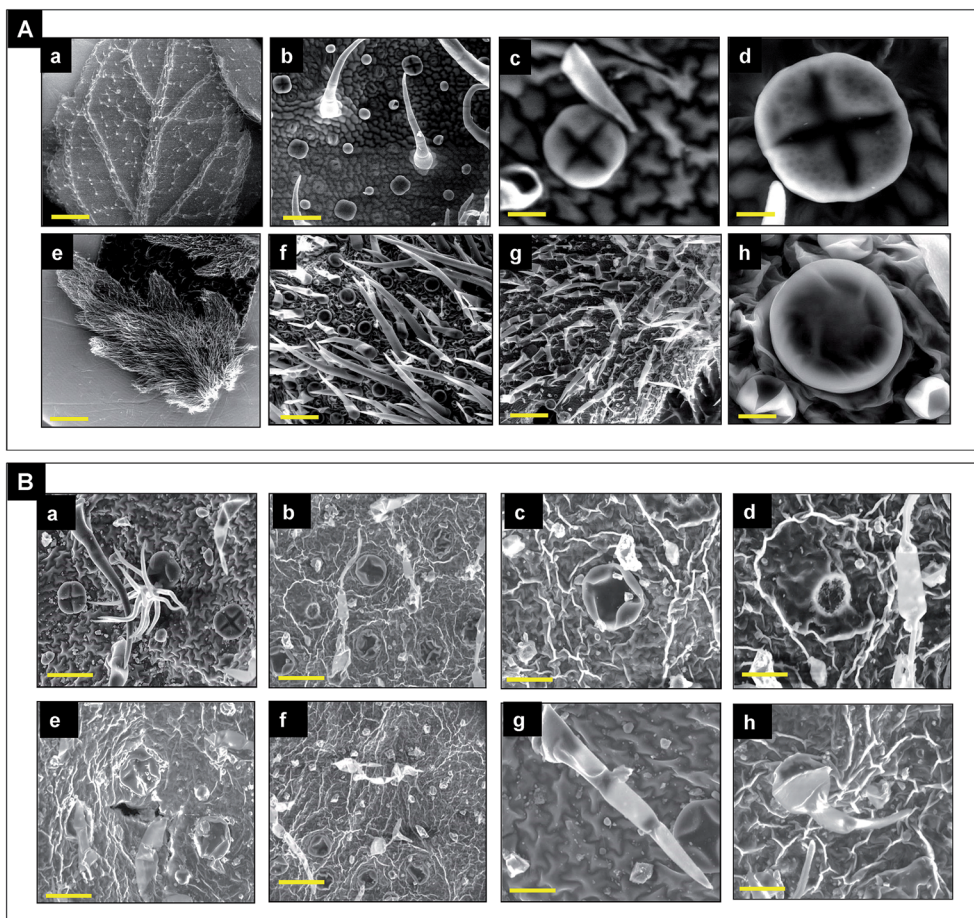


Fig. 4 Scanning electron micrographs of (A) healthy leaf of basil (a–d) and patchouli (e–h) showing trichomes and peltate glands at different magnifications. (B) *Fusarium* infected leaf showing the disease affected peltate gland and trichomes (a–h). The scale for images a and e are 500 μm and other images are 20–100 μm .

mass spectrometric (MS) methods on various bioactive molecules (essential oils, phenolic compounds, flavonoids, *etc.*) in different basil species with their tandem mass spectral data.²⁶ Most of the studies to date on basil have tabulated information on both positive and negative ions of phenolics, flavonoids and essential oils, *etc.*²⁷ So far, preferential detection/extraction of such bioactive compounds have specific requirements of suitable solvents and other instrumental parameters; if those parameters are adapted it is easy to identify the spatial distribution of any targeted metabolite.

As reported,^{26,27} different phenolic compounds were detected in negative ionization mode; here (a) in Fig. 3C shows the fragmentation data for the predominant metabolite peak at m/z 359 in negative ion mode (Fig. 1B), which was identified as rosmarinic acid when the data were analyzed using search tool of databases. Likewise, several metabolites of different pathways (like phenylpropanoid, terpenoids, flavonoids, lipids and fatty acids *etc.*) were identified in this study. Examples are isoeugenol (m/z 165), caffeoyl alcohol (m/z 167), gallic acid (m/z 169), caffeic acid (m/z 179), ferulic acid (m/z 193), syringic acid (m/z 197), 5-hydroxy coniferyl alcohol (m/z 197), quercetin (m/z 301), *etc.* Here, the method highlights a possibility to identify the diversity of compounds as untargeted metabolite profiles

comprising of various classes of small molecular metabolites, without the need for internal standards. There are various factors such as growth stages, seasonal variation, irrigation water, drying, and storage, *etc.*^{28–30} and even, the position of leaf within the same plant could vary in the chemical composition.³¹ It is always difficult to identify and understand transient changes of the eluted metabolite peaks. Here we show that DESI MS imaging gives a snapshot of the transient changes due to the environment stress or any physiological factors.

Conventional identification of *Fusarium* wilt at the field level is time consuming since it involves the accumulation of the pathogen to a sufficient level that can produce visible symptoms. External manifestation of wilt disease as chlorotic leaves, drying leaf tips and stunted growth of plants, wilting of shoots, *etc.*, may overlap with water stress or other diseases. Though wilt disease in basil and patchouli display similar morphological features, wilt in patchouli is caused by *F. solani*.³² Visual differences between healthy and infected leaves are obvious only in advanced stages of infection. Confocal microscopy and thermal imaging^{33,34} were used to image the growth of *Fusarium* pathogen. Scanning electron microscope was used for this study, to observe the changes in the peltate glands and trichomes of both basil and patchouli leaves, as shown in Fig. 4A(a–f).

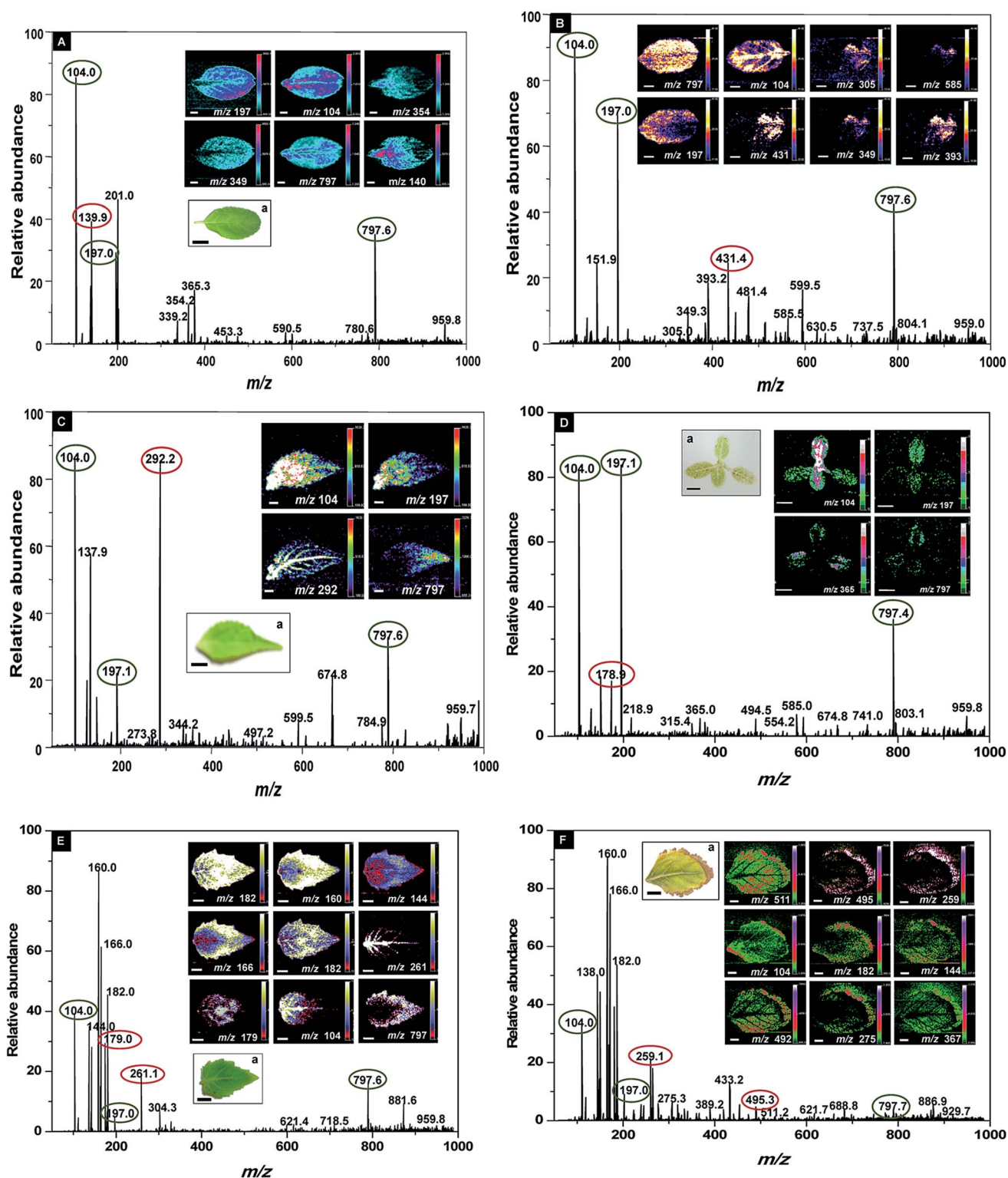


Fig. 5 DESI MS spectra and images showing the changes in predominant metabolites due to *Fusarium* infection in apparently healthy, asymptomatic (A) young leaf, (B) mature leaf of *O. basilicum*, (C) young leaf of *O. gratissimum*, (D) seedling of *O. basilicum* at four leaved stage, (E) asymptomatic young leaf of *P. cablin* and (F) mature leaf of *P. cablin* with visible symptom. Inset (a) in A, C and E shows the photograph of the apparent healthy young leaves used for DESI MS imaging. Inset (a) in D shows the upper surface of TLC-imprint of four leaved seedling of basil. Inset (a) in F is the upper surface of infected leaf showing brown discoloration on the margins. The scale is uniform in all the images (5 mm). The major peaks showing differences in spatial distribution are highlighted in the spectra with black and the fungal toxic metabolite peaks are highlighted with red circles.

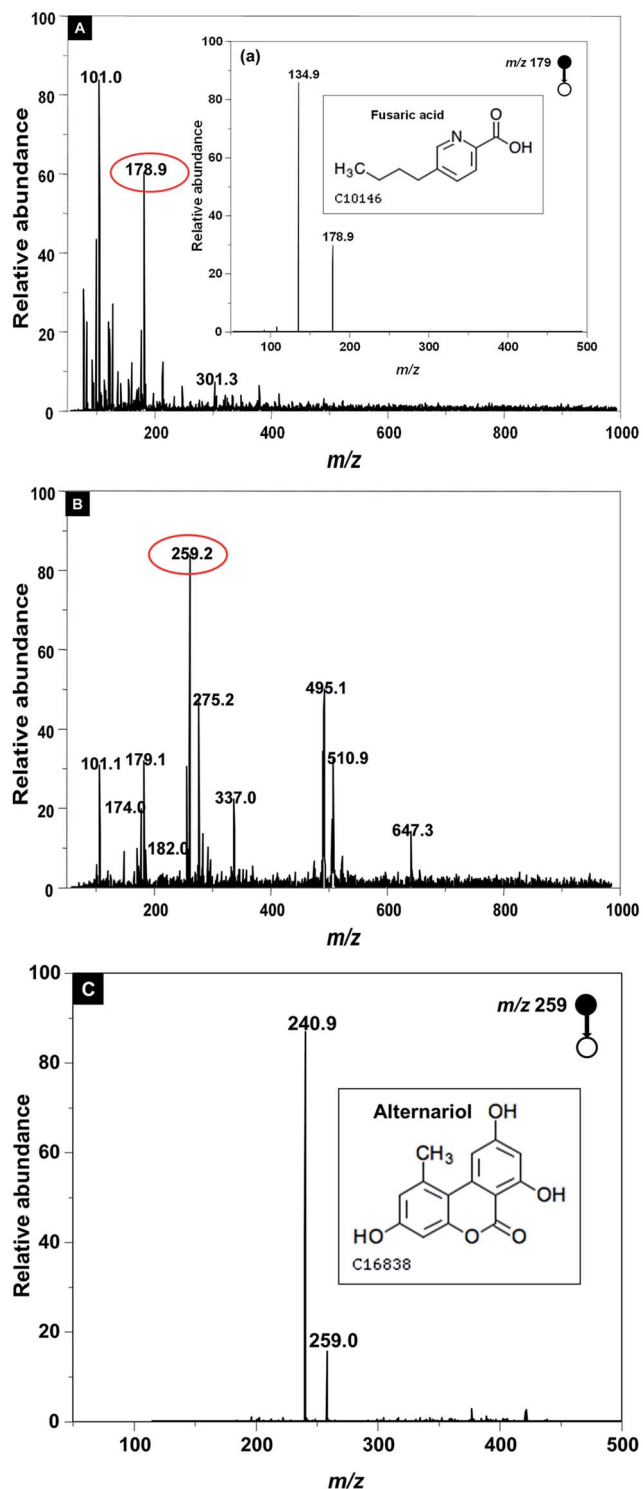


Fig. 6 DESI MS spectrum showing the toxic metabolites due to *Fusarium* (A) *Alternaria* (B) infection; spectrum extracted after subtraction of predominant metabolites peaks of apparently healthy, asymptomatic leaf of *O. basilicum* and *P. cablin*. Insets (a) and (C) show the fragmentation patterns of fusaric acid (m/z 179) and alternariol (m/z 259) respectively.

Both patchouli and basil species have many common features and in particular, terpenoids and phenylpropanoids compounds are reported to be stored in the peltate glands found on the leaf

epidermis.³⁵ The variations in the metabolite profile of basil and patchouli may be due to diversities in the terpenes and phenylpropanoids and the substrate specificity of different enzymes contribute to the production of complex blend of oxygenated linalool derivatives.^{36,37} As shown in (e) of Fig. 4A, young leaf of patchouli has trichomes in high density. During pathogen infection (Fig. 4B), there were necrotic spots in the trichomes and the peltate glands seem to have dilated. It is not feasible to use electron microscope for large scale screening purpose.

The challenge is that apparently healthy leaves that are asymptomatic carriers of the disease have to be identified by accurate, reliable and rapid detection methods. Hence both mature and young leaves showing no visible symptoms were selected for imaging, to identify the *Fusarium* contamination. Illustrations with clove basil given in Fig. 2C and D show that there is slight difference in metabolite profiles of young *versus* mature leaf of healthy plants. Small, apical leaves have a higher density of glands and trichomes (Fig. 4A). Small leaved varieties were reported to be susceptible to the disease.¹⁴ Hence, small, apical leaves with no visible symptoms (insets 'a' of Fig. 5A) were imaged in all selected plants. Typical plant metabolites that could serve as markers are given as DESI MS images (Fig. 5A–C).

Fig. 5B show the DESI MS images of *Fusarium* infected asymptomatic mature leaf of *O. basilicum*. Comparison of young *versus* mature infected basil leaf (Fig. 5A and B) show that a few metabolite ions (m/z 104, 197, 797, etc.) were present in both. Subtraction of metabolite peaks of healthy *versus* contaminated leaf of basil clearly indicated the presence of few metabolites including a metabolite peak at m/z 179, as shown in Fig. 6A. Tandem mass spectrometry along with database search was done and the ion peak at m/z 179 was identified as fusaric acid,³⁸ the primary toxic metabolite of any *Fusarium* pathogenic species. Hence the identification of such characteristic toxic metabolite peaks and their images can delineate the healthy leaf from the contaminated ones. All the three species varied in their responses to *Fusarium*. Spectra of *O. gratissimum* exhibited several other ions assignable to *Fusarium* (m/z 292) besides that corresponding to fusaric acid (m/z 179). In contrast, *O. tenuiflorum* DESI MS spectra did not display any ion corresponding to a known *Fusarium* metabolite. The intensity and spatial distribution of some metabolite ion peaks of the plant also got changed during pathogen infection as observed in all the three *Ocimum* species (Fig. 5A–D). There is species-specific responses to *Fusarium* infection, but several metabolites being common to all the three basil species (like m/z 104, 197, 797), were observed. Several metabolites and genes common in phenylpropanoid pathway is reported in basil or other species of Lamiaceae^{35,36} and the expression of few genes get altered during *Fusarium* infection.^{39a} Changes at germination or seedling stage due to *Fusarium* infection also reported.^{39b} Since the small sized basil seeds and even hydroponically grown basil also bear the *Fusarium* pathogen,¹³ the emerging seedling may contain the symptom; hence, growing seedlings of basil (Fig. S1C†) at four leaved stage was imaged. Fig. 5D shows the spectrum and DESI MS images for the four leaved seedling highlighting the reliability of the imaging method to screen plant leaves collected at any development stage.

The feasibility of extending this protocol to other related plant species/disease is also verified (Fig. 5E and F). In particular, very specific visible symptoms like brown, dried edges on leaf margin often overlap with nutrient stress and/or pathogenic infections. Fig. 5E shows the spectrum and images of an asymptomatic young leaf of patchouli. A mature leaf of patchouli with such visible symptom of brown, dry patches on the leaf margin is imaged and the results are given in Fig. 5F. As shown in inset 'a' of Fig. 5F, the corresponding DESI MS images (Fig. 5F) are very specific in locating the spot of infection. On comparing the contaminated leaf of patchouli (both Fig. 5E and F), with metabolite profile of healthy leaf (Fig. 2C), the predominant metabolite peaks (m/z 104, 144, 176, 182) and their DESI MS images were present in all. In Fig. 5F, DESI MS images of particular metabolite ions (m/z 259, 275, 495, 511) revealed the spatial location of the disease symptom, which were not visible in the TLC-imprint. Tandem mass spectrometry of metabolite ion m/z 259 gave fragment ions at m/z 241, which is identified as alternariol with database search (Fig. 6C). Alternariol is the primary toxin produced by pathogenic fungal species *Alternaria*, and in particular, the occurrence of *Alternaria* infection in basil is reported.⁴⁰ As shown in Fig. 5F, though the intensities of the peaks at m/z 492, 367, 511 were below 10%, still they could be extracted by subtraction of spectra of healthy versus contaminated ones (Fig. 6B). This shows the possibility to image the molecules particularly induced at the site of infection/inter junction, which may be a fungal toxic metabolite or a phytoalexin. It is reported that reddish brown color in pathogen affected area of leaf may be due to flavonoid phytoalexin namely, 3-deoxyanthocyanidins.⁴¹

Comparison of metabolite profiles in contaminated leaves of all the selected plants showed the presence of either or both toxic metabolite peaks *viz.*, fusaric acid (m/z 179) and alternariol (m/z 259), though the presence of other toxic metabolites (like altenuene, altenusin, tenuazoic acid, fusarenone-x *etc.*) were also identified using literature and database search.⁴² ESI Table S1† shows the details on molecular weight, structure, database reference *etc.*, for some of these toxic metabolites. Tandem mass spectral imaging of few of them (m/z 197, 261, 291, 293, *etc.*) showing relationships with each other is given in ESI Fig. S3.† For some of them it was difficult to assign the relationships or do further MSⁿ, because the presence of these metabolites was observed in images but the mass spectral intensity of the peak was below 10% (Fig. 5F). The basic methods for statistical analysis like principal component analysis and log-ratio plot analysis of the healthy and *Fusarium* infected plant samples were done using MZmine software. We checked our results with and without applying statistics and other algorithms; the results on DESI MS imaging are voluminous. Only a few images which are relevant to detection of pathogen contamination are presented in this manuscript. Some of the peaks showing disease symptoms or the intermediate reactions were of very low intensity, though their DESI MS images existed; hence the results given here are without any statistics and background correction. For this study, though we identified some metabolites we did not quantify them because there are no synthetic standard available for different

intermediate and interaction metabolites produced in the leaves during plant pathogen interactions. Hence the results shown here are pertaining only to the qualitative description; additional experiments are required to identify the specific *Fusarium* isolates and *Fusarium*-induced metabolite changes. But for rapid detection, it is relevant to check the presence of fusaric acid (m/z 179) and alternariol (m/z 259).^{38,40} These two metabolites are the principal toxic metabolites of *Fusarium* and *Alternaria*, from which other toxic metabolite ions are produced based on the local environment of the plant or pathogen. Hence, this method of DESI MS imaging is a rapid way to screen the leaves and can be interpreted even by nontechnical persons.

As observed in this study, several fungal metabolites including fusaric acid (m/z 179) and alternariol (m/z 259), are normally detected in positive ionization mode. Mass spectrometry is routinely used for the identification of different mycotoxins (the secondary metabolites produced by *Fusarium* fungi) in food and feed, that causes mycotoxicosis in humans and animals upon ingestion or inhalation.⁴² But it is challenging to determine which metabolite(s) may be responsible for the interaction or infection in plants, under natural growth conditions. Studies show that different metabolic pathways (like pectin, phenylpropanoid and carotenoid) get altered, and various signaling molecules like salicylic acid, methyl jasmonates and peroxidase enzymes are reported as inducing resistance to *Fusarium* in various plants.^{43,44}

Isolation of *Fusarium* species or its toxin(s) from the infected leaf was not attempted in this study, because it is reported that species of *Fusarium* which is nonpathogenic in one plant species may be pathogenic to other.⁴⁵ Besides, different strains or formae species of *Fusarium oxysporum* cannot be distinguished reliably in culture.⁴⁶ Even under controlled experimental conditions, with the inoculation of known strains of the pathogens in barley,⁴⁷ there were differences in the metabolites (like cinnamic acid, sinapoyl alcohol, coniferin, catechin and naringin) induced by trichothecene producing strain and its trichothecene non-producing mutant, thereby differentially regulating defense pathways associated with different resistant levels. In that context, for rapid detection we focused on toxic metabolite ions rather than looking for up/down regulated plant metabolites. Also, *Fusarium* wilt pathogen is reported to produce both toxic and nontoxic metabolites. The levels of contamination of banana fruits with *Fusarium oxysporum* f.sp. *cubense* (Foc) were reported to be too low, to be of concern to humans but appeared to contribute to the pathogenicity of the fungus during infection of banana plants.⁴⁸ For identifying several hundred cytotoxic fungal secondary metabolites, databases are available with details of full-scan high-resolution mass spectra and MS/MS spectra of both positive and negative ions.⁴⁹ Hence, the results illustrated with basil and patchouli suggests that this method may be the most suitable one for rapid screening for the disease, to find the toxic metabolites or the interaction of the *Fusarium* pathogen with any plant. Secondary metabolite biosynthetic genes responsible for the interaction of the *Fusarium* pathogen with of the host plant is decoded⁵⁰ and *Fusarium* genomics database is available.⁶ But intricate compositions of plant genetic, transcriptional and

epigenetic regulation appear to be a possible contributor to susceptibility or resistance to *Fusarium*.

The variations in chemical composition due to the polyploidy and outcrossing nature of the *Ocimum* species posed a great challenge. Hence, for the entire study period, periodically a number of leaf samples were imaged and the results stored as spectra and images for further reference. As there is limited knowledge on the metabolites involved in basil–*Fusarium*–environment interactions, this digitization helped to make comparison between different basil species or find out variations due to seasons on them. Other than the characteristic toxic metabolites of *Fusarium* and/or *Alternaria* species, the changes in the spatial distribution of selected metabolites in all selected plant species were identified in this manuscript. Besides, the identification of species-specific predominant metabolites demonstrated in this study with basil and patchouli strengthens the importance of DESI MS in rapid identification of authentic plant species. Results given here illustrate that it is a simple method suitable for any laboratory condition. However, the mass spectral and DESI MS data that are presented here are comparable, only when similar conditions are used for imaging. As Fob has host, climatic and regional preferences, there are chances for deviations from these results and number of chemical compounds which were present under our field conditions may vary elsewhere in all the three *Ocimum* species. The information and the methodology provided here may be applied precisely to any other crop species but instrumentation and solvent choices must always be tailored to the user defined circumstances and individual diagnostic situations. Handling large number of samples is possible as DESI MS has been successfully integrated into surgery for identification of tumor margins.⁵¹ Hence the methodology adapted here provides a valuable experimental system to address questions of agriculture and quarantine requirements.

Conclusions

Three different basil species (*O. gratissimum*, *O. basilicum* and *O. tenuiflorum*) were screened for *Fusarium* wilt by DESI MS imaging using TLC- imprints of leaves. Data were acquired in both positive and negative ionization modes to get information on predominant metabolite peak(s). The possibility to identify metabolite profile of the healthy plant(s) and compare it with that of the contaminated ones is illustrated with suitable examples. The changes represented in the spatial distribution of selected metabolites served as markers. Identification of toxic metabolites of *Fusarium* is illustrated with examples. The suitability of the method to screen *Fusarium* or other pathogen infection in related plant species is demonstrated using patchouli. The same instrument can be used for imaging the imprints or direct detection in tissues and/or measuring/quantification in extracts. The ease of interpretation of results by nontechnical persons will enable identification of contaminated plants and formulating effective control methods. Hence for rapid detection of contamination in any epidemics of *Fusarium*, DESI MS imaging would be ideal. This method of imaging will be highly useful in agriculture and in quarantine or

even in cases of disease outbreak, where there is urgency to screen large number of plant leaves.

Funding sources

Financial support is from the Department of Biotechnology (DBT) and Department of Science and Technology (DST), Government of India through the Nano Mission.

Conflict of interest

The authors declare no competing financial interest.

Acknowledgements

The authors thank the Department of Science and Technology, Government of India, for equipment support through the Nano Mission.

References

- 1 A. K. Jarmusch and R. G. Cooks, *Nat. Prod. Rep.*, 2014, **31**, 730–738.
- 2 C. Wu, A. L. Dill, L. S. Eberlin, R. G. Cooks and D. R. Ifa, *Mass Spectrom. Rev.*, 2013, **32**, 218–243.
- 3 (a) D. R. Ifa, A. Srimany, L. S. Eberlin, H. R. Naik, V. Bhat, R. G. Cooks and T. Pradeep, *Anal. Methods*, 2011, **3**, 1910–1912; (b) B. Li, N. Bjarnholt, S. H. Hansen and C. Janfelt, *J. Mass Spectrom.*, 2011, **46**, 1241–1246; (c) J. I. Zhang, X. Li, Z. Ouyang and R. G. Cooks, *Analyst*, 2012, **137**, 3091–3098.
- 4 J. Watrous, P. Roach, B. Heath, T. Alexandrov, J. Laskin and P. C. Dorrestein, *Anal. Chem.*, 2013, **85**, 10385–10391.
- 5 K. Chingin, J. Liang and H. Chen, *RSC Adv.*, 2014, **4**, 5768–5781.
- 6 L.-J. Ma, H. C. Van der Does, K. A. Borkovich, J. J. Coleman, M.-J. Daboussi, A. Di Pietro, M. Dufresne, M. Freitag, M. Grabherr, B. Henrissat, P. M. Houterman, S. Kang, W.-B. Shim, C. Woloshuk, X. Xie, J.-R. Xu, J. Antoniwi, S. E. Baker, B. H. Bluhm, A. Breakspear, D. W. Brown, R. A. E. Butchko, S. Chapman, R. Coulson, P. M. Coutinho, E. G. J. Danchin, A. Diener, L. R. Gale, D. M. Gardiner, S. Goff, K. E. Hammond-Kosack, K. Hilburn, A. Hua-Van, W. Jonkers, K. Kazan, C. D. Kodira, M. Koehrsen, L. Kumar, Y.-H. Lee, L. Li, J. M. Manners, D. Miranda-Saavedra, M. Mukherjee, G. Park, J. Park, S.-Y. Park, R. H. Proctor, A. Regev, M. C. Ruiz-Roldan, D. Sain, S. Sakthikumar, S. Sykes, D. C. Schwartz, B. G. Turgeon, I. Wapinski, O. Yoder, S. Young, Q. Zeng, S. Zhou, J. Galagan, C. A. Cuomo, H. C. Kistler and M. Rep, *Nature*, 2010, **464**, 367–373.
- 7 R. Hiltunen and Y. Holm, *Basil: The Genus Ocimum*, Taylor & Francis, 2003.
- 8 R. S. Verma, R. C. Padalia, A. Chauhan and S. T. Thul, *Ind. Crops Prod.*, 2013, **45**, 7–19.
- 9 (a) R. M. Davis, K. D. Marshall and J. Valencia, *Plant Dis.*, 1993, **77**, 537–537; (b) L. E. Datnoff, L. Z. Liang and R. L. Wick, *Plant Dis.*, 1997, **81**, 1214–1214; (c) L. Swart and J. M. Van Niekerk, *Australas. Plant Pathol.*, 2003, **32**, 125–126.

- 10 A. P. Keinath, *Plant Dis.*, 1994, **78**, 1211–1215.
- 11 A. M. Al-Hatmi, A. Bonifaz, G. de Hoog, L. Vazquez-Maya, K. Garcia-Carmona, J. F. Meis and A. D. Van Diepeningen, *BMC Infect. Dis.*, 2014, **14**, 588.
- 12 J. Evans, D. Levesque, A. de Lahunta and H. E. Jensen, *Vet. Pathol.*, 2004, **41**, 510–514.
- 13 (a) A. Chiocchetti, S. Ghignone, A. Minuto, M. L. Gullino, A. Garibaldi and Q. Migheli, *Plant Dis.*, 1999, **83**, 576–581; (b) A. Chiocchetti, L. Sciaudone, F. Durando, A. Garibaldi and Q. Migheli, *Plant Dis.*, 2001, **85**, 607–611; (c) M. Pasquali, P. Piatti, M. L. Gullino and A. Garibaldi, *J. Phytopathol.*, 2006, **154**, 632–636.
- 14 A. Reis, L. S. Boiteux and R. F. Vieira, *J. Gen. Plant Pathol.*, 2008, **74**, 375–381.
- 15 D. Chaimovitch, N. Dudai, E. Putievsky and A. Ashri, *Plant Dis.*, 2006, **90**, 58–60.
- 16 F. Garcia-Bastidas, N. Ordonz, J. Konkol, M. Al-Qasim, Z. Naser, M. Abdelwali, N. Salem, C. Waalwijk, R. C. Ploetz and G. H. J. Kema, *Plant Dis.*, 2014, **98**, 694.
- 17 A. Gamliel, T. Katan, H. Yunis and J. Katan, *Phytopathology*, 1996, **86**, 56–62.
- 18 S. Veillet, V. Tomao and F. Chemat, *Food Chem.*, 2010, **123**, 905–911.
- 19 R. G. Hemalatha and T. Pradeep, *J. Agric. Food Chem.*, 2013, **61**, 7477–7487.
- 20 T. Pluskal, S. Castillo, A. Villar-Briones and M. Oresic, *BMC Bioinf.*, 2010, **11**, 395.
- 21 P. R. N. Vieira, S. M. de Moraes, F. H. Q. Bezerra, P. A. Travassos Ferreira, I. R. Oliveira and M. G. V. Silva, *Ind. Crops Prod.*, 2014, **55**, 267–271.
- 22 X. Zhang, H. Zhang, J. Pu, Y. Qi, Q. Yu, Y. Xie and J. Peng, *PLoS One*, 2014, **8**, e82841.
- 23 (a) K. Carovic-Stanko, A. Salinovic, M. Grdisa, Z. Liber, I. Kolak and Z. Satovic, *Plant Biosyst.*, 2011, **145**, 298–305; (b) M. Aghaei, R. Darvishzadeh and A. Hassani, *Rev. Cienc. Agron.*, 2012, **43**, 312–320.
- 24 S. Rastogi, S. Meena, A. Bhattacharya, S. Ghosh, R. K. Shukla, N. S. Sangwan, R. K. Lal, M. M. Gupta, U. C. Lavania, V. Gupta, D. A. Nagegowda and A. K. Shasany, *BMC Genomics*, 2014, **15**, 588.
- 25 A. K. Badu-Tawiah, L. S. Eberlin, Z. Ouyang and R. G. Cooks, *Annu. Rev. Phys. Chem.*, 2013, **64**, 481–505.
- 26 Z. Wang, P. Chen, L. Yu and P. D. B. Harrington, *Anal. Chem.*, 2013, **85**, 2945–2953.
- 27 C. Jayasinghe, N. Gotoh, T. Aoki and S. Wada, *J. Agric. Food Chem.*, 2003, **51**, 4442–4449.
- 28 A. I. Hussain, F. Anwar, S. T. Hussain Sherazi and R. Przybylski, *Food Chem.*, 2008, **108**, 986–995.
- 29 S. Ekren, C. Sonmez, E. Ozcakal, Y. S. K. Kurttas, E. Bayram and H. Gurgulu, *Agr. Water Manag.*, 2012, **109**, 155–161.
- 30 (a) D. Sarkar, A. Srimany and T. Pradeep, *Analyst*, 2012, **137**, 4559–4563; (b) A. Ghasemi Pirbalouti, E. Mahdad and L. Craker, *Food Chem.*, 2013, **141**, 2440–2449.
- 31 R. Fischer, N. Nitzan, D. Chaimovitch, B. Rubin and N. Dudai, *J. Agric. Food Chem.*, 2011, **59**, 4913–4922.
- 32 S. S. Chavan and S. K. Prashanthi, *Indian Phytopathol.*, 2011, **64**, 258–260.
- 33 A. Bolwerk, A. L. Lagopodi, B. J. Lugtenberg and G. V. Bloemberg, *Mol. Plant-Microbe Interact.*, 2005, **18**, 710–721.
- 34 K. J. Czymmek, M. Fogg, D. H. Powell, J. Sweigard, S.-Y. Park and S. Kang, *Fungal Genet. Biol.*, 2007, **44**, 1011–1023.
- 35 Y. Iijima, R. Davidovich-Rikanati, E. Fridman, D. R. Gang, E. Bar, E. Lewinsohn and E. Pichersky, *Plant Physiol.*, 2004, **136**, 3724–3736.
- 36 F. Deguerry, L. Pastore, S. Wu, A. Clark, J. Chappell and M. Schalk, *Arch. Biochem. Biophys.*, 2006, **454**, 123–136.
- 37 C. Deschamps and J. E. Simon, in *Plant Secondary Metabolism Engineering*, Springer, 2010, pp. 263–273.
- 38 (a) X. Dong, N. Ling, M. Wang, Q. Shen and S. Guo, *Plant Physiol. Biochem.*, 2012, **60**, 171–179; (b) X. Dong, Y. Xiong, N. Ling, Q. Shen and S. Guo, *World J. Microbiol. Biotechnol.*, 2014, **30**, 1399–1408.
- 39 (a) K. Kostyn, M. Czemplik, A. Kulma, M. Bortniczuk, J. Skala and J. Szopa, *Plant Sci.*, 2012, **190**, 103–115; (b) I. Morkunas, M. Stobiecki, L. Marczak, J. Stachowiak, D. Narozna and D. Remlein-Starosta, *Physiol. Mol. Plant Pathol.*, 2010, **75**, 46–55.
- 40 (a) A. H. Aly, R. Edrada-Ebel, I. D. Indriani, V. Wray, W. E. G. Muller, F. Totzke, U. Zirrgiebel, C. Schachtele, M. H. G. Kubbutat and W. H. Lin, *J. Nat. Prod.*, 2008, **71**, 972–980; (b) G. Gilardi, M. L. Gullino and A. Garibaldi, *J. Plant Pathol.*, 2013, **95**, 41–47.
- 41 A. Poloni and J. Schirawski, *Molecules*, 2014, **19**, 9114–9133.
- 42 (a) M. Marchetti-Deschmann, W. Winkler, H. Dong, H. Lohninger, C. P. Kubicek and G. Allmaier, *Food Technol. Biotechnol.*, 2012, **50**, 334–342; (b) P. M. Scott, W. Zhao, S. Feng and B. P. Y. Lau, *Mycotoxin Res.*, 2012, **28**, 261–266.
- 43 (a) W. Wojtasik, A. Kulma, K. Kostyn and J. Szopa, *Plant Physiol. Biochem.*, 2011, **49**, 862–872; (b) A. Boba, A. Kulma, K. Kostyn, M. Starzycki, E. Starzycka and J. Szopa, *Physiol. Mol. Plant Pathol.*, 2012, **76**, 39–47.
- 44 (a) Z. Wang, C. Jia, J. Li, S. Huang, B. Xu and Z. Jin, *Funct. Integr. Genomics*, 2014, 1–16; (b) H. D. Ardila, A. M. Torres, S. T. Martinez and B. L. Higuera, *Physiol. Mol. Plant Pathol.*, 2014, **85**, 42–52.
- 45 T. Kashiwa, K. Inami, M. Fujinaga, H. Ogiso, T. Yoshida, T. Teraoka and T. Arie, *J. Gen. Plant Pathol.*, 2013, **79**, 412–421.
- 46 J. F. Leslie and B. A. Summerell, *The Fusarium Laboratory Manual*, Wiley Online Library, 2007.
- 47 G. K. Kumaraswamy, A. C. Kushalappa, T. M. Choo, Y. Dion and S. Rioux, *Plant Pathol.*, 2012, **61**, 509–521.
- 48 C. Li, C. Zuo, G. Deng, R. Kuang, Q. Yang, C. Hu, O. Sheng, S. Zhang, L. Ma and Y. Wei, *PLoS One*, 2013, **8**, e70226.
- 49 T. El-Elimat, M. Figueroa, B. M. Ehrmann, N. B. Cech, C. J. Pearce and N. H. Oberlies, *J. Nat. Prod.*, 2013, **76**, 1709–1716.
- 50 (a) D. W. Brown, R. A. E. Butchko, M. Busman and R. H. Proctor, *Fungal Genet. Biol.*, 2012, **49**, 521–532; (b) D. W. Brown, R. A. Butchko, S. E. Baker and R. H. Proctor, *Fungal Biol.*, 2012, **116**, 318–331.
- 51 K. S. Kerian, A. K. Jarmusch, V. Pirro, M. O. Koch, T. A. Masterson, L. Cheng and R. G. Cooks, *Analyst*, 2014, **140**, 1090–1098.

Supporting Information

Rapid detection of Fusarium wilt in Basil (*Ocimum* sp.) leaves by desorption electrospray ionization mass spectrometry (DESI MS) imaging

R. G. Hemalatha^a, *Hemanta R. Naik*^a, *Vasundhara Mariappa*^b, and *T. Pradeep*^{a*}

^aDST Unit on Nanoscience and Thematic Unit of Excellence, Department of Chemistry, Indian Institute of Technology Madras, Chennai, India.

^bMedicinal and Aromatic Section, Department of Horticulture, University of Agricultural Sciences, Bangalore, India.

*Corresponding author Email: pradeep@iitm.ac.in

Table of content:

Fig.S1A- Photographs of single leaf of basil species showing variations in leaf margins

Fig. S1B- Photographs of inflorescence of basil species showing variations in flower color

Fig.S1C- Photographs of basil seedling at four and six leaved stage

Fig. S2- DESI MS images of basil leaf collected from a market

Fig. S3- ESI MS tandem mass spectra of toxic metabolites showing fragmentation pattern

Table S1- Identification of toxic metabolites of *Fusarium*/ *Alternaria* using database search

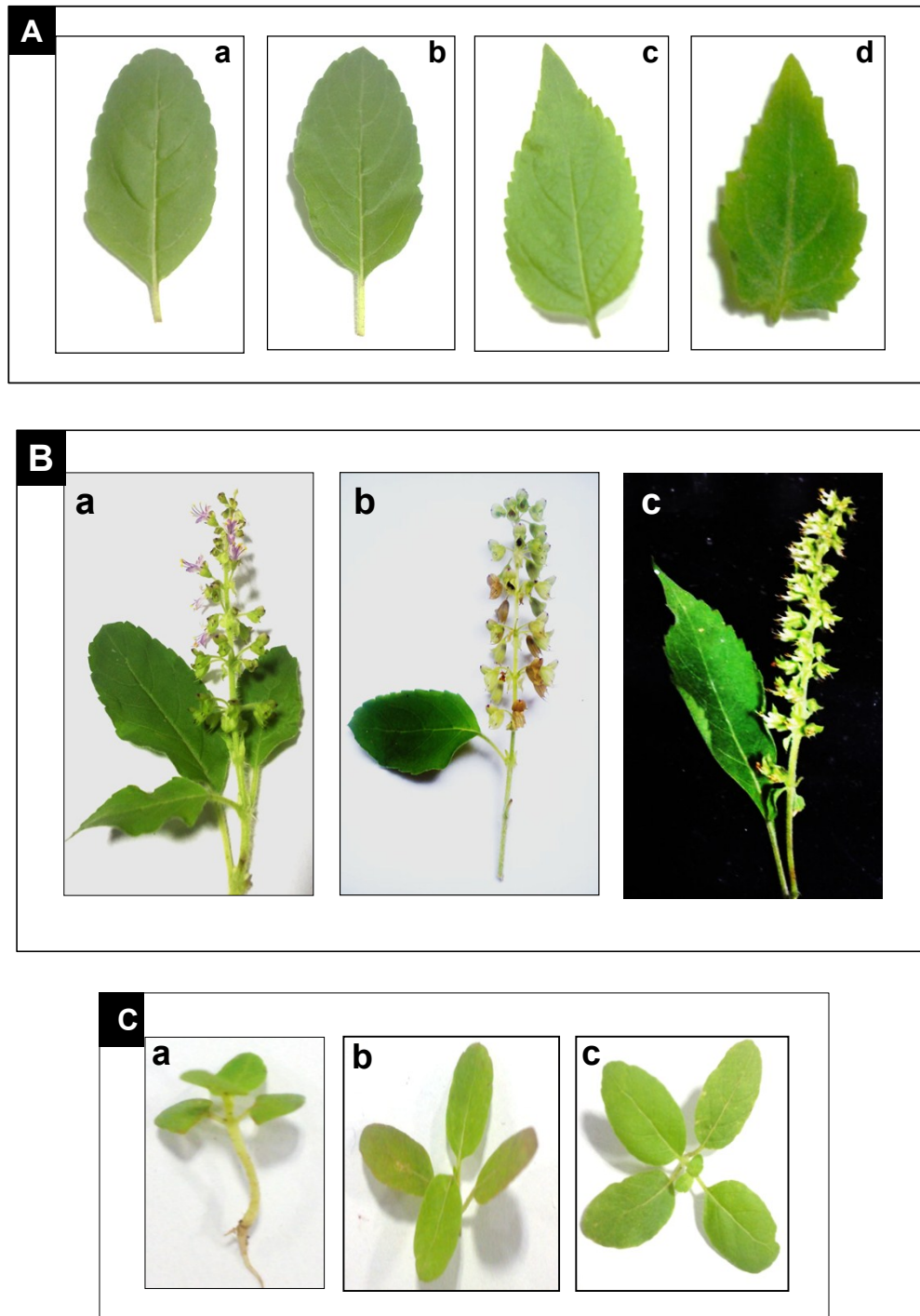


Fig. S1. Photographs of (A) detached healthy leaf in all selected plants showing differences in leaf margins for (a) *O. tenuiflorum*, (b) *O. basilicum*, (c) *O. gratissimum* and (d) *P. cablin*, (B) typical color of inflorescence used for identification of basil species (a) *O. tenuiflorum*, (b) *O. basilicum* and (c) *O. gratissimum* and (C) basil seedling (a) whole plant, (b) four leaved stage and (c) six leaved stage.

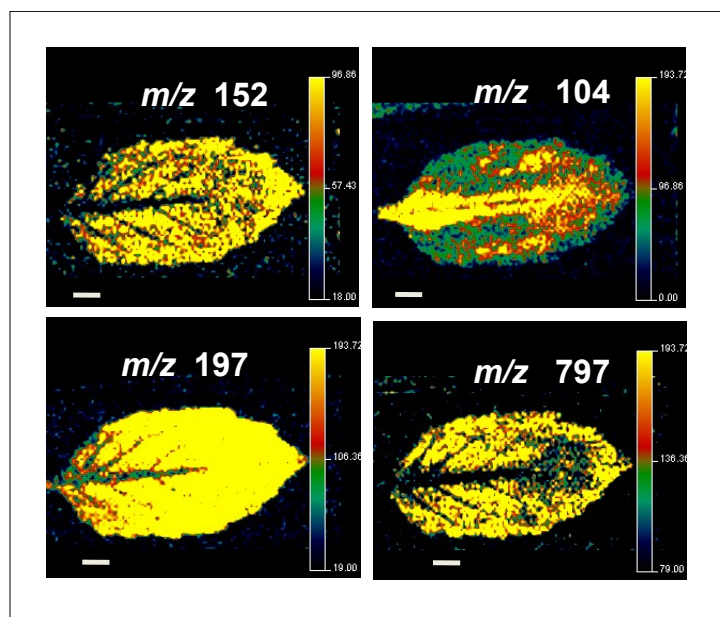


Fig S2. DESI MS images showing the spatial distribution of some molecular ions in basil leaf collected from the local market showing conspicuous leaf margin. The scale is uniform in all the images (5 mm).

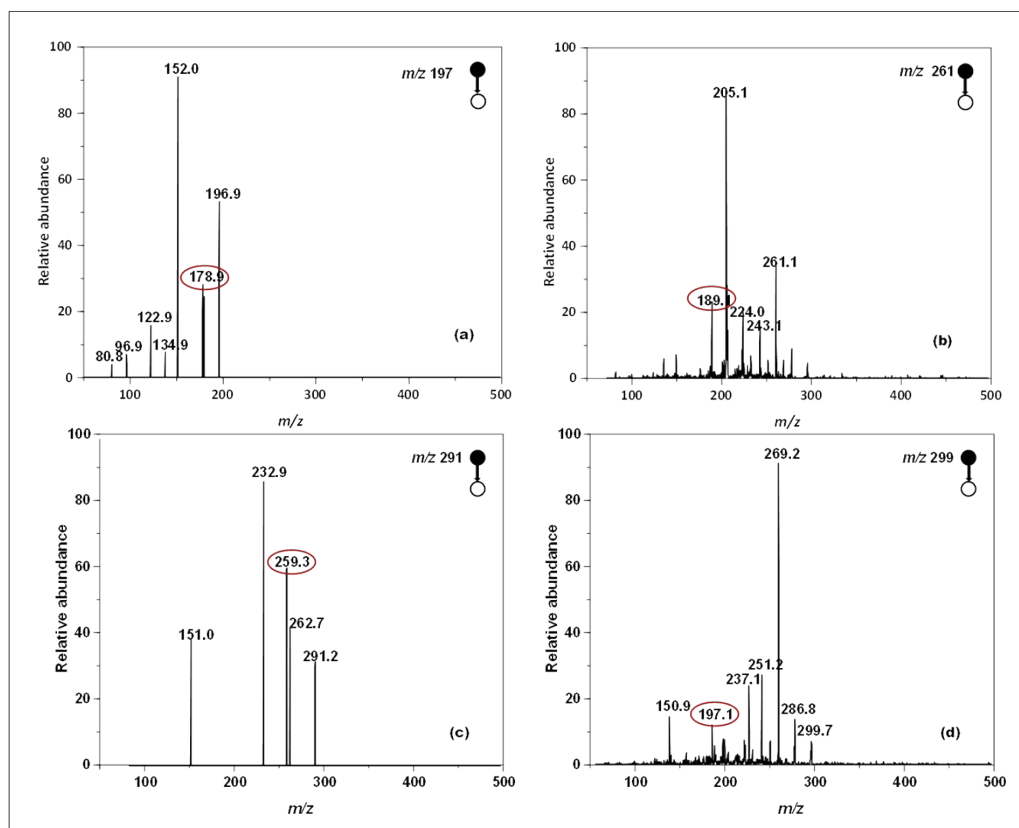
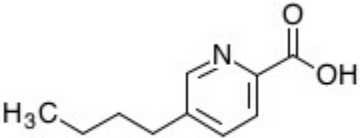
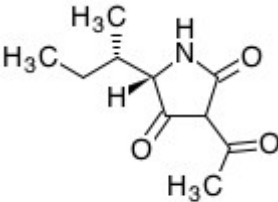
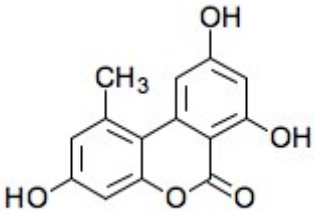
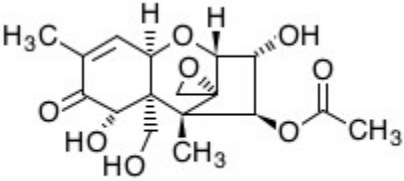
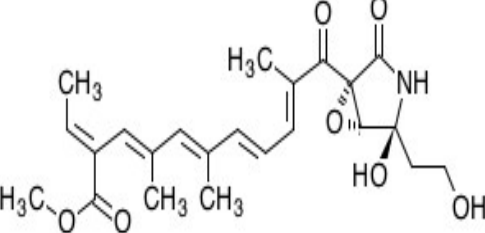


Fig S3. ESI MS tandem mass spectra showing the fragmentation pattern of selected toxic metabolites in contaminated basil leaf. Peaks encircled show their relationships.

Table S1: Identification of toxic metabolite ion peaks of *Fusarium* /*Alternaria* using database search

S.No	Name	Molecular weight	Structure from KEGG database (KEGG-Kyoto Encyclopedia of Genes and Genomes)	Database ID *,**
1.	Fusaric acid	179.2157	 C10146	C10146 MID- 68152
2.	Tenuazonic acid	197.231	 C08511	C08511 MID- 67032
3.	Alternariol	258.2262	 C16838	C16838 MID-71377
4.	Fusarenon-X	354.3518	 C19583	C19583 MID-73245
5.	Fusarin C	431.4789	 C19243	C19243 MID-72964

* C numbers for KEGG database (<http://www.kegg.jp/kegg/compound>) to get additional information on the metabolite(s) including chemical and physical properties, structures, reactions and associated biosynthetic pathways of formation etc.

**MID numbers for METLIN –Metabolite and Tandem MS database (http://metlin.scripps.edu/metabo_advanced.php) to get additional information on the metabolite(s) including data on tandem mass spectra and structures for fragments.

References:

1. M. Kanehisa and S. Goto, *Nucleic Acids Res.*, 2000, **28**, 27-30.
2. C. A. Smith, G. O'Maille, E. J. Want, C. Qin, S. A. Trauger, T. R. Brandon, D. E. Custodio, R. Abagyan and G. Siuzdak, *Ther. Drug Monit.*, 2005, **27**, 747-751.

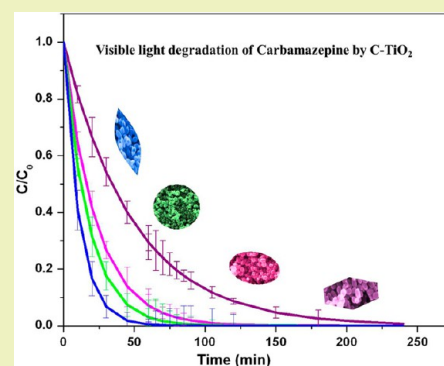
Rapid Synthesis of C-TiO₂: Tuning the Shape from Spherical to Rice Grain Morphology for Visible Light Photocatalytic Application

Balaji Sambandam,[†] Anupama Surenjan,[‡] Ligy Philip,[‡] and Thalappil Pradeep^{*†}[†]DST Unit of Nanoscience and Thematic Unit of Excellence, Department of Chemistry, Indian Institute of Technology Madras, Chennai 600036, India[‡]Department of Civil Engineering, Indian Institute of Technology Madras, Chennai 600036, India

S Supporting Information

ABSTRACT: Visible light-active carbon-loaded anatase TiO₂ (C-TiO₂) nanocrystals of spherical, distorted spherical, rice grain and hexagonal morphologies, with a particle size range of 50–70 nm, have been synthesized by a rapid microwave-assisted route in the solution state. The morphology of these materials is greatly tuned at low concentrations of the precursors used. The absorption band gaps (E_{gap}) are shifted to the visible region due to C loading, and the distorted spherical C-TiO₂ exhibits a maximum energy shift relative to pure TiO₂. Carbon gets deposited predominantly on the surface as graphitic carbon, in the preparative conditions, as confirmed by X-ray photoelectron, scanning electron microscopy elemental mapping and Raman spectroscopic studies. The rapid degradation of an endocrine disrupting agent and a persistent pollutant in wastewater, carbamazepine, by the rice grain shaped C-TiO₂ is attributed to the large surface area (229 m²/g) of the particles and coexposure of the high surface energy and more reactive {001} facets along with the low energy and thermodynamically stable {101} facets.

KEYWORDS: Carbon loaded TiO₂, Microwave synthesis, Morphology control, Photocatalysis, Water pollution, Carbamazepine



INTRODUCTION

Diverse morphological changes in semiconductor nanomaterials can be used for tuning their shape-dependent physical properties, which are consequently useful in applications, for instance, in photocatalysis. Titanium dioxide (TiO₂) is a popular photocatalytic material that has been utilized for a variety of applications.^{1,2} Both theoretical and experimental studies have proven that the anatase phase of TiO₂ is better for photocatalysis than its rutile phase, due to the fast electron–hole recombination and lower surface activity in the latter. But, the large band gap ($E_{\text{gap}} = 3.2$ eV) of anatase TiO₂ makes it active only in the UV region. Thus, several attempts have been made to shift the E_{gap} to the visible region.^{3,4}

Doping is a strategy that is often employed for band gap engineering. It is well accepted that doped titania materials with their long-term stabilities and reduced E_{gap} values will find applications in solar light technologies.^{5,6} In this regard, research is primarily focused on employing nonmetals as dopants.^{7,8} Doping with carbon (C) and nitrogen (N) has attracted significant attention due to a reduction in potential traps for electron/hole recombination, in comparison with the metal dopants.^{9–11} However, the photocatalytic efficiency of C-doped TiO₂ (C-TiO₂) under visible light is still low.¹² Doping of the TiO₂ lattice by C can take place either by substitution of Ti (C@Ti) or by substitution of oxygen (C@O). The corresponding lattice environments can be represented as C–O–Ti–O and Ti–C–Ti–O, respectively. Carbon incorporation on TiO₂ can happen either at anionic (oxygen) or

cationic (Ti) sites, according to a theoretical study.¹³ Experimental evidence are inadequate to precisely describe the type of incorporation.¹⁴ One can achieve such understanding by making precise carbon environments including doping in the lattice, inclusion in the interstitial positions or deposition on the surface.^{14,15} Through a density functional theory-based study, it was shown that C@O reduced E_{gap} of anatase TiO₂ by a small magnitude (0.08 eV) and also generated gap states that were C 2p in character.¹³ In the band structure, these dopant states were found to be positioned between the valence and conduction bands of undoped TiO₂, based on which the shifts in optical absorption edge in C@O doped bulk TiO₂ and TiO₂ nanotubes could be understood. In comparison, C@Ti caused C 2s states to arise just below the original conduction band, so that the calculated E_{gap} was decreased to a value of 2.85 eV (compared to 3.2 eV of undoped anatase TiO₂) corresponding to the visible region.

Complete removal of pharmaceutically active compounds (PhACs) from an aquatic environment and drinking water is a major challenge today.¹⁶ PhACs are found at an alarming rate in drinking water supplies around the world.¹⁷ Although many advanced oxidation processes have been tested for the removal of PhACs,¹⁸ semiconductor photocatalysis using TiO₂ is particularly attractive due to its higher pollutant removal

Received: January 20, 2015

Revised: May 15, 2015

Published: May 20, 2015

efficiency, low cost, easy availability, nontoxicity, and easily modifiable properties.¹⁹ Carbamazepine (CBZ), a common antiepileptic drug, is a persistent pollutant in wastewater. In a recent work, a sol-gel N-doped TiO₂ catalyst surface was reported to have shown enhancement in the photocatalytic removal efficiency of CBZ in visible light with increasing pH between 5 and 9.²⁰ For water spiked with 1 mg/L CBZ, a 45–70% CBZ removal was achieved within this pH range. Increasing alkalinity and natural organic matter was found to cause a significant reduction in CBZ removal capacity of the catalyst. The photocatalytic degradation efficiency also strongly decreased when using surface water and wastewater effluents as water sources.

Generally, efficiency of photocatalysis depends mainly on the surface area and the exposed planes, i.e., surface morphology of the catalyst. Average surface energies of the different facets of anatase TiO₂ predicted from theoretical calculations are as follows: {110} (1.09 J/m²) > {001} (0.90 J/m²) > {100} (0.53 J/m²) > {101} (0.44 J/m²).²¹ Thus, extensive research is currently focused on the exposure of high surface energy facets of TiO₂, as these will have much higher chemical reactivity.^{22–24} This lead to implications in photocatalysis-based environmental cleanup, water splitting hydrogen generation and solar energy as well as Li-ion batteries.²⁵

In this work, C-TiO₂ was synthesized by a rapid technique for visible light photocatalytic applications. By changing the concentrations, in dilute conditions of the reactants, various morphologies, namely, spherical, distorted spherical, rice grain, and hexagonal shapes, were obtained. The photocatalytic activities of these morphologies of C-TiO₂ nanocrystals (NCs) toward CBZ were tested in the visible region, employing certain key parameters derived from the response surface methodology²⁶ for optimal removal efficiency.

EXPERIMENTAL SECTION

Sample Preparation. In a typical synthesis, a solution of 10 mM titaniumoxyacetylacetonate (TOAA) and 10 mM NH₄F was prepared in 50 mL of water. To the above solution was added 20 mg of glucose and then 10 mL of H₂O₂. The resultant mixture was stirred for 10 min and then subjected to microwave digestion. The as-synthesized materials were centrifuged, washed with water and methanol, and dried in an oven at 80 °C for 3 h. To remove the excess glucose, the as-synthesized samples were annealed at 350 °C for 2 h in a nitrogen atmosphere.

A number of solutions were prepared using different combinations of temperature, precursor concentration, reaction time, and volume of the microwave vessel. To understand the effect of these parameters individually, each was varied while keeping the other conditions constant. Table 1 lists the samples synthesized by using different concentrations of TOAA, NH₄F, and H₂O₂ under the same conditions of 80% volume of the Teflon vessel, 150 °C reaction temperature for 30 min and 400 W power. TiO₂ systems produced from variation of other parameters are listed in the Supporting Information, Tables S1–S3 along with the reaction conditions for each set.

Characterization. Powder X-ray diffraction (XRD) measurements were carried out using Bruker Discover D8 diffractometer with default background correction. Raman measurements were recorded using a WiTec GmbH, CRM αS300 instrument with 532 nm Nd:YAG laser line as an excitation source. High-resolution scanning electron microscopy (HRSEM) images were taken using a FEI Quanta FEG 200 with an EDS detector. High-resolution transmission electron microscopy (HRTEM) images were taken using a JEOL 3010 HRTEM instrument. Solid-state UV–vis measurements were performed by a Cary SE UV–vis-NIR spectrophotometer. X-ray photoelectron spectroscopy (XPS) was carried out with an Omicron ESCA probe spectrometer with polychromatic Mg Kα X-rays (hν =

Table 1. Effect of Variation of Concentrations of TOAA, NH₄F, and H₂O₂, Keeping All Other Conditions^a Fixed, on TiO₂ Morphology and Phase

sample code	TOAA (mM)	NH ₄ F (mM)	H ₂ O ₂ (mM)	morphology	crystalline phase
CT-1	10	10	10	spherical	anatase
CT-2	10	20	10	distorted spherical	anatase
CT-3	10	10	0	no specific morphology	anatase
CT-4	10	60	10	spherical	anatase
CT-5	10	100	10	no specific morphology	anatase
CT-6	10	10	5	hexagonal	anatase
CT-7	10	10	15	elongated oval	anatase
CT-8	10	10	2.5	spherical	anatase
CT-9	5	10	10	rice grain	anatase
CT-10	5	10	5	spherical	anatase
CT-11	5	10	2.5	no specific morphology	anatase
CT-12	5	10	15	spherical	anatase
CT-21	30	10	10	spherical	anatase
CT-22	30	15	10	spherical	anatase

^aConditions: volume, 80%; temperature, 150 °C; time, 30 min; power, 400 W.

1253.6 eV). The microwave digestion was done using the CEM Mars 5 microwave digester. The photocatalytic sample was analyzed by high performance liquid chromatography (HPLC) (Dionex, Ultimate 3000). The total organic carbon (TOC) content was measured utilizing the TOC analyzer, Shimadzu, Japan.

Photocatalytic Reaction. In a preceding study,²⁷ we have optimized the following parameters: catalyst concentration, pollutant concentration, light intensity, and time of reaction, for the degradation of CBZ by spherical C-TiO₂, utilizing visible light. To this end, 29 experiments were conducted and the system parameters were determined for optimal CBZ removal efficiency for all the C-TiO₂ morphologies presented herein.

For examining the photocatalytic removal of CBZ, each C-TiO₂ catalyst was suspended in CBZ solution of a desired concentration. Prior to irradiation, the solution was kept in the dark for 45 min to attain adsorption equilibrium (see the Supporting Information, Figure S1). Photocatalytic batch experiments were conducted in a cylindrical photochemical reactor of 400 mL volume, with a water circulation arrangement for maintaining the temperature between 25 and 30 °C. A 150 W high-pressure tungsten visible lamp (λ > 400 nm) was used for irradiation. Constant stirring with an oxygen flow rate of 300 mL/min was maintained throughout the experiment. Stock solution of the pollutant was prepared using ultrapure Millipore water. All intermediate samples were collected at regular intervals of time and analyzed using HPLC.

RESULTS AND DISCUSSION

Tuning Morphology by Different Parameters. More than 20 samples (listed in Table 1 and the Supporting Information, Tables S1–S3) were synthesized by varying the following parameters: temperature, reaction time, precursor concentration, and volume of the microwave vessel. The as-synthesized C-TiO₂ samples were subjected to SEM analysis. Figure 1 shows SEM images of samples CT-1, CT-2, CT-6, and CT-9. The CT-1 sample that was formed at a 1:1 ratio of TOAA:NH₄F exhibits a spherical morphology with a particle size of ~50 nm. However, when the ratio was changed to 1:2 by reducing the TOAA concentration by half (keeping H₂O₂ volume fixed as for CT-1), the morphology changed from a spherical to rice grain shape (CT-9). At the same time, the

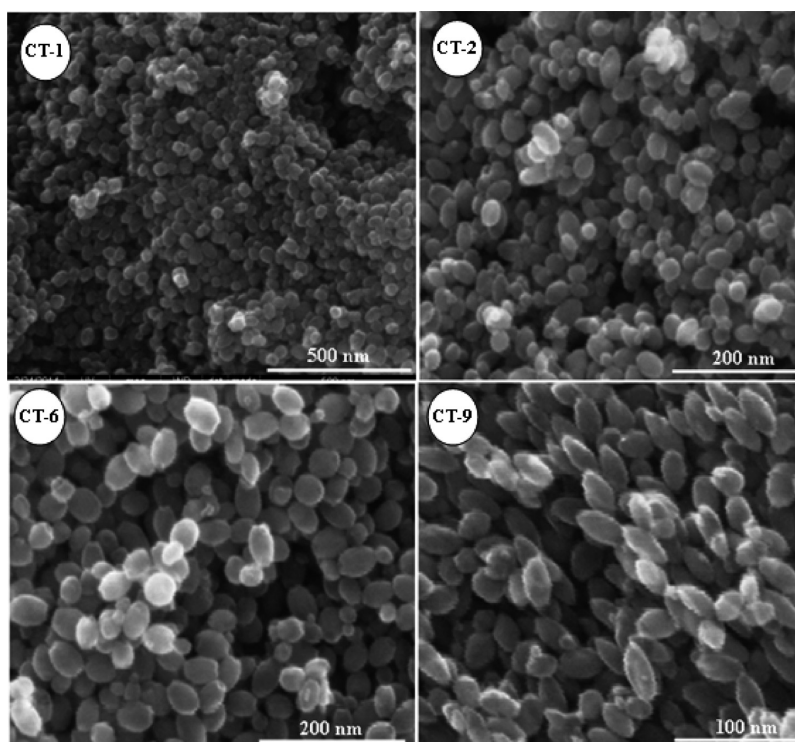


Figure 1. HRSEM images of (CT-1) spherical, (CT-2) distorted spherical, (CT-6) hexagonal, and (CT-9) rice grain shaped C-TiO₂ NCs.

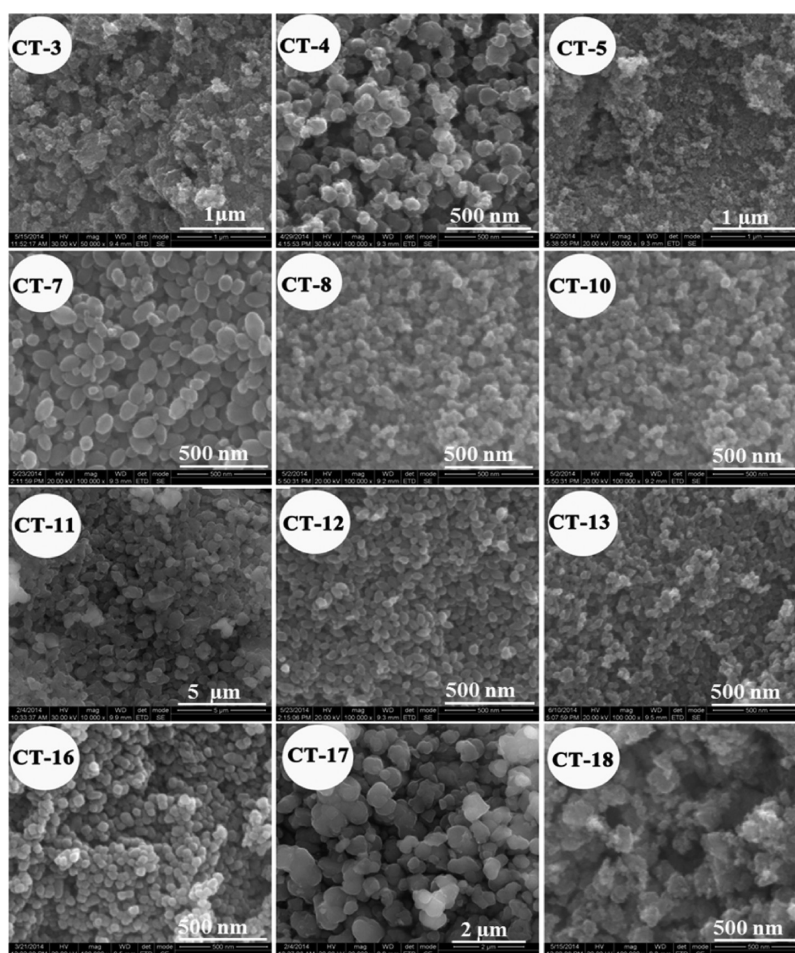


Figure 2. HRSEM images of C-TiO₂ samples prepared using different reaction conditions by microwave digestion technique.

particle size further decreased to less than 50 nm. TOAA:NH₄F = 1:2 was also achieved by doubling the concentration of the NH₄F compared to that used for CT-1. This caused the morphology to change to a distorted spherical (CT-2) shape, along with an increase in particle size. On the other hand if a 1:1 ratio of TOAA:NH₄F was maintained, but the H₂O₂ concentration was decreased by 2-fold to 48.95 mM, an interesting hexagonal morphology was formed (CT-6). Elemental compositions of these four morphologies of C-TiO₂ are presented in the Supporting Information, Figure S2. The morphologies of the remaining C-TiO₂ samples that are listed in Table 1 are shown in Figure 2. However, use of high concentrations of the sources led to no specific morphology of C-TiO₂ with large particle sizes and poor shape control (see the Supporting Information, Figure S3).

The role of H₂O₂ has been found to be that of a structure directing or determining agent. No specific morphology was observed in the absence of H₂O₂ and varying its concentration greatly affected the particle size. Varying the reaction time but keeping the concentration of the precursors unchanged also affected the particle size. Microwave digestion for 18 min resulted in a distorted oval shape for C-TiO₂, which agglomerated with an increased particle size on extending the digestion time to 40 min. Varying the temperature, keeping other parameters constant, affected the morphology too. HRSEM images of C-TiO₂ illustrating the time and temperature dependence of synthesis are shown in the Supporting Information, Figure S4. It is noteworthy that irrespective of the reaction conditions, as given in Table 1 and the Supporting Information, Tables S1–S3, C-TiO₂ was always found in the anatase phase. This is confirmed by powder XRD, as displayed in the Supporting Information, Figure S5.

In the proceeding discussion, we will focus only on the results from the samples synthesized with low concentrations of TOAA and NH₄F, namely, the spherical (CT-1), distorted spherical (CT-2), hexagonal (CT-6), and rice grain (CT-9) shaped NC C-TiO₂ (refer to Table 1). HRTEM images (see Figure 3) confirmed the spherical shape of the CT-1 sample and yielded a particle size of ~50 nm. The measured *d* value of 3.50 Å suggests the existence of a (101) plane in spherical C-TiO₂. In addition, the outer boundary (seen in Figure 3B, corresponding to CT-2) shows layers of carbon accumulated on the periphery. This can be confirmed by measuring EDS line scan of a single spherical shaped C-TiO₂, as given in the Supporting Information, Figure 6. This confirms that carbon is accumulated on the surface. However, there is significant C content in the particle, which is uniform. This carbon is likely to be due to doping. The distorted spherical morphology of CT-2 is easily visible from the figure, with clear lattice fringes at an interplanar distance of 3.51 Å, due to the (101) plane as in CT-1.²⁸ The corresponding particle size was calculated to be ~40–50 nm. The HRTEM image of CT-6 sample clearly exhibits six vertices and a hexagonal morphology in which four sides are long and two are short. Each short side was found to be 10 nm in length, while the remaining sides were measured to be 20 nm in length. The average particle size was found to be 40 nm and was further confirmed by the Scherer formula from XRD. As in the previous two samples, for CT-6 also the measured *d* spacing was found to be 3.51 Å corresponding to a (101) plane. The electron microscopy images of CT-9 showcase the presence of two vertices in each particle with a rice grain shape. From the SEM measurements, a particle size of ~40–50 nm was derived for CT-9. The lattice fringes reveal

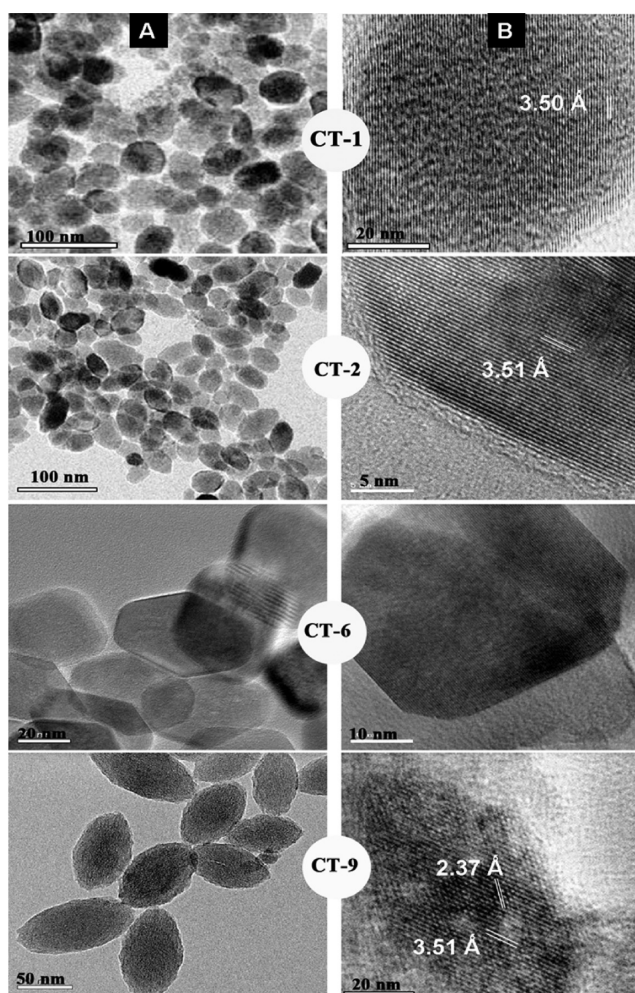


Figure 3. TEM images at (A) low and (B) high magnification of spherical (CT-1), distorted spherical (CT-2), hexagonal (CT-6), and rice grain (CT-9) shaped of C-TiO₂ NCs.

a clear crystallinity and an arrangement of atoms with interplanar distances of 2.37 Å and 3.50 Å corresponding to (004) and (101) planes, respectively of anatase TiO₂. Interestingly, only very few boundary layers (thin layers) of carbon were present in CT-6 and CT-9 samples when compared with CT-1 and CT-2 samples, showcasing that the carbon thickness changes with the sample. More HRTEM images of these four morphologies of C-TiO₂ can be found in the Supporting Information, Figure S7.

Structural Elucidation of C-TiO₂ with Different Morphologies. The powder XRD profiles of the four morphologies of C-TiO₂ are depicted in Figure 4. It is deduced that all the materials index exactly to the anatase phase of bulk TiO₂. The peak at $2\theta = 25.1^\circ$ is due to the (101) plane of anatase TiO₂, while other peaks correspond to the (103), (004), (112), (200), (105), (211), and (204) planes of bulk TiO₂ (JCPDS 89-4921). Though there is a small deviation in the peak positions of the four samples with respect to the bulk form due to carbon accumulation, there are no significant changes in these within the different morphologies of C-TiO₂. However, the full width at half-maxima (fwhm) of any peak (plane) is not the same due to the difference in particles sizes of the four shapes.

Bulk anatase TiO₂ is known to exhibit six Raman active modes (three E_g, two B_{1g} and one A_{1g}).²⁹ These spectral

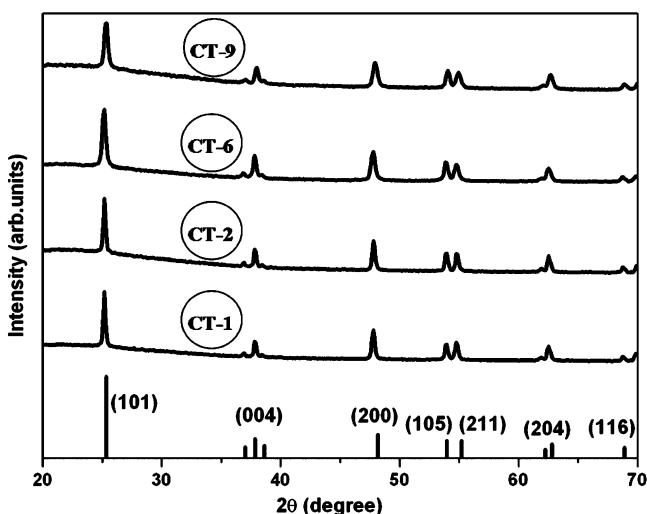


Figure 4. XRD profiles of the four different morphologies of C-TiO₂. For comparison, XRD of bulk anatase TiO₂ is plotted in the bottom (JCPDS 89-4921).

features can also be seen in the low frequency region of the Raman spectra of the four C-TiO₂ NCs displayed in Figure 5A. Thus, in agreement with the XRD analysis, Raman spectroscopy also confirms that these systems were in the anatase phase. The strong phonon peak at 150 cm⁻¹ corresponds to an E_g mode, but its position is shifted by ~6–8 cm⁻¹ relative to bulk TiO₂, possibly due to C content. The peaks at ~400, 510, and 620 cm⁻¹ index well to the B_{1g}, A_{1g}, and E_g modes, respectively. The spectral feature in the high frequency region (see Figure 5B) consists of D and G bands which are normally observed at ~1350 and 1585 cm⁻¹, respectively. These bands correspond to sp² carbon atoms in a disordered (D) environment and to carbons in extended p conjugated graphite-like (G) arrangements. This carbonaceous region upon deconvolution reveals that the disordered character of the D band at 1357 cm⁻¹ is higher in intensity than the graphitic character of the G band at 1585 cm⁻¹.

The ratio of the intensities of the D and G bands (I_D/I_G) or the degree of graphitization is an indication of the amount of graphitic carbon formed at the surface of the nanoparticle; lower the I_D/I_G ratio, higher the degree of graphitization.^{30,31} I_D/I_G was found to be 2.15, 2.06, 1.98, and 1.97, respectively for the distorted spherical, spherical, rice grain, and hexagonal shaped C-TiO₂. These values are greater than the I_D/I_G ratios (1.06–1.66) of previously reported³² C-TiO₂ and are therefore indicative of the presence of lesser graphitic carbon in our samples. It can be further noticed that the I_D/I_G ratio of the rice grain and hexagonal shaped C-TiO₂ is lower than that of the spherical and distorted spherical shaped C-TiO₂. As the D band is reflective of disorder/structural defects, based on I_D , the disorder is likely to be less in the first pair of samples and high in the second pair of C-TiO₂ NCs.

The UV–vis diffuse reflectance spectra of CT-1, CT-2, CT-6, and CT-9 are presented in the Supporting Information, Figure S8. Although P25 Degussa (bulk TiO₂) showed an absorption onset in the UV region, the absorption of all morphologies of C-TiO₂ exhibited a shoulder in the visible region. Absorbance is enhanced with increasing carbon content as follows: distorted spherical > spherical > hexagonal > rice grain shaped C-TiO₂. This trend is in agreement with the TOC results, according to which the percentages of carbon in the distorted spherical (CT-2), spherical (CT-1), hexagonal (CT-6), and rice grain (CT-9) shaped C-TiO₂ samples were 3.35, 2.95, 2.68, and 2.55%, respectively.

Carbon in TiO₂ Network. The carbon environment in the four different morphologies of C-TiO₂ was monitored by XPS, and the results are shown in Figure 6. For comparison, XPS of bulk TiO₂ (P25 Degussa) is also plotted. It can be seen from the figure that after deconvolution, C 1s appears as three distinct peaks at 284.6, 286.3, and 288.5 eV, which are due to adventitious carbon species. The first peak at 284.6 eV is due to graphitic carbon formed at the surface of the nanoparticle, whereas the latter two arise from the C–OH (and C–O–C) and C=O (and COO) bonds of the carbonate-like species due to oxidized carbon species. This carbon species (carbonate-like) are likely to be substituting the Ti site or sitting in interstitial positions.^{33–36,14} The presence of C–O in the TiO₂ was

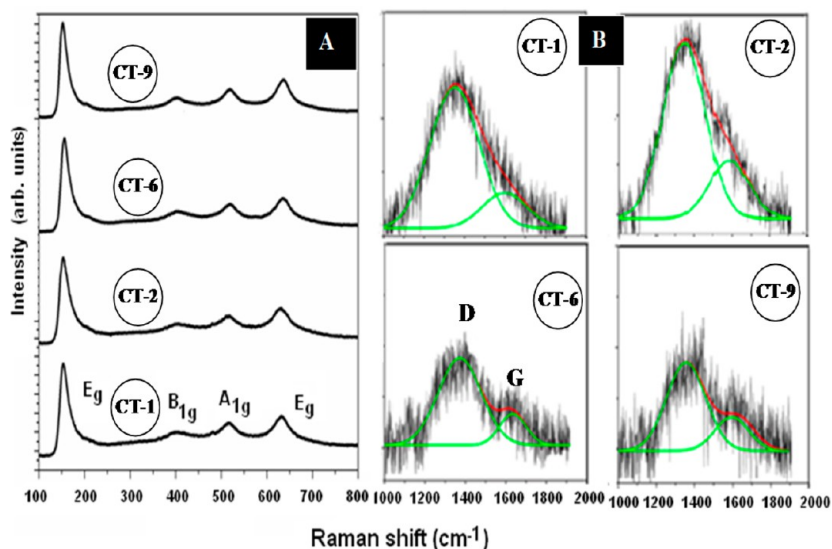


Figure 5. Raman profiles of the spherical (CT-1), distorted spherical (CT-2), hexagonal (CT-6), and rice grain (CT-9) shaped C-TiO₂. (A) TiO₂ bands in the low frequency region; (B) D and G bands in the higher frequency region.

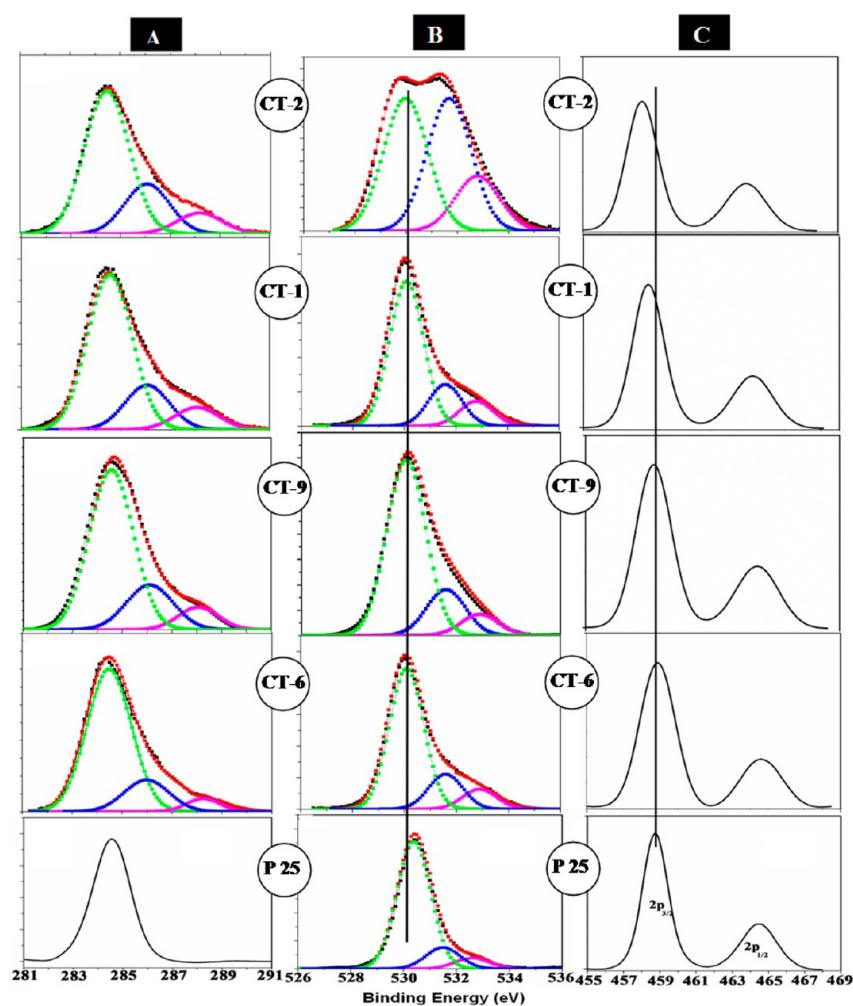


Figure 6. XPS of CT-1, CT-2, CT-6, and CT-9 C-TiO₂ samples. For comparison, XPS of bulk TiO₂ (P25 Degussa) is plotted in the bottom. (A) C 1s, (B) O 1s, and (C) Ti 2p. Color scheme: black-experimental curve; red-fitted; green, blue, and pink-deconvoluted species.

further confirmed by infrared spectra (see the Supporting Information, Figure S9), which exhibit a peak at 1059 cm⁻¹ due to C—O stretching.

Of the three peaks in Figure 6A, intensity of the one due to carbonate-like feature changed with the morphology of C-TiO₂. The measured intensity of this peak at 286.3 eV follows the order: distorted spherical > spherical > hexagonal > rice grain C-TiO₂. This trend is in agreement with the calculated total percentage of carbon from the TOC measurement, mentioned in the previous section. In addition, the absence of a peak around 282.0 eV confirms that the carbon did not substitute oxygen in the lattice.³⁷ The intensity of the 284.6 eV peak implies that the percentage of graphitic carbon is high in the distorted spherical C-TiO₂ and low in the hexagonal C-TiO₂. The uniform C content due to doping within the TiO₂ particle, as proposed from the SEM-EDS line scan, could not be seen distinctly in XPS.

The Ti 2p XPS peak of P25 Degussa in Figure 6C consists of two energy levels of Ti 2p_{1/2} and 2p_{3/2} at 464 and 458 eV, respectively with a separation of ~5.8 eV.³⁸ Two observations are easily noticeable from panel C: (i) the peak shift (with respect to P25 Degussa) toward lower energy is maximum for the distorted spherical C-TiO₂ and is relatively much greater than for other systems and (ii) the distorted spherical morphology exhibits lower line-width than the others. The

fact that the Ti 2p peak position differs for four different morphologies along with the nature of C accumulation on the TiO₂ surface. Thus, the hexagonal and rice grain shaped C-TiO₂ show only a subtle change from the standard TiO₂, whereas the distorted spherical and spherical shapes show greater differences in energy positions. Overall, the distorted spherical C-TiO₂ shows a deviation of nearly 0.45 eV from P25 Degussa, indicative of a partial charge transfer from the surface carbon moiety to the Ti⁴⁺ centers in the TiO₂ network.³⁹

The XPS for O 1s (Figure 6B) shows three different environments in C-TiO₂ for all the four morphologies. The peak positions at 530.3, 531.5, and 532.8 eV in P25 Degussa can be ascribed to Ti—O (O²⁻ lattice oxygen), surface —OH, and adsorbed H₂O, respectively, whereas the peak positions at 530.1, 531.5, and 532.9 eV in all the C-TiO₂ NCs are indexed to Ti—O (O²⁻ lattice oxygen), C=O (and COO), and C—OH (and C—O—C) species, respectively.^{39,40} The enhancement of C=O and C—OH signals in the distorted spherical morphology suggested increased hydration (OH and/or H₂O) with an increase of deposited carbon content (i.e., increased line-width) revealed by the C 1s spectra. The shifting (by 0.2 eV) of the lattice oxygen peak at 530.1 eV in all the C-TiO₂ toward lower energy, relative to the P25 Degussa standard, is indicative of C accumulation.

The Brunauer–Emmett–Teller (BET) surface area data for the four morphological samples are presented in the Supporting Information, Table S4. The BET results show that the C-TiO₂ systems have different surface areas, pore volumes, and pore diameters. Their N₂ adsorption–desorption isotherms are displayed in the Supporting Information, Figure S10. The spherical morphology (CT-1) of C-TiO₂ shows a sharp decline in the desorption branch indicating its mesoporosity, whereas the hysteresis (Type-IV, H1) between the two curves suggests the pores to have a diffusion bottleneck structure.⁴¹ The following parameters were estimated for CT-1: surface area 62 m²/g, pore volume 0.24 cc/g, and BJH pore diameter 18.0 nm. In addition, it showed a unimodal pore size distribution that was a little broad in the range due to its spherical morphology. The reason for the high pore volume may be the fusion of microvoids into macro voids during crystallization. The distorted spherical sample (CT-2) is predicted to have a surface area (61 m²/g) similar to that of the CT-1 sample, but with a smaller pore volume and larger average pore diameter of 0.19 cc/g and 22.4 nm, respectively. CT-2 was found to have two additional pores of sizes 3.6 and 58.6 nm, implying that distorted spherical condensation led to the formation of lower range of mesopores and also macropores due to surface aggregation of these particles. Furthermore, the presence of H3 hysteresis implies nonrigid aggregation of plate-like particles that expose slit-shaped pores.

For the hexagonal shaped C-TiO₂ (CT-6), a type-II isotherm with a still lower surface area of 33 m²/g was observed, with a pore volume and pore diameter of 0.18 cc/g and 19.0 nm, respectively. The BJH pore size distribution exhibits sharp unimodal pores, which are the probable reason for the heterogeneous uptake of carbon and increased pore shrinkage in the region of particle aggregation. Interestingly, the rice grain morphology (CT-9) shows a type-IV isotherm with H4 hysteresis loop and a relatively higher surface area of 229 m²/g with a pore volume of 0.17 cc/g and BJH pore diameter of 3.6 nm. On the basis of the smooth rise in the pore condensation for CT-9, it can be inferred that uniform pores are present, whereas overall results suggest the existence of ordered narrow slit-like mesoporous pores in the micropore region due to the gradual decomposition of carbon.

Photocatalytic Degradation of CBZ. We have previously examined the spherical shaped C-TiO₂ for the photocatalytic degradation of carbamazepine, an emerging contaminant in water. Details of the study and the conditions derived for optimal removal of CBZ are discussed elsewhere.²⁷ Using these optimized parameters (catalyst concentration of 230 mg/L, light intensity of 7700 lux and pollutant concentration of 50 μg/L), the visible light photocatalytic degradation of CBZ was carried out by all four morphologies of C-TiO₂. Additional control experiments were done on undoped TiO₂ and carbon prepared by the same method (CT-1 method). It was found that degradation occurred slowly for both carbon and TiO₂, as shown in the Supporting Information, Figure S11.

As can be seen from Figure 7, the time taken to degrade CBZ using the rice grain, spherical, distorted spherical, and hexagonal shaped C-TiO₂ was 85, 120, 210, and 240 min, respectively. The reaction rates, k (min⁻¹), were determined by plotting $\ln(C/C_0)$ versus time, where C = concentration after time t has elapsed and C_0 = original concentration at $t = 0$. All these trials were found to follow first-order kinetics with a R^2 value of more than 0.90 (see the Supporting Information, Table S5). The rate of CBZ degradation was much faster with the rice

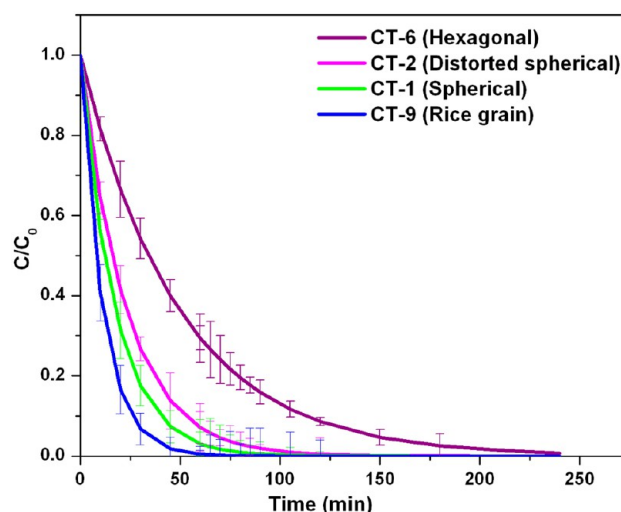


Figure 7. Degradation of carbamazepine by different morphologies of C-TiO₂NCs.

grain shaped C-TiO₂ catalyst than with the other three catalysts. This photocatalytic behavior corroborates well with surface area measurements. The measured surface area (see the Supporting Information, Table S4) is found to be rather large in the rice grain C-TiO₂ (229 m²/g) compared to in the spherical (62 m²/g), distorted spherical (61 m²/g), and hexagonal (33 m²/g) C-TiO₂. Thus, it can be inferred that the high surface area of the rice grain C-TiO₂ is responsible for its high photocatalytic activity.

Chemical Control of Morphology. Our study (tuning morphology by different parameters, vide supra) revealed that low concentrations of H₂O₂ and NH₄F played major roles in controlling morphology and determining the size of C-TiO₂, and it is expected that there may be a competition between them.⁴² F⁻ ions are well-known for their role as etching agents and F⁻ ions from NH₄F can influence the crystallization and growth of TiO₂ due to rapid in situ dissolution and recrystallization.^{43,44} Thus, when H₂O₂ concentration is reduced by 2-fold (to 5 mL) compared to that in the spherical CT-1, the F⁻ ions etch anisotropically leading to the hexagonal shaped C-TiO₂ (CT-6) with clear vertices. We postulate that in all the C-TiO₂ morphologies, this anisotropic etching probably causes the exposure of the (101) plane that has the lowest surface energy. At the same time, the role of H₂O₂⁴⁵ is also crucial, as it was impossible to get the distinct morphologies in its absence. The adsorption of peroxide ions form various intermediate complexes viz., [Ti(O₂)₂(OH₂)OOH]⁻, and/or [Ti(O₂)₂(OH₂)OOH₂], etc., and can lower the surface energy of {001} facets, but these get exposed only in the rice grain shaped C-TiO₂ due to the lower concentration of TOAA.

An interesting observation was noted in the surface morphology of four differently shaped C-TiO₂. In principle, the lower surface energy planes (101), (004), and (200) correspond to the most displayed facets of {101}, {001}, and {100}, respectively in natural anatase crystals.^{46,47} All the four morphologies of C-TiO₂ show the (101) plane of the {101} facet in electron microscopy images. Interestingly, the rice grain shaped C-TiO₂ has coexposed {001} and {101} facets for (004) and (101) planes, respectively as understood from electron microscopy images. Roy et al.⁴⁸ confirmed the presence of high energy {001} reductive facets with low energy {101} oxidative facets of TiO₂, as being responsible for efficient

photocatalytic degradation of a dye. Thus, in our work, the enhanced photocatalytic activity of the rice grain shaped C-TiO₂ could be due to the coexposure of the {001} and {101} facets, as deduced from its TEM images in Figure 3. Different morphologies of TiO₂ have been reported to show mostly {001} facets with enhanced photocatalytic applications even when synthesized using F⁻ ions.^{49,50} Though F⁻ ions have been used for preparing C-TiO₂ in this work, in a given diluted condition ([TOAA/2]), the rice grain C-TiO₂ alone had coexposed {001} and {101} facets due to an competition between F⁻ and H₂O₂. However, a detailed mechanistic study is needed to understand the real factors responsible.

CONCLUSIONS

Various C-TiO₂ morphologies were synthesized by a rapid microwave digestion method. The morphologies were significantly tuned at low concentrations of the precursors for synthesizing anatase C-TiO₂. Among the four different morphologies, the rice grain shaped C-TiO₂ showed enhanced visible light degradation of carbamazepine, a pharmaceutical pollutant in wastewater, due to the presence of coexposed low energy/high energy {101}/{001} facets and its high surface area. These newly synthesized carbon enriched TiO₂ NCs may find useful in applications such as water splitting. Precise understanding of the nature of carbon in these materials needs additional studies.

ASSOCIATED CONTENT

Supporting Information

List of reaction parameters in Tables S1–S4, EDS profile in Figure S2, SEM images at different synthetic parameters (Figures S3 and S4), XRD profiles at various experimental parameters (Figure S5), EDS line scan mapping for CT-1 in Figure S6, HRTEM, UV–vis and FT-IR for samples CT-1 to CT-4 in Figures S7, S8, and S9 respectively, BET surface area results in Figure S10 and Table S4, and rates for photocatalytic CBZ degradation for CT-1 to CT-4 in Table S5 and controlled experiments result found in Figures S1 and S11. This material is available free of charge via the Internet at <http://pubs.acs.org/>. The Supporting Information is available free of charge on the ACS Publications website at DOI: 10.1021/acssuschemeng.5b00044.

AUTHOR INFORMATION

Corresponding Author

*T. Pradeep. E-mail: pradeep@iitm.ac.in.

Notes

The authors declare no competing financial interest.

ACKNOWLEDGMENTS

We thank the Department of Science and Technology, Government of India for financial support. B.S. acknowledges the Indian Institute of Technology Madras for an Institute Postdoctoral Fellowship.

REFERENCES

- (1) Dagherir, R.; Drogui, P.; Robert, D. Modified TiO₂ for environmental photocatalytic applications: A review. *Ind. Eng. Chem. Res.* **2013**, *52*, 3581–3599.
- (2) Carp, O.; Huisman, C. L.; Reller, A. Photoinduced reactivity of titanium dioxide. *Prog. Solid State Chem.* **2004**, *32*, 33–177.

- (3) Dette, C.; Pérez-Osorio, M. A.; Kley, C. S.; Punke, P.; Patrick, C. E.; Jacobson, P.; Giustino, F.; Jung, S. J.; Kern, K. TiO₂ anatase with a bandgap in the visible region. *Nano Lett.* **2014**, *14*, 6533–6538.

- (4) Dong, J.; Han, J.; Liu, Y.; Nakajima, A.; Matsushita, S.; Wei, S.; Gao, W. Defective black TiO₂ synthesized via anodization for visible-light photocatalysis. *ACS Appl. Mater. Interfaces* **2014**, *6*, 1385–1388.

- (5) Zha, C.; Shen, L.; Zhang, X.; Wang, Y.; Korgel, B. A.; Gupta, A.; Bao, N. Double-sided brush-shaped TiO₂ nanostructure assemblies with highly ordered nanowires for dye-sensitized solar cells. *ACS Appl. Mater. Interfaces* **2014**, *6*, 122–129.

- (6) Braham, R. J.; Harris, A. T. Review of major design and scale-up considerations for solar photocatalytic reactors. *Ind. Eng. Chem. Res.* **2009**, *48*, 8890–8905.

- (7) Zhang, J.; Wu, Y.; Xing, M.; Leghari, S. A. K.; Sajjad, S. Development of modified N-doped TiO₂ photocatalyst with metals, nonmetals and metal oxides. *Energy Environ. Sci.* **2010**, *3*, 715–726.

- (8) Chen, D.; Jiang, Z.; Geng, J.; Wang, Q.; Yang, D. Carbon and nitrogen co-doped TiO₂ with enhanced visible-light photocatalytic activity. *Ind. Eng. Chem. Res.* **2007**, *46*, 2741–2746.

- (9) Qian, W.; Alex Greaney, P.; Fowler, S.; Chiu, S. K.; Goforth, A. M.; Jiao, J. Low-temperature nitrogen doping in ammonia solution for production of N-doped TiO₂-hybridized graphene as a highly efficient photocatalyst for water treatment. *ACS Sustainable Chem. Eng.* **2014**, *2*, 1802–1810.

- (10) Irie, H.; Watanabe, Y.; Hashimoto, K. Carbon-doped anatase TiO₂ powders as a visible light sensitive photocatalyst. *Chem. Lett.* **2003**, *32*, 772–773.

- (11) Khan, S. U. M.; Al-Shahry, M.; Ingler, W. B., Jr. Efficient photochemical water splitting by a chemically modified N-TiO₂. *Science* **2002**, *297*, 2243–2245.

- (12) Ohno, T.; Miyamoto, Z.; Nishijima, K.; Kanemitsu, H.; Feng, X. Y. Sensitization of photocatalytic activity of S- or N-doped TiO₂ particles by adsorbing Fe³⁺ cations. *Appl. Catal., A* **2006**, *302*, 62–68.

- (13) Yang, K.; Dai, Y.; Huang, B.; Whangbo, M.-H. Density functional characterization of the visible-light absorption in substitutional C-anion- and C-cation-doped TiO₂. *J. Phys. Chem. C* **2009**, *113*, 2624–2629.

- (14) Zhang, L.; Tse, M. S.; Tan, O. K.; Wang, Y. X.; Han, M. Facile fabrication and characterization of multi-type carbon-doped TiO₂ for visible light-activated photocatalytic mineralization of gaseous toluene. *J. Mater. Chem. A* **2013**, *1*, 4497–4507.

- (15) Wang, S.; Zhao, L.; Bai, L.; Yan, J.; Jiang, Q.; Lian, J. Enhancing photocatalytic activity of disorder engineered C/TiO₂ and TiO₂ nanoparticles. *J. Mater. Chem. A* **2014**, *2*, 7439–7445.

- (16) Kaplan, R. Review: Pharmacological pollution in water. *Crit. Rev. Environ. Sci. Technol.* **2013**, *43*, 1074–1116.

- (17) Benner, J.; Helbling, D. E.; Kohler, H. -P. E.; Wittebol, J.; Kaiser, E.; Prasse, C. Is biological treatment a viable alternative for micropollutant removal in drinking water treatment processes? *Water Res.* **2013**, *47*, 5955–5976.

- (18) Brillas, E.; Sirés, I.; Oturan, M. Electro-Fenton process and related electrochemical technologies based on Fenton's reaction chemistry. *Chem. Rev.* **2009**, *109*, 6570–631.

- (19) Fujishima, A.; Rao, T. N.; Tryk, D. A. Titanium dioxide photocatalysis. *J. Photochem. Photobiol., C* **2000**, *1*, 1–21.

- (20) Avisar, D.; Horovitz, I.; Lozzi, L.; Ruggieri, F.; Baker, M.; Abel, M. L.; Mamane, H. Impact of water quality on removal of carbamazepine in natural waters by N-doped TiO₂ photocatalytic thin film surfaces. *J. Hazard Mater.* **2012**, *244–245*, 463–471.

- (21) Lazzeri, M.; Vittadini, A.; Selloni, A. Structure and energetics of stoichiometric TiO₂ anatase surfaces. *Phys. Rev. B* **2001**, *63*, 155409.

- (22) Han, X.; Kuang, Q.; Jin, M.; Xie, Z.; Zheng, L. Synthesis of titania nanosheets with a high percentage of exposed (001) facets and related photocatalytic properties. *J. Am. Chem. Soc.* **2009**, *131*, 3152–3153.

- (23) Liu, S.; Yu, J.; Jaroniec, M. Anatase TiO₂ with dominant high-energy {001} facets: Synthesis, properties, and applications. *Chem. Mater.* **2011**, *23*, 4085–4093.

- (24) Lee, W.-J.; Sung, Y.-M. Synthesis of anatase nanosheets with exposed {001} facets via chemical vapor deposition. *Cryst. Growth Des.* **2012**, *12*, 5792–5795.
- (25) Liu, S.; Yu, J.; Jaroniec, M. Anatase TiO₂ with dominant high-energy {001} facets: Synthesis, properties, and applications. *Chem. Mater.* **2011**, *23*, 4085–4093.
- (26) Vaez, M.; Moghaddam, A. Z.; Alijani, S. Optimization and modeling of photocatalytic degradation of azo dye using a response surface methodology (RSM) based on the central composite design with immobilized titania nanoparticles. *Ind. Eng. Chem. Res.* **2012**, *51*, 4199–4207.
- (27) We have optimized CBZ removal efficiency using spherical shaped C-TiO₂. The result is unpublished.
- (28) Neville, E. M.; Mattle, M. J.; Loughrey, D.; Rajesh, B.; Rahman, M.; Don MacElroy, J. M.; Sullivan, J. A.; Thampi, K. R. Carbon-doped TiO₂ and carbon, tungsten-codoped TiO₂ through sol–gel processes in the presence of melamine borate: Reflections through photocatalysis. *J. Phys. Chem. C* **2012**, *116*, 16511–16521.
- (29) Shen, J.; Wang, H.; Zhou, Y.; Ye, N.; Li, G.; Wang, L. Anatase/rutile TiO₂ nanocomposite microspheres with hierarchically porous structures for high-performance lithium-ion batteries. *RSC Adv.* **2012**, *2*, 9173–9178.
- (30) Foong, Y. M.; Koh, A. T. T.; Ng, H. Y.; Chua, D. H. C. Mechanism behind the surface evolution and microstructure changes of laser fabricated nanostructured carbon composite. *J. Appl. Phys.* **2011**, *110*, 054904.
- (31) Hu, Z.; Yan, Z.; Shen, P. K.; Zhong, C.-J. Nano-architectures of ordered hollow carbon spheres filled with carbon webs by template-free controllable synthesis. *Nanotechnology* **2012**, *23*, 485404.
- (32) Wang, Y.; Shi, R.; Lin, J.; Zhu, Y. Significant photocatalytic enhancement in methylene blue degradation of TiO₂ photocatalysts via graphene-like carbon in situ hybridization. *Appl. Catal., B* **2010**, *100*, 179–183.
- (33) Kiran, V.; Sampath, S. Enhanced Raman spectroscopy of molecules adsorbed on carbon-doped TiO₂ obtained from titanium carbide: A visible-light-assisted renewable substrate. *ACS Appl. Mater. Interfaces* **2012**, *4*, 3818–3828.
- (34) Liu, J.; Zhang, Q.; Yang, J.; Ma, H.; Tade, M. O.; Wang, S.; Liu, J. Facile synthesis of carbon-doped mesoporous anatase TiO₂ for the enhanced visible-light driven photocatalysis. *Chem. Commun.* **2014**, *50*, 13971–13974.
- (35) Liu, B.; Liu, L.-M.; Lang, X.-F.; Wang, H.-Y.; Lou, X. W.; Aydil, E. S. Doping high-surface-area mesoporous TiO₂ microspheres with carbonate for visible light hydrogen production. *Energy Environ. Sci.* **2014**, *7*, 2592–2597.
- (36) Cao, X. P.; Li, D.; Jing, W. H.; Xing, W. H.; Fan, Y. Q. Synthesis of visible-light responsive C, N and Ce co-doped TiO₂ mesoporous membranes via weak alkaline sol–gel process. *J. Mater. Chem.* **2012**, *22*, 15309–15315.
- (37) Wang, H.; Wu, Z.; Liu, Y. A simple two-step template approach for preparing carbon-doped mesoporous TiO₂ hollow microspheres. *J. Phys. Chem. C* **2009**, *113*, 13317–13324.
- (38) Zhou, W.; Liu, Y.; Zhang, Y.; Yang, G.; Deng, S.; Shen, F.; Peng, H.; Wang, L. Novel multi-layer cross-linked TiO₂/C nanosheets and their photocatalytic properties. *New J. Chem.* **2014**, *38*, 1647–1654.
- (39) Lin, C.; Song, Y.; Cao, L.; Chen, S. Effective photocatalysis of functional nanocomposites based on carbon and TiO₂ nanoparticles. *Nanoscale* **2013**, *5*, 4986–4992.
- (40) Zhong, J.; Chen, F.; Zhang, J. Carbon-deposited TiO₂: Synthesis, characterization, and visible photocatalytic performance. *J. Phys. Chem. C* **2010**, *114*, 933–939.
- (41) Olsen, R. E.; Alam, T. M.; Bartholomew, C. H.; Enfield, D. B.; Woodfield, B. F. Structure analysis of Al-modified TiO₂ nanocatalyst supports. *J. Phys. Chem. C* **2014**, *118*, 9176–9186.
- (42) Cai, J.; Wang, Z.; Lv, K.; Zheng, Y.; Yu, J.; Li, M. Rapid synthesis of a TiO₂ hollow microsphere assembly from hollow nanoparticles with enhanced photocatalytic activity. *RSC Adv.* **2013**, *3*, 15273–15281.
- (43) Liu, N.; Mirabolghasemi, H.; Lee, K.; Albu, S. P.; Tighineanu, A.; Altomare, M.; Schmuk, P. Anodic TiO₂ nanotubes: Double walled vs. single walled. *Faraday Discuss.* **2013**, *164*, 107–116.
- (44) Yu, J. G.; Yu, H.; Cheng, B.; Zhao, X.; Yu, J. C.; Ho, W. The effect of calcination temperature on the surface microstructure and photocatalytic activity of TiO₂ thin films prepared by liquid phase deposition. *J. Phys. Chem. B* **2003**, *107*, 13871–13879.
- (45) Li, T.; Tian, B.; Zhang, J.; Dong, R.; Wang, T.; Yang, F. Facile tailoring of anatase TiO₂ morphology by use of H₂O₂: From microflowers with dominant {101} facets to microspheres with exposed {001} facets. *Ind. Eng. Chem. Res.* **2013**, *52*, 6704–6712.
- (46) Ramamoorthy, M.; Vanderbilt, D.; King-Smith, R. D. First-principle calculations of the energetics of stoichiometric TiO₂ surfaces. *Phys. Rev. B* **1994**, *49*, 16721–16727.
- (47) Diebold, U. The surface science of titanium dioxide. *Surf. Sci. Rep.* **2003**, *48*, 53–229.
- (48) Roy, R.; Sohn, Y.; Pradhan, D. Synergy of low-energy {101} and high-energy {001} TiO₂ crystal facets for enhanced photocatalysis. *ACS Nano* **2013**, *7*, 2532–2540.
- (49) Dozzi, M. V.; Selli, E. Specific facets-dominated anatase TiO₂: Fluorine-mediated synthesis and photoactivity. *Catalysts* **2013**, *3*, 455–485.
- (50) Gu, L.; Wang, J.; Cheng, H.; Zhao, Y.; Liu, L.; Han, X. One-step preparation of graphene-supported anatase TiO₂ with exposed {001} facets and mechanism of enhanced photocatalytic properties. *ACS Appl. Mater. Interfaces* **2013**, *5*, 3085–3093.

Supporting Information

Rapid Synthesis of C-TiO₂: Tuning the Shape from Spherical to Rice Grain Morphology for Visible Light Photocatalytic Applications

Balaji Sambandam^a, Anupama Surejan^b, Ligy Philip^b, and Thalappil Pradeep^a

^aDST Unit of Nanoscience and Thematic Unit of Excellence, Department of Chemistry, Indian Institute of Technology Madras, Chennai 600036, India and

^bDepartment of Civil Engineering, Indian Institute of Technology Madras, Chennai 600036, India.

Table S1: Results from varying reaction time**

S.No	Time in min	Morphology	Crystalline phase
CT-13	10	spherical	Anatase
CT-14	18	spherical and oval	Anatase
CT-15	40	spherical and oval	Anatase

**Conditions: Volume: 80% ; Temperature: 150 °C; Concentrations: Same as in C1 (see Table 1), power: 400 W

Table S2: Results from varying the volume[#]

S.No	Volume	Morphology	Crystalline phase
CT-16	50%	spherical	Anatase
CT-17	40%	distorted spherical	Anatase
CT-18	30%	no specific morphology	Anatase

[#]Conditions: Temperature: 150 °C; Time: 30 min; Concentrations: Same as in C1; power: 400 W

Table S3: Results from varying the temperature[§]

S.No	Temp in (° C)	Morphology	Crystalline phase
CT-19	70	no specific morphology	Anatase
CT-20	100	no specific morphology	Anatase

[§]Conditions: Time: 30 min; Concentrations: Same as in C1; power: 400 W, Volume: 80%

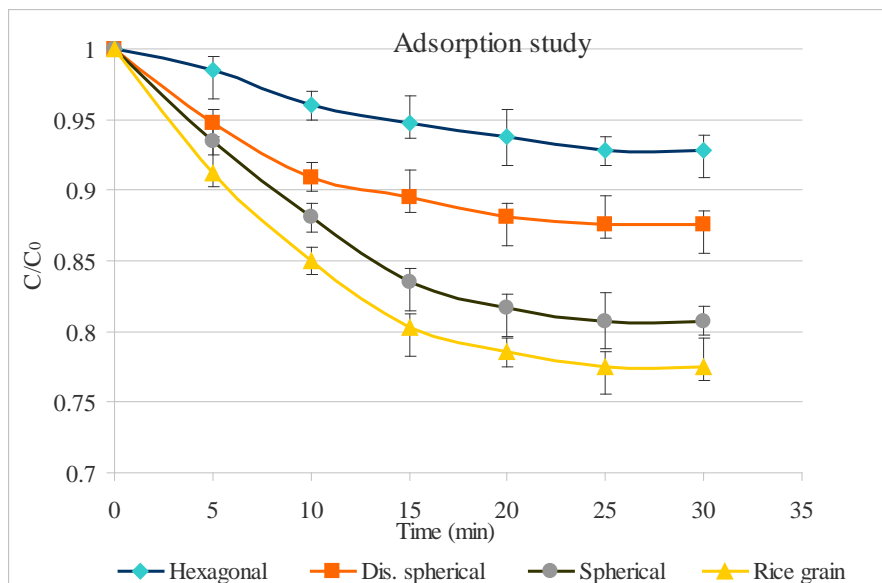


Figure S1. Removal of carbamazepine using different shapes of C-TiO₂ catalysts in dark.

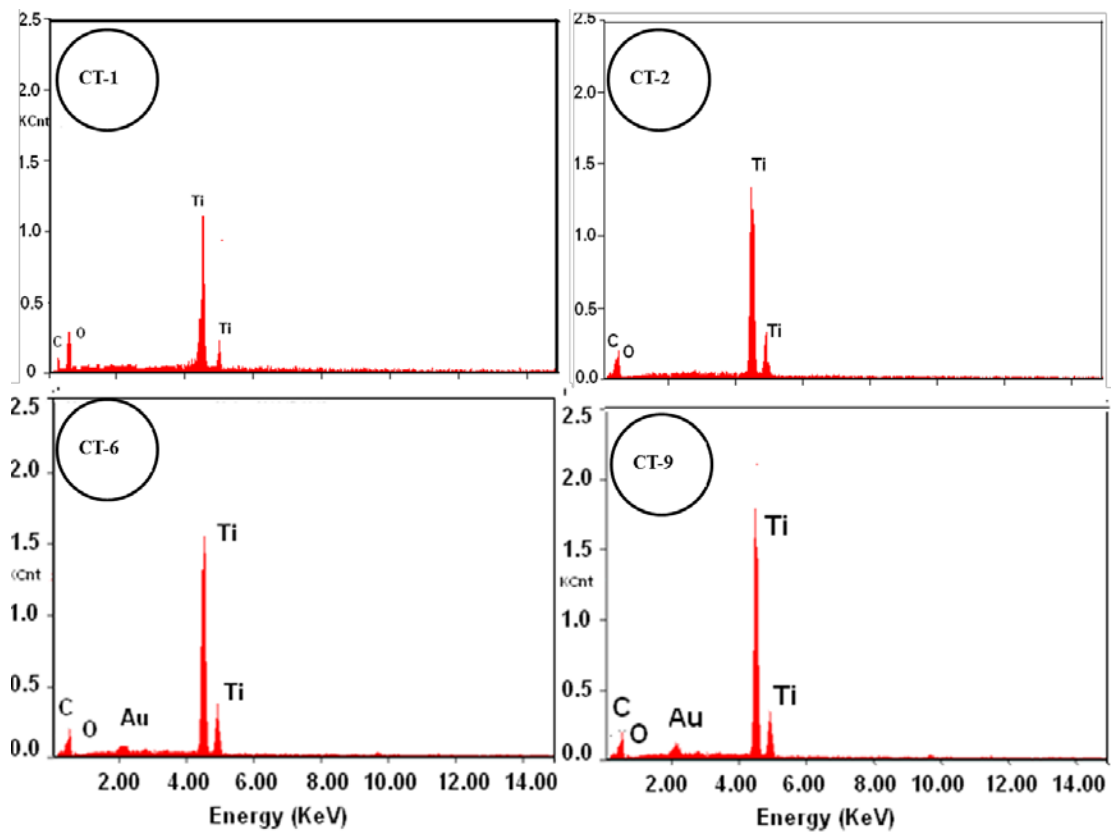


Figure S2. EDS pattern for four different morphologies of C-TiO₂.

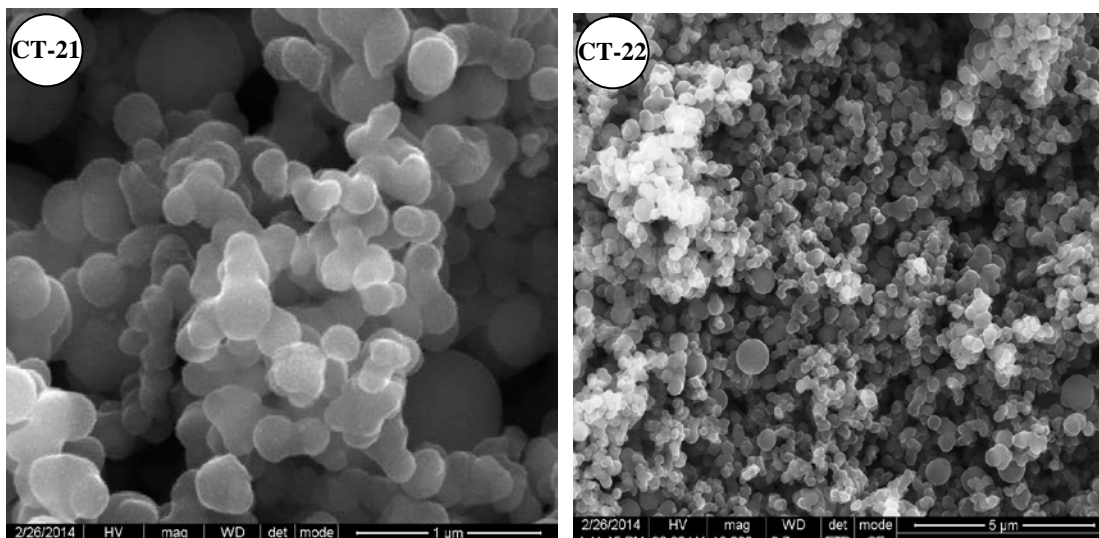


Figure S3. HRSEM images for C-TiO₂ at higher concentration of the ingredients.

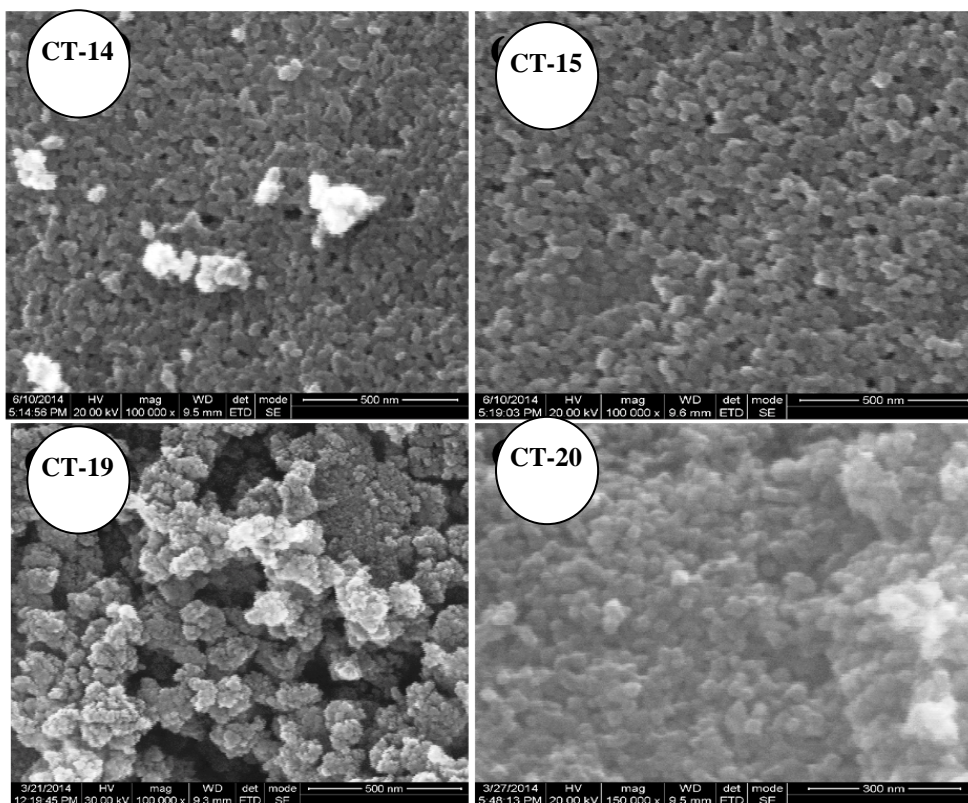


Figure S4. HRSEM images for C-TiO₂ of CT-14 and CT-15 (see Tables S1 and S3) showcasing time and temperature dependence of synthesis.

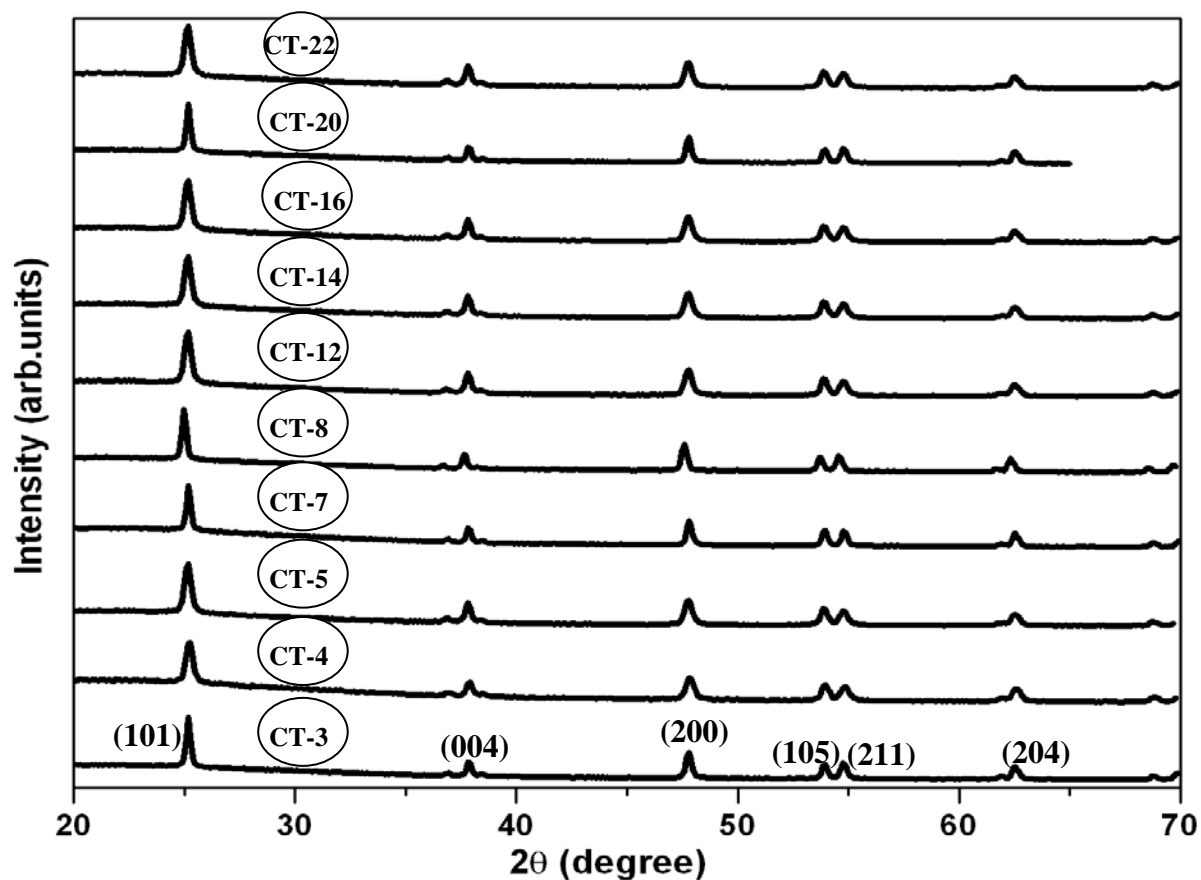


Figure S5. XRD profile for C-TiO₂ at various preparative conditions.

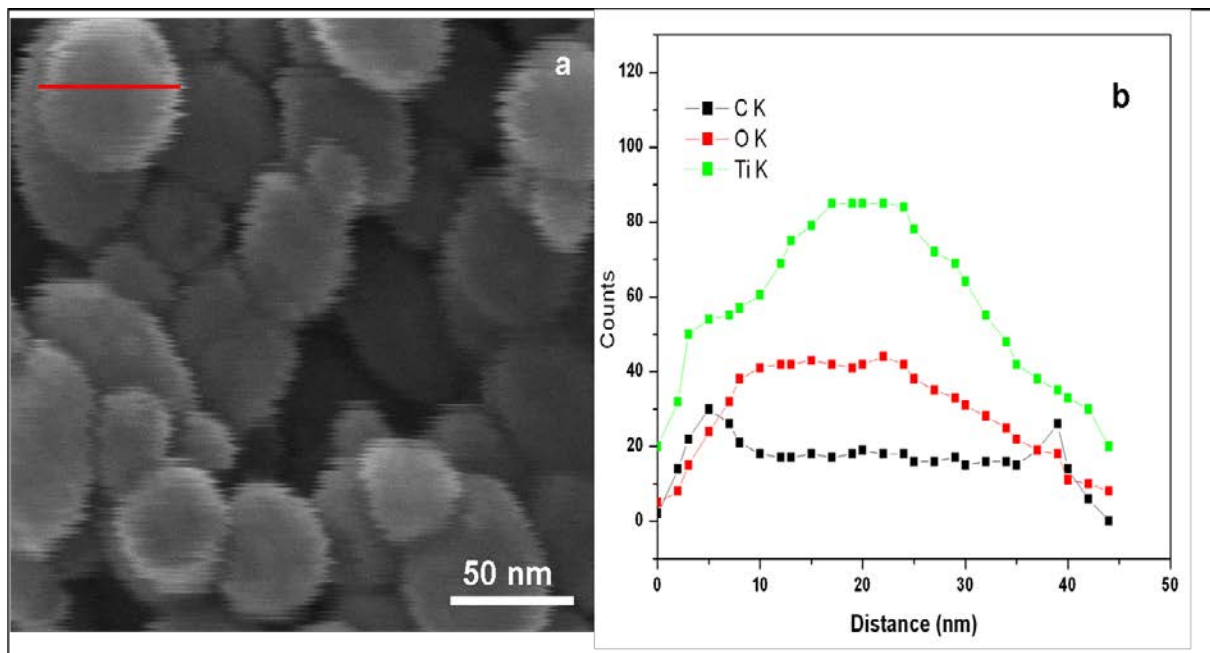


Figure S6. (a) HRSEM image of spherical shaped C-TiO₂ and (b) corresponding EDS line scan data for a single particle as marked by a red line in (a).

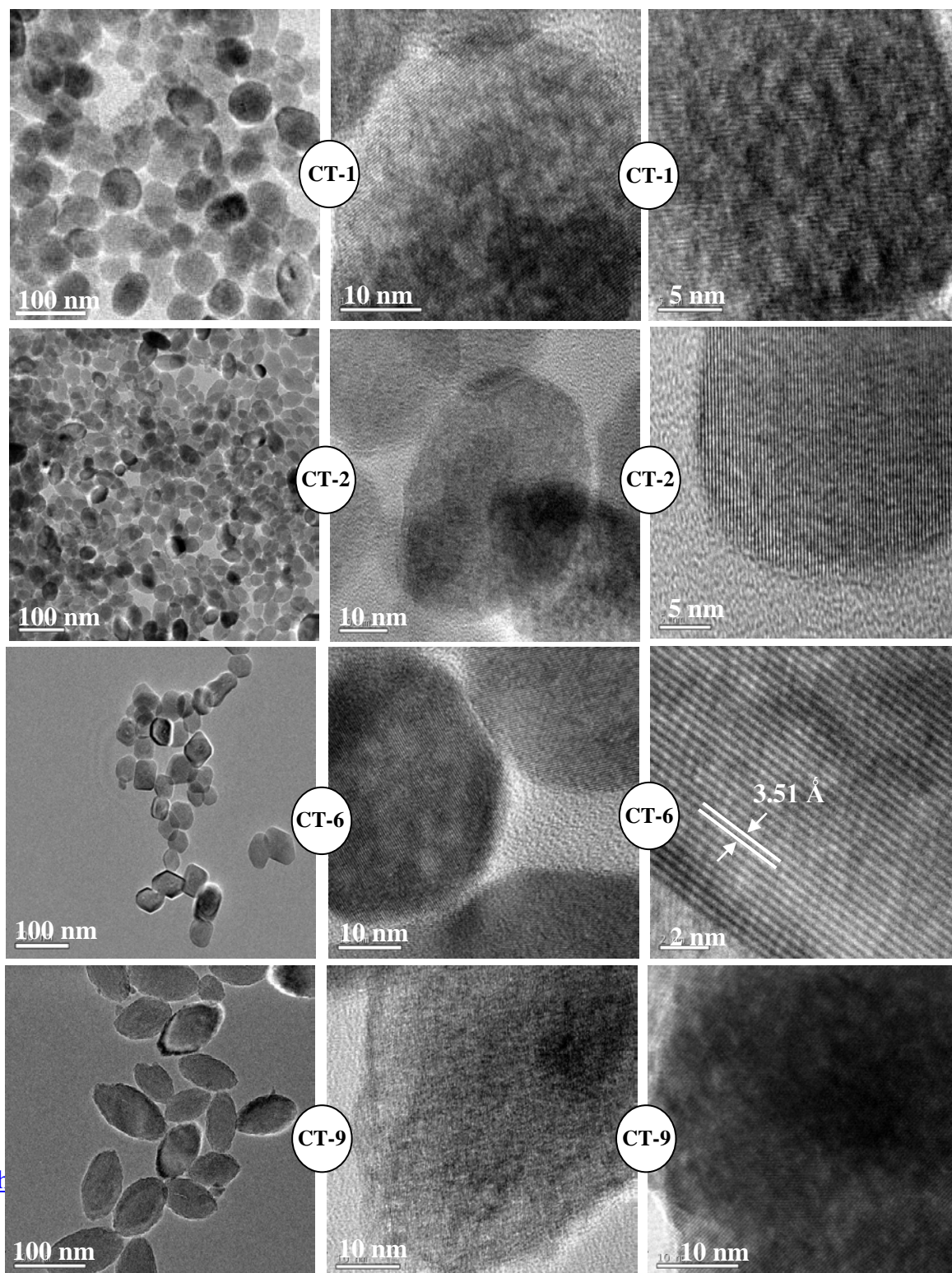


Figure S7. HRTEM images for the four different morphologies of C-TiO₂ nanocrystals.

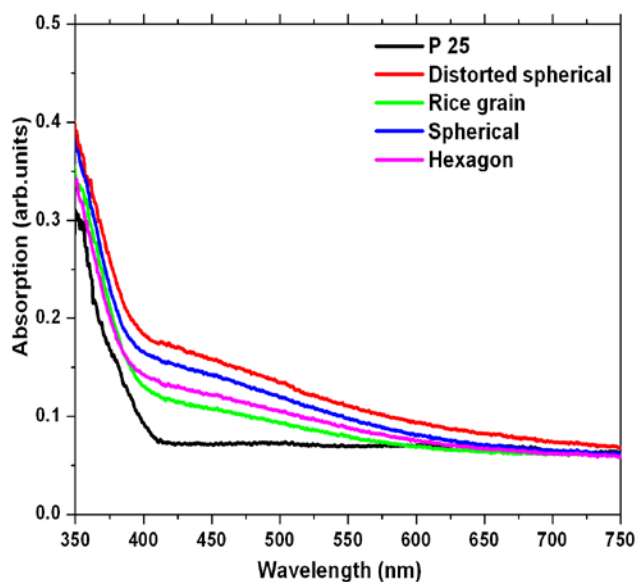


Figure S8. UV-vis diffuse reflectance profiles for four different morphologies of C-TiO₂ in comparison with P25 Degussa (bulk TiO₂).

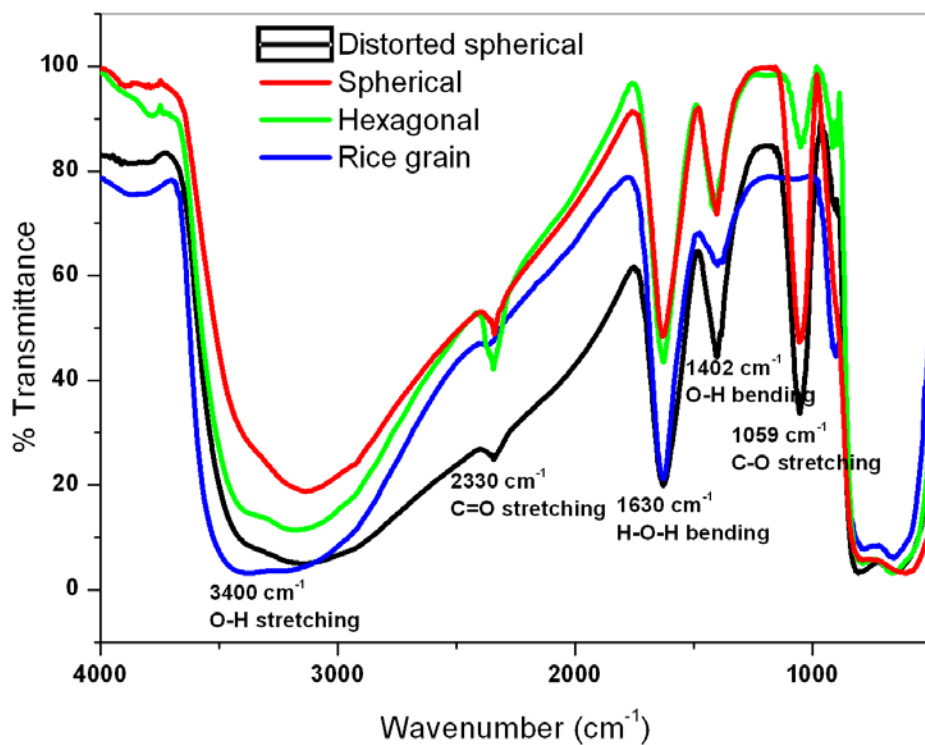


Figure S9. FT-IR spectra for C-TiO₂ of four different morphologies.

Table S4. BET surface area for the different morphologies of C-TiO₂

Sample code	Surface area, m ² /g	Pore volume, cc/g	Pore diameter, Å
Spherical (CT-1)	62	0.24	180
Distorted spherical (CT-2)	61	0.19	224
Hexagonal (CT-6)	33	0.18	190
Rice grain (CT-9)	229	0.17	36

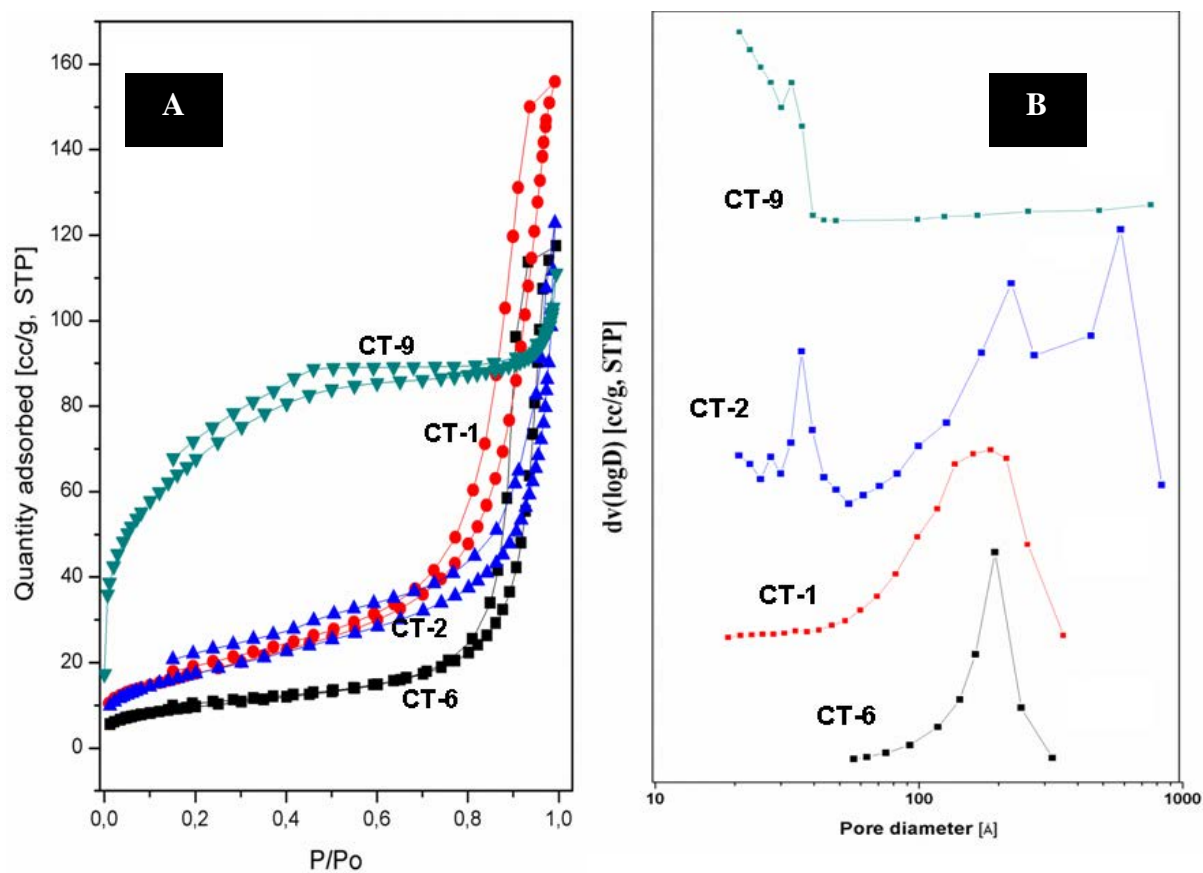


Figure S10. N₂-adsorption-desorption isotherm liner plot (A) and BJH desorption average pore diameter (B) for four different morphologies of C-TiO₂.

Table S5. Rate of degradation of Carbamazepine using different shaped C-TiO₂

Pollutant	Catalyst shape	R ²	K min ⁻¹
Carbamazepine (50µg/L)	Rice grain (CT-9)	0.98	0.094
	Spherical (CT-1)	0.99	0.059
	Distorted spherical (CT-2)	0.99	0.044
	Hexagonal (CT-6)	0.97	0.020

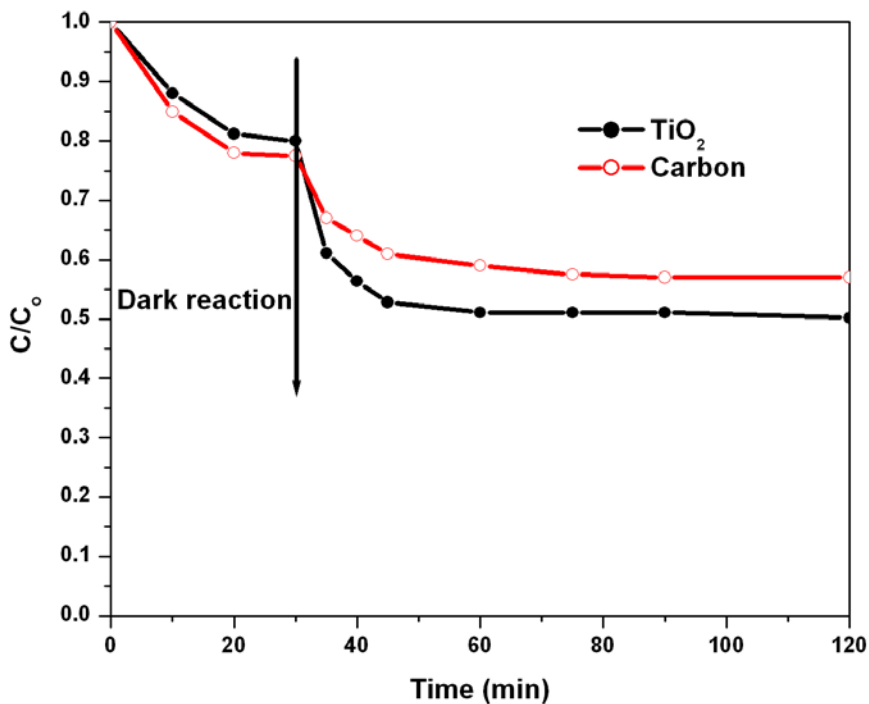


Figure S11. Photocatalytic activity for carbamazepine by TiO_2 and carbon prepared by CT-1 method.


 CrossMark
click for updates

 Cite this: *RSC Adv.*, 2015, 5, 48039

Noble metal clusters protected with mixed proteins exhibit intense photoluminescence†

 Jyoti Sarita Mohanty,‡^a Ananya Baksi,‡^a Haiwon Lee^b and T. Pradeep*^a

In this paper is reported the synthesis and detailed mass spectrometric and spectroscopic characterization of highly luminescent Au and Ag clusters protected with mixed proteins. Taking advantage of the aggregation tendency of the protein, lysozyme (Lyz), an inter-protein conjugate was made from a physical mixture of two proteins, bovine serum albumin (BSA) and Lyz. Based on matrix-assisted laser desorption/ionization mass spectrometry data, the new cluster is assigned as $\sim\text{Au}_{36}\text{@BSA-Lyz}$. This specific system showed a very high red luminescence and the calculated quantum yield was 42% which is the highest to date for such cluster systems. A similar study on an Ag system showed the formation of $\sim\text{Ag}_{35}\text{@BSA-Lyz}$ when a similar metal and protein concentration was used. By varying the concentration of the Ag precursor, different compositions of the cluster protected by the mixed protein were achieved. Such a system with a high quantum yield can be used for various applications such as sensors for ultralow levels of analytes, fluorescent tags and for tracking biomolecules in real systems.

 Received 17th April 2015
Accepted 8th May 2015

DOI: 10.1039/c5ra06964e

www.rsc.org/advances

1. Introduction

Noble metal nanoclusters are one of the most fascinating areas of research in contemporary materials science.^{1–5} Several metals have been used in this context among which gold (Au) and silver (Ag) have drawn the most attention. Most cluster chemistry is concerned with monolayer protected clusters. Thiol ligands are of greater interest as the Au–S bond is strong and by changing the ligand (thiol), the properties of the clusters can be altered. Many thiol protected Au and Ag clusters have been reported and some of them have been crystallized. Examples include: $\text{Au}_{25}(\text{SR})_{18}$,^{6,7} $\text{Au}_{30}(\text{SR})_{18}$,⁸ $\text{Au}_{38}(\text{SR})_{24}$,⁹ $\text{Au}_{36}(\text{SR})_{24}$,¹⁰ $\text{Au}_{102}(\text{SR})_{44}$,¹¹ and $\text{Ag}_{44}(\text{SR})_{30}$.^{12,13} Three types of modifications are possible on such monolayer protected clusters: (i) ligand exchange,^{14–16} (ii) alloying¹² of the core and (iii) alloying and ligand exchange simultaneously. Both of these have been studied in detail for monolayer protected Au clusters. Some of these chemically modified clusters have been crystallized.¹²

Macromolecular templates are another platform for synthesizing such clusters.^{4,17,18} DNA,¹⁹ dendrimers²⁰ and most recently proteins²¹ have been used as templates for cluster

formation. The most often used proteins are bovine serum albumin (BSA),^{21–28} human serum albumin,^{29,30} lactoferrin (Lf),^{31,32} lysozyme (Lyz),^{33–36} insulin,³⁷ and so on. Major characterization methods of such clusters involve mass spectrometry (MS), but matrix-assisted laser desorption/ionization (MALDI) is mainly used,^{21,25,27–29,31,34,38} as none of these clusters could be crystallized so far. The general synthetic route of such clusters involves adduct formation between the protein and the metal and subsequent reduction of the ion to the M(0) state at an elevated pH.^{21,31} During the core formation, inter-protein metal ion transfer takes place which leads to the regeneration of the free protein. As the core evolves to a bigger size, more and more free protein regeneration can be seen.³¹ A variety of cores have been reported, depending on the size and structure of the protein.^{31,34} For smaller proteins such as Lyz, core compositions have been confirmed from the aggregates (formed *via* inter-protein interaction through a salt bridge).³⁴ For a single protein, by changing the experimental conditions and using different parameters, one can modify the core size as shown in a recent study by predefining the protein structure at a specific pH.³⁸ Different methods have been tried for modifying the core and shell composition such as core etching,²³ a sonochemical method,³⁹ microwave synthesis,^{40,41} slow reduction by carbon monoxide,³⁸ and so on. Such clusters exhibit intense luminescence which is highly sensitive to the presence of foreign elements which can interact and quench the luminescence.² This luminescence property has been applied for sensing metal ions^{24,26,33,40} and small molecules,^{30,42–48} as well as *in vitro* and *in vivo* imaging and labeling.^{23,49} A few of the proteins are known to retain biological activity even after cluster formation,³⁷ indicating that the

^aDST Unit of Nanoscience (DST UNS), Thematic Unit of Excellence (TUE), Department of Chemistry, Indian Institute of Technology Madras, Chennai – 600 036, India. E-mail: Pradeep@iitm.ac.in; Fax: +91-44-2257-0545

^bDepartment of Chemistry, Institute of Nanoscience and Technology, Hanyang University, Seoul 133-791, Korea

† Electronic supplementary information (ESI) available: Comparative MALDI-MS of BSA and $\sim\text{Au}_{30}\text{@BSA}$ at higher and lower mass range, MALDI-MS of Lyz and $\text{Au}^+\text{-Lyz}$, BSA-Lyz adducts, XPS spectrum, UV-Vis spectra, concentration dependent MALDI-MS of $\text{Ag}_{\text{QC}}\text{@BSA-Lyz}$. See DOI: 10.1039/c5ra06964e

‡ Contributed equally.

protein remains as it was and the cluster formation does not occur *via* the involvement of the active site of the protein. The presence of another protein might help in enhancing the Förster resonance energy transfer (FRET) probability and thus, the quantum yield may be increased. This could possibly be following the ligand exchange procedure used for monolayer protected clusters where after ligand exchange, properties of both the ligands can be monitored. Niihori *et al.* have separated all the ligand exchange products of $\text{Au}_{25}(\text{SR}_1)_{18-x}(\text{SR}_2)_x$ ($x = 0, 1, 2 \dots 18$) by chromatography and characterized them using MS.¹⁶ The supramolecular chemistry of such clusters *via* ligand exchange by thiolated calixarene has been studied in detail.¹⁴ Taking advantage of ligand and cyclodextrin inclusion complex formation, Mathew *et al.* have recently shown that supramolecular chemistry is possible for such $\text{Au}_{25}(\text{SR})_{18}$ clusters.¹⁵ Exchanging the core with other metals can also enhance the physico-optical properties significantly as shown by Wang *et al.*, where they have exchanged Ag with Au and obtained 200-fold increases in the luminescence (41% quantum yield).⁵⁰

There are reports of ligand exchange and mixed ligand protection for monolayer protected clusters. Recently, ligand exchange of $\text{Au}_{25}(\text{SR})_{18}$ was separated using high-performance liquid chromatography and each of the exchanged products were observed using MALDI-MS.¹⁶ Although a mixed protein matrix such as egg shell membrane⁴⁶ and hair fibre⁴⁴ were used for cluster synthesis, none of these clusters could be characterized to get an idea about their precise core size. Proteins are macromolecules and they behave differently to small thiol ligands. Protein-protein interaction has been studied by biologists and this has strong biological implications. This kind of interaction is very specific and occurs only between specific proteins. Following the ligand exchange of monolayer protected clusters, the effect of addition of an external protein on a preformed protein protected cluster is reported in this paper.

Most of the previous reports have claimed that the luminescence of protein protected clusters is because of FRET between the protein and the cluster.^{4,32} Compared to monolayer protected Au clusters, protein protected clusters have a higher quantum yield but the yield is still not very promising unlike that obtained for the fluorescent dyes (15% for protein protected clusters whereas dyes show more than 95%). Keeping this in mind, an attempt to ligand exchange protein protected clusters was made, where it was hoped to see different properties by protein exchange. More interestingly, we expected to be in a position to regulate the properties of the proteins as well as the cluster core.

In this paper is reported the formation of highly fluorescent Au quantum clusters with the highest quantum yield (42.4%) in a mixed protein system. Two differently sized proteins, namely BSA and Lyz, were used for this study and the reactants as well as the products were probed using MS and optical spectroscopic techniques. A new cluster core, Au_{36} , protected with both BSA and Lyz was obtained with a four-fold increase in the fluorescence intensity which leads to a 42.4% quantum yield for this system.

2. Experimental

2.1. Reagents and materials

Bovine serum albumin at pH 6–7 was purchased from SRL Chemical Co. Ltd., India. Lysozyme and sinapic acid were purchased from Sigma-Aldrich. Tetrachloroauric acid trihydrate ($\text{HAuCl}_4 \cdot 3\text{H}_2\text{O}$) was purchased from CDH, India. Silver nitrate and sodium hydroxide (NaOH) were purchased from Rankem, India. Sodium borohydride (NaBH_4) was purchased from Spectrochem, India. All the chemicals were used without further purification. Milli-Q water was used for all the experiments.

2.2. Instrumentation

Luminescence measurements were carried out using a Jobin Yvon NanoLog spectrofluorometer. Both the excitation and emission spectra were collected with a band pass of 3 nm. MALDI-MS studies were performed using an Applied Biosystems Voyager-DE PRO Biospectrometry Workstation. A pulsed nitrogen laser of 337 nm was used for the MALDI-MS studies. Mass spectra were collected in linear positive mode and an average of 250 shots was used for each spectrum. High resolution transmission electron microscopy (HRTEM) was performed on a Jeol JFD 3010, a 300 kV instrument, equipped with an ultra high resolution pole piece. The samples for HRTEM were prepared by dropping the dispersion on a carbon coated copper grid. Scanning electron microscopy (SEM) and energy dispersive analysis of the X-ray (EDAX) images were carried out using an FEI QUANTA 200 SEM. Samples were spotted on an indium tin oxide conducting glass substrate and dried in ambient conditions prior to SEM and EDAX measurements. X-ray photoelectron spectroscopy (XPS) studies were carried out using an Omicron ESCA probe spectrometer with polychromatic Mg K α X-rays ($h\nu = 1253.6$ eV). The samples were spotted as drop cast films on a sample stub.

2.3. Synthesis

BSA and Lyz were mixed in a 1 : 1 molar ratio and stirred for 10 min. To this 1 mL of 6 mM HAuCl_4 was added. The solution was stirred for another 15 min. Then 100 μL of 1 M NaOH was added to this mixture, and it was stirred further for 12 h to get a clear brown coloured solution. All the samples were taken directly from the reaction mixture for MALDI-MS and other characterization studies. Silver clusters were prepared keeping the protein and Ag concentration exactly the same as those used for the Au cluster synthesis. In this case, NaBH_4 was used as the external reducing agent.

3. Results and discussion

3.1. Gold cluster formation in a mixed protein matrix

Monolayer as well as protein protected Au and Ag clusters were studied extensively.^{1,3,17} Protein protected clusters were typically synthesized by mixing a preferred ratio of protein and metal ions to form a metal bound protein adduct and followed by reduction of the adducts at a basic condition (pH 12). At this

pH, the protein unfolds [seen in circular dichroism]^{27,31,32,34} and disulfide bonds between the cysteine residues break. In a system containing two different proteins, the inter-protein disulfide bonds may create new inter-protein adducts. In these reactions there are a number of different types of possibilities and these are: (i) large protein-large protein, (ii) large protein-small protein and (iii) small protein-small protein. In this paper, the first two possibilities were studied. Lf, a large protein with a mass of 83 kDa and Lyz, a small protein with a mass of 14.3 kDa were chosen in combination with BSA to study the exchange.

Isolated Au and Ag clusters protected with BSA^{25,27} as well as Lyz³⁴ were characterized thoroughly using several spectroscopic and mass spectrometric tools. They show well defined mass spectral signatures as observed from MALDI-MS analysis. The core size of such clusters is assigned by considering the mass shift from the parent protein after cluster formation. In most of the cases, core size depends on the concentration of protein and metal ions in the solution and varies linearly with metal concentration. At a specific Au³⁺ concentration, $\sim\text{Au}_{30}@BSA$ ²⁷ forms (1 : 16 BSA : Au³⁺ molar concentration), whereas an Au₁₀ core is observed for Lyz (1 : 4 Lyz : Au³⁺ molar concentration).³⁴

A physical mixture of 1 : 1 (75 μM) BSA and Lyz was used and the mixture was incubated in the presence of 6 mM Au³⁺ for a few minutes to allow reduction of Au³⁺ to Au⁰ by the aromatic amino acids of the proteins and subsequently NaOH was added. Formation of clusters was confirmed from the appearance of a slight red luminescence under ultraviolet (UV) light after 4 h of incubation. The mixture was further incubated for up to 12 h to allow the complete conversion of Au³⁺ to Au⁰. Fig. 1 shows the comparison of the MALDI-MS spectra of BSA-Lyz and Au_{QC}@BSA-Lyz in linear positive ion mode. In the 60–100 kDa mass range, the BSA-Lyz mixture showed three peaks corresponding to BSA⁺, BSA-Lyz⁺ and BSA-Lyz₂⁺ (see next for details). During cluster formation, a new peak appeared at 88.3 kDa together with $\sim\text{Au}_{30}@BSA$ at 72 kDa (see (ESI) Fig. S1† for the MALDI-MS of $\sim\text{Au}_{30}@BSA$). A corresponding +2 charged species was observed at 44.1 kDa. If it is assumed that there was adduct formation between the proteins, the new peak can be assigned

as $\sim\text{Au}_{36}@BSA-Lyz$. The peak position remained the same after 24 h as well as at 48 h of incubation indicating the formation of a stable species in the solution. The possibility of formation of Au₃₆ in monolayer protected clusters was reported previously.¹⁰ In the lower mass region (<20 kDa), a few Au attachments were observed with Lyz together with the fragments of BSA and Lyz (see ESI Fig. S2†).

3.2. Identification of mixed protein aggregates by MALDI-MS

In order to check the formation of BSA-Lyz adducts in specific reaction conditions, several control experiments were performed and the presence of this species was verified using MALDI-MS. The mass spectra of: (i) pure BSA, (ii) Au⁺-BSA adduct, (iii) Lyz, (iv) Au⁺-Lyz adduct, (v) BSA and Lyz mixture in presence of NaOH and (vi) BSA and Lyz mixture, are shown in Fig. 2. The molecular ion peak of BSA appears at 66.7 kDa as shown in spectrum (i). Corresponding a doubly charged species at 33.3 kDa was also observed. Beyond 66.7 kDa, only the dimer of BSA was observed at 133.4 kDa and no peak was observed in the mass range of 70–100 kDa. Once Au³⁺ was added to the BSA solution, the main protein peak was shifted by 3.2 kDa as shown in (ii) and the resulting adduct was assigned to $\sim\text{Au}_{16}-BSA$. In this state, Au is in the +1 oxidation state (as revealed by XPS).³¹ The monomer of Lyz shows a peak at *m/z* 14.3 kDa and the corresponding doubly charged species was observed at *m/z* 7.2 kDa. Lyz is known to form aggregates in solution and a maximum aggregate of a hexamer of individual protein was observed in the mass range studied. The corresponding dimer, trimer and tetramer peaks were observed at *m/z* 28.6, 42.9 and 57.2 kDa, respectively (see ESI Fig. S3†). Pentamers and hexamers were observed at *m/z* 71.5 and 85.8 kDa, respectively, as shown in (iii). Beyond this the peak intensity was not significant. The Au⁺-Lyz adduct showed multiple Au attachments to the protein monomer as well as to the aggregates. The peaks were separated by a peak at *m/z* 197 which was because of Au and a maximum of up to 10 Au attachments to Lyz were observed (see ESI Fig. S4†). In the lower mass range, gas phase bare clusters were observed, which were reported previously.³⁵

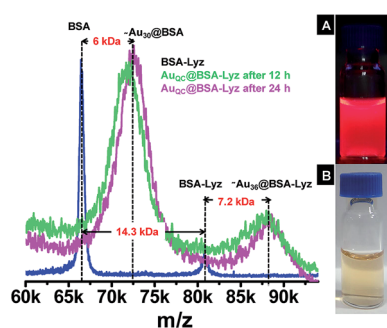


Fig. 1 Comparative MALDI-MS of BSA-Lyz and Au_{QC}@BSA-Lyz in a linear positive ion mode showing the presence of a $\sim\text{Au}_{36}@BSA-Lyz$ peak at *m/z* 88.3 kDa, in the case of a protein mixture, which was not present in the case of Au clusters protected either by BSA or Lyz. The inset shows the photographs of $\sim\text{Au}_{36}@BSA-Lyz$ under UV (A) and visible light (B).

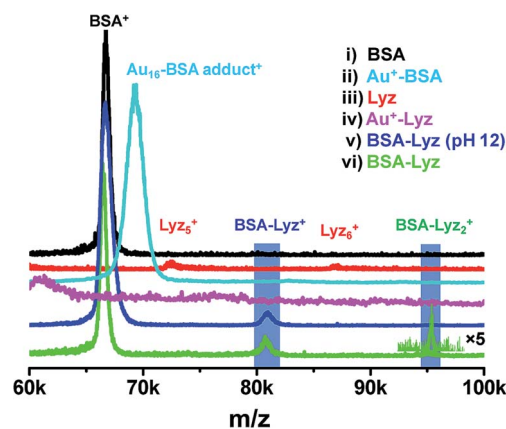


Fig. 2 MALDI-MS of individual proteins, mixture of both the proteins and Au conjugate of individual proteins, showing the formation of BSA-Lyz_n (*n* = 0, 1, 2) conjugate.

When BSA was mixed with Lyz, several possibilities exist such as Lyz_m ($m = 1, 2, 3, 4$), BSA_n ($n = 1, 2$) and Lyz_mBSA_n ($m = 1, 2; n = 1, 2$). All these species were identified using MS in the higher mass region (m/z 80–150 kDa). Two distinct peaks were observed at m/z 81.0 kDa and 95.3 kDa, which appear to be spaced successively at 14.3 kDa from the BSA peak (m/z 66.7 kDa). A similar 14.3 kDa separation was observed in the BSA dimer region (see ESI Fig. S5†) beyond which, because of poor resolution and reduced intensity, other peaks could not be resolved. This separation clearly indicates the possibility of adduct formation between BSA and Lyz. This adduct formation can be explained in terms of the aggregation tendency of Lyz. As was mentioned earlier, Lyz forms aggregates and those can be seen in both MALDI and ESI-MS spectra.³⁴

3.3. Spectroscopic and microscopic characterizations

The presence of Au along with carbon, oxygen, nitrogen, sulfur (S), sodium and chloride was confirmed from the SEM/EDAX spectrum. A Au : S ratio (atomic%) of about 1 : 2 was observed in this case. Elemental mapping of gold using M_α and sulphur using K_α show these elements to be uniform in the sample. The presence of clusters in both the proteins ($\sim\text{Au}_{36}\text{@BSA-Lyz}$) was further confirmed by XPS analysis which showed the presence of a metallic core (Fig. 3E). An Au $4f_{7/2}$ peak appears at 84.1 eV which shows the existence of a zero valent state of the metal. A similar binding energy was observed for $\text{Au}_{25}\text{@LF}$.³¹ A time dependent XPS study during the cluster formation and the corresponding MALDI-MS data was reported by Chaudhari *et al.*, where they showed how a protein–metal complex converts to a zero valent state form during cluster formation and the appearance of a brown colour after the addition of the reducing agent also indicates the reduction of the metal precursor during the cluster formation.³¹ The $\text{S}2p_{1/2}$ peak at 163.3 eV (see ESI Fig. S6†) confirmed the Au–S bonding, through the cysteine residues of the proteins. Protein protected clusters do not show

well defined absorption features such as monolayer protected clusters.

Although the ultraviolet-visible (UV-Vis) technique is not useful for determining the size of the cluster in protein systems, it does help to rule out the possibility of the presence of plasmonic nanoparticles in the solution. UV-Vis spectra show a peak at ~ 280 nm which is because of the presence of aromatic amino acid groups in protein systems (see ESI Fig. S7†). In the case of $\sim\text{Au}_{36}\text{@BSA-Lyz}$, a similar type of absorption feature was observed at 280 nm. In addition, a broad hump was observed at 510 nm which had not been observed before for any such protein protected clusters.

HRTEM analysis of the new cluster showed the core size to be about 1.2 nm as shown in Fig. 4A. However, investigation of the cluster size using HRTEM analysis is not accurate as the electron beam induces the growth of clusters in such soft materials. But this technique helps to determine the approximate size of the samples. Because this is a high resolution instrument with point to point resolution of 0.12 nm, the approximate size is 1.2 ± 0.1 nm. In the present study, this technique showed the absence of bigger plasmonic nanoparticles in the sample. It is important to note that the size of the new species in both these proteins ($\sim\text{Au}_{36}\text{@BSA-Lyz}$) is similar as in the case of individual protein protected clusters. No bigger nanoparticle was found using TEM. Absence of a plasmonic peak in the absorption spectrum also supported the HRTEM data. The photographs of $\sim\text{Au}_{36}\text{@BSA-Lyz}$ together with individual protein protected clusters under UV as well as visible light are shown in Fig. 4B.

3.4. Enhanced photoluminescence and mechanism of cluster formation

The photoluminescence spectra of the parent clusters together with $\sim\text{Au}_{36}\text{@BSA-Lyz}$ are shown Fig. 4C. The emission intensity of $\sim\text{Au}_{36}\text{@BSA-Lyz}$ showed three- and four-fold enhancement when compared to the individual $\text{Au}_{10}\text{@Lyz}$ and $\sim\text{Au}_{30}\text{@BSA}$, respectively, when all the clusters were excited at 365 nm keeping the overall protein concentration the same for all the cases. The calculated quantum yield of $\sim\text{Au}_{36}\text{@BSA-Lyz}$ was

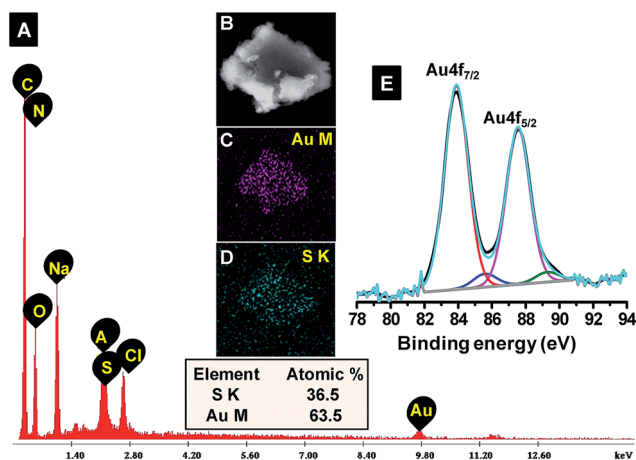


Fig. 3 (A) The SEM/EDAX spectrum of $\sim\text{Au}_{36}\text{@BSA-Lyz}$ together with quantification data. (B) SEM image of a cluster sample. (C and D) EDAX images of the same showing the presence of Au and S. (E) XPS spectrum of $\sim\text{Au}_{36}\text{@BSA-Lyz}$ confirms the presence of Au in the metallic state.

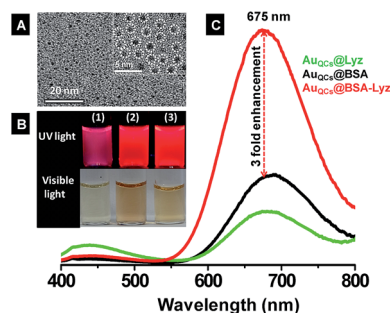


Fig. 4 (A) HRTEM image of $\text{Au}_{\text{QC}}\text{@BSA-Lyz}$ shows a core size of 1.2 ± 0.1 nm. An expanded view is shown in the inset. Some of the clusters are shown in a circle. (B) Photographs of $\text{Au}_{10}\text{@Lyz}$ (1), $\text{Au}_{30}\text{@BSA}$ (2) and $\text{Au}_{\text{QC}}\text{@BSA-Lyz}$ (3) under UV and visible light. (C) Three-fold enhancement in emission intensity of $\text{Au}_{\text{QC}}\text{@BSA-Lyz}$ compared to clusters protected by single proteins was seen, when excited at the same wavelength and at the same metal and protein concentrations.

42.4% considering rhodamine 6G as the reference, which is extremely high compared to all the reported Au clusters in various proteins. Under similar experimental conditions, the quantum yield of $\text{Au}_{\text{QCS}}\text{@BSA}$ and $\text{Au}_{\text{QC}}\text{@Lyz}$ were found to be 10.0% and 15.0%, respectively. These values were comparable to the ones reported previously.³⁴ Like other protein protected clusters, two excitation peaks were observed in the present study, one because of the cluster core (500 nm) and the other because of the protein (365 nm). Both the excitation maxima resulted in the same emission but with different intensities. A higher intensity was observed with 365 nm excitation which was explained in terms of FRET. Muhammed *et al.* have shown metal enhanced luminescence of $\text{Au}_{\text{QC}}\text{@BSA}$ in the presence of Ag nanoparticles where the protein shell acts as a spacer between the cluster and the Ag nanoparticles.²³ The distance between the fluorophore and the metal surface plays an important role in luminescence enhancement. Aggregation induced enhanced luminescence of Au(I) thiolate has been reported by Luo *et al.*, where they have shown that the Au(I) thiolate shell surrounding the Au(0) core drastically increased the luminescence.⁵¹ Wang *et al.* have shown a 200-fold increase in luminescence by replacing Ag atoms with an Au cluster.⁵⁰ In this case, increased emission intensity can be explained by considering the possibility of a FRET between the cluster core and the two proteins. As discussed earlier (in the section on MS), the cluster core is protected by two proteins which implies that both the proteins are in proximity for energy transfer and thus, enhancement in FRET occurs. Here the protein can be a FRET donor and the cluster can be the acceptor. In order to know whether the excess protein can also increase FRET activity, different volumes of BSA were added to $\sim\text{Au}_{30}\text{@BSA}$ solution. No significant increase in photoluminescent (PL) intensity was observed confirming that inter-protein energy transfer is not efficient in this case. Similar observations were also made for $\text{Au}_{\text{QC}}\text{@Lyz}$. Time dependent PL did not exhibit any change in the position of the emission.

As shown in Fig. 1, mixed aggregates of BSA and Lyz are also capable of forming clusters and the cluster was assigned as $\sim\text{Au}_{36}\text{@BSA-Lyz}$. In one possibility, the cluster can form inside one protein (namely BSA, as it is large and can accommodate the 36 atom core) and the other protein, Lyz forms an aggregate with the as-formed BSA protected cluster. Another possibility could be the formation of the cluster in the solution and then subsequent protection by both the proteins. In the case of a mixture of proteins in the Lyz region, only 5–6 Au separations from the parent protein peak was observed, while in the BSA region, the $\text{Au}_{30}\text{@BSA}$ species was seen. However, another peak observed at 88.2 kDa could be because of the separation of 36 Au from the BSA–Lyz adduct. To understand the mechanism of formation, different volumes of Lyz were added to $\sim\text{Au}_{30}\text{@BSA}$ and the change was monitored using MS. After addition, each sample was stirred for 6 h and spotted for MALDI-MS. In the Lyz region, only the intensity enhancement with increase in Lyz concentration was observed but no cluster formation occurred in this situation. In the BSA region, a decrease in core nuclearity with the addition of Lyz was observed in the system. Two humps separated by 5 Au and 16 Au from the parent BSA (initially the

separation was 30 Au) together with the appearance of free BSA were observed. The peak positions were the same for all the concentrations of Lyz used. New humps corresponding to BSA–Lyz, $\text{Au}_8\text{@BSA-Lyz}$ and $\sim\text{Au}_{23}\text{@BSA-Lyz}$ were observed. However, because of poor intensity, peak assignments may vary slightly (Fig. 5).

In this study, large protein-large protein interaction was also considered. For this, Lf with an m/z of 83.0 kDa was chosen. Gold clusters protected by BSA as well as by Lf have already been reported and have been well characterized using MS. $\text{Au}_{\text{QC}}\text{@BSA}$ ²⁷ and $\text{Au}_{\text{QC}}\text{@Lf}$ ³² were synthesized according to a previously reported method. When both $\text{Au}_{\text{QC}}\text{@BSA}$ and $\text{Au}_{\text{QC}}\text{@Lf}$ were mixed together, maintaining certain conditions, no distinct features were observed other than the individual cluster peak in the whole MS range. Different control experiments were also carried out (as mentioned previously) to check the interaction of both the proteins separately and those interactions with the protein protected clusters. But in none of the cases were new features observed which could be because of the bulky nature of the proteins, which restricts them to form inter-protein adducts.

3.5. Silver clusters

Similar studies were also performed for Ag clusters where concentration dependent growth in the cluster core was observed. For a similar concentration of Ag precursor, $\sim\text{Ag}_{28}\text{@BSA}$ and $\sim\text{Ag}_{35}\text{@BSA-Lyz}$ were observed. In the Lyz region, 8 Ag attachments to Lyz were observed. A concentration-dependent study was performed by varying the Ag concentration (final concentrations were 2, 3 and 4 mM) and keeping the protein concentration the same. $\sim\text{Ag}_{16}\text{@BSA}$, $\sim\text{Ag}_{28}\text{@BSA}$ and $\sim\text{Ag}_{34}\text{@BSA}$ were observed in the BSA region, for 2, 3 and 4 mM Ag concentrations, respectively (Fig. 6).

A similar mass shift with respect to Ag concentration was also reflected in the mixed protein adduct mass region where $\sim\text{Ag}_{25}\text{@BSA-Lyz}$, $\sim\text{Ag}_{35}\text{@BSA-Lyz}$ and $\sim\text{Ag}_{42}\text{@BSA-Lyz}$ were

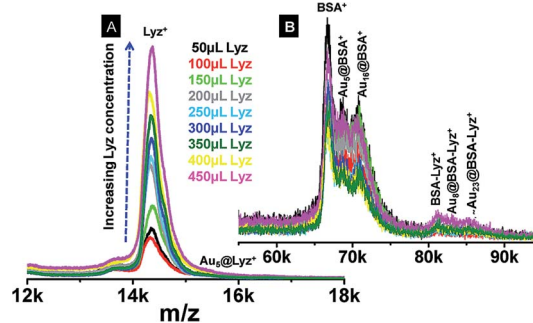


Fig. 5 Different volumes of Lyz solution (75 μM) were added to pre-formed $\text{Au}_{\text{QCS}}\text{@BSA}$ with regular increases in volume by 50 μL . No mass shift was observed in the Lyz region other than an increase in the Lyz peak intensity as shown in A. The Lyz peak has a shoulder and that may be because of a few Au attachments. The main cluster peak in the BSA region splits into two small humps separated by 5 Au and 16 Au from the parent BSA peak. The BSA–Lyz adduct and the $\text{Au}_8\text{@BSA-Lyz}$ and $\sim\text{Au}_{23}\text{@BSA-Lyz}$ were observed in the higher mass spectral region.

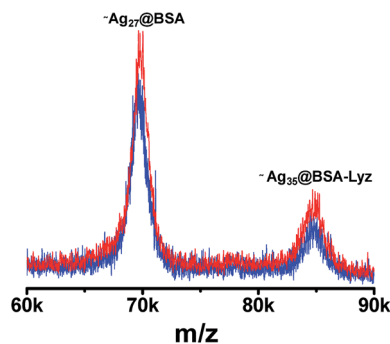


Fig. 6 Time dependent MALDI-MS study on the Ag system which shows the formation of $\sim\text{Ag}_{35}\text{@BSA-Lyz}$ together with the individual cluster peak. The peak positions as well as the peak intensity are the same with time (blue line – after 12 h and red line – after 24 h).

observed for concentrations of 2, 3 and 4 mM Ag, respectively (see ESI Fig. S8†). XPS analysis of this system also showed the presence of a metallic Ag core where Ag is in the Ag^0 state. Also, in this case, increased emission intensity comparable with Au was observed.

By comparing the data obtained for Au and Ag, it can be seen that the mass shift is always more for the mixed protein than for the individual protein. For similar concentrations of Au and Ag, Au_{30} and Ag_{26} cores can be achieved, protected by BSA alone. The other peak (at a higher mass range) was shifted by 36 Au and 35 Ag from the combined mass of BSA and Lyz. If the probabilities mentioned previously are narrowed down, only two possibilities exist: (i) $\sim\text{Au}_{30}/\text{Ag}_{27}\text{@BSA} + \text{Au}_6/\text{Ag}_8\text{@Lyz}$ or (ii) $\sim\text{Au}_{36}/\text{Ag}_{35}\text{@BSA} + \text{Lyz}$. Considering the PL data together with the MS findings, a four-fold enhancement in emission intensity (in the case of Au) was observed which can be attributed to the presence of multiple cluster cores in the system which increases the probability of FRET. In the other case, where the presence of a single core protected by multiple protein is considered, proximity of two different proteins attached to a single core can also enhance FRET efficiently. From the TEM, pairs of clusters separated by a couple of nanometers are not seen, which would support the presence of a single cluster core, while a consequent decrease in the nuclearity of the cluster appears to suggest the idea of the presence of a multiple core. Thus, the mechanism requires further investigation which can be resolved only by crystallization of all the species.

4. Summary and conclusions

In summary, the synthesis of Au clusters protected by mixed protein systems with high quantum yield has been demonstrated. Such clusters were prepared by mixing Au^{3+} with a mixture of both the proteins which were then subsequently reduced to Au^0 at pH 12. Using MALDI-MS, the cluster was assigned as $\sim\text{Au}_{36}\text{@BSA-Lyz}$. Similar observations were also made for the Ag system, $\sim\text{Ag}_{35}\text{@BSA-Lyz}$. The existence of mixed proteins in the form of an adduct was confirmed by extensive MS investigations and control studies. XPS analysis revealed that the Au cluster protected by the mixed protein

system is in zero valent state. HRTEM analysis of these clusters showed that the core size is about 1.2 nm which is in agreement with the size of clusters protected by individual proteins. A four-fold enhancement in the emission intensity of $\sim\text{Au}_{36}\text{@BSA-Lyz}$ was observed, when compared to that of the individual clusters when excited at the same wavelength. The quantum yield of $\sim\text{Au}_{36}\text{@BSA-Lyz}$ was found to be 42.4% which is extremely high compared to that of the already reported clusters. Proximity of two different proteins around a core can enhance FRET and thus, the emission intensity. The presence of multiple cluster species in solution or cluster protected by mixed protein systems might be another reason for such a high quantum yield. Understanding the system in detail is limited by several factors. Separation of the specific entity from the mixture of free proteins and other clusters can help to understand the system in greater detail. Similarly studies such as small angle X-ray scattering and spectroscopy may help to understand the system in more detail, which is part of our future investigations. Such a system can be used for sensing ultralow levels of analytes, because of the sensitivity of protein protected clusters to a range of analytes. Being bio-compatible, these can be used as fluorescent tags and can replace fluorescent dyes for staining biological entities and tracking biomolecules in real systems.

Acknowledgements

AB, JSM and TP thank the Department of Science and Technology, Government of India for continuous support of their research program on nanomaterials. AB thanks the Council of Scientific and Industrial Research (CSIR) for his fellowship. JSM thanks IIT Madras for a fellowship. TP and HL thank the India-Korea research program for a joint project.

References

- 1 R. Jin, *Nanoscale*, 2010, **2**, 343–362.
- 2 A. Mathew and T. Pradeep, *Part. Part. Syst. Charact.*, 2014, **31**, 1017–1053.
- 3 T. Udayabhaskararao and T. Pradeep, *J. Phys. Chem. Lett.*, 2013, **4**, 1553–1564.
- 4 P. L. Xavier, K. Chaudhari, A. Baksi and T. Pradeep, *Nano Rev.*, 2012, **3**, 14767 and the references cited therein.
- 5 D. M. Chevrier, A. Chatt and P. Zhang, *J. Nanophotonics*, 2012, **6**, 064504.
- 6 M. W. Heaven, A. Dass, P. S. White, K. M. Holt and R. W. Murray, *J. Am. Chem. Soc.*, 2008, **130**, 3754–3755.
- 7 M. Zhu, C. M. Aikens, F. J. Hollander, G. C. Schatz and R. Jin, *J. Am. Chem. Soc.*, 2008, **130**, 5883–5885.
- 8 D. Crasto, S. Malola, G. Brososky, A. Dass and H. Hakkinen, *J. Am. Chem. Soc.*, 2014, **136**, 5000–5005.
- 9 H. Qian, W. T. Eckenhoff, Y. Zhu, T. Pintauer and R. Jin, *J. Am. Chem. Soc.*, 2010, **132**, 8280–8281.
- 10 C. Zeng, H. Qian, T. Li, G. Li, N. L. Rosi, B. Yoon, R. N. Barnett, R. L. Whetten, U. Landman and R. Jin, *Angew. Chem., Int. Ed.*, 2012, **51**, 13114–13118.
- 11 P. D. Jadzinsky, G. Calero, C. J. Ackerson, D. A. Bushnell and R. D. Kornberg, *Science*, 2007, **318**, 430–433.

- 12 H. Yang, Y. Wang, H. Huang, L. Gell, L. Lehtovaara, S. Malola, H. Häkkinen and N. Zheng, *Nat. Commun.*, 2013, **4**, 2422.
- 13 A. Desireddy, B. E. Conn, J. Guo, B. Yoon, R. N. Barnett, B. M. Monahan, K. Kirschbaum, W. P. Griffith, R. L. Whetten, U. Landman and T. P. Bigioni, *Nature*, 2013, **501**, 399–402.
- 14 J. Hassinen, P. Pulkkinen, E. Kalenius, T. Pradeep, H. Tenhu, H. Hakkinen and R. H. A. Ras, *J. Phys. Chem. Lett.*, 2014, **5**, 585–589.
- 15 A. Mathew, G. Natarajan, L. Lehtovaara, H. Hakkinen, R. M. Kumar, V. Subramanian, A. Jaleel and T. Pradeep, *ACS Nano*, 2014, **8**, 139–152.
- 16 Y. Niihori, M. Matsuzaki, T. Pradeep and Y. Negishi, *J. Am. Chem. Soc.*, 2013, **135**, 4946–4949.
- 17 T. Pradeep, A. Baksi and P. L. Xavier, in *Functional Nanometer-Sized Clusters of Transition Metals: Synthesis, Properties and Applications*, The Royal Society of Chemistry, 2014, pp. 169–225.
- 18 N. Goswami, K. Zheng and J. Xie, *Nanoscale*, 2014, **6**, 13328–13347.
- 19 J. T. Petty, J. Zheng, N. V. Hud and R. M. Dickson, *J. Am. Chem. Soc.*, 2004, **126**, 5207.
- 20 J. Zheng, C. Zhang and R. M. Dickson, *Phys. Rev. Lett.*, 2004, **93**, 077402.
- 21 J. Xie, Y. Zheng and J. Y. Ying, *J. Am. Chem. Soc.*, 2009, **131**, 888–889.
- 22 L. Shang, Y. Wang, J. Jiang and S. Dong, *Langmuir*, 2007, **23**, 2714–2721.
- 23 M. A. Habeeb Muhammed, P. K. Verma, S. K. Pal, A. Retnakumari, M. Koyakutty, S. Nair and T. Pradeep, *Chem.–Eur. J.*, 2010, **16**, 10103–10112.
- 24 Y. Liu, K. Ai, X. Cheng, L. Huo and L. Lu, *Adv. Funct. Mater.*, 2010, **20**, 951–956.
- 25 A. Mathew, P. R. Sajanalal and T. Pradeep, *J. Mater. Chem.*, 2010, **21**, 11205–11212.
- 26 J. Xie, Y. Zheng and J. Y. Ying, *Chem. Commun.*, 2010, **46**, 961–963.
- 27 J. S. Mohanty, P. L. Xavier, K. Chaudhari, M. S. Bootharaju, N. Goswami, S. K. Pal and T. Pradeep, *Nanoscale*, 2012, **4**, 4255–4262.
- 28 H.-W. Li, K. Ai and Y. Wu, *Chem. Commun.*, 2011, **47**, 9852–9854.
- 29 U. Anand, S. Ghosh and S. Mukherjee, *J. Phys. Chem. Lett.*, 2012, **3**, 3605–3609.
- 30 P.-H. Chan and Y.-C. Chen, *Anal. Chem.*, 2012, **84**, 8952–8956.
- 31 K. Chaudhari, P. L. Xavier and T. Pradeep, *ACS Nano*, 2011, **5**, 8816–8827.
- 32 P. L. Xavier, K. Chaudhari, P. K. Verma, S. K. Pal and T. Pradeep, *Nanoscale*, 2010, **2**, 2769–2776.
- 33 H. Wei, Z. Wang, L. Yang, S. Tian, C. Hou and Y. Lu, *Analyst*, 2010, **135**, 1406–1410.
- 34 A. Baksi, P. L. Xavier, K. Chaudhari, N. Goswami, S. K. Pal and T. Pradeep, *Nanoscale*, 2013, **5**, 2009–2016.
- 35 A. Baksi, T. Pradeep, B. Yoon, C. Yannouleas and U. Landman, *ChemPhysChem*, 2013, **14**, 1272–1282 and the references cited there in.
- 36 A. Baksi and T. Pradeep, *Nanoscale*, 2013, **5**, 12245–12254.
- 37 C.-L. Liu, H.-T. Wu, Y.-H. Hsiao, C.-W. Lai, C.-W. Shih, Y.-K. Peng, K.-C. Tang, H.-W. Chang, Y.-C. Chien, J.-K. Hsiao, J.-T. Cheng and P.-T. Chou, *Angew. Chem., Int. Ed.*, 2011, **50**, 7056–7060.
- 38 Y. Yu, Z. Luo, C. S. Teo, Y. N. Tan and J. Xie, *Chem. Commun.*, 2013, **49**, 9740–9742.
- 39 H.-Y. Liu, X. Zhang, X.-M. Wu, L.-P. Jiang, C. Burda and J.-J. Zhu, *Chem. Commun.*, 2011, **47**, 4237.
- 40 Y. Yue, T.-Y. Liu, H.-W. Li, Z. Liu and Y. Wu, *Nanoscale*, 2012, **4**, 2251–2254.
- 41 L. Yan, Y. Cai, B. Zheng, H. Yuan, Y. Guo, D. Xiao and M. M. F. Choi, *J. Mater. Chem.*, 2012, **22**, 1000–1005.
- 42 T.-H. Chen and W.-L. Tseng, *Small*, 2012, **8**, 1912–1919.
- 43 G. Guan, S.-Y. Zhang, Y. Cai, S. Liu, M. S. Bharathi, M. Low, Y. Yu, J. Xie, Y. Zheng, Y.-W. Zhang and M.-Y. Han, *Chem. Commun.*, 2014, **50**, 5703–5705.
- 44 S. D. Haveli, P. Walter, G. Patriarcho, J. Ayache, J. Castaing, E. E. Van, G. Tsoucaris, P.-A. Wang and H. B. Kagan, *Nano Lett.*, 2012, **12**, 6212–6217.
- 45 M. Li, D.-P. Yang, X. Wang, J. Lu and D. Cui, *Nanoscale Res. Lett.*, 2013, **8**, 182.
- 46 C. Shao, B. Yuan, H. Wang, Q. Zhou, Y. Li, Y. Guan and Z. Deng, *J. Mater. Chem.*, 2011, **21**, 2863.
- 47 X. Wen, P. Yu, Y.-R. Toh, A.-C. Hsu, Y.-C. Lee and J. Tang, *J. Phys. Chem. C*, 2012, **116**, 19032–19038.
- 48 X. Xia, Y. Long and J. Wang, *Anal. Chim. Acta*, 2013, **772**, 81–86.
- 49 M. A. H. Muhammed and T. Pradeep, in *Advanced Fluorescence Reporters in Chemistry and Biology II*, ed. A. P. Demchenko, Springer Berlin Heidelberg, 2010, pp. 333–353.
- 50 S. Wang, X. Meng, A. Das, T. Li, Y. Song, T. Cao, X. Zhu, M. Zhu and R. Jin, *Angew. Chem., Int. Ed.*, 2014, **53**, 2376–2380.
- 51 Z. Luo, X. Yuan, Y. Yu, Q. Zhang, D. T. Leong, J. Y. Lee and J. Xie, *J. Am. Chem. Soc.*, 2012, **134**, 16662–16670.

Electronic Supplementary Information

Clusters protected with mixed proteins exhibiting intense photoluminescence

Jyoti Sarita Mohanty,[‡] Ananya Bakshi,[‡] Haiwon Lee and T. Pradeep*

¹DST Unit of Nanoscience (DST UNS), and Thematic Unit of Excellence (TUE),

Department of Chemistry, Indian Institute of Technology Madras, Chennai - 600 036, India

²Department of Chemistry, Institute of Nanoscience and Technology, Hanyang University,
Seoul- 133-791, Korea.

[‡] Contributed equally

Content

S/N	Description	Page Number
S1	<i>Comparative MALDI MS of BSA and ~Au₃₀@BSA</i>	2
S2	<i>Comparative MALDI MS of ~Au₃₀@BSA, Au₁₀@Lyz and Au_{QC}@BSA-Lyz at lower mass region</i>	3
S3	<i>MALDI MS of Lyz shows the aggregate formation</i>	4
S4	<i>MALDI MS of Au⁺-Lyz adduct showing multiple Au attachments to the parent protein</i>	5
S5	<i>MALDI MS of BSA-Lyz is showing aggregate formation between two proteins</i>	6
S6	<i>XPS survey spectrum of Au_{QC}@BSA-Lyz</i>	7
S7	<i>UV-Vis absorption spectra of Au_{QC}@BSA-Lyz, ~Au₃₀@BSA and Au₁₀@Lyz</i>	8
S8	<i>Concentration dependent MALDI MS of Ag_{QC}@BSA-Lyz</i>	9

Electronic Supplementary Information 1

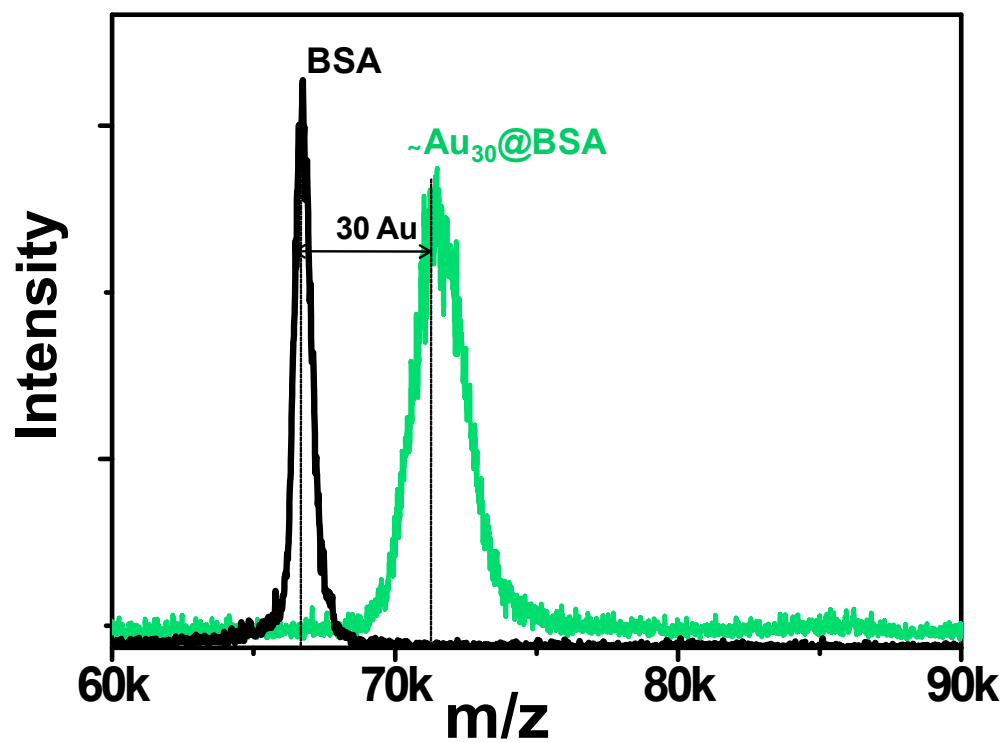


Figure S1: Comparative MALDI MS of BSA and Au_{QC}@BSA showing mass shift of 6 kDa from parent protein after cluster formation. The cluster is assigned as ~Au₃₀@BSA.

Electronic Supplementary Information 2

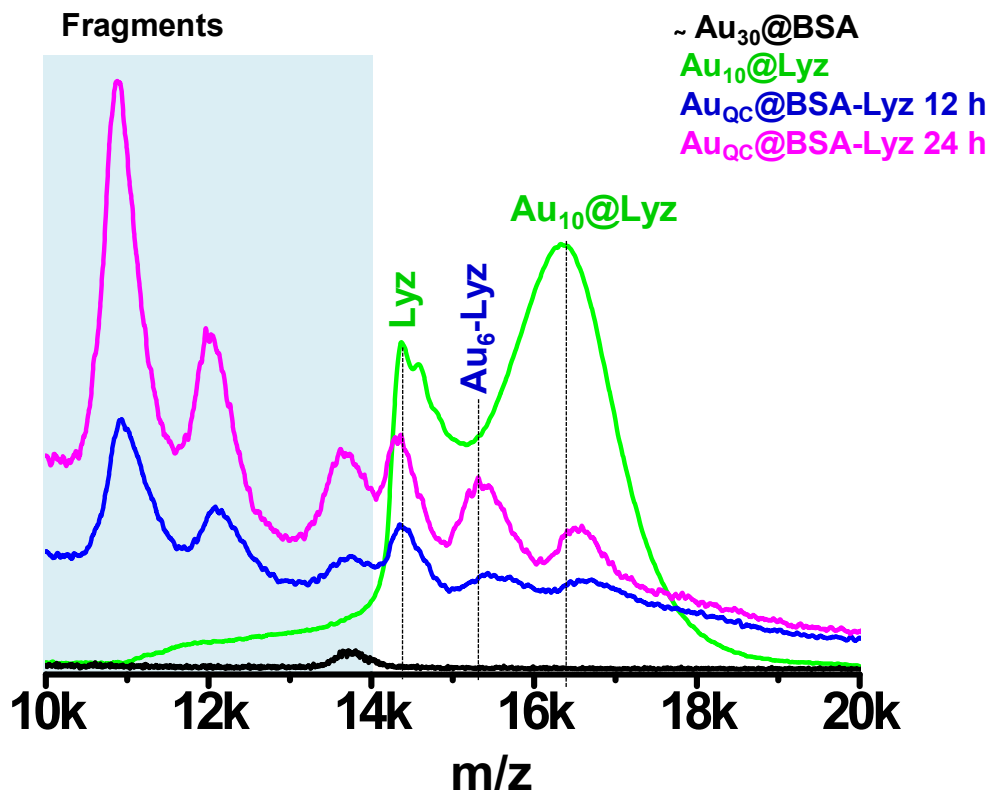


Figure S2: Comparative MALDI MS of ~Au₃₀@BSA, Au₁₀@Lyz and Au_{QC}@BSA-Lyz at lower mass region showing a few Au attachments to Lyz along with other fragments.

Electronic Supplementary Information 3

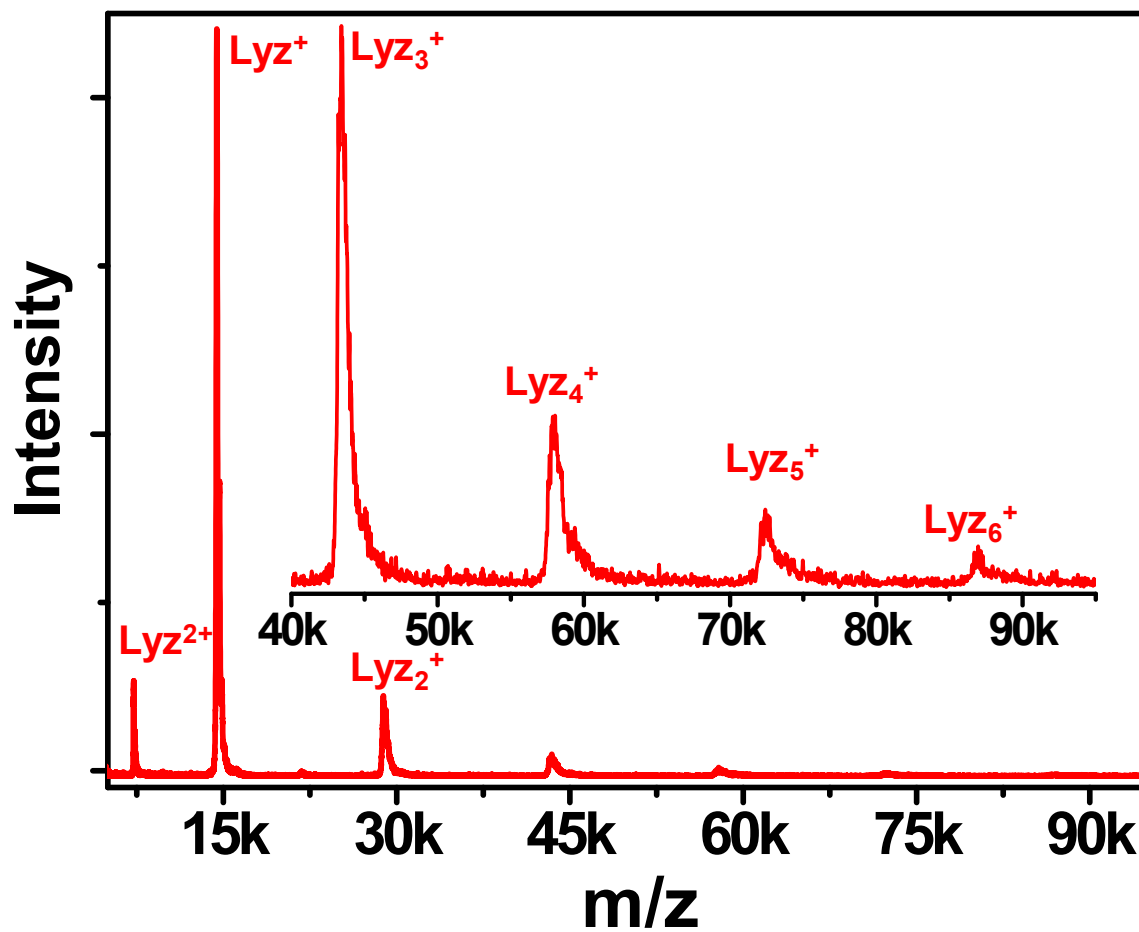


Figure S3: MALDI MS of Lyz is showing aggregate formation. Up to hexamer is clearly visible.

Electronic Supplementary Information 4

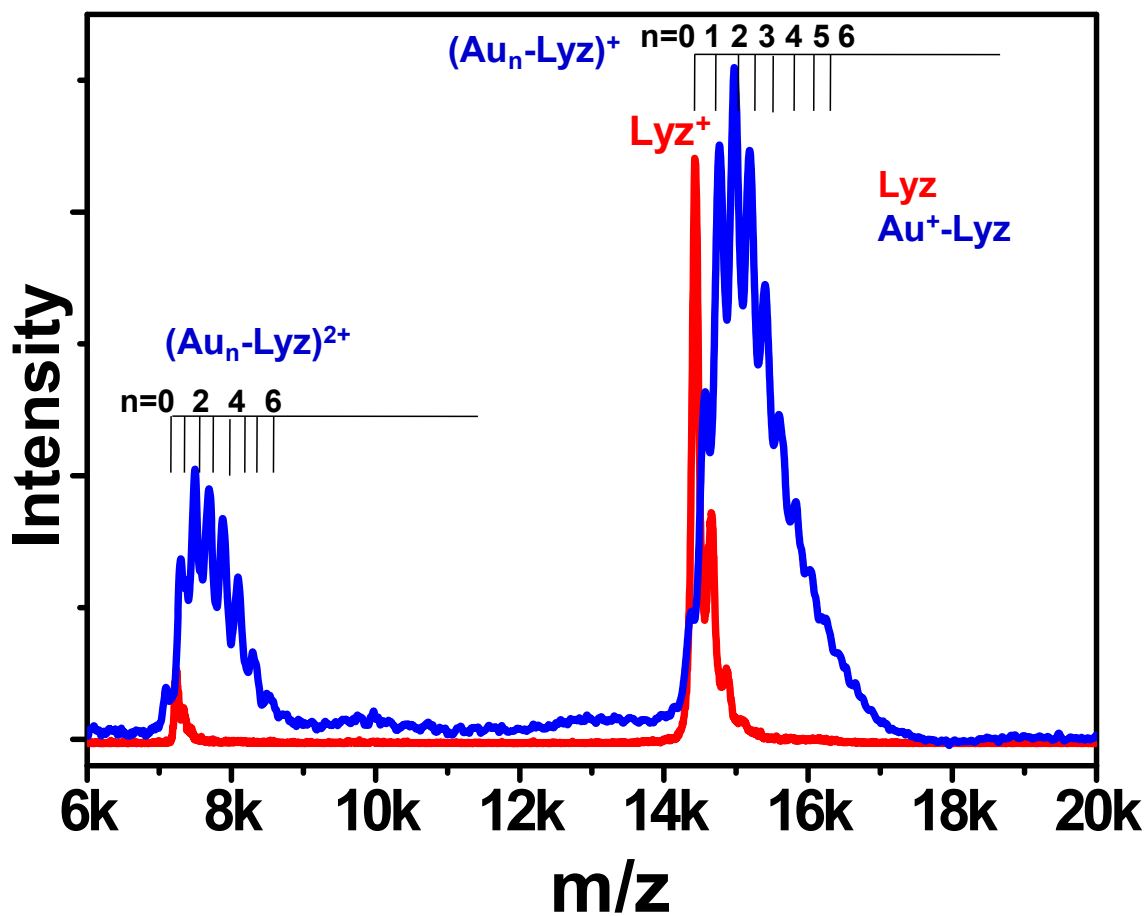


Figure S4: MALDI MS of Au^+ -Lyz adduct showing multiple Au attachments to the parent protein with a separation of m/z 197 due to Au. Corresponding double charge state was also observed with $m/z \sim 99$ separation due to Au^{2+} .

Electronic Supplementary Information 5

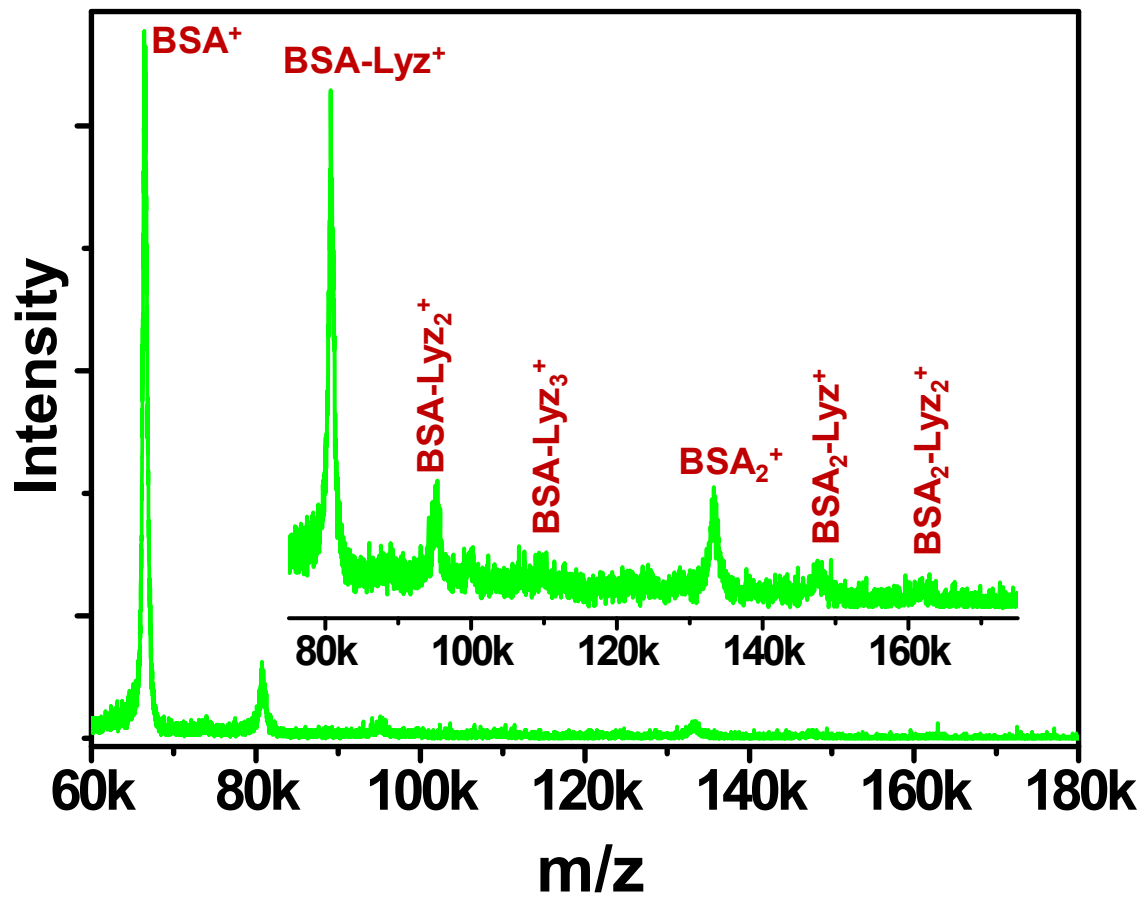


Figure S5: MALDI MS of BSA-Lyz is showing aggregate formation between two proteins.

Electronic Supplementary Information 6

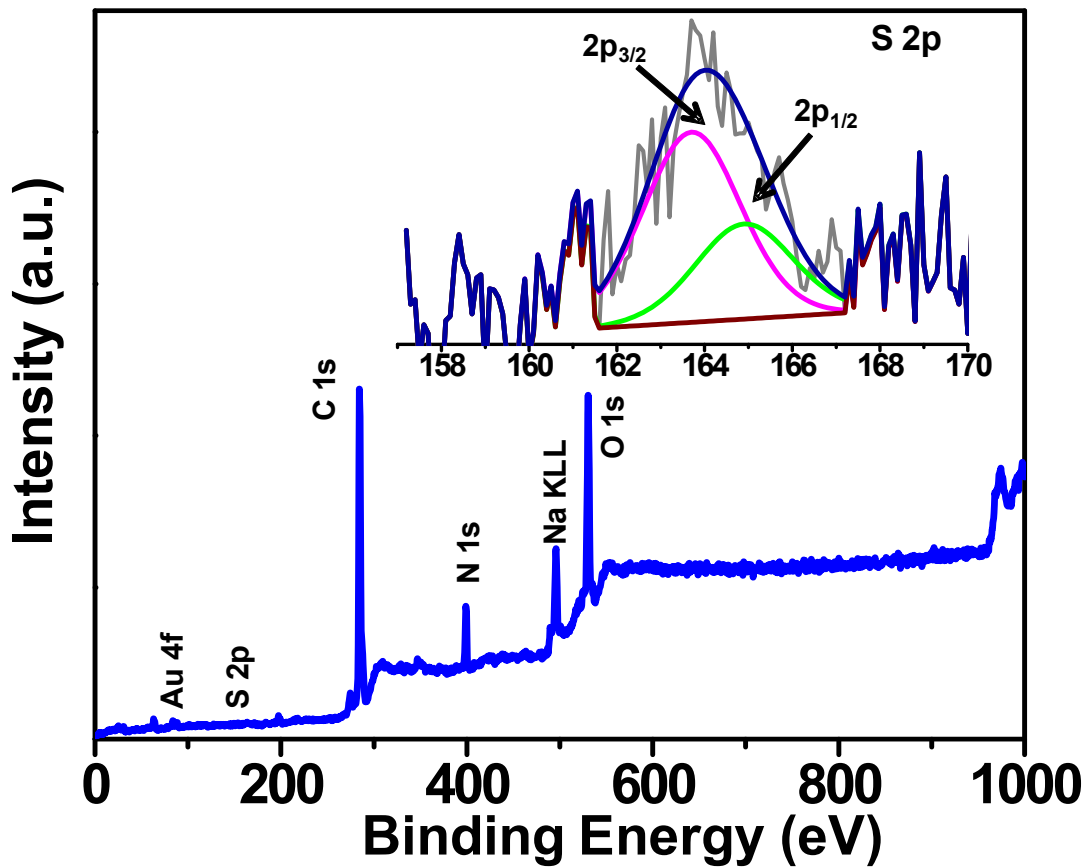


Figure S6: XPS survey spectrum of Au_{QC}@BSA-Lyz is showing the presence of respective elements. The S 2p region is expanded in the inset.

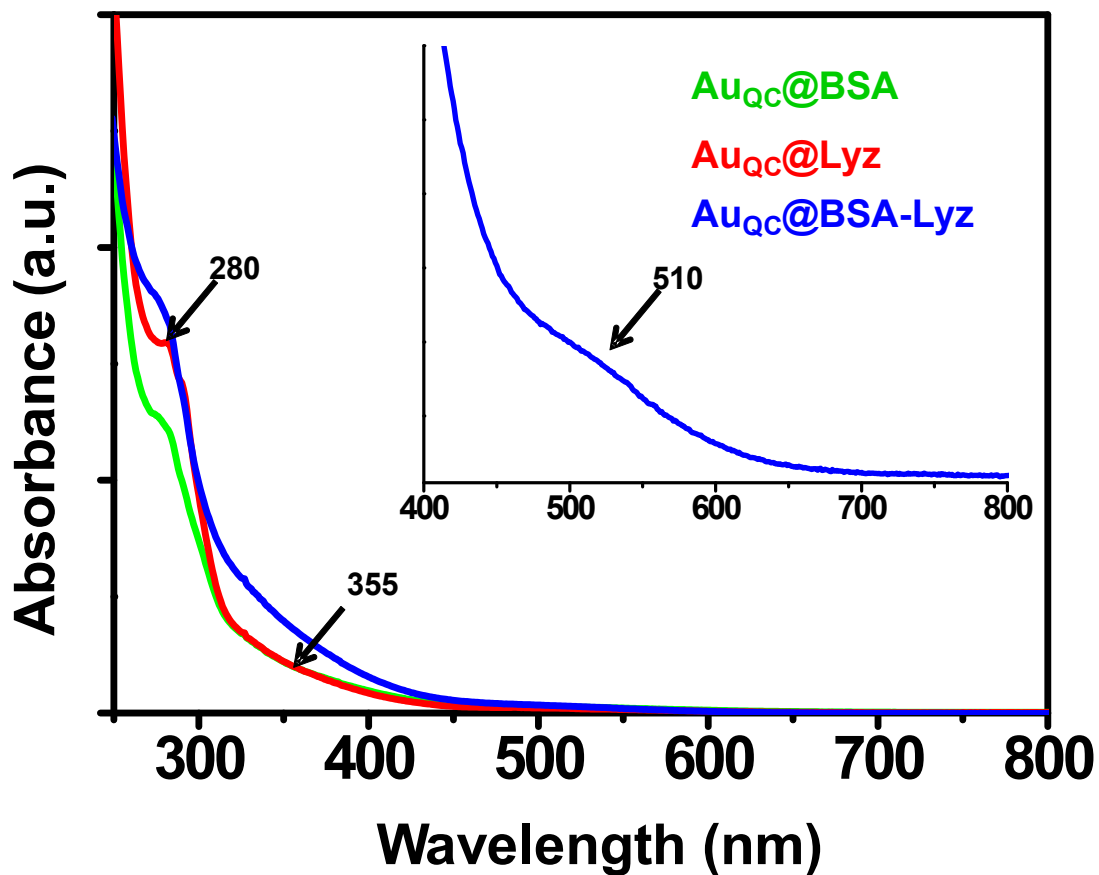


Figure S7: UV-Vis absorption spectra of Au_{QC}@BSA-Lyz is showing a hump at 510 nm which was originally absent for individual clusters, ~Au₃₀@BSA and Au₁₀@Lyz.

Electronic Supplementary Information 8

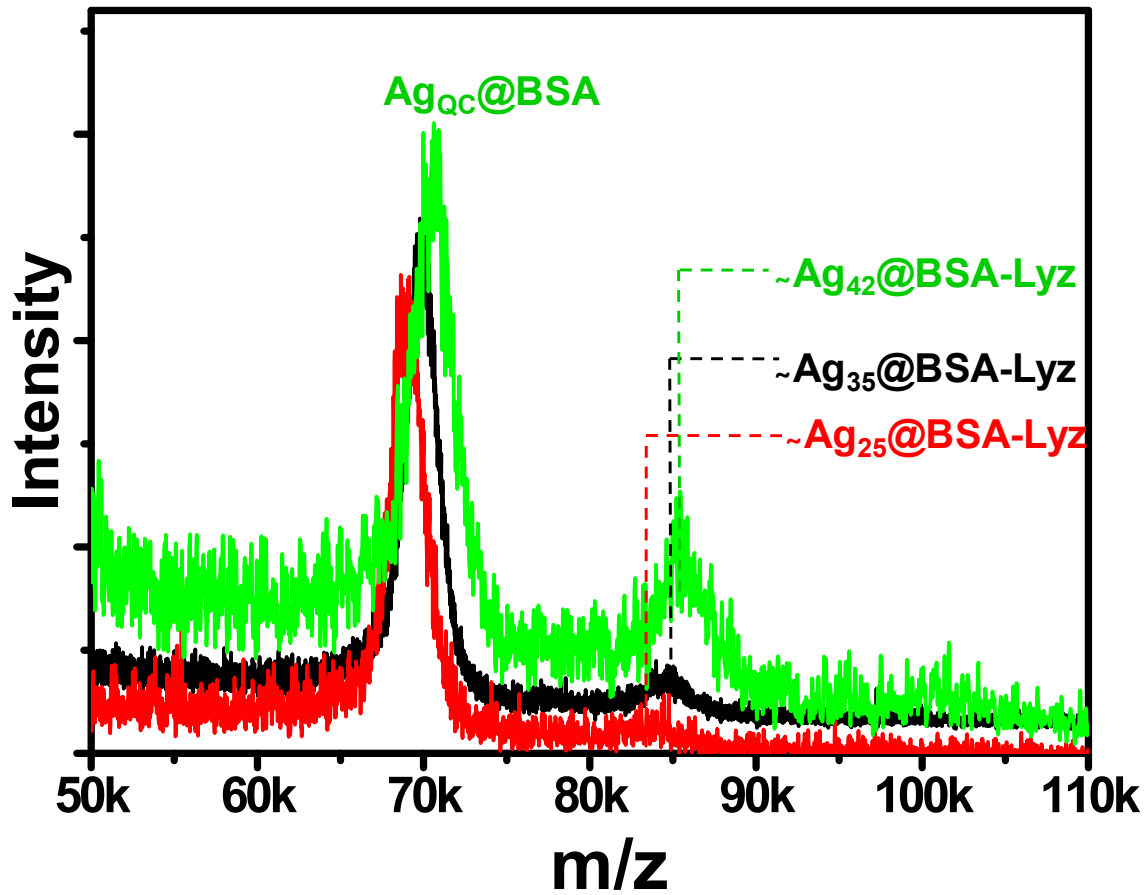


Figure S8: Concentration dependent MALDI MS of $Ag_{QC}@BSA-Lyz$ showing linear dependence of Ag concentration and number of core Ag atoms.

Simultaneous Dehalogenation and Removal of Persistent Halocarbon Pesticides from Water Using Graphene Nanocomposites: A Case Study of Lindane

Soujit Sen Gupta,[†] Indranath Chakraborty,[†] Shihabudheen Mundampra Maliyekkal,[‡] Tuhina Adit Mark,[†] Dheeraj Kumar Pandey,[†] Sarit Kumar Das,[§] and Thalappil Pradeep^{*,†}

[†]DST Unit on Nanoscience and Thematic Unit of Excellence (TUE), Department of Chemistry, Indian Institute of Technology Madras, Chennai 600 036, India

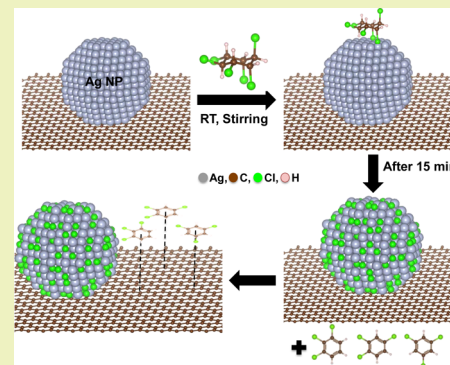
[‡]Environmental Engineering Division, School of Mechanical and Building Sciences, VIT University, Chennai Campus Chennai 600 048, India

[§]Department of Mechanical Engineering, Indian Institute of Technology Madras, Chennai 600 036, India

Supporting Information

ABSTRACT: This paper describes an unusual chemical reaction that takes place on a graphene composite in a concerted fashion. The reaction shows the conversion of a persistent organochlorine pesticide, lindane ($C_6H_6Cl_6$), present in water, to different isomers of trichlorobenzenes (TCBs, $C_6H_3Cl_3$) on the surface of reduced graphene oxide–silver composites (RGO@Ag). The reaction is unique to the composite and does not occur on RGO and nanoparticles of Ag separately. The products of the reaction were isolated and extensively characterized using analytical techniques such as gas chromatography–mass spectrometry, electro-spray ionization mass spectrometry, infrared and NMR, which unequivocally confirmed their identity. The as-formed TCBs were removed from the aqueous medium by adsorption on the same composite. Adsorption of lindane is physical in nature, but that of TCBs is through π – π interactions. The study reveals the unusual chemical reactivity of graphene–metal composites and their potential for water treatment. The uniqueness of the reaction on RGO@Ag is due to the simultaneous removal of three HCl molecules, leading to the formation of aromatic compounds and concomitant formation of silver chloride. Recycling capacity and effect of diverse species present in natural waters were tested for potential applications in sustainable water treatment.

KEYWORDS: Graphene–silver nanocomposite, Pesticides, Lindane, Degradation, Adsorption, Water purification



INTRODUCTION

Since its discovery in 2004,¹ graphene has attracted significant attention in various fields due to its unique physical and chemical properties. Though the physicochemical properties² and the catalytic behavior^{3,4} have been widely investigated, chemistry of its composites has received significant attention these days. Synthesis of different graphene composites, their characterization and applications have been reported in the recent past.^{5–7} Molecular adsorption on graphene/graphene based composites and their applications in water purification^{8–13} have gained momentum recently. Special properties like large surface area,¹⁴ antibacterial nature,^{15–18} reduced cytotoxicity,^{19,20} and tunable chemical properties²¹ make these materials attractive choices for this application. An overwhelming number of related articles published recently support this claim.^{22–33} Attempts are also being made to synthesize graphene from sustainable sources in a cost-effective manner.^{9,24,34} This enables the practical use of graphene for a large-scale application like water purification.

To the best of our knowledge, chemical reactions on graphene and graphene nanocomposites enabling the degradation of halogenated pesticides like lindane (γ -hexachlorocyclohexane) are unexplored. Studies report that the degradation of lindane in water using *Streptomyces* sp. M7^{35,36} and the fungus *Conidiobolus*³⁷ is a slow process and takes nearly 5 days of incubation. Degradation using iron(II) sulfide³⁸ and by iron–palladium bimetallic nanoparticles³⁹ is also possible, but as cyclohexane is the byproduct, it requires additional methods for further deactivation. Although these are useful, more efforts are needed to develop a better system to enable practical utilization. The reaction reported here will provide a new methodology for possible decontamination of lindane in water.

In this paper, we report the chemical reactivity of reduced graphene oxide–silver nanocomposites (RGO@Ag) in degrad-

Received: January 30, 2015

Revised: March 30, 2015

Published: May 4, 2015

ing halogenated pesticides in water taking lindane (γ -hexachlorocyclohexane) as the model pollutant. There are different isomers of lindane namely α -, β -, δ - and ϵ -lindane, which are the byproducts during the production of the potent pesticide γ -lindane. γ -Lindane was chosen owing to its widespread occurrence,⁴⁰ toxicity^{41–43} and persistent nature. According to WHO, the half-life of the γ -isomer ranges from 88 to 1146 days. The paper demonstrates a two-step mechanism of removal, i.e., the degradation of γ -lindane by silver nanoparticles (Ag NPs) supported on RGO and subsequent adsorption of the degraded products by the RGO surface.

MATERIALS AND METHODS

Materials. Natural graphite flakes were procured from Active Carbon India Pvt. Ltd. Sulfuric acid (H_2SO_4 , 95–98%), ammonia (NH_3 , 30%) and hydrochloric acid (HCl , 36%) were purchased from Rankem Chemicals Pvt. Ltd., India. Hydrazine monohydrate ($\text{N}_2\text{H}_4 \cdot \text{H}_2\text{O}$, >99%), phosphorus pentoxide (P_2O_5 , 95%), hydrogen peroxide (H_2O_2 , 98%) and activated carbon (AC of mesh size 300 nm) were purchased from SD Fine Chemicals Pvt. Ltd., India. Potassium peroxydisulfate ($\text{K}_2\text{S}_2\text{O}_8$, 98%) was purchased from Sisco Research Laboratories Pvt. Ltd., India. Potassium permanganate (KMnO_4 , 98.5%) was purchased from Merck, India. γ -Lindane (HPLC assay 95%), δ -lindane (purity 99.9%) and multiwalled carbon nanotubes (MWCNTs) were purchased from Sigma-Aldrich. All chemicals were of analytical grade and used as received, without further purification. Two separate 1000 mg/L of lindane (γ -lindane is termed as lindane throughout the text) stock solutions were prepared by dissolving the required quantity of lindane in pure ethanol (99.9%) and *n*-hexane (99.9%) and were kept under refrigerated condition. Working concentrations of lindane were prepared from the stock solutions. A similar procedure was followed to prepare δ -lindane.

Synthesis of RGO@Ag. A procedure similar to the modified Hummers' method^{44,45} was used to synthesize graphene oxide (GO) from graphite powder. The reduction of GO to RGO was performed by a chemical route as reported by Li et al.^{8,46} Detailed synthetic procedures for GO and RGO are given in the Supporting Information, S1. Working concentrations of RGO were prepared by appropriate dilution of 0.01 wt % stock RGO dispersion. For making RGO@Ag, 100 mL of RGO was taken and calculated amounts of AgNO_3 (0.01, 0.05 and 0.1 mM) were added to it to make three different RGO@Ag composites. Each solution was kept undisturbed for 24 h at room temperature ($30 \pm 2^\circ\text{C}$), which allowed the formation of Ag NPs over graphene. The composites were dialyzed using distilled water to remove unwanted ions and then stored in glass bottles for further use. The composites prepared were labeled based on the Ag precursor concentration used [RGO@Ag^I, RGO@Ag^{II} and RGO@Ag^{III} for 0.01, 0.05 and 0.1 mM AgNO_3 , respectively with constant (0.01 wt %) RGO]. RGO@Ag^I (hereafter termed as RGO@Ag for simplicity) was used for all experiments unless otherwise mentioned. Inductively coupled plasma mass spectrometry (ICPMS) analysis was done with the filtrate (after the removal of RGO@Ag) to confirm the reduction of Ag^+ to Ag NPs. For RGO@Ag, initially 1.1 mg/L (1.1 ppm) of Ag was used. After the formation of the composite, the amount of silver ions present in the supernatant was found to be less than $1 \mu\text{g/L}$ (1 ppb). Therefore, it is likely that all Ag^+ was converted to Ag NPs in the presence of RGO, for the formation of the composite. The specific surface area of RGO was measured to be $1215 \text{ m}^2/\text{g}$ and that of RGO@Ag was $1123 \text{ m}^2/\text{g}$.

Adsorption Experiments. All adsorption studies were done in 20 mL batch reactors at room temperature ($30 \pm 2^\circ\text{C}$) keeping 5 mL of RGO@Ag as the working volume. A required amount of lindane stock solution was spiked to the RGO dispersion to get the working concentration of 2 mg/L in all cases unless mentioned elsewhere. The solutions were stirred for a contact time of 15 min. The liquid was separated from the dispersion using a 200 nm membrane filter paper. The filtrate, extracted with hexane, was analyzed for residual lindane and its degradation products using gas chromatography (GC)

(PerkinElmer, Clarrus 680) equipped with electron capture detection (ECD). The analysis condition was programmed as follows: run time, 38.5 min; injector temperature, 200°C ; injection rate, 12.5 pts/s and carrier gas flow rate, 1 mL/min. The products were detected using ECD (hexane was used as the solvent for all gas chromatography (GC)-ECD characterizations). The effect of contact time, pH and RGO@Ag dose on the removal of pollutants was evaluated by varying the parameters in the appropriate window. All experiments except kinetics' studies were conducted by batch equilibration method. To test the interference of other ions in the degradation of lindane and removal of the degraded products, studies were also conducted by spiking the required concentration of lindane in tap water (TW). All the experiments were performed in duplicate with proper control and the samples were analyzed immediately.

Instrumentation. UV/vis spectra were measured using a PerkinElmer Lambda 25 UV/vis spectrophotometer. Raman spectra of GO and RGO were collected using a confocal Raman spectrometer (WiTec GmbH CRM 200). RGO and RGO@Ag samples were imaged using a high-resolution transmission electron microscopy (HRTEM) instrument with a UHR polepiece (JEOL 3011, 300 kV) equipped with an analyzer for energy dispersive X-ray analysis (EDAX, Oxford). A scanning electron microscopy (SEM) instrument equipped with EDAX (FEI Quanta 200, Czechoslovakia) was also used to record the surface morphology, elemental composition and elemental maps of the samples. Fourier transform infrared (FTIR) spectra were recorded on a Nicolet 6700 spectrometer. Residual concentrations of lindane in water samples were analyzed using GC-ECD. The mass spectrometric studies were done using an electrospray system, 3200 Q-TRAP LC/MS/MS (Applied Biosystems). GC-ECD and GC-MS measurements give different retention times for the species as the GC parameters are different. Surface area measurements were performed using Micromeritics ASAP 2020 porosimeter, and the Brunauer–Emmett–Teller equation was used to calculate the corresponding values. The concentration of silver ion in the solution was measured using inductively coupled plasma mass spectrometry (ICPMS, NexION 300X, PerkinElmer). X-ray photoelectron spectroscopy (XPS) measurements were done with Omicron ESCA Probe spectrometer with polychromatic Mg $K\alpha$ X-rays ($h\nu = 1253.6 \text{ eV}$). Most of the spectra were deconvoluted to their component peaks using the software CasaXPS. The energy resolution of the spectrometer was set at 0.1 eV at a pass energy of 20 eV. Binding energy was corrected with respect to C 1s at 284.5 eV.

RESULTS AND DISCUSSION

Graphene prepared in the solution phase (RGO) showed a characteristic UV/vis peak centered at 271 nm (blue trace in Figure 1). As RGO characterization has been reported extensively,^{8,15,27} we do not discuss this here in detail. RGO@Ag composite was formed through an oxidation–reduction process, in which RGO was oxidized and silver ions were reduced to NPs, which were anchored onto the RGO surface.⁸ The recorded UV/vis spectrum of RGO@Ag (red trace in Figure 1) showed the peak corresponding to RGO (269 nm) and an additional plasmonic peak centered around 420 nm, indicating the formation of Ag NPs on the RGO surface. The small blue shift (2 nm) observed for the RGO peak can be ascribed to the partial oxidation of RGO during the reduction of Ag^+ to Ag NPs (an expanded view of UV/vis is shown in the inset of Figure S1 in the Supporting Information). Figure 1 shows the TEM image of RGO@Ag (silver ion concentration 0.01 mM) and the corresponding image for parent RGO is given in Figure S1 of the Supporting Information. The graphene sheets with characteristic nanometer thin wrinkles are clearly visible (marked with white arrows) in the latter image. The sheets are several micrometers in size and the edges and wrinkles are 1.0–1.5 nm thick, corresponding to a bilayer. The black dots seen in the TEM

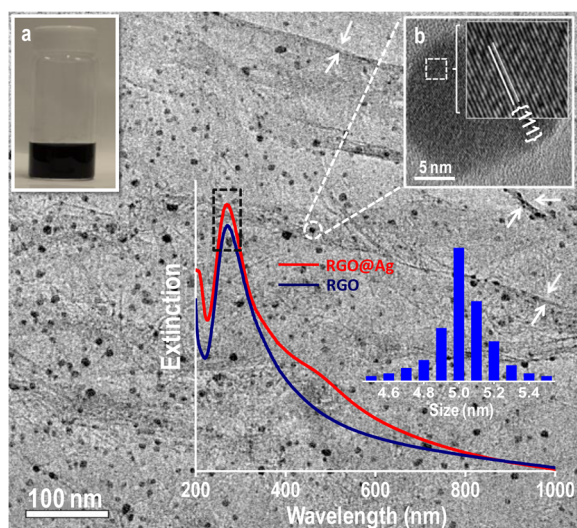


Figure 1. TEM image of RGO@Ag composite (foldings of the RGO sheets are marked with white arrows), the scale bar shows the size distribution of the Ag NPs (5 nm). Inset shows UV/vis spectrum of RGO (blue trace) and RGO@Ag (red trace). Photograph in inset a shows the dispersed nature of RGO@Ag. Inset b is a high resolution image of an Ag particle. Lattice spacing seen in the selected area is expanded further.

image (Figure 1) are due to the presence of Ag NPs over graphene sheets (here also the nanometer thin wrinkles are seen, as the grain boundaries⁴⁷). The well-dispersed particles are almost of uniform size (approximately 5 nm) and spherical in shape. An HRTEM image of one particle is shown in the inset (b) of Figure 1, which shows a lattice spacing of 0.23 nm corresponding to the (111) plane of silver, suggesting that most of the particles are single crystals attached to the RGO sheet. The sizes of the Ag NPs formed are a function of concentration of the silver precursor added initially. An increase in precursor concentration from 0.01 to 0.1 mM of AgNO₃ resulted in the formation of particles of size varying from 5 to 50 nm (a detailed discussion is in the Supporting Information, S2, along with TEM images). The graphenic nature of the sheet is intact even after the formation of the composite. The presence of Ag

peak in the HRTEM-EDAX spectrum of the composite further confirms the deposition of silver on the RGO sheets (see Figure S2D of the Supporting Information). The XPS spectrum of the RGO@Ag (see Figure S3 of the Supporting Information) composite shows the presence of carbon, oxygen and silver as the only elements. A deconvoluted XPS spectrum of Ag (see Figure S3d of the Supporting Information) shows the 3d_{5/2} peak at 368.2 eV, which confirms that silver in the Ag(0) state. Detailed characterizations of these type of RGO composites have been discussed before.^{16,34}

To test the reactivity of the composite, RGO@Ag was taken and lindane (dissolved in ethanol from the stock solution) was spiked, such that the final concentration of lindane in the solution was 2 mg/L (ratio of water:ethanol was 500:1 (v/v)). Characterization of the solution was done using GC-ECD and UV/vis at different time intervals to monitor the change in the concentration of lindane in water. Initially, lindane showed a peak around a retention time of 22 min and the solvent peak (hexane) appeared at 3–4 min in the GC-ECD (Figure 2A). With increase in contact time, the lindane peak started to disappear, implying its removal from the solution. Simultaneously, new peaks around a retention time of 5–7 min appeared, which indicated the formation of some products during the process. When the solution was stirred for 15 min, the peaks of both lindane and the products disappeared because of the degradation of the former and the removal of the latter by the RGO@Ag composite, respectively. The UV/vis spectrum in Figure 2B also indicated the formation of some products as the reaction progresses. The kinetic data in the inset of Figure 2B (red trace) predicts that the removal of lindane is a first-order reaction. The removal of lindane was about 99.9% in 15 min. The blue trace in the same inset shows the formation of product in the solution. It is clearly seen that the product so formed first increased with time, reached a maximum and then it was removed by the composite.

Pristine graphene is hydrophobic in nature, but the carboxylic groups^{48,49} present in RGO make it hydrophilic, thereby helping in the formation of a stable dispersion in water. The reduction of silver to Ag NPs by RGO does not affect the stability of the dispersion. This is evident from the photograph shown in the inset of Figure 1. When a nonpolar solvent like

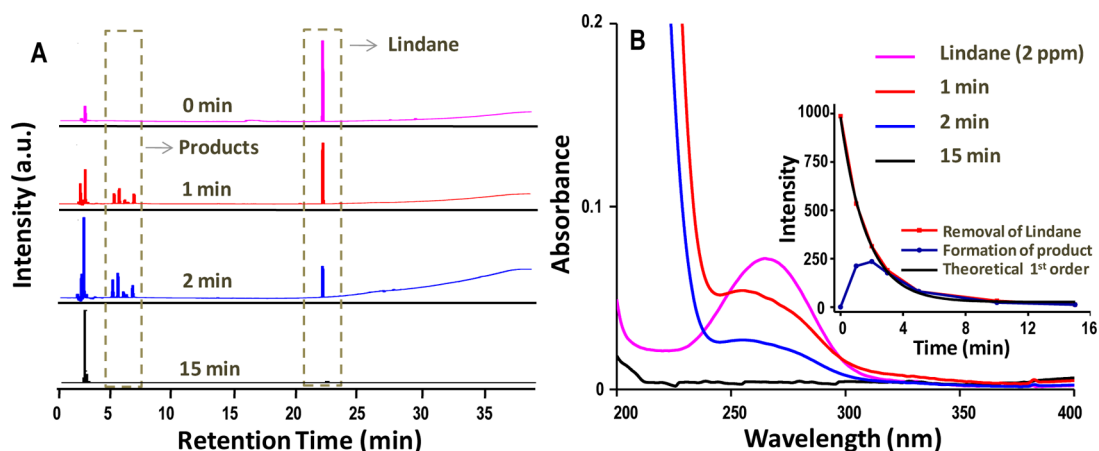


Figure 2. (A) GC-ECD traces and (B) UV/vis data showing the removal of lindane and formation of some products in the solution with respect to time. The dotted areas in A correspond to lindane and product. As can be seen, the lindane peak at the reaction time of 0 min (retention time, 22 min) decreases with time. The peaks of the products increase and then decrease. In panel B, the lindane intensity continuously decreases. The inset in panel B shows the kinetic data for the removal of lindane (red trace) and formation of the product (blue trace).

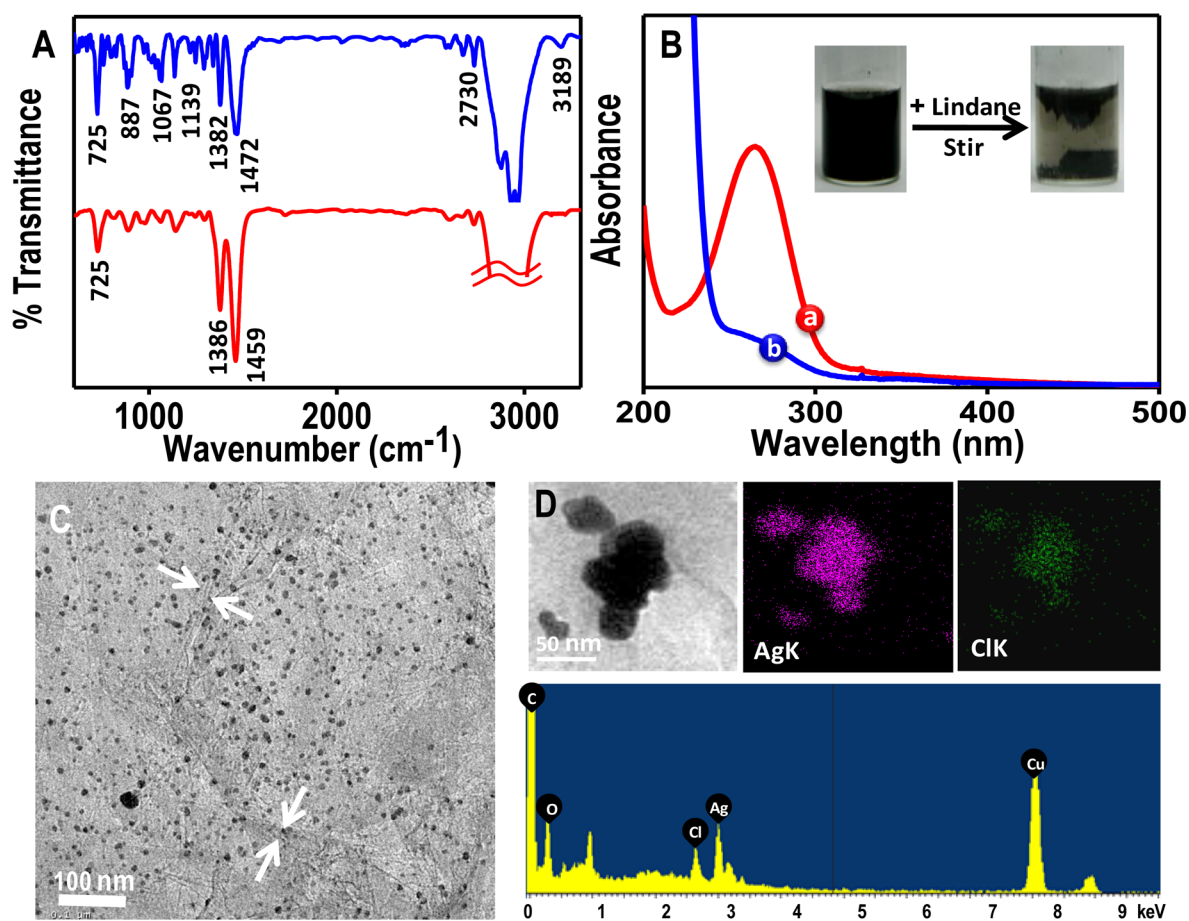


Figure 3. (A) IR spectrum of lindane (red trace) and the product (blue trace), (B) UV/vis spectrum of (a) lindane and the (b) product, inset showing photographs of the reaction mixture before and after reaction, (C) TEM image of RGO@Ag after reaction and (D) TEM-EDAX of the composite after reaction along with elemental mapping data that confirm the presence of silver and chlorine on the surface. Foldings of RGO are marked in panel C.

toluene or hexane is added to RGO dispersed in water, the RGO sheets prefer to stay at the interface and act as interfacial catalysts or reactants; whereas addition of any polar solvent (ethanol/methanol) does not affect their dispersibility. This property helped to isolate the products in the reaction system in the following manner. When lindane (dissolved in hexane) was spiked into the graphene dispersion (0.01 wt %), such that its final concentration was 2 mg/L, the graphene sheets interacted with hexane and lost their dispersibility, as shown in the inset of Figure 3B. Next, the RGO@Ag composites were separated from the solution and extensively characterized with various spectroscopic and microscopic techniques to establish the degradation products; a brief summary of these data is presented below.

The FTIR spectrum of lindane in Figure 3A (red trace) shows a prominent peak at 725 cm^{-1} due to C—Cl stretching and other peaks at 1386 and 1459 cm^{-1} due to rocking and bending vibrations of six C—H groups. The IR spectrum of the product after reacting with RGO@Ag was recorded (Figure 3A (blue trace)). New peaks seen at 887 , 1067 and 1139 cm^{-1} are due to the bending vibrations of the =C—H group and the weak peak at 3189 cm^{-1} is due to aromatic C—H stretching. The results give an indication of the formation of an aromatic product. The peak around $2800\text{--}3000\text{ cm}^{-1}$ is due to the stretching vibration of O—H present in water. UV/vis data of lindane in hexane shows a prominent peak around 264 nm due

to $n\text{--}\sigma^*$ transition, as displayed in Figure 3Ba. The decrease in the intensity of lindane peak after reacting with RGO@Ag (Figure 3Bb) suggests that lindane is getting removed from the solution. It can be further noticed that the absorbance of the solution (Figure 3Bb) starts increasing at 220 nm and continues into the deep UV region (below 200 nm), indicating the formation of a new product in the reaction medium.

A TEM image of was taken after RGO@Ag was reacted with lindane, and an image is shown in Figure 3C. The morphology of the composite does not change even after reacting with lindane. The TEM-EDAX of RGO@Ag after the reaction shows the presence of chlorine (Figure 3D). The elemental mapping of the TEM image in Figure 3D displays that chlorine is present only on silver. The spot SEM-EDAX of the composite confirms the presence of silver along with chlorine (Figure S4 of the Supporting Information) after the reaction. It is also evident from the elemental mapping in the SEM image that there is a one-to-one correspondence with silver and chlorine. In other words, the presence of chlorine is prominent on the surface of silver, which supports the participation of Ag NPs in the degradation of lindane. Similarly, the XPS spectrum of the composite after reaction with lindane shows the presence of AgCl along with C 1s and O 1s (see Figure S5a of the Supporting Information). Figure S5b,c of the Supporting Information shows the deconvoluted spectrum of Cl 2p and Ag 3d, respectively. The deconvoluted XPS spectrum of Ag

(see Figure S5c of the Supporting Information) shows the presence of a Ag $3d_{5/2}$ peak at 367.4 eV, which confirms silver in the Ag(I) state.

To confirm the identity of the products, mass spectrometric studies were conducted. As shown in the GC-ECD trace of Figure S6 of the Supporting Information (also in Figure 2), the lindane peak appeared at a retention time of 22 min and the solvent peak appeared around 2–3 min. The occurrence of new peaks (5–6 min) and decrease in the lindane peak as the reaction proceeds indicate the formation of a new molecular species in the reaction medium. Further confirmation comes from the fact that GC–MS analysis of lindane (GC trace in Figure S7A of the Supporting Information, retention time of 12.20 min) shows its molecular ion at m/z 292 (see Figure S8A of the Supporting Information) with isotope distribution for six chlorines, the spectrum matches with that in the literature.³⁷ The newly formed species, appearing at a retention time of 7.32 min in Figure S8B of the Supporting Information, has a molecular ion peak around m/z 180 (see Figure S7B of the Supporting Information). This can be attributed to the formation of trichlorobenzene (TCB). The isotope pattern with peaks at m/z 179, 181 and 183 is due to the presence of three chlorines in TCB. There is no peak corresponding to m/z 292, indicating the complete degradation of lindane to TCB. It is to be noted that the GC trace showed three distinct peaks for the products (marked as 1, 2 and 3 in Figure S7B of the Supporting Information). The GC–MS of these three peaks is almost similar in nature (given in Figure S9 of the Supporting Information), indicating the existence of TCB isomers in the product.

The product was further confirmed using electrospray ionization mass spectrometry (ESI-MS). Lindane has a set of peaks in the range of m/z 292 (Figure 4A) corresponding to its molecular ion (in the positive mode of ESI). Inset in the figure shows the isotope distribution due to chlorine in the molecular ion (in the positive mode). The degraded product of lindane extracted with hexane was also analyzed by MS (Figure 4B). A set of peaks arising around m/z 180 corresponding to an aromatic benzene ring with three chlorines is observable. The

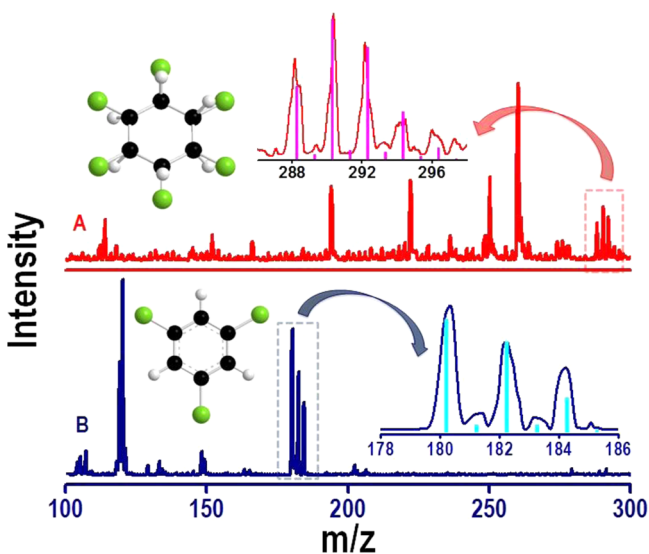


Figure 4. Mass spectrum of (A) lindane (red trace) and the (B) product (blue trace). Inset shows the isotopic distribution of chlorine and the corresponding molecular structure of the analytes.

inset in Figure 4B shows the enlarged spectrum in the region of m/z 180 where the isotope distribution for three chlorine atoms can be seen. The calculated spectrum of TCB matches perfectly with the experimental data. To establish the identity of the product, detailed tandem mass spectrometry (MS/MS or MS^2) studies were undertaken. MS^2 analyses of the peaks at m/z 180, 182 and 184 (corresponding to distinct isotopomers of the product) in Figure 4 exhibiting the predicted isotope patterns was conducted at collision energy of 20 (in the instrumental unit). The MS^2 analyses of m/z 179, 181 and 183 are shown in Figure 5a–c. The peaks at m/z 179, 181 and 183

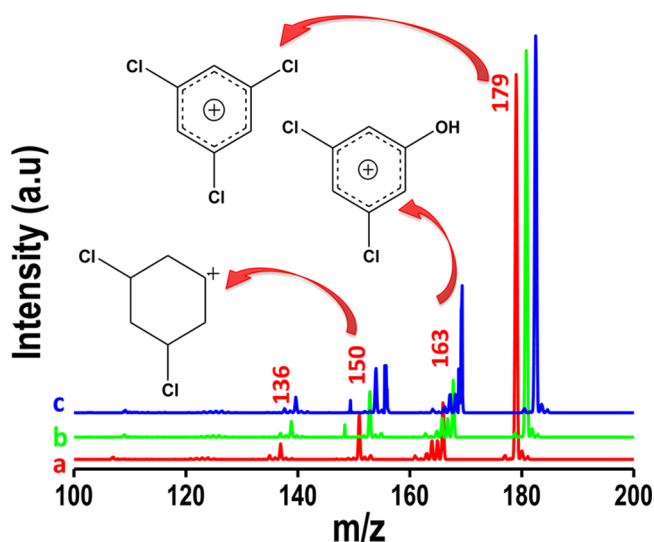


Figure 5. MS-MS of the peaks at m/z 179, 181 and 183 (a, b and c, respectively). The chemical structure of the peak m/z 180, 163 and 150 are shown in the inset. The various isotopologue ions and their fragments are labeled. The ions may have isomeric structures.

in the product are due to $^{35}Cl_3$, $^{35}Cl_2^{37}Cl$ and $^{35}Cl^{37}Cl_2$ isotopomers of TCBS (of various isomers), respectively. The MS^2 of the m/z 179 peak (Figure 5 trace a) gives fragments at m/z 163, 151 and 136. The peak at m/z 163 is due to an exchange of one Cl by the OH group from the parent at m/z 179. The peak arising at m/z 151 is due to $C_6H_9Cl_2^+$. Here, ^{35}Cl is lost in fragmentation. In the MS^2 analysis of m/z 181, all the peaks are shifted by two mass units (trace b in Figure 5) higher than in trace a. Two peaks are seen at m/z 153 and 155 in the MS^2 spectrum of m/z 183 (trace c in Figure 5). Here there is a possibility of losing either ^{35}Cl or ^{37}Cl from the parent material. The enlarged full range MS^2 with higher collision energy of 60 is shown in Figure S10 of the Supporting Information.

Next, the reaction with lindane was carried out at a larger scale and the product was collected for further analysis. About 100 mL of RGO@Ag was taken and 1 mL of lindane stock solution (5000 ppm in hexane) was spiked to it. The reaction was carried out for 1 h with continuous stirring. The product was phase transferred to hexane and kept for crystallization for 1 day, after which needle-like crystals were formed (Figure 6Bi, insets). These crystals were characterized extensively. 1H NMR of lindane (in $CDCl_3$), given in Figure 6A shows the characteristic peak at 4.64 ppm due to the presence of chemically equivalent six C–H bonds. A small peak at 7.26 ppm is due to the solvent, $CDCl_3$. Figure 6B shows the 1H NMR spectrum of the product, in which the peaks between 7.2

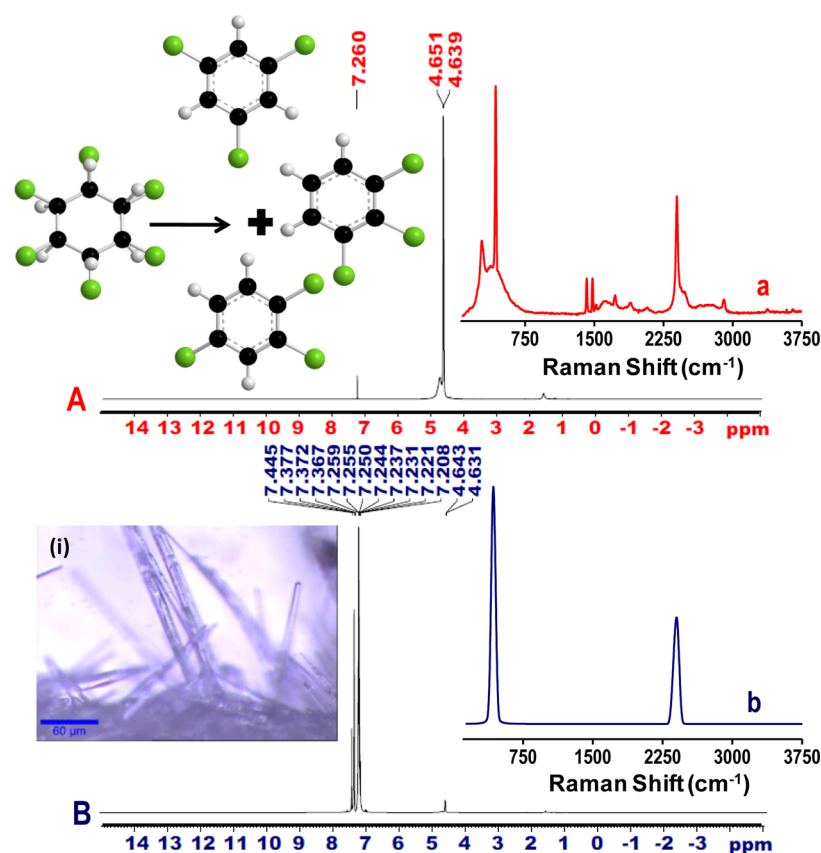


Figure 6. ^1H NMR of (A) lindane and (B) the degraded product. The insets show the Raman spectra of (a) lindane and (b) the product. The schematic in panel A shows the structures of lindane and the products. (i) Optical image of the crystals of TCBS is shown.

and 7.5 ppm confirm the presence of aromatic hydrogen. Multiple peaks in the region confirm that a mixture of TCBS is formed in the reaction. The different isomers of TCB are shown in Figure 6A (inset). A weak peak is visible around 4.63 ppm due to the presence of unreacted lindane, which got attached to the crystals when the crystals along with traces of impurities present in the reaction mixture were dissolved in CDCl_3 . Raman spectrum of lindane in the inset of Figure 6A (Figure 6Aa) shows peaks at 500, 1510 and 1550 cm^{-1} , respectively due to C–Cl and aliphatic C–C stretching modes. In the Raman spectrum of TCBS in the inset of Figure 6B (Figure 6Bb), a peak at 430 cm^{-1} can be seen that confirms the presence of aromatic C–Cl stretching (the image shown here in Figure 6Bb is after baseline correction). The original spectrum has a large fluorescence background due to the conjugated double bond (shown in Figure S11 of the Supporting Information).

Blank tests were performed to check the reactivity of graphene and Ag NPs separately, with lindane. We prepared 50 nm sized citrate capped Ag NPs (Ag@citrate, details of preparation and characterization are given in the Supporting Information, S12). We found that Ag@citrate did not react with lindane, even when kept for 6 h in contact. This can be attributed to the protection of the Ag NPs by the citrate groups, which reduce the accessibility of the silver surface to lindane leading to only a weak interaction between the two. Similarly, RGO did not exhibit any affinity toward lindane. UV/vis spectra in Figure S13A,B of the Supporting Information show that when used independently, Ag@citrate and graphene have a negligible lindane adsorption/degradation capacity. The same

reaction was also performed with other carbon materials such as activated carbon (AC), MWCNTs and AC@Ag. A detailed discussion is given in the Supporting Information, S13 on the preparation of AC@Ag. UV/vis data for the removal of lindane by AC@Ag are presented in Figure S13C of the Supporting Information. Corresponding data for the reaction with MWCNTs is plotted in Figure S13D of the Supporting Information. There was little to no degradation or removal of lindane with these materials. Reactivity of lindane toward elemental silver was checked as well. It was found that elemental silver also degraded lindane. However, the capacity of degradation was much higher in the case of the composite (about 100 times) when an equal amount of silver was considered (see Figure S14A of the Supporting Information). Therefore, it is quite clear that the uncapped silver particles are responsible for this unusual dehalogenation. But the conversion efficiency is higher in the case of the composite due to the synergetic effect of Ag NPs on RGO. RGO does not adsorb lindane, but TCBS can adsorb on it, as they have conjugated π -bonds, which are responsible for adsorption.^{24,50} The bar diagram in Figure S14B of the Supporting Information compares the different carbon-based materials toward the degradation of lindane and clearly illustrates the uniqueness of RGO@Ag for this dehalogenation reaction.

It is known that silver has a great affinity for halogenated compounds.^{51,52} Thus, Ag NPs on RGO react with lindane to form TCBS. This reaction is energetically favorable as the product gains aromaticity, but further degradation of aromatic compounds is thermodynamically unlikely because of the high resonance energy of the benzene ring (152 kJ/mol). Graphene,

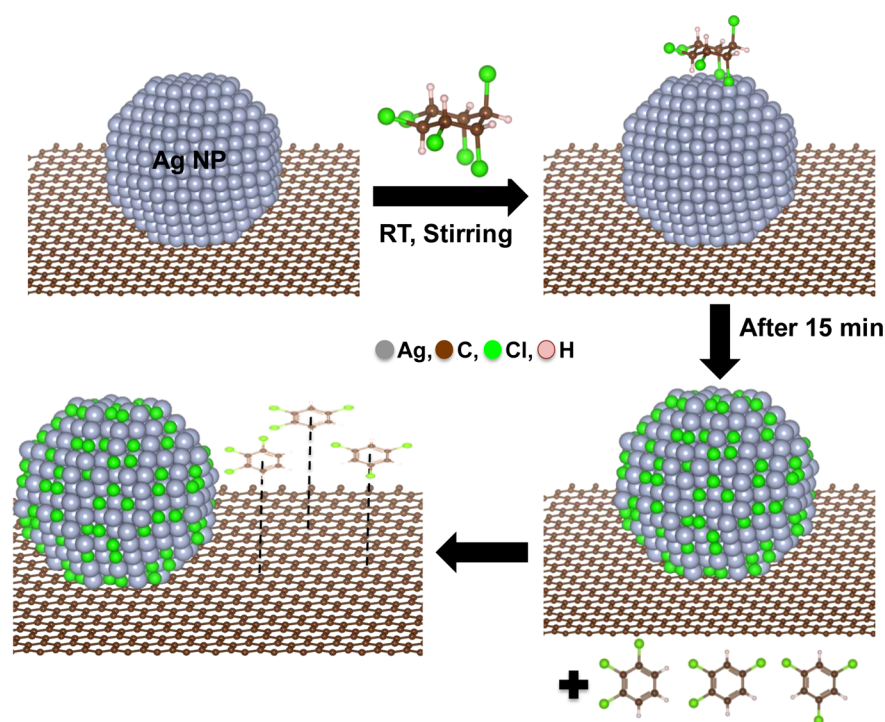


Figure 7. Schematic showing the mechanism of adsorption of lindane on graphene substrate (not to scale).

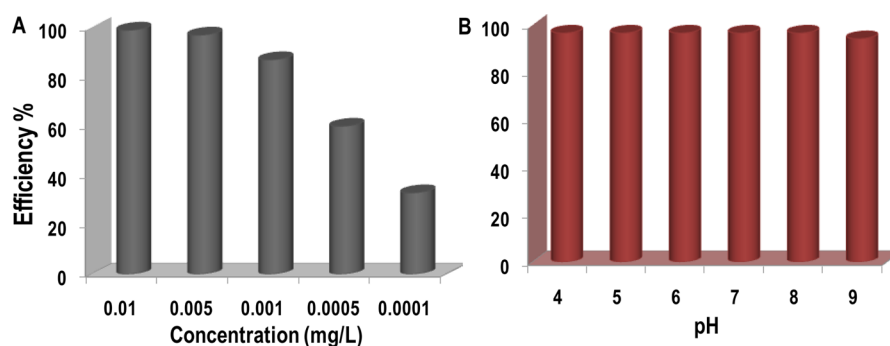


Figure 8. Effect of (A) concentration of the composite and (B) initial pH of the solution on the removal efficiency of lindane.

although promising as an adsorbent, was incapable of removing lindane from the solution when treated alone (see Figure S13B of the Supporting Information). However, it was able to remove TCBs from the solution, as for conjugated organic molecules adsorption occurs via π - π interactions.⁵⁰

A mechanistic pathway for the degradation of lindane by RGO@Ag is proposed in Figure 7. The figure suggests that when lindane is spiked on RGO@Ag, Ag NPs react with lindane to form different isomers of TCBS. Silver on the graphene substrate changes to AgCl, which remains attached on the graphene sheet. The TCBS formed get adsorbed on graphene sheets by π - π interactions. Thus, the removal of lindane from water is a two-step process on the RGO@Ag substrate. To confirm that the adsorption of TCBS is physical in nature, they were extracted with a suitable eluent like hexane. About 2 mL of hexane was added to the composite (after the reaction), and the mixture was stirred vigorously for 10 min. The hexane solution was then characterized with GC-ECD, which gave peaks at a retention time of 5–7 min, characteristic of TCBS as shown in Figure 2A. This confirms that the TCBS were weakly adsorbed on the graphene sheets from where they were dissolved in hexane as a result of the vigorous stirring.

Finally, the reaction was evaluated under various conditions to check the viability of the material for practical applications. As mentioned earlier, increase in silver ion concentration during the preparation of RGO@Ag increased the size and concentration of Ag NP on RGO sheets (shown in the TEM image in Figure S2 of the Supporting Information); this is expected to increase the capacity of the composite to degrade lindane (see Figure S15 of the Supporting Information), but we found that capacity with respect to silver loading (in mg/g of silver) toward degradation of lindane is much higher for smaller particles than for bigger particles (see Figure S15 of the Supporting Information). The removal capacity of RGO@Ag was tested upon dilution. It is seen that lower the concentration of the composite, more is the adsorption capacity in mg/g of the material, which is due to the increase in free surface area available upon dilution (Figure 8A). Increased concentrations of the composite may cause the aggregation of graphene sheets. The maximum removal capacity for lindane was found to be 827 mg/g of the composite. Effect of initial pH toward the removal capacity was also examined and it was found that pH did not have any affect in the window of 3–9 (Figure 8B). The pH was maintained acidic or basic using HNO₃ or NaHCO₃.

The removal capacity decreased with a pH higher than 9 because of the formation of silver hydroxide, which reduces the free silver sites available for the degradation of lindane. The reaction was also performed in TW for real time applications and it showed 70% efficiency compared to the laboratory batch experiments (see Figure S16A of the Supporting Information). The removal capacity of the composite was therefore further examined for common ion effect. For this, 5 mL of RGO@Ag was taken and NaCl solution was spiked to DI water such that the final concentration of the solution was 100 ppm of Cl^- . In the presence of Cl^- ions, the removal efficiency of the composite was found to be 65% versus the laboratory batch experiment, but similar to the efficiency when using TW (see Figure S16B of the Supporting Information). The reaction was also performed with another isomer of lindane (δ -lindane) but no such degradation was observed for this case. Therefore, this type of reaction can open up a new way for isomer selective transformation on graphene substrates, although understanding of the exact mechanism requires additional work. To check the reusability of the composite, repeated adsorption–desorption cycles were performed. For this, the composite was treated with hexane to remove adsorbed TBC and then redispersed in ammoniacal solution through sonication. The analyses of regenerated sample showed no presence of TCB and AgCl. This indicates the possibility of reuse of the material by reloading Ag NPs again on RGO by similar procedure mentioned before. It was seen that the efficiency of the material was around 70–75% even after the fifth cycle of operation (data are presented in Figure S17 of the Supporting Information). Previous studies also show that RGO can be effectively regenerated for repeated use.^{17,37}

CONCLUSION

In conclusion, we presented a sustainable and efficient way for dehalogenation reactions on graphene-silver nanocomposites. The conversion of an alicyclic compound, lindane to an aromatic trichlorobenzene was reported for the first time on graphene substrates. In the reaction, lindane was dehydrohalogenated to yield AgCl and different isomers of trichlorobenzene as products that were adsorbed on the graphene substrate by π - π interactions. This process effectively removed a persistent organochlorine pesticide from water, at efficiency close to 99.9%. It was shown that the high conversion capacity (827 mg/g) observed here for a low concentration of RGO@Ag (0.01 mM) and the recycling ability of the composite could be used effectively for applications in sustainable water treatment. This type of reaction may be employed for the degradation of other toxic halocarbons (studies under progress), which may open up a new method for environmental remediation.

ASSOCIATED CONTENT

Supporting Information

Additional details describing the synthesis of GO and RGO; HRTEM image of RGO and RGO@Ag (at different concentrations of Ag ions); SEM-EDAX image of the composite after the reaction; XPS spectrum of the composite, GC-ECD data showing the removal of lindane; XPS spectrum of the composite after reaction with lindane, GC trace of lindane and the product, GC-MS data of lindane and the degraded product; Raman spectrum of TCBs; synthesis of Ag NPs protected with citrate and their characterization; blank test for RGO, Ag NPs, MWCNTs and AC-Ag composite for the removal of lindane and comparison with elemental silver;

dependence of Ag NP size on the degradation of lindane, the effect of tap water and common ion effect on the removal of lindane and the reusability of the material up-to fifth cycle. The Supporting Information is available free of charge on the ACS Publications website at DOI: 10.1021/acssuschemeng.5b00080.

AUTHOR INFORMATION

Corresponding Author

*T. Pradeep. E-mail: pradeep@iitm.ac.in. Fax: 91-44-2257-0545/0509.

Notes

The authors declare no competing financial interest.

ACKNOWLEDGMENTS

We thank the Nano Mission of the Department of Science and Technology (DST), Government of India, for supporting our research program on nanomaterials. SSG thanks the SERB, CII and Thermax India Pvt. Ltd. for a research fellowship. We also thank Jyoti Sarita Mohanty, K. R. Krishnadas, Shridevi Bhat, and Somraj Guha for help in handling different instruments. D.K.P. was a summer fellow from the Department of Chemistry, University of Hyderabad, while part of this work was performed.

REFERENCES

- (1) Novoselov, K. S.; Geim, A. K.; Morozov, S. V.; Jiang, D.; Zhang, Y.; Dubonos, S. V.; Grigorieva, I. V.; Firsov, A. A. Electric field effect in atomically thin carbon films. *Science* **2004**, *306*, 666–669.
- (2) Geim, A. K.; Novoselov, K. S. The rise of graphene. *Nat. Mater.* **2007**, *6*, 183–191.
- (3) Dhakshinamoorthy, A.; Alvaro, M.; Puche, M.; Fornes, V.; Garcia, H. Graphene oxide as catalyst for the acetalization of aldehydes at room temperature. *ChemCatChem* **2012**, *4*, 2026–2030.
- (4) Su, C.; Acik, M.; Takai, K.; Lu, J.; Hao, S. J.; Zheng, Y.; Wu, P.; Bao, Q.; Enoki, T.; Chabal, Y. J.; Loh, K. P. Probing the catalytic activity of porous graphene oxide and the origin of this behaviour. *Nat. Commun.* **2012**, *3*.
- (5) Gupta, S. S.; Siva, V. M.; Krishnan, S.; Sreepasad, T. S.; Singh, P. K.; Pradeep, T.; K. Das, S. Thermal conductivity enhancement of nanofluids containing graphene nanosheets. *J. Appl. Phys.* **2011**, *110*, 084302–084306.
- (6) Novoselov, K.; Geim, A. K.; Morozov, S.; Jiang, D.; Grigorieva, M. K. I.; Dubonos, S.; Firsov, A. Two-dimensional gas of massless dirac fermions in graphene. *Nature* **2005**, *438*, 197–200.
- (7) Georgakilas, V.; Otyepka, M.; Bourlinos, A. B.; Chandra, V.; Kim, N.; Kemp, K. C.; Hobza, P.; Zboril, R.; Kim, K. S. Functionalization of graphene: Covalent and non-covalent approaches, derivatives and applications. *Chem. Rev.* **2012**, *112*, 6156–6214.
- (8) Sreepasad, T. S.; Maliyekkal, S. M.; Lisha, K. P.; Pradeep, T. Reduced graphene oxide–metal/metal oxide composites: Facile synthesis and application in water purification. *J. Hazard. Mater.* **2011**, *186*, 921–931.
- (9) Sreepasad, T. S.; Gupta, S. S.; Maliyekkal, S. M.; Pradeep, T. Immobilized graphene-based composite from asphalt: Facile synthesis and application in water purification. *J. Hazard. Mater.* **2013**, *246*–247, 213–220.
- (10) Gao, W.; Majumder, M.; Alemany, L. B.; Narayanan, T. N.; Ibarra, M. A.; Pradhan, B. K.; Ajayan, P. M. Engineered graphite oxide materials for application in water purification. *ACS Appl. Mater. Interfaces* **2011**, *3*, 1821–1826.
- (11) Ai, L.; Zhang, C.; Chen, Z. Removal of methylene blue from aqueous solution by a solvothermal-synthesized graphene/magnetite composite. *J. Hazard. Mater.* **2011**, *192*, 1515–1524.
- (12) Zhu, J.; Wei, S.; Gu, H.; Rapole, S. B.; Wang, Q.; Luo, Z.; Haldolaarachchige, N.; Young, D. P.; Guo, Z. One-pot synthesis of magnetic graphene nanocomposites decorated with core@double-shell

nanoparticles for fast chromium removal. *Environ. Sci. Technol.* **2012**, *46*, 977–985.

(13) Chang, C. F.; Truong, Q. D.; Chen, J. R. Graphene sheets synthesized by ionic-liquid-assisted electrolysis for application in water purification. *Appl. Surf. Sci.* **2013**, *264*, 329–334.

(14) Zhu, Y.; Murali, S.; Cai, W.; Li, X.; Suk, J. W.; Potts, J. R.; Ruoff, R. S. Graphene and graphene oxide: Synthesis, properties, and applications. *Adv. Mater.* **2010**, *22*, 3906–3924.

(15) Sreeprasad, T. S.; Maliyekkal, M. S.; Deepti, K.; Chaudhari, K.; Xavier, P. L.; Pradeep, T. Transparent, luminescent, antibacterial and patternable film forming composites of graphene oxide/reduced graphene oxide. *ACS Appl. Mater. Interfaces* **2011**, *3*, 2643–2654.

(16) Liu, S.; Zeng, T. H.; Hofmann, M.; Burcombe, E.; Wei, J.; Jiang, R.; Kong, J.; Chen, Y. Antibacterial activity of graphite, graphite oxide, graphene oxide, and reduced graphene oxide: Membrane and oxidative stress. *ACS Nano* **2011**, *5*, 6971–6980.

(17) Hu, W.; Peng, C.; Luo, W.; Lv, M.; Li, X.; Li, D.; Huang, Q.; Fan, C. Graphene-based antibacterial paper. *ACS Nano* **2010**, *4*, 4317–4323.

(18) Wang, W.; Yu, J. C.; Xia, D.; Wong, P. K.; Li, Y. Graphene and g-C₃N₄ nanosheets cowrapped elemental α -sulfur as a novel metal-free heterojunction photocatalyst for bacterial inactivation under visible-light. *Environ. Sci. Technol.* **2013**, *47*, 8724–8732.

(19) Chang, Y.; Yang, S.-T.; Liu, J. H.; Dong, E.; Wang, Y.; Cao, A.; Liu, Y.; Wang, H. In vitro toxicity evaluation of graphene oxide on A549 cells. *Toxicol. Lett.* **2011**, *200*, 201–210.

(20) Akhavan, O.; Ghaderi, E. Toxicity of graphene and graphene oxide nanowalls against bacteria. *ACS Nano* **2010**, *4*, 5731–5736.

(21) Tuček, J.; Kemp, K. C.; Kim, K. S.; Zbořil, R. Iron-oxide-supported nanocarbon in lithium-ion batteries, medical, catalytic, and environmental applications. *ACS Nano* **2014**, *8*, 7571–7612.

(22) Chandra, V.; Park, J.; Chun, Y.; Lee, J. W.; Hwang, I.-C.; Kim, K. S. Water-dispersible magnetite-reduced graphene oxide composites for arsenic removal. *ACS Nano* **2010**, *4*, 3979–3986.

(23) Gao, H.; Sun, Y.; Zhou, J.; Xu, R.; Duan, H. Mussel-inspired synthesis of polydopamine-functionalized graphene hydrogel as reusable adsorbents for water purification. *ACS Appl. Mater. Interfaces* **2012**, *5*, 425–432.

(24) Gupta, S. S.; Sreeprasad, T. S.; Maliyekkal, S. M.; Das, S. K.; Pradeep, T. Graphene from sugar and its application in water purification. *ACS Appl. Mater. Interfaces* **2012**, *4*, 4156–4163.

(25) Li, H.; Zou, L.; Pan, L.; Sun, Z. Novel graphene-like electrodes for capacitive deionization. *Environ. Sci. Technol.* **2010**, *44*, 8692–8697.

(26) Liu, T.; Li, Y.; Du, Q.; Sun, J.; Jiao, Y.; Yang, G.; Wang, Z.; Xia, Y.; Zhang, W.; Wang, K.; Zhu, H.; Wu, D. Adsorption of methylene blue from aqueous solution by graphene. *Colloids Surf., B* **2012**, *90*, 197–203.

(27) Sreeprasad, T. S.; Pradeep, T. Graphene for environmental and biological applications. *Int. J. Mod. Phys. B* **2012**, *26*.

(28) Hou, C.; Zhang, Q.; Li, Y.; Wang, H. P25-graphene hydrogels: Room-temperature synthesis and application for removal of methylene blue from aqueous solution. *J. Hazard. Mater.* **2012**, *205–206*, 229–235.

(29) Cohen-Tanugi, D.; Grossman, J. C. Water desalination across nanoporous graphene. *Nano Lett.* **2012**, *12*, 3602–3608.

(30) Maliyekkal, S. M.; Sreeprasad, T. S.; Krishnan, D.; Kouser, S.; Mishra, A. K.; Waghmare, U. V.; Pradeep, T. Graphene: A reusable substrate for unprecedented adsorption of pesticides. *Small* **2013**, *9*, 273–283.

(31) Fan, L.; Luo, C.; Li, X.; Lu, F.; Qiu, H.; Sun, M. Fabrication of novel magnetic chitosan grafted with graphene oxide to enhance adsorption properties for methyl blue. *J. Hazard. Mater.* **2012**, *215–216*, 272–279.

(32) Kemp, K. C.; Seema, H.; Saleh, M.; Le, N. H.; Mahesh, K.; Chandra, V.; Kim, K. S. Environmental applications using graphene composites: water remediation and gas adsorption. *Nanoscale* **2013**, *5*, 3149–3171.

(33) Zhao, G.; Li, J.; Ren, X.; Chen, C.; Wang, X. Few-layered graphene oxide nanosheets as superior sorbents for heavy metal ion pollution management. *Environ. Sci. Technol.* **2011**, *45*, 10454–10462.

(34) Ruiz-Hitzky, E.; Darder, M.; Fernandes, F. M.; Zatile, E.; Palomares, F. J.; Aranda, P. Supported graphene from natural resources: Easy preparation and applications. *Adv. Mater.* **2011**, *23*, 5250–5255.

(35) Benimeli, C. S.; Castro, G. R.; Chaile, A. P.; Amoroso, M. J. Lindane removal induction by *Streptomyces* sp. M7. *J. Basic Microbiol.* **2006**, *46*, 348–357.

(36) Benimeli, C. S.; Fuentes, M. S.; Abate, C. M.; Amoroso, M. J. Bioremediation of lindane-contaminated soil by *Streptomyces* sp. M7 and its effects on *Zea mays* growth. *Int. Biodeterior. Biodegrad.* **2008**, *61*, 233–239.

(37) Nagpal, V.; Srinivasan, M. C.; Paknikar, K. M. Biodegradation of γ -hexachlorocyclohexane (lindane) by a non-white rot fungus *conidiobolus* 03-1-56 isolated from litter. *Indian J. Microbiol.* **2008**, *48*, 134–141.

(38) Paknikar, K. M.; Nagpal, V.; Pethkar, A. V.; Rajwade, J. M. Degradation of lindane from aqueous solutions using iron sulfide nanoparticles stabilized by biopolymers. *Sci. Technol. Adv. Mater.* **2005**, *6*, 370–374.

(39) Nagpal, V.; Bokare, A. D.; Chikate, R. C.; Rode, C. V.; Paknikar, K. M. Reductive dechlorination of γ -hexachlorocyclohexane using Fe–Pd bimetallic nanoparticles. *J. Hazard. Mater.* **2010**, *175*, 680–687.

(40) Senthilnathan, J.; Philip, L. Photocatalytic degradation of lindane under UV and visible light using N-doped TiO₂. *Chem. Eng. J.* **2010**, *161*, 83–92.

(41) Silvestroni, L.; Palleschi, S. Effects of organochloride xenobiotics on human spermatozoa. *Chemosphere* **1999**, *39*, 1249–1252.

(42) Hall, R. C. W.; Hall, R. C. W. Long-term psychological and neurological complications of lindane poisoning. *Psychosomatics* **1999**, *40*, 513–517.

(43) Kouras, A.; Zouboulis, A.; Samara, C.; Kouimtzi, T. Removal of pesticides from aqueous solutions by combined physicochemical processes—The behaviour of lindane. *Environ. Pollut.* **1998**, *103*, 193–202.

(44) Hummers, W. S., Jr.; Offeman, R. E. Preparation of graphitic oxide. *J. Am. Chem. Soc.* **1958**, *80*, 1339.

(45) Kovtyukhova, N. I.; Ollivier, P. J.; Martin, B. R.; Mallouk, T. E.; Chizhik, S. A.; Buzaneva, E. V.; Gorchinskiy, A. D. Layer-by-layer assembly of ultrathin composite films from micron-sized graphite oxide sheets and polycations. *Chem. Mater.* **1999**, *11*, 771–778.

(46) Li, D.; Muller, M. B.; Gilje, S.; Kaner, R. B.; Wallace, G. G. Processable aqueous dispersions of graphene nanosheets. *Nat. Nanotechnol.* **2008**, *3*, 101–105.

(47) Yu, S. U.; Park, B.; Cho, Y.; Hyun, S.; Kim, J. K.; Kim, K. S. Simultaneous visualization of graphene grain boundaries and wrinkles with structural information by gold deposition. *ACS Nano* **2014**, *8*, 8662–8668.

(48) Haubner, K.; Murawski, J.; Olk, P.; Eng, L. M.; Ziegler, C.; Adolphi, B.; Jaehne, E. The route to functional graphene oxide. *ChemPhysChem* **2010**, *11*, 2131–2139.

(49) Si, Y.; Samulski, E. T. Synthesis of water soluble graphene. *Nano Lett.* **2008**, *8*, 1679–1682.

(50) Liu, F.; Chung, S.; Oh, G.; Seo, T. S. Three-dimensional graphene oxide nanostructure for fast and efficient water-soluble dye removal. *ACS Appl. Mater. Interfaces* **2011**, *4*, 922–927.

(51) Bootharaju, M. S.; Pradeep, T. Understanding the degradation pathway of the pesticide, chlorpyrifos by noble metal nanoparticles. *Langmuir* **2012**, *28*, 2671–2679.

(52) Bootharaju, M. S.; Deepesh, G. K.; Udayabhaskararao, T.; Pradeep, T. Atomically precise silver clusters for efficient chlorocarbon degradation. *J. Mater. Chem. A* **2013**, *1*, 611–620.

Simultaneous dehalogenation and removal of persistent halocarbon pesticides from water using graphene nanocomposites: A case study of lindane

Soujit Sen Gupta,¹ Indranath Chakraborty,¹ Shihabudheen Mundampra Maliyekkal,² Tuhina Adit Mark,¹ Dheeraj Kumar Pandey¹, Sarit Kumar Das³ and Thalappil Pradeep^{1,*}

¹*DST Unit on Nanoscience and Thematic Unit of Excellence (TUE), Department of Chemistry, Indian Institute of Technology Madras, Chennai 600 036, India*

²*School of Mechanical and Building Sciences, VIT University, Chennai Campus, Chennai 600 048, India*

³*Department of Mechanical Engineering, Indian Institute of Technology Madras, Chennai - 600036, India*

**Email: pradeep@iitm.ac.in; Fax: 91-44-2257-0545/ 0509*

Contents:

Number	Description	Page number
S1	Preparation of GO and RGO	2-4
S2	TEM image of RGO@Ag with varying silver ion concentration	5
S3	XPS spectrum of RGO@Ag composite	6
S4	SEM-EDAX of RGO@Ag	7
S5	XPS spectrum of RGO@Ag after reaction with lindane	8
S6	GC-ECD data of lindane	9
S7	GC trace of lindane and the isomers	10

S8	GC-MS spectrum of lindane and the degraded product	11
S9	GC-MS of three different isomers of TCBS	12
S10	MS2 of the peak of the degraded product, trichlorobenzenes	13
S11	Raman spectrum of the product	14
S12	UV/Vis spectrum of silver nanoparticles	15
S13	UV/Vis spectrum showing degradation capacity of lindane with other adsorbents	16,17
S14	UV/Vis spectrum and comparison for the removal efficiency of lindane with different adsorbents	18
S15	Silver nanoparticle concentration towards the degradation of lindane	19,20
S16	Effect of tap water and 100 ppm of NaCl solution	21
S17	Reuse of RGO@Ag composite	22

Supporting Information 1

S1: Preparation of GO and RGO

Graphene oxide (GO) was synthesized from graphite powder (purchased from R. K. Scientific) based on the Modified Hummers' method. Approximately 2 g of graphite powder was taken and pre-oxidized in a hot solution (temperature maintained around 80-90 °C) of concentrated H₂SO₄ (~ 12 mL) containing K₂S₂O₈ (4 g) and P₂O₅ (4 g) for 6 h. A dark blue mixture was formed which was then cooled to room temperature. About 300 mL distilled water was added carefully and slowly to the mixture. It was filtered using a Whatmann No. 40 filter paper and kept for drying overnight in a hot air oven at 55-60 °C. This pre-oxidized graphite powder (2 g) was added to 100 mL of cold H₂SO₄ at 0 °C (temperature maintained

by an ice bath), to which 12 g of KMnO_4 was added slowly under continuous stirring, making sure that the temperature of the reaction media never crossed $5\text{ }^\circ\text{C}$. The solution was further stirred for 2 h at room temperature and 200 mL of distilled water was added slowly. Care was taken, as the reaction is exothermic. To the mixture, 560 mL of distilled water was added and the reaction was stopped with the addition of 10 mL H_2O_2 (30 %). The resulting bright yellow solution was kept undisturbed overnight. The product was decanted, washed with HCl (1:10) twice and then suspended in water via sonication. Unexfoliated GO was removed by centrifugation at 10000 rpm for 20 min and then suspended in distilled water (1 g in 200 mL of water i.e. 0.5 wt % of GO). The resulting brown dispersion was extensively dialyzed to remove the residual metal ions and to neutralize the pH. The resulting 0.5 wt % of GO (stock solution) was stored in glass bottles for further use.

About 2 ml of GO was taken in a beaker and diluted to 100 mL with distilled water. The solution was heated to $80\text{ }^\circ\text{C}$ and to it 60 μL of NH_3 and 35 μL of hydrazine were added with continuous stirring for 5 min. Stirrer was switched off and the solution was kept at $80\text{ }^\circ\text{C}$ for 2 h. The resulting black colored dispersion was reduced graphene oxide (RGO). This RGO (0.01 wt %) was dialyzed and kept as the stock solution.

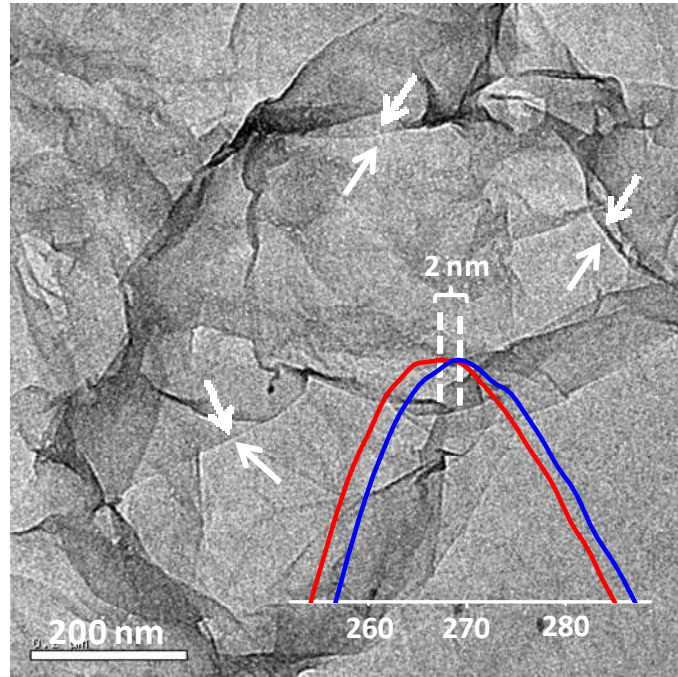


Figure S1: HRTEM image of RGO. Nanometer thick folding of the sheets can be seen. Scale bar is 200 nm. The inset shows an expanded view of the crest of the UV-Vis spectrum shown in Figure 1 (main text), indicating a shift in the graphene peak.

Supporting Information 2

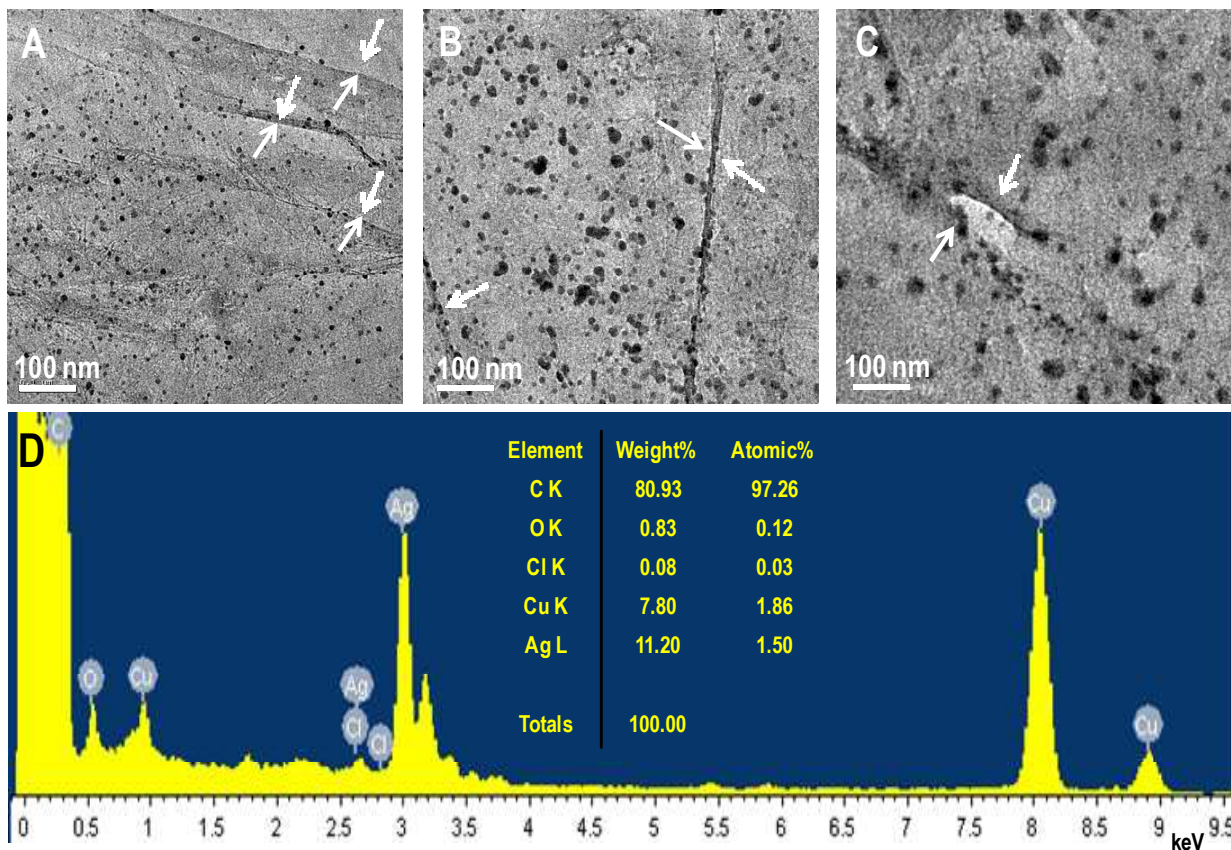


Figure S2: TEM image of RGO@Ag with varying silver ion concentration A) 0.01, B) 0.05 and C) 0.1 mM, respectively, yielding NPs of the size 5, 20 and 50 nm, respectively. D) HRTEM-EDAX spectrum of RGO@Ag.

Here, we have taken three different concentrations (0.01, 0.05 and 0.1 mM, respectively) of AgNO_3 and 25 mL of 0.01 % RGO was added to them separately. It is quite evident from the HRTEM images that with the increase of silver ion concentration (AgNO_3) during the preparation of the composite, the size of the silver nanoparticles formed on the graphene sheets increased. The sizes of silver nanoparticles formed over graphene sheet were 5, 10, and 50 nm for the concentration of 0.01, 0.05 and 0.1 mM, respectively.

Supporting Information 3

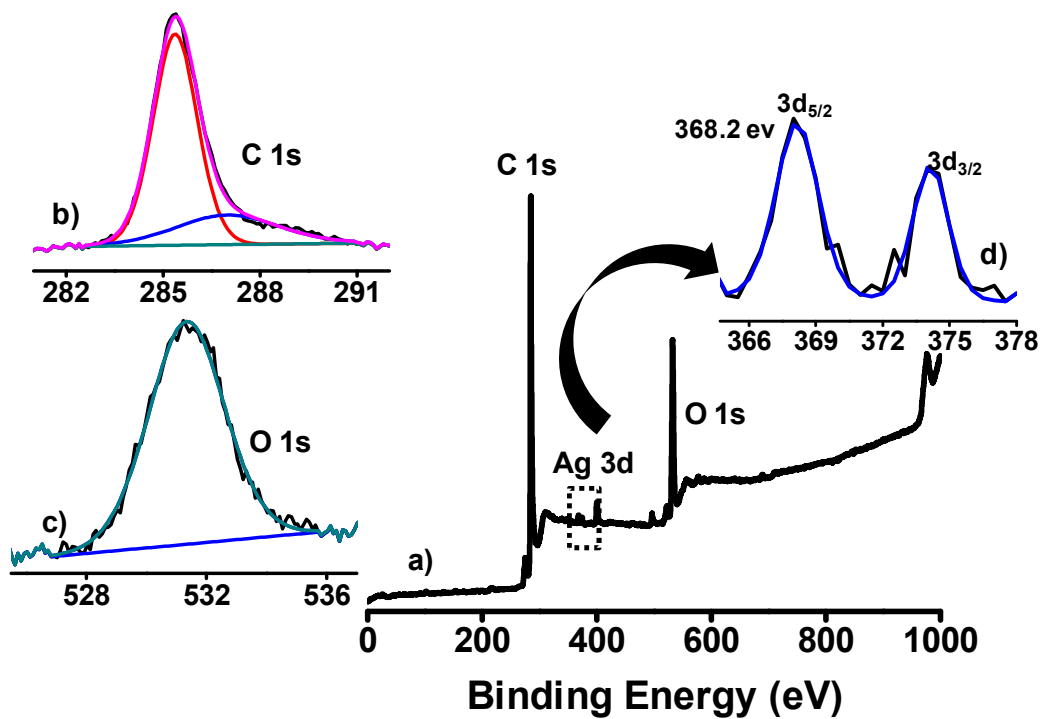


Figure S3: a) XPS survey spectrum of RGO@Ag composite showing the presence of silver, carbon and oxygen. Deconvoluted XPS spectrum of b) carbon, c) oxygen and d) silver.

Supporting Information 4

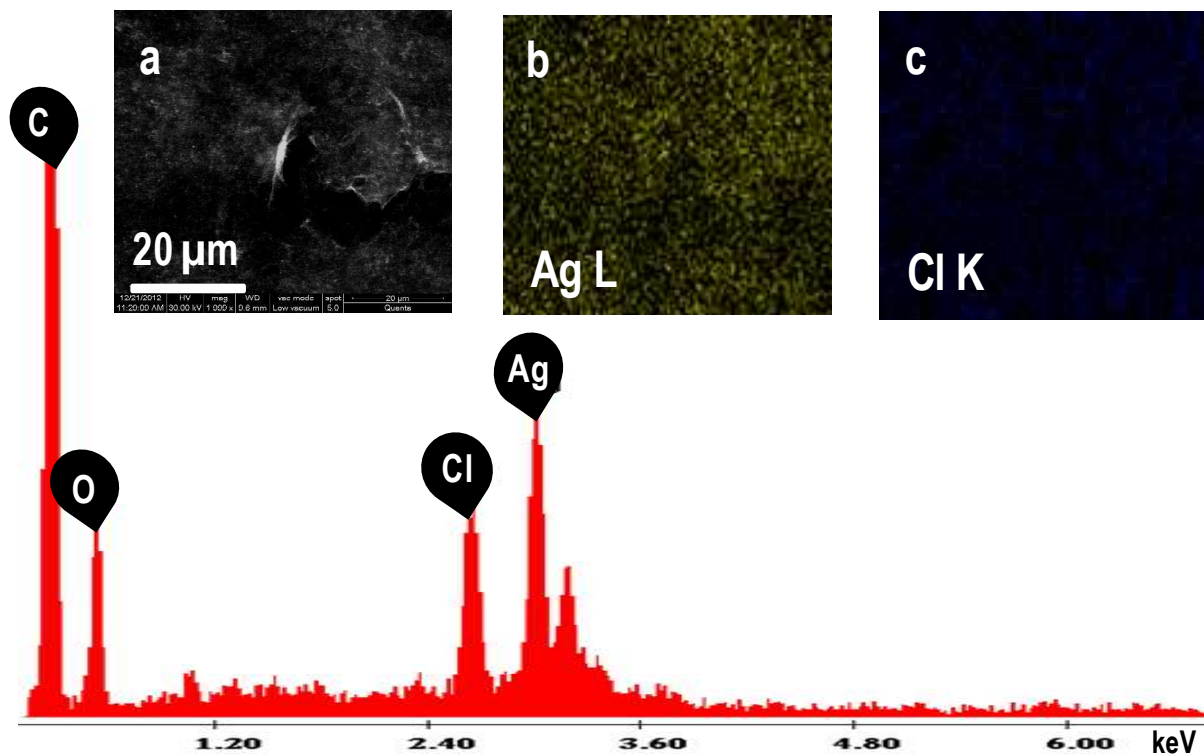


Figure S4: SEM-EDAX spectrum of the image *a* in the inset. *a*) SEM image of RGO@Ag after the reaction. *b* & *c*) Elemental mapping of the image 'a' showing the presence of silver and chlorine, respectively. The scale bar is the same in *a*, *b* and *c*.

Supporting Information 5

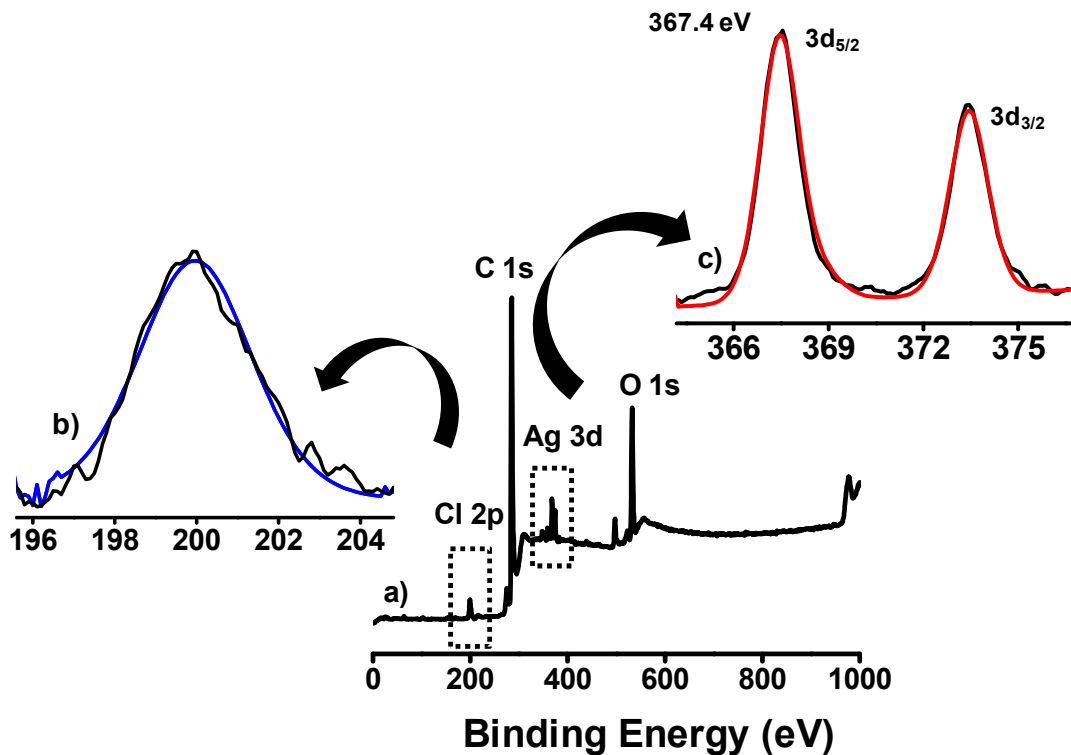


Figure S5: a) XPS survey spectrum of RGO@Ag composite after the reaction with lindane showing the presence of silver, chlorine carbon and oxygen. Deconvoluted XPS spectrum of b) chlorine and c) silver.

Supporting Information 6

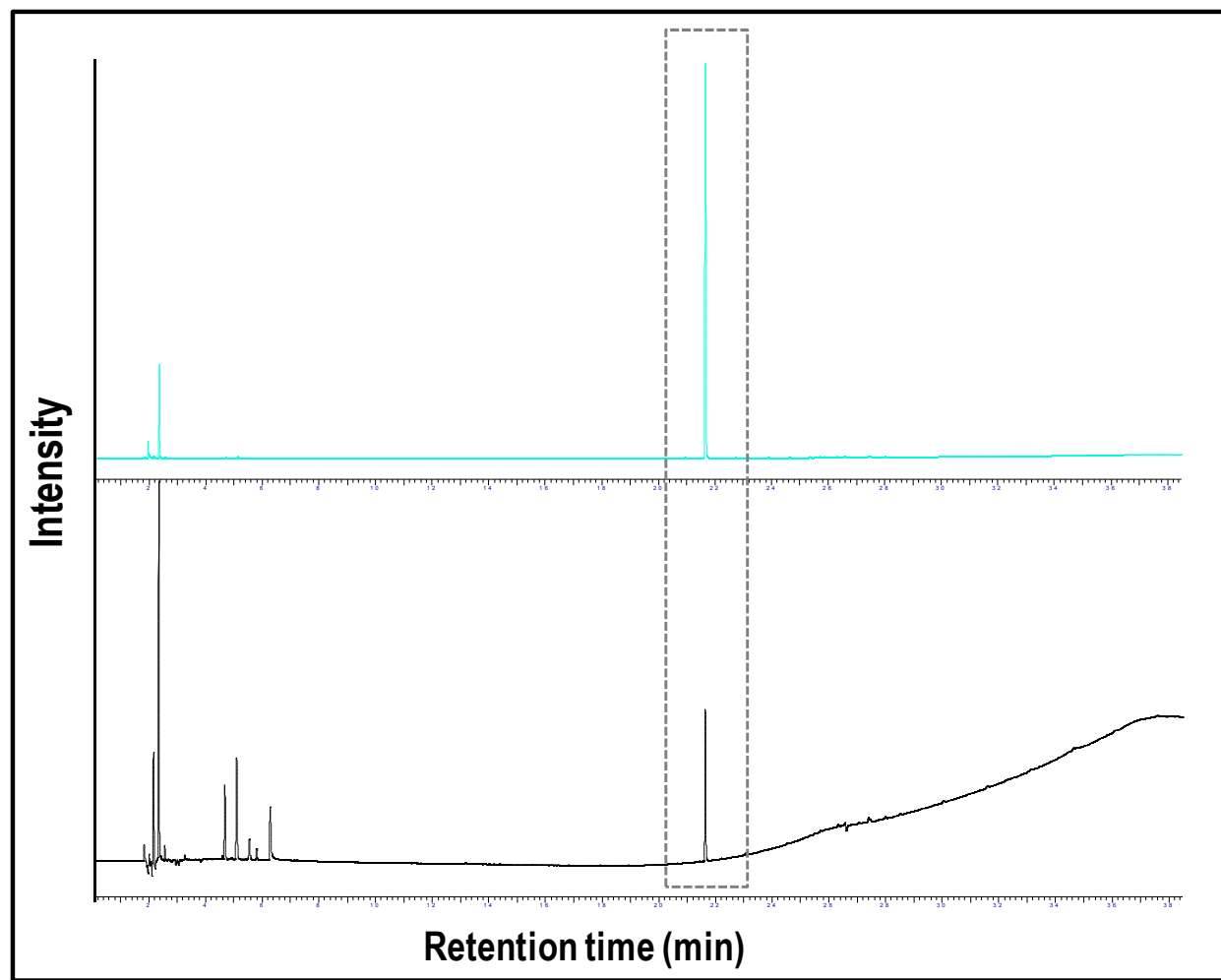


Figure S6: GC-ECD data of lindane (light blue trace) and the degraded product (black trace) after 5 min of reaction (note that in this case, lindane was initially dissolved in hexane and spiked). The dotted box corresponds to the peak of lindane.

Supporting Information 7

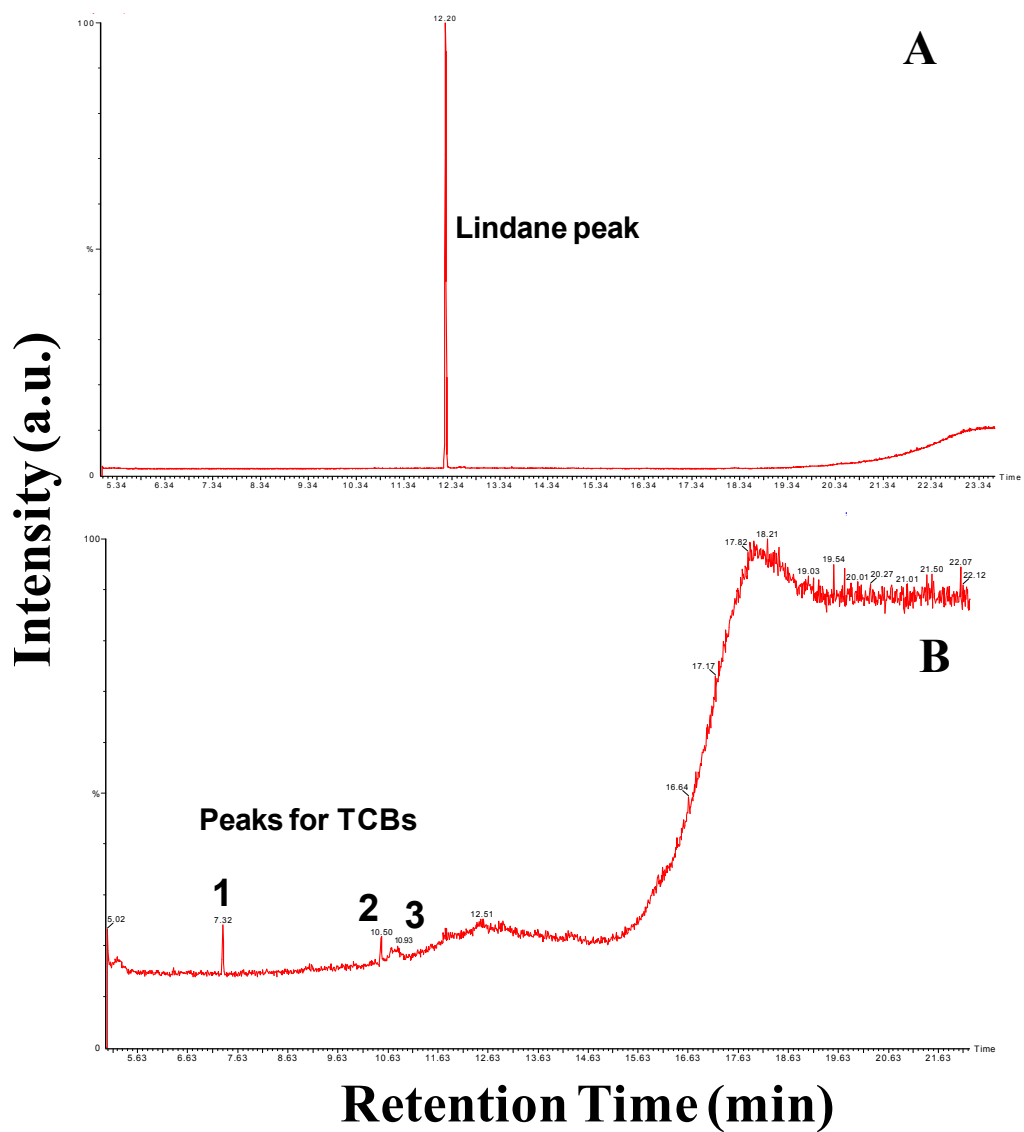


Figure S7: GC-MS trace of A) lindane and B) the isomers of TCB. (1, 2 and 3 are the peaks for TCB).

The GC traces of Figure 2 in the main text give different retention time for lindane and the products, as the parameters are different..

Supporting Information 8

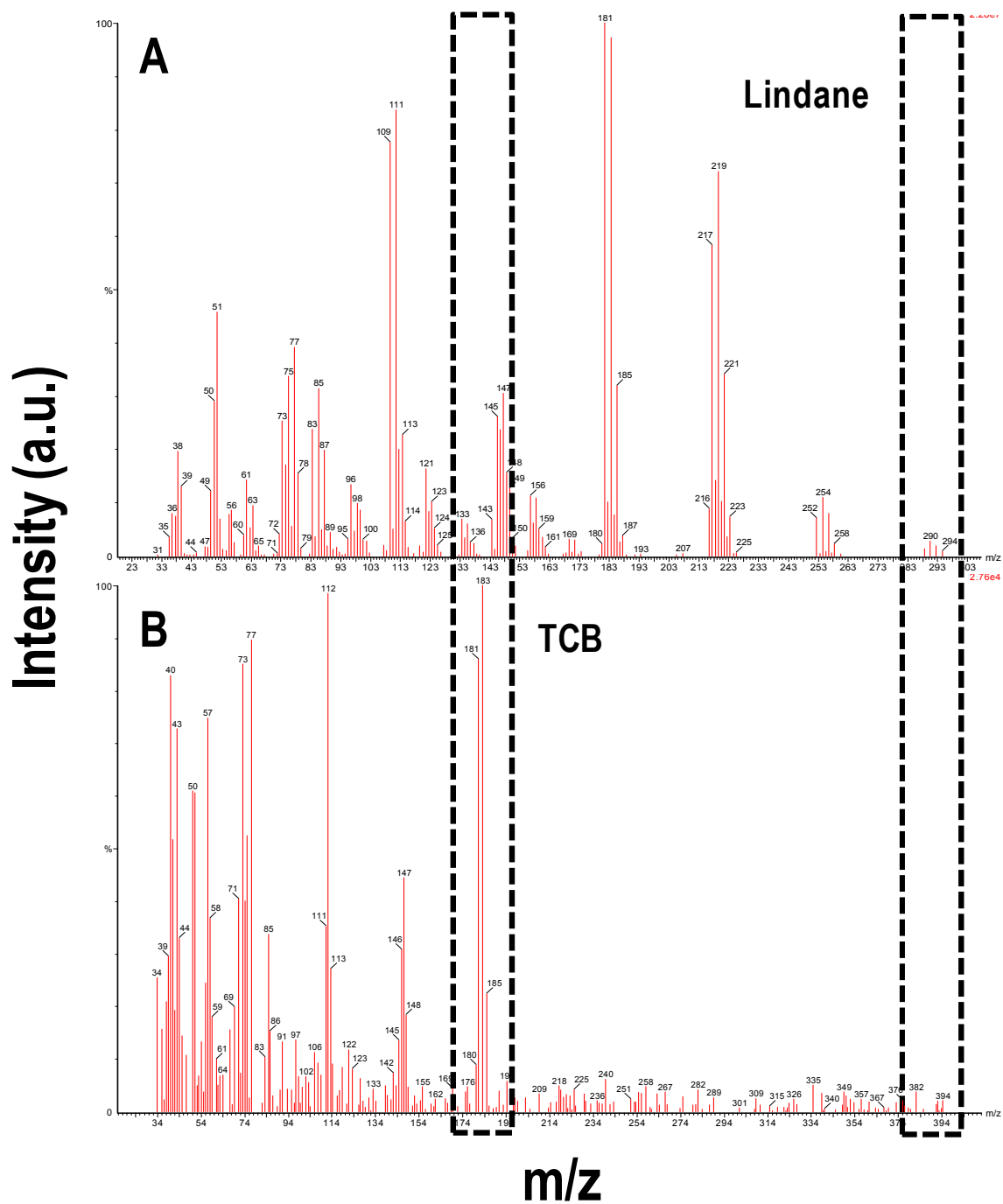


Figure S8: GC-MS spectrum of A) lindane and B) the degraded product appearing at a retention time of 7.32 min in Figure S5B.

Supporting Information 9

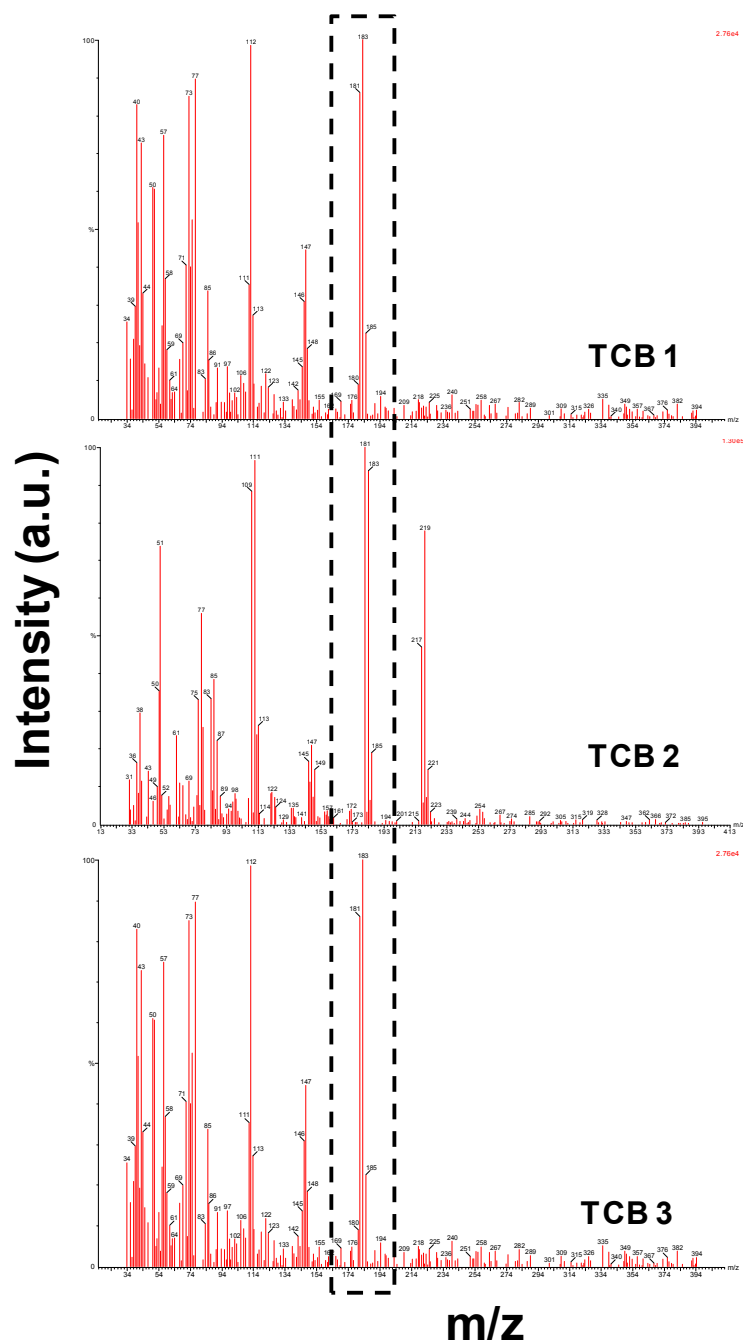


Figure S9: GC-MS of three different isomers of TCB marked as 1, 2, and 3 in Figure S5B.

Supporting Information 10

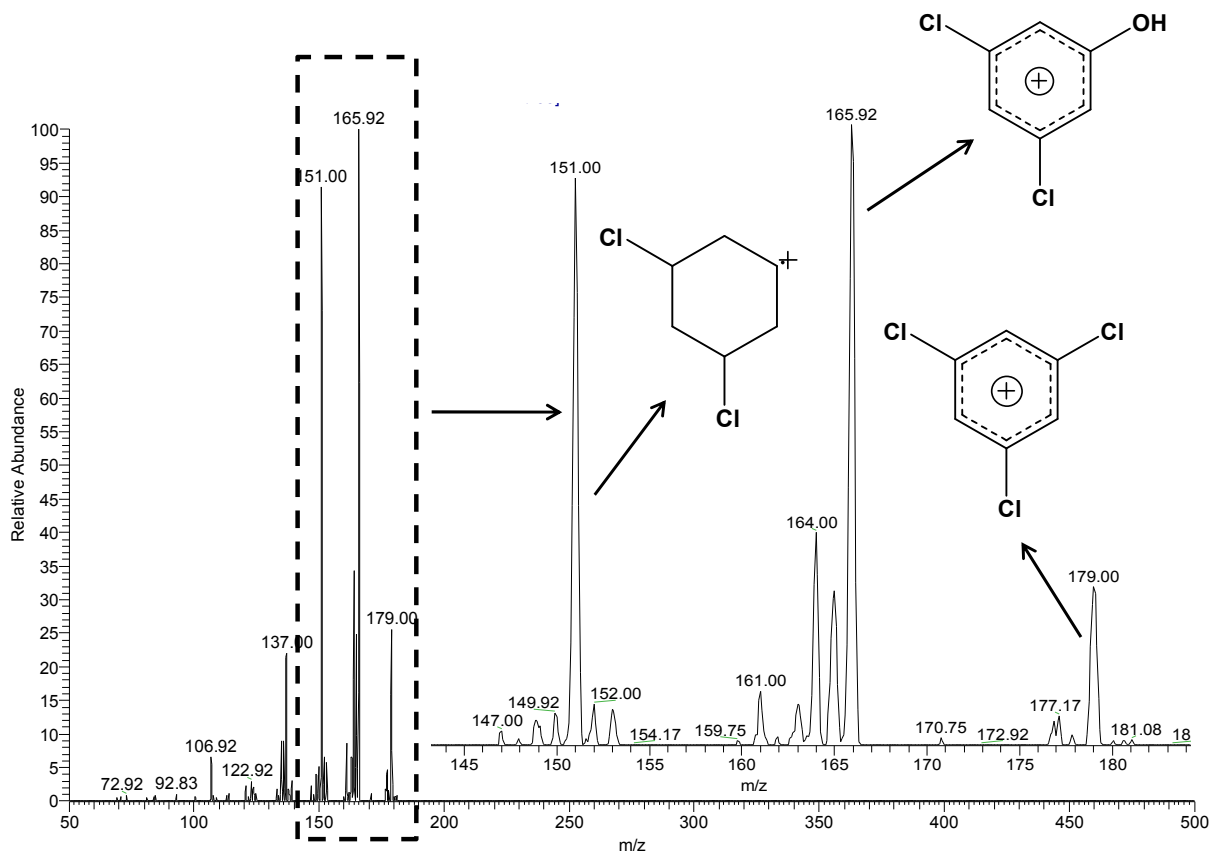


Figure S10: MS2 of the peak of the degraded product, trichlorobenzenes (m/z 180) at collision energy 60 (in instrument unit) measured using ESI MS. Please note that there are isomeric structures for TCBS, only one isomer is shown here.

Supporting Information 11

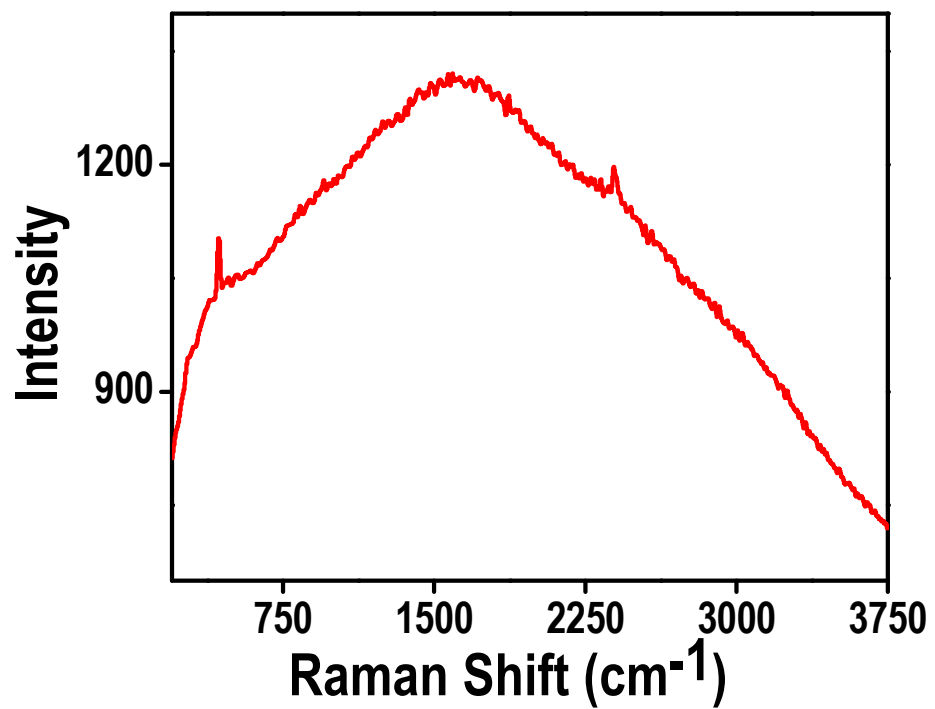


Figure S11: Raman spectrum of the product (trichlorobenzenes), showing the luminescence background.

Supporting Information 12

Preparation of citrate capped silver nanoparticles: Calculated amount of AgNO_3 was dissolved in 50 mL water such that the final concentration of silver in the solution was 5 mM. To the solution, sodium citrate was added and the mixture was heated for 30 min at 80 °C till the color of the solution changed to brown. This brown colored solution was kept for cooling at room temperature for an hour. This was the stock solution for silver nanoparticles (5 mM), which was characterized using UV/Vis spectroscopy and HRTEM. UV/Vis spectrum gives characteristic peaks corresponding to Ag NPs (peak maximum around 420 nm) and TEM image shows that the particle size is around 50 nm. Silver nanoparticles formed by this method are polydisperse.

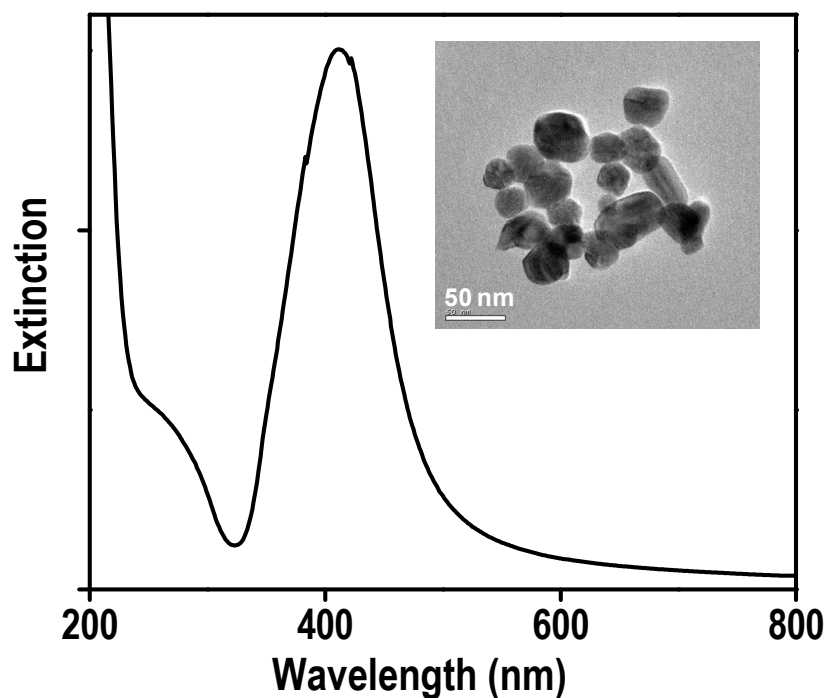


Figure S12: UV/Vis spectrum of silver nanoparticles and the inset shows a typical TEM image of the particles.

Supporting Information 13

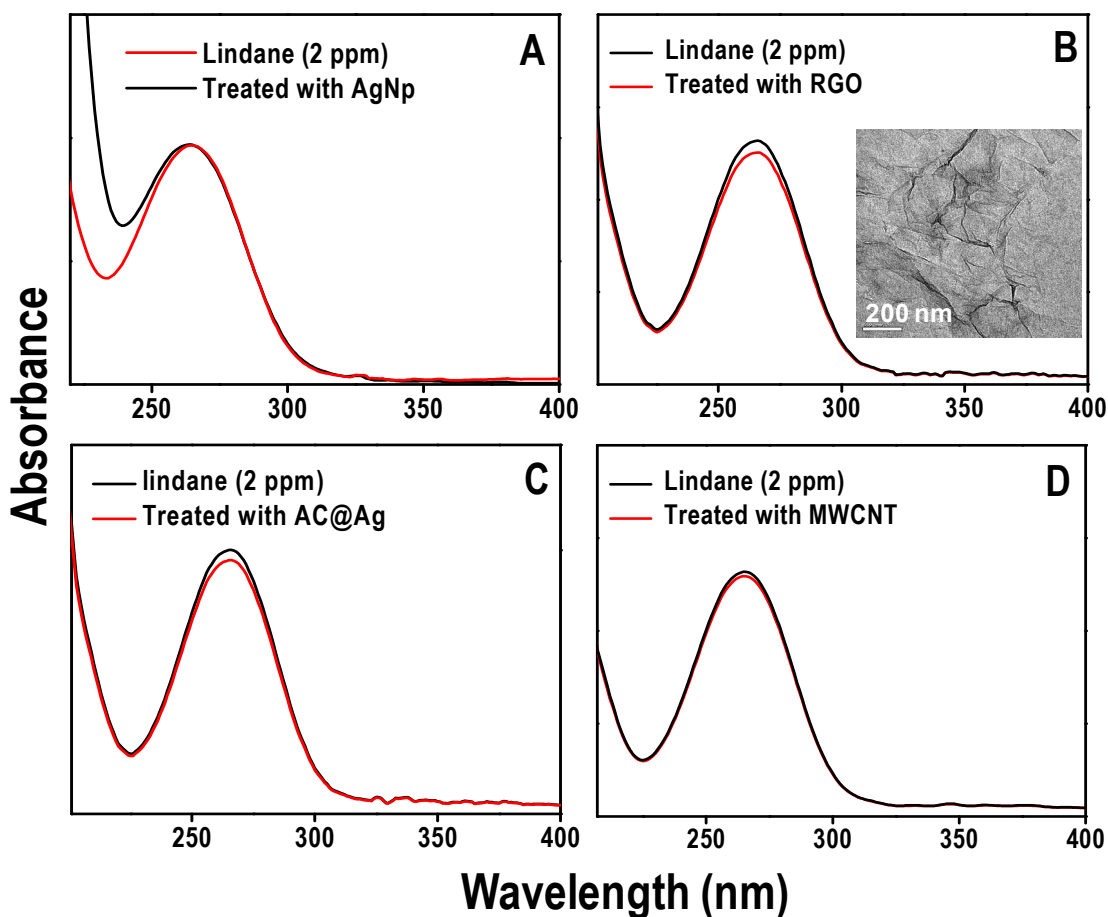


Figure S13: UV/Vis spectrum showing negligible removal/degradation capacity of lindane when treated with A) silver nanoparticles, B) graphene, C) AC@Ag and D) MWCNTs. The inset in Figure B shows the TEM image of graphene.

To test the degradation capacity of lindane with various adsorbents, equal weight of adsorbents were taken (1 mg in 5 mL of water). To each sample, lindane (dissolved in ethanol from stock solution) was spiked, such that final concentration of lindane in the solution was 2 mg/L (ratio of water:ethanol was 500:1 (v/v)). Characterization was done using UV/Vis and the removal percentage was plotted against

adsorbents. The result showed that the composite RGO@Ag was superior than any other adsorbents reported recently.

Preparation of AC@Ag

About 1 mg of AC was taken in 5 mL of DI water and sonicated for 5 min. To it AgNO₃ solution was added such that the final concentration of Ag in the solution was 0.01 wt%. The composite was kept for 24 h, undisturbed. This is referred to as AC@Ag. It was seen that AC does not have the reducing capacity for Ag ions. This was confirmed by ICPMS, the initial and final concentration of Ag was 1.1 ppm and 1.08 ppm, respectively in the solution, which suggest that Ag was not reduced to Ag NP and hence a composite was not formed.

Supporting Information 14

Preparation of elemental silver particles: Calculated amount of AgNO_3 was dissolved in water such that the final silver concentration was 5 mM. To the solution, NaBH_4 was added and heated to 90 °C for an hour, so that reduction of silver takes place. A shiny precipitate was formed on the glass vessel. The precipitate was isolated and dried overnight in vacuum at 50 °C. This precipitate was used as elemental silver with varying concentrations in water. TEM image of this elemental silver was performed but the data were not good as expected due to poor electron beam transmission.

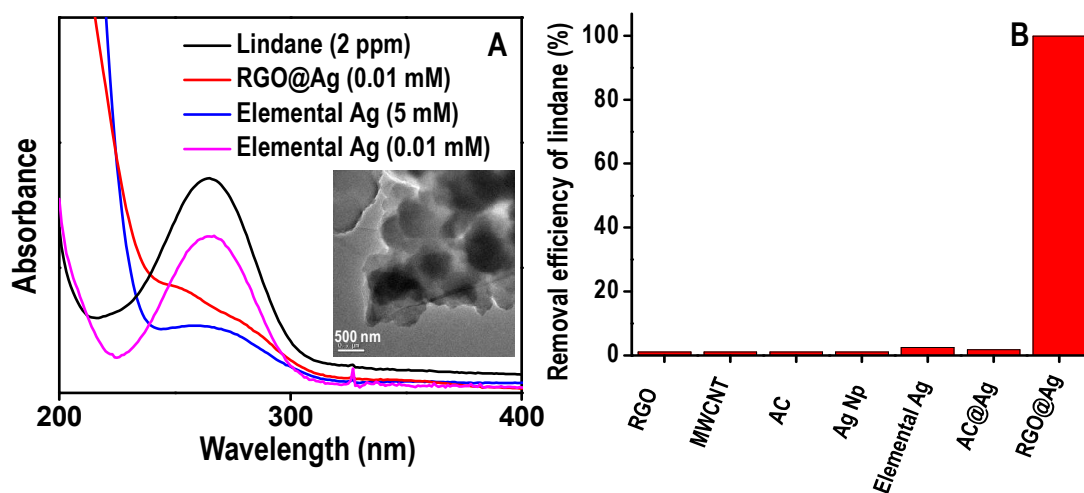


Figure S14: UV/Vis spectrum showing the comparison of the removal capacity of lindane (2 ppm) using the composite and elemental silver (Ag), the values represents the amount of silver used for the degradation reaction. The inset shows a TEM image of the prepared elemental silver. B) Comparison for the removal efficiency of lindane with different adsorbents.

Supporting Information 15

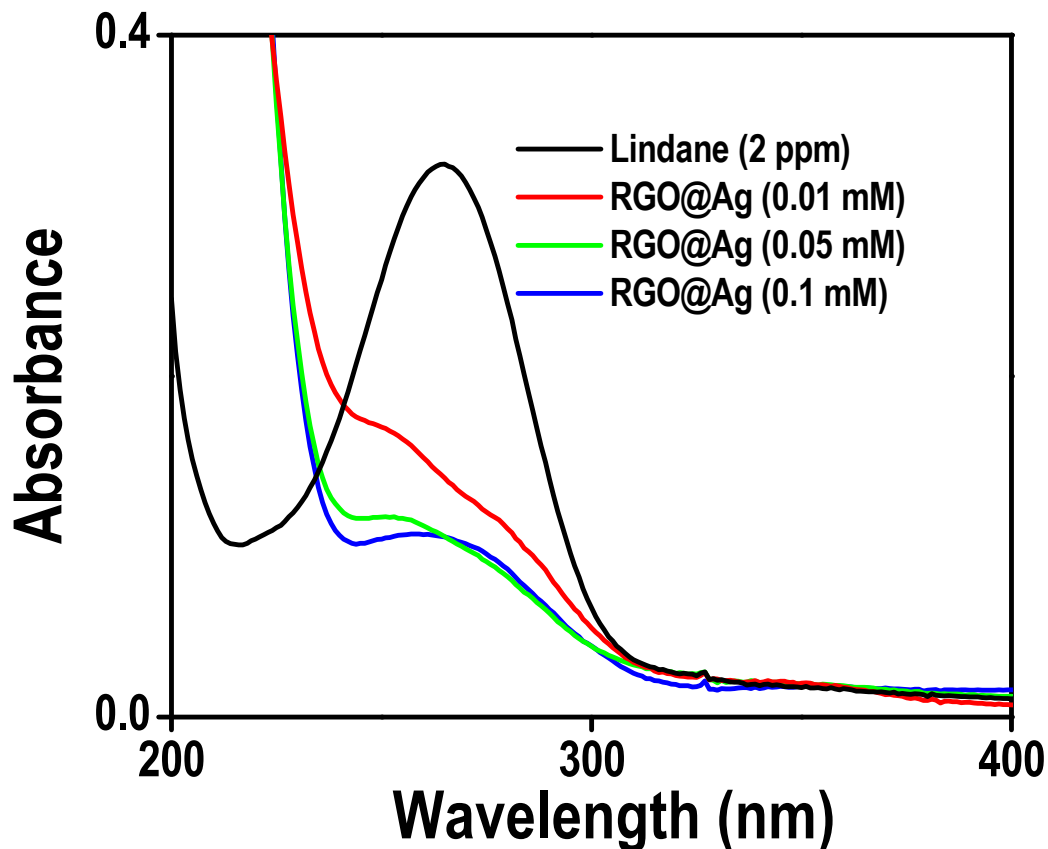


Figure S15: UV/Vis spectrum showing the size dependence of silver nanoparticle on RGO for the degradation of lindane.

Here three different composites, namely, RGO@Ag^I, RGO@Ag^{II}, RGO@Ag^{III} were used to check the efficiency of the composite towards the degradation of lindane which yielded size of 5, 20 and 50 nm of Ag Np on RGO sheet. For this experiment, lindane stock solution (dissolved in hexane) was used such that final concentration of the solution was 5 ppm. It was seen that more the concentration of Ag precursors on RGO, more is the degradation efficiency but the efficiency with respect to mg/g of silver

shows that RGO@Ag^I is much superior to the others. Thus it is concluded that smaller is the size of Np higher is the surface area and hence, higher is the degradation capacity. The data were taken after 15 min.

Supporting Information 16

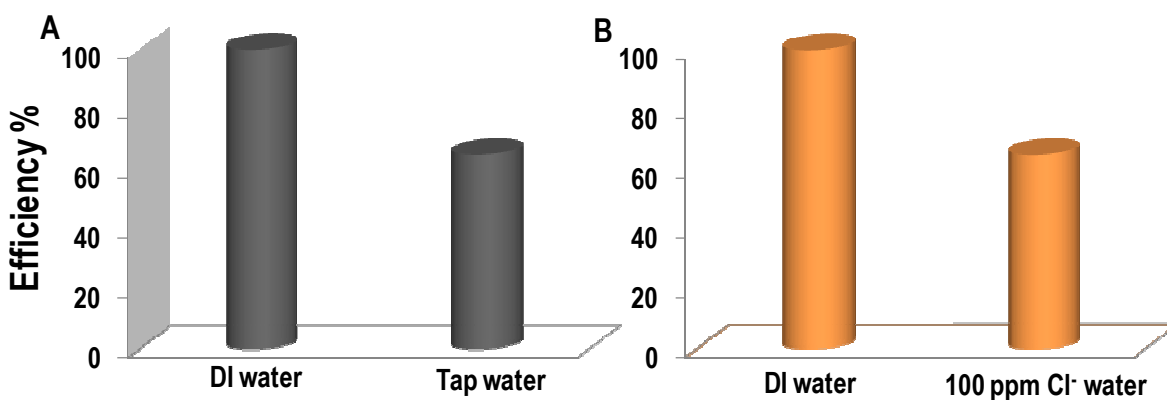


Figure S16: Effect of A) tap water/ground water and B) 100 ppm of NaCl solution (in DI water)_ on the removal efficiency of lindane using RGO@Ag.

Supporting Information 17

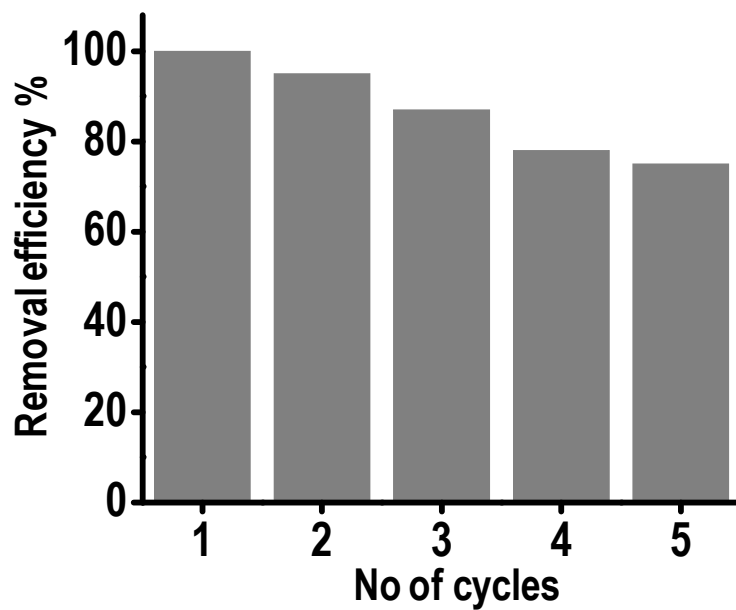


Figure S17: Removal efficiency of lindane by the RGO@Ag composite for multiple cycles, after regeneration.

Interaction of Acetonitrile with Water-Ice: An Infrared Spectroscopic Study

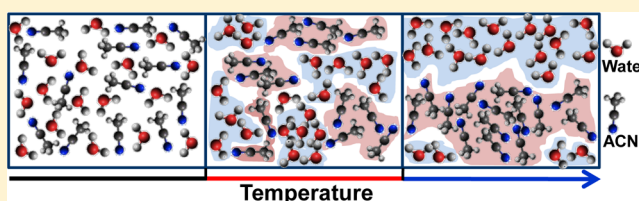
Radha Gobinda Bhuin,^{†,§} Rabin Rajan J. Methikkalam,^{†,§} Bhalamurugan Sivaraman,[‡] and Thalappil Pradeep^{*,†}

[†]DST Unit of Nanoscience (DST UNS) and Thematic Unit of Excellence (TUE), Department of Chemistry, Indian Institute of Technology Madras, Chennai 600 036, India

[‡]Space and Atmospheric Sciences Division, Physical Research Laboratory, Ahmedabad, India

S Supporting Information

ABSTRACT: Interaction of water-ice and acetonitrile has been studied at low temperatures in their codeposited mixtures, in ultrahigh vacuum conditions. They interact strongly at low temperatures (in the temperature range of 40–110 K), which was confirmed from the new features manifested in the reflection absorption infrared spectra of the mixtures. This interaction was attributed to strong hydrogen bonding which weakens upon warming as the acetonitrile molecules phase segregate from water-ice. Complete phase separation was observed at 130 K prior to desorption of acetonitrile from the water-ice matrix. Such a hydrogen-bonded structure is not observed when both the molecular solids are deposited as water on acetonitrile or acetonitrile on water overlayers. A quantitative analysis shows that in a 1:1 codeposited mixture, more than 50% acetonitrile molecules are hydrogen bonded with water-ice at low temperatures (40–110 K).



1. INTRODUCTION

Water-ice is omnipresent in its amorphous form. Studying interactions of different molecules with water-ice is of tremendous interest as it would lead to an understanding of amorphous ice and of various phenomena of environmental and biological importance.¹ These interactions may be physical (as in absorption/adsorption² and trapping³) or chemical⁴ in nature. The latter is the case when water-ice acts as a catalyst to accelerate chemical reactions on its surface or when it participates in a reaction leading to the formation of new chemical species. Such interactions are influenced by the morphology and structure of water-ice.^{5–7} A representative example is the production of dihydrogen via the surface recombination of hydrogen atoms adsorbed on amorphous ice.⁸ Several physical phenomena like adsorption/desorption kinetics,^{2,6} diffusion,^{2,9} and trapping³ are also highly dependent on the morphology of water-ice. Porous amorphous ice can trap several small molecules inside its pores, which can only be released when it undergoes a structural change.

Various factors including local temperature,¹⁰ incident flux,¹¹ incident angle,¹² and kinetic energy¹³ affect the morphology of water-ice. Morphology of water-ice generated by vapor deposition on a cold surface is substantially dependent on temperature. Crystallization and morphological change of amorphous ice has been studied extensively.^{14–16} At temperatures below 120 K vapor deposition, it is known to form amorphous ice.¹⁷ Several studies have revealed that amorphous ice so formed upon heating undergoes a structural change at ~120 K, before crystallizing at ~140 K.^{18,19} Thus, interactions of molecules with water-ice are expected to be temperature-

dependent and are likely to change as it goes through different structural modifications.

A number of factors make acetonitrile (ACN), a very important molecule. The vibrational spectrum of ACN is well-understood in the gas, liquid, and solid phases, and its interaction with a variety of molecules is also well-characterized.^{20–23} ACN is the simplest nitrile and is extensively used in organic syntheses because of its ability to dissolve a wide range of ionic and nonpolar molecules. This makes it a model organic system. The study of interactions of ACN with water-ice is important and is relevant to the Interstellar medium (ISM). Literature is therefore rich in studies of ACN–water systems, examining their gas, liquid, and solid phase interactions.^{20,24–34} It is now known that interaction of ACN with water is mainly due to hydrogen bond formation. In the following section, we present the current understanding of the water–ACN system.

ACN and water systems have been studied extensively.^{25,26,31–34} However, most of the studies were performed on solutions,^{27,31,32,34} a few exist on solid films as well.^{1,24,35} Various studies have been carried out with water and acetonitrile mixtures in the liquid phase.^{31,32,36} Experiments were performed by varying the mole fraction of the components in the mixtures, and studies suggest the formation of different microstructures of the mixtures. A molecular dynamics study proposed a microheterogeneous structure at

Received: December 18, 2014

Revised: May 4, 2015

Published: May 4, 2015

sufficiently high acetonitrile content.³⁷ In such a structure, clusters of one type of molecules are formed (i.e., either of ACN or H₂O and at low ACN content water structure become more ordered). Radial distribution functions of $g_{O-O}(r)$ (O denotes the oxygen of water) significantly increases for 88% ACN solution compared to pure water, which suggests the formation of water clusters. Comparison of $g_{O-O}(r)$ of 12% ACN solution and pure water shows an enhancement of the water structure in the former. On the contrary, Raman spectroscopic study of the CD₃CN–H₂O–HDO system did not support enhancement of the water structure, whereas at intermediate compositions formation of clusters was evident.³⁴ The OH and CN stretching bands in the spectra were monitored for this investigation. However, IR investigation by Gorbunov and Naberukhin was unable to suggest the existence of clusters at any concentration.³⁸ A detailed experimental and theoretical study revealed that microheterogeneity begins above $x_{ACN} = 0.22 \pm 0.11$, and at low concentration, ACN is solvated by H₂O.³⁹ A transmission IR study of ACN–H₂O showed the interaction of ACN with H₂O at different mole fractions. In this, C≡N stretching mode of the CD₃CN–H₂O mixture and OD stretching mode of dilute HDO in the CH₃CN–H₂O mixture were monitored at 20 °C. From a Lorentzian fit of the C≡N band for different mixtures, the percentage of H-bonded ACN has been predicted.³¹ Attenuated total reflection (ATR) spectroscopy was also used to calculate the fraction of H-bonded ACN in the ACN–H₂O mixtures.³² Different compositional mixtures were studied, and the integrated intensity of C≡N stretching band were used to analyze the results. From these studies, it has been revealed that both free and H-bonded ACN molecules coexist in the mixture. Number of H-bonded ACN molecules in the mixture depends on their composition of mixing. Amount of free acetonitrile molecules is constant over a range of acetonitrile concentrations in the acetonitrile–water mixture ($0.7 \leq x_{ACN} \leq 1.0$).³⁶ Another study shows that free acetonitrile molecules present in the acetonitrile–water mixture are not affected by other water molecules, and they survive in the same environment as in pure ACN.³² ACN molecules in the ACN–H₂O mixture formed three-dimensional clusters, and the clusters are surrounded by the water molecules through H-bonding and dipole–dipole interactions.³⁶ Several different models are used to analyze the type and extent of interactions.^{31,32} Ab initio calculations of the ACN–H₂O system has also been performed.³³ In this study, the interaction of water monomer and clusters with the nitrile group has been discussed well. C≡N stretching frequencies for isolated ACN and ACN–water cluster have been calculated. In an ACN–water cluster, isolated ACN molecules were used to form the cluster with one or more water molecules. It was shown that ACN forms σ - and π -type H-bonds with water molecules. σ -Type H-bonded ACN shows a blue shift, whereas the π -type H-bonded ACN shows a red shift in C≡N frequencies. Interaction of ACN with a thin film of water has also been studied.^{20,24} As mentioned earlier, ACN can bind to the free OH/OD groups on the surface through hydrogen bonding or it can purely physisorb on the water-ice surface.^{20,24} Such an H-bonded ACN shows a blue shift in the C≡N stretching frequency.²⁴ Studies show that from the exposures of acetonitrile, presence of free OH group on the surface has been measured quantitatively. The peak appearing at 2264 cm⁻¹ for ACN-*h*₃:H₂O has been attributed to hydrogen-bonded ACN-*h*₃.²⁰ There is no evidence of formation of the hydrogen bond with crystalline ice.²⁰

Although there has been many reports on water–ACN interaction in solution and solid phases, until today there is no such report where interaction of both the molecules is studied in their codeposited mixture. In this paper, we have studied the interaction of ACN molecules with water-ice in their codeposited mixture. Acetonitrile and water were codeposited on a cold surface in order to mimic the ISM conditions. For comparison, layer-on-layer deposited ACN and water-ice systems were also examined. The interaction of the two species was analyzed through reflection absorption infrared spectroscopy, and the effect of temperature was investigated. The distinct difference between codeposited mixtures and overlayer deposition is brought out in these studies.

2. EXPERIMENTAL SECTION

The experimental setup used for this study is given in more detail elsewhere.⁴⁰ The instrument consists of three chambers; namely, the ionization chamber, the octupole chamber, and the scattering chamber. Each chamber was differentially pumped by turbomolecular pumps backed by diaphragm pumps. Base pressure of the instrument was 5.0×10^{-10} mbar, and the pressure was $\sim 2.0 \times 10^{-9}$ mbar during the experiment. Though the chamber has several facilities for probing molecular solids, we have used only a reflection absorption infrared spectrometer (RAIRS), a quadrupole mass spectrometer, and a low-energy alkali ion gun in the study presented here. A Bruker VERTEX 70 FT-IR spectrometer was used to measure the spectra, with external optics, which has been fully described elsewhere.⁴⁰ The spectrometer resolution for the studies reported has been set at 2 cm⁻¹. To describe the experiment, briefly, the substrate is a Ru(0001) single crystal attached at the tip of a closed cycle helium cryostat on a copper holder, fitted with a resistive heater. The substrate can be maintained at any temperature between 8 and 1000 K. The temperature is measured by employing a thermocouple sensor with an accuracy of 0.001 K. Repeated heating at 1000 K ensures surface cleanliness. The temperature ramping is controlled and monitored by a temperature controller (Lakeshore 336). In this work, we have used a temperature window of 40–200 K to investigate the interaction of our ACN–water-ice systems. Temperatures in the range of 40–80 K were tested initially, but significant differences in the IR spectra were not observed. Therefore, in the proceeding experiments, only the temperature range of 80–160 K was examined, in which the IR peaks of the ACN–water-ice system showed a large change.

As received, 99.95% pure acetonitrile (named as ACN-*h*₃) and its deuterated form (named as ACN-*d*₃), both from Sigma-Aldrich, H₂O (Millipore; 99.996%) and D₂O (99.995% purity, Sigma-Aldrich) were further purified by several freeze pump thaw cycles. The above liquids were filled in a glass-to-metal seal adapter tubes fitted in two different sample lines and were connected to a rotary pump. The sample lines were evacuated, the liquid was evaporated, and the vapors were deposited onto the precooled Ru(0001) substrate using all-metal leak valves. The various samples, namely, ACN layer over H₂O layer, H₂O layer over ACN layer, and codeposited ACN and H₂O are referred to as H₂O@ACN, ACN@H₂O, and ACN:H₂O, respectively. For both the deposition techniques, two separate sample gas lines connected with two separate leak valves were used to avoid mixing of vapors in the sample line itself. During deposition, the mass spectral intensity from the quadrupole mass spectrometer was used to calculate the ratio of ACN to water in the mixture. We have consistently kept a 1:1 ratio of

the two in each system. All the samples were deposited on the precooled ruthenium single crystal substrate at 40 K and gradually heated (at a ramping rate of 1 K min⁻¹) to a series of temperatures to collect the temperature-dependent IR spectra. On reaching a particular temperature, the spectrum was collected after a short gap of 3 min to equilibrate the temperature. The 1 K min⁻¹ slow ramping rate helped us to ensure that the temperature change before and during the spectral collection was not significant and was within ± 0.02 K. Each spectrum was obtained by averaging 512 scans, with a resolution of 2 cm⁻¹. The large number of scans ensured that the signal-to-noise ratio was high.

Cs⁺ ion (m/z 133) is a well-known projectile for secondary ion mass spectrometry.⁴¹ Cs⁺ ion scattering is a good technique to characterize solid samples deposited on a substrate at low temperatures. We have performed ion collision experiments using Cs⁺ ions of 1 keV energy generated from a low-energy alkali ion gun (Kimball Physics Inc., IGPS-1016B). These ions were focused to collide at a specific energy on the codeposited acetonitrile water-ice system. The resulting scattered ions were analyzed using a quadrupole mass analyzer fitted on the ion-scattering chamber.

3. RESULTS

We began our investigation by first measuring the temperature-dependent RAIR spectra of ACN-*h*₃. For this, approximately 500 monolayers (ML) (assuming 1 ML = 1×10^{15} number of molecules/cm²) of ACN-*h*₃ were deposited on Ru(0001) at 40 K, and its IR spectrum was measured at different temperatures. The RAIR spectra in the 80 to 135 K range are shown in Figure 1. The spectrum at 80 K shows the presence of almost all the

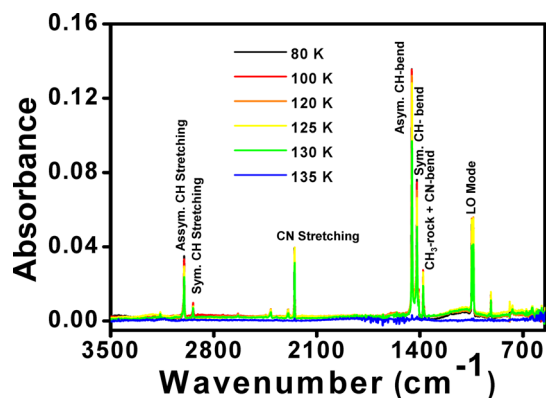


Figure 1. Temperature-dependent RAIRS spectra of pure ACN. 500 ML of ACN was deposited on a cold Ru(0001) surface at 40 K and heated to 135 K, and IR spectra were collected at different temperatures.

vibrational modes and is in good agreement with the reported RAIRS spectrum of pure ACN-*h*₃ at 110 K.⁴² It is also noticeable from the figure that (a) there is no spectral change until 130 K, (b) an intensity loss occurs at 130 K as the ACN-*h*₃ molecules start desorbing from the surface, and (c) the desorption is complete at 135 K.

For studying the interaction of water and acetonitrile molecules, they were codeposited in a 1:1 ratio on a ruthenium substrate at 40 K to form different ice samples. These were subsequently heated up to 160 K, which is the desorption point of water, and the IR spectrum was collected at various temperatures. The spectra at temperatures between 40 and 80

K were similar in appearance, and therefore, in the figures we show only those at 80 K for clarity. In order to understand the changes in the IR peaks at different temperatures more clearly, we used combinations of ACN-*h*₃ and ACN-*d*₃ with H₂O and D₂O.

The full RAIRS spectra for ACN-*h*₃:H₂O at different temperatures are provided in Figure S1 of the Supporting Information. Figure 2a shows the O–H stretching region for

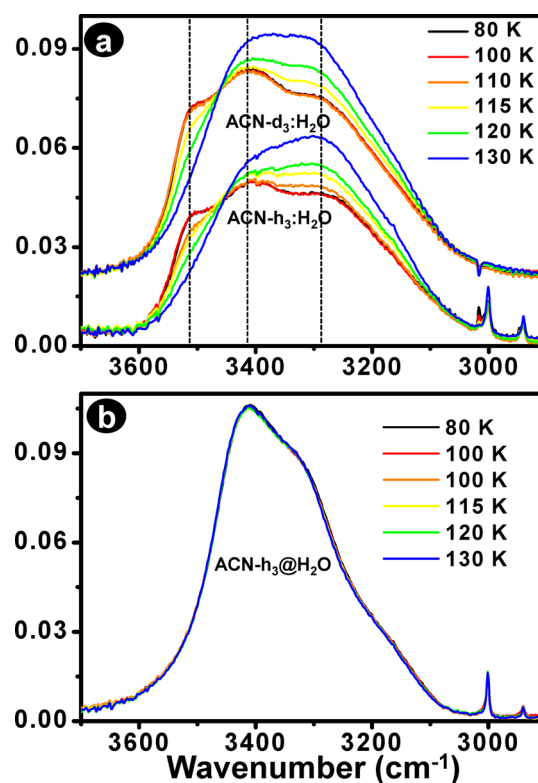


Figure 2. Temperature-dependent RAIRS spectra in the OH stretching region of (a) 1:1 codeposited ACN-*h*₃:H₂O and ACN-*d*₃:H₂O and (b) layer-on-layer ACN-*h*₃@H₂O on cold Ru(0001) surface at 40 K.

ACN-*h*₃:H₂O and ACN-*d*₃:H₂O. Three bands centered at 3510, 3415, and 3290 cm⁻¹ are clearly noticeable at 80 K, and their peak positions are highlighted in the figure by dashed lines. The bands arise due to the interaction of acetonitrile and water and steadily disappear as the temperature increases beyond 115 K, eventually becoming a broad peak centered at ~ 3350 cm⁻¹ that is characteristic of pure water-ice at 130 K. These observations can be understood as follows. In our ACN:H₂O mixture, water can participate in H-bonding with acetonitrile when the free O–H group of water and the C \equiv N group of ACN are in close proximity. The bonding is strong at low temperatures but gets weakened with an increase in temperature. At this stage, ACN molecules probably phase segregate from the water molecules while staying within the water matrix. Complete phase segregation takes place above 130 K where molecular motion of ACN is sufficiently high. Compared to pure ACN on Ru(0001), a relatively higher temperature is needed for ACN to desorb from the water matrix, and complete desorption occurs only during crystallization of water above 140 K.

The next set of experiments was performed for ACN-*h*₃@H₂O, and an enlarged view of the O–H stretching region of the RAIRS spectra is presented in Figure 2b (for complete spectra

see Figure S2 of the Supporting Information). Only a broad absorption feature of O–H stretching centered at $\sim 3400\text{ cm}^{-1}$ is observed at all the temperatures. It is clearly visible that the spectra from 80 to 130 K overlap with each other. The three bands seen in the case of $\text{ACN-}h_3\text{:H}_2\text{O}$ are absent here. Thus, we expect little-to-no interaction between ACN and water molecules in this case compared to the previous experiment. Similar to the codeposited system, $\text{ACN-}h_3$ starts desorbing from the surface at 140 K when water undergoes crystallization and leaves it completely at 145 K. Crystallization of water was clearly seen in the spectra (see Figure S2 of the Supporting Information).

As a next set of experiments, $\text{ACN-}h_3\text{:H}_2\text{O}$ was collided with 1 keV Cs^+ ions at 40 K and a typical mass spectrum (MS) is plotted in Figure 3. Species which are present on the surface

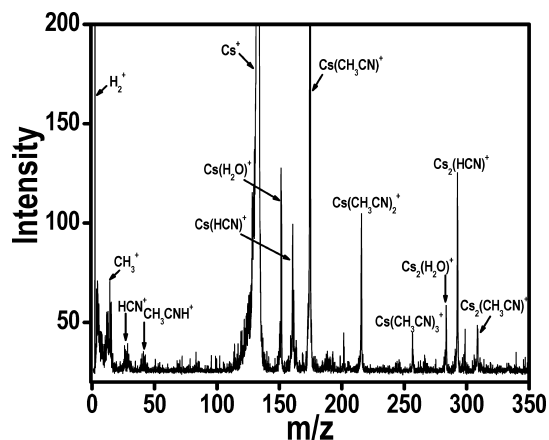


Figure 3. Mass spectrum of $\text{ACN-}h_3\text{:H}_2\text{O}$ mixture obtained on 1 keV Cs^+ ion collision.

can be picked up by Cs^+ ions.⁴¹ The MS for $\text{ACN-}h_3\text{:H}_2\text{O}$ contains peaks corresponding to adducts of Cs^+ ions with both H_2O and $\text{ACN-}h_3$, which indicates the coexistence of these two molecules on the $\text{Ru}(0001)$ surface. The spectrum also shows the formation of the ACN dimer and trimer adducts with Cs^+ ions due to the high-energy impact of Cs^+ ions on the surface. It is possible that when $\text{ACN-}h_3$ and water were deposited together, both got uniformly mixed in the bulk and on the surface, and thus, the mass spectrum obtained shows the presence of both the species. But in mixtures where ACN is covered by water or water is covered by ACN, only one type of molecular species will be accessible to Cs^+ ions, which will therefore form adduct products only with the species that is present on the surface. Indeed when similar studies were performed for $\text{ACN-}h_3\text{@H}_2\text{O}$ and $\text{H}_2\text{O@ACN-}h_3$ systems (with thickness of each layer $\sim 250\text{ ML}$), Cs^+ ions formed adducts only with H_2O and $\text{ACN-}h_3$, respectively.

Figure 4a compares the C–H asymmetric (3000 cm^{-1}) and symmetric (2940 cm^{-1}) stretching regions of the RAIRS spectra of pure $\text{ACN-}h_3$, $\text{ACN-}h_3\text{:H}_2\text{O}$, and $\text{ACN-}h_3\text{@H}_2\text{O}$. The spectral features of pure $\text{ACN-}h_3$ and $\text{ACN-}h_3\text{@H}_2\text{O}$ were found to be quite similar, with two major peaks at 3000 and 2940 cm^{-1} . In the case of the $\text{ACN-}h_3\text{:H}_2\text{O}$ system, an additional peak can be seen in both the C–H asymmetric and symmetric stretching regions (Figure 4a), though the former one is far more prominent. The new peak at $\sim 3017\text{ cm}^{-1}$ visible at 80 K gradually disappeared upon heating. This peak may have arisen due to the interaction of the C–H bond of

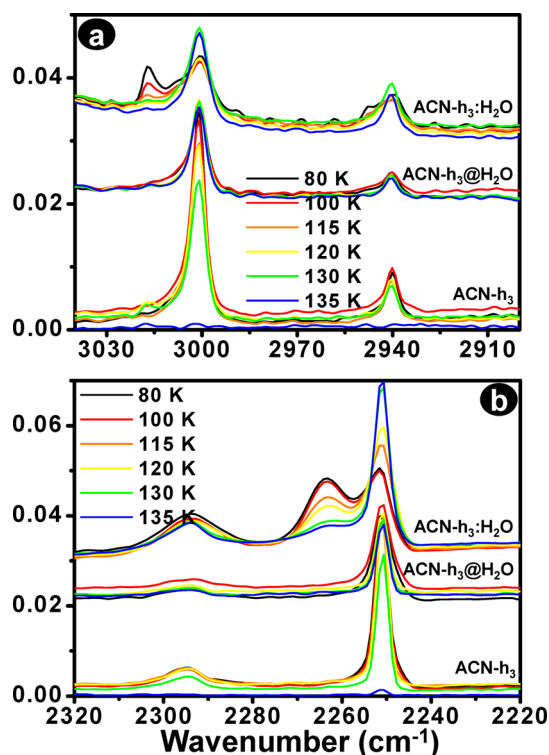


Figure 4. (a) Enlarged view of C–H asymmetric and symmetric stretching regions and (b) $\text{C}\equiv\text{N}$ stretching region of $\text{ACN-}h_3$ of pure acetonitrile, $\text{ACN-}h_3\text{:H}_2\text{O}$, and $\text{ACN-}h_3\text{@H}_2\text{O}$ at different temperatures.

$\text{ACN-}h_3$ with H_2O . Interestingly, this feature was not present in the spectra for the $\text{ACN-}h_3\text{@H}_2\text{O}$ system.

Figure 4b compares $\text{ACN-}h_3\text{:H}_2\text{O}$ with pure $\text{ACN-}h_3$ and $\text{ACN-}h_3\text{@H}_2\text{O}$ in the $\text{C}\equiv\text{N}$ stretching region. It shows an extra peak for $\text{ACN-}h_3\text{:H}_2\text{O}$ at $\sim 2264\text{ cm}^{-1}$ at 80 K whose intensity decreases as temperature is enhanced, and it vanishes completely at 130 K, similar to the disappearance of the bands in the O–H stretching region with a simultaneous regeneration of the H_2O feature (Figure 2a). Simultaneous disappearance of the new bands in the O–H stretching region and of the peak at 2264 cm^{-1} with temperature suggests that the $\text{C}\equiv\text{N}$ bond of $\text{ACN-}h_3$ could participate in bonding with H_2O . However, it is also noted that the above-mentioned peak in the $\text{C}\equiv\text{N}$ stretching region did not appear for $\text{ACN-}h_3\text{@H}_2\text{O}$. This confirms that the interaction between both the molecules takes place only when they are in good contact. An analysis of the temperature-dependent RAIRS spectra was also performed for the $\text{H}_2\text{O@ACN-}h_3$ system (data not shown here), which showed that the trends are similar to $\text{ACN-}h_3\text{@H}_2\text{O}$. In this case, $\text{ACN-}h_3$ desorbed at 135 K, just like pure $\text{ACN-}h_3$, prior to the crystallization of water.

The C–H bending region of the spectra for $\text{ACN-}h_3$, $\text{ACN-}h_3\text{@H}_2\text{O}$, and $\text{ACN-}h_3\text{:H}_2\text{O}$ is plotted in Figure 5a. The figure establishes that there is no change in the C–H bending region on going from pure $\text{ACN-}h_3$ to $\text{ACN-}h_3\text{@H}_2\text{O}$. But a significant change is observed when both the molecules are codeposited. The appearance of a new peak at 1444 cm^{-1} was seen, which slowly vanished upon heating, in a manner similar to the other regions. This further confirms the interaction of $\text{ACN-}h_3$ and H_2O in $\text{ACN-}h_3\text{:H}_2\text{O}$.

In order to gain more insight into the interaction of ACN with water and changes in the IR peaks with temperature, H_2O

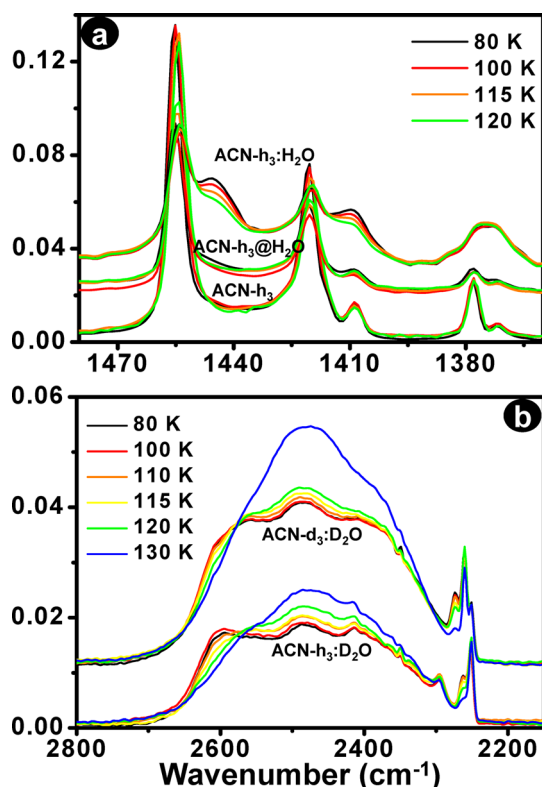


Figure 5. Temperature-dependent RAIRS spectra in (a) bending mode of C–H bond of ACN, ACN- h_3 :H $_2$ O, and ACN- h_3 :D $_2$ O mixtures and (b) O–D stretching mode of codeposited ACN- h_3 :D $_2$ O and ACN- d_3 :D $_2$ O mixtures.

was replaced by D $_2$ O, and mixtures of ACN- h_3 and ACN- d_3 with D $_2$ O were studied. Figure 5b displays the RAIRS spectra for codeposited 1:1 ACN- h_3 :D $_2$ O and ACN- d_3 :D $_2$ O mixtures at 40 K and, subsequently, heated to 130 K. The general features and trends are in good agreement with the ACN- h_3 :H $_2$ O interaction. For instance, there were no changes in the spectra between 40 and 80 K and so, only the spectrum at 80 K is shown. Here too, three peaks can be seen at 80 K, which continue to be noticeable until 120 K, and at 130 K, the pure O–D stretching is regained. However, for these systems, the C \equiv N stretching of acetonitrile overlaps with the broad band of O–D stretching. Figure 6a illustrates the C \equiv N stretching region of pure ACN- d_3 , ACN- h_3 :D $_2$ O, and ACN- d_3 :D $_2$ O at different temperatures. For pure ACN- d_3 , a doublet is observed with the two peaks positioned at 2250 and 2260 cm^{-1} . But a new peak emerges at 2274 cm^{-1} in the ACN- d_3 :D $_2$ O system, and it gradually disappears upon annealing (data for ACN- d_3 :H $_2$ O system is shown in Figure S3 of the Supporting Information). Comparing Figure 6a with Figure 4b, the variation of the C \equiv N stretching mode of ACN- h_3 :D $_2$ O with temperature is similar to that of ACN- h_3 :H $_2$ O. This confirms our earlier prediction that the interaction of acetonitrile and water occurs via a hydrogen bond between the C \equiv N group of acetonitrile and the OD/OH group of water. In Figure 6b, intensity of O–H stretching corresponding to the maximum peak position (as taken from the different codeposited systems) is plotted as a function of temperature. The figure shows that irrespective of the ACN:water system, the (a) intensity remains constant until 110 K, (b) starts increasing at 115 K, and (c) reaches a maximum at 130 K, beyond which desorption occurs.

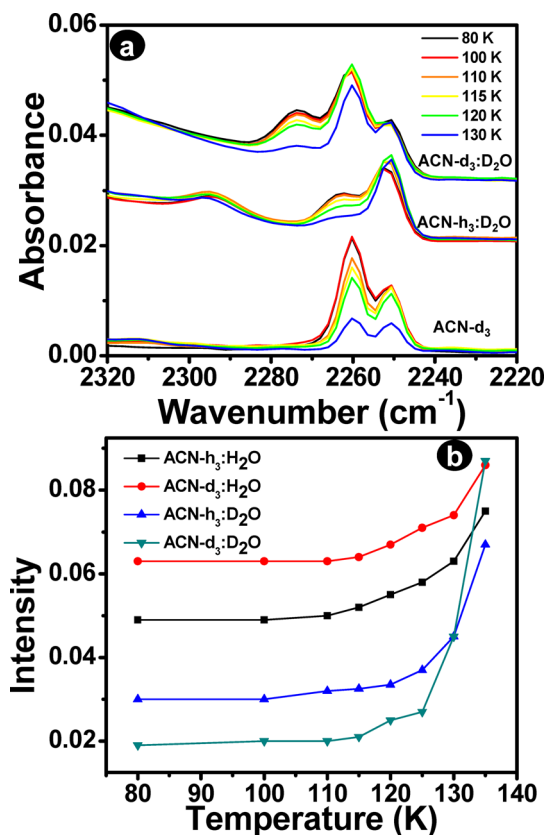


Figure 6. (a) C \equiv N stretching region of ACN- d_3 is shown at different temperatures for three different sets of ice samples. (b) Intensity of O–H stretching (maximum peak position) is plotted with respect to temperature.

4. DISCUSSION

From the data presented so far and in the light of earlier studies presented in the Introduction, let us now focus on the interaction of acetonitrile with water in the bulk ice phase. Strong interaction of codeposited acetonitrile and water at low temperatures (below 115 K) weakened as the temperature was increased. From all the experiments, it is evident that O–H/O–D bands of water and C \equiv N band of ACN are strongly affected by temperature. Three new bands appear in the O–H/O–D stretching region (Figure 2a) due to the interaction of ACN and water via H-bonding. These bands are retained until 110 K but start disappearing at 115 K and vanish completely at 130 K. The H-bonded C \equiv N stretching peak (2264 cm^{-1} for ACN- h_3 and 2274 cm^{-1} for ACN- d_3) starts decreasing in intensity at 115 K, which is reduced to zero at 130 K. From an ab initio study, it has been predicted that if ACNs form a σ -type H-bond, the C \equiv N stretching frequency is blue-shifted by 11.2 cm^{-1} , whereas when it forms the ACN-(H $_2$ O) $_3$ cluster, the C \equiv N stretching frequency is blue-shifted by 24.3 cm^{-1} .³³ We have also observed blue shifts in the C \equiv N frequencies which imply the formation of the σ -type H-bond between ACN and water. However, it was not possible to estimate the exact number of water molecules interacting with one molecule of ACN. In our study, we have seen an \sim 13 cm^{-1} blue shift in the H-bonded C \equiv N stretching frequency from the free C \equiv N stretching frequency irrespective of the samples. In general, calculated IR values do not match exactly with the peak positions obtained in experiments carried out at low temperatures. However, from this observation, we may say that approximately one ACN

molecule is interacting with one water molecule. Interaction of ACN molecules with water-ice is highly temperature sensitive, particularly in the temperature range of 115–130 K, which is evident from the gradual changes in the peak intensity of newly formed peaks in the O–H stretching region and H-bonded peak in the C≡N stretching region.

In our codeposited mixtures, ACN and water were in a 1:1 ratio which allow more ACN molecules to come in direct contact with free OH groups to form hydrogen bonds. The system is quite similar to liquid phase mixing where both the species can mix homogeneously. Here also, both H-bonded and free ACN molecules coexist at temperatures below 115 K, which is evident from the C≡N stretching frequency. C≡N stretching frequency for both free and H-bonded ACN coexist in the codeposited mixture at low temperature (<115 K) and upon increasing the temperature, the H-bonded peak disappears (130 K) and intensity of the free ACN peak shows an increase. At an elevated temperature of ~115–120 K, their molecular motions increase, and the H-bonds between acetonitrile and water-ice weaken, causing phase segregation of ACN molecules from the mixture inside the matrix which completes at 130 K. So at temperatures above 115 K, the intermolecular H-bonding weakens, and H₂O–H₂O and ACN–ACN interactions are enhanced, leading to phase segregation. The phase segregation is evident from the simultaneous disappearance of the bands in the OH stretching region and the peaks in the stretching region of C≡N. Interestingly, phase segregation starts at the same temperature (115 K) and completes at 130 K for the different combinations of ACN (ACN-*h*₃ and ACN-*d*₃) and water (H₂O and D₂O) in the mixture (see Figure 6b).

On the basis of the results obtained at different codeposited experiments, we propose a quantitative analysis. In this analysis, the C≡N stretching region of different mixtures are taken into consideration. We have seen that the C≡N stretching peak consists of both H-bonded and free ACN molecules. The peak was fitted with Lorentzians and the components are analyzed. Spectra at three different temperatures for ACN-*d*₃:H₂O are shown in Figure 7 where the two peaks, namely peak 1 and

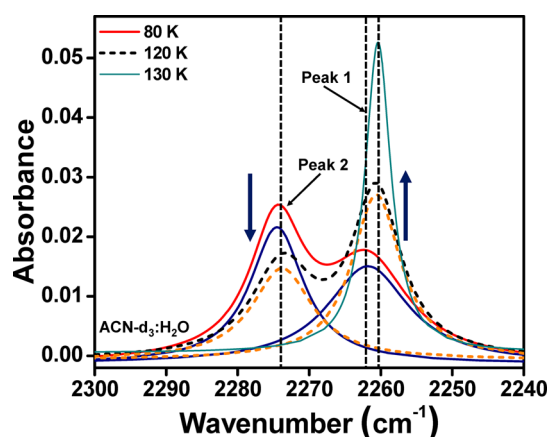


Figure 7. Lorentzian fit of the spectra of 1:1 ACN-*d*₃:H₂O at three different temperatures. Both fitted and cumulative spectra are shown in the figure. Two peaks in the cumulative spectra at each temperature are fitted with two components, peak 1 corresponds to the free ACN molecules and peak 2 corresponds to H-bonded ACN molecules. Fitted spectrum and cumulative spectrum were overlapping at 130 K. Hence, only fitted spectrum is shown in the figure at 130 K.

peak 2 are attributed to contributions from free and H-bonded ACN molecules. Areas of both the peaks are calculated and, from these, a fraction of H-bonded ACN molecules is calculated. A sum of the areas of peaks 1 and 2 gives the contribution due to total number of ACN molecules. Area of peak 2 is divided by the total area, which gives the fraction of H-bonded ACN molecules. This calculation is performed for four different sets of codeposited mixtures at different temperatures. Fraction of H-bonded molecules in different mixtures is plotted against temperature in Figure 8. In this

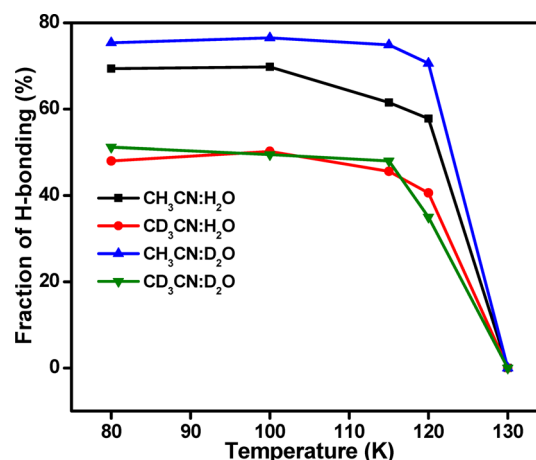


Figure 8. Fraction of H-bonded ACN molecules in different codeposited mixtures, plotted against temperature (see the text for details). Lines are drawn as to guide to eye and they do not represent a fit to the data.

calculation, we assume that once ACN molecules are phase-segregated from the mixture, no H-bonding exists. From the figure, it is evident that in all the different mixtures, more than 50% of ACN molecules are H-bonded with neighboring water molecules in the temperature range of 80–100 K. There is a sudden drop in the intensity of the H-bonded peak in the temperature range of 115–120 K, and finally it tends to zero at 130 K. Molecular motion of the species in the condensed phase is restricted. So the fraction of ACN molecules forming the H bond depends upon how the ACN molecules are oriented and how they are surrounded by H₂O molecules inside the ice matrix. This directly depends upon the concentration of both the molecules in the vapor phase during deposition. During deposition, we maintained the concentration as 1:1, which was closely monitored using a residual gas analyzer and, hence, we assume that the concentration of these molecules in the ice matrix is also 1:1. But it may not be an accurate assumption always as all the 1:1 codeposited mixtures may not give the same fraction of H bonding between ACN and water. More water molecules sitting near to ACN molecules leads to a higher number of H-bonding interaction between both the molecules. However, study reveals that in a 1:1 codeposited system, more than half of the ACN molecules are H-bonded with water molecules at low temperature (below 115 K). While this analysis is informative, it is only approximate. It is assumed that the cross sections of both the peaks (peaks 1 and 2) are the same and so their peak intensities are related to their respective concentrations by the same factor. We assume that interaction between the ACN and H₂O molecules is negligible at 130 K once they get phase segregated, which may not be true as ACN molecules are still in the water matrix and can interact, although

such interactions are weak or small in number to be seen by IR spectroscopy. Desorption of ACN near 135 K is disregarded. Another approach to doing a quantitative analysis is by using the infrared absorbance values along with TPD data. But that approach is not possible in our case due to experimental limitations.

From Figure 7, it is noticeable that free C≡N stretching frequency (peak 1) at 80 K is blue-shifted (shown in the figure by vertical lines) compared to the spectra at 120 and 130 K. Same data, with one more spectrum are shown in Figure S4 of the Supporting Information (spectrum at 100 K is not shown in Figure 7, for clarity). This observation indicates that strong interaction between both the molecules lead to the shift in free C≡N stretching frequency of ACN as well. When the molecules start segregating, the interaction is weakened, and free C≡N stretching frequency start appearing at the same position as in pure ACN.

The study confirms the formation of the H-bond between ACN and water-ice, and we have seen that both the molecules phase segregate above 130 K, where there is no or very limited H-bonding between them. We have also noticed that phase segregation starts at 115 K. But the mechanism of phase segregation remains unclear. To understand the mechanism of phase segregation we need to look at the structure of both the molecules at the temperature regime where phase segregation is occurring. It is reported that vapor deposited ACN at low temperature (below 115 K) is likely to form an amorphous phase with a randomly oriented structure, which on moderate annealing at 115 K initiates transitions to a crystalline phase.⁴³ The study indicates that ACN deposited at 100 K shows an unspecific broad intensity distribution in the XRD pattern, which is characteristic of amorphous structure of solid ACN. The same sample upon annealing to 115 K initiates a phase transition into a stable crystalline phase, which shows reflections in the diffractogram. Water vapor deposited below 120 K is amorphous, and ice undergoes a structural change at 120 K.^{18,19} In this structural transition, porous amorphous ice becomes nonporous at temperatures above 120 K, reducing the number of free OH groups in the process. Another study also revealed that amorphous ice undergoes a structural change of ~130 K before the onset of crystallization, leading to restrained amorphous ice.¹⁰ Other studies also revealed the structure of water-ice at different temperature. Laufer et al. suggested that amorphous ice exists at least in two different forms, one at <85 K and another at 85 < T < 136.8 K, before it undergoes crystallization.⁴⁴ Horimoto et al. also support the formation of microporous structure of amorphous ice, and it becomes pore free at 120 K.⁴⁵ So, all these studies suggest that in the temperature range of 115–130 K, both ACN and H₂O molecules undergo a structural change, which may be the force behind this phase segregation. This in turn starts at the temperature (115 K) where ACN undergoes crystallization. Crystallization leads to the increase in molecular motion. At the same time, amorphous ice also undergoes a structural change (120 K), where the microporous structure of amorphous ice is collapsed. This molecular motion of both the molecules affects the interaction between ACN and water-ice. This is clearly seen from Figure 9. In this figure (Figure 9), the maximum intensity of H-bonded and free C≡N stretching frequency of two different codeposited mixtures is plotted against temperature. The figure indicates that the intensity of both the peaks are constant until 110 K. At 115 K, the intensity of peak 2 shows a decrease and peak 1 shows an increase, which is indicating the

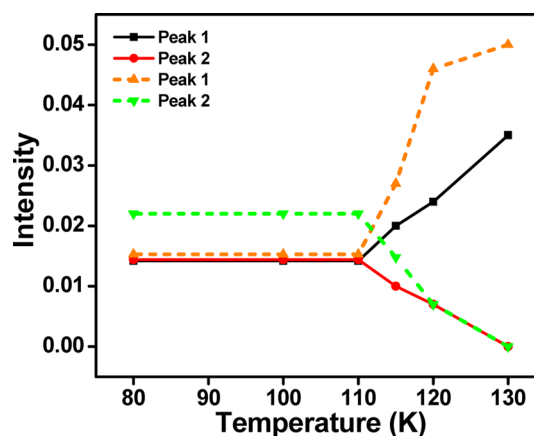


Figure 9. Maximum intensity of fitted (Lorentzian fit) free (peak 1) and H-bonded (peak 2) C≡N stretching frequency of ACN-*h*₃:H₂O (solid line) and ACN-*d*₃:H₂O (dotted line) is plotted against temperature.

breaking of the H-bond between ACN and water-ice. At 130 K, the intensity of peak 1 reaches maximum, whereas the intensity of peak 2 goes to minimum. A similar plot is shown in Figure 6b where maximum peak position of O–H/O–D is plotted against the temperature. This also indicates that the phase segregation starts at the same temperature (115 K) for all the codeposited mixtures. Phase segregation takes place well before the crystallization temperature of water-ice. Hence, nucleation of water-ice does not play any role in the phase segregation process.

Ample molecular motions of ACN at 130 K, where pure ACN starts desorbing from the surface, may also induce ACN molecules to segregate from the mixture. These phase segregated ACN molecules are covered with water-ice. As water-ice is nonporous in nature above 120 K, ACN may not be allowed to sit within the ice pores, rather it segregates to form a separate layer. In this layered structure, ACN molecules are overlaid by water molecules. We make this conclusion as desorption of ACN is not seen until 140 K. Infrared spectral features at high temperatures (above 130 K) also support a layered structure. During crystallization of water, water molecules reorient themselves and open a path for ACN molecules to desorb forming a molecular volcano. With an increase in temperature, there was no increase in pressure in the chamber, until the crystallization of water-ice where we have seen desorption of ACN. This observation indicates that desorption of ACN molecules takes place only when water molecules undergo crystallization.

Compared to ACN:H₂O, no spectral change was observed in the layer-on-layer-deposited ACN@H₂O as a function of temperature. This type of deposition does not allow proper mixing, and so water and ACN are not in 1:1 contact, as a result of which they are not able to form enough H bonds between them. There may be interfacial interaction in the overlayer deposited ACN@H₂O system, but we fail to observe it in our present measurement as we were probing the bulk ice, and hence, such interactions are much less seen by IR. The ACN@H₂O system is closer to the one after phase segregation has occurred (spectrum at 130 K in the ACN:H₂O system) from which ACN was desorbed completely at 145 K at the water crystallization temperature. Hence, we believe that cooling back a codeposited ACN:H₂O mixture after it has phase-separated above 120 K may act like an overlayer deposited ACN@H₂O

system, forming small islands of acetonitrile inside the water matrix with reduced interaction of ACN with water-ice.

Temperature-programmed desorption (TPD) spectroscopy is another way to study this interaction, particularly when molecules interact on the surface.^{20,46} TPD measurements of pure ACN-*h*₃, ACN-*h*₃:D₂O, and ACN-*h*₃@D₂O were performed, and comparison of the data is shown in Figure S5 of the Supporting Information. From the figure it is evident that pure ACN-*h*₃ desorb from the Ru(0001) surface with a peak maximum at ~132 K, whereas the other two cases desorption peak maximum appears above 140 K. Both the TPD spectra of the codeposited (ACN-*h*₃:D₂O) and sequential deposited (ACN-*h*₃@D₂O) systems behave in a similar fashion, which supports our argument that the codeposited system undergoes phase segregation and ACN get trapped inside the water-ice matrix, which is similar to the sequential deposited system. In the sequential deposition system, multilayer and monolayer peaks of ACN-*h*₃ are well-distinguished, but it is not prominent in the codeposited system. Desorption peak of ACN-*h*₃ in the codeposited system appears as a broad peak compared to the sequential deposition system which may be due to phase segregation in the codeposited system forming diffuse islands inside the water matrix. TPD can help to calculate the number of individual type of molecules present in the system. But in this study, it was not possible to measure TPD and RAIRS simultaneously.

5. CONCLUSIONS

The interaction of ACN–water-ice mixtures at low temperature has been studied using RAIRS spectroscopy. ACN and water were codeposited on a Ru(0001) substrate at 40 K and subsequently annealed to higher temperatures. The shifts in the IR peaks confirmed that (a) the molecular interaction between ACN and water-ice involved hydrogen bond formation, (b) the ACN molecules phase separate completely within the ice matrix at ~130 K, and (c) above 140 K, the water molecules reorient themselves causing the trapped ACN molecules to desorb. The study showed that in a 1:1 codeposited mixture of ACN and water-ice, more than 50% of ACN molecules participate in H-bonding with water-ice at a temperature below 115 K. Phase segregation is highly temperature-dependent in the temperature range of 100–130 K, and it is an irreversible process too. This explains how temperature-induced phase separation in an astronomical environment of similar ice mixtures can prevent the molecules from reacting with each other and thereby affect the kinetics of product formation.

Though there have been reports of irradiation processing of ACN–water mixtures, our results reveal the complexity of the interaction between the reacting molecules within the water-ices, which should be taken into account while studying other chemical reactions under similar conditions. Furthermore, the new spectral signatures recorded as a function of temperature may help astronomers to find the interacting molecules, rather than isolated ones in ISM and the atmosphere.

■ ASSOCIATED CONTENT

● Supporting Information

Temperature-dependent RAIR spectra of ACN-*h*₃:H₂O, ACN-*h*₃@H₂O, and ACN-*d*₃:H₂O system. Lorentzian fit of the spectra of 1:1 ACN-*h*₃:H₂O systems. TPD spectra of three different systems. This information is available from The Supporting Information is available free of charge on the ACS Publications website at DOI: 10.1021/jp512607v.

■ AUTHOR INFORMATION

Corresponding Author

*E-mail: pradeep@iitm.ac.in. Fax: + 91-44 2257-0545.

Author Contributions

§R.G.B. and R.R.J.M. contributed equally.

Notes

The authors declare no competing financial interest.

■ ACKNOWLEDGMENTS

T.P. acknowledges the Science and Engineering Research Board (SERB), Department of Science and Technology (DST), Government of India for research funding. R.G.B. thanks Council of Scientific and Industrial Research (CSIR), Government of India for a research fellowship. R.R.J.M. thanks the University Grant Commission (UGC) for his research fellowship. S.B. acknowledges the support from Physical Research Laboratory (PRL) and INSPIRE Grant (IFA-11CH-11).

■ REFERENCES

- (1) Schaff, J. E.; Roberts, J. T. Toward an Understanding of the Surface Chemical Properties of Ice: Differences between the Amorphous and Crystalline Surfaces. *J. Phys. Chem.* **1996**, *100*, 14151–14160.
- (2) Hama, T.; Watanabe, N. Surface Processes on Interstellar Amorphous Solid Water: Adsorption, Diffusion, Tunneling Reactions, and Nuclear-Spin Conversion. *Chem. Rev.* **2013**, *113*, 8783–8839.
- (3) Smith, R. S.; Huang, C.; Wong, E. K. L.; Kay, B. D. The Molecular Volcano: Abrupt CCl₄ Desorption Driven by the Crystallization of Amorphous Solid Water. *Phys. Rev. Lett.* **1997**, *79*, 909–912.
- (4) Cyriac, J.; Pradeep, T.; Kang, H.; Souda, R.; Cooks, R. G. Low-Energy Ionic Collisions at Molecular Solids. *Chem. Rev.* **2012**, *112*, 5356–5411.
- (5) Hornekaer, L.; Baurichter, A.; Petrunin, V. V.; Luntz, A. C.; Kay, B. D.; Al-Halabi, A. Influence of Surface Morphology on D₂ Desorption Kinetics from Amorphous Solid Water. *J. Chem. Phys.* **2005**, *122*, 124701-1–124701-11.
- (6) Ayotte, P.; Smith, R. S.; Stevenson, K. P.; Dohnalek, Z.; Kimmel, G. A.; Kay, B. D. Effect of Porosity on the Adsorption, Desorption, Trapping, and Release of Volatile Gases by Amorphous Solid Water. *J. Geophys. Res.* **2001**, *106*, 33387–33392.
- (7) Azria, R.; Le Coat, Y.; Lachgar, M.; Tronc, M.; Parenteau, L.; Sanche, L. Effects of Morphology in Electron-Stimulated Desorption: O⁻ from O₂ Condensed on D₂O Films Grown at 15–150 K on Pt. *Surf. Sci.* **1999**, *436*, L671–L676.
- (8) Roser, J. E.; Manico, G.; Pirronello, V.; Vidali, G. Formation of Molecular Hydrogen on Amorphous Water Ice. Influence of Morphology and Ultraviolet Exposure. *Astrophys. J.* **2002**, *581*, 276–284.
- (9) Cyriac, J.; Pradeep, T. Probing Difference in Diffusivity of Chloromethanes through Water Ice in the Temperature Range of 110–150 K. *J. Phys. Chem. C* **2007**, *111*, 8557–8565.
- (10) Jenniskens, P.; Blake, D. F. Structural Transitions in Amorphous Water Ice and Astrophysical Implications. *Science* **1994**, *265*, 753–756.
- (11) Smith, R. S.; Petrik, N. G.; Kimmel, G. A.; Kay, B. D. Thermal and Nonthermal Physicochemical Processes in Nanoscale Films of Amorphous Solid Water. *Acc. Chem. Res.* **2012**, *45*, 33–42.
- (12) Stevenson, K. P.; Kimmel, G. A.; Dohnalek, Z.; Smith, R. S.; Kay, B. D. Controlling the Morphology of Amorphous Solid Water. *Science* **1999**, *283*, 1505–1507.
- (13) Smith, R. S.; Zubkov, T.; Dohnalek, Z.; Kay, B. D. The Effect of the Incident Collision Energy on the Porosity of Vapor-Deposited Amorphous Solid Water Films. *J. Phys. Chem. B* **2009**, *113*, 4000–4007.

- (14) Backus, E. H. G.; Grecea, M. L.; Kleyn, A. W.; Bonn, M. Surface Crystallization of Amorphous Solid Water. *Phys. Rev. Lett.* **2004**, *92*, 236101-1–236101-4.
- (15) Kondo, T.; Kato, H. S.; Bonn, M.; Kawai, M. Morphological Change During Crystallization of Thin Amorphous Solid Water Films on Ru(0001). *J. Chem. Phys.* **2007**, *126*, 181103-1–181103-5.
- (16) Kondo, T.; Kato, H. S.; Bonn, M.; Kawai, M. Deposition and Crystallization Studies of Thin Amorphous Solid Water Films on Ru(0001) and on Co-Precovered Ru(0001). *J. Chem. Phys.* **2007**, *127*, 094703-1–094703-14.
- (17) Bag, S.; Bhuin, R. G.; Pradeep, T. Distinguishing Amorphous and Crystalline Ice by Ultralow Energy Collisions of Reactive Ions. *J. Phys. Chem. C* **2013**, *117*, 12146–12152.
- (18) Cyriac, J.; Pradeep, T. Structural Reorganization on Amorphous Ice Films Below 120 K Revealed by near-Thermal (~1 eV) Ion Scattering. *J. Phys. Chem. C* **2008**, *112*, 5129–5135.
- (19) Mate, B.; Rodriguez-Lazcano, Y.; Herrero, V. J. Morphology and Crystallization Kinetics of Compact (HGW) and Porous (ASW) Amorphous Water Ice. *Phys. Chem. Chem. Phys.* **2012**, *14*, 10595–10602.
- (20) Schaff, J. E.; Roberts, J. T. Interaction of Acetonitrile with the Surfaces of Amorphous and Crystalline Ice. *Langmuir* **1999**, *15*, 7232–7237.
- (21) Sexton, B. A.; Avery, N. R. Coordination of Acetonitrile (CH₃CN) to Platinum(111): Evidence for an H₂(C,N) Species. *Surf. Sci.* **1983**, *129*, 21–36.
- (22) Shannon, C.; Campion, A. Raman Spectroscopic Investigation of the Adsorption of Acetonitrile and Methanol on Silicon(100)-2 × 1. *Surf. Sci.* **1990**, *227*, 219–223.
- (23) Meijer, E. L.; van Santen, R. A.; Jansen, A. P. J. Computation of the Infrared Spectrum of an Acidic Zeolite Proton Interacting with Acetonitrile. *J. Phys. Chem.* **1996**, *100*, 9282–9291.
- (24) Bahr, S.; Kempter, V. Interaction of Acetonitrile with Thin Films of Solid Water. *J. Chem. Phys.* **2009**, *130*, 214509-1–214509-9.
- (25) Ahn, D.-S.; Lee, S. Density Functional Theory Study of Acetonitrile - Water Clusters: Structures and Infrared Frequency Shifts. *Bull. Korean Chem. Soc.* **2007**, *28*, 725–729.
- (26) Bako, I.; Megyes, T.; Palinkas, G. Structural Investigation of Water-Acetonitrile Mixtures: An Ab Initio, Molecular Dynamics and X-Ray Diffraction Study. *Chem. Phys.* **2005**, *316*, 235–244.
- (27) Kittaka, S.; Kuranishi, M.; Ishimaru, S.; Umahara, O. Phase Separation of Acetonitrile-Water Mixtures and Minimizing of Ice Crystallites from There in Confinement of Mcm-41. *J. Chem. Phys.* **2007**, *126*, 091103-1–091103-4.
- (28) Melnikov, S. M.; Hoeltzel, A.; Seidel-Morgenstern, A.; Tallarek, U. Adsorption of Water-Acetonitrile Mixtures to Model Silica Surfaces. *J. Phys. Chem. C* **2013**, *117*, 6620–6631.
- (29) Schaff, J. E.; Roberts, J. T. Adsorbed States of Acetonitrile and Chloroform on Amorphous and Crystalline Ice Studied with X-Ray Photoelectron Spectroscopy. *Surf. Sci.* **1999**, *426*, 384–394.
- (30) Zhang, D.; Gutow, J. H.; Eisenthal, K. B. Structural Phase Transitions of Small Molecules at Air/Water Interfaces. *J. Chem. Soc., Faraday Trans.* **1996**, *92*, 539–543.
- (31) Bertie, J. E.; Lan, Z. Liquid Water-Acetonitrile Mixtures at 25 °C: The Hydrogen-Bonded Structure Studied through Infrared Absolute Integrated Absorption Intensities. *J. Phys. Chem. B* **1997**, *101*, 4111–4119.
- (32) Jamroz, D.; Stangret, J.; Lindgren, J. An Infrared Spectroscopic Study of the Preferential Solvation in Water-Acetonitrile Mixtures. *J. Am. Chem. Soc.* **1993**, *115*, 6165–6168.
- (33) Choi, J.-H.; Oh, K.-L.; Lee, H.; Lee, C.; Cho, M. Nitrile and Thiocyanate Ir Probes: Quantum Chemistry Calculation Studies and Multivariate Least-Square Fitting Analysis. *J. Chem. Phys.* **2008**, *128*, 134506.
- (34) Kabisch, G. Raman Spectroscopic Studies on Water-Acetonitrile Mixtures. *Z. Phys. Chem.* **1982**, *263*, 48–60.
- (35) Dello Russo, N.; Khanna, R. K. Laboratory Infrared Spectroscopic Studies of Crystalline Nitriles with Relevance to Outer Planetary Systems. *Icarus* **1996**, *123*, 366–395.
- (36) Takamuku, T.; Tabata, M.; Yamaguchi, A.; Nishimoto, J.; Kumamoto, M.; Wakita, H.; Yamaguchi, T. Liquid Structure of Acetonitrile–Water Mixtures by X-Ray Diffraction and Infrared Spectroscopy. *J. Phys. Chem. B* **1998**, *102*, 8880–8888.
- (37) Kovacs, H.; Laaksonen, A. Molecular Dynamics Simulation and NMR Study of Water-Acetonitrile Mixtures. *J. Am. Chem. Soc.* **1991**, *113*, 5596–605.
- (38) Gorbunov, B. Z.; Naberukhin, Y. I. Structure of Aqueous Solutions of Nonelectrolytes Studied by Vibrational Spectroscopy. ii. Microstratification at Mean Concentrations. *Zh. Strukt. Khim.* **1975**, *16*, 816–25.
- (39) Marcus, Y.; Migron, Y. Polarity, Hydrogen Bonding, and Structure of Mixtures of Water and Cyanomethane. *J. Phys. Chem.* **1991**, *95*, 400–406.
- (40) Bag, S.; Bhuin, R. G.; Methikkalam, R. R. J.; Pradeep, T.; Kephart, L.; Walker, J.; Kuchta, K.; Martin, D.; Wei, J. Development of Ultralow Energy (1 - 10 eV) Ion Scattering Spectrometry Coupled with Reflection Absorption Infrared Spectroscopy and Temperature Programmed Desorption for the Investigation of Molecular Solids. *Rev. Sci. Instrum.* **2014**, *85*, 014103-1–014103-7.
- (41) Kang, H. Chemistry of Ice Surfaces. Elementary Reaction Steps on Ice Studied by Reactive Ion Scattering. *Acc. Chem. Res.* **2005**, *38*, 893–900.
- (42) Abdulgali, A. G. M.; Marchione, D.; Rosu-Finsen, A.; Collings, M. P.; McCoustra, M. R. S. Laboratory Investigations of Irradiated Acetonitrile-Containing Ices on an Interstellar Dust Analog. *J. Vac. Sci. Technol., A* **2012**, *30*, 041505-1–041505-6.
- (43) Tizek, H.; Grothe, H.; Knozinger, E. Gas-Phase Deposition of Acetonitrile: An Attempt to Understand Ostwald's Step Rule on a Molecular Basis. *Chem. Phys. Lett.* **2004**, *383*, 129–133.
- (44) Laufer, D.; Kochavi, E.; Bar-Nun, A. Structure and Dynamics of Amorphous Water Ice. *Phys. Rev. B* **1987**, *36*, 9219–9227.
- (45) Horimoto, N.; Kato, H. S.; Kawai, M. Stepwise Morphological Change of Porous Amorphous Ice Films Observed through Adsorption of Methane. *J. Chem. Phys.* **2002**, *116*, 4375–4378.
- (46) Burke, D. J.; Brown, W. A. Ice in Space: Surface Science Investigations of the Thermal Desorption of Model Interstellar Ices on Dust Grain Analogue Surfaces. *Phys. Chem. Chem. Phys.* **2010**, *12*, 5947–5969.

Interaction of Acetonitrile with Water-Ice: An Infrared Spectroscopic Study

Radha Gobinda Bhui¹, Rabin Rajan J. Methikkalam¹, Bhalamurugan Sivaraman², and Thalappil Pradeep^{1*}

¹DST Unit of Nanoscience (DST UNS) and Thematic Unit of Excellence (TUE), Department of Chemistry, Indian Institute of Technology Madras, Chennai 600 036, India

²Space and Atmospheric Sciences Division, Physical Research Laboratory, Ahmedabad, India.

*Corresponding author: Fax: + 91-44 2257-0545

*E-mail: pradeep@iitm.ac.in

SUPPORTING INFORMATION 1:

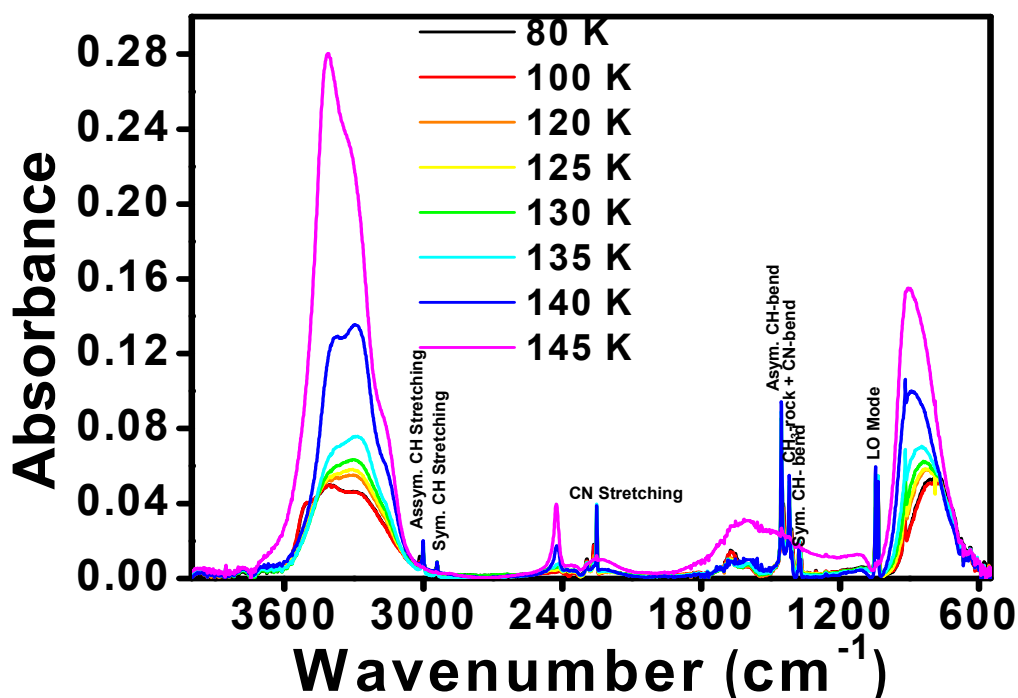


Figure S1: Temperature dependent RAIRS spectra of pure 1:1 ACN-h₃:H₂O deposited on cold Ru(0001) surface at 40 K. Complete desorption of ACN-h₃ takes place at 145 K during crystallization of H₂O.

SUPPORTING INFORMATION 2:

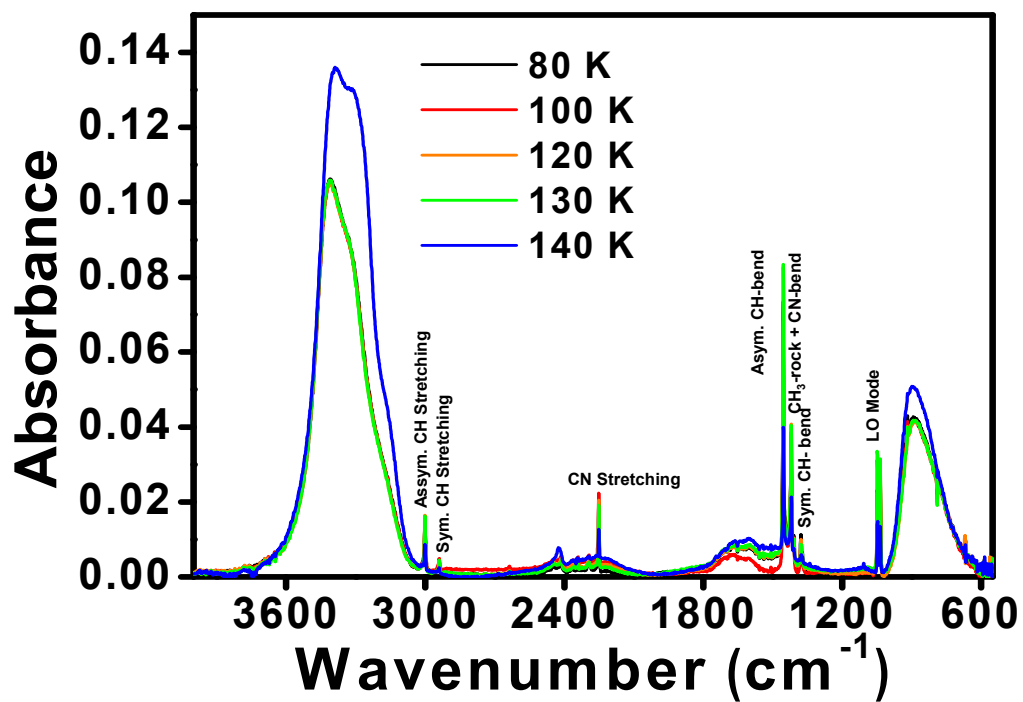


Figure S2: Temperature dependent RAIRS spectra of ACN-h₃@H₂O deposited on cold Ru(0001) surface at 40 K. Desorption of ACN-h₃ takes place during crystallization of H₂O at 140 K and it desorbs completely at 145 K.

SUPPORTING INFORMATION 3:

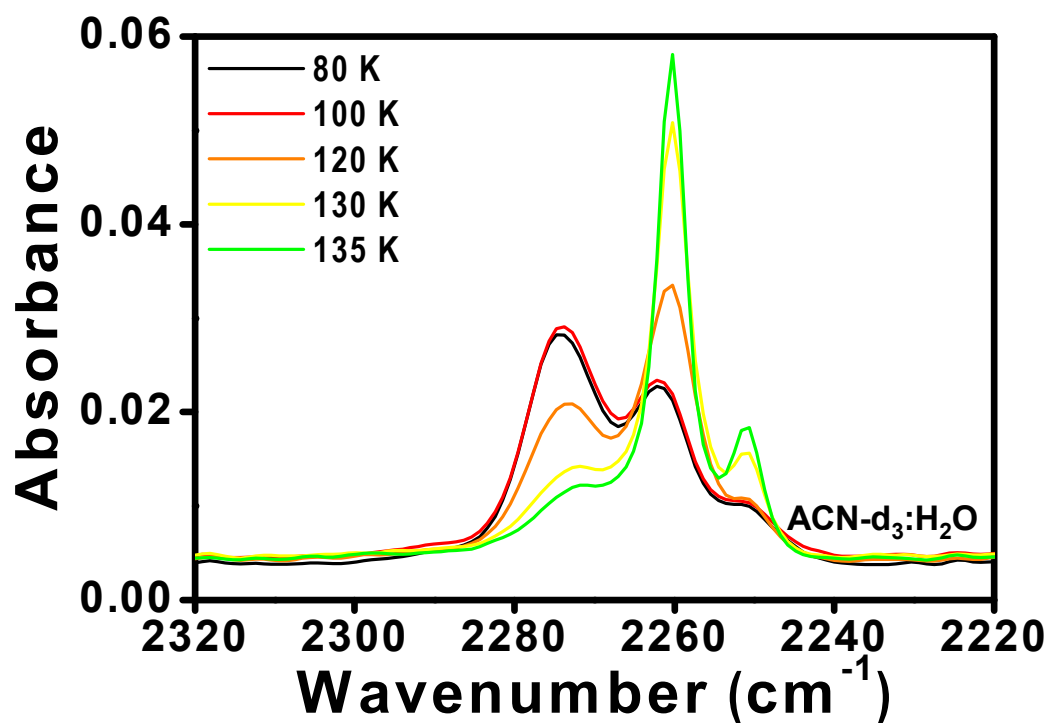


Figure S3: Temperature dependent RAIRS spectra of 1:1 ACN-d₃:H₂O deposited on cold Ru(0001) surface at 40 K. Spectra show the appearance of hydrogen bonded C≡N stretching at 2274 cm⁻¹ and the peak disappears upon warming.

SUPPORTING INFORMATION 4:

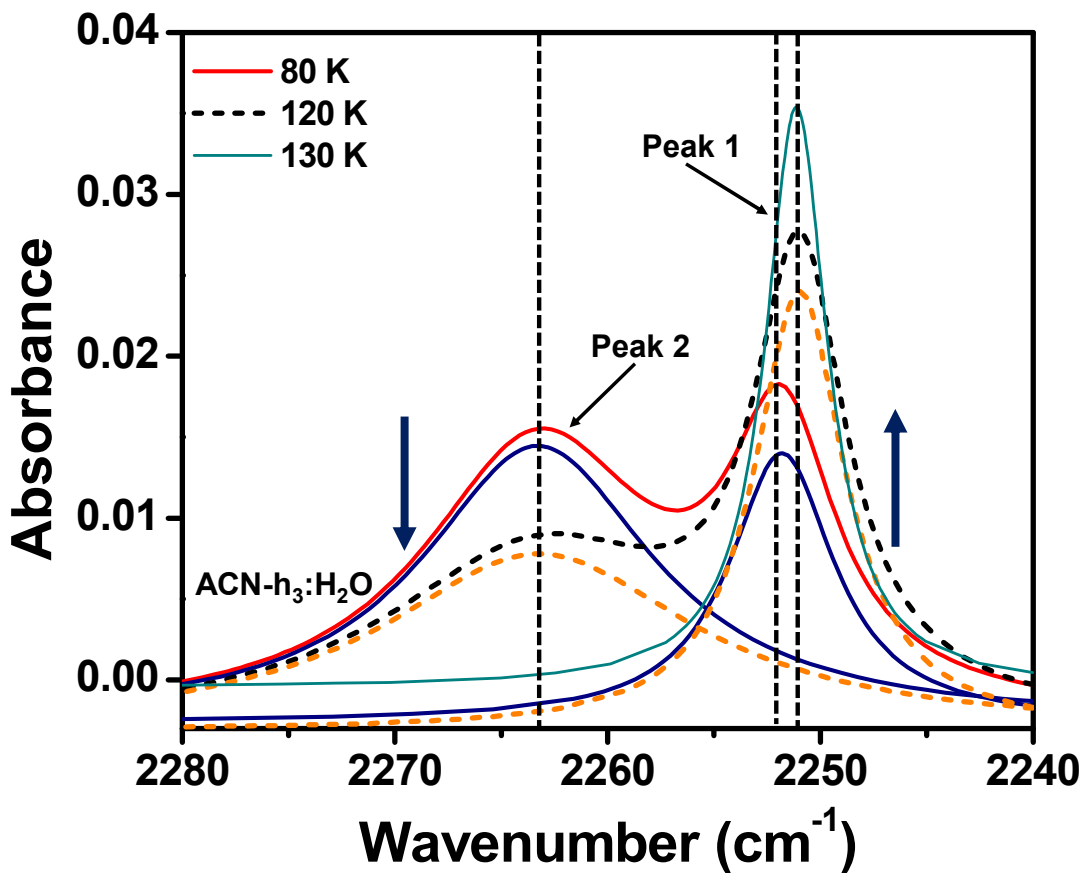


Figure S4: Lorentzian fit of the spectra of 1:1 ACN-h₃:H₂O at three different temperatures. Both fitted and cumulative spectra are shown in the figure. Two peaks in the cumulative spectrum at each temperature are fitted with two components, peak 1 corresponds to the free ACN molecules and peak 2 corresponds to H-bonded ACN molecules. Fitted spectrum and cumulative spectrum were overlapping at 130 K. Hence, only fitted spectrum is shown in the figure at 130 K.

SUPPORTING INFORMATION 5:

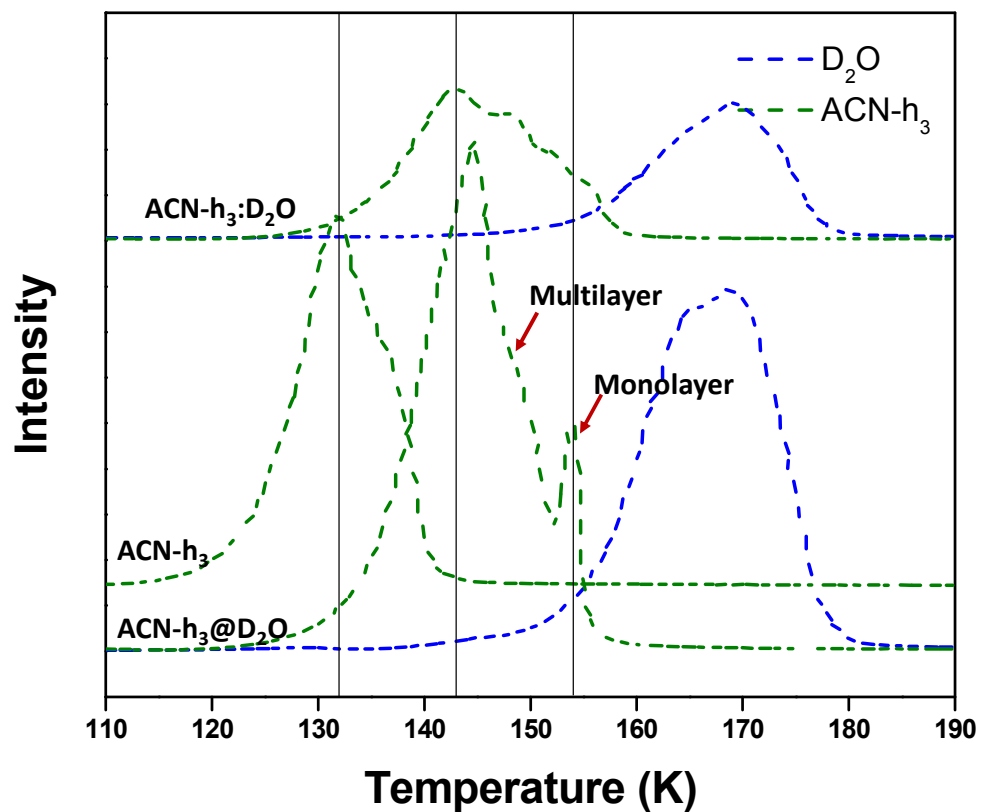


Figure S5: TPD spectra of three different sets of experiments are presented here. Desorption of pure ACN-h₃ is observed at 132 K whereas both co-deposited and overlayer deposited systems desorb at ~145 K, during crystallization of water-ice. Ramping rate was 20 K/min.

ARTICLE

Received 9 Dec 2014 | Accepted 24 Apr 2015 | Published 15 Jun 2015

DOI: 10.1038/ncomms8291

OPEN

Ambient solid-state mechano-chemical reactions between functionalized carbon nanotubes

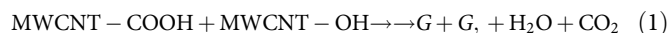
Mohamad A. Kabbani¹, Chandra Sekhar Tiwary^{1,*}, Pedro A.S. Autreto^{2,*}, Gustavo Brunetto^{2,*}, Anirban Som³, K.R. Krishnadas³, Sehmus Ozden¹, Ken P. Hackenberg¹, Yongi Gong⁴, Douglas S. Galvao², Robert Vajtai¹, Ahmad T. Kabbani^{1,5}, Thalappil Pradeep³ & Pulickel M. Ajayan^{1,3,4}

Carbon nanotubes can be chemically modified by attaching various functionalities to their surfaces, although harsh chemical treatments can lead to their break-up into graphene nanostructures. On the other hand, direct coupling between functionalities bound on individual nanotubes could lead to, as yet unexplored, spontaneous chemical reactions. Here we report an ambient mechano-chemical reaction between two varieties of nanotubes, carrying predominantly carboxyl and hydroxyl functionalities, respectively, facilitated by simple mechanical grinding of the reactants. The purely solid-state reaction between the chemically differentiated nanotube species produces condensation products and unzipping of nanotubes due to local energy release, as confirmed by spectroscopic measurements, thermal analysis and molecular dynamic simulations.

¹Department of Materials Science and NanoEngineering, Rice University, Houston, Texas 77005, USA. ²Department of Applied Physics, State University of Campinas, Campinas-SP 13083-959, Brazil. ³DST Unit of Nanoscience and Thematic Unit of Excellence, Department of Chemistry, Indian Institute of Technology Madras, Chennai 600 036, India. ⁴Department of Chemistry Rice University, Houston, Texas 77005, USA. ⁵Department of Natural Science, Lebanese American University, P.O. Box 13-5053 Chouran, Beirut 1102 2801, Lebanon. * These authors contributed equally to this work. Correspondence and requests for materials should be addressed to M.A.K. (email: mak8@rice.edu) or to T.P. (email: pradeep@iitm.ac.in) or to P.M.A. (email: ajayan@rice.edu).

Chemical functionalization of nanoparticles can lead to their surface decoration with a variety of covalently attached functionalities to serve different goals such as drug delivery, cancer therapy, diagnostics and electronic devices^{1–6}. Carbon nanotubes (CNTs) have been the subject of more than two decades of intense research^{7–10}. Various approaches have been used to modify their surfaces via covalent and non-covalent attachments to change both physical and chemical properties. Activation of CNTs by the incorporation of COOH on the exterior surfaces by treating them with concentrated nitric acid has been widely used^{11,12}. CNT-COOH can further be activated by acylation to form CNT-COCl, which can in turn be amidated or esterified^{13,14}. CNTs carrying hydroxyl groups (CNT-OH) on their surfaces have also been synthesized by alkaline hydrothermal treatment of pristine nanotubes in alkaline medium¹⁵. Despite the remarkable CNT mechanical and electronic properties, their large use has been precluded by poor solubility in water or organic solvents, which favours bundle formation, thus limiting their chemical reactivity. Mechano-chemical reactions (MCRs) can be used to overcome such difficulties^{16,17}. MCRs have been extensively used as synthetic protocols to obtain fullerene derivatives. Examples of these methods are fullerene dimers (C₁₂₀), trimers (C₁₈₀), cross dimers (C₆₀-C₇₀) and other fullerene derivatives obtained by the solid-state reactions with potassium salts such as KCN, K₂CO₃, reducing metals such as Mg and Al and solid aromatic amines under the high-speed vibration milling conditions^{18–21}. MCRs of CNT functionalizations with other molecules such as C₆₀, nitrenes, diazoinium compounds and metallic hydroxides under vigorous milling conditions have also been reported^{22–25}. Another way of reacting fullerenes has been through their encapsulation into CNTs²⁶. On the other hand, many methods have been used to produce graphene^{27–31}, including the unzipping of nanotubes to make graphene nanoribbons. A typical chemical unzipping of CNTs makes use of oxidative techniques³¹ in concentrated acid (H₂SO₄) and post treatments with harsh reagents such as highly concentrated potassium permanganate (KMnO₄). These processes involve harsh conditions to get to the final product (graphene), which can contain broken up or unzipped CNT. What has not been done is the use of nanotubes as solid-state reaction templates with specific chemical surface functionalities to induce direct coupling between the functional groups and concomitant breakdown of the cylindrical structure.

Here, we report the demonstration of unzipping of CNTs via a solid-state room temperature reaction between multiwalled CNTs (MWCNTs) containing different reactive functionalities of COOH and OH groups. The reaction is mechano-chemically induced, initiated at room temperature in ambient air, facilitated by the simple grinding of two chemically variant CNT reactants and leading to the unzipping of the nanotube (shown in Fig. 1a). By grinding equal weights of MWCNT-COOH and MWCNT-OH decorated with 1.41% and 0.46% by weight of COOH and OH (see experimental details of grinding and Supplementary Table 1), respectively^{11,15}, a sheet-like lustrous material is formed spontaneously (Fig. 2a). Characterization of the material using different microscopic and spectroscopic methods, described later in the manuscript, suggests that the product consists predominantly of graphene or partially opened CNTs, possibly formed via the unzipping of the MWCNT reactants. The unzipping reaction may be represented by equation (1)



Where G and G' represent the graphenes originating from the carboxylic and hydroxyl MWCNT (functionalized MWCNTs).

Results

Characterization. Attenuated total reflectance-Infrared Spectroscopy (ATR-IR) of the solid-state reaction product reveals almost complete absence of the COOH/O-H stretch in the region 3,600–2,800 cm⁻¹ (Fig. 2a), in agreement with water formation during the reaction. Also, the intensity of the carbonyl band due to either carboxylic group or keto-enol tautomer in the CNT-OH diminishes significantly with the appearance of the adsorbed asymmetric CO₂ mode at 2,345 cm⁻¹. Compatible with these conclusions is the large decrease in the bending infrared mode of the CNTs at 868 cm⁻¹ in the graphene product. The residual intensity is attributed to the unreacted CNTs. These results were further confirmed using X-ray photoelectron spectroscopic measurements.

In the C1s X-ray photoemission spectroscopy (XPS) of the MWCNTs, the signal at 289.2 eV corresponds to the carboxyl group, whereas the shoulders at 286.1 and 285.6 eV correspond to the C–O peak in MWCNT-COOH and MWCNT-OH, respectively^{15,31}. Upon grinding, these features diminish in intensity and the most dominant peak becomes that of C=C at 284.8 eV, as seen in Fig. 2b. This is a strong evidence in favour of a condensation reaction taking place between the COOH and the OH. In addition, according to XPS, oxygen content drops from 0.715% in the unreacted mixture to 0.280% in the observed solid product (XPS data, Supplementary Table 1). The water formed comes from the OH of the carboxylic acid and constitutes half the oxygen of the carboxylic group. The fact that the loss of oxygen (0.715–0.280 = 0.435%) is appreciably larger than half the amount of oxygen of the carboxylic group or oxygen of the hydroxyl group in the unreactive mixture is in agreement with a graphene, H₂O and CO₂ reaction, the yield of which is ~61% (Supplementary Table 1). This is comparable with the infrared data given before as well as with the simulation data presented later. To provide further evidence in favour of the graphene product from the solid-state reaction, we performed Raman spectroscopy of the reactant MWCNTs and that of the solid-state reaction product (Fig. 2c). All the bands in the product are upshifted relative to the reacting MWCNTs, whereas the second-order Raman band (2D) appearing at 2,705 cm⁻¹ is downshifted as compared with the graphite band at 2,714 cm⁻¹ (Fig. 2c). On the other hand, the 2D band in the product was well fitted by a sharp and symmetric Lorentzian in agreement with a few layer graphene-like product (Fig. 2c). The observations of lower 2D peak position relative to graphite, smaller I_D/I_G ratio (0.201) and larger I_{2D}/I_G ratio (1.21) for our reaction product are all in support of the formation of few layer graphene materials^{32,33}.

Water formation during the solid-state reaction between the MWCNTs was also established through an *in-situ* mass spectrometric study of the reaction products. This was performed as described in Supplementary Note 1. Briefly, the experiment involved conducting the solid-state reaction in an enclosed mortar and pestle and sampling of the gases formed directly with a quadruple mass spectrometer, in the mass range of 1–300 amu. A blank measurement was done first without any CNTs in order to estimate the contribution from atmospheric gases and moisture. MWCNT-COOH and MWCNT-OH (1:1 ratio by weight) were then taken in the mortar and ground using a pestle. The gases in the reaction vessel were then allowed into the mass spectrometer inlet by opening a valve (Supplementary Fig. 1a). Intensity of the peak at m/z 18 (due to H₂O⁺) increased significantly than in the blank experiment (Supplementary Fig. 1d). It is to be noted that there was no increase in intensity of nitrogen and oxygen ion currents. Increase in the H₂O⁺ peak intensity with no increase in N⁺ intensity (derived from N₂) clearly shows that this enhancement is due to the water resulting

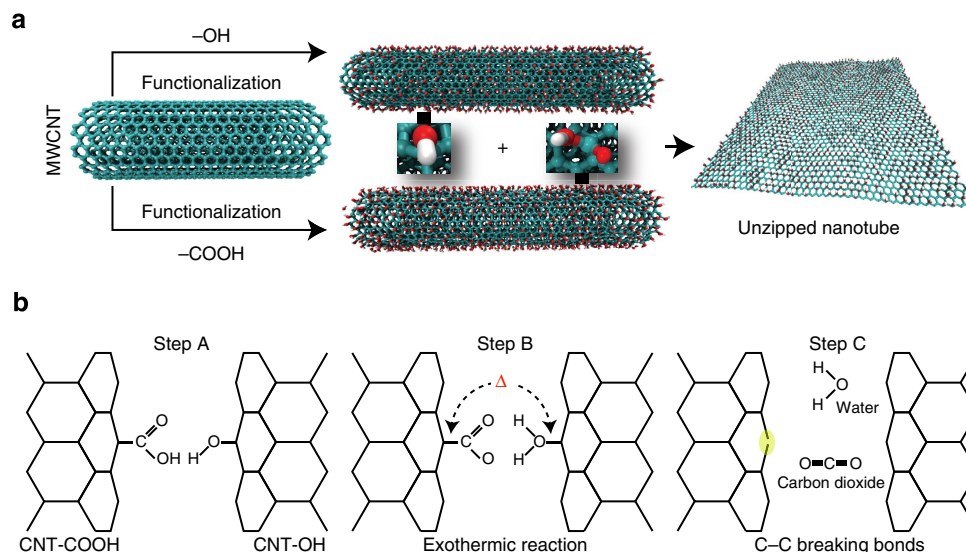


Figure 1 | General scheme of the current work. (a) Solid-state synthetic unzipping scheme. **(b)** Hydrogen bond-mediated proton transfer unzipping mechanism: (Step A) hydrogen-bond formation and (Step B) fast proton-transfer, are followed by (Step C) water and CO_2 as the products of the exothermic reaction. The released heat can induce the breaking of carbon-carbon bonds (highlighted yellow region) leading to unzipped tubes.

from solid-state condensation reaction between MWCNTs. No leak of atmospheric air would explain the increase in H_2O^+ as that would have resulted in an increase in N^+ intensity as well. Corresponding mass spectral (intensity versus m/z) data are given in Supplementary Fig. 1b, which also show that only H_2O^+ intensity increased after the reaction while N^+ and O^+ intensities remained the same. To check whether this increase is due to the desorption of water vapour that was adsorbed on MWCNTs, a control experiment was carried out (Supplementary Fig. 1c). Initially, a blank was measured without MWCNTs. MWCNTs were then kept in the mortar without grinding for 2 min and gases inside were sampled (after the evacuation step). Intensities of N^+ , O^+ and H_2O^+ were almost the same as that of the blank. After the mixture of MWCNTs was ground for 20 min, mass spectral measurement clearly showed an increase in intensity of only H_2O^+ . The OH and COOH functionalized MWCNTs were separately ground and no increase in H_2O^+ was detected in those cases. This shows that H_2O desorption from MWCNTs is not the reason for increased H_2O^+ intensity. No increase in CO_2 intensity was seen as it appears to be adsorbed effectively on the resulting graphene (see above).

Reproducibility of the results was confirmed by repeating these experiments several times with various ratios of the two MWCNT varieties. Furthermore, the decrease in the oxygen content, revealed from the XPS measurements, is supported by our mass spectrometric detection of water. Hence, the *in-situ* mass spectrometric experiments unambiguously give evidence for the solid-state condensation reaction between -COOH and -OH groups of the functionalized MWCNTs.

This was further supported with differential thermal analysis at different temperatures, which gave two distinct peaks, the more intense one occurs at $\sim 50^\circ\text{C}$, whereas the less intense one occurs at $\sim 110^\circ\text{C}$, shown in Supplementary Fig. 2. The peak at 110°C is due to the desorption of water. As the energy evolved at lower temperature is appreciably higher than that due to desorption of water and in light of the strong CO_2 /graphene adsorption, the intense peak is assigned to the desorption of CO_2 . This conclusion is compatible with the infrared and XPS data presented before.

The proposed reaction from above spectroscopic and thermal measurements is further verified using imaging techniques such

as scanning (SEM) and transmission electron microscopy (TEM). Figure 2e,f shows low and higher magnification SEM images revealing the structure of CNTs for the two functionalized raw materials. The amount of graphene-like material is negligible in these samples. On the other hand, the product powder shows predominantly sheet-like structure along with residues of partially reacted nanotubes (Fig. 2g,h). The image analyses of SEM images from different regions are used for calculating the amount of 2D sheets present and the residue of CNTs. The sheets are randomly distributed with a range of sizes with approximately 20% being unreacted CNT. To further confirm the opening of CNTs and the quality of the graphene-like product, TEM imaging was performed. Figure 3a shows bright-field image of the functionalized CNTs. It clearly shows CNTs to be multiwalled with an average diameter of 20 nm. The surfaces of the nanotubes appear disordered, due to heavy functionalization. Figure 3b shows large sheets of graphene-like material with smooth edges. The image shows multilayer structure. It is possible that the graphene flakes formed during the reaction have coalesced to form larger multilayer graphitic sheets. For further confirmation of the structure, selected area diffraction was performed. The result shows the hexagonal lattice of graphene stacks (shown as inset). Several images were taken for different samples of the product at different regions. Figure 3c,d shows products in the intermediate steps of the reaction. Several TEM images from different regions have been used for determining the number of layers in the multilayer sheets and the size of these graphene sheets. Histograms showing the size and number of layers formed due to the reaction are shown in Fig. 3e,f.

Kinetics of the reaction (and product formation) was monitored by measuring the intensity of the 2D Raman band of the graphene product at different temperatures^{30,34–36} (Supplementary Fig. 3). Arrhenius plot (detailed data given in Supplementary Table 2) of $\ln k$ versus $1/T$ (Supplementary Fig. 3) gives an activation energy of $16.63 \text{ kJ mol}^{-1}$ ($3.97 \text{ kcal mol}^{-1}$), a value compatible with the activation energies reported for solid-state hydrogen bond-mediated proton-transfer reactions between many organic compounds such as carboxylic acid/phenol and carboxylic acid/amine combinations^{37–44}.

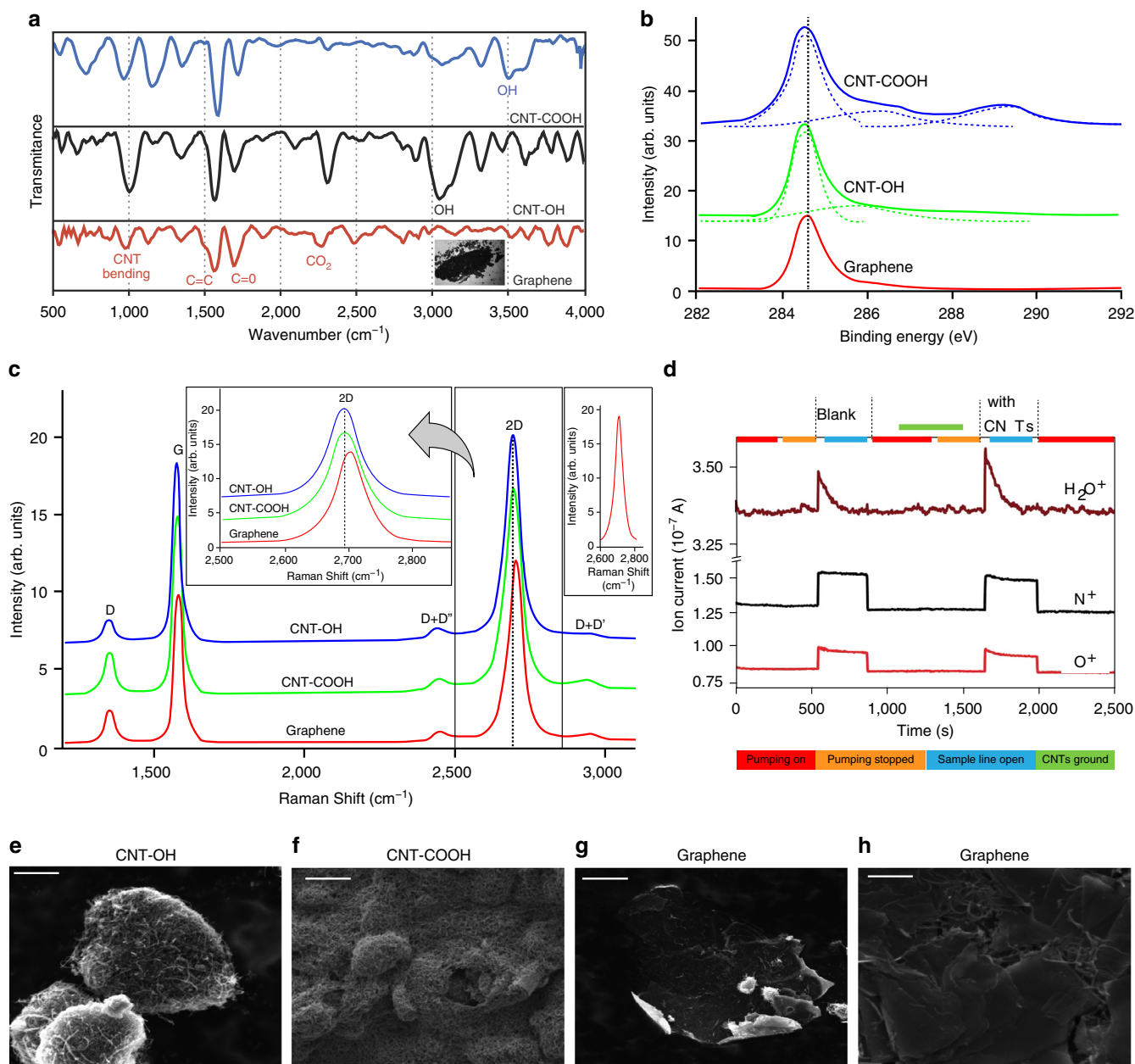


Figure 2 | Materials characterization. (a) ATR-IR spectroscopy of the solid-state reaction graphene product after grinding (red) as compared with MWCNTs starting material MWCNT-COOH (blue) and MWCNT-OH (black). Formation of water in the unzipping process is confirmed by the absence of the COOH/OH stretch band in the $3,600\text{--}2,800\text{ cm}^{-1}$ region of the graphene product. The inset shows an image of the product of the solid-state reaction of MWCNT-COOH and MWCNT-OH. The image shows the thin lustrous sheets of the graphene product formed due to the unzipping of the MWCNTs. These sheets are covered and surrounded with some traces of the unreacted CNTs. (b) High-resolution C1s XPS spectrum of the solid-state reaction graphene product obtained after grinding (red) as compared with MWCNTs starting material (blue and green). (c) Raman spectroscopy of the solid-state reaction mixture after grinding (red) as compared with MWCNTs starting material (green and blue). Insets show a 2D-band spectrum of the product as compared with those in the CNTs starting material, and a single-Lorentzian fit of the 2D band in the product. (d) Ion current versus time plots for N^+ , O^+ and H_2O^+ obtained using *in-situ* mass spectrometric measurements during the solid-state condensation reaction between MWCNTs. SEM image of the two reactants (e) CNT-COOH, scale bar, $2\ \mu\text{m}$; and (f) CNT-OH, scale bar, $2\ \mu\text{m}$. (g,h) The graphene nanosheet product along with residue of CNTs at two magnifications, scale bar: (g) $5\ \mu\text{m}$, (h) $1\ \mu\text{m}$.

CNT unzipping reaction. In light of the above, we suggest that the CNT unzipping reaction consists of a slow step that brings the CNTs together through mechanical grinding allowing the COOH and OH groups to react (Step A in Fig. 1b). Accordingly, this step is followed by fast proton transfer (Step B in Fig. 1c) from the carboxylic group to the hydroxyl group to form $[\text{MWCNT-OH}_2]^+$ and $[\text{MWCNT-COO}]^-$, whose exothermic reactions

produce water and CO_2 (Step C in Fig. 1d). The energy released can induce carbon-carbon bond breaking (highlighted yellow region) leading to unzipped structures.

Owing to the complexity of this process, simulations are divided into two parts. The first one is related to the estimation of the energy barriers associated with the chemical reactions between the CNT functional groups (value and determination of

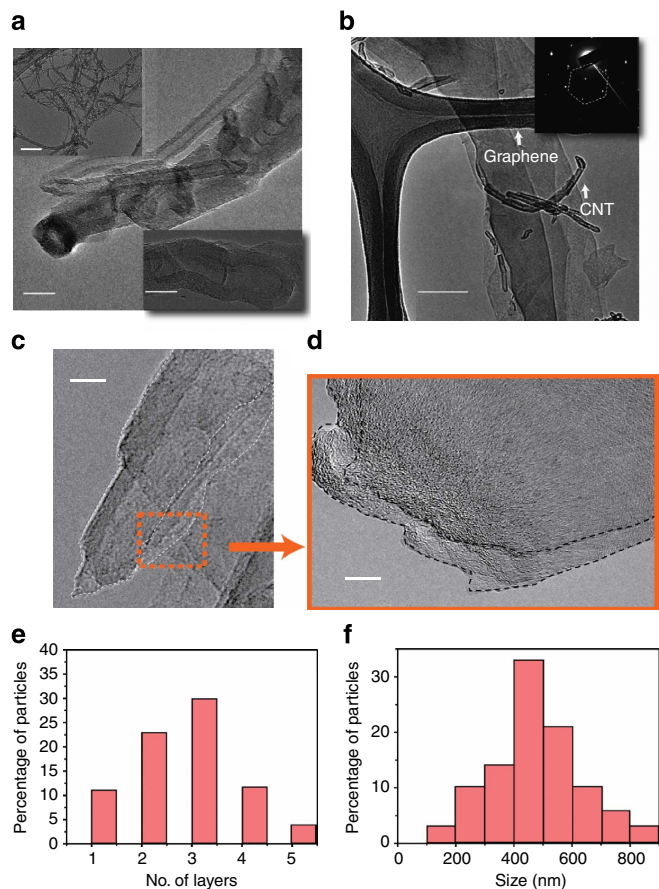


Figure 3 | TEM characterization. Bright-field TEM micrograph of the reactant (a) CNTs, scale bar, 20 nm, with insets showing low-magnification image, scale bar, 200 nm and another HRTEM image, scale bar, 5 nm. HRTEM, high-resolution transmission electron microscopy. (b) Graphene prepared using the current method, scale bar, 200 nm; inset showing diffraction pattern. The image shows multilayer structure. The selected area diffraction performed shows the hexagonal symmetry of graphene. The high-resolution image of these layered structures shows the hexagonal lattice arrangement of graphene. (c,d) The images of partially unzipped CNTs with different magnifications. Scale bar: (c) 10 nm, (d) 5 nm. (e,f) Histogram of number of layers and size, respectively, of the graphene sheets produced using the current method.

the thermodynamical character, exothermic or endothermic). In the second part, we have estimated the minimum required energy (threshold values, using ReaxFF^{45,46}) value to trigger the unzipping (breaking carbon bonds). The unzipping can produce partially or totally opened tubes, thus generating the nanoribbons. The obtained value was then contrasted against the estimated energy released during the chemical reactions. This approach is schematically presented on Fig. 4a–c. The barrier results (Fig. 4d) were obtained through nudged elastic band (NEB) simulations. NEB is one of the standard methods used to determine energy barrier height and the chemical pathways of chemical reactions, assuming the reactants and products are known^{47–49}. Density functional theory calculations (see Supplementary Methods) support the experimental interpretation that water and carbon dioxide are the final products of the reactions between the CNT functional groups (initial and the final states are presented in Fig. 4d).

Energy barrier calculations were performed for different CNT distances (3.5 to 4.0 Å, with stepsize increments of 0.05 Å; see Supplementary Fig. 5). These values were chosen over a range

where it is expected that reaction (3.5 Å) and no reaction (4.0 Å) can occur. Some of these curves are shown in Fig. 4d. The slight differences from the reference values (for instance, 3.88 instead of 3.90) are a consequence of the initial geometry optimization process. Our results indicate that the lowest energy barrier can occur for tubes separated by ~ 3.7 Å, with an associated energy barrier height around 30 kcal mol^{-1} . More detailed information can be obtained from the Supplementary Movie 1.

From these results, we can conclude that these reactions need to be energy assisted. The energy needed to overcome the reaction barriers of CNTs opening can be provided by the exothermic reaction between the carboxylic acid and alcohol functionalities, which in turn provides necessary amount of energy for the cleavage of carbon–carbon bonds and consequently the unzipping of the CNTs. The main mechanical grinding effect is only to bring the CNTs closer. Maximizing the contact area through total or partial axial tube alignment during the grinding, appears to be the key to maximize the number of reactions to produce totally or partially unzipped tubes, which is consistent with the available experimental data. Our results also showed that this reaction is exothermic, which is in agreement with more refined density functional theory calculations that indicate that the released energy is about 25 kcal mol^{-1} (see Supplementary Methods for details). This injected energy can result in thermal (increasing the temperature around the region where the reaction occurred) and/or mechanical (eventual C–C bond breaking) effects, thus leading to tube unzipping, as recently demonstrated by molecular dynamics (MD) simulations⁵⁰.

In the second step, to estimate the minimum amount of energy needed to trigger the unzipping process, we have carried out a systematic MD study. Our models were composed of MWCNTs, where for simplicity of the inner-layers are kept frozen. This approach has been proved effective in the unzipping of carbon⁵¹ and boron nitride⁵² tube studies. To mimic the injected energy generated by the chemical reactions, we used the so-called heating spot protocol^{53,54} (LAMMPS Software manual (<http://lammps.sandia.gov>)). Using this protocol, we randomly added non-translational kinetic energy (heat) to selected atoms within a subregion defined as ‘contact area’ (highlighted strip in Fig. 4e). The atoms belonging to the ‘contact region’ can be thought as the ones that would be in contact with an adjacent tube during the grinding procedure. The investigated injected energy range was from 1.0 up to 30 kcal mol^{-1} (the barrier values). These results are presented in Fig. 4f (limited to the range of 1.5 up to $5.0 \text{ kcal mol}^{-1}$). The percentage of C–C broken bonds is shown for each heating spot value. When the heat transferred to the system is up to $2.0 \text{ kcal mol}^{-1}$, the amount of broken bonds is around 0.3%, which is not enough to produce the tube unzipping. Increasing the heat up to $3.0 \text{ kcal mol}^{-1}$, the number increases to 1.0%, which is enough to create some defects in the tube (red shaded region—Fig. 4f). When the heat delivered to the system is higher than $3.5 \text{ kcal mol}^{-1}$, the amount of broken bonds reaches 1.6%, which is enough to break up the tube along its main axial direction and to produce the unzipping effect (grey shaded region—Fig. 4f). These results show that only a small fraction (in this case, only 14%) of the estimated energy released by the chemical reactions would be enough to provide C–C broken bonds and to trigger the unzipping process.

Discussion

In conclusion, we have reported, for the first time, ambient solid-state mechano-chemical (through simple mechanical grinding) reactions between CNT-COOH and CNT-OH resulting in unzipped nanotubes. The released heat during the process results in C–C bond breaking, which subsequently leads to CNT

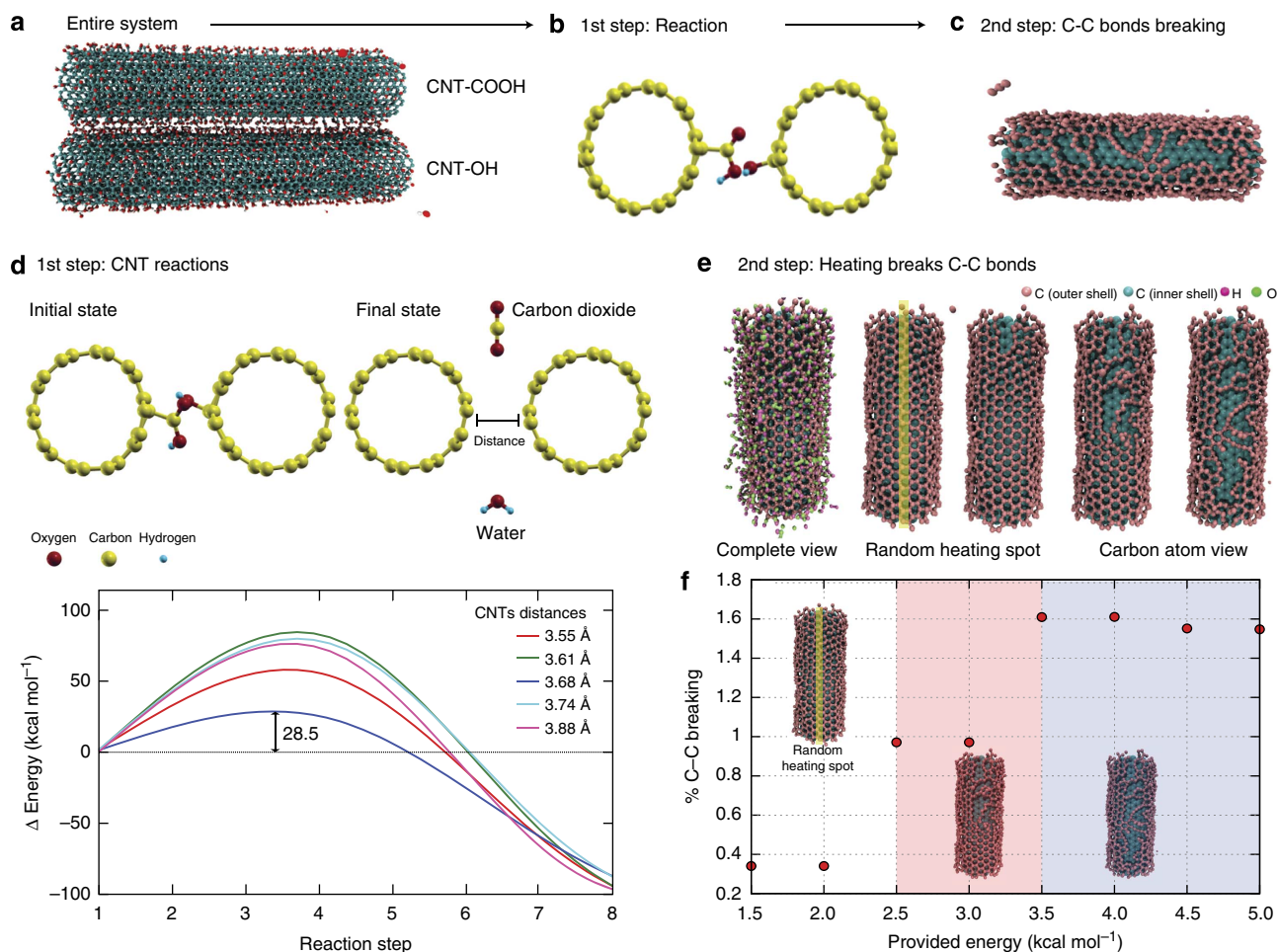


Figure 4 | Simulation of the process. (a) General scheme for the simulated unzipping process; (b) functionalized tubes (CNT-COOH and CNT-OH); (c) initial configuration for energy barrier reaction calculation and resultant unzipped nanotubes. (d) Reactants (different functionalized tubes) and products (tubes, water and carbon dioxide) of the simulated reaction and the corresponding energy barrier values for different tube separations. (e) Schematic view of simulated unzipping process: Initial configuration showing the functionalized tube. For better visualization, the CNT functional groups were made transparent in the following four representative unzipping steps. The yellow line indicates the region where the heating spot was applied. (f) The percentage of C-C bond breaking and the corresponding final configuration for different energies of the heating spot.

unzipping. The proposed method can be used as a generic approach to develop new theoretical and synthetic frameworks where reactions could be designed and controlled via chemically modified solid reactants.

Methods

Synthesis and reactions of CNTs. MWCNTs were prepared by using water-assisted chemical vapour deposition (WACVD) on a Si substrate. Si wafer, on which 10 nm aluminum and 1.5 nm iron layers were deposited via electron beam, was placed in a quartz tube and heated to 775 °C in Ar/H₂ buffer having 15% of H₂-ethylene gas and water vapour were introduced in the quartz tube for 30 min.

Iron impurity from the nanotubes was removed by suspending them overnight in 2.6 M nitric acid at 120 °C. After that the nanotubes were separated by filtration using 0.2 μm GTTP Millipore membrane and washed extensively with water and dried. MWCNT-COOH and MWCNT-OH were prepared from pristine CNTs according to the procedures in refs 1,3, respectively.

The unzipping reaction was done by grinding equal weights of MWCNT-COOH and MWCNT-OH. In current experiment, two different sizes of mortars and pestles (made up of Traditional Agate) with radii of 2.5 and 5 cm were used. Initial experiments are performed using mortar of 5 cm radii and then the same has been repeated for 2.5 cm radii. The samples were collected at different time duration (5, 10, 15 and 20 min). Among all these, the 20-min grinding shows best yield, which is reported in the manuscript. We start observing change in the initial time itself but as the duration of grinding increases, the yield increases as can be observed as lustrous sheets are formed during grinding. As for the reproducibility of the results, the reaction was reproduced in three different labs in three different countries (Professor Ajayan's Lab in Houston (USA), Professor Pradeep's lab in India (Chennai) and Professor Ahmad Kabbani's lab in Lebanon (Beirut)) by

different colleagues and collaborators involved in this paper. As for the environment and temperature, this reaction was done in different environments under vacuum, different labs (that has controlled humidity and temperature) and also outside in open air as well in variable humidity, different temperatures and in different times, seasons and countries (Houston (USA), India (Chennai), Lebanon (Beirut)).

Materials characterization. Raman spectra were measured using a Renishaw Raman spectrometer at 514.5 nm excitation. The variable temperature Raman study was carried out by bringing MWCNT-COOH and MWCNT-OH to same temperatures before grinding them. Grinding was done in a separate vessel at the same temperature. All reaction mixtures were quenched to room temperature before Raman spectra were recorded. 2D line intensities at different temperatures were normalized to the same 2G line intensities. XPS spectra were measured using a Surface Science Instrument SSX-100. SEM image was obtained by using FEI Quanta 400 SEM. TEM image was obtained using a JEOL 2100F TEM. Imaging has been performed using field emission electron microscope with a low current density and low accelerating voltage. Mass spectrometric measurements were carried out using a residual gas analyser (BalzersThermostat with Quadstar 32 bit software). This instrument is basically a residual gas analyser, equipped with an electron impact ionization source and a quadrupole mass analyser. For measurements, we utilized multiple ion detection modes. In multiple ion detection, we measured ion current as a function of time.

Simulation methodology. We used the ReaxFF force field with parameter set from refs 45,46. This parameter set is optimized for structures containing the elements carbon, hydrogen and oxygen, thus appropriated to our systems. For the NEB calculations, we considered eight replicas between the initial and final

configurations. The ‘spring’ that connects each replica has a constant force of $10 \text{ kcal/mol}^{-1} \text{ \AA}^{-1}$. The adopted criterion for NEB convergence was energy differences below $1.0 \times 10^{-4} \text{ kcal mol}^{-1}$. All the calculations using ReaxFF and/or NEB were carried out using the LAMMPS code^{52,53}. For the MD simulations of the CNT unzipping processes, the addition of heat (through the heat spot protocol) into the system is performed every 1.0 ps during 50 ps. The heat is added to the atoms belonging to a circular (4 \AA radius value). We also tested different circle radii values, ranging from 3 to 6 \AA , but no significant differences in the results were observed.

References

- Schulz-Dobrick, M., Sarathy, K. V. & Jansen, M. Surfactant-free synthesis and functionalization of gold nanoparticles. *J. Am. Chem. Soc.* **127**, 12816–12817 (2005).
- Zatas, M., Katz, E., Baron, R. & Willner, I. Reconstitution of Apo-Glucose dehydrogenase on pyrroloquinoline quinone-functionalized Au nanoparticles yields an electrically contacted biocatalyst. *J. Am. Chem. Soc.* **127**, 12400–12406 (2005).
- Wang, L., Wang, L., Zhu, C., Wei, X. & Kan, X. Preparation and application of functionalized nanoparticles of CdS as a fluorescence probe. *Anal. Chim. Acta.* **468**, 35–41 (2005).
- Shenhar, R., Norsten, T. B. & Rotello, V. M. Polymer-mediated nanoparticle assembly: Structural control and applications. *Adv. Mater.* **17**, 657–669 (2005).
- Liu, H. & Alivisatos, A. P. Preparation of asymmetric nanostructures through site selective modification of tetrapods. *Nano Lett.* **4**, 2397–2401 (2004).
- Tomalia, D. A. Birth of a new macromolecular architecture: dendrimers as quantized building blocks for nanoscale synthetic polymer chemistry. *Prog. Polym. Sci.* **30**, 294–324 (2005).
- Iijima, S. Helical microtubules of graphitic carbon. *Nature* **354**, 56–58 (1991).
- Jariwala, D., Sangwan, V. K., Lauhon, L. J., Marks, T. J. & Hersam, M. C. Carbon nanomaterials for electronics, optoelectronics, photovoltaics, and sensing. *Chem. Soc. Rev.* **42**, 2824–2860 (2013).
- Jeng, E. S., Moll, A. E., Roy, A. C., Gastala, J. B. & Strano, M. S. Detection of DNA hybridization using the near-infrared band-gap fluorescence of single-walled carbon nanotubes. *Nano Lett.* **6**, 371–375 (2006).
- Kovtyukhova, N. I., Mallouk, T. E., Pan, L. & Dickey, E. C. Individual single-walled nanotubes and hydrogels made by oxidative exfoliation of carbon nanotubes ropes. *J. Am. Chem. Soc.* **125**, 9761–9769 (2003).
- Liu, J. *et al.* Fullerene pipes. *Science* **280**, 1253–1256 (1998).
- Worsley, K., Kondrat, R., Pal, S., Kalinina, I. & Haddon, R. Isolation and identification of low molecular weight carboxylated carbons derived from the nitric acid treatment of single-walled carbon nanotubes. *Carbon* **49**, 4982–4986 (2011).
- Niyogi, S. *et al.* Chemistry of single-walled carbon nanotubes. *Acc. Chem. Res.* **35**, 1105–1113 (2002).
- Liu, Z. *et al.* Organizing single-walled carbon nanotubes on gold using chemical self-assembling techniques. *Langmuir* **16**, 3569–3573 (2000).
- Yang, D., Guo, G., Hu, J., Wang, C. & Jiang, D. Hydrothermal treatment to prepare hydroxyl group modified multi-walled carbon nanotubes. *J. Mater. Chem.* **18**, 350–354 (2008).
- Zhu, S. E., Fei, F. L. & Wang, G. W. Mechanochemistry of fullerene and related materials. *Chem. Soc. Rev.* **42**, 7535–7570 (2013).
- Drexler, K. E. *Nanosystems: Molecular Machinery, Manufacturing, and Computation* (John Wiley and Sons, 1992).
- Wang, G. W., Komatsu, K., Murata, Y. & Shiro, M. Synthesis and X-ray structure of dumb-bell-shaped C_{120} . *Nature* **387**, 583–584 (1997).
- Komatsu, K., Fujiwara, K., Tanaka, T. & Murata, Y. The fullerene dimer C_{120} and related carbon allotropes. *Carbon* **38**, 1529–1532 (2000).
- Kunitake, M. *et al.* First structural analysis of C_{60} trimers by direct observation with STM. *Angew. Chem. Int. Ed.* **41**, 969–972 (2002).
- Komatsu, K., Fujiwara, K. & Murata, Y. The fullerene cross dimer C_{130} : Synthesis and properties. *Chem. Commun.* **2000**, 1583–1584 (2000).
- Li, X. *et al.* C_{60} modified single-walled carbon nanotubes. *Chem. Phys. Lett.* **377**, 32–36 (2003).
- Holzinger, M. *et al.* Functionalization of single-walled carbon nanotubes with (R)-oxycarbonylnitrenes. *J. Am. Chem. Soc.* **125**, 8566–8568 (2003).
- Dyke, C. A. & Tour, J. Solvent-free functionalization of carbon nanotubes. *J. Am. Chem. Soc.* **125**, 1156–1158 (2003).
- Pan, H. *et al.* Carbon nanotubes from mechanochemical reaction. *Nano Lett.* **3**, 29–32 (2003).
- Smith, B. M., Monthioux, M. & Luzzi, D. L. Encapsulated C_{60} in carbon nanotubes. *Nature* **396**, 323–325 (1998).
- Novoselov, K. S. *et al.* Electric field effect in atomically thin carbon films. *Science* **306**, 666–669 (2004).
- Coleman, J. N. *et al.* Two-dimensional nanosheets produced by liquid exfoliation of layered materials. *Science* **331**, 568–571 (2011).
- Hersam, M. C. *et al.* Chemically resolved interface structure of epitaxial graphene on SiC (0001). *Phys. Rev. Lett.* **111**, 215501 (2013).
- Jiao, L., Wang, X., Diankov, G. & Dai, H. Narrow graphene nanoribbons from carbon nanotubes. *Nature* **458**, 877–880 (2009).
- Kosynkin, D. V. *et al.* Longitudinal unzipping of carbon nanotubes to form graphene nanoribbons. *Nature* **458**, 872–876 (2009).
- Graf, D. *et al.* Spatially resolved Raman spectroscopy of single and few layer graphene. *Nano Lett.* **7**, 238–242 (2007).
- Ferrari, A. C. & Basko, D. M. Raman spectroscopy as a versatile tool for studying the properties of graphene. *Nat. Nanotechnol.* **8**, 235–246 (2013).
- He, R. *et al.* Observation of low energy raman modes in twisted bilayer graphene. *Nano Lett.* **13**, 3594–3601 (2013).
- Ruoff, R. *et al.* Selective-area fluorination of graphene with fluoropolymer and laser irradiation. *Nano Lett.* **12**, 2374–2378 (2012).
- Ferrari, A. C. *et al.* Raman spectrum of graphene and graphene layers. *Phys. Rev. Lett.* **97**, 187401 (2006).
- Stevens, J. *et al.* Proton transfer and hydrogen bonding in the organic solid state. *Phys. Chem* **16**, 1150–1160 (2014).
- Koeppe, B., Tolsay, P. & Limbach, H. Reaction pathways of proton transfer in hydrogen-bonded phenol-carboxylate complexes. *J. Am. Chem. Soc.* **133**, 7897–7908 (2011).
- Hynes, J., Klinman, J., Limbach, H. & Schowen, R. *Hydrogen Transfer Reactions 1–4* (WILEY-vch, 2007).
- Bertran, J. F., Alvarez, J. & Reguera, E. Proton transfer in the solid state: Reactions of organic acids and amines. *Solid State Ionics* **106**, 129–135 (1998).
- Fernández-Bertrán, J. & Reguera, E. Proton transfer in the solid state: mechanochemical reactions of fluorides with acidic substances. *Solid State Ionics* **112**, 351–354 (1998).
- Vinogradov, S. N. & Linnell, R. H. *Hydrogen bonding* (Von Nostrand Reinhold Company, 1971).
- Steiner, T. & Saenger, W. Lengthening of the covalent O–H bond in O–H...O hydrogen bonds. reexamination from low-temperature neutron diffraction data of organic compounds. *Acta Crystallogr* **B50**, 348–357 (1994).
- Limbach, H. H., Deniisov, G. S. & Golubev, N. S. *Hydrogen Bond Isotope Effects Studied by NMR, in isotopes effects in the biological and chemical sciences.* (eds Kohen, A. & Limbach, H. H.) Ch 7 (Taylor and Francis, 2005).
- VanDuijn, A. C. T., Dasgupta, S., Lorant, F. & Goddard, W. A. ReaxFF: a reactive force field for hydrocarbons. *J. Phys. Chem A* **105**, 9396–9409 (2001).
- Chenoweth, K., van Duin, A. C. T. & Goddard, W. A. ReaxFF reactive force field for molecular dynamics simulations of hydrocarbon oxidation. *J. Phys. Chem. A* **112**, 1040–1053 (2008).
- Henkelman, G. & Jónsson, H. Improved tangent estimate in the nudged elastic band method for finding minimum energy paths and saddle points. *J. Chem. Phys.* **113**, 9978–9985 (2000).
- Henkelman, G., Uberuaga, B. P. & Jónsson, H. A climbing image nudged elastic band method for finding saddle points and minimum energy paths. *J. Chem. Phys.* **113**, 9901–9904 (2000).
- Nakano, A. A space–time-ensemble parallel nudged elastic band algorithm for molecular kinetics simulation. *Comp. Phys. Commun.* **178**, 280–289 (2008).
- Santos, dos, R. P. B., Perim, E., Autreto, P. A. S., Brunetto, G. & Galvão, D. S. On the unzipping of multiwalled carbon nanotubes. *Nanotechnology* **23**, 465702 (2012).
- Perim, E., Autreto, P. A. S., Paupitz, R. & Galvão, D. S. Dynamical aspects of the unzipping of multiwalled boron nitride nanotubes. *Phys. Chem. Chem. Phys.* **15**, 19147 (2013).
- Plimpton, S. Fast parallel algorithms for short-range molecular dynamics. *J. Comput. Phys.* **117**, 1–19 (1995).
- Jund, P. & Jullien, R. Molecular-dynamics calculation of the thermal conductivity of vitreous silica. *Phys. Rev. B* **59**, 13707–13711 (1999).
- Chantrenne, P. & Barrat, J.-L. Finite size effects in determination of thermal conductivities: comparing molecular dynamics results with simple models. *J. Heat Transfer* **126**, 577–585 (2004).

Acknowledgements

This work has been supported by US Department of Defense: US Air Force of Scientific Research for the Project MURI: ‘Synthesis and Characterization of 3-D Carbon Nanotube Solid Networks’ Award No. FA9550-12-1-0035. P.A.S.A. acknowledge financial support from the Brazilian Agencies CNPq, CAPES and FAPESP and also thanks the Center for Computational Engineering and Sciences at Unicamp for financial support through the FAPESP/CEPID Grant #2013/08293-7. Work at IIT Madras was supported by a grant through the Nano Mission, Government of India. Part of work was done while MAK was a visiting student at IIT Madras. P.M.A thanks IIT Madras for a Distinguished Visiting Professorship.

Author contributions

M.A.K. and A.T.K. proposed the project. M.A.K. and C.S.T. designed and conducted experiments. P.A.S.A., G.B. performed and D.S.G. supervised the MD simulation. A.S., K.R.K., S.O., K.H., Y.G. helped in characterization. A.S., K.R.K. performed and T.P. supervised the mass spectral measurements. T.P. proposed the mechano-chemical

name for the reaction. M.A.K., C.S.T., R.V., D.S.G., T.P., A.T.K. and P.M.A. analysed the data and wrote the paper. All authors discussed and revised the final manuscript.

Additional information

Supplementary Information accompanies this paper at <http://www.nature.com/naturecommunications>

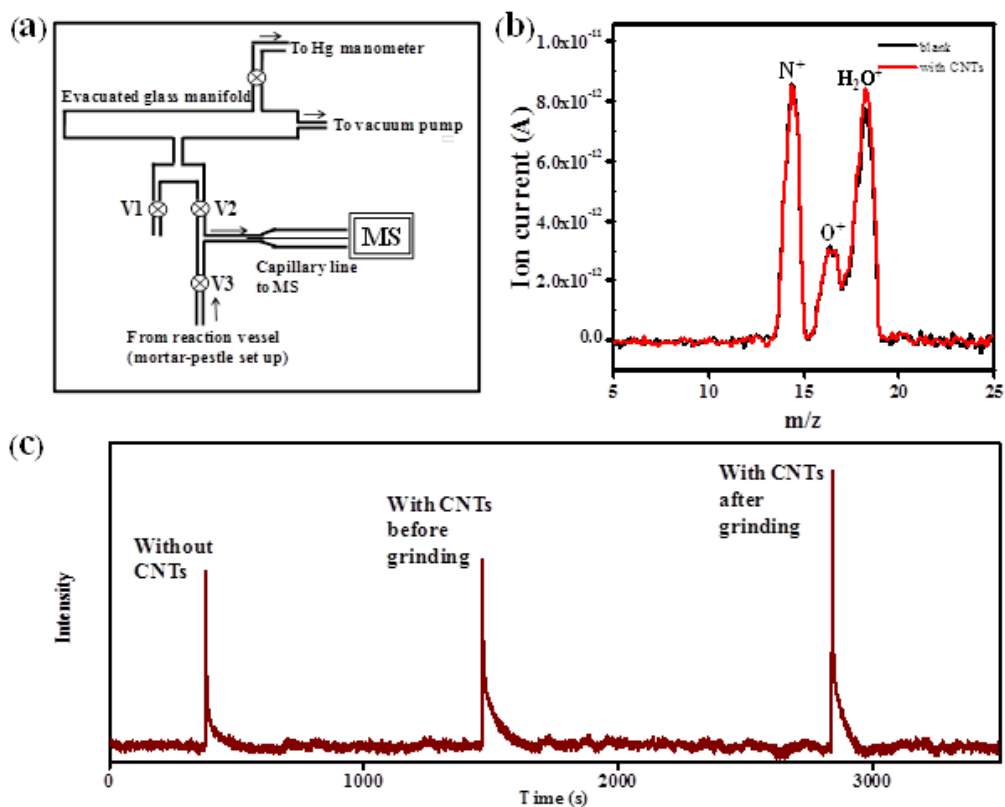
Competing financial interests: The authors declare no competing financial interests.

Reprints and permission information is available online at <http://npg.nature.com/reprintsandpermissions/>

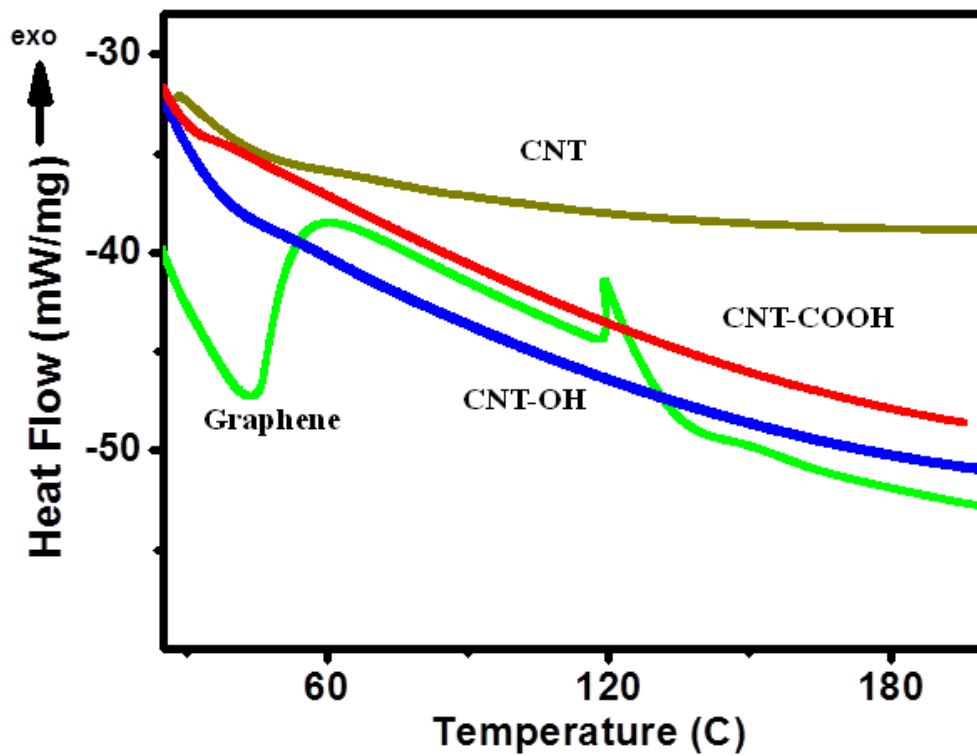
How to cite this article: Kabbani, M. A. *et al.* Ambient solid-state mechano-chemical reactions between functionalized carbon nanotubes. *Nat. Commun.* 6:7291 doi: 10.1038/ncomms8291 (2015).



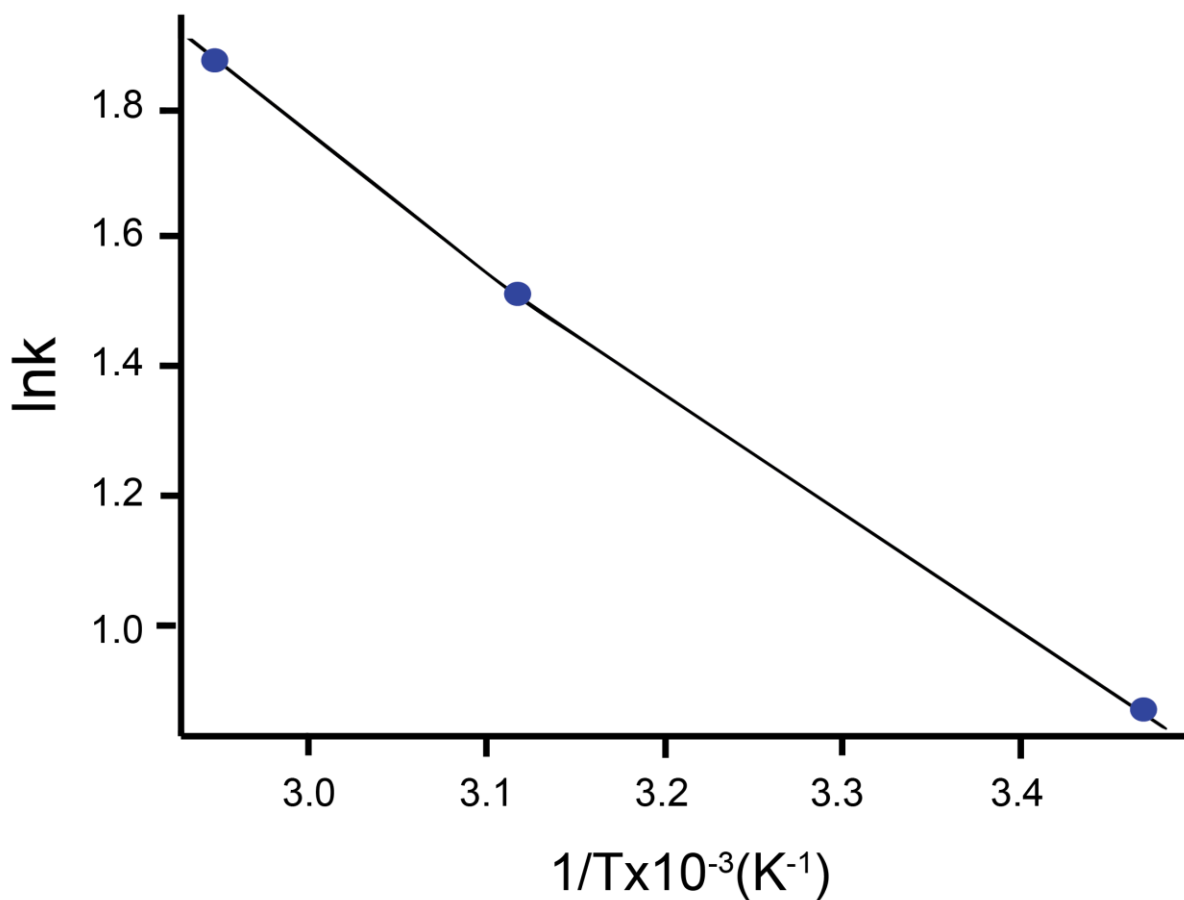
This work is licensed under a Creative Commons Attribution 4.0 International License. The images or other third party material in this article are included in the article's Creative Commons license, unless indicated otherwise in the credit line; if the material is not included under the Creative Commons license, users will need to obtain permission from the license holder to reproduce the material. To view a copy of this license, visit <http://creativecommons.org/licenses/by/4.0/>



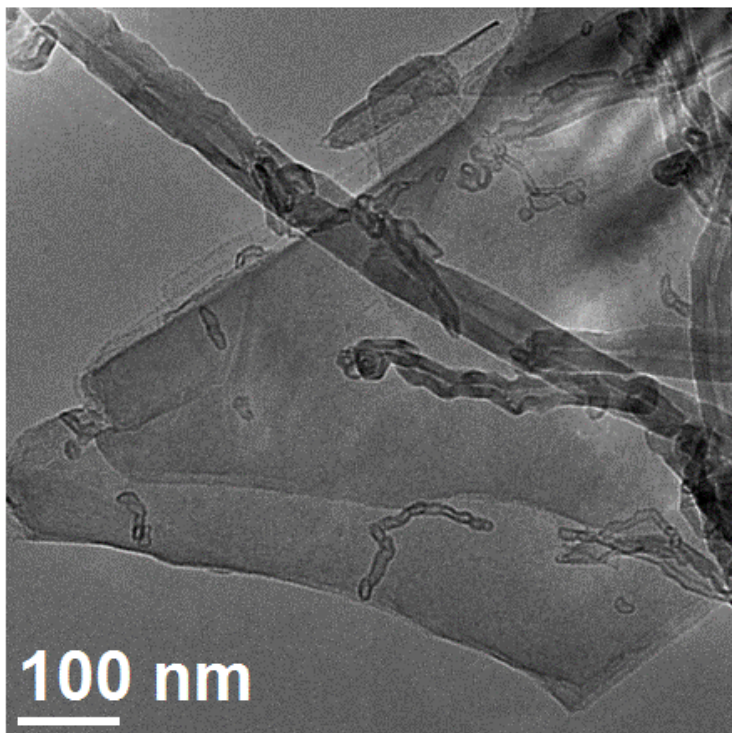
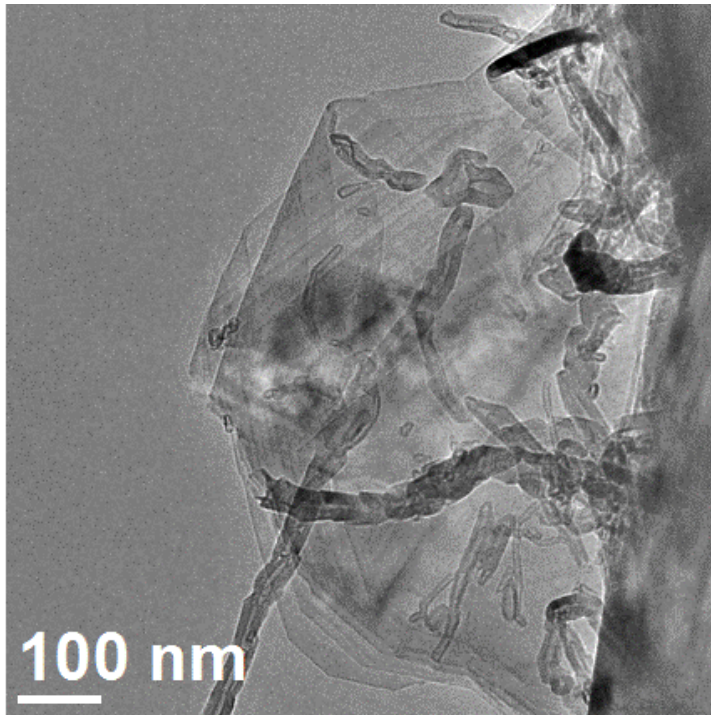
Supplementary Figure 1: (a) Schematic of the experimental set up for the online mass spectrometric detection of water during the solid state condensation reaction between MWCNTs, (b) Mass spectra showing the changes in N^+ , O^+ and H_2O^+ intensities for the blank and the sample after grinding and (c) Ion current vs. time plots for H_2O^+ for blank (without MWCNTs), with MWCNTs before grinding and after grinding.



Supplementary Figure 2: DTA of individual unmixed CNTs and that of the graphene product. First peak is due to desorption of CO₂ while the second is due to desorption of water

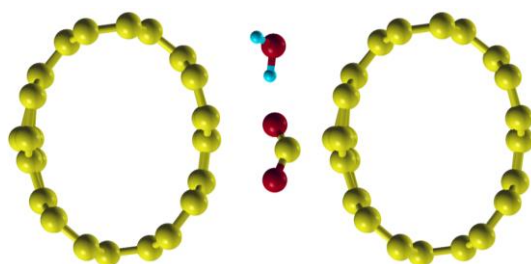


Supplementary Figure 3: In order to evaluate activation energy of the chemical reaction, a variable temperature Raman study was carried out. The two reactants, MWCNT-COOH and MWCNT-OH were mixed and ground at two temperatures (60, 70 °C) on hot plate. The reaction mixtures were quenched to room temperature before the Raman spectra were recorded; this was done for each temperature separately. The intensities of 2D Raman peaks have been used to calculate the rate constants as listed in Table.2. Arrhenius plot of lnk vs. 1/T. Slope = $-R/E_{act} = -2.00 \times 10^3$

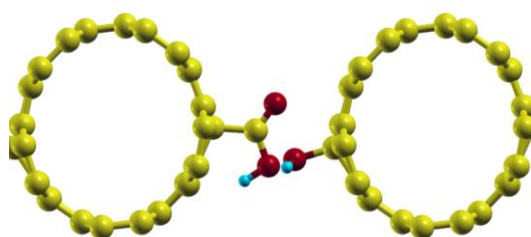


Supplementary Figure 4: Bright field TEM images of graphene observed at different places and in different samples.

(a) $d_{\text{tubes}}=3.5 \text{ \AA}$



(b) $d_{\text{tubes}}=4.5 \text{ \AA}$



Supplementary Figure 5: (a) Geometric optimized structures for nanotubes initially placed at 3.5 \AA , which results in the formation of H_2O and CO_2 . (b) When the distance between the tubes is increased to 4.5 \AA no reaction is observed and the functional groups remain attached to their parent tubes.

Supplementary Table 1: Table 1: % of Oxygen XPS data

Material	% Oxygen
MWCNT-OH	0.430
MWCNT-COOH	1.000
Unreactive mixture	0.715
Solid product after heating to a constant weight at 110 °C	0.280

Calculation of oxygen content:

Expected % oxygen after 60 % yield reaction = $0.715 \times 0.4 = 0.286$

Amount of reacted oxygen due to simple esterification reaction = $0.5/2 = 0.25\% \ll 0.715 - 0.280$
= 0.435% = observed amount of reacted oxygen. This represents $\sim 0.6 \times 0.715 = 0.429\%$ or expected 60% yield oxygen reacted.

Supplementary Table 2: Variable temperature 2D intensity data

T, K	Intensity of the 2D Raman band (au)	ln k	1/T, K⁻¹
286	2.3	0.833	3.497×10^{-3}
319	4.5	1.504	3.134×10^{-3}
341	7.0	1.946	2.932×10^{-3}

Supplementary Note 1

Details of the mass spectrometric measurements for the detection of water

For online monitoring of the reaction, we used a set up schematically shown in Supplementary Fig. 1a. Initially, a mortar and pestle were kept enclosed in a nitrile glove with the pestle protruding through one of its fingers. The glove was then connected to the mass spectrometer inlet using a glass tube through another finger of the glove. In order to ensure that this set up was adequate to detect tiny amounts of water vapor, we placed a drop of water in the mortar and allowed its vapors into the mass spectrometer. We could detect the expected features. To further confirm the adaptability of the method, we heated $\text{CuSO}_4 \cdot 5\text{H}_2\text{O}$ at $63\text{ }^\circ\text{C}$ (at which the loss of two water molecules happens). Here also, we were able to detect water lost from these crystals. These experiments showed that our method was adequate for monitoring the MWCNT reactions. For monitoring the reactions, the set-up was evacuated after keeping the reagents inside the reaction vessel and Valve 3 (see Supplementary Fig. 1a) was closed. After grinding the ingredients for 20 minutes to complete the reaction, Valve 3 was opened and the vapor phase in the reaction vessel was sampled. Changes in the partial pressures of the constituents were evaluated. A blank experiment was performed under the same conditions without the sample, but with equal time for evacuation and reaction. This was done to ensure that artifacts due to potential leaks were avoided. From a quantitative evaluation of the changes in partial pressures, the yield was calculated.

In main figure Fig. 2d, the first peak (for H_2O^+)/first steps (for N^+ and O^+) correspond to blank measurement while second peak/steps correspond to measurement after grinding MWCNTs. For measuring the blank, at first, we kept the valves 1 and 3 closed and 2 open, the whole sample line was then evacuated for 2 h through a glass manifold using a rotary pump (see Supplementary Fig. 1a). Then valve 2 was closed and allowed the residual gases

(N₂ and O₂) and water content present in the volume of this enclosure to mass spectrometer by opening valve 3. Since the gases and moisture enclosed in the reaction vessel enter the mass spectrometer chamber, there was an increase in N⁺, O⁺ and H₂O⁺ intensities (see the first rise in intensity for all traces in the main figure Fig. 2d). After certain time interval, valve 3 was closed and sample line was evacuated for some time (by opening valve 2). Due to this, intensity of all ions drops to initial value (see the fall in intensity of all traces in the first steps/peak of the main figure Fig. 2d). The sample line was pumped for some more time (to reset the base intensities). This finishes the blank measurement. Then, valve 2 was closed; MWCNTs were put into the mortar, ground vigorously. Valve 2 was now closed, and valve 3 was opened allowing the gaseous products into the mass spectrometer capillary for measurement. This result in second rise in intensities of N⁺, O⁺ and H₂O⁺ (see the second rise in intensities for all traces in the main figure Fig. 2d). Please note that intensity of second H₂O⁺ peak (i.e. after grinding MWCNTs) is significantly higher compared to that of blank. This increase is due to the excess amount of water formed due to MWCNTs reaction. After some time, valve 3 was closed; sample line was again pumped, resulting in drop in intensities. This completes a typical experiment. Always, each experiment was carried out by doing a blank one first, followed by the actual sample measurement. Both these were done in a single run, of about one hour duration, to avoid errors that may result from variations in vacuum and the detector response. Mass spectrometer was baked at 100 °C for 24 h prior to any measurement and kept at baking condition during measurements. Also, to avoid condensation of moisture in the mass spectrometer capillary line, it was kept at 150 °C throughout the experiment.

We carried out Density Functional Theory (DFT)¹⁻³ geometry optimizations for model systems in order to investigate the reactions between the functional CNT groups and to validate the results obtained using ReaxFF. For these DFT calculations we did not carried out

a systematic study varying the tube distances. Due to the high computational cost, we just investigated two limit cases: (a) tubes closer enough ($\sim 3.5 \text{ \AA}$) to be reactive, and (b) tubes well separated ($\sim 4.5 \text{ \AA}$), where no chemical reactions are expected to occur and (See Fig. S5). Our results showed that, as expected, the functional groups remain attached to the CNT when the distance is 4.5 \AA (Fig. S5(b)). For the case of an initial 3.5 \AA distance, the geometrical optimization processes lead the functional groups to react, yielding water and carbon dioxide (Fig. S5(a)). The obtained energy difference between the reactants and products was of 24.8 kcal/mol (indicating an exothermic reaction), this energy can be released as heat into the system.

Supplementary Methods

The DFT calculations were carried out within a local density approximation (LDA)⁴ and using the Perdew-Wang functional⁵, as implemented in the Quantum Espresso code⁶. The wave functions were expanded using a standard Plane Wave (PW) basis set⁷. Wavefunctions up to 40 Ry of kinetic energy were considered. A grid of 6×6×1 in the k-space was sampled using the Monkhorst-Pack method⁸.

Supplementary References

1. Fiolhais, C., Nogueira, F. & Marques, M. A. *A primer in density functional theory*. **620**, (Springer, 2003).
2. Koch, W. & Holthausen, M. C. *A chemist's guide to density functional theory*. (Wiley-VCH Verlag GmbH, 2000).
3. Martin, R. M. *Electronic Structure*. (Cambridge University Press, 2008).
4. Kohn, W. & Sham, L. J. Self-Consistent Equations Including Exchange and Correlation Effects. *Phys. Rev.* **140**, A1133–A1138 (1965).
5. Perdew, J. P. & Wang, Y. Accurate and Simple Analytic Representation of the Electron-Gas Correlation-Energy. *Phys. Rev.* **B45**, 13244–13249 (1992).
6. Giannozzi, P. *et al.* QUANTUM ESPRESSO: a modular and open-source software project for quantum simulations of materials. *J. Phys.: Condens. Matter* **21**, 395502 (2009).
7. Dabo, I., Kozinsky, B., Singh-Miller, N. & Marzari, N. Electrostatics in periodic boundary conditions and real-space corrections. *Phys. Rev.* **B77**, 115139 (2008).
8. Monkhorst, H. J. & Pack, J. D. Special Points for Brillouin-Zone Integrations. *Phys. Rev.* **B13**, 5188–5192 (1976).

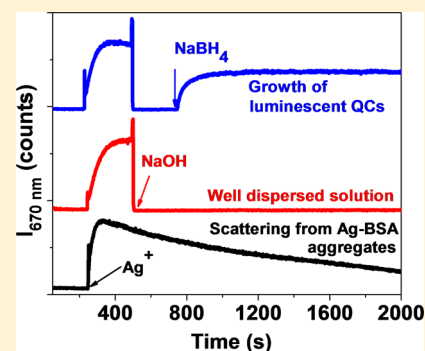
Initial Growth Kinetics of Luminescent Quantum Clusters of Silver within Albumin Family Protein Templates

Kamalesh Chaudhari^{†,‡} and Thalappil Pradeep^{*,‡}

[†]Department of Biotechnology and [‡]DST Unit of Nanoscience (DST UNS) and Thematic Unit of Excellence (TUE), Department of Chemistry, Indian Institute of Technology Madras, Chennai 600 036, India

Supporting Information

ABSTRACT: We probed the initial growth kinetics of luminescent quantum clusters of silver (AgQCs) within two albumin family proteins, bovine serum albumin (BSA) and ovalbumin (Ova). Shorter time scale (seconds to minutes) growth of AgQCs monitored using real time photoluminescence spectroscopy has shown that, at lower concentrations of Ag⁺, only unstable QCs were formed. The major role of basic pH in the synthesis was not only to facilitate Ag⁺-BSA conjugation but also to provide well dispersed medium for controlled nucleation of QCs. Increase in the concentration of NaBH₄ affects growth kinetics greatly and leads to increase in the growth rate of AgQCs; but for NaBH₄ concentrations higher than the optimum value, growth rate becomes constant. Precise measurements have shown that excitation and emission of AgQCs exhibit linear red-shift with the increasing concentration of NaBH₄ whereas protein excitation remains constant. Similar results were observed for both the proteins, Ova and BSA. We believe that various insights provided by this study will be helpful for further improvements in the synthetic methodology and applications of protein protected AgQCs.



INTRODUCTION

Protein protected luminescent noble metal quantum clusters (NMQCs@protein) have found interesting applications in the recent past.^{1–7} NMQCs@protein can be synthesized using various metal ions such as copper, mercury, gold, silver, etc.^{8–10} NMQCs@protein are biocompatible due to their bulky protein ligands and lower metal content.^{4,11,12} Apart from this, protein ligands can be easily conjugated to drug molecules and can be targeted to cancer cells for imaging and therapy applications.^{4,11,13} Photoluminescence (PL) properties of NMQCs@protein have been demonstrated to be useful for sensing amino acids.¹⁴ In the past, NMQCs@protein have been used for the detection of post-translation modification of enzymes and determination of the activity of protease enzymes.^{15,16} Studies have shown that intracellular changes in the properties of NMQCs@protein can be used to sense and monitor the activity of various analytes.^{10,17} Most of these applications are based on photoluminescence of clusters. Such luminescence has been found to be stable at biological pH¹⁸ and it is possible to tune the same by changing multiple synthetic parameters, such as pH, concentrations of reducing agent, etc.^{19–23} For example, Kawasaki et al. and Guével et al. have demonstrated the dependence of AuQC synthesis on pH of the reaction.¹⁹ It was found that growth of smaller clusters can happen at lower pH, whereas larger clusters can be synthesized at basic pH. Synthesis of NMQCs@protein was demonstrated using bovine serum albumin (BSA), lactoferrin, lysozyme, insulin and multiple other proteins.^{2,4,18,24} Variety of synthetic methodologies have been developed for the synthesis of protein template AuQCs and AgQCs.^{21,24–26} Synthetic methodologies

for AuQCs and AgQCs have some basic differences. This is because, gold can be reduced by tyrosine residues of proteins at basic pH but due to lower reduction potential of silver, it requires a stronger reducing agent such as sodium borohydride (NaBH₄).²¹ To optimize the synthetic route for efficient growth of QCs, it is necessary to understand growth process of the same.²⁷ Knowledge of temporal growth mechanism of QCs helps in the determination of relationships between reaction parameters which facilitate tunability of physicochemical properties of the clusters formed.

To monitor such growth processes of QCs, selection of appropriate techniques are important. For slower growth processes which occur at the time scale of hours and days, methods which would involve complex and lengthy sample preparation methods can be used. These techniques can be transmission electron microscopy (HRTEM), scanning electron microscopy (SEM) or mass spectrometric techniques such as matrix assisted laser desorption ionization mass spectrometry (MALDI MS), etc. But, for reactions which occur at time scale of seconds or minutes, real time probing techniques are required. Depending on the intrinsic properties of products, for solution state synthesis, the techniques can be UV–vis absorption, PL spectroscopy, etc. Dharmaratne et al. have shown that for the growth of monolayer protected QCs, which occurs on the time scale of hours, mass spectrometry can be used.²⁸ In this study, size evolution of Au₂₅(SCH₂CH₂Ph)₁₈

Received: January 17, 2015

Revised: April 15, 2015

Published: April 20, 2015

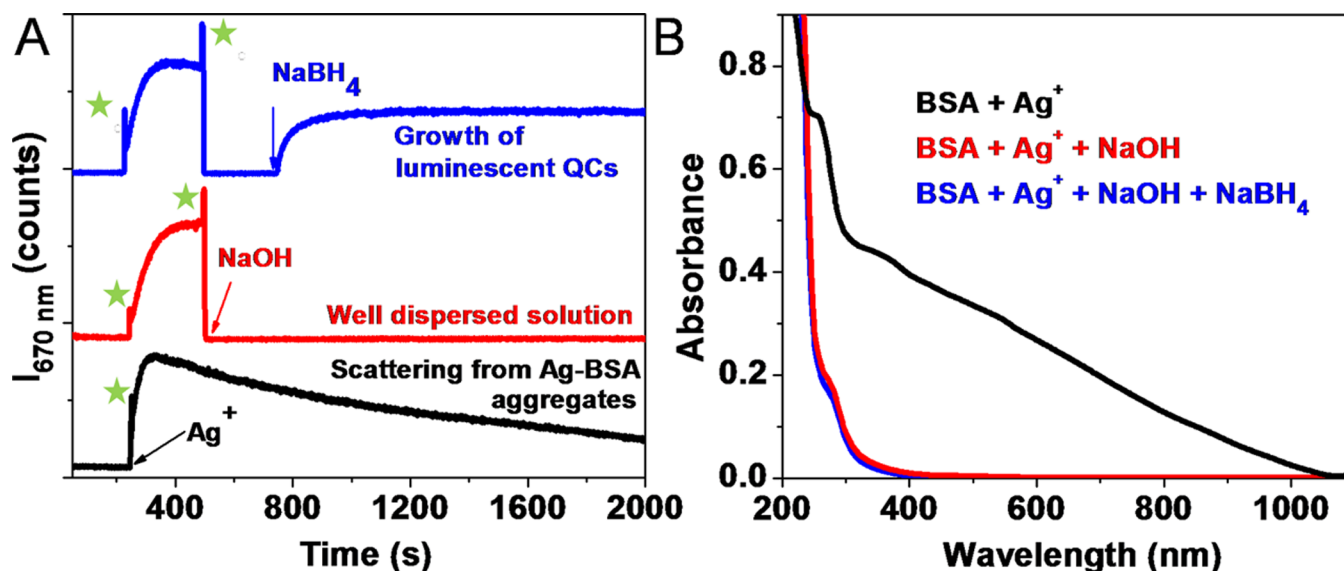


Figure 1. Role of NaOH in the AgQC synthesis. (A) Changes in the PL counts (I_{670}) after the stepwise addition of various reaction components during AgQC synthesis. The black curve shows variations in I_{670} when only Ag^+ ions were added to the BSA solution, and reaction was monitored without adding NaOH and NaBH_4 . The red curve shows variations in I_{670} when addition of Ag^+ was followed by an addition of NaOH. The blue curve shows variations in I_{670} when Ag^+ , NaOH and NaBH_4 were added sequentially. Green stars indicate the occurrence of spikes due to increase in the detector response when stray light got into the spectrometer during the addition of reactants. (B) UV-vis spectra of the aforementioned samples are shown in matching color at 2000 s time of reaction.

nanoclusters was probed using MALDI MS. It was found that initial growth of larger sized clusters such as Au_{102} , Au_{38} and Au_{68} leads to the formation of highly monodisperse Au_{25} nanoclusters. Another study, performed by Xie and co-workers, has used ESI-MS to monitor the time evolution of Au_{25} nanoclusters.²⁹ This study has proposed a two-stage growth process which involves a fast reduction-growth step and a slow intercluster conversion, leading to Au_{25} . Our group has also reported monitoring of growth processes of protein protected clusters.^{21,27,30,31} Our study on the evolution of AuQCs within lactoferrin templates have shown that during the growth of AuQCs, initial addition of Au^{3+} ions in protein solution lead to its reduction to Au^+ which reduces to $\text{Au}(0)$ only when the pH is changed to a basic value.²⁷ This growth process is much slower than the growth process for AgQCs. Growth of AuQCs inside lactoferrin templates involves interprotein metal ion transfer which leads to the emergence of parent protein molecules, at the end of the reaction, beginning from metal-protein adducts. This knowledge obtained from AuQC growth process was used to develop an optimized synthetic route which utilizes the free protein available at the end of reaction. This kind of optimization is mainly necessary when availability of proteins and monodispersity of product are major concerns. A similar phenomenon of the emergence of parent protein was observed when the growth process of AuAg alloy clusters inside BSA templates was monitored.³⁰ Recent studies from our group have used small-angle X-ray scattering (SAXS) and mass spectrometry (MS) for direct visualization of QC growth within protein templates in solution.³¹ In another study, performed by Mathew et al., MALDI MS was used to investigate the effect of NaBH_4 on the synthesis of AgQC@BSA.²¹ It was found that despite the change in concentration of NaBH_4 , the major species formed was Ag_{15} @BSA.²¹ However, as mentioned, due to the use of NaBH_4 as the reducing agent for Ag^+ , growth kinetics of AgQC@protein is much faster as compared to AuQC@protein. Hence, MALDI MS was able to provide

information about the final product only. MALDI MS also has another drawback that the clusters may be formed in the gas phase by reaction between desorbed proteins and the naked clusters produced in the gas phase.⁵ Hence it is risky to correlate the clusters obtained from MALDI MS with the PL properties of QCs measured in solution, in all cases. Hence, in this work, we have used PL spectroscopy to probe the initial growth kinetics of luminescent AgQC@BSA. Unlike MALDI MS, PL spectroscopy allows real time and direct monitoring of the PL properties of clusters growing in the solution state. The study has been performed mainly to check the dependence of growth kinetics on various reaction parameters when NIR luminescent AgQCs are formed. Dependence of excitation and emission wavelengths on the NaBH_4 concentration has been established. Growth process was studied for two albumin family proteins, BSA and Ovalbumin (Ova). To the best of our knowledge, this is the first study on the growth kinetics of rapidly synthesized AgQCs inside protein templates.

EXPERIMENTAL SECTION

Chemicals. Sodium borohydride (99%, Fluka), Ovalbumin (98%, Sigma-Aldrich), Sodium hydroxide (98%, RANKEM, India.), Silver nitrate (99.9%, RANKEM, India.), Bovine serum albumin (96–98%, pH 7, SRL Pvt. Ltd., India.) were used for experiments. Millipore deionized water (DI) (~ 18.2 M Ω) was used throughout the experiments.

Synthesis of AgQCs. A protocol previously reported²¹ from our group was used for the synthesis of AgQC@BSA and AgQC@Ova with slight modifications. Briefly, 200 μL of 100 mM AgNO_3 was added to 2 mL of 25 mg/mL protein solution followed by the addition of 100 μL of 1 M NaOH. Then, 10 mM NaBH_4 was added to initiate cluster growth. Volume of NaBH_4 was varied from 5 to 200 μL according to the experiment. While varying NaBH_4 , final volume of the reaction mixture was maintained constant by adding DI water. No

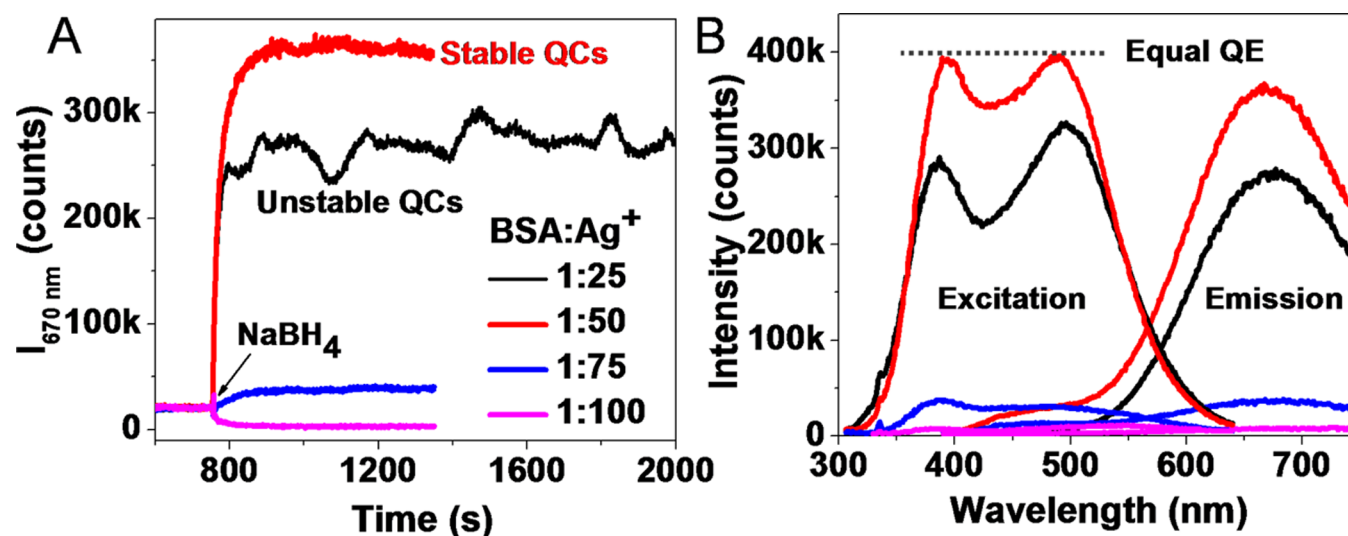


Figure 2. Initial growth kinetics of AgQC@BSA at different Ag⁺ concentrations. (A) Changes in the PL intensity of AgQC@BSA (Ex=380 nm, Em=670 nm) after the addition of NaBH₄ at different concentrations of Ag⁺. (B) Excitation and emission spectra corresponding to the growth curves shown in (A). Colors in B indicate concentrations shown in A. QE stands for quantum efficiency at 670 nm emission.

stirring was used but solution was gently mixed with using 100 μL pipet.

PL spectroscopy. To monitor AgQC growth kinetics in real time, we have carried out reaction in the sample cuvette of PL spectrometer kept within a dark room. HORIBA, JOBIN VYON NanoLog fluorescence spectrometer was used for PL measurements. Protein (BSA or Ova) solution was taken in quartz cuvette and other components were added in the order, AgNO₃, NaOH and NaBH₄. After an addition of every reactant, sufficient time was given to ensure the stability of PL counts. Final volume of the reaction was kept constant by adding deionized water (DI) to achieve better comparison between PL intensity of different products. Care was taken to avoid second order peak of excitation in emission spectra.

UV-vis spectroscopy. UV-visible absorption spectroscopic measurements were performed using PerkinElmer Lambda 25 spectrophotometer (Range -200–1100 nm, scan rate -480 nm per min).

Such clusters were monitored in our earlier studies by a range of techniques such as MALDI MS, XPS, HRTEM, SAXS, etc.^{27,31,32} Although data from those studies are not presented, inferences drawn from these studies will be used here.

RESULTS AND DISCUSSION

Role of NaOH and NaBH₄ in AgQC synthesis. NIR luminescent AgQC@BSA and AgQC@Ova do not form at neutral pH (Figure 1), and neither do they form only by the addition of NaOH. Previous studies from our group have shown using gas phase mass spectrometric studies that basic pH facilitates coordination between Ag⁺ ions and various functional groups of BSA.²¹ PL spectroscopic observations performed in the solution state have shown the importance of NaOH in this reaction. For these observations, reaction was monitored step by step after the addition of various components of the reaction. The mixture was excited at 380 nm and emission was collected at 670 nm (I_{670}). It may be noted that these are the excitation and emission values of AgQC@BSA. As shown in Figure 1, when only Ag⁺ ions were added to BSA solution, a large increase in I_{670} counts was observed, which decayed slowly over long time. This was found to be due to aggregation of BSA

in the presence of Ag⁺ ions. Soon after the addition of Ag⁺, solution became turbid white and I_{670} increases, due to scattering. This was supported by UV-vis spectroscopic data as shown in Figure 1B. Subsequent decrease in I_{670} was due to gradual settling down of aggregates. In the next step of the reaction, after the addition of Ag⁺, it was observed that due to change in the pH of reaction mixture, aggregates break down and form well dispersed solutions of Ag-BSA conjugates.

In this reaction, NaOH does not initiate NIR luminescent AgQC growth even after long time as it can be seen by the red trace shown in Figure 1. This results in an abrupt decrease in I_{670} . At this time, it again reaches the baseline counts, which were observed before the addition of Ag⁺. This baseline count continues for long time without any further change. In the next reaction, addition of Ag⁺ and NaOH was followed by NaBH₄. In this case, I_{670} increases exponentially and reaches a stable count within a few minutes. This time, I_{670} remains steady even after a long time. This suggests stable product formation in the reaction. Hence NaOH provides favorable environment for cluster growth and then NaBH₄ helps in the growth of stable clusters. Apart from the reduction of Ag⁺ to Ag(0), NaBH₄ can affect the reaction in various ways such as change in the reaction pH and disruption of protein structure, which facilitates the binding of Ag⁺ ions to the inner residues of the protein. This suggests that apart from facilitating Ag⁺-BSA conjugation, the other role of NaOH is to provide a well dispersed solution for cluster growth before the addition of NaBH₄ (Figure 1A). We have monitored the same reaction at different concentrations of Ag⁺. These results are discussed in the next section.

Initial growth kinetics of AgQC@BSA at different Ag⁺ concentrations. According to the first report on the synthesis of AgQC@BSA from our group, 1:13 molar ratio of BSA:Ag⁺ was needed for the synthesis of Ag₁₅@BSA.²¹ In this study, even after the addition of large amounts of NaBH₄, no considerable change in the emission of QCs was observed. This was possibly because the number of available silver atoms was adequate only for the synthesis of Ag₁₅. To understand if changes in the relative quantity of NaBH₄ can lead to changes in the cluster growth, at first we have studied growth kinetics

and PL properties at different concentrations of Ag^+ . In this experiment, NaBH_4 (10 mM, 25 μL) and NaOH (1 M, 100 μL) concentrations were kept constant, only Ag^+ concentration was varied. Growth curves for these samples are shown in Figure 2A. When $\sim 1:25$ ratio of $\text{BSA}:\text{Ag}^+$ was used, stable cluster growth was not observed. Fluctuations in the PL intensity were observed at this concentration. Whereas at higher concentration of Ag^+ , that is at $\sim 1:50$ ratio of $\text{BSA}:\text{Ag}^+$, the clusters grown were stabilized. For this sample, even higher PL intensity was observed as compared to clusters grown with 1:25 ratio. It should be noted that, despite using similar NaBH_4 concentration for 1:50 and 1:25 ratios, only 1:50 forms a stable product. Figure 2B shows steady state PL spectra of these samples. These spectra were collected at a time when growth monitoring was stopped (2000 s). For all samples, only one major emission peak was observed at ~ 670 nm. First excitation peak at ~ 376 nm is due to the excitation of Ag-BSA conjugate.²¹ Second excitation peak at ~ 500 nm appears only after NaBH_4 addition and due to the excitation of NIR luminescent AgQC@BSA . When stable and highly emissive clusters were formed, both these excitations exhibit equal intensity for emission at 670 nm (Figure 2B). This implies that for 376 and 500 nm excitation wavelengths, AgQC@BSA exhibit equal quantum efficiency (QE). In the absence of NIR luminescent clusters, excitation at 376 nm leads to emission at ~ 460 nm. It has been shown by previous studies that tryptophan metabolites like kynurenine are responsible for excitation and emission of protein at 375 and 450 nm, respectively.^{8,33} At further higher concentrations of Ag^+ , no NIR luminescent cluster growth was observed. The reason behind this may be the growth of larger size clusters and is discussed in more detail in the subsequent sections with the help of steady state PL spectroscopy of AgQCs .

Growth kinetics of AgQC@BSA at different NaBH_4 concentrations. Figure 3A shows the growth curves of AgQC@BSA when different volumes of NaBH_4 were used to initiate growth of clusters. Figure 3B shows the slopes (growth rates) calculated from the tangents drawn to growth curves just after the addition of NaBH_4 . Initially at lower concentrations of NaBH_4 (5, 10, 25 μL), growth rate increases as the concentration of NaBH_4 increases. To understand the kinetics further, we have tried fitting the growth curves using a single component exponential growth function. Though it was possible to fit curves with the adjusted R square values of ~ 0.97 , no specific correlation between growth constants and NaBH_4 concentration was found. These growth constants and description of exponential growth function are provided in Supporting Information Table 1. Because of this, here we have discussed growth curves only qualitatively. From the I_{670} values at 500 s, for clusters grown with different concentrations of NaBH_4 (Figure 3B), we see that 25 μL of NaBH_4 leads to efficient and stable growth of AgQCs . Further addition of NaBH_4 does not result in change of growth rate but after initial transient growth, formation of nonluminescent clusters dominate the growth of luminescent QCs (Figure 3B). After adding 50 μL of NaBH_4 , QC growth follows a step function; where just after the addition of NaBH_4 , clusters grow abruptly and the concentration remains stable even after long time. This difference between growth curves for 25 and 50 μL concentrations of NaBH_4 suggests that, at lower concentration (25 μL) of NaBH_4 , although clusters start nucleating at high growth rate, after a few seconds, silver atom uptake by the protein is slow. This leads to QC growth in a controlled

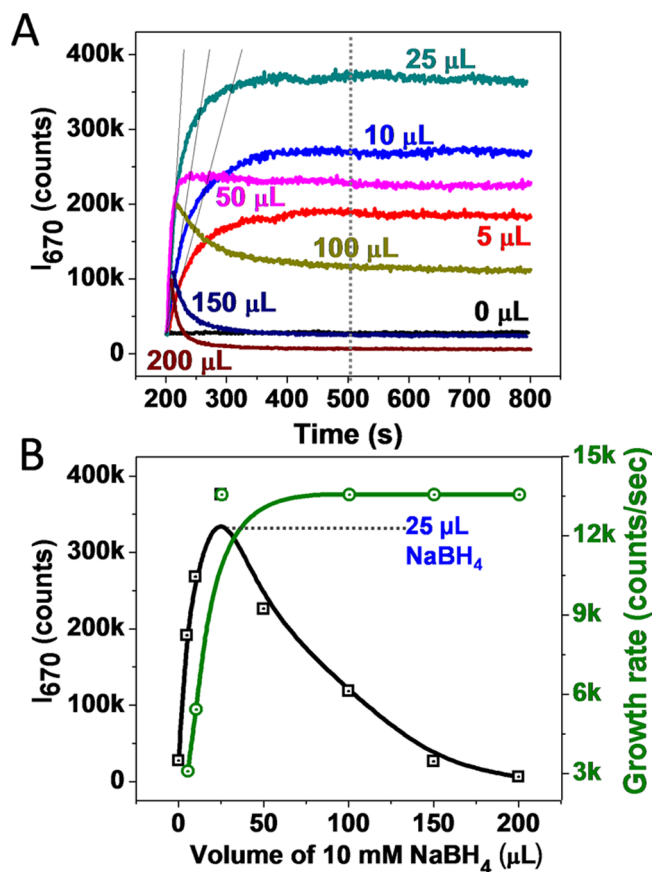


Figure 3. Growth kinetics of AgQC@BSA at different concentrations of NaBH_4 . (A) Changes in the PL intensity of AgQC@BSA (E_x –380 nm, E_m –670 nm) after the addition of NaBH_4 (10 mM). The volume of NaBH_4 added is written adjacent to the growth curves in corresponding colors. Tangents are drawn to determine initial growth rate at different concentrations of NaBH_4 . The dotted line crosses the data points which are plotted in the next figure. (B) The black curve shows changes in the emission intensity of AgQC@BSA after the addition of different amounts of NaBH_4 after 500 s of the reaction. The green curve shows changes in the growth rate of AgQC@BSA .

manner. Whereas, in the case of 50 μL NaBH_4 , formation of larger and nonluminescent QCs dominate the nucleation of luminescent QCs soon after the addition of NaBH_4 . At further higher concentrations of NaBH_4 , growth of larger QCs leads to reduction in I_{670} . Formation of larger clusters was confirmed by red shift observed in steady state PL spectra of aforementioned samples. These observations are discussed in the next section.

Relationship between PL properties of AgQC@BSA and NaBH_4 concentration. Figure 4A shows excitation spectra of AgQC@BSA grown with different concentrations of NaBH_4 . In all these spectra, we see that the excitation peak for Ag-BSA conjugate (E_{x380}) appears even before the addition of NaBH_4 (black trace at the bottom of Figure 4A). E_{x380} remains constant in position but changes in intensity upon change in the concentration of NaBH_4 . But the excitation peak in the region around 500 nm (λ_{ex}) changes in position and intensity, which is attributed to different QCs nucleated in the solution. For 25 μL of NaBH_4 concentration, both E_{x380} and λ_{ex} can be used to excite AgQC@BSA with equal quantum efficiency for emission at 670 nm. But, after increase in the concentration of NaBH_4 , there are corresponding changes in the PL properties of QCs too. Assuming that larger quantum clusters have longer

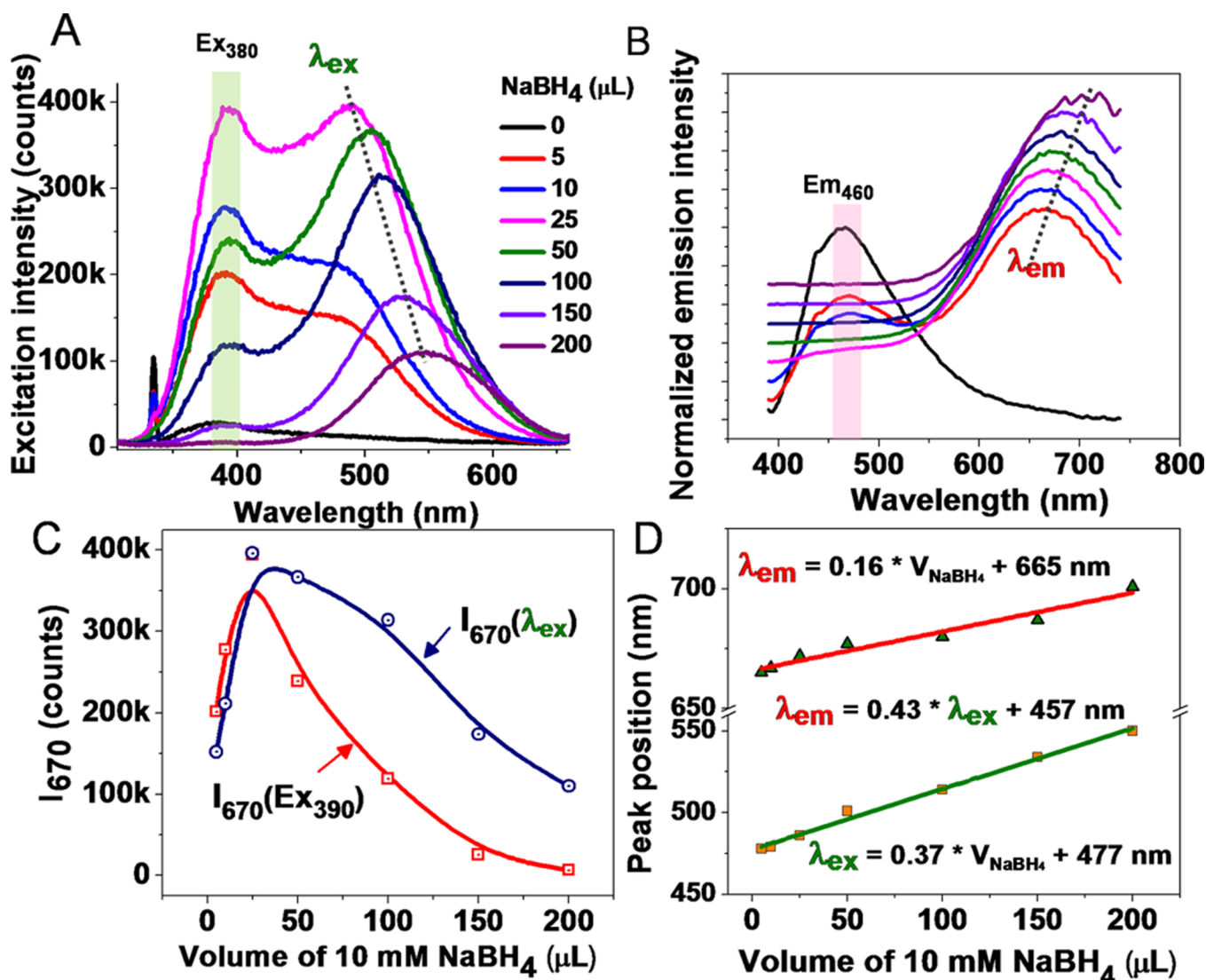


Figure 4. Relationship between PL properties of AgQC@BSA and NaBH₄ concentration. (A) Excitation spectra (Em=670 nm) of AgQC@BSA. (B) Emission spectra (Ex=380 nm) of AgQC@BSA. Matching colors are used for excitation and emission. Emission spectra are normalized and vertically translated for better comparison of peak positions. (C) Changes in I₆₇₀ as a function of NaBH₄ concentration shown for two different excitations, λ_{ex} (blue) and Ex₃₈₀ (red). (D) Relationships between excitation (λ_{ex}) and emission (λ_{em}) wavelengths and volume of NaBH₄ (V_{NaBH₄}) are shown.

excitation wavelength, uniform red-shift in λ_{ex} can be attributed to an increase in the size of clusters. Such red-shift in the cluster emission has also been shown by Petty *et al.* and Gwinn *et al.* for DNA templated AgQCs.^{34,35} In the emission spectra also, Em₄₆₀ remains constant but cluster emission (λ_{em}) exhibits a red shift. Hence, due to red shift, λ_{ex} gradually goes out of Em₄₆₀ range and results in a decrease in the efficiency of Ex₃₈₀.

To compare the excitation and emission peak positions accurately, we have done Gaussian curve fitting of all the excitation and emission spectra. Curve fitting data are shown in Supporting Information Figures S2 and S3. Peak positions obtained from these fittings are plotted in Figure 4D. It was observed that both excitation and emission wavelengths scale linearly with respect to the volume of NaBH₄ (V_{NaBH₄}). The slope values of 0.37 and 0.16 for λ_{ex} and λ_{em} suggest that, excitation is more a prominent function of NaBH₄ concentration as compared to emission. This also implies linear relationship between the excitation and emission of clusters synthesized at different volumes of NaBH₄. To check the possibility of similar behavior in other AgQC@protein systems,

we have performed similar studies on another system of AgQCs stabilized by Ovalbumin (AgQC@Ova). These results are discussed in the next section.

Growth kinetics of AgQC@Ova. To confirm the observations made for AgQC@BSA and to verify whether this behavior can be generalized for other albumin family proteins, we have monitored growth kinetics of AgQC@Ova. Before discussing these observations, it should be noted that molecular weight (MW) and hence amino acid content of Ova is ~2/3 of BSA. Hence these observations can also be used for such MW based comparison. Hence keeping the weight/volume concentration of Ova the same as BSA, NaBH₄ concentration was varied. Results obtained are consolidated in Figure 5. Similar to AgQC@BSA, initial growth rate of AgQC@Ova increases upon increase in the concentration of NaBH₄ and remains constant at an optimum concentration (Supporting Information Figure S6). In the case of AgQC@Ova also, 50 μL concentration of NaBH₄ leads to a growth curve similar to a step function and clusters grow abruptly after the addition of NaBH₄. Figure 5B shows linear relationships

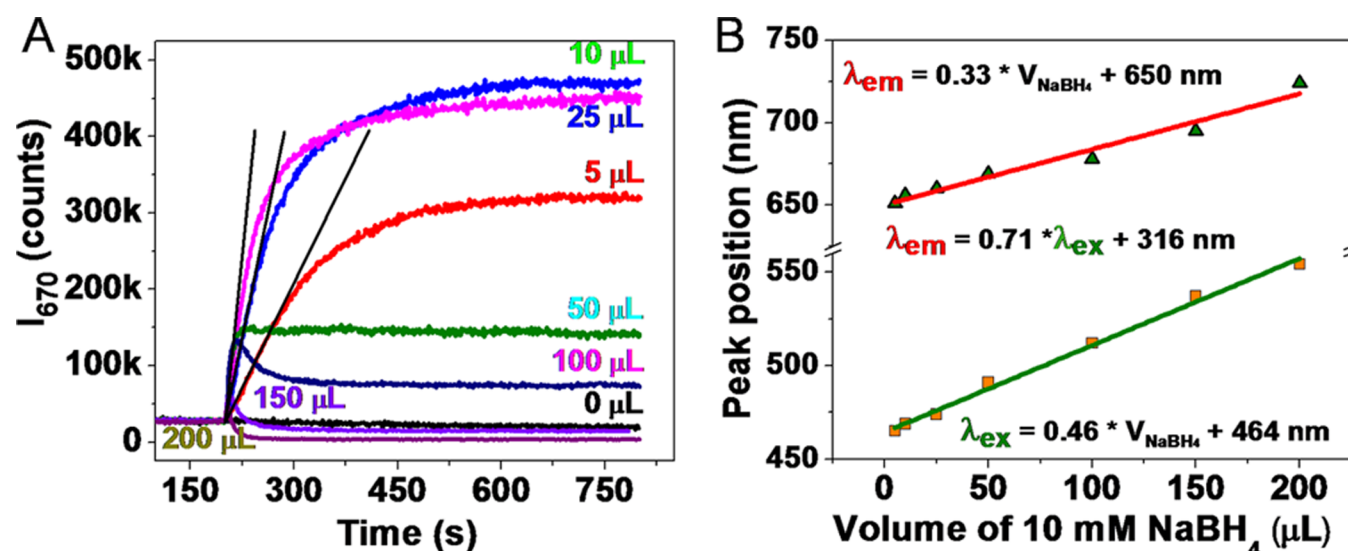


Figure 5. Growth kinetics and PL spectroscopy of AgQC@Ova. (A) Changes in the PL intensity of AgQC@Ova (Ex–380 nm, Em–670 nm) after the addition of NaBH₄. Tangents are drawn to determine initial growth rate at different volumes of 10 mM NaBH₄. (B) Relationships between excitation and emission wavelengths and volume of NaBH₄ are shown.

between excitation, emission and concentration of NaBH₄. Original excitation and emission spectra for these samples are shown in Supporting Information Figure S1 and curve fitting data are shown in Figures S4 and S5. This supports that, the kinetics of AgQC growth inside BSA and Ova can be considered as a generalized kinetics for albumin family proteins. PL data also suggest that Ova provides more tunability over emission (Em = 650–720 nm) as compared to BSA (Em = 660–700 nm).

Unlike gold quantum clusters, for which jellium model has been developed to correlate emission energy with the number of atoms per clusters,^{36,37} for the case of silver clusters, due to the strongly interacting ligands to stabilize cluster core, such a model is unlikely to be followed. However, there have been attempts to apply jellium model for silver-protein nano-bioconjugates.³⁸ If such a model were to be applied in the present study, sizes of AgQCs would have been 24–28 atoms for BSA emission varying between 660 and 700 nm and 23–31 atoms per cluster for Ova emission varying from 650 to 720 nm (Supporting Information Figure S7).

UV–vis spectra of AgQC@BSA and AgQC@Ova do not yield any conclusive information to enlighten the growth process. The possible reasons behind this can be the lack of surface plasmon resonance due to the ultrasmall size of quantum clusters as well as the bulky nature of the protein ligands and their high absorption which may hide the absorption features of the clusters. UV–vis spectra of AgQC@BSA and AgQC@Ova spectra are shown in Supporting Information Figures S8 and S9.

CONCLUSION

We have developed a methodology for monitoring real time growth kinetics of rapidly synthesized luminescent silver quantum clusters. This method allows understanding as well as precise optimization of the synthetic methodology. With the example of AgQC@BSA, we have shown that upon increase in the concentration of NaBH₄, the growth rate of luminescent AgQCs increases and becomes constant for concentrations higher than the optimum value. Studies performed at different concentrations of Ag⁺ have shown that merely the addition of

more NaBH₄ does not lead to stable cluster growth, but sufficient concentration of Ag⁺ is also an important parameter. Steady state PL spectroscopic investigations have shown that excitation and emission properties of clusters are linear functions of NaBH₄ concentration. Similar relationships were observed for both the proteins, Ova, and BSA.

This study also provides a new possibility of using AgQC@BSA as probes for multiple labeling or detection using the ratiometric fluorescence technique. Further probing of this system with advanced techniques and other methodologies may be required to answer questions such as reasons behind the increased tunability of AgQCs by Ova as compared to BSA, larger red-shift in the excitation wavelength of QCs compared to red-shift in the emission, etc. We believe that this study will be helpful for further improvements in the synthetic methodology and applications of protein protected AgQCs.

ASSOCIATED CONTENT

Supporting Information

Excitation and emission spectra of the systems described, spectra after appropriate peak fitting under various conditions, and a table of growth constants derived from the exponential fitting of spectra. The Supporting Information is available free of charge on the ACS Publications website at DOI: 10.1021/acs.jpcc.5b00496.

AUTHOR INFORMATION

Corresponding Author

*E-mail: pradeep@iitm.ac.in.

Notes

The authors declare no competing financial interest.

ACKNOWLEDGMENTS

We thank the Department of Science and Technology, Government of India, for constantly supporting our research program on nanomaterials.

REFERENCES

- (1) Xavier, P. L.; Chaudhari, K.; Baksi, A.; Pradeep, T. Protein-Protected Luminescent Noble Metal Quantum Clusters: An Emerging Trend in Atomic Cluster Nanoscience. *Nano Rev.* **2012**, *3*, 14767.
- (2) Wei, H.; Wang, Z.; Yang, L.; Tian, S.; Hou, C.; Lu, Y. Lysozyme-Stabilized Gold Fluorescent Cluster: Synthesis and Application as Hg²⁺ Sensor. *Analyst* **2010**, *135*, 1406–1410.
- (3) Ghosh, R.; Sahoo, A. K.; Ghosh, S. S.; Paul, A.; Chattopadhyay, A. Blue-Emitting Copper Nanoclusters Synthesized in the Presence of Lysozyme as Candidates for Cell Labeling. *ACS Appl. Mater. Interfaces* **2014**, *6*, 3822–8.
- (4) Liu, C.-L.; et al. Insulin-Directed Synthesis of Fluorescent Gold Nanoclusters: Preservation of Insulin Bioactivity and Versatility in Cell Imaging. *Angew. Chem., Int. Ed.* **2011**, *50*, 7056–7060.
- (5) Baksi, A.; Pradeep, T. Noble Metal Alloy Clusters in the Gas Phase Derived from Protein Templates: Unusual Recognition of Palladium by Gold. *Nanoscale* **2013**, *5*, 12245–12254.
- (6) Luo, Z.; Zheng, K.; Xie, J. Engineering Ultrasmall Water-Soluble Gold and Silver Nanoclusters for Biomedical Applications. *Chem. Commun.* **2014**, *50*, S143–S155.
- (7) Antoku, Y.; Hotta, J.-I.; Mizuno, H.; Dickson, R. M.; Hofkens, J.; Vosch, T. Transfection of Living Hela Cells with Fluorescent Polycytosine Encapsulated Ag Nanoclusters. *Photochemical & Photobiological Sciences* **2010**, *9*, 716–721.
- (8) Goswami, N.; Giri, A.; Bootharaju, M. S.; Xavier, P. L.; Pradeep, T.; Pal, S. K. Copper Quantum Clusters in Protein Matrix: Potential Sensor of Pb²⁺ Ion. *Anal. Chem.* **2011**, *83*, 9676–80.
- (9) Goswami, N.; Giri, A.; Kar, S.; Bootharaju, M. S.; John, R.; Xavier, P. L.; Pradeep, T.; Pal, S. K. Protein-Directed Synthesis of NIR-Emitting, Tunable HgS Quantum Dots and Their Applications in Metal-Ion Sensing. *Small* **2012**, *8*, 3175–3184.
- (10) Durgadas, C. V.; Sharma, C. P.; Sreenivasan, K. Fluorescent Gold Clusters as Nanosensors for Copper Ions in Live Cells. *Analyst* **2011**, *136*, 933–940.
- (11) Retnakumari, A.; Setua, S.; Menon, D.; Ravindran, P.; Muhammed, H.; Pradeep, T.; Nair, S.; Koyakutty, M. Molecular-Receptor-Specific, Non-Toxic, Near-Infrared-Emitting Au Cluster-Protein Nanoconjugates for Targeted Cancer Imaging. *Nanotechnology* **2010**, *21*, 055103.
- (12) Zhang, X. D.; Wu, D.; Shen, X.; Liu, P. X.; Fan, F. Y.; Fan, S. J. In Vivo Renal Clearance, Biodistribution, Toxicity of Gold Nanoclusters. *Biomaterials* **2012**, *33*, 4628–4638.
- (13) Retnakumari, A.; Jayasimhan, J.; Chandran, P.; Menon, D.; Nair, S.; Mony, U.; Koyakutty, M. CD33 Monoclonal Antibody Conjugated Au Cluster Nano-Bioprobes for Targeted Flow-Cytometric Detection of Acute Myeloid Leukaemia. *Nanotechnology* **2011**, *22*, 285102.
- (14) Wang, M.; Mei, Q.; Zhang, K.; Zhang, Z. Protein-Gold Nanoclusters for Identification of Amino Acids by Metal Ions Modulated Ratiometric Fluorescence. *Analyst* **2012**, *137*, 1618–1623.
- (15) Wen, Q.; Gu, Y.; Tang, L. J.; Yu, R. Q.; Jiang, J. H. Peptide-Templated Gold Nanocluster Beacon as a Sensitive, Label-Free Sensor for Protein Post-Translational Modification Enzymes. *Anal. Chem.* **2013**, *85*, 11681–11685.
- (16) Gu, Y.; Wen, Q.; Kuang, Y.; Tang, L.; Jiang, J. Peptide-Templated Gold Nanoclusters as a Novel Label-Free Biosensor for the Detection of Protease Activity. *RSC Adv.* **2014**, *4*, 13753–13756.
- (17) Chatteraj, S.; Bhattacharyya, K. Fluorescent Gold Nanocluster inside a Live Breast Cell: Etching and Higher Uptake in Cancer Cell. *J. Phys. Chem. C* **2014**, *118*, 22339–22346.
- (18) Xavier, P. L.; Chaudhari, K.; Verma, P. K.; Pal, S. K.; Pradeep, T. Luminescent Quantum Clusters of Gold in Transferrin Family Protein, Lactoferrin Exhibiting FRET. *Nanoscale* **2010**, *2*, 2769–2776.
- (19) Kawasaki, H.; Hamaguchi, K.; Osaka, I.; Arakawa, R. pH-Dependent Synthesis of Pepsin-Mediated Gold Nanoclusters with Blue Green and Red Fluorescent Emission. *Adv. Funct. Mater.* **2011**, *21*, 3508–3515.
- (20) Le Guevel, X.; Hotzer, B.; Jung, G.; Hollemeyer, K.; Trouillet, V.; Schneider, M. Formation of Fluorescent Metal (Au, Ag) Nanoclusters Capped in Bovine Serum Albumin Followed by Fluorescence and Spectroscopy. *J. Phys. Chem. C* **2011**, *115*, 10955–10963.
- (21) Mathew, A.; Sajanlal, P. R.; Pradeep, T. A Fifteen Atom Silver Cluster Confined in Bovine Serum Albumin. *J. Mater. Chem.* **2011**, *21*, 11205–11212.
- (22) Baksi, A.; Xavier, P. L.; Chaudhari, K.; Goswami, N.; Pal, S. K.; Pradeep, T. Protein-Encapsulated Gold Cluster Aggregates: The Case of Lysozyme. *Nanoscale* **2013**, *5*, 2009–2016.
- (23) Petty, J. T.; Fan, C.; Story, S. P.; Sengupta, B.; Sartin, M.; Hsiang, J. C.; Perry, J. W.; Dickson, R. M. Optically Enhanced, Near-IR, Silver Cluster Emission Altered by Single Base Changes in the DNA Template. *J. Phys. Chem. B* **2011**, *115*, 7996–8003.
- (24) Xie, J.; Zheng, Y.; Ying, J. Y. Protein-Directed Synthesis of Highly Fluorescent Gold Nanoclusters. *J. Am. Chem. Soc.* **2009**, *131*, 888–889.
- (25) Habeeb Muhammed, M. A.; Verma, P. K.; Pal, S. K.; Retnakumari, A.; Koyakutty, M.; Nair, S.; Pradeep, T. Luminescent Quantum Clusters of Gold in Bulk by Albumin-Induced Core Etching of Nanoparticles: Metal Ion Sensing, Metal-Enhanced Luminescence, and Biolabeling. *Chem.—Eur. J.* **2010**, *16*, 10103–10112.
- (26) Yu, Y.; Chen, X.; Yao, Q.; Yu, Y.; Yan, N.; Xie, J. Scalable and Precise Synthesis of Thiolated Au_{10–12}, Au₁₅, Au₈, and Au₂₅ Nanoclusters Via pH Controlled Co Reduction. *Chem. Mater.* **2013**, *25*, 946–952.
- (27) Chaudhari, K.; Xavier, P. L.; Pradeep, T. Understanding the Evolution of Luminescent Gold Quantum Clusters in Protein Templates. *ACS Nano* **2011**, *5*, 8816–8827.
- (28) Dharmaratne, A. C.; Krick, T.; Dass, A. Nanocluster Size Evolution Studied by Mass Spectrometry in Room Temperature Au₂₅(SR)₁₈ Synthesis. *J. Am. Chem. Soc.* **2009**, *131*, 13604–13605.
- (29) Luo, Z.; Nachammai, V.; Zhang, B.; Yan, N.; Leong, D. T.; Jiang, D. E.; Xie, J. Toward Understanding the Growth Mechanism: Tracing All Stable Intermediate Species from Reduction of Au(I)-Thiolate Complexes to Evolution of Au₂₅ Nanoclusters. *J. Am. Chem. Soc.* **2014**, *136*, 10577–10580.
- (30) Mohanty, J. S.; Xavier, P. L.; Chaudhari, K.; Bootharaju, M. S.; Goswami, N.; Pal, S. K.; Pradeep, T. Luminescent, Bimetallic AuAg Alloy Quantum Clusters in Protein Templates. *Nanoscale* **2012**, *4*, 4255–4262.
- (31) Baksi, A.; Mitra, A.; Mohanty, J. S.; Lee, H.; De, G.; Pradeep, T. Size Evolution of Protein-Protected Gold Clusters in Solution: A Combined SAXS-MS Investigation. *J. Phys. Chem. C* **2015**, *119*, 2148–2157.
- (32) Chakraborty, I.; Govindarajan, A.; Erusappan, J.; Ghosh, A.; Pradeep, T.; Yoon, B.; Whetten, R. L.; Landman, U. The Superstable 25 Kda Monolayer Protected Silver Nanoparticle: Measurements and Interpretation as an Icosahedral Ag₁₅₂(SCH₂CH₂PH)₆₀ Cluster. *Nano Lett.* **2012**, *12*, 5861–5866.
- (33) Goswami, N.; Makhal, A.; Pal, S. K. Toward an Alternative Intrinsic Probe for Spectroscopic Characterization of a Protein. *J. Phys. Chem. B* **2010**, *114*, 15236–15243.
- (34) Petty, J. T.; Zheng, J.; Hud, N. V.; Dickson, R. M. DNA-Templated Ag Nanocluster Formation. *J. Am. Chem. Soc.* **2004**, *126*, 5207–5212.
- (35) Gwinn, E.; Schultz, D.; Copp, S.; Swasey, S. DNA-Protected Silver Clusters for Nanophotonics. *Nanomaterials* **2015**, *5*, 180–207.
- (36) Zheng, J.; Zhang, C.; Dickson, R. M. Highly Fluorescent, Water-Soluble, Size-Tunable Gold Quantum Dots. *Phys. Rev. Lett.* **2004**, *93*, 077402.
- (37) Zheng, J.; Nicovich, P. R.; Dickson, R. M. Highly Fluorescent Noble-Metal Quantum Dots. *Annu. Rev. Phys. Chem.* **2007**, *58*, 409–431.
- (38) Narayanan, S. S.; Pal, S. K. Structural and Functional Characterization of Luminescent Silver–Protein Nanobioconjugates. *J. Phys. Chem. C* **2008**, *112*, 4874–4879.

Supporting information

Initial Growth Kinetics of Luminescent Quantum Clusters of Silver Within Albumin Family Protein Templates

Kamalesh Chaudhari^{†,‡} & Thalappil Pradeep^{‡,}*

[†]Department of Biotechnology and [‡]DST Unit of Nanoscience (DST UNS) and Thematic Unit of Excellence (TUE), Department of Chemistry, Indian Institute of Technology Madras, Chennai 600 036, India.

*Address correspondence to

pradeep@iitm.ac.in

Table of contents

Sl. No.	Title	Page No.
1	Excitation and emission spectra of AgQC@Ova	3
2	Curve fitting of the excitation spectra of AgQC@BSA	4
3	Curve fitting of the emission spectra of AgQC@BSA	5
4	Curve fitting of the excitation spectra of AgQC@Ova	6
5	Curve fitting of the emission spectra of AgQC@Ova	7
6	Changes in the growth rate of AgQC@Ova	8
7	Jellium model applied to AgQC@BSA and AgQC@Ova	9
8	UV-Vis spectra of AgQC@BSA	10
9	UV-Vis spectra of AgQC@Ova	10
10	Growth constants and exponential growth function for AgQC@BSA and AgQC@Ova grown at different volumes of 10 mM NaBH ₄	11

Supporting figure 1

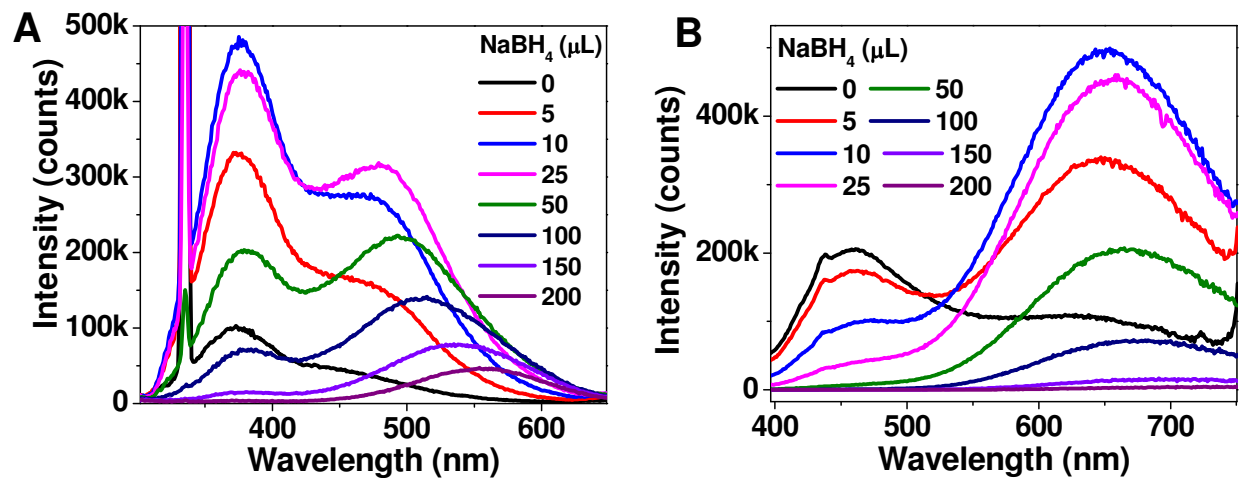


Fig S1: (A) Excitation spectra (Em – 670 nm) of AgQC@Ova. (B) Emission spectra (Ex – 380 nm) of AgQC@Ova.

Supporting figure 2

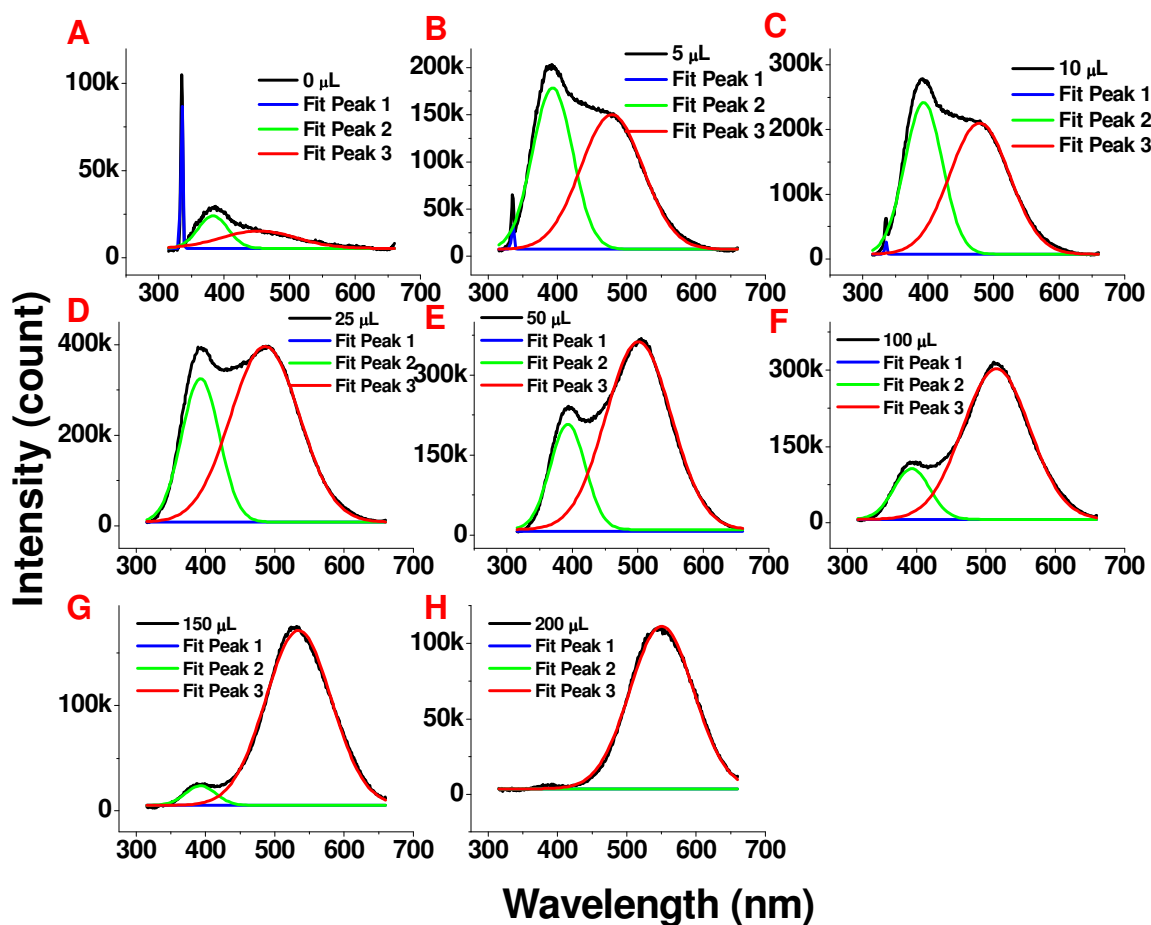


Fig S2: Gaussian peak fitting to excitation spectra ($E_m = 670$ nm) of AgQC@BSA grown using different volumes of 10 mM NaBH₄. Peak 1 was accounted for second order peak of emission. Peak 2 is for the excitation of Ag-BSA conjugates and Peak 3 is for the excitation of AgQCs.

Supporting figure 3

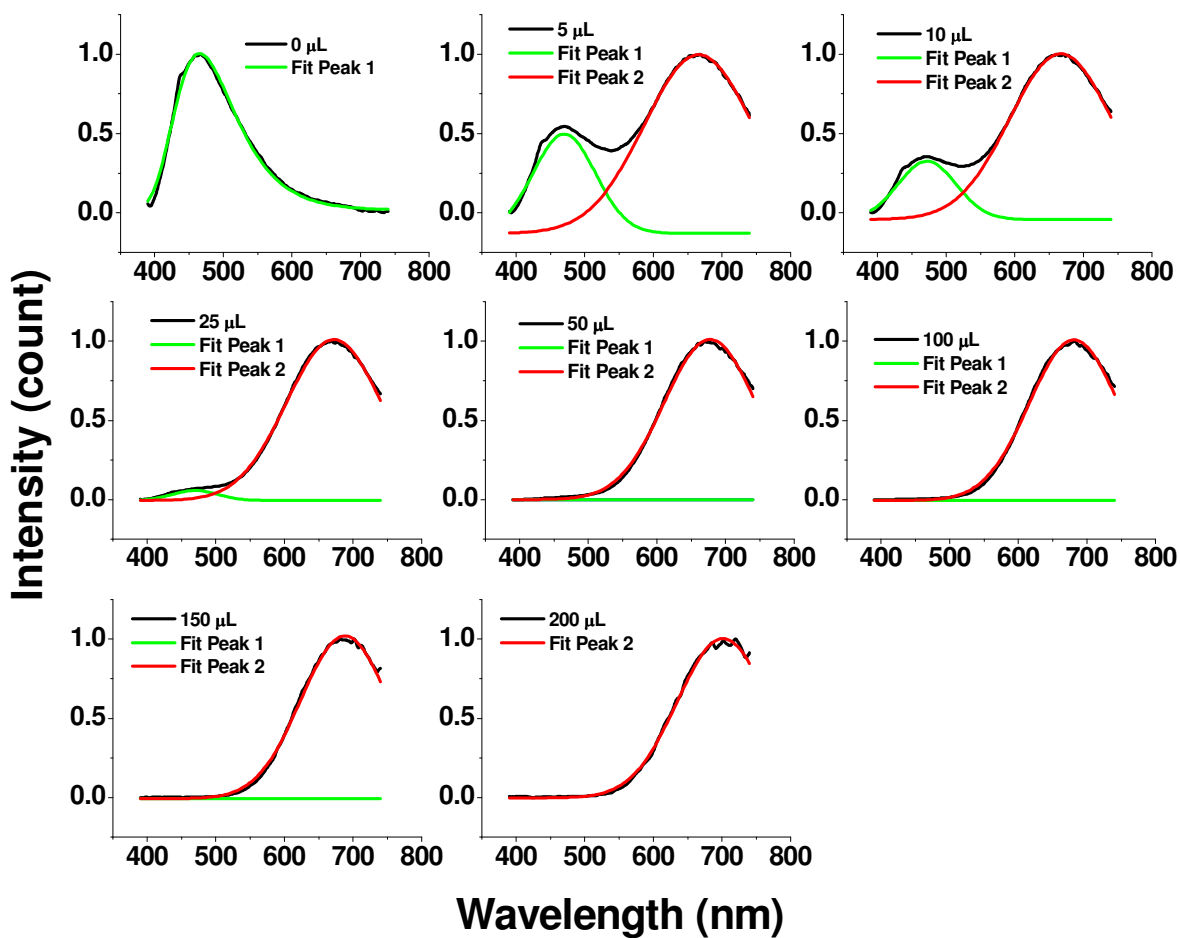


Fig S3: Gaussian peak fitting to emission spectra (Ex – 380 nm) of AgQC@BSA grown using different volumes of 10 mM NaBH₄. For the sample without NaBH₄ (0 μL), curve was fitted using extreme value (amplitude) function. Peak 1 is for the emission of Ag-BSA conjugates and Peak 2 is for the emission of AgQCs.

Supporting figure 4

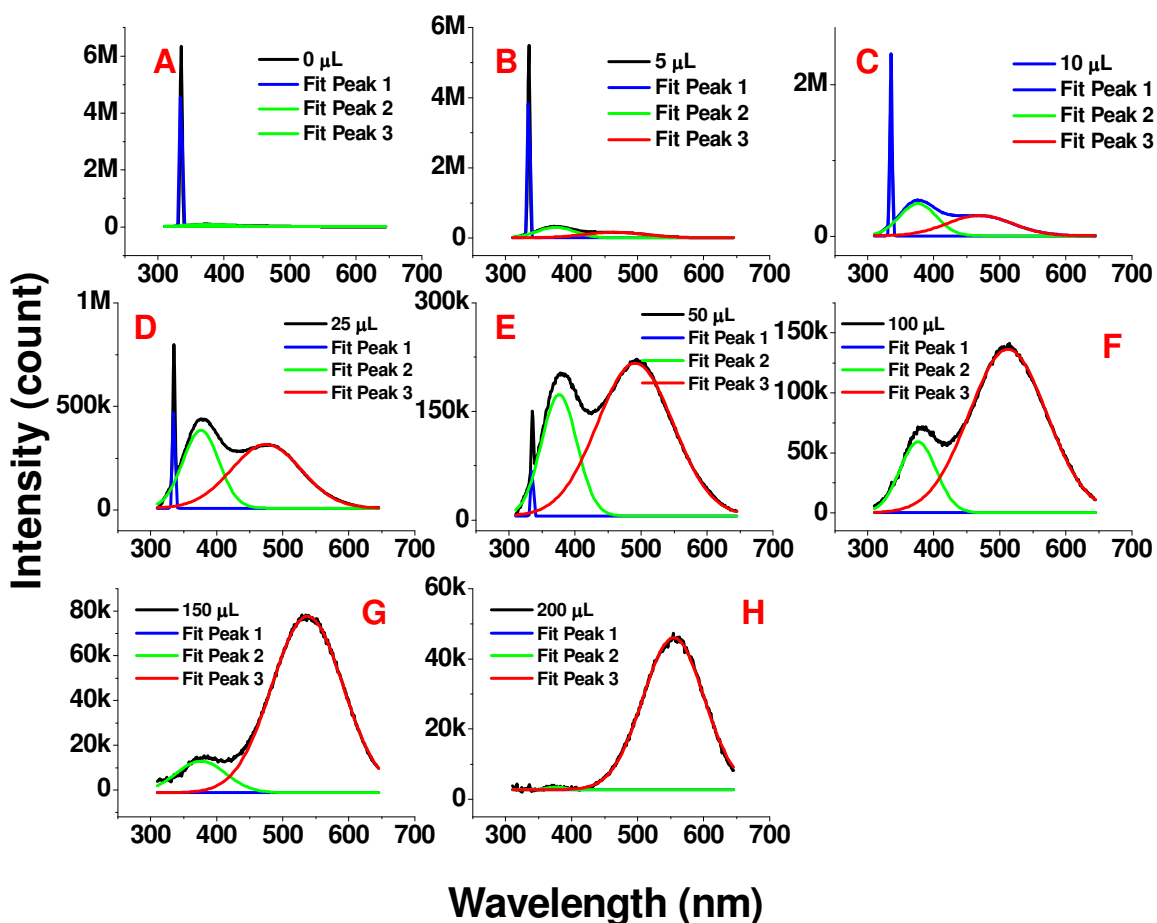


Fig S4: Gaussian peak fitting to excitation spectra ($E_m - 670$ nm) of AgQC@Ova grown using different volumes of 10 mM NaBH_4 . Peak 1 was accounted for second order peak of emission. Peak 2 is for the excitation of Ag-Ova conjugates and Peak 3 is for the excitation of AgQCs.

Supporting figure 5

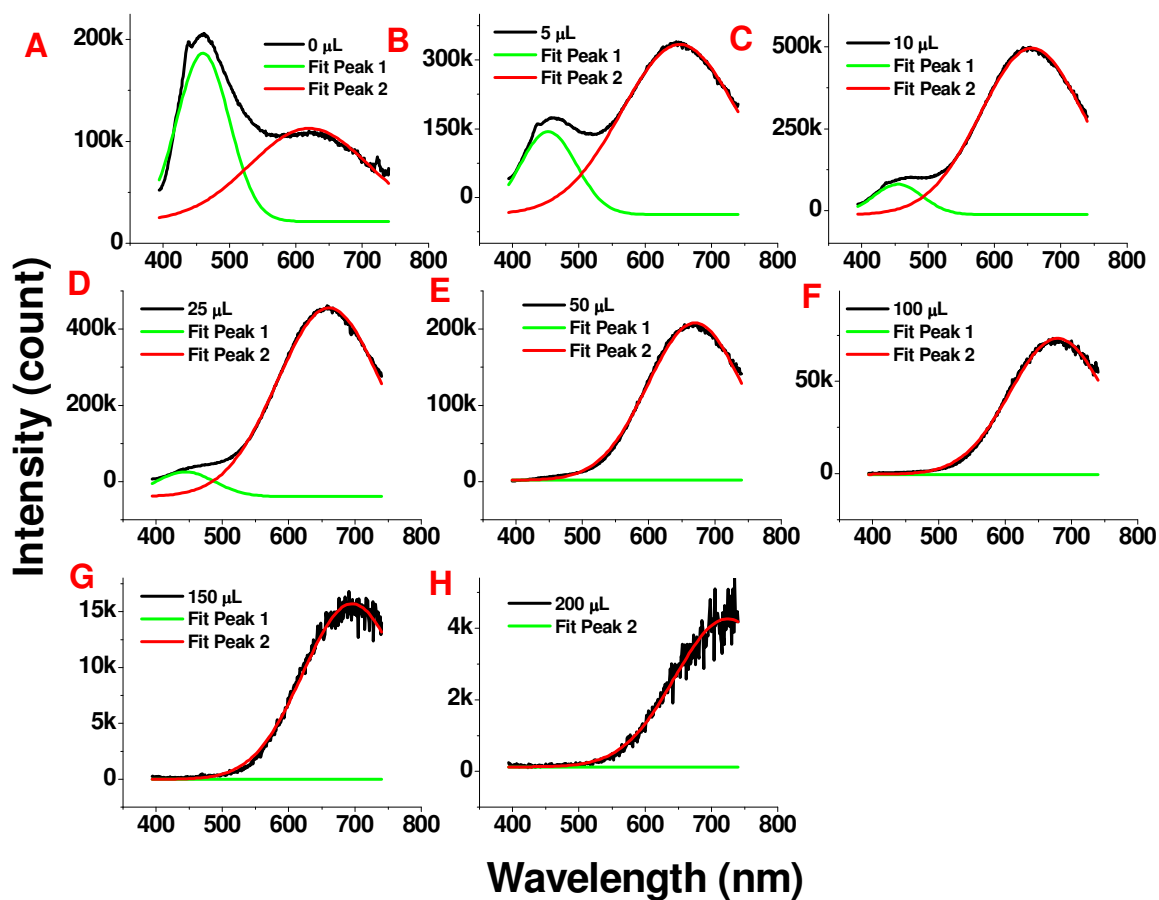


Fig S5: Gaussian peak fitting to emission spectra (Ex – 380 nm) of AgQC@Ova grown using different volumes of 10 mM NaBH₄. Peak 1 is for the emission of Ag-Ova conjugates and Peak 2 is for the emission of AgQCs.

Supporting figure 6

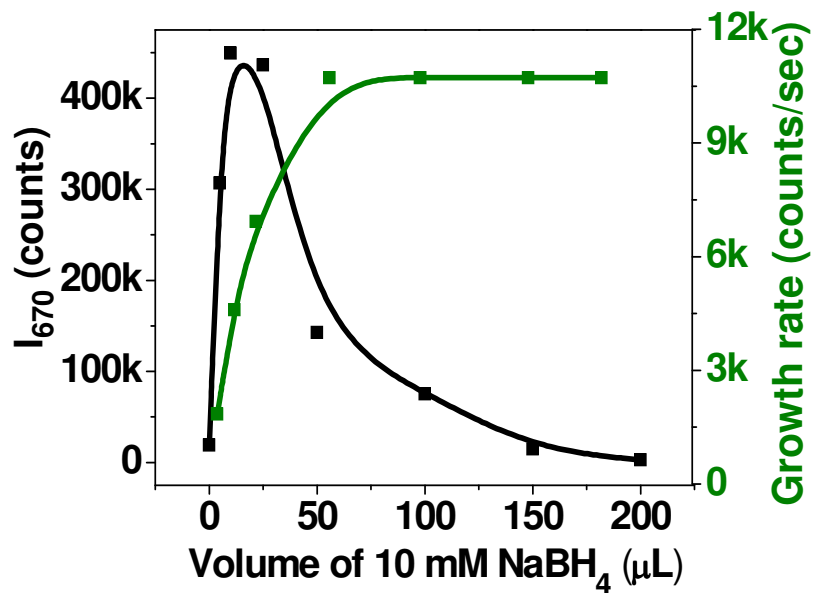


Fig S6: Changes in the emission intensity of AgQC@Ova after the addition of different volumes of 10 mM NaBH₄ after 500 seconds of reaction (black curve). Changes in the growth rate of AgQC@Ova (green curve).

Supporting figure 7

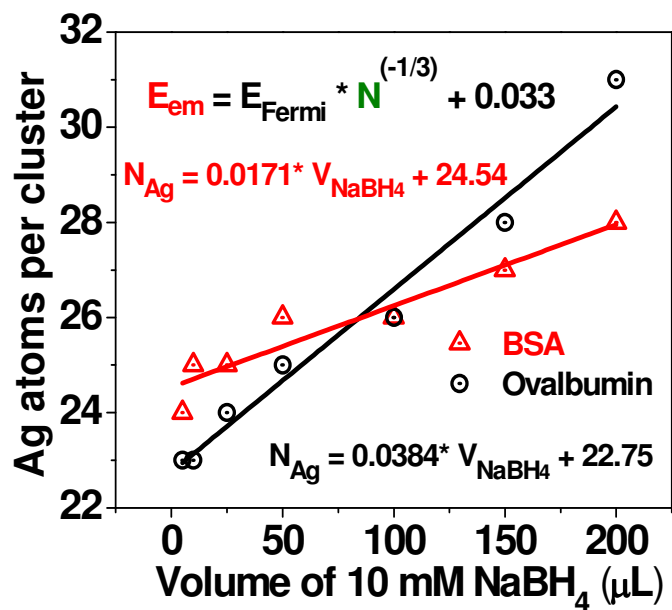


Fig S7: Jellium model¹⁻² was applied to AgQC@BSA and AgQC@Ova and number of silver atoms (N_{Ag}) per clusters was extrapolated from the emission energy values of QCs grown using different volumes of 10 mM NaBH₄ (V_{NaBH_4}). As shown by Zheng *et al.*, the anharmonicity parameter $U = 0.033$ has been added to the spherical jellium model equation.²

Supporting figure 8

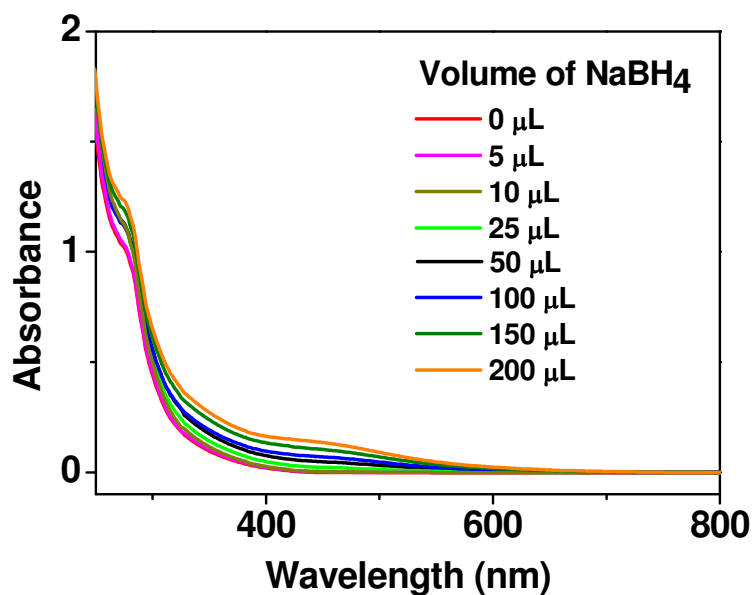


Fig S8: UV-Vis spectra of AgQC@BSA grown using different volumes of 10 mM NaBH₄.

Supporting figure 9

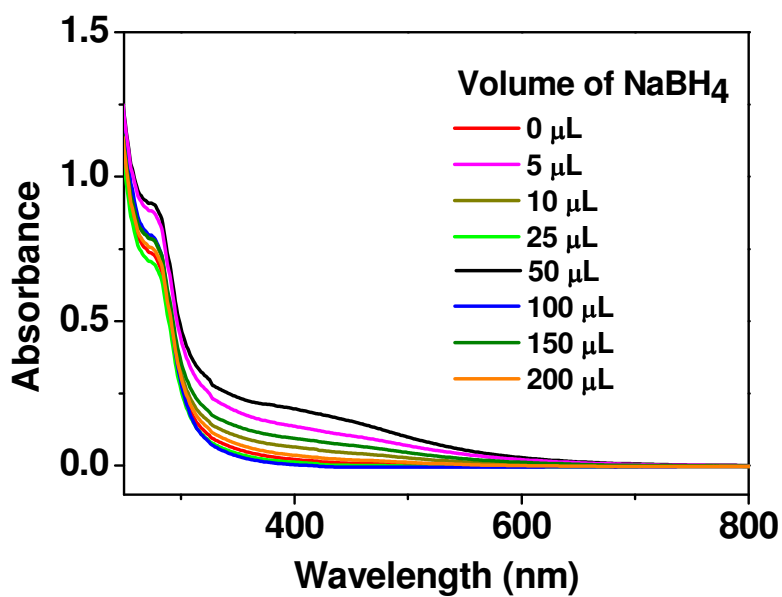


Fig S9: UV-Vis spectra of AgQC@Ova grown using different volumes of 10 mM NaBH₄.

Supporting table1

Concentration of NaBH ₄ (μL)	τ for BSA	τ for Ova
5	-41.7534	-110.546
10	-24.7828	-79.5955
25	-6.33972	-55.6722
50	-42.8316	-6.2128
100	-70.3621	-37.7251
150	-31.8202	-23.355
200	-16.7114	-10.6371

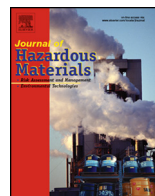
Table 1: Growth curves of AgQC@BSA and AgQC@Ova for different volumes of 10 mM NaBH₄ were fitted using single component exponential growth function given below,

$$I_{670} = C + Ae^{(t/\tau)}$$

Where, I_{670} is the emission intensity at 670 nm in counts, C is offset value for constant baseline, A is amplitude, t is time in seconds and τ is the growth constant. Initial growth transients were removed while fitting the decay curves. Obtained values of growth constants are shown in the table above.

References

1. Zheng, J.; Zhang, C.; Dickson, R. M., Highly Fluorescent, Water-Soluble, Size-Tunable Gold Quantum Dots. *Phys. Rev. Lett.* 2004, **93**, 077402.
2. Zheng, J.; Nicovich, P. R.; Dickson, R. M., Highly Fluorescent Noble-Metal Quantum Dots. *Annu. Rev. Phys. Chem.* 2007, **58**, 409-431.



Translocation of uranium from water to foodstuff while cooking



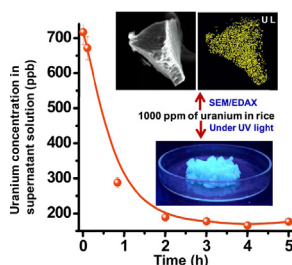
K.C. Krishnapriya¹, Ananya Baksi¹, Swathi Chaudhari¹, Soujit Sen Gupta, T. Pradeep*

DST Unit of Nanoscience (DST UNS), and Thematic Unit of Excellence (TUE), Department of Chemistry, Indian Institute of Technology Madras, Chennai 600 036, India

HIGHLIGHTS

- Rice can efficiently uptake uranium from water contaminated with uranyl nitrate hexahydrate ($\text{UO}_2(\text{NO}_3)_2 \cdot 6\text{H}_2\text{O}$), while cooking.
- Unusual uranium uptake to the extent of about 1000 ppm is observed when rice is cooked in highly concentrated uranium contaminated water (1240 ppm).
- Nature of interaction of uranium with carbohydrates is probed using small monosaccharides like glucose and mannose.
- Electrospray ionization mass spectrometry showed UO_2^{2+} to be the most stable species in water in such solutions which can form complexes with sugars.
- The species (UO_2^{2+}) is also observed in the case of water exposed to the common mineral, uranium oxide (UO_2) and similar type of complexation is observed with sugars.

GRAPHICAL ABSTRACT



ARTICLE INFO

Article history:

Received 8 November 2014

Received in revised form 31 March 2015

Accepted 13 April 2015

Available online 27 April 2015

Keywords:

Uranium contamination
Uranium–rice interaction
Uranyl–carbohydrate adducts
ICP-MS
ESI-MS

ABSTRACT

The present work reports the unusual uranium uptake by foodstuff, especially those rich in carbohydrates like rice when they are cooked in water, contaminated with uranium. The major staple diet in South Asia, rice, was chosen to study its interaction with UO_2^{2+} , the active uranium species in water, using inductively coupled plasma mass spectrometry. Highest uptake limit was checked by cooking rice at very high uranium concentration and it was found to be good scavenger of uranium. To gain insight into the mechanism of uptake, direct interaction of UO_2^{2+} with monosaccharides was also studied, using electrospray ionization mass spectrometry taking mannose as a model. The studies have been done with dissolved uranium salt, uranyl nitrate hexahydrate ($\text{UO}_2(\text{NO}_3)_2 \cdot 6\text{H}_2\text{O}$), as well as the leachate of a stable oxide of uranium, $\text{UO}_2(\text{s})$, both of which exist as UO_2^{2+} in water. Among the eight different rice varieties investigated, Karnataka Ponni showed the maximum uranium uptake whereas unpolished Basmati rice showed the minimum. Interaction with other foodstuffs (potato, carrot, peas, kidney beans and lentils) with and without NaCl affected the extent of chemical interaction but was not consistent with the carbohydrate content. Uranium interaction with D-mannose monitored through ESI-MS, under optimized instrumental parameters, identified the peaks corresponding to uranyl adduct with mannose

* Corresponding author. Tel.: +91 44 2257 4208; fax: 91 44 2257 0545/ 0509.

¹ Contributed equally.

monomer, dimer and trimer and the species were confirmed by MS/MS studies. The product ion mass spectra showed peaks illustrating water loss from the parent ion as the collision energy was increased, an evidence for the strong interaction of uranium with mannose. This study would constitute the essential background for understanding interaction of uranium with various foods. Extension of this work would involve identification of foodstuff as green heavy metal scavengers.

© 2015 Published by Elsevier B.V.

1. Introduction

Heavy metal contamination of the environment and livestock has been a growing concern of multidisciplinary interest, the impact of which has socio-political to scientific implications. The legacy of metal contamination so far comprises mostly of arsenic [1,2] followed by lead, [3–7] cadmium [4,6–10] and mercury [7,11] with more elements being identified as industrial exploitation increases. Extensive studies have been carried out on arsenic contamination of water resources, soil, vegetation and various environmentally relevant systems. Studies on the adverse effects of Cd, Pb and Hg have also been carried out and effective treatment methods have evolved [3,6,7,11–19]. Many documented cases of contamination due to other transition and rare earth elements also exist [1,20,21]. Other heavy metals including radioactive ones are also drawing attention lately [20,22–29]. Uranium has received significant attention over the last few decades owing to its promising applicability as a prospective energy power. These studies are important in India where it is estimated that uranium production will increase, as a result of the use of pressurized heavy water reactor technology utilizing enriched uranium. The principal ores of uranium are urania (mostly UO_2) and coffinite ($\text{U}(\text{SiO}_4)_{1-x}(\text{OH})_{4x}$). Solubility products of these oxides (in terms of $\log K_{\text{sp}}$) are in the range of -8.5 . In natural waters it exists as uranyl hydroxide and carbonate species. Recently efforts have been made to find the basis of uranium mobility and its effects on the environment have been reported. Pompe et al. [30] have investigated the interaction of UO_2^{2+} with humic acids (HAs) with and without modification and found that phenolic OH groups decide the complexation behavior of HAs. Uranium complexes formed after the uptake by plants were studied by Nitsche et al. [28]. In another work, the authors have reported different uranium speciation in water near to uranium mines by experimental determination as well as by modelling for the different U(VI) species, at specific pH range [29]. Compounds of relevance include $\text{Ca}_2\text{UO}_2(\text{CO}_3)_3$ (aq) in carbonate- and calcium-containing mine waters from Schlemma, Germany at pH 7.1. Uranium speciation changes depending on the pH and the ions and concentrations present in water. They have found that in carbonate-containing and calcium-poor tailing water from Helmsdorf at pH 9.8, $\text{UO}_2(\text{CO}_3)_3^{4-}$ is the most abundant uranium species, while UO_2SO_4 (aq) was the most abundant uranium species from sulfate-rich mine water in Königstein, Germany at pH 2.6 [29].

Even though respiratory intake and epidermal contact of uranium can cause health issues, it is through drinking water and food consumption the major propagation and biomagnification of uranium takes place in animals [31]. Recent studies on other mammals like rats and rabbits suggest that even the non-radioactive isotopes can cause hazardous effects in biosphere [23]. Studies based on the intake of uranium by animals showed that solubility of uranium is a crucial factor that determines its metabolism in the body. It appears that the amount of soluble uranium accumulated internally is proportional to the intake from ingestion or inhalation [22,32]. Igarashi et al. [26] has reported that the maximum allowed limit of uranium in humans is $40 \mu\text{g}/\text{kg}$ with approximate 40% present

in the muscles, 20% in the skeleton and 10%, 4%, 1% and 0.3% in the blood, lungs, liver and kidneys, respectively. Health hazards caused by exposure to uranium in rats and rabbits were evaluated by several research groups and changes in organs including kidney and liver were monitored [23,24]. Effect on humans consuming uranium contaminated drinking water in countries all over the world especially in Canada, Finland, Sweden, Ireland and USA suggested renal tissues are affected primarily [25].

The uranium poisoned environment and ecosystem demand effective remediation which should start with research on the basics of uranium interaction with biomolecules. From previous studies, it was found that many heavy metals bind with various carbohydrate moieties and contribute to the spread of contamination in environment and health hazards in vegetation [33,34]. Our investigation substantiates the need to list uranium in the category of heavy metals capable of strongly interacting with foodstuff. Since rice is the staple food in many countries (mainly Asian countries), even small uptake of uranium by the same deserves an extensive study as the permissible World Health Organization (WHO) limit for drinking water is 15 microgram/L. To study the mechanism of uranium-rice interaction, we chose D-mannose as a model monosaccharide and investigated the product using electrospray ionization mass spectrometry (ESI-MS).

2. Experimental section

2.1. Materials

Uranyl nitrate hexahydrate ($\text{UO}_2(\text{NO}_3)_2 \cdot 6\text{H}_2\text{O}$) was purchased from Thomas Bakers. Glucose and mannose were purchased from Sigma-Aldrich and Sisco Research Laboratories Pvt. Ltd., respectively. All the rice varieties and other foodstuff used in the study were obtained from the local market. All the chemicals were used without further purification and deionized water was also used throughout the experiment. Urania (UO_2) was gifted by IGCAR, India.

2.2. Instruments

Inductively coupled plasma-mass spectrometry (ICP-MS) measurements of the samples were done with a PerkinElmer NexION 300X instrument. Prior to ICP-MS analysis, the non liquid samples were digested using an Anton Paar microwave digester at 800 W for 20 min. Scanning electron microscopy (SEM) and energy dispersive analysis of the X-ray (EDAX) images were collected using an FEI QUANTA-200. X-ray photoelectron spectroscopy (XPS) studies were conducted with an Omicron ESCA probe spectrometer with polychromatic Mg $K\alpha$ X-rays ($h\nu = 1253.6 \text{ eV}$). Electrospray ionization mass spectrometry (ESI-MS) analysis was carried out using Applied Biosystems 3200 QTRAP LC/MS/MS system in the mass range of m/z 80 to 1700. The optimized conditions used are as follows: declustering potential (DP) = 60 V, entrance potential (EP) = 10 V, ion spray voltage (IS) = 3 kV, collision energy (CE) = 10–60 V, collision cell exit potential (CXP) = -1 V .

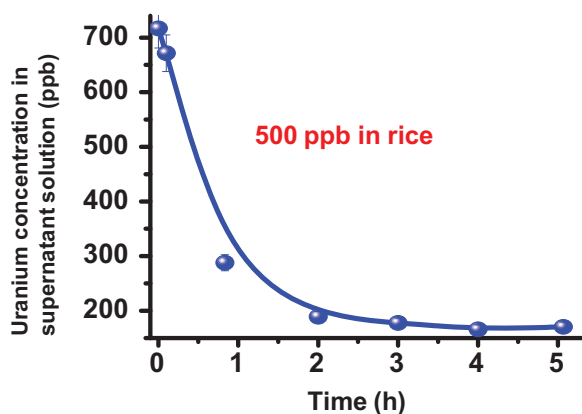


Fig. 1. Decrease in the uranium concentration in the supernatant solution with time during cooking of Karnataka Ponni rice in water containing 720 ppb of uranium.

2.3. Methods

2.3.1. Uranium interaction with rice and other foodstuffs

Eight different rice varieties were chosen for the study including polished and unpolished of each variety. For each one, 2 g of rice was weighed and cooked in 40 mL of 1 ppm $\text{UO}_2(\text{NO}_3)_2 \cdot 6\text{H}_2\text{O}$ solution at 80°C (solution temperature) in a teflon beaker for a period of 2 h. Simultaneously a blank of the rice sample without uranium salt was also cooked under the same conditions. For ICP–MS analysis, it was collected 1 mL of the supernatant (starch) solution with regular time interval (0.5 h) and 43.4 μL of concentrated nitric acid was added (to make it 5% as standards are also made by this procedure for our instrument). After complete cooking, the entire rice was divided in two equal parts in two digestion tubes, followed by the addition of 1 mL water, 2 mL H_2O_2 and 5 mL concentrated HNO_3 and digested using a microwave digester, working at high pressure and temperature (reference method). The digested samples were diluted and subjected to ICP–MS analysis. A sample of the cooked rice was analyzed to estimate the uranium content in it using SEM, EDAX and XPS methods. For this, a small amount of the cooked rice was oven dried and ground into a fine powder prior to analysis.

UO_2 was stirred in water for 1 h, centrifuged and collected the supernatant which was analyzed for its uranium content. This solution was used as stock solution for reactions with UO_2 .

2.3.2. Uranium interaction with a simple carbohydrate as the model system

In order to explore the chemistry of uranium–rice interaction, it was synthesized uranium–mannose adduct following a previously reported method [35]. A 20 mL solution of 2 mM $\text{UO}_2(\text{NO}_3)_2 \cdot 6\text{H}_2\text{O}$ was added to a hot solution of D–glucose (1 mM) in deionized water (30 mL) and heated for 30 min at 80°C . The solution was diluted using deionized water and samples of concentration ranging from 5 ppb to 50 ppm were prepared and analyzed by ESI–MS.

3. Results and discussion

3.1. Uptake of uranium by rice

The results of the investigated uranium interaction with eight different rice samples cooked in water contaminated with uranium is presented in Figs. 1 and 2 and Table 1. Fig. 1A shows a continuous and fast decrease in the uranium concentration in supernatant solution, upon cooking Karnataka Ponni rice which tends to reach a constant value. This implies that rice is uptaking uranium from water while being cooked. Other rice varieties also show more or less similar trend as shown in Fig. 2. Degree of uranium uptake

Table 1

Uranium uptake by different rice varieties per g of the sample. P, UP, B stand for polished, unpolished and boiled, respectively.

Rice variety	Uranium uptake/g of rice (in ppb)
T.N. Ponni (P, B)	314
T.N. Ponni (UP, B)	595
Basmati (P)	465
Basmati (UP)	340
Karnataka ponni	734
Kerala rice	402
Idli rice	375
IR 20	429

depends both on uranium concentration and variety of rice used. Almost all the uranium was uptaken within 2 h which is reflected by a drastic decrease in uranium concentration in the supernatant solution (Fig. 1). After 3 h of cooking, the process attains equilibrium with no significant change in the concentration thereafter confirming that the rice has attained its maximum uranium uptake capacity (see later in Fig. 3). After 5 h of cooking, the rice was digested and analyzed, following the method described above, to estimate the uranium concentration inside and it was found to be in a good agreement with the supernatant solution concentration as the initial concentration of uranium was 720 ppb while after 5 h of cooking, in the supernatant it was found to be 180 ppb and about 500 ppb in the cooked rice. Uranium uptake experiments were performed with different rice varieties considering both polished and unpolished rice. Uranium concentration in rice after cooking is given in Table 1. Among all, Karnataka Ponni (polished) rice showed highest uranium uptake capacity, whereas T.N. Ponni (polished) has the lowest capacity to concentrate uranium from the solution. Compared to the unpolished variety, polished variety of Basmati rice scavenges uranium more readily from solution whereas for T.N. Ponni, the case is opposite. Therefore, it cannot draw any conclusion whether the polish (rice bran) is affecting or not the uranium uptake. This capability seems strongly depends on the rice variety (see Fig. 2).

Although it was seen that rice can uptake high amounts of uranium, the concentration reached in the experiments (Table 1: above 500 ppb) are not adequate to conduct studies using EDAX, XPS, etc. To overcome this problem, it was tried to find the limit of uptake of uranium in rice. For this study, a 1240 ppm uranium solution (prepared from $\text{UO}_2(\text{NO}_3)_2 \cdot 6\text{H}_2\text{O}$) was used and cooked rice was soaked in it. After 4 h of soaking, only 245 ppm of uranium was left in the solution. Under visible light the rice color is yellow and shows light green fluorescence under UV light due to uranium (Fig. 3A). The fluorescence might be masked due to inherent blue fluorescence from rice. A sample of the cooked rice was oven dried, ground and used for XPS, SEM and EDAX analyses and the corresponding data are represented in Fig. 3B–D, respectively. The SEM–EDAX analysis of a small portion of rice shows the presence of uranium along with other elemental components and it is evenly distributed throughout the rice as seen from elemental mapping (Fig. 3B). From XPS analysis, binding energies of U 4f7/2 and 4f5/2 were found to be 381.5 eV and 392.3 eV, respectively with spin–orbit coupling (Δ) of 10.8 eV (standard $\Delta = 10.89$ eV for U), confirming U(VI) state in the rice sample (See Fig. 3 and Fig. S2). Please note that, this study has no relevance to normal cooking and was performed to check maximum uranium uptake limit of rice. This opens up a new possibility of extracting uranium from uranium concentrates by rice or other foodstuff.

3.2. Effect on other metal ion concentration

It is known that other metal ions like iron, manganese, etc., are present in rice in very small quantities. The binding of these met-

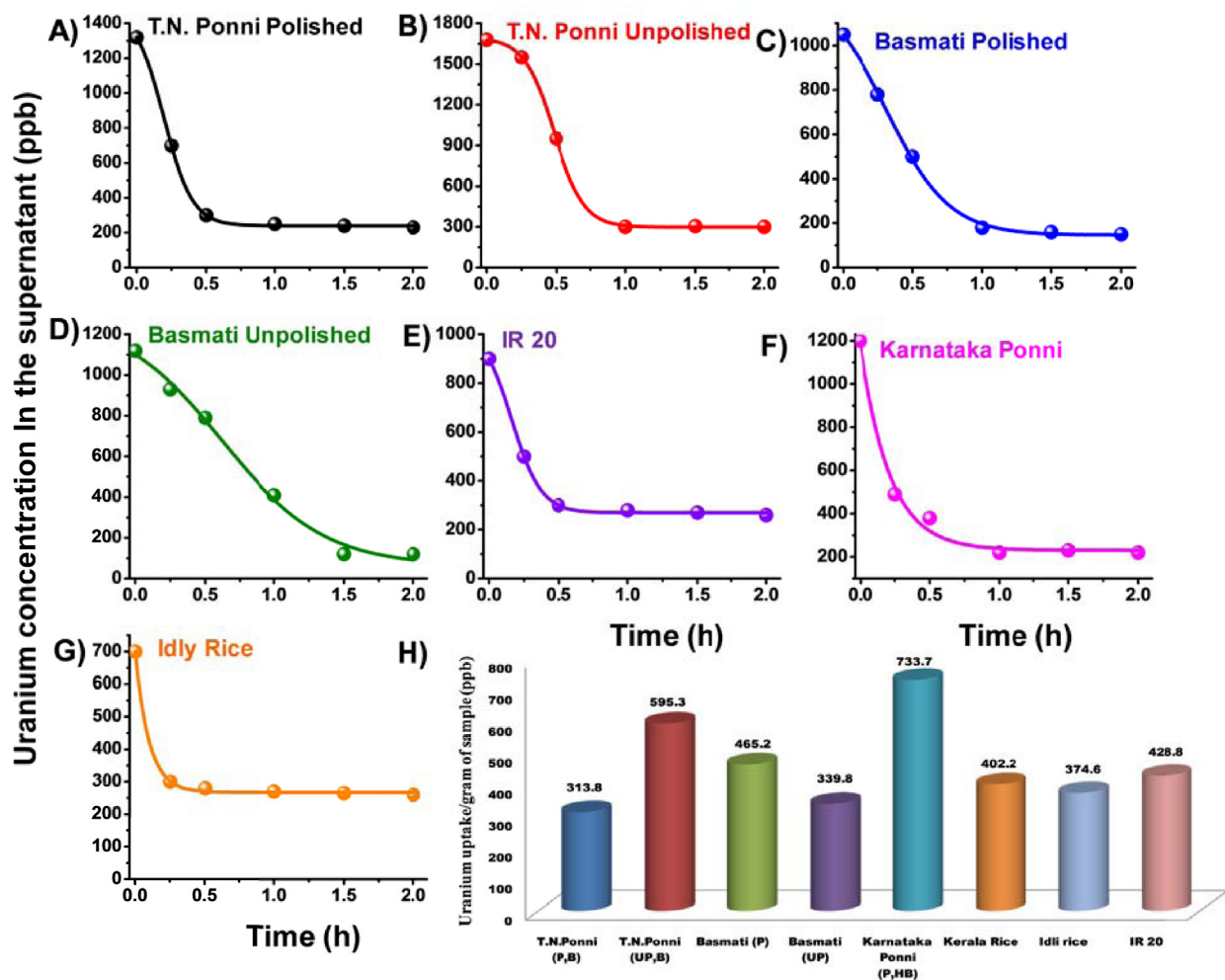


Fig. 2. A–G) Change in uranium concentration in the supernatant solution with time when 2 gram of different rice was cooked at 80 °C. Polynomial fits of the data points are also shown. H) Uranium concentration per g of rice cooked in uranium contaminated water.

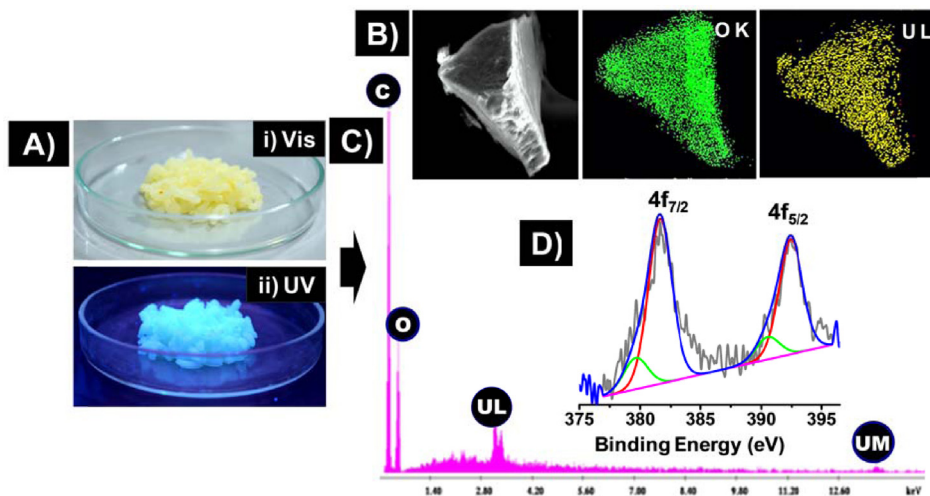


Fig. 3. A) Photographs of cooked rice soaked in highly concentrated uranium-containing water under visible (i) and UV light (ii). B) SEM image and elemental mapping of a cooked rice grain. Corresponding EDAX spectrum is shown in C. Presence of uranium was further proved by XPS in the U 4f region, is shown in D.

als to rice is still to be explored. Another goal of the study was to investigate whether the uptake of uranium affects the concentration of metal ions already present in rice. For this purpose the

concentration of different metal ions such as manganese, iron, nickel, copper, zinc and chromium in rice we monitored in the supernatant solution during regular intervals using ICP–MS. Com-

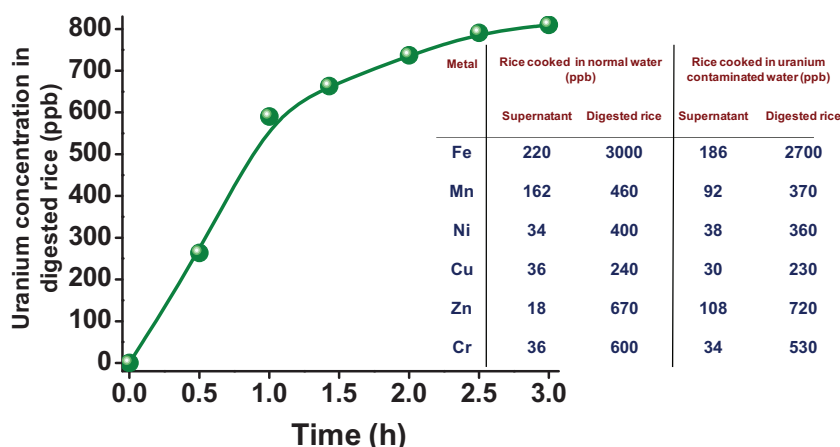


Fig. 4. Change in uranium concentration in the digested rice with time during cooking of Karnataka Ponni rice in water containing 1 ppm of uranium.

paring the concentration change of the transition metal ions during cooking with and without uranium, it was found that uranium uptake does not alter the binding of other metals to any significant extent as evident from Fig. 4.

3.3. Uranium interaction with monosaccharide

The experiments indicate that rice is scavenging uranium from water containing uranium in the form of uranyl ion. The next step was focused on exploring the chemistry of the interaction at the molecular level using mass spectrometry. As it is difficult to monitor directly rice or the supernatant by ESI-MS, the experiments were performed with a simple carbohydrate, mannose as our model system and tried monitoring its interaction with uranium. As it is interesting to probe if uranium naturally interactions occurred in contaminated areas it was used a common uranium mineral, urania (mostly UO_2) as the uranium source. It was found that uranium species existing in water are the same irrespective of whether they are generated from UO_2 or from a suitable commercially available uranium salt as shown in Fig. 5. Uranyl bound mannose monomer, dimer and also trimer were observed in ESI-MS along a few water detachment products from mannose. Uranium can be tetra or hexa-coordinated [35]. Hydroxyl groups in mannose can participate in complexation to give tetra co-ordination for single and hexa co-ordination for double mannose attachment. From previous reports it was known that sugar can coordinate with U through two -OH groups [35]. In aqueous solution UO_2^{2+} is mostly found to be hydrated as most intense peak is due to $\text{UO}_2(\text{OH})^+$. Since the solubility of uranium oxide in water is very low, it was found more appropriate to carry out further mass spectral analysis of uranium carbohydrate interaction using $\text{UO}_2(\text{NO}_3)_2 \cdot 6\text{H}_2\text{O}$ as the uranium source. The mass spectra generated for $\text{UO}_2(\text{NO}_3)_2 \cdot 6\text{H}_2\text{O}$, mannose solution and uranyl-mannose adduct in positive ion mode are shown in the Fig. 6(A). The ESI-MS of mannose in water usually forms Na adduct and the corresponding peak is observed at m/z 203 ($\text{M-Na})^+$ which gives an overall positive charge.

Same tendency was found for mannose dimer and trimer also as shown in Fig. 6C. MS/MS of Na attached dimer or trimer leads to the mannose monomer. Uranyl nitrate can lose one or both the nitrate groups and can form UO_2^{2+} and $\text{UO}_2(\text{NO}_3)^+$. The UO_2^{2+} can capture one electron and can appear as UO_2^+ in positive ion mode. We have observed both the ions $[\text{UO}_2^+]$ and $[\text{UO}_2(\text{NO}_3)^+]$ in positive mode (see Fig. 6B). Corresponding nitrate ion was also observed in the negative ion mode at m/z 62. The UO_2^{2+} can form adduct with water and $\text{UO}_2(\text{OH})^+$ is a well known species and was detected at m/z 287. Uranium has three natural isotopes U^{234} , U^{235} and U^{238} . Among

them, U^{238} is the most abundant one (around 99.3%). The other (radioactive) isotopes, U^{234} (0.0053%) and U^{235} (0.72%) are very hard to detect through ordinary mass spectrometry. The MS/MS study of $\text{UO}_2(\text{OH})^+$ leads to free UO_2^+ but it never decay to free uranium ion which can be explained in terms of the stability of the ion in solution as well as in the gas phase. The important peaks found exclusively in the uranyl-mannose sample compared to the precursor spectra are m/z 449 and m/z 629. They correspond to uranyl adduct with mannose monomer and dimer, respectively. And at higher concentration, a trimer adduct at m/z 809 was also spotted. Detection of a peak at m/z 449 suggests that the species must have been formed by the loss of a proton from one of the hydroxyl groups coordinating UO_2^+ and the as-formed complex is stable in solution as well as in the gas phase.

In order to have more information regarding the species corresponding to m/z 449 and 629 peaks, the MS/MS spectra were also recorded, as shown in Fig. 7 from which it confirmed the adduct formation and strong binding of uranium with mannose.

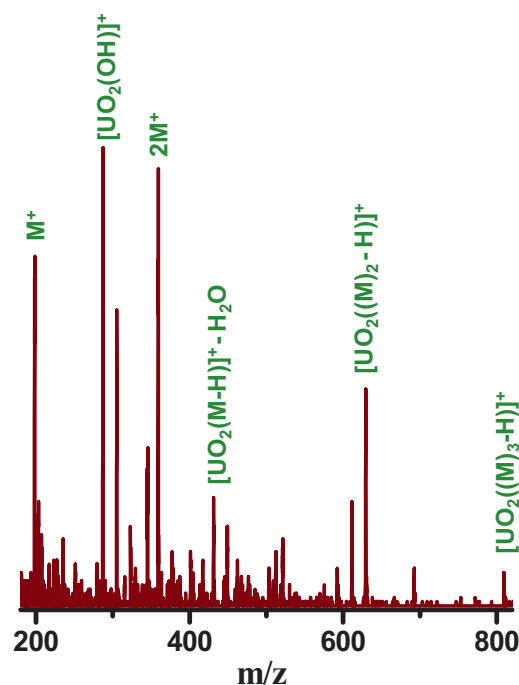


Fig. 5. ESI MS of uranyl-mannose adduct (prepared using urania) in positive ion mode.

In CID (collision induced dissociation), with increasing collision energy (CE), it was found that the intensity of the parent peak decreases and new peaks appear which are separated by m/z 18 due to water loss which is a common fragmentation pattern in all the sugars. The peak at m/z 629 also shows similar kind of water loss at lower collision energy. At higher CE, one mannose unit loss was observed and subsequent water loss species have

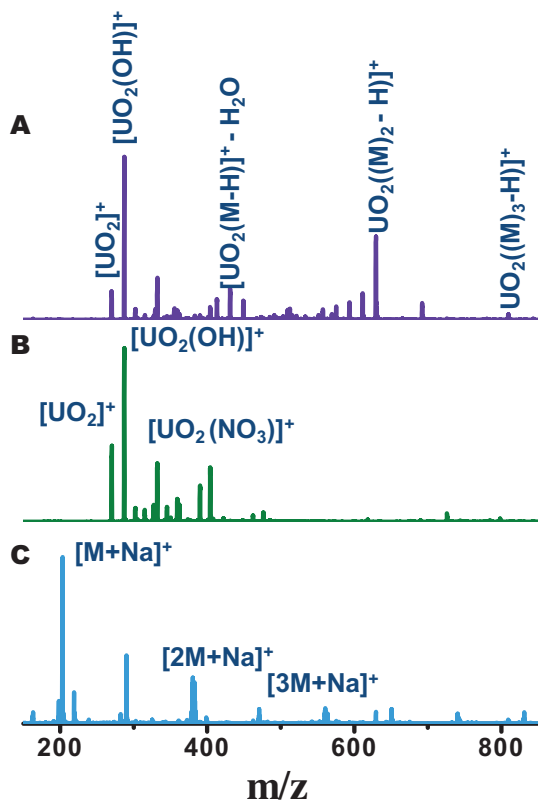


Fig. 6. ESI MS of (A) uranyl-mannose adduct (prepared using $\text{UO}_2(\text{NO}_3)_2 \cdot 6\text{H}_2\text{O}$, (B) $\text{UO}_2(\text{NO}_3)_2 \cdot 6\text{H}_2\text{O}$ and (C) mannose in positive ion mode.

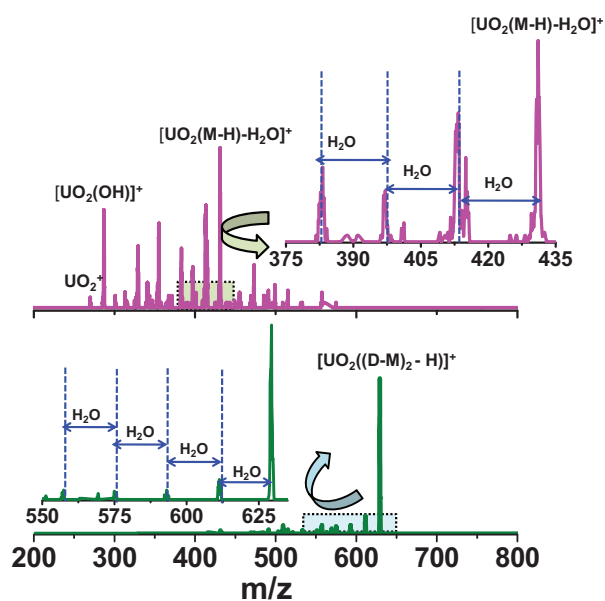


Fig. 7. ESI MS/MS of uranyl-mannose adduct with increase in collision energy (CE) showing water loss products at lower CE. At higher CE, mannose as well as water loss were observed.

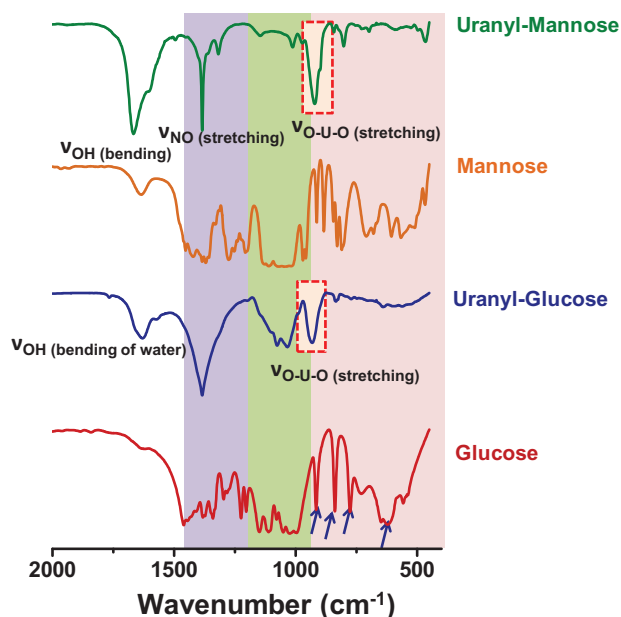


Fig. 8. IR spectra of glucose-uranyl and mannose-uranyl complexes, showing significant differences from the parent glucose and mannose. The arrows are showing the finger print peaks for sugars. Some of peaks at 3140–3460 and 990–1130 cm^{-1} are saturated.

also been formed as shown in Fig. 7. Note that similar kind of adduct formation was observed previously with glucose and the complex was studied using infra-red (IR) and nuclear magnetic resonance (NMR) but not observed in mass spectrometry suggesting that the species might not be stable in the gas phase [35]. It was also monitored glucose, mannose and the corresponding complex formation by IR spectroscopy. The anomeric structure of glucose and mannose can be confirmed from the 950–500 cm^{-1} region where signature peaks of D-glucose were observed around 915, 850, 780 and 600 cm^{-1} (Fig. 8 and Fig. S3 marked with blue arrow). Huge changes were observed in this region confirming appreciable interaction of uranium with glucose/mannose. A strong peak was observed at 930 cm^{-1} which can be attributed as O–U–O stretching in uranyl-glucose/mannose complex as marked in Fig. 8. Several bands due to CH_2 , C–OH and C–CH bending modes come in the 1460–1200 cm^{-1} region. Most of the peaks were absent or shifted after complexation with uranyl. Several other peaks were observed in the 1150–950 cm^{-1} region due to ring C–O stretching vibrations which also changed significantly after complexation. A strong absorption at 1384 cm^{-1} can be confirmed for N–O stretching frequency of nitrate ion which was originally absent in glucose/mannose and appeared only after complexation with uranyl ions. Peak around 1650 cm^{-1} is due to the H_2O bending mode. Significant changes were observed in the 4000–3000 cm^{-1} region where several OH and CH stretching frequencies overlap confirming involvement of OH groups in complexation with UO_2^{2+} . These data are in good agreement with the previously reported glucose-uranyl complex [35].

3.4. Interaction of uranium with other foodstuffs

Unusual uranium uptake by rice inspired to widen the study to different vegetables with varying carbohydrate content. Potato, carrot, peas, lentils and kidney beans were chosen for the purpose. The results presented in Fig. 7 show that not only starchy food but also other foods with less carbohydrate content (potato, carrot, kidney bean, lentil and peas) uptake reasonable quantities of uranium; in some cases uranium uptake is comparable with some rice

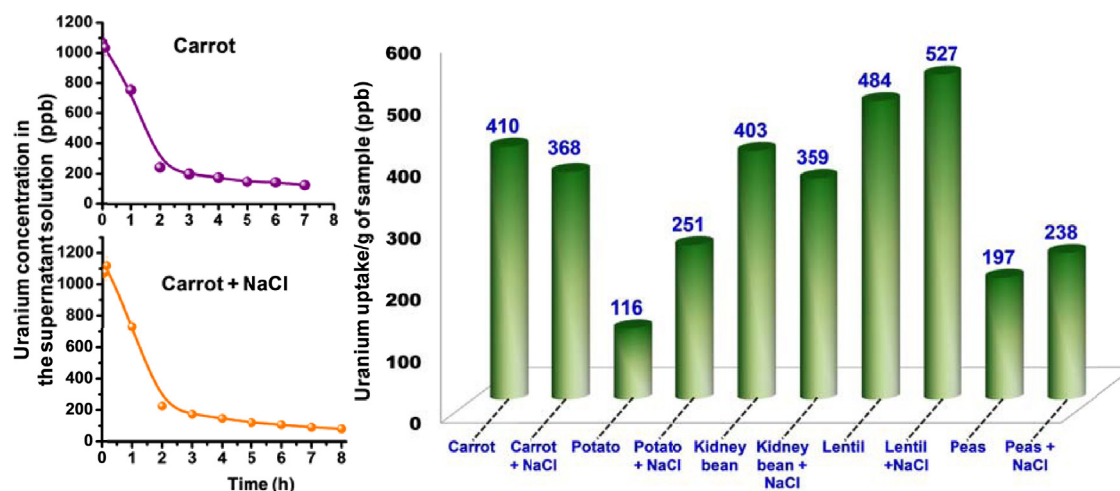


Fig. 9. (A) Decrease of uranium concentration in the supernatant solution with time during cooking of carrot with and without NaCl in water containing uranium. (B) Uranium concentration per gram of the food cooked in 1 ppm uranium contaminated water.

varieties. In the tested foodstuffs, some of them create color in the solution and moreover, they get boiled easily leaving some particles in the solution making it difficult by ICP–MS analysis. Therefore, it was not possible to monitor the release of uranium concentration into the supernatant, except for carrot which results are presented in Fig. 9A. For carrot, just after 2 h of cooking, uranium concentration in the solution decreased to 240 ppb (initial uranium concentration was 1070 ppb) and was saturated within 3 h (190 ppb at 3 h and 125 ppb after 7 h). Cooked carrot sample showed about 410 ppb of uranium.

When cooking, all these foodstuffs are in the presence of salt and other ingredients. As the use of all the ingredients can create additional colors and other effects in foods, the experiments were restricted to NaCl. Each of the food samples was cooked with and without NaCl (50 ppm). Even though the presence of salt changes the uranium uptake (Fig. 9B), it was not possible to reach a conclusion as in some cases uptake increased and in others decreased.

4. Summary and conclusions

In the present study, it was investigated the interaction of uranium (1 ppm) with different cooked foodstuffs. Among the eight different rice varieties Karnataka ponni showed the maximum uranium uptake whereas unpolished basmati rice showed the minimum but all of them uptake maximum uranium content from water after 2 h of cooking. Interaction with other foodstuffs (potato, carrot, peas, kidney beans and lentils) with and without NaCl affected the extent of chemical interaction but was not consistent with the carbohydrate content. The monitored uranium interaction with D-mannose through ESI–MS, under optimized instrumental parameters, identified the peaks which corresponded to uranyl adduct with mannose monomer, dimer and trimer which were also confirmed by MS/MS study. The product ion mass spectra showed peaks illustrating water loss from the parent ion as the collision energy was increased, an evidence for the strong interaction of uranium with mannose. This study would constitute the essential background for understanding interaction of uranium with various foodstuffs. Further extension of this work would be carried out with various heavy metals and other contaminants present in water as many such species are being reported in the recent past.

Acknowledgements

The experimental work was supported by the Department of Science and Technology. K.K.C. and A.B. thank Sudhakar Chennu, E. Sundarraj, Mohd. Azahardin Ganayee for XPS, SEM/EDAX and IR, respectively. A.B. thanks CSIR for a fellowship. S.S.G. thanks the SERB, CII and Thermax India Pvt., Ltd., for a research fellowship.

Appendix A. Supplementary data

Supplementary data associated with this article can be found, in the online version, at <http://dx.doi.org/10.1016/j.jhazmat.2015.04.041>.

References

- [1] B.K. Mandal, K.T. Suzuki, Arsenic round the world: a review, *Talanta* 58 (2002) 201–235.
- [2] M.U. Sankar, S. Aigal, S.M. Maliyekkal, A. Chaudhary, A.A. Anshup, K. Kumar, Chaudhari, T. Pradeep, Biopolymer-reinforced synthetic granular nanocomposites for affordable point-of-use water purification, *Proc. Natl. Acad. Sci. U. S. A.* 110 (2013) 8459–8464, S8459/8426–S 8459/8451.
- [3] G.M.A. Bermudez, R. Jasan, R. Pla, M.L. Pignata, Heavy metal and trace element concentrations in wheat grains: assessment of potential non-carcinogenic health hazard through their consumption, *J. Hazard. Mater.* 193 (2011) 264–271.
- [4] S. Dudka, M. Piotrowska, H. Terelak, Transfer of cadmium, lead, and zinc from industrially contaminated soil to crop plants: a field study, *Environ. Pollut.* 94 (1997) 181–188.
- [5] M. Komarek, V. Ettler, V. Chrastny, M. Mihaljevic, Lead isotopes in environmental sciences: a review, *Environ. Int.* 34 (2008) 562–577.
- [6] G. Nabulo, H. Oryem-Origa, M. Diamond, Assessment of lead, cadmium, and zinc contamination of roadside soils, surface films, and vegetables in Kampala City, Uganda, *Environ. Res.* 101 (2006) 42–52.
- [7] N. Zheng, Q. Wang, D. Zheng, Health risk of Hg, Pb, Cd, Zn, and Cu to the inhabitants around Huludao Zinc Plant in China via consumption of vegetables, *Sci. Total Environ.* 383 (2007) 81–89.
- [8] J. Godt, F. Scheidig, C. Grosse-Siestrup, V. Esche, P. Brandenburg, A. Reich, D.A. Gronenberg, The toxicity of cadmium and resulting hazards for human health, *J. Occup. Med. Toxicol.* (London, U.K.) 1 (2006).
- [9] L. Jaerup, A. Akesson, Current status of cadmium as an environmental health problem, *Toxicol. Appl. Pharmacol.* 238 (2009) 201–208.
- [10] N. Johri, G. Jacquillet, R. Unwin, Heavy metal poisoning: the effects of cadmium on the kidney, *BioMetals* 23 (2010) 783–792.
- [11] Q. Wang, D. Kim, D.D. Dionysiou, G.A. Sorial, D. Timberlake, Sources and remediation for mercury contamination in aquatic systems – a literature review, *Environ. Pollut. (Amsterdam, Neth.)* 131 (2004) 323–336.
- [12] S. Khan, Q. Cao, Y.M. Zheng, Y.Z. Huang, Y.G. Zhu, Health risks of heavy metals in contaminated soils and food crops irrigated with wastewater in Beijing, China, *Environ. Pollut. (Amsterdam, Neth.)* 152 (2008) 686–692.
- [13] Q. Wei, R. Nagi, K. Sadeghi, S. Feng, E. Yan, S.J. Ki, R. Caire, D. Tseng, A. Ozcan, Detection and spatial mapping of mercury contamination in water samples using a smart-phone, *ACS Nano* 8 (2014) 1121–1129.

- [14] J. Wang, X. Feng, C.W.N. Anderson, Y. Xing, L. Shang, Remediation of mercury contaminated sites – a review, *J. Hazard. Mater.* 221–222 (2012) 1–18.
- [15] G. Flora, D. Gupta, A. Tiwari, Toxicity of lead: a review with recent updates, *Interdiscip. Toxicol.* 5 (2012) 47–58.
- [16] R.A. Bernhoft, Mercury toxicity and treatment: a review of the literature, *J. Environ. Public Health* 2012 (2012) 460508.
- [17] B.A. Fowler, Monitoring of human populations for early markers of cadmium toxicity: a review, *Toxicol. Appl. Pharmacol.* 238 (2009) 294–300.
- [18] A. Boudou, R. Maury-Brachet, M. Coquery, G. Durrieu, D. Cossa, Synergic effect of gold mining and damming on mercury contamination in fish, *Environ. Sci. Technol.* 39 (2005) 2448–2454.
- [19] H. Needleman, Lead poisoning, *Annu. Rev. Med.* 55 (2004) 209–222.
- [20] J. Kucera, J. Mizera, Z. Randa, M. Vavrova, Pollution of agricultural crops with lanthanides, thorium and uranium studied by instrumental and radiochemical neutron activation analysis, *J. Radioanal. Nucl. Chem.* 271 (2007) 581–587.
- [21] W. Yantasee, G.E. Fryxell, R.S. Addleman, R.J. Wiacek, V. Koonsiripaiboon, K. Pattamakomsan, V. Sukwarotwat, J. Xu, K.N. Raymond, Selective removal of lanthanides from natural waters, acidic streams and dialysate, *J. Hazard. Mater.* 168 (2009) 1233–1238.
- [22] E.I. Hamilton, Concentration of uranium in man and his diet, *Health Phys.* 22 (1972) 149–153.
- [23] F.J. Bowman, E.C. Foulkes, Effects of uranium on rabbit renal tubules, *Toxicol. Appl. Pharmacol.* 16 (1970) 391–399.
- [24] M. Carriere, L. Avoscan, R. Collins, F. Carrot, H. Khodja, E. Ansoborlo, B. Gouget, Influence of uranium speciation on Normal Rat Kidney (NRK-52E) proximal cell cytotoxicity, *Chem. Res. Toxicol.* 17 (2004) 446–452.
- [25] C.R. Cothorn, W.L. Lappenbusch, Occurrence of uranium in drinking water in the U.S, *Health Phys.* 45 (1983) 89–99.
- [26] Y. Igarashi, A. Yamakawa, N. Ikeda, Plutonium and uranium in Japanese human tissues, *Radioisotopes* 36 (1987) 433–439.
- [27] D. Ribera, F. Labrot, G. Tisnerat, J.-F. Narbonne, Uranium in the environment: occurrence transfer and biological effects, *Rev. Environ. Contam. Toxicol.* 146 (1996) 53–89.
- [28] A. Guenther, G. Bernhard, G. Geipel, T. Reich, A. Rossberg, H. Nitsche, Uranium speciation inplants, *Radiochim. Acta* 91 (2003) 319–328.
- [29] G. Bernhard, G. Geipel, V. Brendler, H. Nitsche, Uranium speciation in waters of different uranium mining areas, *J. Alloys Compd.* 271–273 (1998) 201–205.
- [30] S. Pompe, K. Schmeide, M. Bubner, G. Geipel, K.H. Heise, G. Bernhard, H. Nitsche, Investigation of humic acid complexation behavior with uranyl ions using modified synthetic and natural humic acids, *Radiochim. Acta* 88 (2000) 553–558.
- [31] A.M. Ubios, M. Marzorati, R.L. Cabrini, Skin alterations induced by long-term exposure to uranium and their effect on permeability, *Health Phys.* 72 (1997) 713–715.
- [32] M.L. Zamora, B.L. Tracy, D.P. Zielinski, M.A. Meyerhof, Chronic ingestion of uranium in drinking water: a study of kidney bioeffects in humans, *Toxicol. Sci.* 43 (1998) 68–77.
- [33] J. Szpunar, P. Pellerin, A. Makarov, T. Doco, P. Williams, R. Lobinski, Speciation of metalcarbohydrate complexes in fruit and vegetable samples by size-exclusion HPLC-ICP-MS, *J. Anal. At. Spectrom.* 14 (1999) 639–644.
- [34] J.-F. Verchere, S. Chapelle, F. Xin, D.C. Crans, Metal-carbohydrate complexes in solution, *Prog. Inorg. Chem.* 47 (1998) 837–945.
- [35] H.A. Tajmir-Riahi, D-glucose interaction with uranium ion. Synthesis, spectroscopic and structural characterization of uranyl-glucose adducts and the effect of metal cation binding on the sugar anomeric structures, *Inorg. Chim. Acta* 153 (1988) 155–159.

Supplementary Data

Translocation of Uranium from Water to Foodstuff While Cooking

Krishnapriya K. C., * Ananya Bakshi, * Swathi Chaudhari, * Soujit Sen Gupta and T. Pradeep*

DST Unit of Nanoscience (DST UNS), and Thematic Unit of Excellence (TUE), Department of Chemistry, Indian Institute of Technology Madras, Chennai - 600 036, India

Email: Pradeep@iitm.ac.in, Fax: 91-44-2257-0545/ 0509

* Contributed equally

Content

S/N	Description	Page Number
S1	<i>Change in uranium concentration due to adsorption on Teflon beaker</i>	2
S2	<i>XPS survey spectrum of rice cooked in high concentration of uranium</i>	3
S3	<i>IR spectra of glucose, mannose and their uranyl-bound adduct</i>	4

Supplementary Data 1

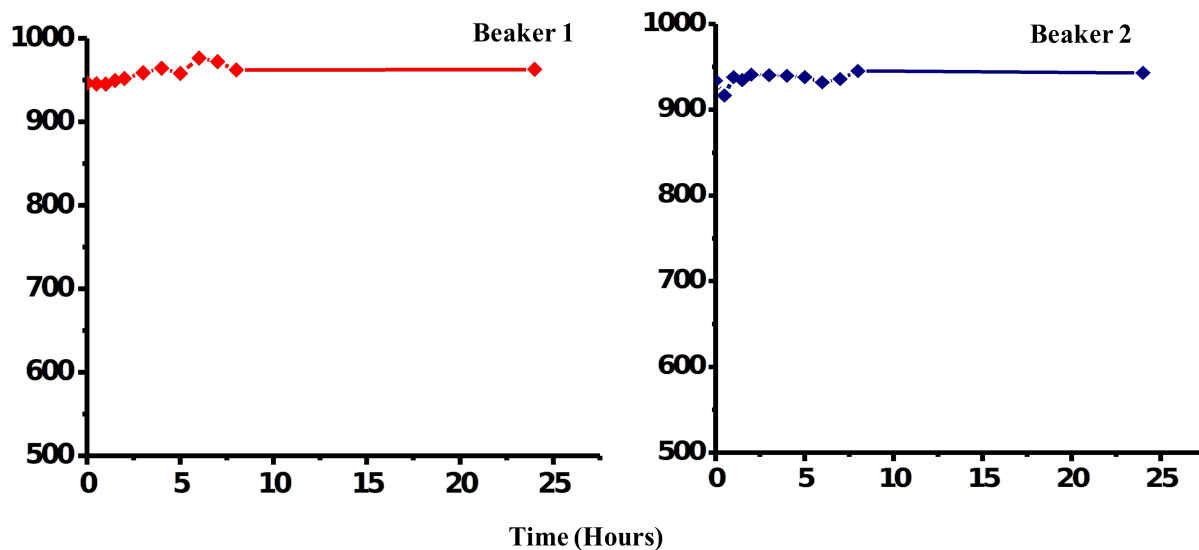


Fig. S1: Change in uranium concentration in the uranyl nitrate solution with time showing that Teflon beakers 1 and 2 used for all cooking and soaking experiments do not absorb uranium from the solution. Experiments were conducted at 80 °C.

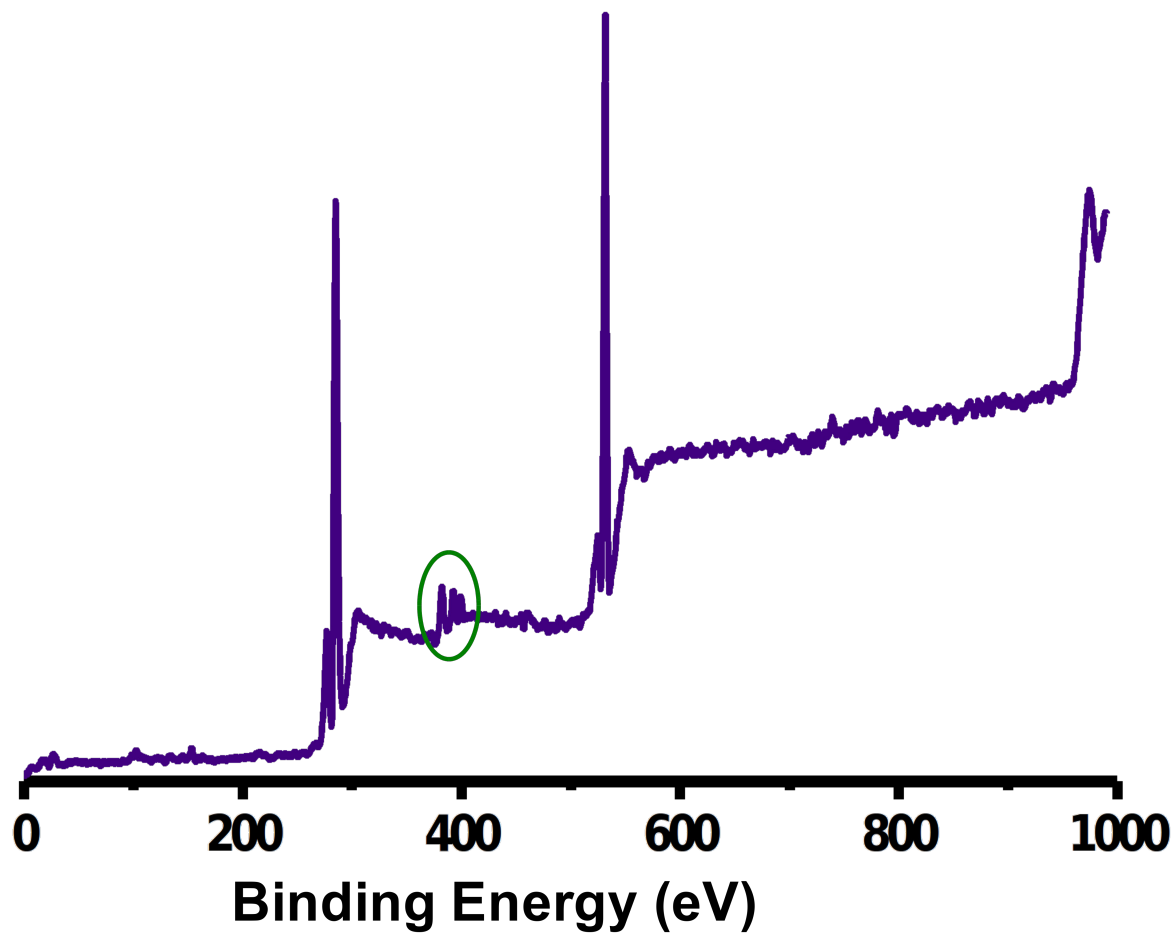


Fig. S2: XPS survey spectrum of rice cooked in uranium contaminated water.

Supplementary Data 3

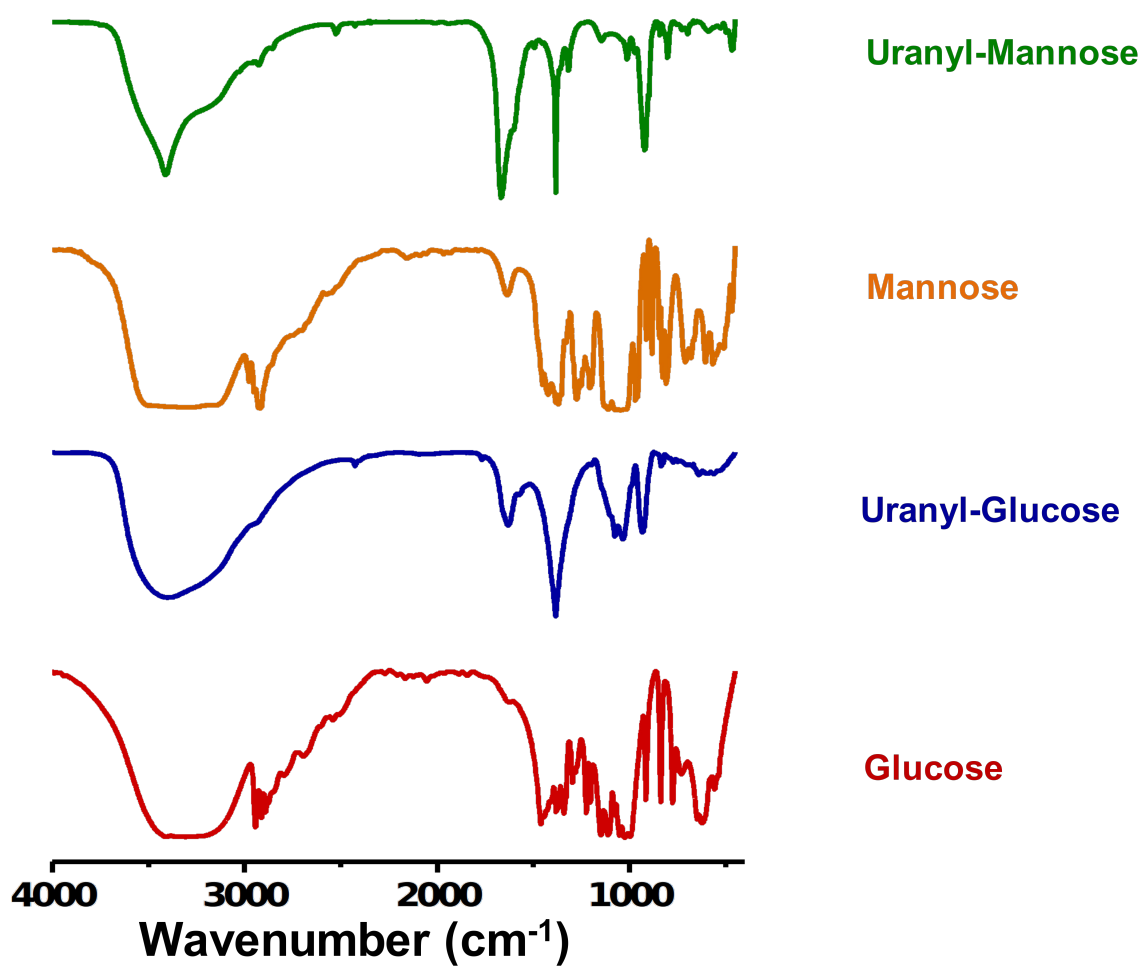


Fig. S3: IR spectra of glucose, mannose and their uranyl-bound adducts. Some of peaks at 3140-3460 and 990-1130 cm⁻¹ are saturated.

Journal of Biomedical Optics

BiomedicalOptics.SPIEDigitalLibrary.org

***In vitro* colocalization of plasmonic nano-biolabels and biomolecules using plasmonic and Raman scattering microspectroscopy**

Kamalesh Chaudhari
Thalappil Pradeep

SPIE.

In vitro colocalization of plasmonic nano-biolabels and biomolecules using plasmonic and Raman scattering microspectroscopy

Kamalesh Chaudhari and Thalappil Pradeep*

Indian Institute of Technology Madras, Department of Chemistry, DST Unit of Nanoscience and Thematic Unit of Excellence, Chennai 600 036, India

Abstract. An insight into the intracellular fate of theranostics is important for improving their potential in biological applications. *In vivo* efficacy of plasmonic theranostics depends on our ability to monitor temporal changes in their size, shape, and state of aggregation, and the identification of molecules adsorbed on their surfaces. We develop a technique which combines plasmonic and Raman scattering microspectroscopy to colocalize plasmonic scattering from metallic nanoparticles with the Raman signatures of biomolecules adsorbed on the surface of the former. Using this technique, we have colocalized biomolecules with the plasmonic scattering from silver nanoparticles in the vicinity of *Escherichia coli* bacteria. To prove the applicability of this setup for the measurements on mammalian cells, imaging of HEK293 cells treated with gold nanoparticles was performed. We discuss the importance of such correlated measurements over individual techniques, although the latter may lead to misinterpretation of results. Finally, with the above-mentioned examples, we have given criteria to improve the specificity of theranostics. We believe that this methodology will be considered as a prime development in the assessment of theranostics. © 2015 Society of Photo-Optical Instrumentation Engineers (SPIE) [DOI: 10.1117/1.JBO.20.4.046011]

Keywords: localized surface plasmon resonance; surface enhanced Raman scattering; colocalization; nano-bioconjugates; microspectroscopy.

Paper 150001R received Jan. 5, 2015; accepted for publication Mar. 20, 2015; published online Apr. 22, 2015.

1 Introduction

Colocalizations of nanoparticles and biomolecules in cellular environments are important for the development of efficient nano-biosensors and theranostics.^{1–4} Detection of theranostics can be based on their plasmonic signals or surface enhanced Raman scattering (SERS) signals obtained from the molecules in the vicinity of particles. To assess the intracellular specificity of theranostics, it is important to verify the exact size, shape, and state (single or dimer or aggregate) of nanoparticles along with the identification of molecules adsorbed on their surfaces.^{5,6} Various techniques have been developed for such observations at the single particle level.^{7–9} Among the available techniques, dark field scattering microspectroscopy (DFSMS) is a well-established technique for the observations of single plasmonic nanoparticles (particularly silver and gold).^{10,11} On the other side, confocal Raman scattering microspectroscopy (RSMS) has been considered as an efficient tool for the detection of single molecules, and where Raman signals from biomolecules are too weak to be detected in a noisy environment, noble metal nanoparticles (NMNPs) can be of help.^{12,13} Due to their SERS activity and thermal properties, NMNPs have been used as theranostics.^{12,13} In a complex environment, nanoparticles of different sizes and shapes may exhibit similar signals or SERS activities.¹⁴ Hence, confirmation of the signals obtained using multiple techniques is essential for improving detection and sensing capabilities.¹⁵ In such cases, the exact nature of particles

can be determined by methodologies based on polarization and excitation wavelength-dependent measurements of their SERS activity or their plasmonic spectra.^{16–19} To precisely monitor specificity, correlated measurements using combined techniques and setups are required. These techniques generally involve correlation between two different signals obtained from the same nanoparticle¹⁵ or precise tracking of single particles in real time.²⁰ In this context, if it is necessary to understand the exact state of nanoparticles and biomolecules responsible for the state change,^{4,21} DFSMS and RSMS are the important techniques which allow such identifications. A few demonstrations of such combined techniques have been done in the past. Lee et al. have demonstrated such correlated measurements for dimeric and trimeric forms of Au–Ag core shell nanoparticles tethered on DNA.²² In this study, Rayleigh scattering, SERS, and atomic force microscopy were used for correlated measurements. These results were used to determine relationships between particle structure, SERS, and Rayleigh scattering with the help of scattering intensity ratio and the incident polarization. In another study, such correlated measurements between Rayleigh scattering and SERS were performed on AgNP aggregates and the data obtained were used to determine the optimized conditions required for maximum SERS.²³ Apart from such physicochemical applications and developments, correlated measurements have major applications in biology. A study from Henry et al. has shown the application of such a technique to collect SERS

*Address all correspondence to: Thalappil Pradeep, E-mail: pradeep@iitm.ac.in

1083-3668/2015/\$25.00 © 2015 SPIE

signals from multiple nanotags at the same time.²⁴ In other studies performed by El-Sayed et al., combined Rayleigh and Raman spectroscopy was used to identify phases of cell cycle or other applications such as the determination of drug efficacy from single cell imaging.^{21,25} In a recent work, we have performed single cell investigations of silver nanoparticles within bacteria using separate DFSMS and RSMS measurements.¹⁰ With this background, development of such techniques is under progress and improvements in terms of resolution, ease of operation, various data analysis, and interpretation techniques are the criteria under consideration.^{21,25} Here, we discuss issues related to the specificity of detection techniques. In sensing and detection of intracellular nanoparticles, while using plasmonic/fluorescence imaging, changes in the scattering/fluorescence signals due to dimerization or aggregation of nanostructures are considered as signals.^{26–28} But due to the complexity of a biological environment, apart from the molecule of interest, many other moieties in the cellular environment can affect the system under investigation. For example, proteins in the cell culture medium itself cause aggregation of nanoparticles.²⁹ Moreover, interactions among the nanoparticles themselves lead to their aggregation.⁵ Also, due to various chemical changes in the surroundings of nanoparticles, changes in the intrinsic properties of nanoparticles may also affect the confidence level of the diagnostic data.³ Hence, in such cases, it is necessary to identify the molecules in the vicinity of the nanoparticles as well as state of the particle such as dimer or aggregate. Similarly, while using SERS-based detection of intracellular nanoparticles, changes in the intensity of Raman signals are considered for the localization of nanoparticles.^{30,31} In such cases, for better understanding of the results, it is important to understand the state of the nanoparticle as well as the mechanisms involved in the SERS activity of the same. To solve the aforementioned issues, in this work, we have demonstrated a combination of high-resolution DFSMS with RSMS. A system of AgNP-treated bacteria was investigated as an example. We have shown successful colocalization between plasmonic signatures of nanoparticles along with the Raman signature of biomolecules in the vicinity of bacteria. Applicability of this setup for the measurements on mammalian cells was demonstrated with the system of HEK293 cells treated with gold nanoparticles. Further, we discuss the mechanism of SERS of nanostructures within cells. To the best of our knowledge, this is the first time such measurements have been used for

intracellular colocalization of plasmonic nanoparticles with biomolecules and to investigate the mechanisms of SERS inside cells.

2 Materials and Methods

2.1 Materials

Tetrachloroauric acid trihydrate ($\text{HAuCl}_4 \cdot 3\text{H}_2\text{O}$) (99.9%), trisodium citrate (>99%), poly-L-lysine solution (0.1% in H_2O), and trypsin-Ethylenediaminetetraacetic acid (0.25% in H_2O) were purchased from Sigma Chemicals. Silver nitrate (99.9%) was purchased from RANKEM, India. Dulbecco's modified Eagle medium (DMEM) with high glucose, GlutaMAX™ Supplement and pyruvate, Antibiotic (100×, penicillin–streptomycin–glutamine), and fetal bovine serum were purchased from Invitrogen. Plasticware for cell culture was purchased from Tarson, India. Millipore deionized water (DI) ($\sim 18.2 \text{ M}\Omega$) was used throughout the experiments.

2.2 Synthesis of Citrate Capped Silver Nanoparticles

AgNPs were synthesized by the Turkevich method.³² Briefly, 17 mg of AgNO_3 was dissolved in 100 mL of DI water. This solution was heated to 100°C and then 40 mg of trisodium citrate was added. Once the color of the solution started changing to pale yellow, it was cooled under tap water. As synthesized, AgNPs were characterized using UV–Vis spectroscopy and transmission electron microscopy (TEM) imaging. A broad surface plasmon resonance (SPR) distribution with a maximum at $\sim 410 \text{ nm}$ was observed [Fig. 1(a)]. TEM suggests nonuniformity in the size and shape of AgNPs.

2.3 Synthesis of Citrate Capped Gold Nanoparticles

GNPs were synthesized by the Turkevich method.³² Briefly, 20 mL of 0.3 mM HAuCl_4 solution in DI water was heated in a synthesizer (400 rpm). Upon boiling, 240 μL of 100 mM trisodium citrate solution was added. After 20 min of boiling, the color of the solution changed to wine red. Then the solution was cooled at room temperature. As synthesized, AuNPs were characterized using UV–Vis spectroscopy and TEM imaging. AuNPs of size $\sim 40 \text{ nm}$ in diameter with SPR around 529 nm were observed [Fig. 1(b)].

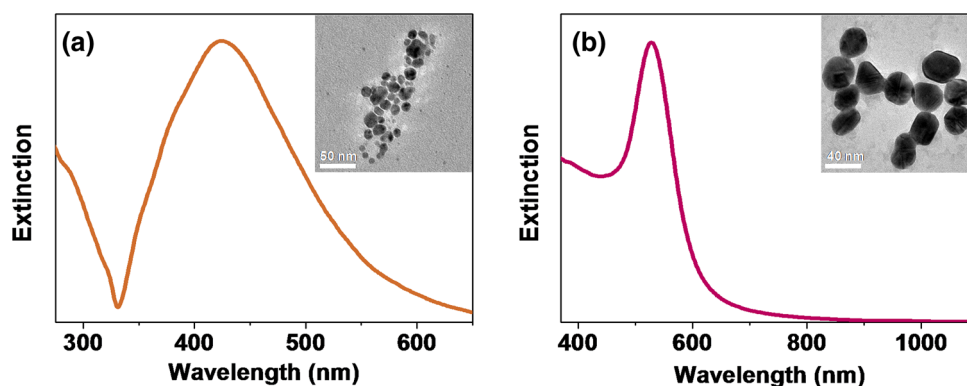


Fig. 1 (a) UV–Vis extinction spectrum of citrate capped AgNPs. Inset shows transmission electron microscopy (TEM) image of these nanoparticles. (b) UV–Vis extinction spectrum of citrate capped AuNPs. Inset shows TEM image of these nanoparticles.

2.4 Bacterial Culture and Sample Preparation

Escherichia coli 739 bacterial culture was grown to an OD₆₀₀ (optical density at 600 nm) value of 1. This culture (5 mL) was washed twice by centrifugation (3000 rpm, 10 min) with DI water. The final pellet was resuspended in the as-prepared AgNP solution and incubated at room temperature for 1 h. After that, this *E. coli*-AgNP suspension was washed twice with DI water and spotted on a poly-L-lysine-coated ultrasonically cleaned glass slide (1-mm thickness, SCHOTT). After 5 min of incubation, the slide was flushed with DI water to remove unbound bacteria and covered with 0.145-mm thick coverslips (SCHOTT) for imaging purposes.

2.5 Mammalian Cell Culture and Sample Preparation

HEK293 cells were cultured on poly-L-lysine-coated glass coverslips in six-well plates. After reaching ~80% confluency, cells were washed twice with 1× phosphate-buffered saline (PBS) and 2 mL DMEM containing 100 μL citrate capped GNPs was added. These cells were incubated overnight inside the incubator at 37°C. After this, the cells were washed thrice with 1× PBS and incubated with paraformaldehyde solution (4% in 1× PBS) for 8 min. Then the cells were washed thrice with 1× PBS and mounted on 1-mm thick glass slides (SCHOTT).

2.6 UV-Visible Extinction Spectroscopy

Ensemble UV-Vis extinction spectroscopic measurements were performed using PerkinElmer Lambda 25 spectrophotometer in the range of 200 to 1100 nm.

2.7 Transmission Electron Microscopy

High resolution transmission electron microscopic measurements were performed using a JEOL 3010, 300 kV instrument. Carbon-coated copper grids were used for measurements. Samples were spotted by drop casting followed by ambient air drying.

2.8 Confocal Raman Scattering Microspectroscopy

Raman microspectroscopic measurements were performed using WiTec GmbH equipment. Frequency doubled Nd:YAG dye laser (532 nm) with a maximum output power of 40 mW was used for excitation of the sample. The laser was focused onto the sample using a 100× oil immersion objective (UPLFLN, Olympus). The signal, after passing through a 532 nm super-notch filter, was dispersed using a grating (600 grooves mm⁻¹) onto a charge-coupled device (CCD). Spectral images were scanned using the sample mounted on a piezo stage.

2.9 Plasmonic and Raman Scattering Microspectroscopy

For plasmonic and Raman scattering microspectroscopy (PRSMS) measurements, an attachment was designed to use a Cytoviva™ high-resolution dark field condenser (oil immersion) and 100× oil immersion objective (UPLFLN, Olympus) in the above-mentioned confocal Raman microscope. For white light illumination (400 to 1000 nm), a L1090-Halogen

Lamp from International Light Technologies Inc. was used. The other details of the instrument for Raman microspectroscopic measurements are the same as above.

3 Results and Discussion

3.1 Setup for Combined Plasmonic and Raman Scattering Microspectroscopy

To accomplish correlated DFSMS and RSMS measurements of biological samples using the same setup, we attached a high-resolution dark field condenser with a conventional point-scan RSMS setup. Schematic and photographs of the actual setup are shown in Fig. 2. In the PRSMS setup, a dark field condenser was used to illuminate samples in the transmitted dark-field configuration. For the DFSMS of samples, a visible-near-infrared (VNIR) light source with a wavelength range from 400 to 1000 nm was used to excite the plasmonic modes of NMNPs. For RSMS, a 532-nm laser was used to excite the Raman spectra and measurements were performed in the reflection mode. Samples sandwiched between a coverslip and glass slide were placed on a piezoelectric scanner and the scattered light was collected using a 100× oil immersion objective. Substantial signal strength in conjunction with confocality was achieved using a 100-μm optical fiber. This fiber was connected to a VNIR spectrometer equipped with appropriate gratings to resolve the spectra. Since for DFSMS a wide range of wavelengths has to be scanned, a grating with 150 grooves/mm was used. For RSMS, a shorter wavelength range but better resolution is necessary. Hence, to resolve RSMS spectra, a grating with 600 grooves/mm was used. It is important to mention that despite the use of wide field illumination in DFSMS, the method of signal collection was confocal due to the configuration of the RSMS setup. Such a signal collection in DFSMS has its pros and cons, which are discussed below.

3.2 Images of AgNP Treated Bacteria Collected with Different Configurations

Figure 3(a) shows a dark field image of bacteria (*E. coli* 739) treated with citrate capped silver nanoparticles. This image was

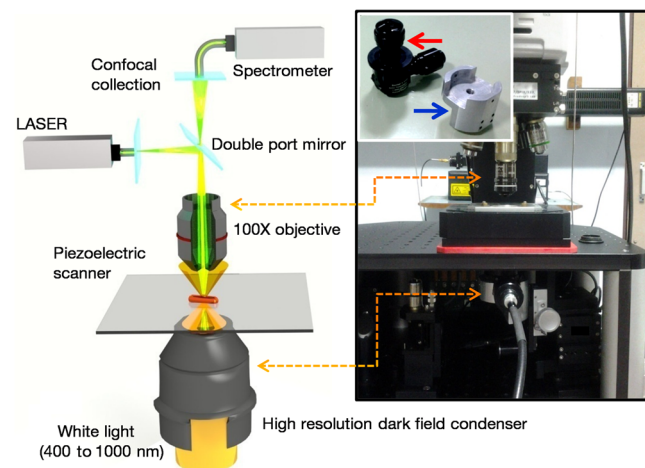


Fig. 2 Schematic of the setup for correlated plasmonic and Raman scattering microspectroscopy (PRSMS) measurements. Briefly, it consists of a high-resolution dark field condenser attached with conventional point-scan confocal RSMS setup. Inset shows a dark field condenser (red arrow, top left) along with the designed attachment (blue arrow, down right).

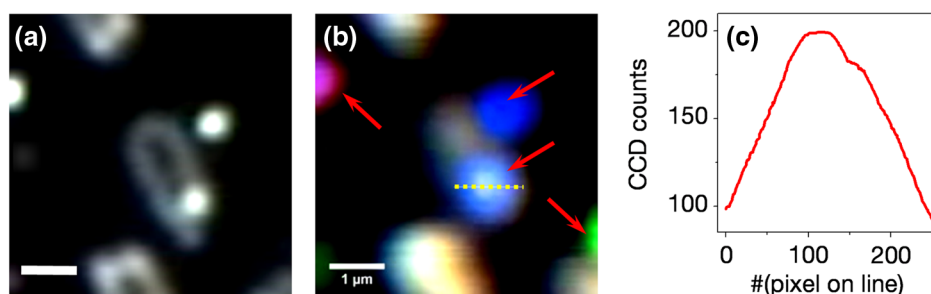


Fig. 3 (a) Dark field image captured using CCD camera of the PRSMS setup. (b) Pseudo-colored dark field scattering microspectroscopy (DFSMS) image collected using the PRSMS setup for the same area. Red arrows indicate the presence of AgNPs which exhibit sharp SPRs. A dotted yellow line shows pixels for which scattering intensity profile is shown in (c). Scale bar is $1\ \mu\text{m}$ for images (a) and (b).

captured using a CCD camera of the PRSMS setup. In such an image, it appears that only borders (cell wall) of the bacteria scatter substantial light, whereas the central portion appears transparent. This is because the wide field image strongly reflects the relative intensity variations which occur due to light collection from all focal planes. But when this sample was measured for DFSMS using the PRSMS setup, the spectral image was captured pixel by pixel using an optical fiber which introduces confocality. Such a confocal signal collection produces an image constructed from the light collected only from a particular focal plane. This image has a diffused appearance as shown in Fig. 3(b). To eliminate the possibility of defocused imaging in the PRSMS setup, care was taken to focus the desired plane of imaging by using a laser spot for confocal RSMS. Figure 3(c) shows a line profile of the scattering intensity along the yellow line in Fig. 3(b). Line profile shows the maximum at the center similar to the airy disc pattern and confirms that the particle was properly focused.

We also observed that when DFSMS images are presented as intensity scaled images, it does not reveal information about locating the NMNPs in complex environments. However, the sharp and nearly monochromatic scattering features of NMNPs allow them to be distinguished as bright and distinct colored spots. This can be achieved by presenting DFSMS images as pseudo-RGB color coded images [Fig. 3(b)]. In pseudo-colored DFSMS images, we have assigned 552-, 615-, and 688-nm wavelengths to blue, green, and red colors, respectively. With this, particles can be clearly located as shown in Fig. 3(b) by red arrows. On this background, we have performed PRSMS measurements on two different systems. These measurements combine our ability to locate NMNPs using DFSMS and colocalizing the same with biomolecules using RSMS.

3.3 Colocalization of AgNPs and Biomolecules in *E. Coli*

A previous study¹⁰ by our group using RSMS has shown that AgNPs interact specifically with the bacterial DNA. It was observed that adenine (A), guanine (G), and cytosine (C) exhibit substantial SERS intensities while thymine (T) shows only limited SERS enhancement. This is because the interactions between AgNPs and A, G, and C are stronger than those with T. This specificity of interaction is due to the interaction between AgNPs and the exocyclic nitrogen present in A, G, and C. In the aforementioned study, DFSMS was used separately to show the attachment of AgNPs to the bacteria.¹⁰ Here, in the present

study, we use PRSMS to colocalize the position of AgNPs with the Raman signatures of biomolecules. Figure 4 shows the consolidated data of these measurements.

Figure 4(a) shows the dark field image captured using a CCD camera with the PRSMS setup. In the region of interest (ROI) selected for imaging, we can see AgNPs labeled 1, 2, 3, and 4 are attached on the surface of bacteria and particle 5 is on the glass slide. The next image shows a pseudo-colored DFSMS image [Fig. 4(b)] for the same ROI. Scattering spectra collected from particle positions are shown in Fig. 4(e). Based on the scattering spectra, it can be observed that particle 1 is possibly a rod or prism-shaped silver nanoparticle,³³ whereas the other particles are relatively smaller and scatter light at lower wavelengths. Among the marked AgNPs, particles 2 and 3 scatter more light as compared to particles 4 and 5. This suggests that AgNPs 2 and 3 are relatively larger particles. Also as compared to AgNP 1, other particles show a broadening in their scattering peak, implying adsorption of biomolecules on their surfaces. Figure 4(c) shows the intensity scaled RSMS image of the same ROI shown in Fig. 4(a). It suggests a maximum intensity enhancement in the vicinity of AgNPs 2 and 4. To understand this data better, we have done cluster analysis of the RSMS image. Cluster analysis helped in grouping and color coding the Raman spectra on the basis of their similarities. Then this color coded image was overlaid with the dark field image as shown in Fig. 4(d). Averages of the spectral clusters are shown in Fig. 4(f) where it can be seen that although some intensity enhancement was observed on AgNP 2 and bacteria at the bottom, actual SERS activity was observed only in the vicinity of AgNP 4 (red colored Raman spectrum). Considering the scattering spectrum of AgNP 4, it can be concluded that in this case, SERS activity is due more to the electronic resonance-charge transfer between the AgNP and the molecule in its vicinity than the electric near-field enhancement. These observations suggest that although many AgNPs attach to the bacteria, all particles do not exhibit SERS activity. This is due to the dependence of SERS activity on the site of molecular adsorption on the surface of the nanoparticle as well as the size and shape of the nanoparticle. Assignments of Raman bands corresponding to the molecule in the vicinity of AgNP 4 are given in Table 1. Most of these bands were found to be due to DNA. These results are in good agreement with our previous observations on the interaction between AgNPs and bacteria.¹⁰ For a further demonstration of the applicability of PRSMS setup with mammalian cells, we have performed measurements on HEK293 cells treated with citrate capped AuNPs. These observations are discussed in Sec. 3.4.

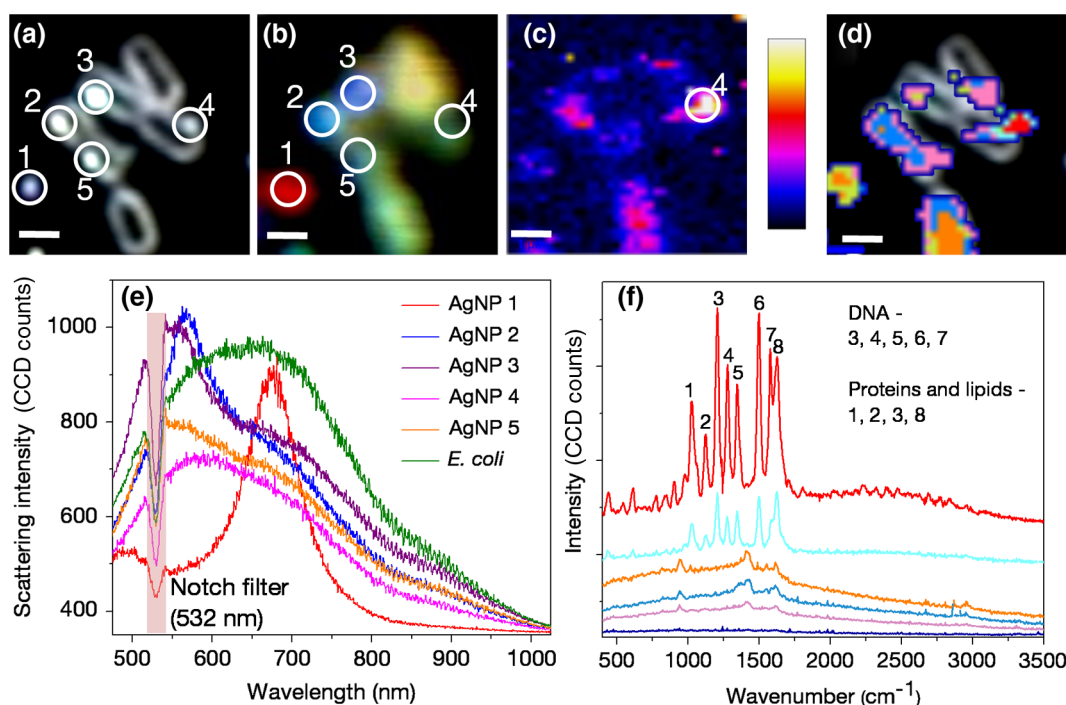


Fig. 4 Images of AgNP treated bacteria collected using PRSMS setup in different configurations. (a) Dark field image captured using CCD camera. (b) Pseudo-colored DFSMS image. (c) Intensity scaled confocal RSMS image and corresponding color scale are shown. (d) Overlay of the clustered RSMS image with dark field image. (e) Scattering spectra of AgNPs 1 to 5 are shown along with the scattering spectrum of bacteria. (f) Averaged cluster spectra corresponding to image (d) are shown in matching colors. Scale bar is 1 μm in all the images.

3.4 Colocalization of AuNPs and Biomolecules Inside HEK293 Cells

Figure 5(a) shows the dark field image of HEK293 cells treated with citrate capped AuNPs of ~ 40 nm in diameter. The Z scanning (focus stacking) measurements performed on these cells have shown that the AuNPs under investigation were within the cells. To prove this, a movie compiled of a Z scanned image stack is shown in Video 1. Figure 5(b) shows a pseudo-colored DFSMS image of the ROI shown in Fig. 5(a). Corresponding scattering spectra shown in Fig. 5(d) suggest

Table 1 Assignments of Raman bands of AgNP treated *Escherichia coli* sample.

Sr. No.	Peak position (cm^{-1})	Assignment	Reference
1	1023	Tryptophan	34
2	1123	Protein/lipids/carbohydrates	10
3	1205	Tyrosine/uridine	10
4	1275	Thymidine	25
5	1348	Adenosine and guanosine	22
6	1496	Adenosine	25
7	1578	dAMP	34
8	1627	Tryptophan + tyrosine	35

that particle 1 has a sharp plasmon resonance and relatively less FWHM, which implies that it is a single AuNP. Other particles (2 and 3) show scattering signatures of aggregates (multiple broad but sharp SPRs). The scattering signal from cellular components exhibits a broad spectrum as well. When the ROI shown in Fig. 5(a) was scanned for RSMS, particle 1 exhibited the most SERS activity [Figs. 5(c) and 5(e)] whereas an aggregate (particle 2) exhibits only a moderate enhancement in the Raman signal as compared to the background. This observation suggests that, although due to the plasmonic coupling effect aggregates are expected to exhibit better SERS activity than single nanoparticles, SERS activity is highly specific to the site of molecule adsorption. Hence, such PRSMS studies are necessary for additional confirmation about the nature of the nanoparticle under investigation. When diagnostic or sensing techniques are solely based on SERS activity or the expected hybridization of NMNPs by specific biomolecules, colocalization using PRSMS is necessary to prove the presence of moieties and nanostructures of interest. In this particular measurement, assignments for Raman bands are given in Table 2. A major band was assigned to protein molecules (1600 to 1700 cm^{-1}) and another band between 1050 and 1125 cm^{-1} was assigned to DNA and RNA O-P-O stretching. It has been reported by previous studies that such an appearance of the Raman band is commonly found for mammalian cells undergoing apoptosis.²⁵

Further, from our observations, it can be seen that when the same ROI containing particle 1 was scanned separately for RSMS [Fig. 5(e), black trace], the Raman spectrum did not repeat with high fidelity upon rescanning [Fig. 5(e), red trace], although in both these measurements, the instrumental parameters were kept exactly the same. This may be due to the

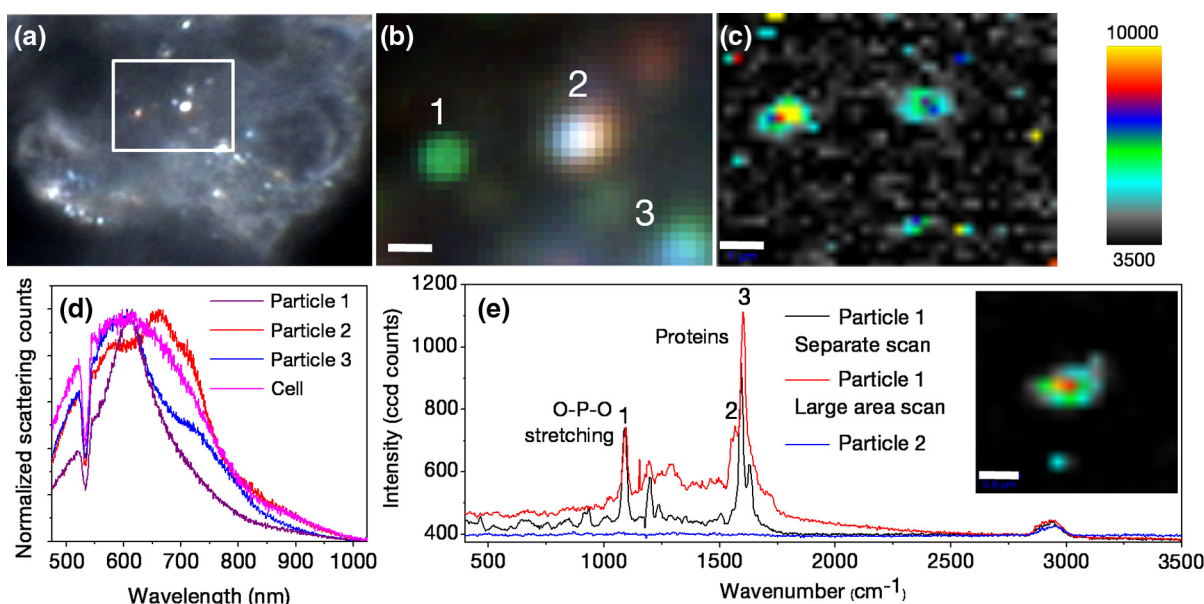


Fig. 5 Images of AuNP-treated HEK293 cells collected using PRSMS setup at different configurations. (a) Dark field image captured using CCD camera. Region of interest (ROI) scanned for PRSMS is shown by the square. Image is taken at such focus that nanoparticles can be seen clearly. Cells can be seen clearly in a movie made of Z stacking of images (Video 1). (b) Pseudo-colored DFSMS image of the ROI shown in (a). Particles are numbered as 1, 2, and 3. Scale bar is 1 micron. (c) Intensity scaled RSMS image. (d) Scattering spectra of AuNPs 1 to 3 are shown along with the scattering spectrum from cellular components. (e) Inset of this image shows RSMS image of particle 1 when it was rescanned. Scale bar is 0.8 μm . Raman spectra corresponding to particles 1 (red) and 2 (blue) from RSMS image (c) are shown along with the Raman spectrum of particle 1 after rescanning (black) (Video 1, MPEG, 0.4 MB). [DOI: <http://dx.doi.org/10.1117/1.JBO.XX.X.XXXXXX.1>].

Table 2 Assignments of Raman bands of AuNP treated HEK293 sample.

Sr. No.	Peak position (cm^{-1})	Assignment	Reference
1	1094	DNA/RNA: O—P—O stretching	35
2	1572	DNA/RNA: ring breathing mode (guanine, adenine)	35
3	1600	Protein, amide I band	34

complexity of the biological samples and sensitivity of the measurements to the surrounding environment. Hence, we suggest that in biosensing measurements, it is first necessary to optimize experimental parameters using standard samples of similar types and then perform measurements with the experimental samples.

4 Conclusions

We have developed a methodology for colocalizing intracellular biomolecules and plasmonic NMNPs by plasmonic and Raman scattering microspectroscopy. We demonstrate the applicability of PRSMS setup by imaging AgNP treated *E. coli* bacteria. SERS signals of biomolecules were detected from the same place where plasmonic scattering signals for nanoparticles were detected. These observations suggest that nanoparticles and observed biomolecules are in such close vicinity that SERS could occur and help us to colocalize the same. In the case of mammalian cells, considering the biocompatibility of AuNPs,

an example of AuNPs treated HEK293 cells was demonstrated. Observations support the fact that the SERS activity of nanoparticles is specific to shape, size, and site of adsorption. Data further suggest that in the case of the samples comprised of multiple complex components, localization of molecules only on the basis of intensity scaled RSMS images or indirectly through the plasmonic features of NMNPs may be risky in sensing applications. In such cases, dual verification of the sensing signals is necessary. We believe that PRSMS provides a solution to such problems and can be efficiently used for molecule and particle colocalization in biological environments which will be of prime importance in improving the specificity of theranostics.

Acknowledgments

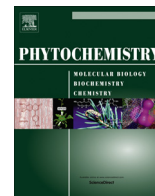
We thank the Department of Science and Technology, Government of India for constantly supporting our research program on nanomaterials. We thank Hitesh Mangain, application scientist, WITec GmbH, Bangalore, India, for discussions.

References

- W. E. Moerner, "A dozen years of single-molecule spectroscopy in physics, chemistry, and biophysics," *J. Phys. Chem. B* **106**(5), 910–927 (2002).
- Y. Gu et al., "Single particle orientation and rotational tracking (SPORT) in biophysical studies," *Nanoscale* **5**(22), 10753–10764 (2013).
- M. Xu et al., "Formation of nano-bio-complex as nanomaterials dispersed in a biological solution for understanding nanobiological interactions," *Sci. Rep.* **2**, 406 (2012).
- P. Nativo, I. A. Prior, and M. Brust, "Uptake and intracellular fate of surface-modified gold nanoparticles," *ACS Nano* **2**(8), 1639–1644 (2008).

5. A. Albanese and W. C. W. Chan, "Effect of gold nanoparticle aggregation on cell uptake and toxicity," *ACS Nano* **5**(7), 5478–5489 (2011).
6. K. Lee et al., "Quantitative imaging of single mRNA splice variants in living cells," *Nat. Nano* **9**, 474–480 (2014).
7. J. Chen and J. Irudayaraj, "Quantitative investigation of compartmentalized dynamics of ErbB2 targeting gold nanorods in live cells by single molecule spectroscopy," *ACS Nano* **3**(12), 4071–4079 (2009).
8. Y.-W. Jun et al., "Continuous imaging of plasmon rulers in live cells reveals early-stage caspase-3 activation at the single-molecule level," *Proc. Natl. Acad. Sci. U. S. A.* **106**(42), 17735–17740 (2009).
9. C. Leduc et al., "A highly specific gold nanoprobe for live-cell single-molecule imaging," *Nano Lett.* **13**(4), 1489–1494 (2013).
10. S. Vishnupriya et al., "Single-cell investigations of silver nanoparticle–bacteria interactions," *Part. Part. Syst. Charact.* **30**(12), 1056–1062 (2013).
11. W. Qian et al., "Dark-field light scattering imaging of living cancer cell component from birth through division using bioconjugated gold nanopores," *J. Biomed. Opt.* **15**(4), 046025 (2010).
12. S. Jung et al., "Theragnostic pH-sensitive gold nanoparticles for the selective surface enhanced Raman scattering and photothermal cancer therapy," *Anal. Chem.* **85**(16), 7674–7681 (2013).
13. C. E. Talley et al., "Intracellular pH sensors based on surface-enhanced Raman scattering," *Anal. Chem.* **76**(23), 7064–7068 (2004).
14. E. Ringe et al., "Plasmon length: a universal parameter to describe size effects in gold nanoparticles," *J. Phys. Chem. Lett.* **3**(11), 1479–1483 (2012).
15. H. Deschout et al., "Correlation of dual colour single particle trajectories for improved detection and analysis of interactions in living cells," *Int. J. Mol. Sci.* **14**(8), 16485–16514 (2013).
16. C. J. Orendorff et al., "Aspect ratio dependence on surface enhanced Raman scattering using silver and gold nanorod substrates," *Phys. Chem. Chem. Phys.* **8**(1), 165–170 (2006).
17. J. Jiao et al., "Polarization-dependent SERS at differently oriented single gold nanorods," *Chemphyschem* **13**(4), 952–958 (2012).
18. K. Munechika et al., "Plasmon line widths of single silver nanoprisms as a function of particle size and plasmon peak position," *J. Phys. Chem. C* **111**(51), 18906–18911 (2007).
19. T. Itoh, K. Hashimoto, and Y. Ozaki, "Polarization dependences of surface plasmon bands and surface-enhanced Raman bands of single Ag nanoparticles," *Appl. Phys. Lett.* **83**(11), 2274–2276 (2003).
20. C. J. Szymanski, W. H. I. V. Humphries, and C. K. Payne, "Single particle tracking as a method to resolve differences in highly colocalized proteins," *Analyst* **136**(17), 3527–3533 (2011).
21. B. Kang, L. A. Austin, and M. A. El-Sayed, "Real-time molecular imaging throughout the entire cell cycle by targeted plasmonic-enhanced Rayleigh/Raman spectroscopy," *Nano Lett.* **12**(10), 5369–5375 (2012).
22. H. M. Lee et al., "High-precision measurement-based correlation studies among atomic force microscopy, Rayleigh scattering, and surface-enhanced Raman scattering at the single-molecule level," *Phys. Chem. Chem. Phys.* **15**(12), 4243–4249 (2013).
23. T. Itoh et al., "Correlated measurements of plasmon resonance Rayleigh scattering and surface-enhanced resonance Raman scattering using a dark-field microspectroscopic system," *J. Photochem. Photobiol. A* **183**(3), 322–328 (2006).
24. A. I. Henry, B. Sharma, and R. P. Van Duyne, "Continuous sensing of blood by dark-field microscopy and surface-enhanced Raman spectroscopy," in *Nanotechnology 2012: Bio Sensors, Instruments, Medical, Environment and Energy*, Vol. **3**, pp. 40–43, Taylor & Francis, Boca Raton (2012).
25. L. A. Austin, B. Kang, and M. A. El-Sayed, "A new nanotechnology technique for determining drug efficacy using targeted plasmonically enhanced single cell imaging spectroscopy," *J. Am. Chem. Soc.* **135**(12), 4688–4691 (2013).
26. M. Liu et al., "Dark-field microscopy in imaging of plasmon resonant nanoparticles," *Colloids Surf. B* **124**(0), 111–117 (2014).
27. N. Kawashima et al., "Reversible dimerization of EGFR revealed by single-molecule fluorescence imaging using quantum dots," *Chem. Eur. J.* **16**(4), 1186–1192 (2010).
28. L. Zhang et al., "Single gold nanoparticles as real-time optical probes for the detection of NADH-dependent intracellular metabolic enzymatic pathways," *Angew. Chem.* **123**(30), 6921–6924 (2011).
29. C. Rosman et al., "A new approach to assess gold nanoparticle uptake by mammalian cells: combining optical dark-field and transmission electron microscopy," *Small* **8**(23), 3683–3690 (2012).
30. X. M. Qian and S. M. Nie, "Single-molecule and single-nanoparticle SERS: from fundamental mechanisms to biomedical applications," *Chem. Soc. Rev.* **37**(5), 912–920 (2008).
31. X. Qian et al., "In vivo tumor targeting and spectroscopic detection with surface-enhanced Raman nanoparticle tags," *Nat. Biotechnol.* **26**(1), 83–90 (2008).
32. J. Turkevich, P. C. Stevenson, and J. Hillier, "The nucleation and growth processes in the synthesis of colloidal gold," *Discuss. Faraday Soc.* **11**, 55–75 (1951).
33. J. N. Anker et al., "Biosensing with plasmonic nanosensors," *Nat. Mater.* **7**(6), 442–453 (2008).
34. B. Kang, L. A. Austin, and M. A. El-Sayed, "Real-time molecular imaging throughout the entire cell cycle by targeted plasmonic-enhanced Rayleigh/Raman spectroscopy," *Nano Lett.* **12**(10), 5369–5375 (2012).
35. F. Draux et al., "Raman spectral imaging of single cancer cells: probing the impact of sample fixation methods," *Anal. Bioanal. Chem.* **397**(7), 2727–2737 (2010).

Biographies of the authors are not available.



Ambient ionization mass spectrometry imaging of rohitukine, a chromone anti-cancer alkaloid, during seed development in *Dysoxylum binectariferum* Hook.f (Meliaceae)

P. Mohana Kumara^a, Amitava Srimany^a, G. Ravikanth^b, R. Uma Shaanker^{b,c}, T. Pradeep^{a,*}

^aDST Unit of Nanoscience (DST UNS) and Thematic Unit of Excellence (TUE), Department of Chemistry, Indian Institute of Technology Madras, Chennai 600036, India

^bAshoka Trust for Research in Ecology and the Environment, Royal Enclave, Srirampura, Jakkur, Bengaluru 560064, India

^cDepartment of Crop Physiology and School of Ecology and Conservation, University of Agricultural Sciences, GKVK, Bengaluru 560065, India

ARTICLE INFO

Article history:

Received 23 September 2014

Received in revised form 4 February 2015

Available online 20 March 2015

Keywords:

Rohitukine

Chromone alkaloids

Dysoxylum binectariferum

Seed

DESI MS

ABSTRACT

Rohitukine, a chromone alkaloid, possesses anti-inflammatory, anti-cancer and immuno-modulatory properties. It has been reported from four species, belonging to the families, Meliaceae and Rubiaceae. Stem bark of *Dysoxylum binectariferum* (Meliaceae) accumulates the highest amount of rohitukine (3–7% by dry weight). In this study, we examine the spatial and temporal distribution of rohitukine and related compounds during various stages of seed development in *D. binectariferum* using desorption electrospray ionization mass spectrometry imaging (DESI MSI). Rohitukine (m/z 306.2) accumulation increased from early seed development to seed maturity stage. The spatial distribution of rohitukine was largely restricted to the cotyledonary tissue followed by the embryo and least in the seed coat. Besides rohitukine, rohitukine acetate (m/z 348.2) and glycosylated rohitukine (m/z 468.2) were also detected, both through mass fragmentation and exact mass analysis through Orbitrap mass spectrometry. These results indicate a dynamic pattern of chromone alkaloid accumulation through seed development in *D. binectariferum*.

© 2015 Elsevier Ltd. All rights reserved.

1. Introduction

Rohitukine (5,7-dihydroxy-8-(3-hydroxy-1-methyl-4-piperidinyl)-2-methyl-4H-chromen-4-one) (Fig. 1E), is a chromone alkaloid where the basic nitrogen ring is linked to 5,7-dihydroxy-2-methylchromone nucleus (Jain et al., 2013). The compound is reported to possess anti-inflammatory, anti-fertility, anti-implantation, anti-cancer and anti-adipogenic activities besides having immuno-modulatory properties (Harmon et al., 1979; Ismail et al., 2009; Mohana Kumara et al., 2010; Naik et al., 1988; Varshney et al., 2014). Several semi or fully-synthetic analogs of rohitukine have been developed of which flavopiridol (also known as HMR 1275 or alvocidib), is a potent CDK inhibitor with broad specificity to several kinases including CDK1, CDK2 and CDK4 (de Souza Noel, 1993). It arrests the cell cycle at both G1 and G2 phases (Senderowicz and Sausville, 2000) and has been shown to be effective against breast and lung cancers and chronic lymphocytic leukemia (Sedlacek et al., 1996; Stadler et al., 2000).

* Corresponding author.

E-mail address: pradeep@iitm.ac.in (T. Pradeep).

Another semi-synthetic compound, L-868276, derived from rohitukine has specific and potent inhibitory effects on CDK2 (De Azevedo et al., 1996).

Rohitukine was first isolated from leaves and stems of *Amoora rohituka* (Meliaceae) (Harmon et al., 1979). Later the alkaloid was also reported from stem bark of *Dysoxylum binectariferum* (Meliaceae) and *Schumanniophyton problematicum* and *Schumanniophyton magnificum* (both belonging to Rubiaceae) (Houghton and Hairong, 1987b; Houghton and Woldemariam, 1993; Naik et al., 1988; Yang et al., 2004). Of these sources, stem bark of *D. binectariferum* is the richest, with yields ranging between 3% and 7% by dry weight (Mohana Kumara et al., 2010). Mahajan et al. (2015) reported a substantial accumulation of rohitukine in leaves and fruits of *D. binectariferum*. Besides the plant sources, endophytic fungi associated with *D. binectariferum*, have also been reported to produce rohitukine in culture, independent of the host (Mohana Kumara et al., 2012, 2014). Recently, dysoline, a new regioisomer of rohitukine was reported from stem bark of *D. binectariferum* (Jain et al., 2013). The biosynthetic pathway of rohitukine in plants is not yet elucidated (Manske and Brossi, 1987) and the functional significance of this compound in the plant is also not clearly known.

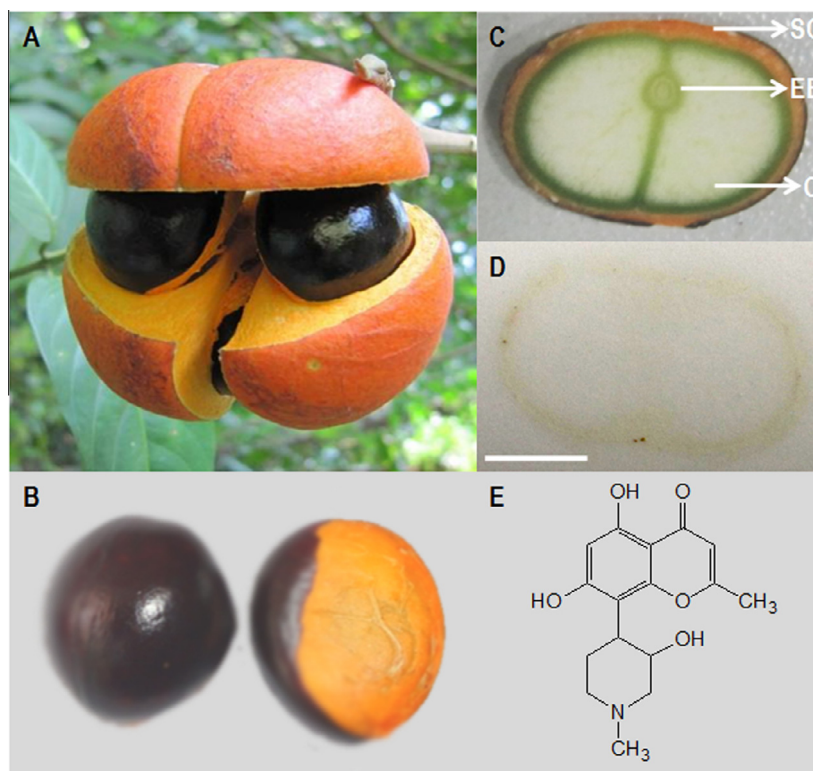


Fig. 1. (A) *Dysoxylum binectariferum* fruit showing the seeds, (B) *D. binectariferum* seed, (C) cross section of the seed through the embryonic region (SC: Seed coat, C: Cotyledon, EB: Embryo), (D) representative TLC imprint of the seed section for DESI MS imaging (scale bar is 5 mm) and (E) structure of rohitukine.

In this study, we examine the spatial and temporal distribution pattern of rohitukine and its analogs in different parts of the seeds during its development. Several studies have addressed the spatial and temporal distribution patterns of primary metabolites and nutrient loading during the seed development in agriculturally important species such as pea (*Pisum sativum*), soybean (*Glycine max*) (Bennett and Spanswick, 1983), broad bean (*Vicia faba*) (Borisjuk et al., 2002), rapeseed (*Brassica napus*) (Fang et al., 2012) and barley (*Hordeum vulgare*) (Gorzolka et al., 2014). With the advent of mass spectrometry techniques such as mass spectrometry imaging (MSI), several studies in the recent past have examined the spatial localization of secondary metabolites in various parts of plant tissue material (Bjarnholt et al., 2014; Hemalatha and Pradeep, 2013; Ifa et al., 2011; Korte et al., 2012; Kueger et al., 2012; Lee et al., 2012). For example, using desorption electrospray ionization mass spectrometry imaging (DESI MSI), efforts have been made to image several secondary metabolites (Bjarnholt et al., 2014; Hemalatha and Pradeep, 2013; Korte et al., 2012; Lee et al., 2012). In DESI MS, electrically charged solvent droplets are directed at the sample of interest to yield desorbed ions which are then conveyed into the mass spectrometer for mass analysis. DESI MS imaging technique has been used in profiling secondary metabolites in *H. vulgare* (Li et al., 2011), capsules of *Papaver somniferum* (Thunig et al., 2011), leaves of *Datura stramonium* (Thunig et al., 2011), and flower petals of *Catharanthus roseus* (Hemalatha and Pradeep, 2013), *Hypericum perforatum* (Li et al., 2013b) and seeds of *Myristica malabarica* (Ifa et al., 2011). Intriguingly, many of these studies have shown a tissue specific and heterogeneous distribution of metabolites, indicating a possible mosaic of genetic expression underlying the observed patterns. In a recent study, DESI MSI was used to show tissue specific distribution of hydroxynitrile glucosides and its relation to the expression of a key

biosynthetic enzyme in *Lotus japonicas* (Li et al., 2013a). A significant advantage of DESI is that it is an ambient ionization technique and thus, even live tissues can be analyzed.

D. binectariferum produces brightly colored fruits within which most frequently four seeds develop. On maturity, the fruits dehisce to reveal arillated seeds (Fig. 1A). Hornbills that regurgitate the seeds after eating the fat rich arils disperse the seeds (Sethi and Howe, 2012). As a typical dicot plant, each seed consists of well-defined cotyledons with an embryo and seed coat. The seeds take approximately 80–90 days to mature. For the purpose of this study, we examined the temporal patterns of accumulation of rohitukine and other related compounds during four discrete seed developmental stages and the spatial distribution of rohitukine and related compounds in different parts of the seeds through their development using HPLC, DESI MSI and ESI (Orbitrap) MS.

2. Results and discussion

2.1. Molecular ions observed from the seeds of *D. binectariferum*

DESI MS analysis of the seeds showed molecular ions signatures in the range of m/z 100–1000 for all stages of seed development (Fig. 2). Among them, the molecular ion signature of m/z 306.2 corresponding to rohitukine was predominant. DESI MS/MS analysis of the ion at m/z 306.2 yielded 3 major peaks at m/z 288, m/z 245, and m/z 222 (Fig. 3A); all of which are characteristic of rohitukine. The peak at m/z 288 is due to the neutral loss of H_2O from the piperidine ring and m/z 245 is due to further fragmentation of the ring. The peak at m/z 222 is due to fragmentation of chromone ring (Mohana Kumara et al., 2012, 2014). Besides rohitukine, a few more ions at m/z 174.1, m/z 328.2, m/z 348.2, m/z 468.2, m/z 610.5, and m/z 915.4 were identified for the first time in the seeds of *D. binectariferum* (Fig. 2). Of these, fragmentation of m/z 348.2

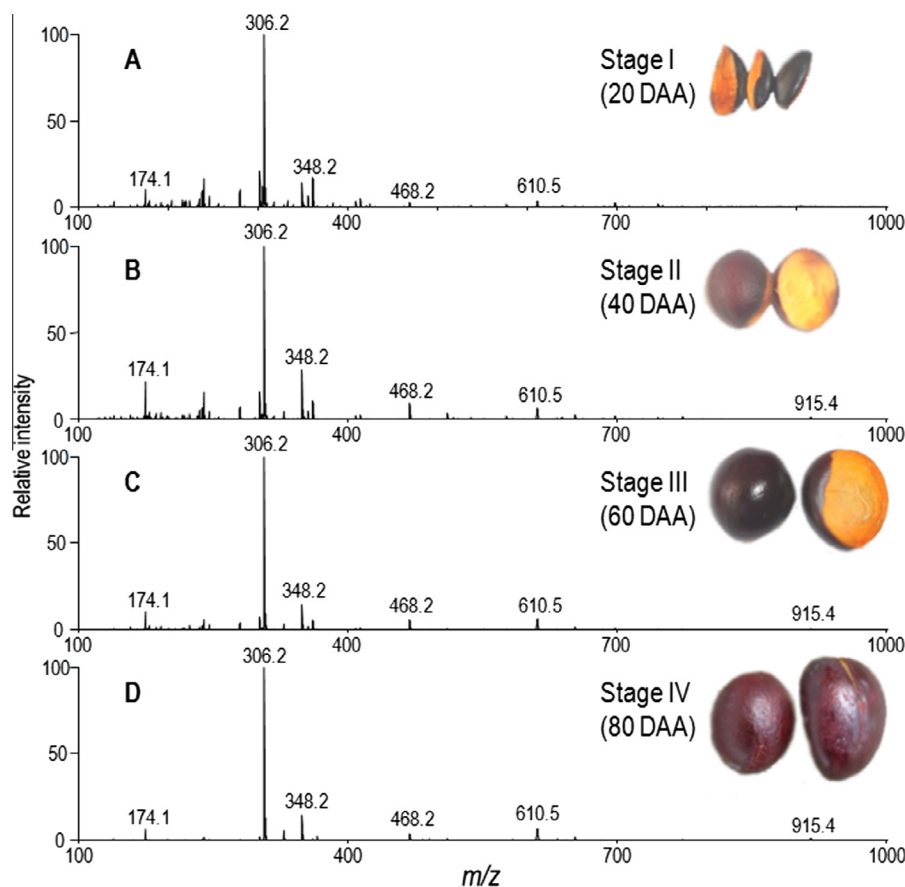


Fig. 2. DESI MS spectra of *D. binectariferum* seeds during different developmental stages. DAA refers to days after anthesis. The spectra represent the average obtained from the line scan of the images from the middle portion of the seed that contains the embryo.

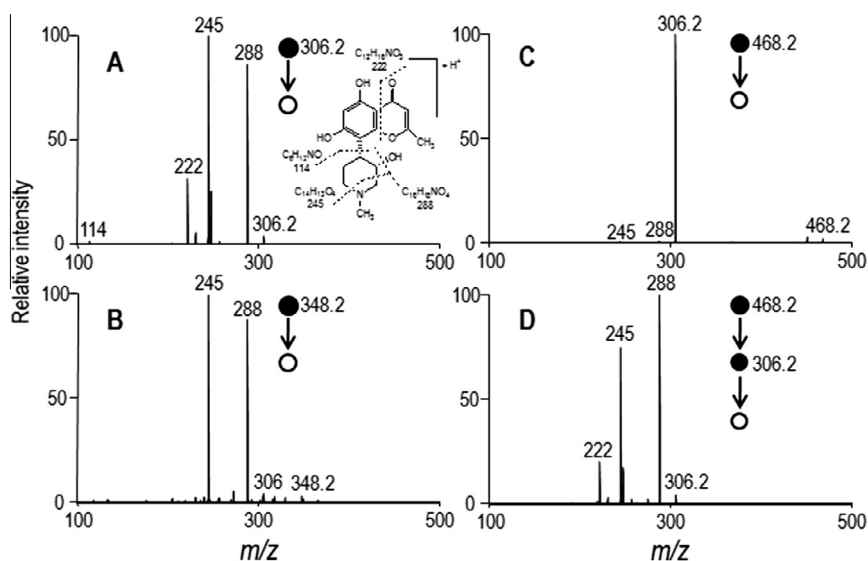


Fig. 3. Tandem DESI MS analysis of (A) rohitukine, m/z 306.2, (B) m/z 348.2, (C) m/z 468.2 and (D) m/z 306.2 (fragment ion from m/z 468.2) obtained from seeds of *D. binectariferum*. Inset in Fig. 3 (A) shows the structure of the three fragments (m/z 222, 245 and 288) obtained from rohitukine (m/z 306.2).

yielded m/z 306.2 (low relative abundance), m/z 288, and m/z 245 (higher abundances for both) (Fig. 3B), while that of m/z 468.2 yielded m/z 306.2 which upon further fragmentation yielded m/z 288, m/z 245, and m/z 222 (Fig. 3C and D). These ions are similar to those obtained on fragmenting rohitukine. Thus, it is likely that besides rohitukine (m/z 306.2), seeds of *D. binectariferum* also

contain at least two other compounds (m/z 348.2 and m/z 468.2) that could be related to the parent molecule, rohitukine. The MS/MS fragmentation of m/z 348.2 yielding m/z 306 could be accounted for by the neutral loss of ketene (CH_2CO). This ketene may have come from an acetyl group that has replaced a hydrogen atom from one of the three hydroxyl groups present in rohitukine.

Since the fragmentation pattern of m/z 348.2 is similar to that of m/z 306.2, the hydroxyl group in the piperidine ring is likely to be acetylated. For the ion at m/z 468.2, the mass difference with the ion at m/z 306.2 is 162 Da. This mass difference can be accounted by the addition of a 6-carbon sugar unit through a glycosidic bond to one of the three hydroxyl groups present in the rohitukine. Again due to a similar fragmentation pattern to that of rohitukine (Fig. 3C and D), it is likely that the sugar unit is attached with the piperidine ring.

To further confirm the identities of these ions (Fig. 2), accurate m/z values of the ions were obtained by Orbitrap MS analysis. Table 1 lists the accurate m/z values of the ions with their probable chemical formulae. For m/z 348.2 and m/z 468.2, the probable chemical formulae obtained from Metlin database are due to $C_{18}H_{22}NO_6$ and $C_{22}H_{30}NO_{10}$, respectively. Based on the fragmentation patterns, these most likely correspond to acetylated and glycosylated rohitukine, respectively.

Exact mass of three other compounds (m/z 174.1237, 328.1155 and 611.2601) indicated probable chemical formulae of $C_7H_{16}N_3O_2$, $C_{16}H_{19}NO_5Na$ and $C_{32}H_{39}N_2O_{10}$, respectively, from Metlin database. While the identities of these compounds remain to be elucidated, it is likely that m/z 611.2601 corresponds to the protonated dimer of rohitukine.

2.2. Temporal and spatial patterns in the occurrence of rohitukine and related compounds during seed development – HPLC and DESI MSI analysis

On a whole seed basis, rohitukine content increased from $0.40 \pm 0.05\%$ in the second stage fruits to $0.65 \pm 0.11\%$ in the fourth stage fruits of *D. binectariferum* (Fig. 4B). Within the seed, the highest mean percentage of rohitukine was obtained in the embryo ($0.44 \pm 0.28\%$) followed by that in the cotyledon ($0.28 \pm 0.09\%$) and in the fruit coat ($0.16 \pm 0.04\%$). Fruit stalk ($0.05 \pm 0.03\%$) and seed coat (0.04 ± 0.02) yielded low levels of rohitukine (Fig. 4A).

The spatial distribution of rohitukine was largely restricted to the cotyledonary tissue followed by the embryo and lastly in the seed coat (Fig. 5). Within the cotyledonary tissue, the outer core of the cotyledon had relatively higher content of rohitukine compared to the inner core. The signatures of rohitukine were most prominent in the fourth stage seeds. The spatial and temporal distribution of m/z 348.2 (acetylated rohitukine) was similar to that of rohitukine with DESI MSI showing relatively higher abundance in cotyledon, followed by seed coat (except embryo). On the other hand, m/z 468.2 (glycosylated rohitukine) was altogether absent from the outer cotyledonary tissue as well as the seed coat. Also within the cotyledons, the distribution of m/z 468.2 was restricted to regions proximal to the embryonic axis. The ion at m/z 174.1 was uniformly distributed in the seed during the early growth stage but at seed maturity, it was patchily distributed. The spatial

Table 1
Mass-to-charge (m/z) values of compounds obtained from seeds of *D. binectariferum* using DESI MS and ESI MS analysis and their probable chemical formulae.

m/z obtained from DESI MS (LTQ XL)	m/z obtained from ESI MS (Orbitrap)	Probable chemical formula of the ion	Exact m/z of the probable ion mentioned in the previous column
174.1	174.1237	$C_7H_{16}N_3O_2$	174.1237
306.2	306.1333	$C_{16}H_{20}NO_5^a$	306.1336
328.2	328.1155	$C_{16}H_{19}NO_5Na$	328.1155
348.2	348.1443	$C_{18}H_{22}NO_6$	348.1442
468.2	468.1867	$C_{22}H_{30}NO_{10}$	468.1864
610.5	611.2601	$C_{32}H_{39}N_2O_{10}$	611.2599
915.4	–	–	–

^a In this case the formula is not probable, it is exact.

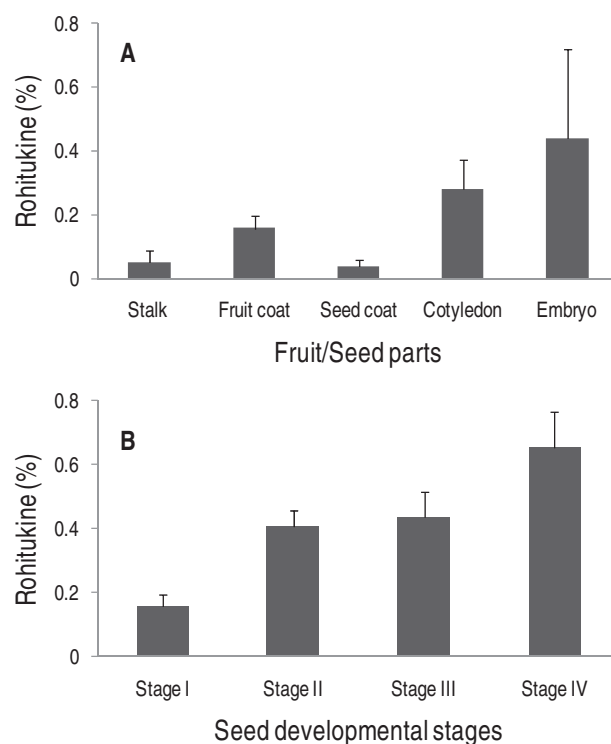


Fig. 4. HPLC analysis of rohitukine content in (A) different parts of fourth stage fruit and (B) during different developmental stages of the seeds of *D. binectariferum*. Bars indicate the standard deviation. Number of samples used for the analysis; Stalk: 4, Fruit coat: 6, Seed coat: 16, Cotyledon: 15, Embryo: 12, different stages of the seeds: 5 each.

distribution of the three ions at m/z 328.2, m/z 610.5, and m/z 915.4 was non-uniform, and tended to decrease in concentration from seed coat to the cotyledon. Distinctly, m/z 328.2 and m/z 348.2 were absent in the embryo (Fig. 5).

In order to visualize the abundance and spatial distribution of molecular ions in relation to each other, DESI MS images of pairwise molecular signatures of mature seeds (Stage IV) were superimposed. Molecular ion m/z 468.2 was localized in the central core of the seed while all other ions tended to be concentrated in the outer core of the seed. The spatial location of this ion was complementary to all other ions identified in the seed. The occurrence of m/z 174.1 was complementary to m/z 328.2, and m/z 915.4 (Fig. 6).

A number of secondary metabolites have been reported to accumulate in developing seeds, presumably to confer resistance against abiotic and biotic stress during the process of seed dispersal and germination (Alves et al., 2007; Dyer et al., 2001; McCall and Fordyce, 2010; Eriksson and Ehrlén, 1998). The secondary metabolites are either synthesized *de novo* in the seed from available precursors (Fang et al., 2012; Radchuk et al., 2011) or transported from their sites of synthesis elsewhere in the plant (Borisjuk et al., 2002; Fang et al., 2012; Patrick and Offler, 2001). In either case, there has been interest in examining the spatial and temporal pattern of accumulation of the secondary metabolites. For instance, Hebbar et al. (1993) showed that trypsin proteinase inhibitors accumulated preferentially in fruits of animal-dispersed species and not in species dispersed by wind or water. Furthermore, the accumulation of trypsin proteinase inhibitors was highest in mature but unripe fruits compared to immature and ripened fruits. They argued that the observed pattern could arise as a selection to deter predators during the mature but unripe stage, while attracting seed and fruit dispersers when the fruits were mature and ripe. In more recent studies, using DESI MSI

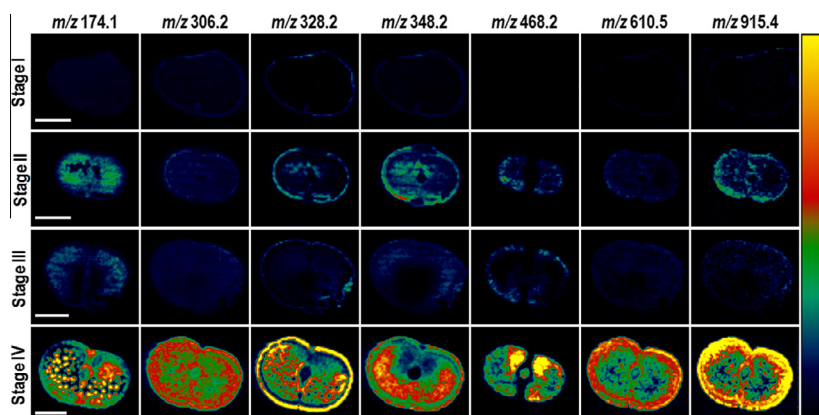


Fig. 5. DESI MS images of *D. binectariferum* seeds during different developmental stages. Intensities are normalized across the columns. The ion m/z 306.2 corresponds to rohitukine. Scale bar of 5 mm applies across each row.

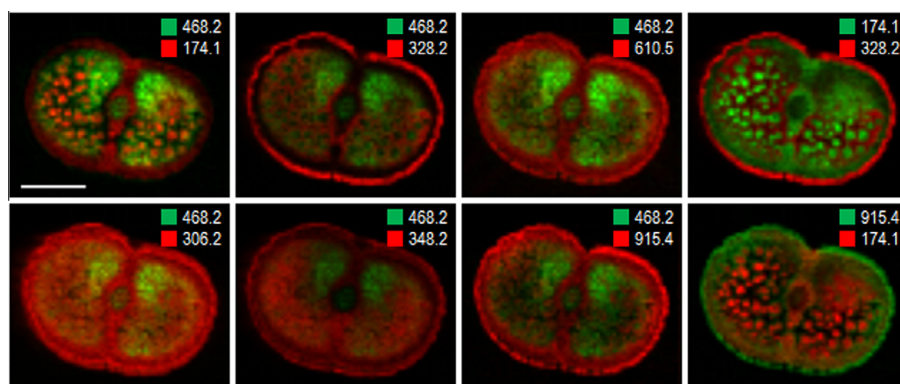


Fig. 6. Superimposed DESI MS images of the fourth stage seeds of *D. binectariferum*. Color codes refer to the specific ions given in each panel. Scale bar of 5 mm applies across each row. (For interpretation of the references to color in this figure legend, the reader is referred to the web version of this article.)

and other mass spectrometric imaging techniques, attempts have been made to spatially and temporally locate secondary metabolites in developing seeds to not only understand the compartmentalization of metabolites, if any, in different parts of the seeds, but also to trace the metabolic pathway from seed initiation to maturity (Gorzolka et al., 2014). With the advent of tissue-specific transcriptomic tools, attempts are being made to couple spatial and temporal localization with gene expression studies, to unravel critical pathway genes (Li et al., 2013a,b). In this context, our study reported here is an initial attempt to examine the spatial and temporal pattern of accumulation of rohitukine, a chromone alkaloid, in developing seeds of *D. binectariferum*. Compared to stem bark, rohitukine yield in seeds was less but substantial. Mature and ripened seeds contain about 0.6% rohitukine compared to 2–3% in stem bark. However, unlike stem bark, the seeds of *D. binectariferum* did not contain rohitukine N-oxide, an analog of rohitukine. While the biosynthetic route of rohitukine is not known, it is suggested that noreugenin (m/z 192) could be the possible upstream precursor of rohitukine (Houghton and Hairong, 1987a; Houghton and Woldemariam, 1993). However, we failed to detect noreugenin in seeds at early seed development stage, suggesting that rohitukine may be transported from sites of synthesis elsewhere in the plant to seeds. Recently, a new regioisomer of rohitukine, dysoline (m/z 306.2) was reported from stem bark of *D. binectariferum* (Jain et al., 2013). The compound differs from rohitukine in its melting point and HPLC retention time. Compared to rohitukine, the concentration of dysoline in the bark extract was very small (0.0003%) (Jain et al., 2013). In this study, we did not detect dysoline in seed tissues.

DESI MSI analysis indicated the occurrence of at least 7 distinct metabolites in seeds. Besides rohitukine (m/z 306.2), two other compounds, m/z 348.2 and m/z 468.2 representing respectively, rohitukine acetate and glycosylated rohitukine, were recovered in the seeds. These masses did not correspond to any of the reported chromone alkaloid, their analogs or natural derivatives reported from *D. binectariferum*. Four other masses of unknown identity were detected in the seeds. Two distinctive features of accumulation were observed; accumulation of rohitukine increased monotonically with seed development and there was a spatial patterning of most of the compounds in the seed. Thus rohitukine was predominantly distributed in the embryo and cotyledon with little in the seed and fruit coat. Within the cotyledon, rohitukine was fairly uniformly distributed. This is in contrast to compounds such as m/z 468.2, whose distribution was restricted to regions proximal to the embryonic axis and altogether absent from the outer cotyledonary tissue as well as the seed coat. Besides these compounds, a few others (m/z 174.1, m/z 328.2, m/z 610.5 and m/z 915.4) were also detected in the different seed developmental stages. The probable chemical formula of three of these (m/z 174.1, m/z 328.2, m/z 610.5) were obtained from the Metlin database, but their chemical structure is yet to be determined.

3. Conclusion

The present study, using DESI MSI, indicated a clear spatial and temporal distribution of rohitukine and related compounds during various stages of seed development in *D. binectariferum*. Rohitukine content increased with seed developmental stages and was largely

localized in the embryo and cotyledon, with little in the seed coat. While the evolutionary or functional significance of rohitukine in seeds is not clear, it is likely that the chromone alkaloid plays an important role as a defense compound considering the fact that rohitukine and its derivative are potent CDK inhibitors. It would be interesting to examine the underlying genetic basis of such temporal and spatial distribution of rohitukine and related compounds.

4. Experimental methods

4.1. Plant material

Fruits of *D. binectariferum* were collected from trees occurring in the Western Ghats, a mountain chain running parallel to the West coast of India and one of the 34 biodiversity hotspots of the world (Myers et al., 2000) between October 2013 and January 2014. Fruits corresponding to four developmental stages were collected, namely, immature (Stage I-20 days after anthesis), semi-mature (stage II-40 days after anthesis), matured (stage III-60 days after anthesis) and ripened (stage IV-80 days after anthesis) (Figs. 1A, B and 2). The harvested fruits were wrapped in aluminum foils and were frozen in liquid nitrogen. The frozen fruits were then transferred to a deep freezer (-80°C) for storage until further use.

4.2. Desorption electrospray ionization mass spectrometry imaging (DESI MSI)

Seeds were removed from fruits corresponding to the four developmental stages. Using a blade, the seeds were neatly cut along their minor axis (cross section) through the embryonic region, which is about 5 mm thick (Fig. 1C). The cut sections were then pressed by hand for 10 s on a hot TLC plate (TLC Silica gel 60 F₂₅₄, Merck KGaA, Germany), pre-wetted with methanol, kept on a heating mantle ($\sim 70^{\circ}\text{C}$) to get an imprint of the molecular signatures present on the cut-end of the seeds. The hand pressing method is a slight modification of an earlier method used for imprinting assisted by both solvent extraction and heating (Cabral et al., 2013). The TLC imprints were imaged using a DESI ion source. Thermo Scientific LTQ XL (Thermo Scientific, San Jose, CA, USA) mass spectrometer coupled with a 2D DESI ion source (Omni Spray Ion Source) from ProSolia, Inc., Indianapolis, IN, USA was used for imaging experiments. Methanol was used as the solvent and was sprayed at an angle of 60° to the surface. Nebulizing gas (dry nitrogen) pressure was 150 psi. Distance between the emitter and inlet was kept at 3 mm and the inlet was positioned 1 mm above the surface. Imaging area was chosen according to the sample dimensions and the spatial resolution used was $250\ \mu\text{m} \times 250\ \mu\text{m}$. Data were acquired in positive ion mode with a spray voltage of 5 kV. After acquisition of the data, they were processed by FireFly software to create the image files (IMG File) and the images were viewed using BioMap software. Collision induced dissociation (CID) was used for fragmentation of ions during MS/MS measurements.

4.3. Exact mass analysis by electrospray ionization mass spectrometry (ESI MS)

The seeds of *D. binectariferum* (Stage IV) were cut into small pieces and soaked in methanol for 12 h. Following this, the solution was filtered and centrifuged at 10,000 rpm for 10 min. The supernatant was taken for ESI MS analysis using a Thermo Scientific Orbitrap (Thermo Scientific, San Jose, CA, USA) mass spectrometer. The data were acquired in positive ion mode with a spray voltage of 5 kV.

4.4. Extraction for rohitukine and HPLC analysis

Fruits and seeds of *D. binectariferum* corresponding to the four developmental stages were oven dried for 1 week at 70°C . Rohitukine was extracted from different parts of the fruit and seeds following the protocol developed by Mohana Kumara et al. (2010). The extracted samples (20 μL) were analyzed by reverse-phase HPLC (Shimadzu, LC20AT, Japan) using RP-18 column ($4.6 \times 250\ \text{mm}$, $5\ \mu\text{m}$) with UV absorbance at 254 nm. HPLC protocol was first standardized for rohitukine using a linear gradient mode using acetonitrile and 0.1% TFA as mobile phases. We used gradient method starting from 0%:100% to 100%:0% of acetonitrile: (0.1%) TFA with a flow rate of 1 mL/min for 30 min. Sharp peak with highest peak intensity was obtained when mobile phase concentration was 30% acetonitrile and 70% TFA. All samples were then analyzed in isocratic mode using 30% acetonitrile: 70% (0.1%) TFA as mobile phase. Care was exercised to ensure that the initial and final volumes of the extract were maintained constant for the sample. Standard curve was developed for the concentration range of 0.125 mg/mL to 1 mg/mL of standard rohitukine obtained from our earlier work (Mohana Kumara et al., 2010). The best fit ($R^2 = 0.99$) was used in calculating the amount of rohitukine in the sample. All estimates were done on 5 replicates.

Acknowledgements

We thank Department of Biotechnology (DBT) and Department of Science and Technology (DST), Government of India for the financial support to carry out this work. P.M.K. thanks IIT Madras, Chennai for a postdoctoral fellowship and A.S. thanks the Council of Scientific and Industrial Research (CSIR), Government of India for PhD fellowship. We thank Prof. Graham Cooks for helpful suggestion in revising the manuscript.

References

- Alves, M., Sartoratto, A., Trigo, J.R., 2007. Scopolamine in *Brugmansia suaveolens* (Solanaceae): defense, allocation, costs, and induced response. *J. Chem. Ecol.* 33, 297–309.
- Bennett, A.B., Spanswick, R.M., 1983. Derepression of amino acid- H^+ cotransport in developing soybean embryos. *Plant Physiol.* 72, 781–786.
- Bjarnholt, N., Li, B., D'Alvise, J., Janfelt, C., 2014. Mass spectrometry imaging of plant metabolites – principles and possibilities. *Nat. Prod. Rep.* 31, 818–837.
- Borisjuk, L., Walenta, S., Rolletschek, H., Mueller-Klieser, W., Wobus, U., Weber, H., 2002. Spatial analysis of plant metabolism: sucrose imaging within *Vicia faba* cotyledons reveals specific developmental patterns. *Plant J.* 29, 521–530.
- Cabral, E., Mirabelli, M., Perez, C., Ifa, D., 2013. Blotting assisted by heating and solvent extraction for DESI-MS imaging. *J. Am. Soc. Mass Spectrom.* 24, 956–965.
- De Azevedo, W.F., Mueller-Dieckmann, H.J., Schulze-Gahmen, U., Worland, P.J., Sausville, E., Kim, S.H., 1996. Structural basis for specificity and potency of a flavonoid inhibitor of human CDK2, a cell cycle kinase. *Proc. Natl. Acad. Sci.* 93, 2735–2740.
- de Souza Noel, J., 1993. Rohitukine and Forskolol. *Human Medicinal Agents from Plants*, vol. 534. American Chemical Society, pp. 331–340.
- Dyer, L., Dodson, C., Beihoffer, J., Letourneau, D., 2001. Trade-offs in antiherbivore defenses in piper cenocladum: ant mutualists versus plant secondary metabolites. *J. Chem. Ecol.* 27, 581–592.
- Eriksson, Ove, Ehrlén, Johan, 1998. Secondary metabolites in fleshy fruits: are adaptive explanations needed? *Am. Nat.* 152, 905–907.
- Fang, J., Reichelt, M., Hidalgo, W., Agnolet, S., Schneider, B., 2012. Tissue-specific distribution of secondary metabolites in rapeseed (*Brassica napus* L.). *PLoS One* 7, e48006.
- Gorzolka, K., Bednarz, H., Niehaus, K., 2014. Detection and localization of novel horadine-like compounds and glycosylated derivatives of horadines by imaging mass spectrometry of barley seeds. *Planta* 239, 1321–1335.
- Harmon, A.D., Weiss, U., Silvertown, J.V., 1979. The structure of rohitukine, the main alkaloid of *Amoora rohituka* (Syn. *Aphanamixis polystachya*) (meliaceae). *Tetrahedron Lett.* 20, 721–724.
- Hebbar, R., Sashidhar, V.R., Shaanker, R.U., Kumar, M.U., Sudharshana, L., 1993. Dispersal mode of species influences the trypsin inhibitor levels in fruits. *Naturwissenschaften* 80, 519–521.
- Hemalatha, R.G., Pradeep, T., 2013. Understanding the molecular signatures in leaves and flowers by desorption electrospray ionization mass spectrometry (DESI MS) imaging. *J. Agric. Food Chem.* 61, 7477–7487.

- Houghton, P.J., Hairong, Y., 1987a. Further chromane alkaloids from *Schumanniohyton magnificum*. *Planta Med.* 52, 262–264.
- Houghton, P.J., Hairong, Y., 1987b. Further chromone alkaloids from *Schumanniohyton magnificum*. *Planta Med.* 53, 262–264.
- Houghton, P.J., Woldemariam, T.Z., 1993. High performance liquid chromatographic analysis of chromone alkaloids from *Schumanniohyton* species. *Phytochem. Anal.* 4, 9–13.
- Ifa, D.R., Srimany, A., Eberlin, L.S., Naik, H.R., Bhat, V., Cooks, R.G., Pradeep, T., 2011. Tissue imprint imaging by desorption electrospray ionization mass spectrometry. *Anal. Methods* 3, 1910–1912.
- Ismail, I.S., Nagakura, Y., Hirasawa, Y., Hosoya, T., Lazim, M.I.M., Lajis, N.H., Shiro, M., Morita, H., 2009. Chromones A–D, chromone alkaloids from *Dysoxylum acutangulum*. *J. Nat. Prod.* 72, 1879–1883.
- Jain, S.K., Meena, S., Qazi, A.K., Hussain, A., Bhola, S.K., Kshirsagar, R., Pari, K., Khajuria, A., Hamid, A., Shaanker, R.U., Bharate, S.B., Vishwakarma, R.A., 2013. Isolation and biological evaluation of chromone alkaloid dysoline, a new regioisomer of rohitukine from *Dysoxylum binectariferum*. *Tetrahedron Lett.* 54, 7140–7143.
- Korte, A.R., Song, Z., Nikolau, B.J., Lee, Y.J., 2012. Mass spectrometric imaging as a high-spatial resolution tool for functional genomics: tissue-specific gene expression of TT7 inferred from heterogeneous distribution of metabolites in *Arabidopsis* flowers. *Anal. Methods* 4, 474–481.
- Kueger, S., Steinhäuser, D., Willmitzer, L., Giavalisco, P., 2012. High-resolution plant metabolomics: from mass spectral features to metabolites and from whole-cell analysis to subcellular metabolite distributions. *Plant J.* 70, 39–50.
- Lee, Y.J., Perdian, D.C., Song, Z., Yeung, E.S., Nikolau, B.J., 2012. Use of mass spectrometry for imaging metabolites in plants. *Plant J.* 70, 81–95.
- Li, B., Bjarnholt, N., Hansen, S.H., Janfelt, C., 2011. Characterization of barley leaf tissue using direct and indirect desorption electrospray ionization imaging mass spectrometry. *J. Mass Spectrom.* 46, 1241–1246.
- Li, B., Knudsen, C., Hansen, N.K., Jørgensen, K., Kannangara, R., Bak, S., Takos, A., Rook, F., Hansen, S.H., Møller, B.L., Janfelt, C., Bjarnholt, N., 2013a. Visualizing metabolite distribution and enzymatic conversion in plant tissues by desorption electrospray ionization mass spectrometry imaging. *Plant J.* 74, 1059–1071.
- Li, B., Hansen, S.H., Janfelt, C., 2013b. Direct imaging of plant metabolites in leaves and petals by desorption electrospray ionization mass spectrometry. *Int. J. Mass Spectrom.* 348, 15–22.
- Mahajan, V., Sharma, N., Kumar, S., Bhardwaj, V., Ali, A., Khajuria, R.K., Bedi, Y.S., Vishwakarma, R.A., Gandhi, S.G., 2015. Production of rohitukine in leaves and seeds of *Dysoxylum binectariferum*: an alternate renewable resource. *Pharm. Biol.* 53 (3), 446–450.
- Manske, R.H., Brossi, 1987. *The Alkaloids Chemistry Pharmacology*, vol. 31. Academic Press Inc., San Diego, California, pp. 123–155.
- McCall, A.C., Fordyce, J.A., 2010. Can optimal defence theory be used to predict the distribution of plant chemical defences? *J. Ecol.* 98, 985–992.
- Mohana Kumara, P., Sreejayan, N., Priti, V., Ramesha, B.T., Ravikanth, G., Ganeshiah, K.N., Vasudeva, R., Mohan, J., Santhoshkumar, T.R., Mishra, P.D., Ram, V., Shaanker, 2010. *Dysoxylum binectariferum* Hook.f (Meliaceae), a rich source of rohitukine. *Fitoterapia* 81, 145–148.
- Mohana Kumara, P., Zuehlke, S., Priti, V., Ramesha, B., Shweta, S., Ravikanth, G., Vasudeva, R., Santhoshkumar, T., Spittler, M., Uma Shaanker, R., 2012. *Fusarium proliferatum*, an endophytic fungus from *Dysoxylum binectariferum* Hook.f, produces rohitukine, a chromone alkaloid possessing anti-cancer activity. *Antonie Van Leeuwenhoek* 101, 323–329.
- Mohana Kumara, P., Soujanya, K.N., Ravikanth, G., Vasudeva, R., Ganeshiah, K.N., Shaanker, R.U., 2014. Rohitukine, a chromone alkaloid and a precursor of flavopiridol, is produced by endophytic fungi isolated from *Dysoxylum binectariferum* Hook.f and *Amoora rohituka* (Roxb). *Wight & Arn. Phytomedicine* 21, 541–546.
- Myers, N., Mittermeier, R.A., Mittermeier, C.G., da Fonseca, G.A.B., Kent, J., 2000. Biodiversity hotspots for conservation priorities. *Nature* 403, 853–858.
- Naik, R.G., Kattige, S.L., Bhat, S.V., Alreja, B., de Souza, N.J., Rupp, R.H., 1988. An antiinflammatory cum immunomodulatory piperidinylbenzopyranone from *Dysoxylum binectariferum*: isolation, structure and total synthesis. *Tetrahedron* 44, 2081–2086.
- Patrick, J.W., Offler, C.E., 2001. Compartmentation of transport and transfer events in developing seeds. *J. Exp. Bot.* 52, 551–564.
- Radchuk, V., Weier, D., Radchuk, R., Weschke, W., Weber, H., 2011. Development of maternal seed tissue in barley is mediated by regulated cell expansion and cell disintegration and coordinated with endosperm growth. *J. Exp. Bot.* 62, 1217–1227.
- Sedlacek, H., Czech, J., Naik, R., Kaur, G., Worland, P., Losiewicz, M., Parker, B., Carlson, B., Smith, A., Senderowicz, A., Sausville, E., 1996. Flavopiridol (L86 8275; NSC 649890), a new kinase inhibitor for tumor therapy. *Int. J. Oncol.* 9, 1143–1163.
- Senderowicz, A.M., Sausville, E.A., 2000. Preclinical and clinical development of cyclin-dependent kinase modulators. *J. Natl Cancer Inst.* 92, 376–387.
- Sethi, P., Howe, H.F., 2012. Fruit removal by hornbills in a semi-evergreen forest of the Indian Eastern Himalaya. *J. Trop. Ecol.* 28, 531–541.
- Stadler, W.M., Vogelzang, N.J., Amato, R., Sosman, J., Taber, D., Liebowitz, D., Vokes, E.E., 2000. Flavopiridol, a novel cyclin-dependent kinase inhibitor, in metastatic renal cancer: a university of Chicago phase II consortium study. *J. Clin. Oncol.* 18, 371.
- Thunig, J., Hansen, S.H., Janfelt, C., 2011. Analysis of secondary plant metabolites by indirect desorption electrospray ionization imaging mass spectrometry. *Anal. Chem.* 83, 3256–3259.
- Varshney, S., Shankar, K., Beg, M., Balaramnavar, V.M., Mishra, S.K., Jagdale, P., Srivastava, S., Chhonker, Y.S., Lakshmi, V., Chaudhari, B.P., Bhatta, R.S., Saxena, A.K., Gaikwad, A.N., 2014. Rohitukine inhibits in vitro adipogenesis arresting mitotic clonal expansion and improves dyslipidemia in vivo. *J. Lipid Res.* 55, 1019–1032.
- Yang, D.-H., Cai, S.-Q., Zhao, Y.-Y., Liang, H., 2004. A new alkaloid from *Dysoxylum binectariferum*. *J. Asian Nat. Prod. Res.* 6, 233–236.

Size Evolution of Protein-Protected Gold Clusters in Solution: A Combined SAXS–MS Investigation

Ananya Baksi,^{†,||} Anuradha Mitra,^{‡,||} Jyoti Sarita Mohanty,[†] Haiwon Lee,[§] Goutam De,^{*,‡} and T. Pradeep^{*,†}

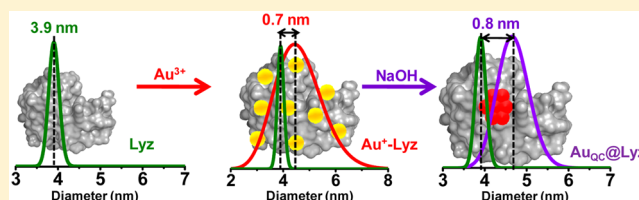
[†]DST Unit of Nanoscience (DST UNS) and Thematic Unit of Excellence, Department of Chemistry, Indian Institute of Technology Madras, Chennai-600 036, India

[‡]Nano-Structured Materials Division, CSIR-Central Glass and Ceramic Research Institute, 196 Raja S. C. Mullick Road, Kolkata-700032, India

[§]Department of Chemistry, Institute of Nanoscience and Technology, Hanyang University, Seoul-133-791, Korea

S Supporting Information

ABSTRACT: We report a combined small-angle X-ray scattering (SAXS) and mass spectrometric (MS) study of the growth of gold clusters within proteins, in the solution state. Two different proteins, namely, lysozyme (Lyz) and bovine serum albumin (BSA), were used for this study. SAXS study of clusters grown in Lyz shows the presence of a 0.8 nm gold core, which is in agreement with the Au₁₀ cluster observed in MS. Dynamic light scattering suggests the size of the cluster core to be 1.2 nm. For BSA, however, a bigger core size was observed, comparable to the Au₃₃ core obtained in MS. Concentration- and time-dependent data do not show much change in the core size in both SAXS and MS investigations. When metal–protein adducts were incubated for longer time in solution, nanoparticles were formed and protein size decreased, possibly due to the fragmentation of the latter during nanoparticle formation. The data are in agreement with dynamic light scattering studies. This work helps to directly visualize cluster growth within protein templates in solution.



1. INTRODUCTION

Noble metal nanoclusters belong to one of the rapidly evolving fields in nanoscience today.^{1–10} Subnanometer sized clusters comprising a few to a hundred atom cores are of specific interest due to their unusual physical and chemical properties. Investigations of such clusters started with their gas phase analogues, which were studied extensively with mass spectrometry.^{1,11–13} Although clusters are many, only very few of the gold and silver clusters have been crystallized so far.^{14–19} Macromolecular templating is one way to create clusters. DNA, dendrimers, and most recently proteins have been introduced to the cluster community.^{3,10,20–23} Many proteins, namely, bovine serum albumin (BSA), human serum albumin (HSA), lactoferrin (Lf), human serum transferrin, pepsin, horseradish peroxidase, ovalbumin, chymotrypsin, insulin, trypsin, lysozyme (Lyz), etc. have been used so far for synthesizing clusters.^{24–37} Protein protected clusters exhibit intense luminescence, which has been exploited mostly for sensing of specific molecules and bioimaging.^{26,29–31,38–43} Besides, retention of biological activity of insulin after cluster formation has also been shown recently.³⁰ Usually proteins are characterized by crystallography, cryo-electron microscopy, nuclear magnetic resonance (NMR), etc. Although crystal structure determination is the best option for analyzing the protein structure,^{44,45} it has not been possible so far to get crystals of protein protected clusters due to the inherent difficulty to form crystals at experimental conditions of cluster

synthesis. Therefore, for assigning cluster composition, mass spectrometry (MS) is often used, as it is possible to determine molecular weights of proteins and related systems with reasonable accuracy. For instance, Au/Ag/Au@Ag_{QC}@BSA,^{28,32,34,46} Au/Ag_{QC}@Lyz,^{24,47} Au_{QC}@Lf,^{36,37} etc. (where the subscript QC refers to quantum clusters, another name for such clusters) have been studied using MS. However, it should be noted that matrix-assisted laser desorption/ionization (MALDI) MS involves studies in the gas phase, but the original synthesis of clusters occurs in the solution phase. Ions observed in MALDI MS need not necessarily correspond to the species in the condensed phase. So, it is essential to correlate the behavior of these clusters in both solution and gas phases. Thus comes the need for solution phase techniques like small-angle X-ray scattering (SAXS) and neutron scattering (SANS) to study the size and structural changes of protein protected clusters.

SAXS enables size analysis using small amounts of sample, even at very low concentrations. Unlike dynamic light scattering (DLS) studies, SAXS analysis does not require any special sample preparation steps (such as preconcentration or predilution) and can be performed at room temperature. Normally, transmission SAXS gives accurate information about species of size less than

Received: September 15, 2014

Revised: December 1, 2014

Published: December 29, 2014

50 nm. SAXS has been widely and successfully used to extract information about size, shape and also secondary structure of biomolecules, especially proteins, in solution.^{48–51} Recently, the behavior of proteins like Lyz and BSA^{48,49} in the presence of salts such as sodium dodecyl sulfonate has been studied in detail using SAXS. Blanchet et al. and Lipfert et al. have described various aspects of SAXS investigations on biomolecules.^{52,53} Besides macromolecules, many studies on the formation and growth of nanoparticles in various media exist. For example, Gang et al. have described DNA-mediated self-assembly of nanoparticles in heterogeneous systems where they programmed nanoparticle-coated DNA molecules to self-assemble into three-dimensional superlattices, and corresponding structural information was obtained from SAXS.⁵⁴ In another report from the same group, nanoparticle dimers linked via DNA were prepared, and the size and other information were collected via DLS and SAXS studies. One dimensional linear meso-structure of nanorod-DNA assembly has also been looked at by in situ SAXS.⁵⁵ The actual solution state mechanism for the formation of citrate-capped gold nanoparticles has also been demonstrated by Kraehnert et al.⁵⁶ using continuous flow SAXS measurement.⁵⁷ There are many other reports on the SAXS study of biological and material interfaces,^{54,55,58–62} although until now very few reports existed on noble metal nanoclusters. In 1995, Murray and group studied alkanethiol protected gold clusters by SAXS and found that their core size was about 1.2 nm, consistent with the TEM data.⁶³ Recently SAXS study of Ag₁₅₂ cluster has been reported.⁵⁶ Most recently, the structure of Au₆₈ has been solved by electron microscopy and the size of the core has been validated by SAXS data.⁶⁴ However, in most cases, such studies have been limited to the basic characterization of the clusters.

Until now, none of the protein protected clusters could be crystallized, and they also have not been seen in electrospray ionization mass spectrometry (ESI MS). Although more than 300 papers have been published to date on protein-protected clusters, there is no direct way to observe these clusters in solution. Thus, it is necessary to acquire additional data on the cluster growth in solution using independent studies. As protein-protected Au clusters are prepared in aqueous solutions, study of the dynamics and growth of proteins in the same phase is more useful. Since proteins are explored widely by SAXS, a study by this methodology has relevance. In this paper, we are reporting a combined MS-SAXS study of the evolution and growth of protein protected clusters for the first time. We have probed the growth of small gold clusters in a relatively small protein, Lyz and correlated the results with mass spectral data. The same procedure is followed for a larger protein, BSA, to validate our point. The sizes of the clusters derived from SAXS profiles are in good agreement with the previously reported cluster size as well as with the mass spectra. The results were further validated using dynamic light scattering.

2. EXPERIMENTAL SECTION

2.1. Reagents and Materials. Lysozyme with >90% purity and sinapic acid with about 99% purity were purchased from Sigma-Aldrich. BSA at pH 6–7 of about 96% purity was purchased from SRL, India. Tetrachloroauric acid trihydrate (HAuCl₄·3H₂O) was purchased from CDH chemicals with 49% gold content. Sodium hydroxide (Rankem, India) was purchased locally. All the chemicals were used without further purification. Milli-Q water was used in all the experiments.

2.2. Synthesis. Au_{QC}@Lyz was prepared by a method reported previously. Briefly, 1:2, 1:4, and 1:8 of Lyz: Au³⁺ were

mixed and stirred for some time to get the Au⁺–Lyz adduct. After that, the pH of the solution was elevated to 12 by NaOH, and the solutions were further incubated to get red luminescent Au_{QC}@Lyz. This luminescence appeared over a period of 12 h. For adduct and nanoparticle formation, the same procedure was followed without the addition of NaOH to the system. For BSA protected clusters, 1:5, 1:10, and 1:20 BSA: Au³⁺ were used, and the same procedure was followed, as described in the case of Lyz.

2.3. Instrumentation. For MALDI TOF MS analysis, an Applied Biosystems Voyager De Pro instrument was used with sinapic acid as the matrix. A pulsed nitrogen laser of 337 nm was used for ionizing the sample. Spectra were collected in the linear positive mode and an average of 250 shots was used for each spectrum. The matrix was prepared by dissolving 10 mg of sinapic acid in a 1:3 mixture of acetonitrile: 0.1% trifluoroacetic acid (overall volume of 1 mL). While preparing the samples for analysis, 5 μ L of the cluster solution (without dilution) was mixed thoroughly with 100 μ L of the matrix mixture. About 2.5 μ L of the resulting mixture was used for spotting. Luminescence measurement was carried out in a Jobin Yvon NanoLog fluorescence spectrometer with a band-pass of 3 nm for both emission and excitation spectra. UV-vis spectra were collected using a PerkinElmer Lambda 25 spectrometer in the range of 200–1100 nm. High-resolution transmission electron microscopic (HRTEM) images were taken using a JEOL 3010 instrument. DLS and zeta potential measurements were done using a Malvern Zetasizer ZSP instrument equipped with a 633 nm (He–Ne) laser.

2.4. Experimental Details of Transmission SAXS Measurements. Transmission SAXS experiments were performed to study the formation and growth of Au_{QC} inside the protein, Lyz. Experiments were carried out as a function of incubation time. We have performed SAXS experiments at different pH and precursor concentrations to observe the change in the overall protein size in a wide time range. The SAXS profiles of the sample solutions were collected in transmission mode using a Rigaku Smart Lab X-ray diffractometer (9 kW; Cu–K α radiation; $\lambda = 1.54059$ Å). Transparent borosilicate capillary tubes (~1.5 mm internal diameter) containing the sample solutions were mounted at a fixed position on a sample holder. Sample alignment and premeasurement scan were carried out before each SAXS measurement. The maximum time taken for each SAXS data acquisition was ~20 min. The NANO-Solver software of Rigaku was used to solve the SAXS profiles. Prior to the data-fitting step, the SAXS profiles of the sample solutions were corrected for background contributions (originating from the solvent and the sample holder).

3. RESULTS AND DISCUSSION

3.1. Formation of Protein Protected Clusters. As luminescent noble metal clusters protected with proteins have been investigated extensively, we introduce only their essential aspects in the following. They are formed upon incubation of the protein with the metal ions for 12 h at a basic pH, and the appearance of the cluster is manifested by the presence of an intense red luminescence upon UV excitation (Figure 1). These clusters in the case of Lyz show an emission at 690 nm when excited at 365 nm (see below, Figure 1).²⁴ As of now, the most widely applied property of such protein protected clusters is their strong luminescence, which has made them useful for sensing, biolabeling, and bioimaging. Cluster formation in such cases proceed through an Au(I)–Lyz complex that we call *adduct* in the subsequent discussion. Such adducts exist in the Au(I) form in

complexation with cysteine residues of the protein. A maximum of 10 Au attachments were seen in such cases with each Lyz molecule when the highest concentration of Au³⁺ was used.⁶⁵ During cluster formation, these adducts get reduced to Au(0) involving interadduct metal transfer and consequent release of free protein (while some proteins contain clusters within them).^{24,36} Depending on the protein involved in cluster formation, various gold cluster cores have been identified in different proteins; among which the most important are Au_{8,25}@BSA,^{34,36} Au_{13,25}@Lf,^{36,37} and Au_{10,11,12}@Lyz²⁴ although many other proteins have been examined.

Proteins differ by their shape and size. Between Lyz and BSA, Lyz is more spherical,⁴⁵ therefore, we have used Lyz as a model protein for our study. Lyz is a small protein (molecular weight 14.3 kDa) with 129 amino acids among which 8 are cysteines forming 4 disulfide bonds. The overall surface structure of the protein shows nearly spherical geometry with mean diameter (considering three-dimensional orientation) of about 3.9 nm.^{45,47} We have studied the formation and growth of gold clusters using SAXS, and the data were compared with mass spectrometric evolution of the clusters within the protein. It is known from a previous study that when protein interacts with Au³⁺, it unfolds to accommodate the Au ions inside. This can lead to the breakage of disulfide bonds and finally the protein's secondary structure is lost (partially).^{36,65} When the protein interacts with Au ions, it may result in a free protein (without any Au attachment) or a protein with single or multiple Au attachments.³⁶ Considering the existence of all these species, we expect to get a broad size distribution due to the presence of various stages of unfolded proteins. This is reflected in the mass spectrum of Au⁺-Lyz, where we can see multiple peaks corresponding to Au attachments, including the parent protein peak.⁶⁵ When NaOH is added to the system, the Au ions start rearranging to form a cluster core, and we are supposed to get only a few possible species present in the system like, some free protein as well as Au attached proteins (not converted to cluster core) and mostly, cluster core containing proteins.²⁴ All these together should show reduced broadness in the size profile, largely because the cluster core distributions are narrower than the *adduct* distributions.

3.2. Solution Phase SAXS Analysis of the Samples. The as-prepared samples were used for SAXS analysis without further purification. Here we briefly describe the working principle of SAXS which may help understand of our results. The discussion is kept to the essential aspects. Particles in the range of 1–50 nm can efficiently scatter the incident X-ray. The larger the electron density difference between the solvent medium and solute particles ($\Delta\rho$), the higher the scattering intensity [$I(q)$]. The scattering amplitude [$A(q)$] is calculated from the Born approximation as

$$A(q) = \int_V \Delta\rho(r) e^{iq \cdot r} dr \quad (1)$$

$$q = (4\pi/\lambda) \cdot \sin(2\theta/2) \quad (2)$$

where, q is the scattering vector, V is the volume for the integral over the entire medium, and λ is the wavelength of the X-ray.

The scattering intensity is expressed as

$$I(q) = A(q)[A(q)]^* \quad (3)$$

If the particles possess definite shape, then $I(q)$ is generalized in terms of the structure factor [$S(q)$] and the form factor [$F(q)$] as follows:

$$I(q) = |F(q)|^2 S(q) \quad (4)$$

The form factor, $F(q)$, is related to the shape of the particle.

- (i) For spherical particles with a radius of R , the form factor is expressed as

$$[F(q, R)]_{\text{sphere}} = \Delta\rho \cdot \frac{4\pi\{\sin(qR) - qR \cos(qR)\}}{q^3} \quad (5)$$

- (i) In the cylinder model, form factor considers the contribution from aspect ratio (a) of the cylinder (or rod):

$$[F(q, \varphi, a, R)]_{\text{cylinder}} = \Delta\rho \cdot \frac{4\pi R^3 a \{\sin(qaR \cos \varphi)(qR \sin \varphi)\}}{(qR)^2 \sin \varphi \cos \varphi} \quad (6)$$

where, φ is the angle formed between the scattering vector and the normal to the surface of the rod.

For irregular particles or in case of particles of unknown shapes “Model Free Analysis” is often helpful, in which the B-spline function is first adopted to generate a “true” scattering profile with scattering intensity, $I^T(q)$ from the raw SAXS profile as given in eq 7:

$$I^T(q) = \sum_{i=0}^N S_i(q - a_i)^b \cdot (b_i - q)^r \quad (7)$$

Fourier transform of the true scattering profile generates the correlation function [$C(R)$], which relates to the interparticle interactions and the distance distribution function $p(r)$ as follows:

$$C(R) = 1/R \cdot \left\{ \int q I^T(q) \sin(qR) dq \div \int q^2 I^T(q) dq \right\} \quad (8)$$

$$p(r) = 4\pi R^2 \cdot C(R) \quad (9)$$

The structure factor, introduced in eq 4, depends upon the interparticle distance and particle–particle arrangements, i.e., it indicates the correlation between particles in a system. Mathematically,

$$S(q) = 1 + \int \{n(r) - n_0\} \cdot e^{iq \cdot r} dr \quad (10)$$

where $n(r)$ is the particle count density function. Usually, short-range interparticle correlations are observed from SAXS analysis. In dilute solutions, the particles are considered to be randomly distributed such that the interparticle distances are very large.⁶⁶

We chose the “sphere” and “cylinder” models of NANO-Solver software, and the simulated profiles are generated based upon eqs 5 and 6. We have considered $S(q) = 1$ while solving the SAXS profiles using these models.⁶⁶ The best profiles are those for which the residual between the raw and simulated profiles (residual factor) is the lowest. To minimize the error in evaluation of average sizes, we have considered only the best fit (simulated) profiles with residual factors less than or around 4%. Normalized dispersion value (σ) is an important parameter that gives us an idea about the polydispersity of particles. For example, a solution containing monodisperse particles with narrow size distribution will have a low σ value. Also, correlation function [$C(R)$] and distance distribution functions [$p(r)$] have been evaluated through the “Model Free Analysis” program of Nanosolver to observe short-range interparticle interactions in the protein solutions under the reaction conditions. It is to be noted that “interparticle distance” shall be recognized as the

distance between centers of two neighboring particles, X and Y, arranged in any possible manner.

To select a suitable model for our interpretation of the solution phase growth of clusters in proteins, the SAXS profiles of pure Lyz and BSA solutions were fitted using both the models (See parts A and B of Supporting Information Figure S1). From the cylinder model, optimized simulated profiles could be generated only when the aspect ratio (a) was fixed in the range of 0.80–1.00 for both Lyz and BSA. It can be clearly seen that by choosing either of these models similar fittings (with the same residual factor) could be obtained in each of the proteins as shown in Figure S1. However, the nature of the size distribution curves of Lyz (shown in Figure S1C) evaluated from the cylinder and the sphere models differs widely; the size of Lyz (and BSA; see Figure S1D) obtained from the sphere model is more in agreement with its reported value (3.9 nm). Moreover, a cylindrical model with aspect ratio in the range of 0.8–1.00 indicates that the particles are more or less spherical and so the simpler sphere model is a better choice. Thus, considering the above observations, we have used the sphere model in the subsequent analyses.^{45,47}

3.3. Evolution of Gold Cluster in Lyz. Figure 1A shows that the simulated SAXS profile of Lyz changes significantly after the addition of Au^{3+} in the system ($\text{Au}^+\text{-Lyz}$ and $\text{Au}_{10}\text{@Lyz}$). Size profiles of Lyz, $\text{Au}^+\text{-Lyz}$ and $\text{Au}_{10}\text{@Lyz}$ have been presented in Figure 1B. Initially, pure Lyz solution shows a narrow size distribution with an average size of 3.9 nm along with the presence of large aggregates ($\sim 11.1\%$; not shown in the figure for simplicity). The average size of this adduct does not change significantly with time (see Figure S2) or at higher pH (Figure S3). However, upon addition of NaOH, the size profiles become relatively broader, possibly due to unfolding of the protein at basic pH (See Figure S4). In all the cases studied here, some amount of aggregates is always present (10–20%). Due to the broad distribution, it is not wise to conclude any size changes in the aggregate region (20 nm and above). The average size of

Lyz increases to 4.6 nm due to $\text{Au}^+\text{-Lyz}$ adduct formation. As multiple Au attachments (maximum 10 Au) are possible, we have observed a relatively broader size distribution in this case. Upon reduction of the adducts in basic medium, luminescent clusters (Figure 1C) form with an overall protein size of 4.7 nm ($\text{Au}_{10}\text{@Lyz}$). Thus, the difference in size of Lyz protein before and after cluster formation is 0.8 nm (3.9 nm for Lyz). The cluster obtained in this process shows emission at 690 nm when excited at 365 nm as shown in Figure 1C. The as-formed cluster showed a mass difference of 10 atoms of Au from the parent protein peak in MALDI MS (Figure 1D). The core size remains the same without any further change with time. A core size of 0.8 nm from SAXS is consistent with the size obtained in TEM (1 nm as shown in Figure 1E). The $C(R)$ profiles of Lyz shows two peaks at 6.31 and 10.82 nm corresponding to the nearest Lyz–Lyz interparticle distances (Figure S5 A). The $C(R)$ -distance profile of $\text{Au}_{10}\text{@Lyz}$ resembles that of the original Lyz solution and incubation of these $\text{Au}_{10}\text{@Lyz}$ (up to 48 h) does not change the correlation pattern. This shows that the cluster formation in Lyz does not involve much change in its overall structure except for the expansion in its size observed from the size distribution profiles (see Figure 1B).

We have conducted a concentration-dependent SAXS study by varying the Au^{3+} concentration, keeping Lyz concentration the same (see Figure 2 and Figure S6). During this study, the core size, analyzed by sphere model, does not change much.²⁴ This was explained in terms of the size of Lyz. Being a small protein, Lyz cannot accommodate larger cluster cores inside it. Less number of cysteines does not help in stabilizing a bigger core. The simulated SAXS profiles of different concentrations of Au^{3+} reveal that the scattering pattern changes a bit and the corresponding size profile shows core sizes ranging from 0.7 to 0.9 nm (0.7, 0.8, and 0.9 nm for 1:2, 1:4, and 1:8 Lyz: Au^{3+} , respectively). Mass spectral study shows that Au_{10-12} cores are possible inside a single molecule of Lyz (see Table S1 for details)

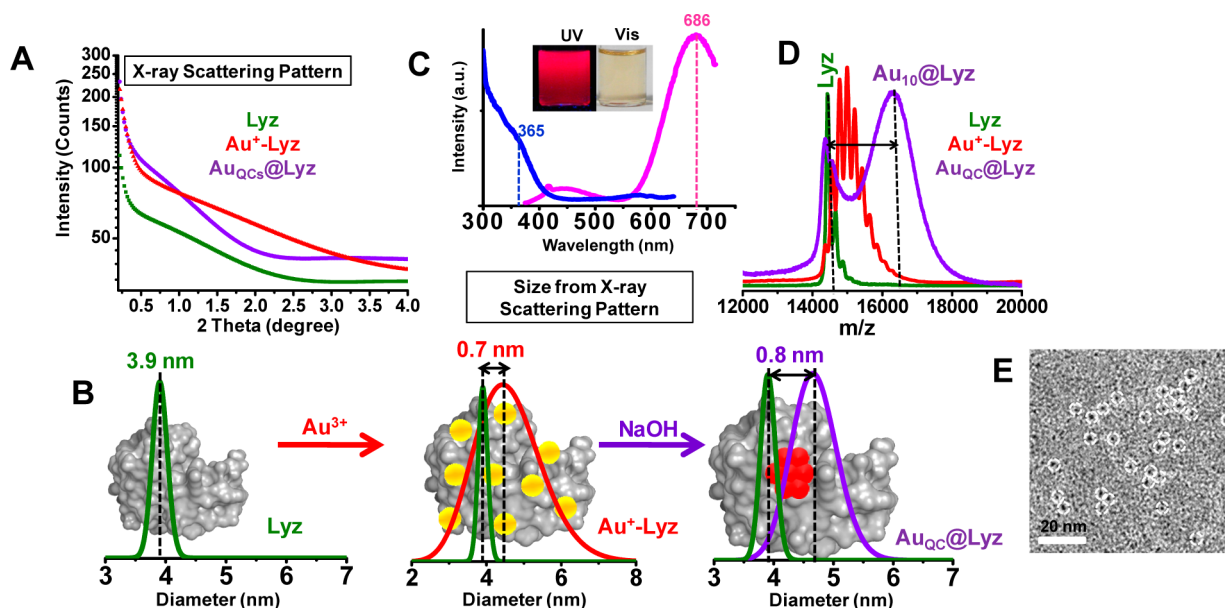


Figure 1. (A) Difference in the SAXS profiles of Lyz, $\text{Au}^+\text{-Lyz}$ adduct and $\text{Au}_{10}\text{@Lyz}$. Size distribution obtained from the SAXS profile is shown in panel B. A 0.8 nm core is observed after cluster formation. The overall state of the protein is schematically represented in the background of each plot. (C) Fluorescence spectra of $\text{Au}_{10}\text{@Lyz}$. In the inset, photographs of $\text{Au}_{10}\text{@Lyz}$ under UV and visible light are shown. (D) Comparative MALDI MS spectra of Lyz, $\text{Au}^+\text{-Lyz}$ and $\text{Au}_{10}\text{@Lyz}$. In the case of $\text{Au}^+\text{-Lyz}$, distinct separation of peaks spaced by m/z 197 due to Au is observed. In $\text{Au}_{10}\text{@Lyz}$, however, a separation of 10 Au atoms from the parent protein peak due to an Au_{10} core is seen. (E) A cluster core of 1 nm was observed in TEM. Some of them are circled.

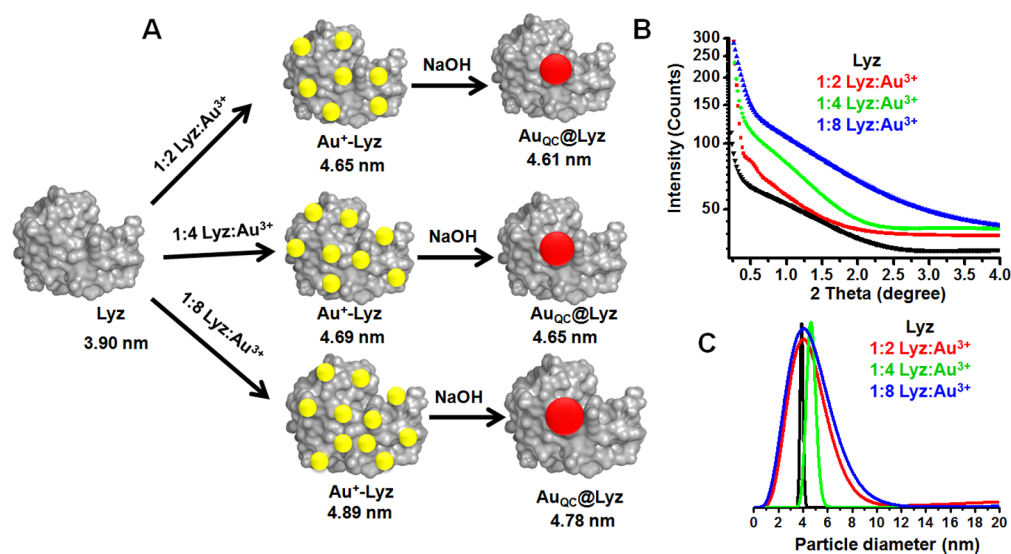


Figure 2. (A) Schematic representation of the concentration-dependent growth of Au⁺–Lyz adduct resulting in Au_{QC}@Lyz. (B) SAXS patterns of Au_{QC}@Lyz samples after 24 h incubation, at various ratios of Lyz:Au³⁺. (C) Size distributions of different Au_{QC}@Lyz samples after 24 h of incubation.

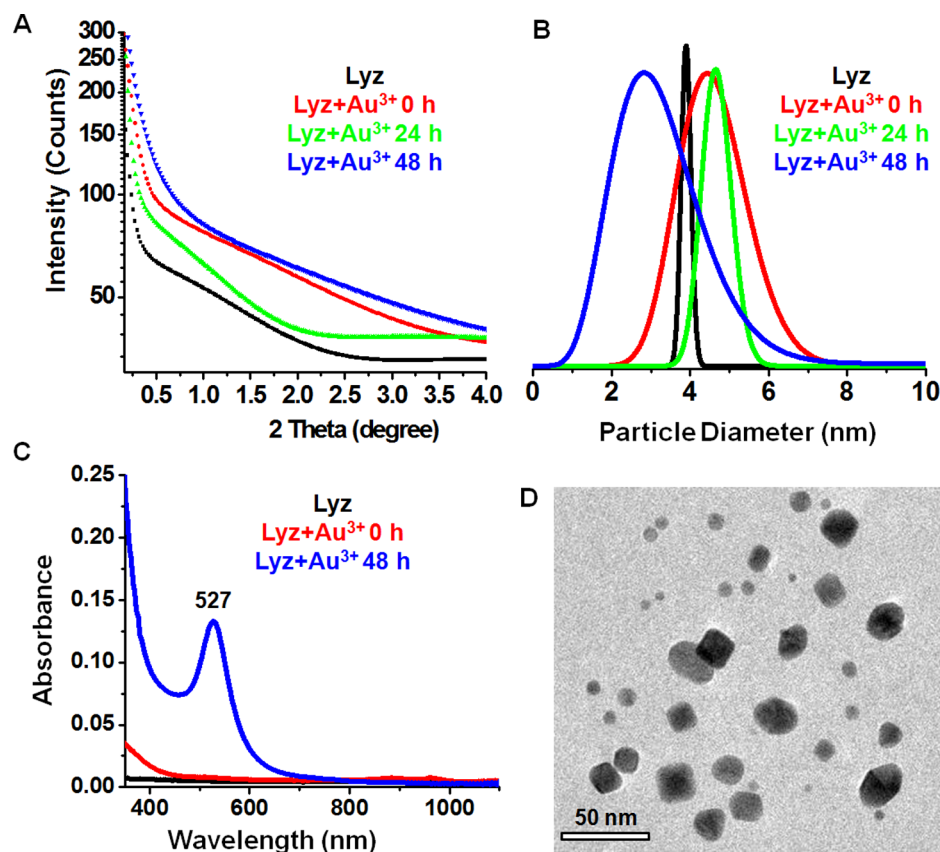


Figure 3. (A) Time-dependent SAXS spectra of Au⁺–Lyz up to 48 h of incubation, when nanoparticles are formed. (B) Corresponding size distribution showing a larger distribution in size, with reduced mean, indicating fragmentation of the protein. (C) UV–vis absorption spectra of Au⁺–Lyz showing a plasmonic feature after 48 h due to nanoparticle formation. (D) TEM image of the Au nanoparticles formed after 48 h of incubation.

in this entire concentration range. These data clearly suggest that it is indeed possible to observe the solution phase growth of the cluster inside a protein, through SAXS.

The change in size was further supported by DLS, which gives the hydrodynamic diameter of the whole particle, including the protein. This study is very much sensitive to concentration (aggregation can happen at higher concentrations), pH and

other factors. All the samples were analyzed at same experimental conditions to avoid errors. Lyz shows a size of 3.2 nm, which increases to 4.2 nm after Au³⁺ addition while Au_{QC}@Lyz has a size of 4.5 nm (see Table 1 and Figure S7). The data are in good agreement with the SAXS result. We have also probed the change in protein during cluster formation through zeta potential measurements. The same sample used for DLS analysis was used for

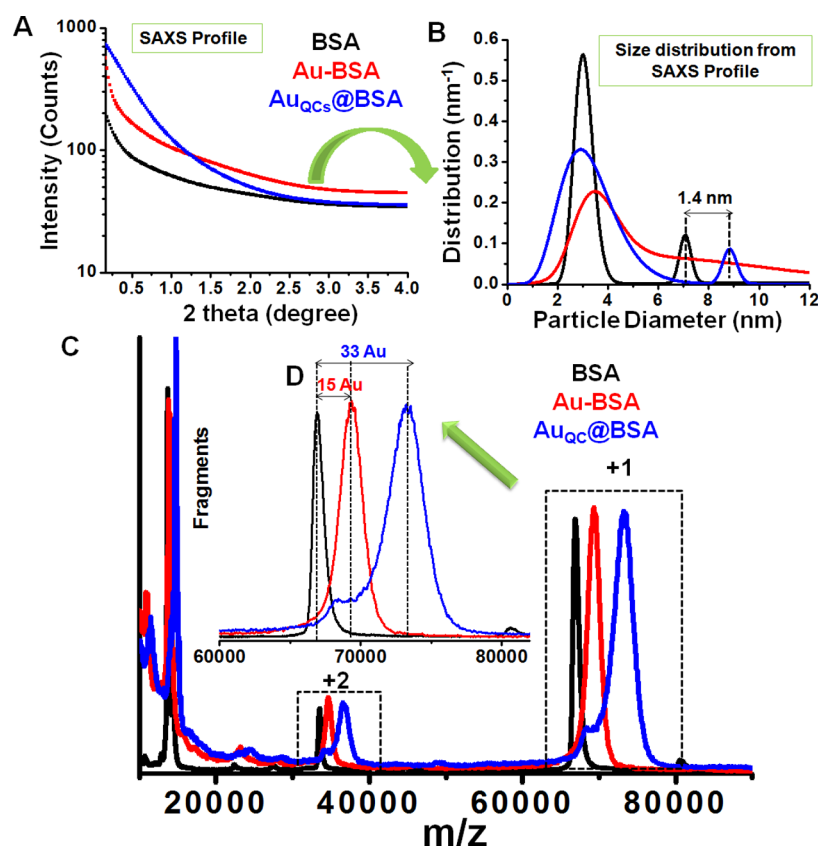


Figure 4. (A) SAXS profile of $\text{Au}_{\text{QCs}}\text{@BSA}$ showing a completely different kind of scattering pattern from the parent BSA as well as $\text{Au}^+\text{-BSA}$. (B) Corresponding size profile showing the presence of about 1.4 nm cluster core. (C) MALDI MS showing the presence of Au_{33} cluster core.

Table 1. Comparative Size (SAXS and DLS) and Zeta Potential for Lyz and Related Systems

sample	size from SAXS (nm)	size from DLS (nm)	zeta potential (mV)
Lyz	3.90	3.20	+12.2
$\text{Au}^+\text{-Lyz}$	4.61	4.20	+39.3
$\text{Au}_{10}\text{@Lyz}$	4.68	4.50	-29.9

zeta potential measurement. Lyz shows a positive zeta potential (+12.2 mV), which increases to +39.3 mV when excess positive charge is introduced in terms of Au^{3+} in the system. When clusters form at basic pH, zeta potential becomes negative (-29.9 mV) (see Table 1).

3.4. Growth of $\text{Au}^+\text{-Lyz}$ Adduct to Nanoparticles. When $\text{Au}^+\text{-Lyz}$ adducts are incubated for longer time (48 h) without changing the pH of the solution, they form Au nanoparticles, distinctly different from luminescent clusters. Formation of nanoparticles is indicated by the appearance of a purple colored solution. Corresponding changes were observed in the SAXS (as well as size) profiles. Size of protein decreases considerably when nanoparticles form (see Figure 3A,B). UV-vis absorption spectra show (Figure 3C) the presence of a plasmonic feature at 527 nm due to the presence of polydispersed Au nanoparticles (Au NPs). The core size of the particles was confirmed by transmission electron microscopic (TEM) analysis. Particles of different shape ranging from 5 to 20 nm in size were observed in TEM. When nanoparticles grow, due to the smaller cavity inside the protein, it cannot accommodate the growing particles within. As a result, nanoparticles come out from the protein cavity causing fragmentation of the protein molecules and

decrease in overall size of the protein. This was supported by increase in the size distribution with reduced mean size (see Table S1 for details).

3.5. Cluster Growth in BSA. To check the validity of SAXS in studying the growth of Au clusters inside proteins in general, we have performed similar experiments with another protein, BSA. It is a widely used serum protein (molecular weight 66.7 kDa) containing 583 amino acids. BSA contains 35 cysteine residues, which form 17 internal disulfide bonds, causing 9 internal loops in the tertiary structure resulting in three primary domains, each containing one small and two large loops. These disulfide bridges are the basis of its compact heart-shaped (equilateral triangle) structure. Two loops are of equal size of 9 nm while the other smaller one is 4 nm.⁴⁴ Considering the three-dimensional orientation of these different lobes, mean size comes around 7.3 nm.

The size distribution profiles of native BSA showed two peaks with the 7.4 nm as the major component (64% population) as shown in Figure 4A,B. Some fragments are observed with 2.7 nm in size in the parent solution itself. These fragments are also seen in MALDI MS, with about 13 kDa mass (see Figure 4C for details). Addition of Au^{3+} facilitates adduct formation; however, this did not show any considerable change in the overall SAXS profile other than an increase in overall size of the protein to 8.3 nm (Figure 5). Addition of NaOH to the as-formed adduct solution drastically changed the overall scattering pattern as well as the size distribution of BSA. After addition of NaOH to the adduct, size of BSA increased to 8.7 nm, which remained almost unchanged (8.8 nm) on further incubation for 24 h (after appearance of red luminescence). So the cluster core size is

about 1.4 nm (size of BSA is 7.4 nm); slightly more than the size observed in TEM reported for this cluster (1.1 nm). After 48 h, the size of BSA in was about 8.9 nm. From a previous study on the time-dependent evolution of BSA protected gold clusters, we know that these clusters grow to bigger cores (Au_{25} to Au_{38} and higher) with time and hence such minute increase in SAXS size is justified.³⁶ The $C(R)$ -distance profiles generated from BSA, Au^+ -BSA adduct, and $\text{Au}_{\text{QC}}@BSA$ have been presented in Figure SSC. The $C(R)$ -distance profile of BSA reveals several interparticle interactions at distances of 3.00, 5.30, 7.67, and 10.10 nm and the corresponding $p(r)$ -distance shows numerous oscillations, characteristic to its multidomain nature. The $C(R)$ pattern of Au^+ -BSA adduct (at pH = 12, at 0 h) is similar to the native BSA solution. Prominent change in the $C(R)$ functions during the growth of $\text{Au}_{\text{QC}}@BSA$ (24–48 h) suggests conformational modifications in the structure of BSA under the reaction conditions. The isoelectric point of BSA is 4.7, and structural change is more likely to happen in this case during cluster formation. BSA also has higher amount of helical structures, which also get affected during cluster formation. This kind of conformational modification through loss in helicity has been reported already for such protein protected clusters.³²

From the mass spectrum of $\text{Au}_{\text{QC}}@BSA$, it is observed that at specific Au^{3+} concentration, Au_{33} core forms inside BSA, and the cluster can be assigned as $\text{Au}_{33}@BSA$. Being a bigger protein, BSA is capable of uptaking more Au inside it. Cluster core size varies linearly with concentration of Au^{3+} used. For higher Au concentration (1:20), 9.2 nm sized BSA was observed. SAXS data show that 0.6 to 1.7 nm Au cluster cores are possible when Au^{3+} concentration is varied from 1:5 to 1:20 ($\text{BSA}:\text{Au}^{3+}$; see Table 2).

After 48 h of incubation of the Au^+ -BSA adducts, nanoparticles form and the size of the protein decreases. The same kind of behavior was also observed for Lyz. Increase in Au concentration increases the amount of Au uptake, which is reflected from the increase in size of BSA. A clear increase in fragmentation can also be observed from MALDI MS data

(see Figure S8). TEM analysis of these nanoparticles shows their polydispersed nature similar to the case of Lyz.

Formation of nanoparticles was further confirmed by UV–vis absorption spectrum showing the 540 nm plasmonic feature. DLS studies shows that the size of BSA (7.4 nm) increases to 8.4 nm when Au^{3+} was introduced in the system (see Figure S9). Incubation of the Au^+ -BSA adduct resulted in nanoparticles after 48 h. Two different prominent peaks were observed when the nanoparticle sample was subjected to DLS. A 5.4 nm peak which corresponds to the fragmented protein and the other peak at 20 nm correspond to Au NPs. Change in protein was further monitored using zeta potential study and a comparison is shown in Table 3.

Table 2. Comparative Size of BSA and Related Systems from SAXS Profile

sample	BSA: Au^{3+}	time of incubation (h)	average particle size from SAXS (nm)
BSA		0	7.45 and 2.73
BSA+NaOH		0	7.08 and 3.06
Au^+ -BSA	1:10	0	8.29 and 3.63
Au^+ -BSA	1:10	24	8.61 and 3.52
Au^+ -BSA (nanoparticle)	1:10	48	6.81 and 2.50
$\text{Au}_{\text{QC}}@BSA$	1:5	0	7.91 and 2.85
$\text{Au}_{\text{QC}}@BSA$	1:5	24	8.04 and 2.69
$\text{Au}_{\text{QC}}@BSA$	1:10	0	8.75 and 3.23
$\text{Au}_{\text{QC}}@BSA$	1:10	24	8.84 and 3.28
$\text{Au}_{\text{QC}}@BSA$	1:10	48	8.87 and 2.47
$\text{Au}_{\text{QC}}@BSA$	1:20	0	9.16 and 3.32

Table 3. Comparative Sizes (SAXS and DLS) and Zeta Potentials for BSA and Related Systems

sample	size from SAXS (nm)	size from DLS (nm)	zeta potential (mV)
BSA	7.30	7.40	-30.3
Au^+ -BSA	8.29	8.40	+18.6
After Au NP formation	6.81	5.40 and 20.30	+32.1
$\text{Au}_{33}@BSA$	8.84	9.00	-39.3

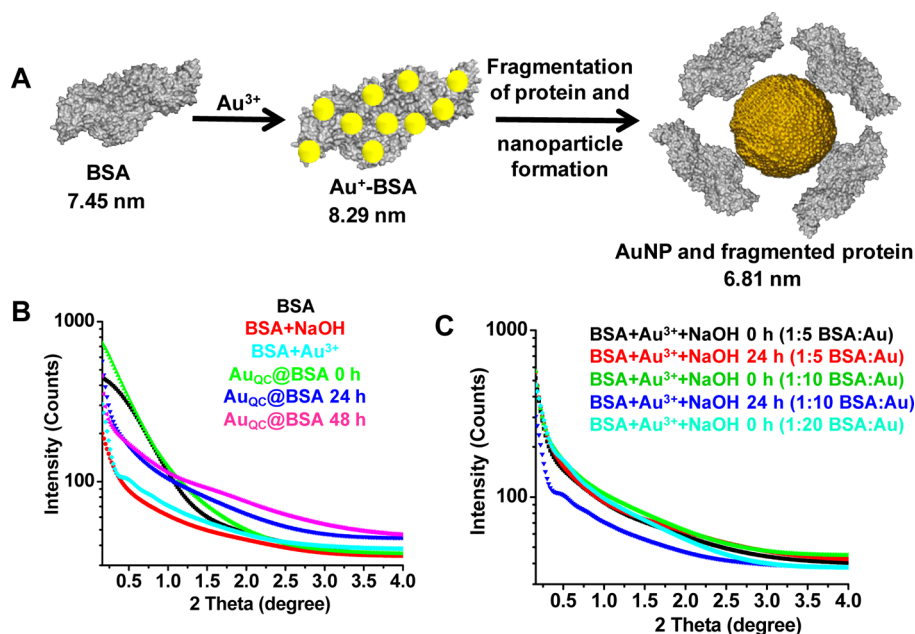


Figure 5. Formation of Au NPs is schematically represented in A along with the corresponding size of BSA. B is showing time dependent SAXS profile of the formation of $\text{Au}_{\text{QC}}@BSA$. Change in SAXS profile due to Au^{3+} concentration is shown in C.

4. SUMMARY AND CONCLUSIONS

In summary, we have presented a detailed SAXS and mass spectrometric study of the formation and growth of luminescent Au clusters inside a small protein, Lyz, for the first time. SAXS data shows the presence of a 0.8 nm core, which is in agreement with the Au₁₀ cluster seen in MALDI MS. Due to the smaller size and availability of less number of cysteine residues, the core size does not change significantly upon further increase in Au³⁺ concentration, which was previously observed to be in the range of Au_{10–12}. Nanoparticle growth can also be monitored using time dependent SAXS along with other microscopic (TEM) and spectroscopic (UV–vis) techniques. We have shown a similar kind of study of cluster growth with a larger protein, BSA. In this case, due to the unsymmetrical structure of the protein, we see an average three-dimensional distribution of the size. The data confirm the presence of Au clusters protected by proteins, in solution.

As of now, none of the protein-protected clusters could be crystallized. There is always a question of whether these clusters form inside a protein cavity or are they an artifact in the MALDI MS. This concern exists as ESI MS is not reported of the same clusters. The present work opens up new possibilities for studying solution phase structure of macromolecule-protected clusters. This study suggests that SAXS can be used to visualize cluster growth in solution regardless of the protein structure. Such studies may be extended to other proteins and several other macromolecules in which cluster growth has been observed.

■ ASSOCIATED CONTENT

● Supporting Information

SAXS profiles and corresponding size of BSA, Lyz and their Au adduct at different time and pH, correlation function and distance distribution function versus distance profiles in Lyz and BSA systems, DLS of BSA and Lyz systems, time-dependent MALDI MS of Au⁺-BSA, table of SAXS parameters of Lyz and Au⁺-Lyz at different conditions, and details of SAXS parameters of Au_{QC}@Lyz at different conditions are shown in the Supporting Information. This material is available free of charge via the Internet at <http://pubs.acs.org>.

■ AUTHOR INFORMATION

Corresponding Authors

*(G.D.) E-mail: gde@cgcri.res.in.

*(T.P.) E-mail: pradeep@iitm.ac.in; Fax: +91-44-2257-0545.

Author Contributions

||Contributed equally.

Notes

The authors declare no competing financial interest.

■ ACKNOWLEDGMENTS

A.B., J.S.M., and T.P. thank the Department of Science and Technology, Government of India for continuous support of our research program on nanomaterials. A.B. and A.M. thank the Council of Scientific and Industrial Research (CSIR) for fellowships. A.B. and J.S.M. thank Swathi R. for help in measuring DLS and zeta potential data. T.P. and H.L. thank an India–Korea research project (Department of Science and Technology, Government of India, in India and National Research Foundation, Korea) for funding.

■ REFERENCES

- (1) Bond, G. C.; Louis, C.; Thompson, D. T., Eds. *Catalysis by Gold*; World Scientific: Singapore, 2006; 384 pp.
- (2) Castleman, A. W. From Elements to Clusters: The Periodic Table Revisited. *J. Phys. Chem. Lett.* **2011**, *2*, 1062–1069.
- (3) Chevrier, D. M.; Chatt, A.; Zhang, P. Properties and Applications of Protein-Stabilized Fluorescent Gold Nanoclusters: Short Review. *J. Nanophoton.* **2012**, *6*, 064504-1–064504-16.
- (4) Feynman, R. There is Plenty of Room at the Bottom. *Caltech Eng. Sci.* **1960**, *23*, 22–36.
- (5) Jena, P. Beyond the Periodic Table of Elements: The Role of Superatoms. *J. Phys. Chem. Lett.* **2013**, *4*, 1432–1442.
- (6) Jin, R. Quantum Sized, Thiolate-protected Gold Nanoclusters. *Nanoscale* **2010**, *2*, 343–362.
- (7) Jena, P.; Castleman, A. W., Jr. *Nanoclusters: A Bridge across Disciplines*; Elsevier Science: Burlington, MA, 2011; Vol. 1.
- (8) Walter, M.; Akola, J.; Lopez-Acevedo, O.; Jadzinsky, P. D.; Calero, G.; Ackerson, C. J.; Whetten, R. L.; Gronbeck, H.; Hakkinen, H. A Unified View of Ligand-Protected Gold Clusters as Superatom Complexes. *Proc. Natl. Acad. Sci. U. S. A.* **2008**, *105*, 9157–9162.
- (9) Wilcoxon, J. P.; Abrams, B. L. Synthesis, Structure and Properties of Metal Nanoclusters. *Chem. Soc. Rev.* **2006**, *35*, 1162–1194.
- (10) Xavier, P. L.; Chaudhari, K.; Baksi, A.; Pradeep, T. Protein-Protected Luminescent Noble Metal Quantum Clusters: An Emerging Trend in Atomic Cluster Nanoscience. *Nano Rev.* **2012**, *3*, 14767 and the references cited therein.
- (11) Alvarez, M. M.; Khoury, J. T.; Schaaff, T. G.; Shafiqullin, M.; Vezmar, I.; Whetten, R. L. Critical Sizes in the Growth of Au Clusters. *Chem. Phys. Lett.* **1997**, *266*, 91–98.
- (12) Antoine, R.; Bertorelle, F.; Broyer, M.; Compagnon, I.; Dugourd, P.; Kulesza, A.; Mitrić, R.; Bonačić-Koutecký, V. Gas-Phase Synthesis and Intense Visible Absorption of Tryptophan–Gold Cations. *Angew. Chem., Int. Ed.* **2009**, *48*, 7829–7832.
- (13) Yoon, B.; Koskinen, P.; Huber, B.; Kostko, O.; von Issendorff, B.; Häkkinen, H.; Moseler, M.; Landman, U. Size-Dependent Structural Evolution and Chemical Reactivity of Gold Clusters. *ChemPhysChem* **2007**, *8*, 157–161 and the references cited therein.
- (14) Qian, H.; Eckenhoff, W. T.; Zhu, Y.; Pintauer, T.; Jin, R. Total Structure Determination of Thiolate-Protected Au₃₈ Nanoparticles. *J. Am. Chem. Soc.* **2010**, *132*, 8280–8281.
- (15) Crasto, D.; Malola, S.; Brosófsky, G.; Dass, A.; Hakkinen, H. Single Crystal XRD Structure and Theoretical Analysis of the Chiral Au₃₀S(S-t-Bu)₁₈ Cluster. *J. Am. Chem. Soc.* **2014**, *136*, 5000–5005.
- (16) Jadzinsky, P. D.; Calero, G.; Ackerson, C. J.; Bushnell, D. A.; Kornberg, R. D. Structure of a Thiol Monolayer-Protected Gold Nanoparticle at 1.1 Å Resolution. *Nanoparticle* **2007**, *318*, 430–433.
- (17) Zeng, C.; Qian, H.; Li, T.; Li, G.; Rosi, N. L.; Yoon, B.; Barnett, R. N.; Whetten, R. L.; Landman, U.; Jin, R. Total Structure and Electronic Properties of the Gold Nanocrystal Au₃₆(SR)₂₄. *Angew. Chem., Int. Ed.* **2012**, *51*, 13114–13118.
- (18) Zhu, M.; Aikens, C. M.; Hollander, F. J.; Schatz, G. C.; Jin, R. Correlating the Crystal Structure of A Thiol-Protected Au₂₅ Cluster and Optical Properties. *J. Am. Chem. Soc.* **2008**, *130*, 5883–5885.
- (19) Yang, H.; Wang, Y.; Huang, H.; Gell, L.; Lehtovaara, L.; Malola, S.; Häkkinen, H.; Zheng, N. All-Thiol-Stabilized Ag₄₄ and Au₁₂Ag₃₂ Nanoparticles with Single-Crystal Structures. *Nat. Commun.* **2013**, *4*.
- (20) Mathew, A.; Pradeep, T. Noble Metal Clusters: Applications in Energy, Environment, and Biology. *Part. Part. Syst. Charact.* **2014**, n/a–n/a.
- (21) Pradeep, T.; Baksi, A.; Xavier, P. L. Noble Metal Clusters in Protein Templates. In *Functional Nanometer-Sized Clusters of Transition Metals: Synthesis, Properties and Applications*; The Royal Society of Chemistry: London, 2014; Chapter 7, pp 169–225.
- (22) Petty, J. T.; Zheng, J.; Hud, N. V.; Dickson, R. M. DNA-Templated Ag Nanocluster Formation. *J. Am. Chem. Soc.* **2004**, *126*, 5207.
- (23) Zheng, J.; Nicovich, P. R.; Dickson, R. M. Highly Fluorescent Noble-Metal Quantum Dots. *Annu. Rev. Phys. Chem.* **2007**, *58*, 409–431.

- (24) Baksi, A.; Xavier, P. L.; Chaudhari, K.; Goswami, N.; Pal, S. K.; Pradeep, T. Protein-Encapsulated Gold Cluster Aggregates: The Case of Lysozyme. *Nanoscale* **2013**, *5*, 2009–2016.
- (25) Kawasaki, H.; Hamaguchi, K.; Osaka, I.; Arakawa, R. pH-Dependent Synthesis of Pepsin-Mediated Gold Nanoclusters with Blue Green and Red Fluorescent Emission. *Adv. Funct. Mater.* **2011**, *21*, 3508–3515.
- (26) Kawasaki, H.; Yoshimura, K.; Hamaguchi, K.; Arakawa, R. Trypsin-Stabilized Fluorescent Gold Nanocluster for Sensitive and Selective Hg^{2+} Detection. *Anal. Sci.* **2011**, *27*, S91–S91.
- (27) Le, G. X.; Hotzer, B.; Jung, G.; Hollemeyer, K.; Trouillet, V.; Schneider, M. Formation of Fluorescent Metal (Au, Ag) Nanoclusters Capped in Bovine Serum Albumin Followed by Fluorescence and Spectroscopy. *J. Phys. Chem. C* **2011**, *115*, 10955.
- (28) Li, H.-W.; Ai, K.; Wu, Y. Fluorescence Visual Gel-separation of Dansylated BSA-Protected Gold-Nanoclusters. *Chem. Commun.* **2011**, *47*, 9852–9854.
- (29) Li, M.; Yang, D.-P.; Wang, X.; Lu, J.; Cui, D. Mixed Protein-Templated Luminescent Metal Clusters (Au and Pt) for H_2O_2 Sensing. *Nanoscale Res. Lett.* **2013**, *8*, 182.
- (30) Liu, C.-L.; Wu, H.-T.; Hsiao, Y.-H.; Lai, C.-W.; Shih, C.-W.; Peng, Y.-K.; Tang, K.-C.; Chang, H.-W.; Chien, Y.-C.; Hsiao, et al. Insulin-Directed Synthesis of Fluorescent Gold Nanoclusters: Preservation of Insulin Bioactivity and Versatility in Cell Imaging. *Angew. Chem., Int. Ed.* **2011**, *50*, 7056–7060.
- (31) Liu, H.-Y.; Zhang, X.; Wu, X.-M.; Jiang, L.-P.; Burda, C.; Zhu, J.-J. Rapid Sonochemical Synthesis of Highly Luminescent Non-oxic AuNCs and Au@AgNCs and Cu (II) Sensing. *Chem. Commun.* **2011**, *47*, 4237.
- (32) Mohanty, J. S.; Xavier, P. L.; Chaudhari, K.; Bootharaju, M. S.; Goswami, N.; Pal, S. K.; Pradeep, T. Luminescent, Bimetallic AuAg Alloy Quantum Clusters in Protein Templates. *Nanoscale* **2012**, *4*, 4255–4262.
- (33) Wei, H.; Wang, Z.; Yang, L.; Tian, S.; Hou, C.; Lu, Y. Lysozyme-Stabilized Gold Fluorescent Cluster: Synthesis and Application as Hg^{2+} Sensor. *Analyst* **2010**, *135*, 1406–1410.
- (34) Xie, J.; Zheng, Y.; Ying, J. Y. Protein-Directed Synthesis of Highly Fluorescent Gold Nanoclusters. *J. Am. Chem. Soc.* **2009**, *131*, 888–889.
- (35) Yan, L.; Cai, Y.; Zheng, B.; Yuan, H.; Guo, Y.; Xiao, D.; Choi, M. F. Microwave-Assisted Synthesis of BSA-Stabilized and HSA-Protected Gold Nanoclusters with Red Emission. *J. Mater. Chem.* **2012**, *22*, 1000–1005.
- (36) Chaudhari, K.; Xavier, P. L.; Pradeep, T. Understanding the Evolution of Luminescent Gold Quantum Clusters in Protein Templates. *ACS Nano* **2011**, *5*, 8816–8827.
- (37) Xavier, P. L.; Chaudhari, K.; Verma, P. K.; Pal, S. K.; Pradeep, T. Luminescent Quantum Clusters of Gold in Transferrin Family Protein, Lactoferrin Exhibiting FRET. *Nanoscale* **2010**, *2*, 2769–2776.
- (38) Habeeb Muhammed, M. A.; Verma, P. K.; Pal, S. K.; Retnakumari, A.; Koyakutty, M.; Nair, S.; Pradeep, T. Luminescent Quantum Clusters of Gold in Bulk by Albumin-Induced Core Etching of Nanoparticles: Metal Ion Sensing, Metal-Enhanced Luminescence, and Biolabeling. *Chem.—Eur. J.* **2010**, *16*, 10103–10112.
- (39) Anand, U.; Ghosh, S.; Mukherjee, S. Toggling Between Blue- and Red-Emitting Fluorescent Silver Nanoclusters. *J. Phys. Chem. Lett.* **2012**, *3*, 3605–3609.
- (40) Chan, P.-H.; Chen, Y.-C. Human Serum Albumin Stabilized Gold Nanoclusters as Selective Luminescent Probes for *Staphylococcus aureus* and Methicillin-Resistant *Staphylococcus aureus*. *Anal. Chem.* **2012**, *84*, 8952–8956.
- (41) Chen, Y.; Wang, Y.; Wang, C.; Li, W.; Zhou, H.; Jiao, H.; Lin, Q.; Yu, C. Papain-Directed Synthesis of Luminescent Gold Nanoclusters and the Sensitive Detection of Cu^{2+} . *J. Colloid Interface Sci.* **2013**, *396*, 63–68.
- (42) Liu, Y.; Ai, K.; Cheng, X.; Huo, L.; Lu, L. Gold-Nanocluster-Based Fluorescent Sensors for Highly Sensitive and Selective Detection of Cyanide in Water. *Adv. Funct. Mater.* **2010**, *20*, 951–956.
- (43) Xie, J.; Zheng, Y.; Ying, J. Y. Highly Selective and Ultrasensitive Detection of Hg^{2+} Based on Fluorescence Quenching of Au Nanoclusters by Hg^{2+} -Au⁺ Interactions. *Chem. Commun.* **2010**, *46*, 961–963.
- (44) Bujacz, A. Structures of Bovine, Equine and Leporine Serum Albumin. *Acta Crystallogr.* **2012**, *68*, 1278–1289.
- (45) Diamond, R. Real-Space Refinement of the Structure of Hen Egg-White Lysozyme. *J. Mol. Biol.* **1974**, *82*, 371–391.
- (46) Mathew, A.; Sajanlal, P. R.; Pradeep, T. A Fifteen Atom Silver Cluster Confined in Bovine Serum Albumin. *J. Mater. Chem.* **2010**, *21*, 11205–11212.
- (47) Baksi, A.; Pradeep, T. Noble Metal Alloy Clusters in the Gas Phase Derived from Protein Templates: Unusual Recognition of Palladium by Gold. *Nanoscale* **2013**, *5*, 12245–12254.
- (48) Stradner, A.; Sedgwick, H.; Cardinaux, F.; Poon, W. C. K.; Egelhaaf, S. U.; Schurtenberger, P. Equilibrium Cluster Formation in Concentrated Protein Solutions and Colloids. *Nature* **2004**, *432*, 492–495.
- (49) Zhang, F.; Skoda, M. W. A.; Jacobs, R. M. J.; Martin, R. A.; Martin, C. M.; Schreiber, F. Protein Interactions Studied by SAXS: Effect of Ionic Strength and Protein Concentration for BSA in Aqueous Solutions. *J. Phys. Chem. B* **2007**, *111*, 251–259.
- (50) Mata, J. P.; Udabage, P.; Gilbert, E. P. Structure of Casein Micelles in Milk Protein Concentrate Powders via Small Angle X-ray Scattering. *Soft Matter* **2011**, *7*, 3837–3843.
- (51) Mertens, H. D. T.; Svergun, D. I. Structural Characterization of Proteins and Complexes Using Small-Angle X-ray Solution Scattering. *J. Struct. Biol.* **2010**, *172*, 128–141.
- (52) Blanchet, C. E.; Svergun, D. I. Small-Angle X-ray Scattering on Biological Macromolecules and Nanocomposites in Solution. *Annu. Rev. Phys. Chem.* **2013**, *64*, 37–54.
- (53) Lipfert, J.; Doniach, S. Small-Angle X-ray Scattering from RNA, Proteins, and Protein Complexes. *Annu. Rev. Biophys. Biomol. Struct.* **2007**, *36*, 307–327.
- (54) Chi, C.; Vargas-Lara, F.; Tkachenko, A. V.; Starr, F. W.; Gang, O. Internal Structure of Nanoparticle Dimers Linked by DNA. *ACS Nano* **2012**, *6*, 6793–6802.
- (55) Vial, S.; Nykypanchuk, D.; Yager, K. G.; Tkachenko, A. V.; Gang, O. Linear Mesosstructures in DNA-Nanorod Self-Assembly. *ACS Nano* **2013**, *7*, 5437–5445.
- (56) Chakraborty, I.; Govindarajan, A.; Erusappan, J.; Ghosh, A.; Pradeep, T.; Yoon, B.; Whetten, R. L.; Landman, U. The Superstable 25 kDa Monolayer Protected Silver Nanoparticle: Measurements and Interpretation as an Icosahedral $Ag_{152}(SCH_2CH_2Ph)_60$ Cluster. *Nano Lett.* **2012**, *12*, 5861–5866.
- (57) Polte, J.; Erler, R.; Thuenemann, A. F.; Sokolov, S.; Ahner, T. T.; Rademann, K.; Emmerling, F.; Kraehnert, R. Nucleation and Growth of Gold Nanoparticles Studied via in Situ Small Angle X-ray Scattering at Millisecond Time Resolution. *ACS Nano* **2010**, *4*, 1076–1082.
- (58) Auyeung, E.; Cutler, J. I.; MacFarlane, R. J.; Jones, M. R.; Wu, J.; Liu, G.; Zhang, K.; Osberg, K. D.; Mirkin, C. A. Synthetically Programmable Nanoparticle Superlattices Using a Hollow Three-Dimensional Spacer Approach. *Nat. Nanotechnol.* **2012**, *7*, 24–28.
- (59) Hamon, C.; Postic, M.; Mazari, E.; Bizien, T.; Dupuis, C.; Even-Hernandez, P.; Jimenez, A.; Courbin, L.; Gosse, C.; Artzner, F.; et al. Three-Dimensional Self-Assembling of Gold Nanorods with Controlled Macroscopic Shape and Local Smectic B Order. *ACS Nano* **2012**, *6*, 4137–4146.
- (60) Polte, J.; Tuae, X.; Wuthschick, M.; Fischer, A.; Thuenemann, A. F.; Rademann, K.; Kraehnert, R.; Emmerling, F. Formation Mechanism of Colloidal Silver Nanoparticles: Analogies and Differences to the Growth of Gold Nanoparticles. *ACS Nano* **2012**, *6*, 5791–5802.
- (61) Kewalramani, S.; Zwanikken, J. W.; Macfarlane, R. J.; Leung, C.-Y.; Olvera de la Cruz, M.; Mirkin, C. A.; Bedzyk, M. J. Counterion Distribution Surrounding Spherical Nucleic Acid–Au Nanoparticle Conjugates Probed by Small-Angle X-ray Scattering. *ACS Nano* **2013**, *7*, 11301–11309.
- (62) Zhang, Y.; Lu, F.; Yager, K. G.; van der Lelie, D.; Gang, O. A General Strategy for the DNA-Mediated Self-assembly of Functional Nanoparticles into Heterogeneous Systems. *Nat. Nanotechnol.* **2013**, *8*, 865–872.
- (63) Terrill, R. H.; Postlethwaite, T. A.; Chen, C.-h.; Poon, C.-D.; Terzis, A.; Chen, A.; Hutchison, J. E.; Clark, M. R.; Wignall, G.; et al.

Monolayers in Three Dimensions: NMR, SAXS, Thermal, and Electron Hopping Studies of Alkanethiol Stabilized Gold Clusters. *J. Am. Chem. Soc.* **1995**, *117*, 12537–48.

(64) Azubel, M.; Koivisto, J.; Malola, S.; Bushnell, D.; Hura, G. L.; Koh, A. L.; Tsunoyama, H.; Tsukuda, T.; Pettersson, M.; Haekkinen, H.; et al. Electron Microscopy of Gold Nanoparticles at Atomic Resolution. *Science* **2014**, *345*, 909–912.

(65) Baksi, A.; Pradeep, T.; Yoon, B.; Yannouleas, C.; Landman, U. Bare Clusters Derived from Protein Templates: Au_{25}^+ , Au_{38}^+ and Au_{102}^+ . *ChemPhysChem* **2013**, *14*, 1272–1282 and the references cited therein.

(66) Manet, S.; Lecchi, A.; Imperor-Clerc, M.; Zholobenko, V.; Durand, D.; Oliveira, C. L. P.; Pedersen, J. S.; Grillo, I.; Meneau, F.; Rochas, C. Structure of Micelles of a Nonionic Block Copolymer Determined by SANS and SAXS. *J. Phys. Chem. B* **2011**, *115*, 11318–11329.

Supporting Information

Size Evolution of Protein Protected Gold Clusters in Solution: A Combined SAXS-MS Investigation

Ananya Baksi^{1†}, Anuradha Mitra^{2†}, Jyoti Sarita Mohanty¹, Haiwon Lee³, Goutam De^{2*} and T. Pradeep^{1*}

¹DST Unit of Nanoscience (DST UNS) and Thematic Unit of Excellence, Department of Chemistry, Indian Institute of Technology Madras, Chennai - 600 036, India.

²Nano-Structured Materials Division, CSIR-Central Glass and Ceramic Research Institute, 196 Raja S. C. Mullick Road, Kolkata-700032, India.

³Department of Chemistry, Institute of Nanoscience and Technology, Hanyang University, Seoul- 133-791, Korea.

† Contributed equally

Content

S/N	Description	Page Number
S1	<i>SAXS and size profiles of freshly prepared aqueous (A) Lyz and (B) BSA solutions using cylinder and sphere models</i>	2
S2	<i>Time dependent SAXS and size profile of Lyz</i>	3
S3	<i>Time dependent SAXS and size profile of Lyz at pH 12</i>	4
S4	<i>Time dependent SAXS and size profile of Au⁺-Lyz</i>	5
S5	<i>Correlation function and distance distribution function versus distance profiles in (A) Lyz and (B) BSA systems</i>	6
S6	<i>Time and concentration dependent SAXS and size profile of Au_{QC}@Lyz</i>	7
S7	<i>DLS of Lyz and related system</i>	7
S8	<i>Time dependent MALDI MS of Au⁺-BSA</i>	8
S9	<i>DLS of BSA and related system</i>	9
S10	<i>Table of SAXS parameters of Lyz and Au⁺-Lyz at different conditions</i>	10
S11	<i>Details of SAXS parameters of Au_{QC}@Lyz at different conditions.</i>	11

Supporting Information 1

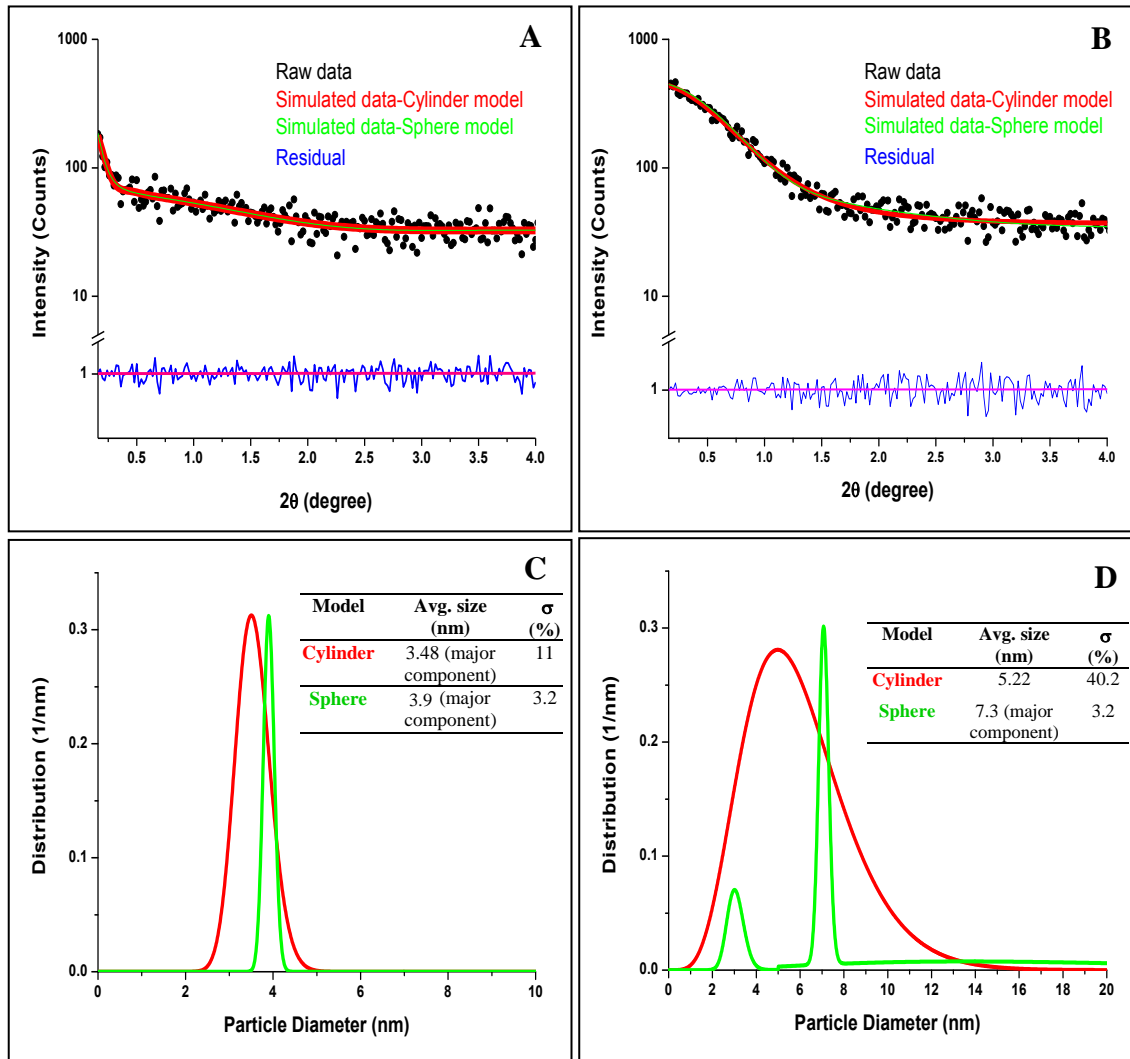


Figure S1: SAXS profiles of freshly prepared aqueous (A) Lyz and (B) BSA solutions evaluated using cylinder and sphere models (same residual factors) are shown for comparison. The corresponding size distribution profiles of (C) Lyz and (D) BSA proteins using the above two models. The average sizes of the proteins are tabulated in the insets of C and D; σ represents normalized dispersion.

Supporting Information 2

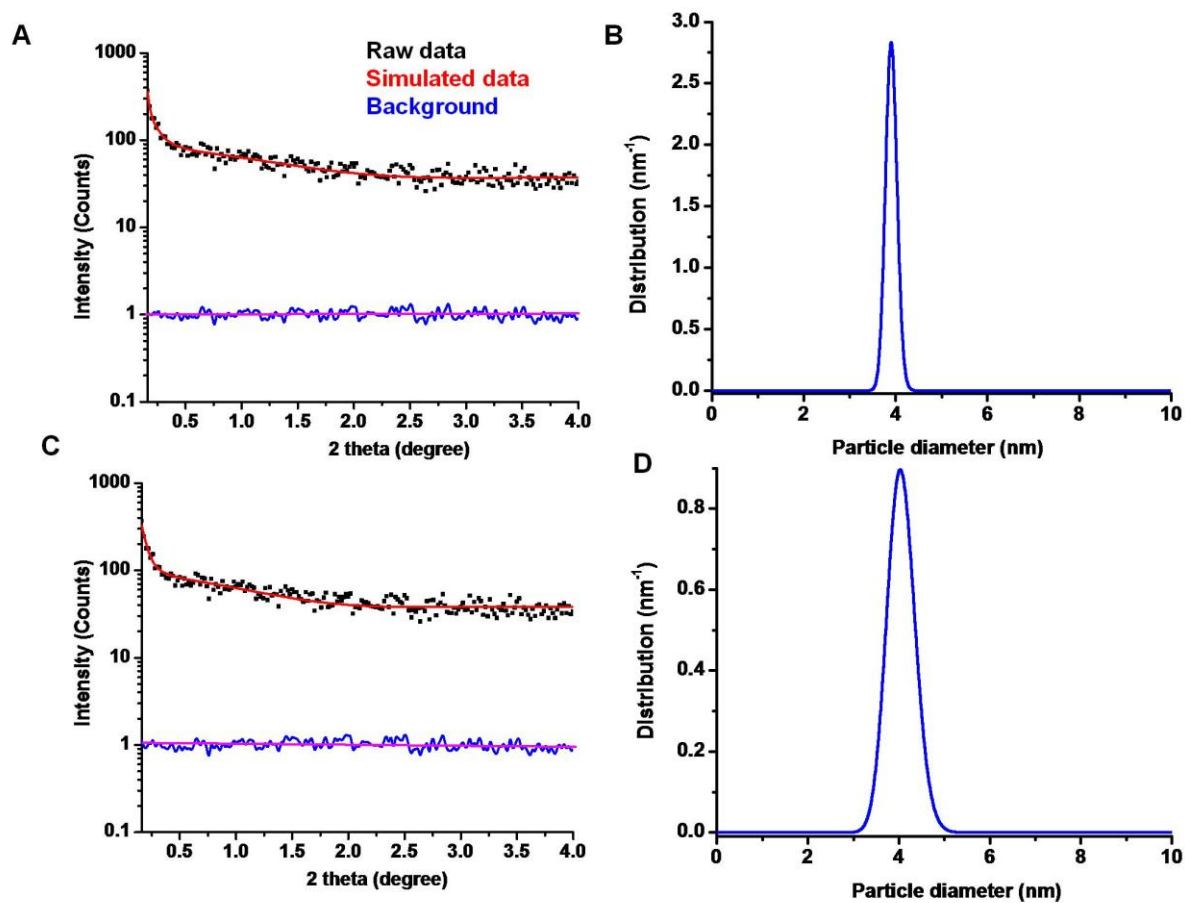


Figure S2: A) SAXS profile of Lyz in water, corresponding size profile is shown in B. C) SAXS profile of Lyz in water after one day, corresponding size profile is shown in D.

Supporting Information 3

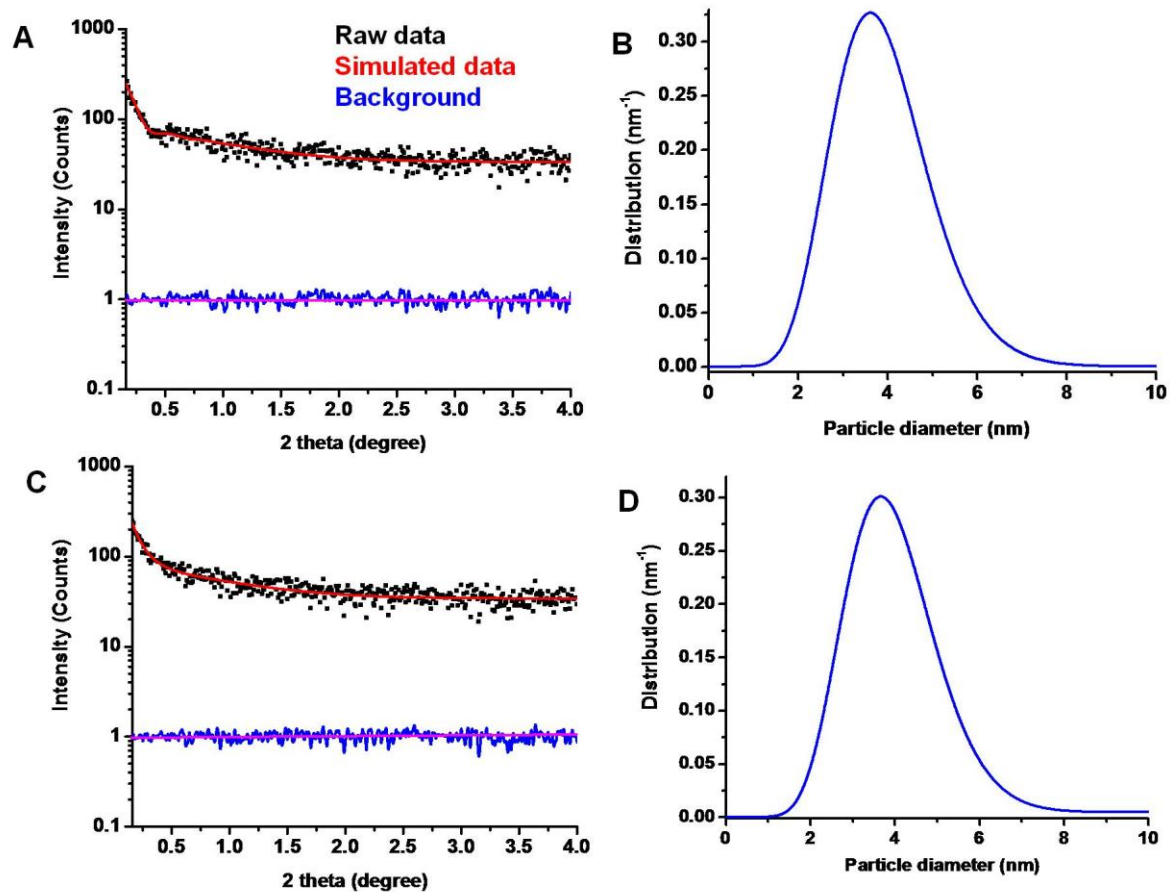


Figure S3: A) SAXS profile of Lyz in presence of NaOH at pH 12, corresponding size profile is shown in B. C) SAXS profile of Lyz in presence of NaOH at pH 12 after one day, corresponding size profile is shown in D.

Supporting Information 4

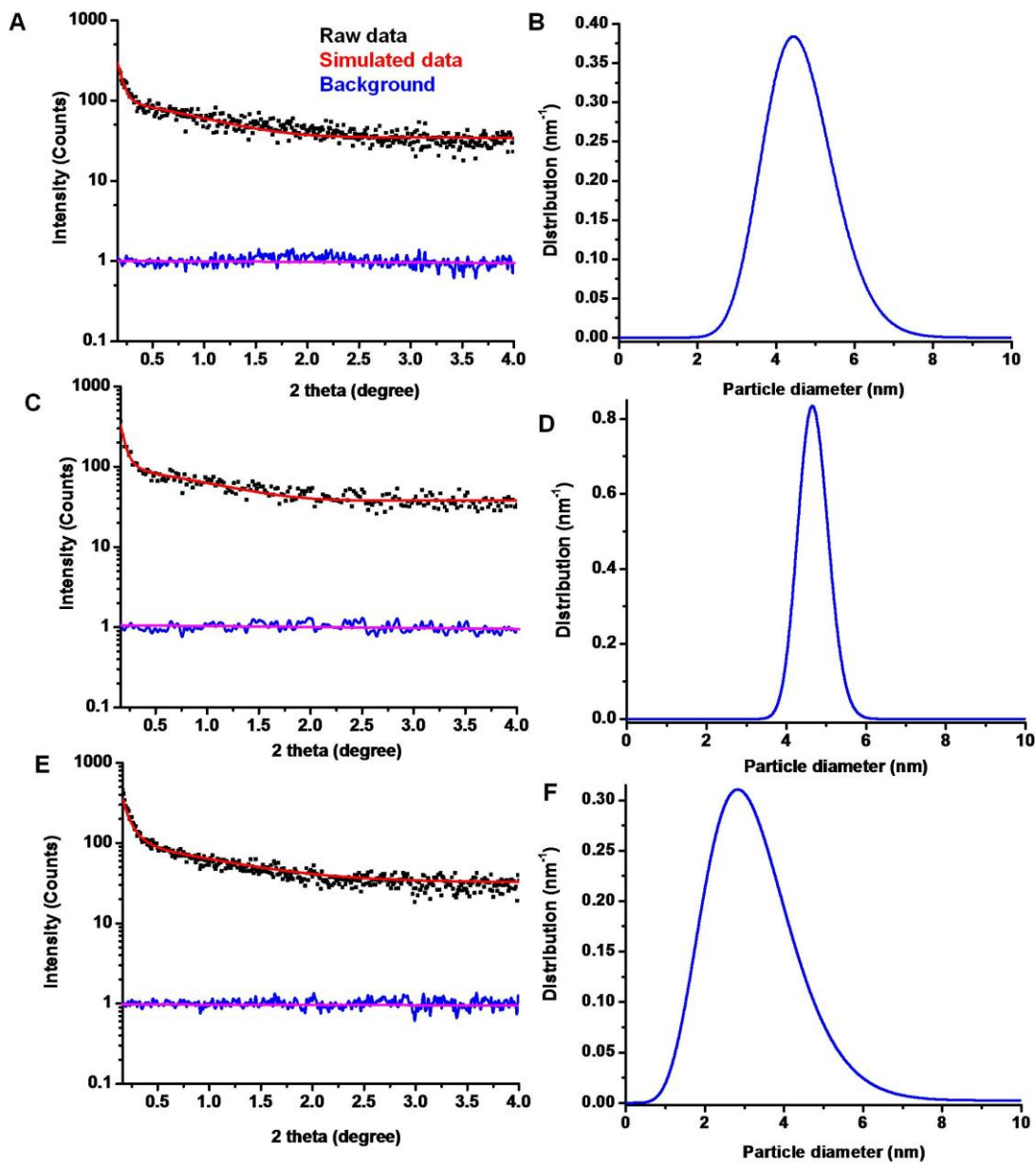


Figure S4: A) SAXS profile of Au⁺-Lyz, corresponding size profile is shown in B. C) SAXS profile of Au⁺-Lyz after 24 h, corresponding size profile is shown in D. After 48 hours of incubation, nanoparticles form. The SAXS profile is shown in E and the corresponding size profile in F is showing overall decrease in protein size after nanoparticle formation.

Supporting Information 5

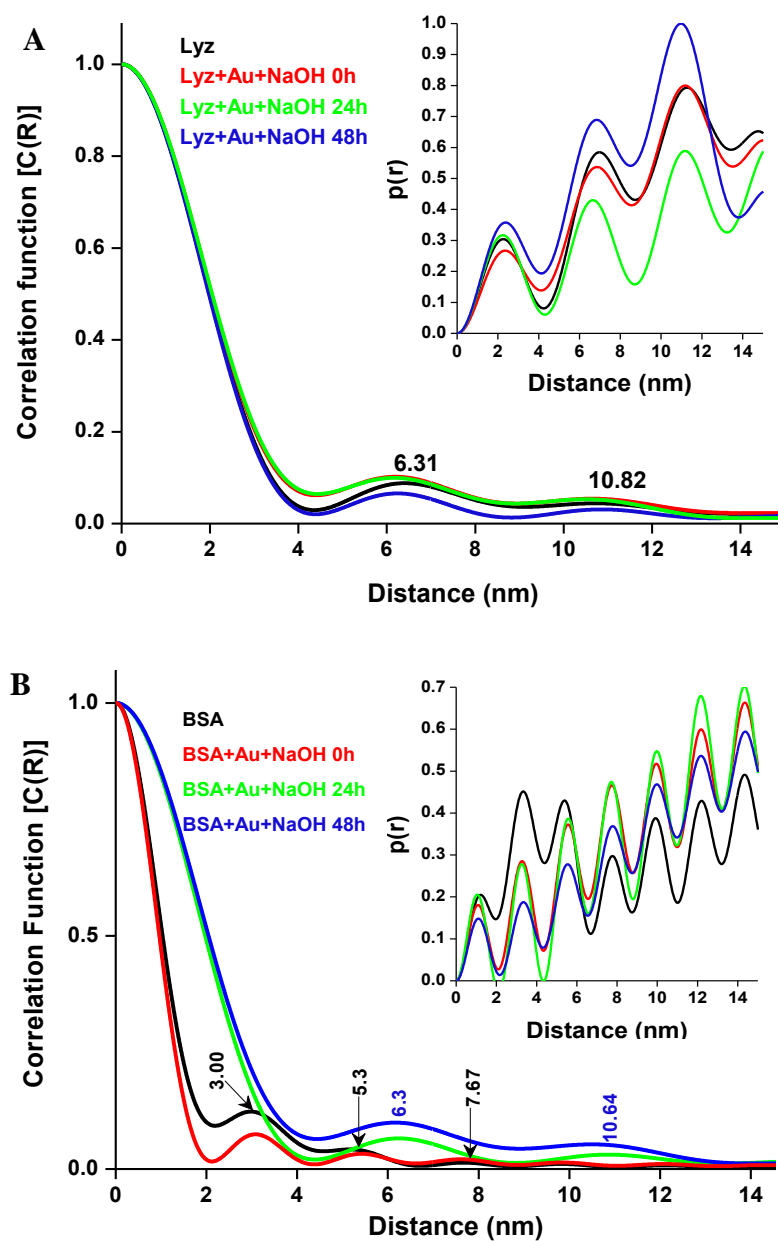


Figure S5. The effect of cluster formation and growth on short range inter-particle interactions in (A) Lyz and (B) BSA systems expressed as correlation function. The corresponding distance distribution functions are presented in the insets.

Supporting Information 6

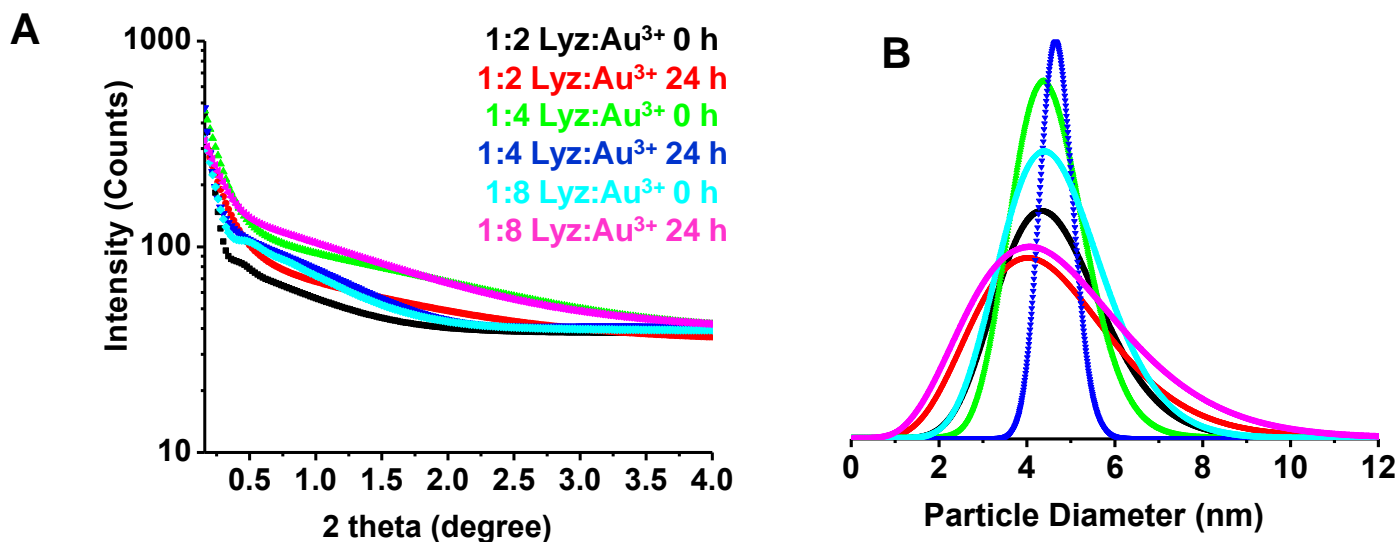


Figure S6: A) Time and concentration dependent SAXS profile of Au_{QC}@Lyz and the corresponding size profile is shown in B.

Supporting Information 7

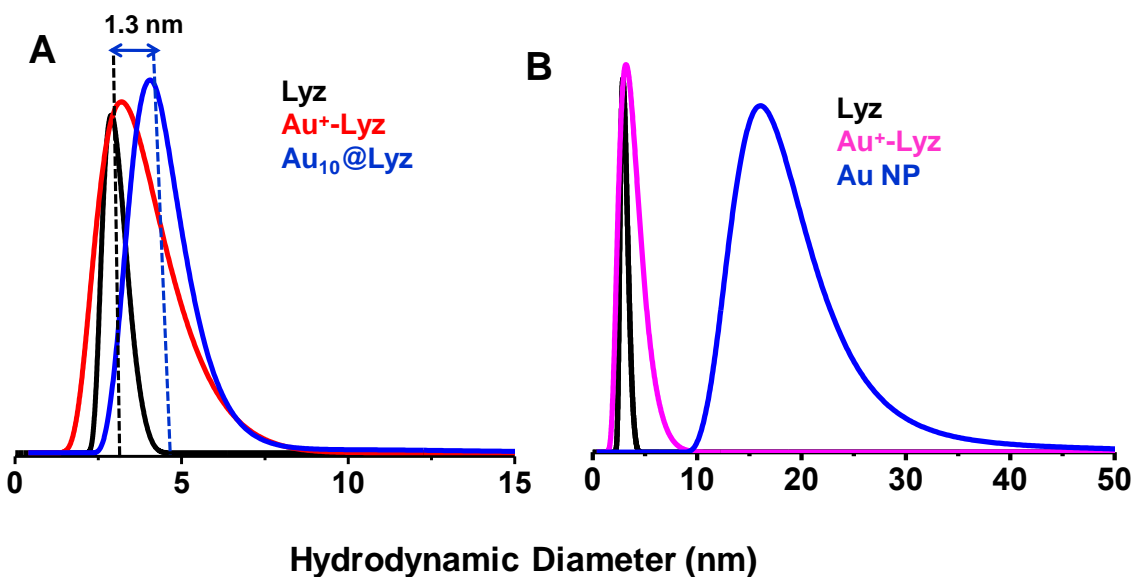


Figure S7: A) DLS data of Lyz, Au⁺-Lyz adduct and Au₁₀@Lyz showing presence of 1.3 nm cluster core. B) Time dependent growth of Au⁺-Lyz adduct lead to nanoparticle formation and the corresponding size of nanoparticle was observed by DLS study.

Supporting Information 8

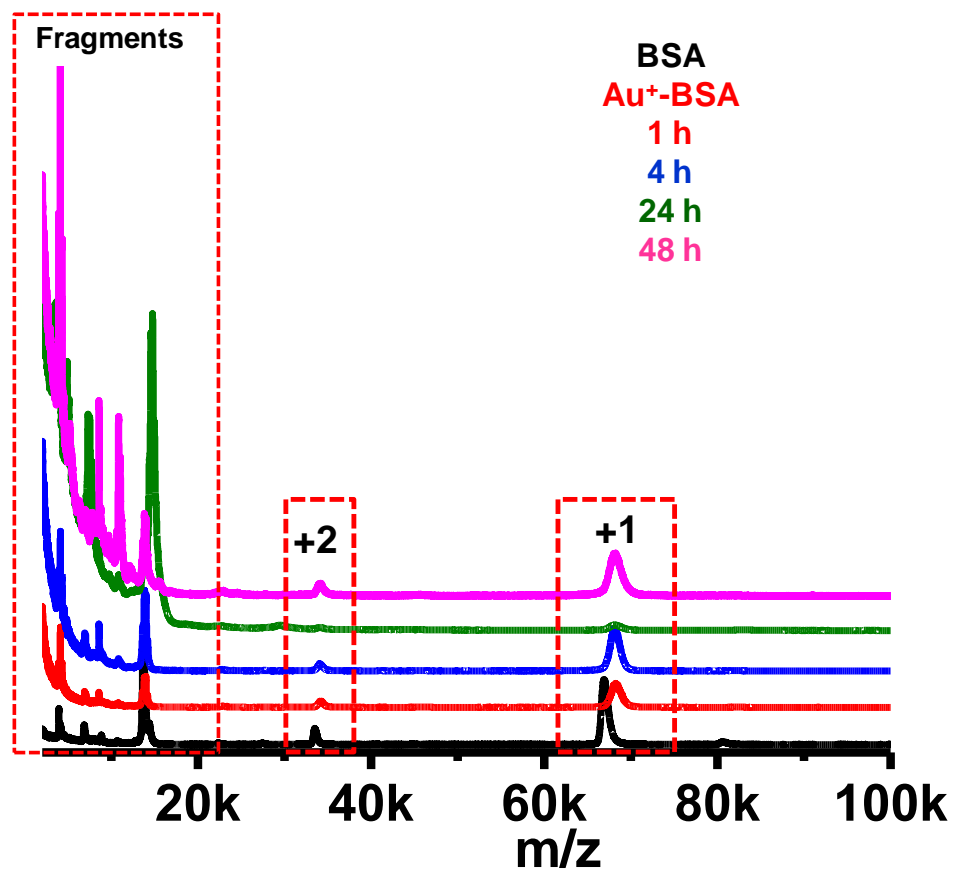


Figure S8: Time dependent MALDI MS of Au⁺-Lyz showing increase in fragmentations at lower mass region (<m/z 20k).

Supporting Information 9

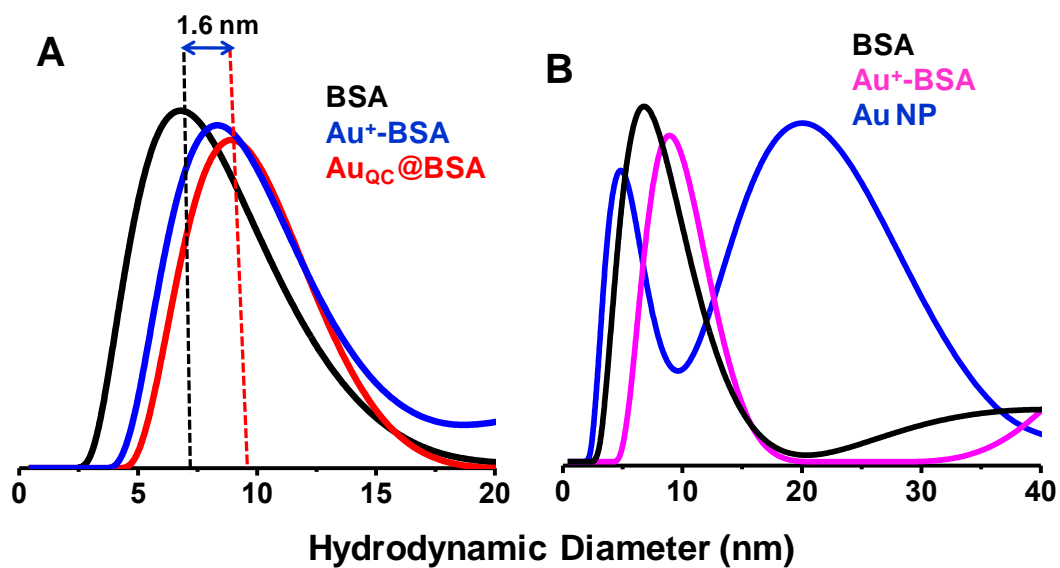


Figure S9: A) DLS data of BSA, Au⁺-BSA adduct and Au₁₀@BSA showing presence of 1.3 nm cluster core. B) Time dependent growth of Au⁺-BSA adduct leads to nanoparticle formation and the corresponding size of nanoparticle was observed by DLS study. After nanoparticle formation, the size of the protein decreases.

Supporting Information 10

Table S1: Details of SAXS parameters of Lyz and Au⁺-Lyz at different conditions.

	Sample	Particle Size (nm)	Normalized Distribution (%)	Volume (%)	R Factor (%)
1	Lyz (0 h)	03.9 37.1	03.2 31.4	88.86 11.14	4.54
2	Lyz (24 h)	04.0 62.8	07.3 20.9	68.12 31.88	3.82
3	Lyz+NaOH (0 h)	03.9 28.5	27.9 03.2	86.52 13.48	4.14
4	Lyz+NaOH (24 h)	04.0 26.9	27.4 61.1	78.85 21.15	4.54
5	Lyz+Au ³⁺ (0 h)	04.6 37.9	19.3 23.7	84.34 15.66	6.25
6	Lyz+Au ³⁺ (24 h)	04.7 42.2	08.1 28.1	79.10 21.90	3.99
7	Lyz+Au ³⁺ (48 h) Nanoparticles	03.3 39.8	35.2 69.3	83.57 16.43	4.19
8	Lyz+Au ³⁺ (high concentration) (0 h)	04.7 30.3	25.0 03.2	88.07 18.93	3.84

Supporting Information 11

Table S2: Details of SAXS parameters of Au_{QC}@Lyz at different conditions.

	Sample	Particle Size (nm)	Normalized Distribution (%)	Volume (%)	R Factor (%)
1	Lyz+Au ³⁺ + NaOH (0 h) (1:4 Lyz: Au ³⁺)	04.5 34.8	18.7 30.5	78.87 21.13	4.00
2	Lyz+Au ³⁺ + NaOH (24 h) (1:4 Lyz: Au ³⁺)	04.7 42.2	08.1 28.1	79.04 20.96	3.99
3	Lyz+Au ³⁺ + NaOH (48 h) (1:4 Lyz: Au ³⁺)	04.7 33.0	31.3 43.7	81.57 18.43	4.18
4	Lyz+Au ³⁺ + NaOH (0 h) (1:2 Lyz: Au ³⁺)	04.6 34.2	26.0 12.7	70.63 29.37	4.11
5	Lyz+Au ³⁺ + NaOH (24 h) (1:2 Lyz: Au ³⁺)	04.6 34.0	35.4 38.2	73.43 26.57	4.59
6	Lyz+Au ³⁺ + NaOH (0 h) (1:8 Lyz: Au ³⁺)	04.9 36.6	31.1 27.5	81.59 18.47	4.14
7	Lyz+Au ³⁺ + NaOH (24 hr) (1:8 Lyz: Au ³⁺)	04.8 32.4	39.7 23.1	88.36 11.64	4.02

Advancing the Use of Sustainability Metrics

Now in its third year, ACS Sustainable Chemistry and Engineering (ACS SCE) continues to receive high-quality manuscripts in the areas of green chemistry, green engineering, and the grand challenges for sustainability in chemistry and chemical engineering. This includes the development and demonstration of renewable feedstocks, fuels, and materials that are less toxic and more sustainable than their functional equivalents. It also includes the development and demonstration of alternative processes and products that are more resource-efficient (in terms of conserving energy and feedstock) and more sustainable compared to conventional chemical processes and products.

In presenting their findings, ACS SCE authors generally justify the contributions of their work to the sustainability of the chemical enterprise by qualitatively invoking the principles of green chemistry¹ and green engineering² or other principles of sustainability.³ This approach is encouraged and acceptable. Ultimately, however, such qualitative approaches will be complemented by rigorous, semiquantitative and quantitative sustainability assessments. These may include life cycle analyses, toxicity assessments, or other indicators of sustainability. More quantitative approaches to sustainability assessments can also help identify the key features to be improved to make a process or product sustainable, providing valuable guidance to further process or product development.

Articles published in ACS SCE and other journals^{4–10} have described and applied such quantitative sustainability assessments, and the editors wish to encourage more authors to consider utilizing *quantitative sustainability metrics* in their submitted work. Toward this end, we offer suggestions and helpful tools and resources that are simple to use and hopefully add more value to manuscripts.

■ GUIDELINES FOR INCORPORATING SUSTAINABILITY METRICS

At the outset, we want to make it clear that ACS SCE will continue to accept manuscripts for review, with or without the inclusion of quantitative sustainability metrics, as we do now. We also continue to welcome contributions that describe new approaches to quantifying sustainability or that are entirely focused on novel and rigorous quantitative sustainability assessments based on life cycle,^{11–15} supply chain,^{16–20} or other concepts.^{21,22} The guidelines provided here are meant to help authors use quantitative metrics, in an evolving process, to demonstrate how their research contribution advances sustainable chemistry or engineering.

Because of the broad scope of research described in ACS SCE, ranging in scale from new nanomaterial development, to process synthesis and analyses of regional or global scale material flows, the types of metrics used by ACS SCE authors will take a variety of forms. These may range from evaluations of the properties of individual chemicals (e.g., toxicity, persistence in the environment, efficiency in material synthesis, or the extent of use of renewable materials) to assessment of a variety of impacts along a supply chain. Although there is great

diversity in the use of metrics, some common principles are emerging and these common principles have been described by ACS SCE authors. For example, in the first issue of ACS SCE, Russell and Shiang⁴ described the sustainability metrics and sustainability tools used by a multinational chemical manufacturer. In Volume 2, Giraud et al.⁵ described results of a survey conducted by the American Chemical Society's Green Chemistry Institute on the commercial use of the principles of Green Chemistry and the metrics used to quantify progress in applying those principles. Multiple tools are now available to assist researchers in applying quantitative metrics. For example, the iSUSTAIN tool²³ is a freely available tool for quantifying progress in the application of the principles of Green Chemistry. The United States Environmental Protection Agency (EPA) has developed and made available online tools that can be used to assess the environmental fate, bioaccumulation, and toxicity of chemicals.²⁴ New computational methods for property estimation, relevant to sustainability assessments, are continuing to develop. Data for supply chains and individual process steps along supply chains are also becoming available. Commercial and public domain Life Cycle Assessment software tools such as *SimaPro*, *GaBi*, and *GREET*^{25–27} can serve as a resource for authors seeking to benchmark their concepts with current supply chains.

On the basis of these considerations, some general guidelines for authors wishing to incorporate quantitative metrics are as follows:

- Whenever possible, place the contribution in the context of the life cycle or supply chain of the relevant product, process, or chemical function. Although a quantitative life cycle assessment will be beyond the scope of most manuscripts, framing the paper's contribution in the context of product and process life cycles will be a valuable addition.
- Cite or briefly describe relevant property data such as environmental persistence or toxicity.
- In describing chemical pathways or processes, consider using metrics such as those associated with the principles of green chemistry, such as atom economy, mass efficiency, E-factor, C efficiency, emission rates, or others.
- When using well established sustainability metrics (e.g., atom economy), detailed methodological descriptions are not necessary; however, if novel metrics are used, the method of their calculation should be described in the manuscript or Supporting Information.
- Authors who incorporate quantitative sustainability metrics are encouraged to highlight their results in the Graphical Abstract.

Recognizing that the field of quantitative sustainability assessments continues to evolve, these guidelines will be periodically reviewed and updated to reflect current trends.

Received: September 4, 2015

Published: September 23, 2015

In closing, we want to reiterate that the current initiative is to encourage authors to assess more critically their work from a sustainability viewpoint via quantitative assessments. We hope that such efforts would not only serve to advance the field but also bring to light sustainability challenges that are nonobvious, and thereby guide process and product development.

D. T. Allen, Editor in Chief
B.-J. Hwang, Associate Editor
P. Licence, Associate Editor
T. Pradeep, Associate Editor
B. Subramaniam, Associate Editor

AUTHOR INFORMATION

Notes

Views expressed in this editorial are those of the authors and not necessarily the views of the ACS.

REFERENCES

- (1) Anastas, P. T.; Warner, J. C. *Green Chemistry, Theory and Practice*; Oxford University Press: Oxford, 1998.
- (2) Anastas, P. T.; Zimmerman, J. B. Design Through the 12 Principles of Green Engineering. *Environ. Sci. Technol.* **2003**, *37*, 94A–101A.
- (3) National Research Council. Sustainability in the Chemical Industry, National Academy Press: Washington, DC, 2006.
- (4) Russell, D. A. M.; Shiang, D. L. Thinking about more sustainable products: Using an efficient tool for sustainability education, innovation, and project management to encourage sustainability thinking in a multinational corporation. *ACS Sustainable Chem. Eng.* **2013**, *1*, 2–7.
- (5) Giraud, R. J.; Williams, P. A.; Sehgal, A.; Ponnusamy, E.; Phillips, A. K.; Manley, J. H. Implementing Green Chemistry in Chemical Manufacturing: A Survey. *ACS Sustainable Chem. Eng.* **2014**, *2*, 2237–2242.
- (6) McGonagle, F. I.; Sneddon, H. F.; Jamieson, C.; Watson, A. J. B. Molar Efficiency: A Useful Metric To Gauge Relative Reaction Efficiency in Discovery Medicinal Chemistry. *ACS Sustainable Chem. Eng.* **2014**, *2*, 523–532.
- (7) Toniolo, S.; Aricò, F.; Tundo, P. A Comparative Environmental Assessment for the Synthesis of 1,3-Oxazin-2-one by Metrics: Greenness Evaluation and Blind Spots Sara. *ACS Sustainable Chem. Eng.* **2014**, *2*, 1056–1062.
- (8) Tabone, M. D.; Cregg, J. J.; Beckman, E. J.; Landis, A. E. Sustainability Metrics: Life Cycle Assessment and Green Design in Polymers. *Environ. Sci. Technol.* **2010**, *44*, 8264–8269.
- (9) Mercer, S. M.; Andraos, J.; Jessop, P. G. Choosing the Greenest Synthesis: A Multivariate Metric Green Chemistry Exercise. *J. Chem. Educ.* **2012**, *89*, 215–220.
- (10) Andraos, J. Unification of Reaction Metrics for Green Chemistry: Applications to Reaction Analysis. *Org. Process Res. Dev.* **2005**, *9*, 149–163.
- (11) Li, Q.; McGinnis, S.; Sydnor, C.; Wong, A.; Renneckar, S. Nanocellulose Life Cycle Assessment. *ACS Sustainable Chem. Eng.* **2013**, *1*, 919–928.
- (12) Mehrkesh, A.; Karunanithi, A. T. Energetic Ionic Materials: How Green Are They? A Comparative Life Cycle Assessment Study. *ACS Sustainable Chem. Eng.* **2013**, *1*, 448–455.
- (13) Zaines, G. G.; Hubler, B. J.; Wang, S.; Khanna, V. Environmental Life Cycle Perspective on Rare Earth Oxide Production. *ACS Sustainable Chem. Eng.* **2015**, *3*, 237–244.
- (14) Piccinno, F.; Hischier, R.; Seeger, S.; Som, C. Life Cycle Assessment of a New Technology To Extract, Functionalize and Orient Cellulose Nanofibers from Food Waste. *ACS Sustainable Chem. Eng.* **2015**, *3*, 1047–1055.
- (15) Li, M.; Ruddy, T.; Fahey, D. R.; Busch, D. H.; Subramaniam, B. Terephthalic Acid Production Via Greener Spray Process: Comparative Economic and Environmental Impact Assessments with Mid-Century Process. *ACS Sustainable Chem. Eng.* **2014**, *2* (4), 823–835.
- (16) Conde-Mejía, C.; Jiménez-Gutiérrez, A.; El-Halwagi, M. M. Assessment of Combinations between Pretreatment and Conversion Configurations for Bioethanol Production. *ACS Sustainable Chem. Eng.* **2013**, *1*, 956–965.
- (17) Yue, D.; Kim, M. A.; You, F. Design of Sustainable Product Systems and Supply Chains with Life Cycle Optimization Based on Functional Unit: General Modeling Framework, Mixed-Integer Nonlinear Programming Algorithms and Case Study on Hydrocarbon Biofuels. *ACS Sustainable Chem. Eng.* **2013**, *1*, 1003–1014.
- (18) Martínez-Guido, S. I.; González-Campos, J. B.; del Río, R. E.; Ponce-Ortega, J. M.; Nápoles-Rivera, F.; Serna-González, M.; El-Halwagi, M. M. A Multiobjective Optimization Approach for the Development of a Sustainable Supply Chain of a New Fixative in the Perfume Industry. *ACS Sustainable Chem. Eng.* **2014**, *2*, 2380–2390.
- (19) Petrou, E. C.; Pappis, C. P. Sustainability of Systems Producing Ethanol, Power, and Lignosulfonates or Lignin from Corn Stover: A Comparative Assessment. *ACS Sustainable Chem. Eng.* **2014**, *2*, 2527–2535.
- (20) Gong, J.; You, F. Value-Added Chemicals from Microalgae: Greener, More Economical, or Both? *ACS Sustainable Chem. Eng.* **2015**, *3*, 82–96.
- (21) Atom Economical Aqueous-Phase Conversion (APC) of Biopolyols to Lactic Acid, Glycols, and Linear Alcohols Using Supported Metal Catalysts Xin, J.; Debdut, R.; Thapa, Prem S.; Subramaniam, B.; Raghunath, R. V. *ACS Sustainable Chem. Eng.* **2013**, *1* (11), 1453–1462.
- (22) Petrucci, C.; Strappaveccia, G.; Giacalone, F.; Gruttadauria, M.; Pizzo, F.; Vaccaro, L. An E-Factor Minimized Protocol for a Sustainable and Efficient Heck Reaction in Flow. *ACS Sustainable Chem. Eng.* **2014**, *2*, 2813–2819.
- (23) iSustain, Green Chemistry Index, www.isustain.com (accessed July 17, 2015).
- (24) U.S. Environmental Green Engineering Software, <http://www.epa.gov/oppt/greenengineering/pubs/software.html> (accessed July 17, 2015).
- (25) Pre Consultants, SIMAPRO Life Cycle Assessment Software, <http://www.pre-sustainability.com/simapro> (accessed July 17, 2015).
- (26) GaBi Life Cycle Assessment Software, <http://www.gabi-software.com/america/index/> (accessed July 17, 2015).
- (27) Argonne GREET Model, <http://greet.es.anl.gov/> (accessed July 17, 2015).

Lectures Delivered

1. Towards point-of-care mass spectrometry: New advances in ambient ionization methods, H3C (International conference of the Ohio State University), Taj Palace Hotel, Mumbai January 15-17, 2015.
2. Clean drinking water and inequality – Technological challenges, addressing economic inequality in India, International Centre for Human Development and National Institute of Advanced Studies, Bengaluru, 8-9 January 2015.
3. Affordable point-of-use water purification using nanomaterials, Plenary lecture at 150 years of BASF, Mumbai, January 23, 2015.
4. Affordable point-of-use water purification using nanomaterials, Nano India 2015 – Plenary lecture, Sastra, Thanjavur, January 29-30, 2015.
5. Understanding the evolution of atomically precise clusters using mass spectrometry, 29th ISMAS Symposium on Mass Spectrometry, Vivanta by Taj Hari Mahal, Jodhpur, February 2-6, 2015.
6. On the birth of metals, Emerging Frontiers of Materials Science, Opening lecture, Maris Stella College, Vijayawada, February 12, 2015.
7. Understanding cancer therapy using mass spectrometry and single particle plasmonics, International symposium on Nanotechnology and Cancer Theranostics, IIT Bombay, Mumbai, February 15-17, 2015.
8. Mass spectrometric imaging of living objects, AgriNANO-2015, Opening lecture, Institute of Frontier Technology, Regional Agricultural Research Station, Tirupati, March 11, 2015.
9. On the birth of metals, Thrust Areas in Chemistry, Govt. Arts College, Nandanam, Chennai March 12, 2015.
10. Atomically precise clusters of noble metals, MANA, Tsukuba, Japan, March 18, 2015.
11. Understanding cancer therapy using mass spectrometry and single particle plasmonics, Kovai Medical Center and Hospital April 25, 2015.
12. Safe water through advanced materials, CII-UNICEF CSR Conference and Exhibition on Swachh Bharat Abhiyan, Chennai May 12, 2015.
13. Optical sensors using synthetic nanostructures, IC-IMPACTS Summer Institute, University of Toronto, June 15, 2015.
14. Affordable clean water using nanomaterials, University of Waterloo, June 17, 2015.

15. Nanotechnology for clean water, University of Alberta, Edmonton, June 19, 2015.
16. Cluster reactions, International Symposium on Monolayer Protected Clusters 2015, Fuji area, Japan, July 13-16, 2015.
17. Affordable clean water using nanomaterials, Emerging Frontiers for Sustainable Water – A Trilateral Partnership, Africa-India-UK Johannesburg, August 3-5, 2015.
18. Affordable clean water using nanomaterials, Plenary lecture, BITRI, Gaborone, August 6, 2015.
19. Chemistry of Noble Metal Clusters, Department of Chemistry, Purdue University, August 19, 2015.
20. Chemistry of Noble Metal Clusters, Professor S. V. Anantkrishnan Memorial Lecture, MCC Chennai, August 28, 2015.
21. Chemistry of Nano molecules, Stella Maris College, Chennai, September 7, 2015.
22. Affordable clean water using nanomaterials, Indian Institute of Toxicology Research, Lucknow, Golden Jubilee Lecture, October 13, 2015.
23. Affordable clean water using nanomaterials, IWA Development Congress, Plenary lecture, Amman, Jordan, October 17, 2015.
24. Extraction of Silver by Glucose, International Toxicology Conclave, Indian Institute of Toxicology Research, November 5, 2015.
25. Clean water and materials, Indian Academy of Sciences Refresher Course, Madikeri, November 16-29, 2015.
26. Fundamental problems at ice surfaces, Indian Academy of Sciences Refresher Course, Madikeri, November 16-29, 2015.
27. Investigating ice surfaces with ions, Indian Academy of Sciences Refresher Course, Madikeri, November 16-29, 2015.
28. Chemistry of Atomically Precise Clusters of Noble Metals, Institute for Nanotechnology, Karlsruhe Institute of Technology, Karlsruhe, Germany, November 24, 2015.

Patents/Technology/Grants

Patents

Applications

- On-line water purifier for hand pumps, Design application, Application No. 271059, April 6, 2015.
- Method for colocalization of plasmonic nanoparticles and biomolecules with plasmonic and Raman scattering microspectroscopy, T. Pradeep and Kamalesh Choudhari, 1864/CHE/2015, April 09, 2015.
- Cellulose derived graphenic fibers for capacitive desalination of brackish water and preparation method of the electrode thereof, T. Pradeep, N. Pugazhenthiran, Soujit Sen Gupta, Anupama Prabhath and J R Swathy, 3951/CHE/2015, July 31, 2015
- Methods of making alloys of precise composition in solution by inter-cluster reactions in solution, T.Pradeep, K. R. Krishnadas, Atanu Ghosh, Ananya Baksi, Indranath Chakrabarti and Ganapathy Natarajan, Filed on December 14, 2015.
- Method for preparing crossed bilayer assembly of 1D nanowires using an atomically precise clusters, T. Pradeep, Anirban Som, Indranath Chakraborty, Tuhina Adit Maark and Shridevi Bhat, Filed on December 28, 2015.
- Composition for sustained release of carbonate and a water purification device based on the same with enhanced biocidal activity, T.Pradeep, Swathy J.R. and Nalendhiran Pugazhenthiran, Filed on December 29, 2015.

Granted

- Gold and Silver quantum clusters in molecular containers, methods for their preparation and use, E. S. Shibu and T. Pradeep, US-8999717, Issued: April 7, 2015.

Technology development

- AMRIT hand-pump model commercialized; 330 units (serving ~100,000 people) were installed in the arsenic affected areas.



Photograph of an installation in a school

- Arsenic free drinking water technology developed by the lab and our incubated company, Inno Nano Research Pvt. Ltd. has been approved for nationwide implementation.

Technology receipts

- Technology licensing fee of \$130,000 for some of our patents was received.
- Cumulative royalty receipts for the pesticide removal patent has crossed Rs. 150,00,000.

New grants

- Indo – UK GITA grant: Development of a novel combined arsenic filtration/monitoring system for community-scale water supplies amounting to Rs. 160,00,000 at the Indian side and £614,000 at the UK side.
- DST Grant: Arsenic free South 24 Parganas using Indian Technology, amounting to Rs. 460,00,000
- Indo-German grant: Cluster-composite nanofibre membranes for rapid, ultra-trace detection of waterborne contaminants, Rs. 200,00,000 at the Indian side and Euro 400,000 at the German side.

SCIENCE & TECHNOLOGY

NASA spacecraft nearing Pluto

NASA's New Horizons spacecraft is at Pluto's doorstep, following an incredible journey of nine years and 3 billion miles (4.83 billion kilometres).

IIT: graphene nanoribbons produced by a novel method

R. PRASAD

For the first time, researchers have been successful in bringing about spontaneous chemical reactions between two different varieties of carbon nanotubes without using any chemicals. In fact, a simple mechanical grinding of the carbon nanotubes with a mortar and pestle was all that was required to induce chemical reactions. The end result was the production of valuable graphene nanoribbons.

Graphene nanoribbons are being increasingly used in composite materials.

To achieve this, carbon nanotubes containing two different chemical additives — carboxyl groups and hydroxyl groups — were chosen for the study. When ground for about 20 minutes, the additives reacted with one another and unzipped the nanotubes to form one atomic layer thin graphene nanoribbons. The reaction of the two different chemical additives is exothermic in nature and the heat released ultimately unzips the nanotubes.

To be certain, the researchers repeated the experiment using various ratios of the two varieties of carbon nanotubes and in many conditions — standard lab conditions, vacuum, in open air and at variable humidity, temperatures, times and seasons.

"Water is formed in this reaction, and its detection during the process of grinding proves the chemical reaction. Mechano-chemistry



K.R. Krishnadas (left) and Anirban Som, co-authors of the study from IIT Madras, observing the variation in intensity of water upon grinding functionalised carbon nanotubes.

— PHOTO: SPECIAL ARRANGEMENT

was proven this way," said Prof. T. Pradeep of the Department of Chemistry, IIT Madras who along with Prof. Pulickel M. Ajayan of the Department of Material Sciences and Nano Engineering, Rice University, Houston undertook this novel study. Prof. Ajayan is also a distinguished visiting professor at IIT Madras. The results of the study were published on June 16 in the journal *Nature Communications*.

Till date, there has not been any reported instance of graphene nanoribbons being formed by grinding the carbon nanotubes and in the complete absence of other chemicals. "This opens up the possibility of producing novel nanostructured products with specific properties by mechanical agitation," Prof. Pradeep said.

The next step is to generalise this in all kinds of nanosystems. The teams are looking at such chemistry with other functionalised

carbon nanotubes. Applications of such chemically synthesised nanoribbons remain to be explored.

"Identification of the process as mechanochemistry was our contribution," he said. "To prove this, we detected the release of water by mass spectrometry. A combination of novel chemistry and modified instrumentation allowed us to observe this."

Prof. Ajayan had observed the disappearance of carbon nanotubes upon grinding and shared this information with Prof. Pradeep.

"I suggested that mechano-chemistry might be the reason. I had just come back after a class which dealt with triboluminescence, the emergence of luminescence by grinding. I showed him that and told him that chemical reactions can happen similarly. Maybe we could detect water to prove this mechano-chemistry. That is how this started," Prof. Pradeep recalled.

NEWS SITES Sign in / Sign up

ETHealthworld.com
An initiative of The Economic Times

GE Founding Partner of ET Health World

ET Home News IndustrySpeak Feature Medical Specialities Health IT Data & Analytics HealthTV Events

Hospitals Pharma Medical Devices Diagnostics Policy **Industry** People Movement Financial Results Health IT

#Industry #Water Purifier #National Rural Drinking Water Programme #nanotechnology #Indian Institute of Technology #Drinking water #Arsenic

Centre approves nationwide use of IIT-M water purifier

A nanotechnology-based water purifier developed by Indian Institute of Technology, Madras that provides arsenic-free water at an affordable cost will soon be installed in all arsenic-affected regions of the country.

TNN | 15 December 2015, 7:35 AM IST

Share 581 Share 2 Share 8 Tweet

Chennai: A nanotechnology-based water purifier developed by Indian Institute of Technology, Madras that provides arsenic-free water at an affordable cost will soon be installed in all arsenic-affected regions of the country.

The purifier is already providing arsenic-free water to more than four lakh people in West Bengal at a cost of less than 5 paise per litre.

The Union ministry of drinking water and sanitation has recommended the replication

Home | News | Notices | Tenders | Downloads | Careers | FAQ | Competitions



Home About Us Research & Development Media Contact Us



Home / Blog / News : BITRI Hosts the 7th Public Seminar

AUGUST 18, 2015



The Botswana Institute for Technology Research and Innovation (BITRI) held the 7th Public Seminar on Thursday August 6, 2015 at the Avani Gaborone Hotel and Casino main conference room.

The guest speaker for the Seminar was Professor Thalapilli Pradeep, a renowned Professor of Chemistry at the Indian Institute of Technology in Madras and a leading expert on the development of affordable technologies for drinking water purification, some of which have been commercialised.

The topic for the seminar "Affordable point-of-use water purification using nanomaterials" could have not been more relevant since availability and quality of potable is a topical issue in Botswana, and indeed the whole globe.

Professor Thalapilli Pradeep presented technical information on nanotechnology and demonstrated the limitless capabilities that



BITRI Hosts Seminar on Open Data
DECEMBER 14, 2015



BITRI Sets Up Centre for Material Science
DECEMBER 14, 2015

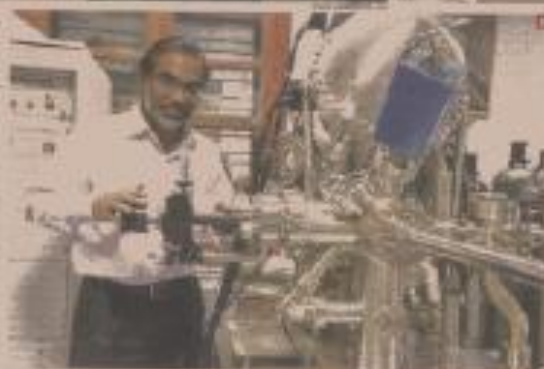


When Ace Scientists Turn Rookie Entrepreneurs



Scientists of distinction are setting up companies that with diligence help solve difficult problems of business and society, writes Hari Palakhat

When Hari Palakhat stepped into the laboratory of the University of California, San Diego (UCSD), he found a world of scientific research that was not only exciting but also profitable. He had just joined the lab of Professor Robert Langer, a pioneer in the field of drug delivery. Langer's research was focused on developing new ways to deliver drugs to the body, and Palakhat was one of the few scientists who had been able to commercialize this technology. He had founded a company, Palakhat Biotech, which was focused on developing new drug delivery systems. Palakhat was a scientist of distinction, and he was now a rookie entrepreneur.



1 A scientist in a white lab coat working in a laboratory setting.

Red-Hot Startup Labs

There are many reasons why scientists are starting their own companies. Some are looking for a new challenge, some are looking for a way to make a difference in the world, and some are looking for a way to make money. In any case, the number of scientists starting their own companies is growing rapidly. This is due to a number of factors, including the increasing number of scientists who are trained in entrepreneurship, the increasing number of scientists who are looking for a way to make a difference in the world, and the increasing number of scientists who are looking for a way to make money.

Palakhat's success in commercializing Langer's technology was due to a number of factors. First, he had a strong understanding of the technology and its potential. Second, he had a strong understanding of the market and its needs. Third, he had a strong understanding of the business and its requirements. Finally, he had a strong understanding of the science and its challenges.



2 A scientist in a white lab coat working in a laboratory setting.



Though CSRE is yet to set up systems that can help equity in companies, it has received the demands of their faculty to create business. The company is currently in the process of setting up systems that can help equity in companies. This is a major challenge, but it is one that the company is committed to addressing. The company is currently in the process of setting up systems that can help equity in companies. This is a major challenge, but it is one that the company is committed to addressing.

Driveway Trend
The number of scientists starting their own companies is growing rapidly. This is due to a number of factors, including the increasing number of scientists who are trained in entrepreneurship, the increasing number of scientists who are looking for a way to make a difference in the world, and the increasing number of scientists who are looking for a way to make money.

Among the recent scientist-entrepreneurs are scientists with a global reputation, and they are looking at entrepreneurship in a new way: bringing research into customers.

Palakhat's success in commercializing Langer's technology was due to a number of factors. First, he had a strong understanding of the technology and its potential. Second, he had a strong understanding of the market and its needs. Third, he had a strong understanding of the business and its requirements. Finally, he had a strong understanding of the science and its challenges.

3 A scientist in a white lab coat working in a laboratory setting.

The company is currently in the process of setting up systems that can help equity in companies. This is a major challenge, but it is one that the company is committed to addressing. The company is currently in the process of setting up systems that can help equity in companies. This is a major challenge, but it is one that the company is committed to addressing.



Acknowledgements

Collaborators and Students

Funding



सत्यमेव जयते

Department of Science and Technology,
Government of India